Published in Journals: Atmosphere, Geosciences,
International Journal of Environmental Research and Public Health
and Remote Sensing

Topic Reprint

Advances in Environmental Remote Sensing

Volume II

Edited by
Zhengqiang Li, Zhongwei Huang, Chi Li, Kai Qin,
Han Wang, Tianhe Wang and Jie Luo

mdpi.com/topics

MDPI

Advances in Environmental Remote Sensing—Volume II

Advances in Environmental Remote Sensing—Volume II

Topic Editors

Zhengqiang Li
Zhongwei Huang
Chi Li
Kai Qin
Han Wang
Tianhe Wang
Jie Luo

MDPI

Basel • Beijing • Wuhan • Barcelona • Belgrade • Novi Sad • Cluj • Manchester

Topic Editors

Zhengqiang Li
Aerospace Information Research Institute, Chinese Academy of Sciences
Beijing
China

Zhongwei Huang
Lanzhou University
Lanzhou
China

Chi Li
Washington University in St. Louis
St. Louis
USA

Kai Qin
China University of Mining and Technology
Xuzhou
China

Han Wang
China University of Mining and Technology
Xuzhou
China

Tianhe Wang
Lanzhou University
Lanzhou
China

Jie Luo
Chinese Academy of Sciences
Beijing
China

Editorial Office
MDPI AG
Grosspeteranlage 5
4052 Basel, Switzerland

This is a reprint of the Topic, published open access by the journals *Atmosphere* (ISSN 2073-4433), *Geosciences* (ISSN 2076-3263), *International Journal of Environmental Research and Public Health* (ISSN 1660-4601) and *Remote Sensing* (ISSN 2072-4292), freely accessible at: https://www.mdpi.com/topics/environment_remote_sensing.

For citation purposes, cite each article independently as indicated on the article page online and as indicated below:

Lastname, A.A.; Lastname, B.B. Article Title. *Journal Name* **Year**, *Volume Number*, Page Range.

Volume II
ISBN 978-3-7258-1479-4 (Hbk)
ISBN 978-3-7258-1480-0 (PDF)
https://doi.org/10.3390/books978-3-7258-1480-0

Set
ISBN 978-3-7258-1475-6 (Hbk)
ISBN 978-3-7258-1476-3 (PDF)

© 2025 by the authors. Articles in this book are Open Access and distributed under the Creative Commons Attribution (CC BY) license. The book as a whole is distributed by MDPI under the terms and conditions of the Creative Commons Attribution-NonCommercial-NoDerivs (CC BY-NC-ND) license (https://creativecommons.org/licenses/by-nc-nd/4.0/).

Contents

About the Editors . . . . . **vii**

Bingqing Liu, Tom Sevick, Hoonshin Jung, Erin Kiskaddon and Tim Carruthers
Quantifying the Potential Contribution of Submerged Aquatic Vegetation to Coastal Carbon Capture in a Delta System from Field and Landsat 8/9-Operational Land Imager (OLI) Data with Deep Convolutional Neural Network
Reprinted from: *Remote Sens.* **2023**, *15*, 3765, https://doi.org/10.3390/rs15153765 . . . . . **1**

Gabriel E. Chanchí Golondrino, Manuel A. Ospina Alarcón and Manuel Saba
Vegetation Identification in Hyperspectral Images Using Distance/Correlation Metrics
Reprinted from: *Atmosphere* **2023**, *14*, 1148, https://doi.org/10.3390/atmos14071148 . . . . . **25**

Lenka Lackoóvá, Juraj Lieskovský, Fahime Nikseresht, Andrej Halabuk, Hubert Hilbert, Klaudia Halászová and Fatemeh Bahreini
Unlocking the Potential of Remote Sensing in Wind Erosion Studies: A Review and Outlook for Future Directions
Reprinted from: *Remote Sens.* **2023**, *15*, 3316, https://doi.org/10.3390/rs15133316 . . . . . **39**

Masashi Hayakawa, Yuriy P. Galuk and Alexander P. Nickolaenko
Integrated Schumann Resonance Intensity as an Indicator of the Global Thunderstorm Activity
Reprinted from: *Geosciences* **2023**, *13*, 177, https://doi.org/10.3390/geosciences13060177 . . . . . **63**

Gang Wang, Zhiying Lu and Ping Wang
Correction: Wang et al. ShuffleCloudNet: A Lightweight Composite Neural Network-Based Method for Cloud Computation in Remote-Sensing Images. *Remote Sens.* 2022, *14*, 5258
Reprinted from: *Remote Sens.* **2023**, *15*, 3022, https://doi.org/10.3390/rs15123022 . . . . . **80**

Moritz Altmann, Katharina Ramskogler, Sebastian Mikolka-Flöry, Madlene Pfeiffer, Florian Haas, Tobias Heckmann, et al.
Quantitative Long-Term Monitoring (1890–2020) of Morphodynamic and Land-Cover Changes of a LIA Lateral Moraine Section
Reprinted from: *Geosciences* **2023**, *13*, 95, https://doi.org/10.3390/geosciences13040095 . . . . . **81**

Yeonghwa Gwon, Dongsu Kim, Hojun You, Su-Han Nam and Young Do Kim
A Standardized Procedure to Build a Spectral Library for Hazardous Chemicals Mixed in River Flow Using Hyperspectral Image
Reprinted from: *Remote Sens.* **2023**, *15*, 477, https://doi.org/10.3390/rs15020477 . . . . . **115**

Chao Wang, Zheng Shi, Yanqing Xie, Donggen Luo, Zhengqiang Li, Decheng Wang and Xiangning Chen
Precipitable Water Vapor Retrieval Based on DPC Onboard GaoFen-5 (02) Satellite
Reprinted from: *Remote Sens.* **2023**, *15*, 94, https://doi.org/10.3390/rs15010094 . . . . . **135**

Haoran Gu, Yuhuan Zhang, Cheng Fan, Zhengqiang Li, Weizhen Hou, Zhenhai Liu, et al.
A Comprehensive Analysis of Ultraviolet Remote Sensing for Aerosol Layer Height Retrieval from Multi-Angle Polarization Satellite Measurements
Reprinted from: *Remote Sens.* **2022**, *14*, 6258, https://doi.org/10.3390/rs14246258 . . . . . **147**

Giulia Iacobucci, Daniela Piacentini and Francesco Troiani
Enhancing the Identification and Mapping of Fluvial Terraces Combining Geomorphological Field Survey with Land-Surface Quantitative Analysis
Reprinted from: *Geosciences* **2022**, *12*, 425, https://doi.org/10.3390/geosciences12110425 . . . . . **170**

Gang Wang, Zhiying Lu and Ping Wang
ShuffleCloudNet: A Lightweight Composite Neural Network-Based Method for Cloud Computation in Remote-Sensing Images
Reprinted from: *Remote Sens.* **2022**, *14*, 5258, https://doi.org/10.3390/rs14205258 . . . . . **190**

Zhi-Qiang Liu, Ping Tang, Weixiong Zhang and Zheng Zhang
CNN-Enhanced Heterogeneous Graph Convolutional Network: Inferring Land Use from Land Cover with a Case Study of Park Segmentation
Reprinted from: *Remote Sens.* **2022**, *14*, 5057, https://doi.org/10.3390/rs14195027 . . . . . **211**

Guangfeng Xiang, Binghuan Meng, Bihai Tu, Xuefeng Lei, Tingrui Sheng, Lin Han, et al.
On-Orbit Autonomous Geometric Calibration of Directional Polarimetric Camera
Reprinted from: *Remote Sens.* **2022**, *14*, 4548, https://doi.org/10.3390/rs14184548 . . . . . **233**

Yang Song, Xiangzheng Tu and Zhengqiang Li
A Detection Method of Atmospheric Neutron Profile for Single Event Effects Analysis of Civil Aircraft Design
Reprinted from: *Atmosphere* **2022**, *13*, 1441, https://doi.org/10.3390/atmos13091441 . . . . . **253**

Lingling Xu, Wei Xiong, Weining Yi, Zhenwei Qiu, Xiao Liu, Dongying Zhang, et al.
Synchronous Atmospheric Correction of High Spatial Resolution Images from Gao Fen Duo Mo Satellite
Reprinted from: *Remote Sens.* **2022**, *14*, 4427, https://doi.org/10.3390/rs14174427 . . . . . **263**

Bangyu Ge, Zhengqiang Li, Cheng Chen, Weizhen Hou, Yisong Xie, Sifeng Zhu, et al.
An Improved Aerosol Optical Depth Retrieval Algorithm for Multiangle Directional Polarimetric Camera (DPC)
Reprinted from: *Remote Sens.* **2022**, *14*, 4045, https://doi.org/10.3390/rs14164045 . . . . . **290**

Ji Wang, Yufeng Hu and Zhenhong Li
A New Coherence Detection Method for Mapping Inland Water Bodies Using CYGNSS Data
Reprinted from: *Remote Sens.* **2022**, *14*, 3195, https://doi.org/10.3390/rs14133195 . . . . . **315**

Fernando Troya, Paulo N. Bernardino and Ben Somers
Inter-Annual Climate Variability Impact on Oil Palm Mapping
Reprinted from: *Remote Sens.* **2022**, *14*, 3104, https://doi.org/10.3390/rs14133104 . . . . . **335**

Donghui Yi, Alejandro Egido, Walter H. F. Smith, Laurence Connor, Christopher Buchhaupt and Dexin Zhang
Arctic Sea-Ice Surface Elevation Distribution from NASA's Operation IceBridge ATM Data
Reprinted from: *Remote Sens.* **2022**, *14*, 3011, https://doi.org/10.3390/rs14133011 . . . . . **355**

Pan Gao, Jun Wang, Yangzi Gao, Jingjing Liu and Dengxin Hua
Observation on the Droplet Ranging from 2 to 16 μm in Cloud Droplet Size Distribution Based on Digital Holography
Reprinted from: *Remote Sens.* **2022**, *14*, 2414, https://doi.org/10.3390/rs14102414 . . . . . **368**

Tao He, Lei Cui, Pengbo Wang, Yanan Guo and Lei Zhuang
A Novel Ultra−High Resolution Imaging Algorithm Based on the Accurate High−Order 2−D Spectrum for Space−Borne SAR
Reprinted from: *Remote Sens.* **2022**, *14*, 2284, https://doi.org/10.3390/rs14092284 . . . . . **387**

Alexander Vasilkov, Nickolay Krotkov, David Haffner, Zachary Fasnacht and Joanna Joiner
Estimates of Hyperspectral Surface and Underwater UV Planar and Scalar Irradiances from OMI Measurements and Radiative Transfer Computations
Reprinted from: *Remote Sens.* **2022**, *14*, 2278, https://doi.org/10.3390/rs14092278 . . . . . **410**

About the Editors

Zhengqiang Li

Zhengqiang Li is a Research Fellow at the Aerospace Information Research Institute of the Chinese Academy of Sciences (CAS). He is the Director of the State Environment Protection Key Laboratory of Satellite Remote Sensing and the Dean of the School of Remote Sensing Science and Technology of Aerospace Information Technology University. Zhengqiang Li received his Ph.D in Optics from CAS in 2004 and worked at the University of Lille in France from 2004 to 2009. He engaged in research covering optical remote sensing, polarized satellite monitoring and the atmospheric environment, and participated in more than 30 research and development projects. He has published over 340 papers, more than 30 patents and 5 monographs, was selected as the winner of the National Outstanding Youth Fund of China and was in the Top 2% of Scientists Worldwide by Stanford University. Zhengqiang Li also serves as the President of the Atmospheric Environment Remote Sensing Society (AERSS) and as a national representative in the international organization of the Space for Climate Observatory (SCO).

Zhongwei Huang

Prof. Huang Zhongwei focuses on lidar remote sensing of the atmosphere, bioaerosol detection and its climate effects. He developed international first-class advanced laser atmospheric detection technologies integrating laser remote sensing, depolarization, Raman and fluorescence. The first lidar atmospheric remote sensing research center with a complete research system in Northwest China was established at Lanzhou University. He proposed a new polarization lidar retrieval method using aerosol microphysical properties, which significantly improved the accuracy of lidar identification of cloud and aerosol types. Furthermore, he proposed and organized a large-scale field observation experiment (DuBi) focusing on dust-bioaerosols in China, significantly bridging the gap in atmospheric microorganism research in certain regions of Northern China. He has conducted extensive and long-term studies pertaining to lidar network observations of aerosol–cloud interactions in Northwest China and has comprehensively analyzed the evolutionary characteristics of aerosol optical properties along dust transport paths. He first found a fast, long-range transport path of dust aerosols from East Asia to the Arctic region, which provided a novel perspective for studying the climate effect of dust aerosols, particularly on the Arctic climate. Based on active remote sensing techniques, he studied the physicochemical properties of dust originating from East Asia after its long-range transport to oceanic regions and observed the real-time evolution of dust aerosols to form water clouds for the first time. By exploring the principles of environmental adaptability, transportation and the dissemination of bioaerosols, he discovered the influence of ambient temperature and humidity on the spread of COVID-19, thereby making remarkable contributions to the advancement of atmospheric remote sensing research in China.

Chi Li

Chi Li is currently a staff scientist in the Department of Energy, Environmental and Chemical Engineering, Washington University, in St. Louis. He obtained a Ph.D in Atmospheric Science from Dalhousie University in 2018. He is broadly interested in the abundances, impacts and processes of various atmospheric compositions that affect the quality of air and the changing climate. His work involves using various observation platforms and modeling tools to unveil how atmospheric composition forms, changes and affects planetary health. Li has published over 40

journal articles and has an H-index of 21 (Web of Science). He has received several prestigious awards, including the Killam Predoctoral Scholarship and the William Leiper Memorial Scholarship. Li was chosen to participate in the 15th Atmospheric Chemistry Colloquium for Emerging Senior Scientists.

Kai Qin

Kai Qin, Ph.D., is a Professor and the Head of the Department of Remote Sensing and GIS at China University of Mining and Technology. He was a Visiting Scientist with the German Aerospace Center in 2016/2017 and a Visiting Professor with Yonsei University in 2022. His research interests include improving satellite retrievals of aerosol and trace gases, assessing air quality using satellite measurements, and estimating methane emissions. He has published around 90 peer-reviewed papers. He organized a series of conferences on the remote sensing of atmospheric environments. Kai Qin serves as Secretary-General of the Atmospheric Environment Remote Sensing Society, Secretary-General of the Commission on Digital Energy of the Chinese National Committee of the International Digital Earth Society (ISDE), a Board Member of *Remote Sensing*, an Editorial board member of *Journal of Remote Sensing* and more.

Han Wang

Han Wang is a master's supervisor, an associate professor at the School of Environment and Spatial Informatics of China University of Mining and Technology, a member of the International Atmospheric Remote Sensing Society (AERSS) and a member of the Remote Sensing and Environmental Science Alliance of Universities in Jiangsu, Hong Kong, and Macao. He graduated from the University of Chinese Academy of Sciences in 2015 with a Ph.D. in Optics. His main research focuses on aerosol inversion based on polarized remote sensing data, analyses of the polarized reflection characteristics of ground surfaces and related works. He refined the spectral relationship between the polarized reflectance of land surfaces and proposed an aerosol adaptive polarization inversion method (adaptive land–atmospheric decoupling algorithm, ALAD). Currently, he has published more than 20 related papers.

Tianhe Wang

Tianhe Wang is a professor at the College of Atmospheric Sciences, Lanzhou University, China. His research focuses on aerosol–cloud remote sensing, dust transport mechanisms, and aerosol–cloud–climate interactions. He has presided over five National Natural Science Foundations of China (NSFCs) and participated in a number of national-level projects, including the Second Tibetan Plateau Scientific Expedition and Research Program (STEP). He has published more than 60 papers in professional academic journals such as *Remote Sensing of Environment*. He has won first prize of the Natural Science of Gansu Province award (3/5, 2012) and second prize of the National Natural Science award (3/5, 2013). Some of his results were selected as research highlights in *Science of the Total Environment* (2021). He is the deputy secretary-general of the Atmospheric Environmental Remote Sensing Society (AERSS) and a reviewer of more than 20 international academic journals.

Jie Luo

Jie Luo obtained his Ph.D from the State Key Laboratory of Fire Science at the University of Science and Technology of China. He previously served as an assistant researcher at the Aerospace Information Research Institute of the Chinese Academy of Sciences and a senior research specialist at the Zhejiang Lab. Currently, he is a professor at Hangzhou Dianzi University, specializing in research on scattering modeling and the climate effects of absorbing aerosols, ocean satellite remote sensing, forest fire

detection and climate effects. He has published over 20 academic papers in prestigious journals such as *Atmospheric Chemistry and Physics*, *Journal of Geophysical Research—Atmospheres*, and *Optics Express*. He has led the National Natural Science Foundation of China Youth Project and participated in national key research and development projects of the Ministry of Science and Technology, the National Natural Science Foundation of China and others. From 2019 to 2020, he visited Washington University in St. Louis, USA, for exchange and collaboration. He has served as a Guest Editor for journals like *Remote Sensing* and *Frontiers in Environmental Science* and he is a reviewer for multiple international academic journals including *Optics Express* and *Atmospheric Measurement Techniques*.

remote sensing

MDPI

Article

Quantifying the Potential Contribution of Submerged Aquatic Vegetation to Coastal Carbon Capture in a Delta System from Field and Landsat 8/9-Operational Land Imager (OLI) Data with Deep Convolutional Neural Network

Bingqing Liu [1,2,*], Tom Sevick [1], Hoonshin Jung [1], Erin Kiskaddon [1] and Tim Carruthers [1]

[1] The Water Institute, 1110 S. River Road, Baton Rouge, LA 70802, USA
[2] School of Geosciences, University of Louisiana at Lafayette, Lafayette, LA 70504, USA
* Correspondence: bingqing.optics.liu@gmail.com; Tel.: +1-225-916-8089

Abstract: Submerged aquatic vegetation (SAV) are highly efficient at carbon sequestration and, despite their relatively small distribution globally, are recognized as a potentially valuable component of climate change mitigation. However, SAV mapping in tidal marshes presents a challenge due to optically complex constituents in the water. The emergence and advancement of deep learning-based techniques in the field of habitat mapping with remote sensing imagery provides an opportunity to address this challenge. In this study, an analytical framework was developed to quantify the carbon sequestration of SAV habitats in the Atchafalaya River Delta Estuary from field and remote sensing observations using deep convolutional neural network (DCNN) techniques. A U-Net-based model, Wetland-SAV Network, was trained to identify the SAV percent cover (high, medium, and low) as well as other estuarine habitat types from Landsat 8/9-OLI data. The areal extent of SAV was up to 8% of the total area (47,000 ha). The habitat areas and habitat-specific carbon fluxes were then used to quantify the net greenhouse gas (GHG) flux of the study area for *with/without SAV* scenarios in a carbon balance model. The total net GHG flux was in the range of -0.13 ± 0.06 to $-0.86 \pm 0.37 \times 10^5$ tonne CO_2e y^{-1} and increased up to 40% (-0.23 ± 0.10 to $-0.90 \pm 0.39 \times 10^5$ tonne CO_2e y^{-1}) when SAV was accounted for within the calculation. At the hectare scale, the inclusion of SAV resulted in an increase of ~60% for the net GHG sink in shallow areas adjacent to the emergent marsh where SAV was abundant. This is the first attempt at remotely mapping SAV in coastal Louisiana as well as a first quantification of net GHG flux at the scale of hectares to thousands of hectares, accounting for SAV within these sub-tropical coastal delta marshes. Remote sensing and deep learning models have high potential for mapping and monitoring SAV in turbid sub-tropical coastal deltas as a component of the increasing accuracy of net GHG flux estimates at small (hectare) and large (coastal basin) scales.

Keywords: submerged aquatic vegetation; carbon balance model; Landsat 8/9-OLI; deep learning

Citation: Liu, B.; Sevick, T.; Jung, H.; Kiskaddon, E.; Carruthers, T. Quantifying the Potential Contribution of Submerged Aquatic Vegetation to Coastal Carbon Capture in a Delta System from Field and Landsat 8/9-Operational Land Imager (OLI) Data with Deep Convolutional Neural Network. *Remote Sens.* **2023**, *15*, 3765. https://doi.org/10.3390/rs15153765

Academic Editor: Dehua Mao

Received: 1 June 2023
Revised: 24 July 2023
Accepted: 24 July 2023
Published: 28 July 2023

Copyright: © 2023 by the authors. Licensee MDPI, Basel, Switzerland. This article is an open access article distributed under the terms and conditions of the Creative Commons Attribution (CC BY) license (https://creativecommons.org/licenses/by/4.0/).

1. Introduction

Submerged aquatic vegetation (SAV) across a broad range of salinity tolerances, including marine species (e.g., seagrasses) and non-marine species, constitutes a key component of shallow aquatic ecosystems [1–3]. SAV can provide a wide range of ecosystem services including stabilizing sediments and reducing shoreline erosion [1,4–6]. SAV can also entrain sediment and reduce nutrients to improve water quality, alter biogeochemical cycles, and provide food and habitat for a number of aquatic species [7–9]. SAV also plays a potential role in mitigating climate change due to its large contribution to global sediment carbon burial [10–12]. During the growing season, SAV captures dissolved carbon dioxide (CO_2) via photosynthesis to support its growth, storing carbon into aboveground and belowground biomass (e.g., leaves, rhizomes, and roots) while oxygenating the surrounding water and sediment (Figure 1). SAV habitats are characterized by a high allochthonous and autochthonous

organic matter deposition [13] and low decomposition rates of belowground organic material in underlying sediment layers [14–17]. Hillmann et al. [18] reported that the carbon stock for fresh to brackish SAV in coastal Louisiana was approximately $231.6 \pm 19.5 \times 106$ g C ha^{-1}. However, in comparison with blue carbon habitats (i.e., salt marsh, mangrove, and seagrass), the carbon sequestration potential of non-marine SAV in fresh-brackish estuarine areas has not been widely quantified [13]. One reason for this is that these SAV habitats have been considered to be highly spatially dynamic over timescales that range from days to decades, partly due to the impact of hurricanes on SAV distribution in these ecosystems [18,19].

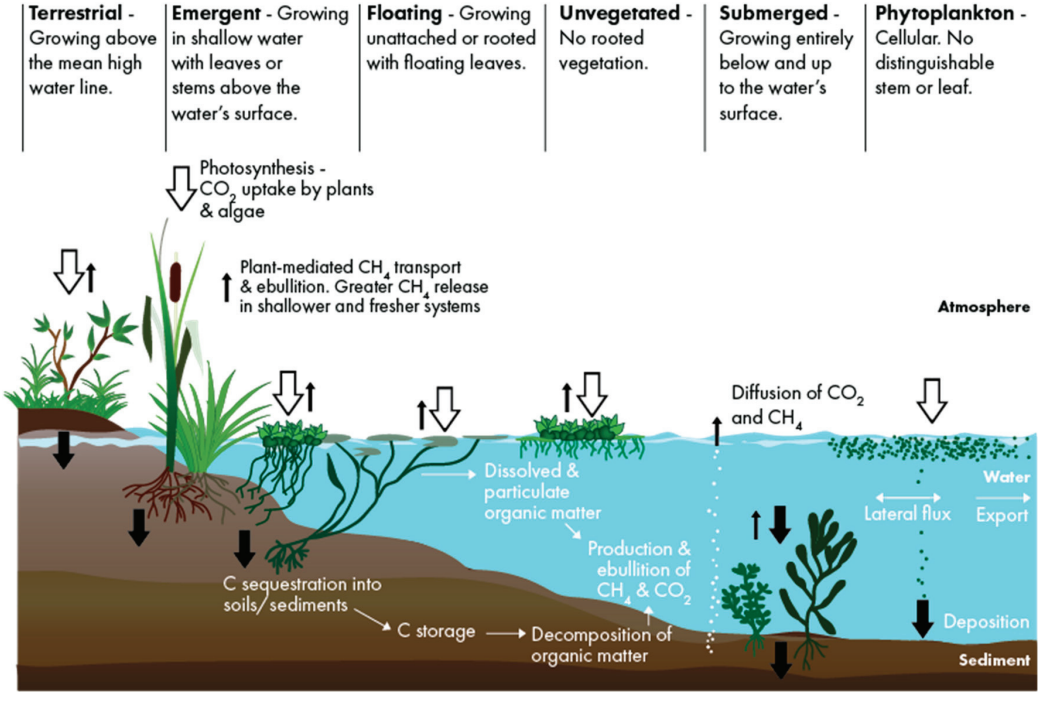


Figure 1. Conceptual representation summarizing prominent carbon fluxes of Louisiana's deltaic fresh to brackish shallow-water coastal ecosystems.

Increasing ecosystem stressors (e.g., large grazing events, eutrophication, storms, high water temperature with low light, and human activities such as dredging) have resulted in a loss in area of tidal marshes and SAV habitat globally [2,3,20,21]. However, in semi-tropical ecosystems, the loss of emergent herbaceous marsh wetland results in a greater area of shallow open water. This expanded area of shallow water brings the potential for an increase in habitat areas suitable for SAV [22–24]. Given future projected wetland loss, the quantification of the current spatial extent of the SAV habitat and continuous long-term monitoring efforts are critical for assessing the distribution and abundance of SAV communities with respect to natural and anthropogenic perturbations [25,26]. SAV quantification and mapping would also inform the estimation of a range of current and future nekton and wildlife ecosystem services, as well as reduce the uncertainty for carbon sequestration and storage estimates [18,27,28].

Optical remote sensing has been effective in the monitoring of terrestrial vegetation (e.g., forestry, tidal wetlands, and agriculture; [29–33]). Remote sensing approaches were also used to map and monitor seagrass distribution and abundance [31,34–36]; however, these applications have largely focused on seagrasses in clear coastal waters [37–39]. In contrast, non-marine SAV mapping presents particular challenges, especially in turbid

estuarine waters where chlorophyll [40,41], dissolved organic carbon [42], and suspended minerals [43] can affect water clarity and the strength of the sensed light signal. Numerous remote sensing methods have been developed to detect SAV for large-scale and long-term monitoring. These methods range from pixel to object-oriented approaches, and from manual to machine learning methods [44–46]. Due to the rapid development of remote sensing techniques, it is essential to use consistent methodologies so as to minimize mapping discrepancies and errors, and to enable comparisons through time. In addition, processes for the simultaneous mapping of SAV in waters that are both clear and turbid can enable regular, routine map creation for the ongoing observation of SAV dynamics [47]. More recently, the emergence and advancement of deep learning-based techniques has achieved remarkable success in various fields [48], including image semantic segmentation. Deep learning-based techniques (e.g., deep convolutional neural network, DCNN) provide better performance against traditional pixel-based methods [49] and the ability to extract image features without human intervention [50,51]. One DCNN architecture with particularly high accuracy, U-Net, was initially developed for biomedical image segmentation [52]. U-Net consists of a contracting path to capture context and a symmetric expanding path, in which a small number of training data can drive U-Net to obtain high accuracy results. Several regional U-Net models have been developed for wetland classification and for vegetation species identification (e.g., black mangrove) [53–55]. The data used to drive these analyses included Landsat 8 (30 m) and Sentinel 2-A/B imagery (10 m), which are satellites with global coverage and a spatial resolution of 10–60 m [56,57]. However, the mapping of non-marine SAV based on deep learning approaches has lagged behind that conducted for marine SAV, mangroves, and coastal wetlands [49].

This study focused on spatiotemporal variation in SAV distribution and the potential role of SAV in carbon sequestration in a subtropical shallow delta system (hereafter, Atchafalaya River Delta Estuary) in Louisiana, USA. A novel combination of DCNN techniques and field and remote sensing observations were used. The four primary objectives of this study were to: (1) develop a DCNN-based model to map the SAV areal extent in the Atchafalaya River Delta Estuary; (2) estimate carbon fluxes of the mapped SAV; (3) estimate the net greenhouse gas (GHG) sink potential of SAV habitats from 2015 to 2022; and (4) assess the impacts of two recent hurricanes on SAV dynamics and net GHG fluxes in the study area.

2. Materials and Methods

2.1. Study Area

This study focused on approximately 47,000 ha in the southern Atchafalaya Basin, Louisiana, USA (Figure 2). Within the Atchafalaya Basin, two deltas (Atchafalaya Delta and Wax Lake Delta) have formed and are extending southward toward the Gulf of Mexico. These deltas are the result of sediment accretion from the Atchafalaya River discharge and from dredged material deposited by the U.S. Army Corps of Engineers [58,59]. The large volume of fresh, sediment, and nutrient-rich water flowing across the deltas has created an extensive habitat for emergent marsh, floating aquatic vegetation (FAV), and SAV [60]. Intermittently flooded upper deltaic areas are dominated by a diverse assemblage of emergent fresh–intermediate marsh species (e.g., *Typha* spp., *Phragmites australis*, and *Zizaniopsis miliacea*; [61]). Emergent marsh vegetation species tolerant of both continuous and partial submergence, FAV, and SAV, dominate the lower regions of the delta system [60,62]. The abundant SAV and FAV communities of the Atchafalaya River Delta Estuary respond strongly to high turbidity events, especially during periods of seasonal high water [63] as well as major tropical events, such as hurricanes Barry in 2019 and Ida in 2021 [64,65].

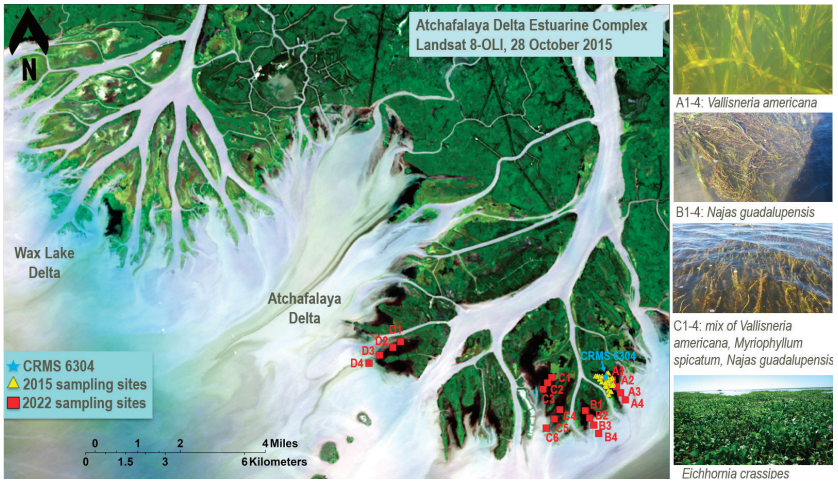


Figure 2. Map of the Atchafalaya River Delta Estuary study area located in southern Louisiana, USA. The map shows the field validation transects (A, B, C, and D; red squares) visited in 2022 and the field calibration sites visited in 2015 (yellow triangles). The Coastwide Reference Monitoring System (CRMS) station nearest to the study area is also indicated. The right panels display photographs of the dominant SAV and FAV species observed in 2022 along transects A–C.

2.2. Field Observations

2.2.1. Historical Data

In this study, historical field measurements of SAV and FAV percent cover (% cover) collected by Darnell et al. (unpublished data) between May and September 2015 were used as input to a U-Net model to classify the two habitat types (described in detail in Section 2.3.2). These data were collected at a mean depth of 0.46 m near the mouth of the Atchafalaya River. Thirty sites were sampled adjacent to Coastwide Reference Monitoring System (CRMS) site 6304 (91.2752272°W, 29.4237544°N; Figure 2). Sites were randomly selected using a generalized random tessellation stratified (GRTS) design. SAV % cover from four replicate 0.25 m quadrats was collected during the monthly sampling at each of the 30 sites from May to September 2015. Data summarized from the CRMS stations describe the ranges of mean salinity (1–2.5 ppt), mean water temperature (20.15–36.1 °C) and mean water depth (0.22–1.25 m) during the period of May–September 2015. The SAV % cover data were categorized for subsequent analyses: high density (60–100%; SAV high), medium density (30–60%; SAV medium), and low density (0–30%; SAV low) based upon a modified Braun–Blanquet scale [64].

2.2.2. Field Data Collection for U-Net Model Validation

To validate the SAV mapping from remote sensing data using the U-Net model, SAV % cover, presence/absence, and dominant species of SAV were assessed in the Atchafalaya River Delta on 19 October 2022. SAV observations were collected along four transects (A, B, C, and D; Figure 2). Four sampling stations were randomly selected along each transect. Due to the low water levels restricting access, some stations had to be re-located along the transects. At each sampling station, five replicate 0.25 m^2 quadrats were measured for SAV % cover. The dominant species of SAV, water temperature (°C), mean water depth (m), salinity (ppt), and location (latitude and longitude) were recorded at each sampling station. The mean % cover of each individual SAV species (±standard deviation) was determined by calculating the average across five replicate samples at each station. The total SAV % cover across all species (versus bare sediment) was then calculated as the sum of the mean % cover measurements for all SAV species observed at each station. The total SAV % cover was then classified into low (0–30%), medium (30–60%), and high (60–100%).

2.3. Deep Learning for Habitat Classification

In this study, a deep learning model based on the U-Net architecture was established to classify the wetland habitat types (fresh forested wetland, fresh marsh, intermediate marsh, brackish marsh, FAV, SAV (high, medium, and low), open water, and bare ground) using Landsat 8/9-OCI. The model developed was named Wetland-SAV Network (hereafter, WSAV-Net).

2.3.1. Remote Sensing Data and Processing

The Operational Land Imager (OLI) sensors onboard Landsat 8 and 9 platforms (Landsat 8/9-OLI) offers innovative opportunities for the long-term observation and monitoring of coastal habitats with a medium spatial resolution at 30 m [66,67]. The orbits of these two satellites are designed to shorten the revisit interval to substantially increase the temporal resolution [68]. In this study, a total of seven Level-1C Landsat 8/9-OLI images (Table 1) were downloaded from USGS Earth Explorer (https://earthexplorer.usgs.gov/, accessed on 31 May 2023). Landsat 8-OLI images obtained on 19 September 2015 were within ±3 days of historical field measurements of % cover (Section 2.2.1). The Landsat 8-OLI imagery obtained on 15 October 2022 were within ±5 days of field measurements of SAV % cover collected on 19 October 2022 (Section 2.2.2). Satellite images acquired in September/October were used to capture the peak growing season for SAV, in addition to a period of low cloud cover. The Level 1C images, which are top of atmosphere (TOA) reflectance (ρ_{TOA}) were processed to obtain bottom of atmosphere (BOA) Level-2A surface reflectance (ρ_s). ENVI's FLAASH (Fast Line-of-sight Atmospheric Analysis of Hypercubes) atmospheric correction tool was used to complete the radiation calibration and atmospheric correction. Surface reflectance at six original bands, including blue, green, red, near-infrared (NIR), shortwave infrared 1 (SWIR1) and 2 (SWIR2) together with the normalization difference vegetation index (NDVI [69] and the modified normalized difference water index; MNDWI [70] were used to generate a 8-band composite image for WSAV-Net training (Figure 3).

Table 1. List of satellite data used in this study.

#	Date	Satellite Sensor	File Name
1	28 October 2015	Landsat 8-OLI	LC08_L1TP_023039_20151028_20200908_02_T1
2	30 October 2016	Landsat 8-OLI	LC08_L1TP_023039_20161030_20200905_02_T1
3	17 October 2017	Landsat 8-OLI	LC08_L1TP_023039_20171017_20200902_02_T1
4	23 October 2019	Landsat 8-OLI	LC08_L1TP_023039_20191023_20200825_02_T1
5	26 September 2021	Landsat 8-OLI	LC08_L1TP_023039_20210926_20211001_02_T1
6	21 September 2022	Landsat 9-OLI	LC09_L1TP_023039_20220921_20220923_02_T1
7	15 October 2022	Landsat 8-OLI	LC08_L1TP_023039_20221015_20221021_02_T1

2.3.2. Louisiana Wetland-SAV Network Model (WSAV-Net)

Land use land cover data (LULC) [71] containing 67 vegetation species across coastal Louisiana were grouped into habitat types according to Visser and Duke-Sylvester [72]. These data were then used to label 8-band composite imagery for the image acquired on 19 September 2015. However, the SAV habitat in the LULC map lacked % cover information. Thus, the SAV % cover data obtained in September 2015 were used to identify SAV % cover as low, medium, or high for the imagery acquired on 19 September 2015. As a result, a total of 2421 polygons were characterized as one of 10 habitat types including fresh forested wetland, fresh marsh, intermediate marsh, brackish marsh, FAV, SAV (high, medium, and low), open water, and bare ground. These polygons were used for supervised classification using the support vector machine (SVM) scheme, where the marshes and bare ground referrer to emergent habitats. The 10-category habitat map from the supervised classification in combination with the 8-band composite image acquired on 19 September 2015 was further cropped to image chips at fixed size (128 × 128 pixels) to train WSAV-Net (Figure 3) to identify habitat types (n = 1802 chips).

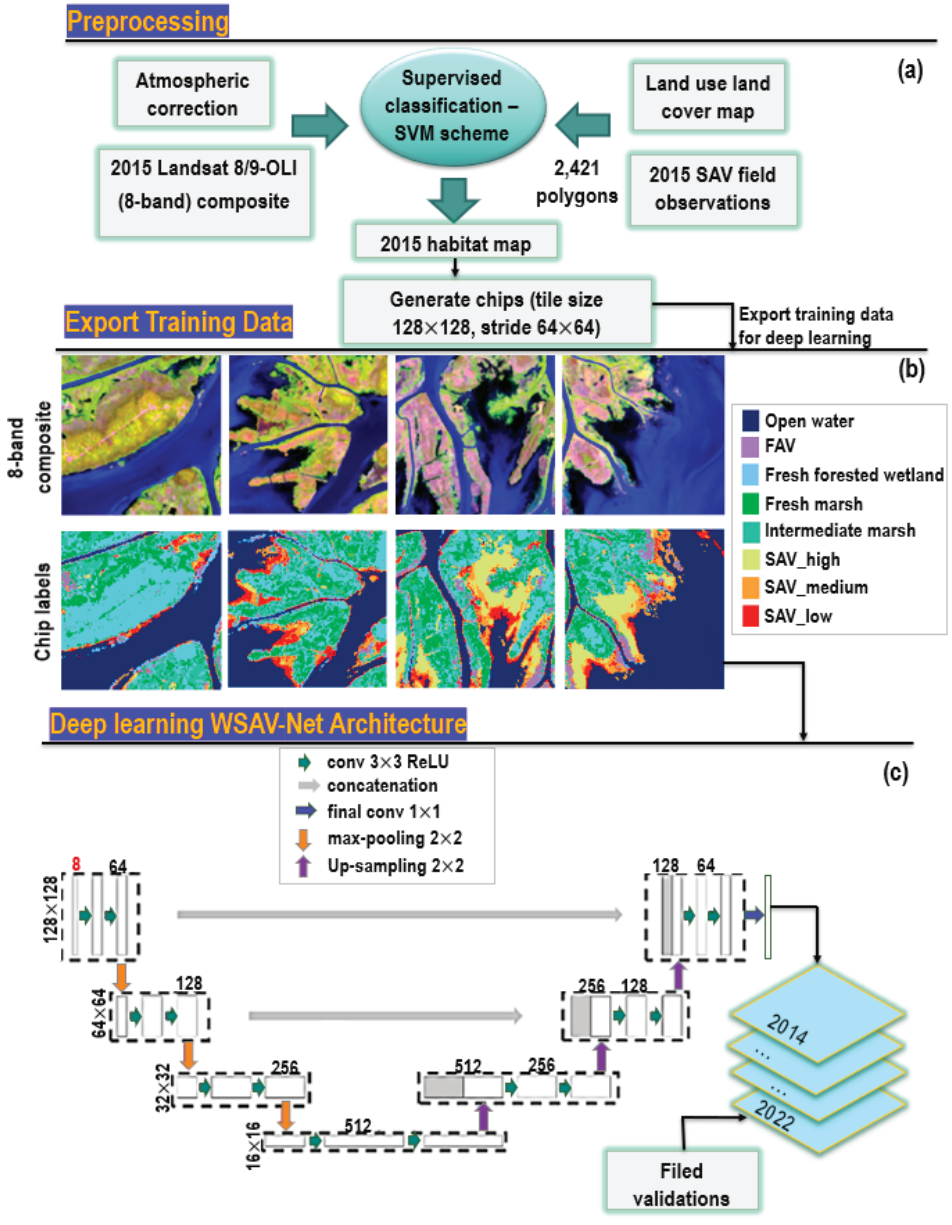


Figure 3. Preprocessing of training data for WSAV-Net and its architecture; (**a**) preprocessing procedure to export training data for deep learning; (**b**) example of training data and validation data (chips) of WSAV-Net; (**c**) architecture of the WSAV-Net with 128 × 128 × 7 as the size of input data.

The encoder–decoder framework of WSAV-Net is a typical U-Net architecture (Figure 3). This was used to extract landscape features and predict vegetation type labels. In WSAV-Net, the encoding path is composed of 3 convolutional blocks including two 3 × 3 convolution layers with a rectified linear unit (ReLU) activation (green arrows; Figure 3) followed by a max-pooling layer with a 2 × 2 pool size. The input 8-band composite chips are down-sampled into a series of feature maps through convolutional blocks. Each block in the decoder path consists

of an up-sampling layer, a concatenation with the corresponding block from the encoder path, and two convolutional layers. The last layer of the network is a 1×1 convolution (blue arrow; Figure 3) with Sigmoid activation. An initial learning rate of 10^{-4} was used. The training batch size was set to eight and the epoch was set to 50, where epoch is defined as the one entire passing of training data through the model. The WSAV-Net employed the Keras library with TensorFlow with its learning processes trained using NVIDIA Tesla T4 GPU.

2.3.3. Habitat Percent Cover

To investigate the effect of changes in habitat % cover on the net GHG flux per hectare (i.e., 100 m × 100 m), habitat maps with 30 m resolution produced from WSAV-Net were converted into habitat % cover using 90 m resolution grids as shown in Equation (1).

$$\text{Habitat \% cover}_i = \frac{\sum \text{Number of habitat pixel}_i \times 30\text{ m} \times 30\text{ m}}{\text{Area of a 90 m} \times \text{90 m grid cell}} \quad (1)$$

where Habitat % cover_i refers to the percentage of coverage for the i-th habitat type, and i represents one of 10 habitat types contained in each 90 m grid cell (i.e., fresh forested wetland, fresh marsh, intermediate marsh, brackish marsh, FAV, SAV in high, medium, and low, open water, and bare ground). The sum of all percentages of habitat types in each grid cell equals 100%.

2.4. Carbon Balance Model

To quantify the carbon captured and stored in coastal habitats, a Net Ecosystem Carbon Balance approach was used (NECB; [73]). This methodology is based on carbon fluxes (e.g., g C m^{-2} y^{-1}) and is frequently used in ecological studies to assess the net carbon balance (gain or loss) of coastal habitats [74–78]. Carbon fluxes of the aboveground net primary productivity (ANPP), sediment/soil accumulation rates ($\text{Sed./Soil}_{\text{accum.}}$), as well as methane ($CH_4$) and nitrous oxide ($N_2O$) emissions are commonly included in the coastal habitat assessments that inform GHG inventories [79–81].

To assess the NECB of non-marine SAV habitats in Louisiana's fresh and intermediate environments, peer-reviewed literature, and scientific data were reviewed to obtain ANPP, soil carbon accumulation rate, and CH_4 emissions; note that N_2O was not considered in the NECB calculation for SAV habitats due to limited data availability. Subsequently, CH_4 emissions were converted into their carbon dioxide equivalent (CO_2e) by multiplying by a global warming potential (GWP) index value of 25 [81–84]. The mean value of all the observational means ("global mean") extracted from peer-reviewed literature and scientific data was used to create an SAV carbon flux look-up table. All units in the look-up table were converted into tonnes CO_2e ha^{-1} y^{-1} with a standard error of the mean (SE). For other wetland habitats, the overall mean carbon fluxes were obtained from Baustian et al. [85,86] (Supplementary Table S2).

The modified NECB is calculated based on habitat-specific carbon fluxes, as shown in Equation (2).

$$\text{NECB}_i = \text{ANPP}_i + \text{Sed./Soil}_{\text{accum. i}} + \text{GHG}_i \quad (2)$$

where i represents 1 of 10 habitats considered in this study (i.e., fresh forested wetland, fresh marsh, intermediate marsh, brackish marsh, FAV, SAV, (high, medium, and low), and open water).

- ANPP = aboveground net primary productivity which represents the live AG biomass produced within one year (tonne CO_2e ha^{-1} y^{-1}).
- $\text{Sed./Soil}_{\text{accum.}}$ = net carbon accumulation in sediment for SAV and open water or in soils for wetlands (tonne CO_2e ha^{-1} y^{-1}). Incorporates the live or net primary productivity of belowground biomass, the accumulation of dead belowground biomass of roots and rhizomes, aboveground litter, and allochthonous carbon [77].
- GHG = GHG emissions (tonne CO_2e ha^{-1} y^{-1}) including CH_4 and N_2O. CO_2 is excluded because ANPP and $\text{Sed./Soil}_{\text{accum.}}$ represent the net value of CO_2 balance.

The net GHG flux of emissions (tonne CO_2e) at each grid cell (90 m) was further determined by the product of the NECB for each habitat and its corresponding habitat area [74], as shown in Equation (3).

$$\text{Net GHG flux}_{\text{grid cell}} = \sum_{i=1 \text{ to } 10} \text{NECB}_i \times F_i \times \text{Area}_{\text{grid cell}} \quad (3)$$

where i represents one of 10 habitats considered in this study (i.e., fresh forested wetland, fresh marsh, intermediate marsh, brackish marsh, FAV, SAV (high, medium, and low), open water, bare ground). F_i represents % cover of habitat_i. The % cover of SAV in high is set to 100%. The % cover of SAV in medium and low categories were set to 56% and 19%, respectively, using the median values of each classification. A positive value for the net GHG flux indicates a GHG source to the atmosphere and a negative value indicates a net GHG sink from the atmosphere.

2.5. Accuracy Analysis

Four evaluation indices were used to assess the accuracy of the WSAV-Net classification: probability of false detection (P_f), precision, recall, and F_1 score. The F_1 score is the measure of a model's accuracy on a dataset, which is a way of combining the precision and recall of the model and is defined as the harmonic mean of the model's precision and recall [87]. The precision, recall, and F_1 scores were calculated for all classes using a macro-average method (an equal weight per class); for more details, refer to Supplement S1.

Furthermore, uncertainty analyses were conducted for (1) carbon fluxes (ANPP, $\text{Sed./Soil}_{\text{accum.}}$, and GHG emissions) per habitat; (2) NECB estimations per habitat; and (3) net flux of GHG emissions for the study area based on U.S. Environmental Protection Agency (EPA) method [81]. The percentage of uncertainty (% uncertainty) in the carbon fluxes was calculated based on the standard error (SE) and the mean of carbon flux as seen in Equation (4).

$$\text{Percentage uncertainty} = \left(\frac{\text{carbon flux}_{\text{SE}}}{\text{carbon flux}_{\text{mean}}}\right) \times 100\% \quad (4)$$

The combined uncertainty was further calculated for NECB using the simple error propagation method, see Equation (5) [88–90]:

$$\text{Combined uncertainty} = \sqrt{\left(\text{ANPP}_{\%\text{ uncertainty}}\right)^2 + \left(\text{Sed./Soil accum.}_{\%\text{ uncertainty}}\right)^2 + \left(\text{GHG emissions}_{\%\text{ uncertainty}}\right)^2} \quad (5)$$

3. Results

3.1. Field Observations of SAV Percent Cover

Overall, the SAV communities observed in transects A–D in 2022 were primarily dominated by *Vallisneria americana* and *Najas guadalupensis* (Table 2). The dominant species observed at each station and their % cover are provided in Table 2 (columns 4 and 5, respectively). The measured SAV % cover ranged from 61% (transect A, site 3) to 95% (transect D, site 2) in the high category, 35% (transect B, site 4) to 44% (transect C, site 5) in the medium category, and 16% (transect C, site 6) to 27% (transect A, site 4) in the low category (Table 2). It was observed that the SAV habitat characterized as low % cover was primarily composed of *N. guadalupensis*, whereas medium and high % cover areas were dominated by *V. americana*. For example, *V. americana* was the primary species observed in transect A, and mean SAV % cover was observed to decrease along the transect (A1–4), with the highest SAV % cover observed at the station closest to the emergent marsh (A1: 79%), decreasing with greater distance from the marsh (A4: 27%). Species composition along transect B was primarily *V. americana* and *N. guadalupensis*, with three of the four sites classified as high SAV % cover. Sampling sites C1–6 were divided into two transects with three sampling sites in each (Figure 2). *V. americana* and *N. guadalupensis* were also the

dominant SAV species present in transects C and D; as in transect A, the % cover decreased with increasing distance from the emergent marsh.

Table 2. Field observation of SAV % cover (% of quadrat covered with SAV vs. bare sediment) obtained from the Atchafalaya River Delta in October 2022; assigned categories of SAV cover were 0–30% (low), 30–60% (medium), and 60–100% (high).

Total SAV % Cover from Field	SAV % Cover Categorized from Field Measurements	SAV % Cover Classified from Remote Sensing	Dominant Species	% Cover of Dominant Species	Sampling Stations
61%	High	SAV medium	*V. americana*	46%	A3
64%	High	SAV medium	*V. americana*	63%	C4
64%	High	SAV medium	*V. americana*	64%	D3
72%	High	SAV high	*V. americana*	72%	C2
73%	High	SAV high	*N. guadalupensis*	67%	B3
75%	High	SAV high	*V. americana*	73%	A2
79%	High	SAV high	*V. americana*	73%	A1
85%	High	SAV high	*V. americana*	85%	B2
86%	High	SAV high	*N. guadalupensis*	63%	B1
95%	High	SAV high	*V. americana*	93%	D2
35%	Medium	SAV low	*N. guadalupensis*	19%	B4
44%	Medium	SAV medium	*V. americana*	44%	C5
51%	Medium	SAV medium	*V. americana*	51%	C1
16%	Low	SAV low	*N. guadalupensis*	15%	C6
22%	Low	SAV low	*N. guadalupensis*	18%	D4
23%	Low	SAV low	*N. guadalupensis*	11%	C3
27%	Low	SAV low	*V. americana*	27%	A4

Total % cover of SAV observed from field observations were further compared with WSAV-Net output of SAV % cover (Section 3.3.1).

3.2. Carbon Flux Look-Up Table

Carbon flux data were limited for fresh and intermediate salinity SAV habitats in Louisiana (Table 3); thus, the $Sed._{accum.}$ and GHG emissions from SAV habitat were obtained from studies conducted outside of Louisiana whose primary focus was the same fresh/intermediate SAV species as that reported in Louisiana. The mean ANPP from the literature ranged from −0.27 to −2.50 tonne CO_2e ha^{-1} y^{-1} and the overall mean (±SE) was −1.40 (±0.31) tonne CO_2e ha^{-1} y^{-1} (Table 3). From these studies, the overall mean $Sed._{accum.}$ was -11.7 ± 6.1 tonne CO_2e ha^{-1} y^{-1}. SAV habitats were observed to sequester more carbon compared to open water habitats (-8.6 ± 6.3 tonne CO_2e ha^{-1} y^{-1}; Supplement S2). GHG gas flux estimates for this study were based on the values of CH_4 emissions observed in fresh–intermediate salinity SAV habitats. The mean GHG flux was 3.20 ± 0.79 tonne CO_2e ha^{-1} y^{-1}. Given the limited availability of N_2O measurements, mean GHG fluxes relied exclusively on CH_4 flux measurements obtained from literature sources. These measurements were derived using distinct methodologies, encompassing static chamber measurements [91,92] and the application of the eddy covariance system [93] (Table 3). Such methodological differences may introduce uncertainties in CH_4 flux assessment for SAV habitats.

Table 3. Major carbon fluxes (ANPP, sediment accumulation rate, and GHG emissions) for fresh and intermediate salinity SAV habitats extracted from the literature. Carbon flux values that could not be sourced from the literature are represented by N/A.

Area of Interest (Location)	Salinity (ppt)	Carbon Fluxes (Tonne CO2e ha^{-1} y^{-1})			
		ANPP	**$Sed._{accum.}$**	**GHG fluxes**	**Citation**
Wuliangsu Lake, China	Fresh	N/A	N/A	4.73	[91]
Luanhaizi wetland, China	Fresh	N/A	N/A	2.84	[92]
Lake Taihu, China	Fresh	N/A	N/A	2.04	[93]
Everglades Stormwater Treatment Areas, FL	0–10	N/A	−17.8	N/A	[94]
Indoor mesocosm of *Myriophyllum spicatum*	Fresh	N/A	−5.60	N/A	[95]
Mississippi River Delta Plain, LA	0–0.2	−2.34	N/A	N/A	[20]
Mississippi River Delta Plain, LA	0.2–7.2	−2.50	N/A	N/A	[20]
Fresh and intermediate marsh SAV, LA	0.5–5	−2.50	N/A	N/A	[96]
Gulf coast sites	0–0.5	−1.32	N/A	N/A	[19]
Atchafalaya delta, LA	0.5–5	−0.27	N/A	N/A	[1]
Birds foot delta, LA	0.5–5	−1.70	N/A	N/A	[97]
Chenier Plain, LA	0.5–6.5	−0.34	N/A	N/A	[98]
Barataria bay, LA	0.5–5	−0.47	N/A	N/A	[99]
Rockefeller State Wildlife Refuge, LA	0–6	−0.78	N/A	N/A	[100]
Overall mean ± SE	-	-1.40 ± 0.31	-11.7 ± 6.1	3.20 ± 0.79	-

The SAV habitat area contained a mix of open water and SAV species; as such, ANPP for both open water and SAV habitats were included in the NECB for SAV habitats. Open-water ANPP for the whole cell was added to SAV ANPP, pro-rated by the mean % cover of SAV. ANPP from the open water habitat was added to SAV ANPP to account for the phytoplankton production in the water column above benthic SAV communities. Therefore, the total NECB of SAV habitats (SAV plus overlying water column) in the study area was -13.6 ± 7.9 tonne CO_2e ha^{-1} y^{-1} (Supplement S2). In addition, the fresh forested wetland (NECB = -0.7 ± 0.4 tonne CO_2e ha^{-1} y^{-1}) served as another GHG sink within the study area (Supplement S2). There were limited available literature values for ANPP, $Sed._{accum.}$, and GHG emissions for FAV habitats; therefore, FAV was combined into a fresh marsh for further analysis. Lastly, all other habitats in the study area were considered as GHG sources (including fresh and intermediate marsh) due to the assumed higher CH_4 emission in fresh and intermediate marsh environments [101,102]. The emergent bare ground in the study area was not modeled in this analysis and thus was assumed to have net zero carbon fluxes for all calculations.

3.3. Remote Sensing of Habitats

3.3.1. Deep Learning Model Performance

The accuracy of the trained WSAV-Net was 83.7% with F_1 scores ranging from 58.2 to 98.4% (Table 4), indicating an overall good performance of WSAV-Net when classifying habitats from remote sensing imagery [103,104]. The lowest F_1 score was observed for brackish marsh due to limited training and validation data. Furthermore, the loss function (or learning curve) of a well-performing U-Net model is expected to show a decreasing asymptotic curve over time [105]. This was the case for the learning curve of WSAV-Net, showing a high training and validation loss at the beginning which decreased to a point of stability with increasing training samples (Figure 4). The gap between the validation and training loss shrinks after each epoch, with a minor difference between the validation and training loss. This illustrates the typical feathers of the learning curve of a good model [106]. In addition, the learning curve is also known to be an efficient approach by which to identify overfitting and underfitting problems [105]. In this study, based on the learning curve, no under- or over-fitting issues were detected. A model which is overfitting will learn training data perfectly with the result that the model misclassifies unseen data. Thus, the learning

curve of an overfitting model has a low training loss at the beginning, which gradually increases with slightly increasing training data and does not reach an asymptote [106]. In addition, the training and validation losses of an overfitting model are far away from each other, which also was not seen in the learning curve from this study. In contrast, the learning curve of an underfitting model, which is unable to recognize meaningful patterns in the data, could be flat or noisy regardless of the amount of training data. Additionally, a gradual increase in training loss at the beginning and sudden dip in both training and validation losses at the end without approaching an asymptote can indicate a model that is underfitting [105].

Table 4. The metrics of WSAV-Net, including precision, recall, and F_1 score, for coastal habitat classification from remote sensing imagery.

Metrics Habitats	Precision (%)	Recall (%)	F_1 Score (%)	Overall Accuracy (%)
Fresh forested wetland	81.2	71.9	76.4	86.7%
Fresh marsh	86.4	73.2	79.8	
Intermediate marsh	74.3	83.1	78.7	
Brackish marsh	52.3	64.2	58.2	
FAV	79.1	79.5	79.2	
SAV high	80.5	77.4	78.9	
SAV medium	69.3	71.9	70.6	
SAV low	78.5 69.3	79.2	78.9	
Open water	97.3	99.6	98.4	

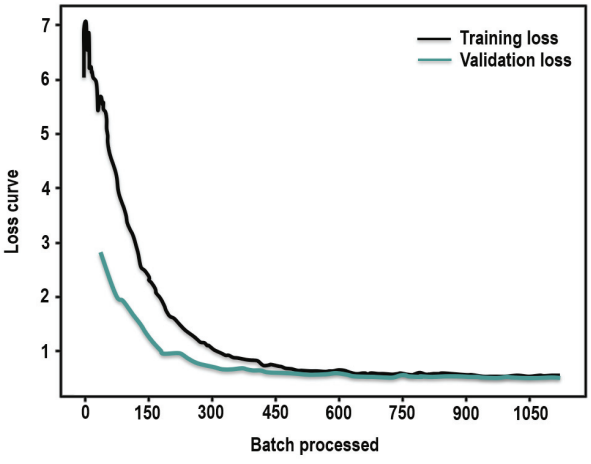


Figure 4. Learning curves including training and validation loss for WSAV-Net.

Field observations of SAV % cover collected in 2022 demonstrated that the WSAV-Net could successfully identify both a high and low % cover of SAV (Table 2). There were some differences, namely that WSAV-Net classified the SAV with up to 65% cover as a break point for the SAV medium, which was higher than the manually classified 60%. For example, there were nine sampling sites with SAV % cover in the range of 60–100%. Only six of these were classified as SAV high by WSAV-Net, and the remainder were classified as SAV medium (A3: 61%, C4: 62.6%, and D4: 64%). In comparison, for low-abundance SAV sites, with an SAV % cover of less than 30%, WSAV-Net correctly classified them all as SAV low. Therefore, based on the classification from WSAV-Net, % cover in the range of 0–30%

was effective for detection as the SAV low. However, the SAV medium and high were more likely to be detected using the ranges of 30%–65% and >65%, respectively.

3.3.2. Habitat Changes from 2015 to 2022

Habitat maps that characterized eight habitat types were developed for the years 2015, 2016, 2017, 2019, 2021, and 2022 (Table 1, Figure 5). Overall, approximately half of the study area was dominated by fresh or intermediate marsh habitats for the years quantified, and the remaining area was open water. The spatial coverage of fresh forested wetlands stayed relatively constant during the study period. The area of SAV habitat was relatively stable between 2015 and 2017, with a minor decline from 3465 ha (2015) to 3123 ha (2017). Most of the areas classified as SAV showed medium-to-high density during the years 2015–2017. The SAV habitat area was observed to decrease from 3125 to 688 ha in 2019, of which 556 ha was classified as medium SAV % (30–65%) cover while the open water habitat areas sharply increased (Figure 6). Although the exact reason for the decline in SAV during the peak growing season of July–October 2019 has not been confirmed yet, it is essential to consider external environmental factors that could potentially contribute to this reduction. Notably, the year 2019 experienced extreme flooding conditions, characterized by record-breaking discharges from both the Mississippi River and Atchafalaya River [107]. The unprecedented flooding during this period led to increased turbidity and sedimentation, which reduced the light penetration to SAV and likely hindered the photosynthetic processes crucial for the growth and survival of SAV [2]. In addition, Hurricane Barry made a landfall as a Category 1 hurricane on Marsh Island, Louisiana, with a maximum reported storm-total rainfall of 580 mm near Ragley, Louisiana [108]. The two deltaic islands are approximately 70 km to the east of Hurricane Barry's track and were exposed to the highest measured storm surge from that storm (~1.86 m near Eugene Island, Louisiana). Barry's heavy rains elevated river flow rates (9601 m^3 s^{-1}) during a flood year (2019) compared to pre-hurricane conditions (8438 m^3 s^{-1}) and caused flooding along the banks of the Atchafalaya River near Morgan City, Louisiana (Figure 6). Hurricanes may have inflicted physical damage onto SAV through wave action, and strong currents, uprooting or burying SAV plants and disrupting their growth [109]. The recovery of SAV was not observed until April 2020. However, identifying the exact SAV recovery time following Hurricane Barry and the 2019 flooding event proved to be challenging due to the unavailability of clear imagery during the peak growing season (September–October) of 2020. The lack of suitable imagery during this critical period hindered our ability to precisely assess the timing and extent of SAV recovery following the extreme weather events in 2019. In addition, major hurricanes in 2020 (Supplement S3), such as Hurricane Laura (Category 4) and Hurricane Zeta (Category 2), may have impacted SAV habitats in the Atchafalaya River Delta Estuary. In 2021, another major hurricane (Hurricane Ida; Category 4) made landfall on 29 August 2021 near Port Fourchon [110]. The highest water levels surrounding the two river deltas during that storm were measured at Eugene Island in Atchafalaya Bay (0.5 m MHHW (mean higher high water); Supplement S3; [110]). The SAV habitat area observed in 2021 (post-Ida) was nearly 1449 ha, which was still less than the pre-hurricane levels (2015–2017). In 2022, the Atchafalaya River experienced the lowest discharge (3125 m^3 s^{-1}) measured during the study period. The aerial extent of SAV recovered to the pre-2019 (Hurricane Barry) conditions of approximately 3284 ha. Throughout this area, more than two-thirds of the SAV was medium % cover. The newly deposited sediment (bare ground) was primarily observed near the head of Wax Lake Delta, prograding into the adjacent freshwater zone. An increase in FAV was observed along the edges of the deltaic islands as well as within the inundated areas of both deltas post Hurricane Barry. Details of each habitat can be found in Supplement S3.

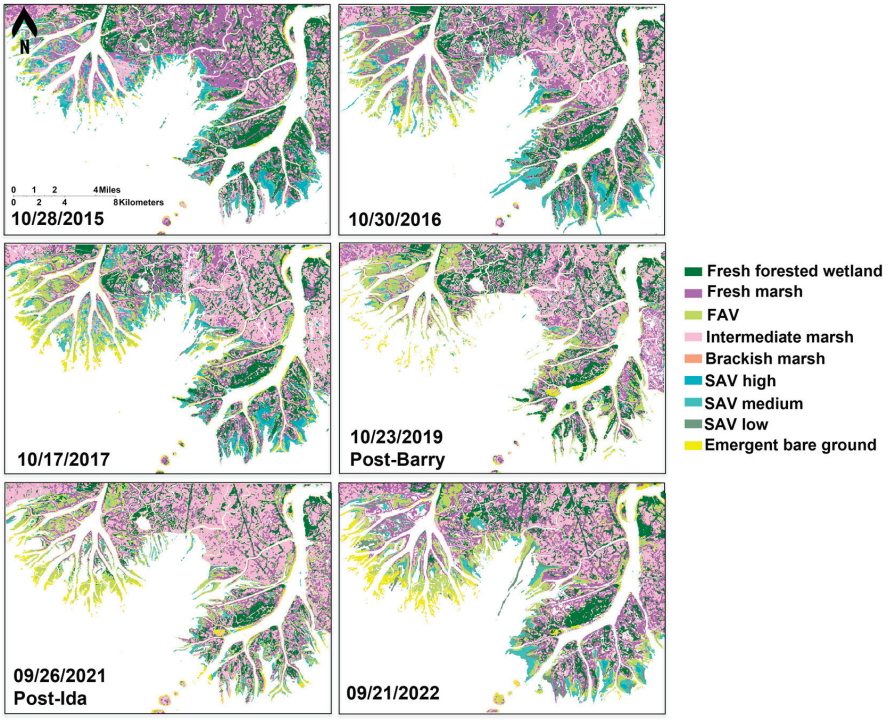


Figure 5. Timeseries of habitats including fresh forested wetland, fresh marsh, intermediate marsh, brackish marsh, FAV, SAV, open water, and bare ground from WSAV-Net.

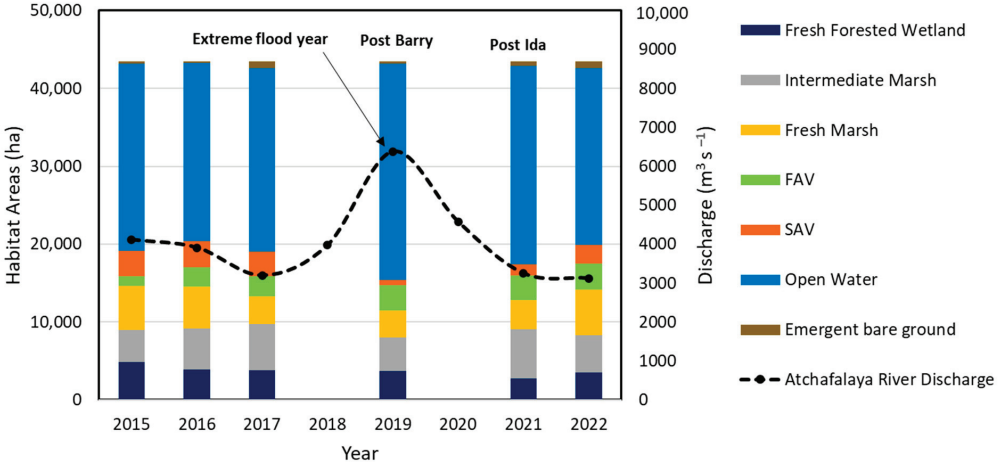


Figure 6. Changes in the habitat area in target years (i.e., 2015, 2016, 2017, 2019, 2021, and 2022). The black line represents the Atchafalaya River mean discharge. SAV = submerged aquatic vegetation. FAV = floating aquatic vegetation.

3.4. The Effect of SAV on Net GHG Flux

The carbon fluxes (Section 3.2) and habitat area (Section 3.3) were used to estimate the net GHG fluxes of the study area using a carbon balance model. The calculations of net GHG flux were conducted under two scenarios: a *with SAV* scenario and a *without*

SAV scenario for the years 2015, 2016, 2017, 2019, 2021, and 2022. In the carbon balance model, habitat maps with 30 m resolution were first converted into habitat % cover using 90 m grids (i.e., 0.81 ha) for the target years. The SAV with different % covers (e.g., SAV high, SAV medium, and SAV low) were considered separately with a different ANPP in carbon calculations by multiplying SAV % cover to the SAV ANPP, estimated from the literature values (Table 3). For the carbon fluxes of SAV habitats from $Sed._{accum.}$ and GHG, the same carbon fluxes were used regardless of the SAV % cover, as the effect of SAV % cover on $Sed._{accum.}$ and GHG emissions could not be quantified based upon the available data extracted from the published literature. An example of habitat % cover for ten habitats generated for the year 2015 is shown in (Figure 7). It was noted that FAV was observed to be more widely distributed in the Wax Lake Delta relative to the Atchafalaya Delta. SAV dominated the area along the margins of wetlands. Emergent bare ground was more aggregated adjacent to the head of Wax Lake Delta, transgressing to open water area. The habitat % cover for other target years can be found in Supplementary Figure S3.

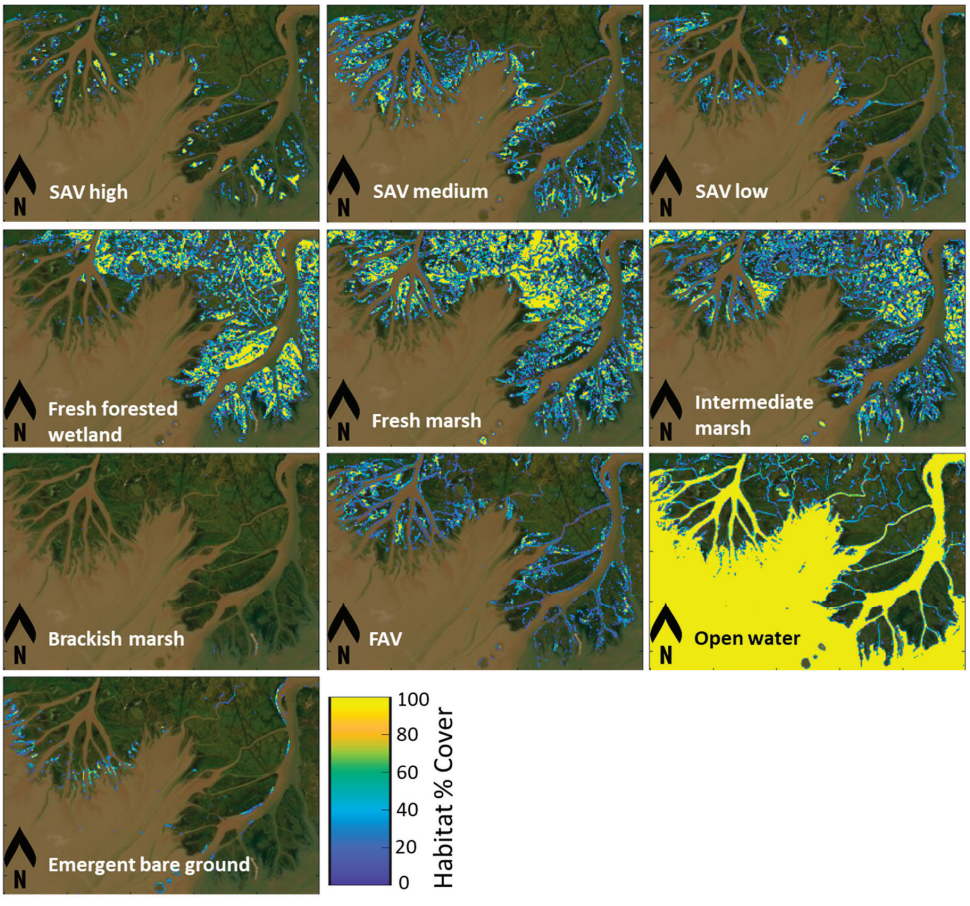


Figure 7. An example of habitat % cover maps for the study area for eight habitats in 2015, with a habitat map produced by the remote sensing analysis. SAV = submerged aquatic vegetation. FAV = floating aquatic vegetation.

3.4.1. Net GHG Fluxes

Net GHG fluxes were estimated as a product of the habitat % cover and NECB for the ten habitats. For the *without SAV* scenario, carbon fluxes for the open water (e.g., ANPP, $Sed._{accum.}$,

and GHG values) were assigned to SAV habitats in the carbon balance model. The estimated net GHG flux (*without SAV* scenario) for the study area presented a larger CO_2 sink in 2019 (-0.09 ± 0.04 MMT CO_2e y^{-1}; Figure 8a) than in 2022 (-0.01 ± 0.01 MMT CO_2e y^{-1}; Figure 8a). The negative and positive values of net GHG fluxes represent net atmospheric carbon sinks and sources, respectively. The increase in net GHG sink from 2016 to 2019 resulted from a reduced area of fresh–intermediate marsh and increased the area of open water habitats. In the study areas, the major net CO_2 sources were fresh marsh and intermediate marsh, while the open water habitat was the dominant CO_2 sink in the *without SAV* scenario (Supplementary Figure S2).

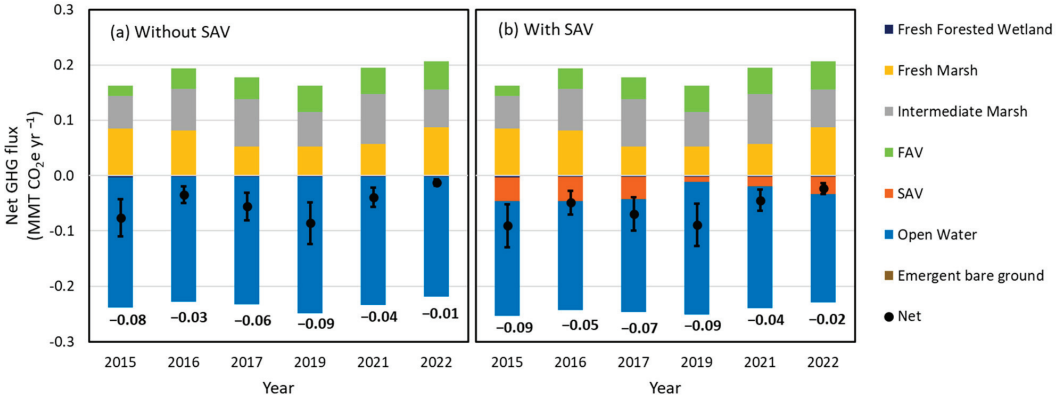


Figure 8. Changes in the total net flux of GHG emissions of habitats for (**a**) *without SAV* and (**b**) *with SAV* scenarios for target years in the study area (Figure 7; total study area is 43,460 ha). Mean and standard error of net flux of GHG emissions are reported. SAV = submerged aquatic vegetation. FAV = floating aquatic vegetation.

For the *with SAV* scenario, the estimated net GHG sinks ranged from -0.02 ± 0.01 to -0.09 ± 0.04 MMT CO_2e y^{-1} during the study period, resulting in an overall higher CO_2 sink observed relative to the *without SAV* scenario. The inclusion of SAV in the carbon balance model increased net GHG sinks, with the greatest carbon sinks from SAV habitats observed in year 2016 (-0.04 ± 0.02 MMT CO_2e y^{-1}; Supplement S4), which contributed to an estimated more negative GHG flux (-0.05 ± 0.02 MMT CO_2e y^{-1}) in comparison to *without SAV* scenario (-0.04 ± 0.02 MMT CO_2e y^{-1}). The smallest difference in estimated net GHG fluxes (3.5% difference) was observed in 2019 between *with SAV* scenario (-0.089 ± 0.04 MMT CO_2e y^{-1}) and *without SAV* scenario (-0.086 ± 0.04 MMT CO_2e y^{-1}) due to the significant loss of SAV post-Hurricane Barry (Supplement S4 and Supplement S5). Despite the significant loss of SAV habitat after Hurricane Barry in 2019, the estimated net GHG sinks in both scenarios were higher than other years, which was associated with an increase in open water area (Figure 8) due to extreme flooding (Figure 6). Details of each habitat can be found in Supplement S4. Overall, a significant difference of estimated net GHG fluxes between *with SAV* and *without SAV* scenarios among years was observed due to the high $Sed._{accum.}$ of SAV habitats (-11.7 ± 6.1 tonne CO_2e ha^{-1} y^{-1}; Supplement S2) combined with the ANPP from phytoplankton in the water above the SAV.

3.4.2. Spatial Distribution of Net GHG Fluxes

Spatial distribution maps of estimated net GHG fluxes *without SAV* and *with SAV* scenarios, as well as difference maps, were produced for each target year. Examples of net GHG fluxes (90 m resolution) in 2015 are shown in Figure 9a,b (results of other years in Supplement S5). The difference in the net GHG flux between *without SAV* and *with SAV* scenarios demonstrated that the SAV increased the estimated net GHG sink by up to 60% ($\sim -5.0 \times 10^{-6}$ MMT CO_2e ha^{-1} y^{-1}) in the open water habitat (Figure 9c). For both scenarios, areas representing a CO_2 source to the atmosphere were highly dominated by

fresh–intermediate marsh. For the *without SAV* scenario (Figure 9a), the areas estimated to be a CO_2 sink in the range of -5.0 to -9.0×10^{-6} MMT CO_2e ha^{-1} y^{-1}) were open water habitats. Under the *with SAV* scenario estimates (Figure 9b), emergent areas were dominated by fresh–intermediate marsh (net CO_2 sources) and were fringed with net GHG sink SAV habitats (ranging from -10 to -15×10^{-6} MMT CO_2e ha^{-1} y^{-1}). The distribution of the net GHG fluxes of SAV in the study area estimated that ~1600 ha of the SAV habitat (i.e., about 50% of total SAV habitats (3225 ha) had a net GHG flux between -14.0 and -11.0×10^{-6} MMT CO_2e ha^{-1} y^{-1} in the study area in 2015 (Figure 9d). Spatial distribution maps of the estimated net GHG fluxes and comparisons between *without SAV* and *with SAV* scenarios for other target years are presented in Supplementary Figure S5.

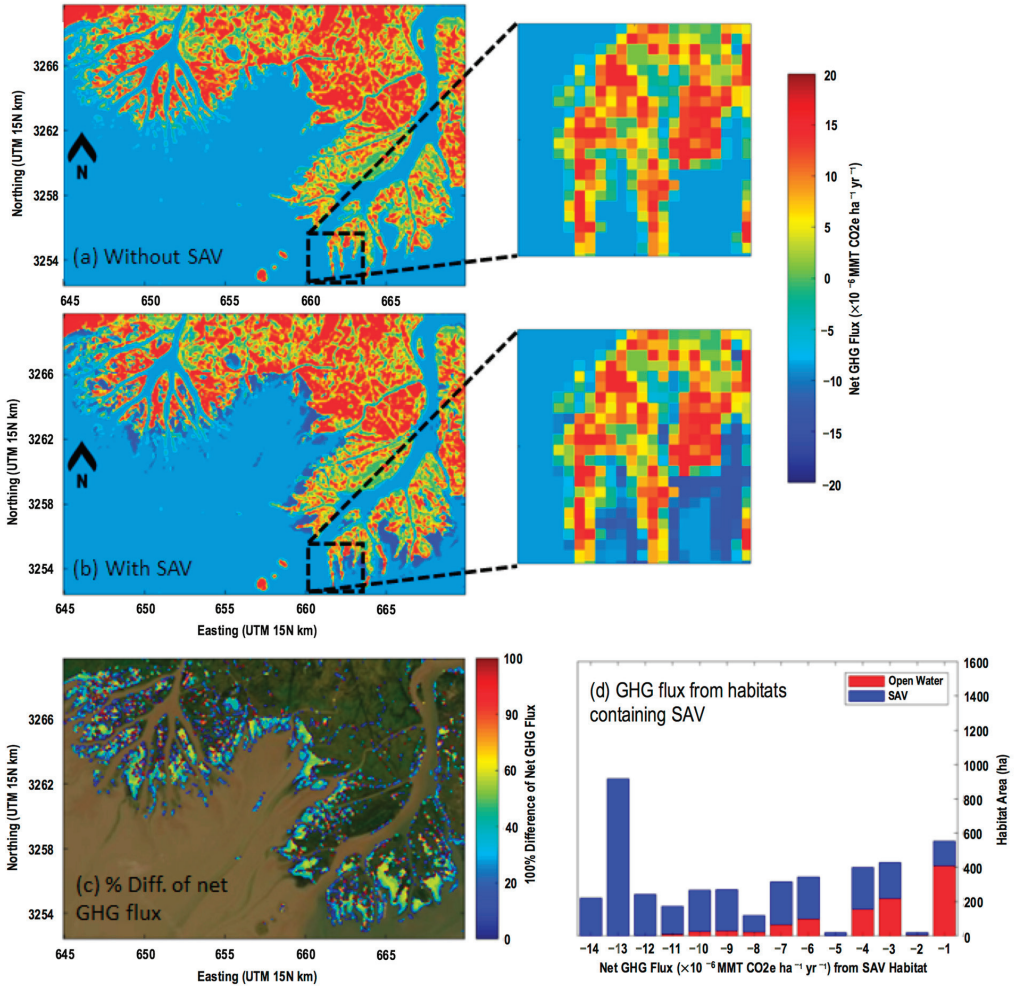


Figure 9. Comparison between the spatial distribution of net GHG flux in 2015: (**a**) net GHG flux for *without SAV* scenario and (**b**) net GHG flux of *with SAV* scenario; (**c**) differences between *with SAV* and *without SAV*, and (**d**) distribution of net GHG flux from SAV. Note that 10^{-6} MMT is more simply MT, provided as MMT for comparison throughout.

3.4.3. Dynamics of Net GHG Fluxes Pre- and Post-Hurricanes

The effects of hurricanes on net GHG fluxes were investigated by comparing the results from before and after hurricanes Barry and Ida (Figure 10). In 2017, SAV area and

net GHG flux were 3125 ha and −0.04 MMT CO_2e y^{-1}, respectively. In comparison, a dramatic decrease in the net GHG flux within the SAV habitat area was observed in 2019 due to a reduction in SAV habitat in the study area (Figure 6). The SAV habitat area was reduced to 688 ha (22% of 2017 SAV area) in the months following Hurricane Barry and extreme flooding event in 2019. As such, the estimated net GHG flux of SAV also reduced to −0.01 MMT CO_2e y^{-1} in September 2019. In the years post-hurricane, the SAV habitat expanded and was approaching pre-hurricane extent by 2022 (Figure 10). In 2022, during hurricane season, no major storms occurred. During that year (one year after Hurricane Ida and three years after Hurricane Barry), the SAV habitat increased in area with an estimated contribution to net GHG flux equivalent to 77% of the 2017 net GHG flux.

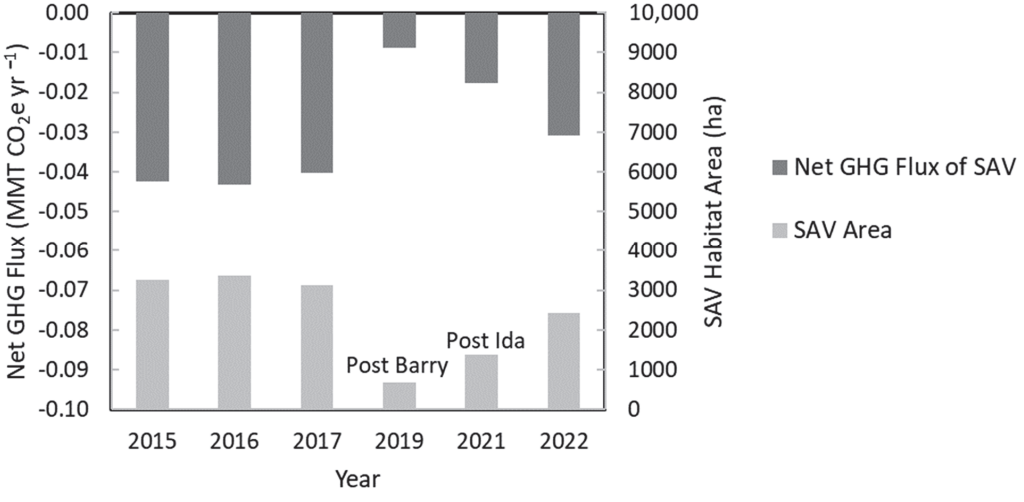


Figure 10. Changes in the estimated net GHG fluxes and SAV area before and after hurricanes Barry (2019) and Ida (2021) in the study area.

4. Discussion

4.1. SAV Habitat Dynamics and Carbon Fluxes

SAV communities are sensitive to short-term changes in environmental conditions [96,111]. The spatial distribution and abundance of SAV in the study area was more dynamic than in other coastal habitat types due to the area's hydrodynamics (e.g., water level) and water quality (e.g., turbidity and salinity; [19]). Two major hurricanes occurred during the study period prior to significant temporary decreases in the SAV spatial extent and density throughout the study area. Major storm events and their associated storm surge can increase salinity, turbidity, and wave energy in shallow coastal habitats [112,113]. These major shifts in abiotic conditions have the potential to negatively affect SAV and its associated biota. Frazer et al. [114] observed the increased mortality in both *V. americana* and *M. spicatum* after seven days of exposure to increased salinity. Similarly, the SAV recovery in the study area post-hurricane was slow due to continued high water and turbid conditions (from increased river flow), and additional storms (2019–2021 hurricane seasons). However, the SAV rebounded in a single growing season when no major storms or hurricanes occurred (2022 hurricane season). As the impact of hurricanes on SAV habitats can vary depending on various factors such as the intensity and duration of the storm, the location of landfall, and the pre-existing condition of the habitat, methods such as remote sensing can be used to regularly monitor the impact of such events on SAV habitats. High-resolution satellite imagery, such as Sentinel 2-MSI, can also provide detailed information on the seasonal dynamics of SAV, enhancing the temporal observations of SAV habitats. This increased temporal resolution aids in understanding how SAV habitats respond to extreme events and assessing the SAV recovery time. This valuable information could be used to better

understand the variability and resilience of SAV meadows, informing management and restoration planning.

Due to the reported high spatial and temporal variation in SAV cover in this region [17,19], the estimation of the net GHG flux for this study was based on existing habitats in the target years in the carbon balance model, rather than on continuous estimates over time (accounting for habitat conversions). Studies of emergent coastal wetlands have estimated carbon loss as emergent wetland converts into open water, ranging from 20% to 100% of soil carbon [115–117]. However, similar estimates related to carbon loss in SAV have not been documented, particularly for fresh- and intermediate-salinity SAV species. Thus, the fate of carbon from lost SAV meadows is highly uncertain and requires further empirical field measurements to reduce uncertainty in the annual estimates of SAV net GHG flux. In coastal Louisiana, projections of emergent wetland loss and the associated potential increase in SAV in shallow open water habitats makes investigating carbon capture and sequestration in the sediments of these open water areas increasingly important to reduce uncertainty in the estimates of coastal habitat net GHG fluxes.

4.2. SAV Contributions to Net GHG Flux

To evaluate the potential contribution of SAV to net GHG flux, 43,460 ha of the Atchafalaya River Delta Estuary was selected to estimate GHG emissions under two scenarios—*without SAV* and *with SAV*—in the target years (i.e., 2015, 2016, 2017, 2019, 2021, and 2022). For both scenarios, open-water habitats dominated the net GHG sinks and accounted for 57% of the study area. Accounting for SAV in open-water areas increased the total net GHG sinks by up to 40% in the study area. Based on available literature, SAV has a high $Sed._{accum.}$ and slightly higher NECB than open-water habitats [18,118,119]. However, for the entire 43,460 ha study area, the total net GHG sinks from SAV were lower than for open water due to their much smaller spatial extent (i.e., SAV covered ~12% of the area of the open water). When considered at a hectare scale, open-water areas dominated by SAV increased the net GHG sink by about 60% in comparison with open water without SAV (Figure 9c). It was also observed that the presence of SAV could switch the net GHG flux from source to sink, depending on the fractions of SAV in mixed habitats with freshwater/intermediate marshes. Therefore, the contribution of carbon sinks from SAV in fresh–intermediate aquatic habitats is valuable to include in hectare-scale net GHG flux accounting.

4.3. Future Methane Quantification

SAV habitats store most of their carbon in the underlying sediments [120], which are water-saturated and thus often anoxic. This lack of oxygen slows microbial decomposition processes and enhances the ability of SAV habitats to sequester and store carbon over long timeframes. However, this same anoxia also creates favorable conditions for methanogenesis—especially in freshwater and oligohaline (i.e., salinity < 5 ppt) habitats [101,121]. The flux of CH_4 from SAV habitats is highly variable across both temporal and spatial scales, which introduces considerable uncertainty into NECB calculations; for instance, the CH_4 emission data used in this study were obtained from other regions with some same SAV species to those found in the Atchafalaya River Delta Estuary, which may introduce regional differences and further enhance the uncertainties. Given that CH_4 has a GWP 25–34 times higher than CO_2 per mole of carbon during a 100-year period [122], even modest amounts of methane emissions can profoundly impact an SAV habitat's overall GHG emissions, potentially shifting an SAV habitat from a net sink to a net source of GHG. Therefore, there is a critical need to better comprehend and quantify the geochemical, hydrological, ecological, and microbial processes that drive CH_4 emissions from SAV habitats. We emphasize the importance of undertaking field data collection efforts for CH_4 emissions from SAV habitats. Such efforts will be essential to clarify the potential for the conservation and restoration of SAV habitats as an effective strategy to mitigate climate change [76,123].

5. Conclusions

This study provides a novel estimation of the carbon sequestration capacity for SAV in fresh-intermediate waters. The SAV species were primarily *V. americana* and *N. guadalupensis*, growing in the prograding deltaic system in the Atchafalaya Basin, Louisiana, which constitutes a large carbon sink in these marshes, with an NECB ~-9.9 ± 6.1 tonne CO_2e ha^{-1} y^{-1}. The grand total of the net GHG flux for the 47,000 ha was in the range of -0.01 ± 0.01 to -0.09 ± 0.04 MMT CO_2e y^{-1}, which increased to -0.02 ± 0.01 to -0.09 ± 0.04 MMT CO_2e y^{-1} when SAV was included. Even though SAV covered only (up to) 8% of the total area in 2015, including SAV in the net GHG flux calculations increased the net GHG sink by up to 40% (-0.05 ± 0.02 MMT CO_2e y^{-1}). This is the first quantification to suggest that accounting for the occurrence and abundance of SAV within annual net GHG flux calculations over 47,000 ha of mixed fresh and intermediate wetlands can shift the net carbon flux from a net GHG source to a net GHG sink. Furthermore, given the patchy distribution of SAV along shallow emergent marsh edges, at the hectare scale, the inclusion of SAV resulted in an increase of ~60% of the net GHG sink in shallow areas adjacent to emergent marsh where SAV was abundant. However, a state of the science literature review conducted in this study revealed that the field measurements of carbon fixed by SAV as well as GHG emissions from SAV (e.g., CH_4 and N_2O) were limited for non-marine SAV. Therefore, this study emphasizes the importance of collecting direct field measurements of GHG exchanges for non-marine SAV species in fresh- and intermediate-salinity coastal areas to reduce uncertainties and better characterize the role of SAV in net GHG flux. The known high spatial and temporal variability of non-marine SAV species has historically been a major barrier to the regular mapping of spatial distribution and biomass over large areas. This study successfully integrated a deep learning approach and satellite imagery to spatially identify non-marine SAV at high, medium, and low % cover in the shallow but highly turbid waters of a large river delta using WSAV-Net with an accuracy of 86.7%. Remote sensing and deep learning models have high potential for the mapping and monitoring of SAV in turbid sub-tropical coastal deltas as a component of increasing accuracy of net GHG flux estimates at small (hectare) and large (coastal basin) scales.

Supplementary Materials: The following supporting information can be downloaded at: https://www.mdpi.com/article/10.3390/rs15153765/s1.

Author Contributions: B.L. and T.C. designed this study. All authors contributed to the draft manuscript during its development and provided a review of the final submission. T.C., E.K. and T.S. acquired and processed the field data. T.S. conducted the literature review of SAV carbon fluxes. B.L. processed all satellite data and developed the deep learning model for habitat analysis. H.J. conducted the carbon calculation via the carbon balance model. All authors have read and agreed to the published version of the manuscript.

Funding: This project was supported, in part, by the Coastal Protection and Restoration Authority.

Data Availability Statement: Landsat 8/9-OLI data can be accessed from https://earthexplorer.usgs.gov/ (accessed on 31 May 2023). The other data presented in this study are available upon request from the corresponding author.

Acknowledgments: The authors are also grateful to Garvin Pittman for providing logistic support for field operations, Charley Cameron, Diana Di Leonardo, and Shawn Doyle helped improve an earlier version of this manuscript through their comments and suggestions. In addition, the authors would like to thank Kelly Darnell for assistance with the analysis of the SAV data from the Atchafalaya River Delta. The authors would also thank the anonymous reviewers for dedicating their time to reviewing an earlier version of this manuscript.

Conflicts of Interest: The authors have no conflict of interest related to this work.

References

1. Castellanos, D.L.; Rozas, L.P. Nekton Use of Submerged Aquatic Vegetation, Marsh, and Shallow Unvegetated Bottom in the Atchafalaya River Delta, a Louisiana Tidal Freshwater Ecosystem. *Estuaries* **2001**, *24*, 184. [CrossRef]
2. Orth, R.J.; Carruthers, T.J.B.; Dennison, W.C.; Duarte, C.M.; Fourqurean, J.W.; Heck, K.L.; Hughes, A.R.; Kendrick, G.A.; Kenworthy, W.J.; Olyarnik, S.; et al. A Global Crisis for Seagrass Ecosystems. *BioScience* **2006**, *56*, 987–996. [CrossRef]
3. Waycott, M.; Duarte, C.M.; Carruthers, T.J.B.; Orth, R.J.; Dennison, W.C.; Olyarnik, S.; Calladine, A.; Fourqurean, J.W.; Heck, K.L.; Hughes, A.R.; et al. Accelerating Loss of Seagrasses across the Globe Threatens Coastal Ecosystems. *Proc. Natl. Acad. Sci. USA* **2009**, *106*, 12377–12381. [CrossRef] [PubMed]
4. Barbier, E.B.; Hacker, S.D.; Kennedy, C.; Koch, E.W.; Stier, A.C.; Silliman, B.R. The Value of Estuarine and Coastal Ecosystem Services. *Ecol. Monogr.* **2011**, *81*, 169–193. [CrossRef]
5. Costanza, R.; Hannon, B.; Limburg, K.; Naeem, S.; O'Neill, R.V.; Raskin, R.G.; Sutton, P. The Value of the World's Ecosystem Services and Natural Capital. *Nature* **1997**, *387*, 253–260. [CrossRef]
6. Heck, K.; Hays, G.; Orth, R. Critical Evaluation of the Nursery Role Hypothesis for Seagrass Meadows. *Mar. Ecol. Prog. Ser.* **2003**, *253*, 123–136. [CrossRef]
7. Carr, J.; D'Odorico, P.; McGlathery, K.; Wiberg, P. Stability and Bistability of Seagrass Ecosystems in Shallow Coastal Lagoons: Role of Feedbacks with Sediment Resuspension and Light Attenuation. *J. Geophys. Res.* **2010**, *115*, G03011. [CrossRef]
8. Gurbisz, C.; Kemp, W.M.; Sanford, L.P.; Orth, R.J. Mechanisms of Storm-Related Loss and Resilience in a Large Submersed Plant Bed. *Estuaries Coasts* **2016**, *39*, 951–966. [CrossRef]
9. McGlathery, K.; Sundbäck, K.; Anderson, I. Eutrophication in Shallow Coastal Bays and Lagoons: The Role of Plants in the Coastal Filter. *Mar. Ecol. Prog. Ser.* **2007**, *348*, 1–18. [CrossRef]
10. McLeod, E.; Chmura, G.L.; Bouillon, S.; Salm, R.; Björk, M.; Duarte, C.M.; Lovelock, C.E.; Schlesinger, W.H.; Silliman, B.R. A Blueprint for Blue Carbon: Toward an Improved Understanding of the Role of Vegetated Coastal Habitats in Sequestering CO_2. *Front. Ecol. Environ.* **2011**, *9*, 552–560. [CrossRef]
11. Fourqurean, J.W.; Duarte, C.M.; Kennedy, H.; Marbà, N.; Holmer, M.; Mateo, M.A.; Apostolaki, E.T.; Kendrick, G.A.; Krause-Jensen, D.; McGlathery, K.J.; et al. Seagrass Ecosystems as a Globally Significant Carbon Stock. *Nat. Geosci.* **2012**, *5*, 505–509. [CrossRef]
12. Tokoro, T.; Hosokawa, S.; Miyoshi, E.; Tada, K.; Watanabe, K.; Montani, S.; Kayanne, H.; Kuwae, T. Net Uptake of Atmospheric CO_2 by Coastal Submerged Aquatic Vegetation. *Glob. Chang. Biol.* **2014**, *20*, 1873–1884. [CrossRef] [PubMed]
13. Hillmann, E.R.; Rivera-Monroy, V.H.; Nyman, J.A.; La Peyre, M.K. Estuarine Submerged Aquatic Vegetation Habitat Provides Organic Carbon Storage across a Shifting Landscape. *Sci Total. Environ.* **2020**, *717*, 137217. [CrossRef]
14. Chmura, G.L.; Anisfeld, S.C.; Cahoon, D.R.; Lynch, J.C. Global Carbon Sequestration in Tidal, Saline Wetland Soils. *Glob. Biogeochem. Cycles* **2003**, *17*, 22-1–22-11. [CrossRef]
15. Hopkinson, C.S.; Cai, W.-J.; Hu, X. Carbon Sequestration in Wetland Dominated Coastal Systems—A Global Sink of Rapidly Diminishing Magnitude. *Curr. Opin. Environ. Sustain.* **2012**, *4*, 186–194. [CrossRef]
16. Mitra, S.; Wassmann, R.; Vlek, P.L.G. An Appraisal of Global Wetland Area and Its Organic Carbon Stock. *Curr. Sci.* **2005**, *88*, 25–35.
17. Watanabe, K.; Kuwae, T. How Organic Carbon Derived from Multiple Sources Contributes to Carbon Sequestration Processes in a Shallow Coastal System? *Glob. Chang. Biol.* **2015**, *21*, 2612–2623. [CrossRef]
18. Hillmann, E.R.; DeMarco, K.E.; Peyre, M.L. Establishing a Baseline of Estuarine Submerged Aquatic Vegetation Resources across Salinity Zones within Coastal Areas of the Northern Gulf of Mexico. *J. Southeast. Assoc. Fish Wildl. Agencies* **2016**, *3*, 25–32.
19. DeMarco, K.; Couvillion, B.; Brown, S.; La Peyre, M. Submerged Aquatic Vegetation Mapping in Coastal Louisiana through Development of a Spatial Likelihood Occurrence (SLOO) Model. *Aquat. Bot.* **2018**, *151*, 87–97. [CrossRef]
20. Massicotte, P.; Bertolo, A.; Brodeur, P.; Hudon, C.; Mingelbier, M.; Magnan, P. Influence of the Aquatic Vegetation Landscape on Larval Fish Abundance. *J. Great Lakes Res.* **2015**, *41*, 873–880. [CrossRef]
21. Zhang, Y.; Jeppesen, E.; Liu, X.; Qin, B.; Shi, K.; Zhou, Y.; Thomaz, S.M.; Deng, J. Global Loss of Aquatic Vegetation in Lakes. *Earth-Sci. Rev.* **2017**, *173*, 259–265. [CrossRef]
22. Day, J.W.; Britsch, L.D.; Hawes, S.R.; Shaffer, G.P.; Reed, D.J.; Cahoon, D. Pattern and Process of Land Loss in the Mississippi Delta: A Spatial and Temporal Analysis of Wetland Habitat Change. *Estuaries* **2000**, *23*, 425. [CrossRef]
23. Yuill, B.; Lavoie, D.; Reed, D.J. Understanding Subsidence Processes in Coastal Louisiana. *J. Coast. Res.* **2009**, *54*, 23–36. [CrossRef]
24. Couvillion, B.R.; Beck, H. Marsh Collapse Thresholds for Coastal Louisiana Estimated Using Elevation and Vegetation Index Data. *J. Coast. Res.* **2013**, *63*, 58–67. [CrossRef]
25. Hamberg, J.; Findlay, S.E.G.; Limburg, K.E.; Diemont, S.A.W. Post-storm Sediment Burial and Herbivory of *Vallisneria Americana* in the Hudson River Estuary: Mechanisms of Loss and Implications for Restoration. *Restor. Ecol.* **2017**, *25*, 629–639. [CrossRef]
26. Kennish, M.J. Coastal Salt Marsh Systems in the U.S.: A Review of Anthropogenic Impacts. *J. Coast. Res.* **2001**, *17*, 731–748.
27. Kuwae, T.; Watanabe, A.; Yoshihara, S.; Suehiro, F.; Sugimura, Y. Implementation of Blue Carbon Offset Crediting for Seagrass Meadows, Macroalgal Beds, and Macroalgae Farming in Japan. *Mar. Pol.* **2022**, *138*, 104996. [CrossRef]
28. Carruthers, T.J.B.; Kiskaddon, E.P.; Baustian, M.M.; Darnell, K.M.; Moss, L.C.; Perry, C.L.; Stagg, C. Tradeoffs in Habitat Value to Maximize Natural Resource Benefits from Coastal Restoration in a Rapidly Eroding Wetland: Is Monitoring Land Area Sufficient? *Restor. Ecol.* **2021**, *30*, e13564. [CrossRef]

29. Asner, G.P. Automated Mapping of Tropical Deforestation and Forest Degradation: CLASlite. *J. Appl. Remote Sens.* **2009**, *3*, 033543. [CrossRef]
30. Johansen, K.; Duan, Q.; Tu, Y.-H.; Searle, C.; Wu, D.; Phinn, S.; Robson, A.; McCabe, M.F. Mapping the Condition of Macadamia Tree Crops Using Multi-Spectral UAV and WorldView-3 Imagery. *ISPRS J. Photogramm.* **2020**, *165*, 28–40. [CrossRef]
31. Phinn, S.; Roelfsema, C.; Dekker, A.; Brando, V.; Anstee, J. Mapping Seagrass Species, Cover and Biomass in Shallow Waters: An Assessment of Satellite Multi-Spectral and Airborne Hyper-Spectral Imaging Systems in Moreton Bay (Australia). *Remote Sens. Environ.* **2008**, *112*, 3413–3425. [CrossRef]
32. Sanders, J.T.; Jones, E.A.L.; Minter, A.; Austin, R.; Roberson, G.T.; Richardson, R.J.; Everman, W.J. Remote Sensing for Italian Ryegrass [*Lolium perenne* L. Ssp. *Multiflorum* (Lam.) Husnot] Detection in Winter Wheat (*Triticum aestivum* L.). *Front. Agron.* **2021**, *3*, 687112. [CrossRef]
33. Tiner, R.W.; Lang, M.W.; Klemas, V.V. *Remote Sensing of Wetlands: Applications and Advances*; CRC Press: Boca Raton, FL, USA, 2015; ISBN 978-1-4822-3738-2.
34. Lyons, M.; Phinn, S.; Roelfsema, C. Integrating Quickbird Multi-Spectral Satellite and Field Data: Mapping Bathymetry, Seagrass Cover, Seagrass Species and Change in Moreton Bay, Australia in 2004 and 2007. *Remote Sens.* **2011**, *3*, 42–64. [CrossRef]
35. Hedley, J.; Roelfsema, C.; Chollett, I.; Harborne, A.; Heron, S.; Weeks, S.; Skirving, W.; Strong, A.; Eakin, C.; Christensen, T.; et al. Remote Sensing of Coral Reefs for Monitoring and Management: A Review. *Remote Sens.* **2016**, *8*, 118. [CrossRef]
36. McKenzie, L.J.; Langlois, L.A.; Roelfsema, C.M. Improving Approaches to Mapping Seagrass within the Great Barrier Reef: From Field to Spaceborne Earth Observation. *Remote Sens.* **2022**, *14*, 2604. [CrossRef]
37. Giardino, C.; Bresciani, M.; Valentini, E.; Gasperini, L.; Bolpagni, R.; Brando, V.E. Airborne Hyperspectral Data to Assess Suspended Particulate Matter and Aquatic Vegetation in a Shallow and Turbid Lake. *Remote Sens. Environ.* **2015**, *157*, 48–57. [CrossRef]
38. Santos, M.J.; Khanna, S.; Hestir, E.L.; Greenberg, J.A.; Ustin, S.L. Measuring Landscape-Scale Spread and Persistence of an Invaded Submerged Plant Community from Airborne Remote Sensing. *Ecol. Appl.* **2016**, *26*, 1733–1744. [CrossRef]
39. Chen, Q.; Yu, R.; Hao, Y.; Wu, L.; Zhang, W.; Zhang, Q.; Bu, X. A New Method for Mapping Aquatic Vegetation Especially Underwater Vegetation in Lake Ulansuhai Using GF-1 Satellite Data. *Remote Sens.* **2018**, *10*, 1279. [CrossRef]
40. Liu, B.; D'Sa, E.J.; Joshi, I. Multi-decadal trends and influences on dissolved organic carbon distribution in the Barataria Basin, Louisiana from in-situ and Landsat/MODIS observations. *Remote Sens. Environ.* **2019**, *228*, 183–202. [CrossRef]
41. Liu, B.; D'Sa, E.J.; Maiti, K.; Rivera-Monroy, V.H.; Xue, Z. Biogeographical trends in phytoplankton community size structure using adaptive sentinel 3-OLCI chlorophyll a and spectral empirical orthogonal functions in the estuarine-shelf waters of the northern Gulf of Mexico. *Remote Sens. Environ.* **2021**, *252*, 112154. [CrossRef]
42. D'Sa, E.J.; Tzortziou, M.; Liu, B. Extreme events and impacts on organic carbon cycles from ocean color remote sensing: Review with case study, challenges, and future directions. *Earth Sci. Rev.* **2023**, *243*, 104503. [CrossRef]
43. D'Sa, E.J.; Joshi, I.; Liu, B. Galveston Bay and coastal ocean optical-geochemical response to Hurricane Harvey from VIIRS ocean color. *Geophys. Res. Lett.* **2018**, *45*, 10–579. [CrossRef] [PubMed]
44. Dierssen, H.M.; Ackleson, S.G.; Joyce, K.E.; Hestir, E.L.; Castagna, A.; Lavender, S.; McManus, M.A. Living up to the Hype of Hyperspectral Aquatic Remote Sensing: Science, Resources and Outlook. *Front. Environ. Sci.* **2021**, *9*, 649528. [CrossRef]
45. Maasri, A.; Jähnig, S.C.; Adamescu, M.C.; Adrian, R.; Baigun, C.; Baird, D.J.; Batista-Morales, A.; Bonada, N.; Brown, L.E.; Cai, Q.; et al. A Global Agenda for Advancing Freshwater Biodiversity Research. *Ecol. Lett.* **2022**, *25*, 255–263. [CrossRef]
46. Orth, R.J.; Dennison, W.C.; Gurbisz, C.; Hannam, M.; Keisman, J.; Landry, J.B.; Lefcheck, J.S.; Moore, K.A.; Murphy, R.R.; Patrick, C.J.; et al. Long-Term Annual Aerial Surveys of Submersed Aquatic Vegetation (SAV) Support Science, Management, and Restoration. *Estuar. Coasts* **2022**, *45*, 1012–1027. [CrossRef]
47. Huber, S.; Hansen, L.B.; Nielsen, L.T.; Rasmussen, M.L.; Sølvsteen, J.; Berglund, J.; Paz von Friesen, C.; Danbolt, M.; Envall, M.; Infantes, E.; et al. Novel Approach to Large-Scale Monitoring of Submerged Aquatic Vegetation: A Nationwide Example from Sweden. *Integr. Environ. Assess Manag.* **2022**, *18*, 909–920. [CrossRef] [PubMed]
48. Liang, J.H.; Yuan, J.; Wan, X.; Liu, J.; Liu, B.; Jang, H.; Tyagi, M. Exploring the use of machine learning to parameterize vertical mixing in the ocean surface boundary layer. *Ocean Model.* **2022**, *176*, 102059. [CrossRef]
49. Zhang, X.; Han, L.; Han, L.; Zhu, L. How Well Do Deep Learning-Based Methods for Land Cover Classification and Object Detection Perform on High Resolution Remote Sensing Imagery? *Remote Sens.* **2020**, *12*, 417. [CrossRef]
50. Mahdianpari, M.; Rezaee, M.; Zhang, Y.; Salehi, B. Wetland Classification Using Deep Convolutional Neural Network. In Proceedings of the IGARSS 2018–2018 IEEE International Geoscience and Remote Sensing Symposium, Valencia, Spain, 22–27 July 2018; pp. 9249–9252.
51. Rezaee, M.; Mahdianpari, M.; Zhang, Y.; Salehi, B. Deep Convolutional Neural Network for Complex Wetland Classification Using Optical Remote Sensing Imagery. *IEEE J. Sel. Top. Appl. Earth Obs. Remote Sens.* **2018**, *11*, 3030–3039. [CrossRef]
52. Ronneberger, O.; Fischer, P.; Brox, T. U-Net: Convolutional Networks for Biomedical Image Segmentation. In Proceedings of the Medical Image Computing and Computer-Assisted Intervention—MICCAI 2015, Munich, Germany, 5–9 October 2015; Navab, N., Hornegger, J., Wells, W.M., Frangi, A.F., Eds.; Springer International Publishing: Cham, Switzerland, 2015; pp. 234–241.
53. Guo, M.; Yu, Z.; Xu, Y.; Huang, Y.; Li, C. ME-Net: A Deep Convolutional Neural Network for Extracting Mangrove Using Sentinel-2A Data. *Remote Sens.* **2021**, *13*, 1292. [CrossRef]

54. Guo, Y.; Liao, J.; Shen, G. Mapping Large-Scale Mangroves along the Maritime Silk Road from 1990 to 2015 Using a Novel Deep Learning Model and Landsat Data. *Remote Sens.* **2021**, *13*, 245. [CrossRef]
55. Hu, Y.; Zhang, Q.; Zhang, Y.; Yan, H. A Deep Convolution Neural Network Method for Land Cover Mapping: A Case Study of Qinhuangdao, China. *Remote Sens.* **2018**, *10*, 2053. [CrossRef]
56. Cisneros, A.; Fiorio, P.; Menezes, P.; Pasqualotto, N.; Van Wittenberghe, S.; Bayma, G.; Furlan Nogueira, S. Mapping Productivity and Essential Biophysical Parameters of Cultivated Tropical Grasslands from Sentinel-2 Imagery. *Agronomy* **2020**, *10*, 711. [CrossRef]
57. Singh, M.; Tyagi, K.D. Pixel Based Classification for Landsat 8 OLI Multispectral Satellite Images Using Deep Learning Neural Network. *Remote Sens. Appl. Soc. Environ.* **2021**, *24*, 100645. [CrossRef]
58. Roberts, H.H. Dynamic Changes of the Holocene Mississippi River Delta Plain: The Delta Cycle. *J. Coastal Res.* **1997**, *13*, 605–627.
59. Thomas, N.; Simard, M.; Castañeda-Moya, E.; Byrd, K.; Windham-Myers, L.; Bevington, A.; Twilley, R.R. High-Resolution Mapping of Biomass and Distribution of Marsh and Forested Wetlands in Southeastern Coastal Louisiana. *Int. J. Appl. Earth Obs. Geoinf.* **2019**, *80*, 257–267. [CrossRef]
60. Carle, M. Spatial Structure and Dynamics of the Plant Communities in a Pro-Grading River Delta: Wax Lake Delta, Atchafalaya Bay, Louisiana. Ph.D. Thesis, Louisiana State University and Agricultural and Mechanical College, Baton Rouge, LA, USA, 2013.
61. Chabreck, R.H.; Condrey, R.E. *Common Vascular Plants of the Louisiana Marsh*; Louisiana State University Center for Wetland Resources: Baton Rouge, LA, USA, 1979; p. 117.
62. Holm, G.O., Jr.; Sasser, C.E. Differential Salinity Response between Two Mississippi River Subdeltas: Implications for Changes in Plant Composition. *Estuaries* **2001**, *24*, 78–89. [CrossRef]
63. Lane, R.R.; Day, J.W.; Marx, B.; Reves, E.; Kemp, G.P. Seasonal and Spatial Water Quality Changes in the Outflow Plume of the Atchafalaya River, Louisiana, USA. *Estuaries* **2002**, *25*, 30–42. [CrossRef]
64. Pasch, R.J.; Roberts, D.P.; Blake, E.S. The 2019 Atlantic Hurricane Season: An Active and Destructive Year. *Weatherwise* **2020**, *73*, 32–39. [CrossRef]
65. Yao, Q.; Cohen, M.C.L.; Liu, K.; de Souza, A.V.; Rodrigues, E. Nature versus Humans in Coastal Environmental Change: Assessing the Impacts of Hurricanes Zeta and Ida in the Context of Beach Nourishment Projects in the Mississippi River Delta. *Remote Sens.* **2022**, *14*, 2598. [CrossRef]
66. Roy, D.P.; Wulder, M.A.; Loveland, T.R.; Woodcock, C.E.; Allen, R.G.; Anderson, M.C.; Helder, D.; Irons, J.R.; Johnson, D.M.; Kennedy, R.; et al. Landsat-8: Science and Product Vision for Terrestrial Global Change Research. *Remote Sens. Environ.* **2014**, *145*, 154–172. [CrossRef]
67. Wulder, M.A.; Hilker, T.; White, J.C.; Coops, N.C.; Masek, J.G.; Pflugmacher, D.; Crevier, Y. Virtual Constellations for Global Terrestrial Monitoring. *Remote Sens. Environ.* **2015**, *170*, 62–76. [CrossRef]
68. Li, J.; Roy, D. A Global Analysis of Sentinel-2A, Sentinel-2B and Landsat-8 Data Revisit Intervals and Implications for Terrestrial Monitoring. *Remote Sens.* **2017**, *9*, 902. [CrossRef]
69. Lin, C.; Gong, Z.; Zhao, W. The Extraction of Wetland Hydrophytes Types Based on Medium Resolution TM Data. *Sheng Tai Xue Bao* **2010**, *30*, 6460–6469.
70. Zhao, D.; Lv, M.; Jiang, H.; Cai, Y.; Xu, D.; An, S. Spatio-Temporal Variability of Aquatic Vegetation in Taihu Lake over the Past 30 Years. *PLoS ONE* **2013**, *8*, e66365. [CrossRef]
71. Couvillion, B. *2017 Coastal Master Plan Modeling: Attachment C3-27: Landscape Data. Version Final*; Coastal Protection and Restoration Authority: Baton Rouge, LA, USA, 2017; p. 84.
72. Visser, J.M.; Duke-Sylvester, S. LaVegMod v2: Modeling Coastal Vegetation Dynamics in Response to Proposed Coastal Restoration and Protection Projects in Louisiana, USA. *Sustainability* **2017**, *9*, 1625. [CrossRef]
73. Chapin, F.S.; Woodwell, G.M.; Randerson, J.T.; Rastetter, E.B.; Lovett, G.M.; Baldocchi, D.D.; Clark, D.A.; Harmon, M.E.; Schimel, D.S.; Valentini, R.; et al. Reconciling Carbon-Cycle Concepts, Terminology, and Methods. *Ecosystems* **2006**, *9*, 1041–1050. [CrossRef]
74. Hopkinson, C.S. Net Ecosystem Carbon Balance of Coastal Wetland-Dominated Estuaries: Where's the Blue Carbon? In *A Blue Carbon Primer*; CRC Press: Boca Raton, FL, USA, 2018; ISBN 978-0-429-43536-2.
75. Poungparn, S.; Komiyama, A.; Sangteian, T.; Maknual, C.; Patanaponpaiboon, P.; Suchewaboripont, V. High Primary Productivity under Submerged Soil Raises the Net Ecosystem Productivity of a Secondary Mangrove Forest in Eastern Thailand. *J. Trop. Ecol.* **2012**, *28*, 303–306. [CrossRef]
76. Taillardat, P.; Thompson, B.S.; Garneau, M.; Trottier, K.; Friess, D.A. Climate Change Mitigation Potential of Wetlands and the Cost-Effectiveness of Their Restoration. *Interface Focus.* **2020**, *10*, 20190129. [CrossRef]
77. Troxler, T.G.; Gaiser, E.; Barr, J.; Fuentes, J.D.; Jaffé, R.; Childers, D.L.; Collado-Vides, L.; Rivera-Monroy, V.H.; Castañeda-Moya, E.; Anderson, W.; et al. Integrated Carbon Budget Models for the Everglades Terrestrial-Coastal-Oceanic Gradient: Current Status and Needs for Inter-Site Comparisons. *Oceanography* **2013**, *26*, 98–107. [CrossRef]
78. Twilley, R.; Castañeda-Moya, E.; Rivera-Monroy, V.H.; Rovai, A.S. Chapter 5: Productivity and Carbon Dynamics in Mangrove Wetlands. In *Mangrove Ecosystems: A Global Biogeographic Perspective: Structure, Function, Services*; Springer: Berlin/Heidelberg, Germany, 2017; pp. 113–162.
79. Cheng, Y.; Zha, Y.; Tong, C.; Du, D.; Chen, L.; Wei, G. Estimating the Gaseous Carbon Budget of a Degraded Tidal Wetland. *Ecol. Eng.* **2021**, *160*, 106147. [CrossRef]

80. Howard, J.; Hoyt, S.; Isensee, K.; Pidgeon, E.; Telszewski, M. *Coastal Blue Carbon: Methods for Assessing Carbon Stocks and Emissions Factors in Mangroves, Tidal Salt Marshes, and Seagrass Meadows*; Conservation International, Intergovernmental Oceanographic Commission of UNESCO, International Union for Conservation of Nature: Arlington, VA, USA, 2014.
81. US EPA Inventory of, U.S. *Greenhouse Gas Emissions and Sinks: 1990–2019*; U.S. Environmental Protection Agency: Washington, DC, USA, 2021.
82. Forster, P.; Ramaswamy, V.; Artaxo, P.; Berntsen, T.; Betts, R.; Fahey, D.W.; Haywood, J.; Lean, J.; Lowe, D.C.; Raga, G.; et al. Changes in Atmospheric Constituents and in Radiative Forcing. In *Climate Change 2007: The Physical Science Basis. Contribution of Working Group I to the Fourth Assessment Report of the Intergovernmental Panel on Climate Change*; Solomon, S.D., Qin, D., Manning, M., Chen, Z., Marquis, M., Averyt, K.B., Tignor, M., Miller, H.L., Eds.; Cambridge University Press: Cambridge, UK; New York, NY, USA, 2007; p. 106.
83. IPCC. *Climate Change 2007: The Physical Science Basis: Contribution of Working Group I to the Fourth Assessment Report of the Intergovernmental Panel on Climate Change*; Cambridge University Press: Cambridge, UK; New York, NY, USA, 2007; ISBN 978-0-521-88009-1.
84. Lane, R.R.; Mack, S.K.; Day, J.W.; Kempka, R.; Brady, L.J. Carbon Sequestration at a Forested Wetland Receiving Treated Municipal Effluent. *Wetlands* **2017**, *37*, 861–873. [CrossRef]
85. Clarito, Q.Y.; Suerte, N.O.; Bontia, E.C.; Clarito, I.M. Determining Seagrassess Community Structure Using the Braun—Blanquet Technique in the Intertidal Zones of Islas de Gigantes, Philippines. *SJES* **2020**, *4*, 1–54. [CrossRef]
86. Baustian, M.M.; Liu, B.; Moss, L.C.; Dausman, A.; Pahl, J.W. Climate Change Mitigation Potential of Louisiana's Coastal Area: Current Estimates and Future Projections. *Ecol. Appl.* **2023**, *33*, e2847. [CrossRef] [PubMed]
87. Sasaki, Y. The Truth of the F-Measure. *Teach Tutor Mater* **2007**, *5*, 1–5.
88. IPCC. *2006 IPCC Guidelines for National Greenhouse Gas Inventories*; Prepared by the National Greenhouse Gas Inventories Programme; Institute for Global Environmental Strategies: Hayama, Japan, 2006.
89. IPCC. *2013 Supplement to the 2006 IPCC Guidelines for National Greenhouse Gas Inventories: Wetlands*; IPCC: Geneva, Switzerland, 2014.
90. IPCC. *2019 Refinement to the 2006 IPCC Guidelines for National Greenhouse Gas Inventories*; IPCC: Geneva, Switzerland, 2019.
91. Duan, X.; Wang, X.; Mu, Y.; Ouyang, Z. Seasonal and Diurnal Variations in Methane Emissions from Wuliangsu Lake in Arid Regions of China. *Atmos. Environ.* **2005**, *39*, 4479–4487. [CrossRef]
92. Hirota, M.; Tang, Y.; Hu, Q.; Hirata, S.; Kato, T.; Mo, W.; Cao, G.; Mariko, S. Methane Emissions from Different Vegetation Zones in a Qinghai-Tibetan Plateau Wetland. *Soil Biol. Biochem.* **2004**, *36*, 737–748. [CrossRef]
93. Zhang, M.; Xiao, Q.; Zhang, Z.; Gao, Y.; Zhao, J.; Pu, Y.; Wang, W.; Xiao, W.; Liu, S.; Lee, X. Methane Flux Dynamics in a Submerged Aquatic Vegetation Zone in a Subtropical Lake. *Sci. Total Environ.* **2019**, *672*, 400–409. [CrossRef]
94. Reddy, K.R.; Hu, J.; Villapando, O.; Bhomia, R.K.; Vardanyan, L.; Osborne, T. Long-Term Accumulation of Macro- and Secondary Elements in Subtropical Treatment Wetlands. *Ecosphere* **2021**, *12*, e03787. [CrossRef]
95. Velthuis, M.; Kosten, S.; Aben, R.; Kazanjian, G.; Hilt, S.; Peeters, E.T.H.M.; van Donk, E.; Bakker, E.S. Warming Enhances Sedimentation and Decomposition of Organic Carbon in Shallow Macrophyte-Dominated Systems with Zero Net Effect on Carbon Burial. *Glob. Chang. Biol.* **2018**, *24*, 5231–5242. [CrossRef]
96. DeMarco, K.E.; Hillmann, E.R.; Nyman, J.A.; Couvillion, B.; La Peyre, M.K. Defining Aquatic Habitat Zones Across Northern Gulf of Mexico Estuarine Gradients through Submerged Aquatic Vegetation Species Assemblage and Biomass Data. *Estuar. Coasts* **2022**, *45*, 148–167. [CrossRef]
97. Taylor, C.; Nyman, J.; La Peyre, M. Nekton Community Dynamics within Active and Inactive Deltas in a Major River Estuary: Potential Implications for Altered Hydrology Regimes. *Aquat. Biol.* **2022**, *31*, 1–18. [CrossRef]
98. O'Connell, J.L.; Nyman, J.A. Marsh Terraces in Coastal Louisiana Increase Marsh Edge and Densities of Waterbirds. *Wetlands* **2010**, *30*, 125–135. [CrossRef]
99. Hillmann, E.; DeMarco, K.; La Peyre, M. Salinity and Water Clarity Dictate Seasonal Variability in Coastal Submerged Aquatic Vegetation in Subtropical Estuarine Environments. *Aquat. Biol.* **2019**, *28*, 175–186. [CrossRef]
100. La Peyre, M.K.; Gossman, B.; Nyman, J.A. Assessing Functional Equivalency of Nekton Habitat in Enhanced Habitats: Comparison of Terraced and Unterraced Marsh Ponds. *Estuar. Coasts* **2007**, *30*, 526–536. [CrossRef]
101. Poffenbarger, H.J.; Needelman, B.A.; Megonigal, J.P. Salinity Influence on Methane Emissions from Tidal Marshes. *Wetlands* **2011**, *31*, 831–842. [CrossRef]
102. Weston, N.B.; Neubauer, S.C.; Velinsky, D.J.; Vile, M.A. Net Ecosystem Carbon Exchange and the Greenhouse Gas Balance of Tidal Marshes along an Estuarine Salinity Gradient. *Biogeochemistry* **2014**, *120*, 163–189. [CrossRef]
103. Dang, K.B.; Nguyen, M.H.; Nguyen, D.A.; Phan, T.T.H.; Giang, T.L.; Pham, H.H.; Nguyen, T.N.; Tran, T.T.V.; Bui, D.T. Coastal Wetland Classification with Deep U-Net Convolutional Networks and Sentinel-2 Imagery: A Case Study at the Tien Yen Estuary of Vietnam. *Remote Sens.* **2020**, *12*, 3270. [CrossRef]
104. Le, Q.T.; Dang, K.B.; Giang, T.L.; Tong, T.H.A.; Nguyen, V.G.; Nguyen, T.D.L.; Yasir, M. Deep Learning Model Development for Detecting Coffee Tree Changes Based on Sentinel-2 Imagery in Vietnam. *IEEE Access* **2022**, *10*, 109097. [CrossRef]
105. Brownlee, J. *Better Deep Learning: Train Faster, Reduce Overfitting, and Make Better Predictions*; Machine Learning Mastery: Melbourne, VIC, Australia, 2018.
106. Li, H.; Li, J.; Guan, X.; Liang, B.; Lai, Y.; Luo, X. Research on Overfitting of Deep Learning. In Proceedings of the 2019 15th International Conference on Computational Intelligence and Security (CIS), Macao, China, 13–16 December 2019; IEEE: Macao, China, 2019; pp. 78–81.

107. Liu, B.; D'Sa, E.J.; Messina, F.; Baustian, M.M.; Maiti, K.; Rivera-Monroy, V.; Huang, W.; Georgiou, I.Y. Dissolved organic carbon dynamics and fluxes in Mississippi-Atchafalaya deltaic system impacted by an extreme flood event and hurricanes: A multi-satellite approach using Sentinel-2/3 and Landsat-8/9 Data. *Front. Mar. Sci.* **2023**, *10*, 1159367. [CrossRef]
108. Huang, W.; Li, C. Contrasting Hydrodynamic Responses to Atmospheric Systems with Different Scales: Impact of Cold Fronts vs. That of a Hurricane. *J. Mar. Sci. Eng.* **2020**, *8*, 979. [CrossRef]
109. Cloern, J.E.; Abreu, P.C.; Carstensen, J.; Chauvaud, L.; Elmgren, R.; Grall, J.; Greening, H.; Johansson, J.O.R.; Kahru, M.; Sherwood, E.T.; et al. Human activities and climate variability drive fast-paced change across the world's estuarine–coastal ecosystems. *Glob. Chang. Biol.* **2016**, *22*, 513–529. [CrossRef] [PubMed]
110. Beven, J.L.; Hagen, A.; Berg, R. *National Hurricane Center Tropical Cyclone Report: Hurricane Ida (AL092021)*; AL092021 National Hurricane Center: Miami, FL, USA, 2021. Available online: www.nhc.noaa.gov/data (accessed on 29 August 2021).
111. Kinney, E.L.; Quigg, A.; Armitage, A.R. Acute Effects of Drought on Emergent and Aquatic Communities in a Brackish Marsh. *Estuar. Coasts* **2014**, *37*, 636–645. [CrossRef]
112. Lou, S.; Huang, W.; Liu, S.; Zhong, G.; Johnson, E. Hurricane Impacts on Turbidity and Sediment in the Rookery Bay National Estuarine Research Reserve, Florida, USA. *Int. J. Sediment Res.* **2016**, *31*, 330–340. [CrossRef]
113. Morton, R.A.; Barras, J.A. Hurricane Impacts on Coastal Wetlands: A Half-Century Record of Storm-Generated Features from Southern Louisiana. *J. Coast Res.* **2011**, *275*, 27–43. [CrossRef]
114. Frazer, T.K.; Notestein, S.K.; Jacoby, C.A.; Littles, C.J.; Keller, S.R.; Swett, R.A. Effects of Storm-Induced Salinity Changes on Submersed Aquatic Vegetation in Kings Bay, Florida. *Estuar. Coasts* **2006**, *29*, 943–953. [CrossRef]
115. Pendleton, L.; Donato, D.C.; Murray, B.C.; Crooks, S.; Jenkins, W.A.; Sifleet, S.; Craft, C.B.; Fourqurean, J.W.; Kauffman, J.B.; Marbà, N.; et al. Estimating Global "Blue Carbon" Emissions from Conversion and Degradation of Vegetated Coastal Ecosystems. *PLoS ONE* **2012**, *7*, e43542. [CrossRef]
116. Sapkota, Y.; White, J.R. Marsh Edge Erosion and Associated Carbon Dynamics in Coastal Louisiana: A Proxy for Future Wetland-Dominated Coastlines World-Wide. *Estuar. Coast Shelf. Sci.* **2019**, *226*, 106289. [CrossRef]
117. Schoolmaster, D.R.; Stagg, C.L.; Creamer, C.; Laurenzano, C.; Ward, E.; Waldrop, M.; Baustian, M.M.; Aw, T.; Merino, S.; Villani, R.; et al. A Model of the Spatiotemporal Dynamics of Soil Carbon Following Coastal Wetland Loss Applied to a Louisiana Salt Marsh in the Mississippi River Deltaic Plain. *J. Geophys. Res. Biogeosci.* **2022**, *127*, e2022JG006807. [CrossRef]
118. Bos, A.R.; Bouma, T.J.; de Kort, G.L.J.; van Katwijk, M.M. Ecosystem Engineering by Annual Intertidal Seagrass Beds: Sediment Accretion and Modification. *Estuar. Coast Shelf. Sci.* **2007**, *74*, 344–348. [CrossRef]
119. Gacia, E.; Duarte, C.M.; Middelburg, J.J. Carbon and Nutrient Deposition in a Mediterranean Seagrass (*Posidonia oceanica*) Meadow. *Limnol. Oceanogr.* **2002**, *47*, 23–32. [CrossRef]
120. Alongi, D.M. Carbon Balance in Salt Marsh and Mangrove Ecosystems: A Global Synthesis. *J. Mar. Sci. Eng.* **2020**, *8*, 767. [CrossRef]
121. Al-Haj, A.N.; Fulweiler, R.W. A Synthesis of Methane Emissions from Shallow Vegetated Coastal Ecosystems. *Glob. Chang. Biol.* **2020**, *26*, 2988–3005. [CrossRef] [PubMed]
122. Myhre, G.; Shindell, D.; Bréon, F.M.; Collins, W.; Fuglestvedt, J.; Huang, J.; Koch, D.; Lamarque, J.F.; Lee, D.; Mendoza, B. *Anthropogenic and Natural Radiative Forcing, Climate Change 2013: The Physical Science Basis. Contribution of Working Group I to the Fifth Assessment Report of the Intergovernmental Panel on Climate Change, 659–740*; Cambridge University Press: Cambridge, UK, 2013.
123. Franz, D.; Koebsch, F.; Larmanou, E.; Augustin, J.; Sachs, T. High Net CO_2 and CH_4 Release at a Eutrophic Shallow Lake on a Formerly Drained Fen. *Biogeosciences* **2016**, *13*, 3051–3070. [CrossRef]

Disclaimer/Publisher's Note: The statements, opinions and data contained in all publications are solely those of the individual author(s) and contributor(s) and not of MDPI and/or the editor(s). MDPI and/or the editor(s) disclaim responsibility for any injury to people or property resulting from any ideas, methods, instructions or products referred to in the content.

atmosphere

MDPI

Article

Vegetation Identification in Hyperspectral Images Using Distance/Correlation Metrics

Gabriel E. Chanchí Golondrino *, Manuel A. Ospina Alarcón and Manuel Saba

Faculty of Engineering, University of Cartagena, Cartagena de Indias 130015, Colombia; mospinaa@unicartagena.edu.co (M.A.O.A.); msaba@unicartagena.edu.co (M.S.)
* Correspondence: gchanchig@unicartagena.edu.co

Abstract: Distance/correlation metrics have emerged as a robust and simplified tool for assessing the spectral characteristics of hyperspectral image pixels and effectively categorizing vegetation within a specific study area. Correlation methods provide a readily deployable and computationally efficient approach, rendering them particularly advantageous for applications in developing nations or regions with limited resources. This article presents a comparative investigation of correlation/distance metrics for the identification of vegetation pixels in hyperspectral imagery. The study facilitates a comprehensive evaluation of five distance and/or correlation metrics, namely, direct correlation, cosine similarity, normalized Euclidean distance, Bray–Curtis distance, and Pearson correlation. Direct correlation and Pearson correlation emerged as the two metrics that demonstrated the highest accuracy in vegetation pixel identification. Using the selected methodologies, a vegetation detection algorithm was implemented and validated using a hyperspectral image of the Manga neighborhood in Cartagena de Indias, Colombia. The spectral library facilitated image processing, while the mathematical calculation of correlations was performed using the numpy and scipy libraries in the Python programming language. Both the approach adopted in this study and the implemented algorithm aim to serve as a point of reference for conducting detection studies on diverse material types in hyperspectral imagery using open-access programming platforms.

Keywords: distance-based method; urban vegetation; vegetation clustering; vegetation classification

Citation: Chanchí Golondrino, G.E.; Ospina Alarcón, M.A.; Saba, M. Vegetation Identification in Hyperspectral Images Using Distance/Correlation Metrics. *Atmosphere* **2023**, *14*, 1148. https://doi.org/10.3390/atmos14071148

Academic Editor: Riccardo Buccolieri

Received: 28 May 2023
Revised: 30 June 2023
Accepted: 12 July 2023
Published: 14 July 2023

Copyright: © 2023 by the authors. Licensee MDPI, Basel, Switzerland. This article is an open access article distributed under the terms and conditions of the Creative Commons Attribution (CC BY) license (https://creativecommons.org/licenses/by/4.0/).

1. Introduction

Remote sensing technology has revolutionized the field of vegetation mapping and monitoring, providing a powerful tool for scientists and researchers to study and understand complex terrestrial ecosystems [1–4]. The ability to obtain high-resolution images of the Earth's surface from satellites, aircraft, and drones has transformed the way humans perceive and analyze vegetation patterns, providing insights into the distribution, structure, and health of plant communities across different regions and biomes [1,5–10].

Despite the significant advances in remote sensing technology over the past few decades, the identification of vegetation in multi- and hyperspectral images remains a challenging task due to the complex spectral signatures of different plant species, as well as the influence of environmental factors, such as soil, water, and atmospheric conditions [11]. Traditional methods for vegetation mapping using remote sensing involve the interpretation of spectral indices, such as the Normalized Difference Vegetation Index (NDVI), which provide a measure of the vegetation cover based on the contrast between the red and near-infrared bands of the electromagnetic spectrum [9,12–21].

While these methods have proven to be effective in many applications, they suffer from several limitations, including the need for manual interpretation and the limited spatial resolution of satellite images. Moreover, traditional methods are often time-consuming and costly, requiring extensive field surveys and ground truth data to calibrate and validate the results [11,22,23].

To overcome these challenges, machine learning techniques have emerged as a promising approach for vegetation mapping and classification, offering a cost-effective and accurate solution for remote sensing applications, especially in developing countries. Machine learning algorithms can analyze vast amounts of hyperspectral data and identify patterns and features that are difficult or impossible to discern through human interpretation, allowing for the automated and objective detection of vegetation cover. The use of machine learning applications in vegetation mapping has been on the rise in recent years [24–26], driven by the availability of large hyperspectral datasets and the development of advanced algorithms and computational tools. Machine learning techniques, such as artificial neural networks [27–29], decision trees [30,31], support vector machines [32], and random forests [33,34], have shown promising results in identifying and classifying vegetation cover from hyperspectral images, offering a more robust, reliable, and cost-effective solution for remote sensing applications.

In addition to machine learning techniques, correlation methods between curves have emerged as another powerful tool for comparing spectral signatures of hyperspectral image pixels and efficiently classifying vegetation in a study area. Spectral signatures are graphical representations of the reflectance values of an object or material across the electromagnetic spectrum. In the context of vegetation mapping, spectral signatures can be used to identify different plant species or vegetation types based on their unique spectral properties [35]. Correlation methods between curves can be used to compare the spectral signatures of different pixels in a hyperspectral image and identify similarities or differences in their spectral properties. Among the most common correlation methods used in vegetation mapping are Pearson's correlation coefficient and spectral angle mapper, among many other methods available [30,36].

Pearson's correlation coefficient measures the linear relationship between the two sets of data and ranges from -1 to 1, with values closer to 1 indicating a strong positive correlation between the two sets of data. In vegetation mapping, Pearson's correlation coefficient can be used to compare the spectral signatures of different pixels and identify areas with similar vegetation cover [37,38].

On the other hand, the spectral angle mapper measures the angular similarity between two spectral signatures and ranges from 0 to 1, with values closer to 1 indicating a high degree of spectral similarity between the two signatures. The spectral angle mapper can be used to compare the spectral signatures of different pixels and identify areas with similar vegetation [30,39,40].

These correlations offer a complementary approach to machine learning techniques. Moreover, these correlation methods can be easily implemented and computationally efficient, making them particularly useful for applications in developing countries or regions with limited resources.

The need to efficiently classify vegetation in a study area using remote sensing technology has led to the development of various methods for comparing spectral signatures of hyperspectral image pixels. The focus of the present work is to determine the best distance/correlation-based method for vegetation detection in hyperspectral images with 380 bands from 400 nm to 2400 nm in an urban area through five different correlation methods, "Correlation methods", "Cosine" "Euclidean", "Bray Curtis", and "Pearson" [41–45].

2. Methodology

For the development of this research, the following 5 methodological phases were considered (Figure 1): identification of reference pixels, obtaining the average or characteristic pixel, determination of distance/correlation metrics, selection of the best metrics, and detection of vegetation in the reference image.

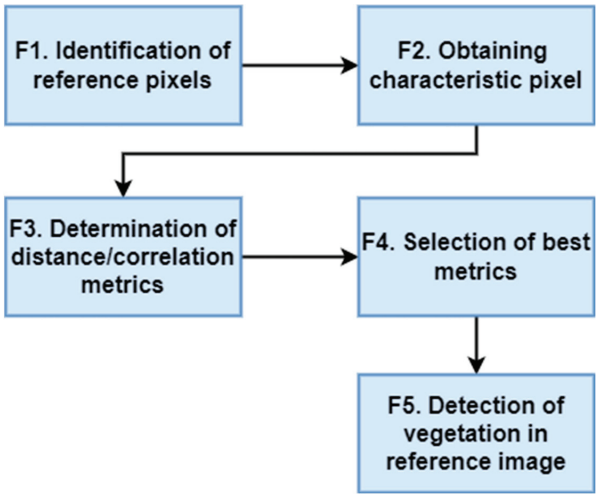


Figure 1. The figure depicts the methodology utilized in the study.

According to Figure 1, in phase 1 of the methodology, a set of 100 coordinates corresponding to vegetation pixels and a set of 100 coordinates corresponding to non-vegetation pixels (roofs, roads, sea, and containers) were obtained manually from the reference image, in order to compare the accuracy of the different distance and correlation metrics in both sets. In phase 2 of the methodology, descriptive statistics were used to determine the characteristic pixel or average pixel. The mean was employed as a measure of central tendency by averaging the 380 positions (frequency bands spanning from 400 nm to 2400 nm) of the 100 vegetation pixels. The aim was for the characteristic pixel to collect, across its 380 positions, the average information from the different frequency bands. Once the characteristic pixel is obtained, in phase 3 of the methodology, the calculation of the distance/correlation metrics between the average pixel and the vegetation and non-vegetation sets is performed, in order to determine the precision of each metric. The 5 distance/correlation metrics used in this phase were direct correlation (correlation distance), similarity or cosine distance, normalized Euclidean distance, Bray–Curtis distance (also known as Normalized Manhattan distance), and Pearson's correlation coefficient. The mathematical description of each of these metrics is presented below.

Direct correlation: It is a measure of dependence between two paired random variables (vectors) of arbitrary dimension, not necessarily equal. That is, it calculates the correlation distance between two one-dimensional arrays. The correlation distance between two vectors $\vec{u}$ and $\vec{v}$ is defined as [41], Equation (1):

$$d_{(\vec{u},\vec{v})} = 1 - \frac{(\vec{u} - \overline{\vec{u}})\cdot(\vec{v} - \overline{\vec{v}})}{\|\vec{u} - \overline{\vec{u}}\|^2 \|\vec{v} - \overline{\vec{v}}\|^2} \quad (1)$$

where $\overline{\vec{u}}$ and $\overline{\vec{v}}$ are the means of the elements of $\vec{u}$ and $\vec{v}$, $(\vec{u} - \overline{\vec{u}})\cdot(\vec{v} - \overline{\vec{v}})$ is the scalar product, and $\|\vec{u} - \overline{\vec{u}}\|^2$ is its norm or variance.

Similarity or cosine distance: It is a measure of similarity between two non-zero vectors defined in an inner product space. The cosine distance is the cosine of the angle between the vectors. It is the scalar product of the vectors divided by the product of their lengths. It differs from direct correlation as it circumvents the utilization of the arithmetic mean or

average of the vectors under examination. The cosine distance, ascribed as the disparity between two vectors $\vec{u}$ and $\vec{v}$, is rigorously delineated as [45], Equation (2):

$$d_{(\vec{u},\vec{v})} = 1 - \frac{\vec{u}\cdot\vec{v}}{\|\vec{u}\|^2\|\vec{v}\|^2} \tag{2}$$

where $\vec{u}\cdot\vec{v}$ is the scalar product and $\|\vec{u}\|^2$ is its norm.

Normalized Euclidean Distance: It gives the squared distance between two vectors, where the lengths have been scaled to have a unit norm. This is useful when the direction of the vector is significant but the magnitude is not [43]. According to [43], the normalized Euclidean distance of two vectors is defined by Equation (3):

$$NED^2_{(\vec{u},\vec{v})} = \frac{1}{2}\cdot\frac{\|(\vec{u}-\overline{\vec{u}})-(\vec{v}-\overline{\vec{v}})\|^2}{(\|(\vec{u}-\overline{\vec{u}})\|^2+\|(\vec{v}-\overline{\vec{v}})\|^2)} = 0.5\frac{var(\vec{u}-\vec{v})}{var(\vec{u})+var(\vec{v})} \tag{3}$$

where $\overline{\vec{u}}$ and $\overline{\vec{v}}$ are the means of the elements of $\vec{u}$ and $\vec{v}$ and $\|\ \|^2$ is the variance.

Bray–Curtis distance: The Bray–Curtis distance is a normalization method commonly used in the field of botany, ecology, and environmental sciences [44]. It is a statistic used to quantify the compositional dissimilarity between two different sites, based on counts at each site. It is defined by Equation (4) [44]:

$$d_{(\vec{u},\vec{v})} = \frac{\sum_{i=1}^{n}(u_i - v_i)}{\sum_{i=1}^{n}(u_i + v_i)} \tag{4}$$

where n is the size of the vectors or sample. The Bray–Curtis distance is in the range [0, 1] if all coordinates are positive and is undefined if the entries are of length zero.

Pearson correlation coefficient: It is a measure of linear dependence between two quantitative random variables (vectors). Unlike covariance, Pearson's correlation is independent of the scale of measurement of the variables [41]. Pearson's population correlation coefficient (also denoted by $r_{(\vec{u},\vec{v})}$) is defined as [43], Equation (5):

$$r_{(\vec{u},\vec{v})} = \frac{\sigma_{(\vec{u},\vec{v})}}{\sigma_{\vec{u}}\cdot\sigma_{\vec{v}}} = \frac{\sum_{i=1}^{n}(u_i-\overline{\vec{u}})\cdot(v_i-\overline{\vec{v}})}{\sqrt{\sum_{i=1}^{n}(u_i-\overline{\vec{u}})^2}\cdot\sqrt{\sum_{i=1}^{n}(v_i-\overline{\vec{v}})^2}} \tag{5}$$

where n is the sample size, $\sigma_{(\vec{u},\vec{v})}$ is the covariance of $(\vec{u},\vec{v})$, $\sigma_{\vec{u}}$ is the standard deviation of vector $\vec{u}$, $\sigma_{\vec{v}}$ is the standard deviation of vector $\vec{v}$, and $\overline{\vec{u}}$ and $\overline{\vec{v}}$ are the means of $\vec{u}$ and $\vec{v}$, respectively.

Based on the previous equations corresponding to correlation metrics and considering that these metrics have values close to 0 when the correlation is high, Equation (6) was proposed to obtain a percentage of correlation or similarity.

$$porc_corr = (1 - abs(corr))\cdot 100 \tag{6}$$

In phase 4 of the methodology, the results obtained by calculating the correlations and similarities described in phase 3 were consolidated in relation to vegetation and non-vegetation pixels. The aim was to determine the precision thresholds for the correlation percentages of each metric in both cases, in order to identify the best metrics to be used in vegetation detection. These metrics are the ones that best classify a pixel as vegetation. Finally, in phase 5, the vegetation detection process was performed on the entire hyperspectral reference image using the selected similarity and/or correlation metrics.

The study area of the present work is shown in Figure 2. It is the Manga neighborhood in the city of Cartagena de Indias, Colombia. Regarding the hyperspectral image, it measures 1500 × 1500 pixels with 380 bands per pixel ranging from 400 nm to 2400 nm. A total of 100 arbitrary vegetation pixels were extracted from various locations across the image. The purpose is to obtain a representative or characteristic pixel by averaging the corresponding spectral signatures of the 100 pixels. This representative pixel was used to compare the correlation and similarity metrics described above. Thus, in Figure 2, the vegetation pixels are shown in blue, while the non-vegetation pixels are shown in red.

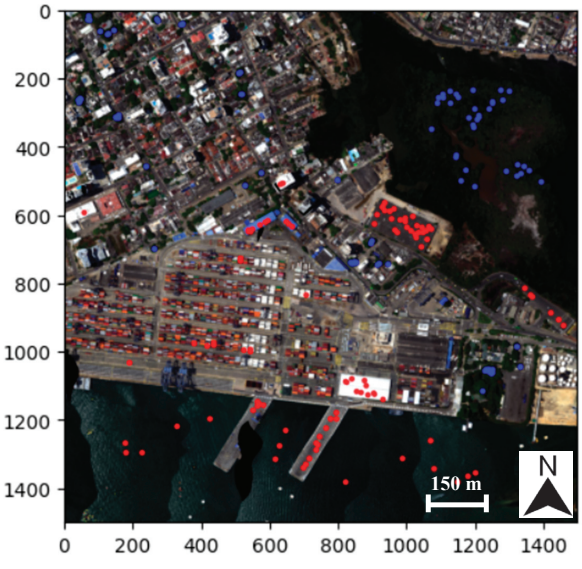


Figure 2. Hyperspectral image used in the present study, in blue vegetation pixels and in red non-vegetation pixels.

3. Results and Discussion

In Figure 3a, the spectral signatures of the selected 100 pixels and their distribution across 380 bands can be observed. It is possible to appreciate that although the reflectance values exhibit variations, the shape of the 100 curves remains the same. They possess a set of peaks that are repeated in a similar manner across different pixels. Similarly, in Figure 3b, the spectral signature corresponding to the zone of no vegetation is presented. Finally, in Figure 3c, the spectral signature corresponding to the characteristic or average pixel can be observed. This pixel is obtained by averaging the curves of the 100 pixels, incorporating the representative maximum and minimum values of the considered sample. The image reading and processing of the different pixels that compose it were performed using the functionalities provided by the Python spectral library. By employing an average pixel normalization approach, it was ascertained that the incorporation of over 100 pixels did not result in significant modifications to the mean pixel value.

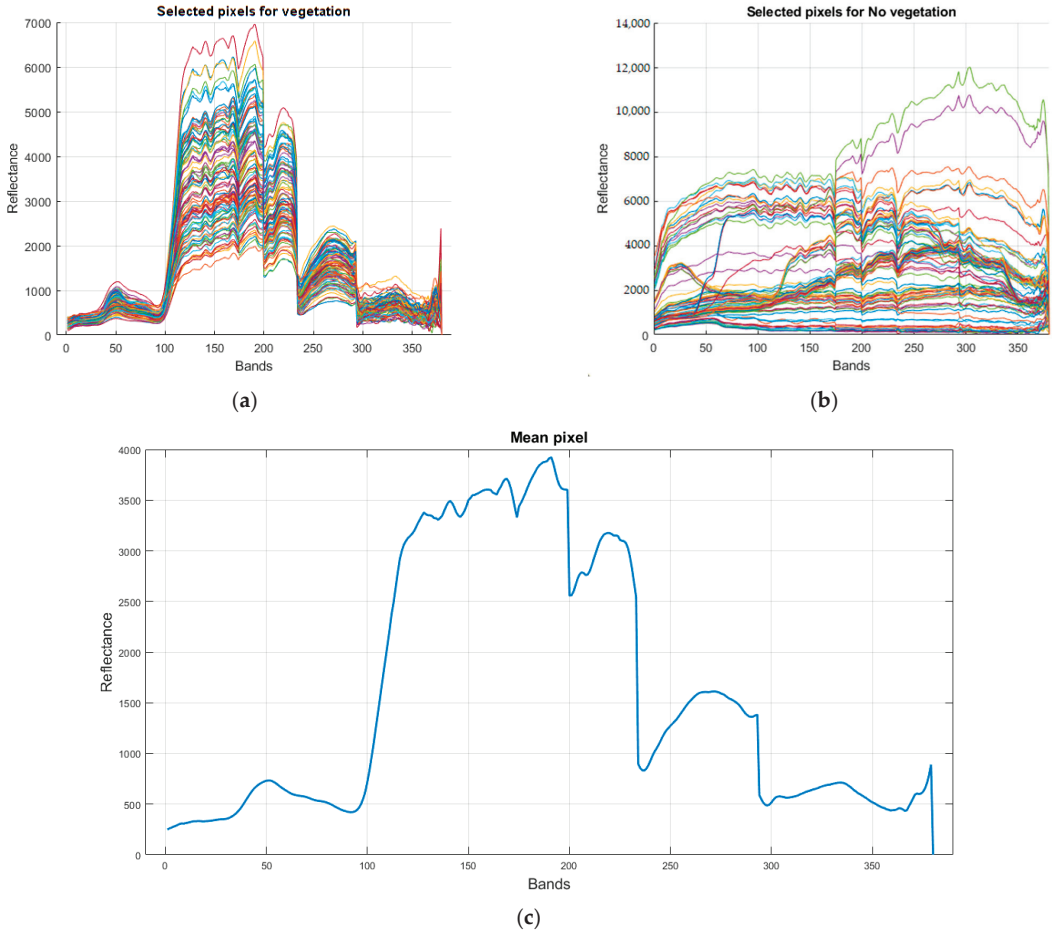


Figure 3. Pixels selected for comparative study: (**a**) vegetation, (**b**) non-vegetation, and (**c**) mean pixel for vegetation.

Based on the above, initially, the representative or average pixel was correlated with each of the 100 selected vegetation pixels using the five metrics considered in Section 2. This was completed to determine both the average and the thresholds obtained for each metric, which helps to identify the most accurate and effective method for identifying the vegetation's spectral signature. For this purpose, the authors started with the idea that each pixel in the image is a vector representation in space. In other words, each pixel is a vector with 380 positions corresponding to the 380 bands, each of which stores a reflectance value. By performing vector operations using the numpy library and the statistical tool from scipy between the average pixel and the 100 vegetation pixels, the bar chart presented in Figure 4 displays the minimum, mean, and maximum values obtained for each of the five metrics considered, as well as the respective standard deviation value for the mean.

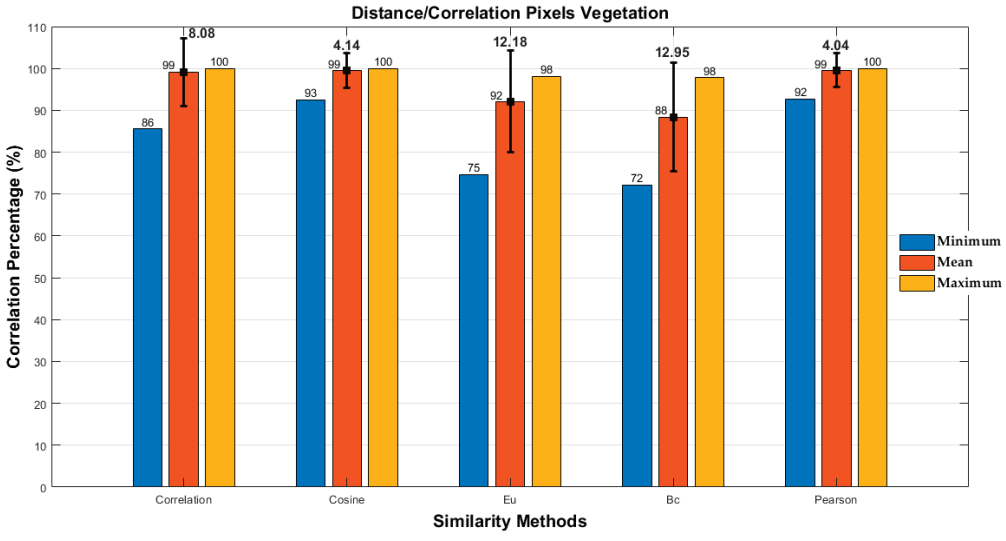


Figure 4. Result of the comparative study of similarity or correlation methods in vegetation pixels.

In Figure 4, it is possible to observe that Pearson correlation, cosine distance, and direct correlation are the metrics that respectively present the highest average values of correlation percentage between the average pixel and the 100 vegetation pixels, with respective values of 99.54%, 99.47%, and 99.09%. Similarly, it can be appreciated that these same three metrics, in the same order, present the highest minimum percentage values of correlation between the average pixel and the 100 vegetation pixels, with respective values of 92.77%, 92.55%, and 85.53%. On the other hand, upon consolidating and comparing the threshold values of these three top metrics, it is possible to observe that the metric with the smallest difference between the maximum and minimum thresholds is Pearson correlation with a difference of 7.2%, followed by cosine distance with a difference of 7.41%.

Once the 100 vegetation pixels were studied, the correlation between the average pixel and the 100 randomly selected non-vegetation pixels was performed using the same five metrics and following a similar procedure as with the vegetation pixels. Hence, by conducting vector operations using the same Python libraries between the average pixel and the 100 non-vegetation pixels, the bar chart in Figure 5 presents the minimum, mean, and maximum values for the five studied metrics, as well as the respective standard deviation value for the mean.

According to Figure 5, it is possible to observe that direct correlation, Bray–Curtis distance (Bc), and Pearson correlation are the metrics that respectively present the lowest average values of correlation percentage between the average pixel and the 100 non-vegetation pixels, with respective values of 31.24%, 56.81%, and 65.62%. Similarly, in Figure 5, it can be appreciated that Bray–Curtis distance (Bc), direct correlation, and Euclidean distance (Eu) are the metrics that respectively present the lowest maximum values of correlation percentage between the average pixel and the 100 non-vegetation pixels, with respective values of 74.24%, 78.52%, and 82.09%. It is also important to mention that cosine distance and Pearson correlation, which showed the two best results for vegetation pixels in this case, have the two highest maximum percentages for non-vegetation pixels with values of 90.12% and 89.26%, respectively. Although these values do not surpass the minimum threshold detected with vegetation pixels, they are close to a difference of 2.43% and 3.51% from the minimum threshold in vegetation pixels.

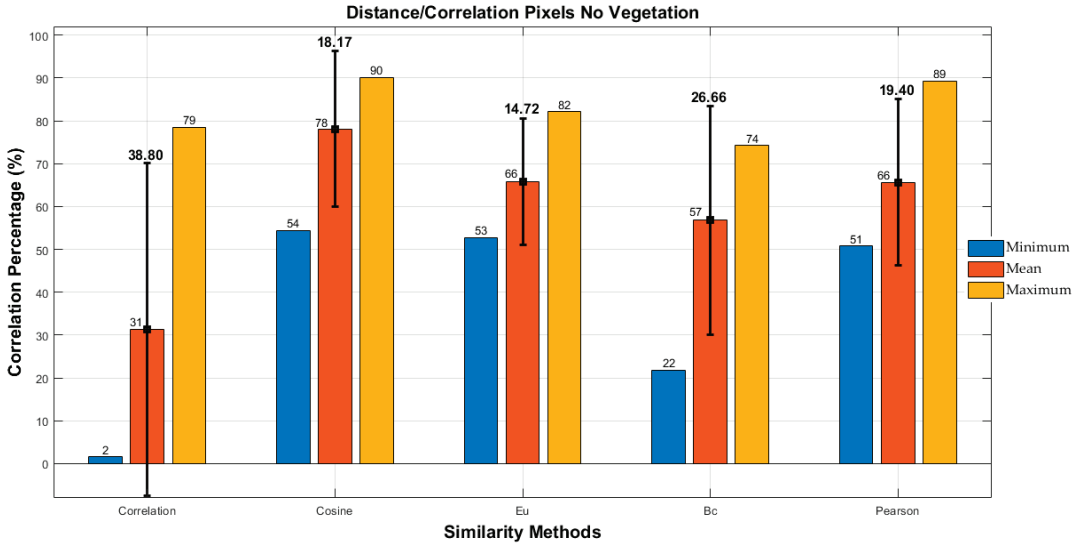


Figure 5. Result of the comparative study of similarity or correlation methods in non-vegetation pixels.

Continuing with the comparison between the results of correlation in vegetation and non-vegetation pixels, Figure 6 presents a comparative graph that shows, for each of the five considered metrics, the minimum correlation percentage value for vegetation and the maximum correlation percentage value for non-vegetation. It can be observed initially that Euclidean distance (Eu) and Bray–Curtis distance (Bc) metrics exhibit an overlap between these thresholds (the maximum value is greater than the minimum value, indicating a negative difference). This implies that applying these methods to the image may lead to confusion between vegetation and non-vegetation pixels. On the other hand, it is evident that the three metrics without overlap between the thresholds are direct correlation, cosine distance, and Pearson correlation. Among them, direct correlation shows the greatest difference between the thresholds (limits), with a percentage difference value of 7.01%.

In Figure 6, it is possible to verify how the overlap of thresholds in the Euclidean distance and Bray–Curtis distance metrics is evidenced by the negative difference between the minimum correlation percentage in vegetation pixels and the maximum correlation percentage in non-vegetation pixels. Similarly, it can be observed that the best results are respectively obtained for the direct correlation and Pearson correlation metrics, with percentage difference values of 7.01% and 3.51%. It is worth mentioning that these metrics are also among the top three metrics with the highest average correlation percentage in vegetation pixels. Therefore, based on the results, they represent the best options for vegetation detection in hyperspectral images.

According to the previous analysis, Figure 7 presents the results of applying the direct correlation and Pearson correlation methods to the hyperspectral image of the Manga neighborhood in Cartagena. This was completed using the spectral library in Python and considering a threshold correlation percentage of 95%. In this regard, the implemented vegetation detection algorithm traverses each pixel of the image matrix, correlating each pixel of the image (a 380 positions vector) with the average vegetation pixel (380 positions) using direct correlation and Pearson correlation to determine the correlation percentage. If the correlation percentage is greater than 98%, the corresponding pixel in the displayed image is colored blue. Visually, it can be observed that in both cases, the detection algorithm adequately identifies the regions where vegetation is present, and the density of the detected vegetation pixels depends on the threshold adjustment for each correlation.

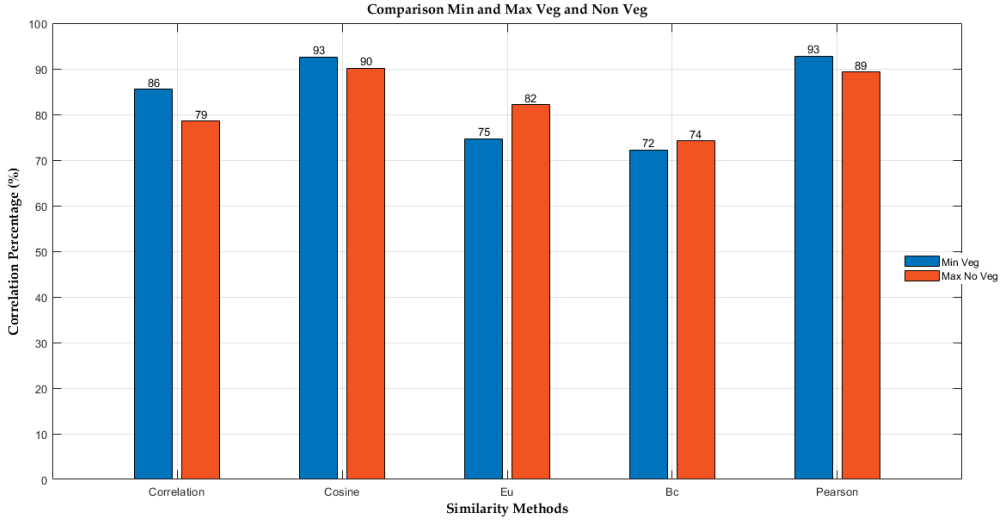
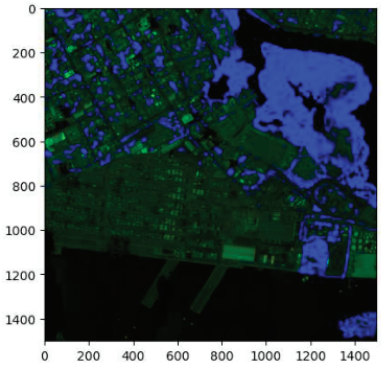


Figure 6. Comparison between minimum and maximum thresholds in vegetation and non-vegetation pixels.

```
In [26]: arr_copia=np.copy(arr)
         tam=arr.shape
         cont_corr=0
         for i in range (0, tam[0]):
             for j in range(0,tam[1]):
                 arr_temp=arr[i,j,:]
                 nz=arr_temp.size - np.count_nonzero(arr_temp)
                 if(nz!=380):
                     corr=ssd.correlation(pix_prom,arr_temp)
                     porc=(1-corr)*100
                     if(porc>95.0):
                         arr_copia[i][j]=150
                         cont_corr+=1

In [27]: view=imshow(arr_copia)
         view

Out[27]: ImageView object:
           Display bands       :  [0, 190.0, 379]
           Interpolation       :  <default>
           RGB data limits     :
             R: [0.0, 14968.0]
             G: [0.0, 15000.0]
             B: [0.0, 150.0]
```




```
In [28]: arr_copia=np.copy(arr)
         tam=arr.shape
         cont_pear=0
         for i in range (0, tam[0]):
             for j in range(0,tam[1]):
                 arr_temp=arr[i,j,:]
                 nz=arr_temp.size - np.count_nonzero(arr_temp)
                 if(nz!=380):
                     corr_pr=np.corrcoef(pix_prom, arr_temp)
                     mean_pr=np.mean(np.absolute(corr_pr))
                     porc=mean_pr*100
                     if(porc>95.0):
                         arr_copia[i][j]=150
                         cont_pear+=1

In [29]: view=imshow(arr_copia)
         view

Out[29]: ImageView object:
           Display bands       :  [0, 190.0, 379]
           Interpolation       :  <default>
           RGB data limits     :
             R: [0.0, 14968.0]
             G: [0.0, 15000.0]
             B: [0.0, 150.0]
```

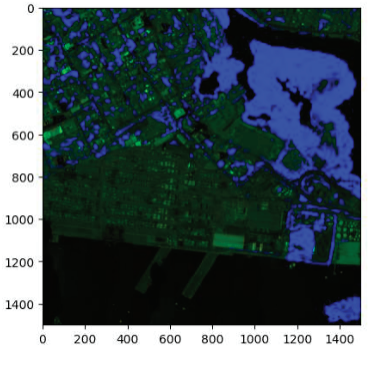


Figure 7. Application of direct correlation and Pearson correlation metrics on the hyperspectral test image.

Finally, by performing a count on the vegetation pixels of the hyperspectral image of the Manga neighborhood that were detected by the algorithm based on correlation metrics, Pearson correlation, and cosine distance, with a 95% threshold, the percentages of detected vegetation were obtained, as presented in Figure 8. It can be observed that, according to the results obtained by the considered metrics, between 15% and 17% of the pixels correspond to vegetation within the hyperspectral image.

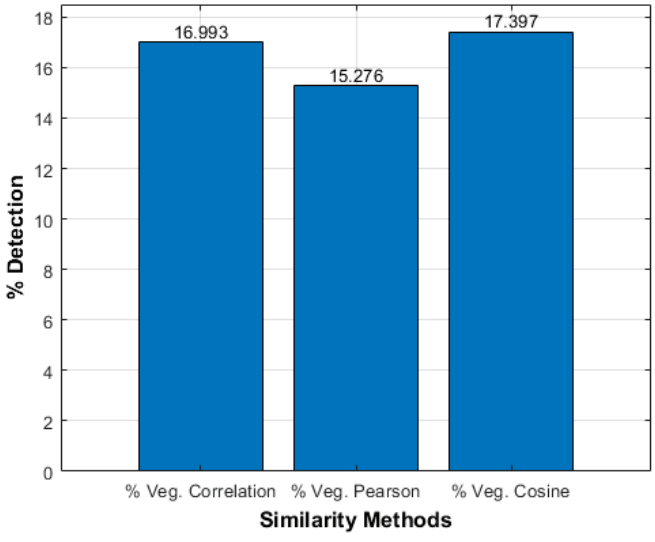


Figure 8. % Vegetation detection.

The present study introduces a novel approach to identify vegetation in hyperspectral images. This research offers valuable insights into the field of remote sensing and image analysis by utilizing distance and correlation metrics. The significance of this study is particularly relevant for developing countries, as it highlights the importance of open-access programming platforms for analyzing hyperspectral images. Accessible tools enable these countries to harness the potential of hyperspectral data, aiding in land monitoring, agricultural management, and environmental conservation efforts.

From a scientific standpoint, in relation to conducting research involving proprietary tools like Environment for Visualising Images Software (ENVI) for analyzing hyperspectral images [46,47], the utilization of open-source technologies like spectral, numpy, and other machine learning libraries such as scikit-learn enables the development of unhindered technological solutions capable of addressing specific remote sensing needs. This approach facilitates the integration of diverse artificial intelligence techniques, exemplifying its potential. These open-source tools allow for the implementation of unrestricted technological solutions that can cater to the unique requirements of remote sensing applications [48], thereby enhancing the accuracy, efficiency, and robustness of the hyperspectral and multispectral image analysis process.

Torres-Gil et al. [11] present distinct spectral signatures (asbestos, oil, soil, and vegetation) suggesting to analyze curve peaks as a viable approach for material detection and similarity determination. According to this, the present study has yielded empirical evidence supporting the effectiveness of the correlation method for comparing curve peaks. This effectiveness stems from the ability to attain a substantial spatial correlation by identifying points of alignment in both the highest and lowest peaks among the curves. However, the findings of the present research indicate that restricting the analysis to specific bands alone is inadequate for comparing the curves comprehensively. It is advisable to perform a correlation analysis between pixels employing the maximum feasible number of

bands, while also considering not only the utmost and lowest points but also the points of inflection.

Ultimately, concerning the techniques employed for vegetation analysis in hyperspectral image processing, specifically the normalized spectral mixture method as outlined in [49], our research introduces an alternative approach that incorporates representative pixel and correlation methods, facilitating the identification and characterization of vegetation in a broader sense. In contrast, the normalized spectral mixture method demonstrates enhanced precision in detecting objects exhibiting greater homogeneity or possessing a higher degree of purity. Consequently, the proposed methodology in our study can find practical application in urban environmental studies, specifically in investigating the correlation between overall green areas and population size. By incorporating the representative pixel and correlation techniques, our approach offers a comprehensive means of discerning vegetative elements within hyperspectral imagery. This methodology surpasses the limitations of solely relying on the normalized spectral mixture method, which primarily excels in detecting homogeneous and pure objects. Therefore, the methodology proposed in our research serves as a valuable tool for analyzing vegetation in a broader context, enabling a more comprehensive understanding of urban environmental dynamics and the relationship between green spaces and population density.

4. Conclusions

This study aimed to propose a comparative approach to assess the accuracy of different distance and correlation metrics in identifying vegetation within hyperspectral images of an urban area in the Manga neighborhood of Cartagena, Colombia. A total of 100 vegetation and non-vegetation pixels were selected from the hyperspectral image to create a reference or average pixel. Subsequently, correlations were computed using five distinct metrics, revealing that the direct correlation and Pearson metrics exhibited superior precision and discrimination of vegetation pixels, outperforming supervised learning-based methods.

Despite the differences between these two metrics, it was observed that the Euclidean and Bray–Curtis distance metrics encountered challenges in accurately classifying pixels as vegetation or non-vegetation. The proposed method based on correlation and/or vector distance metrics proved effective in differentiating spectral signatures within hyperspectral images. Visual inspection confirmed that the detection algorithm employing both metrics correctly identified vegetation in the designated areas, although the number of detected pixels could be adjusted based on specific correlation thresholds. The algorithm implemented using the most effective correlation metrics can be employed in studies related to determining the spatial distribution of vegetation across various latitudes. Furthermore, it can serve as a reference for detecting diverse objects or surfaces, such as water contaminants, asphalt, containers, and asbestos roofs, among others.

An innovative aspect of this study lies in the utilization of open-source software tools for accessing, processing, and analyzing hyperspectral images. The spectral library facilitated image retrieval, reading, and pixel extraction in vector representation, while the Python numpy and scipy libraries were employed for vector operations and correlation calculations. Additionally, the Python matplotlib library facilitated the management and visualization of pixel and hyperspectral image spectral signatures. These tools can serve as a valuable resource for testing and validating detection algorithms within the realm of hyperspectral imaging.

Future endeavors will involve incorporating machine learning models and specialized classification approaches for vegetation pixel detection in hyperspectral images. Furthermore, there are plans to test and calibrate the considered metrics for detecting asbestos-cement on urban rooftops.

Author Contributions: Conceptualization, G.E.C.G. and M.A.O.A.; methodology, G.E.C.G.; software, G.E.C.G.; validation, G.E.C.G. and M.A.O.A.; formal analysis, G.E.C.G.; investigation, G.E.C.G.; resources, M.S.; data curation, M.A.O.A.; writing—original draft preparation, G.E.C.G.; writing—review and editing, M.A.O.A. and M.S.; visualization, M.A.O.A.; supervision, M.S.; project administration, M.S.; funding acquisition, M.S. All authors have read and agreed to the published version of the manuscript.

Funding: This article is considered a product in the framework of the project "Formulation of an integral strategy to reduce the impact on public and environmental health due to the presence of asbestos in the territory of the Department of Bolivar", financed by the General System of Royalties of Colombia (SGR) and identified with the code BPIN 2020000100366. This project was executed by the University of Cartagena, Colombia, and the Asbestos-Free Colombia Foundation.

Institutional Review Board Statement: Not applicable.

Informed Consent Statement: Not applicable.

Data Availability Statement: Not applicable.

Acknowledgments: The authors thank David Enrique Valdelamar Martinez.

Conflicts of Interest: The authors declare no conflict of interest.

References

1. Pérez-Cabello, F.; Montorio, R.; Alves, D.B. Remote sensing techniques to assess post-fire vegetation recovery. *Curr. Opin. Environ. Sci. Health* **2021**, *21*, 100251. [CrossRef]
2. Andreatta, D.; Gianelle, D.; Scotton, M.; Dalponte, M. Estimating grassland vegetation cover with remote sensing: A comparison between Landsat-8, Sentinel-2 and PlanetScope imagery. *Ecol. Indic.* **2022**, *141*, 109102. [CrossRef]
3. Sripada, R.P. *Determining In-Season Nitrogen Requirements for Corn Using Aerial Color-Infrared Photography*; North Carolina State University: Raleigh, NC, USA, 2005.
4. Shikwambana, L.; Xongo, K.; Mashalane, M.; Mhangara, P. Climatic and Vegetation Response Patterns over South Africa during the 2010/2011 and 2015/2016 Strong ENSO Phases. *Atmosphere* **2023**, *14*, 416. [CrossRef]
5. García-Pardo, K.A.; Moreno-Rangel, D.; Domínguez-Amarillo, S.; García-Chávez, J.R. Remote sensing for the assessment of ecosystem services provided by urban vegetation: A review of the methods applied. *Urban For. Urban Green.* **2022**, *74*, 127636. [CrossRef]
6. Neinavaz, E.; Schlerf, M.; Darvishzadeh, R.; Gerhards, M.; Skidmore, A.K. Thermal infrared remote sensing of vegetation: Current status and perspectives. *Int. J. Appl. Earth Obs. Geoinf.* **2021**, *102*, 102415. [CrossRef]
7. Meusburger, K.; Bänninger, D.; Alewell, C. Estimating vegetation parameter for soil erosion assessment in an alpine catchment by means of QuickBird imagery. *Int. J. Appl. Earth Obs. Geoinf.* **2010**, *12*, 201–207. [CrossRef]
8. Henrich, V.; Krauss, G.; Götze, C.; Sandow, C. Index DataBase. A Database for Remote Sensing Indices. 2012. Available online: https://www.indexdatabase.de/db/s-single.php?id=9 (accessed on 29 September 2022).
9. Huang, S.; Tang, L.; Hupy, J.P.; Wang, Y.; Shao, G. A commentary review on the use of normalized difference vegetation index (NDVI) in the era of popular remote sensing. *J. For. Res.* **2021**, *32*, 1–6. [CrossRef]
10. Hernández, D.H.B. *Aplicación de Índices de Vegetación para Evaluar Procesos de Restauración Ecológica en el Parque Forestal Embalse del Neusa*; Universidad Militar Nueva Granada: Neusa, Colombia, 2017.
11. Gil, L.K.T.; Martínez, D.V.; Saba, M. The Widespread Use of Remote Sensing in Asbestos, Vegetation, Oil and Gas, and Geology Applications. *Atmosphere* **2023**, *14*, 172. [CrossRef]
12. Birth, G.S.; McVey, G.R. Measuring the Color of Growing Turf with a Reflectance Spectrophotometer. *Agron. J.* **1968**, *60*, 640–643. [CrossRef]
13. Wolf, A.F. Using WorldView-2 Vis-NIR multispectral imagery to support land mapping and feature extraction using normalized difference index ratios. In Proceedings of the Algorithms and Technologies for Multispectral, Hyperspectral, and Ultraspectral Imagery XVIII, SPIE Defense, Security, and Sensing, Baltimore, MD, USA, 23–27 April 2012; Volume 8390, pp. 188–195. [CrossRef]
14. Rouse, J.W., Jr.; Haas, R.H.; Schell, J.A.; Deering, D.W. *Monitoring Vegetation Systems in the Great Plains with Erts*; Nasa Special Publication; NASA: Washington, DC, USA, 1974.
15. Kauth, R.J.; Thomas, G.S.P. The tasselled cap—A graphic description of the spectral-temporal development of agricultural crops as seen by Landsat. In Proceedings of the Symposium on Machine Processing of Remotely Sensed Data, West Lafayette, IN, USA, 29 June–1 July 1976.
16. Tucker, C.J. Red and photographic infrared linear combinations for monitoring vegetation. *Remote Sens. Environ.* **1979**, *8*, 127–150. [CrossRef]
17. Huete, A.R. A soil-adjusted vegetation index (SAVI). *Remote Sens. Environ.* **1988**, *25*, 295–309. [CrossRef]
18. Crippen, R.E. Calculating the vegetation index faster. *Remote Sens. Environ.* **1990**, *34*, 71–73. [CrossRef]

19. Gitelson, A.A.; Merzlyak, M.N. Remote sensing of chlorophyll concentration in higher plant leaves. *Adv. Sp. Res.* **1998**, *22*, 689–692. [CrossRef]
20. Bannari, A.; Asalhi, H.; Teillet, P.M. Transformed difference vegetation index (TDVI) for vegetation cover mapping. In Proceedings of the IEEE International Geoscience and Remote Sensing Symposium, Toronto, ON, Canada, 24–28 June 2002; Volume 5, pp. 3053–3055. [CrossRef]
21. MaxMax. Enhanced Normalized Difference Vegetation Index (ENDVI). 2015. Available online: https://www.maxmax.com/endvi.htm (accessed on 26 September 2022).
22. Adão, T.; Hruška, J.; Pádua, L.; Bessa, J.; Peres, E.; Morais, R.; Sousa, J.J. Hyperspectral Imaging: A Review on UAV-Based Sensors, Data Processing and Applications for Agriculture and Forestry. *Remote Sens.* **2017**, *9*, 1110. [CrossRef]
23. Wan, L.; Li, H.; Li, C.; Wang, A.; Yang, Y.; Wang, P. Hyperspectral Sensing of Plant Diseases: Principle and Methods. *Agronomy* **2022**, *12*, 1451. [CrossRef]
24. Wang, S.; Guan, K.; Zhang, C.; Jiang, C.; Zhou, Q.; Li, K.; Qin, Z.; Ainsworth, E.A.; He, J.; Wu, J.; et al. Airborne hyperspectral imaging of cover crops through radiative transfer process-guided machine learning. *Remote Sens. Environ.* **2023**, *285*, 113386. [CrossRef]
25. Khan, A.; Vibhute, A.D.; Mali, S.; Patil, C.H. A systematic review on hyperspectral imaging technology with a machine and deep learning methodology for agricultural applications. *Ecol. Inform.* **2022**, *69*, 101678. [CrossRef]
26. Chen, D.; Zhang, F.; Tan, M.L.; Chan, N.W.; Shi, J.; Liu, C.; Wang, W. Improved Na+ estimation from hyperspectral data of saline vegetation by machine learning. *Comput. Electron. Agric.* **2022**, *196*, 106862. [CrossRef]
27. Gakhar, S.; Tiwari, K.C. Spectral–Spatial urban target detection for hyperspectral remote sensing data using artificial neural network. *Egypt. J. Remote Sens. Sp. Sci.* **2021**, *24*, 173–180. [CrossRef]
28. Ma, B.; Zeng, W.; Hu, G.; Cao, R.; Cui, D.; Zhang, T. Normalized difference vegetation index prediction based on the delta downscaling method and back-propagation artificial neural network under climate change in the Sanjiangyuan region, China. *Ecol. Inform.* **2022**, *72*, 101883. [CrossRef]
29. Trombetti, M.; Riaño, D.; Rubio, M.A.; Cheng, Y.B.; Ustin, S.L. Multi-temporal vegetation canopy water content retrieval and interpretation using artificial neural networks for the continental USA. *Remote Sens. Environ.* **2008**, *112*, 203–215. [CrossRef]
30. Davies, B.F.R.; Gernez, P.; Geraud, A.; Oiry, S.; Rosa, P.; Zoffoli, M.L.; Barillé, L. Multi- and hyperspectral classification of soft-bottom intertidal vegetation using a spectral library for coastal biodiversity remote sensing. *Remote Sens. Environ.* **2023**, *290*, 113554. [CrossRef]
31. Badola, A.; Panda, S.K.; Roberts, D.A.; Waigl, C.F.; Jandt, R.R.; Bhatt, U.S. A novel method to simulate AVIRIS-NG hyperspectral image from Sentinel-2 image for improved vegetation/wildfire fuel mapping, boreal Alaska. *Int. J. Appl. Earth Obs. Geoinf.* **2022**, *112*, 102891. [CrossRef]
32. Rumpf, T.; Mahlein, A.-K.; Steiner, U.; Oerke, E.-C.; Dehne, H.-W.; Plümer, L. Early detection and classification of plant diseases with Support Vector Machines based on hyperspectral reflectance. *Comput. Electron. Agric.* **2010**, *74*, 91–99. [CrossRef]
33. Wang, L.; Wang, Q. Fast spatial-spectral random forests for thick cloud removal of hyperspectral images. *Int. J. Appl. Earth Obs. Geoinf.* **2022**, *112*, 102916. [CrossRef]
34. Ding, X.; Wang, Q.; Tong, X. Integrating 250 m MODIS data in spectral unmixing for 500 m fractional vegetation cover estimation. *Int. J. Appl. Earth Obs. Geoinf.* **2022**, *111*, 102860. [CrossRef]
35. Shore, S.N. Astrochemistry. In *Encyclopedia of Physical Science and Technology*; Academic Press: Cambridge, MA, USA, 2003; pp. 665–678. [CrossRef]
36. Galle, N.J.; Brinton, W.; Vos, R.; Basu, B.; Duarte, F.; Collier, M.; Ratti, C.; Pilla, F. Correlation of WorldView-3 spectral vegetation indices and soil health indicators of individual urban trees with exceptions to topsoil disturbance. *City Environ. Interact.* **2021**, *11*, 100068. [CrossRef]
37. Thorp, K.R.; French, A.N.; Rango, A. Effect of image spatial and spectral characteristics on mapping semi-arid rangeland vegetation using multiple endmember spectral mixture analysis (MESMA). *Remote Sens. Environ.* **2013**, *132*, 120–130. [CrossRef]
38. Zhu, Y.; Zhang, Y.; Zheng, Z.; Liu, Y.; Wang, Z.; Cong, N.; Zu, J.; Tang, Z.; Zhao, G.; Gao, J.; et al. Converted vegetation type regulates the vegetation greening effects on land surface albedo in arid regions of China. *Agric. For. Meteorol.* **2022**, *324*, 109119. [CrossRef]
39. Smyth, T.A.G.; Wilson, R.; Rooney, P.; Yates, K.L. Extent, accuracy and repeatability of bare sand and vegetation cover in dunes mapped from aerial imagery is highly variable. *Aeolian Res.* **2022**, *56*, 100799. [CrossRef]
40. Tian, J.; Zhang, Z.; Philpot, W.D.; Tian, Q.; Zhan, W.; Xi, Y.; Wang, X.; Zhu, C. Simultaneous estimation of fractional cover of photosynthetic and non-photosynthetic vegetation using visible-near infrared satellite imagery. *Remote Sens. Environ.* **2023**, *290*, 113549. [CrossRef]
41. Lyons, R. Distance covariance in metric spaces. *Ann. Probab.* **2013**, *41*, 3284–3305. [CrossRef]
42. Székely, G.J.; Rizzo, M.L. Brownian distance covariance. *Ann. Appl. Stat.* **2009**, *3*, 1236–1265. [CrossRef]
43. Connor, R. A tale of four metrics. In *International Conference on Similarity Search and Applications—SISAP 2016*; Lecture Notes in Computer Science; Springer: Cham, Switzerland, 2016; Volume 9939, pp. 210–217. [CrossRef]
44. Bray, J.R.; Curtis, J.T. An Ordination of the Upland Forest Communities of Southern Wisconsin. *Source Ecol. Monogr.* **1957**, *27*, 325–349. [CrossRef]

45. Novotn, V.T. Implementation notes for the soft cosine measure. In Proceedings of the CIKM '18: 27th ACM International Conference on Information and Knowledge Management, Torino, Italy, 22–26 October 2018; pp. 1639–1642. [CrossRef]
46. Curcio, A.C.; Barbero, L.; Peralta, G. UAV-Hyperspectral Imaging to Estimate Species Distribution in Salt Marshes: A Case Study in the Cadiz Bay (SW Spain). *Remote Sens.* **2023**, *15*, 1419. [CrossRef]
47. ESRI. ENVI 2023. 2023. Available online: https://www.esri.com/partners/l3harris-technologie-a2T39000001dNCnEAM/envi-a2d5x000005jPrfAAE (accessed on 28 June 2023).
48. Duarte, L.; Teodoro, A.C.; Monteiro, A.T.; Cunha, M.; Gonçalves, H. QPhenoMetrics: An open source software application to assess vegetation phenology metrics. *Comput. Electron. Agric.* **2018**, *148*, 82–94. [CrossRef]
49. Zhang, Y.; Wang, Y.; Ding, N. Spatial Effects of Landscape Patterns of Urban Patches with Different Vegetation Fractions on Urban Thermal Environment. *Remote Sens.* **2022**, *14*, 5684. [CrossRef]

Disclaimer/Publisher's Note: The statements, opinions and data contained in all publications are solely those of the individual author(s) and contributor(s) and not of MDPI and/or the editor(s). MDPI and/or the editor(s) disclaim responsibility for any injury to people or property resulting from any ideas, methods, instructions or products referred to in the content.

remote sensing

MDPI

Review

Unlocking the Potential of Remote Sensing in Wind Erosion Studies: A Review and Outlook for Future Directions

Lenka Lackoóvá [1,*], Juraj Lieskovský [2], Fahime Nikseresht [1], Andrej Halabuk [2], Hubert Hilbert [2], Klaudia Halászová [1] and Fatemeh Bahreini [3]

[1] Institute of Landscape Engineering, Faculty of Horticulture and Landscape Engineering, Slovak University of Agriculture, 949 76 Nitra, Slovakia; fahime.nikseresht@uniag.sk (F.N.); klaudia.halaszova@uniag.sk (K.H.)
[2] Institute of Landscape Ecology, Slovak Academy of Sciences, 814 99 Bratislava, Slovakia; juraj.lieskovsky@savba.sk (J.L.); andrej.halabuk@savba.sk (A.H.); hubert.hilbert@savba.sk (H.H.)
[3] Research Institute of Forest and Rangelands of Iran, Tehran 13185, Iran
* Correspondence: lenka.lackoova@uniag.sk

Abstract: Remote sensing (RS) has revolutionized field data collection processes and provided timely and spatially consistent acquisition of data on the terrestrial landscape properties. This research paper investigates the relationship between Wind Erosion (WE) and Remote Sensing (RS) techniques. By examining, analyzing, and reviewing recent studies utilizing RS, we underscore the importance of wind erosion research by exploring indicators that influence the detection, evaluation, and modeling of wind erosion. Furthermore, it identifies research gaps particularly in soil erodibility estimation, soil moisture monitoring, and surface roughness assessment using RS. Overall, this research enhances our understanding of WE and RS and offers insights into future research directions. To conduct this study, we employed a two-fold approach. First, we utilized a non-systematic review approach by accessing the Global Applications of Soil Erosion Modelling Tracker (GASEMT) database. Subsequently, we conducted a systematic review of the relevant literature on wind erosion and remote sensing in the core collection of the Web of Science (WoS) database. Additionally, we employed the VOSviewer bibliometric software to generate a cooperative keyword network analysis, facilitating the advancements and identifying emerging areas of WE and RS research. With a non-systematic review, we focused on examining the current state and potential of remote sensing for mapping and analyzing following indicators of wind erosion modelling: (1) soil erodibility; (2) soil moisture; (3) surface roughness; (4) vegetation cover; (5) wind barriers; and (6) wind erosion mapping. Our study highlights the widespread utilization of freely available RS data, such as MODIS and Landsat, for WE modeling. However, we also acknowledge the limitations of high resolution sensors due to their high costs. RS techniques offer an efficient and cost-effective approach for mapping erosion at various scales and call for a more comprehensive and detailed assessment of soil erosion at regional scales. These findings provide valuable guidance for future research endeavors in this domain.

Keywords: advanced remote sensing; wind erosion; wind erosion parameters; wind erosion modelling; non-systematic review; systematic review

Citation: Lackoóvá, L.; Lieskovský, J.; Nikseresht, F.; Halabuk, A.; Hilbert, H.; Halászová, K.; Bahreini, F. Unlocking the Potential of Remote Sensing in Wind Erosion Studies: A Review and Outlook for Future Directions. *Remote Sens.* **2023**, *15*, 3316. https://doi.org/10.3390/rs15133316

Academic Editor: Nicolas Baghdadi

Received: 29 May 2023
Revised: 18 June 2023
Accepted: 27 June 2023
Published: 28 June 2023

Copyright: © 2023 by the authors. Licensee MDPI, Basel, Switzerland. This article is an open access article distributed under the terms and conditions of the Creative Commons Attribution (CC BY) license (https://creativecommons.org/licenses/by/4.0/).

1. Introduction

Wind erosion is a natural soil degradation process [1], often accelerated by human activity [2]. The erosion events caused by wind lead to the depletion of fine particles such as clay and silt [3] and organic matter [4], which can result in decreased soil productivity and degradation of the soil's hydrothermal properties [5]. Wind erosion (WE) predominantly occurs in regions characterized by low precipitation and high evaporation rates, which cover roughly one-third of the global land area and 12% of Europe [6]. Climate change has intensified WE in semi-arid areas by 3.2% from 1980 to 2019 [7]. The United Nations (UN) global soil resources report highlights that a significant proportion of the world's soil is in

suboptimal conditions [8]. Soil erosion, loss of soil carbon, and nutrient imbalance pose significant threats to soil functions.

The process of WE has three phases: (1) initiation of the movement of the soil particles (detachment or deflation), (2) the transportation of the soil particles (suspension, saltation, and surface creep), and (3) the deposition [9,10]. Several models have been developed to simulate the WE [11,12] and estimate the erosion intensity and effectiveness of erosion control strategies [13]. Empirical models are based on observed data and their statistical relationship with analyzed predictors. This approach is simpler, criticized for employing unrealistic assumptions, ignoring heterogeneity of inputs and nonlinear relationships between input parameters [14]. Most empirical models compute soil loss and do not simulate transportation or deposition [11]. Physical models, or process-based models, are based on understanding of the whole process of aeolian transport [15]. The distinction between the models is not always clear, and both approaches could be integrated into one model [2]. Some of the main challenges in aeolian transport modeling have been as identified the fidelity of process representation, up-scaling the presence of heterogeneity, spatial data availability, and large-scale parameter estimation [15].

The management of WE presents a formidable challenge because it involves intricate interplay due to complex interactions among driving forces, pressures, and ecosystem states [16]. Due to the intricate nature of the process, it remains challenging to oversee and measure soil WE on a larger scale [17]. The study of WE involves a range of research techniques, such as laboratory and field measurements, modelling, and the use of remote sensing (RS) technologies. While methods such as wind tunnel testing and direct terrain measurements are commonly employed, they are often constrained by time and environmental factors, and may not fully capture the complex and dynamic spatial and temporal aspects of WE. However, the accuracy of these methods is still being improved [11,18]. In the last two decades, RS [19] and computer technology have made significant progress, with increased technological potential to obtain more relevant data on WE [17]. RS methods are faster than ground methods, can cover large areas, and facilitate repeated monitoring of erosion events or factors affecting the erosion [18,20–22]. The employment of RS technology provides the opportunity to efficiently evaluate soil quality at different scales, with the added benefits of speed and affordability. Nevertheless, the variation in the spectral response of soils at different depths and the disparities in the spatial, spectral, and temporal resolutions of various sensors could necessitate extensive data processing and intricate models [23]. Satellite imagery allows for the quick and timely recording of the presence and intensity of erosion processes, the prediction of their impact on the topography, soils, agricultural land, and landscape systems, and approval of a set of measures to reduce the negative effects on the natural surroundings [24]. The European Space Agency's (ESA) release of the Sentinel 2 sensor, which boasts an average spatial resolution of 10 m and a 5-day revisiting cycle, has made it one of the most widely accessible and practical sources of remote sensing data for soil erosion mapping and modeling, second only to the Landsat series [21]. The new RS systems, including drones and LiDAR, produce the data in higher spatial, temporal, and spectral resolution [18,25]. Additionally, the increasing computer power enables the large-scale application of some detailed approaches used in local scales. Incorporating RS data into WE modeling is anticipated to enhance the accuracy and decrease the level of ambiguity or imprecision present in the model [25,26].

The potential to integrate RS, spatial analysis, geographic information system (GIS), and modelling into WE analyses is still a great challenge. Previous reviews were focused on using RS in erosion or land degradation mapping in general [18,20,22], or were directly focused on WE models [11,12], or the representation of aeolian processes [2,15]. This manuscript reviews the RS approaches used to derive the input parameters for WE models and we analyze the potential of advanced RS methods for improving the quality of main input parameters for WE models.

2. Materials and Methods

To gain a comprehensive understanding of the application of remote sensing (RS) in wind erosion (WE) assessment, we combined a non-systematic and systematic review approach. To conduct the systematic review, the Web of Science (WoS) core collection database was searched for relevant literature on WE and remote sensing. For the non-systematic review, the 'Global Applications of Soil Erosion Modelling Tracker (GASEMT)' database was utilized. This database includes studies published between 1994 and 2018 and is publicly available to users [27]. This review expanded the analysis of the GASEMT database by examining the connection between soil erosion modelling and RS. In this review paper, the impact of six factors that are facilitated in WE studies with the help of RS was evaluated: soil erodibility, soil moisture, surface roughness, vegetation cover, wind barriers, and WE mapping. In each factor, the research and also the future perspectives were examined.

Systematic and Non-Systematic Literature Research

We conducted a bibliographic investigation in September–November 2022 in the WoS database. The query "wind erosion" + "remote sensing" generated 237 research papers, published between 1991 and 2022. We used VOSviewer bibliometric software version 1.6. to draw the cooperative network and keyword co-occurrence map to analyze the research progress and frontier [28].

We used a classical review approach based on non-systematic literature research in databases, SCOPUS, WoS, and Google Scholar. We used search terms such as "Wind erosion modelling, Wind erosion models, Wind erosion mapping, RS, Soil erodibility, Soil moisture, Surface roughness, Vegetation cover, Wind barriers, etc." to obtain a set of papers focusing on wind erosion modelling and then we searched in the reference literature or used specific queries to obtain additional information.

We restricted our review to those model input parameters that are commonly used in WE models [11,12] and are derived or could be derived with use of RS. These WE models include basic parameters such as soil erodibility, soil moisture, soil roughness, vegetation cover, wind barriers, climate inputs, and other inputs such as threshold velocity, management, and so on. Soil erodibility is used in all the models and is derived from the percentage of sand soil particles and for some models forms additional soil physical parameters. Soil moisture is used directly as an input parameter or is estimated indirectly from the climate parameters. Surface roughness is included in models directly as specific input parameter or indirectly as tillage parameter or soil surface condition parameter. Vegetation or crop cover is directly included in most of the models or is covered in management or surface cover parameters. Wind barriers are related to field length, field geometry and wind speed. Additionally, we reviewed the application of RS methods for WE mapping because the RS is often used for verification of WE models, and in some cases the RS approach could be an alternative to WE models.

Figure 1 shows a flowchart with the results at the different stages of this study taken from the initial WoS search to the final selection of possible papers of interest for this review paper. Even though this was a specific and very stringent search, aimed at excluding unrelated articles from the beginning, the WoS output still generated a relatively large number of 40,127 publications for all six factors (a). As shown in Figure 1a, all the research conducted on the six investigated factors are included in the WoS database with the restriction of "remote sensing". Following the evaluation of the papers according to the research interest, the cutting point for considering articles for further evaluation depended on the strong and effective relationship to the topic in this step. In this case, 1371 articles were considered for reading their full abstracts by the terms "Wind Erosion" as a restriction for all six evaluated factors (b). Finally, the relevant articles (n = 207) which emphasize the relationship of chosen factors with the terms "Wind Erosion" and "Remote Sensing" for more interdisciplinary research were investigated (c).

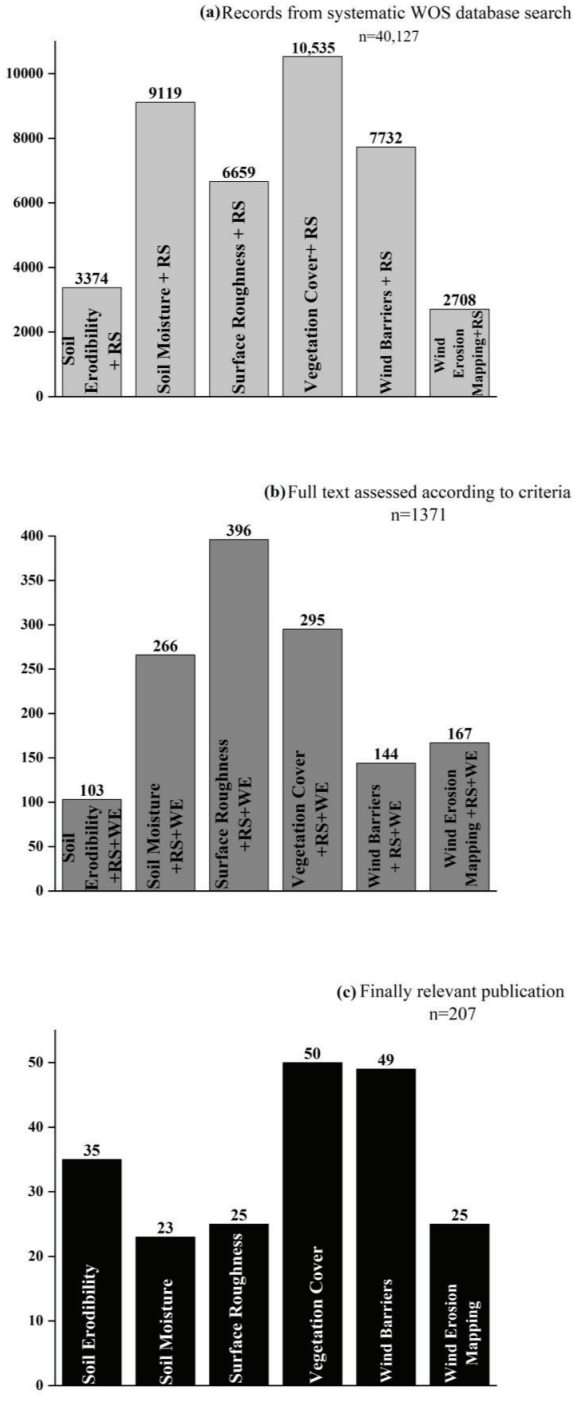


Figure 1. A schematic diagram outlining the process of the literature review according to the WoS database, including overall numbers (**a**), full text according to criteria (**b**), and the final count of publications that were deemed applicable (**c**). WE here is the abbreviation of wind erosion.

Although the climate parameters are crucial for WE modelling, we did not include them in our review, because they are commonly derived from meteorological data and models, and we do not see any potential for RS in this area. In the second phase, we estimated the current and future potential of RS for improving the quality of the input parameters for WE models.

3. Results

3.1. Research Frontiers

In Figure 2, the keyword network analysis map reveals the existence of four groups that represent distinct research areas related to WE and RS. Group 1 is mainly focused on utilizing RS techniques to evaluate land degradation and erosion. This is demonstrated by terms such as "erosion", "land degradation", "desertification", and "impacts". The terms "China" and "loess plateau" indicate an interest in the dominant interest in land degradation in these regions.

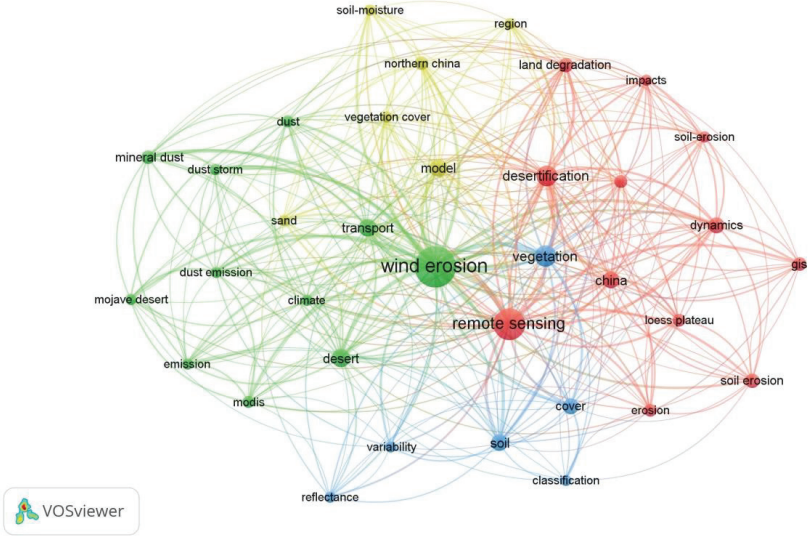


Figure 2. Keyword network analysis.

Groups are identified by color (Group 1—red; 2—green; 3—blue and 4—yellow). The size of the labels and circles in the figure is directly proportional to the frequency of occurrences. The lines connecting the terms indicate significant connections, with the thickness of the lines representing the strength of the association. Additionally, the distance between the terms in the figure also reflects the strength of the association.

The Group 2 research fronts are focused on the effect of WE on dust emission, as indicated by the link to terms "emission", "dust", and "desert" with terms of "modis" and "transport". The time-series MODIS data are utilized for the purpose of identifying the erodibility of landscapes and mapping the hazard of WE during different seasons [29]. Group 3 pertains to the use of RS classification of vegetation cover as a crucial input for WE modeling. This is evident from the presence of terms such as "cover", "variability", "reflectance", and "classification". Group 3's position on the network map suggests that it has a stronger association and greater connectivity with Group 1. On the other hand, Group 4 is focused on WE modeling and has a regional scope, as indicated by the frequent occurrence of terms such as "model" and "region". The application of RS for analyzing the inputs such as "vegetation cover", "soil moisture", and "sand" for erosion models is visible here as well. The frequent use of the term "dust" and "desert" shows the increasing importance of desertification. The co-occurrence groups highlight two distinct trends:

- The majority of studies in the field of WE and RS are completed on a regional scale;
- The research emphasizes more variable and effective factors in the process of erosion. The frequent use of terms such as "vegetation" and "climate change" shows this trend.

3.2. Remote Sensors and Indicators Used in Wind Erosion Modelling

Recent soil survey data, such as the LUCAS topsoil and RS data, have made large-scale soil erosion modeling more feasible. LUCAS Soil, which is an extensive and recurring topsoil survey conducted every three years across the European Union, is an example of such data [30]. The development of dynamic indexes and proxies for soil coverage will be facilitated by the increased availability of surveyed data and the utilization of RS data (MODIS, Landsat) and Copernicus products [31]. Landsat, with its collection of images dating back to the Landsat Multispectral Scanner (MSS) to the Landsat Operational Land Imager (OLI) and Thermal Infrared Sensor (TIRS) is home to the oldest archive of imagery from various sensors. With a spatial resolution of 30 m, it continues to be one of the most utilized satellite images in WE modeling, as shown in Figure 3. Additionally, the Shuttle Radar Topography Mission (SRTM) data, derived from synthetic aperture radar (SAR) imagery, remain a critical source of data for erosion assessment. Other sensors, such as ASTER, Sentinel, and SPOT, among others, offer lower or medium spatial resolution.

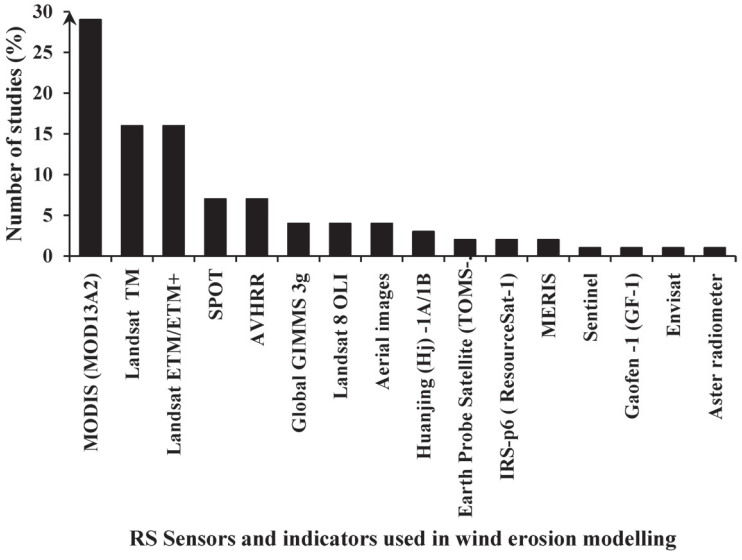


Figure 3. The percentage of global studies that employed various RS sensors and indicators for estimating WE parameters. (Note: this Figure was generated from the GASEMT database).

As illustrated in Figure 3, the number of indicators and RS sensors used through the WE evaluation in this systematic review is very variable. Different usage of RS data is based on its cost. Acquiring most of these images comes with a low cost or is entirely free in some cases. Additionally, high spatial resolution sensors such as IKONOS, GeoEye, and QuickBird can be utilized to evaluate erosion factors. Nonetheless, their usage in erosion assessment over large areas is often limited due to the high costs associated with acquiring them [32]. The MODIS data series was the most applied image during this study (Figure 4). Among these studies, the utilization of freely available Landsat images is frequently observed, followed by images from Google Earth.

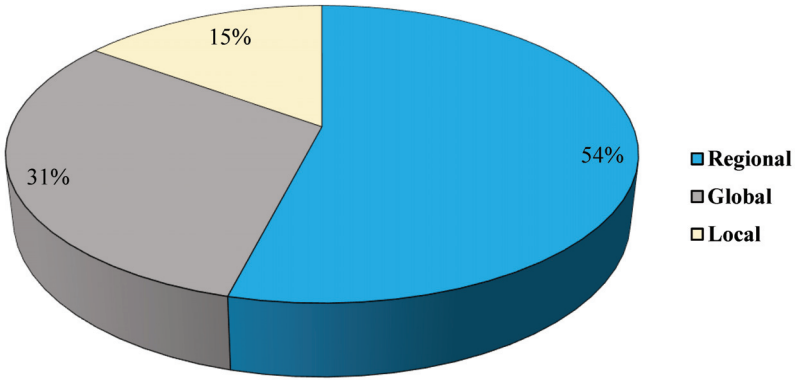


Figure 4. The percentage of studies carried out globally that utilized remote sensing to estimate WE parameters across varying spatial scales of application. (Note: this Figure was generated from the GASEMT database).

Although other soil erosion models can be expensive and time-consuming, RS techniques can map erosion more efficiently and affordably with less expert data, time, and cost in local, global, regional, and plot applications (Figure 4). Until 2018, efforts to quantify and map the extent of soil erosion have been primarily focused on local-scale applications, despite many attempts [21].

As illustrated in Figure 4, with the advancement in RS knowledge, a more comprehensive and detailed assessment of the spatial distribution and magnitude of soil erosion at regional scales is required, along with the development of sustainable management and effective rehabilitation strategies. The occurrence of the term "region" in conjunction with the term "model" suggests a focus on using models at the regional scale.

3.3. Wind Erosion Factors and RS

3.3.1. Soil Erodibility

Current State and Research Gaps

Erodibility, a crucial factor for predicting WE [33–35], refers to a soil's susceptibility to erosion under specific meteorological conditions, or the efficiency of soil erosion on a surface given certain meteorological forcing. The interaction of fine soil particles (silt, clay, and sand) and organic carbon typically determines erodibility and is associated with factors such as soil structure, organic content, surface roughness, and soil texture [36]. However, measuring erodibility can be challenging due to these multiple factors. The influence of soil surface conditions based on soil type is often overlooked as a source of variation in characterizing soil surface erodibility and in using RS for soil assessment [37]. The computation of soil erodibility has been approached differently in various studies [38]. Ref. [39] calculated the wind erodibility of European soils by using a multiple regression equation based on soil texture and chemical properties, while Ref. [40] used soil organic carbon and soil particle size distribution to calculate erodibility in Inner Mongolia, China. However, soil erodibility equations typically require specific physical soil properties that may not be widely available. In the United States, the wind erodibility index (WEI) is available through the USDA Web Soil Survey geographic database [41]. Conducting long-term erosion plot studies is necessary to obtain direct measurements of soil erodibility. Most of the earlier studies [42–45] have been limited only to experimental study areas. Ref. [46] analyzed the soil erodibility of soil moisture, gravel cover, and surface roughness in combination with Landsat8 data to evaluate the direct impact on soil erodibility. Close-range photogrammetry was used to generate a gravel percentage map and the ASTER digital topographic model was used to analyze surface roughness. Ref. [47] highlighted the potential of directional and multi-angular soil reflectance to enhance the knowledge of

erodibility and to detect and quantify soil erosion. In addition, the authors suggested that utilizing ground-based radiometers, as well as current and upcoming versions of angular sensors mounted on aerial and satellite platforms, and multi-angular spectral reflectance holds promise for remotely assessing and computing soil surface characteristics, thereby offering a comprehensive framework. Bi-directional soil spectral reflectance models [48,49] have the potential to establish a framework for integrating the analysis of soil surface erodibility and potentially measuring WE. Ref. [50] employed Landsat MSS and AVIRIS imagery to illustrate the movement of sand from deserted agricultural areas.

Future Directions

Remote sensing is a valuable and economical means of obtaining data for mapping and modeling soil properties, soil resources, and their temporal and spatial variations [47,51–54]. Utilizing Visible, Near Infrared, and Shortwave Infrared sensors, it is possible to calibrate site-specific datasets that depict the correlation between spatiotemporal and quantitative variations in soil information across extensive regions [53]. Ref. [55] estimated soil erodibility by the support vector regression method on Landsat-8 images with relative percent deviation equals 2.01.

The presence of vegetation, crop residues, or clouds can hinder the accuracy of soil property predictions, which is why extracting spectral information solely from bare soil pixels may yield successful results [56]. Ref. [57] stated that a single satellite image provides only 0.5% of valid bare soil pixels, which is inadequate for soil mapping. To address this, new methods of bare soil detection, especially from Landsat and Sentinel images, are being employed. Ref. [58] used the MID-Infrared profile of four images to identify bare soil pixels and established a correlation between the amount of clay content and these pixels to generate a soil clay content map. Refs. [59,60] used a fusion technique, which increased the exposed soil coverage from 36% (single image) to 75%. Meanwhile, Ref. [61] utilized a five-year compilation of Landsat TM imagery and the Barest Soil Composite Image (BSCI) technique to achieve 90% in soil mapping. In a similar attempt, Ref. [62] integrated the reflectance and spectral parameters obtained from Sentinel-2 images with a wider range of spectral and non-spectral covariates to forecast topsoil clay content. Ref. [63] also proved that multi-temporal images performed better in predicting soil properties, then single-date images. The Soil Composite Mapping Processor (SCMaP) was devised by [64] to surmount the obstacle of insufficient soil exposure and to map soil properties in Germany. Further research advancement and improvement is expected as high signal-to-noise ratio spectrometers on space-borne imagery become available, along with the PRISMA, such as EnMAP [65], HISUI [66], SHALOM [67], HySpex [68], and the Sentinel-10/CHIME [69].

3.3.2. Soil Moisture

Current State and Research Gaps

The presence of soil moisture is a significant contributor to the cohesion of soil particles and acts as a mitigating factor for wind erosion [16]. Soil erodibility reaches its peak when the soil is completely dehydrated. However, as the soil moisture content increases beyond this limit, there is a noticeable reduction in erodibility. Erodibility rapidly increases with the soil moisture content [70]. Precisely monitoring and estimating the spatial and temporal changes in soil moisture is of great significance [71]. Estimating soil moisture becomes more challenging in regions with dense vegetation or snow cover, as well as areas with intricate topography [72]. Soil moisture content in correlation with the number of erosive days could predict some mitigation effect for some areas [39].

The production of dust is connected to the annual diversity in plant cover resulting from the variation in soil moisture [50]. Traditional techniques of restoration and reclamation necessitate surface disturbance and rely on adequate moisture to avoid erosion, making them vulnerable to significant erosion risk in the absence of wet conditions [16]. Several machine learning algorithms have been utilized for extracting water bodies and shorelines from remote sensing images, including neural networks, convolutional neural networks,

artificial neural networks, support vector machines, naive Bayes, random forest, gradient boosted machine, recursive partitioning and regression trees, and constraint energy minimizations [73]. Individual spot measurements do not capture high spatial and temporal variability [74,75] and therefore are not suitable for regional and global research [71,76].

Future Directions

The investigation of soil moisture RS commenced during the mid-1970s, after the satellite expansion [71]. Optical and thermal infrared sensors, along with active microwave RS techniques, can be utilized to measure the soil moisture content in the near-surface soil [77]. Several soil moisture estimation outputs have been created via microwave RS, such as SMOS [78], AMSR-E [79], and SMAP [80]. Ref. [81] applied the Landsat and SPOT images for SWI to identify the WE risk in the farming region in Hungary. The driest area (SWI < 6%) exposed WE to a wider scope. Ref. [46] utilized the NDMI and WETNESS spectral index as indicators for estimating soil moisture, enabling the identification of sources for sand and dust storms using RS analysis. Ref. [82] used Sentinel-1 and Landsat-7 data to assess SMC in Egypt and achieved the result with R2 reaching 0.83. Ref. [83] exhibited the capability of estimating soil moisture by integrating on-site soil moisture measurements and MODIS land parameters (LST and NDVI) to generate daily soil moisture products at a resolution of 1 km. The utilization of the presently accessible MODIS time-series products for soil moisture and wind speed can be concurrently employed to detect landscape erodibility and to delineate the seasonal variations of WE hazard [29].

The latest progress in RS have exhibited the capability of quantifying the spatial differences in surface soil moisture across diverse topographic and land cover conditions [84,85]. Unfortunately, there is presently no dataset or model that can accurately determine the deep soil moisture content at a high resolution [76]. In addition, there is no comprehensive map of soil moisture along with its changes during the growing season, land cover, microbial population, etc. Establishing soil moisture prediction methods and combining them with artificial intelligence can help us to solve this problem in the future. Ref. [86] predicted soil surface moisture through the implementation of polarimetric decomposition in tandem with quantile regression forests (QRF). Ref. [87] applied Radial RBFNN and a PCA model to achieve an accurate prediction of farmland moisture. They also developed a range of intelligent prediction techniques for soil moisture content, which significantly enhance the level of agricultural intelligence. The emergence of UAV platforms has now offered an economical approach to measure the soil moisture content on a large scale [76]. Ref. [88] demonstrated that the derived GNSS soil moisture estimates can complement the current global soil moisture databases and offer more frequent retrievals at a resolution of 9 km.

To improve future soil moisture retrieval algorithms, it would be advantageous to integrate spaceborne measurements from multiple sensors, physically based model predictions, and in situ observations in a synergistic manner. Additionally, research should focus on developing approaches for mapping soil moisture in areas with dense vegetation [71].

3.3.3. Surface Roughness

Current State and Research Gaps

Surface roughness refers to the way surfaces are expressed in terms of topography, including features on horizontal and vertical scales ranging from millimeters to a few hundred meters [29]. Precise understanding of surface roughness and its influence on wind speed is crucial for various fields, including climate modeling, wind power meteorology, agriculture, and erosion hazard assessment [89]. Nearly flat surfaces with loose sand-sized particles, lacking any shelter or cover objects, are particularly sensitive to WE [90].

Surface roughness can be considered a direct input parameter or indirectly estimated through soil moisture or vegetation biomass in WE modeling [91,92]. It can be utilized as a WE predictor by determining the potential for soil particle retention, emission, and saltation [93]. However, the measurement accuracy of surface roughness is constrained by the measurement method, instruments used, and data pre-processing [94]. Surface

roughness can be measured using contact or non-contact methods. Contact methods include the grid plate and profiler methods, while non-contact methods include laser profiler, stereophotography, pencil-beam radiometer, and LiDAR [95,96]. Achieving the required measurement accuracy is challenging due to limitations such as large spatial sampling intervals, short sampling segments, temporal variability, and inconvenient operation. However, TLS as a non-contact device [97] can furnish spatial data of high resolution (in mm), depicting surface alterations over time [98]. Other surface properties can be derived from the strength of the reflected signal. The best machine learning approaches for surface roughness estimation consist of both classical machine learning algorithms such as random forest, neural network and support vector machine and artificial neural network (ANN), as well as deep learning algorithms including multilayer perceptron (MLP) and deep belief network (DBN) [99].

Future Directions

RS has proven to be a fast and efficient way to provide high-resolution spatial data over large areas which can be utilized to derive surface roughness parameters. The roughness of a surface can be inferred by analyzing the reflectance of the surface from various angles of illumination and the sensor view, which is characterized by the BRDF [49]. Refs. [100,101] developed correlations between radar backscatter cross sections and surface roughness obtained from wind velocity profile data [102]. Ref. [103] estimated the surface roughness with 92.0% accuracy by using the image features and the combination of IPSO and SVR. Ref. [104] used electromagnetic radiation, particularly low-frequency microwaves, to characterize surface roughness. The limitation of satellite images is the ability to estimate the soil surface characteristics only in areas not covered by vegetation [105].

Although progress has been made in utilizing RS to account for the effects of surface roughness on WE, there are still significant constraints with the methodology and parameterization. For instance, Ref. [104] evaluated the precision and accuracy of LiDAR-based estimations of these parameters in comparison with manual pin-profilers. Their experiments showed that, while the surface RMS can be estimated precisely and accurately from LiDAR data, the correlation length estimates were not as reliable.

The accuracy of LiDAR technologies is constantly improving. Nowadays, the LiDAR reaches relative vertical accuracy in the order of, say, a few centimeters or even millimeters when using UAVs or terrestrial laser scanners [92,106]. Therefore, the constraining factors for surface roughness parameters do not reside in the precision or fidelity of the input data, but rather in the ability to capture the fluctuations in surface roughness due to shifts in vegetation cover, soil moisture levels, or tillage techniques. Accomplishing this necessitates coordinating data acquisition with these occurrences, which can be a time-consuming and an expensive undertaking, and may also be unfeasible for large-scale modeling efforts.

3.3.4. Vegetation Cover

Current State and Research Gaps

Vegetation reduces WE as follows: 1. safeguards the soil from erosive influences by enveloping a portion of its surface; 2. diminishes the velocity of the wind near the ground; 3. traps the soil particles [107]. Vegetation represents mainly standing live and dead biomass (e.g., crops in various development stages) and standing or flat litter (e.g., crop residues). The impact of vegetation on soil erodibility is contingent upon various factors such as the extent of vegetation cover, height, and spatial distribution or arrangement within a landscape [108]. The establishment of vegetation cover and development of windbreaks are the most common erosion control measures [18].

The impact of vegetation on WE in drylands has been primarily studied through wind tunnel experiments, windbreak studies, and field trials [107]. The degree of vegetation's influence on WE is determined by the amount, height, and distribution of vegetation in the landscape. During different seasons, the state of vegetation cover undergoes changes, which in turn affects its ability to mitigate wind erosion. The impact of seasonality on

vegetation cover relates to the growth and development stages of crops or plant species. In some regions, vegetation cover may decrease during dry seasons or winter, leading to reduced erosion control capacity. Conversely, during the rainy seasons or periods of active growth, the vegetation cover tends to increase, providing greater protection against erosion. The extent of vegetation cover is often represented as the ratio of the surface area covered by plants [109]. If the vegetation cover is below 20%, it has a minimal impact on reducing wind velocity, while erosion is essentially halted if the vegetation cover exceeds 60% [110]. Therefore, understanding the seasonality of vegetation cover is crucial for assessing its effectiveness in erosion control throughout the year. The review focusing on erosion monitoring [111] identified Landsat, SPOT, and MODIS data as the most-used RS systems for state-based monitoring of ground cover and identified the products most suitable for erosion monitoring [112–114]. For the WE modelling, the information about vegetation cover, its annual dynamics, and crop residues are important. Vegetation cover for the European scale model [115] was estimated from the Leaf Area Index derived from ENVISAT/MERIS satellite images. For the European WE model (WEELS), the Land Use data were gathered from existing maps, farmers files, agricultural statistics, or the land use dataset was estimated through modeling techniques in case of unavailability [36]. In [116]'s study on the East Africa region, the vegetation cover fraction was obtained from GCLS SPOT/PROBA-V images at a resolution of 1 km. For the East Africa region, Ref. [116] used a fraction of vegetation cover derived from GCLS SPOT/PROBA-V images at 1 km resolution. For the regional studies, the data from MODIS with a resolution of 250 m or 1 km [117–119] or Landsat with a resolution of 30 m [120,121] are often used. The pre-processed data products from Copernicus Global Land Services are also used [122]. For the historical analyses of the vegetation cover development, the MODIS data were combined with 8 km spatial resolution AVHRR [40,123,124] or the Landsat data were used [125].

Vegetation cover is often derived from the Normalised Difference Vegetation Index [126] using a dimidiate pixel model [127] or a specific regression model is developed [122]. From the range of vegetation indexes the Average Maximum Modified Soil Adjusted Vegetation Index was also used [120,128]. A classical RS classification approach was also used for the vegetation cover estimation [125]. In small experimental areas, the vegetation cover could be visually mapped in the field [129], using the line transect method [130] or a pin-type profile meter [131]. The impact of vegetation cover can be disregarded when examining the potential for WE [132], or in the case where the erosion events are expected at a time when there is no vegetation cover in the field [133]. Support Vector Regression and Random Forests are two popular classic machine learning algorithms, and have been widely used in regression and classification of vegetation-related studies [134].

Future Directions

RS has emerged as an effective tool to monitor and analyze vegetation to effectively incorporate seasonality and cover patterns over space and time [135]. Recent advancements in image-based techniques [136] and high-resolution RS [137–139] have enabled rapid and large-scale quantification of plant characteristics such as height, width, and porosity. These data can be utilized to quantify the dynamics of vegetation cover throughout different seasons and improve erosion modeling. RS has also facilitated the refinement of physical and spectral characteristics connected to vegetation cover and surface morphological structures [140–142], particularly by incorporating spatial patterns of vegetation [143,144]. Additionally, RS approaches hold great promise for quickly obtaining tillage information on individual fields over large areas [145]. Estimation of lateral cover with RS represents a great challenge. Depending on the scale of studies, authors use different approximations of lateral cover, based on empirical relations with fractional vegetation cover [146], LAI, or more recently, based on functional relationship with normalized and rescaled albedo resulting in so-called albedo-derived lateral cover [147]. Aerial drones (unmanned aerial vehicles (UAVs)) can be used for low-elevation surveys to collect vegetation transect measurements quickly and inexpensively [148]. Terrestrial laser scanning (TLS) with high

resolution can detect small changes in height around partially vegetated erodible surfaces, aiding in the identification of erosional and depositional regions with high accuracy [107]. High spatial resolution RS allows for the direct imaging of individual plants that are at least the size of the ground resolution of the RS image. This capability enables the effective use of geostatistical methods for describing plant distribution [149]. RS data are becoming increasingly useful for modelling spatial and temporal variability in vegetation [150]. Recent advances in image-based techniques [136] and high-resolution RS [137–139] allow for the rapid quantification of plant characteristics such as height, width, and porosity over relatively large scales. RS approaches also offer a promising option for rapidly collecting tillage information on individual fields over large areas [145].

3.3.5. Living Wind Barriers

Current State and Research Gaps

The windbreaks have various functions in landscapes. Beside the soil protection against wind and water erosion, they positively affect the microclimate, plant productivity [150,151], soil properties [152–154], biodiversity, and also serve other purposes such as protecting buildings, offering thermal comfort to livestock, reducing snow and sand accumulation, and mitigating wind impacts on the transportation infrastructure [155]. Therefore, the effect of windbreaks is evaluated from different perspectives [156,157]. The WE model incorporates three aspects of wind barriers: (1) wind barriers' height; (2) optical porosity; (3) wind barriers' width. The wind barriers' height affects the shelter length [158]. For the erosion modelling purpose, the height is measured by altimeter [159] or from vertical images of the windbreak [132], or is estimated from the average height of windbreak types [160]. Ref. [161] estimated the average tree height of windbreaks from first principal component of GF-1 Multi-Spectral high resolution satellite image. Porosity refers to the proportion of open space to the occupied space of tree stems, branches, twigs, and leaves. It impacts the degree of wind speed reduction and shelter effect of windbreaks [162]. Since measuring aerodynamic porosity is challenging, optical porosity is used as an alternative. Optical porosity is calculated as the ratio of white pixels to the total pixels in digitized black and white pictures taken at a distance of 30 m from the windbreak [163]. These images are processed using software such as ImageTool 3.0 or GIMP 2.10.34 [132,159,164,165]. In RS-based windbreak studies, it is common to assume an approximate shape for the simulated trees. However, this approach often results in notable discrepancies between the simulated and actual results. Ref. [166] employed TLS to obtain parameters used in a quantitative structural model (AdQSM) to reconstruct the tree structure and restore the wind field environment using the computational fluid dynamics software PHOENICS-2022. The findings suggest that TLS can effectively retrieve windbreak parameters and quantify porosity, thereby substantially improving the credibility of windbreak impact investigations in windbreak forests. The wind barriers' width is related to barrier porosity [161,165], but also has a specific effect on wind velocity [167]. Using 10 m SPOT5 images is applicable for windbreaks' width measurement; however, errors may arise when the windbreak is presented on both sides of the road, in the case of sparse or young windbreaks [168]. Aerial images were analyzed using object-oriented image analysis to map the windbreaks [169–171], but also for the automatic extraction of wind barriers' width [172]. The wind barriers are neglected in regional scale models [17,35,39,116,122,173], because such a dataset does not exist for large areas. In most of the local studies, the effect of wind barriers is modelled in the direction of prevailing winds [159,165] or as a Euclidean distance from the nearest windbreak [161]. The most innovative methodology is to calculate the wind reduction for all wind directions and to weight them according to the average occurrence of erosive winds [132]. A unique method is to estimate the shelter area from lateral cover and shadows derived from the multitemporal MODIS albedo images [147].

Future Directions

For the large-scale studies, where wind barrier mapping is not possible, the existing satellite land cover products could be used. The Copernicus Land Monitoring Service provides a GIS layer of High Resolution Layer Small Woody Features, that were mapped from very-high spatial resolution imagery [174] and are available for EEA collaborating countries. The forest areas are included in High Resolution Layer Forest [175], derived from Sentinel 2 images, that also includes information about tree cover, the type of dominant leaves, and the category of the forest.

Remote sensing data obtained from satellites, which are usually calibrated with LiDAR measurements, are commonly utilized to evaluate the height of tree canopies at varying spatial scales and resolutions. For example, MODIS images, trained by Geoscience Laser Altimeter System (GLAS), were utilized to generate a global map of canopy height in 500 m resolution [176]. Landsat images and GLAS were used to produce woody vegetation structure maps with 30 m resolution [177]. Sentinel-2 images and the canopy height model were used to produce a country-wide map of vegetation height in Switzerland in resolution 10 m ("Country-wide high-resolution vegetation height mapping with Sentinel-2", 2019). The Radar images are applicable for tree height estimation as well [178].

The LiDAR scanner is used in forestry research to measure tree height over more than two decades [179]. Current research includes an estimation of canopy base height and bulk density for fire modelling [180], for detection of the sub-canopy structure [181], and mapping of the urban ecological network [182].

The use of existing satellite products such as Copernicus High Resolution Layer Small Woody Features could improve the large scale models, where the effect of wind barriers is neglected [122,183]. The disadvantage is that this dataset does not provide information about windbreak height or porosity and is available only for EEA contributing countries. Satellite images were tested for wind barriers' mapping [168], rough estimation of sheltered areas [147], and for estimation of the wind barriers width, height, and porosity [161] or gaps [184]. The 10 m resolution images are applicable, however better results would be obtained with more detailed images as was shown from aerial images [169–171]. LiDAR was proven as a precise tool for tree height mapping and also as a source of training data for satellite-based tree height estimations. The feature of wind barriers mapping is in application of LiDAR data, very high resolution multispectral satellite images, or in fusion of different RS approaches [185,186].

3.3.6. Wind Erosion Mapping

Current State and Research Gaps

RS approach is used more often for deriving the inputs for WE models, than for mapping the eroded areas. The sole effect of WE is hard to recognize from RS images; therefore, the compound effect with water erosion [187], tillage erosion [188], or land degradation in general [20,21] is mapped.

Monitoring of agricultural soil degradation by RS was reviewed by the authors of [21] and they identified two RS approaches for mapping the WE: (1) mapping direct indicators such as surface lowering or changes in surface roughness; and (2) mapping indirect indicators based on WE relationship with changes in vegetation cover. One illustration of the initial approach involves utilizing radar remote sensing to delineate the patterns of wind-induced land deterioration in the northeast Patagonian region [189]. A second approach could be illustrated by a study that used ASTER images to obtain a WE risk map for Inner Mongolia from the basis of the land use classes, and vegetation height [190].

Ref. [187] summarized the contribution of RS to mapping land depletion in Latin America and Caribbean. The most-used WE indicators were sand dunes, however various surface erosion features such as wind streaks, desert pavements, paleo–aeolian sand features, sand encroachments, blowouts, and changes in vegetation cover were used as well.

Machine learning models commonly employed for wind erosion mapping in various environmental research areas encompass decision tree models, linear equation models,

particle swarm optimization-adaptive network-based fuzzy inference system, genetic algorithms, support vector regression, artificial neural networks, hybrid models, random forest, Wang and Mendel's method, partial least square regression, principal component regression, Cubist, Bayesian additive regression trees, radial basis function, extreme gradient boosting, and regression tree analysis [188].

Future Directions

Detecting the traces of WE from RS images remains challenging. Ref. [20] describes some obstacles in mapping the land degradation at a regional scale: (1) the relationship between RS indicators and soil properties is complex and not straightforward and (2) obtaining data on subsurface soil properties can be challenging. An additional challenge is to distinguish the indicators of WE from other types of land degradation. To direct future research, the community will benefit from multi-temporal and multi-spectral data such as Landsat or Sentinel 2 series [21]. In addition, combining different mapping approaches from several RS platforms [17], using new LiDAR technics detection in changes soil surface [20] or drone-based RS [25] are opportunities in the mapping of WE for future studies. The new very-high resolution satellite systems such as Venus (Israel Space Agency and National Center for Space Studies, France) [191], Gaofen (China) [192], or Planet Satellites [193] bring more detailed images. The spatial and temporal resolution will also increase for upcoming hyperspectral missions such as Copernicus Chime (ESA) [194], HysIS (Indian Space Research Organisation), EnMAP (Environmental Monitoring and Analysis Program) [195], radar mission Copernicus Rose-L [196] and CIMR (ESA) [197], SCATSAT-1 [198], and NovaSAR-01 (CSIRO Centre for Earth Observation) [199].

Landsat 8 has improved spectral and radiometric characteristics that make it suitable for mapping soil erosion at both regional and local scales [200,201]. While the previous Landsat TM series had higher spectral resolution with seven bands (including two mid IR bands) that were more appropriate for degraded landscapes, the SPOT series satellites provide a higher spatial resolution with sensors called High Resolution Visible (HRV) and High Resolution Visible and Infrared (HRVIR), which can detect reflected radiance in three bands at a spatial resolution of 20 m and have been shown to be better at differentiating eroded regions than Landsat TM observations [21]. The cost-effectiveness of the high resolution IKONOS sensor compared to lower resolution air photographs is not significant [202]. SPOT 5 has a lower cost compared to IKONOS and QuickBird, and has been employed in numerous research works [203]; however, the limited spectral resolution of SPOT 5 hinders its potential in mapping soil erosion as it results in restricted spectral observations. The Sentinel 2 sensors, developed by the ESA, have an average spatial resolution of 10 m and a 5-day repeated coverage, making them the most probable and advantageous choices for soil erosion mapping after Landsat data, particularly in developing countries in which the obtaining of high-resolution sensors can be challenging. Sentinel 2 has exhibited its usefulness in the mapping of vegetation [204,205] and water resources' mapping [21].

4. Discussion

Much of WE research uses RS to predict, monitor, and track wind erosion events and assess their impacts, but also as a source of input data for WE modelling, which is third of the challenges of aeolian transport modelling identified by [15]. WE models and RS systems are still under development. New, more detailed datasets are available from RS and other systems, enabling the development of erosion models, which could work with new and different input factors.

The main challenges for mapping soil erodibility is its complexity and spatial and temporal variation together with the fact that spectral information on soil properties could be extracted from bare soil pixels only. The analysis of multitemporal satellite images improves the coverage and quality of the analyses. Additional advancement is expected from forthcoming space-borne imagery spectrometers such as EnMAP, HISUI, SHALOM, HySpex2, and the Sentinel-10/CHIME. Similar challenges occur in soil moisture mapping.

Soil moisture is important in many fields; therefore, the research is more advanced here and soil moisture products and techniques based on modelling or on radar or optical remote sensing are developed. Surface roughness is mapped using radar images; however, it seems that the LiDAR and UAV systems are becoming more suitable due to their increased availability and accuracy. Due to the variations caused by changes in vegetation cover, soil moisture, or tillage practices, the mapping of surface roughness is still challenging. Vegetation mapping is a wide topic; therefore, many remote sensing approaches and products have already been developed. The challenge for WE modelling remains the mapping of lateral cover. The windbreaks are mapped from high resolution satellite images or drones that have become more available in the last decade. Various techniques and products have been developed for woody vegetation mapping. The challenge for WE modelling is the mapping of tree height and porosity. This will be possible with the application of LiDAR, very high-resolution multispectral satellite images, or in fusion of different RS approaches. Direct mapping of WE traces with remote sensing remains challenging, the advances could be reached by multiple use of available systems such as LiDAR, SPOT, HRV, and HRVIR.

Future Research Needs

When evaluating different parameters that affected the WE modelling and could be advanced by RS, several concepts are apparent that could serve as guidance for future research. Some recommendations include:

- EnMAP, HISUI, SHALOM, HySpex2, and the Sentinel-10/CHIME could help to remotely mapping soil erodibility [65–67,69,206];
- GNSS and UAV platforms now provide an economical method for evaluating soil moisture content on a broad level [76,88];
- With the advancement of aerial LIDAR and UAVs, surface roughness measurement has been developed, but the possibility of capturing the variations in surface roughness due to the changes in vegetation cover, soil moisture, or tillage practices is still a big challenge [107];
- Recent advancements in image-based techniques now allow for the rapid and large-scale quantification of vegetation cover [136] and high-resolution RS [137–139];
- The feature of wind barriers mapping is in the application of LiDAR data, very high-resolution multispectral satellite images, or in fusion of different RS approaches [185,186];
- All the mentioned satellites and sensors, especially LiDAR, SPOT, HRV, and HRVIR are helpful in advancing the goal of WE mapping with RS, but unfortunately, a large-scale comprehensive map of WE has not yet been prepared [20,21,25];
- The data obtained from remote sensors primarily focus on surface features mapping, and direct linkage to soil erosion may require the use of inference methods [207]. However, it is important to note that remote sensing data encompass a wide range of information beyond surface features. For instance, atmospheric dust is extensively monitored using remote sensing techniques;
- High resolution data (SPOT-5 and QuickBird) show potential to offer accurate data for soil erosion mapping; however, the acquisition cost of some sensors such as IKONOS and QuickBird can be prohibitive for the large-scale mapping of soil erosion [21].

5. Conclusions

The issue of global warming presents a complex challenge for the world. While certain areas may experience increased vulnerability to WE [102,208,209], it is also important to acknowledge that other regions might witness a reduction in vulnerability [210]. Although numerous researchers have investigated various aspects of water erosion modelling, the implementation of advanced RS techniques in WE modelling has not received much scrutiny. This study presents an outline of the advancements in RS applications for WE modelling across different time periods and spatial scales. The systematic review results showed that most countries have not considered WE as a serious threat yet, and certain

countries have more studies in this field, but the number of studies in the whole world is progressing, and this shows the growing importance of the challenge of WE. It is obvious that bibliometric studies offer only a transient snapshot of a particular research area. The non-systematic review results showed that while RS applications were used to quantify factors in WE, the focus was primarily on small-scale projects. Hence, measuring spatial variability requires a more detailed and widespread effort. The use of RS utilities to monitor WE is largely unattainable in developing countries, which affects WE studies. Hence, the latest sensors such as the Sentinel 2 and Landsat 8 series are currently in high demand because of their enhanced spatial, spectral, radiometric, and temporal resolutions, along with their affordability. High resolution data especially LiDAR, SPOT, HRV, and HRVIR are very helpful for WE mapping. Monitoring of the effective factors in WE has become easier with the help of RS tools, but the possibility of capturing the variations due to the changes in vegetation cover, soil moisture, or tillage practices remains a big challenge.

Author Contributions: Conceptualization: L.L., J.L., F.N., A.H., H.H. and K.H.; Data curation: L.L., J.L., F.N., A.H. and H.H.; Formal analysis: L.L., J.L., F.N., A.H., H.H., K.H. and F.B.; Funding acquisition: L.L., J.L. and A.H.; Investigation: L.L., J.L., F.N., A.H., H.H., K.H. and F.B.; Methodology: L.L., J.L., F.N. and A.H.; Validation: L.L., J.L., F.N., A.H. and H.H.; Visualization: L.L., F.N. and H.H.; Writing—original draft: L.L., J.L., F.N., A.H. and H.H. All authors have read and agreed to the published version of the manuscript.

Funding: This research is the result of the projects: Scientific support of climate change adaptation in agriculture and mitigation of soil degradation, (ITMS2014+ 313011W580) supported by the Integrated Infrastructure Operational Program funded by the ERDF. SUA grant agency no. 09-GASPU-2021: Windbreaks in agricultural landscape—ecological, environmental and economic value of multifunctional structures acting against soil degradation, VEGA 1/0676/22 Blue-green infrastructure as a tool of water management policy in the process of adaptation to climate change, VEGA 1/0186/23 Windbreaks in the agricultural landscape—ecological, environmental and economic value of multifunctional structures acting as soil degradation measures.

Data Availability Statement: Data available on request from the correspondence author.

Conflicts of Interest: The authors declare no conflict of interest.

References

1. Sterk, G.; Riksen, M.; Goossens, D. Dryland Degradation by wind erosion and its control. *Ann. Arid Zone* **2001**, *41*, 351–367.
2. Shao, Y. *Physics and Modelling of Wind Erosion*; Springer Science & Business Media: New York, NY, USA, 2008.
3. Li, J.; Okin, G.S.; Alvarez, L.; Epstein, H. Quantitative effects of vegetation cover on wind erosion and soil nutrient loss in a desert grassland of southern New Mexico, USA. *Biogeochemistry* **2007**, *85*, 317–332. [CrossRef]
4. Yan, H.; Wang, S.; Wang, C.; Zhang, G.; Patel, N. Losses of soil organic carbon under wind erosion in China. *Glob. Chang. Biol.* **2005**, *11*, 828–840. [CrossRef]
5. Peng, F.; Xue, X.; You, Q.; Huang, C.; Dong, S.; Liao, J.; Duan, H.; Tsunekawa, A.; Wang, T. Changes of soil properties regulate the soil organic carbon loss with grassland degradation on the Qinghai-Tibet Plateau. *Ecol. Indic.* **2018**, *93*, 572–580. [CrossRef]
6. Borrelli, P.; Panagos, P.; Montanarella, L. New insights into the geography and modelling of wind erosion in the European agricultural land. Application of a spatially explicit indicator of land susceptibility to wind erosion. *Sustainability* **2015**, *7*, 8823–8836. [CrossRef]
7. Ma, X.; Zhao, C.; Zhu, J. Aggravated risk of soil erosion with global warming—A global meta-analysis. *CATENA* **2021**, *200*, 105129. [CrossRef]
8. Food and Agriculture Organization of the United Nations—FAO; Intergovernmental Technical Panel on Soils—ITPS. *Status of the World's Soil Resources (SWSR)—Main Report*; Food and Agriculture Organization of the United Nations and Intergovernmental Technical Panel on Soils: Rome, Italy, 2015; p. 650.
9. Lyles, L. Erosive wind energy distributions and climatic factors for the West. *J. Soil Water Conserv.* **1983**, *38*, 106–109.
10. Stallings, J.H. *Mechanics of Wind Erosion*; TP 98; U.S. Department of Agriculture, Soil Conservation Service; U.S. Government Publishing Office: Washington, DC, USA, 1951.
11. Jarrah, M.; Mayel, S.; Tatarko, J.; Funk, R.; Kuka, K. A review of wind erosion models: Data requirements, processes, and validity. *CATENA* **2020**, *187*, 104388. [CrossRef]
12. Seo, I.W.; Lim, C.S.; Yang, J.E.; Lee, S.P.; Lee, D.S.; Jung, H.G.; Lee, K.S.; Chung, D.Y. An overview of applicability of WEQ, RWEQ, and WEPS models for prediction of wind erosion in lands. *Korean J. Agric. Sci.* **2020**, *47*, 381–394. [CrossRef]

13. Blanco-Canqui, H.; Lal, R. *Principles of Soil Conservation and Management*; Springer Science & Business Media: Berlin/Heidelberg, Germany, 2008.
14. Merritt, W.; Letcher, R.; Jakeman, A. A review of erosion and sediment transport models. *Environ. Model. Softw.* **2003**, *18*, 761–799. [CrossRef]
15. Raupach, M.R.; Lu, H. Representation of land-surface processes in Aeolian transport models. *Environ. Model. Softw.* **2004**, *19*, 93–112. [CrossRef]
16. Middleton, N.; Kang, U. Sand and Dust Storms: Impact Mitigation. *Sustainability* **2017**, *9*, 1053. [CrossRef]
17. Wang, W.; Samat, A.; Ge, Y.; Ma, L.; Tuheti, A.; Zou, S.; Abuduwaili, J. Quantitative soil wind erosion potential mapping for Central Asia using the Google Earth Engine Platform. *Remote Sens.* **2020**, *12*, 3430. [CrossRef]
18. Dwivedi, R.S. *Geospatial Technologies for Land Degradation Assessment and Management*, 1st ed.; CRC Press: Boca Raton, FL, USA, 2018. [CrossRef]
19. Funk, R. Assessment and measurement of Wind Erosion. In *Novel Methods for Monitoring and Managing Land and Water Resources in Siberia*; Springer Water Book Series; Springer: Cham, Switzerland, 2015; pp. 425–449. [CrossRef]
20. Shoshany, M.; Goldshleger, N.; Chudnovsky, A. Monitoring of agricultural soil degradation by remote-sensing methods: A Review. *Int. J. Remote Sens.* **2013**, *34*, 6152–6181. [CrossRef]
21. Sepuru, T.K.; Dube, T. An appraisal on the progress of remote sensing applications in soil erosion mapping and monitoring. *Remote Sens. Appl. Soc. Environ.* **2018**, *9*, 1–9. [CrossRef]
22. Senanayake, S.; Pradhan, B.; Huete, A.; Brennan, J. A review on assessing and mapping soil erosion hazard using geo-informatics technology for farming system management. *Remote Sens.* **2020**, *12*, 4063. [CrossRef]
23. De Paul Obade, V.; Lal, R. Assessing land cover and soil quality by remote sensing and Geographical Information Systems (GIS). *CATENA* **2013**, *104*, 77–92. [CrossRef]
24. Lukyanchuk, K.A.; Kovalchuk, I.P.; Pidkova, O.M. Application of a remote sensing in monitoring of Erosion Processes. *Geoinform. Theor. Appl. Asp.* **2020**, *2020*, 1–5. [CrossRef]
25. Zhang, J.; Guo, W.; Zhou, B.; Okin, G.S. Drone-based remote sensing for research on wind erosion in drylands: Possible applications. *Remote Sens.* **2021**, *13*, 283. [CrossRef]
26. Jiang, C.; Li, D.; Wang, D.; Zhang, L. Quantification and assessment of changes in ecosystem service in the three-river headwaters region, China as a result of climate variability and land cover change. *Ecol. Indic.* **2016**, *66*, 199–211. [CrossRef]
27. Borrelli, P.; Alewell, C.; Alvarez, P.; Anache, J.A.A.; Baartman, J.; Ballabio, C.; Bezak, N.; Biddoccu, M.; Cerdà, A.; Chalise, D.; et al. Soil erosion modelling: A global review and statistical analysis. *Sci. Total Environ.* **2021**, *780*, 146494. [CrossRef] [PubMed]
28. Batista, P.V.; Davies, J.; Silva, M.L.; Quinton, J.N. On the evaluation of soil erosion models: Are we doing enough? *Earth-Sci. Rev.* **2019**, *197*, 102898. [CrossRef]
29. Yang, X.; Leys, J. Mapping wind erosion hazard in Australia using Modis-derived ground cover, soil moisture and climate data. *IOP Conf. Ser. Earth Environ. Sci.* **2014**, *17*, 012275. [CrossRef]
30. Orgiazzi, A.; Ballabio, C.; Panagos, P.; Jones, A.; Fernández-Ugalde, O. Lucas soil, the largest expandable soil dataset for Europe: A Review. *Eur. J. Soil Sci.* **2017**, *69*, 140–153. [CrossRef]
31. Panagos, P.; Katsoyiannis, A. Soil erosion modelling: The new challenges as the result of policy developments in Europe. *Environ. Res.* **2019**, *172*, 470–474. [CrossRef]
32. Phinzi, K.; Ngetar, N.S. The assessment of water-borne erosion at catchment level using GIS-based Rusle and Remote Sensing: A Review. *Int. Soil Water Conserv. Res.* **2019**, *7*, 27–46. [CrossRef]
33. Bryan, R.B. The development, use and efficiency of indices of soil erodibility. *Geoderma* **1968**, *2*, 5–26. [CrossRef]
34. Geeves, G.W.; Leys, J.F.; McTainsh, G.H. Soil erodibility. In *Soils: Their Properties and Management*; Charman, P.E.V., Murphy, B.W., Eds.; Oxford University Press: New York, NY, USA, 2000; pp. 205–220.
35. Borrelli, P.; Ballabio, C.; Panagos, P.; Montanarella, L. Wind erosion susceptibility of European soils. *Geoderma* **2014**, *232–234*, 471–478. [CrossRef]
36. Cohen, M.J.; Shepherd, K.D.; Walsh, M.G. Empirical reformulation of the universal soil loss equation for erosion risk assessment in a tropical watershed. *Geoderma* **2005**, *124*, 235–252. [CrossRef]
37. Chappell, A.; Zobeck, T.M.; Brunner, G. Using on-nadir spectral reflectance to detect soil surface changes induced by simulated rainfall and wind tunnel abrasion. *Earth Surf. Process. Landf.* **2005**, *30*, 489–511. [CrossRef]
38. Webb, N.P.; Strong, C.L. Soil erodibility dynamics and its representation for wind erosion and dust emission models. *Aeolian Res.* **2011**, *3*, 165–179. [CrossRef]
39. Borrelli, P.; Panagos, P.; Ballabio, C.; Lugato, E.; Weynants, M.; Montanarella, L. Towards a Pan-European assessment of land susceptibility to wind erosion. *Land Degrad. Dev.* **2014**, *27*, 1093–1105. [CrossRef]
40. Zhou, Y.; Guo, B.; Wang, S.; Tao, H. An estimation method of soil wind erosion in Inner Mongolia of China based on Geographic Information System and remote sensing. *J. Arid. Land* **2015**, *7*, 304–317. [CrossRef]
41. Richardson, C.; Sadler, T. Evaluating wind erosion sensitivity for landfill sites in New Mexico using fuzzy analytical hierarchy process (FAHP). *Am. J. Civ. Eng.* **2022**, *10*, 1–12. [CrossRef]
42. Odeh, I.O.; McBratney, A.B. Using AVHRR images for spatial prediction of clay content in the Lower Namoi Valley of Eastern Australia. *Geoderma* **2000**, *97*, 237–254. [CrossRef]

43. Sullivan, D.G.; Shaw, J.N.; Rickman, D. IKONOS imagery to estimate surface soil property variability in two Alabama physiographies. *Soil Sci. Soc. Am. J.* **2005**, *69*, 1789–1798. [CrossRef]
44. Selige, T.; Böhner, J.; Schmidhalter, U. High resolution topsoil mapping using hyperspectral image and field data in multivariate regression modeling procedures. *Geoderma* **2006**, *136*, 235–244. [CrossRef]
45. Gomez, C.; Lagacherie, P.; Coulouma, G. Regional predictions of eight common soil properties and their spatial structures from hyperspectral Vis–Nir Data. *Geoderma* **2012**, *189–190*, 176–185. [CrossRef]
46. Rayegani, B.; Barati, S.; Goshtasb, H.; Gachpaz, S.; Ramezani, J.; Sarkheil, H. Sand and dust storm sources identification: A remote sensing approach. *Ecol. Indic.* **2020**, *112*, 106099. [CrossRef]
47. Chappell, A.; Zobeck, T.M.; Brunner, G. Using bi-directional soil spectral reflectance to model soil surface changes induced by rainfall and wind-tunnel abrasion. *Remote Sens. Environ.* **2006**, *102*, 328–343. [CrossRef]
48. Pinty, B.; Verstraete, M.M.; Dickinson, R.E. A physical model for predicting bidirectional reflectances over bare soil. *Remote Sens. Environ.* **1989**, *27*, 273–288. [CrossRef]
49. Jacquemoud, S.; Baret, F.; Hanocq, J. Modeling spectral and bidirectional soil reflectance. *Remote Sens. Environ.* **1992**, *41*, 123–132. [CrossRef]
50. Okin, G.S.; Murray, B.; Schlesinger, W.H. Degradation of sandy arid shrubland environments: Observations, process modelling, and management implications. *J. Arid. Environ.* **2001**, *47*, 123–144. [CrossRef]
51. Agbu, P.A.; Fehrenbacher, D.J.; Jansen, I.J. Soil property relationships with Spot Satellite Digital Data in East Central Illinois. *Soil Sci. Soc. Am. J.* **1990**, *54*, 807–812. [CrossRef]
52. Ben-Dor, E.; Chabrillat, S.; Demattê, J.; Taylor, G.; Hill, J.; Whiting, M.; Sommer, S. Using imaging spectroscopy to study soil properties. *Remote Sens. Environ.* **2009**, *113*, S38–S55. [CrossRef]
53. Mulder, V.; De Bruin, S.; Schaepman, M.; Mayr, T. The use of remote sensing in soil and terrain mapping—A review. *Geoderma* **2011**, *162*, 1–19. [CrossRef]
54. Wulf, H.; Mulder, T.; Schaepman, M.; Keller, A.; Jörg, P.C. *Remote Sensing of Soils*; University of Zurich, Remote Sensing Laboratories: Zurich, Switzerland, 2015.
55. Chakherlou, S.; Jafarzadeh, A.A.; Ahmadi, A.; Feizizadeh, B.; Shahbazi, F.; Darvishi Boloorani, A.; Mirzaei, S. Soil wind erodibility and erosion estimation using landsat satellite imagery and multiple-criteria decision analysis in Urmia Lake Region, Iran. *Arid Land Res. Manag.* **2022**, *37*, 71–91. [CrossRef]
56. Castaldi, F.; Chabrillat, S.; Don, A.; Van Wesemael, B. Soil Organic Carbon Mapping using lucas topsoil database and sentinel-2 data: An approach to reduce soil moisture and crop residue effects. *Remote Sens.* **2019**, *11*, 2121. [CrossRef]
57. Demattê, J.A.; Fongaro, C.T.; Rizzo, R.; Safanelli, J.L. Geospatial Soil Sensing System (GEOS3): A powerful data mining procedure to retrieve soil spectral reflectance from satellite images. *Remote Sens. Environ.* **2018**, *212*, 161–175. [CrossRef]
58. Shabou, M.; Mougenot, B.; Chabaane, Z.; Walter, C.; Boulet, G.; Aissa, N.; Zribi, M. Soil Clay content mapping using a time series of Landsat TM data in semi-arid lands. *Remote Sens.* **2015**, *7*, 6059–6078. [CrossRef]
59. Demattê, J.A.; Alves, M.R.; Terra, F.D.; Bosquilia, R.W.; Fongaro, C.T.; Barros, P.P. Is it possible to classify topsoil texture using a sensor located 800 km away from the surface? *Rev. Bras. Ciência Solo* **2016**, *40*, e0150335. [CrossRef]
60. Demattê, J.A.M.; Safanelli, J.L.; Paiva, A.F.D.S.; Souza, A.B.; Dos Santos, N.V.; Nascimento, C.M.; De Mello, D.C.; Bellinaso, H.; Neto, L.G.; Amorim, M.T.A.; et al. Bare Earth's surface spectra as a proxy for Soil Resource Monitoring. *Sci. Rep.* **2020**, *10*, 4461. [CrossRef]
61. Diek, S.; Fornallaz, F.; Schaepman, M.E.; De Jong, R. Barest pixel composite for agricultural areas using Landsat Time Series. *Remote Sens.* **2017**, *9*, 1245. [CrossRef]
62. Loiseau, T.; Chen, S.; Mulder, V.L.; Dobarco, M.R.; Richer-De-Forges, A.C.; Lehmann, S.; Bourennane, H.; Saby, N.P.A.; Martin, M.P.; Vaudour, E.; et al. Satellite data integration for soil clay content modelling at a national scale. *Int. J. Appl. Earth Obs. Geoinf.* **2019**, *82*, 101905. [CrossRef]
63. Silvero, N.E.; Demattê, J.A.; Vieira, J.D.S.; Mello, F.A.D.O.; Amorim, M.T.A.; Poppiel, R.R.; Mendes, W.D.S.; Bonfatti, B.R. Soil property maps with satellite images at multiple scales and its impact on management and classification. *Geoderma* **2021**, *397*, 115089. [CrossRef]
64. Rogge, D.; Bauer, A.; Zeidler, J.; Mueller, A.; Esch, T.; Heiden, U. Building an exposed soil composite processor (SCMAP) for mapping spatial and temporal characteristics of soils with landsat imagery (1984–2014). *Remote Sens. Environ.* **2018**, *205*, 1–17. [CrossRef]
65. Guanter, L.; Kaufmann, H.; Segl, K.; Foerster, S.; Rogass, C.; Chabrillat, S.; Kuester, T.; Hollstein, A.; Rossner, G.; Chlebek, C.; et al. The ENMAP Spaceborne Imaging Spectroscopy Mission for Earth Observation. *Remote Sens.* **2015**, *7*, 8830–8857. [CrossRef]
66. Matsunaga, T.; Iwasaki, A.; Tsuchida, S.; Tanii, J.; Kashimura, O.; Nakamura, R.; Yamamoto, H.; Tachikawa, T.; Rokugawa, S. Current Status of Hyperspectral Imager Suite (HISUI) Jadeite. In Proceedings of the 2013 IEEE International Geoscience and Remote Sensing Symposium—IGARSS, Melbourne, Australia, 21–26 July 2013.
67. Varacalli, G.N.; Kafri, A.; Tidhar, G.A.; Chen, M.; Feingersh, T.; Sagi, E.; Cisbani, A.; Baroni, M.; Labate, D.; Nadler, R.; et al. SHALOM—Space-borne hyperspectral applicative land and ocean mission. In Proceedings of the 5th Workshop on Hyperspectral Image and Signal Processing: Evolution in Remote Sensing (WHISPERS), Gainesville, FL, USA, 26–28 June 2013; pp. 1–4.
68. Ward, K.J.; Chabrillat, S.; Brell, M.; Castaldi, F.; Spengler, D.; Foerster, S. Mapping Soil Organic Carbon for airborne and simulated enmap imagery using the Lucas Soil Database and a local PLSR. *Remote Sens.* **2020**, *12*, 3451. [CrossRef]

69. Nieke, J.; Rast, M. Status: Copernicus Hyperspectral Imaging Mission for the Environment (CHIME). In Proceedings of the IGARSS 2019—2019 IEEE International Geoscience and Remote Sensing Symposium, Yokohama, Japan, 28 July–2 August 2019. [CrossRef]
70. Chepil, W.S. *Soil Conditions That Influence Wind Erosion*; Technical Bulletins 157333; United States Department of Agriculture, Economic Research Service: Washington, DC, USA, 1958. [CrossRef]
71. Wang, L.; Qu, J.J. Satellite remote sensing applications for Surface Soil Moisture Monitoring: A Review. *Front. Earth Sci. China* **2009**, *3*, 237–247. [CrossRef]
72. Ahmed, A.; Nichols, S.; Zhang, Y. Review and evaluation of remote sensing methods for soil-moisture estimation. *J. Photonics Energy* **2011**, *2*, 028001. [CrossRef]
73. Niu, L.; Kaufmann, H.; Xu, G.; Zhang, G.; Ji, C.; He, Y.; Sun, M. Triangle Water Index (TWI): An Advanced Approach for More Accurate Detection and Delineation of Water Surfaces in Sentinel-2 Data. *Remote Sens.* **2022**, *14*, 5289. [CrossRef]
74. Engman, E.T. Applications of microwave remote sensing of soil moisture for water resources and Agriculture. *Remote Sens. Environ.* **1991**, *35*, 213–226. [CrossRef]
75. Wood, E.F.; Lettenmaier, D.P.; Zartarian, V.G. A land-surface hydrology parameterization with subgrid variability for general circulation models. *J. Geophys. Res.* **1992**, *97*, 2717. [CrossRef]
76. Cheng, M.; Li, B.; Jiao, X.; Huang, X.; Fan, H.; Lin, R.; Liu, K. Using multimodal remote sensing data to estimate regional-scale soil moisture content: A case study of Beijing, China. *Agric. Water Manag.* **2022**, *260*, 107298. [CrossRef]
77. Walker, J.P. Estimating Soil Moisture Profile Dynamics from Near-Surface Soil Moisture Measurements and Standard Meteorological Data. Ph.D. Thesis, University of Newcastle, Ourimbah, Australia, 1999.
78. Kerr, Y.H.; Waldteufel, P.; Wigneron, J.-P.; Delwart, S.; Cabot, F.; Boutin, J.; Escorihuela, M.-J.; Font, J.; Reul, N.; Gruhier, C.; et al. The smos mission: New tool for monitoring key elements ofthe global water cycle. *Proc. IEEE* **2010**, *98*, 666–687. [CrossRef]
79. Karthikeyan, L.; Pan, M.; Konings, A.G.; Piles, M.; Fernandez-Moran, R.; Nagesh Kumar, D.; Wood, E.F. Simultaneous retrieval of global scale vegetation optical depth, surface roughness, and soil moisture using X-band AMSR-e Observations. *Remote Sens. Environ.* **2019**, *234*, 111473. [CrossRef]
80. Mao, Y.; Crow, W.T.; Nijssen, B. Dual State/rainfall correction via soil moisture assimilation for improved streamflow simulation: Evaluation of a large-scale implementation with soil moisture active passive (SMAP) Satellite Data. *Hydrol. Earth Syst. Sci.* **2020**, *24*, 615–631. [CrossRef]
81. Mezösi, G.; Szatmári, J. Assessment of wind erosion risk on the agricultural area of the southern part of Hungary. *J. Hazard. Mater.* **1998**, *61*, 139–153. [CrossRef]
82. Mohamed, E.; Ali, A.; El-Shirbeny, M.; Abutaleb, K.; Shaddad, S.M. Mapping soil moisture and their correlation with crop pattern using remotely sensed data in arid region. *Egypt. J. Remote Sens. Space Sci.* **2020**, *23*, 347–353. [CrossRef]
83. Wang, L.; Qu, J.J.; Zhang, S.; Hao, X.; Dasgupta, S. Soil moisture estimation using MODIS and ground measurements in eastern China. *Int. J. Remote Sens.* **2007**, *28*, 1413–1418. [CrossRef]
84. Czajkowski, K.P.; Goward, S.N.; Stadler, S.J.; Walz, A. Thermal remote sensing of near surface environmental variables: Application over the Oklahoma Mesonet. *Prof. Geogr.* **2000**, *52*, 345–357. [CrossRef]
85. Chauhan, N.S.; Miller, S.; Ardanuy, P. Spaceborne soil moisture estimation at high resolution: A microwave-optical/IR synergistic approach. *Int. J. Remote Sens.* **2003**, *24*, 4599–4622. [CrossRef]
86. Zhang, L.; Lv, X.; Wang, R. Soil moisture estimation based on polarimetric decomposition and quantile regression forests. *Remote Sens.* **2022**, *14*, 4183. [CrossRef]
87. Li, W.; Liu, C.; Yang, Y.; Awais, M.; Ying, P.; Ru, W.; Cheema, M.J.M. A UAV-aided prediction system of soil moisture content relying on thermal infrared remote sensing. *Int. J. Environ. Sci. Technol.* **2022**, *19*, 9587–9600. [CrossRef]
88. Lei, F.; Senyurek, V.; Kurum, M.; Gurbuz, A.C.; Boyd, D.; Moorhead, R.; Crow, W.T.; Eroglu, O. Quasi-global machine learning-based soil moisture estimates at high spatio-temporal scales using CYGNSS and SMAP observations. *Remote Sens. Environ.* **2022**, *276*, 113041. [CrossRef]
89. Petersen, R.L. A wind tunnel evaluation of methods for estimating surface roughness length at industrial facilities. *Atmos. Environ.* **1997**, *31*, 45–57. [CrossRef]
90. MacKinnon, D.J.; Clow, G.D.; Tigges, R.K.; Reynolds, R.L.; Chavez, P. Comparison of aerodynamically and model-derived roughness lengths (zo) over diverse surfaces, central Mojave Desert, California, USA. *Geomorphology* **2004**, *63*, 103–113. [CrossRef]
91. Levin, N.; Ben-Dor, E.; Kidron, G.J.; Yaakov, Y. Estimation of surface roughness (Z0) over a stabilizing coastal dune field based on vegetation and topography. *Earth Surf. Process. Landf.* **2008**, *33*, 1520–1541. [CrossRef]
92. Turner, R.; Panciera, R.; Tanase, M.A.; Lowell, K.; Hacker, J.M.; Walker, J.P. Estimation of soil surface roughness of agricultural soils using Airborne Lidar. *Remote Sens. Environ.* **2014**, *140*, 107–117. [CrossRef]
93. Moreno, R.G.; Álvarez, M.D.; Alonso, A.T.; Barrington, S.; Requejo, A.S. Tillage and soil type effects on soil surface roughness at semiarid climatic conditions. *Soil Tillage Res.* **2008**, *98*, 35–44. [CrossRef]
94. Zheng, X.; Zhao, K.; Li, X.; Li, Y.; Ren, J. Improvements in farmland surface roughness measurement by employing a new laser scanner. *Soil Tillage Res.* **2014**, *143*, 137–144. [CrossRef]
95. Davidson, M.; Thuy Le Toan Mattia, F.; Satalino, G.; Manninen, T.; Borgeaud, M. On the characterization of Agricultural Soil Roughness for radar remote sensing studies. *IEEE Trans. Geosci. Remote Sens.* **2000**, *38*, 630–640. [CrossRef]

96. Zribi, M.; Ciarletti, V.; Taconet, O. Validation of a rough surface model based on fractional Brownian geometry with SIRC and Erasme Radar Data over orgeval. *Remote Sens. Environ.* **2000**, *73*, 65–72. [CrossRef]
97. Buckley, S.J.; Howell, J.; Enge, H.; Kurz, T. Terrestrial Laser Scanning in geology: Data Acquisition, processing and accuracy considerations. *J. Geol. Soc.* **2008**, *165*, 625–638. [CrossRef]
98. Nield, J.M.; Bryant, R.G.; Wiggs, G.F.; King, J.; Thomas, D.S.; Eckardt, F.D.; Washington, R. The dynamism of salt crust patterns on playas. *Geology* **2015**, *43*, 31–34. [CrossRef]
99. Hu, X.; Shi, L.; Lin, L.; Magliulo, V. Improving surface roughness lengths estimation using machine learning algorithms. *Agric. For. Meteorol.* **2020**, *287*, 107956. [CrossRef]
100. Greeley, R.; Blumberg, D.G.; McHone, J.F.; Dobrovolskis, A.; Iversen, J.D.; Lancaster, N.; Rasmussen, K.R.; Wall, S.D.; White, B.R. Applications of Spaceborne Radar Laboratory data to the study of Aeolian Processes. *J. Geophys. Res. Planets* **1997**, *102*, 10971–10983. [CrossRef]
101. Greeley, R.; Gaddis, L.; Lancaster, N.; Dobrovolskis, A.; Iversen, J.; Rasmussen, K.; Saunders, S.; Van Zyl, J.; Wall, S.; Zebker, H.; et al. Assessment of aerodynamic roughness via airborne radar observations. In *Aeolian Grain Transport*; Springer: Vienna, Austria, 1991; pp. 77–88. [CrossRef]
102. Marticorena, B.; Chazette, P.; Bergametti, G.; Dulac, F.; Legrand, M. Mapping the aerodynamic roughness length of desert surfaces from the polder/adeos bi-directional reflectance product. *Int. J. Remote Sens.* **2004**, *25*, 603–626. [CrossRef]
103. Ge, J.; Liu, H.; Yang, S.; Lan, J. Laser cleaning surface roughness estimation using enhanced GLCM feature and ipso-SVR. *Photonics* **2022**, *9*, 510. [CrossRef]
104. Abdelkareem, M.; Gaber, A.; Abdalla, F.; El-Din, G.K. Use of optical and radar remote sensing satellites for identifying and monitoring active/inactive landforms in the driest desert in Saudi Arabia. *Geomorphology* **2020**, *362*, 107197. [CrossRef]
105. Vrieling, A. Satellite Remote Sensing for Water Erosion Assessment: A Review. *CATENA* **2006**, *65*, 2–18. [CrossRef]
106. Herodowicz, K.; Piekarczyk, J. Effects of soil surface roughness on soil processes and remote sensing data interpretation and its measuring techniques—A Review. *Pol. J. Soil Sci.* **2018**, *51*, 229. [CrossRef]
107. Mayaud, J.; Webb, N. Vegetation in drylands: Effects on wind flow and aeolian sediment transport. *Land* **2017**, *6*, 64. [CrossRef]
108. Webb, N.P.; McGowan, H.A.; Phinn, S.R.; McTainsh, G.H. Auslem (Australian land erodibility model): A tool for identifying wind erosion hazard in Australia. *Geomorphology* **2006**, *78*, 179–200. [CrossRef]
109. Fryrear, D.W.; Bilbro, J.D.; Saleh, A.; Schomberg, H.; Stout, J.E.; Zobeck, T.M. RWEQ: Improved Wind Erosion Technology. *J. Soil Water Conserv.* **2000**, *55*, 183–189.
110. Zhao, Y.; Wu, J.; He, C.; Ding, G. Linking wind erosion to ecosystem services in drylands: A landscape ecological approach. *Landsc. Ecol.* **2017**, *32*, 2399–2417. [CrossRef]
111. Leys, J.; McTainsh, G.; Strong, C.; Heidenreich, S.; Biesaga, K. DustWatch: Using community networks to improve wind erosion monitoring in Australia. *Earth Surf. Process. Landf.* **2008**, *33*, 1912–1926. [CrossRef]
112. Donohue, R.J.; Roderick, M.L.; McVicar, T.R. Deriving consistent long-term vegetation information from AVHRR reflectance data using a cover-triangle-based framework. *Remote Sens. Environ.* **2008**, *112*, 2938–2949. [CrossRef]
113. Goulevitch, B.; Danaher, T.; Walls, J. The statewide Landcover and trees study (slats) monitoring land cover change and greenhouse gas emissions in Queensland. In Proceedings of the IEEE 1999 International Geoscience and Remote Sensing Symposium, IGARSS'99 (Cat. No.99CH36293), Hamburg, Germany, 28 June–2 July 1999. [CrossRef]
114. Guerschman, J.P.; Hill, M.J.; Renzullo, L.J.; Barrett, D.J.; Marks, A.S.; Botha, E.J. Estimating fractional cover of photosynthetic vegetation, non-photosynthetic vegetation and bare soil in the Australian Tropical Savanna Region upscaling the EO-1 Hyperion and Modis sensors. *Remote Sens. Environ.* **2009**, *113*, 928–945. [CrossRef]
115. Panagos, P.; Borrelli, P.; Meusburger, K.; Alewell, C.; Lugato, E.; Montanarella, L. Estimating the soil erosion cover-management factor at the European scale. *Land Use Policy* **2015**, *48*, 38–50. [CrossRef]
116. Fenta, A.A.; Tsunekawa, A.; Haregeweyn, N.; Poesen, J.; Tsubo, M.; Borrelli, P.; Panagos, P.; Vanmaercke, M.; Broeckx, J.; Yasuda, H.; et al. Land susceptibility to water and wind erosion risks in the East Africa Region. *Sci. Total Environ.* **2020**, *703*, 135016. [CrossRef]
117. Guo, B.; Zhang, F.; Yang, G.; Sun, C.; Han, F.; Jiang, L. Improved estimation method of soil wind erosion based on remote sensing and geographic information system in the Xinjiang Uygur autonomous region, China. *Geomat. Nat. Hazards Risk* **2017**, *8*, 1752–1767. [CrossRef]
118. Guoli, G.; Jiyuan, L.; Quanqin, S.; Jun, Z. Sand-fixing function under the change of vegetation coverage in a wind erosion area in northern China. *J. Resour. Ecol.* **2014**, *5*, 105–114. [CrossRef]
119. Mezősi, G.; Blanka, V.; Bata, T.; Kovács, F.; Meyer, B. Estimation of regional differences in wind erosion sensitivity in Hungary. *Nat. Hazards Earth Syst. Sci.* **2015**, *15*, 97–107. [CrossRef]
120. Saadoud, D.; Hassani, M.; Martin Peinado, F.J.; Guettouche, M.S. Application of fuzzy logic approach for wind erosion hazard mapping in Laghouat region (Algeria) using remote sensing and GIS. *Aeolian Res.* **2018**, *32*, 24–34. [CrossRef]
121. Yue, Y.; Shi, P.; Zou, X.; Ye, X.; Zhu, A.; Wang, J. The measurement of wind erosion through field survey and remote sensing: A case study of the mu us desert, China. *Nat. Hazards* **2015**, *76*, 1497–1514. [CrossRef]
122. Baumgertel, A.; Lukić, S.; Belanović Simić, S.; Kadović, R. Identifying areas sensitive to wind erosion—A case study of the AP vojvodina (Serbia). *Appl. Sci.* **2019**, *9*, 5106. [CrossRef]

123. Chi, W.; Zhao, Y.; Kuang, W.; He, H. Impacts of anthropogenic land use/cover changes on soil wind erosion in China. *Sci. Total Environ.* **2019**, *668*, 204–215. [CrossRef]
124. Li, J.; Ma, X.; Zhang, C. Predicting the spatiotemporal variation in soil wind erosion across Central Asia in response to climate change in the 21st Century. *Sci. Total Environ.* **2020**, *709*, 136060. [CrossRef]
125. Rezaei, M.; Sameni, A.; Fallah Shamsi, S.R.; Bartholomeus, H. Remote Sensing of land use/cover changes and its effect on wind erosion potential in southern Iran. *PeerJ* **2016**, *4*, e1948. [CrossRef]
126. Huete, A.; Didan, K.; Miura, T.; Rodriguez, E.; Gao, X.; Ferreira, L. Overview of the radiometric and biophysical performance of the Modis vegetation indices. *Remote Sens. Environ.* **2002**, *83*, 195–213. [CrossRef]
127. Gutman, G.; Ignatov, A. The derivation of the green vegetation fraction from NOAA/AVHRR data for use in numerical weather prediction models. *Int. J. Remote Sens.* **1998**, *19*, 1533–1543. [CrossRef]
128. Qi, J.; Chehbouni, A.; Huete, A.; Kerr, Y.; Sorooshian, S. A modified soil adjusted vegetation index. *Remote Sens. Environ.* **1994**, *48*, 119–126. [CrossRef]
129. Panebianco, J.E.; Buschiazzo, D.E. Effect of temporal resolution of wind data on wind erosion prediction with the revised wind erosion equation (RWEQ). *Cienc. Suelo* **2013**, *31*, 189–199.
130. Rakkar, M.; Blanco-Canqui, H.; Tatarko, J. Predicting soil wind erosion potential under different corn residue management scenarios in the Central Great Plains. *Geoderma* **2019**, *353*, 25–34. [CrossRef]
131. Pi, H.; Sharratt, B.; Feng, G.; Lei, J. Evaluation of two empirical wind erosion models in arid and semi-arid regions of China and the USA. *Environ. Model. Softw.* **2017**, *91*, 28–46. [CrossRef]
132. Bartus, M.; Barta, K.; Szatmári, J.; Farsang, A. Modeling wind erosion hazard control efficiency with an emphasis on shelterbelt system and plot size planning. *Z. Geomorphol.* **2017**, *61*, 123–133. [CrossRef]
133. Kozlovsky Dufková, J.; Mašíček, T.; Lackóová, L. Using of Wind Erosion Equation in GIS. *Infrastruct. Ecol. Rural Areas* **2019**, *2*, 39–51. [CrossRef]
134. Bao, Z.; Zhang, J.; Wang, G.; Guan, T.; Jin, J.; Liu, Y.; Li, M.; Ma, T. The sensitivity of vegetation cover to climate change in multiple climatic zones using machine learning algorithms. *Ecol. Indic.* **2021**, *124*, 107443. [CrossRef]
135. Ito, A.; Kok, J.F. Do dust emissions from sparsely vegetated regions dominate atmospheric iron supply to the Southern Ocean? *J. Geophys. Res. Atmos.* **2017**, *122*, 3987–4002. [CrossRef]
136. Karl, J.W.; Gillan, J.K.; Barger, N.N.; Herrick, J.E.; Duniway, M.C. Interpretation of high-resolution imagery for detecting vegetation cover composition change after fuels reduction treatments in Woodlands. *Ecol. Indic.* **2014**, *45*, 570–578. [CrossRef]
137. Omasa, K.; Hosoi, F.; Konishi, A. 3D lidar imaging for detecting and understanding plant responses and canopy structure. *J. Exp. Bot.* **2006**, *58*, 881–898. [CrossRef] [PubMed]
138. Jupp, D.L.; Culvenor, D.; Lovell, J.; Newnham, G.; Strahler, A.; Woodcock, C. Estimating forest LAI profiles and structural parameters using a ground-based laser called 'Echidna®. *Tree Physiol.* **2008**, *29*, 171–181. [CrossRef] [PubMed]
139. Sankey, J.B.; Law, D.J.; Breshears, D.D.; Munson, S.M.; Webb, R.H. Employing lidar to detail vegetation canopy architecture for prediction of Aeolian Transport. *Geophys. Res. Lett.* **2013**, *40*, 1724–1728. [CrossRef]
140. Bradley, B.A.; Mustard, J.F. Identifying land cover variability distinct from land cover change: Cheatgrass in the Great Basin. *Remote Sens. Environ.* **2005**, *94*, 204–213. [CrossRef]
141. Okin, G.S.; Painter, T.H. Effect of grain size on remotely sensed spectral reflectance of sandy desert surfaces. *Remote Sens. Environ.* **2004**, *89*, 272–280. [CrossRef]
142. Weeks, R.J.; Smith, M.; Pak, K.; Li, W.; Gillespie, A.; Gustafson, B. Surface roughness, radar backscatter, and visible and near-infrared reflectance in Death Valley, California. *J. Geophys. Res. Planets* **1996**, *101*, 23077–23090. [CrossRef]
143. Caylor, K.; Dowty, P.; Shugart, H.; Ringrose, S. Relationship between small-scale structural variability and simulated vegetation productivity across a regional moisture gradient in Southern Africa. *Glob. Chang. Biol.* **2003**, *10*, 374–382. [CrossRef]
144. Okin, G.S.; Roberts, D.A.; Murray, B.; Okin, W.J. Practical limits on hyperspectral vegetation discrimination in arid and semiarid environments. *Remote Sens. Environ.* **2001**, *77*, 212–225. [CrossRef]
145. Sudheer, K.P.; Gowda, P.; Chaubey, I.; Howell, T. Artificial neural network approach for mapping contrasting tillage practices. *Remote Sens.* **2010**, *2*, 579–590. [CrossRef]
146. Shao, J. Resampling Methods in Sample Surveys. *Statistics* **1996**, *27*, 203–254. [CrossRef]
147. Chappell, A.; Webb, N.P.; Guerschman, J.P.; Thomas, D.T.; Mata, G.; Handcock, R.N.; Leys, J.F.; Butler, H.J. Improving ground cover monitoring for wind erosion assessment using MODIS BRDF parameters. *Remote Sens. Environ.* **2018**, *204*, 756–768. [CrossRef]
148. Cruzan, M.B.; Weinstein, B.G.; Grasty, M.R.; Kohrn, B.F.; Hendrickson, E.C.; Arredondo, T.M.; Thompson, P.G. Small unmanned aerial vehicles (Micro-Uavs, drones) in plant ecology. *Appl. Plant Sci.* **2016**, *4*, 1600041. [CrossRef]
149. McGlynn, I.O.; Okin, G.S. Characterization of shrub distribution using high spatial resolution remote sensing: Ecosystem implications for a former Chihuahuan Desert Grassland. *Remote Sens. Environ.* **2006**, *101*, 554–566. [CrossRef]
150. Cleugh, H.A. Effects of windbreaks on airflow, microclimates and crop yields. *Agrofor. Syst.* **1998**, *41*, 55–84. [CrossRef]
151. Zheng, X.; Zhu, J.; Xing, Z. Assessment of the effects of shelterbelts on crop yields at the regional scale in Northeast China. *Agric. Syst.* **2016**, *143*, 49–60. [CrossRef]

152. Chang, X.; Sun, L.; Yu, X.; Jia, G.; Liu, J.; Liu, Z.; Zhu, X.; Wang, Y. Effect of windbreaks on particle concentrations from agricultural fields under a variety of wind conditions in the farming-pastoral ecotone of Northern China. *Agric. Ecosyst. Environ.* **2019**, *281*, 16–24. [CrossRef]
153. Holden, J.; Grayson, R.; Berdeni, D.; Bird, S.; Chapman, P.; Edmondson, J.; Firbank, L.; Helgason, T.; Hodson, M.; Hunt, S.; et al. The role of hedgerows in soil functioning within agricultural landscapes. *Agric. Ecosyst. Environ.* **2019**, *273*, 1–12. [CrossRef]
154. Wiesmeier, M.; Lungu, M.; Cerbari, V.; Boincean, B.; Hübner, R.; Kögel-Knabner, I. Rebuilding soil carbon in degraded steppe soils of Eastern Europe: The importance of windbreaks and improved cropland management. *Land Degrad. Dev.* **2018**, *29*, 875–883. [CrossRef]
155. Engineering Sciences Data Unit (ESDU). *Estimation of Shelter Provided by Solid and Porous Fences*; ESDU Data Item 97031; Engineering Sciences Data Unit (ESDU): London, UK, 2000.
156. Li, B.; Sherman, D.J. Aerodynamics and morphodynamics of Sand Fences: A Review. *Aeolian Res.* **2015**, *17*, 33–48. [CrossRef]
157. Miri, A.; Dragovich, D.; Dong, Z. Wind flow and sediment flux profiles for vegetated surfaces in a wind tunnel and field-scale windbreak. *CATENA* **2021**, *196*, 104836. [CrossRef]
158. Yukhnovskyi, V.; Polishchuk, O.; Lobchenko, G.; Khryk, V.; Levandovska, S. Aerodynamic properties of windbreaks of various designs formed by thinning in central Ukraine. *Agrofor. Syst.* **2020**, *95*, 855–865. [CrossRef]
159. Kučera, J.; Podhrázská, J.; Karásek, P.; Papaj, V. The effect of windbreak parameters on the wind erosion risk assessment in Agricultural Landscape. *J. Ecol. Eng.* **2020**, *21*, 150–156. [CrossRef]
160. Schmidt, S.; Meusburger, K.; Figueiredo, T.; Alewell, C. Modelling hot spots of soil loss by wind erosion (solowind) in Western Saxony, Germany. *Land Degrad. Dev.* **2016**, *28*, 1100–1112. [CrossRef]
161. Yang, X.; Li, F.; Fan, W.; Liu, G.; Yu, Y. Evaluating the efficiency of wind protection by windbreaks based on remote sensing and Geographic Information Systems. *Agrofor. Syst.* **2021**, *95*, 353–365. [CrossRef]
162. Loeffler, A.E.; Gordon, A.M.; Gillespie, T.J. Optical porosity and windspeed reduction by coniferous windbreaks in southern Ontario. *Agrofor. Syst.* **1992**, *17*, 119–133. [CrossRef]
163. Kenney, W. A method for estimating windbreak porosity using digitized photographic silhouettes. *Agric. For. Meteorol.* **1987**, *39*, 91–94. [CrossRef]
164. Středová, H.; Podhrázská, J.; Litschmann, T.; Středa, T.; Rožnovský, J. Aerodynamic parameters of windbreak based on its optical porosity. *Contrib. Geophys. Geod.* **2012**, *42*, 213–226. [CrossRef]
165. Vigiak, O.; Sterk, G.; Warren, A.; Hagen, L.J. Spatial modeling of wind speed around windbreaks. *CATENA* **2003**, *52*, 273–288. [CrossRef]
166. An, L.; Wang, J.; Xiong, N.; Wang, Y.; You, J.; Li, H. Assessment of permeability windbreak forests with different porosities based on laser scanning and computational fluid dynamics. *Remote Sens.* **2022**, *14*, 3331. [CrossRef]
167. Yusaiyin, M.; Tanaka, N. Effects of windbreak width in wind direction on wind velocity reduction. *J. For. Res.* **2009**, *20*, 199–204. [CrossRef]
168. Deng, R.X.; Li, Y.; Xu, X.L.; Wang, W.J.; Wei, Y.C. Remote estimation of shelterbelt width from spot5 imagery. *Agrofor. Syst.* **2016**, *91*, 161–172. [CrossRef]
169. Burke, M.; Rundquist, B.; Zheng, H. Detection of Shelterbelt density change using historic APFO and NAIP aerial imagery. *Remote Sens.* **2019**, *11*, 218. [CrossRef]
170. Ghimire, K.; Dulin, M.W.; Atchison, R.L.; Goodin, D.G.; Shawn Hutchinson, J.M. Identification of windbreaks in Kansas using object-based image analysis, GIS techniques and field survey. *Agrofor. Syst.* **2014**, *88*, 865–875. [CrossRef]
171. Wiseman, G.; Kort, J.; Walker, D. Quantification of shelterbelt characteristics using high-resolution imagery. *Agric. Ecosyst. Environ.* **2009**, *131*, 111–117. [CrossRef]
172. Yang, X.; Yu, Y.; Fan, W. A method to estimate the structural parameters of windbreaks using remote sensing. *Agrofor. Syst.* **2016**, *91*, 37–49. [CrossRef]
173. Pásztor, L.; Négyesi, G.; Laborczi, A.; Kovács, T.; László, E.; Bihari, Z. Integrated Spatial Assessment of Wind Erosion Risk in Hungary. *Nat. Hazards Earth Syst. Sci.* **2016**, *16*, 2421–2432. [CrossRef]
174. Fraucqueur, L.; Morin, N.; Masse, A.; Remy, P.-Y.; Hugé, J.; Kenner, C.; Dazin, F.; Desclée, B.; Sannier, C. A new Copernicus High Resolution Layer at pan-European scale: Small woody features. In *Remote Sensing for Agriculture, Ecosystems, and Hydrology XXI*; SPIE: Bellingham, WA, USA, 2019. [CrossRef]
175. EEA. *High Resolution Layer Forest 2018 Product User Manual*; European Environment Agency: Copenhagen, Denmark, 2020; p. 56.
176. Lefsky, M.A. A global forest canopy height map from the Moderate Resolution Imaging Spectroradiometer and the Geoscience Laser Altimeter System. *Geophys. Res. Lett.* **2010**, *37*, L15401. [CrossRef]
177. Potapov, P.; Tyukavina, A.; Turubanova, S.; Talero, Y.; Hernandez-Serna, A.; Hansen, M.; Saah, D.; Tenneson, K.; Poortinga, A.; Aekakkararungroj, A.; et al. Annual continuous fields of woody vegetation structure in the lower Mekong Region from 2000-2017 Landsat Time-Series. *Remote Sens. Environ.* **2019**, *232*, 111278. [CrossRef]
178. Kugler, F.; Schulze, D.; Hajnsek, I.; Pretzsch, H.; Papathanassiou, K.P. Tandem-X Pol-Insar Performance for Forest Height Estimation. *IEEE Trans. Geosci. Remote Sens.* **2014**, *52*, 6404–6422. [CrossRef]
179. Næsset, E. Determination of mean tree height of forest stands using Airborne Laser Scanner Data. *ISPRS J. Photogramm. Remote Sens.* **1997**, *52*, 49–56. [CrossRef]

180. Chamberlain, C.P.; Sánchez Meador, A.J.; Thode, A.E. Airborne lidar provides reliable estimates of canopy base height and canopy bulk density in southwestern ponderosa pine forests. *For. Ecol. Manag.* **2021**, *481*, 118695. [CrossRef]
181. Jarron, L.R.; Coops, N.C.; MacKenzie, W.H.; Tompalski, P.; Dykstra, P. Detection of sub-canopy forest structure using Airborne Lidar. *Remote Sens. Environ.* **2020**, *244*, 111770. [CrossRef]
182. Choi, H.; Song, Y.; Kang, W.; Thorne, J.H.; Song, W.; Lee, D.K. Lidar-derived three-dimensional ecological connectivity mapping for urban bird species. *Landsc. Ecol.* **2021**, *36*, 581–599. [CrossRef]
183. Borrelli, P.; Robinson, D.A.; Fleischer, L.R.; Lugato, E.; Ballabio, C.; Alewell, C.; Meusburger, K.; Modugno, S.; Schütt, B.; Ferro, V.; et al. An assessment of the global impact of 21st Century land use change on soil erosion. *Nat. Commun.* **2017**, *8*, 2013. [CrossRef] [PubMed]
184. Kriese, J.; Hoeser, T.; Asam, S.; Kacic, P.; Da Ponte, E.D.; Gessner, U. Deep learning on synthetic data enables the automatic identification of deficient forested windbreaks in the Paraguayan Chaco. *Remote Sens.* **2022**, *14*, 4327. [CrossRef]
185. Kwong, I.H.; Fung, T. Tree height mapping and crown delineation using lidar, large format aerial photographs, and unmanned aerial vehicle photogrammetry in subtropical urban forest. *Int. J. Remote Sens.* **2020**, *41*, 5228–5256. [CrossRef]
186. Lucas, R.; Van De Kerchove, R.; Otero, V.; Lagomasino, D.; Fatoyinbo, L.; Omar, H.; Satyanarayana, B.; Dahdouh-Guebas, F. Structural characterisation of mangrove forests achieved through combining multiple sources of remote sensing data. *Remote Sens. Environ.* **2020**, *237*, 111543. [CrossRef]
187. Metternicht, G.; Zinck, J.A.; Blanco, P.D.; Del Valle, H.F. Remote sensing of land degradation: Experiences from Latin America and the Caribbean. *J. Environ. Qual.* **2010**, *39*, 42–61. [CrossRef]
188. Žížala, D.; Juřicová, A.; Zádorová, T.; Zelenková, K.; Minařík, R. Mapping soil degradation using remote sensing data and ancillary data: South-East Moravia, Czech Republic. *Eur. J. Remote Sens.* **2018**, *52* (Suppl. 1), 108–122. [CrossRef]
189. Del Valle, H.F.; Blanco, P.D.; Metternicht, G.I.; Zinck, J.A. Radar Remote Sensing of wind-driven land degradation processes in northeastern Patagonia. *J. Environ. Qual.* **2010**, *39*, 62–75. [CrossRef]
190. Reiche, M.; Funk, R.; Zhang, Z.; Hoffmann, C.; Reiche, J.; Wehrhan, M.; Li, Y.; Sommer, M. Application of satellite remote sensing for mapping wind erosion risk and dust emission-deposition in Inner Mongolia grassland, China. *Grassl. Sci.* **2012**, *58*, 8–19. [CrossRef]
191. Dick, A.; Raynaud, J.-L.; Rolland, A.; Pelou, S.; Coustance, S.; Dedieu, G.; Hagolle, O.; Burochin, J.-P.; Binet, R.; Moreau, A. Venμs: Mission characteristics, final evaluation of the first phase and data production. *Remote Sens.* **2022**, *14*, 3281. [CrossRef]
192. Chen, L.; Letu, H.; Fan, M.; Shang, H.; Tao, J.; Wu, L.; Zhang, Y.; Yu, C.; Gu, J.; Hong, J.; et al. An introduction to the Chinese high-resolution Earth observation system: Gaofen-1~7 civilian satellites. *J. Remote Sens.* **2022**, *2022*, 9769536. [CrossRef]
193. Rufin, P.; Bey, A.; Picoli, M.; Meyfroidt, P. Large-area mapping of active cropland and short-term fallows in smallholder landscapes using PlanetScope Data. *Int. J. Appl. Earth Obs. Geoinf.* **2022**, *112*, 102937. [CrossRef]
194. Celesti, M.; Rast, M.; Adams, J.; Boccia, V.; Gascon, F.; Isola, C.; Nieke, J. The copernicus hyperspectral imaging mission for the environment (CHIME): Status and planning. In Proceedings of the IGARSS 2022—2022 IEEE International Geoscience and Remote Sensing Symposium, Kuala Lumpur, Malaysia, 17–22 July 2022. [CrossRef]
195. Bracken, A.; Coburn, C.; Staenz, K.; Rochdi, N.; Segl, K.; Chabrillat, S.; Schmid, T. Detecting soil erosion in semi-arid Mediterranean environments using simulated enmap data. *Geoderma* **2019**, *340*, 164–174. [CrossRef]
196. Pierdicca, N.; Davidson, M.; Chini, M.; Dierking, W.; Djavidnia, S.; Haarpaintner, J.; Hajduch, G.; Laurin, G.V.; Lavalle, M.; López-Martínez, C.; et al. The Copernicus L-band SAR mission rose-L (Radar observing system for europe) (conference presentation). In *Active and Passive Microwave Remote Sensing for Environmental Monitoring III*; SPIE: Bellingham, WA, USA, 2019. [CrossRef]
197. Kilic, L.; Prigent, C.; Aires, F.; Boutin, J.; Heygster, G.; Tonboe, R.T.; Roquet, H.; Jimenez, C.; Donlon, C. Expected performances of the Copernicus Imaging Microwave Radiometer (CIMR) for an all-weather and high spatial resolution estimation of ocean and sea ice parameters. *J. Geophys. Res. Ocean.* **2018**, *123*, 7564–7580. [CrossRef]
198. Singh, S.; Tiwari, R.K.; Gusain, H.S.; Sood, V. Potential applications of SCATSAT-1 Satellite Sensor: A systematic review. *IEEE Sens. J.* **2020**, *20*, 12459–12471. [CrossRef]
199. Zhou, Z.S.; Parker, A.; Brindle, L.; Rosenqvist, A.; Caccetta, P.; Held, A. Initial NovaSAR-1 Data Processing and Imagery Evaluation. In Proceedings of the IGARSS 2020—2020 IEEE International Geoscience and Remote Sensing Symposium, Waikoloa, HI, USA, 26 September–2 October 2020; pp. 6154–6157. [CrossRef]
200. Pickup, G.; Nelson, D. Use of landsat radiance parameters to distinguish soil erosion, stability, and deposition in arid Central Australia. *Remote Sens. Environ.* **1984**, *16*, 195–209. [CrossRef]
201. Dhakal, A.S.; Amada, T.; Aniya, M.; Sharma, R.R. Detection of Areas Associated with Flood and Erosion Caused by a Heavy Rainfall Using Multitemporal Landsat TM Data. *Photogramm. Eng. Remote Sens.* **2002**, *68*, 233–239.
202. Nichol, J.E.; Shaker, A.; Wong, M. Application of high-resolution stereo satellite images to detailed landslide Hazard assessment. *Geomorphology* **2006**, *76*, 68–75. [CrossRef]
203. Lu, D.; Weng, Q. A survey of image classification methods and techniques for improving classification performance. *Int. J. Remote Sens.* **2007**, *28*, 823–870. [CrossRef]
204. Shoko, C.; Mutanga, O.; Dube, T. Progress in the remote sensing of C3 and c4 grass species aboveground biomass over time and space. *ISPRS J. Photogramm. Remote Sens.* **2016**, *120*, 13–24. [CrossRef]
205. Sibanda, M.; Mutanga, O.; Rouget, M. Discriminating rangeland management practices using simulated HyspIRI, Landsat 8 OLI, Sentinel 2 MSI, and VENμS Spectral Data. *IEEE J. Sel. Top. Appl. Earth Obs. Remote Sens.* **2016**, *9*, 3957–3969. [CrossRef]

206. Michel, S.; Gamet, P.; Lefèvre-Fonollosa, M. HYPXIM—A hyperspectral satellite defined for science, security and defence users. In Proceedings of the 2011 3rd Workshop on Hyperspectral Image and Signal Processing: Evolution in Remote Sensing (WHISPERS), Lisbon, Portugal, 6–9 June 2011; pp. 1–4.
207. Vrieling, A.; De Jong, S.M.; Sterk, G.; Rodrigues, S.C. Timing of erosion and satellite data: A multi-resolution approach to soil erosion risk mapping. *Int. J. Appl. Earth Obs. Geoinf.* **2008**, *10*, 267–281. [CrossRef]
208. Huang, J.; Yu, H.; Guan, X.; Wang, G.; Guo, R. Accelerated dryland expansion under climate change. *Nat. Clim. Chang.* **2016**, *6*, 166–171. [CrossRef]
209. Négyesi, G.; Lóki, J.; Buró, B.; Bertalan-Balázs, B.; Pásztor, L. Wind erosion researches in Hungary—Past, present and future possibilities. *Hung. Geogr. Bull.* **2019**, *68*, 223–240. [CrossRef]
210. Sharratt, B.S.; Tatarko, J.; Abatzoglou, J.T.; Fox, F.A.; Huggins, D. Implications of climate change on wind erosion of agricultural lands in the Columbia plateau. *Weather Clim. Extrem.* **2015**, *10*, 20–31. [CrossRef]

Disclaimer/Publisher's Note: The statements, opinions and data contained in all publications are solely those of the individual author(s) and contributor(s) and not of MDPI and/or the editor(s). MDPI and/or the editor(s) disclaim responsibility for any injury to people or property resulting from any ideas, methods, instructions or products referred to in the content.

geosciences

MDPI

Article

Integrated Schumann Resonance Intensity as an Indicator of the Global Thunderstorm Activity

Masashi Hayakawa [1,2,*], Yuriy P. Galuk [3] and Alexander P. Nickolaenko [4]

[1] Hayakawa Institute of Seismo Electromagnetics Co., Ltd. (Hi-SEM), UEC Alliance Center #521, 1-1-1 Kojima-cho, Chofu-shi, Tokyo 182-0026, Japan
[2] Advanced Wireless & Communications Research Center (AWCC), The University of Electro-Communications (UEC), 1-5-1 Chofugaoka, Chofu-shi, Tokyo 182-8585, Japan
[3] Department of Applied Mathematics and Control Processes, Saint-Petersburg State University, 35, University Ave., Peterhof, Saint-Petersburg 198504, Russia; j.galuk@spbu.ru
[4] O.Ya. Usikov Institute for Radio-Physics and Electronics, National Academy of Sciences of the Ukraine, 12, Acad. Proskura Street, 61085 Kharkov, Ukraine; sashanickolaenko@gmail.com
* Correspondence: hayakawa@hi-seismo-em.jp

Abstract: This paper addresses the accuracy of estimates for the contemporary level of global thunderstorm activity found from the synchronous records of integrated Schumann resonance (SR) intensity at two high-latitude observatories in the Northern and Southern hemispheres. The results are based on numerical simulations of electromagnetic fields in the frequency band of the global (Schumann) resonance in the Earth–ionosphere cavity characterized by a realistic conductivity profile in the middle atmosphere. The credible distribution is used for global thunderstorm activity in space and time. The paired observatory locations are considered either at the geographic poles or at Svalbard and the Antarctic Peninsula. The seasonal variations in the spatial distribution of global thunderstorms are adopted from the OTD satellite observations. The diurnal variations imply the spatial and temporal distribution of lightning strokes measured by the WWLLN network for an arbitrarily chosen date of 18 January 2022. The results obtained suggest that simultaneous records of the integrated SR intensity at Svalbard and in Antarctica provide errors below 3% in the diurnal variations of global thunderstorm activity with a temporal resolution of 10 min. The seasonal changes in global thunderstorm intensity are estimated with an error of ~10%. Since the level of global thunderstorm activity varies by a factor of two on the both time scales, the estimates confirm the appropriate accuracy of the estimate of thunderstorm activity from the concurrent measurements at the high-latitude SR observatories in the Arctic and Antarctic.

Keywords: Schumann resonance (SR) intensity; global thunderstorm activity; diurnal variations; seasonal variations

Citation: Hayakawa, M.; Galuk, Y.P.; Nickolaenko, A.P. Integrated Schumann Resonance Intensity as an Indicator of the Global Thunderstorm Activity. *Geosciences* **2023**, *13*, 177. https://doi.org/10.3390/geosciences13060177

Academic Editors: Pao K. Wang and Jesus Martinez-Frias

Received: 24 April 2023
Revised: 30 May 2023
Accepted: 13 June 2023
Published: 14 June 2023

Copyright: © 2023 by the authors. Licensee MDPI, Basel, Switzerland. This article is an open access article distributed under the terms and conditions of the Creative Commons Attribution (CC BY) license (https://creativecommons.org/licenses/by/4.0/).

1. Introduction

Geoscience incorporates three great areas corresponding to three media: the solid earth, the ocean, and the Earth's atmosphere. The present paper is concerned with the terrestrial atmosphere, namely, it addresses the global electric activity of the Earth's atmosphere.

It is well known that the global electromagnetic (Schumann) resonance in the Earth–ionosphere cavity is driven by electromagnetic radiation from global thunderstorms. Schumann resonance (SR) and its observations are described in detail in the literature. The necessary information and the bibliography may be found in previous works [1–8]. SR is observed in the vertical electric or (more often) in the horizontal magnetic field. Power spectra of global SR have maxima (modes) at frequencies of 8, 14, 20 Hz, etc., and the resonance intensity might be used for estimating the level of global lightning activity. The major obstacle to such measurements arises from the distance dependence of the modal amplitudes.

The latter emerges in the closed spherical Earth–ionosphere cavity bounded by the ground surface and the lower ionosphere. This is why the amplitude of the recorded oscillations varies non-monotonously with the source–observer distance: the field amplitude acquires the maxima and minima in space arising from the interaction of the direct and antipodal waves propagating through the cavity. For compensating spatial variations, an application was proposed of the total resonance intensity, i.e., the spectral density integrated over the frequency band covering several resonance modes [1,9–12].

Usually, the power spectral density is integrated over the first three modes: from about 5 to 23 Hz. The quantitative estimates for the accuracy of this technique were discussed in [10] in a realistic Earth–ionosphere cavity model when excited by a point vertical dipole source. It was shown that frequency integration reduces deviations in the estimated source intensity from ~6 dB to a level of about 1 dB. Unfortunately, these estimates were relevant only to a compact field source, while actual thunderstorm activity covers substantial areas over the globe. Thus, it is highly desirable to obtain similar estimates for the actual position and size of global thunderstorms relative to the observer. The demand for such a study becomes especially obvious from a recent study based on multi-stationed SR observations [13]. In this context, the modeling is necessary of simultaneous SR monitoring at globally separated observatories. This particular subject is the goal of the present study.

2. Formulation of the Problem

We apply the uniform Earth–ionosphere cavity model: a spherical cavity uniform along the angular coordinates, which is formed by the perfectly conducting ground and the horizontally stratified atmosphere of conductivity gradually increasing with height. We use the vertical profile of air conductivity suggested in [14]. This profile is used in the full-wave solution for computing the propagation constant of extremely low frequency (ELF) radio waves $\upsilon(f)$ and the normalizing factor $N(f)$; they both depend on the signal frequency f as seen in [14–17]. Since two orthogonal components of the horizontal magnetic field are usually recorded in experimental observations, we use the west–east $H_{WE} = H_X$ and the south–north $H_{SN} = H_Y$ components. These fields are formally described by the zero-order mode of the Earth–ionosphere waveguide at ELF. The power spectra of these fields are described by the following expressions [5]:

$$|H_X|^2 = \left|\frac{1}{4aN}\right|^2 \sum_{i=-\infty}^{\infty} \left| M_i \frac{P_\nu^1(-\cos\theta_i)}{\sin \pi\nu} \right|^2 \cos^2(Az_i), \quad (1)$$

$$|H_Y|^2 = \left|\frac{1}{4aN}\right|^2 \sum_{i=-\infty}^{\infty} \left| M_i \frac{P_\nu^1(-\cos\theta_i)}{\sin \pi\nu} \right|^2 \sin^2(Az_i). \quad (2)$$

Each sum in Equations (1) and (2) accounts for the mutually independent lightning strokes, which are distributed over the Earth's surface. The following notations are used: a is the Earth's radius; $N(f)$ is the normalization coefficient (the excitation factor); $\upsilon(f)$ is the propagation constant; $P_\nu^1(-\cos\theta_i)$ is the associated Legendre function of the complex index υ; θ_i is the angular distance from the observer to the i-th lightning stroke; Az_i denotes the particular source azimuth at the observation point; M_i is the current moment of the i-th discharge.

Equations (1) and (2) describe the accumulation of pulsed power arriving from the individual lightning strokes. These relations are valid when the global thunderstorms form the Poisson succession of ELF radio pulses. Such an assumption is quite natural, since the random individual lightning discharges are mutually independent.

3. Model Daily Variations

For introducing the model daily variations in the level of global lightning activity, one must specify the coordinates and occurrence times of particular lightning strokes.

These data are used in our computations of the SR intensity. The real records of the World Wide Lightning Location Network (WWLLN) are well suited for this purpose. The network operates in the very low frequency (VLF) band [18–22]. The relative closeness of the WWLLN operating frequency band 6–18 kHz to the SR band of 4–40 Hz serves in favor of utilizing these data in modeling of the global electromagnetic resonance signals. The WWLLN exploits the observation sites covering the entire globe, which synchronously register the pulses arriving from the lightning discharges. The network data provide the occurrence time of particular strokes and their coordinates derived from the mutual delay of pulses arriving at different sites. The radiated energy is also estimated by WWLLN [18–22].

The computations are organized in the following way. As the first step, we find the source–observer distance and the arrival angle (source bearing) of particular radio pulse by using known position of lightning strokes. We compute the SR power spectra in two orthogonal components of the horizontal magnetic field at the observatory. In Equations (1) and (2), we account for the radiated energy of a stroke provided by the WWLLN. In fact, we assume that the spectral density radiated by a lightning stroke being directly proportional to $|M_i|^2$ is independent of frequency (the source current moments have the 'white' spectra).

We selected an arbitrary date of the WWLLN record for our modeling, 18 January 2022. Prior to calculating the SR power spectra, we inspected the WWLLN data and eliminated the pulses with energy significantly exceeding the typical level in the data set; the reason for these deviations remains unknown (reading error?). In order to demonstrate general features of the WWLLN data, we show in Figure 1 the spatial distribution of lightning strokes in the time interval 12:00–13:00 UTC. This figure presents the world map in the rectangular projection. Geographic longitude and latitude are plotted in degrees along the abscissa and ordinate. The map outlines the continents. Positions of all 28,703 lightning strokes are shown in the figure by the red diamonds. One may observe that the majority of lightning strokes appear southward of the equator, which reflects the seasonal drift of global thunderstorm activity. The strokes are often detected over land, and discharges concentrate around Indonesia, Australia, South Africa, Madagascar, and South America during this particular time interval. All these features agree with climatology data on the global thunderstorm distribution.

We divided the original record of the WWLLN network into 10-min intervals, for which the field components were computed and the contributions accumulated of individual lightning strokes into the SR power spectra. Thus, the 144 cumulative power spectra were obtained in two orthogonal magnetic field components at an arbitrary observatory during the day. To obtain estimates of the contemporary intensity of SR oscillations (over 10 min), we integrated the power spectra over the frequency band 5–23 Hz with a step of 0.1 Hz. The integrated spectra of individual field components were then summed, providing the integrated power of the total horizontal magnetic field as seen below.

Energy radiated by the lightning activity according to WWLLN data was also summed over the same 10-min time intervals thus providing the level of the ongoing intensity of global thunderstorms. This value was compared with the integrated intensity of SR.

It is clear that the integrated intensity of SR at a site will slightly increase when global thunderstorms approach the observer and decrease when the thunderstorms move away from him. It is necessary to somehow compensate for this remaining distance-dependence of the integrated spectral power. The simplest way is to use the simultaneous records at a couple of 'conjugate' observatories located in such a way that the observed increase in the intensity at one point is compensated by an equal decrease at the other field site.

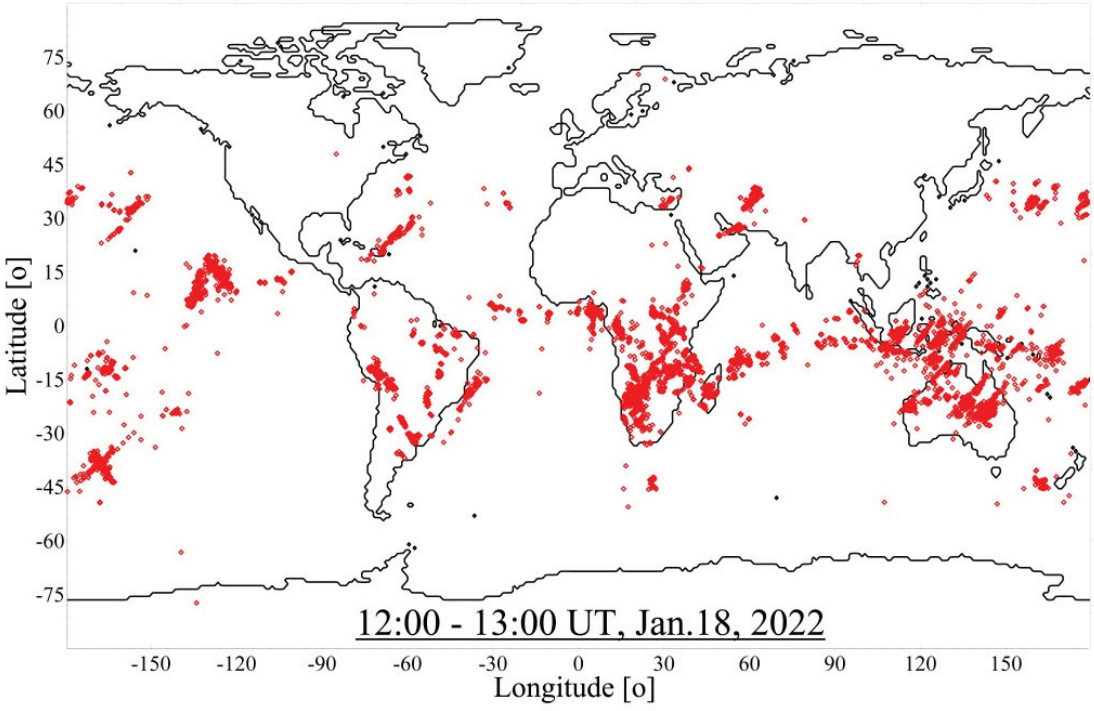


Figure 1. Spatial distribution of lightning discharges (red dots) over the globe according to the WWLLN data for the interval 12–13 h UTC on 18 January 2022.

3.1. Polar Observers

One may expect that the most promising pair of observatories should occupy the geographic North and South Poles. We know that global thunderstorm activity is concentrated at low latitudes. We may expect therefore that the diurnal drift of thunderstorms around the globe will not cause considerable alterations in the source distance from a polar observatory. Simultaneously, a moderate decrease in the distance from one observer will be compensated by relevant increase from the other one. Consequently, the sum of the integrated SR intensities recorded at the poles will be insensitive to the daily movement of lightning activity: this sum will adequately reflect alterations in the level of global thunderstorm activity.

Figure 2 demonstrates the simulated dynamic power spectra of the total horizontal magnetic field in the SR band. Daily variations in the spectra were computed for observers positioned at the North (left panel) and South Pole (right panel). The horizontal axis shows the Universal Time (UT) in hours, and the vertical axis depicts the frequency in Hertz. The total magnetic field power $|H(f)|^2 = |H_{WE}(f)|^2 + |H_{SN}(f)|^2$ is shown by the color, and the common color scale is found to the right of the dynamic spectra.

A remark is appropriate here that the term 'west–east direction' has no sense at the poles. We postulated that the H_{SN} field component is directed along the Greenwich zero meridian, while the orthogonal H_{WE} component is orthogonal to it.

The spectral peaks of the global electromagnetic resonance are visible in the dynamic spectra as the horizontal yellow-red stripes in the vicinity of 8, 14, 20, 26 Hz. These areas are separated by the dark-blue bands corresponding to the minima in the power spectral density. The figure illustrates a high similarity of the dynamic spectra at the opposite poles of the Earth, although the resonance intensity is slightly higher at the South Pole than at

the North Pole. The general outline of the SR pattern indicates their close relationship to the diurnal variations in the thunderstorm activity rather than to their positions.

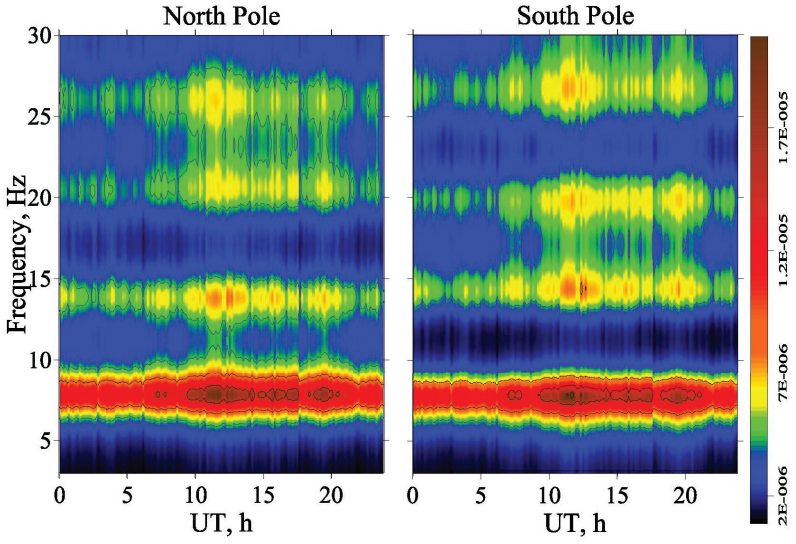


Figure 2. Dynamic spectra of SR for observers at the geographic North and South Poles.

We show in Figure 3 the temporal changes in the cumulative intensities of resonance oscillations: the power spectral density $\int_{f_1}^{f_2} |H_{WE}(f)|^2 df$ and $\int_{f_1}^{f_2} |H_{SN}(f)|^2 df$ integrated over the frequency band 5–23 Hz with a step of 0.1 Hz. Individual curves in Figure 3 show the power spectra integrated over the frequency, i.e., along the vertical lines in Figure 2. The abscissa in Figure 3 shows the UT in hours, and the integrated intensity is plotted along the ordinate in relative units. The red curves in this figure correspond to the South Pole data, and the blue curves show the data from the North Pole.

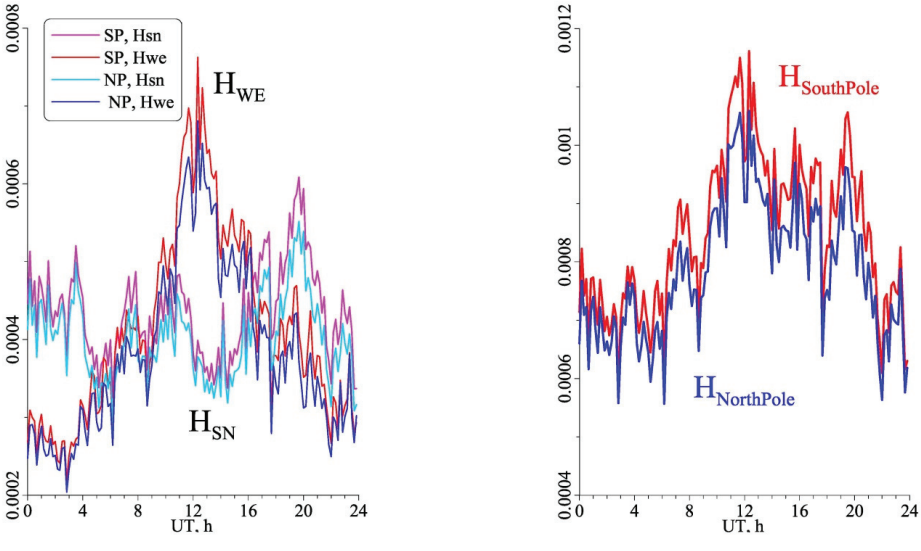


Figure 3. Daily variations of the integrated intensity of the field components (**left panel**) and the total horizontal magnetic field (**right panel**) at the North and the South Poles.

The left panel in Figure 3 shows temporal changes in the integrated intensity of separate field components west–east and south–north. The right panel allows us to compare diurnal variations in the total horizontal magnetic field H at the poles. These plots demonstrate the degree of mutual similarity of the curves calculated for the opposite poles.

Diurnal variations in the intensity of the H_{WE} field at both poles have a clear maximum in the vicinity of the UTC noon. In contrast, the power of H_{SN} component has a minimum in this time interval. It shows an increase occurring around 20:00 UTC, and the smaller local maxima are present in the interval 0–4:00 and around 10:00 UTC. The maxima are easily explained. The growth in the H_{WE} component is conditioned by the increase in thunderstorm activity in Madagascar and South Africa, which is natural for the boreal winter. This activity reaches its maximum around the UTC noon hours. The maxima in the intensity of the orthogonal H_{SN} field component are associated with the thunderstorms in South America (20 h), Oceania (0–4 h), and Southeast Asia with Australia (10 h). Hence, the temporal behavior of these fields is conditioned by the above-chosen orientation of magnetic field components at the poles.

It is important to note that SR signals at the South Pole slightly exceed those detected at the North Pole. These variations indicate that the distance-dependence in the integrated field intensity was not completely compensated by applying the frequency-integrated individual field components.

The right panel in Figure 3 depicts the SR power in the total horizontal magnetic field at the North and the South Poles. The total magnetic field power is characterized by a single wide daily maximum at both the polar sites. The maximum is located in the vicinity of 11–12 h UTC. Obviously, the residual effect of the varying source–observer distance might be further reduced by summing the integrated SR intensities observed at the poles. The results of such an operation are presented in Figure 4.

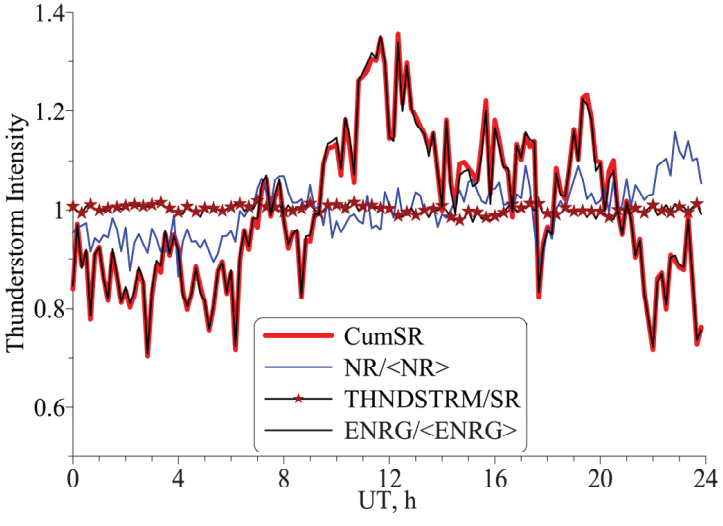


Figure 4. Diurnal variations of the sum of the integrated SR intensities at the poles and changes in the parameters of global lightning activity.

Figure 4 shows the diurnal changes of the following values obtained in the model computations. The thin blue curve depicts variations of the normalized number of lightning strokes $\frac{N_{Strokes}}{\langle N_{Strokes}\rangle}$ recorded during each 10-min interval by the WWLLN network on 18 January 2022. From now on, the angular brackets denote the averaging over the day. The thin black line shows changes in time of the normalized total energy emitted by the global lightning strokes $\frac{ENRG}{\langle ENRG\rangle}$ also corresponding to every 10-min interval of observations

by WWLLN. The bold red curve originates from the SR data: it depicts the normalized cumulative resonance intensity at the North and South Poles $\frac{|H_{NP}|^2 + |H_{SP}|^2}{\langle |H_{NP}|^2 + |H_{SP}|^2 \rangle}$. It is clear that the black and the red lines in Figure 4 are practically coincident, i.e., the cumulative SR power in the polar records follows in time the energy radiated by the global lightning activity.

The black curve with brown stars illustrates the accuracy of the measurement technique: this is the ratio of the normalized energy radiated by the lightning strokes to the normalized cumulative intensity of SR. The daily mean of this ratio is equal to 1.0004, and its standard deviation is 0.9%. Thus, the results of numerical modeling bring us to the conclusion that simultaneous records of SR at the North and South Poles allow for accurate monitoring of changes in the level of global thunderstorm activity on the daily scale.

3.2. Diurnal Variations for High-Latitude Observers

After completing the modeling of diurnal variations at the Earth's poles, let us turn to more realistic records at the coupled high-latitude observatories in the Arctic and Antarctic. These should be equipped with the same calibrated receiving hardware and exploit the same processing technique. There is such a pair of facilities: the Ukrainian Antarctic Observatory "Akademik Vernadsky" (UAS; 65.25° S and 64.24° W) and the Norwegian observatory on Svalbard SOUSY (78.15° N and 16.05° E); the details can be found in [23,24].

Figure 5 shows the model dynamic spectra of SR computed for these two observatories and based on the WWLLN thunderstorm data for the same date of 18 January 2022. We computed the power spectra of the H_{WE} and H_{SN} horizontal magnetic field components and obtained afterwards the power spectra of the total magnetic field $|H(f)|^2 = |H_{WE}(f)|^2 + |H_{SN}(f)|^2$ relevant to the 10-min tine intervals. These dynamic power spectra of total field H at UAS and SOUSY are shown in Figure 5 as the 2D maps above the time–frequency plane. The abscissas in both panels depict the UTC in hours, and the ordinate displays the ELF frequency in Hertz. The power spectral density of the total horizontal magnetic field is shown by color and the corresponding color scale is placed on the right. The Arctic and the Antarctic spectrograms are found on the right and left panels of Figure 5.

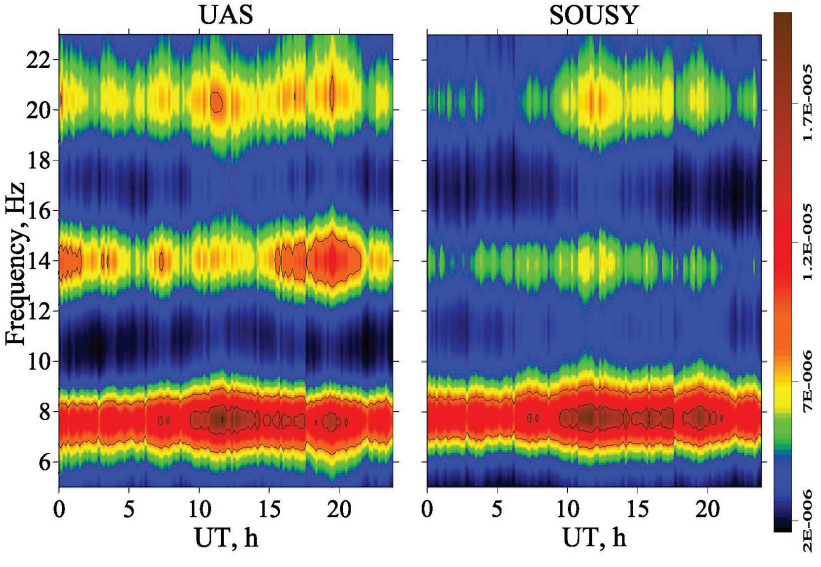


Figure 5. Model dynamic spectra of SR at high-latitude observatories in the Arctic and Antarctic.

The SR peaks are clearly visible at the sub-polar field sites in form of the horizontal red and yellow bands. The spectral minima separating the peaks are outlined by dark-blue horizontal areas. The spectrograms demonstrate that diurnal variations in the global resonance intensity have much in common at each observatory. One may notice the maximum in the intensity of electromagnetic signal in the vicinity of UTC noon present both in the Arctic and Antarctic sites. At the same time, definite variations are observed and the resonance intensity in the Arctic is slightly smaller than that in the Antarctic. The disparities arise from the longitudinal separation of the field sites by almost 90° and by the winter displacement of global thunderstorms into the Southern hemisphere.

Figure 6 shows temporal variations of the cumulative intensity of SR oscillations similarly to Figure 4: the power spectral density integrated in the frequency band 5–23 Hz. The abscissas here show the UT in hours, and the ordinate depicts the integrated resonance intensity in arbitrary units. The red curves in this figure correspond to the data from the Southern hemisphere, and the bluish curves are relevant to the Northern hemisphere.

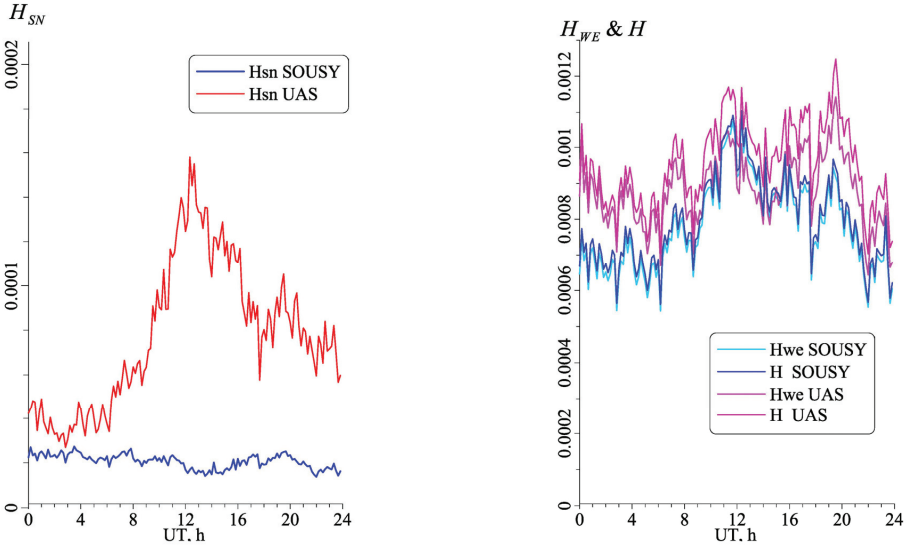


Figure 6. Daily variations in the integrated intensity of horizontal magnetic fields computed for the Arctic and Antarctic observatories.

The left panel of Figure 6 demonstrates temporal changes in the integrated intensity of the south–north field component H_{SN} of the horizontal magnetic field. The plots showing diurnal variations of the integrated intensity of the west–east component H_{WE} and of the total horizontal magnetic field H occupy the right panel of Figure 6. The south–north field component is noticeably smaller than the west–east component, which is explained by the problem geometry: the particular spatial distribution of lightning strokes. One may conclude that in this particular case of the sub-polar position of observatories, an outstanding similarity is observed of the model curves relevant to the total field and to the west–east component computed in opposite hemispheres.

The west–east and south–north components at the high latitudes in the Arctic and Antarctic demonstrate a comprehensive increase in resonance intensity during the time intervals of high lightning activity at the global thunderstorm centers in Madagascar and South Africa (around 12 h) and in South America (20 h). The influence of thunderstorms in Oceania (0–4 h) and Southeast Asia including Australia (10 h) is less pronounced than that observed at the polar observatories. As a whole, variations at the high-latitude sites significantly deviate from the patterns computed for the poles. However, the resonance

signals in the Antarctic slightly exceed those in the Arctic again, which indicates that the distance-dependence in the integrated field intensity was not compensated completely.

Figure 7 compares the diurnal changes in the level of global thunderstorm activity (global lightning radiated power) and the cumulative SR intensity. The legend in Figure 7 is similar to that of Figure 5. The blue curve depicts the normalized variations of the number of lightning strokes recorded by the WWLLN in each 10-min interval of 18 January 2022. The black curve shows changes in the normalized radiated energy ENRG/<ENRG> of all lightning discharges summed during every 10-min interval. The thick red curve shows changes in the normalized cumulative integrated SR intensity at the SOUSY and UAS sites. The black curve with brown stars outlines the daily changes in the ratio of the normalized cumulative SR intensity and the normalized lightning energy. The scheme of this figure repeats the arrangement used in Figure 5.

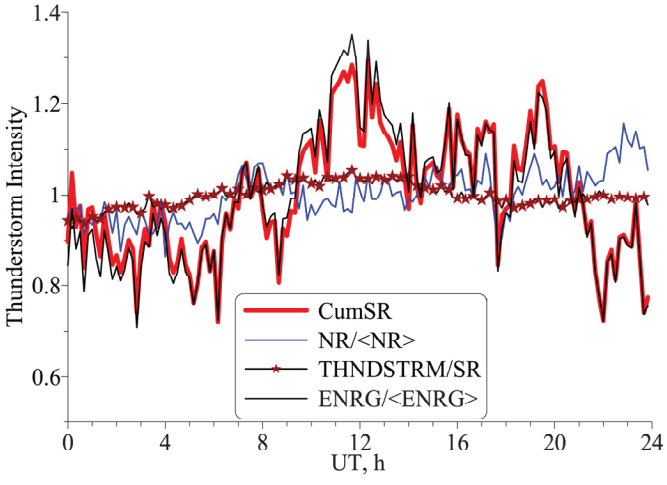


Figure 7. Diurnal variations in the cumulative integral intensities of SR observed in the Arctic and Antarctic, changes in the stroke rate and in the global lightning radiated power.

Similarly to speculative positioning of the observers at the poles, the computations for the existing high-latitude observatories indicate that the cumulative intensity of the global electromagnetic resonance is almost coincident with the daily variations in the radiation energy of global thunderstorm activity. One may observe that the black curve with brown stars in Figure 7 does not essentially deviate from the constant equal to unity. Its daily median value is equal to 0.998, and the standard deviation is equal to 2.7%. Thus, the simultaneous records of SR at the currently operating high-latitude observatories SOUSY and UAS allow for accurate estimating of the level of global thunderstorm activity on the time scales of 10 min or higher.

4. Model Seasonal Variations

Let us model the seasonal variations in global thunderstorm activity and its reflection in the SR records performed at different observation sites. To model the spatial distribution of the field sources, we use the monthly averaged maps of global thunderstorm activity according to the OTD (Optical Transient Detector) satellite observations [25]. These data have the form of tables for each month of the year, averaged over several years of orbital observations. We divide the entire globe along latitude and longitude into cells of the size of 2.5° by 2.5°. Global lightning activity is proportional to the average number of lightning flashes observed in a particular cell during a given month for the entire observation period.

A figure showing all 12 maps with the spatial distribution of global thunderstorms for each month turns out to be very cumbersome. Therefore, we present in Figure 8 only maps

for the four seasons of the year: for the periods December–January–February, March–April–May, June–July–August, and September–October–November. The geographic longitude is plotted in degrees along the abscissa on these maps, and the latitude is shown along the ordinate. The spatial distribution of lightning flashes is shown by the color. One may easily recognize the continents outlined by the spatial distribution of lightning strokes. The north–south and west–east seasonal grifts are visible in these maps of global thunderstorm activity.

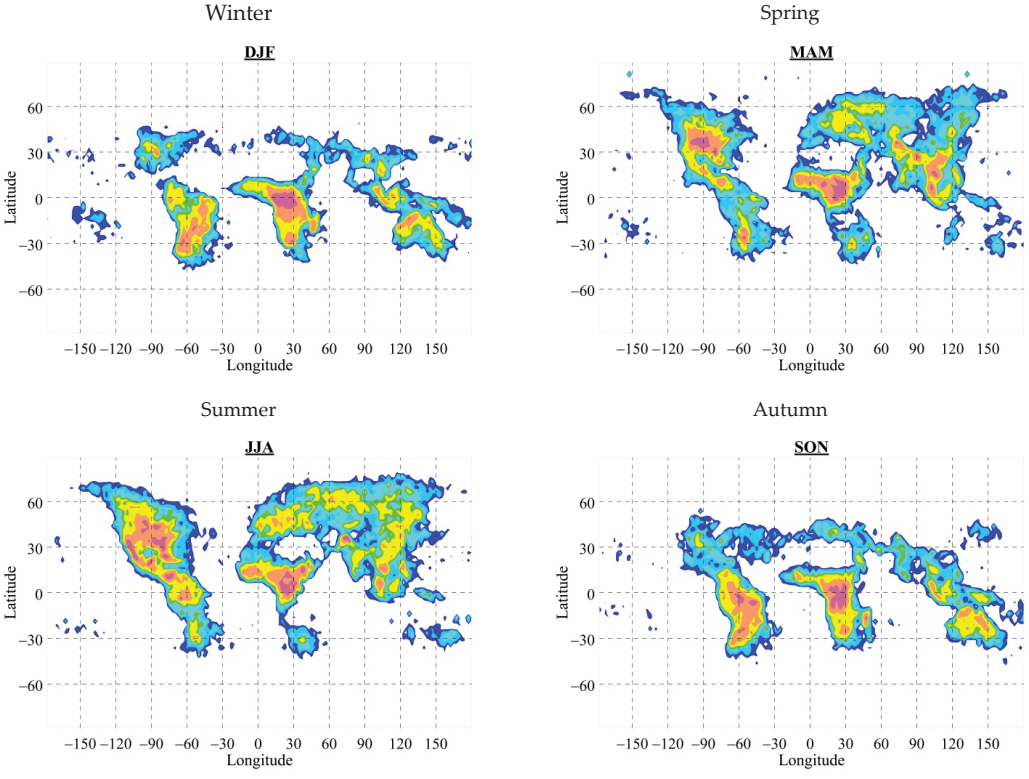


Figure 8. Global distribution of lightning discharges in four annual seasons.

In computations, we use the coordinates of the center of the corresponding cell of 2.5° by 2.5° as the position of the elementary source. The radiated power of such an elementary source is considered to be directly proportional to the number of optical lightning flashes observed in this cell. By moving from cell to cell, we calculate the geometric parameters of elementary propagation paths (the source–observer distance and the arrival angle of the radio wave at the observation point) and compute by using Equations (1) and (2) the power spectra of individual field components and of the total horizontal magnetic field at a given observatory for each month of a year.

Such an approach is not a great novelty: the similar spatial distribution of global thunderstorm activity was taken into account 50 years ago in the paper [26]. The significant distinction of the present study is that in [26] the yearly averaged distribution of the 'thunder days' over the Earth's surface was used, i.e., the days in a year when the sound of thunder was heard at a given meteorological station (see [27]). To model the daily changes in global thunderstorm activity, the authors of [26] used a standard sinusoidal 'modulation factor' depending on time, by which they multiplied the number of thunder days within the longitude sectors of the 15° width. This product of the spatial thunderstorm

distribution and of the temporal modulating factor provided the model diurnal variations. In the previous part of this study, we used the updated diurnal variations based on the actual global observations of lightning strokes by the WWLLN.

To model seasonal changes, we apply 12 maps of the global distribution of lightning flashes observed aboard the OTD satellite during each month and averaged over the whole period of its observations [25]. A detailed description of applying the OTD data in the SR computations may be found in [6,11,12].

One may expect that the integrated intensity of SR will slightly increase when the global thunderstorms come closer to an observer and will decrease when the thunderstorms drift away from him. As we note before, the simplest way to compensate for this remnant distance-dependence is to simultaneously monitor the integrated resonance intensity at two observatories located such that an increase in the intensity at one of them is combined with its corresponding decrease at the other site.

When treating seasonal variations, we initially consider positioning of the coupled observatories at the North and the South Poles. As might be seen from the maps of Figure 8, global thunderstorm activity is always confined to low latitudes. Therefore, one might expect that a decrease in the distance from one observer will be compensated by its increase relative to another one during the seasonal drift of thunderstorms relative to polar observatories. Then, the sum of the integrated power measured at the poles should be insensitive to the seasonal drift of global thunderstorms and will tend to reflect alterations in the intensity of global thunderstorm activity.

4.1. Polar Observers

We show in Figure 9 the model spectrograms of the total horizontal magnetic field power in the SR band. Seasonal variations in the power spectra of the total magnetic field $|H(f)|^2 = |H_{WE}(f)|^2 + |H_{SN}(f)|^2$ were computed using the monthly OTD maps for observers positioned at the South (left panel) and the North Pole (right panel). The abscissa shows the month of the year, and the ordinate depicts the frequency of SR radio signal in Hertz. The total field power is shown by color, and the color scale is positioned at the right of the dynamic spectra.

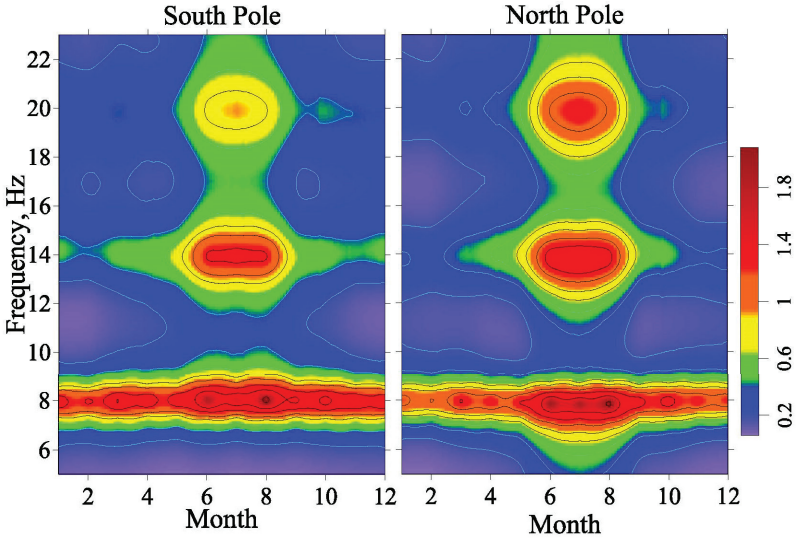


Figure 9. Annual spectrograms of the total horizontal magnetic field of SR computed for the South and North Poles.

The spectra on the seasonal scale acquire an outline deviating of spectra in Figures 2 and 5. The major distinction is in the 'isolated' summer peaks especially visible as the spots at the higher modes. As in the case of diurnal variations, the northern and southern spectrograms remain similar in spite of the fact that the computations were made for the opposite poles of the Earth. The behavior of resonance intensity at the poles is close, but not coincident. Deviations in the general resonance pattern at the observatories indicate the traces of their link to the source–observer distance, which is different owing to seasonal displacements of global thunderstorm activity.

Figure 10 shows separately the monthly averaged power spectra of SR in the total horizontal magnetic field at the North and the South Poles. The frequency in Hertz is plotted along the abscissa, and the power spectral density in relative units is plotted along the ordinate. The spectra for January are shown by the black lines, and those for July are shown by the red lines. The data for the South Pole are marked with red circles, and those for the North Pole are marked with blue circles.

The spectra in Figure 10 demonstrate a pronounced resonance pattern, and some details might be seen in a more vivid manner than in the plots in Figure 9. The resonance peaks in the power spectra corresponding to the first three resonance modes are clearly visible. The resonance intensity tends to decrease when the distance to the source increases. In addition, a slight deformation of the spectra as a whole is also visible, which alters the form of resonance curve and the heights of individual peaks. Therefore, the seasonal changes in the outline of resonance spectra at the Poles are not coincident. In contrary to optimistic expectations, the seasonal drifts in the global thunderstorm position provide changes at a pole that could not be completely compensated by changes at the other pole even in the integrated power spectra.

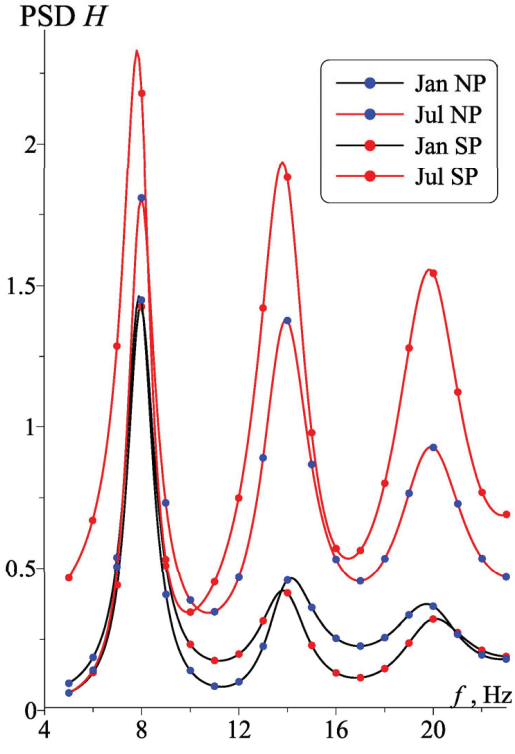


Figure 10. Model SR spectra at the North and South Poles in January and July.

Validity of this conclusion is clearly demonstrated in Figure 11. Months are plotted along the abscissa and the intensity of SR and of global thunderstorms is plotted along the ordinate in relative units. All data shown in this figure were normalized in such a way that their annual mean value was equal to 100.

The thin blue line with blue circles depicts the seasonal variations in the integrated SR intensity at the North Pole. The thin red line with red circles shows the simultaneous seasonal changes in the integrated SR intensity at the South Pole. As might be seen, the polar seasonal changes are highly similar in spite of some variations in details. In particular, the intensity of the SR noticeably increases at both hemispheres during the boreal summer. The thick black line with black circles corresponds to the half-sum of the integrated intensities at the North and the South Pole. It occupies an intermediate position between the individual curves relevant to the poles.

The bold blue line in Figure 11 shows the seasonal variations in the monthly mean of the global thunderstorm activity observed by the OTD satellite. We have scaled the data so that the annual average values became equal to 100, and this involves the blue line and the thick black line with black dots. After such scaling, these two lines would become coincident in an ideal case. Unfortunately, this did not happen. We observe that seasonal variations in the SR intensity are more pronounced than alterations in the thunderstorm activity following from the orbital optical observations.

When comparing the seasonal model data, we acted in the following way. First, we calculated the yearly average $M_{SR} = < P_{SR} >$, where P_{SR} is the half-sum of integrated SR intensities detected at the poles during particular month. We computed similarly the yearly average of global thunderstorm activity $M_{Th} = < S_{Th} >$, where S_{Th} is directly proportional to the cumulative number of global lightning strokes observed by OTD during a month. The median values M_{SR} and M_{Th} allow us to obtain the normalized seasonal variations of both parameters $R_{SR} = \frac{P_{SR}}{M_{SR}}$ and $R_{Th} = \frac{S_{Th}}{M_{Th}}$. The accuracy of estimating the seasonal changes of global thunderstorm activity by using SR records is equal to the ratio of the normalized seasonal variations $\frac{R_{SR}}{R_{Th}}$.

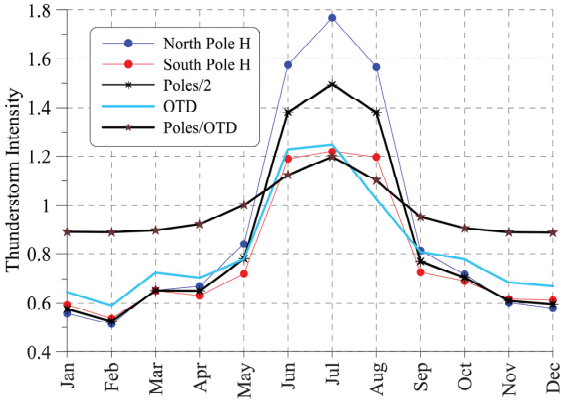


Figure 11. Seasonal changes in the integral SR intensity at the North and the South Pole compared with the level of global thunderstorms according to the OTD observations.

The bold black line with brown stars described as Poles/OTD in the legend of Figure 11 shows the sought seasonal variation ratio $\frac{R_{SR}}{R_{Th}}$. This curve illustrates relative deviations of global thunderstorm activity derived from the SR records against the "actual" intensity of global lightning activity recorded by OTD. The assessment of the level of global thunderstorm activity by using the half-sum of the integrated SR power at the North and the South Pole deviates from the postulated thunderstorm activity by +20 and –11%, depending on the particular month. (The annual means of these data are coincident by default.)

The observed variations are apparently associated with an uneven distribution of thunderstorms along the longitude and with their seasonal drift along the latitude and the longitude. These features are related to the geographical allocation of continents in the Northern and Southern hemispheres because thunderstorms tend to concentrate over solid land. The resulting estimate allows us to speak about a modest evaluation accuracy of the global thunderstorm level based on the concurrent ELF observations at the poles.

Since, according to OTD data, the amount of lightning stokes varies by a factor of two depending on the season, the polar observers provide a modest accuracy in assessing the seasonal changes in the level of global thunderstorms. Unfortunately, it is impossible to apply the above results in practice, since there are no sites monitoring the SR at the terrestrial poles. Therefore, we return to modeling the observations at the existing operating couple of high-latitude sites: UAS (65.25° S and 64.24° W) and SOUSY (78.15° N and 16.05° E).

4.2. High-Latitude Observers in the Northern and Southern Hemispheres

We present below the model seasonal results for UAS and SOUSY points based on the OTD maps. Using the power spectra of the orthogonal west–east and south–north components, we find the power spectra of the total magnetic field for each month of a year. These spectra are shown in Figure 12 as the 2D maps above the month–frequency plane.

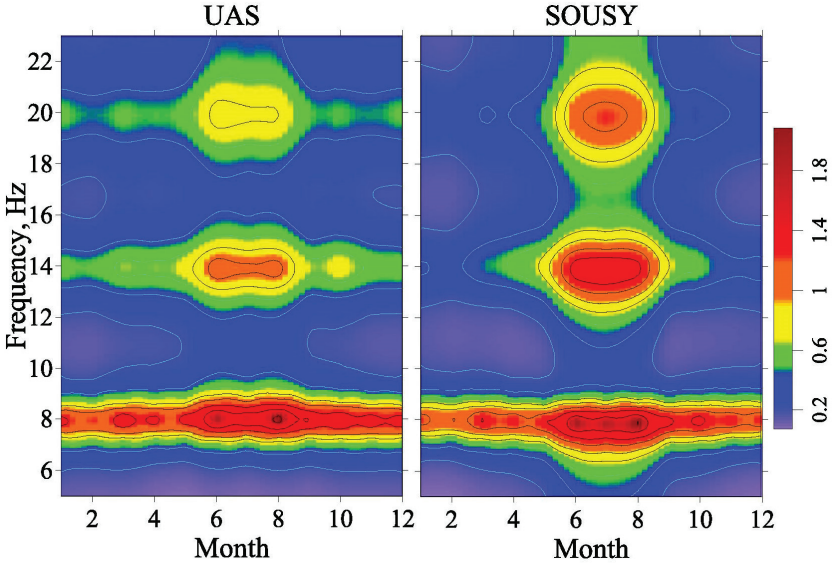


Figure 12. SR spectrograms at the UAS and SOUSY observatories.

The abscissas in Figure 12 show the months, and the frequency of the signal is plotted along the ordinate. The power spectral density is shown by color, and the corresponding color scale is placed on the right. Resonance peaks are clearly visible, and the seasonal changes in the SR intensity are well resolved at each observatory. There is a pronounced increase in the intensity of electromagnetic signal recorded both in the Arctic and Antarctic during the boreal summer. Simultaneously, the relative summer intensity increase in the Arctic exceeds that in the Antarctic, which is explained by the distance-dependence of the resonance field. The major conclusion that might be drawn from Figure 12 is that SR observations at any of the hemispheres reflect seasonal changes in the level of global thunderstorm activity. Since the magnitude of seasonal changes in the SR intensity in the Northern hemisphere significantly exceeds the changes in the Southern hemisphere, the realistic estimate of global thunderstorms must imply the half-sum of the resonance powers observed in both the hemispheres.

Figure 13 shows seasonal variations of the integrated SR intensity at the two sub-polar sites. The interval of 12 months' duration is shown along the abscissa in Figure 13, and the resonance intensity is plotted in arbitrary units along the ordinate. The blue line with blue dots represents the Arctic data (Svalbard) and the red line with red dots shows the Antarctic observations (Antarctic Peninsula). The bold black line with the black asterisks presents the half-sum of the Arctic and Antarctic data. The bold blue line outlines changes in global thunderstorm activity, which is directly proportional to the mean number of planetary lightning strokes observed from orbit during a given month. The seasonal changes are obviously similar in global thunderstorm activity and in the half-sum of integrated SR intensities at the high-latitude observatories.

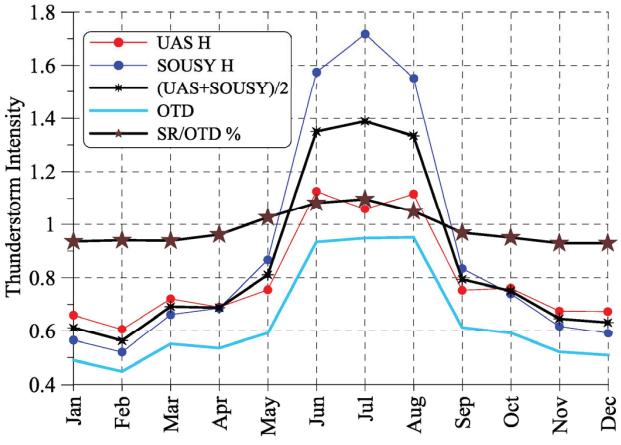


Figure 13. Estimated seasonal variations in global thunderstorm activity found from observations at the high-latitude observatories.

As before, we derive the ratio of the seasonal variations in the SR to changes in the OTD record $\frac{R_{SR}}{R_{Th}}$. Here, $R_{SR} = \frac{P_{SR}}{M_{SR}}$ is the normalized cumulative SR intensity and $R_{Th} = \frac{S_{Th}}{M_{Th}}$ denotes the normalized global thunderstorm activity in the OTD data. This ratio is depicted by the black bold line with the brown stars in Figure 13. It indicates that in the framework of the OTD global thunderstorm distribution, the simultaneous monitoring of SR at the high latitude Arctic and Antarctic stations allows estimation of the contemporary level of global thunderstorm activity with an accuracy ranging from -6 to +10%. This result confirms the fortunate positioning of these particular observatories, which facilitates the remote sensing of changes in the current global thunderstorm activity with an error of about $\pm$10% on the annual time scale.

5. Summary

1. The numerical simulations showed a rather high accuracy of the estimates for the diurnal variations in the level of global thunderstorm activity by using the concurrent records of the integrated SR intensity at two high-latitude observatories, UAS and SOUSY. The relative error does not exceed 3% for the daily time resolution of 10 min or more;
2. Alterations in the relative intensity of global thunderstorms on the seasonal time-scale are estimated from the SR data with an error of about 10%;
3. Since the rate of changes in the level of global thunderstorm activity on the considered time-scales is approximately one octave (the factor of two), the above errors indicate an acceptable overall accuracy of the estimates acquired using simultaneous SR monitoring at the high-latitude observatories in the Arctic and Antarctic.

6. Conclusions

Geoscience studies the processes that occur in the three media, being the solid Earth, the ocean, and the Earth's atmosphere. The present work is addressed to one of these media: to the terrestrial atmosphere. We model and discuss the scheme of possible remote sensing of the level of global thunderstorm activity by using the natural electromagnetic radiation from the lightning strokes captured in the Earth–ionosphere cavity. Model computations indicate that the global electromagnetic (Schumann) resonance might serve as a reliable tool for such measurements, provided that ELF radio signals are concurrently monitored in the Northern and the Southern Hemispheres at high-latitude or at polar observatories.

We must emphasize that the modeling procedure has used the particular realistic planetary distributions of lightning strokes. Of course, the generalization of the estimates obtained to reality may seem ambiguous, since particular random distributions might deviate from those used in the model. Nevertheless, we dare to express an optimistic opinion that the actual relative errors will not cross the corridor of 10% width. This belief is supported by the fact that the models applied were based on modern observations of thunderstorm activity.

The model data obtained indicate that concurrent high-latitude ELF measurements in the Northern and the Southern Hemispheres will allow adequate estimates for the diurnal and seasonal patterns in the level of global thunderstorm activity to be obtained.

Author Contributions: Conceptualization, M.H. and A.P.N.; Methodology, Y.P.G. and A.P.N.; Software, Y.P.G. All authors have read and agreed to the published version of the manuscript.

Funding: This research received no external funding.

Institutional Review Board Statement: Not applicable.

Informed Consent Statement: Not applicable.

Data Availability Statement: All data can be provided by the corresponding author upon request.

Acknowledgments: The authors are grateful to the colleagues of WWLLN for providing us with the data.

Conflicts of Interest: The authors declare no conflict of interest.

References

1. Polk, C. Relation of ELF noise and Schumann resonances to thunderstorm activity. In *Planetary Electrodynamics*; Coronoti, S.C., Hughes, J., Eds.; Gordon and Breach: New York, NY, USA, 1969; Volume 2, pp. 55–83.
2. Polk, C. Schumann resonances. In *Handbook of Atmospherics*; Volland, H., Ed.; CRC Press: Boca Raton, FL, USA, 1982; Volume 1, pp. 111–178.
3. Bliokh, P.V.; Nickolaenko, A.P.; Filippov, Y.F. *Schumann Resonances in the Earth-Ionosphere Cavity*; Peter Perigrinus: New York, NY, USA; London, UK; Paris, France, 1980; p. 168.
4. Sentman, D.D. Schumann Resonances. In *Handbook of Atmospheric Electrodynamics*; Volland, H., Ed.; CRC Press: Boca Raton, FL, USA; London, UK; Tokyo, Japan, 1995; Volume 1, pp. 267–298.
5. Nickolaenko, A.P.; Hayakawa, M. *Resonances in the Earth-Ionosphere Cavity*; Kluwer Academic Publishers: Dordrecht, The Netherlands, 2002; p. 388.
6. Nickolaenko, A.; Hayakawa, M. *Schumann Resonance for Tyros*; Springer: Tokyo, Japan; Heidelberg, Germany; New York, NY, USA; Dordrecht, The Netherlands; London, UK, 2014; p. 348. [CrossRef]
7. Price, C. ELF electromagnetic waves from lightning: The Schumann resonances. Review. *Atmosphere* **2016**, *7*, 116. [CrossRef]
8. Nickolaenko, A.P.; Shvets, A.V.; Hayakawa, M. Propagation at Extremely Low-Frequency Radio Waves. In *Wiley Encyclopedia of Electrical and Electronics Engineering*; Webster, J., Ed.; John Wiley & Sons, Inc.: Hoboken, NJ, USA, 2016; pp. 1–20. [CrossRef]
9. Sentman, D.D.; Fraser, B.J. Simultaneous observation of Schumann resonances in California and Australia: Evidence for intensity modulation by local height of D. region. *J. Geophys. Res.* **1991**, *96*, 15973–15984. [CrossRef]
10. Nickolaenko, A.P. Modern aspects of the Schumann resonance studies. *J. Atmos. Solar-Terr. Phys.* **1997**, *59*, 805–816. [CrossRef]
11. Nickolaenko, A.P.; Hayakawa, M.; Sekiguchi, M. Variations in global thunderstorm activity inferred from the OTD records. *Geophys. Res. Lett.* **2006**, *33*, L06823. [CrossRef]
12. Sekiguchi, M.; Hayakawa, M.; Nickolaenko, A.P.; Hobara, Y. Evidence of a link between the intensity of Schumann resonance and global surface temperature. *Ann. Geophys.* **2006**, *24*, 1809–1817. [CrossRef]

13. Bozóki, T.; Sátori, G.; Williams, E.; Guha, A.; Liu, Y.; Steinbach, P.; Leal, A.; Atkinson, M.; Beggan, C.D.; DiGangi, E.; et al. A Schumann Resonance-based quantity for characterizing day-to-day changes in global lightning activity. *J. Geophys. Res. Atmos.* 2023, *in press*. [CrossRef]
14. Kudintseva, I.G.; Nickolaenko, A.P.; Rycroft, M.J.; Odzimek, A. AC and DC global electric circuit properties and the height profile of atmospheric conductivity. *Ann. Geophys.* **2016**, *59*, A0545. [CrossRef]
15. Hynninen, E.M.; Galuk, Y.P. The field of vertical electric dipole source over the spherical Earth with non-uniform along the height ionosphere. In *Problems of Radio Wave Diffraction and Propagation*; LSU Publ.: St. Petersburg, Russia, 1972; pp. 109–120.
16. Galuk, Y.P.; Ivanov, V.I. Propagation characteristics of VLF fields in the waveguide Earth–vertically non-uniform anisotropic ionosphere. In *Problems of Radio Wave Diffraction and Propagation*; LSU Publ.: St. Petersburg, Russia, 1978; pp. 148–153.
17. Galuk, Y.P. Schumann resonance in the model of global thunderstorm activity uniformly distributed over the Earth. *Radio-Phys. Electron.* **2015**, *6*, 3–9.
18. Lay, E.H.; Rodger, C.J.; Holzworth, R.H.; Dowden, R.L. Introduction to the World Wide Lightning Location Network (WWLLN). *Geophys. Res. Abstr.* **2005**, *7*, 02875; 2005 SRef-ID: 1607-7962/gra/EGU05-A-02875.
19. Rodger, C.J.; Werner, S.; Brundell, J.B.; Lay, E.H.; Thomson, N.R.; Holzworth, R.H.; Dowden, R.L. Detection efficiency of the VLF World-Wide Lightning Location Network (WWLLN): Initial case study. *Ann. Geophys*. 2006, 24, pp. 3197–3214. Available online: www.ann-geophys.net/24/3197/2006 (accessed on 10 January 2023).
20. Hutchins, M.L.; Holzworth, R.H.; Brundell, J.B.; Rodger, C.J. Relative detection efficiency of the World Wide Lightning Location Network. *Radio Sci.* **2012**, *47*, RS6005. [CrossRef]
21. Rodger, C.J.; Brundell1, J.B.; Hutchins, M.; Holzworth, R.H. The world wide lightning location network (WWLLN): Update of status and applications. In Proceedings of the 2014 XXXIth URSI General Assembly and Scientific Symposium (URSI GASS), Beijing, China, 16–23 August 2014. [CrossRef]
22. Holzworth, R.H.; Brundell, J.B.; McCarthy, M.P.; Jacobson, A.R.; Rodger, C.J.; Anderson, T.S. Lightning in the Arctic. *Geophys. Res. Lett.* **2021**, *48*, e2020GL091366. [CrossRef]
23. Koloskov, A.V.; Bezrodny, V.G.; Budanov, O.V.; Yampolski, Y.M. Polarization monitoring of the Schumann resonances in the Antarctic and recognition of the world thunderstorm activity characteristics. *Radiofiz. I Radioastron.* **2005**, *10*, 11–29.
24. Koloskov, O.V.; Nickolaenko, A.P.; Yampolski, Y.M.; Budanov, O.V. Electromagnetic seasons in Schumann resonance records. *J. Geophys. Res. Atmos.* **2022**, *127*, e2022JD036582. [CrossRef]
25. Christian, H.J.; Blakeslee, R.J.; Boccippio, D.J.; Boeck, W.L.; Buechler, D.E.; Driscoll, E.T.; Goodman, S.J.; Hall, J.M.; Koshak, W.J.; Mach, D.M.; et al. Global frequency and distribution of lightning as observed from space by the Optical Transient Detector. *J. Geophys. Res.* **2003**, *108*, 4005. [CrossRef]
26. Ogawa, T.; Murakami, Y. Schumann resonance frequencies and conductivity profiles in the atmosphere. *Contr. Geophys. Inst. Kyoto Univ.* **1973**, *13*, 13–20.
27. Israel, H. *Atmospherische Elekrizitat*; Akademische Verlaggeseltschaft: Leipzig, Germany, 1961; Volume 2, 503p.

Disclaimer/Publisher's Note: The statements, opinions and data contained in all publications are solely those of the individual author(s) and contributor(s) and not of MDPI and/or the editor(s). MDPI and/or the editor(s) disclaim responsibility for any injury to people or property resulting from any ideas, methods, instructions or products referred to in the content.

remote sensing

MDPI

Correction

Correction: Wang et al. ShuffleCloudNet: A Lightweight Composite Neural Network-Based Method for Cloud Computation in Remote-Sensing Images. *Remote Sens.* 2022, *14*, 5258

Gang Wang [1,2], Zhiying Lu [1,*] and Ping Wang [1]

[1] School of Electrical and Information Engineering, Tianjin University, Tianjin 300072, China
[2] CETC Key Laboratory of Aerospace Information Applications, Shijiazhuang 050081, China
* Correspondence: luzy@tju.edu.cn; Tel.: +86-138-2057-3798

Figure Legend

In the original publication [1], there was a mistake in "Figure 4. Diagram of the fusion evaluation rules for the composite neural network." as published. The title content in Figure 4 is the same as that in Figure 5. The corrected caption of Figure 4 appears below. The authors state that the scientific conclusions are unaffected. This correction was approved by the Academic Editor. The original publication has also been updated.

Figure 4. Diagram of the comparison between ShuffleNet V2 and ShuffleCloudNet network structure.

Reference

1. Wang, G.; Lu, Z.; Wang, P. ShuffleCloudNet: A Lightweight Composite Neural Network-Based Method for Cloud Computation in Remote-Sensing Images. *Remote Sens.* **2022**, *14*, 5258. [CrossRef]

Citation: Wang, G.; Lu, Z.; Wang, P. Correction: Wang et al. ShuffleCloudNet: A Lightweight Composite Neural Network-Based Method for Cloud Computation in Remote-Sensing Images. *Remote Sens.* 2022, *14*, 5258. *Remote Sens.* **2023**, *15*, 3022. https://doi.org/10.3390/rs15123022

Received: 10 March 2023
Accepted: 30 May 2023
Published: 9 June 2023

Disclaimer/Publisher's Note: The statements, opinions and data contained in all publications are solely those of the individual author(s) and contributor(s) and not of MDPI and/or the editor(s). MDPI and/or the editor(s) disclaim responsibility for any injury to people or property resulting from any ideas, methods, instructions or products referred to in the content.

Copyright: © 2023 by the authors. Licensee MDPI, Basel, Switzerland. This article is an open access article distributed under the terms and conditions of the Creative Commons Attribution (CC BY) license (https://creativecommons.org/licenses/by/4.0/).

geosciences

MDPI

Article

Quantitative Long-Term Monitoring (1890–2020) of Morphodynamic and Land-Cover Changes of a LIA Lateral Moraine Section

Moritz Altmann [1,*], Katharina Ramskogler [2,3], Sebastian Mikolka-Flöry [4], Madlene Pfeiffer [5], Florian Haas [1], Tobias Heckmann [1], Jakob Rom [1], Fabian Fleischer [1], Toni Himmelstoß [1], Norbert Pfeifer [4], Camillo Ressl [4], Erich Tasser [2] and Michael Becht [1]

1 Department of Physical Geography, Catholic University of Eichstätt-Ingolstadt, 85072 Eichstätt, Germany
2 Institute for Alpine Environment, Eurac Research, 39100 Bolzano, Italy
3 Department of Botany, Universität Innsbruck, 6020 Innsbruck, Austria
4 Research Unit Photogrammetry E120.7, Department of Geodesy and Geoinformation, TU Wien, 1040 Vienna, Austria
5 Institute of Geography, University of Bremen, 28359 Bremen, Germany
* Correspondence: maltmann@ku.de

Abstract: Aerial photographs of the European Alps usually only reach back to the middle of the 20th century, which limits the time span of corresponding studies that quantitatively analyse long-term surface changes of proglacial areas using georeferenced orthophotos. To the end of the Little Ice Age, this leads to a gap of about 100 years. Using digital monoplotting and several historical terrestrial photographs, we show the quantification of surface changes of a Little Ice Age lateral moraine section until the late second half of the 19th century, reaching a total study period of 130 years (1890–2020). The (initial) gully system expands (almost) continuously over the entire study period from 1890 to 2020. Until 1953, the vegetation-covered areas also expanded (mainly scree communities, alpine grasslands and dwarf shrub communities), before decreasing again, especially between 1990 and 2003, due to large-scale erosion within the gully system. Furthermore, our results show that the land-cover development was impacted by temperature and precipitation changes. With the 130-year study period, we contribute to a substantial improvement in the understanding of the processes in the proglacial by analysing the early phase and thus the immediate response of the lateral moraine to the ice exposure.

Keywords: aerial photos; Central Eastern Alps; digital monoplotting; historical terrestrial oblique photos; long-term mapping; paraglacial slope adjustment; proglacial area; upper Kauner Valley (Ötztal Alps)

Citation: Altmann, M.; Ramskogler, K.; Mikolka-Flöry, S.; Pfeiffer, M.; Haas, F.; Heckmann, T.; Rom, J.; Fleischer, F.; Himmelstoß, T.; Pfeifer, N.; et al. Quantitative Long-Term Monitoring (1890–2020) of Morphodynamic and Land-Cover Changes of a LIA Lateral Moraine Section. *Geosciences* **2023**, *13*, 95. https://doi.org/10.3390/geosciences13040095

Academic Editors: Fedor Lisetskii and Jesus Martinez-Frias

Received: 28 February 2023
Revised: 15 March 2023
Accepted: 20 March 2023
Published: 23 March 2023

Copyright: © 2023 by the authors. Licensee MDPI, Basel, Switzerland. This article is an open access article distributed under the terms and conditions of the Creative Commons Attribution (CC BY) license (https://creativecommons.org/licenses/by/4.0/).

1. Introduction

Since the end of the Little Ice Age (LIA) around the middle of the 20th century, glacier retreat in high alpine mountains, caused by global warming, has led to a continuous expansion of the glacier forelands, the so-called proglacial areas [1,2]. Glacial environments and corresponding proglacial areas are among the most rapidly changing areas on earth, as they are strongly affected by climate change. After ice release, the exposed areas, especially the steep and, to a high degree, unvegetated lateral moraines, are reworked by different geomorphological processes, such as fluvial and nival erosion, debris flows, slope failures and landslides, which can be associated with high erosion rates [3–6]. Generally, this phase is described as the paraglacial slope adjustment process, which can last several decades to centuries [7–9]. These processes have led to a high number of deeply incised lateral moraine sections in which correspondingly strongly developed gully systems have formed [5,9–12].

The upcoming vegetation can in turn act as a consequence but also as a cause of slope stabilisation on the lateral moraines [13–16]. Knoflach et al. [17] showed in the

proglacial areas of the Fürkele-, Zufall- and Langenferner (Ortler-Cevedale Group/Eastern Italian Alps), using in situ observations in combination with NDVI time series the increase in vegetation-covered areas from 1986 to 2015 from 0.25 km^2 (5.6%) to 0.9 km^2 (11.2%), whereby the mean annual rate of change shows a significant acceleration during the study period. Hohensinner et al. [18] showed, by a long-term analysis from 1820 to 2015 of land-cover change in a proglacial area of the Jamtalferner (Silvretta, Central Eastern Alps), based on historical maps and orthophotos, mainly the development of alpine grassland and krummholz on such areas, however wasteland predominates.

Thus, historical and current aerial photographs offer effective possibilities to document the landscape evolution of proglacial areas, as several studies underlined [4,5,19,20]. However, historical aerial photographs of the European Alps mostly only go back to the middle of the 20th century, which leads to a limitation of these studies and leaves a gap of about 100 years until the end of the LIA (around 1850). In particular, the early phase of the paraglacial slope adjustment process and thus the early response of the lateral moraines to the ice loss remains unknown.

On the other hand, the advent of alpinism and the availability of cameras, historical terrestrial oblique photographs from the late second half of the 19th century and the first half of the 20th century are already available. Many of the photos are stored in public and private archives, e.g., the archives of the German or Austrian Alpine Club (DAV/ÖAV) or private archives of enthusiastic Alpine pioneers. The enormous relevance of these photos is evident from the fact that these photographs are the only visual source of these landscapes from this epoch. The photogrammetric method of digital monoplotting offers the effective possibility to analyse also historical terrestrial oblique photos. After estimating the position and orientation of the camera, the position of mapped image contents (e.g., forest areas, glacial extents and rivers) can be exported as spatial referenced vector data sets into a three-dimensional (3D) object space with global coordinates [21,22]. Finally, real lengths or areas can be calculated. This enables quantitative measurements of object dimensions in addition to qualitative image descriptions. The availability of the WSL monoplotting tool from the Swiss Federal Institute for Forest, Snow and Landscape Research (WSL) [21,22] has already led to several studies that have been able to quantify environmental long-term changes in alpine areas using individual historical terrestrial oblique photographs. Research has included land-cover/vegetation change [21–28], natural hazards [29,30], LIA glacier extents [31] and rock glacier movement [32]. However, no studies have shown the long-term mapping of surface changes of LIA lateral moraines until the second half of the 20th century using historical terrestrial photos.

Therefore, the aim of this study is to investigate the long-term evolution of a steep LIA lateral moraine section in a proglacial area in high spatial and temporal resolution. In particular, we aim to identify the unknown early response in terms of morphodynamics and development of land-cover types. For this purpose, we map different surface types, with a focus on morphodynamic areas and land-cover types, by processing different historical terrestrial oblique photos (1890 to ~1940) with the newly developed monoplotting tool "Mono3D" of the Department of Geodesy and Geoinformation (TU Wien, Austria). This tool was developed as part of the research project SEHAG ("Sensitivity of High Alpine Geosystems to Climate Change since 1850") funded by the German Research Foundation (DFG) and the Austrian Science Fund (FWF). Based on this, the mapping will be continued using historical and current aerial photographs (respectively georeferenced orthophotos) from 1953 to 2020 in order to quantify the surface changes over the entire period in high temporal and spatial resolution (entire period of 130 years from 1890 to 2020). Additionally, the long-term temperature development (1850 to 2020) and corresponding effects on the proglacial area are shown using simulated climate data. Therefore, we focus on three research questions:

- To what extent can spatial and temporal changes in morphodynamic areas and land-cover types on a LIA lateral moraine section be quantified by digital monoplotting using

historical terrestrial oblique photographs from the second half of the 19th and the first half of the 20th century and subsequent orthophotos based on aerial photographs until 2020?
- How far can long-term mapping improve the knowledge about paraglacial slope adjustment processes and what are besides morphodynamics the driving variables for the land-cover change?
- Could the long time series provide new opportunities for a better understanding of the relationships between climate, morphodynamics, and land-cover development?

2. Study Area

The survey was conducted on a LIA lateral moraine in the proglacial area of the Gepatsch glacier (Gepatschferner) in the upper Kauner Valley (upper Kaunertal) in Tyrol, Austria, located in the Ötztal Alps, which is situated in the central Eastern Alps (Figure 1). Geologically, the Kauner Valley belongs to the Austroalpine crystalline complex, in which mainly crystalline rocks such as ortho- and paragneisses predominate [33–35]. Climatically, the valley is characterised by the Central Alpine dry region [36,37]. The valley is oriented north-south and borders Italy and the main Alpine ridge to the south. The maximum glacier extent at the end of the LIA was observed at the Gepatschferner in 1856 [38]. Apart from two glacier advances in 1920/21 and between 1977 and 1988 [38,39] the Gepatschferner has experienced continuous glacier retreat. Our Area of Interest (AoI, see Figure 1c,d, Table 1) is located in the upper part of an approximately 150 m high lateral moraine and is characterised by high morphodynamics and steep slope gradients. Typical moraine material both vegetated and nearly vegetation-free areas can be found.

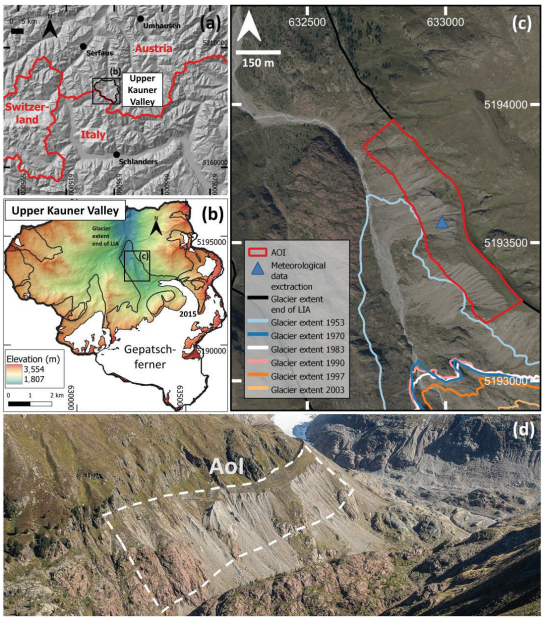


Figure 1. (**a**) Location of the study area in the upper Kauner Valley (Tyrol, Austria) with (**b**) the location of the proglacial area of Gepatschferner. (**c**) AoI (red) in the proglacial area of Gepatschferner in the upper Kauner Valley with glacier extents in different years and (**d**) course mapping of the AoI in a photo (white dashed line) from 2021 (taken by Anton Brandl). Sources of glacier extents: End of LIA: Groß and Patzelt [40], 1953 to 2003: Own mapping by change detection based on DoDs published by Piermattei et al. [20] (mapping method also includes mapping of debris-covered glacier parts), 2015: Buckel and Otto [41]. Large-scale elevation data (DSM, 25 m) (**top left**) are based on SRTM and ASTER GDEM [42]. DEM 2017 (1 m) (**bottom left**) based on Airborne LiDAR data [4]. The 2020 orthophoto (**right**) is from the Province of Tyrol (see Appendix A, Table A1).

Table 1. Characteristics of the Area of Interest (values were derived from 2017 DEM).

Location (Centre) (ETRS89/UTM Zone 32N, EPSG Code: 25832)	632987, 5193575
Elevation (ellipsoidal heights) [m]	2096–2346
Mean aspect [°]	251.36 (West)
Size [ha]	12.1
Mean slope gradient (min./max.) [°]	38.09 (1–82)
Min. ice-free since	1940 [1] / 1953 [2]
Dead ice influence at the foot of the slope up to max.	1982 [3]

[1] based on a historical terrestrial oblique image (monoplotting, see Sections 3.2 and 4), [2] based on the Euclidean distance between two glacier extents (calculated following Betz-Nutz et al. [5] determined by change detection using DEMs of Difference (DoD) published by Piermattei et al. [20]. The different annual data are thus mainly due to the debris cover of the glacier, [3] based on DoD interpretations published by Piermattei et al. [20].

3. Material and Methods

3.1. Photo Material

To enable the long-term observation of the development of the lateral moraine section, several terrestrial and aerial photographs were analysed. For the second half of the 19th century and the first half of the 20th century, historical terrestrial oblique photographs (Figure 2, Appendix B, Table A2) and from the second half of the 20th century onwards, aerial photographs were processed and analysed (Figure 2, Appendix A, Table A1).

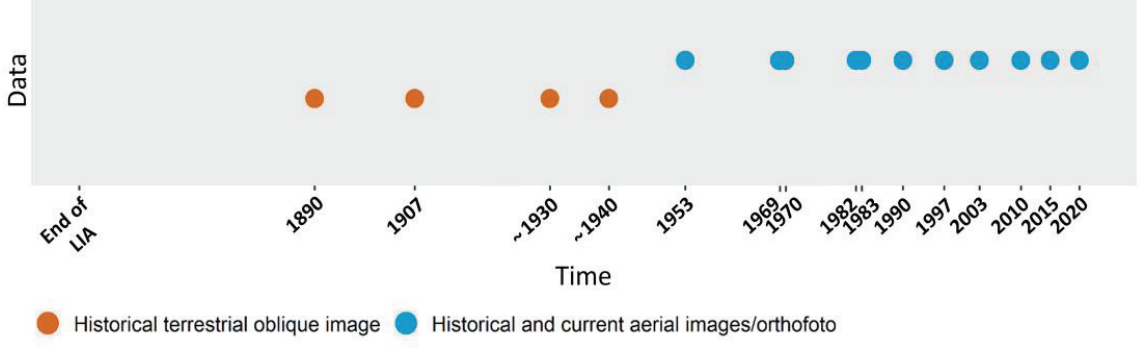


Figure 2. Overview of the temporal distribution of the analysed terrestrial and aerial photographs.

3.2. Methods of Image Processing and Mapping

3.2.1. Processing of the Terrestrial Photos

In order to map the extent of the different surface types, mainly the morphodynamic area and land-cover types, within the AoI since 1890, a monoplotting tool was used [43]. With this tool the historical terrestrial photos from 1890, 1907, ~1930 and ~1940 (Figure 3; Appendix B, Table A2, Figure A1) were analysed. Using monoplotting, for each pixel of a photo the corresponding point in a (3D) global coordinate system is calculated by intersecting rays from the projection centre (O in Figure 3a) through each image pixel of the photo with a reference DTM (Figure 3a) [21,22,30].

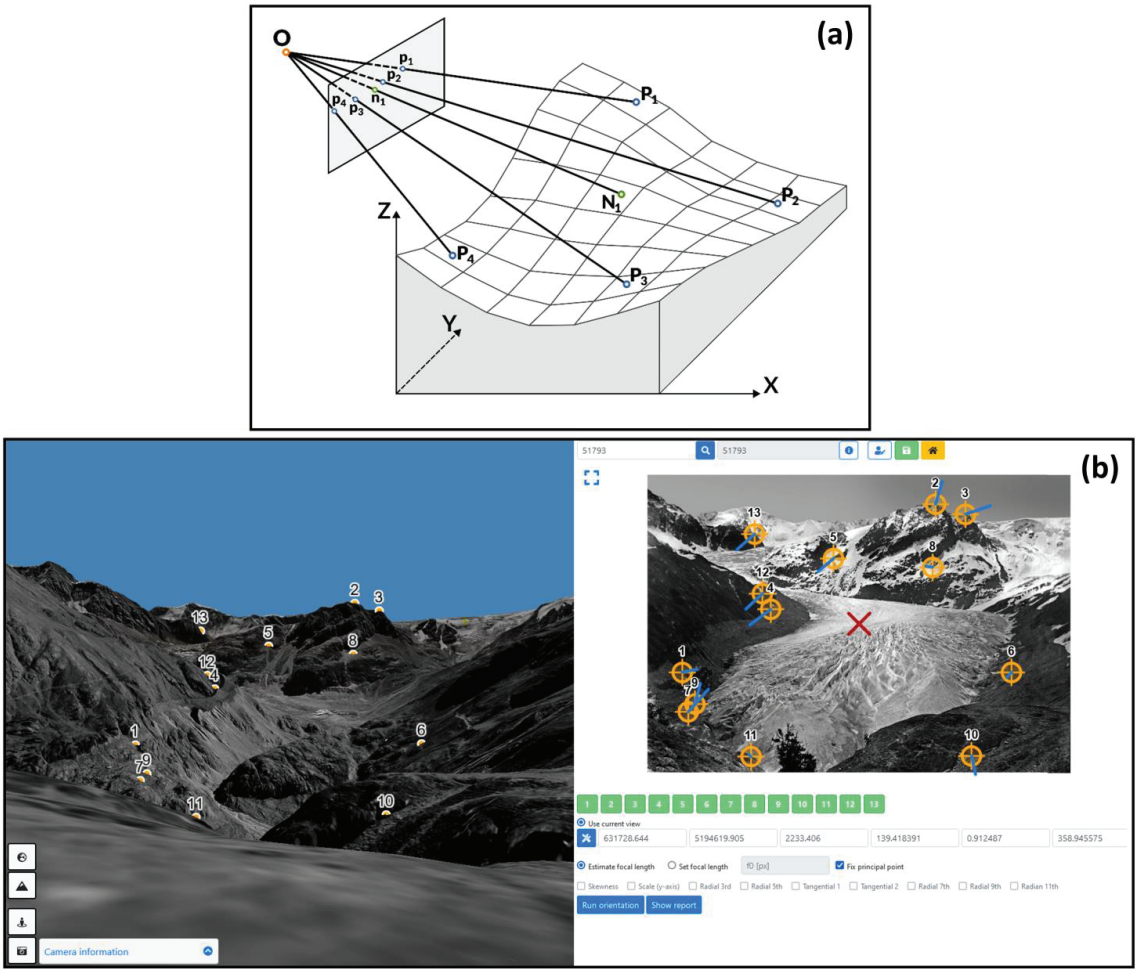


Figure 3. (**a**) GCPs (P1–P4) both in the image and object space can be used to estimate the unknown camera parameters. Using the estimated camera parameters, the position of an image point (n1) can be calculated in the object space (N1) by monoplotting. Figure adapted from Kraus [44]. (**b**) Selection of ground control points on the 1890 photograph in the 3D Viewer and the following calculation of the camera information.

Thus, each pixel of a photograph can be assigned a coordinate in a 3D object space [30]. Prior to monoplotting the interior (focal length f, coordinates of the principal point x0 and y0) and exterior orientation (coordinates of the projection centre and three rotation angles) of the camera have to be estimated as they are generally unknown for historical terrestrial photos [21]. For this purpose, approximately uniformly distributed ground control points (GCPs) were identified in each historical terrestrial oblique image as well as on the 1970 orthophoto with deposited 2017 DTM using a 3D viewer (Figure 3b; Appendix B, Tables A3 and A4).

Then, both the interior and exterior orientation of each image were estimated using OrientAL [45]. Subsequently, the object coordinates of the image pixels corresponding to the outlines of the different surface types, mainly the morphodynamic area and land-cover types, were calculated by monoplotting using the estimated camera parameters and the reference DTM (2017, 1 m). The results from the orientation are shown in Figure 4 and

Table 2. The coordinates of the principal point x_0 and y_0 were fixed in the image centre and only the remaining seven unknown camera parameters were estimated.

The calculated camera positions and orientations show that they were taken in the north-west direction of the AoI (Figure 4). The shortest distance to the AoI is 971 m (photo 1907), 1010 m (photo 1930), 1104 m (photo 1940) and 1242 m (photo 1890) metres respectively. In addition, Figure 4 shows the georeferenced orthophotos of the individual historical terrestrial photos.

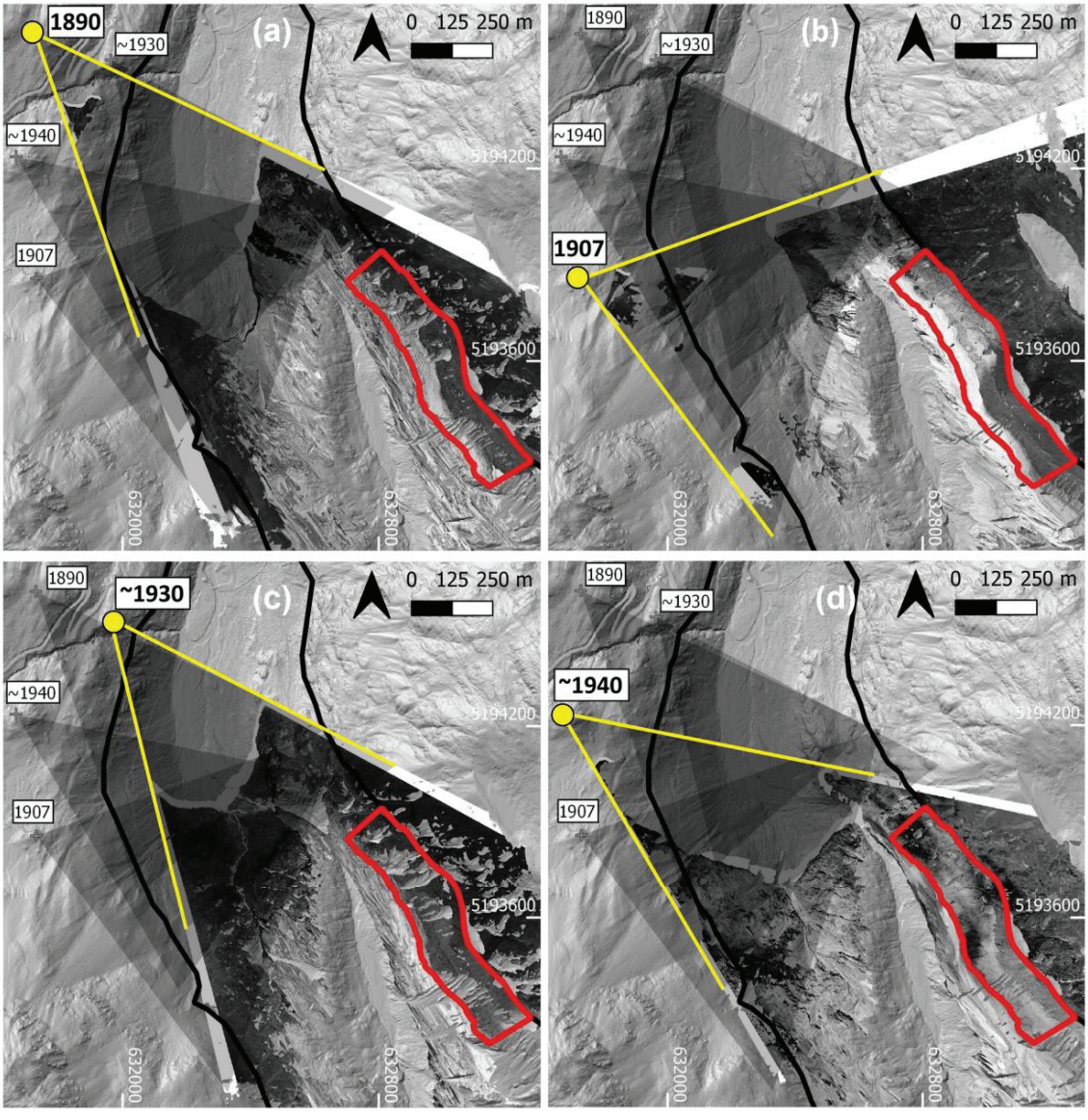


Figure 4. Determination of the position and field of view (yellow marking) of the individual historical terrestrial oblique photographs computed with Mono3D: (**a**) 1890, (**b**) 1907, (**c**) ~1930 and (**d**) ~1940, whereas the black line determines the glacier extent at the end of the LIA and the red polygon the AoI. The historical orthophotos are projected on the hillshade of 2017 published by Piermattei et al. [20].

Table 2. Calculated coordinates of the projection centre (east [E], north [N], height [H]) and the corresponding height above ground [H_{Ground}], rotation angle of the camera (Alpha, Zeta, Kappa), coordinates of the principal point (x0, y0) and focal length f. σ_0 represents the mean reprojection error. The corresponding standard deviations are given in brackets. The coordinates refer to the ETRS89/UTM Zone 32N coordinate system (EPSG code: 25832).

Estimation of Interior and Exterior Orientation	1890	1907	~1930	~1940
σ_0 [px]	16.1	7.2	13.8	19.7
E [m]	631728.6 (±2.074)	631728.6 (±0.363)	631963.2 (±2.969)	631667.4 (±7.260)
N [m]	5194619.9 (±1.620)	5193858.1 (±0.266)	5194538.2 (±2.761)	5194236.8 (±6.239)
H [m]	2233.4 (±0.570)	2265.9 (±0.173)	2169.7 (±1.013)	2254.3 (±2.317)
H_{Ground} [m]	3.2	1.0	12.3	13.7
Alpha [°]	−48.146 (±0.056)	−16.866 (±0.043)	−51.964 (±0.055)	−35.351 (±0.078)
Zeta [°]	269.081 (±0.053)	271.069 (±0.045)	268.187 (±0.054)	266.540 (±0.087)
Kappa [°]	−88.929 (±0.203)	−88.268 (±0.110)	−89.364 (±0.107)	−90.610 (±0.144)
x0 [px]	2302.5	2305.5	4606.5	4488.0
y0 [px]	−1535.5	−1535.5	−3071.0	−3071.0
f [px]	5425.1 (±22.7)	3129.0 (±7.2)	101,14.8 (±38.6)	100,06.9 (±50.3)

3.2.2. Processing of the Aerial Photos

For quantitative mapping of the extent of different surface types, mainly the morphodynamic area and land-cover types, the area-wide and overlapping historical and current aerial photographs from the mid-20th century onwards (1953 to 2015) were processed into georeferenced orthophotos using Agisoft Metashape Professional (Version 1.6.6; Agisoft LLC, St. Petersburg, Russia) and Trimble Inpho (Version 9.2) for the 2003 aerial photo series. For a detailed description of the processing of the orthophotos we refer to [4,20,46,47]

3.3. Mapping of Morphodynamic and Land-Cover Types

In order to identify temporal and spatial changes within the AoI, morphodynamic and land-cover types were mapped using QGIS (version 3.16.7) [48] (Table 3). In morphodynamics, a classification was made between the (initial) gully system and the sediment accumulation at the glacier margin. In addition, geomorphological non-active areas (areas outside the gullies, which can mostly be considered as more stable) and glacier areas were mapped (lower part of the mapped glacier extent). Regarding the different land-cover types (Table 3) we mapped different land-cover types, but also the bedrock, and the glacier extent. The most abundant species for the land cover types scree slope, scree communities, alpine grassland and dwarf shrubs are listed in Table 3, which are based on vegetation surveys done in 2020. The mapping of the morphodynamic and land-cover types was carried out at intervals of 7–23 years, depending on the availability of photos (see Figure 2). If photo materials were temporally within 1–3 years, it was assumed that only very small changes in land-cover have occurred. In contrast to this, all photos were used for mapping the morphodynamics, as very short-term events can also occur. The analyses for showing the development over time were carried out in R (version 4.2.2) [49]. For further processing, all georeferenced shapefiles were converted into raster files with a resolution of 1×1 m. The rate of change in land-cover types over time on the whole AoI as well as the 1890 initial glaciated area, area with the initial gully system, and the more stable area respectively was displayed with alluvial diagrams using the packages tidyverse [50], raster [51], and ggalluvial [52,53].

Table 3. Categories used for the morphodynamic and land-cover types mapping with the most abundant species per type based on vegetation surveys in 2020 in brackets.

Morphodynamic	Glacier [1]
	(Initial) Gully system
	Sediment accumulation at the glacier margin
	Geomorphological not active area
Land-cover types	Glacier
	Rock
	Scree slope (<5%) (e.g., *Atocion rupestre*, *Cardamine resedifolia*, *Linaria alpina*)
	Scree community (vegetation cover 5–60%) (e.g., *Achillea moschata*, *Tussilago farfara*, *Saxifraga bryoides*)
	Alpine grassland (e.g., *Carex sempervirens*, *Nardus stricta*, *Festuca halleri*, *Lotus corniculatus*, *Leontodon hispidus*, *Potentilla aurea*)
	Wetland
	Dwarf shrub (e.g., *Rhododendron ferrugineum*, *Empetrum hermaphroditum*, *Salix helvetica*)
	Shrub
	Trees, woodland

[1] to complete the mapping within the AoI.

The mapping was done manually through digitising the relevant objects of interest in the orthophotos, whether linear or areal and creating the corresponding spatially referenced vector datasets (line and polygon shapefiles) in QGIS (version 3.16.7) [48], which could then be exported. After that, the spatial and temporal extent of all surface types of the AoI was calculated. We compiled ten historical states of the AoI step-by-step going backwards in time to the first photograph. After one historical situation had been completed, we evaluated its relevance for the temporally younger situations and whether corrections would have to be made. Such a regressive-iterative approach allows for permanent critical revision of the reconstructed time segments already processed.

3.4. Generating Meteorological Data of the Study Area

Using simulated climate data generated by a regional climate model (RCM), the long-term air temperature (2 m above ground) as well as the precipitation of the AoI since the end of the LIA was determined. For the corresponding dynamic downscaling of climate data (from 1850 to 2015), the Advanced Research Version of the Weather Research and Forecasting (ARW-WRF) model (version 4.3) was used [54]. Therefore, the 20th Century Reanalysis version 3 (20CRv3) dataset was used as input [55–57]. To perform the simulations, the physical and dynamic options proposed by Collier and Mölg [58] were used (Appendix C, Table A5). In addition, the Noah land surface model, the Eta values of Collier et al. [59] and the 24 land use categories of the United States Geological Survey (USGS) were applied. Finally, simulated temperature data with a temporal and spatial resolution of one hour and two km respectively could be generated. For the subsequent period from 2016 to 2020, the ERA5 reanalysis dataset Hersbach et al. [60] was used, available with a temporal and spatial resolution of one hour and 55 $\times$ 55 km. The corresponding temperature data was extracted using the centre of the AoI (Figure 1). Additionally, an elevation correction of the temperature data was applied. The five years running mean of the average annual temperature and sum of summer (Mid-April to mid-October of each year) as well as winter precipitation (Mid-October to mid-April of each year) were used for the statistical analysis of the development of the land cover types.

3.5. Statistical Analysis of Land Cover Changes

For getting an information if there are other variables than the morphodynamic influencing the development of the land cover types on lateral moraines in the long-term, we performed a beta-regression using the package betareg [61] which is the suitable method for proportions. Therefore, the proportions have to be converted into values between zero and one using the formula $\frac{y*(n-1)+0.5}{n}$ [62] where y is the proportion, and n the sample size. We used the variables age (years to the end of the observation period), amount of glacier per year (gla), the mean annual temperature (temp), the sum of summer (pre_sum) and winter precipitation (pre_win), and the amount of the more stable areas within the AoI (inact) for every year as independent variables. The equation for the different land cover types was the same and is shown in the following equation:

$$g\left(E\left[y^{type}\right]\right) = \beta_0 + \beta_1\, age + \beta_2 gla + \beta_3 temp + \beta_4 pre_sum + \beta_5 pre_win + \beta_6 inact + \varepsilon$$

where g (.) is the link function (logit link) and E [.] the expection; y^{type} the transformed ratio of the land cover type following a beta distribution; β_0 is the overall intercept, the β_s capture the effects, and ε is the remainder noise.

4. Results

4.1. Long-Term Morphodynamic Development

While the AoI was fully glaciated at the end of the LIA, the glacier melted completely, over the years 1890, 1907, ~1930, by ~1940 (Figures 5 and 6); Appendix D, Table A6). From 1890 (5.1%) to 2020 (47.7%), there is an (almost) constant increase in the area of the (initial) gully system (Figure 5 and 6; Appendix D, Table A6; Appendix E, Figures A3 and A4). However, between 1970 and 1982, there is a decrease (from 43.61% to 42.23% of the total AoI) in the extent of the mapped gully system (Appendix D, Table A6). Due to erosion processes, debris cones were formed at the glacier margin, which were visible from 1907 onwards and disappeared from the AoI by 1953 (Proportion of accumulated debris in 1907: 18.4%, ~1930: 23.9%, ~1940: 35%). The area defined as geomorphologically not active (more stable) is subject to greater variations. In the beginning (1890) with a high proportion (of 53.7%), this area expanded (almost) continuously until 1983 (60%) before it decreased again until 2020 (52.3%). In 2020, the gully system (47.7%) and the geomorphologically not active area (52.3%) had approximately the same share of area.

The initial gully system, already visible in 1890, had formed on the area exposed by the glacier until then (Figure 6). Between 1890 and 1953 the size of the (initial) gully system increased subsequently. These areas previously not detected as impacted by erosion, developed into gullies over time. Gullies were formed on previous area of the debris cone (sediment accumulation at the glacier margin) which was transported downslope on the melting glacier. Due to a strong headcut retreat, the size of the gully system increased (almost) continuously from 1953 to 2020, so that formerly geomorphologically not active areas became active. However, it is also evident that areas mapped as active gully system can certainly become stable again (throughout the investigation period) (Figure 6).

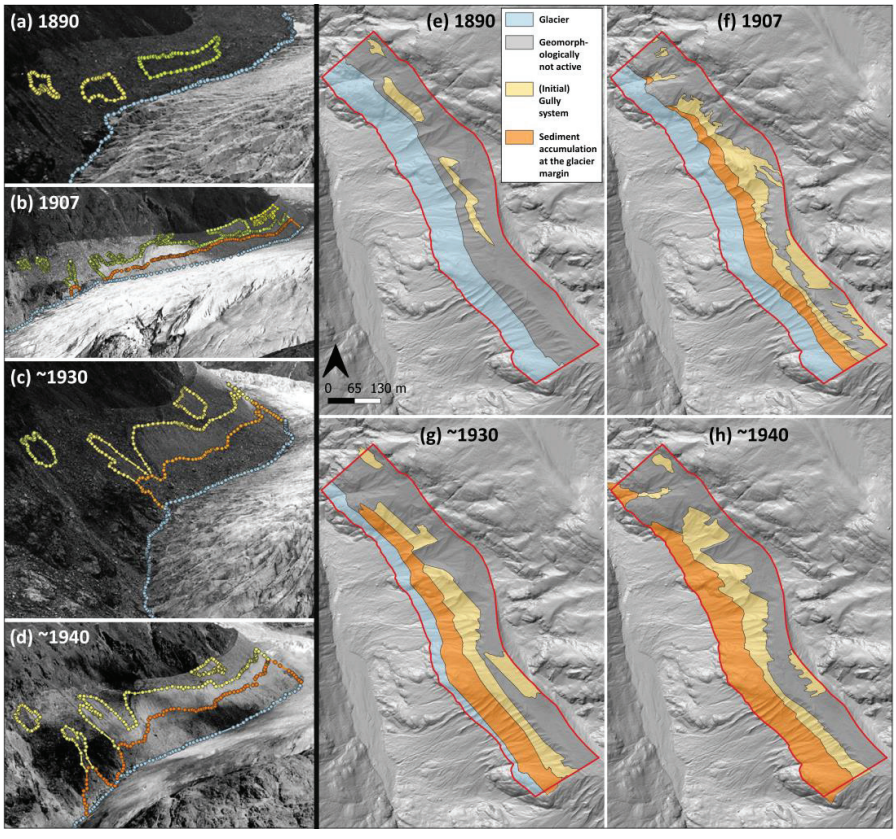


Figure 5. Mapping of the different surface types (morphodynamic mapping), in the historical terrestrial photos (**a**–**d**) and the corresponding visualisation of the extracted georeferenced vector data sets on a 2017 digital elevation model (DEM) (**e**–**h**). In (**e**–**h**) the red polygon indicates the AoI.

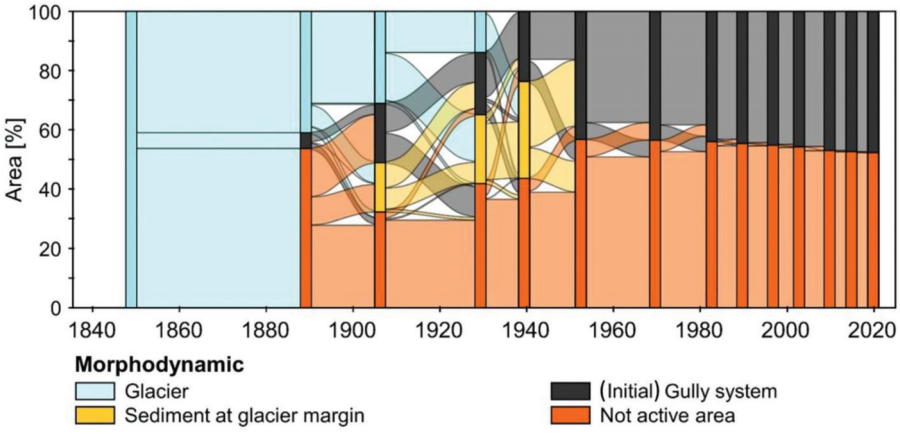


Figure 6. Changes in morphodynamic types of the AoI from 1890 to 2020 (For reasons of visualisation, the 1969 and 1982 mappings were excluded from this figure, which can be, however, found in the Appendix D, Table A6).

4.2. Long-Term Development of the Land-Cover Types

The entire AoI was covered by glaciers at the end of the LIA (Figures 7 and 8 and Appendix D, Table A7). Until 1890 a small part was covered by bedrock (0.6%), the largest part by scree slope (46.5%), and further small parts to scree community with a low cover of vegetation (9.6%), alpine grassland (1.7%) and even dwarf shrubs (0.6%) (Figures 7 and 8; Appendix D, Table A7). From ~1940 onwards, many of the scree slope stabilised and primary succession took place. As a result, the proportion of areas at the expense of scree slope communities, alpine grassland and dwarf shrubs increased to about 72.88% (Appendix E, Figures A5 and A6). This share remained largely stable until 1990, but then there was another massive increase in scree slope. This indicates a renewed dynamic in these areas (Figure 8; Appendix D, Figure A2, Tables A7 and A8). Mostly, these were alpine grasslands and scree communities that underwent a transition back into scree slopes. To a smaller extent, however, dwarf shrub communities were also affected (Figure 8; Appendix D, Figure A2, Tables A7 and A8). The dispersal of wetlands, shrubs and trees/woodland started in 1953 and reached together until 2020 a proportion of 0.9% (Figure 8; Appendix D, Figure A2, Tables A7 and A8; Appendix E, Figures A5 and A6).

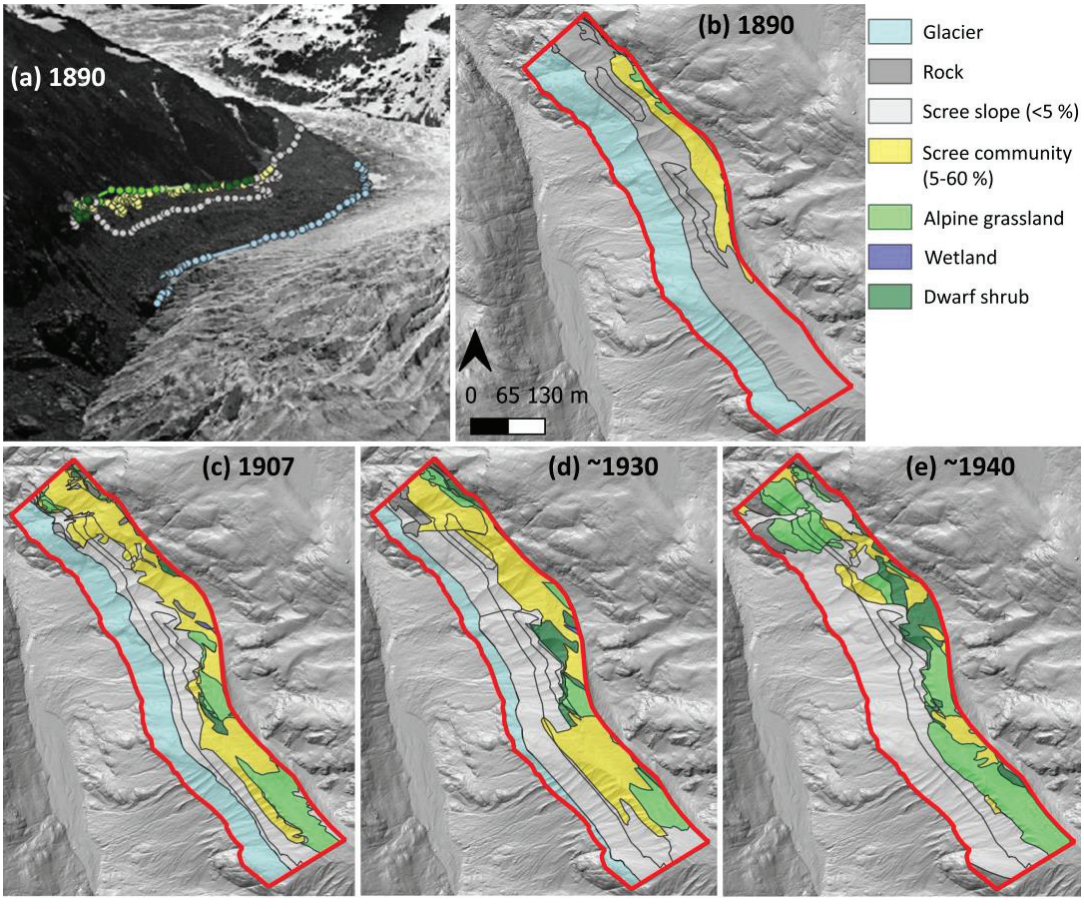


Figure 7. Example of the mapping of the different land-cover types of the year (**a**) 1890 in the historical terrestrial photo and (**b**–**e**) the corresponding visualisation of the extracted vector datasets on the 2017 DEM in QGIS (version 3.16.7). The red line indicates the area of interest (AoI).

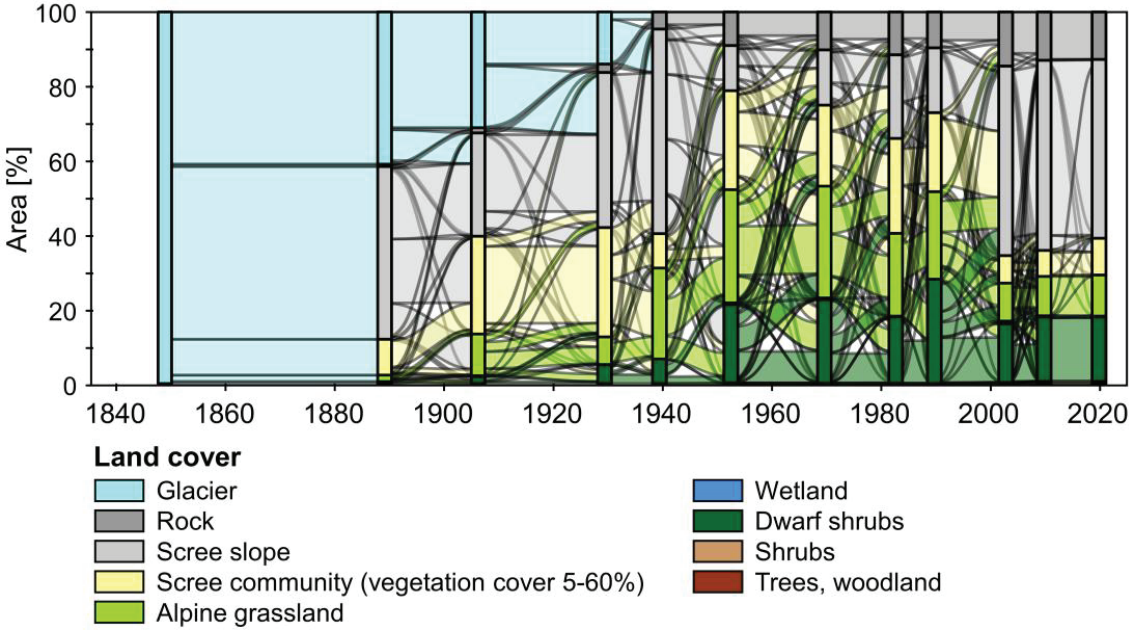


Figure 8. Development of land-cover types from the end of the Little Ice Age to 2020.

4.3. Development of Land-Cover Types in Geomorphologically Active and Not Active Areas

The development of the land-cover types within the gully systems as well as in the geomorphologically inactive (more stable) areas showed clear differences. The active gully systems were mainly characterised by scree slope (Figure 9a). However, due to the expansion of different vegetation types, these declined until 1953 (100 to 23.7%). After a strong decline from 1907 to 1940 (40.8 to 11.7%), mainly scree communities increased until 1990 (11.7 to 38.6%) (Figure 9b). Alpine grasslands and dwarf shrubs spread from 1907 (8%/0.2%) until 1953 (23.6%/19%) before declining again until 1990 (11.2%/13%) (Figure 9c,d). Between 1990 and 2003, a strong expansion of scree slope area (35.3% to 92.2%) is evident and a simultaneously strong decline of scree slope communities (38.6% to 3.5%), alpine grassland (11.2 to 1.3%) and dwarf shrubs (13 to 1.7%) (Figure 9c,d). Between 2003 and 2020, a slow increase in scree communities (3.5 to 10.6%) (Figure 9b) and alpine grassland (1.3 to 2.6%) (Figure 9c) can be observed, accompanied by a decline in scree slope areas (92.9 to 84.4%). Dwarf shrubs have remained at a similar level during this epoch (1.7 to 1.4%) (Figure 9d).

The geomorphologically non-active area (more stable) had clearly higher proportions of land-cover types, except scree slope (Figure 9a–d). Scree slope decreased strongly from 1890 (76.7%) to 1907 (5.9%) and, with some fluctuations, always remained below 20% until 2020 (Figure 9a). Scree communities increased clearly from 1890 to 1907 (18% to 54.6%) before decreasing strongly with fluctuations until 2020 (9.2%) (Figure 9b). Alpine grasslands also increased from 1890 to 1940 (from 3.2% to 52.6%) before also decreasing with variation by 2020 (18.8%) (Figure 9c). Dwarf shrubs increased almost continuously from 1890 to 2020 (from 1.1% to 31.8%), with the largest area in 1990 (40.2%) (Figure 9d).

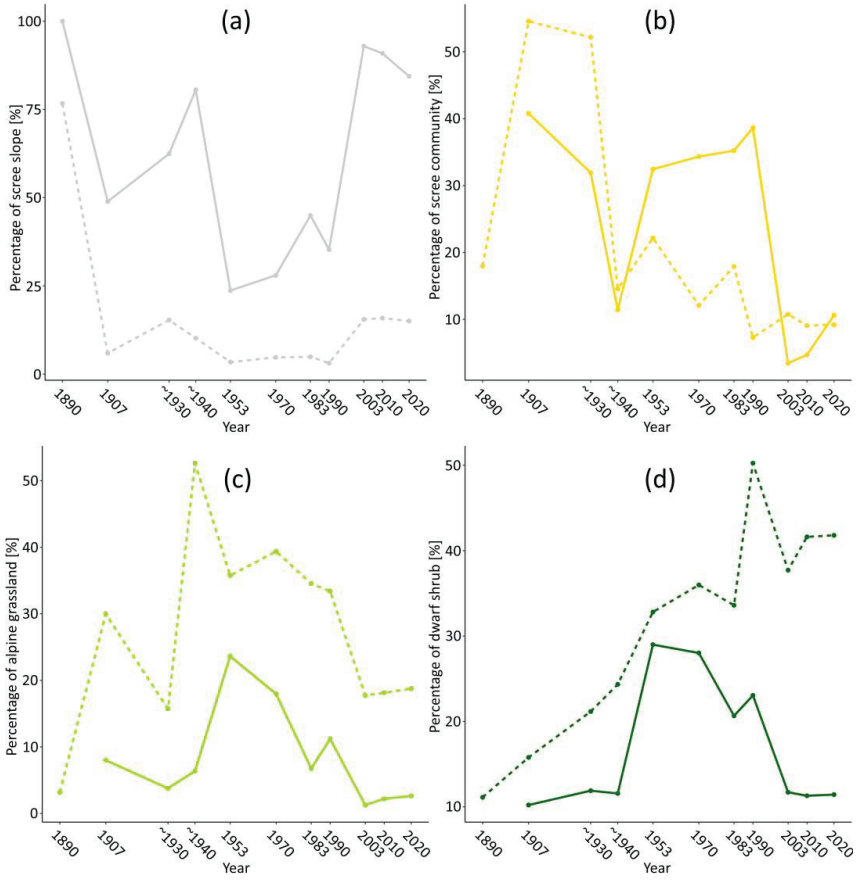


Figure 9. Change in the proportion of the land-cover types within the gully systems (solid line) and non-active areas (dashed line) (**a**) scree slope, (**b**) scree community, (**c**) alpine grassland and (**d**) dwarf shrub.

4.4. Land-Cover Change in Context with Morphodynamic and Meteorological Data

Figure 10 shows the running mean of the annual air temperature (2 m above ground) and the sums of the annual precipitation since 1850.

The analysis showed that the amount of glacier had only an impact on higher developed land-cover types. All analysed land-cover types except the dwarf shrubs were influenced by temperature. Summer and winter precipitation influenced the less developed land-cover types. The effect of age (years since observation) had a significant negative effect on scree slope ($p = 0.038$) and the amount of glacier per year was only significant for the land-cover types alpine grassland and dwarf shrub ($p < 0.001$ and $p = 0.003$, respectively) (Table 4). Temperature had a significant positive effect on scree slope ($p < 0.001$) and a significant negative effect on the land-cover types scree community ($p = 0.002$) alpine grassland ($p = 0.006$ (Table 4). Land cover types were also affected by summer precipitation with a significant negative effect on scree slope ($p = 0.013$) and a significant positive one on scree community ($p = 0.041$), respectively. Winter precipitation influenced scree slope significantly positive ($p = 0.004$) and scree community negative ($p = 0.005$) (Table 4). Concerning the morphodynamic more stable areas, we observed only a significant positive effect for dwarf shrubs (Table 4). The other three land-cover types were not significantly affected by the morphodynamic more stable areas. For the four analysed land-cover types the pseud

R^2 was high (0.718, 0.728, 0.872, and 0.912, respectively). Also, the precision parameter (phi) was good for all four models (Table 4).

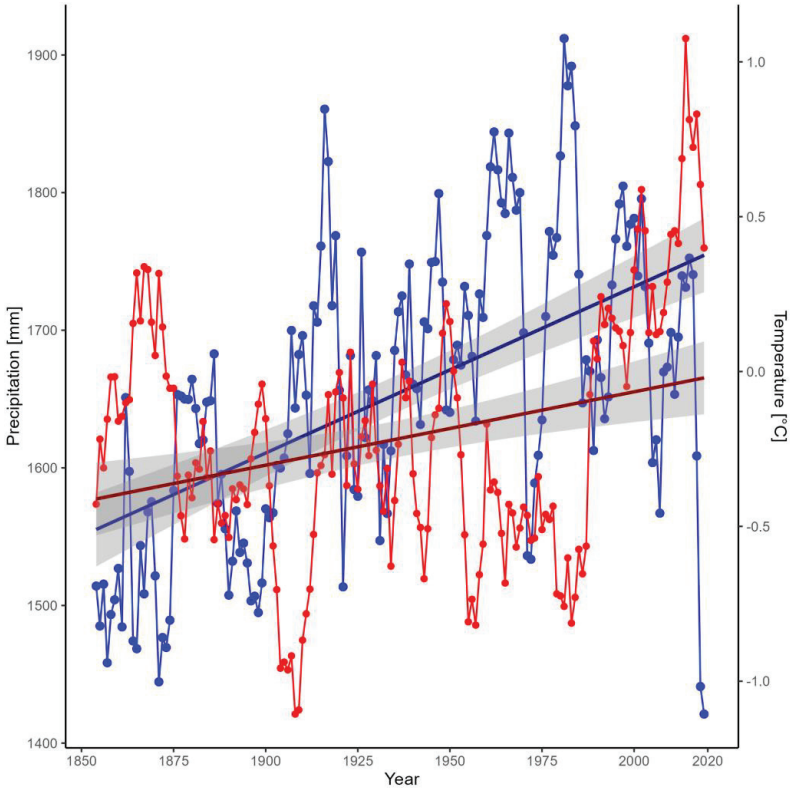


Figure 10. Development of the five years running mean of the mean annual air temperature (red; 2 m above ground) and five years running mean of the sums of the annual precipitation (blue) of the AoI between 1850 and 2020 with corresponding trend lines for the entire epoch (thick line). The 95% confidence interval is included (grey).

Table 4. Effects of the years since observation (age), the glacier retreat (gla), the five years running mean temperature (temp), of the five years running mean summer precipitation (pre_sum) and the five years running mean winter precipitation (pre_win), and more stable areas within the AoI (inact) on the main land-cover types. Estimates (est.), standard errors (se), and *p*-values (*p*) for the independent variables, and phi are shown (*p*-values below 0.05 are in bold).

	Scree Slope			**Scree Community**			**Alpine Grassland**			**Dwarf Shrub**		
	est.	**se**	***p***	**est.**	**se**	***p***	**est.**	**se**	***p***	**est.**	**se**	***p***
Intercept	−9.940	4.255	**0.019**	7.614	3.908	0.051	2.466	3.326	0.458	0.082	2.962	0.978
age	0.014	0.007	**0.038**	−0.006	0.006	0.316	0.005	0.005	0.344	−0.007	0.005	0.147
gla	−0.009	0.015	0.560	0.004	0.015	0.794	−0.071	0.013	**<0.001**	−0.047	0.016	**0.003**
temp	2.267	0.476	**<0.001**	−1.408	0.445	**0.002**	−1.034	0.375	**0.006**	−0.355	0.307	0.249
pre_sum	−0.003	0.001	**0.013**	0.003	0.001	**0.041**	−0.005	0.003	0.139	0.001	0.001	0.222
pre_win	0.015	0.005	**0.004**	−0.012	0.004	**0.005**	0.000	0.001	0.900	−0.006	0.003	0.067
inact	−0.026	0.017	0.123	−0.021	0.016	0.206	0.000	0.019	0.981	0.046	0.022	**0.033**
phi	38.100	16.090	**0.018**	63.090	26.840	**0.019**	98.580	42.070	**0.019**	158.690	68.130	**0.020**
R^2	0.718			0.728			0.872			0.912		

5. Discussion

5.1. Assessment of Technical Uncertainties and Errors

The accuracy and precision of the digital monoplotting results are influenced by several factors [21–26,28–32] including the distribution and number of the GCPs, the accuracy and precision of the DTM, the accuracy of the estimated camera parameters (interior and exterior orientation of the camera) and the angle of incidence between the image ray and the DTM. Furthermore, the quality of the historical terrestrial photos is not comparable to modern photos (e.g., lens distortion), further reduced by the way they were stored in the archives (e.g., stains, scratches), influencing the potentially achievable accuracy. When selecting the GCPs, we made sure to identify only terrain points in stable areas, further avoiding the highly dynamic proglacial area as much as possible, except for example rocky outcrops. Despite these restrictions, it was possible to identify more than 10 GCPs for each camera, distributed over the entire image. The use of a current (3D) object space (in this case the DTM 2017 (1 m)) and a historical terrestrial photo (from 1890 onwards) can also lead to errors in the mapping, as the mapping was carried out on the historical terrestrial photos, but the current surface might have changed considerably due to erosion processes such as landslides and debris flows [28,29]. This could be remedied by DTMs that are much closer in time to the historical terrestrial photos and thus possibly contain less changes in the surface topography, however, no corresponding DTM exists from this early period. Due to the strong surface changes on the AoI, especially due to the incision of the gullies, throughout the study period, there is strong shadowing of the georeferenced orthophotos based on the terrestrial photos, especially of the 1890 and ~1930 image (due to the low angle of incidence), as can be seen in Figure 5.

To estimate the spatial error of the GCPs, the corresponding theoretical 3D error was computed. This was calculated using the Euclidean distance between the user defined GCPs and the GCPs calculated by monoplotting. The determined error values of the GCPs show high variability. It ranges from minimum values of a few centimetres to maximum values of several tens of metres, although in extreme cases several hundred metres, or no value at all, could be reached, while the median of the GCPs of the four historical photos ranged from 3.5 to 17.5 m (Tables 5, A3 and A4). The extreme cases occurred only at the top of hills or mountains where the calculated point was computed on the opposite slope or not at all (1890 photo: GCP numbers 2, 3 and 11 in Figure 3b and in Appendix B, Table A2 and ~1930 photo: GCP number 8 in Appendix B, Table A4).

Table 5. Minimum value, maximum value and median of the theoretical 3D error of the corresponding photos: The complete values can be found in Appendix B, Tables A3 and A4.

Year	Number of GCPs	Minimum [m]	Maximum [m]	Average (Median) Monoplotting Accuracy (RMSE) [m]
1890	13	1.1	877.7	17.5
1907	12	0.2	62.3	9.1
~1930	13	0.3	23.7	3.5
~1940	12	0.8	15.5	4.1

The height above ground of the determined camera locations shows heights of 1.0 or 3.2 m, but also up to 12.3 and 13.7 m (Table 3), whereby the steep slopes of the location where the photos were taken play an important role, as a horizontal shift can quickly add up to a few metres in height. In any case, the determined coordinates of the camera locations mostly have an accuracy of a few decimetres to metres (up to a maximum of 7.3 m) (Table 3), which means that we consider the calculated camera locations to be acceptable. Bozzini et al. [21] show a theoretical 3D error of less than 10 m respectively less than 5 m for the prototype version of the WSL tool, if all basic requirements like a high image quality, a good distribution of control points, a DTM with high resolution and a good camera

calibration are considered. Nevertheless, under optimal conditions, accuracies of less than one metre to decimetres are possible [22]. Conedera et al. [29,30] and Scapozza et al. [32] also report a possible spatial (3D) error of less than one metre (up to several metres) under optimal conditions, although even within the same photo higher errors can occur in flatter versus steeper areas due to the different angle of incidence.

Studies using photos from the Mountain Legacy Project [23,25] show clearly higher error values, but these studies used photos that cover larger and wider areas in high mountain regions (Rocky Mountains, Canada). Therefore, they are prone to higher error values (similar to the photos from the SEHAG project used in this study), as the accuracy decreases with increasing distance from the camera, due to the uncertainties in the orientation (angle). Stockdale et al. [23] show that especially the angle of incidence is of high importance, but that also the distance to the camera plays an important role, as it is difficult to set GCPs that have a very long distance, such as mountain peaks several kilometres away. In addition, we consider the angles of incidence in our study on the AoI to be high and therefore acceptable, due to the elevated position of the photo locations on the opposite slope and the steep slope of the lateral moraine itself. McCaffrey and Hopkinson [25] give a mean error vector length (between test points) of 23.9 m (range from 2 to 63.8 m) and a landscape level displacement of 7 m using seven photos. After removing two outliers, corresponding values of 16.5 m and 5.9 m were obtained, which are comparable to the values of Stockdale et al. [23] with 14.4 m and 2.9 m, respectively.

5.2. Opportunities and Limitations

While aerial photographs show an area-wide coverage of the surface, for terrestrial photographs, due to the oblique viewing geometry in combination with the complex topography especially in high mountain regions, some areas within the field of view cannot be observed due to occlusion [28]. We can confirm this, as the AoI is limited to a small area in the upper part of the lateral moraine. In the south-eastern part, the AoI is limited due to the curved topography of the lateral moraine, and in the north-western part, the AoI ends because rock exposures occurred on the slope (mainly in ~1930 and ~1940) and the mapping of the (initial) gully systems in several areas was not possible anymore due to the shadowing effect. While the upper boundary of the AoI was defined by the maximum glacier extent at the end of the LIA, the lower boundary was defined by the glacier extent in ~1940, so that a focus was placed on the erosion area in the upper part of the lateral moraine. This shows that although it is possible to map different surface types in high mountain regions using this approach, it can only be applied locally, and not over a wide area as with aerial photographs. While larger areas could be analysed with a greater number of historical terrestrial photos, these are usually available to a very limited extent and the identification of potential photos in the archives is time consuming. With very steep rock faces, however, aerial photos can reach their limits and the advantages of terrestrial photos can outweigh them, as due to the oblique geometry the angle of incidence is correspondingly higher [28]. Nevertheless, and most importantly, due to their temporal coverage into the 19th century, these photos provide a unique source for quantifying the change of different surface types in proglacial areas.

However, manual mapping is challenging and therefore prone to error. To minimise interpretation errors, only photos of good quality (e.g., photographic glass plates) and taken from a short distance from the AoI were selected, meaning that some photos that would have been available were not included in the analysis. Concerning the mapping of land-cover types, there exists a limitation by the quality of the photos and difficulties in mapping on black-white photos. Therefore, small errors of the mapping of the different land cover types may also be due to quality and difficulties in differentiation of the black-white photos and also by interpretation of the areas with shadow. By using a regressive-iterative approach the number of errors can be reduced as an unlikely sequence can be better detected. Due to the remote sensing data used (terrestrial photos and aerial photographs), it was not possible for us to identify individual species and to reconstruct them accordingly

over the entire period. Nevertheless, based on field data collected in 2020, we can specialize the scree slope, scree community, alpine grassland, and dwarf shrub in more detail (Table 3).

5.3. Development of the Morphodynamic and Land-Cover Changes

The use of individual historical oblique photos by monoplotting has shown that it is possible to determine the changing extents of different surface types between the end of the LIA and the mid-20th century, thus quantifying to a certain point the approximately 100-year unknown initial response of surfaces to glacier retreat of proglacial areas, demonstrating the immense value of these photographs. By continuing the mapping using georeferenced orthophotos from the middle of the 20th century onwards and ensuring the compatibility of both mapping approaches, it was possible to continue this until 2020, covering a total period of 130 years. The results of the mapping of the upper lateral moraine section show a correspondingly high dynamic in recent decades. Also, for land-cover maps the development in the AoI was highly dynamic.

5.3.1. Morphodynamic Area

The mapping shows a continuous melting of the glacier from the end of LIA until ~1940. Although the visible glacier extents were mapped (and the lower surface determined as glacier), it must be assumed that the debris deposits on the glacier cover some parts of the glacier margin and thus the actual glacier extent is underestimated. However, this problem occurs in all terrestrial photographs (but mainly from 1907 to ~1940). This is evident in Figure 1, where the ~1940 (lower border of the AoI) and 1953 glacier extent overlap at two points, but the 1953 glacier extent is based on a DoD mapping (DEMs from 1970 and 1953) where volume changes were used to determine the full glacier extent even under debris deposits. Also, several studies show the occurrence of dead ice in this slope [4,5,20], at least until 1983 [20], which influenced the development of the erosion area for decades.

Although, an (almost) continuous increase in the area of the gully system within the AoI was observed from the end of LIA until 2020, several studies show a clear decrease in the corresponding erosion rate (based on quantitative volume data derived by DoDs) on the same slope, such as Altmann et al. [4] from the 1970s or Betz-Nutz et al. [5], Piermattei et al. [20] and Altmann et al. [6] from the 1950s onwards to present. However, between 1970 and 1982, there is a decrease in the extent of the gully system (Appendix D, Table A6), due to a part of an erosion area, previously (1971) mapped as geomorphologically active, which in turn were mapped in 1982 as bare rock and thus not geomorphologically active anymore (Appendix D, Table A6). Since several rocks were exposed over the entire period, this phenomenon occurs several times, but only predominates in the example mentioned. The geomorphologically inactive area was separated as well as possible from the (initial) gully system, although it cannot be excluded that some material was mobilised in the inactive area. Nevertheless, the (initial) gully system is well visible and was mapped due to its linear erosion form.

5.3.2. Land-Cover Types

The massive increase in scree slope between 1907 and 1930 was mainly caused by the release of new areas by the glacier (Appendix D Figure A2a). In 1953 we observed small flat areas within the gullies with alpine grassland or dwarf shrubs which eroded in the following periods. This can explain the high amount of dwarf shrubs and alpine grassland in 1953. The small flat areas with vegetation might be due to gliding down of whole areas with vegetation and erosion between vegetated areas. The detected large increase in alpine grassland, especially in the accumulation area might also be due to the glide down of larger parts in its entirety. The small flatter areas with denser vegetation eroded within the next periods. The clear decrease in higher developed land-cover types (mainly alpine grassland, and dwarf shrubs) as well as scree community and the accompanied increase in scree slope between 1990 and 2003 can be explained by the impact of geomorphic processes on the emergent and developing vegetation. For example the large-scale (wide

area) erosion processes within the gully systems, as seen in a DoD of our AoI published by Piermattei et al. [20] between 1997 and 2003, have covered the upcoming vegetation. From 2003 (until 2020), a very slow increase in these land-cover types (scree community, alpine grassland and dwarf shrubs) can be observed again. The AoI experiences clearly less geomorphic activity during these epochs [20]. In the period 2010 to 2020 we could observe further stabilisation with mainly an evolvement from the scree slope to scree community and less changes for the other land-cover types.

There was nearly no comparable mapping for land-cover types found in literature, except the one by Hohensinner et al. [18]. However, in contrast to this study, they used historical maps for the long-term mapping rather than historical terrestrial photos, which, however, achieves a much lower spatial resolution. Using historical maps can cause problems in high elevations, especially above the timberline due to lower resolution and is therefore not appropriate for analysis on a small scale as these maps are often drawn at a coarser scale. The problems concerning scale, projection system, and reference points for elevation calculation as well as the precision during the field surveys and the accuracy are shown by Stäuble et al. [63].

Although morphodynamic activity highly influences land-cover development, the increase in alpine grassland and dwarf shrub might be due to the increasing temperature since the 1980s and faster change since 2011 as shown by Knoflach et al. [17], but it seems that the morphodynamic processes influence vegetation development more than the increasing temperature due to climate change. In contrast to Eichel et al. [14] we could only observe slope stabilisation when the morphodynamic activity already decreased.

6. Conclusions

To analyse quantitative landscape changes in the European Alps, mapping of different surface types, for example, can be carried out using georeferenced orthophotos based on aerial photos. However, the corresponding aerial photo series only extends up to about half of the 20th century, which limits the research design of many studies in time. Using digital monoplotting, it is possible to extend the time frame of mapping studies analysing landscape changes in high alpine geosystems using single terrestrial oblique photos by several decades into the late 19th and first half of the 20th century. By linking a single image to a 3D object space, quantitative analysis is possible by enabling real surface measurements of different image contents. Using several historical terrestrial oblique photographs from 1890 onwards (to ~1940) and georeferenced orthophotos based on aerial photos from 1953 to 2020, we show by mapping the quantitative changes of different surface types of a LIA lateral moraine section. The main conclusions of this study are listed below:

- Using the monoplotting approach, it was possible to extend the temporal scope of a quantitative mapping study based on historical terrestrial oblique photographs within a proglacial area into the second half of the 19th century (1890), covering a total study period of over 130 years (1890–2020). This shows that the different orthophotos (based on terrestrial photos and aerial photographs) can be combined in a productive manner.
- The (initial) gully systems expanded (almost) continuously since 1890 (respectively since the end of the LIA). However, several studies show that the erosion volume (mean annual erosion rate), between the 1950s/1970s and today, on the same slope is decreasing.
- The vegetation covered areas show a clear increase within the AoI from 1890 (respectively since the end of the LIA) to 1953, as mainly scree communities (vegetation cover 5–60%), alpine grassland and dwarf shrubs expand. From 1953 to 2020, vegetation covered areas are clearly reduced as the scree expand again due to erosion processes. Especially in this epoch, rocks within the lateral moraine were also exposed. Land-cover types are clearly less developed in the active gully system than in the geomorphologically non-active areas, as erosion processes deplace or cover corresponding vegetated areas. The development of land-cover types is also significantly influenced by temperature and precipitation changes.

- The approach of this study allows a better analysis of the paraglacial adjustment process, as in particular the early phase of the lateral moraine's response to the ice loss can be determined and thus the initial gully formation as well as the development of the land-cover types can be detected, which previously remained unclear.

However, the digital monoplotting approach is highly dependent on the availability, number and quality of the corresponding historical oblique photos, and shadowing effects in high alpine regions can quickly lead to corresponding limits. Nevertheless, the study shows the enormous potential of these photos. Therefore, we encourage scientists to conduct further long-term studies using digital monoplotting with terrestrial historical oblique photos to better reconstruct corresponding climate change consequences in high alpine geosystems.

Author Contributions: Conceptualization, M.A., K.R., F.H., E.T. and M.B.; methodology, M.A., S.M.-F., K.R., M.P., J.R., F.F., T.H. (Toni Himmelstoß), F.H., T.H. (Tobias Heckmann), N.P., C.R., E.T. and M.B.; software, M.A., S.M.-F., K.R., M.P., N.P. and C.R.; formal analysis, M.A., K.R. and M.P.; investigation, M.A., K.R. and M.P.; data curation, M.A., K.R. and M.P.; writing—original draft preparation, M.A. and K.R.; writing—review and editing, M.A., S.M.-F., K.R., M.P., J.R., F.F., F.H., T.H. (Toni Himmelstoß) and E.T.; visualization, M.A., K.R., M.P. and E.T.; supervision, F.H., E.T., N.P. and M.B.; project administration, F.H., T.H. (Tobias Heckmann), E.T. and M.B; funding acquisition, F.H., T.H. (Tobias Heckmann), E.T. and M.B. All authors have read and agreed to the published version of the manuscript.

Funding: The study was part of the SEHAG project ("SEnsitivity of High Alpine Geosystems to climate change since 1850") and financially supported by the German Research Foundation (DFG) project number 3,942,00609, the Austrian Science Fund (FWF) and the Autonomous Province of Bozen/Bolzano, South Tyrol (Grant numbers: BE 1118/38-1, BE 1118/39-1, BE 1118/40-1, HA 5740/10-1, HE 5747/6-1, ER 905/1-1, MA 6966/4-1, LA 4426/1-1, 4062-N29 and IT-DFG 781,607).

Data Availability Statement: Aerial photos have been provided by the *Federal Office* of *Metrology* and *Surveying* of *Austria, Vienna* (BEV) and the Department of Geoinformation of the Province of Tyrol (Innsbruck, Austria). The orthophoto 2020 was downloaded from the Department of Geoinformation of the Province of Tyrol (TIRIS maps, https://tiris.maps.arcgis.com/home/index.html, accessed on 2 May 2022). The historical oblique photos have been made available by the archive of the German and Austrian Alpine Club (1890 und 1907) as well as by Martin Frey (~1930 und ~1940), a local chronicler in the Kauner Valley. The DEM 2017, which is based on airborne LiDAR data, comes from an own field campaign of the Chair of Physical Geography of the University of Eichstätt-Ingolstadt. The meteorological data were generated within the SEHAG project ("Sensitivity of High Alpine Geosystems to Climate Change since 1850"). The data can be requested from the authors.

Acknowledgments: We would like to thank the German Research Foundation (DFG), the Austrian Science Fund (FWF), and the Autonomous Province of Bozen/Bolzano, South Tyrol for their financial support. We would also like to thank the Federal Office of Metrology and Surveying (BEV, Vienna, Austria) and the Department of Geoinformation of the Province of Tyrol (Innsbruck, Austria) for providing the aerial photographs. Furthermore, we would like to thank the Archive of the German Alpine Club and Martin Frey, a local chronicler of the Kaunertal, for providing the historical terrestrial oblique photos of the Gepatsch glacier.

Conflicts of Interest: The authors declare no conflict of interest. The funders had no role in the design of the study; in the collection, analyses, or interpretation of data; in the writing of the manuscript; or in the decision to publish the results.

Appendix A

Table A1. Attributes of historical and current aerial photos.

Year of Recording	Source/ Purpose and Designation	Photos [1]	Camera Model, Band	Focal Length [mm]	Flying Altitude [m a.s.l.]	Type/Scanning Resolution [μm]	Result	Resolution Orthophoto [m]
5 June/31 August and 8 September 1953 [2]	BEV/Forest condition estimation, C	124	Wild RC5, BW	210.1	ca. 3330	film/15	Orthophoto	0.23
7 October 1976	BEV/Austrian Glacier Overall Survey	23	Wild RC5/RC8, BW	152.0	ca. 3450	film/15	Orthophoto	0.5
29 September 1970	Land Tirol/Overall flight Tyrol	26	Wild RC5/RC8	210.4	ca. 8665	film/12	Orthophoto	0.2
18 August 1971	Land Tirol/Overall flight Tyrol	91	Wild RC5/RC8, BW	209.5	ca. 3080	film/12	Orthophoto	0.2
14 September 1982	BEV/High Flight Tyrol/80	34	Wild RC10, BW	152.6	ca. 6090	film/15	Orthophoto	0.5
24 September 1983	BEV/Kaunertal	7	Wild RC10, BW	152.6	ca. 4840	film/15	Orthophoto	0.4
10 October 1990	BEV/KF 171–173	35	Wild RC10, BW	152.6	ca. 5850	film/15	Orthophoto	0.53
11 September 1997	BEV/KF 173	25	Wild RC10, BW	152.7	ca. 6010	film/15	Orthophoto	0.55
5 September 2003	BEV/Ötztaler Alpen/Oberinntal	59	N/A, RGB	305.1	ca. 4800	film/15	Orthophoto	0.35
31 July 2010	Land Tirol/Reutte-Sölden	413	N/A, RGBN	—	ca. 2870	digital	Orthophoto	0.2
5 October 2015	Land Tirol/Landeck	94	UltraCamX, RGBN	—	ca. 3250	digital	Orthophoto	0.4
8 September 2020 [3]	Land Tirol/ Landeck	N/A	N/A, N/A	—	N/A	digital	Orthophoto	0.2

[1] Photos were used to process the entire catchment of the upper Kaunertal, [2] Data set were processed into one orthophoto, [3] the Province of Tyrol (Office of the Provincial Government of Tyrol/Department of Geoinformation) provided the orthophoto as download (https://www.tirol.gv.at/sicherheit/geoinformation/geodaten/orthophotos/, accessed on 2 May 2022).

Appendix B

Table A2. Attributes of historical terrestrial oblique photos.

Year of Recording	Photographer	Source	Image Medium	Type	Colour	Width and Height [pixel, cm]	Resolution [dpi]	Image Depth [BIT]
1890	N/A	Archive of the ÖAV (Innsbruck, Austria)	Negative glass plate	Digitised	B&W	4607 × 307, 19.5 × 13	600	24
1907	N/A	Archive of the ÖAV (Innsbruck, Austria)	Negative glass plate	Digitised	B&W	4607 × 307, 19.5 × 13	600	24
~1930 (estimated)	N/A	Martin Frey (Local archivist of the Kaunertal)	N/A	Digitised	B&W	9213 × 614, 19.5 × 13	1200	8
~1940 (estimated)	N/A	Martin Frey (Local archivist of the Kaunertal)	N/A	Digitised	B&W	8976 × 614, 19.5 × 13	1200	8

Table A3. Monoplotting accuracy of 1890 and 1907 photos: Coordinates of the user defined GCPs (East, North and Height), by monoplotting calculated GCPs (East monoplotting, North monoplotting and Height monoplotting) and corresponding Euclidean distance as error value (Delta 3D). In two cases, no coordinates could be determined using monoplotting. Used coordinate system: ETRS89/UTM Zone 32N coordinate system (EPSG code: 25832).

Historical Terrestrial Image	GCP Number	East [m]	North [m]	Height [m]	East Monoplotting [m]	North Monoplotting [m]	Height Monoplotting [m]	Delta 3D [m]
1890	1	632,685.9	5,194,046.4	2153.5	632,683.9	5,194,044.5	2154.1	2.8
	2	633,755.7	5,191,665.6	3034.7	-	-	-	-
	3	633,620.1	5,191,552.4	2981.4	-	-	-	-
	4	633,228.3	5,193,382.3	2312.4	633,167.3	5,193,441.0	2303.8	85.1
	5	634,099.5	5,192,196.0	2682.9	634,097.6	5,192,210.5	2673.2	17.5
	6	632,267.2	5,193,552.0	2160.9	632,266.8	5,193,555.0	2159.9	3.1
	7	632,554.6	5,194,113.3	2096.5	632,567.4	5,194,101.5	2097.8	17.5
	8	633,537.9	5,191,990.8	2606.3	633,541.6	5,191,992.0	2607.1	4.0

Table A3. *Cont.*

Historical Terrestrial Image	GCP Number	East [m]	North [m]	Height [m]	East Monoplotting [m]	North Monoplotting [m]	Height Monoplotting [m]	Delta 3D [m]
	9	632,583.6	5,194,081.1	2104.3	632,588.8	5,194,077.0	2106.9	7.1
	10	631,871.4	5,194,377.8	2176.2	631,870.9	5,194,378.5	2175.4	1.1
	11	631,771.5	5,194,586.7	2221.7	632,450.3	5,194,062.0	2036.3	877.7
	12	633,316.5	5,193,349.7	2371.0	633,286.8	5,193,380.5	2362.6	43.7
	13	635,653.5	5,191,577.7	3079.1	635,650.3	5,191,598.5	3062.5	26.8
1907	1	633,903.8	5,191,802.8	3001.5	633,898.3	5,191,800.5	2996.7	7.7
	2	633,788.7	5,191,703.1	3038.4	633,782.3	5,191,696.0	3033.9	10.6
	3	635,966.8	5,192,804.1	3319.8	635,962.1	5,192,808.0	3308.6	12.8
	4	636,185.9	5,192,836.2	3513.2	636,171.9	5,192,847.5	3495.6	25.1
	5	632,880.3	5,193,919.6	2285.5	632,878.6	5,193,920.0	2283.3	2.8
	6	633,178.7	5,193,634.4	2351.9	633,176.8	5,193,635.5	2350.6	2.6
	7	632,468.7	5,193,780.7	2075.9	632,471.6	5,193,780.0	2078.3	3.8
	8	635,078.2	5,192,954.0	2797.6	635,078.6	5,192,958.5	2795.6	5.0
	9	633,600.1	5,192,238.7	2516.7	633,610.6	5,192,234.0	2524.3	13.8
	10	634,146.5	5,192,466.7	2554.4	634,156.1	5,192,466.0	2559.9	11.1
	11	631,784.8	5,193,797.0	2252.2	631,785.0	5,193,797.0	2252.2	0.2
	12	633,152.3	5,193,425.2	2309.2	633,212.1	5,193,408.5	2314.2	62.3

Table A4. Monoplotting accuracy of ~1930 and ~1940 photos: Coordinates of the user defined GCPs (East, North and Height), by monoplotting calculated GCPs (East monoplotting, North monoplotting and Height monoplotting) and corresponding Euclidean distance as error value (Delta 3D). In two cases, no coordinates could be determined using monoplotting. Used coordinate system: ETRS89/UTM Zone 32N coordinate system (EPSG code: 25832).

Historical Terrestrial Image	GCP Number	East [m]	North [m]	Height [m]	East Monoplotting [m]	North Monoplotting [m]	Height Monoplotting [m]	Delta 3D [m]
~1930	1	632,555.5	5,194,112.2	2096.4	632,552.9	5,194,114.5	2095.2	3.8
	2	632,594.4	5,194,061.4	2108.8	632,594.6	5,194,061.0	2108.8	0.5
	3	633,263.0	5,193,341.0	2327.6	633,252.7	5,193,351.0	2323.6	14.9
	4	632,279.4	5,193,591.3	2136.4	632,279.9	5,193,590.0	2136.4	1.4
	5	633,775.0	5,191,663.0	3040.9	633,772.8	5,191,664.5	3039.1	3.2
	6	632,502.6	5,193,815.5	2074.7	632,501.0	5,193,815.5	2073.4	2.1
	7	632,460.0	5,194,170.6	2072.8	632,460.6	5,194,170.5	2072.6	0.7
	8	636,614.9	5,190,978.5	3546.9	-	-	-	-
	9	632,432.6	5,193,770.2	2050.1	632,432.6	5,193,770.0	2050.3	0.3
	10	633,259.8	5,192,088.3	2412.6	633,251.1	5,192,106.0	2399.5	23.7
	11	633,628.1	5,191,548.1	2986.9	633,625.8	5,191,557.5	2979.1	12.4
	12	633,272.8	5,193,521.1	2400.0	633,272.2	5,193,516.5	2402.6	5.3
	13	633,820.9	5,192,338.5	2502.0	633,804.7	5,192,349.0	2491.6	22.0
~1940	1	632,544.0	5,193,660.3	2126.0	632,542.9	5,193,664.5	2125.4	4.4
	2	633,207.9	5,193,569.0	2363.0	633,207.6	5,193,567.5	2362.8	1.6
	3	636,190.2	5,192,839.9	3516.1	636,189.6	5,192,840.0	3516.8	0.9
	4	633,563.4	5,191,691.1	2790.6	633,563.2	5,191,678.5	2799.6	15.5
	5	632,299.4	5,193,577.7	2142.1	632,298.3	5,193,576.0	2142.4	2.1
	6	633,535.3	5,191,986.0	2607.7	633,533.6	5,191,999.0	2600.8	14.8
	7	633,665.8	5,193,738.3	2565.9	633,663.6	5,193,733.5	2567.9	5.6
	8	633,151.3	5,193,427.7	2309.2	633,147.5	5,193,432.5	2307.7	6.3
	9	633,327.3	5,193,333.1	2382.1	633,325.4	5,193,341.0	2378.7	8.8
	10	632,325.2	5,193,633.5	2105.9	632,325.8	5,193,633.0	2106.0	0.8
	11	633,904.9	5,191,943.1	2873.0	633,907.3	5,191,941.0	2875.3	3.9
	12	632,456.5	5,193,736.9	2073.9	632,456.7	5,193,735.0	2074.4	2.0

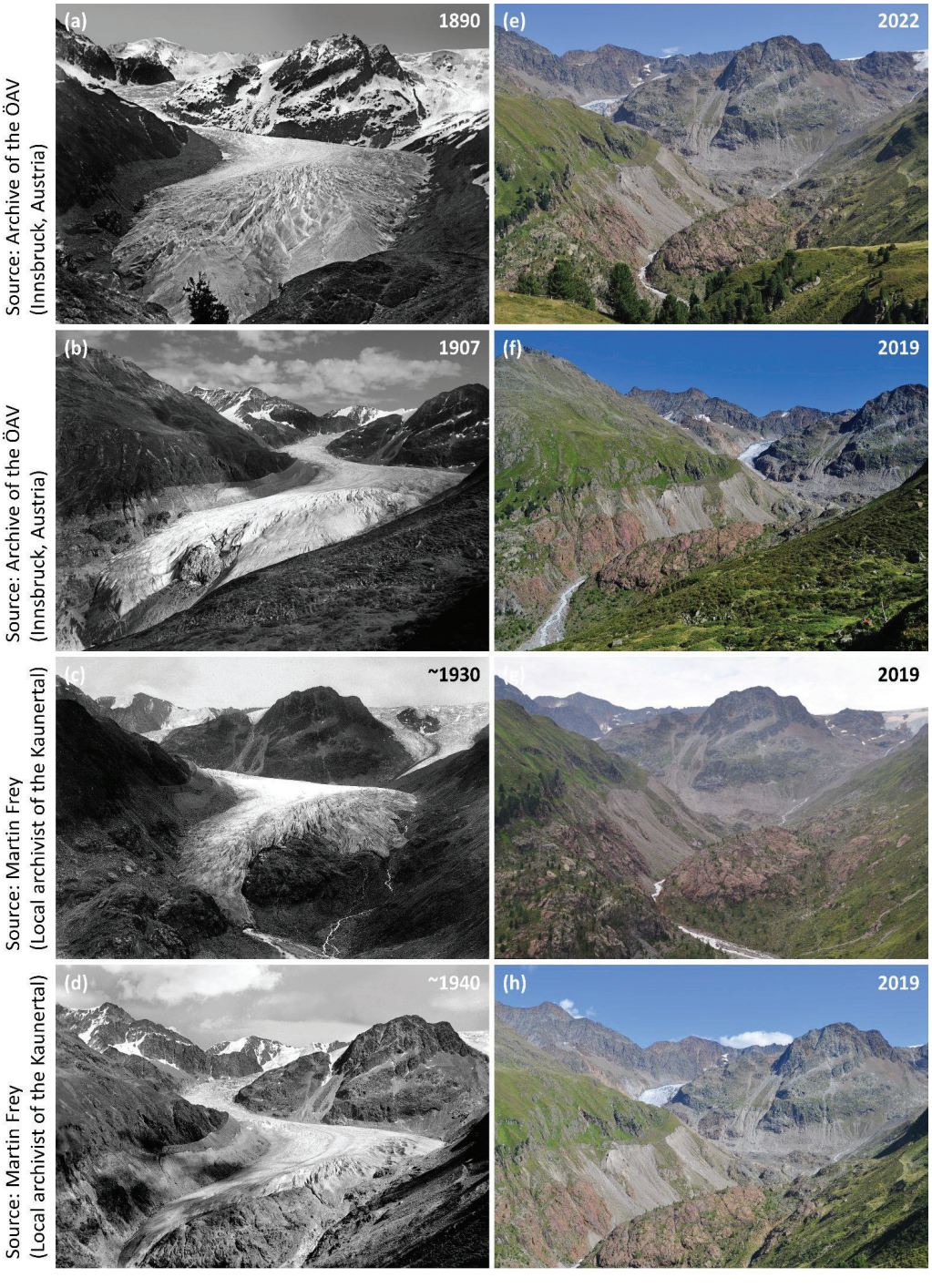


Figure A1. Historical terrestrial photos (**a**–**d**) and the correspondingly reproduced photos from the same location between 2019 and 2022 (**e**–**h**).

Appendix C

Table A5. Summary of the WRF configuration.

Domain Configuration	
Horizontal grid spacing	18-, 6-, 2-km (D1, D2 and D3)
Grid dimensions	190 × 190, 151 × 142, 121 × 139
Lateral boundary condition	variable (20CRv3 at 1° × 1°, 3-h)
Time step	90, 30, 10 s
Vertical levels	50
Model top pressure	10 hPa
Model physics	
Microphysics	Morrison [64]
Cumulus	Kain-Fritsch (none in D3) [65]
Radiation	RRTMG [66]
Planetary boundary layer	Yonsei State University [67]
Atmospheric surface layer	Monin Obukhov [68]
Land surface	Noah [69]
Dynamics	
Top boundary conditions	Rayleigh damping
Diffusion	Calculated in physical space

Appendix D

Table A6. Changes of surface types/morphodynamic area from End of LIA to 2020 with the proportion [%].

Surface Type/Morphodynamic Area	**End of LIA**	**1890**	**1907**	**~1930**	**~1940**	**1953**	**1969**	**1970**
(Initial) Gully system	0	5.13	22.71	23.82	26.82	43.34	43.49	43.61
Geomorphological not active area	0	53.71	28.30	39.12	38.21	56.66	56.51	56.39
Sediment accumulation at the glacier margin	0	0	18.40	23.85	34.97	0	0	0
Glacier	100	41.16	30.59	13.21	0	0	0	0
Surface Type/Morphodynamic Area	**1982**	**1983**	**1990**	**1997**	**2003**	**2010**	**2015**	**2020**
(Initial) Gully system	42.23	44.05	44.62	45.24	45.77	47.04	47.43	47.70
Geomorphological not active area	57.77	59.95	55.38	54.76	54.23	52.96	52.57	52.30
Sediment accumulation at the glacier margin	0	0	0	0	0	0	0	0
Glacier	0	0	0	0	0	0	0	0

Table A7. Changes of land cover types from End of LIA to 2020 with the proportion of each land-cover type in the area of interest (AoI).

Land-Cover Type	1850	1890	1907	~1930	~1940	1953	1970	1983	1990	2003	2010	2020
Glacier	100.0	40.98	31.10	14.02	0.00	0.00	0.00	0.00	0.00	0.00	0.00	0.00
Rock	0.00	0.56	1.42	2.23	4.57	8.98	10.21	11.50	9.62	14.57	12.97	12.74
Scree slope	0.00	46.52	27.79	41.76	55.09	12.19	14.88	22.54	17.46	50.95	51.15	48.14
Scree community	0.00	9.63	26.34	29.45	9.27	26.61	21.79	25.53	21.28	7.42	7.01	9.87
Alpine grassland	0.00	1.70	11.25	7.36	24.45	30.50	30.05	22.30	23.49	10.19	10.64	11.07
Wetland	0.00	0.00	0.20	0.12	0.00	0.42	0.45	0.12	0.00	0.77	0.27	0.27
Dwarf shrub	0.00	0.60	1.91	5.06	6.62	21.16	22.51	17.90	28.11	15.81	17.35	17.31
Shrub	0.00	0.00	0.00	0.00	0.00	0.08	0.07	0.00	0.01	0.25	0.53	0.53
Trees, woodland	0.00	0.00	0.00	0.00	0.00	0.06	0.05	0.11	0.04	0.04	0.08	0.08

Table A8. Changes of land-cover types from End of LIA to 2020 with the proportion [%], on the 1890 initially glaciered area (upper part), on the 1890 initially morphodynamic active area (initial gully system) (middle part), and on the initially more stable (not active) area (lower part).

1890 initially glaciered area											
Land-Cover Type	**1890**	**1907**	**~1930**	**~1940**	**1953**	**1970**	**1983**	**1990**	**2003**	**2010**	**2020**
Glacier	100.0	75.89	34.22	0.00	0.00	0.00	0.00	0.00	0.00	0.00	0.00
Rock	0.00	1.35	4.05	7.72	17.80	20.49	24.51	21.26	26.26	24.07	24.03
Scree slope	0.00	20.27	60.34	82.70	14.66	15.93	23.05	19.11	57.55	56.60	50.55
Scree community	0.00	1.63	1.39	2.01	27.38	27.99	31.19	30.95	8.74	5.76	11.49
Alpine grassland	0.00	0.86	0.00	7.57	23.59	18.22	11.13	17.37	3.44	5.92	6.36
Wetland	0.00	0.00	0.00	0.00	0.00	0.00	0.00	0.00	0.00	0.00	0.00
Dwarf shrub	0.00	0.00	0.00	0.00	16.57	17.37	10.04	11.31	4.00	7.51	7.44
Shrub	0.00	0.00	0.00	0.00	0.01	0.00	0.00	0.00	0.00	0.08	0.08
Trees, woodland	0.00	0.00	0.00	0.00	0.00	0.00	0.07	0.00	0.01	0.06	0.06
1890 initially morphodynamic active area (initial gully system)											
Land-Cover Type	**1890**	**1907**	**~1930**	**~1940**	**1953**	**1970**	**1983**	**1990**	**2003**	**2010**	**2020**
Glacier	0.00	0.00	0.00	0.00	0.00	0.00	0.00	0.00	0.00	0.00	0.00
Rock	0.00	0.34	0.48	0.65	0.53	1.98	10.63	3.26	16.94	12.84	12.64
Scree slope	100.0	58.84	63.42	59.37	10.62	19.24	48.83	35.21	60.54	62.35	57.19
Scree community	0.00	32.06	21.04	5.80	23.85	13.52	8.69	20.34	2.57	5.18	10.11
Alpine grassland	0.00	3.85	11.89	32.41	39.23	31.98	13.89	17.33	7.39	5.98	6.57
Wetland	0.00	0.00	0.00	0.00	0.00	0.00	0.00	0.00	0.00	0.00	0.00
Dwarf shrub	0.00	4.91	3.18	1.78	25.50	33.12	22.95	23.86	11.65	12.91	12.75
Shrub	0.00	0.00	0.00	0.00	0.22	0.15	0.00	0.00	0.91	0.74	0.74
Trees, woodland	0.00	0.00	0.00	0.00	0.06	0.00	0.00	0.00	0.00	0.00	0.00

Table A8. *Cont.*

1890 initially more stable (not active) area											
Land-Cover Type	**1890**	**1907**	**~1930**	**~1940**	**1953**	**1970**	**1983**	**1990**	**2003**	**2010**	**2020**
Glacier	0.00	0.00	0.00	0.00	0.00	0.00	0.00	0.00	0.00	0.00	0.00
Rock	1.05	1.58	1.02	2.57	3.10	3.20	1.65	1.39	5.42	4.49	4.10
Scree slope	76.70	30.36	25.35	33.54	10.48	13.67	20.02	14.42	45.01	45.96	45.47
Scree community	17.95	44.72	51.75	15.17	26.27	17.86	22.84	13.97	6.90	8.16	8.61
Alpine grassland	3.18	19.92	12.54	36.56	34.95	38.89	31.81	28.85	15.57	14.71	15.13
Wetland	0.00	0.37	0.22	0.00	0.79	0.85	0.22	0.00	1.42	0.49	0.49
Dwarf shrub	1.12	3.04	9.12	12.16	24.20	25.34	23.31	41.28	25.23	25.23	25.23
Shrub	0.00	0.00	0.00	0.00	0.12	0.12	0.00	0.02	0.37	0.86	0.86
Trees, woodland	0.00	0.00	0.00	0.00	0.10	0.08	0.15	0.07	0.07	0.11	0.11

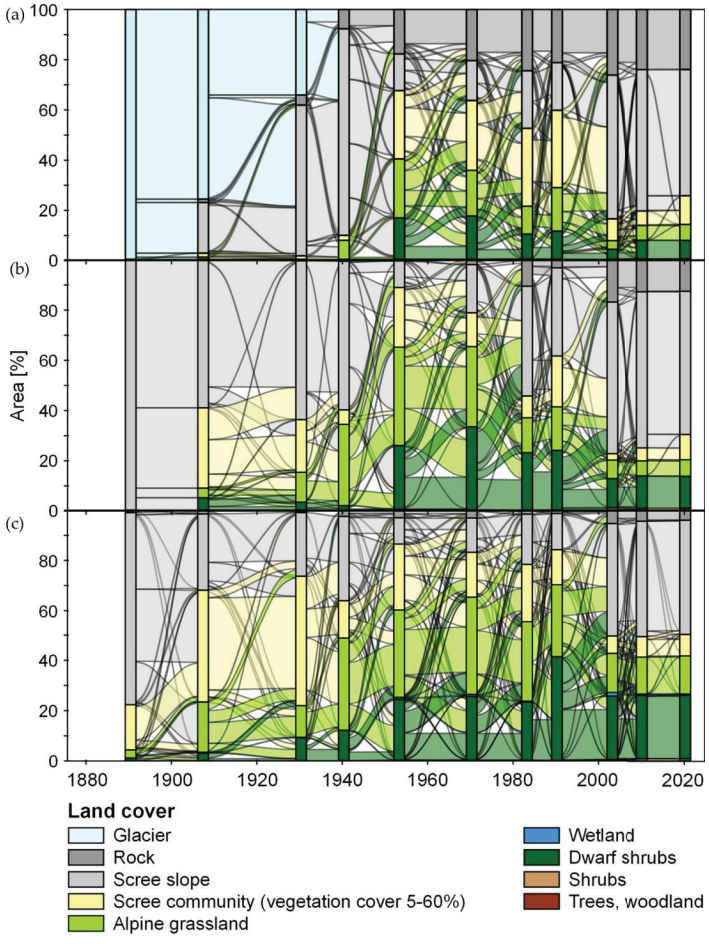


Figure A2. Changes of the land-cover types on in 1890 (**a**) initial glaciated area, (**b**) the initial active area (initial gully system), and (**c**) the initial more stable (not active) area; the different colours indicate the different land-cover types.

Appendix E

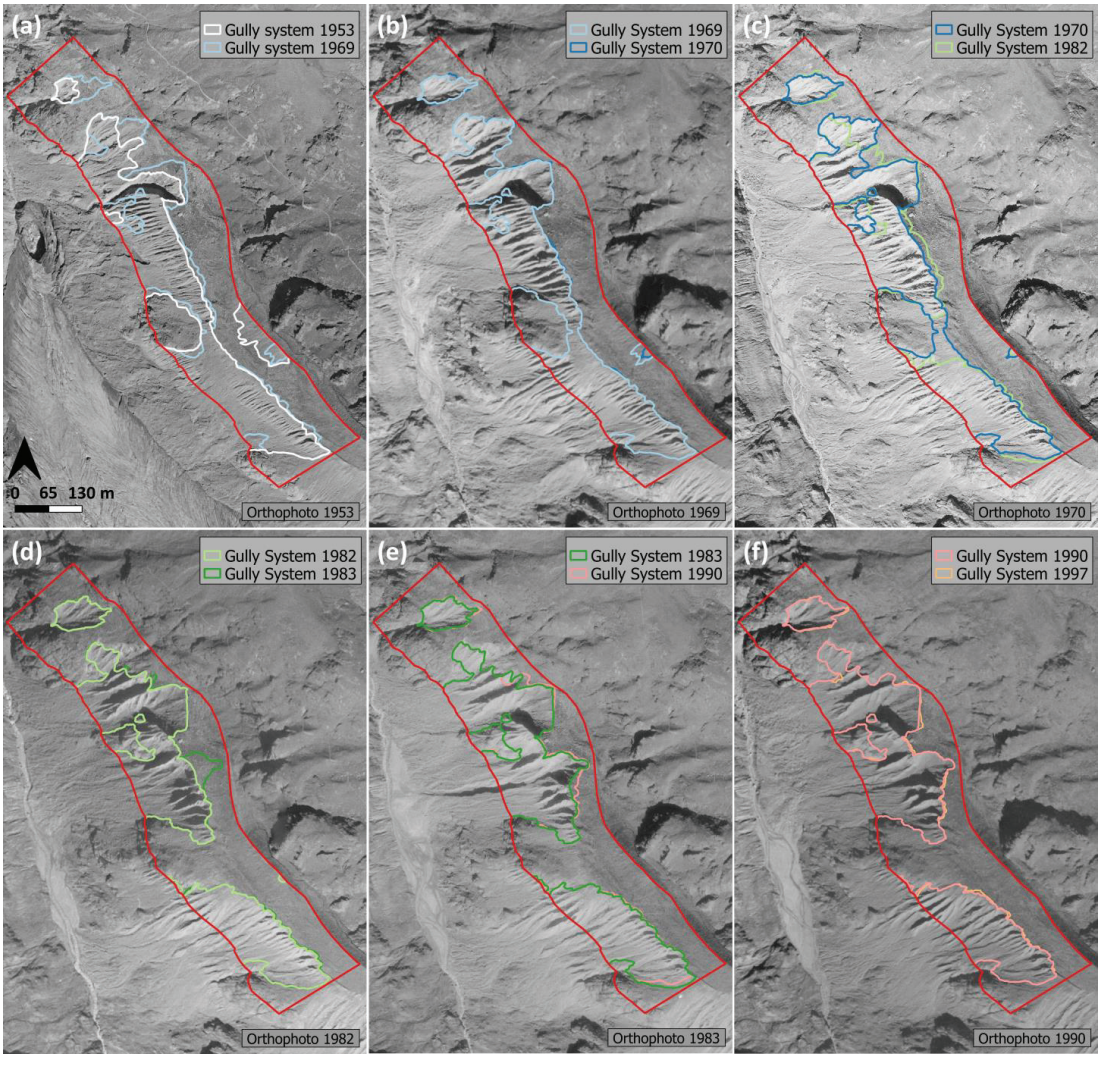


Figure A3. Continued mapping of the different surface types (morphodynamic mapping) using georeferenced orthophotos based on overlapping area-wide aerial photographs from 1953 to 1990 (**a**–**f**). The red line indicates the area of interest.

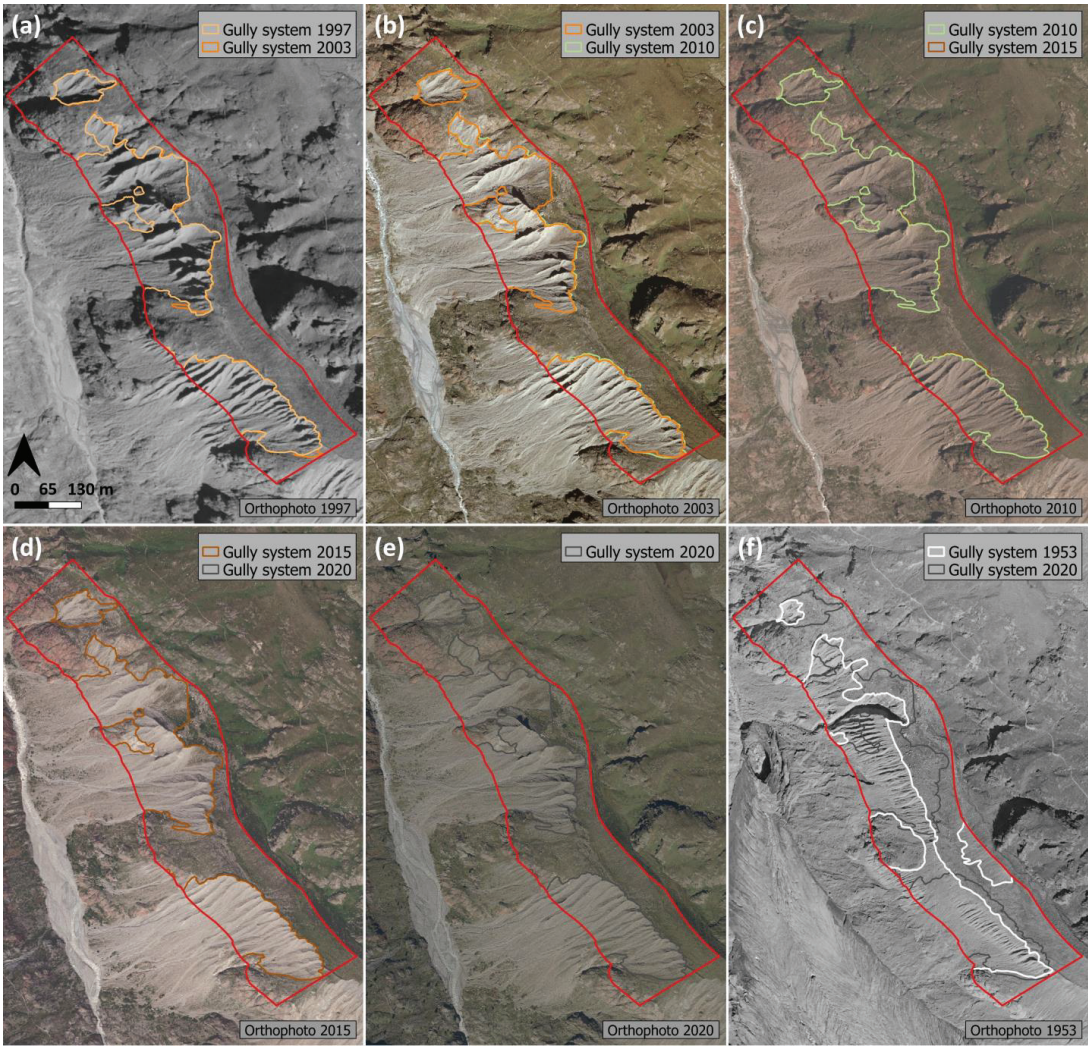


Figure A4. Continued mapping of the different surface types (morphodynamic mapping) using georeferenced orthophotos based on overlapping area-wide aerial photographs from 1997 to 2020 (**a**–**f**). The red line indicates the area of interest.

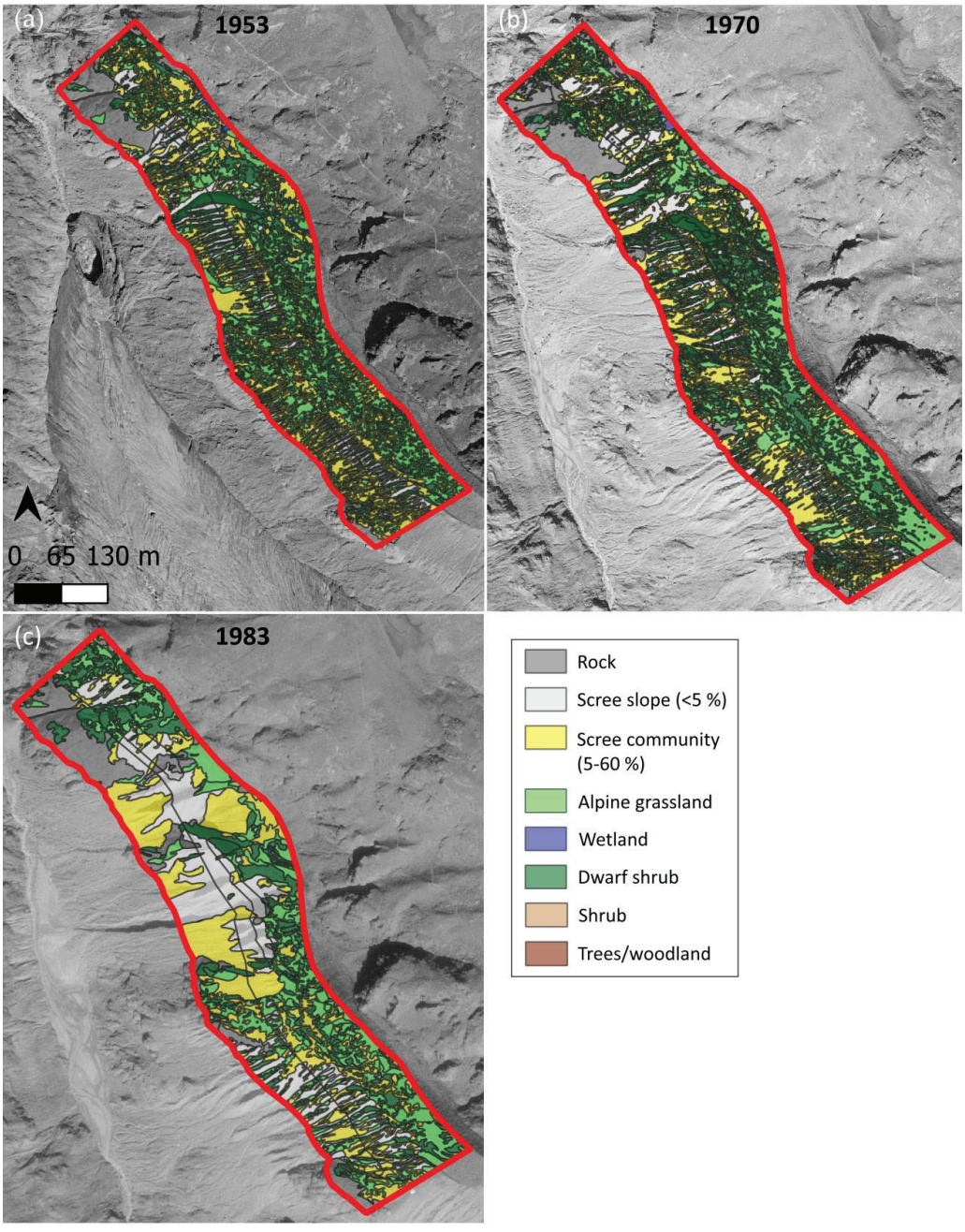


Figure A5. Continued mapping of the different surface types (land-cover mapping) using georeferenced orthophotos based on overlapping area-wide aerial photographs from 1953 to 1983 (**a**–**c**). The red line indicates area of interest (AoI).

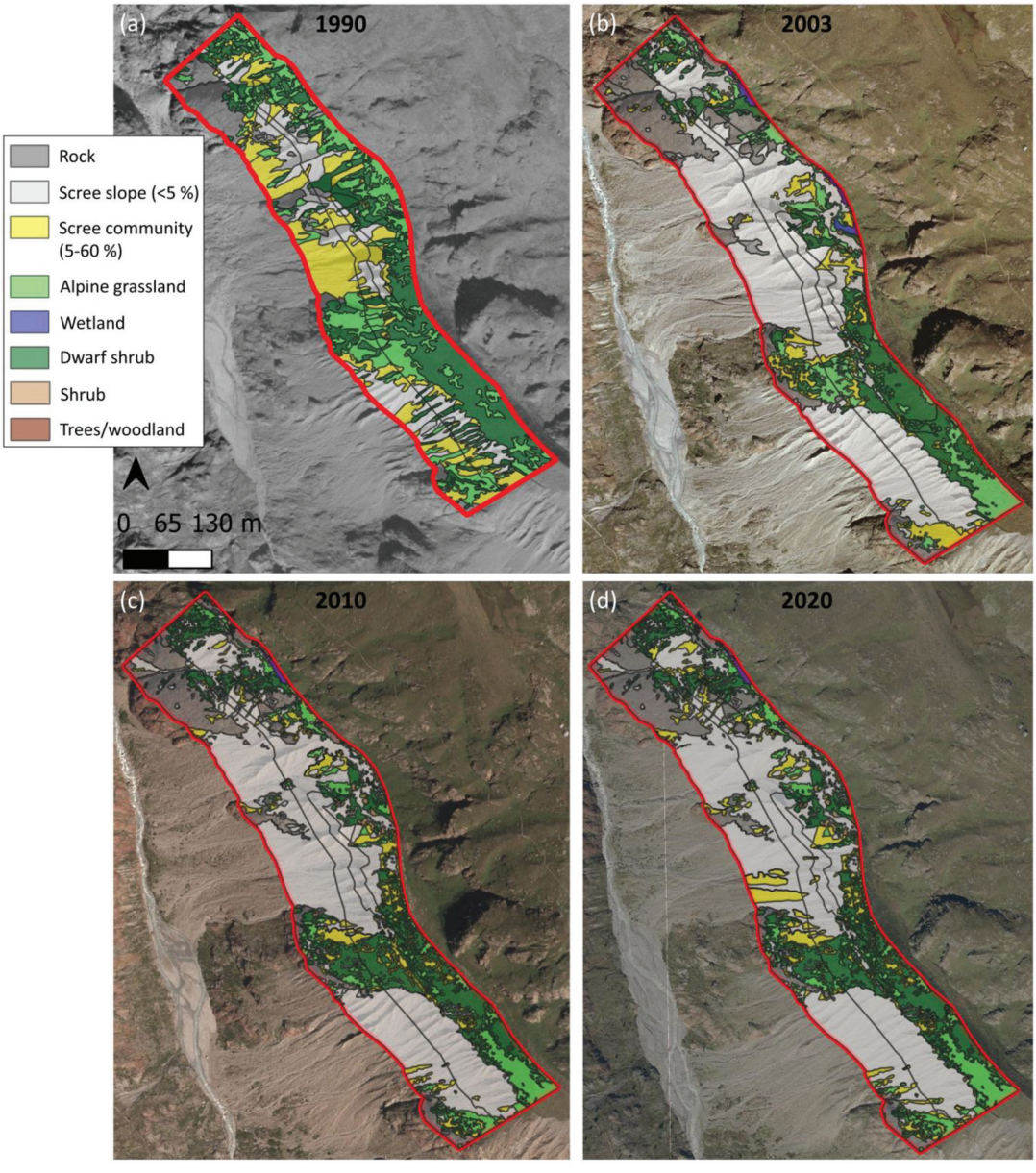


Figure A6. Continued mapping of the different surface types (land-cover mapping) using georeferenced orthophotos based on overlapping area-wide aerial photographs from 1990 to 2020 (**a**–**d**). The red line indicates the area of interest.

References

1. Heckmann, T.; Morche, D. *Geomorphology of Proglacial Systems: Landform and Sediment Dynamics in Recently Deglaciated Alpine Landscapes*; Springer: Cham, Switzerland, 2019; ISBN 9783319941820.
2. Hock, R.; Rasul, G.; Adler, C.; Cáceres, B.; Gruber, S.; Hirabayashi, Y.; Jackson, M.; Kääb, A.; Kang, S.; Kutuzov, S.; et al. High Mountain Areas. In *IPCC Special Report on the Ocean and Cryosphere in a Changing Climate*; Pörtner, H.-O., Roberts, D.C., Masson-Delmotte, V., Zhai, P., Tignor, M., Poloczanska, E., Mintenbeck, K., Alegría, A., Nicolai, M., Okem, A., et al., Eds.; Cambridge University Press: Cambridge, UK; New York, NY, USA, 2019; pp. 131–202. [CrossRef]
3. Deline, P.; Gruber, S.; Delaloye, R.; Fischer, L.; Geertsema, M.; Giardino, M.; Hasler, A.; Kirkbride, M.; Krautblatter, M.; Magnin, F.; et al. Chapter 15—Ice Loss and Slope Stability in High-Mountain Regions. In *Snow and Ice-Related Hazards, Risks, and Disasters*; Haeberli, W., Whiteman, C., Shroder, J.F., Eds.; Academic Press: Cambridge, MA, USA, 2015; pp. 521–561. [CrossRef]
4. Altmann, M.; Piermattei, L.; Haas, F.; Heckmann, T.; Fleischer, F.; Rom, J.; Betz-Nutz, S.; Knoflach, B.; Müller, S.; Ramskogler, K.; et al. Long-Term Changes of Morphodynamics on Little Ice Age Lateral Moraines and the Resulting Sediment Transfer into Mountain Streams in the Upper Kauner Valley, Austria. *Water* **2020**, *12*, 3375. [CrossRef]
5. Betz-Nutz, S.; Heckmann, T.; Haas, F.; Becht, M. Development of the morphodynamics on LIA lateral moraines in ten glacier forefields of the Eastern Alps since the 1950s. *Earth Surf. Dynam. Discuss.* 2022; *in review*. [CrossRef]
6. Altmann, M.; Pfeiffer, M.; Haas, F.; Rom, J.; Fleischer, F.; Heckmann, T.; Piermattei, L.; Wimmer, M.; Braun, L.; Stark, M.; et al. Long-term monitoring (1953–2019) of geomorphologically active sections on LIA lateral moraines under changing meteorological conditions. *EGUsphere* **2023**. [CrossRef]
7. Ballantyne, C.K. A general model of paraglacial landscape response. *Holocene* **2002**, *12*, 371–376. [CrossRef]
8. Ballantyne, C.K. Paraglacial geomorphology. *Quat. Sci. Rev.* **2002**, *21*, 1935–2017. [CrossRef]
9. Curry, A.M.; Cleasby, V.; Zukowskyj, P. Paraglacial response of steep, sediment-mantled slopes to post-'Little Ice Age' glacier recession in the central Swiss Alps. *J. Quat. Sci.* **2006**, *21*, 211–225. [CrossRef]
10. Ballantyne, C.K.; Benn, D.I. Paraglacial Slope Adjustment and Resedlmenfation following Recent Glacier Retreat, Fåbergstølsdalen, Norway. *Arct. Alp. Res.* **1994**, *26*, 255–269. [CrossRef]
11. Ballantyne, C.K.; Benn, D.I. Paraglacial slope adjustment during recent deglaciation and its implications for slope evolution in formerly glaciated environments. In *Advances in Hillslope Processes*; Anderson, M.G., Brooks, S.M., Eds.; Wiley: Chichester, UK, 1996; Volume 2, pp. 1173–1195.
12. Curry, A.M.; Ballantyne, C.K. Paraglacial modification of glacigenic sediment. *Geogr. Ann. Ser. A Phys. Geogr.* **1999**, *81*, 409–419. [CrossRef]
13. Eichel, J.; Corenblit, D.; Dikau, R. Conditions for feedbacks between geomorphic and vegetation dynamics on lateral moraine slopes: A biogeomorphic feedback window. *Earth Surf. Process. Landf.* **2016**, *41*, 406–419. [CrossRef]
14. Eichel, J.; Draebing, D.; Meyer, N. From active to stable: Paraglacial transition of Alpine lateral moraine slopes. *Land Degrad. Dev.* **2018**, *29*, 4158–4172. [CrossRef]
15. Gurnell, A.M.; Corenblit, D.; García de Jalón, D.; Del González Tánago, M.; Grabowski, R.C.; O'Hare, M.T.; Szewczyk, M. A Conceptual Model of Vegetation-hydrogeomorphology Interactions Within River Corridors. *River Res. Appl.* **2016**, *32*, 142–163. [CrossRef]
16. Haselberger, S.; Ohler, L.-M.; Junker, R.R.; Otto, J.-C.; Glade, T.; Kraushaar, S. Quantification of biogeomorphic interactions between small-scale sediment transport and primary vegetation succession on proglacial slopes of the Gepatschferner, Austria. *Earth Surf. Process. Landf.* **2021**, *46*, 1941–1952. [CrossRef]
17. Knoflach, B.; Ramskogler, K.; Talluto, M.; Hofmeister, F.; Haas, F.; Heckmann, T.; Pfeiffer, M.; Piermattei, L.; Ressl, C.; Wimmer, M.H.; et al. Modelling of Vegetation Dynamics from Satellite Time Series to Determine Proglacial Primary Succession in the Course of Global Warming—A Case Study in the Upper Martell Valley (Eastern Italian Alps). *Remote Sens.* **2021**, *13*, 4450. [CrossRef]
18. Hohensinner, S.; Atzler, U.; Fischer, A.; Schwaizer, G.; Helfricht, K. Tracing the Long-Term Evolution of Land Cover in an Alpine Valley 1820–2015 in the Light of Climate, Glacier and Land Use Changes. *Front. Environ. Sci.* **2021**, *9*, 683397. [CrossRef]
19. Schiefer, E.; Gilbert, R. Reconstructing morphometric change in a proglacial landscape using historical aerial photography and automated DEM generation. *Geomorphology* **2007**, *88*, 167–178. [CrossRef]
20. Piermattei, L.; Heckmann, T.; Betz-Nutz, S.; Altmann, M.; Rom, J.; Fleischer, F.; Stark, M.; Haas, F.; Ressl, C.; Wimmer, M.; et al. Evolution of an Alpine proglacial river during seven decades of deglaciation quantified from photogrammetric and LiDAR digital elevation models. *Earth Surf. Dynam. Discuss.* **2022**. [CrossRef]
21. Bozzini, C.; Conedera, M.; Krebs, P. A new tool for obtaining cartographic georeferenced data from single oblique photos. In Proceedings of the XXIIIrd International CIPA Symposium, Prague, Czech Republic, 12–16 September 2011.
22. Bozzini, C.; Conedera, M.; Krebs, P. A New Monoplotting Tool to Extract Georeferenced Vector Data and Orthorectified Raster Data from Oblique Non-Metric Photographs. *Int. J. Herit. Digit. Era* **2012**, *1*, 499–518. [CrossRef]
23. Stockdale, C.-A.; Bozzini, C.; Macdonald, S.-E.; Higgs, E. Extracting ecological information from oblique angle terrestrial landscape photographs: Performance evaluation of the WSL Monoplotting Tool. *Appl. Geogr.* **2015**, *63*, 315–325. [CrossRef]
24. Stockdale, C.A.; McLoughlin, N.; Flannigan, M.; Macdonald, S.E. Could restoration of a landscape to a pre-European historical vegetation condition reduce burn probability? *Ecosphere* **2019**, *10*, e02584. [CrossRef]
25. McCaffrey, D.R.; Hopkinson, C. Assessing Fractional Cover in the Alpine Treeline Ecotone Using the WSL Monoplotting Tool and Airborne Lidar. *Can. J. Remote Sens.* **2017**, *43*, 504–512. [CrossRef]

26. McCaffrey, D.; Hopkinson, C. Repeat Oblique Photography Shows Terrain and Fire-Exposure Controls on Century-Scale Canopy Cover Change in the Alpine Treeline Ecotone. *Remote Sens.* **2020**, *12*, 1569. [CrossRef]
27. Gabellieri, N.; Watkins, C. Measuring long-term landscape change using historical photographs and the WSL Monoplotting Tool. *Landsc. Hist.* **2019**, *40*, 93–109. [CrossRef]
28. Bayr, U. Quantifying historical landscape change with repeat photography: An accuracy assessment of geospatial data obtained through monoplotting. *Int. J. Geogr. Inf. Sci.* **2021**, *35*, 2026–2046. [CrossRef]
29. Conedera, M.; Bozzini, C.; Scapozza, C.; Rè, L.; Ryter, U.; Krebs, P. Anwendungspotenzial des WSL-Monoplotting-Tools im Naturgefahrenmanagement. *Schweiz. Z. Forstwes.* **2013**, *164*, 173–180. [CrossRef]
30. Conedera, M.; Bozzini, C.; Ryter, U.; Bertschinger, T.; Krebs, P. Using the Monoplotting Technique for Documenting and Analyzing Natural Hazard Events. In *Natural Hazards—Risk Assessment and Vulnerability Reduction*; Carmo, J.S.A.d., Ed.; IntechOpen: London, UK, 2018; pp. 107–123. ISBN 978-1-78984-820-5.
31. Wiesmann, S.; Steiner, L.; Pozzi, M.; Bozzini, C.; Bauder, A.; Hurni, L. Reconstructing historic glacier states based on terrestrial oblique photographs. In Proceedings of the AutoCarto International Symposium on Automated Cartography, Columbus, OH, USA, 16–18 September 2012.
32. Scapozza, C.; Lambiel, C.; Bozzini, C.; Mari, S.; Conedera, M. Assessing the rock glacier kinematics on three different timescales: A case study from the southern Swiss Alps. *Earth Surf. Process. Landf.* **2014**, *39*, 2056–2069. [CrossRef]
33. Tollmann, A. *Geologie von Österreich: Die Zentralalpen*; Deuticke: Wien, Austria, 1977.
34. Hoinkes, G.; Thöni, M. Evolution of the Ötztal-Stubai, Scarl-Campo and Ulten Basement Units. In *Pre-Mesozoic Geology in the Alps*; Von Raumer, J.F., Neubauer, F., Eds.; Springer: Berlin/Heidelberg, Germany, 1993. [CrossRef]
35. Vehling, L. Gravitative Massenbewegungen an alpinen Felshängen: Quantitative Bedeutung in der Sedimentkaskade proglazialer Geosysteme (Kaunertal, Tirol). Doctoral Thesis, Friedrich-Alexander-Universität Erlangen-Nürnberg, Erlangen, Germany, 2016.
36. Fliri, F. *Klima der Alpen im Raume von Tirol: Monographien zur Landeskunde Tirol, Folge 1*; Univ. Verl. Wagner: Innsbruck, Austria, 1975.
37. Hilger, L. Quantification and Regionalization of Geomorphic Processes Using Spatial Models and High-Resolution Topographic Data: A Sediment Budget of the Upper Kauner Valley, Ötztal Alps. Doctoral Thesis, Catholic University of Eichstätt-Ingolstadt, Eichstätt, Germany, 2017.
38. Nicolussi, K.; Patzelt, G. Untersuchungen zur holozänen Gletscherentwicklung von Pasterze und Gepatschferner (Ostalpen). *Z. Gletsch. Glazialgeol.* **2001**, *36*, 1–88.
39. Pepin, N.C.; Arnone, E.; Gobiet, A.; Haslinger, K.; Kotlarski, S.; Notarnicola, C.; Palazzi, E.; Seibert, P.; Serafin, S.; Schöner, W.; et al. Climate Changes and Their Elevational Patterns in the Mountains of the World. *Rev. Geophys.* **2022**, *60*, e2020RG000730. [CrossRef]
40. Groß, G.; Patzelt, G. The Austrian Glacier Inventory for the Little Ice Age Maximum (GI LIA) in ArcGIS (shapefile) format. *PANGAEA* **2015**. [CrossRef]
41. Buckel, J.; Otto, J.-C. The Austrian Glacier Inventory GI 4 (2015) in ArcGis (shapefile) format, supplement to: Buckel, Johannes; Otto, Jan-Christoph; Prasicek, Günther; Keuschnig, Markus (2018): Glacial lakes in Austria—Distribution and formation since the Little Ice Age. *Glob. Planet. Chang.* **2018**, *164*, 39–51. [CrossRef]
42. Copernicus. Hillshade Derived from EU-DEM Version 1.0. Available online: https://land.copernicus.eu/imagery-in-situ/eu-dem/eu-dem-v1-0-and-derived-products/hillshade?tab=metadata (accessed on 3 June 2021).
43. Flöry, S.; Ressl, C.; Puercher, G.; Pfeifer, N.; Hollaus, M.; Bayr, A.; Karel, W. Development of a 3D Viewer for georeferencing and monoplotting of historical terrestrial images. *EGU Gen. Assem. Conf. Abstr.* **2020**, 22327. [CrossRef]
44. Kraus, K. *Photogrammetrie: Geometrische Informationen aus Photographien und Laserscanneraufnahmen*; Walter de Gruyter: Berlin, Germany, 2012.
45. Karel, W.; Doneus, M.; Verhoeve, G.; Bries, C.; Ressl, C.; Pfeifer, N. OrientAL—Automatic geo-referencing and otho-rectification of archaeological aerial photographs. ISPRS Ann. Photogramm. Remote Sens. *Spat. Inf. Sci.* **2013**, *II-5/W1*, 175–180. [CrossRef]
46. Stark, M.; Rom, J.; Haas, F.; Piermattei, L.; Fleischer, F.; Altmann, M.; Becht, M. Long-term assessment of terrain changes and calculation of erosion rates in an alpine catchment based on SfM-MVS processing of historical aerial images. How camera information and processing strategy affect quantitative analysis. *J. Geomorphol.* **2022**. [CrossRef]
47. Rom, J.; Haas, F.; Heckmann, T.; Altmann, M.; Fleischer, F.; Ressl, C.; Betz-Nutz, S.; Becht, M. Spatio-temporal analysis of slope-type debris flow activity in Horlachtal, Austria, based on orthophotos and lidar data since 1947. *Nat. Hazards Earth Syst. Sci.* **2023**, *23*, 601–622. [CrossRef]
48. QGIS Development Team. *QGIS Geographic Information System*; Open Source Geospatial Foundation: Chicago, IL, USA, 2020; Available online: http://qgis.orgeo.org (accessed on 13 October 2019).
49. R Core Team. *R: A Language and Environment for Statistical Computing*; R Foundation for Statistical Computing: Vienna, Austria, 2020.
50. Wickham, H.; Averick, M.; Bryan, J.; Chang, W.; McGowan, L.; François, R.; Grolemund, G.; Hayes, A.; Henry, L.; Hester, J.; et al. Welcome to the tidyverse. *J. Open Source Softw.* **2019**, *4*, 1686. [CrossRef]
51. Hijmans, R.J.; Etten, J.v. Raster: Geographic Analysis and Modeling with Raster Data: R Package Version 2.0-12. 2012. Available online: http://CRAN.R-project.org/package=raster (accessed on 5 September 2022).
52. Brunson, J.C. ggalluvial: Layered Grammar for Alluvial Plots. *J. Open Source Softw.* **2020**, *5*, 2017. [CrossRef]

53. Brunson, J.C.; Read, Q.D. ggalluvial: Alluvial Plots in 'ggplot2'. R Package Version 0.12.3: Ggalluvial (Brunson JC, Read QD (2020). "ggalluvial: Alluvial Plots in 'ggplot2'." R Package Version 0.12.3. 2020. Available online: http://corybrunson.github.io/ggalluvial/ (accessed on 10 January 2023).
54. Skamarock, W.C.; Klemp, J.B. A time-split nonhydrostatic atmospheric model for weather research and forecasting applications. *J. Comput. Phys.* **2008**, *227*, 3465–3485. [CrossRef]
55. Compo, G.P.; Whitaker, J.S.; Sardeshmukh, P.D.; Matsui, N.; Allan, R.J.; Yin, X.; Gleason, B.E.; Vose, R.S.; Rutledge, G.; Bessemoulin, P.; et al. The Twentieth Century Reanalysis Project. *Q. J. R. Meteorol. Soc.* **2011**, *137*, 1–28. [CrossRef]
56. Giese, B.S.; Seidel, H.F.; Compo, G.P.; Sardeshmukh, P.D. An ensemble of ocean reanalyses for 1815–2013 with sparse observational input. *J. Geophys. Res. Ocean.* **2016**, *121*, 6891–6910. [CrossRef]
57. Slivinski, L.C.; Compo, G.P.; Whitaker, J.S.; Sardeshmukh, P.D.; Giese, B.S.; McColl, C.; Allan, R.; Yin, X.; Vose, R.; Titchner, H.; et al. Towards a more reliable historical reanalysis: Improvements for version 3 of the Twentieth Century Reanalysis system. *Q. J. R. Meteorol. Soc.* **2019**, *145*, 2876–2908. [CrossRef]
58. Collier, E.; Mölg, T. BAYWRF: A high-resolution present-day climatological atmospheric dataset for Bavaria. *Earth Syst. Sci. Data* **2020**, *12*, 3097–3112. [CrossRef]
59. Collier, E.; Sauter, T.; Mölg, T.; Hardy, D. The Influence of Tropical Cyclones on Circulation, Moisture Transport, and Snow Accumulation at Kilimanjaro During the 2006–2007 Season. *J. Geophys. Res. Atmos.* **2019**, *124*, 6919–6928. [CrossRef]
60. Hersbach, H.; Bell, B.; Berrisford, P.; Biavati, G.; Horányi, A.; Muñoz Sabater, J.; Nicolas, J.; Peubey, C.; Radu, R.; Rozum, I.; et al. ERA5 Hourly Data on Single Levels from 1979 to Present: Copernicus Climate Change Service (C3S) Climate Data Store (CDS). Available online: https://cds.climate.copernicus.eu/cdsapp#!/dataset/reanalysis-era5-single-levels?tab=overview (accessed on 13 October 2019).
61. Cribari-Neto, F.; Zeileis, A. Betaregression in R. *J. Stat. Softw.* **2010**, *34*, 1–24. [CrossRef]
62. Smithson, M.; Verkuilen, J. A better lemon squeezer? Maximum-likelihood regression with beta-distributed dependent variables. *Psychol. Methods* **2006**, *11*, 54–71. [CrossRef] [PubMed]
63. Stäuble, S.; Martin, S.; Reynard, E. Historical mapping for landscape reconstruction. Examples from the Canton of Valais (Switzerland). In Proceedings of the 6th ICA Mountain Cartography Workshop Mountain Mapping and Visualisation, Lenk, Switzerland, 11–15 February 2008; pp. 207–211.
64. Morrison, H.; Thompson, G.; Tatarskii, V. Impact of Cloud Microphysics on the Development of Trailing Stratiform Precipitation in a Simulated Squall Line: Comparison of One- and Two-Moment Schemes. *Mon. Wea. Rev.* **2009**, *137*, 991–1007. [CrossRef]
65. Kain, J.S. The Kain–Fritsch Convective Parameterization: An Update. *J. Appl. Meteorol. Climatol.* **2004**, *43*, 170–181. [CrossRef]
66. Iacono, M.J.; Delamere, J.S.; Mlawer, E.J.; Shephard, M.W.; Clough, S.A.; Collins, W.D. Radiative forcing by long-lived greenhouse gases: Calculations with the AER radiative transfer models. *J. Geophys. Res.* **2008**, *113*, 1–8. [CrossRef]
67. Hong, S.Y.; Noh, Y.; Dudhia, J. A new vertical diffusion package with an explicit treatment of entrainment processes. *Mon. Weather Rev.* **2006**, *134*, 2318–2341. [CrossRef]
68. Jiménez, P.A.; Dudhia, J.; González-Rouco, J.F.; Navarro, J.; Montávez, J.P.; García-Bustamante, E. A Revised Scheme for the WRF Surface Layer Formulation. *Mon. Wea. Rev.* **2012**, *140*, 898–918. [CrossRef]
69. Chen, F.; Dudhia, J. Coupling an Advanced Land Surface–Hydrology Model with the Penn State–NCAR MM5 Modeling System. Part II: Preliminary model validation. *Mon. Wea. Rev.* **2001**, *129*, 569–585. [CrossRef]

Disclaimer/Publisher's Note: The statements, opinions and data contained in all publications are solely those of the individual author(s) and contributor(s) and not of MDPI and/or the editor(s). MDPI and/or the editor(s) disclaim responsibility for any injury to people or property resulting from any ideas, methods, instructions or products referred to in the content.

remote sensing

MDPI

Article

A Standardized Procedure to Build a Spectral Library for Hazardous Chemicals Mixed in River Flow Using Hyperspectral Image

Yeonghwa Gwon [1], Dongsu Kim [1,*], Hojun You [2], Su-Han Nam [3] and Young Do Kim [3]

[1] Department of Civil & Environmental Engineering, Dankook University, Yongin-si 16890, Geyonggi-do, Republic of Korea
[2] K-water Institute, Daejeon-si 34045, South Chungcheong, Republic of Korea
[3] Department of Civil & Environmental Engineering, Myongji University, Yongin-si 17058, Geyonggi-do, Republic of Korea
* Correspondence: dongsu-kim@dankook.ac.kr; Tel.: +82-31-8005-3611

Abstract: The occurrence of natural disasters as a consequence of accidental hazardous chemical spills remains a concern. The inadequate, or delayed, initial response may fail to mitigate their impact; hence, imminent monitoring of responses in the initial stage is critical. Classical contact-type measurement methods, however, sometimes miss solvent chemicals and invoke risks for operators during field operation. Remote sensing methods are an alternative method as non-contact, spatially distributable, efficient and continuously operatable features. Herein, we tackle challenges posed by the increasingly available UAV-based hyperspect ral images in riverine environments to identify the presence of hazardous chemical solvents in rivers, which are less investigated in the absence of direct measurement strategies. We propose a referable standard procedure for a unique spectral library based on pre-scanning hyperspectral sensors with respect to representative hazardous chemicals registered on the national hazardous chemical list. We utilized the hyperspectral images to identify 18 types of hazardous chemicals injected into the river in an outdoor environment, where a dedicated hyperspectral ground imaging system mounted with a hyperspectral camera was designed and applied. Finally, we tested the efficiency of the library to recognize unknown chemicals, which showed >70% success rate.

Keywords: hyperspectral; hazardous chemicals; spectral library; chemical accident; recognition test

Citation: Gwon, Y.; Kim, D.; You, H.; Nam, S.-H.; Kim, Y.D. A Standardized Procedure to Build a Spectral Library for Hazardous Chemicals Mixed in River Flow Using Hyperspectral Image. *Remote Sens.* **2023**, *15*, 477. https://doi.org/10.3390/rs15020477

Academic Editor: Paul Scheunders

Received: 3 October 2022
Revised: 4 January 2023
Accepted: 5 January 2023
Published: 13 January 2023

Copyright: © 2023 by the authors. Licensee MDPI, Basel, Switzerland. This article is an open access article distributed under the terms and conditions of the Creative Commons Attribution (CC BY) license (https://creativecommons.org/licenses/by/4.0/).

1. Introduction

There are increasing social concerns regarding water pollution and natural disaster attributed to hazardous chemicals spills. With industrialization, accidental hazardous chemical spills in riverine environments occur more frequently, which has adverse effects on humans and the ecological environment [1]. The inadequate or delayed initial response may lead to serious environmental disasters and fail to mitigate their impact; thus, appropriate actions and responses in the initial stages are critical. However, the leakage of chemicals into rivers is particularly challenging to detect as they are mostly transparent solvents. For example, when transparent sodium hypochlorite was leaked after an accidental damage to a storage tank filled with a detergent on 11 May 2018, the leaked chemical flowed into Gam stream and caused significant harm to aquatic life, such as fish [2]. Local authorities were able to recognize the type of chemical and its leaked location by indirectly tracking a fire in a nearby factory. No detecting protocol worked, while the chemical was never detected in the middle of the spilling accident. The imminent sensing of solvent chemical leaked in the river has been difficult to perform since identifying the chemical occurred only after detecting the certain suspicious spill in rivers where "direct" and "contact" in-situ detectors were conventionally applied as subsequent sensing devices, such as pH

paper, simple identification and detection kits or detector tube devices, as well as electronic detectors, such as a portable ion spectrometer or portable Fourier transform infrared (FT-IR) spectroscope. These contact-type measurement methods, however, may not be able to detect the presence of chemicals due to sensor's local positioning and contact nature when spilled chemicals are disseminated spatially biased on opposite sides of a river cross-section. Also, this type of direct sensing invokes risks for field operators while performing system installation, measurement and checking status of toxic chemicals. Therefore, there have been increasing needs for the development of alternatively efficient, spatially distributable and safe technologies enabling seamless monitoring against hazardous chemicals spilled in river water. Among various alternative ways, remote sensing is a potential candidate when considering its advantages such as minimal contact, spatial distribution, efficiency and ease of operation. Recent advances in platforms, such as CCTV and UAV, made remote sensing more plausible for this kind of river monitoring.

From such a perspective, the present study specifically proposes a remote sensing method of using hyperspectral images to identify the type of hazardous chemicals, where spectral images are continuously monitored along a cross-section of river. More specifically, we developed a dedicated spectral library of solvent hazardous chemicals that helped to characterize specific features of a given spectrum. Already, hyperspectral images have been increasingly applied for assessing the hydraulic and ecological characteristics of rivers. For example, monitoring river water quality (e.g., Chl-a, TSS and turbidity) using aerial and satellite-based hyperspectral images has been developed [3–7]. River depth measurements based on drone-based hyperspectral images are being actively investigated [8]. The present study expands their applications for detecting and identifying dissolved or floating chemicals spilled in a river using a hyperspectral image [9–11]. The motivation for using hyperspectral images for chemical identification is to construct a unique spectral library for each chemical. In fact, spectral libraries have played a key role in the identification of terrain objects, such as minerals, soils, vegetation, artifacts and liquids [12], when spectral images began to be available following the era of satellites. However, there have been very few spectral libraries researched for substances based on solvents, such as chemicals mixed in river water, mainly due to the fact that spatial resolution of conventional spectral image from conventional satellites supporting spectral images (i.e., 30 m) is not suitable to detect chemicals spilled in relatively small rivers. Furthermore, existing spectral libraries for identification of substances mixed in water, such as those developed by USGS [13], Johns Hopkins University [14], NASA [14] and the ECOSTRESS spectral library version 1.0, are mostly unable to detect non-chemical materials, such as frost, ice, distilled water, seafoam, seawater, coarse granular snow and red-coated algae water [15]. Additionally, these studies have mainly constructed spectral libraries based on indoor spectrometers while missing critical signatures for water solvent, light-transmittable substances applicable to natural rivers under sunlight.

Considering that a reliable spectral library is enough to utilize hyperspectral images acquired from river environment for monitoring hazardous chemicals, very few prior studied spectral libraries are available. In this context, this study helps to derive a spectral library for identifying various hazardous chemicals floating in or mixed in river water. Several issues must be prioritized before newly streamlining a spectral library, where the hyperspectral images acquired from platforms, such as UAVs, raise new issues in contrast to those obtained from former spectral investigations conducted in controlled indoor conditions. First, when building a unique chemical spectral library, the spectral characteristics of river water must be removed as it exhibits higher reflective properties than the dissolved chemicals. Also, the spectral characteristics for each river water may differ. The spectral impact from the surrounding solvent should be discriminated and eliminated to isolate pure spectrum from the chemicals. Second, unlike with point spectroradiometer, when building a standard spectral library from hyperspectral images recorded in-plane units, post-processing and averaging of multiple spectral signatures are required.

Thus, outlining the procedure for averaging multiple spectral information for targeted chemicals with outlier removal to obtain a representative spectrum as the unique spectral trend for further versatile usages is essential. Third, chemicals dissolved in river water with the same properties exhibit, to some extent, different spectral characteristics depending on field observation conditions, i.e., solar intensity and angle. Thus, conversion to reflectance requires standard quantification through radiometric calibration using multiple reflection tarps with known absolute reflectance. Fourth, despite similar spectral patterns, the same chemicals may show different reflectance levels depending on the chemical concentration and solar intensity. Hence, the reflectance levels must be standardized to avoid challenges in future identification. Consequently, in addition to the existing method for building a spectral library, a new standard procedure for building a unique spectral library for each chemical should be established. This spectral library will allow the identification of dissolved chemicals, in river water, from UAV-based hyperspectral images. The core contribution of this study is the proposed standard procedure and method for building a spectral library.

From the above perspective, we tackle the challenges posed by the increasingly available UAV-based hyperspectral images in riverine environments to identify the presence of hazardous chemical solvents in rivers which have been less investigated in the absence of direct measurement. We propose a referable standard procedure for constructing a unique spectral library based on pre-scanning hyperspectral sensors mounted on a drone with respect to representative hazardous chemicals registered on the national hazardous chemical list. The spectral library for the chemicals was built on the condition that the chemicals are basically mixed with natural rivers in the form of dissolved or floating ions on river water. We utilized the hyperspectral images for 18 types of hazardous chemicals injected into river water in an outdoor environment, where a dedicated hyperspectral ground imaging system mounted with a hyperspectral camera was designed and applied.

2. Materials and Methods

2.1. Target River and Hazardous Chemicals

The hazardous chemicals supplied to build a unique spectral library are close to undiluted solutions of high concentrations. To build a spectral library of hazardous chemicals mixed in river water, we collected water from Gam Stream of the Nakdong River water system located in the southern part of South Korea. There are industrial complexes located upstream of the Gam Stream, where several former spill incidents of hazardous chemicals occurred, such as the detection of perchlorate at major water intake sites on the Nakdong River in July 2006; a phenol spill due to a fire accident in the Gimcheon site of Kolon Industries in March 2008; and the temporary suspension of water intake due to phenol detection in Gumi Metropolitan Water Treatment Plant. Thus, the Gam Stream was selected as a testing subject in this study since there is a real concern regarding water quality due to chemical spills in this area.

As mentioned, 18 types of chemicals were selected as hazardous chemicals, consisting of five types of organic matter and 13 types of inorganic matter (Table 1). By pH, the hazardous chemical samples of 3000 ppm consisted of 8 types of acidic chemicals, seven types of neutral chemicals and 3 types of basic chemicals. The hazardous chemicals were turned into 0.5 M stoke solutions by diluting in distilled water, considering the molecular weight and purity of each chemical. Samples were produced by diluting these 0.5 M stoke solutions in river water. The samples prepared to capture hyperspectral images were placed in a wide shallow container with a glass cover to secure stability and minimize light diffraction that occurs on a spherical surface. Handling hazardous chemicals that have no cover is challenging; therefore, 250 mL samples were collected in covered crystallizing dishes with a diameter of 80 mm and a height of 45 mm. Hyperspectral images of samples in these containers were captured.

Table 1. Hazardous chemicals used to build a spectral library.

No.	CAS No.	Name	Chemical Formula	Color	Organic	pH
1	107-07-3	2-Chloroethanol	C_2H_5ClO	Colorless	Organic	7.42
2	556-52-5	Glycidol	$C_3H_8O_2$	Colorless	Organic	8.29
3	78-93-3	Methyl ethyl ketone	C_4H_8O	Colorless	Organic	8.22
4	7664-39-3	Hydrogen fluoride	HF	Colorless	Inorganic	2.18
5	7726-95-6	Bromine	Br_2	Dark reddish-brown, Dark red	Inorganic	5.8
6	7784-34-1	Arsenic trichloride	$AsCl_3$	Colorless, Yellow oily fuming liquid	Inorganic	6.69
7	7719-12-2	Phosphorus trichloride	PCl_3	Colorless, Yellow oily fuming liquid	Inorganic	1.53
8	143-33-9	Sodium cyanide	NaCN	White crystalline solid, Colorless liquid	Inorganic	10.90
9	7664-41-7	Ammonia	NH_3	Colorless liquid	Inorganic	10.47
10	7647-01-0	Hydrogen chloride	HCl	Colorless	Inorganic	1.05
11	869-24-9	2-Chloroethyldiethylammonium chloride	$C_6H_{14}ClN{\cdot}HCl$	Colorless liquid	Organic	6.50
12	7719-09-7	Thionyl chloride	$SOCl_2$	Colorless to yellow to reddish liquid	Inorganic	1.41
13	10025-87-3	Phosphorus oxychloride	$POCl_3$	Colorless to yellow, oily liquid	Inorganic	1.46
14	1341-49-7	Ammonium bifluoride	$(NH_4)HF_2$	White crystals, Colorless liquid	Inorganic	3.49
15	108-88-3	Toluene	C_7H_8	Colorless	Organic	(basic)
16	7681-49-4	Sodium fluoride	NaF	White powder or colorless crystals, colorless liquid	Inorganic	6.85
17	7789-23-3	Potassium fluoride	KF	White crystalline, colorless liquid	Inorganic	7.27
18	7664-93-9	Sulfuric acid	H_2SO_4	Colorless to dark-brown, oily liquid	Inorganic	1.34

2.2. Hyperspectral Image Collection

The hyperspectral sensors are generally passive types that collect light reflected from objects after they absorb sunlight. The hyperspectral sensor used in this study was Corning's microHSI 410 SHARK, as shown in Figure 1a [16]. This hyperspectral sensor has a wavelength range of VNIR, i.e., 400–1000 nm, a spectral resolution of 4 nm, and provides a total of 150 spectral bands. The sensor size, including the lens, is 13.6 cm × 8.7 cm × 7.0 cm, with a weight of 0.68 kg. Since the sensor is lightweight, it can be easily mounted on UAVs. The sensor collects the spectral information using the line scanning method with a push-broom that spatially records the light passing through a prism [17]. Basically, spectral outliers were removed using a Kalman filter. The observation angle is 29.5°, while 682 pixels are collected per scanning line at a frequency of 300 Hz. Hyperspectral images captured using the line scanning technology enable the measurement of space as the spectral characteristics collected at each observation are stored linearly. The linearly stored spectral characteristics along the traveling path of the platform were recorded (Figure 1b).

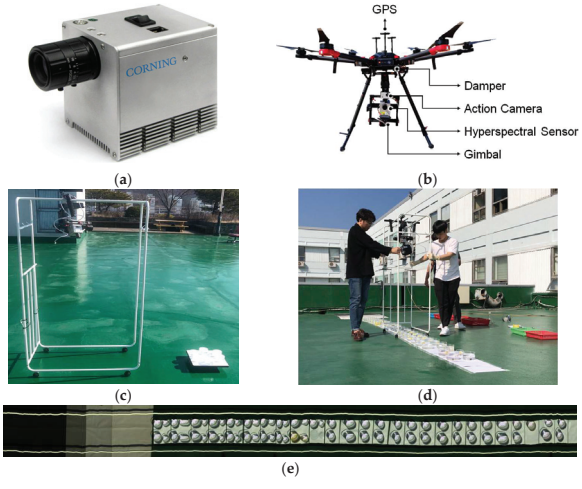


Figure 1. Hyperspectral image sensor and its ground-based outdoor portable holder to obtain spectral images for various hazardous chemicals. (**a**) Hyperspectral sensor used for building spectral image; (**b**) a drone system with hyperspectral sensor, GPS and gimbal supposed to monitor hazardous chemicals in riverine environments; (**c**) a portable holder mounted with hyperspectral sensor on the ground and chemical samples to be photographed; (**d**) manual mobile operation of the portable holder on top of biker containing chemicals; (**e**) resultant hyperspectral image where prepared samples of hazardous chemical were monitored concurrently.

As seen in Figure 1c, the hazardous chemical samples were captured with a hyperspectral camera mounted on a portable holder at a height of approximately 1.4 m to enable portable photography according to the line scanning method for collecting various samples concurrently. By slowly migrating the holder with a hyperspectral camera at a constant speed, various chemical samples could be collected almost simultaneously under natural light conditions (Figure 1d,e). Due to the pre-scanning method, the hyperspectral camera mounted on a UAV or a ground holder is sensitive to wind, flight vibrations and observation angle. The vibration of the mounted drone and its portable holder should be considered, which occurs when the flight path is changed compared to a relatively stable manned airplane. Thus, it was challenging to generate hyperspectral images without proper post-processing since line scanned images could not be properly combined. Consequently, clear hyperspectral images were often not obtained due to the failure of proper image registration. To cope with this issue, the installation of a gimbal was indispensable to minimize and correct shaking mathematically. In this study, hyperspectral raw data with minimal shaking could be obtained by applying DJI's RONIN-MX (Figure 1b,c); the results are shown in Figure 1e. Further, white A4 sheets were placed below the samples to be captured, for minimizing the effects of the floor material.

The hyperspectral image depicted in Figure 1e was captured at 1:30 pm on 16 October 2019, when the solar angle elevation was very high. The temperature was 15.3 °C, and the relative humidity was 72.6%. The solar azimuth was 215°53′18.25″, and its altitude was 38°5 4′12.9″.

Notably, the reflectance, a normalized spectral signal, mainly utilized to build a library or to conduct further analysis, is obtained by dividing the intensity of the light source and the intensity of the reflected light from objects. A conventional ground-based spectrometer and spectroradiometer can calculate relatively accurate reflectance without further processing.

However, the line scan-based hyperspectral sensor stores the light intensity in the form of a radiance and, hence, should be converted into reflectance in the post-process with respect to an absolute reference, such as a white plate (i.e., a standard reference panel (Spectralon (Labsphere, North Sutton, NH, USA)) with 99.9% reflectance applied where the reflectance derived from radiance can be expressed in Equation (1). When single reference like white plate is not sufficient, a couple of reference plates with different reflectance values can be alternatively applied. This study applied the latter approach that will be explained later on.

$$\text{Reflectance } (\lambda) = \frac{\text{Radiance } (\lambda)}{\text{Radiance}_{\text{white plate}} (\lambda)} \times 100 \quad (1)$$

Figure 2b shows the raw spectral signature expressed as radiance extracted from 100 pixels at the center of the container in the photographed chemicals (Figure 2a). Although there are subtle differences between all chemicals, the differences between chemicals mixed in river water are insignificant (Figure 2b–d). Furthermore, the usual spectral library acquired from the spectrometer (i.e., point and time-averaged) through artificial lights in the existing laboratory can be used to distinguish between chemicals without a separate standard processing procedure since it provides one spectral signature. However, as with the approach adopted here, multiple spectral signatures (e.g., 100 spectrums) could be acquired from one material using the line-scan hyperspectral imaging system. If the solvent, such as the river water, has a strong reflectance compared to the chemical, the utility of such a library, based on raw spectral signature (Figure 2), can be limited in future identification.

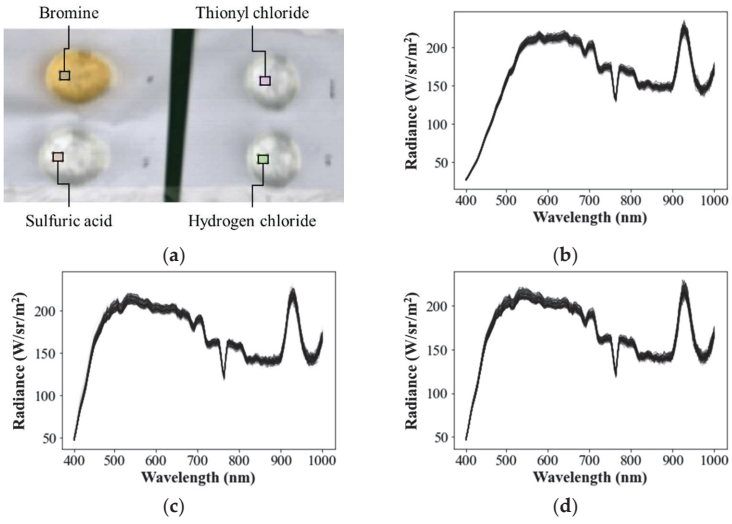


Figure 2. Example of spectral extraction and extracted spectral signatures. (**a**) Example of extraction of the spectral signature; (**b**) spectral signatures of river water and bromine mixture; (**c**) spectral signatures of river water and sulfuric acid mixture; (**d**) spectral signatures of river water and hydrogen chloride mixture.

3. Results and Discussion

3.1. Procedure for Building a Spectral Library

3.1.1. Deriving Radiometric Calibration Equation

Radiometric calibration must be performed for the obtained hyperspectral images in order to remove the atmospheric absorption and scattering effect. Generally, this process involves the conversion of radiance to the reflectance as well as removing the atmospheric effects [18]. It is desirable to collect the coincident spectral radiation measurements (i.e., to the hyperspectral image acquisition) using a field spectroradiometer [19]. However, it may be challenging to approach the site during image acquisition or to operate the hyperspectral sensor and spectroradiometer concurrently. Therefore, we concluded that the collected spectral data (i.e., radiance) can be better converted into reflectance using a standard reference panel (Spectralon (Labsphere, North Sutton, NH, USA)) or calibration panel. Furthermore, since different signatures may be derived from the same chemical depending on the optical and equipment conditions at the time of hyperspectral imaging, reference values for converting the measurements (i.e., DN and radiance) to reflectance are required. For this purpose, the so called "reflectance tarps" made of specific materials maintaining standard stepwise reflectance values of 55, 44, 22 and 5% (Figure 3a) were applied using a calibration panel together with the hyperspectral images of hazardous chemicals. The stepwise reflectance tarps would guarantee better performance in conversion of radiance to reflectance rather than using a single white plate of 99%. Since the accurate reflectance values of the reflectance tarps are known and mostly fixed for any spectral bands as seen in Figure 3b, a reflectance-radiance relationship for each spectral band (Figure 3e) can be established by constructing a relational equation and standardizing imaging conditions for both the reflectance tarps and chemicals. Notably, the hyperspectral sensor (microHSI (Corning Advanced Optics, Corning, NY, USA)) provides raw data as DN (or radiance), which is the light intensity, for a total of 150 spectral bands in 4 nm intervals in the spectral range of 400–1000 nm. The actual reflectance values of the reflectance tarps are already set in all the 150 bands. For example, the 55% reflectance tarp shows 55% reflectance in all the wavelengths. In this study, we verified the reflectance values of the reflectance tarps using a spectroradiometer (PSR-2500 (Spectral Evolution Inc., Haverhill, MA, USA)). The

PSR-2500 spectroradiometer is a well-established and highly reliable passive device for collecting spectral information (Figure 3b). The results were highly similar to the values of reflectance tarps in most wavelengths except 400–420 nm. However, the spectral data of the reflectance tarps, collected using a hyperspectral sensor (microHSI (Corning Advanced Optics, Corning, NY, USA)) and used to build a library, started at 520 nm, unlike the spectroradiometer data shown in Figure 3c. Also, constant reflectance was not observed from 700 nm.

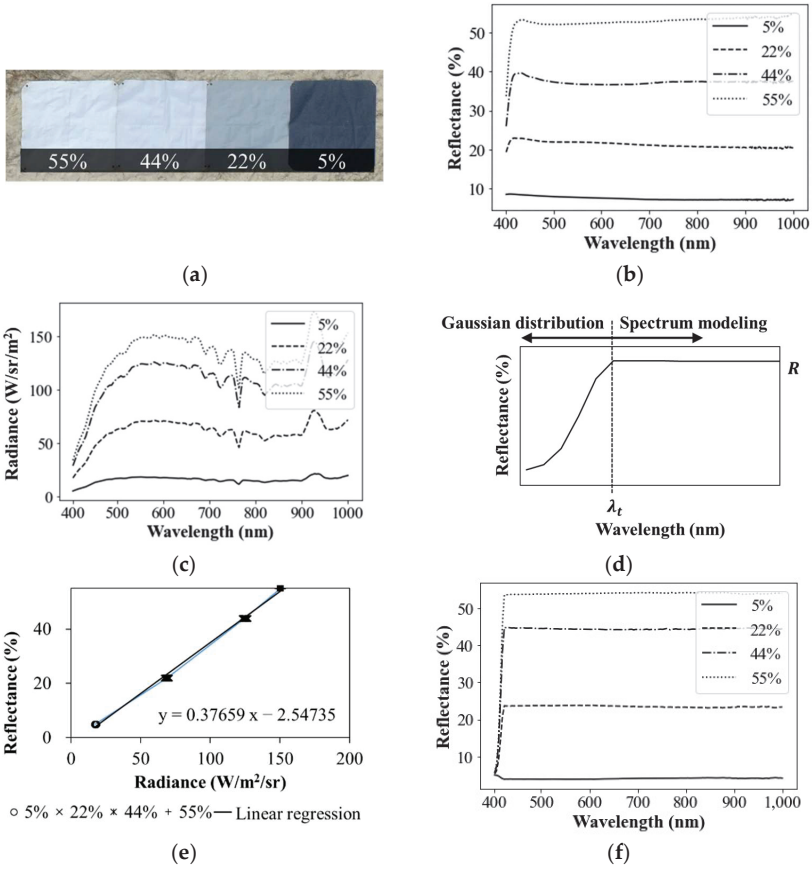


Figure 3. Derivation of radiometric calibration equation for a hyperspectral image using reflectance tarps. (**a**) The reflectance tarps; (**b**) spectrometer data from reflectance tarps; (**c**) hyperspectral sensor data from reflectance tarps; (**d**) concept of radiometric calibration; (**e**) radiance to reflectance rating at 597.66 nm; (**f**) calibrated reflectance tarps from hyperspectral sensor.

Therefore, reflectance modeling at 400–420 nm was based on the normal distribution (Equation (2)), by assuming the spectroradiometer data as the truth, so that similar trends are shown. For wavelengths above 420 nm, radiometric calibration was performed so that constant reflectance would be shown (Figure 3d).

$$N\left(\text{xvert}\mu, \sigma^2\right) = \frac{1}{\left(2\pi\sigma^2\right)^{1/2}} \exp -\frac{1}{2\sigma^2}(x-\mu)^2 \quad (2)$$

where μ is the mean and σ^2 is the variance. Since it must have the R-value at λ_t, $\frac{1}{\sqrt{2\pi\sigma^2}} \exp(\sigma) = R$ must be satisfied. In this study, σ was calculated using the spectral

information of an actual spectrometer and applied to radiometric calibration, as shown in Figure 3d and Equation (3).

$$\begin{cases} N(\text{xvert}\lambda_t,\ \sigma^2) & \text{if}) \ \lambda < \lambda_t \\ R & \text{if}) \ \lambda \geq \lambda_t \end{cases} \tag{3}$$

The above radiometric calibration, by building a specified radiance-reflectance relation, was performed for each individual 150 spectral bands collected from the hyperspectral sensor, respectively. The results are summarized in Table 2. Figure 3e shows an example of deriving the equation for converting radiance to reflectance at the wavelength 597.66 nm (No. 45, Table 2).

Table 2. The correlation coefficients between each 18 spectral samples and characteristic spectral libraries.

No.	Chemicals	Correlation Coefficient	No.	Chemicals	Correlation Coefficient
1	2-Chloroethanol	0.871	10	Hydrogen chloride	0.910
2	Glycidol	0.926	11	2-Chloroethyldiethylammonium chloride	0.934
3	Methyl ethyl ketone	0.989	12	Thionyl chloride	0.977
4	Hydrogen fluoride	0.948	13	Phosphorus oxychloride	0.912
5	Bromine	0.994	14	Ammonium bifluoride	0.861
6	Arsenic trichloride	0.814	15	Toluene	0.717
7	Phosphorus trichloride	0.881	16	Sodium fluoride	0.906
8	Sodium cyanide	0.948	17	Potassium fluoride	0.881
9	Ammonia	0.962	18	Sulfuric acid	0.977

Based on the radiometric calibration method presented aforehand, radiometric calibration was performed by applying radiance-reflectance relation established for each of the 150 bands in the entire captured collection of hyperspectral images (pixels). The complete process of the radiometric calibration was scripted using a dedicated software application for future use.

3.1.2. Extraction of Spectral Signatures

After applying the aforementioned radiometric calibration, spectral signatures rated as reflectance were extracted from the radiometrically calibrated hyperspectral images based on multiple pixels of the beaker holding the hazardous chemicals. Considering the outlier removal at a later step, more than 100 pixels were selected for the extraction of spectral information in the parts that are not affected by the scattered light due to the curved surface of the glass container (Figure 4a). This bundle of spectral signals will be averaged afterward to build a representative spectral signature for a given hazardous chemical. The extracted reflectance data pertained to the mixed samples (i.e., river water and chemicals), which has 2.5 cm depth of water in common. Herein, the spectral response could be differentiated to be commensurate with water depth. In this regard, we accordingly proposed and maintained a specified water depth for each container mentioned above to build a standardized spectral library. This way of consideration should be taken plausibly when certain soluble objects in liquid should be spectrally liberalized. In this study, a bundle of the spectral signatures derived from 100 pixels of the river water mixed with hydrofluoric acid image is shown in Figure 4b. As mentioned, we attempted to build a spectral library for overall 19 hazardous chemical samples, which were taken concurrently as shown in Figure 1e and enabled pulling out of the spectral signatures in an analogous environment. To facilitate this process, a dedicated in-house tool was developed to deal with a hyperspectral image, which basically allows the building of radiance-reflectance relations for each spectral band (Figure 4c,d) and simultaneously applies the relationships to the collected hyperspectral image. Subsequently, the software enabled the selection of multiple locations (i.e., 100 pixels) for each chemical container and the extraction of the spectral bundles (Figure 4a,b). The software was designed to efficiently load the heavy size of the hyperspectral image (2.4 GB); however, such large size tends to substantially slow down the conventional memory size of a personal computer. We resolved this by partially

loading specific bands or pulling out all band information for some designated pixels for a targeted analysis.

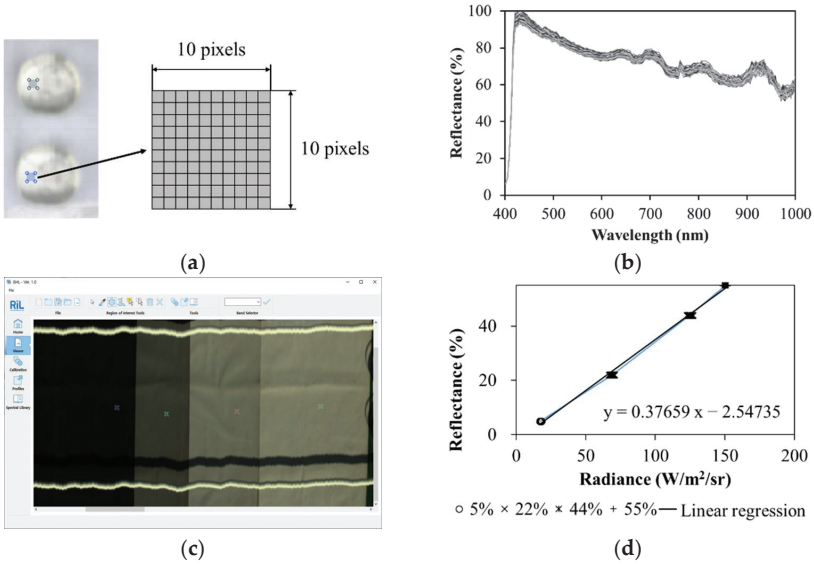


Figure 4. Extraction of spectral signatures from a hyperspectral image containing 19 chemicals using a mobile portable holder. (**a**) selection of specified pixels within a chemical container used as ingredient for building a spectral library for that chemical; (**b**) a bundle of hyperspectral signature extracted from selected pixels, where radiometric calibration was previously applied; (**c**) building radiance-reflectance relation using various reflectance tarps, where crossing point indicates a selected pixel corresponding to each reflectance percentile as well as raw radiance by the present hyperspectral camera (Corning microHSI); (**d**) a developed in-house software to make radiance-reflectance relation based on the previous step for conducting radiometric calibration and to apply the relations to entire bands and pixels.

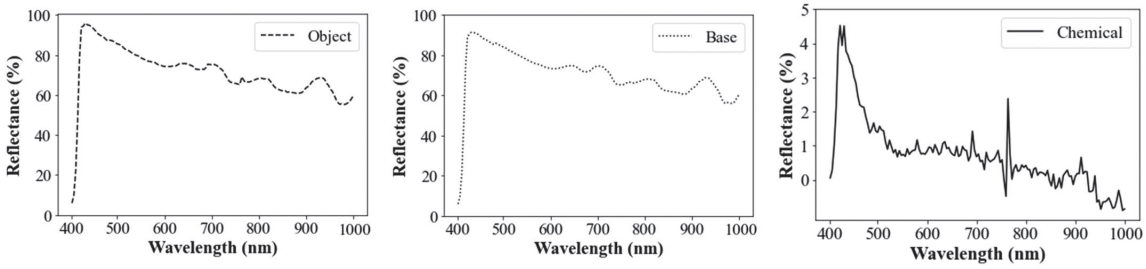
3.1.3. Spectral Subtraction of Backgrounded Impacts

The radiance data of liquid collected through hyperspectral imaging includes base reflection, absorption by a water column, water surface reflection and absorption by the atmosphere. The equation for the total radiance is as follows:

$$L_T(\lambda) = L_b(\lambda) + L_c(\lambda) + L_s(\lambda) + L_p(\lambda) \simeq L_b(\lambda) \quad (4)$$

where L_T is the radiance; λ is the wavelength; L_b is the base reflection; L_c is the water column absorption; L_s is the water surface reflection; and L_p is the atmospheric absorption. Bearing in mind that raw reflectance for chemical solvent river water encompassed several other backgrounded factors, spectral signatures were derived following the procedure described in Figure 3, which showed a considerably similar pattern irrespective of different types of chemicals. This output addresses the background impacts on spectral characteristics that exist inevitably for solvent materials and will differ for other cases accordingly with the specific spectral characteristics of river water. More specifically, the result shown in Figure 5a,b indicated that the background river impact was dominant to a much higher degree, rather than the chemicals. Consequently, the spectral signature of pure river water was eliminated in order to characterize the impact solely from solvent chemicals; otherwise the original spectral pattern would be inappropriate as the library was supposed to identify individual chemicals afterward. We assumed that the spectral signature for individual chemical will be differentiated to play a librarian role. In this regard, pure

river water without chemicals was also spectrally photographed and used to subtract from raw reflectance for each solvent chemical. Figure 5a,b exemplified a spectral signature of hydrogen fluoride in both conditions of mixed and pure river water, respectively, denoting that their spectral pattern looks remarkably analogous. When the spectra of pure water were subtracted from the mixed water, the residual spectral pattern became pronounced as shown in Figure 5c; this sort of residual spectral signature was identifiable and differentiable for each solvent chemical. The residual spectra can be negative when reflection of pure river water in certain spectral bands is higher than the solvent chemical. Collectively, the subtraction of backgrounded spectral impacts driven by river water was necessitated; subsequently, we adapted this background subtraction as a standardized step to build the spectral library of solvent chemicals.



(**a**) (**b**) (**c**)

Figure 5. Derivation of spectral signature characterizing hazardous chemicals mixed with river water in terms of residual spectral pattern for solvent chemicals subtracted from a given pure river water. (**a**) Raw spectral signature exemplified for a solvent chemical mixed river water and hydrogen fluoride; (**b**) spectral signature of pure river water without any solvent chemicals; (**c**) residual spectral pattern for solvent hydrogen fluoride subtracting impact by pure river water.

3.1.4. Delineation of Mean Spectral Signature

A bundle of spectral signature using approximately 100 locations was taken from a spatially adjacent region as illustrated in Figure 6a. Interestingly, their resultant spectral patterns stemming from the identical chemical and monitoring environment demonstrated slightly different fluctuations, despite a similar main trend as described in Figure 6. Also, there exists spikes or outliers in spectral information, whose elimination is recommended. Therefore, it was necessary to select a method to eliminate outlier and then decompose a representative and mean spectral signature among a bundle of spectral signatures. There will be several useful methods to accomplish such a purpose. In this study, we applied a classic filtering algorithm to remove the spectral signatures, including the reflectance corresponding to outliers that leaves only the data within $\pm 3\sigma(\lambda)$, i.e., a 99.73% confidence interval of the reflectance values. To obtain the mean spectral value corresponding to each band, the Super Smoother method [20] was applied as one of the non-parametric regression methods as likely as loess or lowess [21,22]. The Super Smoother [23] computes the most probable value by applying weighted linear regression in each section after dividing bivariate data into elastic bandwidths and then determines a smoothed trend curve by estimating the most probable values, repeatedly in a given span, and connects them. Bandwidth is used to estimate the local pattern. If the bandwidth is too large, a flat curve close to a straight line is obtained (i.e., under-fitting); if it is too small, a curve with considerable bending of the regression function is obtained (i.e., overfitting). Therefore, a small bandwidth (i.e., optimal width size) was set to remove variations due to random behaviors and to reflect a local trend while maintaining the reflectance of each wavelength as much as possible. Such filtering and finding mean path algorithm of the super smoother was iterated, and finally, the overall trend after removing variations due to random behaviors of the collected data was obtained as shown in Figure 6b.

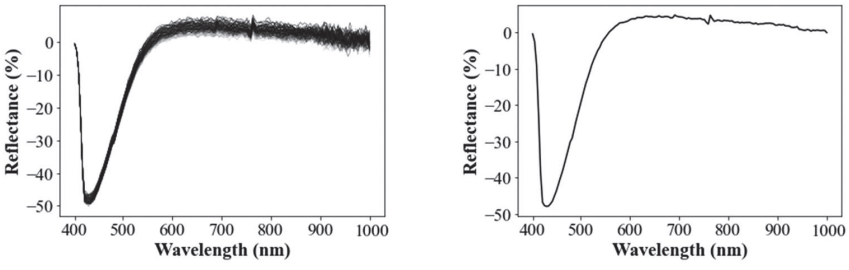


Figure 6. Derivation of a mean and filtered spectral signature for a hazardous chemical (bromine) using the super smoother. (**a**) A bundle of residual reflectance for bromine; (**b**) a derived spectral signature after applying filter and the super smoother.

3.1.5. Normalization of Mean Residual Reflectance

Spectral intensity responding to individual spectral band could differ according to in-situ conditions for the same solvent chemical, such as concentration of chemical, sunlight strength and type of hyperspectral camera. Although a major spectral factor of backgrounded river water was eliminated by the forced subtraction, the presence of such other remaining variants should be considered to build a generalized spectral library. This aspect is essential to diagnose an unknown solvent chemical based on the established library, but the new one could be possibly taken in different conditions. To address this, we normalized the residual spectral information using vector normalization with respect to total magnitude (I) cumulated by all residual reflectance as denoted in Equation (5).

$$R'(\lambda) = \frac{R(\lambda)}{I},\ I = \sqrt{\int_{\lambda_{min}}^{\lambda_{max}} R(\lambda)^2} \tag{5}$$

$R'(\lambda)$ is the vector-normalized residual reflectance; $R(\lambda)$ is a raw residual reflectance; I is the magnitude cumulated for the vectorized residual reflectance; and λ_{max} and λ_{min} are the maximum and minimum wavelength of residual spectral signature, respectively. Figure 7 lists normalized residual spectral signatures for the designated 18 hazardous solvent chemicals. There could be distinctive features between chemicals, yet some are similar. For example, methyl ethyl ketone showed similar trend with Hydrogen fluoride but completely opposite compared with bromine. Hydrogen fluoride looks similar to Arsenic trichloride in the pattern, but their details in higher spectral band are different. On the other hand, sodium cyanide showed a unique feature that is very distinctive from other chemicals.

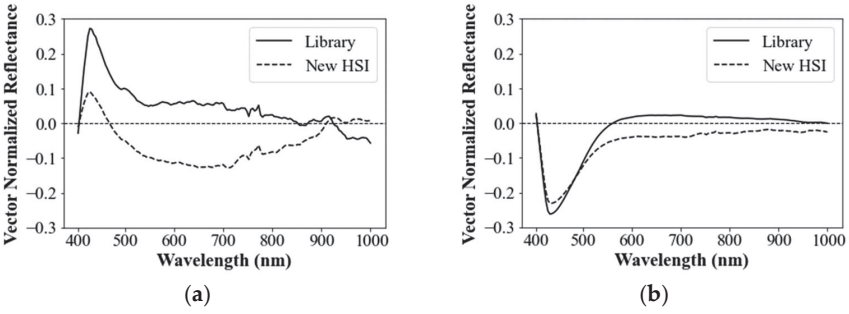


Figure 7. *Cont.*

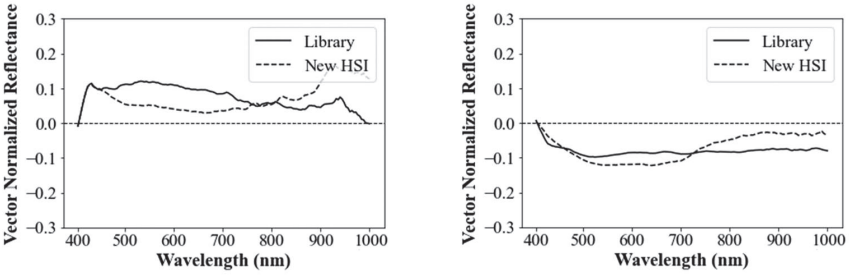


Figure 7. Exemplified comparison of the spectral spectrum between the spectral library and the HSI (Hyperspectral Image). (**a**) Hydrogen fluoride; (**b**) bromine; (**c**) phosphorus oxychloride; (**d**) ammonium bifluoride.

Spectral signature, such as that observed in normalized residual spectra in Figure 6, could have been immediately streamlined in a spectral library for identifying solvent chemicals, whereas full spectral signature has been generally used to identify and classify surface materials such as land cover [18–20]. Beyond using raw spectral information, we expected that various aforementioned steps to make raw spectral data more distinctive could be further augmented with the addition of backgrounded water spectra subtraction and normalization. However, the resultant normalized residual spectra can be prone to other submerged factors, like sunlight intensity; hence, this tentative spectral library should be validated to determine whether additional modification is necessary. In this regard, we conducted a preliminary diagnosis test, where the derived spectral library represented in Figure 7 was compared with newly captured hyperspectral signatures for 18 hazardous chemicals lagged with 2 h intervals where only sunlight strength was changed. Figure 7 demonstrates the feasibility of the developed library (Lib) in terms of sampled comparison for hydrogen fluoride, bromine, phosphorus oxychloride and ammonium bifluoride, respectively, where their spectral signatures were extracted from the new hyperspectral images (New HSI) in exactly the same way as described above.

The comparative results however indicated that, whereas bromine clearly showed highly analogous pattern and spectral value with new sample from qualitative perspective, hydrogen fluoride and ammonium bifluoride revealed less similarity in terms of spectral value, despite overall similar feature. Moreover, phosphorus oxychloride was hardly acceptable in terms of strong similarity. In fact, review of remaining chemicals did not show feasible agreement between developed library and new input. To evaluate quantitative comparison, the correlation coefficient between the two spectral spectrums was assessed. The correlation coefficient between the spectral library and the new HSI spectrum of each group was calculated for all the wavelength groups as follows:

$$r_{lib,new} = \frac{\sum_{i=1}^{n}\left\{R(\lambda_{lib,i}) - \overline{R(\lambda_{lib})}\right\}\left\{R(\lambda_{new,i}) - \overline{R(\lambda_{new})}\right\}}{(n-1)s_{lib}s_{new}} \quad (6)$$

where $\overline{R(\lambda_{lib})}$ and $\overline{R(\lambda_{new})}$ are the mean reflectance of the spectral library and the new HSI spectrum, respectively; s_{lib} and s_{new} are the standard deviations of reflectance of the spectral library and the new HSI spectrum, respectively. In conjunction with prior qualitative view, bromine stood out with a high correlation coefficient of 0.979; however, correlation for most of the 17 hazardous chemicals showed highly poor performance of <0.6 and negatively correlated in other cases. For example, correlations for ammonium bifluoride and hydrogen fluoride were 0.63 and 0.26, respectively. Phosphorus oxychloride resulted in a negative correlation of −0.44. This may be attributed to the fact that only bromine has chromaticity, while other chemicals were mostly invisible, which can prominently account

for the superior performance of bromine. The results suggested further modification of the spectral library.

3.1.6. Characteristics of Spectral Library

When the whole spectrum was applied as a library, as shown in Figure 7, we found that the spectral bands irrelevant to reflective characteristics of chemical could be randomly different according to spectral nature and ambient measurement conditions. These irrelevant spectral bands negatively affected the correlation assessment against reference in high degree, thus should be better excluded from the spectral library. Subsequently, it would be optimal to identify unique bands that enable to characterize specific chemicals. In fact, the approach of solely using optimal bands (not whole) has been widely accepted in various hyperspectral applications, such as NDVI for vegetation [24], NDWI for water [25] and optimal band ratio analysis (OBRA) for submerged bathymetry [8]. In this study, however, we did not develop a specialized index or finding optimal band ratio similarly with former studies. Rather, we selected specific band groups among whole spectrum to characterize a specific chemical as likely as a signature. We presume that such signatures should discriminate each other within the targeted chemicals. This is an important perspective and also a limitation since our objective was to only identify a chemical among the given pool of hazardous chemicals, where concept of ranking was adapted to prioritize candidates. We referred to this specific signature of chemical as "characteristic spectral library for hazardous chemicals", which was built on top of a previously processed spectrum following the aforementioned procedure.

To derive such characteristic library, various plausible ways can be used for further manipulation of the given processed library. As a top principle, it is necessary to extract common and unique parts from multiple spectrums acquired on various measurement conditions. In this way, the greater number of spectrums will better pull-out uniqueness of the spectral reflectance, where data mining techniques, such as machine learning, will work in certain degree to delineate specific patterns. Nevertheless, spectral samples in the presence of hazardous chemicals in the natural rivers are especially hard to obtain compared with other conventional natural objects. The safe way of handling chemicals was to bring such river water and artificially dissolve and mix them in a controlled experiment.

In this study, therefore, we followed a simple correlation defined in Equation (6) and preliminarily applied available only two different spectrums to manually pull-out common characteristics, though it would not be sufficiently generic and automated.

More specifically, in the two spectrums captured per each chemical, we defined 146 pairs, each having approximately 20 nm of coverage and applied the entire wavelength range of 400–1000 nm with 150 spectral bands. Then the correlation coefficient was assessed for each pair and ranked in order of highest value. For example, phosphorus trichloride was sorted in top five highly correlated pairs of 689.76–709.79, 633.7–653.72, 469.52–485.54, 509.56–525.58 and 733.81–785.87 nm, where the correlation coefficients in those pairs were 0.932, 0.909, 0.881, 0.834 and 0.711, respectively (Figure 8a). In addition, we attempted to further move the average cascadedly starting from the first two (i.e., 0.932 and 0.909) down to the fifth rank until the highest mean correlation coefficient was acquired.

As a result, phosphorus revealed that the first two bands had the highest moving average (Figure 9b), which characterized phosphorus in the spectral library. Herein, the number of characteristic coverages can be 2–5. Given that the number of maximum characteristic coverage of 5 was arbitrarily chosen, it is sufficient to characterize the uniqueness and similarity but can be more. Figure 9 shows signatured coverage to represent spectral characteristic of all 18 solvent chemicals, where multiple spans of bands were adapted to characterize the chemicals. For example, glycidol pertained five coverages as a characteristic spectral signature. An examination of the characteristic spectral libraries indicated that all 18 chemicals exhibited different characterized spectral properties. In particular, bromine, light brown in color, revealed significantly lower reflectance than other chemicals until 500 nm at which it turned blue. Interestingly, the overall shape of the spectrum of

bromine was similar to that of sodium cyanide, having no chromaticity cyanide especially in the lower reflectance. Similarly, fluorine compounds, i.e., sodium fluoride and potassium fluoride, showed similar overall spectral patterns. In addition, 2-chloroethyl, glycidol, hydrogen fluoride, bromine, phosphorous trichloride, 2-chloroethyl-diethyl ammonium chloride, thionyl chloride, sodium fluoride and potassium fluoride showed similar patterns in the wavelength range of 749.83–773.86 nm.

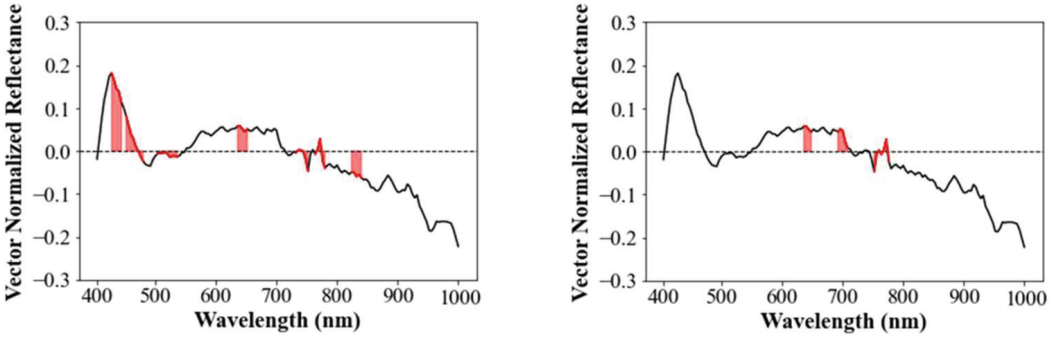


Figure 8. Characteristic spectral library of phosphorus trichloride (red color). (**a**) Primary characteristic spectral library of Phosphorus trichloride; (**b**) final characteristic spectral library of phosphorus trichloride.

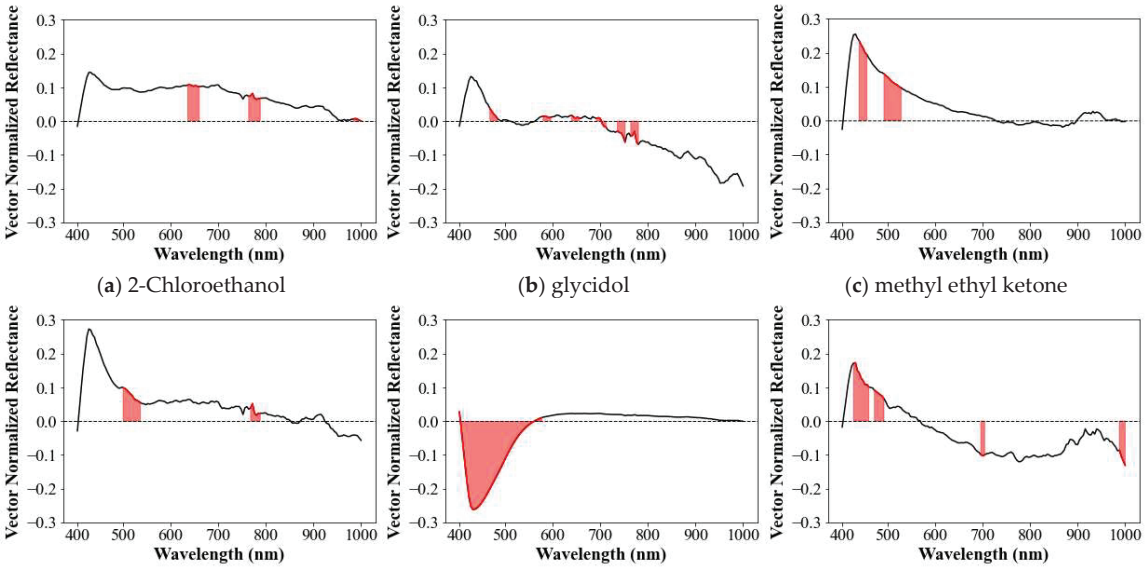


Figure 9. *Cont.*

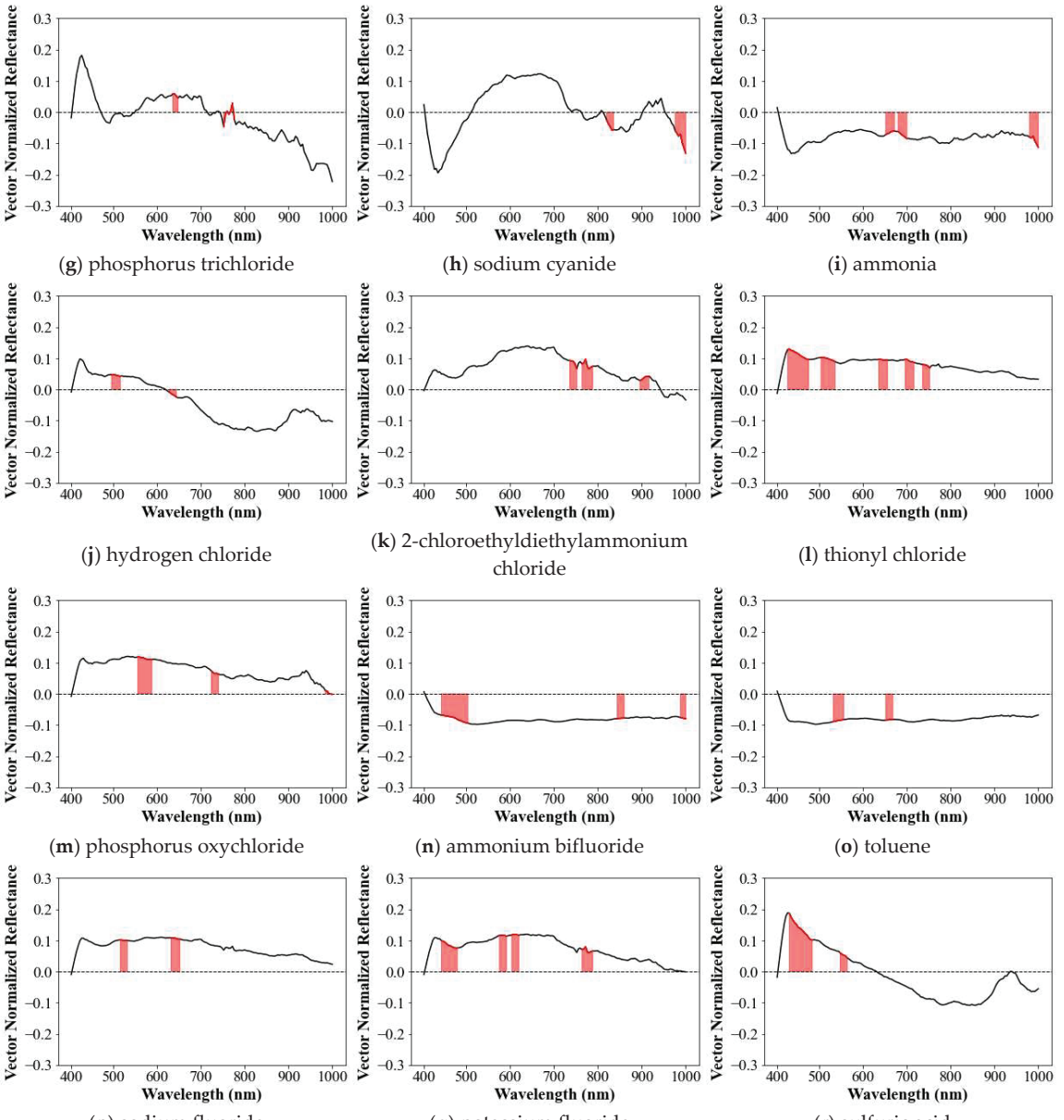


Figure 9. Characteristic spectral library. (**a**) 2-Chloroethanol; (**b**) glycidol; (**c**) methyl ethyl ketone; (**d**) hydrogen fluoride; (**e**) bromine; (**f**) arsenic trichloride; (**g**) phosphorus trichloride; (**h**) sodium cyanide; (**i**) ammonia; (**j**) hydrogen chloride; (**k**) 2-chloroethyldiethylammonium chloride; (**l**) thionyl chloride; (**m**) phosphorus oxychloride; (**n**) ammonium bifluoride; (**o**) toluene; (**p**) sodium fluoride; (**q**) potassium fluoride; (**r**) sulfuric acid.

Basically, the strategy of present study imposed several characteristic coverages as signature in case certain chemicals have different overall patterns, which is anticipated to better characterize and recognize a specified one. For the chemicals with similar patterns after ap-

plying steps of vector normalization, however, this strategy does not consistently guarantee high recognition between them. For example, the characteristic library of bromine can work suitably with that similar spectral coverage of sodium cyanide; thus, recognition process will yield to sodium cyanide as the best match rather than bromine that can be a secondary feasible match. We postulated that above drawback is unavoidable. Consequently, we suggested further recognition guideline to recommend more candidates (e.g., within ranking 3) in addition to the most similar one, where correlation coefficient between new and library account for the plausible criteria as a sort of probability. In fact, this approach is also useful in practice since we can substantially narrow down and specify the type of chemicals and track nearby spilling locations, such as chemical factory if chemical database was priorly established (e.g., among chemical factories located in upstream of Gam Stream in this study). Despite the different number of coverages for each chemical and certain degree of similarity, the resulted characteristic spectral library in Figure 9 is useful to identify and classify the type of leaked chemical.

Noting that only two spectral resources in an analogous environment (e.g., 2 h difference) were ingested, these characteristic spectral libraries are not certainly conclusive, thus limitedly applicable for identifying a new unknown chemical. Nevertheless, the results demonstrated that the derived spectral library well documented their distinctive features, and proof and good example of applying proposed procedure, indicating that the more spectral resources from various environment and variable are added, the better consolidated spectral characteristics of chemicals will be obtainable. In Figure 10, we summarized an end-to-end step to build a characteristic spectral library.

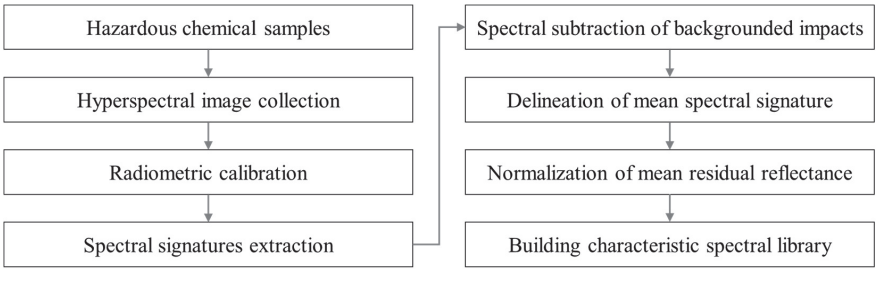


Figure 10. A flow chart to describe an end-to-end step for building characteristic spectral library for hazardous chemicals proposed solvent in rivers.

3.2. Recognition Process

Given that a spectral library for 18 solvent hazardous chemicals was established, we demonstrated how the library reliably recognizes a new unknown chemical (Figure 11). The unknown spectral information will be compared with the librarized chemicals one by one and ranked accordingly with the computed correlation. Note that whole recognition process only occurs among the given spectral library and mandatorily suggests suitable candidates within ranking 3 by referencing correlation coefficient, rather than assertively designating a single one. We herein exemplified chemical recognition process using newly photographed hyperspectral images for each hazardous chemical. For each chemical, spectral information was extracted and normalized after excluding ambient water as illustrated so far. Such manipulated spectral information was partially utilized up to characteristic spectral coverages specific to librarized chemicals. We prepared the same 18 samples of chemicals as in the library and took hyperspectral images in the slightly different environment when used during library construction. The unknown chemicals were hyperspectrally imaged at around 6 pm with the other conditions being identical. During sampling, the light intensity was lower than when imaging for constructing the spectral library. Then we individually applied the recognition procedure for 18 unknown chemicals and tested how feasibly the library yielded right candidates.

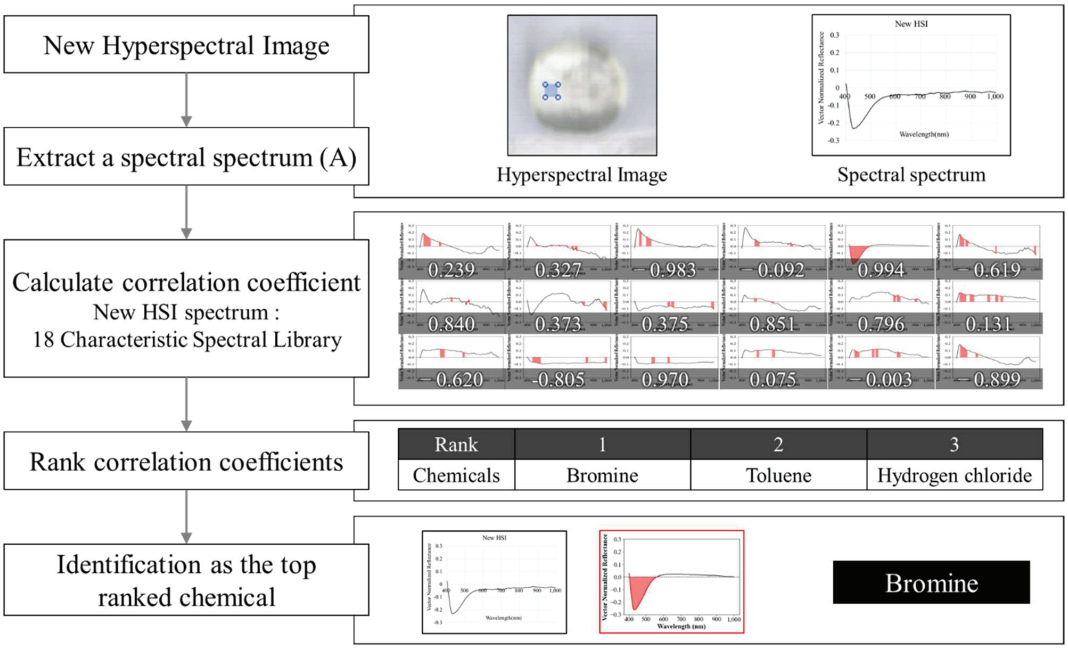


Figure 11. Chemicals recognition concept using a characteristic spectral library.

The correlation coefficients between each of 18 spectral samples and characteristic spectral libraries were assessed in Table 2 and ranked accordingly with correlation and simultaneously provided the rank to fit with each sample in Table 3. For example, the library recognized 2-chloroethanol correctly as first rank, but arsenic trichloride was ranked thirdly. In particular, bromine was firstly ranked in spite of having significantly lower reflectance than chemicals until 500 nm at which it turned blue. Low concentrations of chemicals with chromaticity could be better ranked though most chemicals in the library were transparent. We proposed that, when the rank of a chemical was within third, it became conceded as the library worked by narrowing down candidates for the unknown chemical. The greater number of chemicals in the library corresponds to higher accuracy of capturing the type of chemicals. Overall, the recognition rate showed that the developed library gave precisely correct answers for more than one-half of the samples (10 samples) as first ranked, and a total of 13 chemicals were among the top three chemicals (i.e., the recognition rate of 72.2%). Table 2 demonstrated the correlations between 18 spectral samples and a spectral library, which led to more than 0.8 except one sample (e.g., Toluene), implying an analogous nature of the derived library. In low rank cases, Table 3 imposed that practitioners narrow down possible candidates of leaked chemicals. This recognition rate indicated that our efforts to adapt a characterizing process substantially enhanced the success rate, considering that prior to using the characteristic library (meaning that full spectrum was used as signature to assess correlation), the recognition rate was approximately 53.3%. Nevertheless, five chemicals could not reach within the third rank, such that a characteristic library missed matching them. They were mostly transparent solvent subordinate of sodium and hydrogen type. In particular, toluene was completely out of ranking scope (ranked tenth), though this chemical was slightly visible as floating texture when it was mixed with water like spilled oil. The score of unmatched 27.8% of samples (i.e., beyond third rank) implied that, though we considered and standardized all different environmental conditions and furthermore adapted the characteristic concept, there might be other factors that were not considered.

Table 3. Evaluation of recognition rate—Example identification using a characteristic spectral library.

Rank	Number	Chemicals
1	10	2-Chloroethanol, glycidol, methyl ethyl ketone, hydrogen fluoride, bromine, ammonia, thionyl chloride, ammonium bifluoride, potassium fluoride, and sulfuric acid
2	2	2-Chloroethyldiethylammonium chloride and phosphorus oxychloride
3	1	Arsenic trichloride
4	2	Hydrogen chloride and Sodium fluoride
5	1	Sodium cyanide
6	1	Phosphorus trichloride
10	1	Toluene

In addition, the present chemical samples were only taken at difference in light intensity. In general, chemical samples can be measured in other higher order of difference in the measurement equipment (i.e., spectroradiometer or hyperspectral sensor), platform (terrestrial or airborne), weather, chemical concentration, different type of ambient river water, the bed materials (sand, gravel, mud, vegetated) and the container for holding samples. In those cases, the recognition success rate can be lower. Unfortunately, given the difficulties of securing hazardous chemicals in those conditions, it was not possible to obtain diverse cases of samples and was limited to developing a more solid spectral library for sampling chemicals, which was an unavoidable limitation of handling hazardous chemicals. Nevertheless, given such limited conditions, we suggest that the derived characteristic library work in certain acceptable range and can enhance the recognition rate. Also, considering previous similar studies, the developed library in this study was measured on condition where air correction was ignored; thus, those spectral images from low altitude UAV and terrestrial hyperspectral system can be eligible.

4. Conclusions

In this study, we developed a strategy for building a standard spectral library by characterizing hazardous chemicals using a hyperspectral sensor. Upon recognizing that various limitations occur when the spectral library is directly applied to the identification of chemical, the characteristic spectral library reflected several distinctive characteristic wavelength bands for each chemical and used them to better recognize an unknown chemical. Summarized procedures for building a characteristic spectral library are outlined here: (a) assuming that hazardous chemical samples have the analogous concentration, hyperspectral images are captured per container with identical hyperspectral sensor in operation and surrounding imaging conditions; (b) the collected spectral information is converted into reflectance through radiometric calibration where the spectral signatures of the sampled chemicals are extracted from the calibrated hyperspectral images; (c) spectral subtraction of backgrounded impact stemmed particularly from ambient river water; (d) outliers are removed from the extracted data and checked for validity, then mean spectral signature is delineated using a smoothing method (e.g., super smoother); (e) each spectrum per chemical is normalized for further standardized correlation assessment; (f) characteristic features from the normalized full spectrum are extracted to uniquely distinguish the spectral signature of a chemical. Based on the above procedure, we have developed a characteristic library for 18 hazardous chemicals assuming a scenario of leaking them into rivers and tested the feasibility of the library to recognize unknown chemicals, which meaningfully worked with >70% success rate.

Throughout developing a standardized procedure to develop a spectral library and perform a recognition test, we have the following conclusions and suggestions for future research:

(1) Hyperspectral-based detection of solvent hazardous chemicals in the riverine environment was scarce, thus very little former research was referable. In this regard, though our initial effort proposed in this study is preliminary and should be more

verified, such a library will be referenceable for further research. Practically, the library can be useful for the real-time detection and distinction between hazardous chemicals by facilitating a response to the occurrence of chemical accidents. We highly anticipate that more subtle aspects of enhancing performance of the spectral library will continue to be investigated. From this perspective, further research efforts as well as appropriate guidelines to synthesize various water environment indices such as the concentration of organic matters, concentration of algae, turbidity and water depth are required.

(2) At the initial stages of this study, we considered more than 100 hazardous chemicals, but only covering a small portion of them given the danger of handling them since several of them were forbidden to be treated without permission from national security. In addition, practical abundance to fulfill a solid library even for available chemicals was therefore limited, because it was impossible to obtain sufficient in-situ samples. Instead, the mobile carrier mounting hyperspectral camera was useful for mimicking line-scanning hyperspectral imaging process in outdoor hyperspectral sampling of very low concentration of hazardous chemical samples.

(3) We arbitrarily assigned a criterion for the maximum number of characteristic bands (or coverage) as five. Similarly, ranking criteria to define recognition success was set up as less than third rank. Though we verified that these criteria are suitable to build and utilize a spectral library, such ambiguity in properly defining the optimal criteria remained and should be resolved. For example, we speculate that spectral libraries can better work if developed with the greater number of spectral images, reflecting diverse measurement environments with applying advanced AI techniques to train the capacity to recognize chemicals' signature. Also, the rank in the recognition process was provided in this study as correlation coefficient, rather than considered to suggest probability.

(4) Characterizing distinctive features among the full spectrum was effective in addition to excluding the ambient spectral impact, such as river water, and normalizing to reduce the impacts from concentration. However, other factors influencing spectral signature should be considered.

(5) Beyond identifying hazardous chemicals, the approach proposed herein for building a characteristic spectral library can also be applied for recognizing other types of solvent materials.

(6) For the better recognition rate and practical uses, various water environment indices, such as the concentration, weather conditions, turbidity, water depth and water color, should be considered ensuring they contain a great number of in-situ spectral images. In those cases, artificial intelligence techniques might be a good solution.

Author Contributions: Conceptualization, D.K. and Y.D.K.; methodology, H.Y.; software, H.Y.; validation, Y.G. and S.-H.N.; formal analysis, Y.G.; investigation, Y.G. and D.K.; resources, Y.D.K.; data curation, S.-H.N. and Y.G.; writing—original draft preparation, Y.G.; writing—review and editing, D.K.; visualization, Y.G.; supervision, D.K. and Y.D.K.; project administration, Y.D.K.; funding acquisition, Y.D.K. and D.K. All authors have read and agreed to the published version of the manuscript.

Funding: Korea Agency for Infrastructure Technology Advancement (KAIA) grant funded by Korea Ministry of Environment (MOE) (Grant 22DPIW-C153746-04).

Institutional Review Board Statement: Not applicable.

Informed Consent Statement: Not applicable.

Data Availability Statement: Not applicable.

Acknowledgments: This research was supported by the Korea Agency for Infrastructure Technology Advancement (KAIA) grant funded by Korea Ministry of Environment (MOE) (Grant 22DPIW-C153746-04).

Conflicts of Interest: The authors declare no conflict of interest.

References

1. You, J.S.; Chung, Y.J. Case analysis of the harmful chemical substances' spill. *Fire Sci. Eng.* **2014**, *28*, 90–98. [CrossRef]
2. Lee, J.S.; Jung, M.S.; Cho, M.S.; Ahn, S.Y.; Kim, K.J.; Yoon, Y.S.; Yoon, J.H.; Seok, K.S. Review on detection analysis and environmental impacts for nitric acid spill response. *Korean J. Hazard. Mater.* **2013**, *1*, 25–30.
3. Kisevic, M.; Morovic, M.; Andricevic, R. The use of hyperspectral data for evaluation of water quality parameters in the river Sava. *Fresenius Environ. Bull.* **2016**, *25*, 4814–4822.
4. Fan, C.L. Spectral Analysis of Water Reflectance for Hyperspectral Remote Sensing of Water Quality in Estuarine Water. *J. Geosci. Environ. Prot.* **2014**, *2*, 19–27.
5. Pokrzywinski, K.; Johansen, R.; Reif, M.; Bourne, S.; Hammond, S.; Fernando, B. Remote sensing of the cyanobacteria life cycle: A mesocosm temporal assessment of a *Microcystis* sp. bloom using coincident unmanned aircraft system (UAS) hyperspectral imagery and ground sampling efforts. *Harmful Algae* **2022**, *117*, 102268. [CrossRef] [PubMed]
6. Lu, Q.; Si, W.; Wei, L.; Li, Z.; Xia, Z.; Ye, S.; Xia, Y. Retrieval of Water Quality from UAV-Borne Hyperspectral Imagery: A Comparative Study of Machine Learning Algorithms. *Remote Sens.* **2021**, *13*, 3928. [CrossRef]
7. Kwon, S.; Shin, J.; Seo, I.; Noh, H.; Jung, S.; You, H. Measurement of suspended sediment concentration in open channel flows based on hyperspectral imagery from UAVs. *Adv. Water Resour.* **2022**, *159*, 104076. [CrossRef]
8. You, H.J. Development of riverine bathymetry survey technique using drone-based hyperspectral image. Ph.D. Dissertation, Dankook University, Yongin, Republic of Korea, 2018.
9. Warren, R.; Cohn, D. Chemical detection on surfaces by hyperspectral imaging. *J. Appl. Remote Sen.* **2017**, *11*, 015013. [CrossRef]
10. Nakamura, T. Non-Destructive Trace Detection of Explosives Using Pushbroom Scanning Hyperspectral Imaging System. *Sensors* **2019**, *19*, 97.
11. Zhou, S.; Kaufmann, H.; Bohn, N.; Bochow, M.; Kuester, T.; Segl, K. Identifying distinct plastics in hyperspectral experimental lab-, aircraft-, and satellite data using machine/deep learning methods trained with synthetically mixed spectral data. *Remote Sens. Environ.* **2022**, *281*, 113263. [CrossRef]
12. Yang, J.W.; Cho, G.S. Construction and evaluation of spectral library for SWIR hyperspectral image analysis. *J. KOGSIS* **2019**, *27*, 3–12. [CrossRef]
13. Kokaly, R.F.; Clark, R.N.; Swayze, G.A.; Livo, K.E.; Hoefen, T.M.; Pearson, N.C.; Wise, R.A.; Benzel, W.M.; Lowers, H.A.; Driscoll, R.L.; et al. *USGS Spectral Library Version 7*; U.S. Geological Survey: Reston, VA, USA, 2017.
14. Baldridge, A.M.; Hook, S.J.; Grove, C.I.; Rivera, G. The ASTER spectral library version 2.0. *Remote Sens. Environ.* **2009**, *113*, 711–715. [CrossRef]
15. Meerdink, S.K.; Hook, S.J.; Roberts, D.A.; Abbott, E.A. The ECOSTRESS spectral library version 1.0. *Remote Sens. Environ.* **2019**, *203*, 111–196. [CrossRef]
16. Corning. Corning microHSI 410 SHARK: Integrated, Coherent, Airborne Hyperspectral Imaging System. 2017. Available online: https://www.corning.com/microsites/coc/oem/documents/hyperspectral-imaging/Corning-MicroHSI-410-SHARK-Brochure.pdf (accessed on 23 December 2022).
17. Fowler, J.E. Compressive pushbroom and whiskbroom sensing for hyperspectral remote-sensing imaging. In Proceedings of the 2014 IEEE International Conference on Image Processing (ICIP), Paris, France, 27–30 October 2014.
18. Mustard, J.F.; Staid, M.I.; Fripp, W.J. A semianalytical approach to the calibration of AVIRIS data to reflectance over water. *Remote Sens. Environ.* **2001**, *75*, 335–349. [CrossRef]
19. McCoy, R.M. *Field Methods in Remote Sensing*; The Guilford Press: New York, NY, USA, 2005.
20. Friedman, J.H. *A Variable Span Scatterplot Smoother*; Laboratory for Computational Statistics, Stanford University Technical Report No. 5; Stanford University: Stanford, CA, USA, 1984.
21. Cleveland, W.S.; Devlin, S.J. Locally Weighted Regression: An Approach to Regression Analysis by Local Fitting. *J. Am. Stat. Assoc.* **1988**, *83*, 596–610. [CrossRef]
22. Fox, S.; Southam, P.; Pantin, F.; Kennaway, R.; Robinson, S.; Castorina, G.; Sánchez-Corrales, Y.E.; Sablowski, R.; Chan, J.; Grieneisen, V.; et al. Spatiotemporal coordination of cell division and growth during organ morphogenesis. *Environ. Sci. Biol.* **2018**, *16*, e2005952. [CrossRef] [PubMed]
23. Friedman, J.H. *SMART User's Guide*; Laboratory for Computational Statistics, Stanford University Technical Report No. 1; Stanford University: Stanford, CA, USA, 1984.
24. Kriegler, F.J.; Malila, W.A.; Nalepka, R.F.; Richardson, W. Preprocessing Transformations and Their Effects on Multispectral Recognition. *Proc. Sixth Int. Symp. Remote Sens. Environ.* **1969**, *2*, 13–16.
25. McFeeters, S.K. The Use of Normalized Difference Water Index (NDWI) in the Delineation of Open Water Features. *Int. J. Remote Sens.* **1996**, *17*, 1425–1432. [CrossRef]

Disclaimer/Publisher's Note: The statements, opinions and data contained in all publications are solely those of the individual author(s) and contributor(s) and not of MDPI and/or the editor(s). MDPI and/or the editor(s) disclaim responsibility for any injury to people or property resulting from any ideas, methods, instructions or products referred to in the content.

remote sensing

MDPI

Technical Note

Precipitable Water Vapor Retrieval Based on DPC Onboard GaoFen-5 (02) Satellite

Chao Wang [1], Zheng Shi [2,3,*], Yanqing Xie [4], Donggen Luo [5], Zhengqiang Li [2,3], Decheng Wang [1] and Xiangning Chen [1]

[1] Space Information Academy, Space Engineering University, Beijing 101416, China
[2] State Environment Protection Key Laboratory of Satellite Remote Sensing, Aerospace Information Research Institute, Chinese Academy of Sciences, Beijing 100094, China
[3] University of Chinese Academy of Sciences, Beijing 100049, China
[4] Shanghai Institute of Satellite Engineering, Shanghai 201109, China
[5] Anhui Institute of Optics and Fine Mechanics, Hefei Institutes of Physical Science, Chinese Academy of Sciences, Hefei 230031, China
* Correspondence: shizheng@radi.ac.cn

Abstract: GaoFen-5 (02) (GF5-02) is a new Chinese operational satellite that was launched on 7 September 2021. The Directional Polarimetric Camera (DPC) is one of the main payloads and is mainly used for the remote sensing monitoring of atmospheric components such as aerosols and water vapor. At present, the DPC is in the stage of on-orbit testing, and no public DPC precipitable water vapor (PWV) data are available. In this study, a PWV retrieval algorithm based on the spectral characteristics of DPC data is developed. The algorithm consists of three parts: (1) the construction of the lookup table, (2) the calculation of water vapor absorption transmittance (WVAT) in the band at 910 nm, and (3) DPC PWV retrieval. The global PWV results derived from DPC data are spatially continuous, which can illustrate the global distribution of water vapor content well. The validation based on the Aerosol Robotic Network (AERONET) PWV data shows that the DPC PWV data have accuracy similar to that of Moderate-resolution Imaging Spectroradiometer (MODIS) PWV data, with coefficient correlation of determination (R^2), mean absolute error (MAE), and relative error (RE) of 0.32, 0.30, and 0.93 using the DPC and 0.23, 0.36, and 0.96 using the MODIS, respectively. The results show that our proposed DPC PWV retrieval algorithm is feasible and has high accuracy. By analyzing the errors, we found that the calibration coefficients of the DPC in the 865 nm and 910 nm bands need to be updated.

Keywords: GF5-02 satellite; Directional Polarimetric Camera (DPC); precipitable water vapor (PWV); remote sensing retrieval

Citation: Wang, C.; Shi, Z.; Xie, Y.; Luo, D.; Li, Z.; Wang, D.; Chen, X. Precipitable Water Vapor Retrieval Based on DPC Onboard GaoFen-5 (02) Satellite. *Remote Sens.* **2023**, *15*, 94. https://doi.org/10.3390/rs15010094

Academic Editor: Kenji Nakamura

Received: 28 November 2022
Revised: 18 December 2022
Accepted: 20 December 2022
Published: 24 December 2022

Copyright: © 2022 by the authors. Licensee MDPI, Basel, Switzerland. This article is an open access article distributed under the terms and conditions of the Creative Commons Attribution (CC BY) license (https://creativecommons.org/licenses/by/4.0/).

1. Introduction

Water vapor is one of the important sources of the greenhouse effect [1,2] and a key factor affecting precipitation and severe weather [3,4]. The main source of atmospheric water vapor is the evaporation of water and the transpiration of plants. Although water vapor makes up only a small part of the entire atmosphere, it plays important roles in the Earth's weather system and climate change. In addition, water vapor emits and absorbs radiation in a specific spectral range, which significantly affects the accuracy of quantitative remote sensing, such as aerosol property retrieval and atmospheric correction of remote sensing data [5–7]. Driven by thermodynamics, atmospheric water vapor shows distinct spatial and temporal differences in certain regions [8,9]. Precipitable water vapor (PWV) can characterize the water vapor content in the atmosphere. The PWV is the water vapor content in a vertical column per unit cross-sectional area from the ground to the top of the atmosphere. A study found that the total water vapor in the atmosphere increases by about 1% every 10 years [10]. Therefore, the satellite remote sensing of PWV has great significance

for monitoring water vapor content on a large spatial scale and for supporting studies on climate change, weather systems, and atmospheric correction of remote sensing data.

GaoFen-5 (02) (GF5-02) is a new Chinese satellite that was launched on 7 September 2021. The multi-view polarization camera Directional Polarimetric Camera (DPC) is one of the main payloads. The DPC has eight spectral observation channels in the spectral range from 0.4 μm to 0.9 μm, and it has enhanced observation information for aerosol remote sensing [11,12]. Since the DPC aerosol retrieval channels are affected by water vapor absorption, PWV data are needed to –eliminate the water vapor absorbing effect before aerosol retrieval. At present, researchers have developed many types of high-precision PWV data for different satellite sensors, such as Moderate-resolution Imaging Spectroradiometer (MODIS) PWV data and Medium Resolution Spectral Imager-2 (MERSI-2) PWV data [13–15]. However, due to the different transit times of different satellites and the significant temporal difference in the distribution of atmospheric water vapor, it is difficult to achieve accurate water vapor absorption correction of DPC data using an external PWV dataset. To solve this problem, the water vapor absorption band (910 nm) for water vapor retrieval was set in the DPC. It allows PWV results to be produced by means of DPC observation directly. In addition, as a new satellite PWV source, DPC PWV data can also provide data support for research on, e.g., climate change and weather systems.

At present, the DPC on the GF5-02 satellite is still in the on-orbit test period, and no public PWV data are available. Therefore, it is necessary and urgent to develop a DPC PWV retrieval algorithm for the production of a PWV dataset. We can roughly divide the existing water vapor retrieval algorithms into four categories according to the wavelength used: visible light algorithms, near-infrared algorithms, thermal infrared algorithms, and microwave algorithms. Visible light algorithms are developed based on the absorption characteristics of water vapor in the visible light spectrum. Such algorithms have been successfully used for water vapor retrieval with sensors such as Ozone Monitoring Instrument (OMI) and Global Ozone Monitoring Experiment-2 (GOME-2) [16,17]. Since these algorithms require observation in the visible light spectrum, they can only be implemented in cloudless areas during the daytime. Near-infrared algorithms use data from the near-infrared band, which requires the sensor to have both the water vapor absorption band and the non-absorption band in the spectral range of 850–1250 nm. Near-infrared algorithms have been applied to water vapor retrieval using satellite data, such as MODIS and MERSI-2 [13,14]. Because near-infrared algorithms perform in high-land-surface-reflectance conditions, they are only suitable for PWV retrieval in cloudless land and ocean glint areas during the daytime. Thermal infrared algorithms are developed based on thermal infrared split window channels. They are developed for and have been applied to sensors such as Advanced Very High Resolution Radiometer (AVHRR) and Spinning Enhanced Visible and Infrared Imager (SEVIRI) [18,19]. Since these algorithms only use thermal infrared data to retrieve water vapor, they can be used for both day and night water vapor detection in cloud-free areas. Microwave algorithms are suitable for sensors with microwave observation capabilities and have been successfully applied to water vapor retrieval with sensors such as Calibration Microwave Radiometer (CMR) and Microwave Radiation Imager (MWRI) [20,21]. Since microwaves have a certain penetration ability, these methods can be used for water vapor detection in both cloudless and cloudy areas, which is also a unique advantage over other water vapor retrieval algorithms.

Since the DPC has a water vapor absorption channel in the 910 nm band, only a near-infrared water vapor retrieval algorithm can be developed for water vapor retrieval with the DPC. The water vapor absorption band at 910 nm and the nearby band at 865 nm located in the atmospheric window are used to quantify the water vapor absorption transmittance (WVAT) in the DPC 910 nm channel according to the difference in the top of the atmosphere (TOA) reflectance in these two bands. PWV is then retrieved based on the calculated WVAT. We evaluated the accuracy of DPC PWV using AERONET PWV data as ground-truth data and MODIS PWV data for intercomparison. The structure of this paper is as follows: We introduce the dataset used in Section 2.1 and the retrieval strategy for DPC PWV retrieval

in Section 2.2. Then, the global distribution of DPC PWV is shown in Section 3.1. After that, we show the accuracy assessment of DPC PWV in Section 3.2, including validation against ground-based PWV and intercomparison with MODIS PWV data. In Section 4, we discuss the improvement of the existing bias of DPC PWV data. Finally, the paper is concluded in Section 5.

2. Materials and Methods

2.1. Dataset

2.1.1. DPC Data

The Chinese GF5-02 satellite was launched on 7 September 2021, at the local time of descending node of 13:30. The DPC is one of seven payloads of GF5-02 and is mainly used for the retrieval of atmospheric parameters. The DPC has multi-angle observation capabilities and can achieve a maximum of 17 effective observations in different views of one target. A DPC image has a swath width of 1850 km and a spatial resolution of 1.62 km at the nadir point. The DPC has eight spectral channels with a spectral range from visible to near-infrared wavelengths. Only the channels at 490 nm, 670 nm, and 865 nm have extra polarization observation, and the other five channels at 443 nm, 565 nm, 763 nm, 765 nm, and 910 nm can only realize intensity observation. Among them, the laboratory calibration uncertainty of DPC intensity data is better than 3.94%, and the detection accuracy of polarization data is better than 0.0066. In this study, we used data from two near-infrared bands of the DPC (865 nm and 910 nm) to retrieve water vapor. The signal received in the 865 nm band is not affected by atmospheric absorption, and the signal received in the 910 nm band is strongly affected by water vapor absorption. The spectral response functions (SRFs) of these two bands and the WVAT spectrum are shown in Figure 1. The blue line in the legend indicates the WVAT when the view zenith angle and the solar zenith angle are both equal to 0° and PWV is equal to 1 cm. The yellow line is the WVAT when the zenith angle of the satellite and the sun is equal to 0° and PWV is equal to 3 cm. In this study, we used 10 days of DPC data from 20 January 2022 to 29 January 2022 provided by the China Centre for Resources Satellite Data and Application (CRESDA) during the on-orbit testing of the GF5-02 satellite.

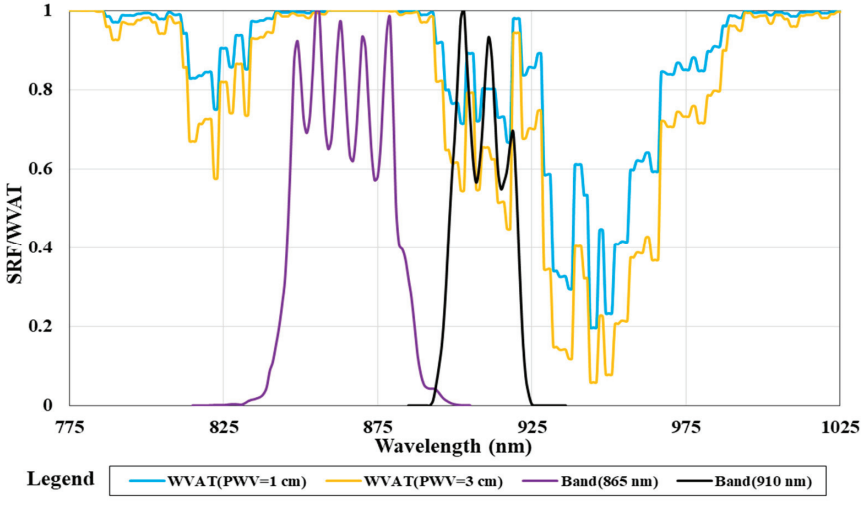


Figure 1. The SRFs of two near-infrared bands of DPC are illustrated by a purple line (denotes 865 nm) and a black line (denotes 910 nm), respectively. The blue line and yellow line represent the WVAT when PWV is equal to 1 and 3 cm, respectively [22].

2.1.2. MODIS PWV

The MODIS sensors on board the Terra and Aqua satellites have five near-infrared bands that can be used for water vapor retrieval: Band 2 (865 nm), Band 5 (1240 nm), Band 17 (905 nm), Band 18 (936 nm), and Band 19 (940 nm). Band 2 and Band 5 are located in the atmospheric window region and are not affected by the absorption of atmospheric gases, while Bands 17–19 are located in the spectral region of strong water vapor absorption, and the absorption effect of gases other than water vapor on these three bands is negligible. National Aeronautics and Space Administration (NASA) released official MODIS PWV data based on the above five bands. The basic principle of the official MODIS PWV retrieval algorithm is as follows: firstly, the TOA reflectance in Bands 17–19 without considering water vapor absorption is calculated using the TOA reflectance in MODIS Band 2 and Band 5 by means of linear interpolation; then, the water vapor absorption transmittance in these three water vapor absorption bands is calculated according to the TOA reflectance in Bands 17–19 and the actual TOA reflectance in Bands 17–19 when water vapor absorption is not considered. Finally, water vapor retrieval can be realized according to the obtained water vapor absorption transmittance [13]. Since we used the same PWV retrieval strategy using near-infrared channels as MODIS, and the MODIS PWV data have been extensively validated with high accuracy [23–27], we performed an intercomparison between DPC-derived PWV and MODIS official PWV data (MYD05) to comprehensively evaluate the accuracy of our developed algorithm in this research. Due to the large number of MODIS PWV data and due to the accuracies of MOD05 data developed based on Terra/MODIS data and MYD05 data developed based on Aqua/MODIS data being close [28], MYD05 data were randomly selected as the representatives of MODIS PWV data to participate in the intercomparison. The MODIS official water vapor product (MOD05/MYD05) mentioned above can be accessed at the NASA data website (https://ladsweb.modaps.eosdis.nasa.gov, accessed on 25 February 2022).

2.1.3. Ground-Based PWV Data

Aerosol Robotic Network (AERONET) is a global atmospheric aerosol observation network currently consisting of hundreds of solar photometers [29]. AERONET has been in continuous operation for more than 25 years. Although its major task is to monitor aerosol properties, it can also provide high-precision PWV data. AERONET PWV data have an uncertainty of about 10% [30,31]. Because AERONET can provide high-precision PWV data for long time series and AERONET sites are widely distributed around the world, AERONET PWV data are widely used as verification data for water vapor remote sensing retrieval results [32–34]. In this study, remote sensing PWV data were validated using level 1.5 AERONET data version 3 (data after cloud masking and quality control) [35], which can be downloaded from the AERONET homepage (https://aeronet.gsfc.nasa.gov, accessed on last accessed on 5 March 2022).

2.2. Methods

The PWV retrieval algorithm developed for the DPC in this study is mainly composed of three parts: (1) the construction of the DPC water vapor retrieval lookup table, (2) the calculation of WVAT in the DPC 910 nm band, and (3) DPC PWV retrieval. The flowchart of DPC PWV retrieval is shown in Figure 2.

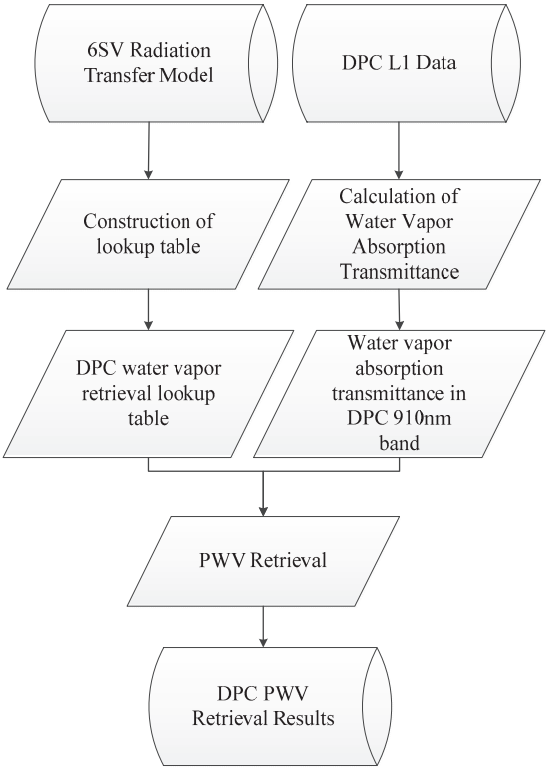


Figure 2. Flow chart of DPC water vapor retrieval.

2.2.1. Construction of DPC Water Vapor Retrieval Lookup Table

In this study, the radiative transfer model Second Simulation of a Satellite Signal in the Solar Spectrum vector (6SV) [36] was used to simulate the water vapor absorption transmittance in the DPC 910 nm band under different observed geometries and water vapor content. Then, we achieved water vapor retrieval by minimizing the simulated water vapor absorption transmittance and the actual water vapor absorption transmittance. Running 6SV in real time to calculate the water vapor absorption transmittance for PWV retrieval for each pixel is time-consuming, resulting in low retrieval efficiency. To improve the efficiency of DPC PWV retrieval, a 4-dimensional lookup table was constructed using 6SV before PWV retrieval. These four dimensions are solar zenith angle (0–72°, interval of 4°), observed zenith angle (0–72°, interval of 4°), PWV (0–8 cm, interval of 0.1 cm), and DPC 910 nm band water vapor absorption transmittance.

2.2.2. WVAT Calculation of DPC 910 nm

The received signal of DPC in near-infrared channels can be expressed as [10]

$$L_{sen}^{\lambda} = T_{g}^{\lambda}\left(L_{c}^{\lambda} + L_{0}^{\lambda}T_{\uparrow}^{\lambda}T_{\downarrow}^{\lambda}\rho_{s}^{\lambda}\right) \quad (1)$$

where L_{sen}^{λ} represents the radiance received at the TOA, T_{g}^{λ} represents the atmospheric absorption transmittance, L_{0}^{λ} represents the solar irradiance at the top of the atmosphere, $T_{\uparrow}^{\lambda}T_{\downarrow}^{\lambda}$ represents the atmospheric total transmittance from the sun-surface–sensor path, ρ_{s}^{λ} represents the surface reflectance, and L_{c}^{λ} represents the atmospheric path radiance.

Dividing the two sides of Formula (1) by solar irradiance L_0^λ, the formula for calculating the TOA reflectance of the DPC near-infrared band can be obtained [14].

$$R_{TOA}^\lambda = T_g^\lambda \left(\rho_0^\lambda + T_\uparrow^\lambda T_\downarrow^\lambda \rho_s^\lambda \right) \tag{2}$$

where R_{TOA}^λ represents the TOA reflectance and ρ_0^λ represents the atmospheric path reflectance.

Due to the relatively close wavelengths of the DPC bands at 865 nm and 910 nm, the difference between the path reflectance and atmospheric total transmittance in these two bands can be ignored. In addition, the surface reflectance difference between the two bands is small. Based on these reasons, it can be assumed that the TOA reflectance of the DPC in the 910 nm band is equal to that in the 910 nm band without considering atmospheric absorption [22].

In addition, the influence of atmospheric gases other than water vapor on the radiation absorption of DPC Band 8 is neglectable, which means that the WVAT in DPC Band 8 is equal to the atmospheric absorption transmittance. Since the influence of the atmosphere on the absorption at DPC 865 nm can be neglected, the WVAT at 910 nm can be calculated by dividing the TOA reflectance at 910 nm by the TOA reflectance at 865 nm.

$$T_g^{910\ nm} = R_{TOA}^{910\ nm} / R_{TOA}^{865\ nm} \tag{3}$$

where $T_g^{910\ nm}$ represents the atmospheric absorption transmittance in the DPC 910 nm band, which can also be considered as the WVAT in the DPC 910 nm band, and $R_{TOA}^{865\ nm}$ and $R_{TOA}^{910\ nm}$ represent the TOA reflectance of the DPC in the 865 nm band and 910 nm band, respectively.

2.2.3. DPC PWV Retrieval Strategy

For any pixel to be retrieved, we can simulate 81 water vapor absorption transmittances in the 910 nm band for different water vapor contents (PWV range of 0–8 cm, interval of 0.1 cm) according to the pre-constructed lookup table and the corresponding solar zenith angle and observation zenith angle of the pixel and then calculate the water vapor absorption transmittance in the DPC 910 nm band according to Formula (3) (for convenience of description, it is called T_1). Then, we can realize water vapor retrieval based on the simulated and actual WVAT in the 910 nm channel by means of linear interpolation. The specific process of retrieving water vapor by means of interpolation is as follows: two adjacent water vapor absorption transmittances are found from the 81 water vapor absorption transmittances simulated above, one of which is not less than T_1 (called T_2) and the other is not greater than T_1 (called T_3), after which we can perform water vapor inversion according to Equation (4) [37].

$$V_1 = V_2 + \frac{(V_3 - V_2) \times (T_1 - T_2)}{(T_3 - T_2)} \tag{4}$$

where V_1 represents the PWV retrieval results, and V_2 and V_3 represent PWV corresponding to T_2 and T_3, respectively.

3. Results

3.1. Global Distribution of PWV Retrieved from DPC Data

Figure 3 shows the mean values of global water vapor from 20 January 2022 to 29 January 2022. The blank areas denote no retrieval results, which happens in cloud-contaminated regions. During the last winter season, most of the regions were dry in the Northern Hemisphere. The inland areas of North America, Europe, Asia, and northern Africa had low water vapor contents (<2 cm). Coastal and off-shore regions such as southeastern India and southwestern Africa had relatively high water vapor values, about 2 cm. The PWV contents were high (>3 cm) in Myanmar and Thailand, which have considerable rainforest coverage. Places such as Brazil, Congo, and northern Australia with

rainforest land cover had high water vapor contents. In this period, the DPC PWV data derived from our developed algorithm illustrate the climate-influenced global water vapor content distribution well.

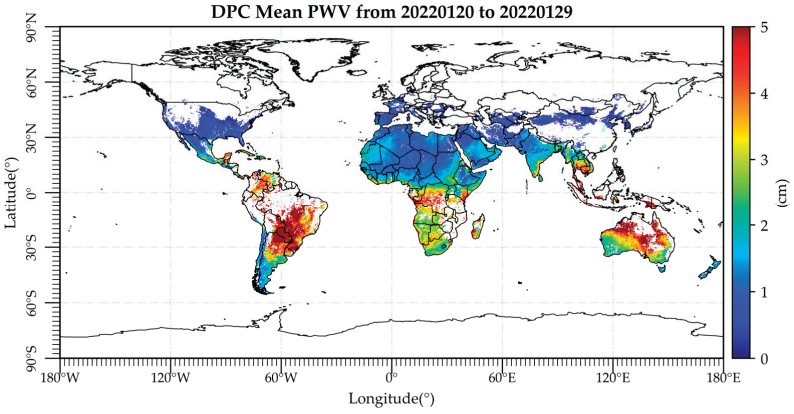


Figure 3. Global mean PWV values derived from DPC data for 20 January 2022 and 29 January 2022.

Since PWV has obvious zonal distribution characteristic, we calculated the zonally averaged absolute PWV values, which are depicted in Figure 4. As expected, the PWV content was higher at the mid-lower latitudes of the southern summer hemisphere. The mean PWV content was higher than 2 cm at latitudes from -40° to 10°. Two obvious peaks of PWV were found at -7° and -21°, with PWV content being higher than 4 cm. Rainfall, continuous cloud cover, and the transpiration of plants contribute to rainforest moisture in these mid-lower-latitude regions.

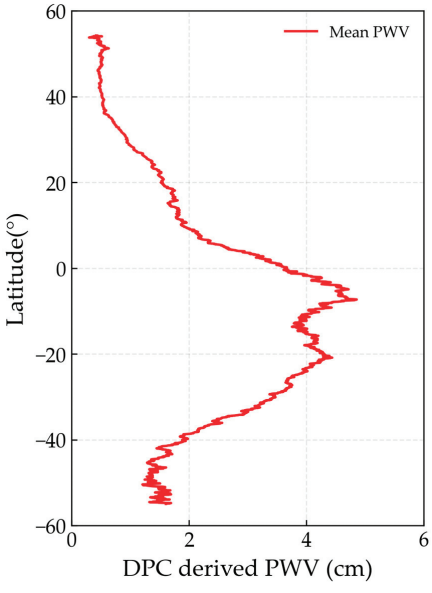


Figure 4. The 10-day zonally averaged PWV values observed using the DPC.

Figure 5 shows the variation in the statistical results of global mean PWV derived using the DPC. The highest global mean PWV value was 2.032 cm on 20 January 2022, and

the lowest value was 1.541 on 29 January 2022. A clear downward trend could be seen, except for two instances of PWV value increment on 25 January 2022 and 27 January 2022.

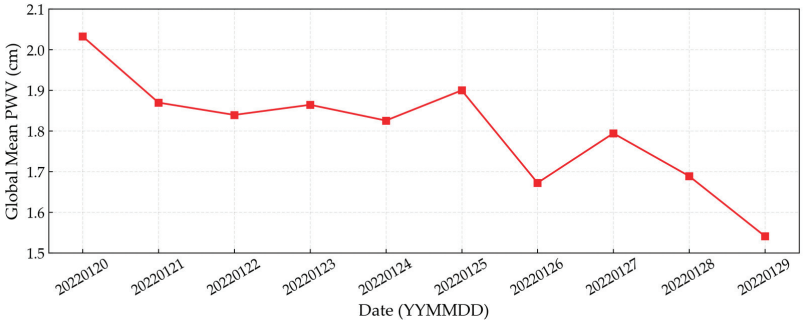


Figure 5. Global mean PWV variation from 20 January 2022 to 29 January 2022.

3.2. Accuracy Assessment

In this study, AERONET PWV data were used to evaluate the accuracy of DPC PWV data. The matching of AERONET PWV data and remote sensing PWV data was achieved according to the spatial and temporal matching method: The temporal mean of AERONET PWV data within half an hour of satellite transit was used to match the spatial mean of remote sensing PWV data in the range of 10×10 km^2 centered on the ground station [38]. We used three metrics to evaluate the accuracy of remote sensing PWV data, including mean absolute error (MAE), mean bias (MB), relative error (RE), and the coefficient of determination (R^2). The MAE was used to characterize the absolute error of remote sensing PWV data, the RE was used to characterize the relative error of remote sensing PWV data, and the MB was used to characterize whether the remote sensing PWV data were overestimated or underestimated. The calculation formulas of MAE, MB, and RE are as follows:

$$MAE = \sum_{i=1}^{N} \left| P_i - P_i' \right| / N \tag{5}$$

$$MB = \sum_{i=1}^{N} \left(P_i - P_i' \right) / N \tag{6}$$

$$RE = \sum_{i=1}^{N} \left| P_i - P_i' \right| / \sum_{i=1}^{N} P_i' \tag{7}$$

where i represents a serial number, N represents the number of valid matching results between remote sensing PWV data and AERONET PWV data, P_i represents remote sensing PWV data, and $P_i^{'}$ is the date corresponding to AERONET PWV data related to P_i. R^2 indicates the correlation between satellite PWV and AERONET PWV. To more comprehensively evaluate the accuracy of the DPC PWV data developed in this study, this study not only used ground-based data to verify the DPC PWV data but also validated the accuracy of MODIS PWV data released by NASA for comparison. The verification results of DPC PWV data and MODIS PWV data are shown in Figure 6. The MAE and RE of DPC PWV data were 0.32 cm and 0.30, respectively, and the MAE and RE of MODIS PWV data released by NASA were 0.23 cm and 0.26, respectively. The DPC and MODIS PWV results presented an overestimation situation with MB values of 0.29 and 0.21, respectively. Both DPC PWV and MODIS PWV had a high correlation with AERONET PWV, with R^2 values of 0.93 and 0.96, respectively. In general, DPC PWV data and MODIS PWV data had similar accuracy, with relatively close absolute error and relative error values. This meant that the overall accuracy of DPC PWV data was close to that of MODIS PWV data released by NASA. Since MODIS PWV data are high-precision PWV data [23], it can be considered that the DPC PWV data developed in this study have high accuracy.

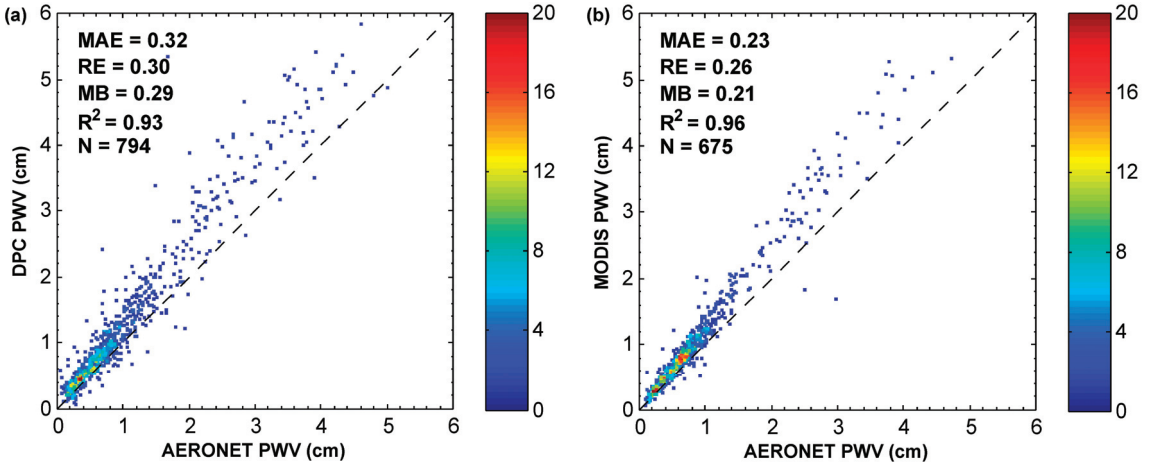


Figure 6. Validation results of satellite PWV data based on AERONET PWV data: (**a**) validation results of DPC PWV data; (**b**) validation results of MODIS PWV data. The color of each point denotes the number density at its location. The dotted line is the 1:1 line.

4. Discussion

Although the PWV data developed based on DPC data in this study have a low absolute error and relative error, the DPC PWV data still have some room for improvement. We analyzed the validation results and found that the DPC PWV data had a distinct overestimation trend (MB = 0.29 cm). To further explain this bias, we analyzed the DPC TOA reflectance in the 865 nm and 910 nm channels. We removed the absorption effect of water vapor on the 910 nm channel to obtain the corrected TOA reflectance, using the 6SV model with AERONET PWV data as input. Then, we compared the TOA reflectance in the 865 nm band with the corrected TOA reflectance in the 910 nm band. Figure 7 illustrates this comparison. Previous studies have shown that the TOA reflectance at 865 nm and the 910 nm TOA reflectance after water vapor absorption correction should be equal [37]. However, a distinct and systematic deviation is shown in Figure 7, which is inconsistent with the previous research conclusions. Since the DPC data used in this study were obtained during the on-orbit test period, the above inconsistency should be mainly because the calibration coefficients of the DPC 865 nm and 910 nm channels were not updated in time. A more detailed analysis of Figure 7 shows that the TOA reflectance in the DPC 865 nm band was systematically greater than the TOA reflectance in the DPC 910 nm band after water vapor absorption correction, which caused the WVAT in the DPC 910 nm band to be underestimated, resulting in an overestimation of PWV retrieval. Therefore, to further improve the accuracy of DPC PWV data in the future, it is necessary to update the calibration parameters of DPC 865 nm and 910 nm channels in time.

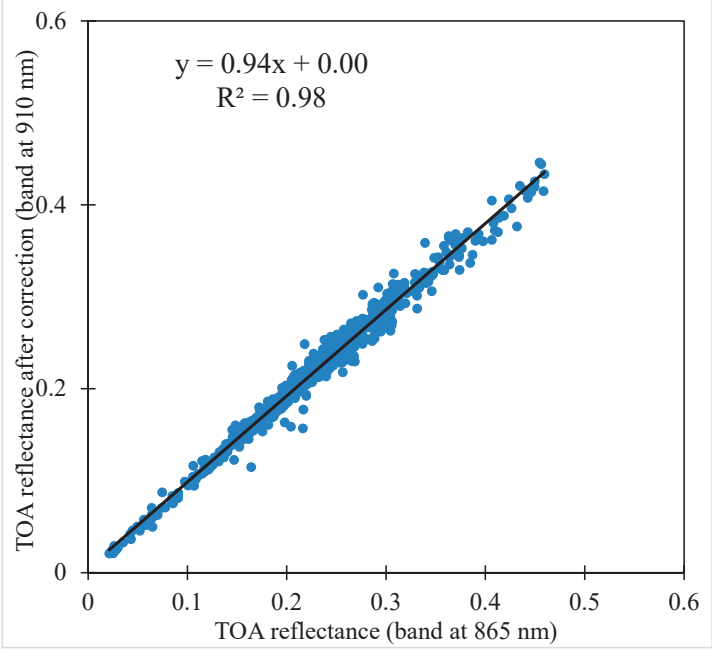


Figure 7. Comparison between DPC TOA reflectance in the 865 nm band and DPC TOA reflectance in the 910 nm band after water vapor absorption correction. The correction is implemented using 6SV with AERONET PWV as input.

5. Conclusions

The DPC is one of the main payloads on board the newly launched GF5-02 satellite. At present, the DPC is in the stage of on-orbit testing, and no publicly released DPC PWV data are available. In this study, we developed a DPC-suited water vapor retrieval algorithm based on the spectral characteristics of DPC data. The DPC water vapor retrieval algorithm consists of three parts: (1) the construction of the PWV retrieval lookup table, (2) the calculation of the WVAT in the DPC 910 nm band, and (3) DPC water vapor retrieval. The DPC PWV data are spatially continuous and can reflect the global water vapor content distribution. The validation results based on ground-based data show that the DPC PWV data developed in this study have metric values close to those of the widely used and accurate MODIS PWV data published by NASA. Although the DPC PWV data developed in this study have low absolute error and relative error, we still found a systematic overestimation trend in DPC PWV data. We found it was mainly caused by the calibration error. The DPC needs an updated calibration coefficient to further improve the accuracy of PWV products in the future.

Author Contributions: This work was carried out in collaboration with all the authors. Conceptualization, C.W., Z.S., Y.X., Z.L. D.L. and X.C.; Methodology, C.W., Z.S., Y.X. Z.L. and D.L.; Data acquisition, Z.S. and Y.X.; Supervision, Z.S. and Y.X.; Visualization, C.W., Z.S., Y.X. and D.L.; Validation; C.W. and Y.X.; Original draft preparation, C.W. and Y.X.; Writing—review and editing, Z.S., Y.X., Z.L., D.W. and X.C. All authors have read and agreed to the published version of the manuscript.

Funding: This work was supported by National Key R&D Program of China (grant No. 2020YFE0200700), National Natural Science Foundation of China (grant No. 42175147), and National Outstanding Youth Foundation of China (grant No. 41925019).

Data Availability Statement: The DPC data can be obtained from China Centre for Resources Satellite Data and Application (available online: http://www.cresda.com (accessed on 20 February 2022)).

The AERONET data can be downloaded from the official website of AERONET (https://aeronet.gsfc.nasa.gov/, last accessed on 5 March 2022). The MODIS data can be downloaded from the official website of NASA (https://ladsweb.modaps.eosdis.nasa.gov/, last accessed on 25 February 2022).

Acknowledgments: The authors thank Jun Lin, Zhongzheng Hu, and Lanlan Fan from China Centre for Resources Satellite Data and Application for providing DPC L1 data during the on-orbit testing of the Gaofen5-02 satellites. We would also like to thank the PI(s), Co-I(s), and their staff for their efforts in establishing and maintaining the AERONET sites for providing valuable validation datasets. In addition, we thank NASA for providing us with MODIS water vapor data.

Conflicts of Interest: The authors declare no conflict of interest.

References

1. Held, I.M.; Soden, B.J. Water Vapor Feedback and Global Warming. *Annu. Rev. Energy Environ.* **2000**, *25*, 441–475. [CrossRef]
2. Solomon, S.; Rosenlof, K.H.; Portmann, R.W.; Daniel, J.; Davis, S.M.; Sanford, T.J.; Plattner, G.-K. Contributions of Stratospheric Water Vapor to Decadal Changes in the Rate of Global Warming. *Science* **2010**, *327*, 1219–1223. [CrossRef] [PubMed]
3. Lyngwa, R.V.; Nayak, M.A. Atmospheric river linked to extreme rainfall events over Kerala in August 2018. *Atmos. Res.* **2021**, *253*, 105488. [CrossRef]
4. Reid, K.J.; Rosier, S.M.; Harrington, L.J.; King, A.D.; Lane, T.P. Extreme rainfall in New Zealand and its association with Atmospheric Rivers. *Environ. Res. Lett.* **2021**, *16*, 044012. [CrossRef]
5. Xie, Y.; Li, Z.; Guang, J.; Hou, W.; Salam, A.; Ali, Z.; Fang, L. Aerosol Optical Depth Retrieval Over South Asia Using FY-4A/AGRI Data. *IEEE Trans. Geosci. Remote Sens.* **2022**, *60*, 1–14. [CrossRef]
6. Levy, R.C.; Mattoo, S.; Munchak, L.A.; Remer, L.A.; Sayer, A.M.; Patadia, F.; Hsu, N.C. The Collection 6 MODIS aerosol products over land and ocean. *Atmos. Meas. Tech.* **2013**, *6*, 2989–3034. [CrossRef]
7. Xue, Y.; He, X.; Xu, H.; Guang, J.; Guo, J.; Mei, L. China Collection 2.0: The aerosol optical depth dataset from the synergetic retrieval of aerosol properties algorithm. *Atmos. Environ.* **2014**, *95*, 45–58. [CrossRef]
8. Jade, S.; Vijayan, M.S.M. GPS-based atmospheric precipitable water vapor estimation using meteorological parameters interpolated from NCEP global reanalysis data. *J. Geophys. Res.* **2008**, *113*, D03106. [CrossRef]
9. Wang, Z.; Sun, M.; Yao, X.; Zhang, L.; Zhang, H. Spatiotemporal Variations of Water Vapor Content and Its Relationship with Meteorological Elements in the Third Pole. *Water* **2021**, *13*, 1856. [CrossRef]
10. Allan, R.P.; Willett, K.M.; John, V.O.; Trent, T. Global Changes in Water Vapor 1979–2020. *J. Geophys. Res. Atmos.* **2022**, *127*, e2022JD036728. [CrossRef]
11. Li, Z.; Hou, W.; Hong, J.; Zheng, F.; Luo, D.; Wang, J.; Gu, X.; Qiao, Y. Directional Polarimetric Camera (DPC): Monitoring aerosol spectral optical properties over land from satellite observation. *J. Quant. Spectrosc. Radiat. Transf.* **2018**, *218*, 21–37. [CrossRef]
12. Li, Z.; Hou, W.; Hong, J.; Fan, C.; Wei, Y.; Liu, Z.; Lei, X.; Qiao, Y.; Hasekamp, O.P.; Fu, G.; et al. The polarization crossfire (PCF) sensor suite focusing on satellite remote sensing of fine particulate matter $PM_{2.5}$ from space. *J. Quant. Spectrosc. Radiat. Transf.* **2022**, *286*, 108217. [CrossRef]
13. Gao, B.-C.; Kaufman, Y.J. Water vapor retrievals using Moderate Resolution Imaging Spectroradiometer (MODIS) near-infrared channels. *J. Geophys. Res.* **2003**, *108*, 4389. [CrossRef]
14. Wang, L.; Hu, X.; Xu, N.; Chen, L. Water Vapor Retrievals from Near-infrared Channels of the Advanced Medium Resolution Spectral Imager Instrument onboard the Fengyun-3D Satellite. *Adv. Atmos. Sci.* **2020**, *38*, 1351–1366. [CrossRef]
15. Abbasi, B.; Qin, Z.; Du, W.; Fan, J.; Zhao, C.; Hang, Q.; Zhao, S.; Li, S. An Algorithm to Retrieve Total Precipitable Water Vapor in the Atmosphere from FengYun 3D Medium Resolution Spectral Imager 2 (FY-3D MERSI-2) Data. *Remote. Sens.* **2020**, *12*, 3469. [CrossRef]
16. Wagner, T.; Beirle, S.; Sihler, H.; Mies, K. A feasibility study for the retrieval of the total column precipitable water vapour from satellite observations in the blue spectral range. *Atmos. Meas. Tech.* **2013**, *6*, 2593–2605. [CrossRef]
17. Wang, H.; Souri, A.H.; González Abad, G.; Liu, X.; Chance, K. Ozone Monitoring Instrument (OMI) Total Column Water Vapor version 4 validation and applications. *Atmos. Meas. Tech.* **2019**, *12*, 5183–5199. [CrossRef]
18. Zhang, X.; Pang, J. A comparison between atmospheric water vapour content retrieval methods using MSG2-SEVIRI thermal-IR data. *Int. J. Remote Sens.* **2015**, *36*, 5075–5086. [CrossRef]
19. Eck, T.F.; Holben, B.N. AVHRR split window temperature differences and total precipitable water over land surfaces. *Int. J. Remote Sens.* **1994**, *15*, 567–582. [CrossRef]
20. Wu, Z.; Liu, Y.; Liu, Y.; Wang, J.; He, X.; Xu, W.; Ge, M.; Schuh, H. Validating HY-2A CMR precipitable water vapor using ground-based and shipborne GNSS observations. *Atmos. Meas. Tech.* **2020**, *13*, 4963–4972. [CrossRef]
21. Du, B.; Ji, D.; Shi, J.; Wang, Y.; Lei, T.; Zhang, P.; Letu, H. The Retrieval of Total Precipitable Water over Global Land Based on FY-3D/MWRI Data. *Remote Sens.* **2020**, *12*, 1508. [CrossRef]
22. Xie, Y.; Hou, W.; Li, Z.; Zhu, S.; Liu, Z.; Hong, J.; Ma, Y.; Fan, C.; Guang, J.; Yang, B.; et al. Columnar Water Vapor Retrieval by Using Data from the Polarized Scanning Atmospheric Corrector (PSAC) Onboard HJ-2 A/B Satellites. *Remote Sens.* **2022**, *14*, 1376. [CrossRef]

23. Prasad, A.K.; Singh, R.P. Validation of MODIS Terra, AIRS, NCEP/DOE AMIP-II Reanalysis-2, and AERONET Sun Photometer Derived Integrated Precipitable Water Vapor Using Ground-Based GPS Receivers over India. *J. Geophys. Res. Atmos.* **2009**, *114*, D05107. [CrossRef]
24. Zhao, Y.; Zhao, H.; Li, J.; Xiao, G. Comprehensive Validation and Calibration of MODIS PWV over Mainland China. *Atmosphere* **2022**, *13*, 1763. [CrossRef]
25. Liu, Z.; Wong, M.S.; Nichol, J.; Chan, P.W. A Multi-Sensor Study of Water Vapour from Radiosonde, MODIS and AERONET: A Case Study of Hong Kong. *Int. J. Climatol.* **2013**, *33*, 109–120. [CrossRef]
26. Khaniani, A.S.; Nikraftar, Z.; Zakeri, S. Evaluation of MODIS Near-IR water vapor product over Iran using ground-based GPS measurements. *Atmos. Res.* **2020**, *231*, 104657. [CrossRef]
27. Vaquero-Martínez, J.; Antón, M.; Galisteo, J.P.O.d.; Cachorro, V.E.; Costa, M.J.; Román, R.; Bennouna, Y.S. Validation of MODIS integrated water vapor product against reference GPS data at the Iberian Peninsula. *Int. J. Appl. Earth Obs. Geoinf.* **2017**, *63*, 214–221. [CrossRef]
28. Bright, J.M.; Gueymard, C.A.; Killinger, S.; Lingfors, D.; Sun, X.; Wang, P.; Engerer, N.A. Climatic and Global Validation of Daily MODIS Precipitable Water Data at AERONET Sites for Clear-sky Irradiance Modelling. In Proceedings of the 12th International Conference on Solar Energy for Buildings and Industry (ISES EuroSun), Fachhochschule Ostschweiz, Hochschule Technik Rapperswil, Rapperswil, Switzerland, 10–13 September 2018; pp. 1490–1501. [CrossRef]
29. Holben, B.N.; Eck, T.F.; Slutsker, I.; Tanré, D.; Buis, J.-P.; Setzer, A.W.; Vermote, E.F.; Reagan, J.A.; Kaufman, Y.J.; Nakajima, T.; et al. AERONET-a federated instrument network and data archive for aerosol Characterization. *Remote Sens. Environ.* **1998**, *66*, 1–16. [CrossRef]
30. Pérez-Ramírez, D.; Whiteman, D.N.; Smirnov, A.; Lyamani, H.; Holben, B.N.; Pinker, R.T.; Andrade, M.; Alados-Arboledas, L. Evaluation of AERONET precipitable water vapor versus microwave radiometry, GPS, and radiosondes at ARM sites. *J. Geophys. Res. Atmos.* **2014**, *119*, 9596–9613. [CrossRef]
31. Alexandrov, M.D.; Schmid, B.; Turner, D.D.; Cairns, B.; Oinas, V.; Lacis, A.A.; Gutman, S.I.; Westwater, E.R.; Smirnov, A.; Eilers, J. Columnar water vapor retrievals from multifilter rotating shadowband radiometer data. *J. Geophys. Res.* **2009**, *114*, D02306. [CrossRef]
32. Xie, Y.; Li, Z.; Hou, W.; Guang, J.; Ma, Y.; Wang, Y.; Wang, S.; Yang, D. Validation of FY-3D MERSI-2 Precipitable Water Vapor (PWV) Datasets Using Ground-Based PWV Data from AERONET. *Remote Sens.* **2021**, *13*, 3246. [CrossRef]
33. Makarau, A.; Richter, R.; Schläpfer, D.; Reinartz, P. APDA Water Vapor Retrieval Validation for Sentinel-2 Imagery. *IEEE Geosci. Remote Sens. Lett.* **2017**, *14*, 227–231. [CrossRef]
34. Wang, Y.; Liu, H.; Zhang, Y.; Duan, M.; Tang, S.; Deng, X. Validation of FY-4A AGRI layer precipitable water products using radiosonde data. *Atmos. Res.* **2021**, *253*, 105502. [CrossRef]
35. Giles, D.M.; Sinyuk, A.; Sorokin, M.G.; Schafer, J.S.; Smirnov, A.; Slutsker, I.; Eck, T.F.; Holben, B.N.; Lewis, J.R.; Campbell, J.R.; et al. Advancements in the Aerosol Robotic Network (AERONET) Version 3 database—Automated near-real-time quality control algorithm with improved cloud screening for Sun photometer aerosol optical depth (AOD) measurements. *Atmos. Meas. Tech.* **2019**, *12*, 169–209. [CrossRef]
36. Vermote, E.F.; Tanré, D.; Deuze, J.L.; Herman, M.; Morcette, J.-J. Second Simulation of the Satellite Signal in the Solar Spectrum, 6S: An overview. *IEEE Trans. Geosci. Remote. Sens.* **1997**, *35*, 675–686. [CrossRef]
37. Li, Z.; Xie, Y.; Hou, W.; Liu, Z.; Bai, Z.; Hong, J.; Ma, Y.; Huang, H.; Lei, X.; Sun, X.; et al. In-orbit Test of the Polarized Scanning Atmospheric Corrector (PSAC) onboard Chinese Environmental Protection and Disaster Monitoring Satellite Constellation HJ-2 A/B. *IEEE Trans. Geosci. Remote Sens.* **2022**, *60*, 4108217. [CrossRef]
38. Martins, V.S.; Lyapustin, A.I.; Wang, Y.; Giles, D.M.; Smirnov, A.; Slutsker, I.; Korkin, S. Global validation of columnar water vapor derived from EOS MODIS-MAIAC algorithm against the ground-based AERONET observations. *Atmos. Res.* **2019**, *225*, 181–192. [CrossRef]

Disclaimer/Publisher's Note: The statements, opinions and data contained in all publications are solely those of the individual author(s) and contributor(s) and not of MDPI and/or the editor(s). MDPI and/or the editor(s) disclaim responsibility for any injury to people or property resulting from any ideas, methods, instructions or products referred to in the content.

remote sensing

MDPI

Article

A Comprehensive Analysis of Ultraviolet Remote Sensing for Aerosol Layer Height Retrieval from Multi-Angle Polarization Satellite Measurements

Haoran Gu [1,2], Yuhuan Zhang [3,*], Cheng Fan [2], Zhengqiang Li [2,4], Weizhen Hou [2,4], Zhenhai Liu [5], Yisong Xie [2], Hua Xu [2,4], Luo Zhang [2] and Jinji Ma [1]

1 School of Geography and Tourism, Anhui Normal University, Wuhu 241003, China
2 State Environmental Protection Key Laboratory of Satellite Remote Sensing, Aerospace Information Research Institute, Chinese Academy of Sciences, Beijing 100101, China
3 Satellite Application Center for Ecology and Environment, Ministry of Ecology and Environment, Beijing 100094, China
4 University of Chinese Academy of Sciences, Beijing 100049, China
5 Anhui Institute of Optics and Fine Mechanics, Chinese Academy of Sciences, Hefei 230031, China
* Correspondence: zhangyh@secmep.cn

Abstract: Based on the optimal estimation (OE) theory and information content analysis method, we discuss the ability to include the multi-angle satellite ultraviolet polarization channel to retrieve the aerosol layer height (ALH) for ten typical aerosol types in the China region. We also quantitatively evaluate the effects of polarization measurements and the number of viewing angles on ALH retrieval under different conditions (aerosol model, aerosol optical depth, etc.). By comparing the different degree of freedom for signal (DFS) results of ALH caused by the theoretical retrieval error changes in different microphysical parameters in the aerosol and surface model, we identify the key factors affecting ALH retrieval. The results show that the extended ultraviolet band provides important information for ALH retrieval and is closely related to the scattering and absorption characteristics of aerosol models. The polarization measurements in fine mode reduce the posterior error of ALH retrieval by 6–39%; however, this is relatively small for coarse mode. In particular, when it is applied to the transported dust and background dust aerosol types, the posterior error is only reduced by 1–8% after adding polarization measurements. For these two aerosol types with weak absorption at the ultraviolet band, increasing the number of angles observed in addition to increasing the polarization channel will more effectively improve ALH inversion. Compared with other aerosol and surface model parameters, the retrieval errors for the total volume column, effective variance, real part of the complex refractive index, and surface reflectance are the main factors affecting ALH retrieval. Therefore, reducing the theoretical retrieval error of these parameters will be helpful.

Keywords: information content analysis; aerosol layer height; optimal estimation inversion; multiangle polarimetric remote sensing; a posteriori error

Citation: Gu, H.; Zhang, Y.; Fan, C.; Li, Z.; Hou, W.; Liu, Z.; Xie, Y.; Xu, H.; Zhang, L.; Ma, J. A Comprehensive Analysis of Ultraviolet Remote Sensing for Aerosol Layer Height Retrieval from Multi-Angle Polarization Satellite Measurements. *Remote Sens.* **2022**, *14*, 6258. https://doi.org/10.3390/rs14246258

Academic Editor: Tamas Várnai

Received: 6 November 2022
Accepted: 8 December 2022
Published: 10 December 2022

Publisher's Note: MDPI stays neutral with regard to jurisdictional claims in published maps and institutional affiliations.

Copyright: © 2022 by the authors. Licensee MDPI, Basel, Switzerland. This article is an open access article distributed under the terms and conditions of the Creative Commons Attribution (CC BY) license (https://creativecommons.org/licenses/by/4.0/).

1. Introduction

Aerosols are liquid or solid particles suspended in gas with a certain level of stability that have significant impacts on the global radiative energy balance and climate change. The aerosol vertical distribution is an important parameter associated with the retrieval of highly precise aerosol microphysical properties (a previous study has shown the spectral dependence of the radiation effect on the aerosol layer height) that plays an important role in the study of radiative forcing [1]. For example, it is necessary to consider aerosol scattering in trace gas and ocean color retrieval and modify the aerosol vertical distribution parameters accordingly [2–4]. The aerosol layer height (ALH) is a major determining factor in the passive remote sensing monitoring of atmospheric fine particulate matter, such

as $PM_{2.5}$, near the ground. One such approach is the spaceborne $PM_{2.5}$ remote sensing method (PMRS) [5,6]. ALH is commonly used in model calculation, while in the passive remote sensing measurements, it can be always be replaced by planetary boundary layer height (PBLH). The planetary boundary layer is the lowest layer of the atmosphere and, which contains the vast majority of aerosols of the low troposphere [6,7]. At the same time, the height information on smoke, volcanic, and dust aerosols can provide the initial conditions for the modeling of their emissions and the physics of plume formation [8–10]. Consequently, it is imperative to observe the vertical distribution of aerosols on a global scale in order to validate transport models and better understand the impact of aerosols on the climate and environment of the Earth [10,11].

Satellite remote sensing offers the possibility of measuring aerosol height information on a global scale. Active remote sensing measurements, such as ground-based, flight-based, and space-based measurements, can effectively measure the vertical distribution of aerosols. For instance, Cloud-Aerosol Lidar with Orthogonal Polarization (CALIOP) can measure the backscatter at each vertical layer, resulting in detailed aerosol extinction coefficient profiles based on the backscatter ratio [12]. Passive remote sensing measurements, while not having the same accuracy or resolution as active remote sensing, can provide considerable spatial coverage and higher temporal resolution by using ultraviolet (UV), visible/near infrared (VNIR), and thermal infrared (TIR) band observations [10]. In passive remote sensing, most studies focus on the O_2 A band [12–14]. Comprehensive studies have shown that the vertical distribution of oxygen absorption bands is generally stable and not affected by the emissions [13], which is one of the important ways to retrieve ALH. In practice, it is challenging to reach an agreement between the retrieved aerosol height from real O_2 A band measurements and LIDAR measurements, which depend on ad hoc assumptions. Often, higher spectral resolution sensors are used or, given the advantage of reducing interference from the surface, measurements are combined with the O_2 B band to improve the retrieval accuracy [14]. The stereoscopic technique, which relies on the principle of parallax, is applicable for the retrieval of plume-type aerosols with discernable textures, while it is not affected by complex aerosol microphysical properties and radiative transfer computation [15,16].

Applying the UV-A band (315–400 nm) is another approach for ALH passive retrieval, because in the ultraviolet and near-ultraviolet bands, the elevated aerosol layer partly shields the polarization signal from Rayleigh scattering, providing sensitivity to the aerosol layer height [17,18]. On the other hand, the aerosol information will be improved when the surface albedo decreases, and the lower surface reflectance in the UV wavelength is also beneficial for the retrieval of ALH. A previous study performed retrievals with Research Scanning Polarimeter (RSP) measurements in the near-ultraviolet and blue spectral bands. The validation against measurements from a CALIOP showed good agreement with an absolute ALH difference of less than 1 km. The study also indicates the possibility for future satellite instruments to better retrieve aerosol height information if they may include wavelengths shorter than 410 nm [10]. There are some existing sensors that already include polarization channels in the single-angle UV band, such as the Ozone Monitoring Instrument (OMI) [19], Particulate Observing Scanning Polarization (POSP), and so on [20]. However, there is a lack of evidence that multi-angle polarization measurements are better for ALH inversion in UV than near UV. More and more multi-angle polarized instruments are being launched in China for remote sensing studies of atmospheric aerosol properties [21–24]. Since the inversion of the aerosol layer height in the UV band often requires additional constraints, the aerosol model should be assumed in the inversion algorithm in advance, which may introduce errors [25]. Multi-angle polarization provides just enough observational information to improve the accuracy of the inversion.

In this paper, we focus on the typical aerosol types in China and further quantitatively investigate the influence of multi-angle polarization measurements on the retrieval of ALH based on these models. The aim of this study is to determine whether the multi-angle polarization measurements of the UV band can provide enough information to retrieve

ALH and to investigate how UV multi-angle polarization observations can be used for remote sensing inversion of ALH of different aerosol types. We also demonstrate the influence of aerosol and surface model parameter errors by the degree of freedom for signal (DFS) of ALH retrieval under different conditions (aerosol loads, model types, multi viewing observation and so on). The results of this study could be used to develop the next generation spaceborne polarimetric sensors and corresponding ALH retrieval algorithms.

2. Materials and Methods

2.1. Optimal Estimation Theory

Following the optimal estimation (OE) theory [26], ALH retrieval is the process of obtaining the best matching ALH parameter based on satellite observations. The forward model can be described as

$$\boldsymbol{y} = F(\boldsymbol{x}, \boldsymbol{b}) + \boldsymbol{\epsilon} \tag{1}$$

where $\boldsymbol{x}$ is a state vector, $\boldsymbol{b}$ comprises parameters that are not present in $\boldsymbol{x}$ but have a quantitative impact on TOA measurements, $\boldsymbol{y}$ is an observation vector, F is a forward model, and $\boldsymbol{\epsilon}$ represents an experimental error term that integrates observation noise and forward model uncertainty.

Meanwhile, the maximum likelihood analysis of $\boldsymbol{x}$ can be described as

$$\hat{\boldsymbol{x}} = \boldsymbol{x}_a + \left(\boldsymbol{K}^T \boldsymbol{S}_\epsilon^{-1} \boldsymbol{K} + \boldsymbol{S}_a^{-1}\right)^{-1} \boldsymbol{K}^T \boldsymbol{S}_\epsilon^{-1} (\boldsymbol{Y} - \boldsymbol{K}\boldsymbol{x}_a) \tag{2}$$

where the superscript "-1" is the inverse operation of the matrix, $\boldsymbol{S}_\mathrm{a}$ is the error covariance matrix of the a priori estimate $\boldsymbol{x}_\mathrm{a}$, and $\boldsymbol{K}$ is the Jacobian matrix, which consists of the partial derivatives of $F(\mathbf{x})$ with respect to $\boldsymbol{x}$ and describes the sensitivity of the forward model to the state vector. $\boldsymbol{S}_\epsilon$ is the covariance matrix of the error. The a priori estimate provides constraints for the retrieval of the optimal estimation algorithm to prevent the generation of unreasonable results.

In Equation (2), $\hat{x}$ corresponds to the minimum value of the scalar-valued cost function after convergence, and the scalar-valued cost function $\boldsymbol{J}$ is used as the form of

$$\boldsymbol{J} = (\boldsymbol{y} - \boldsymbol{K}\boldsymbol{x})^T \boldsymbol{S}_\epsilon^{-1} (\boldsymbol{y} - \boldsymbol{K}\boldsymbol{x}) + (\boldsymbol{x} - \boldsymbol{x}_a)^T \boldsymbol{S}_a^{-1} (\boldsymbol{x} - \boldsymbol{x}_a) \tag{3}$$

The posteriori error is also known as the theoretical retrieval error. It can be calculated by combining the prior error with error propagation, which can be written as

$$\hat{\boldsymbol{S}} = \left(\boldsymbol{S}_a^{-1} + \boldsymbol{K}^T \boldsymbol{S}_\epsilon^{-1} \boldsymbol{K}\right)^{-1} \tag{4}$$

This indicates that the statistical uncertainties in retrieved $\hat{\boldsymbol{x}}$ due to noise in measurements and error propagation, as well as the posterior errors (absolute errors), are equal to the square root of the diagonal elements.

Besides the posterior error covariance matrix, another key parameter that measures the amount of information about the parameters recovered from observations is the averaging kernel function $\boldsymbol{A}$:

$$\boldsymbol{A} = \frac{\partial \hat{\boldsymbol{x}}}{\partial \boldsymbol{x}} = \left(\boldsymbol{K}^T \boldsymbol{S}_\epsilon^{-1} \boldsymbol{K} + \boldsymbol{S}_a^{-1}\right)^{-1} \boldsymbol{K}^T \boldsymbol{S}_\epsilon^{-1} \boldsymbol{K} \tag{5}$$

The degree of freedom for signal (DFS), also known as the trace of the averaging kernel matrix $\boldsymbol{A}$, denotes the amount of information about the retrieved parameters that can be explored from the satellite data. When the matrix is the identity matrix, the retrieved state can fully reflect the true state; Typically, we may assume that the parameter can be retrieved when the DFS result is >0.5 [27,28]. Each diagonal element, in turn, describes the information contained in each retrieved parameter, given that the averaging kernel specifies the relative weight of information about the state vector contained in satellite measurements as well as from a priori measurements [29]. Considering that the averaging kernel describes the relative weight of information about the state vector from the satellite

measurements compared with that from the a priori measurements, the DFS value depends on the a priori uncertainty assumption. In other words, a higher "degree of freedom for signal" corresponds to a lower posterior error with the same a priori measurement. Therefore, in this work, we quantified the ALH information supplied by UV band satellite data by comparing the posterior uncertainty to the prior uncertainty. The model simulates the Jacobians of the retrieved and supplementary parameters ($\boldsymbol{K}$ and $\boldsymbol{K}_b$), whereas the error covariance matrices are determined empirically (Section 3.2.3).

2.2. Radiative Transfer Simulation

The Unified Linearized Vector Radiative Transfer Model (UNL-VRTM) is used to simulate satellite observations and related weighting functions regarding parameters retrieved for multi-angle viewing geometries. For UNL-VRTM to simulate TOA reflectance and polarization, the sensor setup, atmospheric profile, aerosol characteristics, and surface reflectance are also required as inputs. The vertical profiles of atmospheric temperature, pressure, and trace gases are presumed to be based on the mid-latitude summer atmospheric profiles from Optical Properties of the Atmosphere, Third Edition, AFCRL-72-0497. The 49-layer standard atmospheric profile is mapped to the GEOS-5 vertical grids with 47 hybrid pressure-sigma layers to increase the vertical resolution [30]. Meanwhile, the MT CKD model created by Mlawer, D.C. Tobin, and S.A. Clough is used to determine the continuum absorption of water vapor [31]. The UNL-VRTM is based on the VLIDORT model for calculating the Stokes vector $[I, Q, U, V]^T$, and details about each module in UNL-VRTM can be found in [32], where I represents the total radiant intensity, Q represents the difference between the linearly polarized components parallel to and perpendicular to the reference plane, U describes the linearly polarized irradiance on the polarization plane at an angle of $\pm 45^\circ$ from the reference plane, and V describes the circular polarization. We consider an observation vector comprising I and the degree of linear polarization (*DoLP*) which can eliminate the influence of absolute calibration, where *DoLP* is defined by

$$DoLP = \frac{\sqrt{Q^2 + U^2}}{I} \tag{6}$$

Furthermore, the Jacobian matrix of the *DoLP* for each component of the state vector can be described as

$$\frac{\partial DoLP}{\partial x} = -\frac{DoLP \frac{\partial I}{\partial x_i}}{I} + \frac{Q\frac{\partial Q}{\partial x_i} + U\frac{\partial U}{\partial x_i}}{I\sqrt{Q^2 + U^2}} \tag{7}$$

Using the superscripts v_1–v_M to note each viewing in multiple observations, the measurement vector y can be described as

$$y = \left[I_\lambda^{v_1}, \ldots, I_\lambda^{v_M}, DOLP_\lambda^{v_1}, \ldots, DOLP_\lambda^{v_M}\right]^T \tag{8}$$

The Jacobian matrix calculation of $\boldsymbol{y}$ to $\boldsymbol{x}$ is performed by the UNL-VRTM. Combined with the simulated propagation of errors and the posterior errors, DFS and a posterior error of ALH under different aerosol types and observed geometry can be derived from Equations (4) and (5). According to the results, we can carry out the sensitivity analysis.

3. Instrument and Simulation Assumptions

3.1. Observation Geometry Setting

The instrument in this study is a pre-developed sensor with extra capacity to measure polarization at multi-angle observations in the UV band. We refer to it as Multi-Angle Polarization Measurements with Ultraviolet band (MAPMU). Microphysical and optical properties of aerosols are derived from multi-angle measurements in 11 spectral bands from 388 to 2140 nm with bands near 388, 490, 670, 865, 1370,1640, and 2140 nm performing polarimetric measurements in addition to radiance. The properties of MAPMU are listed

in Table 1 and the fundamental simulation presumptions, such as the aerosol model, the surface model, and the error covariance matrix, are discussed in this part.

Table 1. Basic characteristics of MAPMU.

Parameter	Value	Parameter	Value
Spatial res. (m)	500 (vertical resolution)	Multi-angle	5
Instrument FOV	±45°	Polarized angle	0°, 60°,120°
Pol. Cal. Error	≤2%	Stokes parameters	I, Q, U
Rad. Cal. Error	≤5%	Band width (nm)	20, 20, 20, 20, 10, 40, 20, 40, 40, 40, 40
Central wavelength/nm	388 (P), 443, 490 (P), 670 (P), 555, 865 (P), 910, 1045, 1370 (P), 1640 (P), 2140 (P)		

Four multi-viewing observation geometries were taken into consideration with the combinations of various solar zenith angles (θ_0), viewing zenith angles (θ_v), and relative azimuth angles (φ) to represent the typical observations in various locations in order to obtain synthetic MAPMU data for the information content analysis, just as listed in Table 2. Here, summer low and summer high refer to observations at low and high solar zenith angles, respectively. Figure 1a shows the polar-plot observational geometries, in which the radius means the θ_v change from 0° to 60° with steps of 20°, and the circle represents the change in φ from 0° to 360°. Correspondingly, Figure 1b plots the scattering angles based on the observational geometries within the ranges of [137.76°, 173.68°], [105.05°, 121.30°], [80.28°, 109.40°], and [104.04°, 145.82°].

Table 2. Multi-viewing observation geometries for forward simulations (corresponding to Figure 1).

Geometry Scenarios	Solar Zenith Range (°)	Viewing Zenith Range (°)	Relative Azimuth Range (°)	Scattering Angle Range (°)
Geometry 1	54.12~54.79	44.39~64.09	5.78~330.03	137.76~173.68
Geometry 2	32.86~33.59	25.59~58.64	106.99~248.41	105.05~121.30
Geometry 3	53.18~53.74	28.8~61.06	97.15~229.85	80.28~109.40
Geometry 4	77.63~78.08	37.15~61.87	0.65~298.07	104.04~145.82

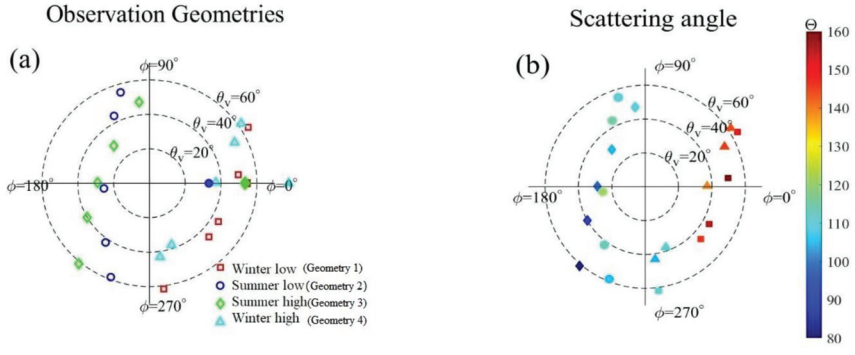


Figure 1. Observation geometries (**a**) with its corresponding scatter angle (**b**) of MAPMU sensor adopted in the simulation. In panel (**a**), the different geometries with $\varphi = 0°$ represent the corresponding positions of the sun for summer low, summer high, winter low, and winter high scenarios, respectively.

3.2. Simulation Assumptions

3.2.1. Aerosol Model

The optical and microphysical characteristics of global aerosols vary greatly throughout both space and time. The climatic variables that control their removal and transport processes have significant impacts on their vertical and horizontal dispersion. There is a large range of values for the optical and microphysical characteristics of different forms of aerosol [33]. A theoretical analysis employing every form of aerosol is a difficult and unrealistic method. In order to simplify this method, previous studies have often analyzed some typical aerosol types (such as fine-dominated and coarse-dominated types) [7,28,34]. We hope to use a more realistic aerosol model classification while building a more sophisticated ALH retrieval framework for the Chinese region in order to explore the ability of UV multi-angle polarization measurements to undergo ALH retrieval for different aerosol types.

Based on the ground-based remote sensing measurements of the Sun-sky radiometer Observation NETwork (SONET), ten fundamental aerosol models used in China were derived in a cluster study by Li et al., and the classifications are summarized in Table 3 [35].

Table 3. Aerosol model classification with SONET [35].

Mode	Aerosol Type	Description of Characteristics
Fine Mode	Urban polluted (F-ULW)	Urban-polluted fine-mode aerosols with high particle concentrations
	Continental background (F-UHS)	Background fine-mode aerosols with low particle concentrations
	Secondary polluted (F-BLW)	Secondary aerosols containing mainly polluted particles with low refractivity and a higher scattering capacity
	Combined polluted (F-BNS)	Mixture of direct anthropogenic emissions and secondary aerosols with high light absorption
	Polluted fly ash (F-BNM)	Mixture of anthropogenic-polluted particles and fine fly ash particles with large submicron fine particles
Coarse Mode	Summer fly ash (C-ULW)	Background of fly ash coarse particles with low light absorption, for example, natural emissions of primary organic aerosols
	Winter fly ash (C-UHS)	Background of fly ash coarse particles with high light absorption, for example, fly ash polluted by anthropogenic components
	Primary dust (C-UNW)	Coarse particles of natural dust with a very high volume concentration
	Transported dust (C-BNM)	Dust particles after long-term transportation and sedimentation
	Background dust (C-BHM)	Background dust suspended over continental regions with a large coarse standard mode

The ten clusters suggest five typical fine particle aerosol models and five coarse models, including urban polluted, secondary polluted, combined polluted, polluted fly ash, and continental background, summer fly ash, winter fly ash, primary dust, transported dust, and background dust. Table 4 lists the details of the microphysical parameters, including the total aerosol volume ($\boldsymbol{V_0}$), effective radius (r_{eff}) and variance (v_{eff}) as well as the refractive index, as shown in the results in Figure 2. In the fine-particle size range, there are five single-peak aerosol models (F-ULW, F-UHS, C-ULW, C-UHS, and C-UNW) and five double-peak (F-BLW, F-BNS, F-BNM, C-BNM and C-BHM) aerosol models. It should be noted that

the double-peak feature may not be obvious, because one small peak may be covered by another big peak [35].

Table 4. Microphysical parameters of ten typical aerosol models in China.

Type	r_{eff}	r_{eff}^{sm}	v_{eff}	v_{eff}^{sm}	Refractive Index	V_0	V_0^{sm}	Refractivity	Absorptivity
Fine Modes									
F-ULW	0.175	\	0.300	\	1.414-0.007i	0.136	\	Low	Weak
F-UHS	0.126	\	0.334	\	1.515-0.014i	0.063	\	High	Strong
F-BLW	0.132	0.283	0.152	0.257	1.392-0.007i	0.087	0.069	Low	Weak
F-BNS	0.103	0.204	0.089	0.334	1.459-0.016i	0.046	0.089	Normal	Strong
F-BNM	0.124	0.387	0.189	1.766	1.477-0.011i	0.073	0.058	Normal	Moderate
Coarse Modes									
C-ULW	2.208	\	0.522	\	1.437-0.006i	0.089	\	Low	Weak
C-UHS	2.558	\	0.500	\	1.522-0.015i	0.090	\	High	Strong
C-UNW	1.970	\	0.305	\	1.495-0.003i	0.482	\	Normal	Weak
C-BNM	1.211	2.973	0.345	0.552	1.492-0.009i	0.059	0.105	Normal	Moderate
C-BHM	1.626	4.481	0.552	0.142	1.518-0.008i	0.121	0.076	High	Moderate

V_0 is the total aerosol volume ($\mu m^3/\mu m^2$), The subscript sm is for the submicron fine mode or super-micron coarse mode.

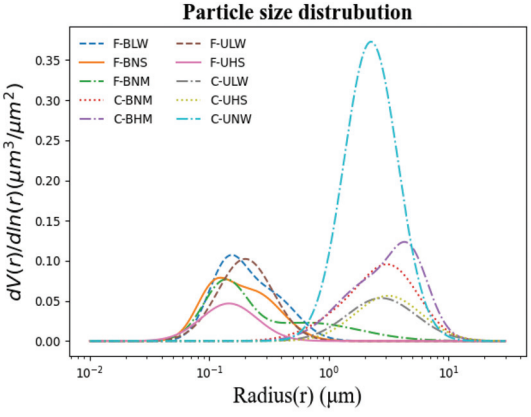


Figure 2. The aerosol volume size distributions for the ten aerosol types defined in Table 4.

The scattering phase matrix $\boldsymbol{P}$ is simulated using a linearized Mie code once these microphysical characteristics have been input:

$$\boldsymbol{P} = \begin{bmatrix} P_{11} & P_{12} & 0 & 0 \\ P_{21} & P_{22} & 0 & 0 \\ 0 & 0 & P_{33} & P_{34} \\ 0 & 0 & P_{43} & P_{44} \end{bmatrix} \quad (9)$$

where $P_{12} = P_2$ and $P_{34} = P_{43}$. P_{11} is the normalized phase function that describes the scalar component of particle scattering, whereas $-P_{12}/P_{11}$ is the polarized scattering that corresponds to DoLP.

The single scattering albedo (SSA) in the UV and VIS bands for ten typical aerosol models is also shown in Table 5. SSA represents the ratio of the scattering efficiency to the total extinction efficiency. Compared with the VIS band (443 nm), the SSA in the UV band is higher for the fine mode, while the SSA of the coarse mode is lower.

Table 5. SSA of ten aerosol models at 338 nm and 443 nm.

SSA	F-BLW	F-BNS	F-NM	F-ULW	F-UHS	C-ULW	C-BNM	C-BHM	C-UHS	C-UNW
SSA (388 nm)	0.9541	0.9020	0.9572	0.9277	0.9413	0.7642	0.7906	0.7666	0.6194	0.6338
SSA (443 nm)	0.9498	0.8895	0.9569	0.9261	0.9377	0.7817	0.8082	0.7842	0.6333	0.6496

Table 5 indicates stronger absorption for F-ULW, F-BNS, and F-BNS compared to F-BLW and F-BNM. Similarly, weaker absorption is shown for C-BNM and C-BHM compared to C-ULW, C-UHS, and C-UNW for the wavelength at 388 nm.

The wavelength-dependent P_{11} and $-P_{12}/P_{11}$ of various aerosol types vary with different scattering angles, as shown in Figure 3a–d resulting in diverse scattering properties that impact TOA measurements. Figure 3c,d additionally show four multi-viewing observation geometries with varying sensitivities to TOA radiance and DoLP with respect to ALH. As an example, when the scattering angle gradually moves closer to 180°, the aerosol DoLP ($-P_{12}/P_{11}$) with scattering angles for C-BHM and C-BNM is obviously different from the other three coarse aerosol models, and the overall value is negative. This bimodal aerosol model has the characteristics of Asia dust and transport dust. Due to the high aerosol layer and special optical characteristics of the UV band, the absorption is weak.

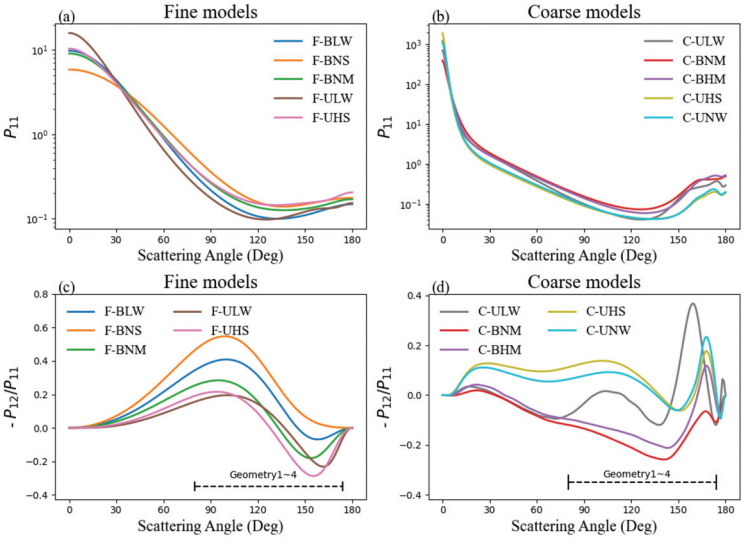


Figure 3. Scattering phase functions (**a**,**b**) and polarized phase functions (**c**,**d**) of ten typical aerosol models at a wavelength of 388 nm. (**a**,**c**) represents fine mode aerosol types and (**b**,**d**) represents coarse mode aerosol types.

From the perspective of passive remote sensing, we assume that only one aerosol layer is present in the atmosphere, and the definition of the aerosol height depends on how the profile is represented. Meanwhile, the suitable choice of representation often depends on the actual applications. It also depends on whether the measurement can meet the profile model parameters which are in the state vectors to solve at the same time. In the simulation, we assume that the profile of the aerosol extinction coefficient follows an exponential-decay profile, which is often used in atmospheric correction algorithms and can be written in the form of [7,32,36]:

$$\int_{TOA}^{Z} \tau(z)dz = \tau_0 \exp\left(-\frac{z}{H}\right) \quad (10)$$

where τ_0 is the columnar aerosol optical depth (AOD), and H is the scale height, which represents the height of the aerosol layer when the columnar aerosol optical depth (AOD) decays to 1/e of the ground. To simplify this, we only include H in our retrieval's state vector, while the other aerosol-related characteristics (AOD, effective radius, variance, and refractive index) are specified as model parameters.

3.2.2. Surface Model

The surface reflectance has a significant impact on ALH information; hence, it is vital to choose the proper surface reflectance model. Many studies have suggested that compared with bare soil (bright surface case), surface types with relatively higher absorption (seawater, vegetation, etc.) show higher sensitivity to the ALH [1,29]. However, the surface reflectance of different types is relatively low at the UV band, and the difference is small. For instance, we use the improved kernel-driven bidirectional reflectance distribution function (BRDF) model of vegetated surface, which has been proven to provide a better retrieval performance than the traditional Ross-Li model in the multi-angle polarization satellite observation retrieval framework [37]. For surface reflectance, the used BRDF is

$$\rho_S(\mu_0, \mu_v, \phi, \lambda) = f_{iso}(\lambda)[1 + k_1 f_{geom}(\mu_0, \mu_v, \phi) + k_2 f_{vol}(\mu_0, \mu_v, \phi)] \quad (11)$$

where μ_0 and μ_v represent the cosine of the solar zenith angles and the viewing zenith angle, respectively; f_{iso}, f_{geom}, and f_{vol} correspond to the isotropic, geometric-optical (Li-sparse kernel), and volumetric (Ross-thick kernel) surface scattering, respectively. k_1 and k_2 are the coefficients of the BRDF kernels at the given wavelength. In this paper, the surface reflectance f_{iso} was set to 0.0186, a value chosen from the surface reflectance databases USGS and ASTER [38,39]. The values of k_1 and k_2 were chosen from Litvinov's work as equal to 0.087 and 0.668 [40].

3.2.3. Error Covariance Matrix

As described in Section 2, we constructed the inversion framework as described in [10]. The state vector has only one parameter, which is

$$\boldsymbol{x} = [H]^T \quad (12)$$

At the same time, the other aerosol model surface parameters were retrieved from other satellite channels with certain retrieval errors under the known inversion framework. For the double-peak aerosol models, the vector is

$$\boldsymbol{b} = \left[V_0, V_0^{sm}, r_{eff}, r_{eff}^{sm}, v_{eff}, v_{eff}^{sm}, m_r, m_i, m_r^{sm}, m_i^{sm}, \rho_s, k_1, k_2\right]^T \quad (13)$$

where V_0 and V_0^{sm}, r_{eff} and r_{eff}^{sm}, v_{eff} and v_{eff}^{sm}, m_r and m_r^{sm}, m_i and m_i^{sm} correspond to the total aerosol volume, effective radius, variance, as well as the real and imaginary parts of the refractive index in fine-mode (coarse-mode) or submicron fine mode (super-micron coarse mode); ρ_s, k_1, k_2 are the improved BRDF model parameters.

For the error covariance matrix, here, we assume that σH = 75% H; and the prior error covariance matrix is an identity matrix.

$$\boldsymbol{S}_a = \left[\sigma_H^2\right], \quad (14)$$

The prior error is 20% for V_0^f and V_0^{sm}, and 10% for ρ_s. For the fine-mode, the a priori errors r_{eff}, v_{eff}, m_r, m_i, k_1, and k_2 are 15%, 15%, 0.025, 50%, 15%, and 15%, respectively, while for the coarse-mode, the a priori errors r_{eff}, v_{eff}, m_r, m_i, k_1, and k_2 are 35%, 35%, 0.04,

50%, 35%, and 35%, respectively. Here, the a priori error refers to the retrieval errors of SONET [41,42]. The diagonal error covariance matrix of $\boldsymbol{b}$ (S_b) is

$$\boldsymbol{S}_b = \mathrm{diag}\left(\left[(\Delta V_0)^2, (\Delta V_0^{sm})^2, \ldots, (\Delta m_i^{sm})^2, (\Delta \rho_s)^2, \ldots, (\Delta k_2)^2\right]\right) \quad (15)$$

The uncertainties of satellite measurements ($\boldsymbol{S}_y$), as part of the observation uncertainty, include systematic and random errors that occur during the instrument observation process. For the MAPMU instrument, we estimated radiance and polarized measurement errors of 5% and 2%, respectively. The correlations of observations between multiple viewing angles should be considered in multi-angle satellite observations, but polarization and intensity measurements can still be assumed to be independent. Therefore, $\boldsymbol{S}_y$ is a 10×10 off-diagonal matrix, and the details of the construction are shown in Equation (A1).

4. Results

4.1. Simulated TOA Results

To provide synthetic data from the MAPMU measurements, we defined the TOA reflectance (R^{TOA}) and polarized reflectance (R_P^{TOA}) as follows. All of the synthetic data were cloud free.

$$\begin{cases} R^{TOA} = \pi I/\mu_0 \\ R_P^{TOA} = \pi\sqrt{Q^2+U^2}/\mu_0 \end{cases} \quad (16)$$

Figure 4 illustrates the TOA normalized radiance and polarized radiance of different multi-viewing observation geometries at 388 nm for the F-ULW and C-ULW aerosol types. These two models (coappearance probability greater than 5%) also represent aerosol characteristics in the China region. TOA measurements for the other seven aerosol types are not shown in the figures for simplicity, although the characteristics are similar.

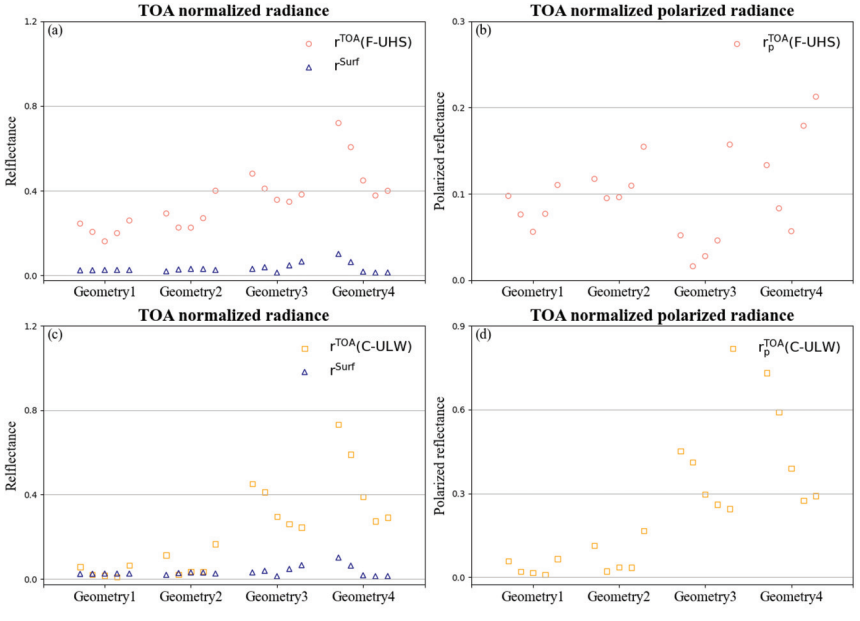


Figure 4. Contributions of TOA reflectance and TOA polarized reflectance at 388 nm with vegetated surface, and AOD = 0.6 at 550 nm. (**a**,**b**) correspond to the F-UHS aerosol type, while (**c**,**d**) correspond to the C-ULW aerosol type.

4.2. ALH Retrieval Capability for Typical Cases

In this section, we analyze the ability of MAPMU to detect ALH in the UV band. Four multi-angle observation geometries were used for the forward simulations, and each mean DFS of the observation geometries was calculated under the conditions of AOD = 0.6 (550 nm) and H = 2 km. Figure 5 further illustrates the DFS and posterior errors of ALH retrieval for different aerosol models in the form of histograms, and the error bars correspond to four multi-viewing observation geometries. The gray bottom column represents the prior estimation error for the aerosol layer height, and the visible part of the gray bottom column shows the reduction in the posterior error relative to the prior error in Figure 5c,d (absolute a priori error is 1.5 km).

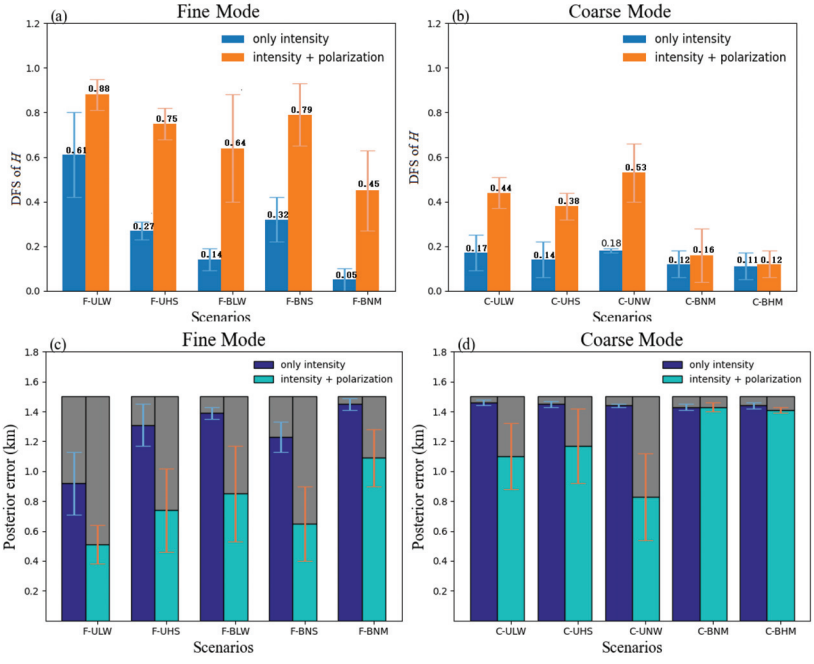


Figure 5. The DFS and posterior error of *H* for different aerosol models with AOD = 0.6 for two aerosol types over vegetation surfaces. The error bar are the mean value and standard deviation of different geometries and the aerosol profile H is defined as 2 km. (**a**,**c**) represents fine mode aerosol types and (**b**,**d**) represents coarse mode aerosol types.

(1) The results show that the multi-angle polarization measurements of ALH retrieval performed well (DFS > 0.5) in the UV band for the main aerosol models. Previous studies have shown that the surface reflectance on the information content of ALH often has more impact than the optical aerosol properties [29]. It can be seen that the optical properties of aerosols also play crucial roles in ultraviolet ALH retrieval.

(2) The determination of ALH for the coarse mode is relatively difficult compared with the fine mode, and the information content of ALH is closely related to the scattering and absorption characteristics of the aerosol model. Combined with the aerosol model SSA presented in Section 3.2.1, the fly ash pollution type (F-BNM) has the strongest scattering characteristics in the five fine modes, as a result of having the lowest DFS result, which is even lower than that found for some coarse modes. Similarly, the difference between the primary dust type (C-UNW) with the highest DFS and background dust with the lowest DFS is 0.07, and the difference grew further to above

0.4 after adding the polarization measurements. The result also indicates a better performance of the MAPMU observations for absorbing aerosol in ALH retrieval.

(3) Comparing intensity observation and polarization observation, it can be seen that, regardless of the type of aerosol (except F-ULW), it is difficult to retrieve the scale height parameter using only the intensity observation in the UV band, and the addition of polarization observation information effectively improves ALH retrieval. We supplement and test the information related to ALH retrieval under different aerosol conditions in Section 5.1 and evaluate the improvement produced by adding polarization measurements.

(4) As shown in Figure 5c,d, due to the different aerosol models, when only the intensity measurements are included, the posterior error for fine mode is in the range of 1.45 km to 0.92 km; however, once polarization measurements are included, the posterior error can drop to a range of 1.09 km to 0.51 km. For Coarse mode, the posterior error is in the range of 1.46 km to 1.43 km when just intensity measurements are used, while it is in the range of 1.43 km to 0.62 km when polarization measurements are added. In summary, the DFS of the ALH is significantly improved with the addition polarization measurements, and the posterior error is gradually reduced.

In addition, we assume that if the wrong aerosol model is chosen, the theoretical error due to the intensity and polarization measurement model choice can be quantitatively assessed by calculating the relative error of the posterior error between different models. As results shown in Figure 6, in extreme cases, the aerosol model used for the actual intensity measurement is the urban pollution type (F-ULW), but we chose the background dust type (C-BHM) for ALH inversion. The absolute error corresponding to the posterior error of the two models is, at most, 59.1%. After adding the polarization measurement, the difference between different models increases further and can reach 180.39%. That is to say, the uncertainty of the aerosol model has an important impact on ALH retrieval.

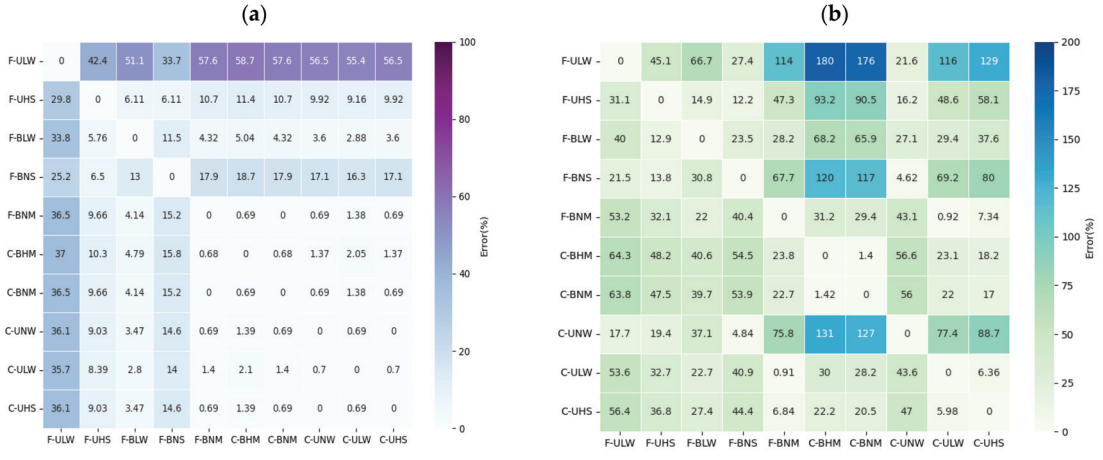


Figure 6. Heat maps of the absolute error corresponding to the posterior error caused by inaccurate aerosol models. (**a**) represents intensity measurements only; (**b**) represents "intensity + polarization" multi-angle measurements.

5. Discussion

5.1. The Influence of Adding Polarization Measurements

In Section 4.2, we analyze the ability of MAPMU to detect the aerosol layer height for typical cases and show the impact of uncertainty for aerosol models. However, previous studies have shown that the aerosol vertical distribution is also affected by the aerosol model parameters (AOD, H), while the impact of these parameters generally appears to

be similar in different aerosol types [7,29]. Therefore, in this section, we test the changes in ALH information under different aerosol optical depth conditions (AOD is from 0.2 to 1.0) and scale height conditions including near-ground aerosols and transported aerosols above the boundary layer (H is from 1 km to 5 km) for the vegetation surface. At the same time, combined with the corresponding posterior error, the improvements in the information quantity and posterior error after adding polarization measurements under different aerosol conditions are analyzed.

Figure 7a,b shows the variation in the DFS for the parameter H for ten typical aerosol models used in China with the aerosol condition (AOD, H) used for the intensity measurements. The figure is presented in the form of a box plot. Figure 7c,d corresponds to the DFS after adding polarization measurements, and the other parameters are the same as those used in Figure 7a,b. When the AOD varies from 0.2 to 1.0, each box in Figure 7a–f depicts the DFS and the uncertainty reduction of ALH. On each box, the median value (solid line in the box), maximum value (whisker top), and minimum value (whisker bottom) correspond to AOD values of 0.6, 1.0, and 0.2, respectively. Figure 7e,f represents to extent to which uncertainty reduction might be improved by including polarization measurements by comparing the reduction in posterior uncertainties of H for intensity measurements with the addition of polarization measurements. The uncertainty reduction is similar to the percentage of prior error assumed in the prior error covariance matrix, which is discussed in Section 3.2.3. In this way, we can evaluate the improvement achieved by adding polarization measurements. For Figure 7, we conclude the following:

(1) Comparing Figure 7a–d, it can be seen that no matter which aerosol model is used, the DFS of ALH increases at larger AOD values. For the intensity measurements, the DFS increases gradually with the increase in H. After adding the polarization measurements, the DFS gradually decreases, but the overall value is much higher than that of the intensity measurements. The polarization especially improves the ALH retrieval when the prior setting of the scale height is less than 3 km. At the same time, the difference between aerosol models has a greater impact on DFS than the changes in AOD and H, which is especially obvious for the coarse modal aerosol types.

(2) As shown in Figure 7e,f, the influence of polarization measurements on ALH retrieval gradually decreases. This is because the troposphere contains more height information, and the detection accuracy of the aerosol height is relatively high in this range. As H increases, the enhancement effect of polarization gradually weakens. Similar to the study presented in [33], DoLP measurements increase the sensitivity to H, and polarization multi-angle observations offer a high potential for ALH detection, but the polarization improvement shows obvious differences between aerosol models.

(3) The comparison of different models shows that the difference between the fine-mode aerosol types is small, while the difference is generally higher than that for the coarse mode aerosols. The ALH retrieval uncertainty can be reduced by 10–39% at most through the addition of polarized measurements for F-ULW, but it can only be reduced by 6–24% for F-BNM. In contrast, the differences among the coarse mode aerosol types affected by polarization are large. For instance, when the scale height is 1 km, the uncertainty reduction might change by as much as 49%, but the H retrieval uncertainty will only be reduced by 1–5% (1–8%) for C-BHM(C-BNM). It can be seen that the polarization enhancement effect is very limited for the above two coarse mode aerosol types with a moderate particle radius and weak absorption in the UV band.

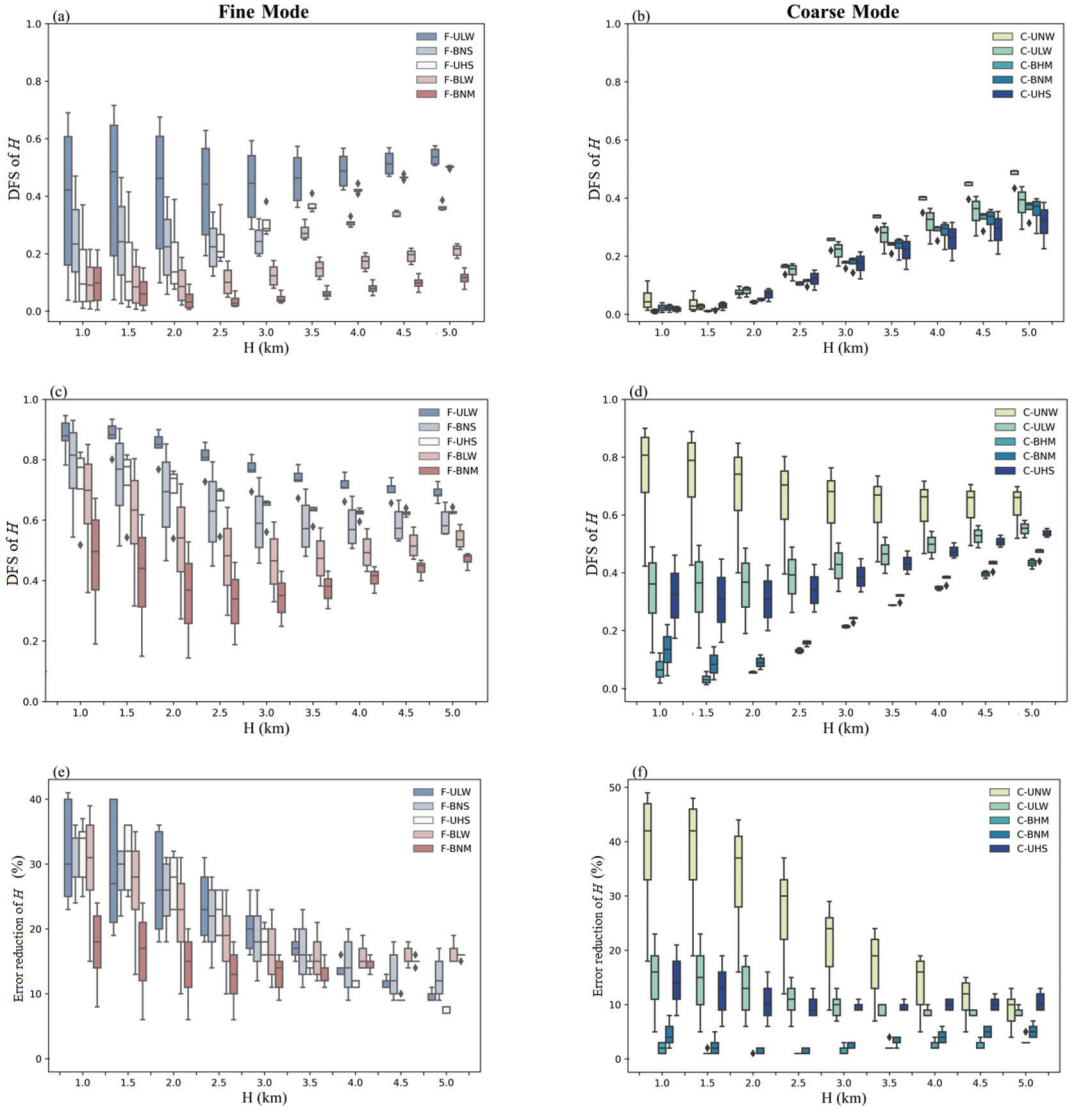


Figure 7. The DFS of H from multi-angle radiance measurements (**a**,**b**) and adding DoLP measurements (**c**,**d**), as well as the posterior error uncertainty reduction between these two types measurements (**e**,**f**) under different aerosol conditions for ten aerosol models over vegetation surface. (**a**,**c**,**e**) represent fine mode aerosol types and (**b**,**d**,**f**) represent coarse mode aerosol types.

5.2. The Influence of Multi-Angle Measurements

The scattering angle determined by the satellite observation geometry often determines the Rayleigh scattering and aerosol scattering, which has an important impact on ALH retrieval. Based on multi-angle satellite observations, it should be determined whether the height information obtained by the number of observation angles is sufficient for ALH retrieval. To explore the ALH inversion potential corresponding to polarization multi-angle measurements when the number of observation angles is further increased from 1 to 14, detailed geometric parameters are shown in Table A1. In Section 4.2, Figure 8 shows that even with multi-angle observations such as MAPMU with five viewing angles, it is

difficult to retrieve ALH information using only intensity measurements in the UV band (DFS < 0.5). Therefore, in this section, following the addition of the polarization measurements, we examine how the DFS of ALH depends on the quantity of the observation angles to analyze whether increasing the observation angle can improve the ALH retrieval, particularly for coarse mode aerosols (C-BHM and C-BNM). When the retrieval involves multi-angle observations, the angles are selected according to the quantification of the intensity measurements with H using the Jacobian matrix from the highest (sub-satellite point) to the lowest values. Through this method, we get the following conclusions:

(1) Figure 8a,b show that the increase in the DFS with the angle number in fine mode is larger than that in coarse mode. When the angle number is 1, even in the F-UHS type with the highest DFS for fine mode, the value is only 0.28. Combined with the single-angle observation presented in Figure 9, it can be seen that, under the same conditions, when the scattering angle is around 90° and F-UHS is 120–150°, the DFS can approach 0.5. In that case, the use of single-angle polarization measurements to retrieve ALH is often limited, so the development of multi-angle polarization sensors has great significance for ALH retrieval in the UV band.

(2) In addition, given the constrained observation period in the actual multi-angle observation mode, if numerous angles focus on the same object, the target's spatial coverage or the overall number of targets will be decreased [29]. Therefore, it is necessary to find the optimal number of angles to reduce the observation time of each target while maintaining a high level of ALH information. It can be seen that, as the observation angle increases, the increase in DFS gradually decreases, but as the number of observation angles rises from 1 to 5, it basically meets the requirements of ALH retrieval (DFS > 0.5) for the main aerosol models. Even for the two aerosol types with limited polarization enhancement, C-BNM and C-BHM, the DFS is significantly improved when the observation angles increased to about 7–8. This also shows that the multi-angle observation is an effective way to improve the ALH retrieval of weak absorbing aerosol types at the UV band.

(3) As the observation angle continues to increase, the DFS increase gradually slows down with the number of angles and finally converges, which means that as the number of angles continues to increase, the inversion framework constructed in this study is easily extensible. In a future study, we will add to and evaluate the potential for retrieving more aerosol properties from the UV band through the addition of multi-angle measurements.

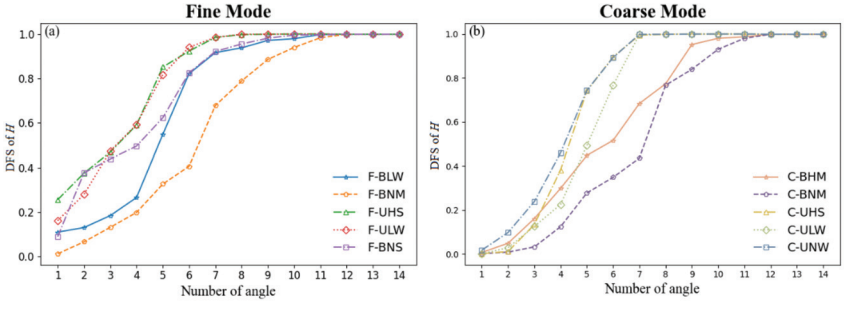


Figure 8. The DFS of *H* as a function of number of viewing angles for different aerosol models with AOD = 0.6 for the two aerosol types. The scale height is defined as 2 km. (**a**) represents fine mode aerosol types and (**b**) represents coarse mode aerosol types.

In order to analyze the upper limit of ALH information of single-angle polarization observations, we simulated two typical observation geometries (solar zenith angles of 40° and 60°, respectively), and there were 25 observation angles in each group. The scattering angle varied from 60° to 140° with a step size of 5°. By using the same parameter

settings as before in the forward simulation, we found that for the single-angle polarization observation, the mean value between two typical observation geometries of DFS as a function of the scattering angle is as shown in Figure 9:

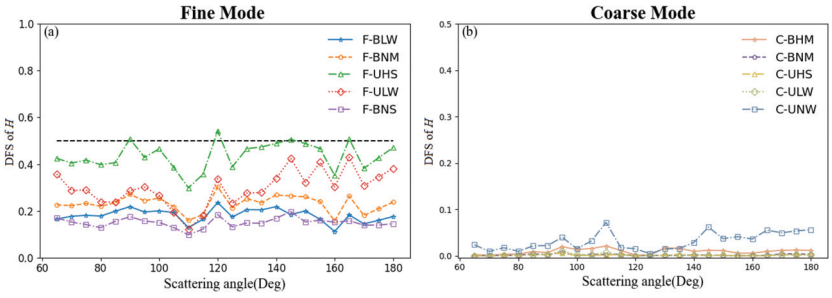


Figure 9. The DFS of H as a function of the scattering angle with single-angle polarization observations. (**a**) represents fine aerosol model types and (**b**) represents coarse aerosol model types.

5.3. The Influence of Model Errors

We also needed to quantitatively investigate the influence of predefined model errors on the retrieval results of ALH, because the predefined aerosol model will inevitably introduce model errors into the retrieval of critical aerosol and surface parameters in our inversion framework. Using Equation (15), we used the specified constant measurement errors from the previous section to calculate the DFS results resulting from various model errors. Previous research has shown that the DFS of the aerosol layer height will be affected by the aerosol types and has shown the differences, but the impact of AOD generally appear similar in different aerosol types [7,29]. Therefore, we concentrated on AOD = 0.6 and scale height = 2 km as a demonstration. Additionally, we have given an example of AOD = 0.2 in Figure A1 as a comparison. It was assumed that all aerosol and surface parameters change from 5% to 100%, as defined in Section 3.2.3 It was found that for both fine mode and coarse aerosol types, the DFS of ALH decreases with an increase in the parameter error, but the influence of each parameter is not the same, as shown in Figures 10 and 11. We obtained the following conclusions:

(1) For aerosol model parameters, the F-ULW and F-UHS aerosol types, the total aerosol volume, and the effective radius have the greatest influences, and decreases in DFS are all above 0.3. For the other three fine particle aerosol types, although the real part of the complex refractive index is an important factor that affects the scattering, the difference in DFS caused by the change of aerosol parameters is controlled within 0.1 (Figure 10). However, for the five coarse mode aerosol types, the influence of the total aerosol volume and the imaginary part of refractive index on the DFS occupies the main role (Figure 11).

(2) Similarly, for fine-mode aerosol types, the error of k_1 of surface parameters has the greatest influence on the DFS of ALH retrieval. In coarse mode, the DFS is much more affected by the surface BRDF ρ_s error than the other two parameters.

(3) When combined, the aerosol model coappearance probability is greater than 5% (F-ULW, F-UHS, F-BLW, C-BHM, C-UHS and C-ULW). For the ten typical aerosol models used in China, an iteration procedure among several predefined typical aerosol models has been designed to further decrease the probability of choosing a very bad value for the actual retrieval, and priority should be given to reducing the retrieval errors of three key parameters: the aerosol volume column concentration, effective variance, and imaginary part of the refractive index in the aerosol model, as well as the surface BRDF ρ_s and k_1 parameters will effectively improve the DFS of the aerosol retrieval in the UV band.

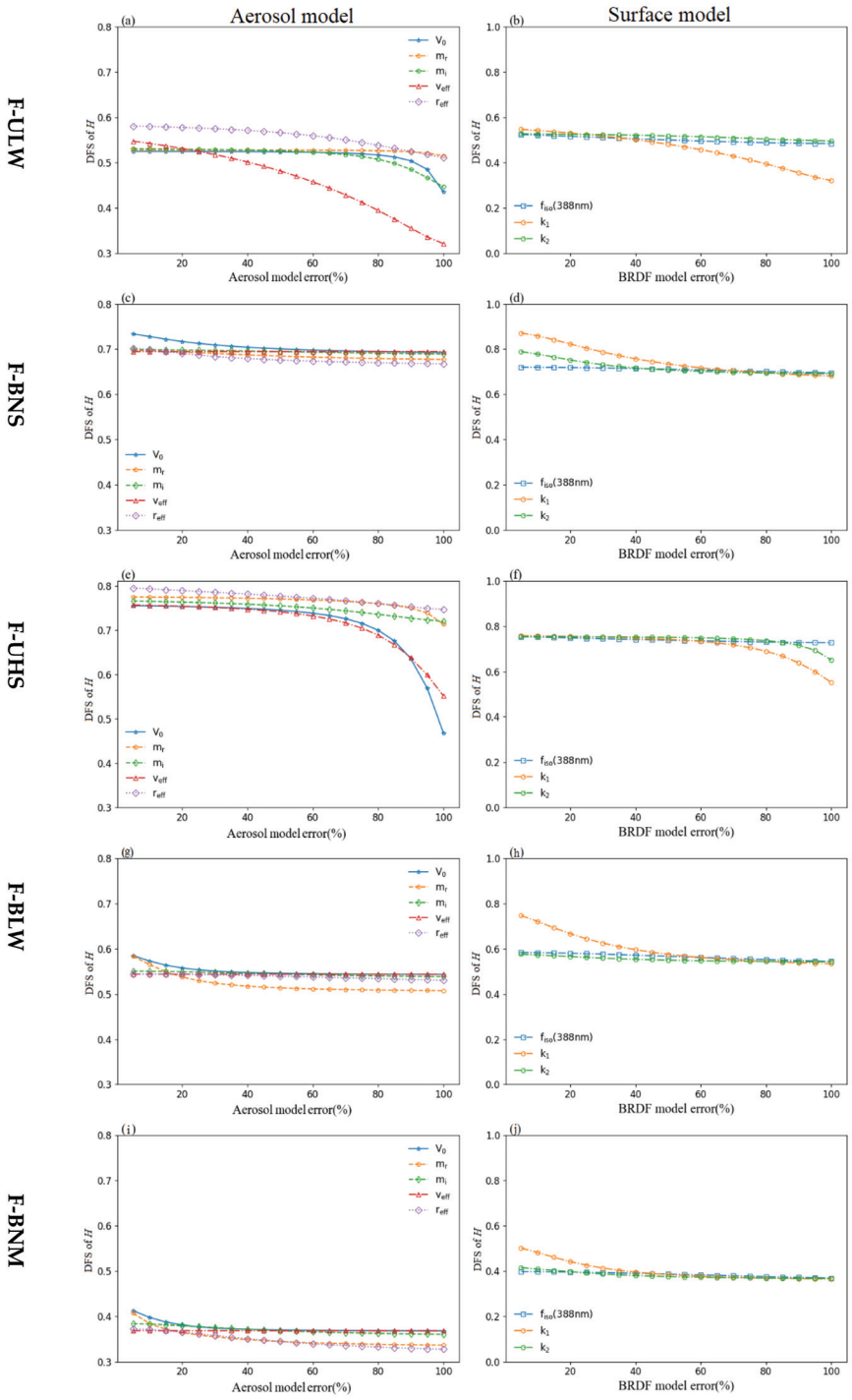


Figure 10. DFS of H as a function of the fine aerosol model and surface model parameter errors from 5% to 100% in steps of 5% with AOD = 0.6, in which left (**a**,**c**,**e**,**g**,**i**) and right panel (**b**,**d**,**f**,**h**,**j**) corresponds to the aerosol model and surface model respectively.

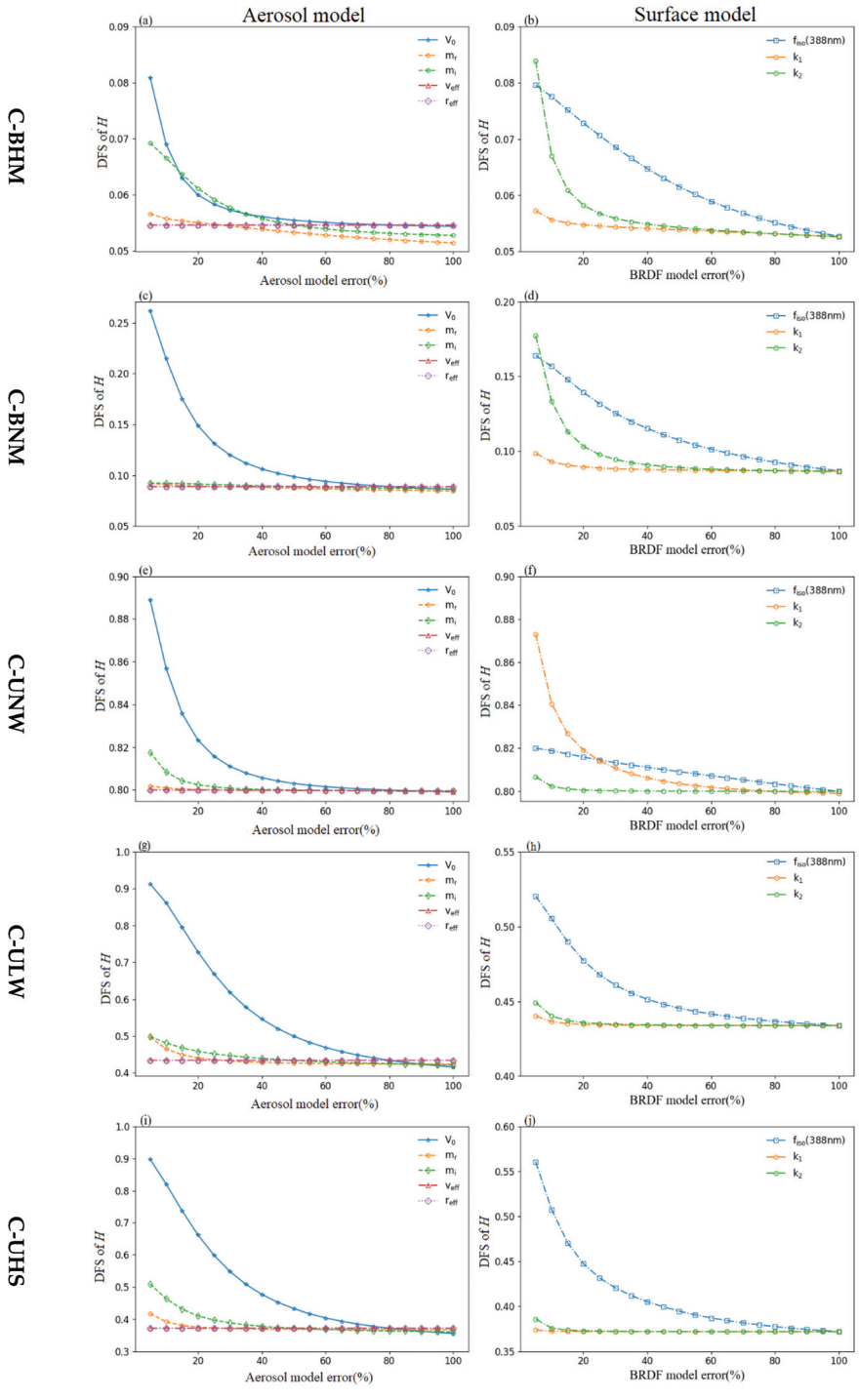


Figure 11. The same as Figure 10, but DFS of H as a function of the coarse aerosol model and surface model parameter errors from 5% to 100% in steps of 5% with AOD = 0.6, in which left (**a**,**c**,**e**,**g**,**i**) and right panel (**b**,**d**,**f**,**h**,**j**) corresponds to the aerosol model and surface model respectively.

6. Conclusions

In this paper, we used the extended ultraviolet band (388 nm) to simulate multi-angle polarization synthetic data and fully evaluate the performance of multi-angle polarization measurements in the UV channel for passive remote sensing of the aerosol layer heights of ten typical aerosol model types used in the Chinese region. The research results show that

(1) The extended ultraviolet 388 nm band is an important information source for passive remote sensing ALH retrieval. With additional constraints, such as the aerosol single scattering albedo and AOD from independent sources (thought to be obtained by retrieval from other channels), MAPMU can theoretically retrieve ALH under different conditions by combining polarization measurements with multi-angle measurements.
(2) Polarization measurements have important impacts on ALH retrieval at the UV band, but the improvement is different for each typical aerosol model due to their different optical properties. For example, the reduction in posterior uncertainties of ALH retrieval is 6–39% for the fine mode aerosol types following the addition of polarization measurements. However, the improvement for coarse mode aerosol types is relatively small, especially for C-BHM and C-BNM which characterize the types of dust found in North China and have larger median radii and low absorption rates in the UV band. The retrieved reduction of posterior uncertainties is only 1–8%.
(3) Compared with single-angle polarization observations, which have difficulty retrieving the ALH for coarse mode aerosol types, the multi-angle observation mode effectively improves the DFS of ALH retrieval. In particular, for the ALH retrieval of C-BHM and C-BNM, the combination of polarization and multi-angle measurements could be used to improve the aerosol layer height information. When the number of viewing angles is increased to 6, the DFS increment is above 0.4, on average, for different aerosol types.
(4) The predefined model errors include the error of the total aerosol volume and the effective radius and the imaginary part of the complex refractive index as well as the error of the surface reflectivity ρ_s and the k_1 parameter, which will lead to the largest change in the DFS of ALH retrieval. The effect of other parameter errors on the aerosol and surface models is relatively small.

In summary, the addition of polarization and multi-angle measurements can effectively improve ALH retrieval compared with single-angle intensity measurements in the UV band. For ALH retrieval under coarse-mode aerosol types, in addition to considering the polarization channel, multi-angle observations also need to be considered. We suggest that the number of viewing angles should be 5–6 to achieve a good level of performance (DFS > 0.5) for ALH retrieval in the UV band for the typical aerosol model types. Additionally, reducing the retrieval errors of these key parameters, as presented above, will effectively improve the uncertainty associated with ALH retrieval in the UV band.

Author Contributions: Conceptualization, Y.Z., Z.L. (Zhengqiang Li) and W.H.; Formal analysis, H.G., Z.L. (Zhengqiang Li), W.H. and C.F.; Methodology, H.G., Z.L. (Zhenhai Liu), J.M. and C.F.; Supervision, C.F. and Z.L. (Zhengqiang Li); Visualization, H.G., Y.Z., Y.X. and L.Z. (Zhenhai Liu); Writing—original draft, H.G.; Writing—review and editing, H.G., C.F. and H.X. All authors have read and agreed to the published version of the manuscript.

Funding: This study was supported by the National Natural Science Foundation of China (Grant No. 41871269), the Major Projects of High Resolution Earth Observation Systems of National Science and Technology (05-Y30B01-9001-19/20-3), the National Outstanding Youth Foundation of China (Grant No. 41925019), and the Space Pre-research Projects (No. D010206).

Data Availability Statement: Not applicable.

Acknowledgments: We acknowledge the work of Zhu Jun of DFH Satellite Co., Ltd. and Hong Jin and Qiu Zhenwei of the Hefei Institutes of Physical Science, Chinese Academy of Sciences who were involved with the design of the new instrument. In addition, we thank the Fine Mechanics Unified Linearized Vector Radiative Transfer Model UNL-VRTM (www.unl-vrtm.org (accessed on 6 January

2022)) developed by Jun Wang of The University of Iowa and Xiaoguang Xu of the University of Maryland, Baltimore County for their technical support. Meanwhile, thanks to the reviewers and editor for their helpful comments.

Conflicts of Interest: The authors declare no conflict of interest.

Appendix A

Table A1. Multi-viewing observation geometries for forward simulations (corresponding to Figure 8).

Number	Geometry 1	Geometry 2	Geometry 3	Geometry 4
NO. 1	[54.12, 64.09, 30.44]	[32.8, 59.78, 104.02]	[53.08, 57.8, 88.40]	[77.63, 61.87, 34.08]
NO. 2	[54.17, 60.77, 26.19]	[32.86, 55.18, 106.99]	[53.13, 52.95, 92.08]	[77.67, 57.78, 30.81]
NO. 3	[54.22, 57.20, 20.87]	[32.92, 49.86, 111.05]	[53.18, 47.42, 97.15]	[77.72, 53.14, 26.5]
NO. 4	[54.27, 53.52, 14.19]	[32.98, 43.81, 116.83]	[53.23, 41.29, 104.48]	[77.76, 47.98, 20.64]
NO. 5	[54.33, 49.95, 5.78]	[33.04, 37.22, 125.53]	[53.28, 34.99, 115.55]	[77.80, 42.47, 12.4]
NO. 6	[54.38, 46.90, 355.42]	[33.10, 30.78, 139.24]	[53.33, 29.63, 132.40]	[77.85, 37.15, 0.65]
NO. 7	[54.43, 44.89, 343.23]	[33.16, 26.16, 160.34]	[53.38, 27.11, 155.45]	[77.89, 33.09, 344.34]
NO. 8	[54.48, 44.39, 330.03]	[33.22, 25.59, 186.76]	[53.43, 28.80, 179.32]	[77.94, 31.67, 324.35]
NO. 9	[54.53, 45.52, 317.10]	[33.28, 29.43, 209.63]	[53.48, 33.72, 197.55]	[77.90, 33.52, 304.71]
NO. 10	[54.58, 47.99, 305.6]	[33.34, 35.61, 224.89]	[53.53, 39.92, 209.64]	[78.03, 37.83, 289.07]
NO. 11	[54.63, 51.28, 296.03]	[33.4, 42.23, 234.53]	[53.58, 46.11, 217.59]	[78.08, 43.20, 277.9]
NO. 12	[54.69, 54.92, 288.36]	[33.47, 48.42, 240.86]	[53.64, 51.76, 223.04]	[78.12, 48.65, 270.06]
NO. 13	[54.74, 58.56, 282.26]	[33.53, 53.89, 245.23]	[53.69, 56.74, 226.94]	[78.17, 53.73, 264.45]
NO. 14	[54.79, 62.01, 277.41]	[33.59, 58.64, 248.41]	[53.74, 61.06, 229.85]	[78.21, 59.06, 257.35]

The three parameters in parentheses [] represent the solar zenith range (Deg), viewing zenith range (Deg) and relative azimuth range (Deg), respectively.

Appendix B

Equation (A1) uncertainties of satellite measurement matrices (S_y)

$$S_y = \begin{bmatrix} (\varepsilon_1)^2, & c1\times\varepsilon_1\varepsilon_2, & c2\times\varepsilon_2\varepsilon_3, & c3\times\varepsilon_1\varepsilon_4, & c4\times\varepsilon_1\varepsilon_5 & & & & & \\ c1\times\varepsilon_1\varepsilon_2, & (\varepsilon_2)^2, & c5\times\varepsilon_2\varepsilon_3, & c6\times\varepsilon_2\varepsilon_4, & c7\times\varepsilon_2\varepsilon_5 & & & & & \\ c2\times\varepsilon_2\varepsilon_3, & c5\times\varepsilon_2\varepsilon_3, & (\varepsilon_3)^2, & c8\times\varepsilon_3\varepsilon_4, & c9\times\varepsilon_3\varepsilon_5 & & & 0 & & \\ c3\times\varepsilon_1\varepsilon_4, & c6\times\varepsilon_2\varepsilon_4, & c8\times\varepsilon_3\varepsilon_4, & (\varepsilon_4)^2, & c10\times\varepsilon_4\varepsilon_5 & & & & & \\ c4\times\varepsilon_1\varepsilon_5, & c7\times\varepsilon_2\varepsilon_5, & c9\times\varepsilon_3\varepsilon_5, & c10\times\varepsilon_4\varepsilon_5, & (\varepsilon_5)^2 & & & & & \\ & & & & & (\varepsilon_6)^2, & c11\times\varepsilon_6\varepsilon_7, & c12\times\varepsilon_6\varepsilon_8, & c13\times\varepsilon_6\varepsilon_9, & c14\times\varepsilon_6\varepsilon_{10} \\ & & & & & c11\times\varepsilon_6\varepsilon_7, & (\varepsilon_7)^2, & c15\times\varepsilon_7\varepsilon_8, & c16\times\varepsilon_7\varepsilon_9, & c17\times\varepsilon_7\varepsilon_{10} \\ & & 0 & & & c12\times\varepsilon_6\varepsilon_8, & c15\times\varepsilon_7\varepsilon_8, & (\varepsilon_8)^2, & c18\times\varepsilon_8\varepsilon_9, & c19\times\varepsilon_8\varepsilon_{10} \\ & & & & & c13\times\varepsilon_6\varepsilon_9, & c16\times\varepsilon_7\varepsilon_9, & c8\times\varepsilon_3\varepsilon_4, & (\varepsilon_9)^2, & c20\times\varepsilon_9\varepsilon_{10} \\ & & & & & c14\times\varepsilon_6\varepsilon_{10}, & c17\times\varepsilon_7\varepsilon_{10}, & c19\times\varepsilon_8\varepsilon_{10}, & c20\times\varepsilon_9\varepsilon_{20}, & (\varepsilon_{10})^2 \end{bmatrix} \quad \text{(A1)}$$

Combined with statistical data, c1~c20 refer to the measurement correlation coefficients between different observation angles. ε_1–ε_{10} correspond to the intensity and polarization measurement errors between the five observation angles for each multi-viewing observation.

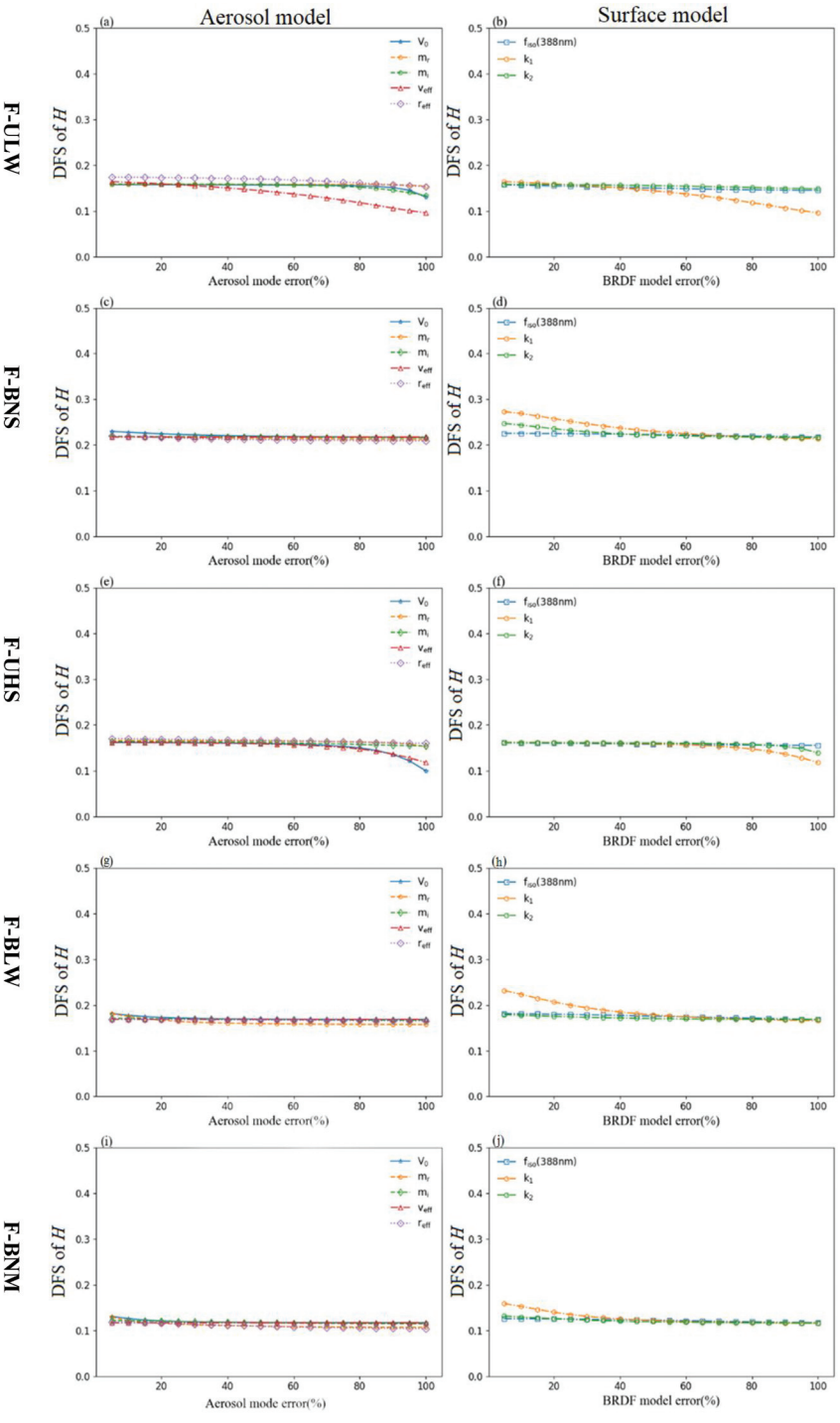


Figure A1. DFS of H as a function of the fine aerosol model and surface model parameter errors from 5% to 100% in steps of 5% but with AOD = 0.2, in which left (**a**,**c**,**e**,**g**,**i**) and right panel (**b**,**d**,**f**,**h**,**j**) corresponds to the aerosol model and surface model respectively.

References

1. Mishra, A.K.; Koren, I.; Rudich, Y. Effect of Aerosol Vertical Distribution on Aerosol-Radiation Interaction: A Theoretical Prospect. *Heliyon* **2015**, *1*, e00036. [CrossRef]
2. Gordon, H.R. Atmospheric Correction of Ocean Color Imagery in the Earth Observing System Era. *J. Geophys. Res.* **1997**, *102*, 17081–17106. [CrossRef]
3. Duforêt, L.; Frouin, R.; Dubuisson, P. Importance and Estimation of Aerosol Vertical Structure in Satellite Ocean-Color Remote Sensing. *Appl. Opt.* **2007**, *46*, 1107. [CrossRef] [PubMed]
4. Butz, A.; Guerlet, S.; Hasekamp, O.; Schepers, D.; Galli, A.; Aben, I.; Frankenberg, C.; Hartmann, J.-M.; Tran, H.; Kuze, A.; et al. Toward Accurate CO_2 and CH_4 Observations from GOSAT: GOSAT CO_2 AND CH_4 VALIDATION. *Geophys. Res. Lett.* **2011**, *38*, n/a-n/a. [CrossRef]
5. Zhang, Y.; Li, Z. Remote Sensing of Atmospheric Fine Particulate Matter (PM2.5) Mass Concentration near the Ground from Satellite Observation. *Remote Sens. Environ.* **2015**, *160*, 252–262. [CrossRef]
6. Wang, H.; Li, Z.; Lv, Y.; Xu, H.; Li, K.; Li, D.; Hou, W.; Zheng, F.; Wei, Y.; Ge, B. Observational Study of Aerosol-Induced Impact on Planetary Boundary Layer Based on Lidar and Sunphotometer in Beijing. *Environ. Pollut.* **2019**, *252*, 897–906. [CrossRef]
7. Hou, W.Z.; Wang, H.F.; Li, Z.Q.; Qie, L.L.; Ge, B.Y.; Fan, C.; Li, S. PRELIMINARY SENSITIVITY STUDY OF AEROSOL LAYER HEIGHT FROM SYNTHETIC MULTIANGLE POLARIMETRIC REMOTE SENSING MEASUREMENTS. *Int. Arch. Photogramm. Remote Sens. Spat. Inf. Sci.* **2019**, *XLII-3/W9*, 63–69. [CrossRef]
8. Kahn, R.A.; Chen, Y.; Nelson, D.L.; Leung, F.-Y.; Li, Q.; Diner, D.J.; Logan, J.A. Wildfire Smoke Injection Heights: Two Perspectives from Space. *Geophys. Res. Lett.* **2008**, *35*, L04809. [CrossRef]
9. Yang, Z.; Wang, J.; Ichoku, C.; Hyer, E.; Zeng, J. Mesoscale Modeling and Satellite Observation of Transport and Mixing of Smoke and Dust Particles over Northern Sub-Saharan African Region: DUST AND SMOKE MIXING OVER SAHEL. *J. Geophys. Res. Atmos.* **2013**, *118*, 12139–12157. [CrossRef]
10. Wu, L.; Hasekamp, O.; van Diedenhoven, B.; Cairns, B.; Yorks, J.E.; Chowdhary, J. Passive Remote Sensing of Aerosol Layer Height Using Near-UV Multiangle Polarization Measurements. *Geophys. Res. Lett.* **2016**, *43*, 8783–8790. [CrossRef]
11. Yu, H.; Chin, M.; Winker, D.M.; Omar, A.H.; Liu, Z.; Kittaka, C.; Diehl, T. Global View of Aerosol Vertical Distributions from CALIPSO Lidar Measurements and GOCART Simulations: Regional and Seasonal Variations. *J. Geophys. Res.* **2010**, *115*, D00H30. [CrossRef]
12. Winker, D.M.; Vaughan, M.A.; Omar, A.; Hu, Y.; Powell, K.A.; Liu, Z.; Hunt, W.H.; Young, S.A. Overview of the CALIPSO Mission and CALIOP Data Processing Algorithms. *J. Atmos. Ocean. Technol.* **2009**, *26*, 2310–2323. [CrossRef]
13. Zeng, J.; Han, Q.; Wang, J. High-Spectral Resolution Simulation of Polarization of Skylight: Sensitivity to Aerosol Vertical Profile. *Geophys. Res. Lett.* **2008**, *35*, L20801. [CrossRef]
14. Chen, X.; Wang, J.; Xu, X.; Zhou, M.; Zhang, H.; Castro Garcia, L.; Colarco, P.R.; Janz, S.J.; Yorks, J.; McGill, M.; et al. First Retrieval of Absorbing Aerosol Height over Dark Target Using TROPOMI Oxygen B Band: Algorithm Development and Application for Surface Particulate Matter Estimates. *Remote Sens. Environ.* **2021**, *265*, 112674. [CrossRef]
15. Fisher, D.; Muller, J.-P.; Yershov, V.N. Automated Stereo Retrieval of Smoke Plume Injection Heights and Retrieval of Smoke Plume Masks from AATSR and Their Assessment with CALIPSO and MISR. *IEEE Trans. Geosci. Remote Sens.* **2014**, *52*, 1249–1258. [CrossRef]
16. Zakšek, K.; Hort, M.; Zaletelj, J.; Langmann, B. Monitoring Volcanic Ash Cloud Top Height through Simultaneous Retrieval of Optical Data from Polar Orbiting and Geostationary Satellites. *Atmos. Chem. Phys.* **2013**, *13*, 2589–2606. [CrossRef]
17. Hasekamp, O.P.; Landgraf, J. Retrieval of Aerosol Properties over the Ocean from Multispectral Single-Viewing-Angle Measurements of Intensity and Polarization: Retrieval Approach, Information Content, and Sensitivity Study. *J. Geophys. Res.* **2005**, *110*, D20207. [CrossRef]
18. Kalashnikova, O.V.; Garay, M.J.; Davis, A.B.; Diner, D.J.; Martonchik, J.V. Sensitivity of Multi-Angle Photo-Polarimetry to Vertical Layering and Mixing of Absorbing Aerosols: Quantifying Measurement Uncertainties. *J. Quant. Spectrosc. Radiat. Transf.* **2011**, *112*, 2149–2163. [CrossRef]
19. Torres, O.; Tanskanen, A.; Veihelmann, B.; Ahn, C.; Braak, R.; Bhartia, P.K.; Veefkind, P.; Levelt, P. Aerosols and Surface UV Products from Ozone Monitoring Instrument Observations: An Overview. *J. Geophys. Res.* **2007**, *112*, D24S47. [CrossRef]
20. Lei, X.; Zhu, S.; Li, Z.; Hong, J.; Liu, Z.; Tao, F.; Zou, P.; Song, M.; Li, C. Integration Model of POSP Measurement Spatial Response Function. *Opt. Express* **2020**, *28*, 25480. [CrossRef]
21. Lei, X.; Liu, Z.; Tao, F.; Hou, W.; Huang, H.; Xie, Y.; Zhao, X.; Dong, H.; Zou, P.; Song, M.; et al. Geolocation Error Estimation Method for the Wide Swath Polarized Scanning Atmospheric Corrector Onboard HJ-2 A/B Satellites. *IEEE Trans. Geosci. Remote Sens.* **2022**, *60*, 1–9. [CrossRef]
22. Li, Z.; Xie, Y.; Hou, W.; Liu, Z.; Bai, Z.; Hong, J.; Ma, Y.; Huang, H.; Lei, X.; Sun, X.; et al. In-Orbit Test of the Polarized Scanning Atmospheric Corrector (PSAC) Onboard Chinese Environmental Protection and Disaster Monitoring Satellite Constellation HJ-2 A/B. *IEEE Trans. Geosci. Remote Sens.* **2022**, *60*, 1–17. [CrossRef]
23. Shi, Z.; Li, Z.; Hou, W.; Mei, L.; Sun, L.; Jia, C.; Zhang, Y.; Li, K.; Xu, H.; Liu, Z.; et al. Aerosol Optical Depth Retrieval Based on Neural Network Model Using Polarized Scanning Atmospheric Corrector (PSAC) Data. *IEEE Trans. Geosci. Remote Sens.* **2022**, *60*, 1–18. [CrossRef]

24. Ge, B.; Li, Z.; Chen, C.; Hou, W.; Xie, Y.; Zhu, S.; Qie, L.; Zhang, Y.; Li, K.; Xu, H.; et al. An Improved Aerosol Optical Depth Retrieval Algorithm for Multiangle Directional Polarimetric Camera (DPC). *Remote Sens.* **2022**, *14*, 4045. [CrossRef]
25. Satheesh, S.K.; Torres, O.; Remer, L.A.; Babu, S.S.; Vinoj, V.; Eck, T.F.; Kleidman, R.G.; Holben, B.N. Improved Assessment of Aerosol Absorption Using OMI-MODIS Joint Retrieval. *J. Geophys. Res.* **2009**, *114*, D05209. [CrossRef]
26. Rodgers, C.D. *Inverse Methods for Atmospheric Sounding: Theory and Practice*; World Scientific: Singapore, 2000; ISBN 978-981-4498-68-5.
27. Hou, W.; Wang, J.; Xu, X.; Reid, J.S.; Han, D. An Algorithm for Hyperspectral Remote Sensing of Aerosols: 1. Development of Theoretical Framework. *J. Quant. Spectrosc. Radiat. Transf.* **2016**, *178*, 400–415. [CrossRef]
28. Hou, W.; Wang, J.; Xu, X.; Reid, J.S. An Algorithm for Hyperspectral Remote Sensing of Aerosols: 2. Information Content Analysis for Aerosol Parameters and Principal Components of Surface Spectra. *J. Quant. Spectrosc. Radiat. Transf.* **2017**, *192*, 14–29. [CrossRef]
29. Chen, X.; Xu, X.; Wang, J.; Diner, D.J. Can Multi-Angular Polarimetric Measurements in the Oxygen-A and B Bands Improve the Retrieval of Aerosol Vertical Distribution? *J. Quant. Spectrosc. Radiat. Transf.* **2021**, *270*, 107679. [CrossRef]
30. Zhu, Y.; Gelaro, R. Observation Sensitivity Calculations Using the Adjoint of the Gridpoint Statistical Interpolation (GSI) Analysis System. *Mon. Weather Rev.* **2008**, *136*, 335–351. [CrossRef]
31. Mlawer, E.J.; Payne, V.H.; Moncet, J.-L.; Delamere, J.S.; Alvarado, M.J.; Tobin, D.C. Development and Recent Evaluation of the MT_CKD Model of Continuum Absorption. *Philos. Trans. R. Soc. A* **2012**, *370*, 2520–2556. [CrossRef]
32. Xu, X.; Wang, J. UNL-VRTM, A Testbed for Aerosol Remote Sensing: Model Developments and Applications. In *Springer Series in Light Scattering*; Kokhanovsky, A., Ed.; Springer Series in Light Scattering; Springer International Publishing: Cham, Switzerland, 2019; pp. 1–69, ISBN 978-3-030-20586-7.
33. Hess, M.; Koepke, P.; Schult, I. Optical Properties of Aerosols and Clouds: The Software Package OPAC. *Bull. Am. Meteorol. Soc.* **1998**, *79*, 831–844. [CrossRef]
34. Hou, W.; Wang, J.; Xu, X.; Reid, J.S.; Janz, S.J.; Leitch, J.W. An Algorithm for Hyperspectral Remote Sensing of Aerosols: 3. Application to the GEO-TASO Data in KORUS-AQ Field Campaign. *J. Quant. Spectrosc. Radiat. Transf.* **2020**, *253*, 107161. [CrossRef]
35. Li, Z.; Zhang, Y.; Xu, H.; Li, K.; Dubovik, O.; Goloub, P. The Fundamental Aerosol Models Over China Region: A Cluster Analysis of the Ground-Based Remote Sensing Measurements of Total Columnar Atmosphere. *Geophys. Res. Lett.* **2019**, *46*, 4924–4932. [CrossRef]
36. Wang, J.; Xu, X.; Ding, S.; Zeng, J.; Spurr, R.; Liu, X.; Chance, K.; Mishchenko, M. A Numerical Testbed for Remote Sensing of Aerosols, and Its Demonstration for Evaluating Retrieval Synergy from a Geostationary Satellite Constellation of GEO-CAPE and GOES-R. *J. Quant. Spectrosc. Radiat. Transf.* **2014**, *146*, 510–528. [CrossRef]
37. Li, Z.; Hou, W.; Hong, J.; Zheng, F.; Luo, D.; Wang, J.; Gu, X.; Qiao, Y. Directional Polarimetric Camera (DPC): Monitoring Aerosol Spectral Optical Properties over Land from Satellite Observation. *J. Quant. Spectrosc. Radiat. Transf.* **2018**, *218*, 21–37. [CrossRef]
38. Baldridge, A.M.; Hook, S.J.; Grove, C.I.; Rivera, G. The ASTER Spectral Library Version 2.0. *Remote Sens. Environ.* **2009**, *113*, 711–715. [CrossRef]
39. *USGS Spectral Library Version 7*; Data Series; USGS: Reston, VA, USA, 2017; p. P67.
40. Litvinov, P.; Hasekamp, O.; Dubovik, O.; Cairns, B. Model for Land Surface Reflectance Treatment: Physical Derivation, Application for Bare Soil and Evaluation on Airborne and Satellite Measurements. *J. Quant. Spectrosc. Radiat. Transf.* **2012**, *113*, 2023–2039. [CrossRef]
41. Ma, Y.; Li, Z.; Li, Z.; Xie, Y.; Fu, Q.; Li, D.; Zhang, Y.; Xu, H.; Li, K. Validation of MODIS Aerosol Optical Depth Retrieval over Mountains in Central China Based on a Sun-Sky Radiometer Site of SONET. *Remote Sens.* **2016**, *8*, 111. [CrossRef]
42. Li, Z.Q.; Xu, H.; Li, K.T.; Li, D.H.; Xie, Y.S.; Li, L.; Zhang, Y.; Gu, X.F.; Zhao, W.; Tian, Q.J.; et al. Comprehensive Study of Optical, Physical, Chemical, and Radiative Properties of Total Columnar Atmospheric Aerosols over China: An Overview of Sun–Sky Radiometer Observation Network (SONET) Measurements. *Bull. Am. Meteorol. Soc.* **2018**, *99*, 739–755. [CrossRef]

geosciences

MDPI

Article

Enhancing the Identification and Mapping of Fluvial Terraces Combining Geomorphological Field Survey with Land-Surface Quantitative Analysis

Giulia Iacobucci, Daniela Piacentini * and Francesco Troiani

Department of Earth Sciences, Sapienza University of Rome, 00185 Rome, Italy
* Correspondence: daniela.piacentini@uniroma1.it

Abstract: A methodological approach to refining the identification and mapping of fluvial terraces has been applied, combining geomorphological field surveys with the computation and assessment of different morphometric parameters (local, statistical, and object-oriented), derived from a high-resolution digital terrain model (DTM) obtained from a LiDAR survey. The mid-sector floodplain of the Misa River basins was taken as a valid example of the main river valleys draining the northern Marche Apennines (Italy) and was considered an ideal site to test a combination of different geomorphological techniques for enhancing fluvial terraces' detection and mapping. In this area, late Pleistocene–Holocene fluvial terraces are well exposed, and their geomorphological and geochronological characteristics have largely already been studied. However, a reliable distinction of the different Holocene terrace levels, including a detailed geomorphological mapping of different terrace features, is still lacking due to the very complex terrace geometry and the lack of good-quality deposit outcrops. Land-surface quantitative (LSQ) analysis has been coupled with the available outcomes of previous studies and ad-hoc geomorphological field surveys to enhance the identification and mapping of fluvial terraces. The results of this work provided information for the discernment of terrace remnants belonging to the full-glacial fill terrace generation (late Pleistocene) as well as reconstruction of the terrace top–surface, and can be used to distinguish the inner terrace limits coinciding with the margin of the floodplain. It has also been possible to identify and delimit the late Pleistocene terrace from a staircase of three younger strath terraces formed during the Holocene. The results of this study demonstrated that the investigation of fluvial landforms, at different scales, can strongly benefit from the integration of field surveys and quantitative geomorphic analysis based on high-resolution digital topographic datasets. In particular, the integration of LSQ analysis with ground-truth geomorphological data can be dramatically helpful for the identification and mapping of fluvial terraces.

Keywords: fluvial terraces; geomorphometry; geomorphological mapping; Holocene; northern Apennines

Citation: Iacobucci, G.; Piacentini, D.; Troiani, F. Enhancing the Identification and Mapping of Fluvial Terraces Combining Geomorphological Field Survey with Land-Surface Quantitative Analysis. *Geosciences* **2022**, *12*, 425. https://doi.org/10.3390/geosciences12110425

Academic Editors: Jesus Martinez-Frias and Rosa Nappi

Received: 22 September 2022
Accepted: 15 November 2022
Published: 18 November 2022

Publisher's Note: MDPI stays neutral with regard to jurisdictional claims in published maps and institutional affiliations.

Copyright: © 2022 by the authors. Licensee MDPI, Basel, Switzerland. This article is an open access article distributed under the terms and conditions of the Creative Commons Attribution (CC BY) license (https://creativecommons.org/licenses/by/4.0/).

1. Introduction

Fluvial deposits provide one of the most-studied continental records of climate changes, and consequently, fluvial terraces represent important geomorphological features in diverse morphoclimatic contexts worldwide [1]. There is now a wide consensus on the role of climate variability in producing alternation in the fluvial incision and sedimentation processes recorded in fluvial terraces [2,3]. Therefore, the cyclical interchange between the erosional and depositional processes during quaternary can be considered the main response of fluvial systems to climate change [1]. Further, many studies have demonstrated that fluvial terrace staircases are responses to regional uplift at a long time scale (10^4–10^6 year) [4]. Therefore, the sensitivity of fluvial dynamics to tectonics and climate variability allows for the use of geomorphic and stratigraphic records as quantitative archives of past climatic conditions and tectonics.

Focusing on the last glacial–interglacial cycle, the fluvial sequence is often represented by several fill-cut episodes, which have formed two/three (or more) terrace steps since the last glacial maximum during the Holocene [5,6]. Minor aggradation phases along the inner valley sectors from the Holocene can be recognized at several places in the world. These phases are often accelerated either by increased mass wasting along hillslopes or by anthropogenic soil erosion. Although the late glacial and Holocene terrace sequences are among the best studied and exposed alluvial records worldwide, their complexity and intriguing arrangement stimulates further research perspectives aimed at unraveling the types and ages as well as the altimetric arrangement and along-valley distribution. Indeed, the late glacial and Holocene terrace sequences are often dissimilar not only because of the diverse morphoclimatic and geodynamic contexts, but even along adjacent valleys in the same region.

Along the river valleys draining the Adriatic side of the northern Marche Apennines (Figure 1), a late Pleistocene-to-Holocene terrace sequence constitutes the present valley floors hanging from a few meters up to maximum of 18–20 m above the thalweg. Even though mapping fluvial terraces in the field is a standard geomorphological procedure, over wide and low-relief floodplains, traditional geomorphological mapping is particularly challenging [7], as is the case along the valley floors within the northern Marche Apennines [8]. In facts, the difficulty of detecting Holocene fluvial terraces in the field, as well as distinguishing the latter from the ancient late Pleistocene terrace generation, has many origins, including (i) the size of the terrace surfaces, often too large to be completely seen in the field, and (ii) the subjectivity of the examiner in detecting all terrace features and their geometric and geomorphological characteristics (e.g., external scarp, inner edge, lateral edges, basal strath, deposit thickness and composition, and terrace surface) with adequate accuracy and detail. From this perspective, fluvial terraces exposed along the northern Marche river valleys are ideal for testing a geomorphological approach to enhancing the detection and interpretation of fluvial terraces and better comprehending their morpho-evolutive implications.

The introduction of digital terrain models (DTMs) has provided a great opportunity for the remote analysis of terrace morphology and surficial geometry using geographic information systems (GIS). Different efforts have been carried out over the course of the last twenty years for the automatic extraction of terrace features, such as terrace surfaces or terrace scarps, using low-resolution interpolated DTMs [9] and high-resolution DTMs derived from light detection and ranging (LiDAR) [10,11]. Automated methods for the extraction of fluvial terraces have proven to be supportive in different contexts, and they have often been often for extracting terrace features, even where terrace remnants were scarcely observable [12]. Nonetheless, the analysis of late Pleistocene–Holocene floodplains, characterized by a very complex spatial arrangement of terrace morphology and structure, can be difficult to perform, and the purely automatic detection of terrace features is challenging. Therefore, a great opportunity is offered by the combination of land-surface quantitative (LSQ) analysis based on high-resolution DTMs with ground-truth geomorphological investigations, which have proven to be effective for the analysis of Earth surface processes and landforms at different space–time scales [6,13–15].

In this work, a combined approach is presented for the identification and mapping of the late Pleistocene–Holocene fluvial terraces exposed along the mid sector of the Misa River valley. This approach is based on geomorphological field surveys and mapping combined with the computation and assessment of different morphometric parameters (local, statistical, and object-based). These parameters have been calculated from high-resolution DTM derived from LiDAR surveys conducted in the frame of the national project called "Not Ordinary Plan of Remote Sensing" [16]. After a short presentation of the study area and the exhibition of the complete methodological approach, the main results are presented, and their general methodological implications are discussed together with site-specific geomorphological findings and implications.

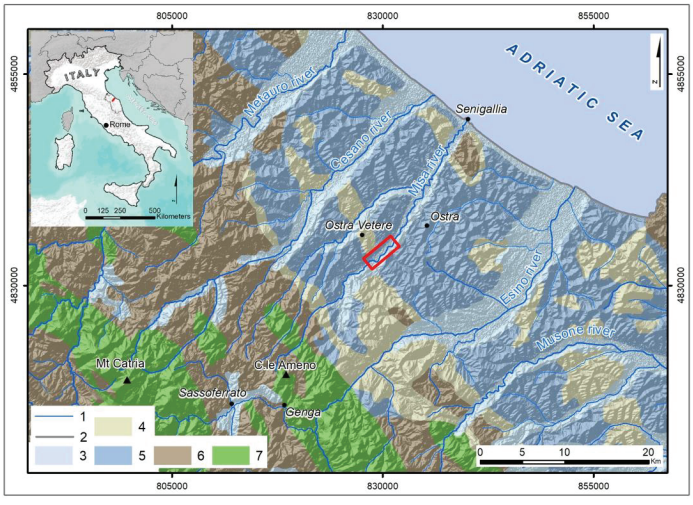


Figure 1. Geological sketch, derived from a geo-lithological map of Italy [17], of the northern Marche Apennines, encompassing the study area. In the mainframe: 1. River; 2. Coastline; 3. Pleistocene and Holocene fluvial deposits; 4. Plio-Pleistocene sands and conglomerates; 5. Plio-Pleistocene clays; 6. Miocene marly-calcareous, evaporitic, and terrigenous unit; 7. Mesozoic limestones. In the top left corner: the location of the study area in the Italian peninsula. Coordinate references are provided in World Geodetic System (WGS) 1984, Universal Transverse Mercator (UTM) Zone 32N (EPSG: 32632).

2. Study Area

The northern Marche Apennines consist of an inner, mainly mountainous area merging to the NE into a hilly coastal zone (Figure 1), the latter developing for about 65 km along the western side of the central Adriatic Sea. The first area pertains to the Meso-Cenozoic carbonatic and marly-carbonatic, autochthonous Umbria–Marche geological domain, while the latter zone is shaped from Neogene terrigenous formations. The inland Umbria–Marche domain is characterized by two regionally extended anticlines (i.e., the Umbria–Marche Ridge to the SW and the Marche Ridge to the SE), separated by a broad, mainly terrigenous syncline where several minor carbonate anticlines also rise. The fold shape is typically imprinted on the planform of the derived sub-parallel, NW–SE-trending morphostructures (Figure 1).

Tectonic uplift rates over the last 1 Ma have been estimated to be comprised of between 0.3 and 0.5 mm/year in the inner sectors of the chain, and between 0.15 and 0.18 mm/year along the Adriatic coastal sectors [8].

The main watercourses mostly drain eastward, cross cutting the main geological structures and forming sub-parallel valleys. The last ones, along their middle and lowermost sectors expose a well-preserved terrace staircase hanging at different heights along the valley sides and flat floodplains up to 2–4 km wide (Figure 2A). Floodplains typically enlarge in proximity of the river mouths, showing bell-shaped planforms that have been interpreted by [18] as the surficial expression of wide coastal fan bodies developed during the last sea level rise but still under low stand conditions in the late Pleistocene–early Holocene. The complex arrangement of the fluvial terrace staircase has been widely studied and discussed in the past (see the works by [19,20]). In general, up to ten levels compose an ideal fluvial terraces staircase, which, as a rule, starts with the remnants of ancient strath terraces. These hang at heights above the present thalweg higher than 150–180 m, and their origin has widely been accepted to be related to tectonic uplift [20 and references therein]. The fill terraces sequence is mainly represented by remnants of up to five generations of gravel-dominated terraces, from middle-Pleistocene to Holocene in age, hanging at heights above the thalweg from a few of meters up to 120–150 m, named, from the ancient ones, T1a-1b, T2, T3, and T4 (Figure 2A). This latter is a complex series of nested minor terrace levels formed dur-

ing a general post-glacial downcutting phase [18–20] (Figure 2B). Late Quaternary climate changes, in a context of active regional tectonic uplift, principally accounts for the genesis and development of different fill terrace generations. During the Pleistocene, the northern Marche inland was glacier-free, therefore the influence of small local glaciers on fluvial terraces' development must be considered as irrelevant [20]. The terrace deposits belonging to the different generations are generally composed of a fluvial depositional sequence that starts at the base with thick gravels and sands of braided-type river channels, representing the main alluvial infilling during glacial cold conditions, which often superimposes late-glacial alluvial fan deposits [21]. These latter show different thickness, with maxima at the tributary junctions, and represent the termination of the depositional phase of each terrace generation, especially the ancient ones, after which the valley entrenchment started. This cyclical deposition pattern principally characterizes the highest, ancient depositional terrace generations (i.e., T1a–1b, T2, and, partially, T3), being an exception the youngest terrace generation starting from the T3 [20,22–24] (Figure 2B). Moreover, the late Pleistocene–Holocene terrace is characterized by a series of sub-horizontal terrace treads, slightly dipping towards the present channel, separated by minor terrace scarps (with heights often less than 2–3 m), which are often slightly convex slope breaks remolded by shallow mass movements and surficial running waters. The present floodplains, composed by these terrace generations, are often covered by patches of arboreal and shrubby vegetation, hosting intense agricultural practices and deep anthropogenic changes since the first urbanization of the area as far back as the Roman times [25]. In fact, the current valley floors host several Roman archeological sites and connected structures. The ancient Ostra Roman village along the Misa River, as well as the Forum Sepronii along the Metauro River and the ancient Suasa Roman village along the Cesano River, developed above the T3 terrace surface or immediately below along the inner margin of the Holocene minor terrace levels, indicating complex interrelations between early human occupation and the watercourses [24,25].

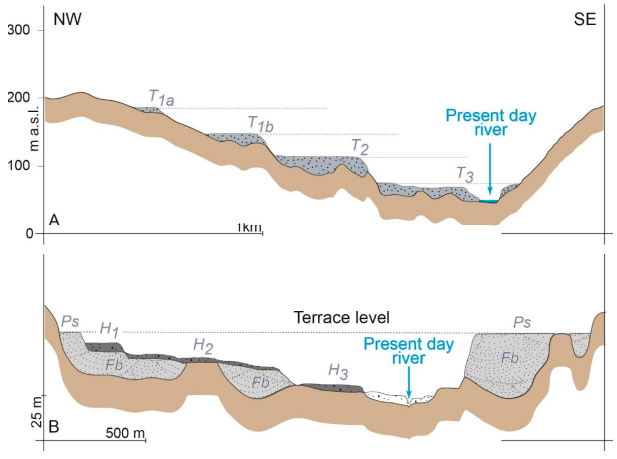


Figure 2. Schematic profiles along an ideal valley sector along the Adriatic side of the northern Marche Apennines. (**A**) Schematic altimetric profile across an ideal mid-valley illustrating the altimetric distribution of different terrace generations composing the typical middle-to-late Pleistocene terraces staircase (after [20], modified). (**B**) Schematic cross-section within an ideal valley showing the nested configuration of the different terrace generations composing the late Pleistocene–Holocene sequence (T3–T4 terraces) that denotes the present floodplain (after [20], redrawn). Relevant are (i) the late Pleistocene, full-glacial main valley filling characterized by braided-type deposits (Fb) and the corresponding remnants of the terrace top–surface (Ps) delineating the T3 terrace level as well as (ii) the different Holocene fill-cut episodes (H1–3) characterizing the general, post-glacial downcutting phase and (iii) the present-day flooding zone fringing the thalweg above the channel bankfull.

3. Materials and Methods

The available datasets on fluvial terraces along the Adriatic margin of the Marche Apennines partially provide details on the most recent fluvial terrace generation starting from the T3. Indeed, also considering the cartographic scale, they just report the general spatial information and sedimentological data, lacking geomorphological details. For example, the updated geological map [26,27] only reports the types of the predominant deposits and their spatial distribution along the main floodplains, whereas neither provides a precise morpho-stratigraphic, nor have geometric distinctions been made among the different terrace levels younger than the late Pleistocene and, eventually, the evidence of fill-cut episodes starting from late Pleistocene terrace generation [19] (Figure 2A). In fact, in the available geological dataset, the Holocene fluvial terraces are considered as an indistinct terrace level. Consequently, minor terrace features, such as terraced surfaces and scarps forming different minor Holocene terrace generations, result as undistinguishable. These terrace features are important, as geomorphological evidence for several depositional and/or erosional episodes occurred during the Holocene.

In this work, a combination of field-based and remote sensing techniques consisting of geomorphological surveys and LSQ analysis [13,14] was performed along a sector, ca. 4 km long, of the Misa River floodplain. The topographic dataset, available for the study area in vector format at a scale of 1:10,000, was used as a base map for the field work performed on a Samsung Galaxy S7+ tablet equipped with the QField app (https://qfield.org/, accessed on 21 September 2022). Field surveys were preliminarily supported by the interpretation of panchromatic orthophotos, available for the years 1988–1989 and 1994–1998 at www.pcn.minambiente.it (accessed on 21 September 2022) as a web map service (WMS), together with panchromatic aerial photos available in stereo-pair at the scale of 1:33,000 (year 1954) and 1:75,000 (year 1989). Google Earth optical satellite imagery was also used for the preliminary geomorphological interpretations, and Google Street Map has been used to virtually run across the main roads network for the preliminary checking of possible outcrops and/or geomorphological features useful for the successive fieldworks.

LSQ analysis was performed starting with a DTM derived from the LiDAR survey with density of points > 1.5 per square meter. The dataset for the Italian floodplains is available at www.pcn.minambiente.it (accessed on 21 September 2022) [16]. The DTM, with a ground resolution of 1 m, presents an error accuracy lower than $\pm$ 15 cm in elevation and $\pm$ 30 cm in plane [16].

A geographic information system (GIS) using the ESRI ArcGIS 10.8.1 desktop software platform was principally used for storing the geomorphological data derived from field works, managing the whole dataset, other than for performing images processing and LSQ analysis, and for preparing the layouts of the final products. QGIS 3.2 software has also been adopted for completing some morphometric analyses and for the synchronization of the GIS layers with the QGIS mobile app during the surveys.

3.1. Geomorphological Field Survey

A series of geomorphological field surveys was carried out in order to corroborate previous datasets derived from the works by [28–30] and the one already reported in the new geological map available for the study area at the scale of 1:50,000 [26,27]. Specifically, the surveys performed in this work aimed at refining the detection and mapping of fluvial processes and landforms as well as at acquiring major details about the types and spatial arrangement of the terrace deposits with a particular attention to those starting from the late Pleistocene main terrace generation. Moreover, the geometry and morphology of the features associated with each terrace generation, such as the inner and external edges, main scarps, and top–surfaces, were the object of the surveys. Field works have also been concentrated upon the present active channel in order to distinguish the channel sectors presently incising into bedrock from those that display depositional behavior. On the field, a general screening of the anthropogenic landforms has also been performed to eventually filter these artifacts from the DTM. The main outputs are reported on a geomorphological

scheme created with the cartographic accuracy corresponding to a scale < 1:10,000 (Figure 3). Field surveys have been supported by the interpretations of remote sensing imagery such as panchromatic orthophotos and aerial photos in addition to Google Earth optical satellite data. This support has turned out to be profitable in identifying terrace features through their surface expression (i.e., color, texture, structure) and for defining the landform state of activity based on the multitemporal interpretation of images taken in different years.

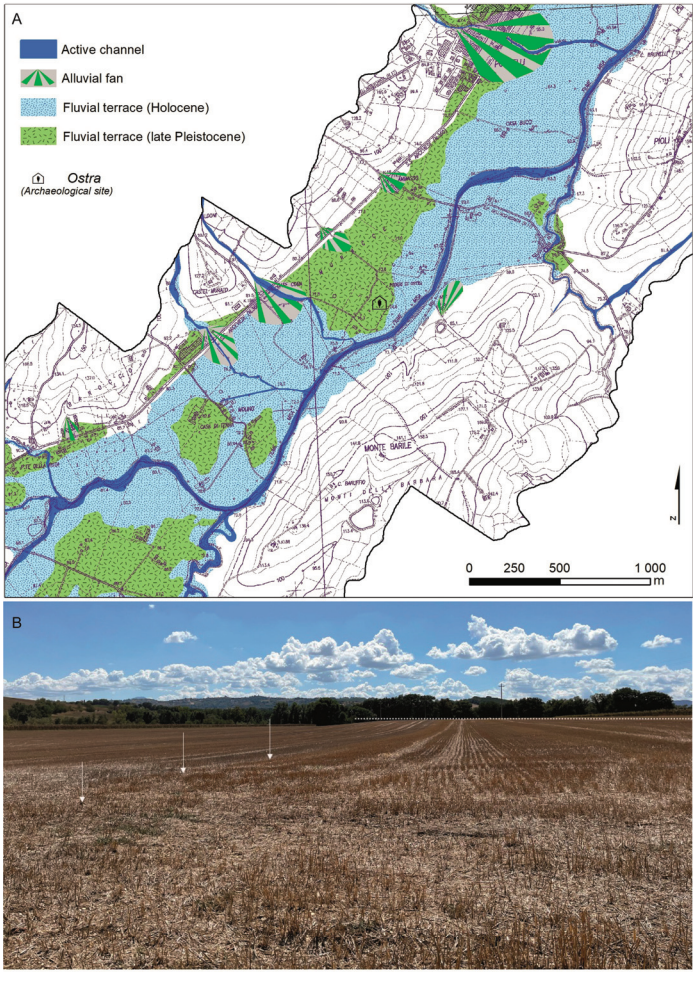


Figure 3. Geomorphological characteristics of the studied section of the Misa River valley floor with a particular emphasis on the fluvial terraces derived from field surveys. (**A**) Geomorphological scheme showing the distribution of the main fluvial terraces composing the late Pleistocene–Holocene floodplain. In this scheme, alluvial fans at the margin of the floodplain and the configuration of the present active channel are also reported. (**B**) Panoramic view of a portion of the floodplain where the planar configuration of the top–surface of the late Pleistocene fill terrace generation can be observed (white-dashed straight line) separated by a remolded scarp (approximately 3 m high) from the younger terrace (white arrows). The remodeled scarp separating the oldest terrace from the younger ones can be detected with continuity along the floodplain; on the contrary, an objective distinction of the different steps composing the Holocene terraces staircase is almost impossible to observe directly on the field due to the very low-relief of the floodplain, agricultural practices, and the scarce continuity of the scarps separating the different terrace steps.

3.2. Land-Surface Quantitative (LSQ) Analysis

The quantitative characterization of the topography, aimed at identifying the fluvial terraces, was carried out considering the geometric properties of the specific landforms being detected. As a result, 7 morphometric parameters, both primary and secondary [31], were selected. Namely, the computed morphometric parameters are slope (S), curvature (C), roughness (R), elevation standard deviation (ESD), topographic position index (TPI), terrain ruggedness index (TRI), and geomorphons. The primary parameters, which consider a moving window with respect to the central cell in the computation, comprise local parameters both of geometric (slope and curvature) and statistical types (roughness and elevation standard deviation). Between the secondary parameters, both indexes (the topographic position index and terrain ruggedness index) and objects (geomorphons) have been considered. The first was intended as a combination of primary parameters [32], while the second was conceived as an elementary unit expressing geometric terrain types [33]. These parameters have been selected with the purpose of remotely supporting the identification of terraces and evaluating their specific statistics in each terrace order. The considered morphometric parameters consist of 6 of continuous type (slope, curvature, roughness, elevation standard deviation, topographic position index, and terrain ruggedness index) and 1 of categorical type (geomorphons).

S (Figure 4A) has been calculated by exploiting the algorithm running in the Spatial Analyst tool of the ArcGIS software, which considers the parameter as the first derivative of the elevation surface or the maximum change in elevation on a cell-by-cell basis [34]. This geometric parameter has been considered, as it is considered to be a basic variable for defining the specific signature of several geomorphic processes [35].

C (Figure 4B) was calculated by combining the planform and the profile values in order to estimate the magnitude of the concavity and convexity of the land surface and to describe the general shape of the slopes [36]. Curvature was computed by exploiting the algorithm running in the Spatial Analyst tool of the ArcGIS software.

R (Figure 4C) is a local-statistical parameter and was computed by considering the largest inter-cell absolute difference of a focal cell and its surroundings [14,37], defined as a 3×3 cell moving window. The R values were computed using the focal statistics approach in the Spatial Analyst tool of the ArcGIS software and the Raster calculator tool.

ESD (Figure 4D) is a parameter of the local-statistic type and was computed by performing a neighborhood operation using a 3×3 moving window, wherein the output value for each cell represents the standard deviation value within the considered window. ESD is a measure of the amount of variation in height within the selected area, with values close to zero indicating flat zones. The ESD values were computed using the focal statistics approach in the Spatial Analyst tool of the ArcGIS software.

TPI (Figure 4E) measures the difference between the elevation at a central point with respect to the average elevation of its neighborhood, and it is used to describe the relative position of the cells of the DTM with respect to the surrounding area [38,39]. This parameter is highly scale-dependent and enables one quantitatively express the morphology of the area being considered. In this study, TPI values were computed by considering an area corresponding to the 3×3 windows adopted in the calculation of other morphometric parameters. TPI was calculated with the specific GDAL tool available in the QGIS software.

TRI (Figure 4F) represents a measurement of the topographic heterogeneity quantifying the mean value of the absolute difference in elevation between a focal cell and its surroundings [40]. In our study, it is defined in in a 3×3 cell window. TRI was calculated with the specific GDAL tool available in the QGIS software.

Geomorphons (Figure 5) are an object-based parameter which identifies geomorphological types based on pattern recognition rather than differential geometry. This parameter consists of 10 classes which classify the terrain in terms of the following features: depression (or pit), flat, footslope, hollow, ridge, shoulder, slope, spur, summit (or peak), and valley [33]. The geomorphon parameter was calculated using the specific GRASS tool available in the QGIS software. Geomorphons were computed considering several combinations of

input information, among which the best-performing example considered an outer search radius equal to 3, an inner search radius of 0, and a flatness threshold equal to 3°.

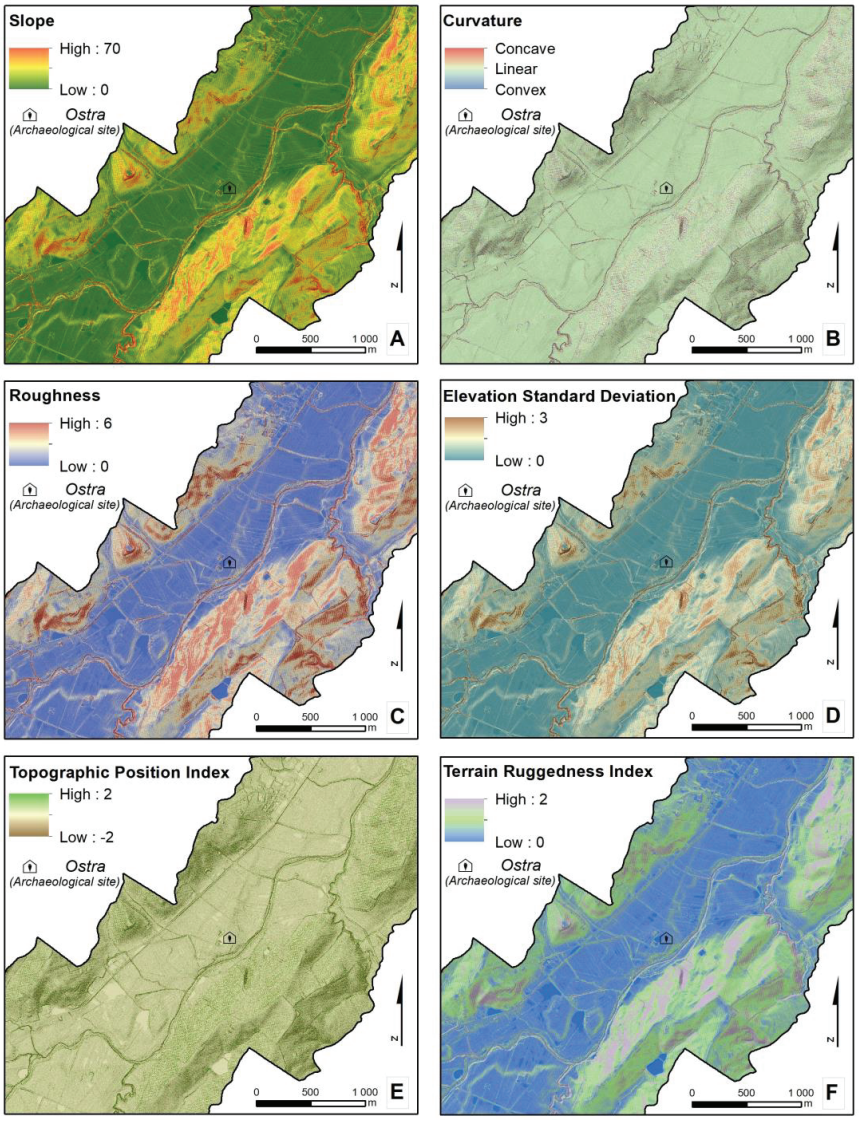


Figure 4. Spatial distribution of the selected continuous morphometric parameters in the study area: slope (**A**), curvature (**B**), roughness (**C**), elevation standard deviation (**D**), topographic position index (**E**), and terrain ruggedness index (**F**).

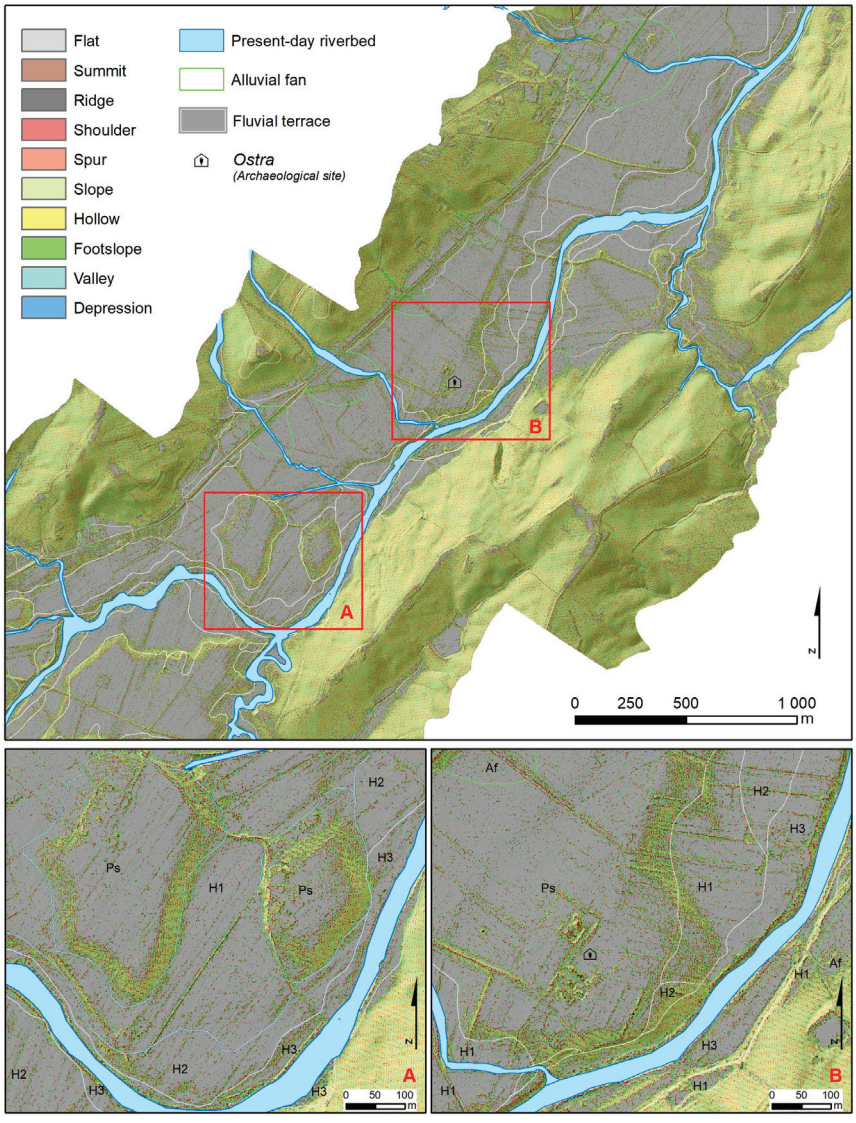


Figure 5. Comparison between the geomorphon output and fluvial features (present-day riverbed, alluvial fan, and fluvial terrace) mapped from field surveys. In the (**A**,**B**) insets, Af: alluvial fan, Ps: late Pleistocene fill terrace, H1: Holocene—first terrace level, H2: Holocene—second terrace level, and H3: Holocene—third terrace level.

4. Results

The field survey allowed us to distinguish the main terrace generation (Figure 3), corresponding to the late Pleistocene fill terrace, thanks to the good preservation of the planar geometry of the terrace top–surface, which hangs at a mean of 12–16 m above the present thalweg, and the large presence, above and immediately below of this thalweg, of well-rounded fluvial cobbles of different dimensions, taken as markers of the late Pleistocene gravel deposits ([16] and references therein). The presence of gravel above the terrace surface seems to diminish starting at the higher terrace level and continuing to the lower ones. Despite the good preservation of the original geometry of the late Pleistocene terrace

top–surface, the inner and external edges of the main terrace have not been successfully recognized in the field because of the profound remodeling caused by agricultural practices, hydraulic works, urbanization, and the overall very low altitudinal differences between the single terrace features. Furthermore, the inner terrace edge, corresponding to the inner margin of the present valley floor, is often crossed by a main road, is fringed by a shallow colluvial cover, and, at the main tributary streams, is at places hidden by wide alluvial fan bodies (Figure 3). The latter have been reported in the geomorphological scheme, and their limits have been mapped using aerial photo interpretation based on the different colors and textures shown by different landforms [41]. The limits between the main, late Pleistocene fill terrace reported in the present geological map and the Holocene terraces have been checked and adjusted where possible thanks to the presence of a remolded scarp that, at places, preserved the original landform geometry (Figure 3b). On the contrary, as expected, the distinction between different minor terrace steps starting from those of the late Pleistocene (hanging at heights from few meters up to about 10 m from the present thalweg) has not been possible due to the apparent absence in the field of recognizable landforms and deposit outcrops. In addition, field survey allows for the recognition that the active river channel is characterized by bedrock typology and, at places, is covered by a thin alluvial cover represented by shallow gravel bars. The bedrock incising tendency of the active river channel is also testified to by the presence of 2–3 m high, sub-vertical active river banks fringing the active channel with a relative spatial continuity.

To support the field survey findings, a visual inspection of the spatial distribution of the selected morphometric parameters was carried out (Figures 4 and 5). This visual inspection was conducted by cross-checking the outputs, specifically symbolized to optimize the thresholds between significant values, of the LSQ analysis.

In the S output, the contrast between the floodplain and the slope sector is evident as well as the location of the present active channels (Figure 4A). Major S values are found in correspondence with the present-day riverbeds and along slopes that are mainly occupied by landslides and alluvial fans. Furthermore, in the defined floodplain, the geometric delineation between the late Pleistocene and Holocene fluvial terraces is evident, as the former are surrounded by noticeable slope breaks which contoured the terrace top–surface. Likewise in the R, ESD, and TRI outputs (Figure 4C,D,F) where these same distinctions are detectable, with differences are mainly due to the range of values computed and the graduated color scale employed. The C and TPI outputs (Figure 4B,E), conversely, do not supply an effective visual support for terrace identification, as the wide value range is opposed by a limited variance of around zero. Finally, the 10 classes of geomorphons (Figure 5) allow for a more detailed description of the local morphology and relative changes, especially when a 1 m resolution DTM is employed, as is the case in this study site; however, they require a large-scale interpretation and an overall generalization in order to be functional for fluvial terrace delimitation (Figure 5A,B). The floodplain, clearly distinguishable from the slope sectors, is dominated by the flat class interspersed with alternating geometries (i.e., hollow, footslope, and spur) which describe the slope breaks and corresponding fluvial terrace limit.

The computed S values show a value range from 0° to 69.78° (Figure 4A, Table 1) with a mean value of about 7°, median value of about 5°, and a third quartile of about 10°. If only terraced deposits are considered, then the mean value drops by about to 2° with 87% of the values less being than 5°, and 94% of the values being less than 10°. Differences in S-value distribution between the Ps terraces and H terraces are slightly delineable, as the former have a mean value of 2.53°, while the latter present a mean value of 3.50°. More detectable, especially in relation to the small range of values, are the distinctions that fit out in the S values of the three Holocene terrace levels; H1 shows a lower median value equal to 1.30° in comparison with the median value of the H3 level, which is equal to 2.43° (Figure 6A).

Table 1. Descriptive statistics of the considered morphometric parameters. The presented values are divided into total area, late Pleistocene terraces (Ps), and Holocene terraces (H); these latter are subdivided in the three terrace levels (H1–H2–H3).

		Total Area	Ps	H		
				H1	H2	H3
S	MIN-MAX	0.00–69.78	0.00–60.18		0.00–69.78	
				0.00–58.04	0.00–63.78	0.00–66.33
	MEAN	6.86	2.53		3.50	
				1.80	2.04	4.98
	1ST QUARTILE	1.67	0.92		0.82	
				0.70	0.80	1.16
	MEDIAN	4.8	1.74		1.61	
				1.30	1.47	2.43
	3RD QUARTILE	10.27	3.08		3.09	
				2.20	2.48	5.11
C	MIN-MAX	−516.82–547.03	−310.19–283.14		−516.82–461.92	
				−357.98–268.02	−300.20–356.29	−409.71–349.99
	MEAN	0.13	0.15		0.33	
				0.23	0.13	−0.31
	1ST QUARTILE	−4.80	−3.13		−3.03	
				−2.63	−2.93	−4.11
	MEDIAN	0.00	0.00		0.03	
				0.00	0.10	0.00
	3RD QUARTILE	4.99	3.54		3.73	
				3.11	3.27	4.43
R	MIN-MAX	0.00–5.68	0.00–4.46		0.00–5.68	
				0.00–3.72	0.00–4.75	0.00–5.68
	MEAN	0.33	0.13		0.12	
				0.09	0.11	0.25
	1ST QUARTILE	0.09	0.06		0.05	
				0.05	0.05	0.07
	MEDIAN	0.23	0.09		0.08	
				0.07	0.08	0.12
	3RD QUARTILE	0.47	0.15		0.13	
				0.11	0.12	0.25
ESD	MIN-MAX	0.00–2.31	0.00–1.47		0.00–1.85	
				0.00–1.45	0.00–1.66	0.00–1.85
	MEAN	0.11	0.04		0.04	
				0.03	0.04	0.08
	1ST QUARTILE	0.03	0.02		0.02	
				0.02	0.02	0.02
	MEDIAN	0.08	0.03		0.03	
				0.02	0.03	0.04
	3RD QUARTILE	0.15	0.05		0.04	
				0.04	0.04	0.08

Table 1. *Cont.*

		Total Area	Ps	H		
				H1	**H2**	**H3**
TPI	MIN-MAX	−2.58–2.78	−1.16–1.10	−1.38–1.00	−1.16–1.10 −1.17–1.43	−1.73–1.84
	MEAN	0.00	0.00	0.00	0.00 0.00	0.00
	1ST QUARTILE	−0.02	−0.02	−0.01	−0.02 −0.01	−0.02
	MEDIAN	0.00	0.00	0.00	0.00 0.00	0.00
	3RD QUARTILE	0.02	0.02	0.01	0.02 0.01	0.02
TRI	MIN-MAX	0.00–2.78	0.00–1.39	0.00–1.42	0.00–2.01 0.00–1.71	0.00–2.01
	MEAN	0.1	0.04	0.03	0.04 0.03	0.08
	1ST QUARTILE	0.03	0.02	0.02	0.02 0.02	0.02
	MEDIAN	0.07	0.03	0.03	0.03 0.03	0.04
	3RD QUARTILE	0.15	0.05	0.04	0.04 0.04	0.08

The C values present a mean value of 0.13 × 10^{-2} m and a median value of about 0.00 × 10^{-2} m, with a third quartile of 4.99 × 10^{-2} m (Figure 4B, Table 1). Taking into account the terraced deposits, the mean value is 0.15 × 10^{-2} m for the Ps terraces and 0.33 × 10^{-2} m for the H ones. The zones with positive C values represent about 50% of the total terraced deposits, while the flat zones represent 6%, and the zones with negative C values represent about 44%. Despite the high range in values, 94% of the values are in the range from −15 × 10^{-2} m to 15 × 10^{-2} m (Figure 6B). C value distribution does not considerably differ between Ps and H terraces; in fact, respectively, the median values are 0.00 and 0.03 × 10^{-2} m, the mean values are 0.15 and 0.33 × 10^{-2} m, and the third quartile is 3.54 and 3.73× 10^{-2} m. Even the contrast between the three H terrace levels is marginally marked, except for the H3 level, which presents distinct values for the first and third quartiles, respectively, equal to −4.11 and 4.43 × 10^{-2} m.

The R morphometric parameter exhibits values ranging from 0 m to 5.68 m (Figure 4C, Table 1) with a mean value of 0.33 m, a median value of 0.23 m, and a third quartile of about 0.47 m. Considering terraced deposits, the mean value is 0.12 m, with 91% of the values being less than 0.23 m and 97% of the values being less than 0.47 m (Figure 6C). As for S values, differences in value distribution between Ps terraces and H terraces are hardly delineable, as all parameters are very close in value, but the distinction between the three Holocene terraces appears to be identifiable. Though H1 and H2 are distinguished by limited differences in value distribution, H3 presents a different distribution, with a median value of 0.12 m and a third quartile equal to 0.25 m.

ESD values range between 0.00 and 2.31 m (Figure 4D, Table 1) with a median value of 0.08 m and with first and third quartiles, respectively, of 0.03 and 0.15 m. A total of 97% of the terraced deposits show values less than 0.15 m (Figure 6D). Ps statistics do not differ from H values, but for this parameter some differences are notable between the three H levels and, in particular, in the H3 level.

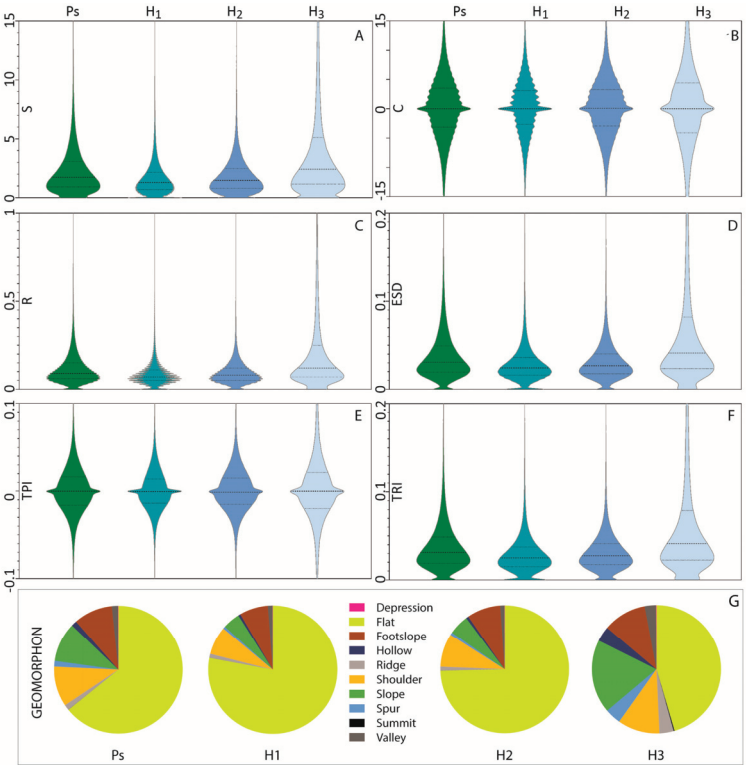


Figure 6. Violin plots of morphometric continuous parameters, namely S (**A**), C (**B**), R (**C**), ESD (**D**), TPI (**E**), and TRI (**F**), and pie charts of the categorical geomorphon parameter (**G**) considering the PS fill terrace and the three Holocene terrace levels (H1, H2, and H3).

TPI morphometric index offers values which are more difficult to interpret both through visual inspection and numerical interpretation. Values range between −2.58 m and 2.78 m (Figure 4E, Table 1), but the descriptive statistics show an equivalent distribution, as 91% of the total study area presents values ranging between −0.1 and 0.1 m, and this percentage rises to 98% if only terraced deposits are considered. The small range of values does not allow for the detection of significant differences, only the H3 level stands out slightly, as already noted in the other morphometric parameters, with the first and third quartiles, respectively, being equal to −0.02 and 0.02 m (Figure 6E).

The computed TRI values show a value range from 0 to 2.78 m (Figure 4F, Table 1) with a mean value of about 0.1 m, a median value of 0.07 m, and a third quartile of about 0.15 m. If only terraced deposits are considered, then the mean value drops to about 0.04 m, with 90% of the values being less than 0.07 m, and 97% of the values being less than 0.15 m. Differences in the TRI value distribution between Ps terraces and H terraces are, as shown by the above-mentioned morphometric parameters, slightly delineable, as the descriptive statistic values are close to be equal. Appreciable are, instead, the distinctions that fit out between the H3 terrace level and the other two H1 and H2 levels (Figure 6F). In particular, H3 shows high values for the median and third quartile equal to 0.04 and 0.08 m, respectively.

Geomorphon outputs are of categorical type, and they consequently have been analyzed by means of visual inspection (Figure 5) and with consideration for the general distribution of the 10 classes within the alluvial terraces (Figure 6G, Table 2). The study area feature types are predominantly slope (38%) and flat (32%), followed by shoulder (7%), spur (7%), footslope (6%), hollow (6%), and then the remaining classes. In the alluvial terraces, the dominant feature is

flat, with a percentage of 64% for Ps terraces and 72% for H terraces (respectively 78%, 75%, and 45%). Next in line are footslope and shoulder with percentages of 10% in Ps terraces and 8% in H terraces. Slope type represents a percentage of 10% in the Ps terraces and 7% in H terraces. Other features are irrelevant with percentages less than 2% both for Ps and H terraces. Considering the distribution characterizing the three H levels, notably the H3 distinction with flat features less than 50% and a relatively high percentage of slope, footslope, and shoulder types as well as a generalized percentage higher that both Ps and other H terraces.

Table 2. Percentage distribution in geomorphon classes of fluvial terraces. The presented values are divided into total area, late Pleistocene terraces (Ps), and Holocene terraces (H), these latter subdivided in the three terrace levels (H1, H2, and H3).

		Total Area	Ps	H		
				H1	H2	H3
GEOMORPHON	Depression	0%	0%		0%	
				0%	0%	0%
	Flat	32%	64%		72%	
				78%	75%	45%
	Footslope	6%	10%		8%	
				7%	8%	11%
	Hollow	6%	1%		1%	
				1%	1%	4%
	Ridge	2%	1%		1%	
				1%	1%	4%
	Shoulder	7%	10%		8%	
				7%	8%	11%
	Slope	38%	1		7%	
				4%	5%	19%
	Spur	7%	1%		1%	
				1%	1%	4%
	Summit	0%	0%		0%	
				0%	0%	0%
	Valley	2%	2%		1%	
				1%	1%	3%

The spatial distribution of morphometric continuous parameters has been also compared, considering their trends (Figure 7) along with selected altimetric profiles (P1–P6 in Figure 8). S, R, ESD, and TRI show observable peaks, denoting evident changes in values, which are supportive to locating the boundaries between different terrace levels as well as to top surface identification. Meanwhile, C and TPI exhibit fluctuating trends which are not interpretable for terrace delimitation. In Figure 7, by way of example, the trends along P1 and P4 are shown. In both, S, R, ESD, and TRI display analogous trends with peak values, those higher than the mean corresponding with terrace limits and low steady values, those lower than the mean, in correspondence with the terrace top–surface. All of the parameters show a noticeable peak at the first flex point above the talweg, potentially marking the height of the channel bankfull. In particular, the C parameter shows a rapid switch from negative to positive values, confirming the occurrence of a flex point at the external margin of the floodplain, above the present active channel.

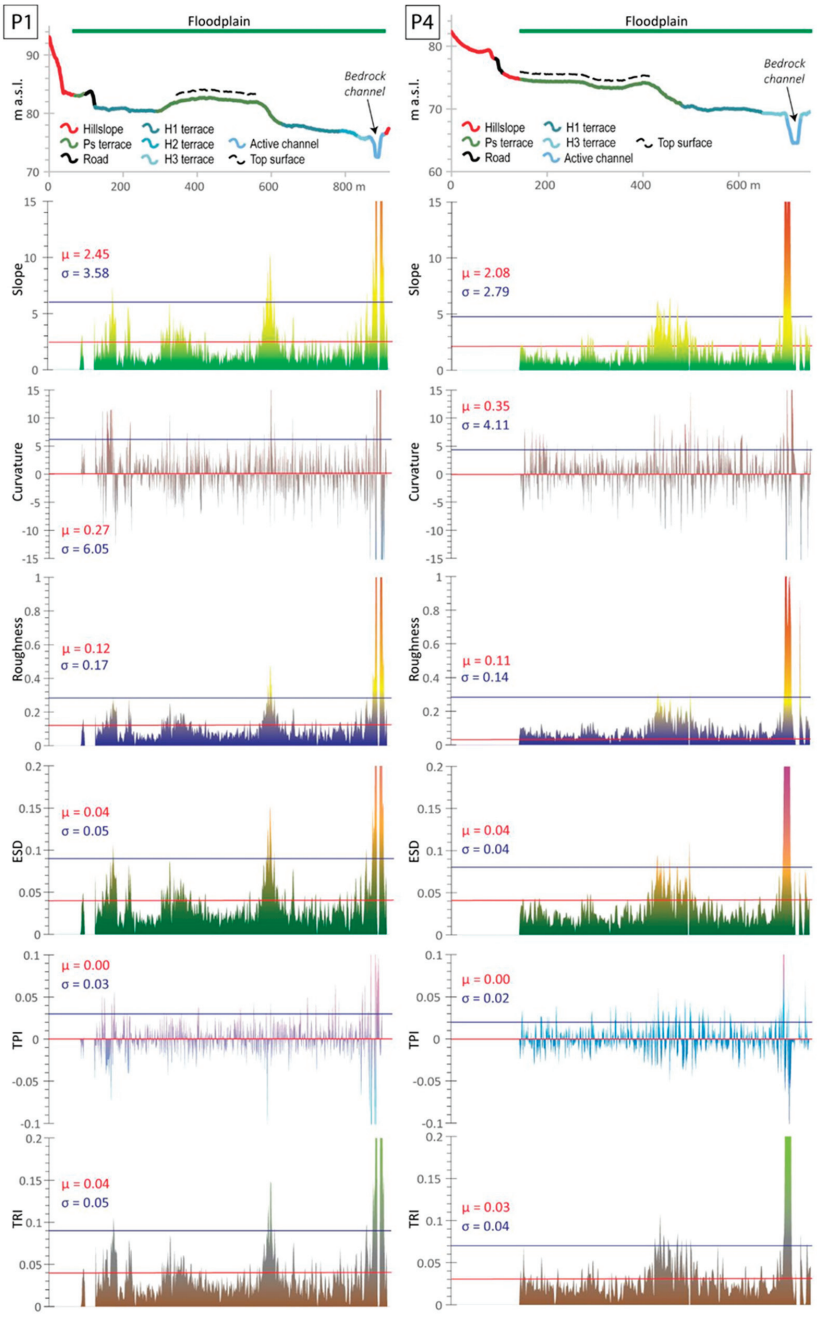


Figure 7. Altimetric profiles along the two most-significant traces (P1 and P4 in Figure 8) and the profile distribution of the morphometric parameters calculated. For each parameter, the values of the mean and standard deviation have been reported as strength lines for a better visual interpretation of the parameter distribution. The altimetric profiles report the fluvial terrace generations according with the color scheme and nomenclature of Figure 8. See the text for further details. The altimetric profiles P2, P3, P5, and P6 (locations in Figure 8) are consultable in the Supplementary Files.

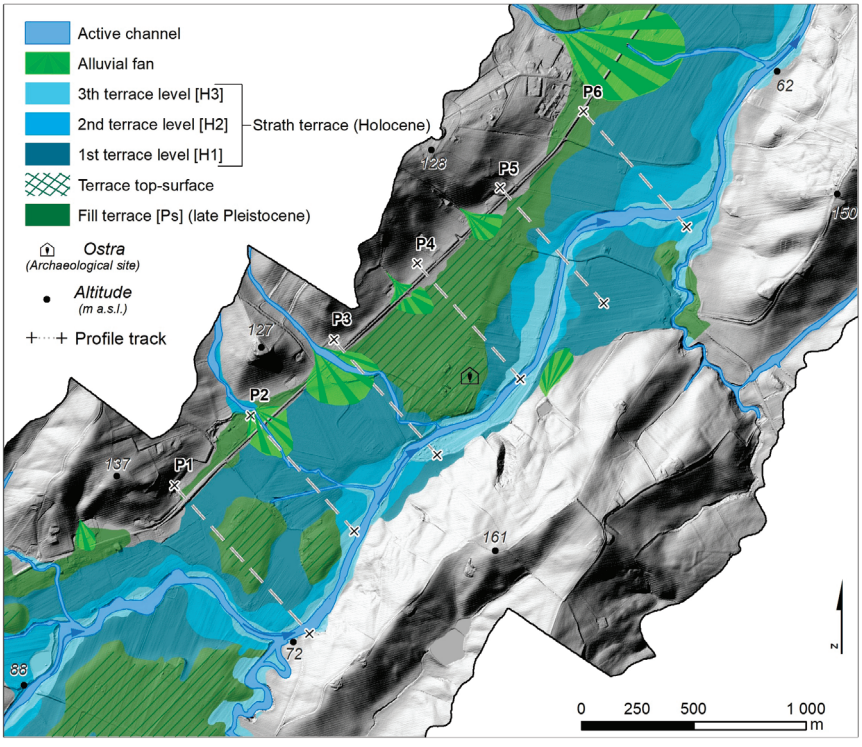


Figure 8. Final geomorphological map derived from the field surveys combined with LSQ analysis showing the distribution of the late Pleistocene terraces and the three Holocene terrace levels, characterizing the studied section of the Misa River valley. Alluvial fans at the margin of the floodplain and the configuration of the present active channel are also reported.

5. Discussion

Despite previous studies and the efforts made in the field, the individuation of some terrace features and the assessment of their spatial distribution and continuity remained elusive, therefore, LSQ analysis has been supportive to obtaining more detailed identifications and precise mapping.

Field surveys have proven to be of basic relevance in identifying the terrace typologies (fill and strath) for both Ps and H levels. A main terrace of fill typology (Ps on Figure 2B) and three different discontinuous levels of strath terraces (H1, H2, and H3 on Figure 2B) compose the fluvial terraces staircase in the analyzed sector of the Adriatic side of the northern Marche Apennines, confirming the model proposed [16] for the arrangement of the main floodplains in the study region (Figures 7 and 8). The highest and most continuous fill terrace, corresponding to the T3 terrace generation [20], formed during the late Pleistocene under cold, full-glacial conditions. Gravels and sands of braided-type river pattern compose the terrace deposits, whose sedimentation ended at about 14 ka (see the scheme of valley development reported in [18], which is valid for the mid and lowermost section of the river valleys draining the Adriatic side of the Marche Apennines). The main late-Pleistocene fill terrace shows a sub-planar terrace top–surface, well-continued along the valley and slightly dipping toward the main channel at the valley bottom and hanging at heights between 10 and 16 m above the present thalweg. The terrace surface at places results as being remolded by tributary streams' entrenchment and human activities. Starting from this terrace surface, at lower heights between 3–4 and 9–10 m above the preset thalweg, a series of discontinuous terrace steps can be found due to episodic

overbank sedimentation during a general entrenchment phase [42], changing river regimes coupled with lateral river migrations [43], and/or in-grown meanders [20,24]. Therefore, considering the thin depositional cover never exceeding 2–3 m in thickness [20,23,24], these terrace levels can reasonably be interpreted as strath terraces generated in short episodes of river stationarity. Accordingly, minor filling stages account for thin gravel and sand deposition during a general post-glacial downcutting phase, the latter characterizing the entirety of the Holocene fluvial morphodynamics at the inner portion of the river basins in the study region. Extreme flooding events, such as the one which occurred on 16 September 2022, to cite the most recent, have reached the heights of the lowest terrace levels. Therefore, at places, it is somewhat difficult to distinguish these younger and lower levels from the flooding area. The latter is due to the plain inundation by either the main watercourse or tributary streams along their lowermost sectors crossing the floodplain.

In this research, no chronological investigations have been done, and therefore the chronology of the terrace generations here described has been extrapolated by adopting mere extra-valley correlation criteria which have already been adopted and accepted for the study region [8,18–20,24] based on similar terrace generations located at the same position along valley sides and floodplains. Nonetheless, the position of the ancient Roman village of Ostra, lying at the margin of the late Pleistocene fill terrace top–surface, supports the adopted relative chronology, interpreting the three strath terrace levels, according to [28–30], as early Holocene (10–8.0 ka BP) and late Holocene (ca. 3–2 ka BP and VI–VII century AD) in age, from the higher to the lower one, respectively. Obviously, the lack of absolute chronological constraints in the specific study site provides a wide margin of uncertainty with regard to the hypothesized terrace chronology, and, considering the climate and tectonic relevance of the terrace record here described, the geomorphological results of this work should be taken as stimulus for further targeted research.

The computation and the assessment (both visual and objective) of the selected morphometric parameters have indeed allowed for the refinement of terrace features' identification, completing the conventional geomorphological field surveys and remote imagery interpretations. In particular, the LSQ analysis allows for evaluation of the general along-valley continuity of the Ps surface, refinement of the identification of the terrace top–surfaces, as well as relocation of the Holocene terrace boundaries (H1, H2 and H3), also identifying their along-valley continuity.

The morphometric parameters S, R, ESD, TRI, and geomorphons (Figure 4A,C,D,F and Figure 5) have proven to be effective in supporting the visual interpretation of the investigated fluvial landforms. Conversely, C and TPI were demonstrated to be unreliable in highlighting the limits of fluvial terrace sequence, even if they did contribute to delineating the overall morphology of the considered sector (Figure 4B,E). Corresponding consideration also emerged from the quantitative evaluation of the descriptive statistics of the parameter values (Tables 1 and 2 and Figure 6). It is noticeable that these assessments can support the distinction between the slope sectors and the fluvial terraced deposits as well as the detection of the three Holocene terrace levels. Among these, the characterization of the most recent one (H3) turned out to be particularly evident, as it shows distinctive values for most parameters (Tables 1 and 2).

The interpretation of parameters' values along some profiles and their comparison with the high-detail altimetry derived from LiDAR (Figure 7) allowed for the inner margin of the higher terrace generation to be clearly distinguished, and thus the boundary between the hillslope and floodplain. Along the single profiles, both principal and minor terrace scarps can be identified, thus allowing for a good distinction between the single terrace generations. Moreover, marked by a peak in the C parameter, the channel bankfull can be identified, resulting in the first flex point above the thalweg and the external, channel-wards margin of the floodplain.

The main limitations of the proposed approach are the impossibility of estimating the terrace deposits belonging to the ancient fill terrace generation, and intrinsic difficulties in identifying some small terrace remnants belonging to the youngest strath generations due

to the very small altimetric differences between some of them and the presence of some DTM artifacts.

6. Conclusions

In this work a combined geomorphological approach based on a field survey and land-surface quantitative (LSQ) analysis has been applied for better identification and the detailed mapping of fluvial terraces along low-relief floodplains. The late Pleistocene–Holocene fluvial terrace staircase along a segment in the mid-Misa River valley has been taken as an example of the floodplains developing along the Adriatic side of the Marche Apennines. Here, the combination of fieldwork with the assessment of some morphometric parameters (S, C, ESD, R, TPI, TRI, and geomorphons) derived from a high-resolution DTM, were demonstrated to enhance the identification and mapping of fluvial terraces. Thus, this combined approach allowed for distinguishing and mapping in detail the main terrace generation characterized by the fill typology, the well-developed and continuous terrace surface, and the remodeled, ca. 3 m-high, low-angle terrace scarp that separates the terrace top–surface from the lower and younger terrace generations. These latter are of strath typology, formed during the Holocene, rarely display a well-developed surface, and are discontinuous, though the first Holocene terrace is the most developed. The main terrace was formed during the late Pleistocene under full-glacial, cold conditions, whereas the younger ones were formed at periods of channel stationarity during the general post-glacial downcutting phase.

From a methodological point of view, the field surveys were revealed to be precious for distinguishing the terrace typologies and verifying the results from the quantitative remote analyses. These latter were helpful for distinguishing the different Holocene terrace levels and assessing their along-valley distribution, as well as for objectively identifying and mapping the top–surface of the main fill terrace generation.

The proposed approach, which includes both field surveys and quantitative analysis based on a high-resolution DTM, led to distinguishing the late Pleistocene–Holocene fluvial terrace staircase, thus taking advantage of the quantitative characterization of the geometric properties of these specific fluvial landforms.

The presented approach can potentially be adopted as a preliminary investigation for remote study areas, where field surveys can more-or-less be conducted. Moreover, the early distinction between fluvial terrace features (i.e., top–surface and main scarps) is useful for a preliminary selection of sampling areas, where dating and additional analysis can be conducted for the chronological and sedimentological characterization of the fluvial deposits. Finally, the proposed approach can be reliable for detailing previous geomorphological maps as well as their first fulfillment.

Supplementary Materials: The following supporting information can be downloaded at: https://www.mdpi.com/article/10.3390/geosciences12110425/s1, Supplementary Files: Altimetric profiles P2, P3, P5, and P6 (locations in Figure 8).

Author Contributions: Conceptualization, D.P. and F.T.; formal analysis, G.I. and D.P.; investigation, F.T.; writing—original draft preparation, G.I., D.P. and F.T. All authors have read and agreed to the published version of the manuscript.

Funding: This research was funded by the Sapienza University of Rome to F. Troiani through the project RM120172A260A846 (Progetti di Ateneo 2020) "Geomorphic response of fluvial systems to climate change during the last glacial-interglacial cycle in the northern Apennines of Italy".

Acknowledgments: The authors thank O. Nesci and D. Savelli, retired from the University of Urbino "Carlo Bo", for their suggestions in the genesis and development of fluvial terraces within the Marche Apennines and for the precious discussions about geomorphological techniques which actually inspired this new research on the fluvial terraces within the Marche Apennines.

Conflicts of Interest: The authors declare no conflict of interest.

References

1. Bridgland, D.R.; Westaway, R. Climatically controlled river terrace staircases: A worldwide Quaternary phenomenon. *Geomorphology* **2008**, *98*, 285–315. [CrossRef]
2. Bridgland, D.R. River terrace systems in north-west Europe: An archive of environmental change, uplift and early human occupation. *Quat. Sci. Rev.* **2000**, *19*, 1293–1303. [CrossRef]
3. Tao, Y.; Xiong, J.; Zhang, H.; Chang, H.; Li, L. Climate-driven formation of fluvial terraces across the Tibetan Plateau since 200 ka: A review. *Quat. Sci. Rev.* **2020**, *237*, 106303. [CrossRef]
4. Maddy, D. Uplift-driven valley incision and river terrace formation in southern England. *J. Quat. Sci.* **1997**, *12*, 539–545. [CrossRef]
5. Starkel, L. Climatically controlled terraces in uplifting mountain areas. *Quat. Sci. Rev.* **2007**, *22*, 2189–2198. [CrossRef]
6. Tlapáková, L.; Pánek, T.; Horácková, S. Holocene fluvial terraces reveal landscape changes in the headwater streams of the Moravskoslezské Beskydy Mountains, Czechia. *Geomorphology* **2021**, *377*, 107589. [CrossRef]
7. Iacobucci, G.; Troiani, F.; Milli, S.; Mazzanti, P.; Piacentini, D.; Zocchi, M.; Nadali, D. Combining satellite multispectral imagery and topographic data for the detection and mapping of fluvial avulsion processes in lowland areas. *Remote Sens.* **2020**, *12*, 2243. [CrossRef]
8. Troiani, F.; Della Seta, M. Geomorphological responses of fluvial and coastal terraces to late Quaternary tectonics and climate change as revealed by geostatistic topographic analysis. *Earth Surf. Proc. Land.* **2011**, *36*, 1193–1208. [CrossRef]
9. Demoulin, A.; Bovy, B.; Rixhon, G.; Cornet, Y. An automated method to extract fluvial terraces from digital elevation models: The Vesdre valley, a case study in eastern Belgium. *Geomorphology* **2007**, *91*, 51–64. [CrossRef]
10. del Val, M.; Iriarte, E.; Arriolabengoa, M.; Aramburu, A. An automated method to extract fluvial terraces from LIDAR based high resolution Digital Elevation Models: The Oiartzun valley, a case study in the Cantabrian Margin. *Quat. Int.* **2015**, *364*, 35–43. [CrossRef]
11. Hassenruck-Gudipati, H.J.; Ellis, T.; Goudge, T.A.; Mohrig, D. A multi-proxy assessment of terrace formation in the lower Trinity River valley, Texas. *Earth Surf. Dynam.* **2022**, *10*, 635–651. [CrossRef]
12. Stout, J.C.; Belmont, P. TerEx Toolbox for semi-automated selection of fluvial terrace and floodplain features from lidar. *Earth Surf. Process. Landf.* **2013**, *39*, 569–580. [CrossRef]
13. Troiani, F.; Martino, S.; Marmoni, G.M.; Menichetti, M.; Torre, D.; Iacobucci, G.; Piacentini, D. Integrated field surveying and land surface quantitative analysis to assess landslide proneness in the Conero promontory rocky coast (Italy). *Appl. Sci.* **2020**, *10*, 4793. [CrossRef]
14. Piacentini, D.; Troiani, F.; Torre, D.; Menichetti, M. Land-Surface Quantitative Analysis to Investigate the Spatial Distribution of Gravitational Landforms along Rocky Coasts. *Remote Sens.* **2021**, *13*, 5012. [CrossRef]
15. Tsanakas, K.; Karymbalis, E.; Gaki–Papanastassiou, K.; Maroukian, H. Geomorphology of the Pieria Mtns, Northern Greece. *J. Maps* **2019**, *15*, 499–508. [CrossRef]
16. Ministero dell'Ambiente e della Tutela del Territorio e del Mare—Geoportale Nazionale. Not Ordinary Plan of Remote Sensing. Available online: http://www.pcn.minambiente.it/mattm/en/not-ordinary-plan-of-remote-sensing/ (accessed on 21 September 2022).
17. Ministero dell'Ambiente e della Tutela del Territorio e del Mare—Geoportale Nazionale. Carta Geolitologica 500,000. Available online: http://www.pcn.minambiente.it/viewer/index.php?services=geolitologica (accessed on 21 September 2022).
18. Calderoni, G.; Della Seta, M.; Fredi, P.; Lupia Palmieri, E.; Nesci, O.; Savelli, D.; Troiani, F. Late Quaternary geomorphological evolution of the Adriatic coast reach encompassing the Metauro, Cesano and Misa river mouths (Northern Marche, Italy). *GeoActa* **2010**, *3*, 109–124.
19. Wegmann, K.W.; Pazzaglia, F.J. Late Quaternary fluvial terraces of the Romagna and Marche Apennines, Italy: Climatic, lithologic, and tectonic controls on terrace genesis in an active orogen. *Quat. Sci. Rev.* **2009**, *28*, 137–165. [CrossRef]
20. Nesci, O.; Savelli, D.; Troiani, F. Types and development of stream terraces in the Marche Apennines (central Italy): A review and remarks on recent appraisals. *Géomophologie Relief Process. Environ.* **2012**, *18*, 215–238. [CrossRef]
21. Nesci, O.; Savelli, D.; Troiani, F. Late Quaternary alluvial fans in the Northern Marche Apennines: Implications of climate changes. *Il Quat. Ital. J. Quat. Sci.* **2010**, *23*, 145–156.
22. Coltorti, M. Human impact in the Holocene fluvial and coastal evolution of the Marche region, Central Italy. *Catena* **1997**, *30*, 311–335. [CrossRef]
23. Dall'Aglio, P.L.; Marchetti, G.; Nesci, O.; Pellegrini, L.; Savelli, D.; Calderoni, G. Geomorfologia e popolamento antico nella media valle del Fiume Cesano (Marche-Italia). *Il Quat. Ital. J. Quat. Sci.* **2004**, *17*, 213–219.
24. Dall'Aglio, P.L.; Giorgi, E.; Silani, M.; Aldrovandi, M.; Fanceschelli, C.; Nesci, O.; Savelli, D.; Troiani, F.; Pellegrini, L.; Zizioli, D. Ancient landscape changes in the North Marche region: An archeological and geomorphological appraisal in the Cesano valley. In *Variabilitès Environnementales, Mutations Sociales, Proceedings of XXXII° Rencontres Internationales d'Archéologie et d'Histoire d'Antibes, Editions APDCA, Antibes, France, 23–25 October 2012*; Bertoncello, F., Braemer, F., Eds.; Editions APDCA: Antibes, France, 2012; pp. 101–112.
25. Savelli, D.; Luni, M.; Mei, O. La città di Forum Sempronii e i suoi rapporti con il paesaggio attuale: Una discussione basata su evidenze geologico-geomorfologiche e archeologiche. *Alp. Mediterr. Quat.* **2004**, *17*, 185–193.
26. Guerrera, F.; Tramontana, M. *Note Illustrative della Carta Geologica d'Italia in scala 1:50,000, Foglio 281—Senigallia*; ISPRA, Servizio Geologico d'Italia: Rome, Italy, 2011; pp. 1–116.

27. Guerrera, F.; Tramontana, M. *Note Illustrative della Carta Geologica d'Italia alla scala 1:50,000 Foglio 292—Jesi*; ISPRA, Servizio Geologico d'Italia: Rome, Italy, 2012; pp. 1–122.
28. Dall'Aglio, P.L.; Franceschelli, C.; Nesci, O.; Pellegrini, L.; Savelli, D. La gestione dell'acqua nella città romana di Ostra (Ostra Vetere, AN): Adduzione, distribuzione, evacuazione. In *Aqua Publica dans la ville Romaine: Droit, Technique, Structures (Clermont-Ferrand, 9 Novembre 2016)*; Franceschelli, C., Dall'Aglio, P.L., Lamoine, L., Eds.; Agri Centuriati: Washington, DC, USA, 2016; Volume 13, pp. 107–127.
29. Dall'Aglio, P.L.; Franceschelli, C.; Roversi, G.; Nesci, O.; Pellegrini, L.; Savelli, D. Il sistema fognario della città romana di Ostra (Ostra Vetere, AN). In *I Sistemi di Smaltimento delle Acque nel Mondo Antico*; Buora, M., Magnani, S., Eds.; Antichità Altoadriatiche: Aquileia, Italy, 2018; Volume LXXXVII, pp. 453–472.
30. Dall'Aglio, P.L.; Franceschelli, C.; Nesci, O.; Pellegrini, L.; Savelli, D. La geografia dei luoghi. In *Ostra: Archeologia di una città romana delle Marche (scavi 2006–2019)*; Dall'Aglio, P.L., Franceschelli, C., Eds.; Ante Quem: Bologna, Italy, 2020; pp. 35–43.
31. Wilson, J.P.; Gallant, J.C. Digital terrain analysis. In *Terrain Analysis: Principles and Applications*; Wilson, J.P., Gallant, J.C., Eds.; John Wiley and Sons: New York, NY, USA, 2000; pp. 1–27.
32. Szypuła, B. Digital Elevation Models in Geomorphology. In *Hydro-Geomorphology—Models and Trends*; Shukla, D.P., Ed.; IntechOpen: London, UK, 2017. [CrossRef]
33. Jasiewicz, J.; Stepinski, T.F. Geomorphons—A Pattern Recognition Approach to Classification and Mapping of Landforms. *Geomorphology* **2013**, *182*, 147–156. [CrossRef]
34. Burrough, P.A.; Mcdonnel, R.A. *Principles of Geographical Information Systems*, 2nd ed.; Oxford University Press: Oxford, UK, 1998; pp. 1–352.
35. Wilson, J.P.; Bishop, M.P. Geomorphometry. In *Treatise on Geomorphology, Remote Sensing and GIScience in Geomorphology*; Shroder, J.F., Bishop, M.P., Eds.; Academic Press: San Diego, CA, USA, 2013; Volume 3, pp. 162–186.
36. Olaya, V. Basic land-surface parameters. In *Geomorphometry: Concepts, Software, Applications*; Hengl, T., Reuter, H.I., Eds.; Elsevier: Amsterdam, The Netherlands, 2009; pp. 141–169.
37. Wilson, M.F.J.; O'Connell, B.; Brown, C.; Guinan, J.C.; Grehan, A.J. Multiscale Terrain Analysis of Multibeam Bathymetry Data for Habitat Mapping on the Continental Slope. *Mar. Geod.* **2007**, *30*, 3–35. [CrossRef]
38. Weiss, A. Topographic position and landforms analysis. In Proceedings of the ESRI User Conference 2001, San Diego, CA, USA, 9–13 July 2001.
39. Jenness, J.; Brost, B.; Beier, P. *Land Facet Corridor Designer: Extension for ArcGIS*; Jenness Enterprise: Flagstaff, AZ, USA, 2011.
40. Riley, S.; DeGloria, S.D.; Elliot, R. A terrain ruggedness index that quantifies topographic heterogeneity. *Intermt. J. Sci.* **1999**, *5*, 23–27.
41. Iacobucci, G.; Troiani, F.; Milli, S.; Nadali, D. Geomorphology of the Lower Mesopotamia Plain at Tell Zurghull archaeological site. *J. Maps* **2022**, 1–14. [CrossRef]
42. Straffin, E.C.; Blum, M.D. Holocene fluvial response to climate change and human activities; Burgundy, France. *Neth. J. Geosci.* **2002**, *81*, 417–430. [CrossRef]
43. Kalicki, T.; Calderoni, G.; Zernitskaya, V.P. River response to the Holocene climatic fluctuations: A case study from Zelvianka river valley (Belorussia). *Il Quat. Ital. J. Quat. Sci.* **2004**, *17*, 165–180.

remote sensing

MDPI

Article

ShuffleCloudNet: A Lightweight Composite Neural Network-Based Method for Cloud Computation in Remote-Sensing Images

Gang Wang [1,2], Zhiying Lu [1,*] and Ping Wang [1]

[1] School of Electrical and Information Engineering, Tianjin University, Tianjin 300072, China
[2] CETC Key Laboratory of Aerospace Information Applications, Shijiazhuang 050081, China
* Correspondence: luzy@tju.edu.cn; Tel.: +86-138-2057-3798

Abstract: The occlusion of cloud layers affects the accurate acquisition of ground object information and causes a large amount of useless remote-sensing data transmission and processing, wasting storage, as well as computing resources. Therefore, in this paper, we designed a lightweight composite neural network model to calculate the cloud amount in high-resolution visible remote-sensing images by training the model using thumbnail images and browsing images in remote-sensing images. The training samples were established using paired thumbnail images and browsing images, and the cloud-amount calculation model was obtained by training a proposed composite neural network. The strategy used the thumbnail images for preliminary judgment and the browsing images for accurate calculation, and this combination can quickly determine the cloud amount. The multi-scale confidence fusion module and bag-of-words loss function were redesigned to achieve fast and accurate calculation of cloud-amount data from remote-sensing images. This effectively alleviates the problem of low cloud-amount calculation, thin clouds not being counted as clouds, and that of ice and clouds being confused as in existing methods. Furthermore, a complete dataset of cloud-amount calculation for remote-sensing images, CTI_RSCloud, was constructed for training and testing. The experimental results show that, with less than 13 MB of parameters, the proposed lightweight network model greatly improves the timeliness of cloud-amount calculation, with a runtime is in the millisecond range. In addition, the calculation accuracy is better than the classic lightweight networks and backbone networks of the best cloud-detection models.

Keywords: cloud-amount calculation; lightweight neural network; multi-scale confidence fusion; bag-of-words; composite network structure

Citation: Wang, G.; Lu, Z.; Wang, P. ShuffleCloudNet: A Lightweight Composite Neural Network-Based Method for Cloud Computation in Remote-Sensing Images. *Remote Sens.* **2022**, *14*, 5258. https://doi.org/10.3390/rs14205258

Academic Editors: Kai Qin, Chi Li, Zhengqiang Li, Zhongwei Huang, Han Wang, Tianhe Wang and Jie Luo

Received: 3 September 2022
Accepted: 19 October 2022
Published: 20 October 2022
Corrected: 9 June 2023

Publisher's Note: MDPI stays neutral with regard to jurisdictional claims in published maps and institutional affiliations.

Copyright: © 2022 by the authors. Licensee MDPI, Basel, Switzerland. This article is an open access article distributed under the terms and conditions of the Creative Commons Attribution (CC BY) license (https://creativecommons.org/licenses/by/4.0/).

1. Introduction

With the development of space technology and the continuous launch of remote-sensing satellites, the data volume of remote-sensing images has seen rapid growth. Statistics show that, continuously, more than 66% of the Earth's surface is covered by clouds [1], which makes the ground observation of optical remote-sensing images challenging. Additionally, this causes many optical remote-sensing images to become cloudy and thus be judged as invalid data. The general processing method implements cloud-detection methods to exclude the interference of cloud regions, remove redundant and invalid data to some extent, and concentrate the subsequent image interpretation on the cloud-free images or regions. However, two scenarios require new consideration: the processing of in-orbit remote sensing and the management of enormous remote-sensing images. Since the computing and storage capabilities of the in-orbit platform are constrained, a simple and efficient cloud-amount calculation method is urgently required. To manage nearly ten million different types of remote-sensing images, the management system for huge remote-sensing images generally adopts a database server and a disk array. At the same time, the system itself has limited computing power. When the cloud judgment of remote-sensing

data before warehousing is not accurate enough, it introduces difficulties to subsequent user retrieval and data usage. Therefore, a method that is less computationally intensive and can calculate the cloud amount of remote-sensing images more accurately without directly calculating the original images is needed to ensure the efficient operation of data management.

With the development of remote-sensing image processing, cloud detection and amount calculation has been an important research topic. Numerous representative methods [2–9] have been proposed to solve this challenge. These methods fall into two main categories: threshold-based methods and statistical-based methods. The former sets a threshold to detect clouds based on information such as spectral reflectance, brightness, and temperature. However, this threshold is not global and does not apply to all scenarios. Therefore, its value must be set according to the different remote-sensing images to be processed. The statistical-based approach is to design manual features based on the physical properties of the cloud (e.g., texture, geometric relationships, and color) and then to use statistical machine-learning methods to classify them pixel by pixel. This method also calculates the cloud amount of the whole image, which facilitates the qualitative and quantitative analysis of remote-sensing images by operators. However, such statistical machine learning-based methods are completely dependent on the feature design level of the researchers. These methods do not work well in practical applications, mainly because the environment captured by remote-sensing images is so diverse that it is difficult to meet the requirements of stability applications.

The rapid development of deep learning in recent years has led to the application of methods involving deep convolutional neural networks to cloud detection, which has facilitated the rapid development of cloud detection and cloud-amount computing due to its very powerful feature representation and scene application capabilities [10–18]. The convolutional neural network-based approach can achieve automatic feature acquisition and automatic classification by establishing a nonlinear mapping from input to output. Experiments have proved that with enough representative samples, better cloud detection and cloud-amount calculation results can be obtained through continuous training and learning. The convolutional neural network-based approach has achieved the best results to date, but it still faces some problems and limitations.

First, most existing CNN-based models improve the performance of cloud detection and cloud-amount calculation by increasing the width and depth of neural networks. Therefore, to obtain a higher accuracy of cloud detection, greater computational resources are required. Such huge neural network models limit their ability to be applied in resource-constrained situations, such as in-orbit processing and data management centers. It is also important to note that the variability in the shape and size of the clouds themselves, as well as the complexity of the background, makes cloud detection and cloud-amount calculation extremely challenging.

As shown in Figure 1 featuring thumbnails of original remote-sensing images, there are many disruptive factors and difficult situations in cloud detection and cloud-amount calculation. The eight remote-sensing images in Figure 1 are derived from ChineseGF-series satellites and ZY-series satellites. In Figure 1a, there is a certain degree of integration between clouds and ground objects. At the same time, a semi-transparent situation also exists. In the original cloud-amount calculation software, the cloud amount is only 12 (a percentage of the whole image), but as can be seen by visual interpretation, it is much more than 12. Thin clouds in Figure 1b are not calculated into the cloud amount by the general algorithm, which is obviously not accurate enough. The clouds in Figure 1c obscure almost all the ground objects, which is an invalid image. Additionally, the original cloud-calculation software calculates it as 8, which is not accurate enough either. In cloud-amount calculation, ice and thin clouds existing in Figure 1d are easily confused, which affects the accuracy of the calculation. The situation in Figure 1e is more complicated: there are thick clouds, thin clouds, ice, and snow, and the thin clouds are not distinguished from the ground objects. There are mainly thin clouds in Figure 1f, and they are evenly distributed

throughout the whole image, making it difficult to calculate the cloud amount. In Figure 1g, there is mainly snow and ice and no clouds, but the original cloud-calculation software calculates them as clouds. In Figure 1h, there is a thick cloud almost completely covering the whole map, and the original cloud-calculation software calculates it as 0, which is clearly wrong. In summary, thin clouds, snow and ice interference, background and cloud integration, and other issues greatly complicate cloud-amount calculation.

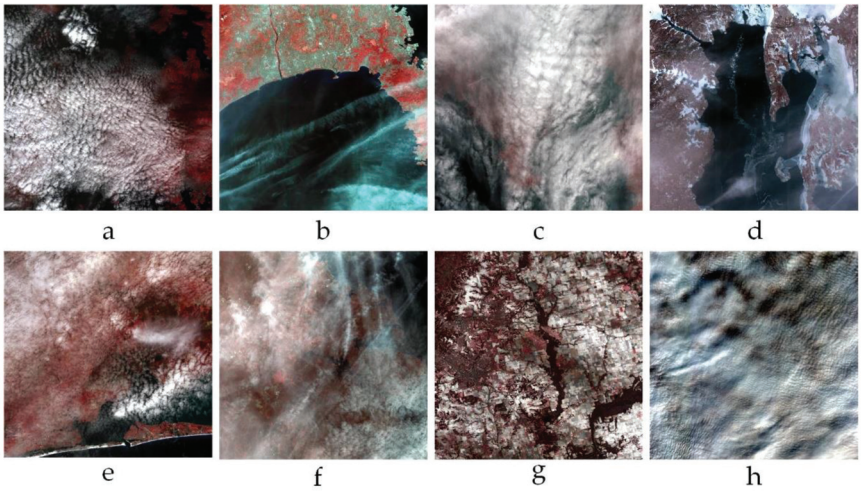


Figure 1. Analysis diagram of some challenging examples of cloud detection in remote-sensing images, featuring: (**a**) a certain degree of integration between clouds and ground objects; (**b**) thin cloud not calculated as part of the cloud amount; (**c**) cloud obscuring almost all the ground objects; (**d**) ice and thin clouds that can be easily confused; (**e**) thick clouds, thin clouds, ice, and snow; (**f**) thin clouds evenly distributed throughout the whole image; (**g**) mainly snow and ice; (**h**) thick cloud almost completely covering the whole image.

Therefore, it is highly significant in research and application to design an efficient and lightweight neural network model to solve the above-mentioned difficulties. Among them, the most straightforward approach is to design the model with as few parameters and operators as possible. Based on what has been mentioned above, a ShuffleCloudNet network structure for cloud-amount computation is designed in this paper. In contrast to the traditional neural network model, ShuffleCloudNet is inspired by the unique operation structure of the channel split in ShuffleNetV2. Furthermore, it adopts the concatenation operation to obtain the perception ability of small-sized clouds. Moreover, the physical features of clouds are very complex and variable. To overcome this challenge, this paper designs a relevant multi-scale confidence fusion module to enhance the distinguishability of different backgrounds and foregrounds. Furthermore, this paper also defines a bag-of-words loss function so that the model can be optimized during the training process and thereby more directly distinguish cloud boundaries, small clouds, etc., from complex backgrounds (e.g., desert, seawater, glaciers, and snow). From the engineering practice experience of remote-sensing image management, we found that thumbnail images and browsing images in remote-sensing images contain good cloud cover information. Operators in the remote-sensing field often pay attention to the general cloud amount in the remote-sensing image rather than the specific cloud location. Therefore, we divide the cloud amount into 11 levels, 0–10, which simplifies the cloud-amount calculation.

To summarize, the main contributions of this paper can be outlined as follows.

1. Differing from the traditional CNN method, an efficient and lightweight network model architecture for remote-sensing image cloud-amount computation is constructed, referred to as ShuffleCloudNet, and which can use fewer model parameters to obtain better results of cloud-amount computation.
2. Based on the diversity of clouds and the complexity of backgrounds, a multi-scale confidence fusion module is proposed to optimize the performance of cloud-amount computation under different scales, backgrounds, and cloud types. Multi-scale confidence fusion, which fuses multi-scale confidence into the final cloud-amount results, notably conforms to a voting principle of human cloud-amount interpretation, itself inspired by the business process of multi-person cloud-amount interpretation.
3. A bag-of-words loss function is designed to optimize the training process and better distinguish complex cloud edges, small clouds, and cloud-like backgrounds.
4. To verify the effectiveness of the proposed model, a cloud-amount calculation dataset, CTI_RSCloud, is built using GF series satellites and ZY series images. It includes thumbnail images, browsing images, and cloud-amount information of remote-sensing images. The data is open-sourced on https://pan.baidu.com/s/1qgvc5j2dxCDl2ei05khxzg (access on 1 September 2022).

The excellent performance of the proposed method is demonstrated in the results of this paper's dataset and other publicly available datasets.

The remainder of the paper is organized as follows. In Section 2, we review the related work of the method generally. Section 3 details the structure of the proposed model and possible improvements to it. Section 4 shows the construction process of the dataset, the ablation experiments, and the experimental results. Finally, the relevant information on this approach is summarized in Section 5.

2. Related Work

Cloud detection and cloud-amount calculation have been widely used and experimentally studied in the field. In this section, we briefly review some related research work on our proposed method.

2.1. CNN-Based Method for Cloud Detection and Cloud-Amount Calculation

In recent years, CNN-based methods have made great progress [19–23], mainly due to their capacity for automatic learning and automatic feature extraction. Xie et al. designed a cloud-detection method based on multi-level CNN [19] and utilized the simple linear iterative clustering (SLIC) method for cloud superpixel segmentation to overcome the wide-magnitude problem of remote-sensing images. Li et al. employed multi-scale fusion using convolutional features to improve the accuracy of cloud detection and cloud-amount calculation. Additionally, their consideration of waveform information improves the detection accuracy to some extent [20]. To better apply the useful regions of remote-sensing images, Shao et al. presented a multi-scale multi-feature convolutional neural network MF-CNN [21] to detect thin clouds, thick clouds, and cloud-free regions in a more refined remote-sensing cloud-processing stage. Yang et al. introduced a cloud-detection network CDnet [22] to directly process thumbnail images for the standard data of remote-sensing images, which is time- and labor-saving and has very important engineering applications. Mohajerani et al. determined whether each pixel is a cloud or not using a fully convolutional neural network and significantly increased the accuracy of cloud-amount calculation using a gradient-based reconfirmation method designed to distinguish clouds from snow and ice [23].

2.2. Lightweight Convolutional Neural Networks

With the rapid rise in the computer vision field, the application of deep networks with powerful performance in embedded platforms and mobile smart devices has encountered problems, which are cleverly solved by the emergence of lightweight networks for such

applications. Based on traditional convolution, the emergence of MobileNetV1 [24], a lightweight CNN network, has dramatically improved the operation speed of traditional networks, whose novelty is the proposed Depthwise Separable Convolution. Although the speed of MobileNetV1 was improved, the feature loss was large, and the accuracy improvement was not obvious. Subsequently, the Inverted Residuals module and Linear Bottlenecks module were added to MobileNetV2 [25], thus increasing the gradient propagation and reducing the memory usage [26]. Based on MobileNetV2, MobileNetV3 was proposed in 2019 [21], whose two versions, MobileNetV3-Large and MobileNetV3-Small, demonstrated improved accuracy and speed. In 2017, Mandola et al. [27] proposed a lightweight network named SqueezeNet, which utilizes a Fire Module to reduce the parameters and the number of input channels, and its pooling layer is placed at the end of the network to improve the accuracy. Earlier in 2018, Zhang et al. proposed ShuffleNetV1 [28], exploiting the idea of pointwise group convolution and channel shuffle, which greatly improved the network inference capability of deep network models in resource-constrained environments. Later in 2018, Ma et al. [29] proposed the lightweight network ShuffleNetV2, which comprises deep convolution and group convolution and introduces a new operation: channel split. Compared to lightweight networks such as ShuffleNetV1, it achieves a speed and accuracy balance. Lightweight convolutional neural networks are more suitable for computer vision applications in mobile devices due to their smaller model size, reduced memory occupation, and faster-running speed while ensuring that accuracy is not reduced. The processing of remote-sensing images, especially in-orbit processing and preprocessing before accessioning in data centers, is conducted with very limited resources. Thus, it is necessary to adopt a lightweight network to realize cloud-amount calculation to reduce computing volume and ensure accuracy.

2.3. Complex Neural Networks

After the introduction of neural networks, they became an increasingly common means to solve problems in different domains by increasing their architectural complexity. Before 2012, notably from 2006, a composite neural network design had become commonplace for solving problems in automatic control, planning, and decision making relating to problems such as computing power and network gradient disappearance. In 2001, Xia et al. had proposed a dual neural network model [30] to solve the kinematic control problem of redundancy robots, which has been demonstrated to be globally stable. In 2004, Zhang et al. constructed a dual neural network to solve the obstacle-avoidance problem of redundancy degree robots, whose network is mainly a combination of a recurrent neural network and a fully connected neural network [31]. In 2006, Liu et al. presented a pairwise neural network and analyzed its application in task planning as well as KWTA tasks [32]. The above-mentioned composite neural networks solve certain optimization and control problems, but they still lack effective solutions in applications such as image-processing classification because the number of neural network layers and feature-expression capabilities are not in place. Since the development of deep learning in 2012, many neural networks for image classification have been established. Among them, there are many models that use composite neural networks to solve multi-source information input. In 2017, Hao et al. proposed a composite neural network framework to solve the plane-detection problem for ultrasound annotation [33]. The deep neural network was designed to carry out relevant research on image classification. Their relevant design ideas were influenced by the composite neural network in the control field, and they began to design multiple neural networks for cross-validation or mutual assistance. In 2019, Zhu et al. introduced a dual-way neural network model that could input images and text to solve the classification problem of small-sample images, and described a fusion strategy of image and text information which improved the training efficiency [34]. In 2021, Tian et al. built a dual-way neural network that utilized different feature-extraction and target-detection ideas for final fusion, which obtained an excellent object-detection result for UAVs in remote-sensing images, especially for small objects [35]. Li et al. reported binary composite neural networks that can handle binary

complex data inputs and weights through complex convolution with limited hardware computational resources while showing outperformance compared to the best existing models using Cifar10 and ImageNet datasets [36].

In remote-sensing processing, most professionals use cloud-detection methods to solve information occlusion and too much interference in remote-sensing images to better complete the extraction of ground object information. This approach gradually develops from a method based on band characteristics to a method based on deep neural networks. In cloud detection, several important datasets are proposed, including GF-1 WFV [37] and AIR-CD [38]. The application scenario to be solved in this paper involves quickly calculating the cloud amount of each standard remote-sensing image product in the massive remote-sensing image data management file to determine whether it will be further distributed and processed. In this scene, we do not pay attention to the location of the cloud but focus on the number of clouds and whether this will seriously affect the information extraction and visual interpretation of images.

3. Proposed Method

As shown in Figure 2, the L1 and L2 remote-sensing image products include the original remote-sensing image, metadata, RPB data, browsing image, and thumbnail image. Among them, the size of the browsing image is about 1024 × 1024, the size of the thumbnail image is about 60 × 60, and the size of the original image is about 7000 × 7000; metadata is used to describe the satellite number, shooting time, bands and other information of the remote-sensing image product; RPB data have detailed RPC model parameters for image orthorectification. Through observation and analysis, we found that the cloud details described in the thumbnail and browsing images are sufficient to identify the cloud amount. Therefore, we used the thumbnail image and browsing image in the standard remote-sensing image products as the input of the designed neural network. At the same time, the designed neural network also needs two structures to process the thumbnail image and browsing image, respectively, and finally, it uses the fusion structure to fuse the results.

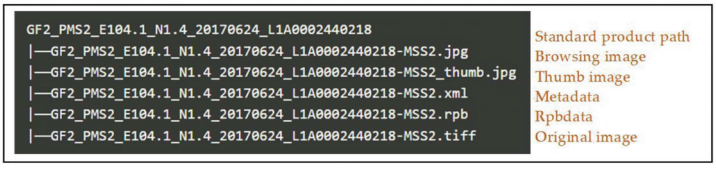


Figure 2. Structure of cloud-amount calculation based on a composite neural network.

A lightweight neural network model, ShuffleCloudNet, is proposed for the cloud-amount calculation of remote-sensing images. Through feature extraction and training optimization, it can obtain the cloud amount from the browsing image and thumbnail image in the standard data of the remote-sensing image. By analyzing the diversity of clouds and the complexity of backgrounds, a multi-scale confidence fusion module is presented to optimize the calculation performance of cloud amounts under different scales, backgrounds, and cloud types. Furthermore, the bag-of-words loss function is introduced to optimize the training process and to better distinguish complex cloud edges, small clouds, and cloud-like backgrounds. The ShuffleCloudNet framework proposed in this paper is shown in Figure 3 and consists of three main parts: (1) the lightweight backbone networks ShuffleCloudNet-L and ShuffleCloudNet-S; (2) the multi-scale confidence fusion (MSCF) module; and (3) the bag-of-words loss function. In the following, a general overview of the algorithm model is provided first, and then the implementation details of the three key steps within the cloud-amount calculation framework are described in detail.

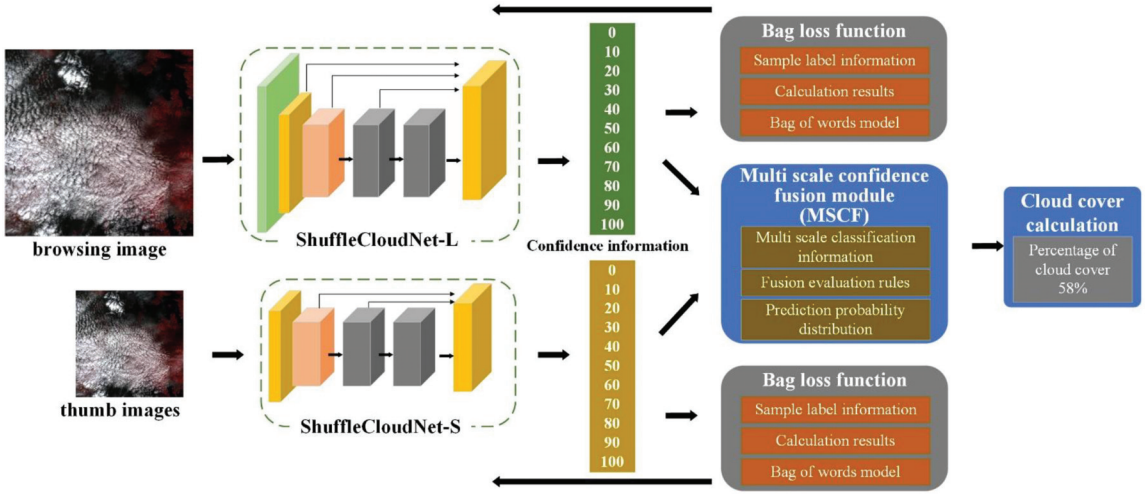


Figure 3. Structure of cloud-amount calculation based on composite neural network.

3.1. Model Description

In our investigation, we found that clouds are generally large in scale, greater than 100 m [2,5–12,22,37–39]. Hence, cloud-amount calculation using high-resolution remote-sensing images consumes too many computational resources while the accuracy improvement is too limited. Generally, browsing images can be a good way to obtain cloud-amount information from remote-sensing images, and thumbnail images can obtain cloud-amount information from remote-sensing images on a more global scale.

First, the cloud-amount calculation problem of remote-sensing images can be described as the following process. Suppose the remote-sensing image used for cloud-amount calculation is d, and the backbone neural network model is applied to calculate the convolutional features of the remote-sensing image. In general, the more complex the structure of the backbone neural network is, the better its feature-extraction capability and the more robust the semantic representation is. However, if the network size is continuously increased to make its structure complex, then the parameters and computation of the whole network will continuously increase. The most straightforward way to solve such problems is to design lightweight network structures to accomplish the convolutional feature extraction in the cloud-amount calculation, to obtain more efficient and fast computational efficiency. Nevertheless, this operation inevitably ignores the semantic need for deep-level features, which reduces the network's performance. Thus, contextual and background knowledge feature information are employed to improve and stabilize the model's computational power and solve this problem. Although some existing methods [19–21] have built some context and background extraction units, these models are difficult to adaptively adjust to remote-sensing images from different loads. Moreover, they adopt the more mature but complex neural networks in the field as the backbone network, which also intrinsically contributes to the difficulty in adaptation to remote-sensing processing.

As mentioned above, the purpose of the method in this paper is to design a lightweight and high-accuracy method for cloud-amount calculation. To achieve this goal, we first build a lightweight backbone neural network N_{SCN} to extract convolutional features. It should be noted that the backbone neural network N_{SCN} contains two parts: the small neural network N_{SCN-L} for extracting the convolutional features of the browsing images from remote-sensing images and the tiny neural network N_{SCN-S} for extracting the convolutional features of the thumbnail images from remote-sensing images. Next, we transform these

features into a multi-scale pyramidal feature representation. The details are shown in the following equation:

$$N_{MPR} = N_{MSN}(N_{SCN}) \tag{1}$$

Here, N_{MPR} denotes the features of the obtained multi-scale pyramidal network and N_{MSN} indicates the processing operation of the multi-scale feature extraction module. On this basis, MSCF is combined to perform the fusion calculation of the probability distribution of the multi-scale multi-cloud amount to obtain the final cloud-amount calculation results of remote-sensing images.

$$N_{result} = N_{\mathrm{MSCF}}(N_{MPR}) \tag{2}$$

In this way, MSCF can use background knowledge and fusion rules to perform fusion calculations based on the output individual cloud-amount probabilities, yielding a final output as a cloud-amount result that considers both detailed information and overall features while integrating multiple cloud-amount possibilities.

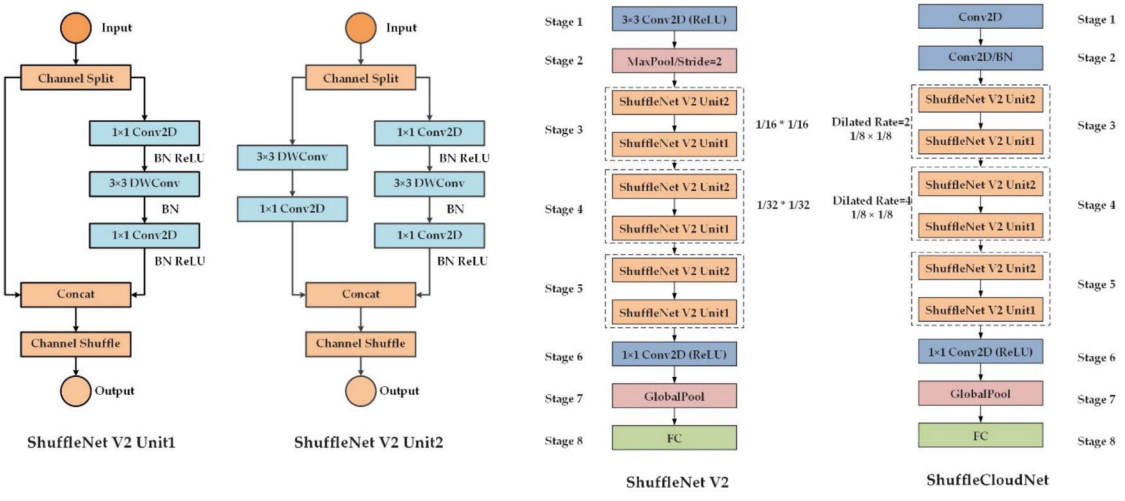
In the forward inference process, it is already possible to accomplish the related work. However, it is also necessary to fully consider how both the proposed module and the final results can be fed into the training process. Thus, the model can be continuously optimized during the training phase to achieve efficient feature extraction that balances various cloud types and multiple cloud scales. We define a bag-of-words loss function L_{bw} to train the entire network and update the network parameter θ.

$$N_{SCN}^{\theta} = \underset{N_{SCN} \in N}{\arg} \min_{\theta} \max L_{bw}(N_{SCN}, \theta) \tag{3}$$

where N is the hypothetical hyperparameter space of the search. In this paper, a complete composite neural network model is developed. However, only the core backbone neural network N_{SCN} is really needed to enter the training phase, and the other parts are only used for information processing in feedback. As a result, the entire network can be used with maximum efficiency both in the training and testing phases.

3.2. ShuffleCloudNet

To improve the efficiency of the cloud-amount calculation network as much as possible, we designed ShuffleCloudNet, a lightweight backbone network inspired by ShuffleNetV2. The main units and network structure of ShuffleNetV2 are shown in Figure 4. The original ShuffleNetV2 network uses numerous downsampling operations, which hides many details of the image, and is very disadvantageous to perceiving the cloud amount in the full image distribution of remote-sensing images. For example, many small clouds are difficult to be perceived by the general network and are included in the final cloud-amount calculation results because they occupy few pixels and are easily lost in the neural network convolution operation. If it is possible to pass the high-resolution information of the thumbnail images and the browsing images of remote-sensing images through the model and to ensure that the output information can represent the main content of the input information, then the neural network parameters can be tuned down during the training process thus enabling the network to learn to obtain the basic information of small clouds.



(**a**) ShuffleNetV2 unit (**b**) ShuffleNetV2 and ShuffleCloudNet structures.

Figure 4. Diagram of the comparison between ShuffleNet V2 and ShuffleCloudNet network structure.

In the design of neural networks, the most straightforward way to preserve the high-resolution information of the model is to remove the downsampling units from the network directly. However, directly removing the downsampled units reduces the perceptual field of the next layer, which is not conducive to the extraction of global contextual information. Therefore, it is a good choice to adopt the expanded convolutional unit to improve the high-level perceptual field. As shown in Figure 4b, the downsampling modules in stages 1 and 2 of ShuffleNetV2 are replaced with standard convolutional modules that can retain more information. To compensate for the decrease in receptive fields, expansion convolutions with 2 and 4 rates were used in stages 3 and 4, respectively. Different from the 32-fold downsampling of ShuffleNetV2, the model designed in this paper only conducts 8-fold downsampling, which greatly preserves the detailed information. Moreover, there is no change in the parameter number and network layers, which keeps the characteristics of the lightweight network well and provides the basis for subsequent efficient computation of the cloud amount. The features extracted by the backbone network of ShuffleCloudNet retain more detailed information and more overall weak feature information, which is an excellent solution for small-cloud detection and considers the overall information extraction of thin clouds. To ensure the convergence of the proposed model and avoid overfitting, we add a batch normalization layer.

After the backbone neural network model, we add a multi-scale confidence fusion module to improve the support capability of multi-scale information for cloud-amount calculation. By adding the multi-scale confidence fusion module, the CNN can adaptively obtain a more explicit representation of spatial features in remote-sensing images after training. This helps to separate the structural information of similar objects (i.e., clouds and snow) and better capture long-term dependencies. Additionally, this long-term dependency on the model is the main reason the business system of cloud-amount calculation can operate steadily.

3.3. Multi-Scale Confidence Fusion (MSCF) Module

In terms of data sources and different algorithms used in the past, this paper designs a two-way neural network and employs thumbnail images and browsing images as inputs for cloud-amount calculation instead of the original remote-sensing images. This operation reduces the computational workload and can better perceive the cloud distribution at the

full scale of remote-sensing images, which is efficient and accurate. However, we found through experiments that due to the different sizes of thumbnail images and browsing images, there are some differences in extracting cloud-amount information. Therefore, we propose the multi-scale confidence fusion module MSCF to effectively balance the effects of inconsistent scale information introduced by the two images.

3.3.1. Multi-Scale Classification Information

To clarify the step characteristics of clouds, we divide the cloud amount into 11 classes, i.e., 0, 10, 20, 30, 40, 50, 60, 70, 80, 90, and 100, which makes it easier to distinguish different cloud amounts for classification networks. If the cloud amount is only split into two categories by 50, it may lead to an extremely rapid decrease in model convergence.

3.3.2. Rules for Fusion Evaluation

To accommodate the different granularities of detailed cloud information reflected in both the thumbnail image and the browsing image in remote-sensing images, we set up a fusion-evaluation rule. The main principle of this fusion-evaluation rule is that the thumbnail image is faster and more efficient in distinguishing large-scale cloud amounts. For example, it more easily distinguishes cloud amounts of 0, 50, 80, and 100. However, when we distinguish the 20, 30, and 40 cloud amounts in the close range, we mainly refer to the classification results provided by the browsing image.

The rules we set can be presented by two Gaussian curves, as shown in Figure 5.

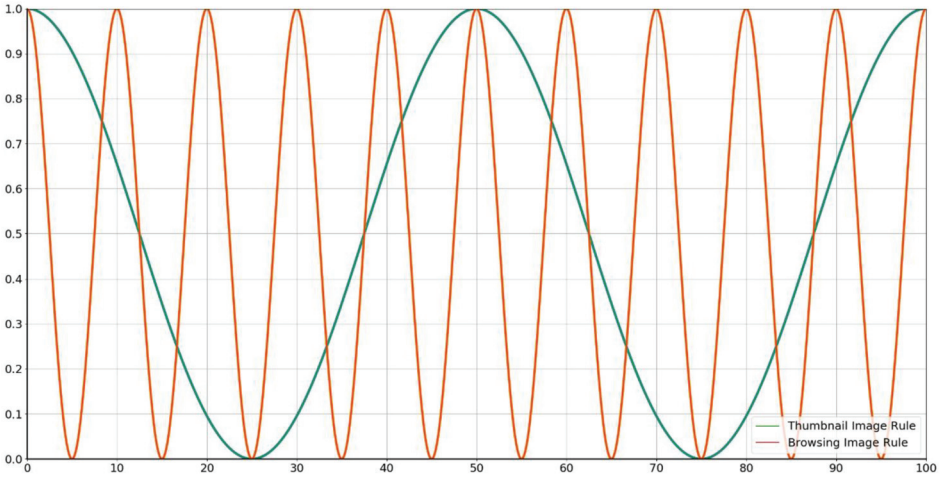


Figure 5. Diagram of the fusion-evaluation rules for the composite neural network.

3.3.3. Probability Distribution Prediction

The predicted probability of the obtained cloud-amount calculation is a list of probability predictions for each cloud-amount phase, as represented in Table 1.

Table 1. Probability distribution table of cloud-amount calculation.

Cloud-Amount Level	**0**	**10**	**20**	**30**	**40**	**50**	**60**	**70**	**80**	**90**	**100**
Probability	P^0	P^1	P^2	P^3	P^4	P^5	P^6	P^7	P^8	P^9	P^{10}

According to the probability distribution, several adjacent probabilities of the cloud amount with the highest probability are accumulated. The specific process is as follows:

1. Find the cloud-amount class with the highest probability in the output of the classification result, denoted as C_n, corresponding to the probability as P^n, where $0 \leq n \leq 10$ is a natural number;
2. Determine the selection number M of the adjacent cloud-amount levels for the highest cloud-amount level;
3. Normalize the cloud-amount level probability, $P'^{n+m} = P^n \cdot \frac{P^n}{\sum_{-\frac{M}{2}}^{\frac{M}{2}} P'^{n+m}}$, where $m \in \left[-\frac{M}{2}, \frac{M}{2}\right]$;
4. The final cloud amount is $C = \sum_{m=-\frac{M}{2}}^{\frac{M}{2}} C_{n+m} \cdot P'^{n+m}$.

Several adjacent cloud-amount levels are selected for calculation and relevant experiments. M is set to 0, 2, 4, 6, and 8. Cloud-amount prediction is performed using the above steps and compared with the real values, and the final experimental results are statistically analyzed with an error of less than 5. Among them, 55 samples are selected for this statistical experiment, and their real cloud-amount levels are uniformly distributed from 0 to 100. The experimental results show that the selection of M = 2 is most suitable. The specific experimental situation is shown in Table 2.

Table 2. Table of experimental results for cloud-amount level selection.

Cloud-Amount Level	0	10	20	30	40	50	60	70	80	90	100	Total	Accuracy
Total Number	5	5	5	5	5	5	5	5	5	5	5	55	100%
M = 0 Correct Number	5	4	4	3	4	4	3	3	3	3	4	40	72.73%
M = 2 Correct Number	5	4	4	4	4	5	4	4	5	5	5	49	89.09%
M = 4 Correct Number	4	4	4	3	3	3	3	2	3	4	3	36	65.45%
M = 6 Correct Number	4	4	4	3	3	4	3	3	3	4	3	38	69.09%
M = 8 Correct Number	5	4	4	3	3	3	3	3	3	4	3	38	69.09%

4. Experimental Results

In this section, we focus on showing the comparative experimental results of the proposed ShuffleCloudNet on the dataset CTI_RSCloud and other publicly available datasets (GF-1 WFV [37] and AIR-CD [38]). First, we briefly introduce each dataset; then, we preprocess all datasets according to the requirements to meet our experimental requirements. Among them, we focus on preparing the cloud-amount calculation dataset CTI_RSCloud for remote sensing. Next, we demonstrate the ablation experiments of key components of ShuffleCloudNet. Finally, the overall performance of the model is analyzed quantitatively and qualitatively.

4.1. Experimental Data

To quantitatively evaluate the performance of ShuffleCloudNet, we conducted experiments on three datasets of cloud detection and cloud-amount calculation for optical remote-sensing images. The first is our own constructed dataset CTI_RSCloud for the cloud-amount calculation of remote-sensing images; the second is the cloud-detection dataset of remote-sensing images of GF-1 WFV; and the third is the AIR-CD dataset composed of remote-sensing images of GF-2.

- CTI_RSCloud: This mainly includes 1829 browsing images of remote-sensing images and an equal number of thumbnail images, with images mainly from GF-1, GF-2, ZY series, etc.

- GF-1 WFV: This was created by the SENDIMAGE lab. The dataset contains 108 complete scenes at level 2A, where all masks are labeled with cloud, cloud shadow, clear sky, and non-value pixels. The spatial resolution of the dataset is 16 m and consists of one NIR band and three visible bands. Since our study concentrates on detecting cloud pixels, all other classes of masks are set to background pixels (i.e., non-cloud pixels). Specifically, the cloud shadows, clear sky, and non-value pixels in the original masks are set to 0, and the cloud pixels are set to 1.
- AIR-CD: This is based on GF-2 high resolution, which includes 34 complete scenes collected by GF-2 satellite from different regions of China between February 2017 and November 2017. AIR-CD is one of the earliest publicly available cloud-detection datasets of remote-sensing images collected from GF-2 satellites. In addition, the scenes in AIR-CD are more complex than in previous datasets, making it more challenging to achieve high-accuracy cloud detection and cloud-amount calculation. The dataset contains various land-cover types, including urban, wilderness, snow, and forest. The dataset consists of near-infrared and visible bands with a spatial resolution of 4 m and a size of 7300 × 6908 pixels. Considering the radiation difference between PMS1 and PMS2 sensors in the GF-2 satellite imaging system, the scenes of both sensors are used as experimental data to ensure the generalization ability of the model.

4.2. Data Preprocessing

To obtain training and test data adapted to the model, we conducted relevant preprocessing for the CTI_RSCloud, GF-1 WFV, and AIR-CD datasets, respectively.

1. CTI_RSCloud: The main elements of preprocessing are data filtering, cloud-amount level classification, cloud-amount judgment rules, sample annotation, etc.

- Selection of remote-sensing images

To find the characteristics of remote-sensing image clouds more objectively, we try to filter remote-sensing images according to the season, month, region, and satellite for balanced interpretation and translation. Presently, it includes the remote-sensing data of four seasons—the spring, summer, autumn, and winter, January to December; four continents—Asia, Europe, Africa, and America; and satellites, such as GF1, GF2, ZY, and CB04. Additionally, at the same level, we selected as many different types of cloud amounts as possible.

- Cloud-amount level division

To clarify the step characteristics of the cloud amount, we divide the cloud amount into 11 levels, i.e., 0, 10, 20, 30, 40, 50, 60, 70, 80, 90, and 100.

- Cloud-amount interpretation rules

In the manual interpretation of the labeled cloud-amount calculation samples, three rules, or principles, are followed. (i) The principle of balancing multiple types of clouds, i.e., thick clouds, thin clouds, etc. Therefore, when we manually collect and sort remote-sensing images, we generally control the proportion of thin clouds, thick clouds, and point clouds at each cloud level. For example, 35 thin clouds, 39 thick clouds, 25 thin–thick clouds, and 18 others are included in the cloud-amount calculation samples of remote-sensing images with a level of 50. (ii) The principle of grid-assisted interpretation, using horizontal, vertical, and grid lines to assist in cloud-amount division. (iii) The principle of upward rounding, considering the complexity of cloud-amount calculation and the enhancement effect of human visual ability. Therefore, after interpreting the cloud amount of a remote-sensing image, it is directly rounded upward; for example, 46 is rounded up and grouped into 50. Figure 6 shows a schematic diagram of cloud-amount division with the aid of horizontal, vertical, and grid lines. If the cloud amount is simple and the horizontal distribution is large, the horizontal line shall be used for auxiliary interpretation. If the vertical distribution angle is large, the vertical line shall be used for auxiliary interpretation. Considering the efficiency and the cloud-amount level of 0–10 set by us, the cloud amount

can be divided into five horizontal lines and five vertical lines. If the cloud-amount distribution is complex, the 5 × 5 vertical and horizontal lines shall be used to intersect.

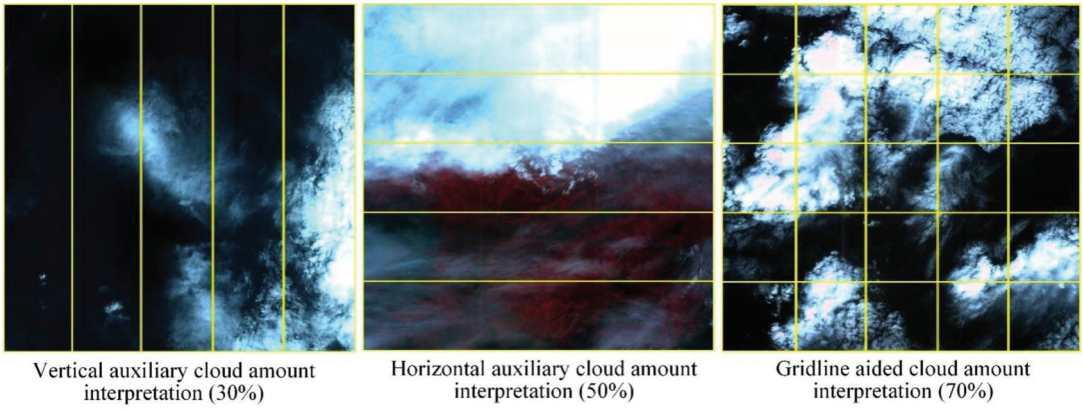


Figure 6. Schematic diagram of grid cloud-amount calculation.

Finally, through the above operations, the remote sensing cloud-amount calculation dataset CTI_RSCloud is obtained, which contains 225 cloud-free samples, 449 10-rank samples, 192 20-rank samples, 158 30-rank samples, 145 40-rank samples, 117 50-rank samples, 106 60-rank samples, 110 70-rank samples, 106 80-rank samples, 108 90-rank samples, and 113 100-rank samples, with a total of 1829 samples.

2. GF-1 WFV and AIR-CD

Both GF-1 WFV and AIR-CD are raw data from remote-sensing images, which need to be changed into the size of the browsing image and thumbnail image and given the corresponding cloud-amount level labels. In calculating the cloud-amount levels for the above two datasets, the detailed cloud-amount percentage calculation is performed using the already-obtained cloud-detection masks and then rounded upwards to obtain the cloud-amount level label. Among them, GF-1 WFV obtained 6 cloud-free samples, 32 10-grade samples, 19 20-grade samples, 17 30-grade samples, 6 40-grade samples, 6 50-grade samples, 4 60-grade samples, 4 70-grade samples, 7 80-grade samples, 5 90-grade samples, and 0 100-grade samples, for a total of 100 samples. AIR-CD obtained 10 cloud-free samples, 11 10-grade samples, 7 20-grade samples, 2 30-grade samples, 2 40-grade samples, 1 50-grade sample, 0 60-grade samples, 0 70-grade samples, 0 80-grade samples, 1 90-grade sample, and 0 100-grade samples, for a total of 34 samples.

4.3. Implemental Details

4.3.1. Evaluation Metrics

To evaluate the performance of different methods in the cloud-amount calculation of remote-sensing images, four widely used quantitative metrics, namely precision (top 3), precision (top 5), overall parameters of the model (Params), and inference runtime, are utilized. It should be noted that precision (top 3) and precision (top 5) are utilized as classification accuracy metrics—and the larger the value, the higher the accuracy; Params and the inference runtime are considered efficiency metrics, where smaller is usually better.

4.3.2. Comparative Models

The model proposed in this paper is compared with typical CNN-based cloud-amount calculation methods, including three classic lightweight neural network architectures, MobileNetV2, SqueezeNet, and ShuffleNetV2. MobileNetV2 is a classification backbone network proposed by the Google team in 2018, which is an improved version of MobileNet

with the addition of Linear Bottleneck and Inverted Residual. SqueezeNet was proposed in the same period as MobileNet, and its core idea is a fire module that adopts the structure of squeeze and expand, thus improving the training efficiency and reducing the parameter number. ShuffleNetV2, guided by four design principles of lightweight networks and based on ShuffleNetV1, introduces the idea of Channel Split and proposes a novel convolutional block architecture, a practical network architecture that can be deployed industrially.

Because we have not used deep neural networks to directly calculate the cloud cover of remote-sensing images, most algorithms have cloud detection as the ultimate goal. Therefore, we selected three cloud-detection algorithms based on deep neural networks as comparison algorithms and selected their backbone networks as the main comparison models to join in the comparison experiment. They are the backbone networks of MFFS-Net (improved Resnet101), MSCFF (CBRR module combination), and CDNet (improved Resnet50). At the same time, to ensure that the three network models can reach the highest level, we fully trained and taught the three models the cloud-detection dataset GF-1 WFV and AIR-CD. Later, along with other comparison models, the cloud-amount calculation data set CTI_RSCloud was trained.

Since the lightweight backbone network of the proposed method is mainly redesigned based on the ShuffleNetV2, we also analyzed ShuffleCloudNet in the ablation studies.

4.3.3. Experimental Setup

All models in the experiments are trained on the training set and tested on the corresponding test set, where samples obtained from GF-1 WFV and AIR-CD preprocessing are all used for testing. All models use RGB images as input, and only the cloud amount is calculated without detecting the specific location of the clouds. In the training process, we classify the browsing and thumbnail images as separate training sets in ShuffleCloudNet-L and ShuffleCloudNet-S. Data augmentation is conducted by flipping horizontally and rotating at a specific angle. The models are optimized using the Adam algorithm. In particular, we set the hyperparameters $\beta 1 = 0.9$, $\beta 2 = 0.999$, and $\varepsilon = 10^{-8}$. The initial learning rate is set to 1×10^{-4} and reduced by half every 10 epochs for a total of 300 epochs. All experiments are implemented in the Pytorch framework with an NVIDIA RTX 3090 GPU.

4.4. Ablation Experiments

To better validate the superiority of the proposed method, we conducted ablation studies in ShuffleCloudNet-L, ShuffleCloudNet-S, MSCF, and BW loss.

1. Effect of ShuffleCloudNet-L and ShuffleCloudNet-S

We conducted the experiments using ShuffleNetV2, ShuffleCloudNet-L, ShuffleCloudNet-S, and ShuffleCloudNet, respectively. The corresponding results in this ablation experiment are shown in Table 3. It can be seen that there is a certain loss of accuracy or time consumption in the cloud-amount calculation results when using ShuffleNetV2, ShuffleCloudNet-L, and ShuffleCloudNet-S only. Additionally, the combination of ShuffleCloudNet-L and ShuffleCloudNet-S meets the lower time requirement with the highest accuracy guaranteed.

Table 3. Effects of the ShuffleNet module with different combinations on the CTI_RSCloud dataset.

Method	Precision (Top 3) (%)	Precision (Top 5) (%)	Params (MB)
ShuffleNetV2 [29]	71.20	82.85	5.28
ShuffleCloudNet-L	76.70	88.02	5.6
ShuffleCloudNet-S	70.23	79.11	5.6
ShuffleCloudNet	82.85	92.56	12.2

2. Effect of MSCF

To evaluate the performance of the MSCF module, we take "ShuffleCloudNet-L+ ShuffleCloudNet-S+RN" as the benchmark so that the whole network does not consider the feature pyramid mechanism. Furthermore, the MSCF module is added to achieve the final result. As shown in Table 4, adding the MSCF module significantly improves the accuracy of the cloud-amount calculation.

Table 4. Effects of the MSCF module on the CTI_RSCloud dataset.

Method	Precision (Top 3) (%)	Precision (Top 5) (%)	Params (MB)
Baseline	77.67	89.97	11.2
+MSCF	82.85	92.56	12.2

3. Effect of BW loss

To verify the effect of the loss function, we train the network in two ways. Formally, the first method is "BCE loss" (i.e., training with BCE loss), and the other method is "BW loss" (i.e., training with BW loss). As shown in Figure 7, the network model trained by BW loss has better results in processing remote-sensing images that contain thin clouds and debris clouds, which are more difficult to calculate. Table 5 shows the corresponding quantitative results, and BW loss achieves good results in precision (top3) and precision (top5) accuracy metrics. The results show that BW loss can guide the network to learn strong semantics and help optimize the stability and representativeness of cloud-amount calculation.

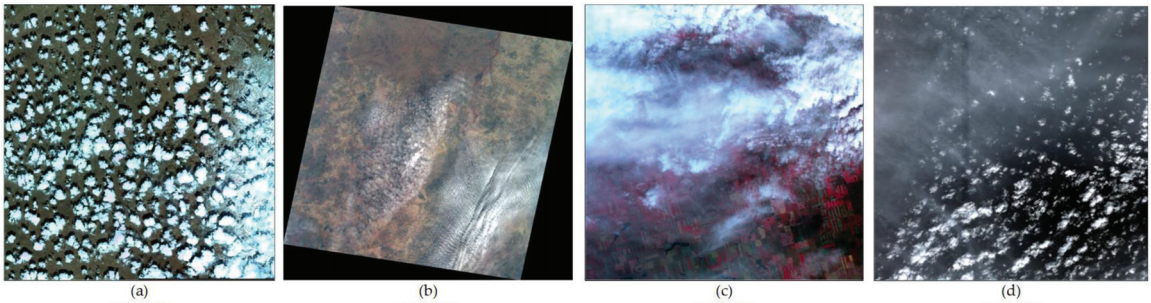


Figure 7. Results with BW loss compared to BCE loss. (**a**) is an example of cloud amount calculation result of remote sensing image of speckled cloud. (**b**) is an example of cloud amount calculation results of thin cloud remote sensing image. (**c**) is an example of cloud amount calculation result of remote sensing image of thin cloud and thick cloud mixture. (**d**) is an example of cloud amount calculation results of remote sensing images of thin clouds and speckled clouds.

Table 5. Effects of different loss functions on the CTI_RSCloud dataset.

Method	Precision (Top 3) (%)	Precision (Top 5) (%)	Params (MB)
BCE Loss	77.99	87.70	12.2
BW Loss	82.85	92.56	12.2

4.5. Comparison with State-of-the-Art Methods

1. Quantitative analysis

Table 6 shows the performance of our ShuffleCloudNet and other state-of-the-art methods on CTI_RSCloud, AIR-CD, and GF-1 WFV datasets. Considering the parameters

and multiple additions, ShuffleCloudNet has a significant advantage over other models in terms of efficiency. Our method produces accuracies of 82.85 (precision (top 3)), 92.56 (precision (top 5)), 97.06 (precision (top 3)), 100.00 (precision (top 5)), 72.74 (precision (top 3)), and 83.02 (precision (top 5)), which reaches the accuracy of the complex cloud detection and computation model.

Table 6. Comparison of the performance of different methods for cloud-amount calculation.

Method	Accuracy						Efficiency	
	CTI_RSCloud		AIR-CD		GF-1 WFV			
	Precision (Top 3) (%)	Precision (Top 5) (%)	Precision (Top 3) (%)	Precision (Top 5) (%)	Precision (Top 3) (%)	Precision (Top 5) (%)	Params (MB)	Inf Time (ms)
SqueezeNet [27]	73.46	84.47	82.35	94.12	67.92	79.25	4.8	1.3
MobileNetV2 [25]	72.17	85.76	85.29	91.18	67.92	77.36	3.5	1.5
ShuffleNetV2 [29]	77.67	89.03	88.24	97.06	63.21	76.42	5.2	1.5
MFFSNet backbone [39]	81.88	90.61	94.12	100.0	71.70	82.08	63.1	215.3
MSCFF backbone [20]	80.91	89.32	94.12	100.0	69.92	80.19	42	158.6
CDNet backbone [22]	81.88	90.61	94.12	100.0	71.70	82.08	45.6	145.0
ShuffleCloudNet	82.85	92.56	97.06	100.00	72.74	83.02	12.2	1.5

In Table 7, we evaluate the inference runtimes of these networks. The runtimes are calculated based on input data of 1024 × 1024 pixels, respectively. The runtime of ShuffleCloudNet is much lower than other cloud-detection methods. Especially for large data inputs, the advantage is more obvious. The runtime can be used to intuitively evaluate the model efficiency (i.e., complexity), which mainly depends on the parameters and computations (multiple additions) of the model. The smaller the parameters and multiple additions, the more efficient the model is and the shorter the inference runtime. Since the runtime also depends on memory access, some comparison methods seem very close to this metric. In our further work, we will optimize the model structure of ShuffleCloudNet to further reduce the inference runtime.

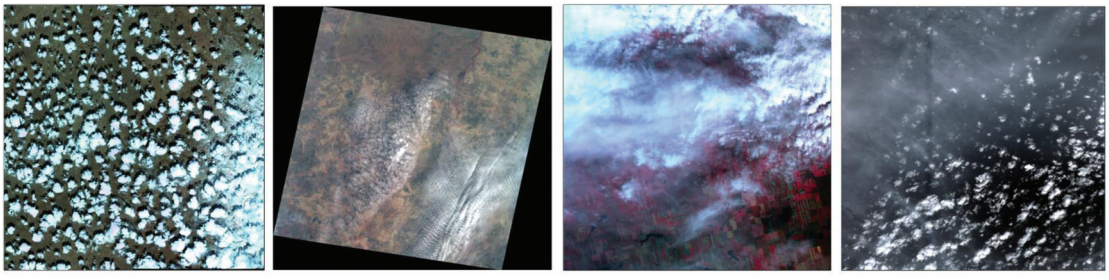
Table 7. Comparison of the parameters and the inference runtime of different methods of cloud detection.

Method	Precision (Top 3) (%)	Params (MB)	Runtime (ms)
MFFSNet [39]	100	73.32	307.3
MSCFF [20]	100	49.46	312.5
CDNet [22]	100	85.52	326.8
ShuffleCloudNet	97.06	12.2	1.5

2. Qualitative analysis

Figures 8–10 compare different methods on CTI_RSCloud, AIR-CD, and GF-1 WFV datasets. We select some representative image-visualization results, including thin clouds, small clouds, and the coexistence of clouds and snow. The results show that our method is significantly superior to others. Specifically, the MobileNet method generates more misclassification results in snowy regions. Due to the introduction of a multi-scale feature-extraction mechanism, SqueezeNet and ShuffleNet are significantly improved. MFFSNet and CDNet backbones use improved Resnet 101 and Resnet50, respectively, which have strong feature-extraction and convergence abilities and cloud-computing effects superior to lightweight models such as MobileNet. However, the runtime of the MFFSNet backbone and CDNet backbone is long, and they do not meet the application scenarios of high time efficiency and low resources. When the MSCFF backbone loses its multi-scale fusion module, which is the most characteristic of a cloud-detection network, its cloud-computing

effect is relatively general. Unlike them, ShuffleCloudNet has a lightweight multi-scale architecture, which greatly reduces the total number of parameters and calculations. By implementing the MSCF module and BW loss, cloud and snow pixels with similar colors can be effectively distinguished, and the results of the cloud-amount calculation are more accurate. Therefore, our ShuffleCloudNet has an excellent generalization capability for the cloud-amount calculation task of optical remote-sensing images.



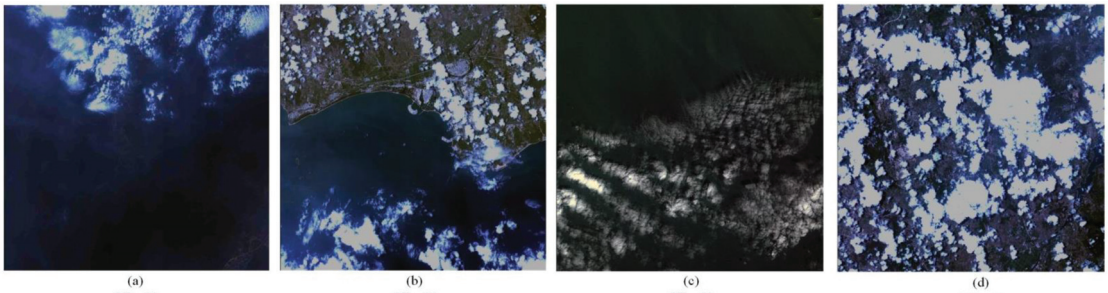
(a)
GT：40
MobileNet v2：60
SqueezeNet：50
Shufflenet v2：50
MFFSNet backbone：40
MSCFF backbone：50
CDNet backbone：40
ShuffleCloudNet：40

(b)
GT：20
MobileNet v2：10
SqueezeNet：10
Shufflenet v2：0
MFFSNet backbone：10
MSCFF backbone：0
CDNet backbone：10
ShuffleCloudNet：20

(c)
GT：60
MobileNet v2：70
SqueezeNet：50
Shufflenet v2：70
MFFSNet backbone：60
MSCFF backbone：50
CDNet backbone：60
ShuffleCloudNet：60

(d)
GT：70
MobileNet v2：50
SqueezeNet：40
Shufflenet v2：30
MFFSNet backbone：50
MSCFF backbone：40
CDNet backbone：50
ShuffleCloudNet：70

Figure 8. Test example diagram of CTI_RSCloud dataset. (**a**) is an example of cloud amount calculation result of remote sensing image of speckled cloud. (**b**) is an example of cloud amount calculation results of thin cloud remote sensing image. (**c**) is an example of cloud amount calculation result of remote sensing image of thin cloud and thick cloud mixture. (**d**) is an example of cloud amount calculation results of remote sensing images of thin clouds and speckled clouds.



(a)
GT：20
MobileNet v2：60
SqueezeNet：50
Shufflenet v2：50
MFFSNet backbone：40
MSCFF backbone：50
CDNet backbone：40
ShuffleCloudNet：40

(b)
GT：20
MobileNet v2：10
SqueezeNet：10
Shufflenet v2：20
MFFSNet backbone：20
MSCFF backbone：0
CDNet backbone：20
ShuffleCloudNet：20

(c)
GT：30
MobileNet v2：80
SqueezeNet：70
Shufflenet v2：40
MFFSNet backbone：40
MSCFF backbone：50
CDNet backbone：40
ShuffleCloudNet：20

(d)
GT：40
MobileNet v2：10
SqueezeNet：20
Shufflenet v2：20
MFFSNet backbone：40
MSCFF backbone：30
CDNet backbone：40
ShuffleCloudNet：40

Figure 9. Test example diagram of AIR-CD dataset. (**a**) is an example of cloud amount calculation result of remote sensing image of thin cloud and thick cloud mixture. (**b**) is an example of the cloud amount calculation result of remote sensing image in the sea land scene. (**c**) is an example of the cloud amount calculation result of remote sensing image in the evening time. (**d**) is an example of cloud amount calculation result of remote sensing image of speckled cloud.

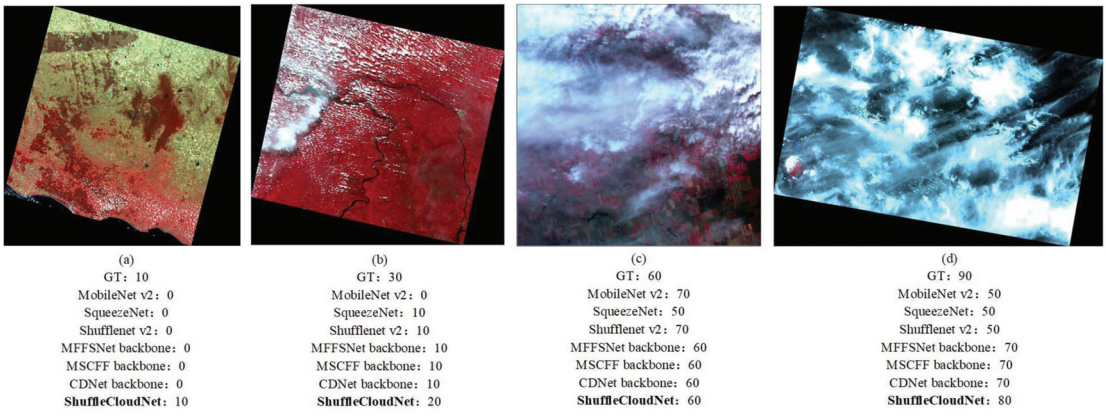


Figure 10. Test example diagram of GF-1 WFV dataset. (**a**) is an example of cloud amount calculation results of remote sensing image with a few clouds. (**b**) is an example of cloud amount calculation results of remote sensing image of large-scale speckled cloud. (**c**) is an example of cloud amount calculation result of remote sensing image of thin cloud and thick cloud mixture. (**d**) is an example of cloud amount calculation results of remote sensing image with multi type cloud mixture.

4.6. Limitations

ShuffleCloudNet can achieve decent cloud-amount calculation in many difficult scenarios but still suffers from some errors in cases such as thin cloud, fog, ice, and mixing of snow clouds. Thin clouds are usually visually recognizable. When the surface below is faintly visible, most thin clouds appear almost the same as subsurface objects. Thus, the problem of thin clouds missing in the calculation results easily occurs. Snow and ice have similar characteristics to clouds in some cases and are also easily misidentified by the human eye. Figure 11 shows three cases of incorrectly calculated cloud amounts. The last case (Figure 11c) has poor cloud-amount calculation, mainly due to the information loss after 16-bit to 8-bit image conversion. In the future, we will optimize the model to further improve the robustness of the proposed method in situations such as thin clouds, ice, and snow.

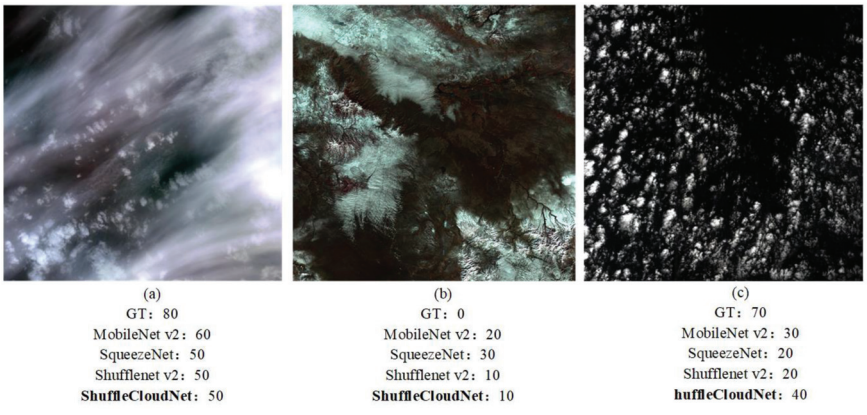


Figure 11. Example diagram of poor cloud-amount calculation results. (**a**) is an example of the cloud amount calculation result of remote sensing image with thin cloud covering thick cloud. (**b**) is an example of cloud amount calculation result of remote sensing image of ice snow cloud mixture. (**c**) is an example of the cloud amount calculation result of remote sensing image at low contrast in the evening.

5. Discussion

From the precision (top 3) and precision (top 5) values in Table 3, it can be seen that the improved ShuffleCloudNet achieves an accuracy of about 10 percentage points higher than ShuffleNetV2 on the CTI_RSCloud dataset; of course, due to the model design, its parameters are also larger than ShuffleNetV2 by a factor of two. As can be seen from Table 4, the design and addition of the MSCF module increased the precision (top 3) and precision (top 5) values by 5% and 3%, respectively. Figure 7 and Table 5 show the role of the BW loss function. The trained model mainly improves the cloudiness calculation capability of speckle clouds, thin clouds, and their combination. The test results of the three datasets in Table 6 and Figures 8–10 show that the proposed ShuffleCloudNet model has the best performance in remote-sensing cloud computing and has a small number of parameters. In Table 7, we compare it with the current best cloud-detection models and find that its precision (top 3) is 100% (our model is 97.06), but the runtime and parameters are far greater than the proposed ShuffleCloudNet. The amount of parameters is 4 to 7 times that of ShuffleCloudNet, and the runtime is 200 times that of ShuffleCloudNet. However, the experiment also clarified the areas where future research is needed to improve it. First of all, the directivity of the model in the cloud-cover calculation is not clear enough. Therefore, there are cases where the calculation of thin clouds and fog is inaccurate, and ice and snow are included in cloud cover. With data reaching the tens of millions, there are still many cases. Another area of improvement is how to quickly obtain the browsing and thumbnail images of remote-sensing images under in-orbit deployment and quickly update the model. In summary, we will continue to improve the model, fully considering the current popular lightweight model structures, to obtain a more stable and precise classification calculation effect.

6. Conclusions

In this paper, we propose an effective cloud-amount calculation method, named ShuffleCloudNet, for optical remote-sensing images. Compared with the results of currently published lightweight cloud-amount calculations, the accuracy of ShuffleCloudNet can attain even better performance. An MSCF module is utilized in our method to extract multi-scale features adaptively based on the shape and size features of clouds. Moreover, we have designed ShuffleCloudNet-L for the feature extraction of browsing images and ShuffleCloudNet-S for the feature extraction of thumbnail images in remote-sensing images. Furthermore, a novel BW loss function is also constructed, leading the network to pay more attention to the pixels near the cloud boundary. To better test the method's effectiveness in this paper, we built our own remote-sensing cloud-amount calculation dataset, CTI_RSCloud. The experiments based on CTI_RSCloud, AIR-CD, and GF-1 WFV datasets demonstrate that our method outperforms the baseline method and achieves better efficiency than the existing algorithms. In the future, we will try to optimize the model structure to improve the computational performance for situations such as thin clouds, snow, and ice. Moreover, we will explore model designs based on specific onboard computing platforms (e.g., FPGAs and ASICs) to further improve operational efficiency.

Author Contributions: Conceptualization, G.W. and Z.L.; methodology, G.W.; software, G.W.; validation, G.W. and Z.L.; formal analysis, G.W. and Z.L.; investigation, G.W.; resources, G.W.; data curation, G.W.; writing—original draft preparation, G.W.; writing—review and editing, Z.L.; visualization, G.W.; supervision, P.W.; project administration, G.W.; funding acquisition, G.W. All authors have read and agreed to the published version of the manuscript.

Funding: This research was funded by the Key Program National Natural Science Foundation of China, grant number U20B2064.

Data Availability Statement: The dataset used in this article will be published on Baidu Netdisk.

Acknowledgments: We thank Jinyong Chen for revising and improving the method proposed in this paper and Min Wang for his contribution to the quantitative calculation of this paper. We also thank Wei Fu for financially supporting this article.

Conflicts of Interest: The authors declare no conflict of interest.

References

1. Zhang, Y.; Rossow, W.B.; Lacis, A.A.; Oinas, V.; Mishchenko, M.I. Calculation of radiative fluxes from the surface to top of atmosphere based on ISCCP and other global data sets: Refinements of the radiative transfer model and the input data. *J. Geophys. Res. Atmos.* **2004**, *109*, D19105. [CrossRef]
2. Lu, D. Detection and substitution of clouds/hazes and their cast shadows on IKONOS images. *Int. J. Remote Sens.* **2007**, *28*, 4027–4035. [CrossRef]
3. Mackie, S.; Merchant, C.J.; Embury, O.; Francis, P. Generalized Bayesian cloud detection for satellite imagery. Part 1: Technique and validation for night-time imagery over land and sea. *Int. J. Remote Sens.* **2010**, *31*, 2595–2621. [CrossRef]
4. He, Q.-J. A daytime cloud detection algorithm for FY-3A/VIRR data. *Int. J. Remote Sens.* **2011**, *32*, 6811–6822. [CrossRef]
5. Marais, I.V.Z.; Preez, J.A.D.; Steyn, W.H. An optimal image transform for threshold-based cloud detection using heteroscedastic discriminant analysis. *Int. J. Remote Sens.* **2011**, *32*, 1713–1729. [CrossRef]
6. Han, Y.; Kim, B.; Kim, Y.; Lee, W.H. Automatic cloud detection for high spatial resolution multi-temporal images. *Remote Sens. Lett.* **2014**, *5*, 601–608. [CrossRef]
7. Lin, C.H.; Lin, B.Y.; Lee, K.Y.; Chen, Y.C. Radiometric normalization and cloud detection of optical satellite images using invariant pixels. *ISPRS J. Photogramm. Remote Sens.* **2015**, *106*, 107–117. [CrossRef]
8. Adrian, F. Cloud and Cloud-Shadow Detection in SPOT5 HRG Imagery with Automated Morphological Feature Extraction. *Remote Sens.* **2014**, *6*, 776–800.
9. Bai, T.; Li, D.; Sun, K.; Chen, Y.; Li, W. Cloud Detection for High-Resolution Satellite Imagery Using Machine Learning and Multi-Feature Fusion. *Remote Sens.* **2016**, *8*, 715. [CrossRef]
10. Wieland, M.; Li, Y.; Martinis, S. Multi-sensor cloud and cloud shadow segmentation with a convolutional neural network. *Remote Sens. Environ.* **2019**, *230*, 111203. [CrossRef]
11. Tian, M.; Chen, H.; Liu, G. Cloud Detection and Classification for S-NPP FSR CRIS Data Using Supervised Machine Learning. In Proceedings of the IGARSS 2019—2019 IEEE International Geoscience and Remote Sensing Symposium, Yokohama, Japan, 28 July–2 August 2019.
12. Ji, S.; Dai, P.; Lu, M.; Zhang, Y. Simultaneous Cloud Detection and Removal From Bitemporal Remote Sensing Images Using Cascade Convolutional Neural Networks. *IEEE Trans. Geosci. Remote Sens.* **2020**, *59*, 732–748. [CrossRef]
13. Sudhakaran, S.; Lanz, O. Convolutional Long Short-Term Memory Networks for Recognizing First Person Interactions. In Proceedings of the IEEE International Conference on Computer Vision Workshop, Venice, Italy, 22–29 October 2017.
14. Jeppesen, J.H.; Jacobsen, R.H.; Inceoglu, F.; Toftegaard, T.S. A cloud detection algorithm for satellite imagery based on deep learning. *Remote Sens. Environ.* **2019**, *229*, 247–259. [CrossRef]
15. Xie, W.; Yang, J.; Li, Y.; Lei, J.; Zhong, J.; Li, J. Discriminative feature learning constrained unsupervised network for cloud detection in remote sensing imagery. *Remote Sens.* **2020**, *12*, 456. [CrossRef]
16. Dai, P.; Ji, S.; Zhang, Y. Gated convolutional networks for cloud removal from bi-temporal remote sensing images. *Remote Sens.* **2020**, *12*, 3427. [CrossRef]
17. Li, X.; Zheng, H.; Han, C.; Zheng, W.; Chen, H.; Jing, Y.; Dong, K. SFRS-net: A cloud-detection method based on deep convolutional neural networks for GF-1 remote-sensing images. *Remote Sens.* **2021**, *13*, 2910. [CrossRef]
18. Ma, N.; Sun, L.; Zhou, C.; He, Y. Cloud detection algorithm for multi-satellite remote sensing imagery based on a spectral library and 1D convolutional neural network. *Remote Sens.* **2021**, *13*, 3319. [CrossRef]
19. Xie, F.; Shi, M.; Shi, Z.; Yin, J.; Zhao, D. Multilevel Cloud Detection in Remote Sensing Images Based on Deep Learning. *IEEE J. Sel. Top. Appl. Earth Obs. Remote Sens.* **2017**, *10*, 3631–3640. [CrossRef]
20. Li, Z.; Shen, H.; Cheng, Q.; Liu, Y.; You, S.; He, Z. Deep learning based cloud detection for medium and high resolution remote sensing images of different sensors. *ISPRS J. Photogramm. Remote Sens.* **2019**, *150*, 197–212. [CrossRef]
21. Shao, Z.; Pan, Y.; Diao, C.; Cai, J. Cloud Detection in Remote Sensing Images Based on Multiscale Features-Convolutional Neural Network. *IEEE Trans. Geosci. Remote Sens.* **2019**, *57*, 4062–4076. [CrossRef]
22. Yang, J.; Guo, J.; Yue, H.; Liu, Z.; Hu, H.; Li, K. CDnet: CNN-Based Cloud Detection for Remote Sensing Imagery. *IEEE Trans. Geosci. Remote Sens.* **2019**, *57*, 6195–6211. [CrossRef]
23. Mohajerani, S.; Krammer, T.A.; Saeedi, P. Cloud Detection Algorithm for Remote Sensing Images Using Fully Convolutional Neural Networks. In Proceedings of the 2018 IEEE 20th International Workshop on Multimedia Signal Processing (MMSP), Vancouver, BC, Canada, 29–31 August 2018.
24. Howard, A.G.; Zhu, M.; Chen, B.; Kalenichenko, D.; Wang, W.; Weyand, T.; Andreetto, M.; Adam, H. MobileNets: Efficient Convolutional Neural Networks for Mobile Vision Applications. *arXiv* **2017**, arXiv:1704.04861.

25. Sandler, M.; Howard, A.; Zhu, M.; Zhmoginov, A.; Chen, L.C. MobileNetV2: Inverted Residuals and Linear Bottlenecks. In Proceedings of the 2018 IEEE/CVF Conference on Computer Vision and Pattern Recognition (CVPR), Salt Lake City, UT, USA, 18–23 June 2018.
26. Howard, A.; Sandler, M.; Chu, G.; Chen, L.-C.; Chen, B.; Tan, M.; Wang, W.; Zhu, Y.; Pang, R.; Vasudevan, V. Searching for mobilenetv3. In Proceedings of the IEEE/CVF International Conference on Computer Vision, Seoul, Korea, 27 October–2 November 2019; pp. 1314–1324.
27. Iandola, F.N.; Han, S.; Moskewicz, M.W.; Ashraf, K.; Dally, W.J.; Keutzer, K. SqueezeNet: AlexNet-level accuracy with 50x fewer parameters and <0.5 MB model size. *arXiv* **2016**, arXiv:1602.07360.
28. Zhang, X.; Zhou, X.; Lin, M.; Sun, J. ShuffleNet: An Extremely Efficient Convolutional Neural Network for Mobile Devices. In Proceedings of the 2018 IEEE/CVF Conference on Computer Vision and Pattern Recognition (CVPR), Salt Lake City, UT, USA, 18–23 June 2018.
29. Ma, N.; Zhang, X.; Zheng, H.-T.; Sun, J. ShuffleNet V2: Practical Guidelines for Efficient CNN Architecture Design. In Proceedings of the European Conference on Computer Vision (ECCV); Springer: Cham, Switzerland, 2018; pp. 122–138.
30. Xia, Y.; Wang, J. A dual neural network for kinematic control of redundant robot manipulators. *IEEE Trans. Syst. Man Cybern. Part B (Cybern.)* **2001**, *31*, 147–154.
31. Zhang, Y.; Wang, J. Obstacle avoidance for kinematically redundant manipulators using a dual neural network. *IEEE Trans. Syst. Man Cybern. Part B (Cybern.)* **2004**, *34*, 752–759. [CrossRef] [PubMed]
32. Liu, S.; Wang, J. A simplified dual neural network for quadratic programming with its KWTA application. *IEEE Trans. Neural Netw.* **2006**, *17*, 1500–1510.
33. Chen, H.; Wu, L.; Dou, Q.; Qin, J.; Li, S.; Cheng, J.-Z.; Ni, D.; Heng, P.-A. Ultrasound standard plane detection using a composite neural network framework. *IEEE Trans. Cybern.* **2017**, *47*, 1576–1586. [CrossRef]
34. Zhu, F.; Ma, Z.; Li, X.; Chen, G.; Chien, J.-T.; Xue, J.-H.; Guo, J. Image-text dual neural network with decision strategy for small-sample image classification. *Neurocomputing* **2019**, *328*, 182–188. [CrossRef]
35. Tian, G.; Liu, J.; Yang, W. A dual neural network for object detection in UAV images. *Neurocomputing* **2021**, *443*, 292–301. [CrossRef]
36. Li, Y.; Geng, T.; Li, A.; Yu, H. Bcnn: Binary complex neural network. *Microprocess. Microsyst.* **2021**, *87*, 104359. [CrossRef]
37. Li, Z.; Shen, H.; Li, H.; Xia, G.; Gamba, P.; Zhang, L. Multi-feature combined cloud and cloud shadow detection in GaoFen-1 wide field of view imagery. *Remote Sens. Environ.* **2017**, *191*, 342–358. [CrossRef]
38. He, Q.; Sun, X.; Yan, Z.; Fu, K. DABNet: Deformable contextual and boundary-weighted network for cloud detection in remote sensing images. *IEEE Trans. Geosci. Remote Sens.* **2021**, *60*, 1–16. [CrossRef]
39. Yan, Z.; Yan, M.; Sun, H.; Fu, K.; Hong, J.; Sun, J.; Zhang, Y.; Sun, X. Cloud and cloud shadow detection using multilevel feature fused segmentation network. *IEEE Geosci. Remote Sens. Lett.* **2018**, *15*, 1600–1604. [CrossRef]

remote sensing

MDPI

Article

CNN-Enhanced Heterogeneous Graph Convolutional Network: Inferring Land Use from Land Cover with a Case Study of Park Segmentation

Zhi-Qiang Liu [1,2], Ping Tang [1], Weixiong Zhang [1,2] and Zheng Zhang [1,*]

[1] Aerospace Information Research Institute (AIR), Chinese Academy of Sciences (CAS), Beijing 100094, China
[2] University of Chinese Academy of Sciences (UCAS), Beijing 100049, China
* Correspondence: zhangzheng@aircas.ac.cn

Abstract: Land use segmentation is a fundamental yet challenging task in remote sensing. Most current methods mainly take images as input and sometimes cannot achieve satisfactory results due to limited information. Inspired by the inherent relations between land cover and land use, we investigate land use segmentation using additional land cover data. The topological relations among land cover objects are beneficial for bridging the semantic gap between land cover and land use. Specifically, these relations are usually depicted by a geo-object-based graph structure. Deep convolutional neural networks (CNNs) are capable of extracting local patterns but fail to efficiently explore topological relations. In contrast, contextual relations among objects can be easily captured by graph convolutional networks (GCNs). In this study, we integrated CNNs and GCNs and proposed the CNN-enhanced HEterogeneous Graph Convolutional Network (CHeGCN) to incorporate local spectral-spatial features and long-range dependencies. We represent topological relations by heterogeneous graphs which are constructed with images and land cover data. Afterwards, we employed GCNs to build topological relations by graph reasoning. Finally, we fused CNN and GCN features to accomplish the inference from land cover to land use. Compared with other homogeneous graph-based models, the land cover data provide more sufficient information for graph reasoning. The proposed method can achieve the transformation from land cover to land use. Extensive experiments showed the competitive performance of CHeGCN and demonstrated the positive effects of land cover data. On the IoU metric over two datasets, CHeGCN outperforms CNNs and GCNs by nearly 3.5% and 5%, respectively. In contrast to homogeneous graphs, heterogeneous graphs have an IoU improvement of approximately 2.5% in the ablation experiments. Furthermore, the generated visualizations help explore the underlying mechanism of CHeGCN. It is worth noting that CHeGCN can be easily degenerated to scenarios where no land cover information is available and achieves satisfactory performance.

Keywords: land use; semantic segmentation; heterogeneous graph; graph convolutional network (GCN)

Citation: Liu, Z.-Q.; Tang, P.; Zhang, W.; Zhang, Z. CNN-Enhanced Heterogeneous Graph Convolutional Network: Inferring Land Use from Land Cover with a Case Study of Park Segmentation. *Remote Sens.* **2022**, *14*, 5027. https://doi.org/10.3390/rs14195027

Academic Editor: Giuseppe Scarpa

Received: 26 August 2022
Accepted: 3 October 2022
Published: 9 October 2022

Publisher's Note: MDPI stays neutral with regard to jurisdictional claims in published maps and institutional affiliations.

Copyright: © 2022 by the authors. Licensee MDPI, Basel, Switzerland. This article is an open access article distributed under the terms and conditions of the Creative Commons Attribution (CC BY) license (https://creativecommons.org/licenses/by/4.0/).

1. Introduction

Land use information is critical for understanding complex human–environment relationships and promoting human socioeconomic development, such as environmental change [1], ecosystem deterioration [2], and urban planning [3]. There is a tremendous demand for land use mapping for sustainable urban development in this era of rapid urbanization and population growth. However, land use, in contrast to land cover, is more difficult to distinguish. Land cover can be directly identified from images as it relates to the physical characteristics of the ground surface [4], while land use reflects the socio-economic activities that take place on that surface. A land use unit may comprise a variety of diverse land cover types, resulting in dramatic differences in spatial arrangement and spectral characteristics, even in a homogeneous land use region [5]. Thus, it is challenging to obtain

reliable land use segmentation using low-level image features, such as spectral and textural features. Meanwhile, information about land use is implicitly provided as patterns or high-level semantic functions in very fine spatial resolution (VFSR) satellite images [6]. Hence, it is essential to extract high-level semantic features from detailed images for accurate land use segmentation.

The topological relations among land cover elements are beneficial for narrowing the semantic gap between land cover and land use [7–9]. Topological relations can describe the complicated spatial configuration of land cover objects, which are beneficial for land use identification. This assumption is built on the fact that land use parcels with similar structures tend to possess similar functional attributes [5]. From another perspective, accurate land use segmentation necessitates a thorough understanding of complex urban structures. This structure is a global perception of urban areas, which is built on the long-range dependencies of land cover units. According to the perceptual organization theory, humans group visual objects together to recognize the visual as a whole, where topological relations play an important role in the grouping process.

The positive effects of topological relations can be illustrated by the application of urban park segmentation. Urban parks (hereinafter referred to as parks) are designated areas of natural, semi-natural, or planted space inside cities for human recreation. There are usually multiple land cover types inside a park unit, such as water, buildings, and forest. Thus, the spectral feature distribution of park pixels is irregular and difficult to distinguish. For instance, a building area in a park is easily recognized as non-park because most buildings do not appear in parks. Land cover data are advantageous for solving this problem, as topological relations can be better depicted. For example, a building surrounded by forests is more likely to belong to a park than one surrounded by buildings. As a result, land use segmentation can be further improved by the topological relation inference using land cover data. Meanwhile, land cover classification is one of the most fundamental tasks in remote sensing [10]. There are many well-known public land cover products available, such as GlobeLand30 [11], Finer Resolution Observation and Monitoring of Global Land Cover (FROM-GLC) [12], and ESA's Land Cover Climate Change Initiative (LC-CCI). Therefore, an appealing idea is to use land cover to support land use segmentation, and models capable of effectively extracting topological relationships are required.

In recent decades, many investigations have been conducted to improve the accuracy of land use segmentation. These approaches can be generally divided into two categories regarding the use of spatial information: grid-based and object-based. Grid-based algorithms learn image representation from regular regions, and the most basic strategy is to use only spectral characteristics for pixel-wise segmentation. Researchers have tried to increase the size of grids to get spatial context features since pixel-wise methods fail to describe the spatial structure of land use. The most successful design among them are deep CNNs, as CNNs provide a powerful framework for local pattern modeling by end-to-end and hierarchical learning. Many attempts have been made to better exploit spatial information. Dilated convolutions are exploited to enlarge receptive fields [13]. Local features are enhanced with a global context vector obtained by global pooling [14]. A pyramid pooling module was employed to collect semantic features [15,16], and on this basis, the atrous special pyramid pooling (ASPP) further incorporates the atrous algorithm [17–20]. It is worth mentioning that the use of spatial context boosts models' performance and robustness. Thus, CNNs, such as fully convolutional network (FCN) [21], U-net [22], pyramid scene parsing network (PSPNet) [15], and DeepLabv3 [19] have achieved outstanding results in semantic segmentation. However, these models are highly inefficient in describing long-distance relationships because they are composed of the local operations of convolution and pooling [23,24].

It is preferable to depict relationships between objects rather than regular grids (the comparison can be seen in Figure 1). On the one hand, interregional dependencies are of significantly longer range than those represented by local convolutions [23]. On the

other hand, objects and regions are of arbitrary shape in the real world, and object-based methods are more capable of describing the "reality" of human perception than pixel-level approaches [25]. Furthermore, object-based techniques are more ideal for expressing topological relations among land cover objects inside a land use parcel, which, as mentioned before, is extremely beneficial for bridging the semantic gap between land cover and land use. As previous deep learning models are prepared for Euclidean data, complex topological relations among land cover objects are frequently neglected.

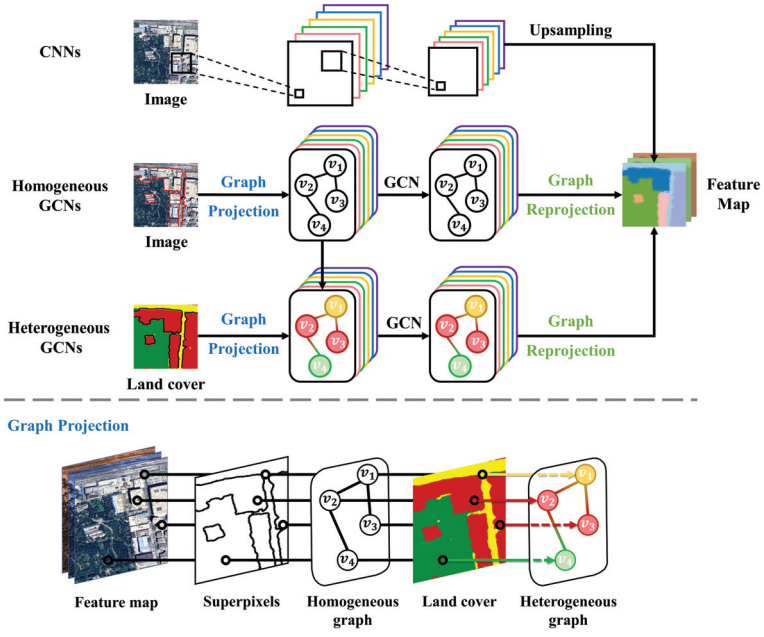


Figure 1. Comparison of CNNs, homogeneous GCNs, and heterogeneous GCNs in feature extraction. The CNNs employ convolutions and pooling on regular regions to obtain feature maps and upsample them to the pixel level. Homogeneous GCNs first transform images into graphs by graph projection, and then apply GCN to obtain node-level features, and finally produce pixel-level feature maps by graph re-projection. Heterogeneous graphs differ from homogeneous graphs in the graph construction. Nodes of heterogeneous graphs are labeled with land cover classes in graph projection. Edge weights are determined by the corresponding node pair's class. Graph projection is described in detail at the bottom, and graph reprojection is the inverse process of this.

It is natural to consider graphs to explore relationships, because images can be easily converted into graphs with vertices and edges indicating image regions and their similarities. Graphs are a widely used data structure as well as a universal language for describing complex systems, and Euclidean data such as images (2D grids) can be regarded as instances of graphs. Graphs, which focus on relationships among objects rather than the attributes of individual objects [26], have shown great expressive power in various domains, including social science [27], protein–protein interaction networks [28], and network biology [29]. Subsequently, context modeling is typically postulated as an inference issue on graphs [30]. In practice, the process of relation reasoning, i.e., context modeling, is realized by the aggregation of node information. The aggregation process depends on the graph structure, which is dominated by the topological relationships of geo-objects. Finally, a land use segmentation problem is converted into a node classification problem.

However, most current models are built on homogeneous graphs and fail to fully employ the rich semantic information of heterogeneous data. Recently, GCNs [31] have

received increasing attention for their ability to aggregate information by generalizing convolutions to graph-structure data. By employing GCNs on graphs transformed from images, relations among objects can be explicitly inferred along graph edges, and spatial structures can be better portrayed. For example, GCNs are used to model contextual structures in hyperspectral image classification problems [32–35]. In detail, GCNs are employed through graph reprojection [23], in which vertex features are projected back to grid space based on region assignments. Then, the projected features are integrated (using operations such as addition) into the CNN feature maps. As mentioned above, it is suggested to accomplish land use segmentation with land cover data. However, these homogeneous graph-based approaches are severely limited in their ability to merge additional data. For instance, a co-occurrence matrix of node classes [36] is employed in an implicit and inefficient way, and the use of coarse prediction maps [37] ignores inter-class relationships and treats nodes of different classes equally.

Heterogeneous graphs [38] are introduced to solve the aforementioned issues, which can appropriately infer land use from land cover. In a heterogeneous graph, the total number of node types and edge types is greater than two, whereas there is only one node type and one edge type in a homogeneous graph (see Figure 1 for the difference).This work [38] fully exploits the heterogeneity and rich semantic information embedded in the multiple node and edge types by using hierarchical attention, which consists of node-level and semantic-level attention. Specifically, the node and edge types are taken into consideration when aggregating features. Heterogeneous graphs are experts in portraying complex relationships among various classes of nodes. Thus, heterogeneous graph-based methods can better mine topological relations among different land cover nodes.

Our model is proposed based on heterogeneous graphs to bridge the semantic gap between land cover and land use. Specifically, in the case of park segmentation, there are m node types and $\frac{m(m+1)}{2}$ edge types, where m denotes the number of land cover types. Thus, we can build heterogeneous graphs with land cover data. It makes sense to define different edge calculation functions among the nodes of different land cover classes. For instance, reducing weights between road and forest objects is beneficial given that roads frequently appear outside parks. Moreover, the parameters of class-specific edge calculation functions are automatically learned, making the relation inference more adaptive. Similarly to the feature fusion framework [32,39], we integrate CNNs and our heterogeneous graph-based model to derive long-distance relationships among objects while preserving spatial details, since the shallow features of CNNs retain more spatial information. To this end, we propose the CNN-enhanced HEterogeneous Graph Convolutional Network(CHeGCN) for land use segmentation. The main distinction between CHeGCN and the existing models [32,39] is that CHeGCN is constructed on heterogeneous graphs, whereas these existing models are intended for homogeneous graphs and are thus unable to make use of extra data, such as land cover data. Furthermore, CHeGCN can also be easily degraded to situations without additional land cover data, which is detailed in ablation experiments.

Experiments have been conducted to show the capability of CHeGCN in land use segmentation, and visualization results reveal that land cover information can significantly improve the graph inference. It can be observed that the contributions of objects with various land cover labels are different by visualizing the weights of graph edges, which is consistent with our knowledge. The main contributions of our work are summarized as follows:

1. We propose a novel CHeGCN that fully explores the relations between land cover and land use. CHeGCN is able to infer and extract high-level semantic features based on the heterogeneous graphs, which can significantly improve land use segmentation. Furthermore, our model provides a general framework that can be applied not only to land cover and land use segmentation, but also to land use segmentation with additional land cover data;
2. CHeGCN is an early attempt to investigate heterogeneous graph neural networks in the field of remote sensing. CHeGCN is a good example of successfully exploiting

heterogeneous data, which further strengthened the inference ability of graphs with additional data. This work may encourage the integration of other Earth observation products;

3. CHeGCN outperforms CNNs and homogeneous graph-based models in our park segmentation datasets, mainly owing to the incorporation of local spectral-spatial features and long-distance topological relationships. In particular, class-specific calculation functions of edge weight boost the representation of the topology of land cover objects within land use parcels.

2. Materials and Methods

In this section, we describe our proposed CHeGCN model. As shown in Figure 2, it is an encoder–decoder network, where the encoder is composed of two modules. The CNN module mainly focuses on local features, and the GCN module concentrates more on global relations among objects. The latter module is actually to apply GCN on heterogeneous graphs. Thus, it is necessary to construct heterogeneous graphs first. After that, convolution operations are employed on these graphs. Features extracted from graph-structure data are fused with CNN features to accomplish the final segmentation task. The decoder is actually a pixel-wise classifier, which determines the label of each pixel. Then, we detail our CHeGCN, which is mainly composed of four parts: (1) the CNN module; (2) the heterogeneous graph construction; (3) the GCN model; and (4) the feature fusion and the classifier.

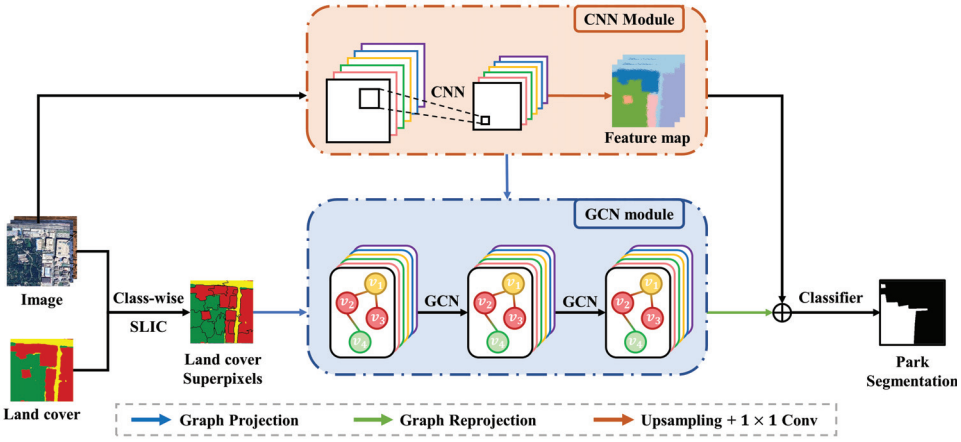


Figure 2. The architecture of CNN-enhanced HEterogeneous Graph Convolutional Network (CHeGCN) model. CHeGCN contains a CNN module and a GCN module, where the former focuses more on a local extraction pattern and the latter concentrates more on long-range dependency modeling. Before the GCN module is applied, the heterogeneous graph needs to be constructed. Nodes in the heterogeneous graph are determined by land cover superpixels and attributed by CNN feature maps. Edges are linked based on topological relations among nodes. Finally, GCN features are reprojected and fused with CNN features to accomplish park segmentation.

2.1. CNN Module

CNNs are generally selected as the backbone network for semantic segmentation because of their strong ability to describe local patterns. However, it is problematic to employ CNNs on a small dataset, which can easily lead to overfitting [40]. In order to reduce the risk of overfitting, we adopt ResNet [41] pretrained with ImageNet [42] as the CNN module. ResNet uses stacked residual blocks with skip connections between each one to solve the optimization problem posed by the network's growing depth. As a result, this structure makes it quite successful across various segmentation datasets. Specifically, we select the pretrained ResNet-18 and remove the last four convolutional layers, the

average pooling layer, and the fully connected layer. The last four layers in ResNet-18 contain 256, 256, 512, and 512 convolution kernels, respectively. These four layers consist of too many parameters for our datasets. By removing them, the number of parameters declines from 11.18 M to 0.69 M. The robustness to overfitting can be increased due to the considerably decreased size of the pretrained module. Furthermore, we upsample the output feature maps of the CNN module to obtain pixel-level features using bilinear interpolation. The upsampled output is then fed into a 1×1 convolutional layer to reduce dimensions. Finally, the output is entered into the heterogeneous graph construction part and the feature fusion part.

2.2. Heterogeneous Graph Construction

It is necessary to convert images from grid-structure into graph-structure data before applying graph convolution. We take the feature maps of the CNN module as the input for heterogeneous graph construction, as the spectral band number of VFSR images is limited. The extended features provide more discriminating features to enhance our model. Although a pixel can be regarded as a node in a graph [35,43], this would result in a large graph with intractable computation. Meanwhile, topological relations among land cover objects inside land use units are advantageous for land use segmentation. Therefore, we transformed the feature maps to an undirected graph $\mathcal{G} = (\mathcal{V}, \mathcal{E})$ using land cover data, where $\mathcal{V}$ and $\mathcal{E}$ denote the vertices and edges of the graph, respectively. The vertex set $\mathcal{V}$ is composed of land cover superpixels obtained by the simple linear iterative clustering (SLIC) algorithm [44]. The link set $\mathcal{E}$ is determined by the topological relations of nodes, where the nodes of each edge in $\mathcal{E}$ are spatially adjacent. In detail, land cover superpixels are obtained in two steps. First, we obtain the masks of each land cover class from land cover data. Then, we apply SLIC to images with land cover masks to obtain land cover superpixels. Because directly applying SLIC to land cover data is actually random clustering in local regions, the values inside a land cover region are the same. This class-wise SLIC method makes use of an image texture to achieve clustering and guarantees that all pixels in a superpixel belong to the same land cover category. It is worth noting that directly adopting land cover masks as land cover nodes is not recommended because node features will be over-smoothed.

In practice, the $\mathcal{V}$ and $\mathcal{E}$ are presented by a vertex feature matrix $X \in \mathbb{R}^{|\mathcal{V}| \times d}$ and an adjacency matrix $A \in \mathbb{R}^{|\mathcal{V}| \times |\mathcal{V}|}$, where $|\mathcal{V}|$ and d indicate the number and the dimensions of nodes, respectively. The ith row of X indicates the feature vector $\mathbf{x}_i \in \mathbb{R}^d$ of node v_i. Node features are obtained by graph projection, which assigns the pixels located in the same superpixel to the related node. Then, the features of this node are the average signatures of the pixels involved. A_{ij} denotes the edge weight between node v_i and node v_j. The higher the value of A_{ij}, the closer the nodes v_i and v_j are connected. The adjacency matrix of the undirected graph is symmetric and thus A_{ij} equals A_{ji}. The symmetric adjacency matrix A is calculated with the attention mechanism [45] as:

$$A_{ij} = \begin{cases} \text{softmax}_i(\mathbf{x}_i^T \mathbf{x}_j), & \text{if } v_i \in N(v_j) \\ 0, & \text{otherwise.} \end{cases} \tag{1}$$

where $\mathbf{x}_i, \mathbf{x}_j$ indicate the features of nodes v_i and v_j, and $N(v_j)$ represents the set composed of the neighboring nodes of v_j. In addition, the adjacency matrix is normalized in row direction by the softmax function to make coefficients comparable across nodes.

As previously stated, topological relations among land cover elements are of importance to land use segmentation. However, homogeneous graphs fail to fully take advantage of land cover information in graph construction processes, treating nodes of different land cover classes equally in Equation (1). Thus, they are insufficient for modeling dependencies among heterogeneous regions (regions with different land cover labels). We propose to adaptively model the relations based on land cover categories through heterogeneous graphs. As seen in Figure 1, the graph projection operation transforms raster data into graph-structure data, where pixel-level feature maps are projected to the node level. At

the same time, each node is assigned a land cover label that it is colored against. The node label is selected by the mode value of the land cover category the involved pixels. The meta-path P is taken into consideration in the adjacency matrix calculation. Relations among nodes with different labels are better explored since relations among land cover objects are closely related to their land cover types. In the case of park segmentation, it makes sense to modify the edge weight based on the land cover type of the corresponding node pair. For instance, reducing the weight between road and forest objects is beneficial, given that roads frequently appear outside parks. Meta-path $P = v_i \xrightarrow{R} v_j$ describes relation R between node v_i and v_j, where R is determined by the land cover labels of node pair (i, j). In fact, the meta-path can be regarded as an edge type, where the edge e_{ij} in Figure 1 is rendered by the gradient color of node v_i to node v_j. The meta-path of node pair (i, j) is the same as the meta-path of node pair (j, i) because graphs are undirected. As a result, the total number of meta-path types is $\frac{(m(m+1))}{2}$, where m denotes the number of land cover classes. Given a vertex pair (i, j) that is connected though meta-path P, the edge calculation function in heterogeneous graphs is

$$A_{ij} = \begin{cases} \text{softmax}_i(a_P(\mathbf{x}_i^T \mathbf{x}_j) + b_P), & \text{if } v_i \in N(v_j) \\ 0, & \text{otherwise.} \end{cases} \tag{2}$$

where a_P and b_P are scalar parameters to adjust the importance of meta-path P. In contrast to [38], we use a simpler yet effective method to compute node embedding. The node-level attention calculation formula is the same for nodes with different land cover labels since all nodes are located in the same feature space. The semantic-level attention is a linear function whose parameters a_P and b_P vary with respect to the meta-path P.

2.3. Graph Convolutional Network

Motivated by CNN, GCN is proposed to generalize convolutions from Euclidean data to non-Euclidean data. Euclidean data, such as images, speech, and videos, has an underlying Euclidean structure. In contrast, non-Euclidean data, such as graphs and manifolds, are data whose underlying domain does not obey Euclidean distance as a metric between points in the domain. Consequently, basic operations such as convolution cannot be directly applied to non-Euclidean data since non-Euclidean data lack shift invariance [46]. GCN successfully translates the deep learning methods designed for Euclidean data, such as CNN, to non-Euclidean data. Specifically, GCN inherits the key elements of CNNs: (1) a locally connected structure; (2) shared weights to reduce the computational cost; and (3) the use of multiple layers to exploit hierarchical information. The architecture of GCN is built on the basis of a localized first-order approximation of spectral graph convolutions [31], which updates the node embedding by aggregating information from 1 to hop neighboring nodes. To be specific, the single graph convolutional layer is a combination of graph convolution, with a trainable weight matrix, and a non-linear function. The forward propagation process of a GCN layer can be formulated as:

$$X^{l+1} = \sigma(\tilde{A} X^l W^l) \tag{3}$$

where $X^l \in \mathbb{R}^{|\mathcal{V}| \times d^l}$ and $X^{(l+1)} \in \mathbb{R}^{|\mathcal{V}| \times d^{l+1}}$ are the input and output node feature matrix of lth layer, respectively. Both of them have $|\mathcal{V}|$ rows, but the column number of X^{l+1} is determined by W^l. $W^l \in \mathbb{R}^{d^l \times d^{l+1}}$ is a learnable matrix, which linearly maps the input feature space to the output feature space. The $\tilde{A} = \hat{D}^{-\frac{1}{2}} \hat{A} \hat{D}^{-\frac{1}{2}}$ is a symmetric normalized adjacency matrix (with self-loops) which is used to fuse the features of neighboring nodes. $\hat{A} = A + I$, where A denotes the adjacency matrix and I indicates the identical matrix. The identical matrix is used to add self-loop connections, which ensures that the previous node embedding is engaged in the node feature update process. $\hat{D}$ is the diagonal degree matrix of $\hat{A}$ and is employed to normalize $\hat{A}$. It is necessary to keep the magnitude of node features consistent because aggregation operations can be extremely sensitive to node

degrees. The normalized adjacency matrix is useful to overcome numerical instabilities and optimization difficulties [26]. $\sigma(\cdot)$ is a non-linear activation function, and rectified linear units (ReLU) [47] were selected in this paper.

Afterwards, we can build a powerful model by stacking multiple graph convolutional layers in the form of Equation (3), where different layers of the same graph share the same adjacency matrix. By doing this, GCN is able to implicitly operate beyond the first-order polynomials of the adjacency matrix, and then extract global context information. In fact, the insight of graph convolution is a weighted sum of all adjacent nodes, including the node itself. Thus, the graph convolution is equivalent to a local node-level filter, whose receptive field is defined as the neighboring nodes. As the size of neighboring nodes can be arbitrary, the filter is adaptively determined by the local neighborhood structure. This is the key difference between GCN and CNN, where the filters in CNN are identical in all positions of grids.

As a result, the determination of the adjacency matrix is critical because the weight matrix $\tilde{A}$ is calculated by A. The simplest solution is to set A_{ij} to one if node v_i and v_j are adjacent, otherwise set A_{ij} to zero. This method is equivalent to take a simple average of neighborhoods, which restricts the complexity of GCN. Considering the importance of different nodes varies, weighted adjacency matrix emerges, such as RBF kernel [33,34], semidefinite kernel [48], and self-attention mechanism [45]. However, these methods are disabled to leverage additional information. In our heterogeneous graph, we take land cover labels into consideration to calculate A, which further strengthen the relations expression of GCN. Meanwhile, the parameters of this function are learnable, which is adaptively adjusted in the training process.

2.4. Feature Fusion and Classifier

The VFSR image representations obtained by different network architectures vary greatly. CNNs focus on spectral-spatial features, and GCNs pay more attention to topological relations among objects. Typically, features provided by a single architecture are limited, which makes it hard to obtain optimal results. Therefore, we enhance the GCN module with CNN features to attain better performance. Before feature fusion, we have to map the node-level outputs of the GCN module to pixels, which is an inverse process of graph projection, called graph reprojection. The graph reprojection assigns the features of a node to pixels located in that node. Then, element-wise addition is performed on the reprojected GCN feature maps and the upsampled CNN feature maps. Finally, pixel-level segmentation results are obtained after feeding fused feature maps into the classifier, which comprises a 1×1 convolutional layer, a softmax function, and an arg max operation on the feature dimension, as shown in Equation (4).

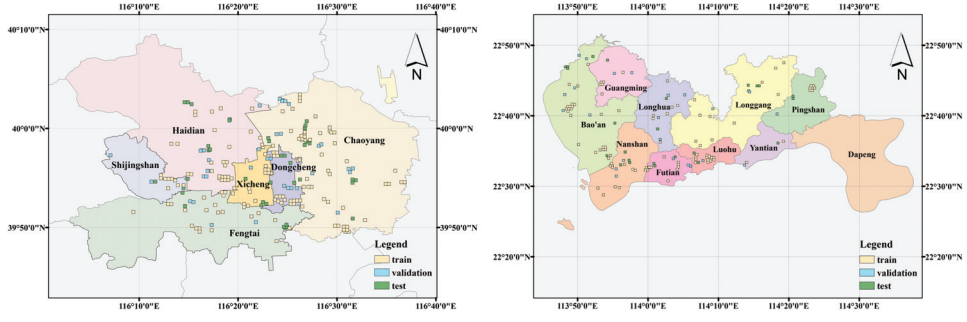
$$\text{Output} = \arg\max_{d}(\text{softmax}(\text{Conv}(X_{CNN} + X_{GCN}))) \tag{4}$$

3. Results

In the experiments, our proposed CHeGCN model is evaluated on our two park segmentation datasets. Six state-of-the-art deep learning approaches are compared with our method: FCN [21], U-net [22], PSPNet [15], DeepLabv3 [19], CNN-enhanced graph convolutional network (CEGCN) [32], and global reasoning unit (GloRe unit) [24]. Three metrics, overall accuracy (OA), kappa coefficient (Kappa), and intersection over union (IoU), are adopted to measure the performance of models. Since the Kappa and IoU can better describe the segmentation results, we will focus on them more in the following analysis. The mean and standard deviation of these three indicators are presented after each experiment is repeated five times. Finally, ablation experiments and visualization results are conducted to demonstrate the benefits brought by heterogeneous graphs, which are constructed with land cover data.

3.1. Dataset

We created two new land use segmentation datasets with two categories: park and non-park. Parks that are too large or too small are excluded, because topological relationships among land cover objects in a park area cannot be well expressed by fixed-size image blocks at the current resolution. For a large park, an image block cannot reflect the overall spatial structure of it. For a small park, land cover data are not sufficiently refined to support the segmentation of tiny regions. In the Beijing dataset, we selected 157 parks of appropriate size in Beijing, China. In the Shenzhen dataset, we selected 99 parks in Shenzhen, Guangdong province, China. Due to the different shapes of these parks, we cropped them into image blocks of size 256×256 to facilitate the subsequent process. These samples are then randomly split into training, validation, and test sets in a 4:1:1 ratio using parks as units, which prevents data leakage. Samples in these sets are evenly distributed across districts (see Figure 3). Each sample has three components obtained in 2015: a VFSR image, a park label, and a land cover label.



(a) Beijing dataset (b) Shenzhen dataset

Figure 3. Distribution of samples. These samples are divided into training, validation, and test sets in a ratio of 4:1:1. The data in each set are evenly distributed across districts.

The VFSR images with RGB bands come from Google Earth imagery. These images are at a zoom level of 16, with a resolution of 1.8 m for the Beijing dataset and 2.2 m for the Shenzhen dataset. They are cloud free after careful selection, and most of them were taken between July and September of 2015. To expand the dataset, we realized dataset augmentation through adaptively sliding windows with the premise of preserving the park's integrity as much as possible. The augmented training dataset is abbreviated as "training-aug". The distribution of samples in these two datasets can be seen in Tables 1 and 2.

Table 1. The distribution of samples in Beijing dataset.

Dataset	Dongcheng	Xicheng	Haidian	Chaoyang	Fengtai	Shijingshan	Total
Training	17	14	32	52	22	7	144
Training-aug	53	52	166	199	85	27	532
Validation	4	4	9	14	4	2	37
Test	5	4	9	14	6	2	40

Table 2. The distribution of samples in the Shenzhen dataset.

Dataset	Luohu	Futian	Nanshan	Yantian	Bao'an	Longgang	Pingshan	Longhua	Guangming	Total
Training	13	12	11	2	23	11	6	7	7	92
Training-aug	30	40	37	8	73	46	14	24	22	294
Validation	1	3	2	1	6	3	1	4	3	24
Test	2	3	4	1	6	3	2	2	1	24

Park labels are made by manual correction on the basis of the OpenStreetMap (OSM) project and area of interest (AOI) data collected from Baidu Map. After reprojection and rasterization, the corrected park vector data are then transformed into raster labels. The land cover product, with a spatial resolution of 2 m, is generated from GF-1 data and contains 13 categories. By visual interpretation, we label unknown regions with the other 12 categories. Afterwards, these 12 categories (except the unknown class) are merged into five classes: grass, forest, buildings, road, and water. The class distribution of the processed land cover data is shown in Figure 4. Blue bars indicate the distribution of samples in all areas, while green bars denote the distribution of park regions. It is worth noting that land cover labels are reprojected and resampled as the coordinate system and resolution of this product do not match images.

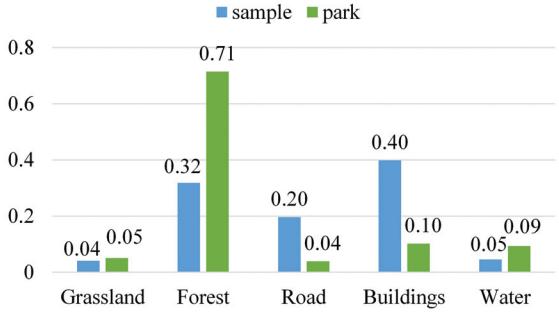


Figure 4. Land cover category distribution of all samples and park areas.

3.2. Hyperparameters Configuration

CHeGCN has four components: the CNN module, the heterogeneous graphs construction, the GCN module, and the classifier. The output dimensions of the CNN module are 32. The segment number n and compactness c of SLIC are set to 50 and 10, respectively. Parameter n is the approximate number of segments, and c balances the color proximity and space proximity. There are 3 layers each with 32 units in the GCN module. Each GCN layer is followed by a batch normalization [49] layer and a ReLU activation layer. The fused feature maps are followed by a 1×1 convolutional layer, a softmax function, and the cross-entropy loss. We use the Adam optimizer [50] to train CHeGCN for 130 epochs, with four examples per mini-batch. All hyperparameters are determined by the performance in the validation dataset, and the same hyperparameter configuration is used for both qualitative and quantitative results. Our code (Code is available at: https://github.com/Liuzhizhiooo/CHeGCN-CNN_enhanced_Heterogeneous_Graph) is implemented with Python-3.6 and PyTorch-1.10.2 and is accessed on 6 October 2022.

The learning rate (lr) parameters of modules should be different because the architectures of the CNN module and the GCN module are different. Meanwhile, the ResNet backbone is pretrained, thus the lr of it is set lower than convolutional layers that are used in dimension deduction and the classifier. Specifically, the maximum lr of the GCN module, the ResNet-18 backbone, and the 1×1 convolutional layers are 6×10^{-4} , 1×10^{-4}, and 2×10^{-4}, respectively. Furthermore, we adopt the warm-up strategy [41], the cosine annealing warm restarts schedule [51], and periodically decay the amplitude. The lr curves are shown in Figure 5, and the lr schedule is formulated as Equation (5):

$$lr_t = \frac{1}{2}\beta^{t'} lr_{max}(1 + \cos(t'\pi)) \tag{5}$$

where:

lr_t is the learning rate at current epoch t;
β is the periodic decay factor and is set to $\sqrt{1/2}$;
lr_{max} is the maximum learning rate of modules,

t' is a temporary variable and $t' = \frac{t-T_0}{T}$;
T_0 is the number of epochs for warm-up and is set to 30;
T is the number of epochs between two warm restarts and is set to 20.

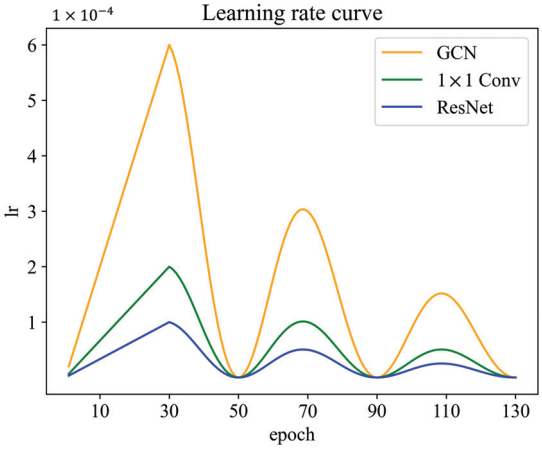


Figure 5. Learning rate schedule, which combines the warm-up strategy, cosine annealing warm restarts schedule, and periodic decay. The maximum learning rates of different components in CHeGCN are different.

Moreover, the training details of these state-of-the-art models for comparison are as follows. The pretrained ResNet-18, with the last two down-sampling layers removed, serves as the backbone for FCN, PSPNet, DeepLabv3, and GloRe. All compared models adopt the learning rate schedule in Equation (5) with $lr_{max} = 1 \times 10^{-4}$. We employ a heuristic strategy rather than grid search to determine the model structure and the hyperparameters because there are a lot of parameters in our model. Specifically, we first determine the model's configuration, then the learning rate hyperparameters, and finally other parameters such as batch size and segmentation scale. All of these parameters are determined by the performance in the validation dataset. For some key parameters, such as model depth and segmentation scale, we conducted detailed experiments in the discussion section. It is worth noting that all quantitative metrics are obtained by the model with the maximum OA index on the validation dataset.

3.3. Comparison of Classification Performance

Tables 3 and 4 exhibit the segmentation scores (%) of CHeGCN and six state-of-the-art models in terms of OA, Kappa, and IoU in two datasets. Meanwhile, we show the qualitative segmentation results of all methods in Figure 6.

Table 3. Quantitative comparison of different methods in the Beijing dataset.

Model	OA	Kappa	IoU
FCN	87.78 ± 0.67	71.05 ± 1.98	66.40 ± 2.22
U-net	85.33 ± 0.65	65.99 ± 2.00	62.22 ± 2.18
PSPNet	87.61 ± 0.31	70.82 ± 0.96	66.30 ± 1.12
DeepLabv3	87.86 ± 0.20	71.46 ± 0.65	66.97 ± 0.80
CEGCN	79.67 ± 0.26	51.67 ± 0.91	49.42 ± 0.95
GloRe	88.02 ± 0.63	71.67 ± 1.93	67.03 ± 2.26
CHeGCN	**89.07 ± 0.29**	**74.71 ± 0.49**	**70.48 ± 0.49**

Table 4. Quantitative comparison of different methods in the Shenzhen dataset.

Model	OA	Kappa	IoU
FCN	87.46 ± 0.39	65.17 ± 1.57	57.85 ± 1.75
U-net	87.51 ± 0.39	66.07 ± 1.42	59.10 ± 1.58
PSPNet	87.66 ± 0.21	66.37 ± 0.53	59.33 ± 0.50
DeepLabv3	87.17 ± 0.20	64.50 ± 0.98	57.28 ± 1.18
CEGCN	82.64 ± 0.20	52.76 ± 1.04	47.25 ± 1.09
GloRe	87.33 ± 0.33	64.83 ± 0.89	57.52 ± 0.88
CHeGCN	**88.37 ± 0.45**	**69.11 ± 1.79**	**62.45 ± 2.11**

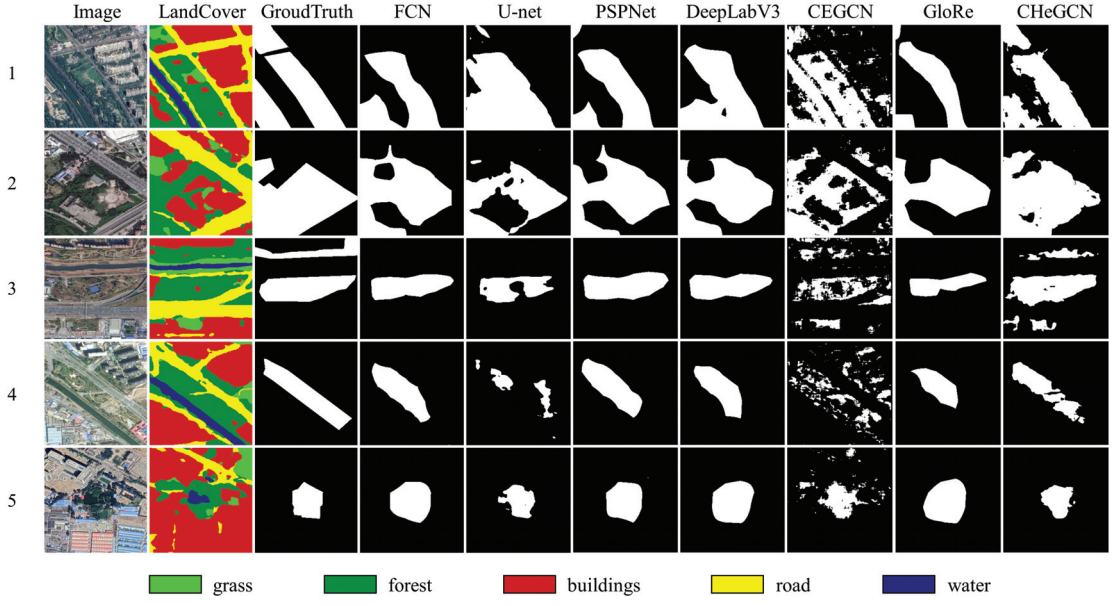


Figure 6. Qualitative segmentation results of different methods. Five examples are provided for comparison of models. The first column is the images, the second one indicates the land cover data, the third one lists the corresponding ground truth, and the following columns exhibit the segmentation results of different models. The color table for land cover categories is listed at the bottom.

In the Beijing dataset, our model performs the best and outperforms the second one by nearly 3.5% on the IoU metric. All CNNs achieve a similar performance, except U-net. Under the condition of limited samples, U-net behaves worse than other CNNs because it is trained from scratch. Meanwhile, we observe that the performance of the graph-based model CEGCN is unsatisfactory. This could be due to insufficient local spatial feature extraction. CEGCN is developed for hyperspectral images with abundant spectral information, which extracts pixel-level features. GloRe has a marginal improvement over CNNs, which benefits from the constructed long-distance relationships. However, GloRe builds graphs by applying convolutions to images, resulting in mismatches between nodes in interaction space and land cover units. Therefore, the improvement is not significant. Compared to GloRe, CHeGCN builds graphs based on land cover elements and achieves better performance.

Similarly to the previous dataset, the Shenzhen dataset demonstrates CHeGCN's advantages over other models. CHeGCN outperforms CNNs (e.g., DeepLabv3) and homogeneous GCNs (e.g., GloRe) by approximately 5% on the Kappa and IoU indices. GloRe, on the other hand, performs worse than PSPNet and U-net, demonstrating its instability. The topological relationships among land cover units cannot be properly established since

GloRe builds graphs on virtual nodes. In contrast, CHeGCN achieves stable improvement over CNNs.

We further display the qualitative segmentation results of several test samples in Figure 6. CNNs and CEGCN tend to classify all forest and water pixels as parks (see sample 1), regardless of the topological positions of these pixels. Meanwhile, CNNs, CEGCN, and GloRe fail to treat park regions as a whole. They classify buildings in the marked area of sample 2 as non-park. CNNs ignore the narrow park area in sample 3 as pooling operations of deep CNN severely destroy the spatial structure. In contrast, CHeGCN removes the last four convolutional layers of ResNet-18 to extract shallow CNN features, which are beneficial for small object recognition. The same goes for samples 4 and 5, where the predictions of CNNs tend to be over-smoothed and blurred. The noisy results of CEGCN indicate its lack of spatial features. Comparatively, CHeGCN yields more accurate results.

3.4. Ablation Experiments

The improvement in the performance of CHeGCN model can be attributed to two factors: the heterogeneous graph-based reasoning and the pretrained CNN module. We designed the following experiments on the Beijing dataset to demonstrate the effectiveness of these factors. It is worth noting that hyperparameters in ablation experiments remain unchanged unless otherwise specified.

First, we conduct experiments to demonstrate the effectiveness of graph reasoning. We build a CNN model with the same structure as CHeGCN, except that the CNN model substitutes the GCN module with three convolutional layers. These layers have the same hidden units as the GCN layers. As a result, rows 3 and 5 in Table 5 show that the GCN module plays an important role, improving the accuracy by nearly 3.5%, 8.5%, and 8.5% in terms of OA, Kappa, and IoU, respectively.

Table 5. The quantitative comparison of different models in ablation experiments.

Model	OA	Kappa	IoU
HoGCN	78.60 ± 0.83	50.04 ± 1.80	48.77 ± 1.57
HeGCN	83.12 ± 0.27	61.86 ± 0.67	59.25 ± 0.82
CNN	85.63 ± 0.40	66.10 ± 1.35	61.85 ± 1.57
CHoGCN	88.05 ± 0.62	72.13 ± 1.32	67.80 ± 1.20
CHeGCN	$\mathbf{89.07 \pm 0.29}$	$\mathbf{74.71 \pm 0.49}$	$\mathbf{70.48 \pm 0.49}$

Furthermore, considering the situation in which there are no land cover data available, CHeGCN cannot use meta-path parameters to refine edge weights and degenerates to the CNN-enhanced HOmogeneous Graph Convolutional Network (CHoGCN). The sole difference from CHeGCN is that nodes in CHoGCN do not have land cover labels. Therefore, CHoGCN calculates the edge weights by (1). Compared with CHeGCN, there is a performance drop (nearly 2.5% in Kappa and IoU) in CHoGCN. This suggests that heterogeneous graphs have a stronger inference capability than homogeneous graphs. Meanwhile, CHoGCN outperforms the CNN model, demonstrating the effectiveness of graph reasoning once again.

Moreover, CNN features boost the performance of graph-based models. We report the accuracy metrics of the HOmogeneous Graph Convolutional Network (HoGCN) and HEterogeneous Graph Convolutional Network (HeGCN), neither of which employs a CNN module. The differences between HeGCN and CHeGCN are the initialization of node features and feature fusion. Node features in HeGCN are the average spectral features in superpixels of the input image, whereas CHeGCN takes the mean value of the CNN module's feature maps as node features. Moreover, HeGCN only employs the GCN output to classify without using CNN feature maps. The same goes for the differences between HoGCN and CHoGCN. The CNN module significantly improves the Kappa of HoGCN

and HeGCN, as shown in Table 5. Meanwhile, HeGCN outperforms HoGCN, which is consistent with the previous conclusion that land cover data are beneficial.

3.5. Visualization Analysis

In this section, we analyze the underlying mechanism of CHeGCN. We visualize edge weights among adjacent land cover objects to observe topological relations among land cover objects in parks. CHoGCN is compared with the proposed CHeGCN to illustrate the advantages of heterogeneous graphs. Furthermore, we interpret segmentation results with meta-path parameters. We select two samples to show the edge weights and segmentation results of CHoGCN and CHeGCN in Figure 7. The top row contains land cover data overlaid with superpixel boundaries, and the edge weights of models. The second row includes the zoomed-in views of the highlight boxes in the first row. The third row consists of the ground truth label, and the predictions of models.

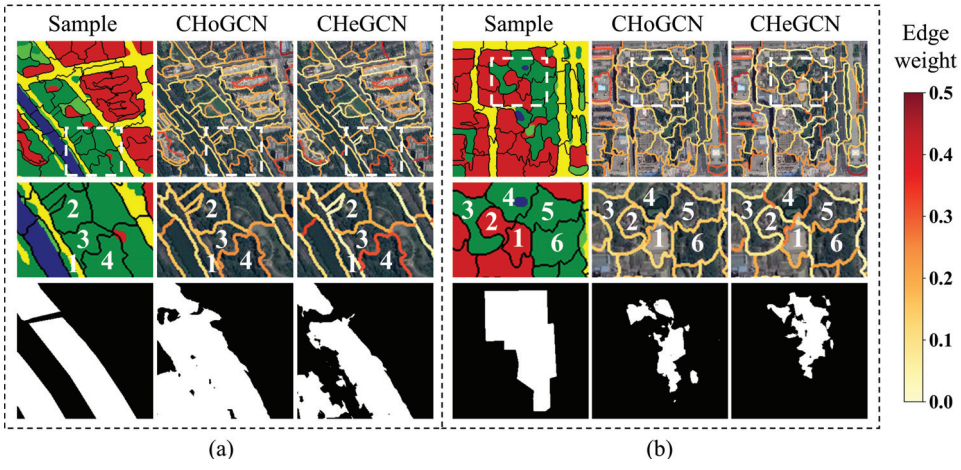


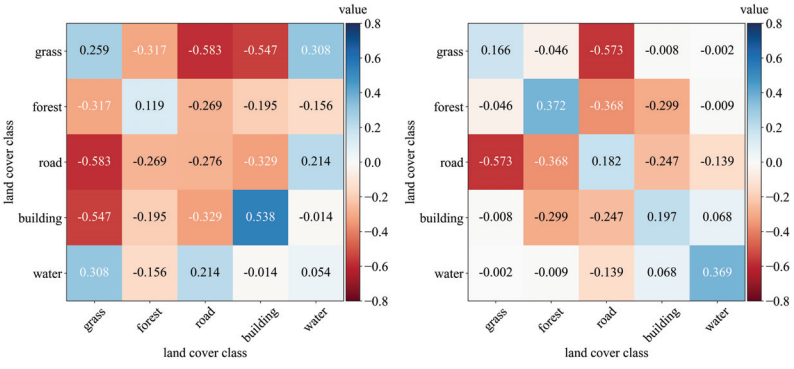
Figure 7. Visualization of edge weights among land cover objects and the segmentation results. There are two examples shown in (**a**,**b**) and the numbers in the second row denote the index numbers of different nodes. The color bar on the right is used to render edge weights, with higher values making edges redder.

As shown in Figure 7a, CHoGCN misclassifies the road and water regions in the lower left of the image. Due to the improper selection of edge weights, the topological relationships are insufficiently constructed. As mentioned previously, roads generally form the boundaries of parks. This is consistent with land cover distribution statistics in Figure 4, where the number of road pixels in parks is much less than that in all regions. However, the edge weight of CHoGCN between a road object and a forest object is high. Specifically, the edges between a road node (1) and forest nodes (2, 3, 4) in CHoGCN are high, which are orange-colored. This will reduce the interclass variance in the feature aggregation, leading to the false positive classification. CHeGCN decreases the edge weights (rendered in yellow) between road and forest objects, making these nodes further apart in the feature space.

Figure 7b shows another example. Because of inadequate use of neighboring information, CHoGCN incorrectly labels the building area in the park as non-park. CHeGCN reduces intraclass variance during feature aggregation to smooth local variations, which finally achieves global perception. In detail, the forest superpixels (nodes 3, 4, 5, 6) surrounding the building are more closely connected than those of CHoGCN, and the corresponding edges in CHeGCN tend to be red. As a result, the features of the building regions (nodes 1, 2) tend to be similar to those of their neighbors, making them easier to recognize as parks.

We visualize meta-path parameters a_P, b_P in Figure 8 because they play a critical role in heterogeneous graph construction (the calculation equation is seen in Equation (2)).

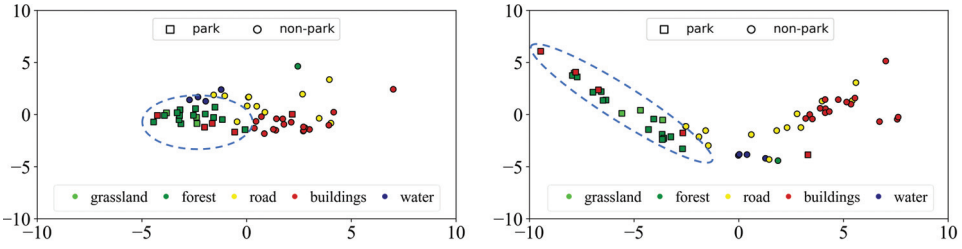
Combined with the above cases, we find these parameters interpretable. Almost all parameters of the self-connection meta-path are positive, which is profitable for decreasing the intraclass variance. Most of the values related to roads are negative, especially the parameters of meta-path "road-grass" and "road-forest". As such, meta-path parameters are advantageous for the segmentation of the scene in Figure 7a. Meanwhile, despite being negative, the absolute values of the parameters of the meta-path "buildings-forest" are relatively small. These behaviors make it possible to realize global recognition for segmentation, such as the case in Figure 7b. From the above analysis, we find that meta-path-based adjacency matrix calculation in Equation (2) greatly enhances graph reasoning capability.



(a) Meta-path Parameter a_P (b) Meta-path Parameter b_P

Figure 8. Symmetric meta–path parameters a_P,b_P in edge calculation. The values are rendered with the color bar on the right, with positive values appearing in blue and negative values in red.

To summarize, the mechanism of the heterogeneous graph-based model is to adaptively adjust interclass and intraclass variance based on topological relations. We take the sample in Figure 7a to show the difference in feature distribution before and after the GCN module, where the feature dimension is reduced to two by principal component analysis (PCA) [52]. As shown in Figure 9a, the CNN features of water nodes are close to those of park nodes since the water regions are located in the middle of two parks. After the GCN module, the interclass variance between the forest and water nodes are increased (see Figure 9b), which is consistent with the analysis of the edge weights in Figure 7a. Moreover, the intraclass variance of buildings is increased after the node feature aggregation. This makes it possible to distinguish building nodes inside parks from those outside parks. The building nodes outside parks are gathered together and move away from the park cluster because the a_P of the meta-path "buildings-buildings" is high. Finally, park nodes form a pure cluster.



(a) Node features of CNN (b) Node features of GCN

Figure 9. Node feature distributions of the CNN module and the GCN module, where PCA reduces the feature dimension to two. The park cluster is highlighted with a blue dashed circle and nodes are rendered by their land cover categories.

4. Discussion

In this section, we further investigated some critical hyperparameters on the Beijing dataset. Meanwhile, we analyze the reasons behind these phenomena in combination with previous findings.

4.1. Influence of Segmentation Scale

Graph size is determined by the segmentation scale. The larger n is, the more nodes there are in the graph. Large objects are easily over-smoothed, whereas small objects are noisy. Figure 10 shows that, on the first sample, the model performs better with a smaller $n = 20$, which filters out the noisy regions. When $n = 100$, however, the long and narrow park can be better identified.

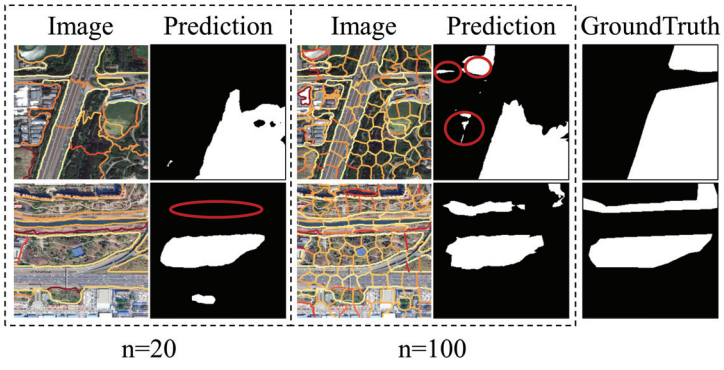


Figure 10. Comparison of qualitative results at different segmentation scales. Segmentation results of different segmentation scales are placed on the image. Predicted differences are marked with red circles.

Generally, we prefer appropriate over-segmentation, which ensures that the segmented regions are homogeneous and preserves more spatial details. Furthermore, we believe that proper over-segmentation can better establish topological relationships. When relations are described by large objects in Figure 11a, the "surrounded" relation is the same as the "adjacent" relation because there is only a single edge between node 2 and node 1, and the same thing between node 2 and node 3. By contrast, there are more edges between node 1 and its surrounding nodes in Figure 11b if over-segmented. Thus, node 1 is more likely to be identified as a park node. However, when there is a large building in a park, such as node 4 in Figure 11c, the prediction result will be unsatisfactory if over-segmented. As aforementioned, CHeGCN can reduce intraclass variation, causing node 4 in Figure 11d to move away from the park cluster after over-segmentation. As a result, the accuracy of CHeGCN rises at first, and then falls as n increases in Figure 12. Meanwhile, the standard deviation is high when n is too high or too low, indicating that using an appropriate segmentation scale can produce more stable results. The determination of the segment number is data-dependent and heuristic.

4.2. Influence of Network Depth

Although GCNs have shown promise, their architectures are much shallower than those of CNNs. Because of the vanishing gradient problem, most current GCNs generally contain 2–4 layers. The variation of model depth will greatly influence the performance of the model as the layer number is limited. We investigate the impact of CHeGCN depth in the following experiments. In more detail, we evaluate the performance of CHeGCN with 1–5 layers, where the number of hidden units in each layer is 32. Other hyperparameters are unchanged from previously.

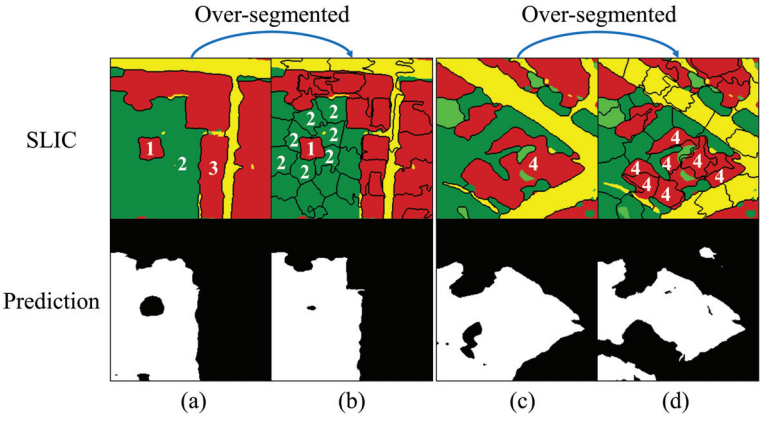


Figure 11. Two examples are provided to illustrate how the segmentation scale affects the construction of topological relations. In some cases, over-segmentation is beneficial for describing the topological relations of small objects. For instance, the "surrounding" relationship in (**b**) can be better expressed when the sample in (**a**) is over-segmented. However, describing the actual topological relations of large objects becomes more challenging when they are over-segmented. For example, (**d**) is the over-segmentation of (**c**). Since the topological relationship of node 4 is incorrectly expressed as being surrounded by buildings, the segmentation result of (**d**) is unsatisfactory.

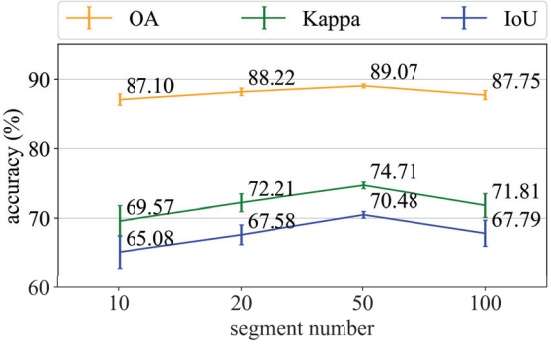


Figure 12. Quantitative comparison of CHeGCN at different segmentation scales.

As seen in Figure 13, the best choice of model depth is three. Excessively shallow or excessively deep networks have larger deviation values. The model with fewer layers captures an insufficient global context, resulting in a large variation in the extracted features. The model with more layers, on the other hand, is prone to over-smoothing, which ultimately makes nodes of different types indistinguishable in the feature space. Figure 14 depicts the feature distributions of the last GCN layer in the single-layer CHeGCN and the five-layer CHeGCN. The intraclass variance of the shallow GCN is high, where the building nodes are discretely distributed. Meanwhile, the interclass variance of the deeper GCN is minor. The water and forest nodes are mixed together, and it is difficult to distinguish. As a result, building an extremely shallow or deep GCN is not recommended. In all of the other experiments, the layer number is fixed to three.

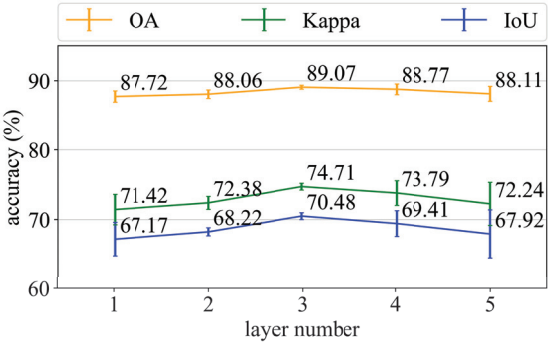


Figure 13. Quantitative comparison of models with different depths.

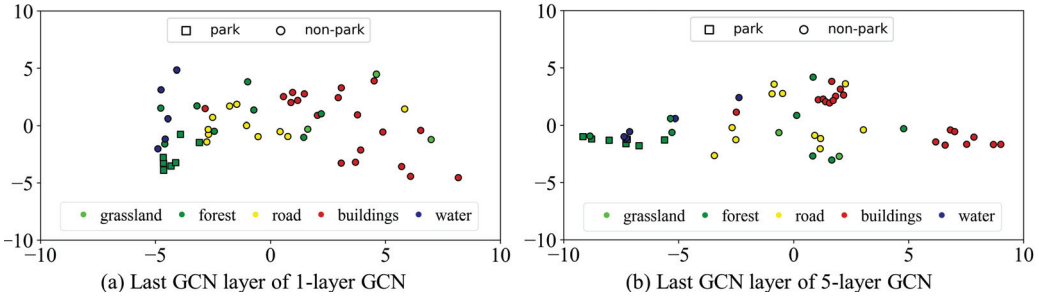


Figure 14. The feature distributions of the last GCN layer in 1-layer CHeGCN and 5-layer CHeGCN.

4.3. Spatially Adjacent vs. Global Adjacent

As mentioned above, land use segmentation requires global context information. CHeGCN stacks k GCN layers to aggregate features from k-hop neighborhoods based on topological relations. Another solution is to connect a pixel to all pixels [43,53]. Inspired by it, we propose a non-local CHoGCN and a non-local CHeGCN, which calculate the response at a given superpixel as a weighted sum of all superpixels. We compare the results between non-local models and the local connected models. Each experiment is repeated five times, with the average of the indices (OA, Kappa, and IoU) recorded in Table 6.

We observe that both non-local CHoGCN and non-local CHeGCN models perform worse than CHoGCN and CHeGCN, respectively, as model depth is three. Considering that fully connected non-local models are prone to overfitting, we compare these models in a single-layer structure. However, these single-layer non-local networks still fail to compete with the single-layer local connected models. On the one hand, it is difficult to train a fully connected network with limited samples. On the other hand, park segmentation relies heavily on topological relations, where non-local models fail to extract dependencies among heterogeneous regions and cannot capture local spatial structures. Furthermore, we discover that a non-local structure has far more negative effects on CHeGCN than on CHoGCN. When adopting the non-local strategy, IoU drops (ΔIoU) by 4.55% and 6.89% for 3-layer CHoGCN and 3-layer CHeGCN, respectively. This demonstrates that the performance of heterogeneous graph-based models will suffer greatly when meta-path parameters are not appropriately selected.

Table 6. Quantitative comparison of local and non-local CHeGCN.

Layer	Model	OA	Kappa	IoU	Δ IoU
1-layer	CHoGCN	87.44	70.69	66.39	
	Non-local CHoGCN	86.90	69.30	64.97	−1.42
	CHeGCN	87.72	71.42	67.17	
	Non-local CHeGCN	86.87	69.67	65.69	−1.48
3-layer	CHoGCN	88.05	72.13	67.80	
	Non-local CHoGCN	86.05	67.39	63.25	−4.55
	CHeGCN	89.07	74.71	70.48	
	Non-local CHeGCN	86.32	67.87	63.59	−6.89

4.4. Other Types of Land Use

Based on the aforementioned experiments and analysis, we demonstrated the great improvements in park segmentation with land cover data. Furthermore, we believe that, in addition to parks, there are other types of land use that can benefit from the land cover information. Some land use categories are combinations of multiple land cover components, and different land use categories have distinct combination patterns. For example, wetlands typically consist of water and grass regions while urban parks may also contain buildings. In addition, the location of land use units is closely tied to the land cover distribution. For instance, commercial areas regularly emerge in the center of building areas, and fields are rarely seen among buildings. However, several land use categories, such as forest, grass, and water, may obtain slight improvements given that they share similar definitions with land cover.

4.5. Imagery with Multiple Spectral Bands

In this article, the images in our datasets only contain RGB bands, while most of VFSR images contain four spectral bands (RGB + near-infrared). The simple method to generalize our model to VFSR images with four bands is to take the RGB bands. On the one hand, the primary information for land use segmentation is included in RGB bands. On the other hand, as the short-wave infrared spectrum predominantly provides relevant information for vegetation recognition, the additional land cover information provides supplemental information for vegetation. In addition, we could modify the CNN module to better exploit the multi-spectral data. For example, we can substitute the ResNet-18 backbone with U-net, which does not restrict the band number at 3. Meanwhile, the U-net trained from scratch may require more data to obtain comparable results.

5. Conclusions

In this paper, we propose a heterogeneous graph-based model, CHeGCN, to infer land use from land cover. Unlike prior work that builds graphs solely on images, we introduce land cover data to better estimate the topological relations among geo-objects. With the assistance of land cover information, CHeGCN achieves approximately 2.5% IoU improvements over CHoGCN in two datasets. The mechanism behind this is that the ability of graph reasoning is enhanced by adaptively adjusting the edge weights of labeled nodes. In addition, our CHeGCN produces more accurate segmentation results. CHeGCN performs nearly 3.5% and 5% better than current methods, namely CNNs and GCNs, respectively. Meanwhile, we comprehensively analyze the underlying mechanisms. In conclusion, CHeGCN is capable of processing heterogeneous data, which greatly improves land use segmentation results. Inspired by the image pyramid, we believe the multi-scale architecture of graphs will be beneficial for building topological relationships. In future work, the multi-scale structure will be explored to better exploit pretrained deep CNN features and GCN features at different segmentation scales.

Author Contributions: Conceptualization, Z.-Q.L. and Z.Z.; methodology, Z.-Q.L. and P.T.; software, Z.-Q.L. and W.Z.; data curation, Z.-Q.L.; writing—original draft, Z.-Q.L.; writing—review and editing,

Z.-Q.L. and Z.Z.; visualization, Z.-Q.L.; supervision, Z.Z. All authors have read and agreed to the published version of the manuscript.

Funding: This research was funded by the National Key R&D Program of China (Grant No. 2021YFB3900503), the Youth Innovation Promotion Association, CAS (No. 2022127), and "Future Star" Talent Plan of Aerospace Information Research Institute, Chinese Academy of Sciences (No. 2020KTYWLZX03 and No. 2021KTYWLZX07).

Acknowledgments: We gratefully acknowledge the free access to land cover data (https://data.casearth.cn/sdo/detail/60e55fca819aec59a2af708d and https://data.casearth.cn/sdo/detail/60e55fca819aec59a2af708f, accessed on 7 July 2021) provided by the Big Earth Data Science Engineering Project (CASEarth) launched by the Chinese Academy of Sciences (CAS) and the International Research Center of Big Data for Sustainable Development Goals (CBAS).

Conflicts of Interest: The authors declare no conflict of interest.

References

1. Patino, J.E.; Duque, J.C. A review of regional science applications of satellite remote sensing in urban settings. *Comput. Environ. Urban Syst.* **2013**, *37*, 1–17. [CrossRef]
2. Vitousek, P.M.; Mooney, H.A.; Lubchenco, J.; Melillo, J.M. Human domination of Earth's ecosystems. *Science* **1997**, *277*, 494–499. [CrossRef]
3. Zhu, Z.; Zhou, Y.; Seto, K.C.; Stokes, E.C.; Deng, C.; Pickett, S.T.; Taubenböck, H. Understanding an urbanizing planet: Strategic directions for remote sensing. *Remote Sens. Environ.* **2019**, *228*, 164–182. [CrossRef]
4. Comber, A.J.; Brunsdon, C.F.; Farmer, C.J. Community detection in spatial networks: Inferring land use from a planar graph of land cover objects. *Int. J. Appl. Earth Obs. Geoinf.* **2012**, *18*, 274–282. [CrossRef]
5. Li, M.; Stein, A. Mapping land use from high resolution satellite images by exploiting the spatial arrangement of land cover objects. *Remote Sens.* **2020**, *12*, 4158. [CrossRef]
6. Zhang, C.; Sargent, I.; Pan, X.; Li, H.; Gardiner, A.; Hare, J.; Atkinson, P.M. An object-based convolutional neural network (OCNN) for urban land use classification. *Remote Sens. Environ.* **2018**, *216*, 57–70. [CrossRef]
7. Cihlar, J.; Jansen, L.J. From land cover to land use: A methodology for efficient land use mapping over large areas. *Prof. Geogr.* **2001**, *53*, 275–289. [CrossRef]
8. Walde, I.; Hese, S.; Berger, C.; Schmullius, C. From land cover-graphs to urban structure types. *Int. J. Geogr. Inf. Sci.* **2014**, *28*, 584–609. [CrossRef]
9. Barnsley, M.J.; Barr, S.L. Distinguishing urban land-use categories in fine spatial resolution land-cover data using a graph-based, structural pattern recognition system. *Comput. Environ. Urban Syst.* **1997**, *21*, 209–225. [CrossRef]
10. Zhang, W.; Tang, P.; Corpetti, T.; Zhao, L. WTS: A Weakly towards strongly supervised learning framework for remote sensing land cover classification using segmentation models. *Remote Sens.* **2021**, *13*, 394. [CrossRef]
11. Chen, J.; Chen, J. GlobeLand30: Operational global land cover mapping and big-data analysis. *Sci. China Earth Sci.* **2018**, *61*, 1533–1534. [CrossRef]
12. Gong, P.; Wang, J.; Yu, L.; Zhao, Y.; Zhao, Y.; Liang, L.; Niu, Z.; Huang, X.; Fu, H.; Liu, S.; et al. Finer resolution observation and monitoring of global land cover: First mapping results with Landsat TM and ETM+ data. *Int. J. Remote Sens.* **2013**, *34*, 2607–2654. [CrossRef]
13. Yu, F.; Koltun, V. Multi-scale context aggregation by dilated convolutions. *arXiv* **2015**, arXiv:1511.07122.
14. Liu, W.; Rabinovich, A.; Berg, A.C. Parsenet: Looking wider to see better. *arXiv* **2015**, arXiv:1506.04579.
15. Zhao, H.; Shi, J.; Qi, X.; Wang, X.; Jia, J. Pyramid scene parsing network. In Proceedings of the IEEE Conference on Computer Vision and Pattern Recognition, Honolulu, HI, USA, 21–26 July 2017; pp. 2881–2890.
16. Li, H.; Xiong, P.; An, J.; Wang, L. Pyramid attention network for semantic segmentation. *arXiv* **2018**, arXiv:1805.10180.
17. Chen, L.C.; Papandreou, G.; Kokkinos, I.; Murphy, K.; Yuille, A.L. Semantic image segmentation with deep convolutional nets and fully connected crfs. *arXiv* **2014**, arXiv:1412.7062.
18. Chen, L.C.; Papandreou, G.; Kokkinos, I.; Murphy, K.; Yuille, A.L. Deeplab: Semantic image segmentation with deep convolutional nets, atrous convolution, and fully connected crfs. *IEEE Trans. Pattern Anal. Mach. Intell.* **2017**, *40*, 834–848. [CrossRef]
19. Chen, L.C.; Papandreou, G.; Schroff, F.; Adam, H. Rethinking atrous convolution for semantic image segmentation. *arXiv* **2017**, arXiv:1706.05587.
20. Chen, L.C.; Zhu, Y.; Papandreou, G.; Schroff, F.; Adam, H. Encoder-decoder with atrous separable convolution for semantic image segmentation. In Proceedings of the European Conference on Computer Vision (ECCV), Munich, Germany, 8–14 September 2018; pp. 801–818.
21. Long, J.; Shelhamer, E.; Darrell, T. Fully convolutional networks for semantic segmentation. In Proceedings of the IEEE Conference on Computer Vision and Pattern Recognition, Boston, MA, USA, 7–12 June 2015; pp. 3431–3440.

22. Ronneberger, O.; Fischer, P.; Brox, T. U-net: Convolutional networks for biomedical image segmentation. In Proceedings of the International Conference on Medical Image Computing and Computer-Assisted Intervention, Munich, Germany, 5–9 October 2015; Springer: Berlin/Heidelberg, Germany, 2015; pp. 234–241.
23. Li, Y.; Gupta, A. Beyond grids: Learning graph representations for visual recognition. *Adv. Neural Inf. Process. Syst.* **2018**, *31*, 9225–9235.
24. Chen, Y.; Rohrbach, M.; Yan, Z.; Shuicheng, Y.; Feng, J.; Kalantidis, Y. Graph-based global reasoning networks. In Proceedings of the IEEE/CVF Conference on Computer Vision and Pattern Recognition, Long Beach, CA, USA, 16–20 June 2019; pp. 433–442.
25. Lucas, R.; Rowlands, A.; Brown, A.; Keyworth, S.; Bunting, P. Rule-based classification of multi-temporal satellite imagery for habitat and agricultural land cover mapping. *ISPRS J. Photogramm. Remote Sens.* **2007**, *62*, 165–185. [CrossRef]
26. Hamilton, W.L. Graph representation learning. *Synth. Lect. Artifical Intell. Mach. Learn.* **2020**, *14*, 1–159.
27. Hamilton, W.; Ying, Z.; Leskovec, J. Inductive representation learning on large graphs. *Adv. Neural Inf. Process. Syst.* **2017**, *30*, 1025–1035 .
28. Fout, A.; Byrd, J.; Shariat, B.; Ben-Hur, A. Protein interface prediction using graph convolutional networks. *Adv. Neural Inf. Process. Syst.* **2017**, *30*, 6533–6542.
29. Rhee, S.; Seo, S.; Kim, S. Hybrid approach of relation network and localized graph convolutional filtering for breast cancer subtype classification. *arXiv* **2017**, arXiv:1711.05859.
30. Malisiewicz, T.; Efros, A. Beyond categories: The visual memex model for reasoning about object relationships. *Adv. Neural Inf. Process. Syst.* **2009**, *22*, 1222–1230.
31. Kipf, T.N.; Welling, M. Semi-supervised classification with graph convolutional networks. *arXiv* **2016**, arXiv:1609.02907.
32. Liu, Q.; Xiao, L.; Yang, J.; Wei, Z. CNN-enhanced graph convolutional network with pixel-and superpixel-level feature fusion for hyperspectral image classification. *IEEE Trans. Geosci. Remote Sens.* **2020**, *59*, 8657–8671. [CrossRef]
33. Wan, S.; Gong, C.; Zhong, P.; Pan, S.; Li, G.; Yang, J. Hyperspectral image classification with context-aware dynamic graph convolutional network. *IEEE Trans. Geosci. Remote Sens.* **2020**, *59*, 597–612. [CrossRef]
34. Wan, S.; Gong, C.; Zhong, P.; Du, B.; Zhang, L.; Yang, J. Multiscale dynamic graph convolutional network for hyperspectral image classification. *IEEE Trans. Geosci. Remote Sens.* **2019**, *58*, 3162–3177. [CrossRef]
35. Hong, D.; Gao, L.; Yao, J.; Zhang, B.; Plaza, A.; Chanussot, J. Graph convolutional networks for hyperspectral image classification. *IEEE Trans. Geosci. Remote Sens.* **2020**, *59*, 5966–5978. [CrossRef]
36. Cui, W.; Yao, M.; Hao, Y.; Wang, Z.; He, X.; Wu, W.; Li, J.; Zhao, H.; Xia, C.; Wang, J. Knowledge and Geo-Object Based Graph Convolutional Network for Remote Sensing Semantic Segmentation. *Sensors* **2021**, *21*, 3848. [CrossRef] [PubMed]
37. Hu, H.; Ji, D.; Gan, W.; Bai, S.; Wu, W.; Yan, J. Class-wise dynamic graph convolution for semantic segmentation. In Proceedings of the European Conference on Computer Vision, Glasgow, UK, 23–28 August 2020; Springer: Berlin/Heidelberg, Germany, 2020; pp. 1–17.
38. Wang, X.; Ji, H.; Shi, C.; Wang, B.; Ye, Y.; Cui, P.; Yu, P.S. Heterogeneous graph attention network. In Proceedings of the World Wide Web Conference, San Francisco, CA, USA, 13–17 May 2019; pp. 2022–2032.
39. Ouyang, S.; Li, Y. Combining deep semantic segmentation network and graph convolutional neural network for semantic segmentation of remote sensing imagery. *Remote Sens.* **2020**, *13*, 119. [CrossRef]
40. Marmanis, D.; Datcu, M.; Esch, T.; Stilla, U. Deep learning earth observation classification using ImageNet pretrained networks. *IEEE Geosci. Remote Sens. Lett.* **2015**, *13*, 105–109. [CrossRef]
41. He, K.; Zhang, X.; Ren, S.; Sun, J. Deep residual learning for image recognition. In Proceedings of the IEEE Conference on Computer Vision and Pattern Recognition, Las Vegas, NV, USA, 26 June–1 July 2016; pp. 770–778.
42. Krizhevsky, A.; Sutskever, I.; Hinton, G.E. Imagenet classification with deep convolutional neural networks. *Adv. Neural Inf. Process. Syst.* **2012**, *25*, 84–90. [CrossRef]
43. Mou, L.; Lu, X.; Li, X.; Zhu, X.X. Nonlocal graph convolutional networks for hyperspectral image classification. *IEEE Trans. Geosci. Remote Sens.* **2020**, *58*, 8246–8257. [CrossRef]
44. Achanta, R.; Shaji, A.; Smith, K.; Lucchi, A.; Fua, P.; Süsstrunk, S. SLIC superpixels compared to state-of-the-art superpixel methods. *IEEE Trans. Pattern Anal. Mach. Intell.* **2012**, *34*, 2274–2282. [CrossRef] [PubMed]
45. Velickovic, P.; Cucurull, G.; Casanova, A.; Romero, A.; Lio, P.; Bengio, Y. Graph attention networks. *Stat* **2017**, *1050*, 20.
46. Bronstein, M.M.; Bruna, J.; LeCun, Y.; Szlam, A.; Vandergheynst, P. Geometric deep learning: Going beyond euclidean data. *IEEE Signal Process. Mag.* **2017**, *34*, 18–42. [CrossRef]
47. Nair, V.; Hinton, G.E. Rectified linear units improve restricted boltzmann machines. In Proceedings of the ICML, Haifa, Israel, 21–24 June 2010; pp. 807–814.
48. Camps-Valls, G.; Marsheva, T.V.B.; Zhou, D. Semi-supervised graph-based hyperspectral image classification. *IEEE Trans. Geosci. Remote Sens.* **2007**, *45*, 3044–3054. [CrossRef]
49. Ioffe, S.; Szegedy, C. Batch normalization: Accelerating deep network training by reducing internal covariate shift. In Proceedings of the International Conference on Machine Learning, PMLR, Lille, France, 6–11 July 2015; pp. 448–456.
50. Kingma, D.P.; Ba, J. Adam: A method for stochastic optimization. *arXiv* **2014**, arXiv:1412.6980.
51. Loshchilov, I.; Hutter, F. Sgdr: Stochastic gradient descent with warm restarts. *arXiv* **2016**, arXiv:1608.03983.

52. Tipping, M.E.; Bishop, C.M. Probabilistic principal component analysis. *J. R. Stat. Soc. Ser. (Stat. Methodol.)* **1999**, *61*, 611–622. [CrossRef]
53. Wang, X.; Girshick, R.; Gupta, A.; He, K. Non-local neural networks. In Proceedings of the IEEE Conference on Computer Vision and Pattern Recognition, Salt Lake City, UT, USA, 18–22 June 2018; pp. 7794–7803.

remote sensing

MDPI

Article

On-Orbit Autonomous Geometric Calibration of Directional Polarimetric Camera

Guangfeng Xiang [1,2,3], Binghuan Meng [1,3,*], Bihai Tu [1,3], Xuefeng Lei [1,2,3], Tingrui Sheng [1,2,3], Lin Han [1,3], Donggen Luo [1,3] and Jin Hong [1,3]

[1] Anhui Institute of Optics and Fine Mechanics, Hefei Institutes of Physical Science, Chinese Academy of Sciences, Hefei 230031, China
[2] University of Science and Technology of China, Hefei 230026, China
[3] Key Laboratory of Optical Calibration and Characterization, Chinese Academy of Sciences, Hefei 230031, China
* Correspondence: bhmeng@aiofm.ac.cn

Abstract: The Directional Polarimetric Camera (DPC) carried by the Chinese GaoFen-5-02 (GF-5-02) satellite has the ability for multiangle, multispectral, and polarization detection and will play an important role in the inversion of atmospheric aerosol and cloud characteristics. To ensure the validity of the DPC on-orbit multiangle and multispectral polarization data, high-precision image registration and geolocation are vital. High-precision geometric model parameters are a prerequisite for on-orbit image registration and geolocation. Therefore, on the basis of the multiangle imaging characteristics of DPC, an on-orbit autonomous geometric calibration method without ground reference data is proposed. The method includes three steps: (1) preprocessing the original image of the DPC and the satellite attitude and orbit parameters; (2) scale-invariant feature transform (SIFT) algorithm to match homologous points between multiangle images; (3) optimization of geometric model parameters on-orbit using least square theory. To verify the effectiveness of the on-orbit autonomous geometric calibration method, the image registration performance and relative geolocation accuracy before and after DPC on-orbit geometric calibration were evaluated and analyzed using the SIFT algorithm and the coastline crossing method (CCM). The results show that the on-orbit autonomous geometric calibration effectively improves the DPC image registration and relative geolocation accuracy. After on-orbit calibration, the multiangle image registration accuracy is better than 1.530 km, the multispectral image registration accuracy is better than 0.650 km, and the relative geolocation accuracy is better than 1.275 km, all reaching the subpixel level (<1.7 km).

Keywords: geometric calibration; directional polarimetric camera; geolocation accuracy; image registration; remote sensing

Citation: Xiang, G.; Meng, B.; Tu, B.; Lei, X.; Sheng, T.; Han, L.; Luo, D.; Hong, J. On-Orbit Autonomous Geometric Calibration of Directional Polarimetric Camera. *Remote Sens.* **2022**, *14*, 4548. https://doi.org/10.3390/rs14184548

Academic Editor: Dongdong Wang

Received: 28 July 2022
Accepted: 8 September 2022
Published: 12 September 2022

Publisher's Note: MDPI stays neutral with regard to jurisdictional claims in published maps and institutional affiliations.

Copyright: © 2022 by the authors. Licensee MDPI, Basel, Switzerland. This article is an open access article distributed under the terms and conditions of the Creative Commons Attribution (CC BY) license (https://creativecommons.org/licenses/by/4.0/).

1. Introduction

On 7 September 2021, China successfully launched the GaoFen-5-02 (GF-5-02) satellite into a predetermined sun-synchronous orbit with a CZ-4C-Y40 carrier rocket at the Taiyuan Satellite Launch Center, with a nominal orbit altitude of 705 km. The satellite carries two Earth observation payloads and five atmospheric sounding payloads: Advanced Hyperspectral Imager (AHSI) [1], Visual and Infrared Multispectral Imager (VIMI) [2], Greenhouse Gas Monitoring Instrument (GMI) [3], Environment Monitoring Instrument (EMI) [4], Directional Polarization Camera (DPC) [5–9], Particulate Observing Scanning Polarimeter (POSP) [5], and Absorptive Aerosol Sensor (AAS) [10]. Through the cooperation of various payloads, China's hyperspectral observation capacity in the atmosphere, water, and land will be comprehensively improved, meeting the urgent needs of China's comprehensive environmental monitoring and providing effective data guarantee for environmental protection operations such as atmospheric environment monitoring, water environment monitoring, and ecological environment monitoring.

Among them, the DPC developed by the Anhui Institute of Optics and Fine Mechanics (AIOFM) of the Chinese Academy of Sciences (CAS) has multiangle, multispectral, and polarization detection capabilities. Combined with the inversion model of atmospheric properties based on polarization information, the DPC will play an important role in the inversion of atmospheric aerosol and cloud parameters [11–13]. In addition to the already launched GF-5-01, GF-5-02, and DQ-1 satellites, subsequent CM satellites are also planned to carry DPC. As shown in Figure 1, the DPC optical system consists of an objective lens, a filter and polarizer wheel, and an area array charge-coupled device (CCD). The design concept is similar to the French Polarization and Directionality of the Earth Reflectances (POLDER) [14–18] series of instruments. The objective lens has a wide field of view (FOV) and image space telecentric characteristics. The wide FOV imaging capability based on DPC can observe the target from multiple angles along the track. The design of the image space telecentric ensures that there is enough space to install the filter and polarizer wheel. The filter and polarizer wheel adopt the time-sharing detection mode, which can analyze the multispectral and polarized radiation information of the target. The area array CCD is used to complete the photoelectric conversion of remote sensing images, and it should meet the design requirements of the instrument's working band, dynamic range, and spatial resolution. Table 1 shows the DPC parameters to be configured for each satellite. The GF-5-02 and DQ-1 satellites use a 2 × 2 pixel combination to ensure the same nadir resolution as the GF-5-01 satellite. The follow-up research object of this paper is the DPC carried by the GF-5-02 satellite.

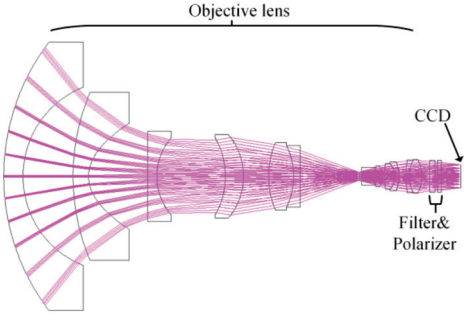


Figure 1. Optical structure of DPC.

Table 1. DPC parameters.

Parameter		GF-5-01	GF-5-02	DQ-1	CM
Focal length (mm)		4.83	5.54	5.54	4.83
FOV (degree)	Along-track	±50	±50	±50	±50
	Cross-track	±50	±50	±50	±40
Relative aperture		1:4	1:4.26	1:4.26	1:4
CCD array size		512 × 512	1024 × 1024	1024 × 1024	360 × 512
Pixel size (μm)		22.5 × 22.5	13 × 13	13 × 13	22.5 × 22.5
Orbit altitude (km)		705	705	705	505
Band (nm)	Polarized		490 (20) 670 (20) 865(40)		
	Nonpolarized		443 (20) 565 (20) 763 (10) 765 (40) 910(20)		
Swath (km)	Along-track	1850	1850	1850	1250
	Cross-track	1850	1850	1850	850
Observation angle		9	17	17	9
Nadir resolution (km)		3.3	1.7	1.7	2.5

To take full advantage of the multiangle and multispectral polarization detection advantages of DPC, not only are radiation and polarization detection accuracy required, but high-precision image registration and geolocation are also extremely important. Therefore, it is necessary to establish the mapping relationship between object points in 3D

space and image points on the instrument's 2D image plane with high-precision geometric calibration. The geometric calibration of spaceborne optical instruments is generally divided into two stages: pre-launch laboratory geometric calibration and on-orbit geometric calibration. The geometric model parameters calibrated by the laboratory cannot effectively represent the geometric performance of the instrument on-orbit because of the violent vibration during launch and the difference between the on-orbit environment and the laboratory environment. Therefore, the validity of on-orbit observation data of spaceborne optical instruments depends largely on high-precision on-orbit geometric calibration. Traditional on-orbit geometric calibration methods are usually based on the reference data of high-precision ground calibration fields [19,20]. The ground calibration field can provide satellites with ground control points with high-precision geographic coordinate information as an absolute reference for on-orbit geometric calibration. This method matches the calibration field image acquired by the on-orbit instrument with the reference image and then realizes the on-orbit geometric calibration using dense control point constraint. However, due to the dependence on calibration field reference data, this method has the opportunity to calibrate only when the satellite passes through the calibration field, and its timeliness is greatly limited. The calibration field size is usually only tens to hundreds of kilometers, for DPC, which is a spaceborne optical instrument with a swath width of thousands of kilometers, the ground calibration field cannot be used for all-around on-orbit geometric calibration. To solve the limitations of the traditional on-orbit geometric calibration method based on a ground calibration field, it is urgent to explore an on-orbit autonomous geometric calibration method without reference data from the ground calibration field. In the field of computer vision, camera autonomous calibration methods have always been a hot research topic [21–24]. In the field of satellite remote sensing, on-orbit autonomous geometric calibration methods have also attracted more and more attention from researchers in recent years [17,25–28]. Gresloud et al. [25], on the basis of the agile imaging capabilities of the Pleiades [29], used two imaging methods of along-track push-broom and cross-track swing-scanning to obtain cross images with a yaw angle difference of nearly 90° during a satellite transit. Then, the on-orbit autonomous geometric calibration was carried out according to the geometric constraint relationship of the homologous points between the cross images. However, the corresponding calibration model and solution method were not described in detail in [25]. Moreover, the calibration method requires the satellite to have agile imaging ability, which is not suitable for satellites without agile imaging ability (such as GF-5-01 satellite, GF-5-02 satellite, DQ-1 satellite, and CM satellite). Wang et al. [26] proposed an on-orbit geometric calibration method based on two ground control points and homologous points evenly distributed between the two images in their research on the on-orbit geometric calibration of the GaoFen-4 satellite. Although this method greatly reduces the need for ground control points compared with the traditional on-orbit geometric calibration method based on the ground calibration field, there is still a gap with the on-orbit autonomous geometric calibration method (no ground control points at all) we pursue. Zhang et al. [27] proposed using at least three images with overlapping regions to match homologous points and calculate the internal distortion of the instrument according to the forward intersection residual between the homologous points. However, this method only considers the calibration of the internal distortion of the spaceborne push-broom instrument. Fougnie et al. [17] proposed that the multiangle detection capability based on Polarization and Anisotropy of Reflectance for Atmospheric Sciences coupled with Observations from a Lidar (PARASOL) can perform on-orbit autonomous geometric calibration of the instrument installation angle error, but there is no public calibration model and specific implementation method. In a word, there are relatively few studies on the on-orbit autonomous geometric calibration methods in the field of satellite remote sensing, especially for instruments similar to DPC with a wide FOV, low resolution, and area array imaging. However, the DPC's multiangle imaging capability along the track makes it possible for its on-orbit autonomous geometric calibration.

In this paper, a geometric model of on-orbit imaging is constructed on the basis of the collinear equation and the imaging characteristics of DPC. Using the geometric model of on-orbit imaging, the errors of the model are classified and analyzed, and the geometrical parameters that require on-orbit calibration are determined. Secondly, on the basis of the multi-angle observation characteristics of the DPC, an on-orbit autonomous geometric calibration method that does not require a ground calibration field is proposed to perform the on-orbit geometric calibration of the DPC. Lastly, through the comparative analysis of the image registration and geolocation accuracy before and after the DPC on-orbit geometric calibration, the effectiveness of the on-orbit autonomous geometric calibration method in this paper is confirmed.

2. Geometric Model of DPC On-Orbit Imaging

The geometric model of DPC on-orbit imaging is used to describe the geometric mapping relationship between object points in 3D space and image points on the 2D image plane, and it is the basis for DPC on-orbit geolocation and image registration. The geometric model of DPC on-orbit imaging is shown in Figure 2, which involves a series of related coordinate systems, including the image coordinate system, DPC instrument coordinate system, GF-5-02 satellite body coordinate system, orbit coordinate system, and World Geodetic System 1984 (WGS-84). Assuming that the optical system is an ideal optical system, according to the transformation relationship between the coordinate systems and the basic principle of the collinear equation (namely, collinearity of image point M, projection center C, and object point G), the geometric model of DPC on-orbit imaging can be expressed as follows:

$$\begin{bmatrix} X_G \\ Y_G \\ Z_G \end{bmatrix} = \begin{bmatrix} X_{GPS} \\ Y_{GPS} \\ Z_{GPS} \end{bmatrix} + \begin{bmatrix} \Delta X \\ \Delta Y \\ \Delta Z \end{bmatrix} + \lambda \cdot R_{orbit}^{WGS-84} \cdot R_{body}^{orbit} \cdot R_{DPC}^{body} \begin{bmatrix} \sin\theta\cos\varphi \\ \sin\theta\sin\varphi \\ \cos\theta \end{bmatrix}, \quad (1)$$

where $\begin{bmatrix} X_G & Y_G & Z_G \end{bmatrix}^T$ represents the coordinates of object point G in the WGS-84, $\begin{bmatrix} X_{GPS} & Y_{GPS} & Z_{GPS} \end{bmatrix}^T$ represents the coordinates of the Global Position System (GPS) phase center in WGS-84, $\begin{bmatrix} \Delta X & \Delta Y & \Delta Z \end{bmatrix}^T$ represents the relative deviation between the GPS phase center and DPC projection center C, $\begin{bmatrix} \sin\theta\cos\varphi & \sin\theta\sin\varphi & \cos\theta \end{bmatrix}^T$ represents the direction of the incident ray corresponding to the image point M in the DPC instrument coordinate system, and θ and φ represent the field angle and azimuth angle of the incident ray, respectively. The corresponding relationship between the direction of incident ray and the coordinates of ideal image points can be described according to the ideal imaging formula of optical system. λ is the proportionality coefficient, R_{orbit}^{WGS-84} represents the rotation matrix from the orbit coordinate system to WGS-84. $R_{orbit}^{WGS-84} = \begin{bmatrix} (\vec{X_o})_1 & (\vec{Y_o})_1 & (\vec{Z_o})_1 \\ (\vec{X_o})_2 & (\vec{Y})_2 & (\vec{Z_o})_2 \\ (\vec{X_o})_3 & (\vec{Y_o})_3 & (\vec{Z_o})_3 \end{bmatrix}$, $\vec{Z_o} = -\frac{\vec{P_t}}{\|\vec{P_t}\|}$, $\vec{X_o} = \frac{\vec{V_t} \times \vec{Z_o}}{\|\vec{V_t} \times \vec{Z_o}\|}$, $\vec{Y_o} = \vec{Z_o} \times \vec{X_o}$, $\vec{P_t}$ is the satellite position at the imaging time t, and $\vec{V_t}$ is the satellite speed at the imaging time t, interpolated from GPS data. $R_{body}^{orbit} = R_{yaw} \cdot R_{roll} \cdot R_{pitch}$ represents the rotation matrix from GF-5-02 satellite body coordinate system to the orbit coordinate system, $(roll, pitch, yaw)$ represents the attitude parameters of the satellite at the time of imaging, which can be obtained by interpolation of the Attitude Determination System (ADS) data, $R_{DPC}^{body} = R_\gamma \cdot R_\alpha \cdot R_\beta$ represents the rotation matrix from the DPC instrument coordinate system to GF-5-02 satellite body coordinate system, and (α, β, γ) is the installation angle of DPC measured in the laboratory in the GF-5-02 satellite body coordinate system.

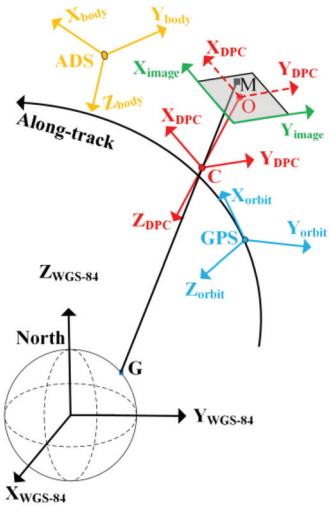


Figure 2. Geometric model of DPC on-orbit imaging.

Due to the influence of the distortion of the actual optical system, the actual image point M′ does not coincide with the ideal image point M, and the ideal object–image relationship needs to be corrected. Therefore, the laboratory established the corresponding relation between the incident ray direction and the coordinate of the actual image point, as shown in Figure 3.

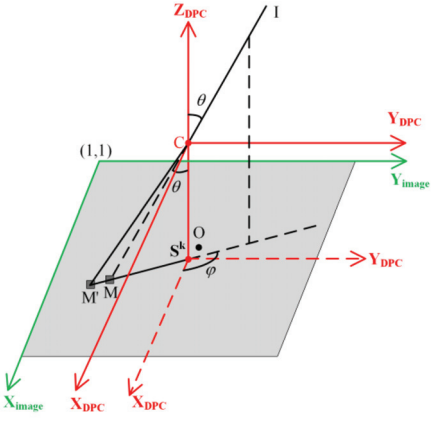


Figure 3. Object-image geometric relationship of DPC.

The actual image point on the CCD imaged by the incident light I with the field angle θ and the azimuth angle φ is M′ and the imaging process can be described by the following mathematical model:

$$\begin{cases} x^k_{M'} = x^k_S - D^k \cdot \cos\varphi \\ y^k_{M'} = y^k_S - D^k \cdot \sin\varphi \\ D^k = f^k_1 \cdot \tan\theta + f^k_3 \cdot \tan^3\theta + f^k_5 \cdot \tan^5\theta + f^k_7 \cdot \tan^7\theta + f^k_9 \cdot \tan^9\theta \end{cases}, \quad (2)$$

where S^k is the distortion center of band k, $\left(x^k_S, y^k_S\right)$ denotes the coordinates of the distortion center of band k, D^k is the distance between the distortion center S^k and the actual image

point M′, and $(f_1^k, f_3^k, f_5^k, f_7^k, f_9^k)$ is the distortion coefficient of the band k. In the laboratory, a geometric calibration method based on a separated two-dimensional turntable and the least square optimization theory was used to calibrate the distortion center coordinates $\left(x_S^k, y_S^k\right)$ and distortion coefficient $(f_1^k, f_3^k, f_5^k, f_7^k, f_9^k)$ of each band of DPC [30–32].

In the actual projection process, the geometric model of on-orbit imaging composed of Equations (1) and (2) is adopted, combined with the digital elevation model (DEM) and the reference Earth ellipsoid model, to calculate the position of each pixel detection target in the WGS-84 at the imaging time.

According to the physical significance of the parameters of the geometric model of DPC on-orbit imaging, the model parameters can be divided into two categories: the external parameters (installation angle, attitude angle, and projection center position) used to describe the position and attitude of DPC in the WGS-84, and the internal parameters (distortion center and distortion coefficient) used to describe the imaging process of the optical system. To improve the accuracy and efficiency of subsequent on-orbit geometric calibration, it is necessary to further analyze the above two types of model parameters to determine the geometric model parameters to be calibrated.

The installation angle error $(\Delta\alpha, \Delta\beta, \Delta\gamma)$ is a systematic error, including the change in the installation state of the DPC on the satellite platform and the rotation of the CCD. This is due to factors such as vibration during satellite launch and the difference between the on-orbit operating environment and the laboratory environment. The attitude angle error $(\Delta roll, \Delta pitch, \Delta yaw)$ is a random error, which originates from the ADS measurement error (the ADS measurement accuracy is better than 0.005° (3σ)) and the interpolation error caused by the mismatch between the ADS sampling time and the DPC imaging time. The projection center positioning error $(\Delta X_C, \Delta Y_C, \Delta Z_C)$ includes systematic error and random error. The systematic error is the change in the relative position of the projection center and GPS phase center caused by vibration and environmental changes. The random error is caused by GPS orbit measurement error (the orbit measurement accuracy is better than 20 m) and interpolation error caused by the mismatch between GPS sampling time and DPC imaging time. The influence of the projection center positioning error on the geolocation accuracy is equivalent to the error magnitude. It can be ignored for low-resolution instruments such as DPC. Moreover, it can be approximately considered that the projection center of the DPC coincides with the GPS phase center. Equation (1) can, thus, be simplified as follows:

$$\begin{bmatrix} X_G \\ Y_G \\ Z_G \end{bmatrix} = \begin{bmatrix} X_{GPS} \\ Y_{GPS} \\ Z_{GPS} \end{bmatrix} + \lambda \cdot R_{orbit}^{WGS-84} \cdot R_{body}^{orbit} \cdot R_{DPC}^{body} \begin{bmatrix} \sin\varphi \sin\theta \\ \cos\varphi \sin\theta \\ \cos\theta \end{bmatrix}. \quad (3)$$

The distortion center error $(\Delta x_S^k, \Delta y_S^k)$ is a systematic error, representing the horizontal offset of the area array CCD and the optical axis, caused by the vibration during the satellite launch and changes in the space environment. The distortion coefficient error $(f_1^k, f_3^k, f_5^k, f_7^k, f_9^k)$ is a systematic error caused by the change in the environment of the optical system (such as environmental refractive index, temperature, and other factors). The scaling of CCD pixel size caused by temperature changes can also be described by changes in distortion coefficients. For example, using Zemax analysis, it was found that, when the environment of the DPC optical system is changed from the standard atmosphere to vacuum, the imaging position of the incident beam of the same FOV on the image plane presents an error, as shown in Figure 4. However, the changes in the actual optical system environment are more complicated, and the on-orbit geometric performance of the instrument needs to be determined by on-orbit geometric calibration.

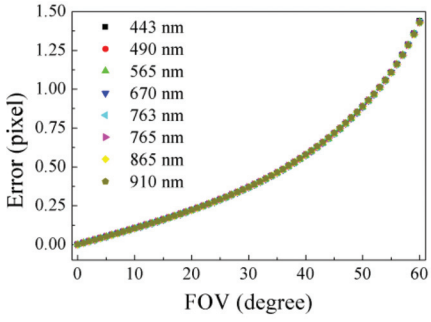


Figure 4. DPC geometric performance environmental difference analysis results.

According to the above analysis, after removing the random error term and the error term with a slight influence, the parameters to be calibrated on-orbit include the installation angle (α, β, γ) of the external parameter and the distortion center (x_S^k, y_S^k) and distortion coefficient $(f_1^k, f_3^k, f_5^k, f_7^k, f_9^k)$ of the internal parameter. However, it was found that the accuracy of geolocation and image registration is higher when the distortion center remains unchanged. Referring to PARASOL of the same type as DPC, the variation of the distortion center is not considered in its on-orbit geometric calibration [17]. Therefore, the subsequent on-orbit geometric calibration parameters in this paper only include the installation angle (α, β, γ) in the external parameter and the distortion coefficient $(f_1^k, f_3^k, f_5^k, f_7^k, f_9^k)$ in the internal parameter.

3. On-Orbit Autonomous Geometric Calibration Method

The DPC on-orbit autonomous geometric calibration method benefits from the multiangle observation characteristics of the instrument. The principle of DPC on-orbit multiangle observation is shown in Figure 5. Due to the instrument's wide FOV imaging capability in the along-track direction, the same ground object can be photographed 17 times in a single satellite transit.

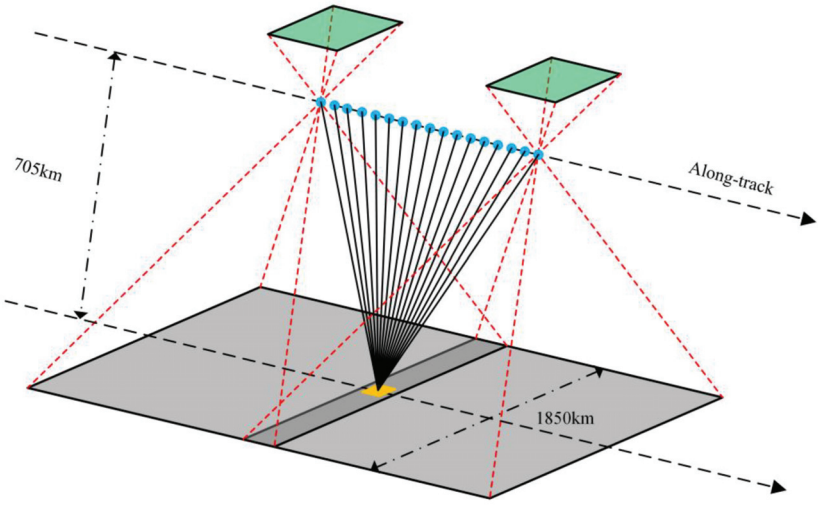


Figure 5. On-orbit multiangle observation principle of DPC.

As shown in Figure 6, if the same object G is imaged twice by DPC, the image points are M_a and M_b, respectively. In practice, objects are imaged up to 17 times. When the

parameters of the geometric model of DPC on-orbit imaging are ideal and error-free, calculating the coordinates $\begin{bmatrix} X_G & Y_G & Z_G \end{bmatrix}^T$ of the target G in the WGS-84 according to the geometric model parameters of the image points M_a and M_b at the imaging time should have the same results. However, the errors in the geometric model parameters often lead to deviations in the calculation results of the target geographic location. The difference between the geolocation result of each image point and the theoretical target point coordinates represents the geolocation error. Differences between homologous point pair geolocation results represent image registration errors.

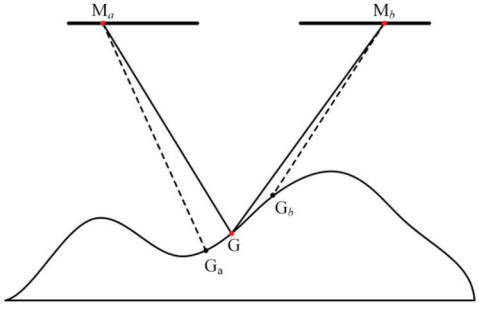


Figure 6. Schematic diagram of geolocation and registration error of DPC.

On the basis of the above analysis, this paper proposes an on-orbit autonomous geometric calibration method that does not require ground calibration field reference data. This method optimizes the geometric model parameters only according to the geometric constraint that homologous points between multiangle images have unique coordinates in WGS-84. The on-orbit autonomous geometric calibration method includes three steps: data preprocessing, multiangle image homologous points matching, and geometric parameter optimization.

(1) Data preprocessing

The data preprocessing stage includes two aspects: preprocessing of the L0-level image data of DPC, and preprocessing of the attitude and orbit parameters. The L0-level image preprocessing includes CCD dark current correction, frame transfer correction, relative response correction, optical system relative response correction, and stray light correction. The attitude and orbit parameter preprocessing needs to analyze the attitude and orbit data from the engineering parameters of the satellite platform, and then obtain the attitude and orbit parameters of each frame of image imaging time according to the imaging time interpolation of DPC.

(2) Homologous point matching

After preprocessing, the scale-invariant feature transform (SIFT) [33,34] algorithm is used to extract feature points in multiangle images. The SIFT algorithm is an image local feature extraction algorithm that finds extreme points as feature points in the Gaussian difference scale space. The feature points extracted by the SIFT algorithm remain invariant to rotation, scaling, and brightness changes, while also maintaining a certain stability to viewing angle changes, affine transformation, and noise. The SIFT algorithm includes four steps of scale space extreme value detection, feature point localization, orientation assignment, and feature point description. After completing the localization and description of the feature points of each angle image, the homologous points between the multiangle images can be matched according to the similarity of the descriptor of the feature points. When matching homologous points, any two of the 17 angle images are paired, with C_{17}^2 combinations, and then homologous point matching is performed on the two images of each combination. A cloud-free image is selected as best as possible. Because the elevation information of the cloud is unknown, and the cloud is not fixed during multiangle image acquisition, to ensure that there are no cloud pixels at the matched homologous points, cloud pixels need

to be removed. In this study, a simple threshold method is adopted to remove cloud pixels. In this method, a reflectivity threshold is set for each band. When the reflectivity of the pixels is higher than this threshold, clouds are identified and removed. Additionally, to eliminate the mismatched points, the random sample consensus (RANSAC) [35] algorithm and the homologous point geographic location constraint threshold are used to eliminate mismatched points. The RANSAC algorithm is an algorithm that removes outliers from a set of sample datasets containing outliers and inliers. The basic principle of using the homologous point geographic location constraint threshold to eliminate mismatched points is that there is no huge deviation when calculating the geographic coordinates of a pair of homologous points using the initial geometric parameters of DPC. Therefore, when the geographic coordinate deviation exceeds a set threshold, it can be regarded as a mismatch. Finally, the homologous point datasets DATA_A and DATA_B are formed, as shown in Equation (4). Data points in the two datasets are matched one by one. The information in a single data point i includes the coordinates of the image point, attitude, and orbit data at the time of imaging. The precise geographic coordinates of the ground object corresponding to the homologous point are unknown. The on-orbit autonomous geometric calibration method proposed in this paper does not need to know the high-precision geographic coordinate information of these homologous points. This enables the method in this paper to complete the on-orbit autonomous geometric calibration without relying on the reference data of the ground calibration field.

$$\mathrm{DATA}_A = \left\{ \begin{array}{c} (x^k_{A,i}, y^k_{A,i}) \\ [X_{\mathrm{GPS}}, Y_{\mathrm{GPS}}, Z_{\mathrm{GPS}}]^k_{A,i} \\ \overrightarrow{V}^k_{A,i} \\ (roll^k_{A,i,}, pitch^k_{A,i}, yaw^k_{A,i}) \end{array} \right\}, \mathrm{DATA}_B = \left\{ \begin{array}{c} (x^k_{B,i}, y^k_{B,i}) \\ [X_{\mathrm{GPS}}, Y_{\mathrm{GPS}}, Z_{\mathrm{GPS}}]^k_{B,i} \\ \overrightarrow{V}^k_{B,i} \\ (roll^k_{B,i}, pitch^k_{B,i}, yaw^k_{B,i}) \end{array} \right\}. \quad (4)$$

(3) Geometrical parameter optimization

Combined with the geometric model of DPC on-orbit imaging and the geometric constraints of homologous points between multiangle images, the least-squares method can be used to optimize the geometrical parameters to be calibrated. The initial values of the distortion coefficient $(f^k_1, f^k_3, f^k_5, f^k_7, f^k_9)_{\mathrm{L}}$ and installation angle $(\alpha, \beta, \gamma)_{\mathrm{L}}$ are the results of laboratory calibration tests. The geometrical parameter optimization process can be divided into three steps.

The first step is to use the homologous point data of each band to simultaneously optimize the distortion coefficient and installation angle band by band. The objective equation is shown in Equation (5). In the formula, $(X_{\mathrm{G},A,i}, Y_{\mathrm{G},A,i}, Z_{\mathrm{G},A,i})$ and $(X_{\mathrm{G},B,i}, Y_{\mathrm{G},B,i}, Z_{\mathrm{G},B,i})$ correspond to the coordinates of the ground object G_i in WGS-84 calculated from the ith pair of homologous point data in the datasets DATA_A and DATA_B, respectively. The first step optimization results include the distortion coefficient $(f^k_1, f^k_3, f^k_5, f^k_7, f^k_9)_1$ and installation angle $(\alpha^k, \beta^k, \gamma^k)_1$ of each band.

$$E_1 = \min \sum_{i=1}^{m} \left(\begin{array}{l} (X_{\mathrm{G},A,i}(f^k_1, f^k_3, f^k_5, f^k_7, f^k_9, \alpha, \beta, \gamma) - X_{\mathrm{G},B,i}(f^k_1, f^k_3, f^k_5, f^k_7, f^k_9, \alpha, \beta, \gamma))^2 \\ +(Y_{\mathrm{G},A,i}(f^k_1, f^k_3, f^k_5, f^k_7, f^k_9, \alpha, \beta, \gamma) - Y_{\mathrm{G},B,i}(f^k_1, f^k_3, f^k_5, f^k_7, f^k_9, \alpha, \beta, \gamma))^2 \\ +(Z_{\mathrm{G},A,i}(f^k_1, f^k_3, f^k_5, f^k_7, f^k_9, \alpha, \beta, \gamma) - Z_{\mathrm{G},B,i}(f^k_1, f^k_3, f^k_5, f^k_7, f^k_9, \alpha, \beta, \gamma))^2 \end{array} \right). \quad (5)$$

In the second step, it is considered that all bands should have the same installation angle; however, due to the influence of random errors such as attitude and orbit parameters and the possible correlation between internal and external parameters, the installation angles obtained from each band in the first step are slightly different. Therefore, the average $(\alpha, \beta, \gamma)_1$ of the installation angles of each band in the first step is taken as the optimization result of the first step. The second step only optimizes the distortion coefficient band by band. The installation angle $(\alpha, \beta, \gamma)_1$ obtained from the first step is set as the true

value. The objective equation of this process is shown in Equation (6). The second step optimization result includes the distortion coefficient $(f_1^k, f_3^k, f_5^k, f_7^k, f_9^k)_2$ of each band.

$$E_2 = \min \sum_{i=1}^{m} \begin{pmatrix} (X_{G,A,i}(f_1^k, f_3^k, f_5^k, f_7^k, f_9^k) - X_{G,B,i}(f_1^k, f_3^k, f_5^k, f_7^k, f_9^k))^2 \\ +(Y_{G,A,i}(f_1^k, f_3^k, f_5^k, f_7^k, f_9^k) - Y_{G,B,i}(f_1^k, f_3^k, f_5^k, f_7^k, f_9^k))^2 \\ +(Z_{G,A,i}(f_1^k, f_3^k, f_5^k, f_7^k, f_9^k) - Z_{G,B,i}(f_1^k, f_3^k, f_5^k, f_7^k, f_9^k))^2 \end{pmatrix}. \quad (6)$$

The third step is to set the distortion coefficient $(f_1^k, f_3^k, f_5^k, f_7^k, f_9^k)_2$ of each band obtained in the second step as the true value and optimize the installation angle band by band. The objective equation of this process is shown in Equation (7). The third step optimization result $(\alpha, \beta, \gamma)_2$ can be obtained by averaging the installation angles obtained from all band optimizations.

$$E_3 = \min \sum_{i=1}^{m} \begin{pmatrix} (X_{G,A,i}(\alpha, \beta, \gamma) - X_{G,B,i}(\alpha, \beta, \gamma))^2 \\ +(Y_{G,A,i}(\alpha, \beta, \gamma) - Y_{G,B,i}(\alpha, \beta, \gamma))^2 \\ +(Z_{G,A,i}(\alpha, \beta, \gamma) - Z_{G,B,i}(\alpha, \beta, \gamma))^2 \end{pmatrix}. \quad (7)$$

Lastly, when the differences $\left|(f_1^k, f_3^k, f_5^k, f_7^k, f_9^k)_1 - (f_1^k, f_3^k, f_5^k, f_7^k, f_9^k)_2\right|$ and $|(\alpha, \beta, \gamma)_1 - (\alpha, \beta, \gamma)_2|$ of two adjacent distortion coefficient optimization results and two adjacent installation angle optimization results are less than the set threshold, the cycle exits, and the on-orbit distortion coefficient $(f_1^k, f_3^k, f_5^k, f_7^k, f_9^k)_1$ and installation angle $(\alpha, \beta, \gamma)_1$ are output; otherwise, steps 2 and 3 are repeated.

4. Experiment and Discussion

4.1. On-Orbit Geometric Calibration

In this paper, the remote sensing images of the Red Sea region taken by DPC on 21 September 2021, are selected for on-orbit geometric calibration, and the corresponding region is shown in the red box in Figure 7. This region is basically cloud-free, and the ground features (surface textures such as coastlines) are relatively wealthy, which is conducive to feature matching to obtain more homologous point pairs and improve the accuracy and stability of on-orbit geometric calibration. In addition, the acquisition time of the calibration image was about 2 weeks after the launch of the satellite, the state of the satellite platform and DPC had stabilized, and the conditions for on-orbit geometric calibration were available.

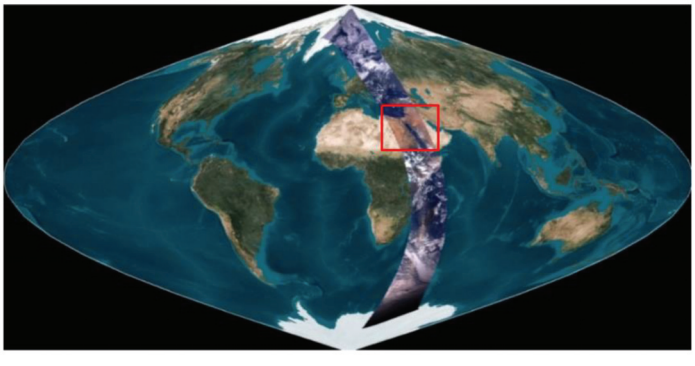


Figure 7. L1-level data preview of DPC. Corresponding to orbit 202.

The DEM reference dataset was GMTED2010 [36], with a spatial resolution of 30 arc seconds, covering most of the world from −180° W to 180° E, −90° S to 84° N, and the global total vertical accuracy was 25–42 m (RMSE). For DPC, an instrument with a nadir

spatial resolution of about 1.7 km, along with the resolution and accuracy of the DEM data, could meet the application requirements.

On-orbit initial geometric parameters are provided by laboratory calibration tests. The laboratory calibration test results are shown in Table 2. The laboratory uses a geometric calibration method based on a separated two-dimensional turntable and the least squares optimization theory to calibrate the distortion characteristics of the instrument in a standard atmospheric environment. The calibration results show that the fitting residual between the geometric model and the measured data is better than 0.1 pixel, which confirms the rationality of the geometric model. The laboratory uses the method of prism transfer to measure the installation angle of DPC in the GF-5-02 satellite body coordinate system.

Table 2. Results of laboratory geometric calibration.

Parameter	443 nm	490 nm	565 nm	670 nm	763 nm	765 nm	865 nm	910 nm
x_S^k(pixel)	512.055	512.073	512.025	512.047	512.044	511.985	512.041	512.058
y_S^k(pixel)	519.338	519.334	519.308	519.321	517.297	519.312	519.318	519.354
f_1^k(pixel)	434.884	433.724	432.767	432.092	431.743	431.758	431.494	431.425
f_3^k(pixel)	1.776	2.869	3.995	5.139	5.838	5.768	6.415	6.533
f_5^k(pixel)	−1.646	−2.261	−2.903	−3.600	−4.026	−3.940	−4.393	−4.422
f_7^k(pixel)	−0.731	−0.629	−0.519	−0.378	−0.291	−0.333	−0.209	−0.228
f_9^k(pixel)	0.246	0.242	0.238	0.230	0.224	0.231	0.217	0.223
α(degree)				−0.001				
β(degree)				0.022				
γ(degree)				−0.058				

On the basis of the above DEM dataset, laboratory geometric calibration results, the geometric model of DPC on-orbit imaging, and the on-orbit autonomous geometric calibration method proposed in this paper, the geometric parameters are calibrated on-orbit. The on-orbit calibration results are shown in Table 3. By matching multiple groups of images, tens of thousands of homologous point pairs are matched in each band for on-orbit geometric calibration. Among them, the 443 nm band with the least amount of data matched 28,929 homologous point pairs. The distribution of these homologous points on the DPC image plane is shown in Figure 8. It can be seen from the figure that the homologous points were basically evenly distributed on the image plane. This is beneficial for obtaining valid on-orbit geometry parameters. The application of a large amount of data can effectively reduce the influence of random matching error, attitude, and orbit measurement error on the precision of geometric calibration.

Table 3. Results of on-orbit autonomous geometric calibration.

Parameter	443 nm	490 nm	565 nm	670 nm	763 nm	765 nm	865 nm	910 nm
x_S^k(pixel)	512.055	512.073	512.025	512.047	512.044	511.985	512.041	512.058
y_S^k(pixel)	519.338	519.334	519.308	519.321	517.297	519.312	519.318	519.354
f_1^k(pixel)	430.671	429.612	428.661	428.306	428.137	427.899	427.824	427.861
f_3^k(pixel)	0.112	2.297	3.977	5.330	6.269	6.363	6.912	6.668
f_5^k(pixel)	2.745	0.282	−0.762	−1.692	−2.146	−2.214	−2.444	−1.944
f_7^k(pixel)	−2.876	−1.632	−1.334	−1.082	−1.069	−1.001	−1.001	−1.285
f_9^k(pixel)	0.650	0.416	0.376	0.351	0.370	0.349	0.359	0.409
α(degree)				0.047				
β(degree)				−0.024				
γ(degree)				0.219				

The residual data of the on-orbit geometric calibration in the 670 nm band are shown in Figure 9. The blue points correspond to the initial residuals (obtained using laboratory geometric parameters), and the orange points correspond to the final residuals (obtained using on-orbit geometric parameters). Figure 9a1–a3 correspond to the residuals of the *X*-,

Y-, and *Z*-coordinates, respectively. The mean values of *X*, *Y*, and *Z* in the initial residual data were −1.459 km, 1.364 km, and 0.567 km, respectively, and the standard deviations (STDs) were 2.054 km, 1.901 km, and 2.501 km, respectively. The mean values of *X*, *Y*, and *Z* in the final residual data were 0.049 km, −0.016 km, −0.140 km, respectively, and the STDs were 0.964 km, 0.861 km, and 1.714 km, respectively. The above results show that, compared with the laboratory geometric parameters, the geometric parameters obtained by the on-orbit autonomous geometric calibration method in this paper were more consistent with the actual on-orbit data, which proves the effectiveness of the method in this paper.

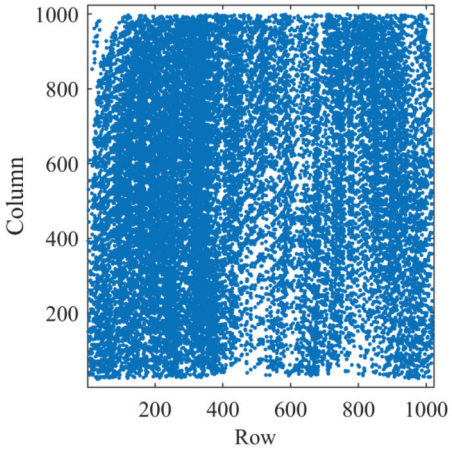


Figure 8. Distribution of homologous points in the 443 nm band.

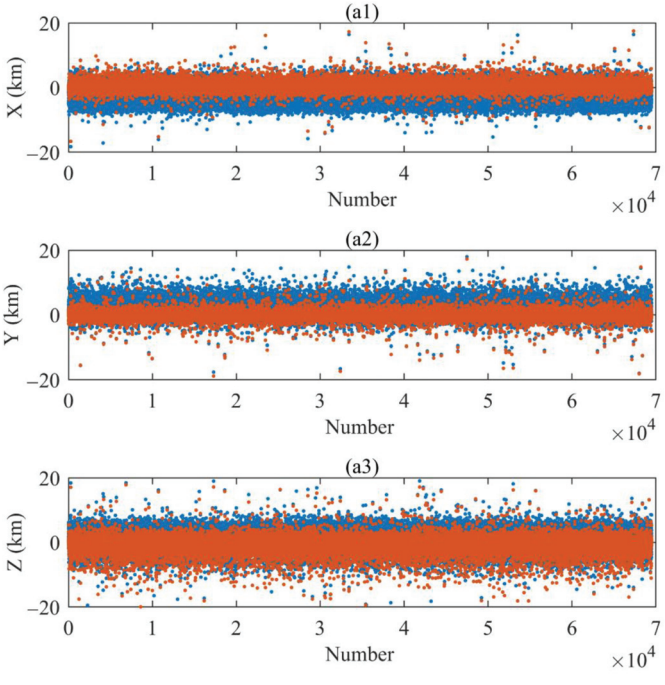


Figure 9. Residual comparison before and after calibration at 670 nm. The blue points correspond to the initial residuals, and the orange points correspond to the final residuals. Subgraphs (**a1**), (**a2**), and (**a3**) correspond to the residuals of the *X*-, *Y*-, and *Z*-coordinates, respectively.

4.2. Relative Geolocation Accuracy Evaluation

To verify the validity of the on-orbit autonomous geometric calibration method. In this paper, the GSHHG [37] coastline data were used as a reference to evaluate the relative geolocation accuracy before and after DPC on-orbit geometric calibration. Two sets of geometric parameters before and after the on-orbit geometric calibration were used to project the original image. Taking the 910 nm band as an example, the results are shown in Figure 10. Figure 10a,b represent the matching relationship between the local area projection results of the original image and the reference coastline before and after the on-orbit geometric calibration, respectively. The results shown in Figure 10 correspond to the original resolution (nadir resolution 1.7 km) of the DPC without merging pixels. The results show that the DPC projection results after the on-orbit autonomous geometric calibration were significantly more consistent with the reference coastline data, which can preliminarily prove the effectiveness of the on-orbit autonomous geometric calibration method in this paper.

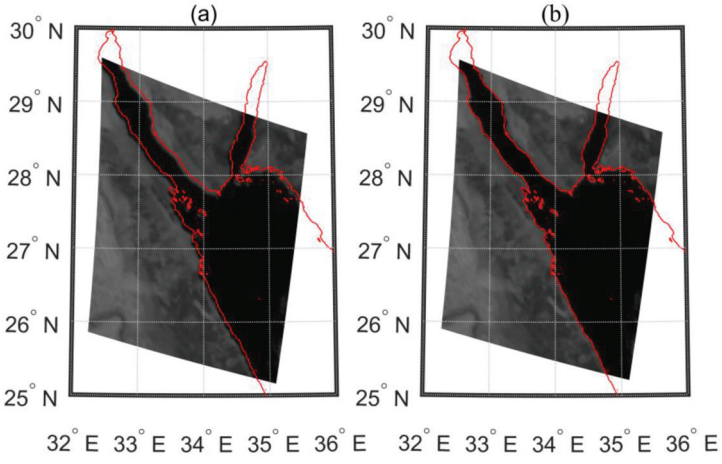


Figure 10. Result of coastline comparison, with no pixels merged, corresponding to the original resolution of the image: (**a**) before the on-orbit geometric calibration; (**b**) after the on-orbit geometric calibration.

In order to further quantitatively analyze the impact of on-orbit geometric calibration on the geolocation accuracy of DPC, the coastline crossing method (CCM) [38–40] was used for quantitative evaluation. The CCM was originally developed for the Earth Radiation Budget Experiment (ERBE) scanner [38]. The basic idea of this method is that there is a significant difference in brightness temperature between the sea surface and land; hence, there is a large gradient change at the junction of sea and land. The subpixel location of the coastline can be achieved by fitting a cubic polynomial to the brightness temperature of four consecutive pixels (along the row or column direction) near the coastline. The cubic polynomial form is as follows:

$$L_j = ax_j^3 + bx_j^2 + cx_j + d, (j = 1, 2, 3, 4), \tag{8}$$

where L_j represents the brightness temperature of pixel j, and x_i represents the longitude or latitude of pixel j. (a, b, c, d) is a polynomial coefficient with the solution shown as follows:

$$\begin{bmatrix} a \\ b \\ c \\ d \end{bmatrix} = \begin{bmatrix} x_1^3 & x_1^2 & x_1 & 1 \\ x_2^3 & x_2^2 & x_2 & 1 \\ x_3^3 & x_3^2 & x_3 & 1 \\ x_4^3 & x_4^2 & x_4 & 1 \end{bmatrix}^{-1} \begin{bmatrix} L_1 \\ L_2 \\ L_3 \\ L_4 \end{bmatrix}. \tag{9}$$

After the polynomial coefficients are known, the inflection point position $x = -b/3a$ can be calculated. When x is between x_2 and x_3, and $|L_1 - L_4|$ is greater than the set threshold, the inflection point represents the coastline. Finally, the coastline data located by the CCM is matched with the reference coastline data, and the outliers are eliminated. The deviation between the two represents the relative geolocation error of the instrument.

In this paper, an improved CCM is proposed. The method first uses the Canny [41] operator for pixel-level edge localization, and then uses the polynomial fitting method of the original CCM for subpixel localization. After calculating the position of the subpixel inflection point, if it is located in the pixel where the Canny operator initially locates the edge, and $|L_1 - L_4|$ is greater than the set threshold, then the inflection point is considered the coastline. The method first uses the Canny operator to initially locate the pixel-level edge, which can quickly identify the potential coastline position, eliminate a large amount of invalid data, locate the subpixel-level coastline position more quickly, and improve the algorithm efficiency.

The improved CCM was used to evaluate the relative geolocation accuracy of the DPC, taking the 910 nm band as an example. To fully verify the improvement effect of the on-orbit autonomous geometric calibration method on the relative geolocation accuracy, three sets of completely independent DPC data were used to evaluate the relative geolocation accuracy. One of the sets of data was the orbit 202 data acquired on 21 September 2021, which is the same as the data used for on-orbit geometric calibration. The additional two datasets were acquired on 19 September 2021 and 23 September 2021, corresponding to orbits 173 and 231. In the short term, the geometric performance of DPC could remain stable. The relative geolocation evaluation results of the three groups of data before and after the on-orbit geometric calibration are shown in Figures 11–13, respectively, where (a1), (a2), and (a3) represent the latitude error, longitude error, and total error between the coastline geolocation by DPC before on-orbit geometric calibration and the reference coastline, respectively, while (b1), (b2), (b3) are the results after on-orbit geometric calibration. Figures 11–13 contain 2209, 2150, and 1902 statistical data points, respectively. All three sets of validation data show that on-orbit geometric calibration significantly improved the on-orbit relative geolocation accuracy of DPC. The error in the longitude direction, the error in the latitude direction, and the total error were significantly improved after geometric calibration. The mean and STD of the data in the histogram were calculated, and the results are shown in Table 4. The relative geolocation evaluation results of the three sets of data were basically the same. Among the three sets of results, the maximum mean value of the total error before the on-orbit geometric calibration was about 2.725 km, with the maximum STD of 2.238 km. After on-orbit geometric calibration, the maximum mean value of the total error was about 1.275 km, with the maximum STD of 1.157 km.

Table 4. On-orbit relative geolocation accuracy results for DPC.

Stage	No.	Mean (km)			STD (km)		
		Latitude	Longitude	Total	Latitude	Longitude	Total
Before	202	−0.720	−1.291	2.725	2.120	2.088	1.902
	173	−0.593	−0.645	2.221	2.231	2.050	2.238
	231	−0.247	−0.805	2.443	2.062	2.258	2.022
After	202	0.386	0.175	1.131	1.050	1.076	1.076
	173	0.461	0.019	1.192	1.015	0.971	0.966
	231	0.555	0.308	1.275	1.270	1.225	1.157

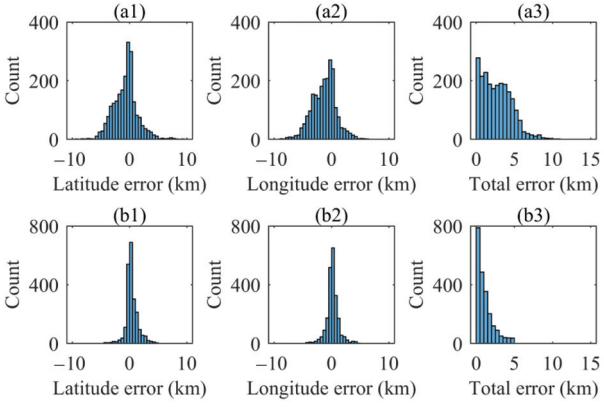


Figure 11. On-orbit relative geolocation accuracy results for DPC, corresponding to orbit 202: (**a1**–**a3**) before the on-orbit geometric calibration; (**b1**–**b3**) after the on-orbit geometric calibration.

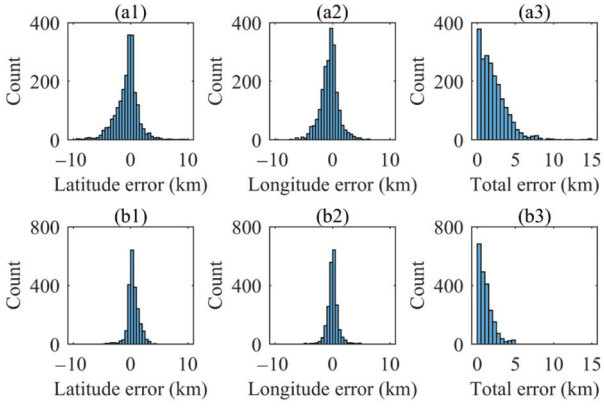


Figure 12. On-orbit relative geolocation accuracy results for DPC, corresponding to orbit 173: (**a1**–**a3**) before the on-orbit geometric calibration; (**b1**–**b3**) after the on-orbit geometric calibration.

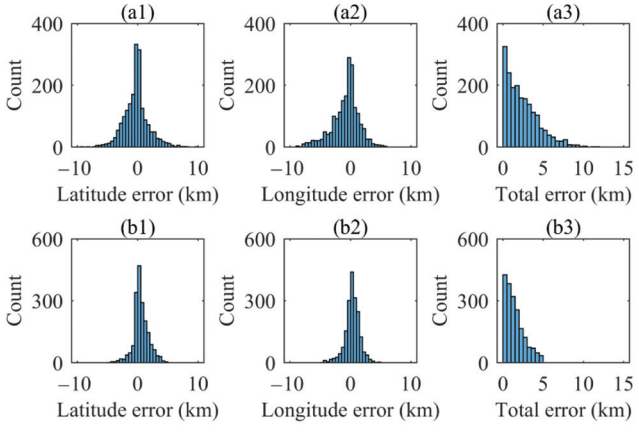


Figure 13. On-orbit relative geolocation accuracy results for DPC, corresponding to orbit 231: (**a1**–**a3**) before the on-orbit geometric calibration; (**b1**–**b3**) after the on-orbit geometric calibration.

Additionally, the FOV correlation of the aforesaid total error data was analyzed by taking the orbit 202 data as an example, and the relationship between the error mean and the FOV is shown in Figure 14. The results show that the relative geolocation error increased with the increasing FOV before the on-orbit geometric calibration, but the relative geolocation accuracy remained the same with the increase in FOV after the on-orbit geometric calibration. This further demonstrates the effectiveness of the proposed method in improving the relative geolocation accuracy of DPC on-orbit.

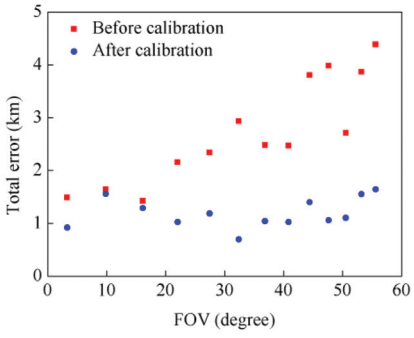


Figure 14. FOV correlation analysis of DPC relative geolocation accuracy. Red represents before the on-orbit geometric calibration, while blue represents after the on-orbit geometric calibration.

4.3. Image Registration Accuracy Evaluation

The performance of DPC on-orbit image registration was evaluated using the SIFT algorithm, including multiangle image registration and multispectral image registration. The data used to evaluate the image registration performance are consistent with the data used for the relative geolocation accuracy assessment. In the evaluation of multi-angle image registration performance, this paper took the ninth angle image of each band as the reference image to evaluate the registration accuracy of the remaining 16 angle images relative to the reference image. The reason is that the images of the ninth angle and the other 16 angles have a relatively large overlap area, which is conducive to matching more feature points and avoids the inability to accurately evaluate the multiangle image registration performance due to insufficient feature points. The evaluation results of each band are shown in Figure 15. Figure 15a1,b1 correspond to the mean and STD of the orbit 202 evaluation results. Figure 15a2,b2 correspond to the mean and STD of the orbit 173 evaluation results. Figure 15a3,b3 correspond to the mean and STD of the orbit 231 evaluation results. Red represents before the on-orbit geometric calibration, while blue represents after the on-orbit geometric calibration. All three sets of results show that the on-orbit geometric calibration could effectively improve the multiangle registration accuracy of DPC, especially when the angle number difference is large. Furthermore, the on-orbit geometric calibration could greatly improve the consistency of the registration performance between each angle image and the reference image. The short-wave bands (443 nm, 490 nm) are greatly affected by aerosols; hence, there are certain differences in the STD of the short-wave bands in the three sets of data results. Among the three sets of results, the maximum mean and STD of the multiangle registration error before on-orbit geometric calibration were about 9.607 km and 1.852 km respectively. The maximum mean and STD after on-orbit geometric calibration were 1.530 km and 1.130 km, respectively. Considering that the ground sampling distance (GSD) corresponding to the DPC L1-level data grid was 3.3 km, the mean and STD of the above registration errors were 2.911 GSD, 0.562 GSD, 0.464 GSD, and 0.342 GSD, respectively, when the GSD was taken as the unit.

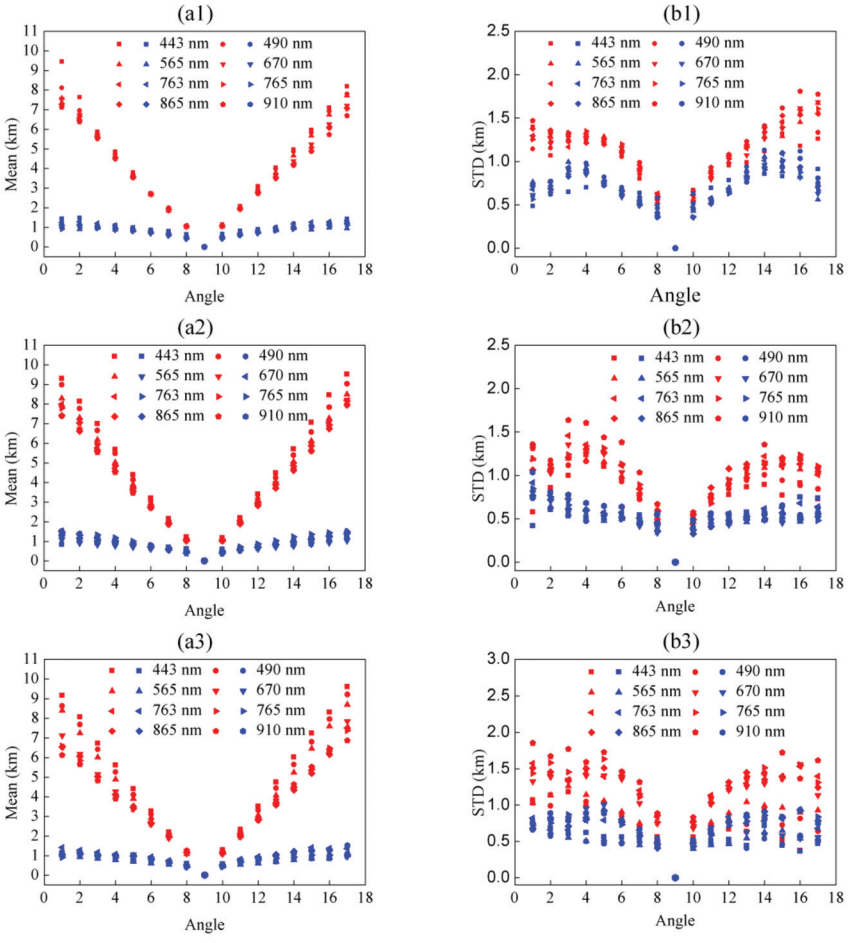


Figure 15. On-orbit multi-angle image registration performance of DPC. Red represents before the on-orbit geometric calibration, while blue represents after the on-orbit geometric calibration: (**a1**,**b1**) corresponding to orbit 202; (**a2**,**b2**) corresponding to orbit 173; (**a3**,**b3**) corresponding to orbit 231.

The multispectral image registration performance evaluation took the 670 nm band as the reference band and evaluated the registration accuracy of other bands relative to the reference band. The 670 nm band was used as a reference mainly because the imaging time of this band is in the middle of an imaging cycle of DPC, and there is a large overlap area with the data of each band. The 670 nm band is less affected by aerosols, and there is no effect of gas absorption. The results are shown in Figure 16. Figure 16a,b respectively represent the mean and STD. After the geometric calibration, the multispectral image registration performance was significantly improved, and the consistency of the registration performance of all bands was also improved. The evaluation results of the three sets of data were basically the same. Among the three sets of results, before the on-orbit geometric calibration, the maximum mean and maximum STD of multispectral image registration errors were about 1.859 km (0.563 GSD) and 1.033 km (0.313 GSD), respectively. After the on-orbit geometric calibration, they were 0.650 km (0.197 GSD) and 0.555 km (0.168 GSD), respectively. However, the registration accuracy of the 443 nm band and 490 nm band relative to the reference band was relatively low both before and after

geometric calibration. The reason is that the signals of these two bands were relatively weak, the signal-to-noise ratio was low, and the atmospheric radiation signal was strong, which led to the blurring of the surface feature information. Therefore, the matching error of the SIFT algorithm increased when the algorithm was used for matching, which led to the registration performance declining to a certain extent compared with other bands.

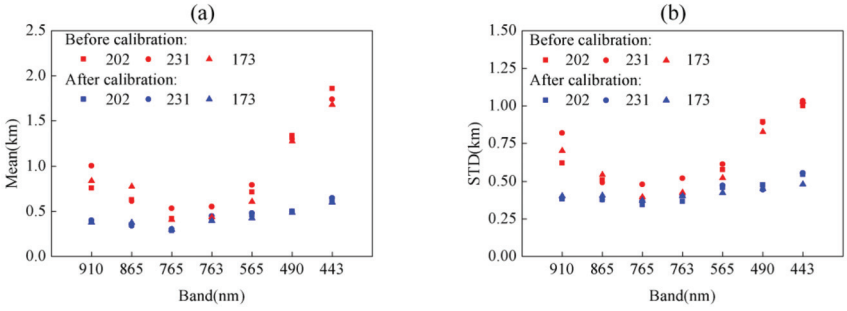


Figure 16. On-orbit multi-spectral image registration performance of DPC. Red represents before the on-orbit geometric calibration, while blue represents after the on-orbit geometric calibration. Subgraphs (**a**,**b**) represent the mean and STD of multi-spectral image registration performance, respectively.

5. Conclusions

In this paper, an on-orbit autonomous geometric calibration method was proposed, which does not require reference data from the ground calibration field. The on-orbit autonomous geometric calibration method is based on the multiangle imaging characteristics of DPC, and the geometric model parameters are optimized by the geometric constraints of the homologous points between the multiangle images. Using this method, the installation angle (α, β, γ) and the instrument distortion coefficient $(f_1^k, f_3^k, f_5^k, f_7^k, f_9^k)$ in the geometric model of DPC are calibrated on-orbit. To verify the effectiveness of this method, the DPC relative geolocation accuracy and image registration performance were compared and verified. The evaluation method of on-orbit relative geolocation accuracy is based on the improved CCM, and the reference coastline data are GSHHG. The SIFT algorithm was used to evaluate the image registration performance, including multiangle image registration performance and multispectral image registration performance. The results demonstrate that the proposed on-orbit autonomous geometric calibration method could effectively improve the accuracy of DPC relative geolocation and image registration. It is proven that this method could realize the on-orbit autonomous geometric calibration of spaceborne optical instruments without the ground calibration field. However, there were still some errors in relative geolocation and image registration after geometric calibration on-orbit, which may be from the following aspects: (1) the deviation between the geometric model of DPC on-orbit imaging and the actual model; (2) measurement error and interpolation error of attitude and orbit data; (3) error of coastline subpixel positioning algorithm; (4) image registration algorithm error; (5) influence of the accuracy of the on-orbit autonomous geometric calibration method itself. Therefore, to further improve the accuracy of DPC on-orbit relative geolocation and image registration, it is necessary to further study the above problems. Additionally, it is necessary to further evaluate and analyze the long-term variation characteristics of DPC geometric model parameters, image registration performance, and relative geolocation accuracy.

Author Contributions: Conceptualization, G.X. and B.M.; methodology, G.X. and B.M.; software, G.X.; validation, G.X. and B.M.; formal analysis, G.X.; investigation, G.X. and B.M.; resources, G.X., B.T. and B.M.; data curation, G.X., X.L., T.S. and B.T.; writing—original draft preparation, G.X.; writing—review and editing, G.X., L.H. and B.M.; visualization, G.X.; supervision, B.M. and J.H.; project administration, D.L. and J.H.; funding acquisition, D.L. and J.H. All authors have read and agreed to the published version of the manuscript.

Funding: This research was funded by the K. C. Wong Education Foundation "International team of Advanced Polarization Remote Sensing Technology and Application" (GJTD-2018-15).

Data Availability Statement: Not applicable.

Acknowledgments: We thank the DPC team for their contributions to the project and the manuscript.

Conflicts of Interest: The authors declare no conflict of interest.

References

1. Liu, Y.; Sun, D.; Hu, X.; Ye, X.; Li, Y.; Liu, S.; Cao, K.; Chai, M.; Zhou, W.; Zhang, J.; et al. The Advanced Hyperspectral Imager: Aboard China's GaoFen-5 Satellite. *IEEE Trans. Geosci. Remote Sens.* **2019**, *7*, 23–32. [CrossRef]
2. Zhao, Y.; Li, Y. Technical Characteristics and Application of Visible and Infrared Multispectral Imager. In Proceedings of the 6th International Symposium of Space Optical Instruments and Applications, Delft, The Netherlands, 24–25 September 2021; Space Technology Proceedings. Urbach, H.P., Yu, Q., Eds.; Springer International Publishing: Cham, Switzerland, 2021; Volume 7, pp. 197–208.
3. Shi, H.; Li, Z.; Ye, H.; Luo, H.; Xiong, W.; Wang, X. First Level 1 Product Results of the Greenhouse Gas Monitoring Instrument on the GaoFen-5 Satellite. *IEEE Trans. Geosci. Remote Sens.* **2021**, *59*, 899–914. [CrossRef]
4. Zhao, M.; Si, F.; Zhou, H.; Jiang, Y.; Ji, C.; Wang, S.; Zhan, K.; Liu, W. Pre-Launch Radiometric Characterization of EMI-2 on the GaoFen-5 Series of Satellites. *Remote Sens.* **2021**, *13*, 2843. [CrossRef]
5. Dubovik, O.; Li, Z.; Mishchenko, M.I.; Tanré, D.; Karol, Y.; Bojkov, B.; Cairns, B.; Diner, D.J.; Espinosa, W.R.; Goloub, P.; et al. Polarimetric remote sensing of atmospheric aerosols: Instruments, methodologies, results, and perspectives. *J. Quant. Spectrosc. Radiat. Transf.* **2019**, *224*, 474–511. [CrossRef]
6. Huang, C.; Chang, Y.; Xiang, G.; Han, L.; Chen, F.; Luo, D.; Li, S.; Sun, L.; Tu, B.; Meng, B.; et al. Polarization measurement accuracy analysis and improvement methods for the directional polarimetric camera. *Opt. Express* **2020**, *28*, 38638–38666. [CrossRef]
7. Huang, C.; Xiang, G.; Chang, Y.; Han, L.; Zhang, M.; Li, S.; Tu, B.; Meng, B.; Hong, J. Pre-flight calibration of a multi-angle polarimetric satellite sensor directional polarimetric camera. *Opt. Express* **2020**, *28*, 13187–13215. [CrossRef]
8. Yao, P.; Tu, B.; Xu, S.; Yu, X.; Xu, Z.; Luo, D.; Hong, J. Non-uniformity calibration method of space-borne area CCD for directional polarimetric camera. *Opt. Express* **2021**, *29*, 3309–3326. [CrossRef]
9. Huang, C.; Zhang, M.; Chang, Y.; Chen, F.; Han, L.; Meng, B.; Hong, J.; Luo, D.; Li, S.; Sun, L.; et al. Directional polarimetric camera stray light analysis and correction. *Appl. Opt.* **2019**, *58*, 7042–7049. [CrossRef]
10. Shi, E.; Wang, Y.; Jia, N.; Mao, J.; Lu, G.; Liang, S. Absorbing Aerosol Sensor on Gao-Fen 5B satellite. *Adv. Opt. Technol.* **2018**, *7*, 387–393. [CrossRef]
11. Shang, H.; Letu, H.; Chen, L.; Riedi, J.; Ma, R.; Wei, L.; Labonnote, L.C.; Hioki, S.; Liu, C.; Wang, Z.; et al. Cloud thermodynamic phase detection using a directional polarimetric camera (DPC). *J. Quant. Spectrosc. Radiat. Transf.* **2020**, *253*, 107179. [CrossRef]
12. Li, Z.; Hou, W.; Hong, J.; Zheng, F.; Luo, D.; Wang, J.; Gu, X.; Qiao, Y. Directional Polarimetric Camera (DPC): Monitoring aerosol spectral optical properties over land from satellite observation. *J. Quant. Spectrosc. Radiat. Transf.* **2018**, *218*, 21–37. [CrossRef]
13. Yu, H.; Ma, J.; Ahmad, S.; Sun, E.; Li, C.; Li, Z.; Hong, J. Three-Dimensional Cloud Structure Reconstruction from the Directional Polarimetric Camera. *Remote Sens.* **2019**, *11*, 2894. [CrossRef]
14. Durieux, A.; Neubert, S.; Petitbon, I. POLDER: A wide field-of-view instrument for earth-polarized observation. *Proc. SPIE* **1994**, *2209*, 160–169.
15. Bret-Dibat, T.; Andre, Y.; Laherrere, J.M. Preflight calibration of the POLDER instrument. *Proc. SPIE* **1995**, *2553*, 218–231.
16. Hagolle, O.; Guerry, A.; Cunin, L.; Millet, B.; Perbos, J.; Laherrere, J.M.; Bret-Dibat, T.; Poutier, L. POLDER level-1 processing algorithms. *Proc. SPIE* **1996**, *2758*, 308–319.
17. Fougnie, B.; Bracco, G.; Lafrance, B.; Ruffel, C.; Hagolle, O.; Tinel, C. PARASOL in-flight calibration and performance. *Appl. Opt.* **2007**, *46*, 5435–5451. [CrossRef]
18. Fougnie, B.; Marbach, T.; Lacan, A.; Lang, R.; Schlüssel, P.; Poli, G.; Munro, R.; Couto, A.B. The multi-viewing multi-channel multi-polarisation imager—Overview of the 3MI polarimetric mission for aerosol and cloud characterization. *J. Quant. Spectrosc. Radiat. Transf.* **2018**, *219*, 23–32. [CrossRef]
19. Wang, M.; Tian, Y.; Cheng, Y. Development of On-orbit Geometric Calibration for High Resolution Optical Remote Sensing Satellite. *Geo. Spat. Inf. Sci.* **2017**, *42*, 1580–1588.
20. Wang, M.; Yang, B.; Hu, F.; Zang, X. On-Orbit Geometric Calibration Model and Its Applications for High-Resolution Optical Satellite Imagery. *Remote Sens.* **2014**, *6*, 4391–4408. [CrossRef]
21. Zhang, Z.; Tang, Q. Camera Self-Calibration Based on Multiple View Images. In Proceedings of the 2016 Nicograph International (NicoInt), Hanzhou, China, 6–8 July 2016; pp. 88–91.
22. Hemayed, E.E. A survey of camera self-calibration. In Proceedings of the IEEE Conference on Advanced Video and Signal Based Surveillance, Miami, FL, USA, 21–22 July 2003; pp. 351–357.
23. Malis, E.; Cipolla, R. Camera self-calibration from unknown planar structures enforcing the multiview constraints between collineations. *IEEE Trans. Pattern Anal. Mach. Intell.* **2002**, *24*, 1268–1272. [CrossRef]

24. Yilmaztürk, F. Full-automatic self-calibration of color digital cameras using color targets. *Opt. Express* **2011**, *19*, 18164–18174. [CrossRef] [PubMed]
25. Greslou, D.; Lussy, F.D.; Delvit, J.M.; Dechoz, C.; Amberg, V. Pleiades-HR innovative techniques for geometric image quality commissioning. *ISPRS Int. Arch. Photogramm. Remote Sens. Spatial Inf. Sci.* **2012**, *XXXIX-B1*, 543–547. [CrossRef]
26. Wang, M.; Cheng, Y.; Tian, Y.; He, L.; Wang, Y. A New On-Orbit Geometric Self-Calibration Approach for the High-Resolution Geostationary Optical Satellite GaoFen4. *IEEE J. Sel. Top. Appl. Earth Obs. Remote Sens.* **2018**, *11*, 1670–1683. [CrossRef]
27. Zhang, G.; Xu, K.; Zhang, Q.; Li, D. Correction of Pushbroom Satellite Imagery Interior Distortions Independent of Ground Control Points. *Remote Sens.* **2018**, *10*, 98. [CrossRef]
28. Zhang, G.; Deng, M.; Cai, C.; Zhao, R. Geometric Self-Calibration of YaoGan-13 Images Using Multiple Overlapping Images. *Sensors* **2019**, *19*, 2367. [CrossRef]
29. Gleyzes, M.A.; Perret, L.; Kubik, P. Pleiades system architecture and main performances. ISPRS Int. Arch. Photogramm. *Remote Sens. Spatial Inf. Sci.* **2012**, *XXXIX-B1*, 537–542.
30. Chen, L.; Zheng, X.; Hong, J.; Qiao, Y.; Wang, Y. A novel method for adjusting CCD camera in geometrical calibration based on a two-dimensional turntable. *Optik* **2010**, *121*, 486–489. [CrossRef]
31. Huang, C.; Chang, Y.; Han, L.; Wu, S.; Li, S.; Luo, D.; Sun, L.; Hong, J. Geometric calibration method based on Euler transformation for a large field of view polarimetric imager. *J. Mod. Opt.* **2020**, *67*, 1524–1533. [CrossRef]
32. Huang, C.; Meng, B.; Chang, Y.; Chen, F.; Zhang, M.; Han, L.; Xiang, G.; Tu, B.; Hong, J. Geometric calibration method based on a two-dimensional turntable for a directional polarimetric camera. *Appl. Opt.* **2020**, *59*, 226–233. [CrossRef]
33. Lowe, D.G. Distinctive image features from scale-invariant keypoints. *Int. J. Comput. Vis.* **2004**, *60*, 91–110. [CrossRef]
34. Lowe, D.G. Object recognition from local scale-invariant features. In Proceedings of the Seventh IEEE International Conference on Computer Vision, Kerkyra, Greece, 20–27 September 1999; pp. 1150–1157.
35. Fischler, M.A.; Bolles, R.C. Random Sample Consensus: A Paradigm for Model Fitting with Applications to Image Analysis and Automated Cartography. *Commun. ACM* **1981**, *24*, 381–395. [CrossRef]
36. Jeffrey, J.D.; Dean, B.G. Global Multi-Resolution Terrain Elevation Data 2010 (GMTED2010). U.S. Geological Survey Open-File Report 2011–1073. Available online: https://pubs.er.usgs.gov/publication/ofr20111073 (accessed on 23 April 2022).
37. Wessel, P.; Smith, W.H.F. A global self-consistent, hierarchical, high resolution shoreline database. *J. Geophys. Res. Solid Earth* **1996**, *101*, 7989–8743. [CrossRef]
38. Hoffman, L.F.; Weaver, W.L.; Kibler, J.F. Calculation and Accuracy of ERBE Scanner Measurement Locations. NASA Technical Paper 2670; NASA Langley Research Center: Hampton, VA, USA, 1981.
39. Han, Y.; Weng, F.; Zou, X.; Yang, H.; Scott, D. Characterization of geolocation accuracy of Suomi NPP Advanced Technology Microwave Sounder measurements. *J. Geophys. Res. Atmos.* **2016**, *121*, 4933–4950. [CrossRef]
40. Tang, F.; Zou, X.; Yang, H.; Weng, F. Estimation and Correction of Geolocation Errors in FengYun-3C Microwave Radiation Imager Data. *IEEE Trans. Geosci. Remote Sens.* **2016**, *54*, 407–420. [CrossRef]
41. Canny, J. A Computational Approach to Edge Detection. *IEEE Trans. Pattern Anal. Mach. Intell.* **1986**, *8*, 679–698. [CrossRef]

atmosphere

MDPI

Article

A Detection Method of Atmospheric Neutron Profile for Single Event Effects Analysis of Civil Aircraft Design

Yang Song *, Xiangzheng Tu and Zhengqiang Li

Shanghai Aircraft Design and Research Institute, Shanghai 201210, China
* Correspondence: songyang@comac.cc; Tel.: +86-021-20866355

Abstract: High-energy particles such as neutron act as serious threats to electronic equipment on board aircraft via Single Event Effects (SEE), but atmospheric neutron flux profile which could cover civil aviation altitude is rarely observed. To address the representative of atmospheric radiation data in SEE analysis, we propose a new method of detecting atmospheric neutron profile for civil aviation altitude. Using the sounding balloon carrying one nuclear radiometer, the radiation dose could be observed with high accuracy. Subsequently, the profile of atmospheric neutron flux can be derived on the basis of the conversion equation between radiation dose and the neutron flux. We implement two experiments, and the results show that this low-cost method could reliably obtain the vertical distribution of atmospheric neutron and might be integrated into SEE analysis of civil aircraft design.

Keywords: radiation detection; atmospheric neutron; single event

Citation: Song, Y.; Tu, X.; Li, Z. A Detection Method of Atmospheric Neutron Profile for Single Event Effects Analysis of Civil Aircraft Design. *Atmosphere* **2022**, *13*, 1441. https://doi.org/10.3390/atmos13091441

Academic Editor: Olaf Scholten

Received: 31 July 2022
Accepted: 1 September 2022
Published: 6 September 2022

Publisher's Note: MDPI stays neutral with regard to jurisdictional claims in published maps and institutional affiliations.

Copyright: © 2022 by the authors. Licensee MDPI, Basel, Switzerland. This article is an open access article distributed under the terms and conditions of the Creative Commons Attribution (CC BY) license (https://creativecommons.org/licenses/by/4.0/).

1. Introduction

The radiations in the atmosphere, created by cosmic rays, are serious threats to civil aviation [1]. In the atmospheric radiation environment, there is a high flux of various energetic particles, including neutrons, protons, and pion [2]. The radiations are not only harmful to the crews [3] but could also cause damage to the electronic equipment on board civil aircraft [4]. The impact of these high-energy particles on aircraft system electronic components is called the Single Event Effects (SEE). At the altitude of civil aviation, neutrons are of the main concern [5]. SEE contains various fault conditions, such as hazardous misleading information and system failure in avionics equipment. The conditions might mislead signals instantaneously or alter the physical layer permanently, resulting in the loss of a component or function [6].

With the rapid development of aircraft avionics in recent years, the scale of electronic circuits in aircraft exhibits geometric growth. Meanwhile, the electronic computing components are highly integrated in aircraft system equipment, and the operation logic is getting more and more complex. All of these lead to a higher occurrence of single events [7], especially in the high-latitude and high-altitude civil aviation routes where many high-energy particles are present. The influence of high-energy particles in the atmosphere on the safety design of civil aircraft should receive more attention [8].

In the development of newly designed civil aircraft, the SEE analysis is recommended to be taken into consideration in system safety design as aircraft level requirements [9]. However, in the preliminary preparations for the first flight of newly designed aircraft, safety risks caused by SEE have emerged, which could affect the aircraft's flight altitude. For the consideration of system safety, particular risk analysis research on SEE should be performed. A standard of the International Electrotechnical Commission (IEC) has given the profile of the neutron flux at 45° N in the form of tables [10]. Nevertheless, in the preparation phase of the first flight, it is difficult to perform the safety assessment by calculating the failure rate of equipment caused by atmospheric radiation due to the lack of detection data of atmospheric neutron flux in the flight environment. There were limited ways to detect the radiation background at low cost [11].

To study the radiation background, some theoretical methods based on Monte Carlo simulation were also developed [12,13], and dedicated detectors for radiation detection were explored [14,15].

In the former research on radiation dose on the aircrews, detection of the dose rate on board carried by aircraft has been studied [16,17]. In the framework of the CONCORD, dose rates in the radiation field at aviation altitudes were obtained with several instruments on board during joint flights [17]. Based on the measurements performed on flights with an altitude of 40,000 and 32,000 ft in narrow target areas between 42° N and 57° N, the relationship between the dose equivalent rate and its dose components onboard aircraft has been researched [18].

In the safety assessment of civil aircraft development such as the first flight, the requirement for radiation environment data is the profile of the neutron flux (1–10 MeV) of the place where the aircraft would take off. To get the vertical distribution of the neutron flux, there are three ways to carry the radiation detector to perform in situ detection: rocket [19], unmanned aerial vehicle [20], and sounding balloon [21]. Apparently, compared with the former two means, balloons are low cost and convenient to operate [22,23].

In this paper, we propose a new method of detecting atmospheric neutron radiation profile covering the altitude of civil aviation, aiming to polish an important element in SEE analysis of civil aircraft with low cost and convenience. The instruments and procedure used in this method are described in Section 2. Section 3 introduces the two experiments implemented in Northwest China. Observational results and concluding remarks are given in Sections 4 and 5, respectively.

2. Detection Method

In order to perform SEE analysis, the profile of atmospheric neutron flux needs to be detected. Since the lack of effective remote sensing means to detect the neutron flux and the limitation of the experiment cost, we proposed the new method for in situ measurements of the vertical distribution of atmospheric neutron flux at low cost. The equipment consists of the radiosonde system and one nuclear radiometer. In this method, the radiation dose could be observed by the nuclear radiation detector. The profile of the atmospheric neutron flux could be derived from the basis of the conversion equation between the radiation dose and the neutron flux.

2.1. Equipment

The atmospheric high-energy particles are generally detected in the form of field experiments using high-energy particle detection equipment carried by rockets, airplanes, airships, or other carriers in the atmosphere. Then the profile of high-energy particle parameters with height is derived through detection data analysis.

In the detection, constrained by the expense, the lowest cost-choice for the carrier can be selected as the radiosonde system. The radiosonde system is an important tool for measuring and studying the high-altitude stratospheric atmosphere. It is mainly composed of a sounding balloon and a ground receiver, as shown in Figure 1.

In high-energy particle detection, high-energy particle mass spectrometer is generally used, but it is difficult for high-altitude detection in practical space detection because of its huge size and high price. Instead of the mass spectrometer, the high-energy particle detector used in the method is a nuclear radiometer, as shown in Figure 2. The specifications of the nuclear radiometer are shown in Table 1. This nuclear radiometer could provide detection of the radiation dose situation all day. Not only environmental pollution, but also the cumulative value and change rate of radiation dose could be monitored with a wide detection range and proper detection accuracy. Since the nuclear radiometer is much smaller than a high-energy particle mass spectrometer in size, it can conveniently be carried by the radiosonde balloon.



Figure 1. The radiosonde balloon equipped with the radiation detector in this study.



Figure 2. The photo of the nuclear radiometer used in this study.

Table 1. Parameter specifications for the radiometer used in this study.

Parameter	Specification
Detector	GM tube
Dose Rate Display	0.01 uSv/h~1 Sv/h, H*(10)
Dose Rate Accuracy	±20%
Energy Range	10 keV–20 MeV
Temperature	−40~60 °C
Environmental Protection	IP67
Size	87 × 72 × 35 mm
Weight	≤150 g

2.2. Detection Procedure

The neutron flux detection procedure is shown below:

Step 1: The radiation detector shown in Figure 2 is placed into an equipment cabin consisting of a well-grooved foam box with a GPS device. Then the communication equipment inside can be connected, and the reception of signals checked. Finally, the equipment cabin containing the instruments should be sealed and connected to the sounding balloon. After the balloon is filled with helium, it is ready to launch.

Step 2: The balloon is released, and the detection devices carried in the cabin detect the dose equivalent and dose-equivalent rate along the flight path.

Step 3: The atmospheric radiation dose data and altitude data are exported from the recycled detector.

Step 4: According to the conversion relationship of data process, the neutron flux at each altitude can be calculated with the radiation dose rate.

2.3. Data Process

In the safety analysis of civil aircraft design, the major requirement for radiation environment data is the neutron flux (1–10 MeV). The energy spectrum is not very important. It

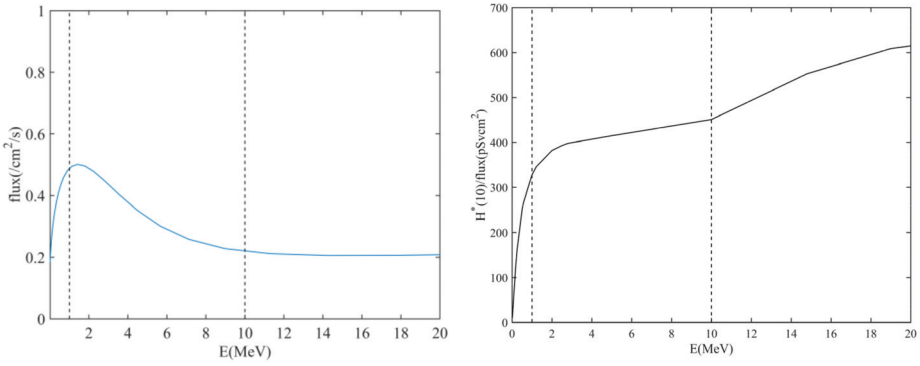
would be a convenient way to use the dose rate to deduce the neutron flux ranging from 1 to 10 MeV. However, it is difficult to use the dose to get flux without any assumptions of energy spectrum. Based on the assumption of analytic energy spectrum, the data-processing method is derived by modifying the flux-dose conversion relationship.

According to the research on unitied conversion function [24], the radiation dose at monoenergetic energy can be converted into the neutron flux. The conversion function of radiation dose equivalent rate and neutron flux ϕ is described in Equation (1),

$$\log_{10}\frac{H^*(10)}{\phi} = \frac{a}{1+(b+cx)^2} + \frac{d}{1+e^{f-gx}} + \frac{h}{1+e^{j-kx}} \quad (1)$$

where x stands for the natural logarithm of electron volts in eV, $a = 1.02$, $b = 0.0102$, $c = 0.208$, $d = 2.33$, $f = 9.56$, $g = 1.98$, h = 0.187, j = 93.3, and k = 13.1.

In this case, with the input of the longitude and latitude of the experiment location, typical energy spectrum at the altitude of 15 km could be obtained by the model EXPACS [25]. Using the Equation (1) in the paper, the coefficient H*(10)/flux variation with energy could be obtained. Since the energy range of the detector is 10 keV–20 MeV, the flux varies with energy in the range 0.01–20 MeV and the coefficient H*(10)/flux varies with energy in the range 0.01–20 MeV, as shown in Figure 3. The dash-lines in both figures are E = 1 MeV and E = 10 MeV respectively.



(**a**) (**b**)

Figure 3. (**a**) The flux varies with energy at the altitude of 15 km above the experimental location, (**b**) the coefficient H*(10)/flux varies with energy. The dash-lines in (**a**,**b**) are E = 1 MeV and E = 10 MeV, respectively.

From Figure 3a,b, the low energy part for which energy is lower than 1 MeV could be ignored for the low flux and little contribution to the dose rate. For the part (E > 1 MeV) in the Figure 3a, we can see the whole energy spectrum could be approximately viewed as uniform distribution. For the part (E > 1 MeV) in the Figure 3b, the coefficient and energy could be viewed as a linear relationship so that we can take the coefficient at 10 MeV as the average value to convert the dose rate to total flux. To get the flux in the range 1–10 MeV, the radiation weight (1–10 MeV) is employed. The flux in the range 1–10 MeV is obtained by Equation (2).

$$\phi_{1-10\mathrm{MeV}} = H^*(10) \times C_{10\mathrm{MeV}} \times w_{1-10\mathrm{MeV}} \quad (2)$$

where $\phi_{1-10\mathrm{MeV}}$ is the flux in the range of 1–10 MeV, $C_{10\mathrm{MeV}}$ is the coefficient H*(10)/flux at the energy E = 10 MeV, $w_{1-10\mathrm{MeV}}$ is the radiation weight factor of 1–10 MeV in total flux (0.01–20 MeV) which could be derived from the energy spectrum in Figure 3a.

3. Detection Experiment

On the day of releasing the radiosonde balloon, the detection device was taken to the designated location and then packed in a foam box in the equipment cabin, which was tied to the balloon with a rope. Nine bottles of 35 kg helium were thereafter pumped into the 1000-cubic-metre balloon.

For the recycling of the experiment equipment, the location where the detection equipment would land should be determined by a sounding balloon with wind measurements. Therefore, before the launch of the sounding balloon carrying the radiation detector, one sounding balloon with GPS was released. On the basis of both the flying time of the sounding balloon and the wind profile obtained by the weather report (as shown in Figure 4), we can ascertain the location where the detection equipment would be recycled. Figure 5 presents the GPS trace results of the sounding balloon and the location of the landing site.

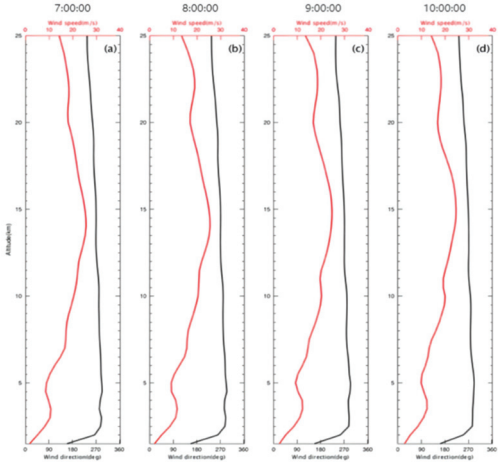


Figure 4. Wind profiles obtained from weather report before the experiment, (**a**–**d**) are the wind profiles at the time of 7:00:00, 8:00:00, 9:00:00, and 10:00:00 respectively. The red curve represents the wind speed and the black curve represents the direction of the wind.

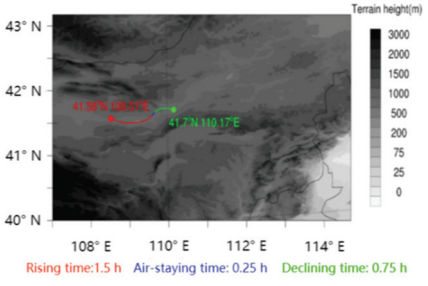


Figure 5. The locations where the equipment box was launched (red point) and recycled (blue point).

(1) The first launch on Day 1

At 10:10:19 on the morning of Day 1, the radiosonde balloon was launched. The geographic coordinates of the releasing place were (41.58608° N, 108.4906° E). The initial altitude was 1295 m, temperature was 4.2 °C, air pressure was 869.88 hPa, and the rising speed gradually increased with altitude. At 11:35:12, the sounding balloon rose to its highest point (41.6428° N, 109.4726° E) with the altitude, temperature, and pressure being 24,417 m, −24.6 °C, and 25.25 hPa, respectively. Then the balloon flew horizontally at an average speed of 1 m/s for 5 min. At 10:25, the rope between the box and balloon was cut

via remote control and the equipment cabin began to descend. At 12:29:12, the equipment cabin landed at (41.65476° N, 110.042° E), altitude 2206.9 m.

(2) The second launch on Day 2

At 8:58 on the morning of Day 2, the balloon was released. The coordinates of the flying place were (41.586° N, 108.4906° E). The initial altitude was 1300 m, temperature 1.7 °C, air pressure 863.83 hPa. At 10:20, the sounding balloon reached its highest point (41.804° N, 109.4905° E) with the altitude, temperature, and pressure being 24,686.3 m, −14.8 °C, and 25.94 hPa, respectively. After flying horizontally at an average speed of 0.2 m/s for 5 min, the rope between the balloon and the equipment cabin was cut and the equipment cabin began to descend at 10:25. At 10:53:33, the equipment cabin finally landed at (41.886° N, 109.8826° E), altitude 2655.9 m.

The position of the equipment cabin was archived in real-time by the GPS receiver. The altitude monitored by GPS on Day 1 and Day 2 was shown in Figure 6. When the balloon reached the predetermined height (~25 km), the equipment cabin was separated from the sounding balloon. The longitude and latitude of the equipment cabin were obtained according to the landing position of the equipment cabin GPS feedback.

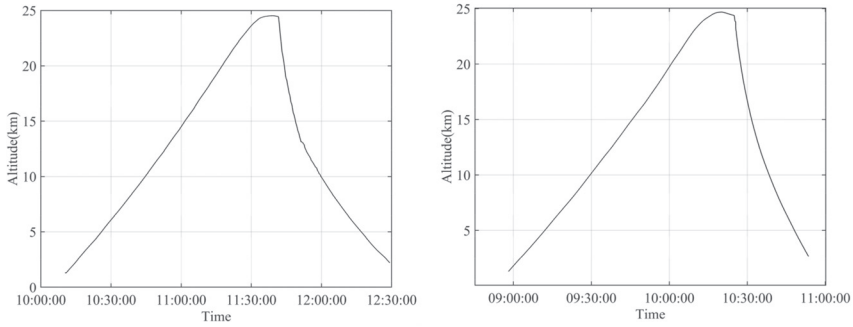


Figure 6. The altitude monitored by GPS on (**a**) Day 1 and (**b**) Day 2, respectively.

4. Results

The data from the radiation detector, accumulating through the infrared (IR) communication channel and stored in the non-volatile memory, was sent to the computer via radio. The radiation dose rate distribution recorded on Day 1 and Day 2 were shown in Figure 7, respectively.

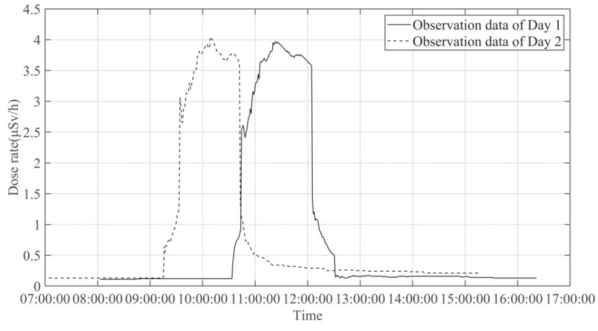
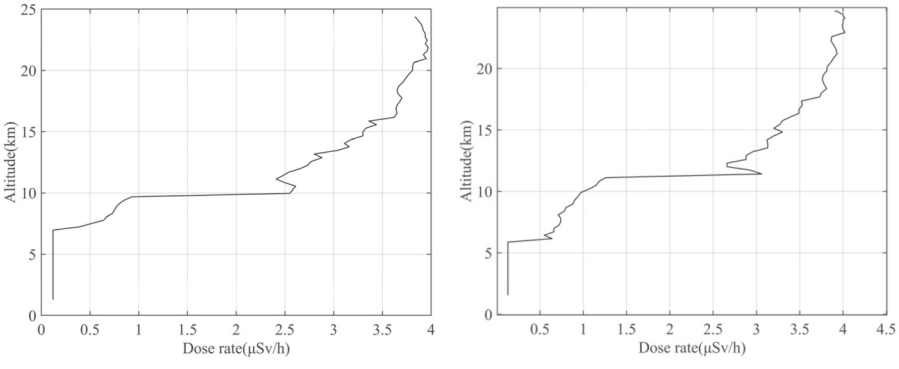


Figure 7. Time series of the radiation dose rate detected on Day 1 (solid line) and Day 2 (dash line), respectively.

Comparing the results from the two sounding experiments, it was obvious that the curves of the radiation dose equivalent rate were basically of the same trend. In the beginning, it was no more than 0.2 μSv/h and barely changed with time. Over the following 15–20 min, it increased gradually to 0.8–1.2 μSv/h with the steady ascent of the sounding balloon and the detector. Subsequently, a sharp enhancement in the radiation dose equivalent rate was followed by persistance at a level of >3.0 μSv/h. Consistent observations on these two days in the same detection environment may indicate this detection method is rather stable.

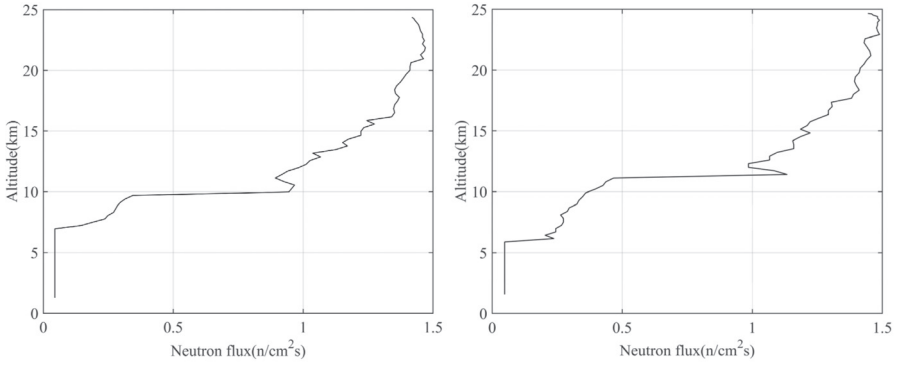
On the basis of the relevance of time line, the dose rate variance with altitude could be obtained from the GPS altitude data and the time series of the radiation dose rate, as shown in Figure 8.



(**a**) (**b**)

Figure 8. Profiles of the dose rate with altitude on (**a**) Day 1 and (**b**) Day 2, respectively.

Figure 9a,b presents the profiles of the neutron flux (1–10 MeV) on Day 1 and Day 2, respectively. The neutron flux also exhibited a similar pattern in vertical distribution. The neutron flux profiles were characterized by approximately zero below 6 km but >1.0 $cm^{-2}s^{-1}$ at the height of civil aviation. The profiles of the neutron flux could serve as crucial inputs to the calculation of the upset rate for SEE analysis.



(**a**) (**b**)

Figure 9. Profiles of the neutron flux (1–10 MeV) varies with altitude on (**a**) Day 1 and (**b**) Day 2, respectively.

5. Discussion

To validate our observational results, the neutron flux data were compared with the results published by Normand and Baker [4] which is also called the Boeing model in IEC 62396-1 [10]. The Boeing model showed the variation of 1–10 MeV neutron flux in the atmosphere with an altitude at the latitude of 45° N. The comparison between our observations and the Boeing model is shown in Figure 10.

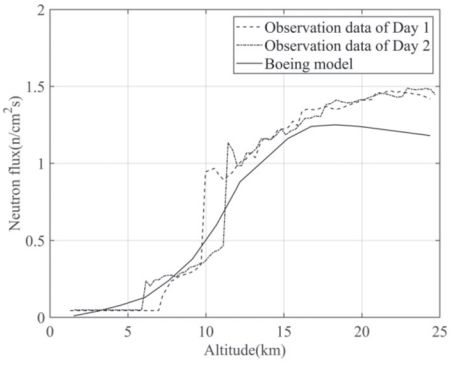


Figure 10. The neutron flux profiles on Day 1 (solid line) and Day 2 (dot dash line) and in the Boeing model (dash line).

Comparing the profiles of the neutron flux shown in Figure 9a,b with the results of Boeing model, the curve distribution obtained in these experiments could be considered as essentially consistent with the trend of the known profile. Both the experiments and the Boeing model show the neutron flux increases with altitude from 6 to 15 km and remains nearly consistent at the altitudes of 15–25 km.

The differences between observation data and Boeing model lie in two parts. One significant difference is the neutron flux below the altitude of 6 km. The Boeing model indicates that the neutron flux from 0 to 6 km increases with height. For the observational results of Day 1 and Day 2, the neutron flux is nearly constant. This is mainly caused by the detection threshold of the radiometer used in the experiment. Constrained by the cost, the dose rate display range of the radiometer starts at 0.01 μSv/h, so the value of the dose rate in the experiment at low altitude is nearly constant. To get more accurate result of neutron flux, the radiation detector should be more sensitive with a lower detection threshold. The other difference between the observation data and the Boeing model is the specific value at high altitude (>12 km). The trend of the curves is similar but the values corresponding to the observed data are greater than those in the model. This might be caused by solar activity or regional differences. It indicates that in order to get a complete comprehension of the background of radiation for civil aircraft design, the detection experiment should be performed at different latitudes and places. With the enrichment of the detection data, the neutron flux model could be updated.

6. Conclusions and Future Work

A new method of detecting atmospheric neutron for the altitude of civil aviation is proposed in this paper. Based on the method, the vertical distribution of atmospheric neutron flux could be well detected with convenience and low cost. The trend consistency between the observation data and the Boeing model indicates that this method is validated and reliable. Besides, the idea to use a nuclear radiometer could also be applied to other flying platforms such as aircraft.

In the test flight of civil aircraft, the nuclear radiometer could be carried by the radiosonde balloon for wind-field detection. In the wind-field detection before the flight test [26], the detection of atmospheric neutrons profiles could be completed through apply-

ing this method by carrying the nuclear radiometer as extra equipment on the radiosonde balloon. To improve the accuracy of the detection of the neutron flux, the radiometer should be replaced with detectors with higher accuracy.

With the detection results, the safety assessment of the first flight could be performed via the SEE analysis. Multiple measurements of the neutron flux could form an atmospheric radiation background database for single event research, which could greatly benefit the verification of single event effect in the safety design of aircraft systems.

Author Contributions: Conceptualization, Y.S.; methodology, Y.S., X.T. and Z.L.; data curation & formal analysis & writing—original draft preparation, Y.S.; writing—review and editing, Y.S., X.T. and Z.L.; Funding acquisition: Z.L. All authors have read and agreed to the published version of the manuscript.

Funding: Not applicable.

Institutional Review Board Statement: Not applicable.

Informed Consent Statement: Not applicable.

Data Availability Statement: Not applicable.

Acknowledgments: The authors would like to thank Chen Zhou for the help of outdoor experiment support.

Conflicts of Interest: The authors declare no conflict of interest.

References

1. Meier, M.M.; Copeland, K.; Klöble, K.E.J.; Matthiä, D.; Plettenberg, M.C.; Schennetten, K.; Wirtz, M.; Hellweg, C.E. Radiation in the Atmosphere—A Hazard to Aviation Safety? *Atmosphere* **2020**, *11*, 1358. [CrossRef]
2. Tezari, A.; Paschalis, P.; Stassinakis, A.; Mavromichalaki, H.; Karaiskos, P.; Gerontidou, M.; Alexandridis, D.; Kanellakopoulos, A.; Crosby, N.; Dierckxsens, M. Radiation Exposure in the Lower Atmosphere during Different Periods of Solar Activity. *Atmosphere* **2022**, *13*, 166. [CrossRef]
3. Baczynska, K.A.; Brown, S.; Chorley, A.C.; Lyachev, A.; Wittlich, M.; Khazova, M. Measurements of UV—A Exposure of Commercial Pilots Using Genesis-UV Dosimeters. *Atmosphere* **2020**, *11*, 475. [CrossRef]
4. Normand, E.; Baker, T.J. Altitude and Latitude Variations in Avionics SEU and Atmospheric Neutron Flux. *IEEE Trans. Nucl. Sci.* **1993**, *40*, 1484. [CrossRef]
5. Normand, E. Single-Event Effects in Avionics. *IEEE Trans. Nucl. Sci.* **1996**, *43*, 461. [CrossRef]
6. Normand, E.; Taber, A.H. *Investigation and Characterization of SEU Effects and Hardening Strategies in Avionics*; Defense Nuclear Agency: Alexandria, VA, USA, 1995.
7. Baumann, R.C. Radiation-induced soft errors in advanced semiconductor technologies. *IEEE Trans. Device Mater. Reliab.* **2005**, *5*, 305–316. [CrossRef]
8. Dominik, L. Incorporating Atmospheric Radiation Effects Analysis into the System Design Process. *SAE Int. J. Aerosp.* **2012**, *5*, 224–232. [CrossRef]
9. Mike, D.; Laura, D. Incorporation of Atmospheric Neutron Single Event Effects Analysis into a System Safety Assessment. *SAE Int. J. of Aerosp.* **2011**, *4*, 619–632.
10. IEC. *IEC/TS-62396-1*; Process Management for Avionics Atmospheric Radiation Effects—Part 1: Accommodation of Atmospheric Radiation Effects via Single Event Effects within Avionics Electronic Equipment. International Electrotechnical Commission: Geneva, Switzerland, 2006.
11. Song, Y. A Detection Method of Atmospheric Neutron at the Civil Aviation Height. *J. Phys. Conf. Ser.* **2022**, *2220*, 012009. [CrossRef]
12. Dyer, C.; Lei, F. Monte Carlo Calculations of the Influence on Aircraft Radiation Environments of Structures and Solar Particle Events. *IEEE Trans. Nucl. Sci.* **2001**, *48*, 1987. [CrossRef]
13. Matthiä, D.; Meier, M.M.; Reitz, G. Numerical calculation of the radiation exposure from galactic cosmic rays at aviation altitudes with the PANDOCA core model. *Space Weather* **2014**, *12*, 161–171. [CrossRef]
14. Berger, T.; Marsalek, K.; Aeckerlein, J.; Hauslage, J.; Matthiä, D.; Przybyla, B.; Rohde, M.; Wirtz, M. The German Aerospace Center M-42 radiation detector—A new development for applications in mixed radiation fields. *Rev. Sci. Instrum.* **2019**, *90*, 125115. [CrossRef]
15. Spurný, F.; Dachev, T. Aircrew onboard dosimetry with a semiconductor spectrometer. *Radiat. Prot. Dosim.* **2002**, *100*, 525–528. [CrossRef]
16. Federico, C.A.; Gonçalez, O.L.; Caldas, L.V.E.; Pazianotto, M.T.; Dyer, C.; Caresana, M.; Hands, A. Radiation measurements onboard aircraft in the South Atlantic region. *Radiat. Meas.* **2015**, *82*, 14–20. [CrossRef]

17. Meier, M.M.; Trompier, F.; Ambrozova, I.; Kubancak, J.; Matthiä, D.; Ploc, O.; Santen, N.; Wirtz, M. CONCORD: Comparison of cosmic radiation detectors in the radiation field at aviation altitudes. *J. Space Weather Space Clim.* **2016**, *6*, A24. [CrossRef]
18. Lindborg, L.; Beck, P.; Bottolier-Depois, J.F.; Latocha, M.; Lillhök, J.; Rollet, S.; Roos, H.; Roth, J.; Schraube, H.; Spurny, F.; et al. Determinations of H*(10) and its dose components onboard aircraft. *Radiat. Prot. Dosim.* **2007**, *126*, 577–580. [CrossRef]
19. Zhou, L.; Sheng, Z.; Fan, Z.; Liao, Q. Data Analysis of the TK-1G Sounding Rocket Installed with a Satellite Navigation System. *Atmosphere* **2017**, *8*, 199. [CrossRef]
20. Lampert, A.; Altstädter, B.; Bärfuss, K.; Bretschneider, L.; Sandgaard, J.; Michaelis, J.; Lobitz, L.; Asmussen, M.; Damm, E.; Käthner, R.; et al. Unmanned Aerial Systems for Investigating the Polar Atmospheric Boundary Layer—Technical Challenges and Examples of Applications. *Atmosphere* **2020**, *11*, 416. [CrossRef]
21. Pfotzer, G. History of the use of balloons in scientific experiments. *Space Sci. Rev.* **1972**, *13*, 199–242. [CrossRef]
22. Sushko, A.; Tedjarati, A.; Creus-Costa, J.; Maldonado, S.; Marshland, K.; Pavone, M. Low cost, high endurance, altitude-controlled latex balloon for near-space research (ValBal). In Proceedings of the 2017 IEEE Aerospace Conference, Big Sky, MT, USA, 4–11 March 2017; pp. 1–9. [CrossRef]
23. Nagaoka, K.; Hiraide, I.; Sato, K.; Yamagami, T.; Nakamura, T.; Yabutani, T. Measurements of neutron dose rates with a balloon in Japan. *Radiat. Prot. Dosim.* **2007**, *126*, 585–589. [CrossRef]
24. Wager, S.R.; Grosswendt, B.; Harvey, J.R.; Mill, A.J.; Selbach, J.-J.; Siebert, B.R.L. Unitied conversion function for the new ICRU operation protection quantities. *Radiat. Prot. Dosim.* **1985**, *12*, 231–235.
25. Sato, T. Analytical Model for Estimating Terrestrial Cosmic Ray Fluxes Nearly Anytime and Anywhere in the World: Extension of PARMA/EXPACS. *PLoS ONE* **2015**, *10*, e0144679. [CrossRef]
26. Wolfson, M.M.; Clark, D.A. Advanced Aviation Weather Forecasts. *Linc. Lab. J.* **2006**, *16*, 31–58.

remote sensing

MDPI

Article

Synchronous Atmospheric Correction of High Spatial Resolution Images from Gao Fen Duo Mo Satellite

Lingling Xu [1,2], Wei Xiong [1], Weining Yi [1], Zhenwei Qiu [1], Xiao Liu [1], Dongying Zhang [1], Wei Fang [1], Zhengqiang Li [3], Weizhen Hou [3], Jun Lin [4], Zhongzheng Hu [4], Tao Wang [5] and Wenyu Cui [1,*]

[1] Hefei Institutes of Physical Science, Chinese Academy of Sciences, Hefei 230031, China
[2] Department of Automation, University of Science and Technology of China, Hefei 230026, China
[3] Aerospace Information Research Institute, Chinese Academy of Sciences, Beijing 100101, China
[4] China Centre for Resources Satellite Data and Application, Beijing 100094, China
[5] National Satellite Meteorological Center, Beijing 100081, China
* Correspondence: cuiwenyu@aiofm.ac.cn; Tel.: +86-0051-65593066

Abstract: Atmospheric conditions vary significantly in terms of the temporal and spatial scales. Therefore, it is critical to obtain atmospheric parameters synchronized with an image for atmospheric correction based on radiative transfer calculation methods. On 3 July 2020, the high resolution and multimode imaging satellite, Gao Fen Duo Mo (GFDM), which was the first civilian high-resolution remote sensing satellite equipped with the Synchronization Monitoring Atmospheric Corrector (SMAC), was launched. The SMAC is a multispectral and polarization detection device that is used to retrieve atmospheric parameters that are time-synchronized with the image sensor of GFDM in the same field-of-view. On the basis of the atmospheric parameters obtained from the SMAC, a synchronization atmospheric correction (Syn-AC) method is proposed to remove the influence of the atmosphere and the adjacency effects to retrieve the surface reflectance. The Syn-AC method was applied in the experiments of synchronous atmospheric correction for GFDM images, where the surface reflectance retrieved via the Syn-AC method was compared with the field-measured values. In addition, the classical correction method, the FLAASH, was applied in the experiments to compare its performance with that of the Syn-AC method. The results indicated that the image possessed better clarity and contrast with the blurring effect removed, and the multispectral reflectance was in agreement with the field-measured spectral reflectance. The deviations between the reflectance retrievals of Syn-AC and the field-measured values of the selected targets were within 0.0625, representing a higher precision than that of the FLAASH method (the max deviation was 0.2063). For the three sites, the mean relative error of Syn-AC was 19.3%, and the mean relative error of FLAASH was 76.6%. Atmospheric correction based on synchronous atmospheric parameters can improve the quantitative accuracy of remote sensing images, and it is meaningful for remote sensing applications.

Keywords: Synchronization Monitoring Atmospheric Corrector (SMAC); Gao Fen Duo Mo (GFDM); synchronization atmospheric correction

Citation: Xu, L.; Xiong, W.; Yi, W.; Qiu, Z.; Liu, X.; Zhang, D.; Fang, W.; Li, Z.; Hou, W.; Lin, J.; et al. Synchronous Atmospheric Correction of High Spatial Resolution Images from Gao Fen Duo Mo Satellite. *Remote Sens.* **2022**, *14*, 4427. https://doi.org/10.3390/rs14174427

Academic Editor: Linlu Mei

Received: 22 July 2022
Accepted: 29 August 2022
Published: 5 September 2022

Publisher's Note: MDPI stays neutral with regard to jurisdictional claims in published maps and institutional affiliations.

Copyright: © 2022 by the authors. Licensee MDPI, Basel, Switzerland. This article is an open access article distributed under the terms and conditions of the Creative Commons Attribution (CC BY) license (https://creativecommons.org/licenses/by/4.0/).

1. Introduction

During optical satellite imaging of the Earth, the observed radiance of a satellite sensor is mainly influenced by three aspects: the illumination, observation geometry, and interaction between solar radiation with the atmosphere and ground surface [1]. The scattering and absorption of molecules and aerosols play a significant role in the radiation extinction [2]. In addition, the interference contribution of the surrounding pixels is a major cause of blurred visual effects of images, called the adjacency effect [3]. The purpose of atmospheric correction (AC) is to reduce the influence of the atmosphere and adjacency effects to retrieve the real reflectance of ground objects for high spatial resolution satellite

imagery [4]. Atmospheric parameters, such as aerosol optical depth (AOD) and column water vapor (CWV), are key factors affecting the quantitative estimation of the influence of atmospheric radiation. However, atmospheric conditions vary significantly in terms of temporal and spatial scales [5]. Therefore, synchronous acquisition of atmospheric parameters is important. Several efforts have been made to obtain atmospheric parameters that are synchronized with the space-time of the image to be corrected, and currently, three kinds of approaches are available.

In the first method, the atmospheric parameters are measured using ground-based technologies, such as the Aerosol Robotic Network (AERONET) [6]. However, ground-based data solely represent the atmospheric conditions restricted to the observation site area and cannot be applied for large-scale spatial analyses [7]. In the second method, the spectral information of the sensor such as the Moderate-resolution Imaging Spectroradiometer (MODIS) is used for aerosol retrieval [8]. However, the ground sample distance of these aerosol retrieval products is greater than 10 km, and the accuracy of aerosol retrieval products with higher spatial resolution should be further improved [9]. Furthermore, sensors with high-spatial resolution are used to obtain detailed ground information, though generally, their imaging bandwidth is relatively wide, which is insufficient for atmospheric detection [7].

In the third method, the atmospheric parameters for atmospheric correction are simultaneously measured by an instrument, which is equipped on the platform of a satellite. This method can solve the spatial and temporal matching between atmospheric parameters and images, and improve the accuracy of the parameters, which has been a development direction in recent years for remote sensing with high spatial resolution [10].

On 21 November 2000, the Earth Observing-1 (EO-1) satellite was launched successfully by the National Aeronautics and Space Administration (NASA). The satellite platform was equipped with a Linear Etalon Imaging Spectrometer Array (LEISA) Atmospheric Corrector (LAC) for the atmospheric correction of the multispectral imagery from the Advanced Land Imager (ALI) [11]. In August 2014, a commercial US company (DigitalGlobe) launched the WorldView-3 satellite, which was equipped with an instrument to detect atmospheric conditions [12]. The Clouds, Aerosols, water Vapor, Ice, and Snow (CAVIS) sensor covers 12 wavelength bands ranging from 405 nm (ultraviolet) to 2245 nm (shortwave infrared) with a spatial resolution of approximately 30 m. Atmospheric correction can be performed based on the atmospheric parameters from CAVIS for the high resolution remote sensing images of the WorldView-3 satellite [11].

On 3 July 2020, the China National Space Administration (CNSA) launched the high-resolution and multimode imaging satellite, Gao Fen Duo Mo (GFDM). The main imaging sensor onboard the satellite is configured with 1 panchromatic and 8 multispectral bands, and the spatial resolutions are 0.42 m and 1.6 m, respectively. In addition, the platform is also equipped with the Synchronization Monitoring Atmospheric Corrector (SMAC) to detect atmospheric parameters. The SMAC can offer atmospheric measurements that are time-synchronized with the image sensor of GFDM in the same field-of-view for synchronous atmospheric correction. The SMAC equipment was developed by the Anhui Institute of Optics and Fine Mechanics, Hefei Institutes of Physical Science, Chinese Academy of Sciences (CAS).

In this study, a synchronous atmospheric correction (Syn-AC) method is proposed based on the SMAC. First, the data processing procedures of the SMAC are detailed. Then, a brief introduction of the atmospheric parameters inversion methods based on the SMAC is presented. Third, the main principles of the atmospheric correction method based on synchronous atmospheric parameters provided by the SMAC are stated. To evaluate the performance of Syn-AC, six images under different atmospheric conditions, which are from three radiometric calibration sites [13–15] (Dunhuang, Songshan, and Baotou) were selected to conduct atmospheric correction experiments. Then, the visual effects before and after AC were compared. In addition, the average reflectance of the selected targets in the surface reflectance image of Syn-AC was compared with the field-measured reflectance for

evaluating the performance of correction methods, as well as the evaluation of fast line-of-sight atmospheric analysis of spectral hypercubes (FLAASH). Finally, the performance of Syn-AC and FLAASH were compared.

2. Satellite and Equipment

2.1. The GFDM Satellite

The GFDM satellite operates in a Sun-synchronous orbit with an orbital altitude of 643.8 km and a global average revisit period of less than 2 days [16]. The detailed parameters are listed in Table 1. The spectral response function of GFDM satellite is depicted in Figure 1. The GFDM satellite is equipped with a high-resolution optical camera, an atmospheric synchronization corrector, and auxiliary equipment [17]. As the first scientific optical remote sensing civilian satellite with submeter-scale resolution in China [16], the spatial resolution of a panchromatic band and 8 multispectral bands are 0.42 m and 1.6 m at the nadir, respectively. In addition, considering the high performance of this agile platform and its multiple imaging modes, the GFDM satellite can accurately and efficiently acquire satellite images, with large data volumes expected to be widely used in surveying and mapping, agriculture, and other industries to further meet the demand of high precision data for emergency management, disaster mitigation, and monitoring of construction activities and natural resources [18].

Table 1. Parameters of GFDM satellite.

Satellite	Type	Sun-synchronous circular orbit
	Orbit altitude	643.8 km
	Revisit	less than 2 days
High Resolution Camera	Swath Width	$\geq$15 km
	Resolution	Panchromatic: 0.42 m; Multispectral: 1.6 m
Band Setting /nm	pan	450–900
	band 1	450–520
	band 2	520–590
	band 3	630–690
	band 4	770–890
	band 5	400–450
	band 6	590–625
	band 7	705–745
	band 8	860–1040

2.2. The SMAC Equipment

The SMAC onboard the GFDM satellite platform is capable of multispectral and polarization detection and can record atmospheric observations on the surface to obtain atmospheric parameters that are synchronized with the main image sensor [16]. The configuration details of the SMAC are presented in Table 2. The SMAC operates over eight wavelength bands, ranging from 490 nm (visible) to 2250 nm (short-wave infrared), with a spatial resolution of approximately 6.7 km. Five polarized bands of SMAC are centered at 490, 670, 870, 1610, and 2250 nm, and marked with superscript P in Table 2. During synchronous observation, the detection of different atmospheric parameters were accomplished based on spectrum and polarization information from different wavelengths.

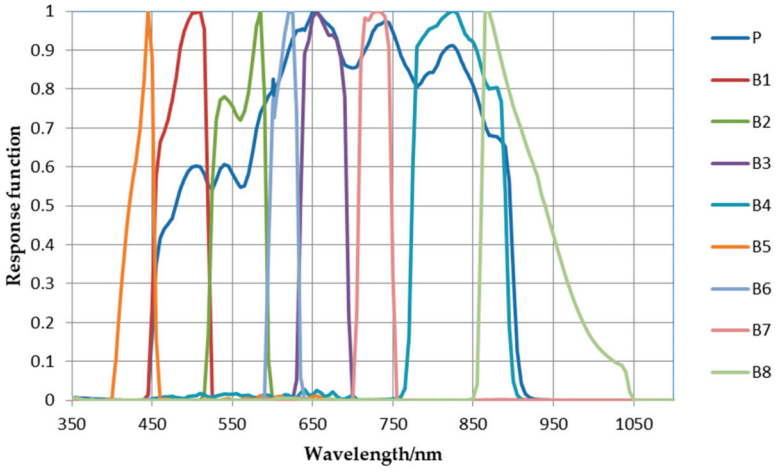


Figure 1. Spectral response function of GFDM satellite.

Table 2. Settings of SMAC equipment.

Spatial resolution	6.7 km	Polarizer orientation	0°, 60°, 120° (490, 670, 870, 1610 nm) 0°, 60°, 120°, 145° (2250 nm)
Instrument FOV	1.48°	Band width	20, 20, 20, 40, 20, 40, 60, 80 nm
Swath width	2 pixels	Rad. Cal. Error	≤5% (490, 550, 670, 870, 910 nm) ≤6% (1380, 1610, 2250 nm)
Imaging	No	Pol. Cal. Error	≤0.01 (DOLP ≥ 0.02)
Band/nm		Observation mission	
490 ^{P}		Aerosol and Clouds	
550		Aerosol and Clouds	
670 ^{P}		Aerosol and Clouds	
870 ^{P}		Aerosol and Water vapor	
910		Water vapor	
1380		Cirrus	
1610 ^{P}		Aerosol and Surface	
2250 ^{P}		Aerosol and Surface	

DOLP Degree of linear polarization; ^{P} Bands with polarization.

To achieve the simultaneous measurement of each polarized channel, the SMAC equipment utilizes a split-aperture detection method, and each channel adopts a dual pixel shooting mode [19]. The synchronous detection mode is depicted in Figure 2. In Figure 2a, the arrow denotes the flight direction of the GFDM satellite. The SMAC measurements are indicated by the two square pixels corresponding to the dual detector. For detecting the covered spatial area, the SMAC starts up before and shuts down after the main CCD. Therefore, in Figure 2b, the golden-filled boxes cover a larger area than the entire image during one observation, and the breadth of the two box pixels is slightly larger than the image width. The central longitude and latitude of the two pixels are represented by the green dotted lines. In addition, because the SMAC performs intensive shooting with a frequency of 10 times per second, the green dotted lines form redundant along-tracks, as illustrated in Figure 2b.

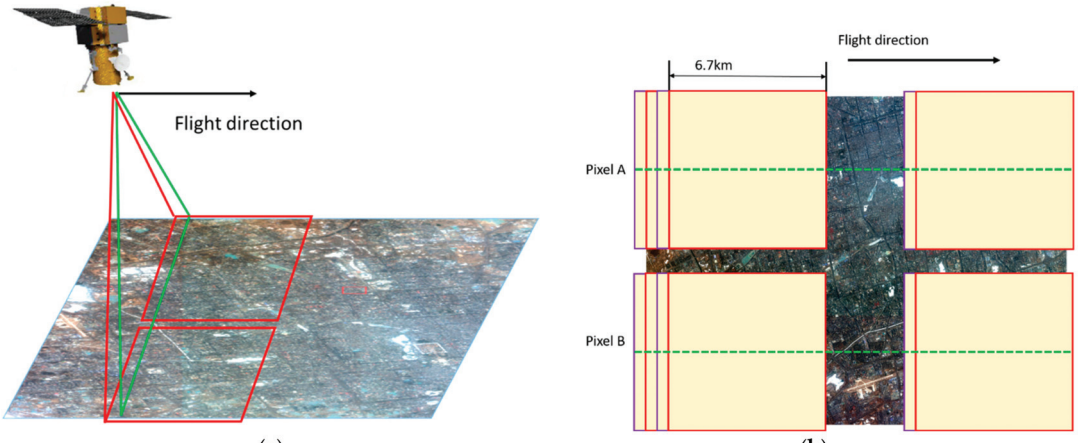


Figure 2. (**a**) Synchronous detection mode. (**b**) Shooting tracks of SMAC. The black arrow represents the flight direction of satellite, and the bottom image represents the multispectral images from main sensor. The base of the green triangle in (**a**) refers to the swath width of the remote sensing image. The red box pixels in (**a**) and the golden-filled box pixels in (**b**) mean the measurements of SMAC, and the spatial resolution of SMAC is 6.7 km.

3. Atmospheric Synchronization Correction Method Based on the SMAC

The main ideas proposed in the developed synchronization atmospheric correction technique are presented in this section, including data processing steps for the SMAC, brief techniques of atmospheric parameter inversion, and principles of atmospheric synchronization correction.

3.1. Data Processing for SMAC

Synchronized with the auxiliary data of the main CCD, the raw data of the SMAC, called Level-0 data, comprise digital number (DN) values stored in frames, and the size of one frame is 930 bytes, which are obtained through consecutive observations per second. The raw data are used as an input for data processing and processed following the steps illustrated in Figure 3, to invert atmospheric parameters in the subsequent step.

First, to ensure the validity of all of the retained data, data validation is conducted to check for anomalous attributes, for example, the working mode (observation or holding state) and temperature of the detector.

In step 2, according to the current temperature of the detector, the background under the heat sink temperatures obtained from the calibration profile is calculated via linear interpolation and subtracted from the DN.

In step 3, the spectral radiance of each band without polarization (550, 910, and 1380 nm) is calculated as

$$L_\lambda = \frac{DN_\lambda}{A_\lambda * Z_\lambda}, \tag{1}$$

where λ denotes the band, A_λ and Z_λ refer to the absolute spectral response and gain of each band, respectively. The radiance unit is equal to $\mu Wcm^{-2}nm^{-1}sr^{-1}$.

In step 4, considering the polarized bands (490, 670, 870, 1610, and 2250 nm), combined with the calibration data, the Stokes parameters including I, Q, and U are expressed [20] as

$$\begin{bmatrix} I_\lambda \\ Q_\lambda \\ U_\lambda \end{bmatrix} = \frac{1}{A_{\lambda,2} * Z_{\lambda,2}} \begin{bmatrix} 1 & \cos(2(\alpha_\lambda + \alpha_{\lambda,1})) & -\sin(2(\alpha_\lambda + \alpha_{\lambda,1})) \\ 1 & \cos(2(\alpha_\lambda + \alpha_{\lambda,2})) & -\sin(2(\alpha_\lambda + \alpha_{\lambda,2})) \\ 1 & \cos(2(\alpha_\lambda + \alpha_{\lambda,3})) & -\sin(2(\alpha_\lambda + \alpha_{\lambda,3})) \end{bmatrix}^{-1} \begin{bmatrix} DN_{\lambda,1}/T_{\lambda,1} \\ DN_{\lambda,2} \\ DN_{\lambda,3}/T_{\lambda,3} \end{bmatrix} \tag{2}$$

where i denotes the channels with different polarization angles, as mentioned in Table 2, $DN_{\lambda,i}$, $\alpha_{\lambda,i}$ and $T_{\lambda,i}$ represent the DN value, polarization orientation angle, and relative transmittance for band λ and channel i, respectively. Polarized detection is relatively more sensitive to atmosphere, and the retrieval of aerosol parameters can benefit from this sensitivity as a result [21–24]. Furthermore, the degree of polarization P_λ can be calculated as

$$P_\lambda = \frac{\sqrt{(Q_\lambda)^2 + (U_\lambda)^2}}{I_\lambda}. \quad (3)$$

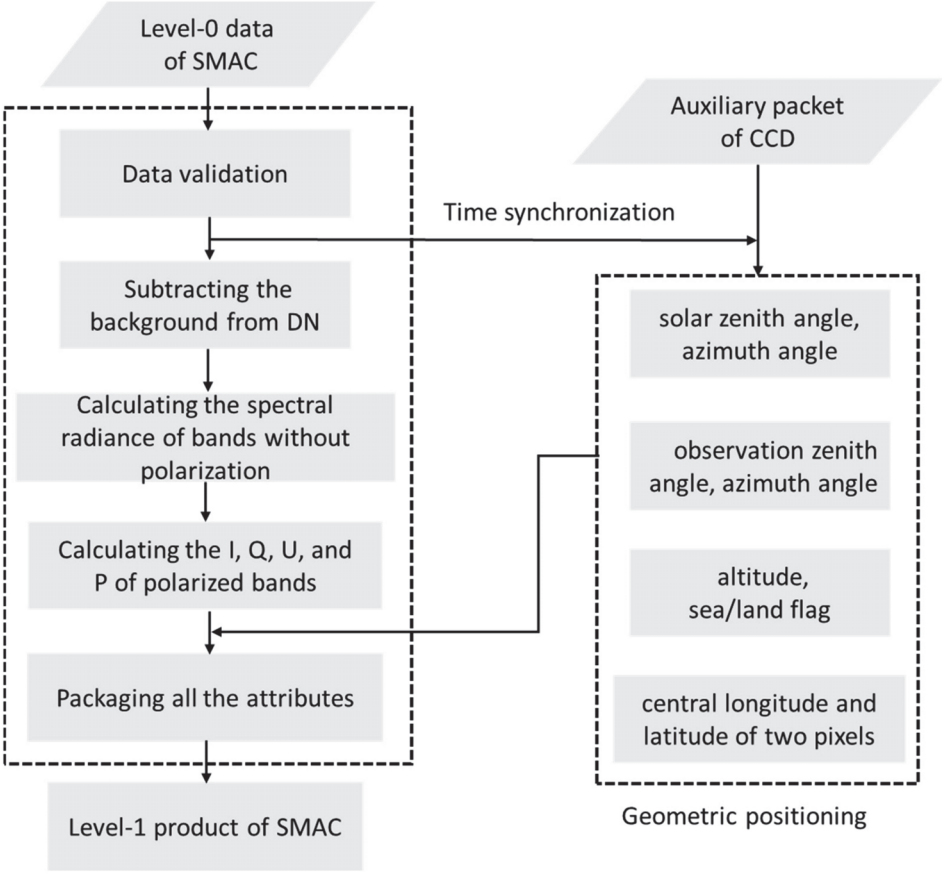


Figure 3. Procedures for processing raw data of SMAC.

Step 5 involves the satellite geometric positioning. Based on the principle of time synchronization, geometric data, including the zenith and azimuth angles of the Sun and the SMAC sensor, the sea/land flag and altitude, and the central longitude and latitude of the two pixels of SMAC, are calculated via a combination with the auxiliary data packets of the CCD provided by the satellite platform.

Finally, the Level-0 data of the SMAC are processed in a time sequence to obtain the Level-1 product of the SMAC. As shown in Table 3, the radiation information and polarization information of the ground target are packaged along with the time stamps and geometry data of the detector. Thus, the aerosol and water vapor parameters can be retrieved according to the Level-1 product, as detailed in the following step.

Table 3. Level-1 product of SMAC.

Parameter	Instruction	Parameter	Instruction
Identification of SMAC data	1 column; Filled with 0 × 62;	Sea-land flag	1 column for each pixel (A and B); 0-Sea;1-Land
Package number	1 column; Filled with C000~FFFFH	Altitude	1 column for each pixel (A and B)
Latitude and longitude	2 columns for each pixel (A and B);	Time stamp	1 column; Coordinated universal time
Solar zenith angle and azimuth angle	2 columns;	I, Q, U, and P of polarized bands	4 columns for each pixel (A and B); 20 columns in total
Viewing zenith angle and azimuth angle	2 columns for each pixel (A and B);	Spectral radiance of non-polarized bands	1 column for each pixel (A and B)

(A and B) two pixels of SMAC.

3.2. Atmospheric Parameters Inversion

In this section, the identification of cloud-covered pixels and the inversion of aerosol and water vapor are described in detail.

- Cloud identification

The lapse in identifying any small, broken, or thin clouds alters the satellite-observed apparent reflectance [17]. Therefore, identifying and removing cloud-covered pixels is a prerequisite for the retrieval of atmospheric parameters from the Level-1 product of the SMAC [17]. A threshold-based judgment method is used for the identification of clouds in this study [16]. A pixel is recognized as a cloud-covered pixel when at least one of the following conditions on ρ_{490}^{TOA}, ρ_{1380}^{TOA}, Normalized Difference Dust Index (NDDI), or Normalized Difference Snow Index (NDSI) are satisfied.

First, considering that thick clouds are usually brighter than their thin counterparts, the TOA reflectance at 490 nm obtained from the Level-1 product of the SMAC is used for the detection of thick clouds as [25]

$$\rho_{490}^{TOA} > 0.4, \tag{4}$$

Subsequently, cirrus clouds are identified based on the TOA reflectance at 1380 nm as [25].

$$\rho_{1380}^{TOA} > 0.0025, \tag{5}$$

Based on the above result, a further judgment is formulated to determine the presence of a cloud-covered pixel or a highlighted surface.

For a desert surface, the NDDI is used as [26]

$$NDDI = \frac{\rho_{2250nm}^{TOA} - \rho_{490nm}^{TOA}}{\rho_{2250nm}^{TOA} + \rho_{490nm}^{TOA}} < 0, \tag{6}$$

Thereafter, for a bright surface covered with ice and snow, the NDSI is used as [27]

$$NDSI = \frac{\rho_{550nm}^{TOA} - \rho_{1610nm}^{TOA}}{\rho_{550nm}^{TOA} + \rho_{1610nm}^{TOA}} > 0.13, \tag{7}$$

Finally, all of the judgments are fused to produce a cloud mask for all of the pixels of the SMAC measurements, and the pixel is recognized as a cloud-covered pixel when at least one of the Equations from (4) to (7) are satisfied.

- Aerosol

For a simpler representation, the TOA polarized reflectance $\rho_{p,\lambda}^{TOA}$ can be expressed as [28,29]

$$\rho_{p,\lambda}^{TOA}(\theta_s, \theta_v, \phi) = \rho_{p,\lambda}^{Atm}(\theta_s, \theta_v, \phi) + T_{p,\lambda}^{\downarrow}(\theta_s)\rho_p^{Surf}(\theta_s, \theta_v, \phi)T_{p,\lambda}^{\uparrow}(\theta_v) \quad (8)$$

where λ denotes the wavelength, θ_s, θ_v, and ϕ correspond to the solar zenith angle, observation zenith angle, and relative azimuth angle for the observation geometry, respectively; $\rho_{p,\lambda}^{Atm}$ symbolizes the polarized scattering interference of aerosols and molecules; ρ_p^{Surf} is the surface polarized reflectance, which is independent of wavelength. It can be approximately calculated by following the work of Litvinov et al. [30]; $T_{p,\lambda}^{\downarrow}$ and $T_{p,\lambda}^{\uparrow}$ represent the upwelling and downwelling transmittance factors, respectively. $T_{p,\lambda}^{\downarrow}$ and $T_{p,\lambda}^{\uparrow}$ can be represented as [29]

$$T^{\downarrow} = \exp[-(\frac{\xi\tau_{\alpha,\lambda} + \zeta\tau_{m,\lambda}}{\cos\theta_s})], \quad (9)$$

$$T^{\uparrow} = \exp[-(\frac{\xi\tau_{\alpha,\lambda} + \zeta\tau_{m,\lambda}}{\cos\theta_v})], \quad (10)$$

where $\tau_{\alpha,\lambda}$ and $\tau_{m,\lambda}$ denote the AOD and Rayleigh scattering optical depth at wavelength λ, respectively; ξ and ζ represent the experiential coefficients, respectively.

Additionally, the TOA polarized reflectance $\rho_{p,\lambda}^{TOA}$ can be expressed as [31]

$$\rho_{p,\lambda}^{TOA} = \pi L_p / \cos\theta_s, \quad (11)$$

where L_p denotes the polarized radiance.

Thus, for optimal estimation (OE) inversion [22], the simplified cost function J_p can be expressed as

$$J_p(AOD, C, FMF_v) = \sum_{i=1}^{d}\left[\frac{L_p^{meas} - L_p^{simu}(AOD, C, FMF_v)}{L_p^{meas}}\right]^2 / d, \quad (12)$$

where i denotes the polarized channel, d denotes the total number of the polarized channel, L_p^{meas} and L_p^{simu} represent the observed polarized radiance and the simulated polarized radiance, respectively; C symbolizes the parameter for the bidirectional polarized distribution function (BPDF); FMF_v depicts the volume fine-mode fraction.

Then, based on the unified Linearized Vector Radiative Transfer Model (UNL-VRTM) [32], a look-up table (LUT) under different θ_s, θ_v, ϕ, and AOD (550 nm) is established for timeliness. The polarized scattering contribution of aerosols and molecules $\rho_{p,\lambda}^{Atm}$ is obtained from the LUT, and the simulated polarized radiance L_p^{simu} is the output of the LUT. Therefore, the corresponding vector (AOD, C, FMF_v) is the combination of parameters when the minimum value of the function J_p is obtained, and the AOD can be calculated [17].

- Water vapor

In this study, the atmospheric column water vapor is retrieved on the basis of the channel ratio between the window channel centered at 865 nm and the water vapor absorption channel centered at 910 nm [33].

On the basis of the Lambert surface assumption and considering the gaseous absorption, the TOA reflectance can be represented as [34]

$$\rho_\lambda^{TOA}(\theta_s, \theta_v, \phi) = T_g(\mathrm{OG})\left[\rho_\lambda^{Atm}(\theta_s, \theta_v, \phi) + \frac{T_\lambda^{\downarrow}(\theta_s)\rho_\lambda^{Surf}(\theta_s, \theta_v, \phi)T_\lambda^{\uparrow}(\theta_v)}{1 - S_\lambda\rho_\lambda^{Surf}(\theta_s, \theta_v, \phi)}T_g(\mathrm{H_2O})\right] \quad (13)$$

where ρ_{λ}^{Surf} denotes the surface reflectance; ρ_{λ}^{Atm} symbolizes the path reflectance contributed by the aerosols and molecules; $T_g(\mathrm{H_2O})$ and $T_g(\mathrm{OG})$ represent the gaseous transmissions by water vapor and other atmospheric gases, such as O_3 and CO_2; $T_{\lambda}(\theta_s)^{\downarrow}T_{\lambda}(\theta_s)^{\uparrow}$ represents the transmittance in total; and S_{λ} denotes the hemispherical albedo.

Moreover, assuming that the difference in the surface reflectance of the two bands is negligible, the ratio of the reflectance between 870 and 910 nm of the SMAC can be expressed as the water vapor absorption transmittance along the ground-to-sensor direction [17].

$$\frac{\rho_{910}^{TOA} - \rho_{910}^{Atm}}{\rho_{870}^{TOA} - \rho_{870}^{Atm}} \cong \frac{T_{910}^{\downarrow}(\theta_s)T_{910}^{\uparrow}(\theta_v)}{T_{870}^{\downarrow}(\theta_s)T_{870}^{\uparrow}(\theta_v)} \equiv T, \tag{14}$$

The water vapor content can subsequently be calculated by using an empirical formula [35,36] as

$$U_{cwv} = \frac{A + B\ln(T) + C[\ln(T)]^2}{m}, \tag{15}$$

where $m = 1/(\cos\theta_s) + 1/(\cos\theta_v)$, $A = 0.1946$, $B = 0.5202$, and $C = 28.11$ represent the fitting coefficients of empirical formula [17].

3.3. Synchronization Atmospheric Correction

Considering atmospheric scattering, together with the radiance directly reflected off the corresponding ground surface along the ground-to-sensor direction, a single sensor pixel collects two different contributions [37–39]: radiation diffused by the atmosphere without interaction with the ground (called path radiance); then, radiance scattered by the neighbor pixels through scattering events (called adjacency effect). The main contributions are depicted in Figure 4. Atmospheric correction mainly removes the influence of atmospheric and adjacency effects for retrieving the real reflectance of ground objects [4]. The principles of atmospheric correction follow those reported in a study by Tang et al. [40].

First, radiometric calibration is performed on each pixel to transform the DN value into the spectral radiance as

$$L = C_0 \cdot DN + C_1, \tag{16}$$

where C_0 denotes the gain coefficient, and its unit is equal to $\mathrm{Wm^{-2}sr^{-1}\mu m^{-1}}$, and C_1 represents the offset. C_0 and C_1 are obtained from the calibration file provided by the CNSA.

Additionally, the spectral radiance L can be expressed as

$$L = L_{path} + T(\theta_v)\frac{\rho_1 E_g(0)}{\pi(1 - \rho_1 S)}, \tag{17}$$

where L_{path} denotes the path radiance. θ_v symbolizes the viewing zenith angle. ρ_1 denotes the surface reflectance, which includes the interference of the adjacency effect.$T(\theta_v)$ represents the atmospheric transmittance in total along the ground-to-sensor direction; $E_g(0)$ represents the solar irradiance corresponding to the position; and S denotes the atmospheric hemispheric albedo. For this step, the image parameters are used as inputs for 6SV model [39]. Thereafter, considering all of the reasonably likely atmospheric conditions, a LUT is established, containing L_{path} and $T(\theta_v)$, etc.

Subsequently, the initial surface reflectance ρ_1 can be calculated as

$$\rho_1 = \frac{L - L_{path}}{\frac{T(\theta_v)E_g}{\pi} + (L - L_{path})S}, \tag{18}$$

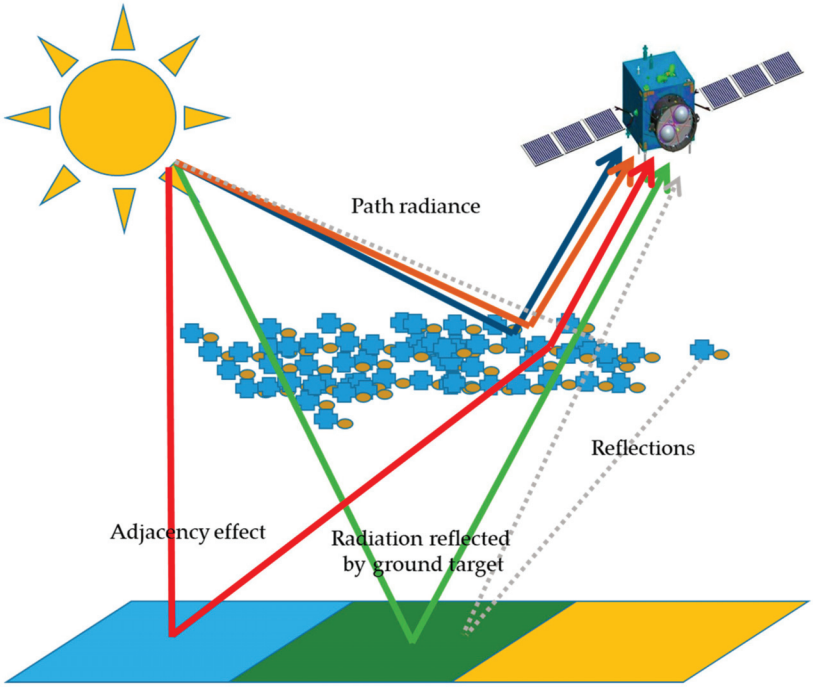


Figure 4. Main contributions to the received radiance of a single sensor pixel.

Accordingly, the contribution ρ_M of the surrounding pixels can be calculated as [40]

$$\rho_M = \sum_k \sum_l \rho'(x,y) P(x,y,\theta_v), \tag{19}$$

where $\rho'(x,y)$ is the reflectance of the neighboring pixel in row x and column y, and $P(x,y,\theta_v)$ is a weight function describing the contribution rate of the neighboring pixel, which depends on the distance, r, from the target pixel. The weight factor changes dynamically according to the spatial distance from the central pixel to its neighboring pixels and the reflectance difference between the central pixel and its neighboring pixels [4].

Finally, adjacency effect correction is performed, and the surface reflectance ρ_t can be obtained as [40]

$$\rho_t = \rho_1 + q(\rho_1 - \rho_M), \tag{20}$$

where q represents the coefficient of the adjacency effect correction, and it equals to the ratio of the background radiance and the pixel radiance [41]. The principles of synchronization atmospheric correction based on the SMAC are illustrated in Figure 5.

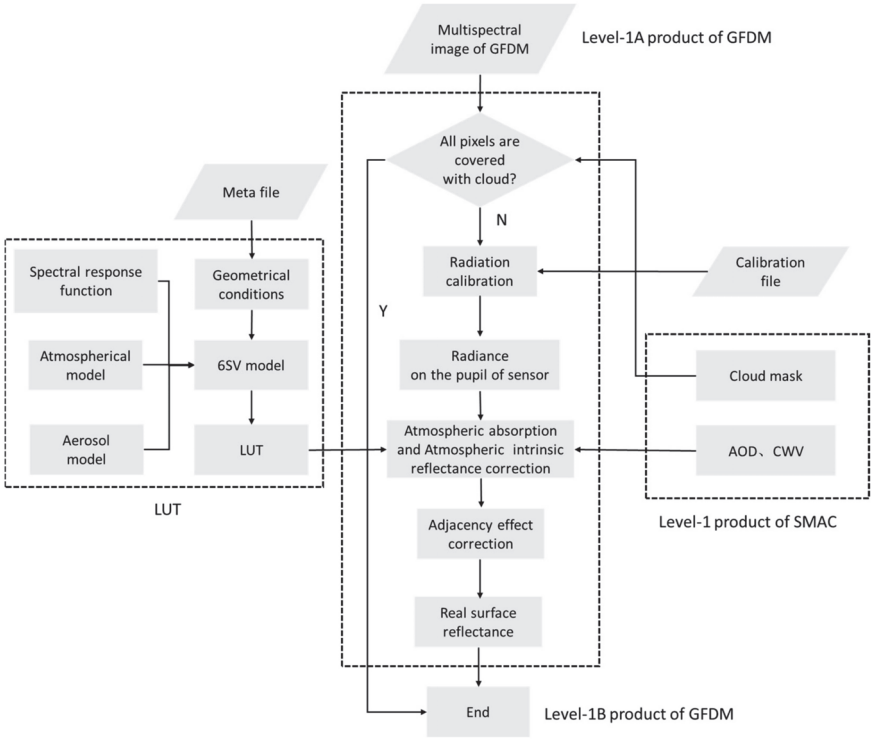


Figure 5. Procedures for synchronization atmospheric correction.

4. Experiments

4.1. Data Sets

- Satellite data

The GFDM satellite provides high-resolution satellite images with a 0.42 m panchromatic resolution and a 1.6 m multispectral resolution. In the experiments, six multispectral images under various atmospheric conditions were chosen to apply atmospheric correction. The scenes are centered on three radiometric calibration sites located in Dunhang, Songshan, and Baotou, respectively. Furthermore, field-based test measurements were conducted on the sites, and the collected data could be used for performance tests of Syn-AC. Table 4 lists the corresponding geometric observation conditions of the images, and the imaging time means the start time and date of main sensor shooting on the ground targets. Based on the previous experience and data analyses, the "Continental" aerosol model tends to perform better in the selected cases.

- Study area

As shown in Figure 6, the fields marked with red square are study areas, where field-based test measurements were conducted. In the Dunhuang site, the Gobi surface (Figure 6a) commonly used in radiometric calibration was selected as the experimental target in this study [13]. Additionally, the black target with 5% reflectivity and the white target with 60% reflectivity [14] in the Songshan site (Figure 6b) were chosen as experimental targets. In the Baotou calibration site shown in Figure 6c, three targets with different reflectivity [15] were selected as experimental targets.

Table 4. Atmospheric parameters and observed geometric conditions of the images of Dunhuang, Songshan, and Baotou.

	Location	Imaging Time (UTC)	Image Center	Satellite Zenith	Satellite Azimuth	Aerosol Model
Example 1	Dunhuang	2020/7/27 4:34:17	40.092°N, 94.404°E	4.319°	90.854°	Continental
Example 2	Songshan	2020/8/26 3:24:14	34.514°N, 113.103°E	31.087°	217.135°	Continental
Example 3		2021/2/4 3:40:24	34.553°N, 113.109°E	36.934°	283.133°	Continental
Example 4		2021/2/8 3:37:06	34.554°N, 113.1°E	31.696°	286.942°	Continental
Example 5	Baotou	2020/8/26 3:21:55	40.843°N, 109.636°E	28.782°	96.381°	Continental
Example 6		2020/8/31 3:42:14	40.895°N, 109.65°E	10.389°	285.117°	Continental

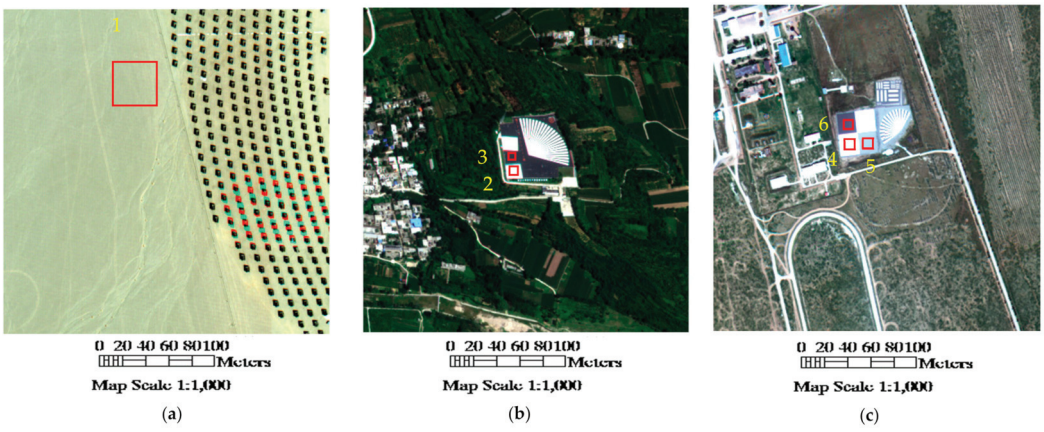


Figure 6. Study areas (marked with red square and number) of the radiometric calibration sites. (**a**) Sand of Dunhuang site. The small squares on the right side are solar panels. (**b**) White and black artificial targets of Songshan site. (**c**) White, gray, and black artificial targets of Baotou site.

In the field-based test measurements, a spectroradiometer produced by Analytical Spectral Devices (ASD) was used to collect spectral data on the target surface. The spectroradiometer collected wavelengths in a spectral range from 400 to 1600 nm with 1 nm sampling interval. Following the spectral measurement specification [42], the measurements were conducted under cloudless atmosphere condition. For each target, three repeated observations perpendicular to the target surface were taken, and the average value was taken as the target spectrum.

In order to compare the reflectance retrievals of AC with the field-measured values, the normalized average reflectance corresponding to each band of the GFDM satellite was obtained using Equation (21) as [43]

$$\rho_{average} = \frac{\int_{\lambda_1}^{\lambda_2} L(\lambda)\rho_{field}(\lambda)d\lambda}{\int_{\lambda_1}^{\lambda_2} L(\lambda)d\lambda}, \quad (21)$$

where ρ_{field} denotes the average reflectance spectrum and L represents the relative spectral radiance response of the GFDM multispectral band; λ_1= 400 nm, and λ_2= 1040nm. As shown in Table 5, the detailed information of the field-based test measurements is listed. The maximum standard deviation of the measurements for six targets were 0.0089, 0.01109, 0.00180, 0.00462, 0.0018, and 0.00039, respectively. It can be seen that the target spectra from the Dunhuang and Songshan sites were synchronously measured as the GFDM satellite passed over on 27 July 2020 and 26 August 2020, respectively. Therefore, it is assumed that the spectral reflectance of the target surface within a short time changes insignificantly, and the artificial target has a uniform Lambert surface [44], so the field measured data could be used for experimental analyses.

- AOD (550 nm) and CWV

Table 5. Detailed information of field-based test measurements.

Location		**Dunhuang**	**Songshan**		**Baotou**		
Time (UTC)		**2020/7/27 12:34**	**2020/8/26 3:24**		**2020/9/10 3:19**		
Targets		**Sand**	**White**	**Black**	**White**	**Gray**	**Black**
Average reflectance	485 nm	0.173	0.432	0.040	0.429	0.116	0.059
	555 nm	0.211	0.484	0.040	0.464	0.147	0.068
	607.5 nm	0.232	0.508	0.040	0.478	0.159	0.071
	660 nm	0.237	0.512	0.040	0.482	0.161	0.073
	725 nm	0.240	0.516	0.040	0.493	0.166	0.076
	830 nm	0.240	0.507	0.041	0.498	0.171	0.072
	950 nm	0.236	0.477	0.038	0.497	0.172	0.066
Max standard deviation of field-based measurement		0.0089	0.0110	0.0018	0.0046	0.0018	0.0004

The accuracy of atmospheric parameters has a great influence on the accuracy of AC, therefore, it is necessary to analyze the accuracy of the retrieved AOD and CWV before applying Syn-AC. In this study, the products from ground-based sites were used for a comparative analysis of the selected cases. In terms of temporal matching, the average value of at least two ground-based observations within 30 min before and after the satellite passed over is used [45]. For the Dunhuang case, the atmospheric parameters measured by the CNSA during on-orbit calibration on 27 July 2020 were used. The data in Table 6 are detailed information of the ground-based sites and the corresponding ground observations used in the experiment's analysis.

4.2. Comparison of Visual Effects before and after AC

The scattering of solar radiation by the atmospheric molecules and aerosol tend to cause the blurring of satellite images [46]. Atmospheric correction can effectively remove the influence of the atmosphere, and the blurring effect of the atmosphere is reduced after atmospheric correction. In particular, if the adjacency effect is corrected, better clarity and contrast are achieved [47]. Therefore, the visual effects of the satellite images before and after atmospheric correction were compared in the study.

Table 6. Ground-based sites and observations.

	Imaging Time (UTC)	Data Source	Site		Observation Time 1 (UTC)	Observation Time 2 (UTC)
			Longitude	Latitude		
Example 1	2020/7/27 4:34:17	CNSA	94.404°E	40.092°N	2020/7/27 4:34:17	-
Example 2	2020/8/26 3:24:14	SONET	113.114°E	34.511°N	2020/8/2 3:15:27	2020/8/26 3:30:28
Example 3	2021/2/4 3:40:24				-	2021/2/4 4:08:58
Example 4	2021/2/8 3:37:06				2021/2/8 3:28:00	2021/2/8 3:42:55
Example 5	2020/8/26 3:21:55	AERONET	109.629°E	40.852°N	2020/8/26 3:14:19	2020/8/26 3:29:26
Example 6	2020/8/31 3:42:14				2020/8/31 3:27:51	2020/8/31 3:42:52

4.3. Correction Precision

As described in Section 3, the output of Syn-AC is the surface reflectance after removing atmospheric influence and the interference contribution of the surrounding pixels. The accuracy of the reflectance retrievals is critical for remote sensing quantitative application. To validate the correction precision of Syn-AC, the average reflectance of the selected targets in the surface reflectance image of Syn-AC was compared with the field-measured value, and the absolute error (E_A) and the relative error (E_R, %) between reflectance retrievals and field measurements was calculated for each band following Equations (22) and (23), respectively.

$$E_A = \left| \rho_t - \rho_{field} \right|, \tag{22}$$

$$E_R = \left| \rho_t - \rho_{field} \right| / \rho_{field}, \tag{23}$$

where ρ_t denotes the reflectance retrieval and ρ_{field} denotes the field-measured value.

4.4. Comparison with FLAASH

The fast line-of-sight atmospheric analysis of spectral hypercubes (FLAASH), a classical atmospheric correction model, was introduced into the experiments [48]. Then, the validation of the correction precision of FLAASH was conducted in the same way as for Syn-AC. FLAASH is based on the radiative transfer model code, MODTRAN 4.0, which is written in FORTRAN [48]. The model is the first principle atmospheric correction model that can correct wavelengths from visible and near-infrared (VNIR), short-wave infrared (SWIR), and 3000 nm spectral range [49]. Moreover, the FLAASH model considers the adjacency effect, and the input data must be the calibrated image. Moreover, the imaging parameters were inputted according to the metadata of the image. The atmospheric model was calculated according to the flight date and scene center location [49]. The aerosol model was the same as the input of Syn-AC. Independent of the synchronously measured atmospheric parameters, FLAASH can estimate atmospheric properties on the basis of spectral information from each pixel of the image to be corrected [48]. Meanwhile, the correction precision between Syn-AC and FLAASH was compared.

5. Results

5.1. Atmospheric Retrieval Results of SMAC

A preliminary validation of the atmospheric parameters retrieved from the SMAC against AERONET was performed, with the results indicating that the synchronized atmospheric parameters retrieved from the SMAC are consistent with the ground mea-

surements [16]. The data in Table 7 are the atmospheric parameters retrieved from the SMAC corresponding to the selected examples contrasting with those obtained from the ground-based sites, and the relative error (E_R, %) were calculated. The results indicate that the synchronized atmospheric parameters retrieved from SMAC have good agreement with the ground measurements, and the atmospheric retrievals could be used for atmospheric correction in Syn-AC.

Table 7. Comparison between AOD (550 nm) and CWV (g/cm^2) retrieved from SMAC and the ground-based observation.

	Site	Date	AOD (550 nm)			CWV (g/cm^2)		
			Ground Measured	SMAC	E_R (%)	Ground Measured	SMAC	E_R (%)
Example 1	Dunhuang	27 July 2020	0.164	0.200	22	1.808	1.67	8
Example 2	Songshan	26 August 2020	0.200	0.225	13	2.506	2.42	3
Example 3		4 February 2021	0.417	0.421	1	0.486	0.42	14
Example 4		8 February 2021	1.061	1.19	12	0.871	0.72	17
Example 5	AOE_Baotou	26 February 2020	0.314	0.338	8	1.455	1.42	2
Example 6		31 February 2020	0.081	0.092	14	1.179	1.14	3

5.2. Comparison of Visual Effects before and after AC

Based on the synchronous AOD and CWV retrieved from the SMAC, synchronization atmospheric correction was applied to each image of the datasets. For the sake of simplicity, three images under different atmospheric conditions were selected, and parts of the images before and after Syn-AC are depicted in Figure 7. The AC parameters retrieved from SMAC data are the AOD of 0.2, 0.421, and 0.092, and the CWV of 1.67, 0.42, and 1.14 g/cm^2 for images (a)–(c), respectively. In the upper panel, Figure 7a–c present the true color images (formed by band 3, 2, and 1 for red, green, and blue, respectively) before AC, which are blurred. In contrast, the true color images after AC exhibit clear image edges and rich textures, as shown in the bottom panel.

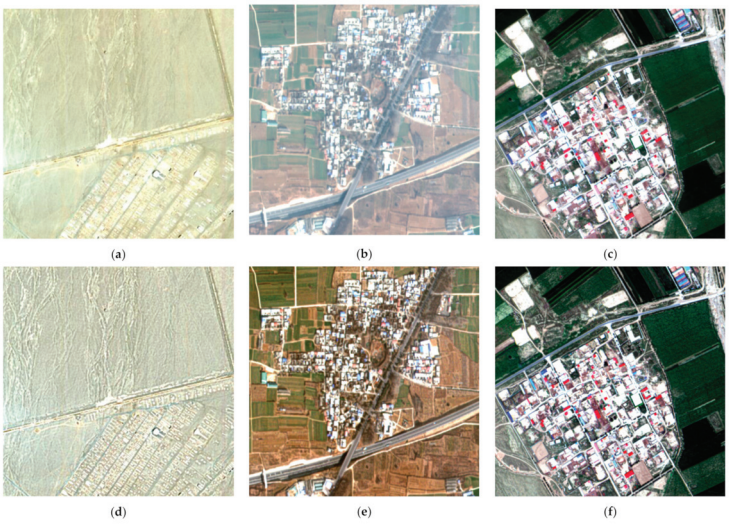


Figure 7. True color images of main sensor of GFDM satellite. Image (**a**) is part of the image in Dunhuang on 27 July 2020. Image (**b**) is part of the image in Songshan on 4 February 2021. Image (**c**) is part of the image in Baotou on 31 August 2020. Images (**a**–**c**) are original images, and images (**d**–**f**) are corrected images. The AC parameters are retrieved from SMAC with AOD of 0.2, 0.421, and 0.092, and the CWV of 1.67, 0.42, and 1.14 g/cm^2 for images (**a**–**c**), respectively.

5.3. Correction Precision

An image composed of reflectance retrievals was generated after atmospheric correction. In this part, the images of the study area in the original and corrected images are displayed. Then, the average reflectance of the targets in the surface reflectance image obtained after atmospheric correction was calculated and compared with the field-based measurement value to verify the accuracy of AC in quantitative applications. In order to compare the correction accuracy, the reflectance retrievals of Syn-AC and FLAASH are listed, and the absolute error (E_A) and the relative error (E_R, %) between the reflectance retrievals and field-based measurement values were calculated.

- Dunhuang

The Syn-AC and FLAASH methods were applied to perform AC on the GFDM multispectral image of Dunhuang (Figure 8a). The average surface reflectance in the study region of each image of Figure 8b,c was analyzed, and the results are illustrated in Figure 9. As indicated in Figure 9, the values obtained from the surface reflectance images of the Syn-AC and FLAASH methods are in good agreement with the field-measured data. As indicated in Table 8, the E_R values between the reflectance retrievals from Syn-AC and the ground-measured value are smaller. The absolute error values of Syn-AC are within 0.0201, and the max absolute error of FLAASH is 0.0415. The mean relative error values of Syn-AC and FLAASH are 4.0% and 8.7%, respectively.

- Songshan

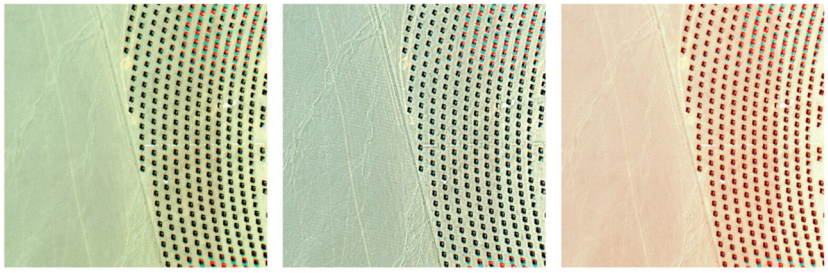


Figure 8. Images of Dunhuang on 27 July 2020. (**a**) Original image; (**b**) corrected image after Syn-AC; (**c**) corrected image after FLAASH. The retrieved AOD at 550 nm and retrieved CWV are 0.2 and 1.67 g/cm^2, respectively.

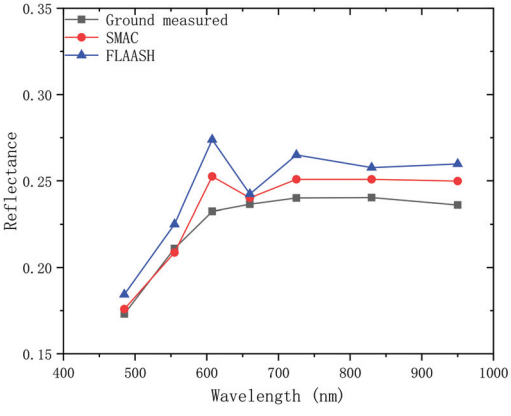


Figure 9. The average surface reflectance of sand in the corrected image of Dunhuang on 27 July 2020 obtained from Syn-AC and FLAASH and the field-measured reflectance.

Table 8. Performance comparison for sand between Syn-AC and FLAASH, based on Example 1.

Site	Songshan—Example 1			
Target	Sand			
	Syn-AC		FLAASH	
Band/nm	E_A	E_R (%)	E_A	E_R (%)
485	0.0028	1.6	0.0112	6.5
555	0.0024	1.1	0.0141	6.7
607.5	0.0201	8.7	0.0415	17.9
660	0.0037	1.6	0.0059	2.5
725	0.0108	4.5	0.0249	10.4
830	0.0106	4.4	0.0174	7.2
950	0.0139	5.9	0.0238	10.1

For the artificial target site located in Songshan, three multispectral images under different atmospheric conditions were selected for quantitative research. Syn-AC and FLAASH were applied to perform AC on these images. The atmospheric correction parameter retrievals are obtained from the SMAC with AOD of 0.225, 0.421, and 1.19, as well as CWV of 2.42, 0.42, and 0.72 g/cm^2 for Figure 10a, Figure 12a and Figure 14a, respectively.



(**a**) (**b**) (**c**)

Figure 10. Images of Songshan on 26 August 2020. (**a**) Original image; (**b**) corrected image after Syn-AC; (**c**) corrected image after FLAASH. The retrieved AOD at 550 nm and retrieved CWV are 0.225 and 2.42 g/cm^2, respectively.

For the case of the slightly polluted atmosphere (Figure 10a), the surface reflectance images after AC are shown in Figure 10b,c. As shown in Figure 11, the overall results of Syn-AC of the white target are proximate to the measured values. As shown in Table 9, the relative errors between the surface reflectance of the black target of Syn-AC and the ground measurements are smaller than that of FLAASH. For the white target, the absolute error values of Syn-AC are within 0.0416, and the max absolute error of FLAASH is 0.0981. The mean relative error values of Syn-AC and FLAASH were 5.14% and 11.25%, respectively. For the black target, the absolute error values of Syn-AC are within 0.0364, and the max absolute error of FLAASH is 0.0884. The mean relative error values of Syn-AC and FLAASH are 46.3% and 139.6%, respectively.

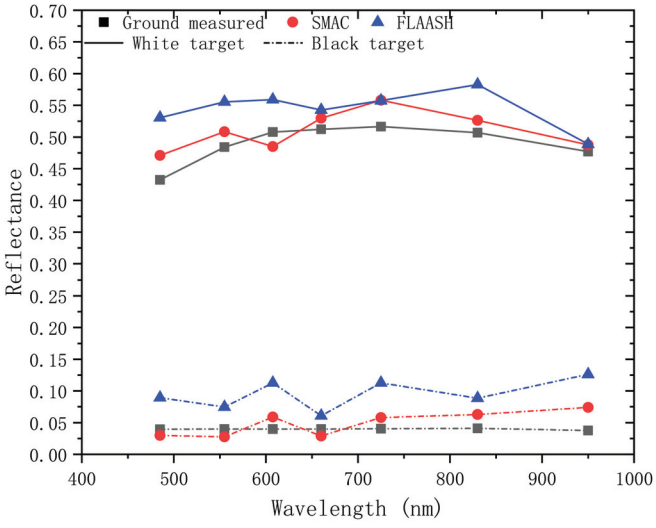


Figure 11. The average surface reflectance of white and black targets in the corrected image of Songshan on 26 August 2020 obtained from Syn-AC and FLAASH and the field-measured reflectance.

Table 9. Performance comparison between Syn-AC and FLAASH, basing on Example 2.

Site	**Songshan—Example 2**							
Target	**White Target**				**Black Target**			
	Syn-AC		**FLAASH**		**Syn-AC**		**FLAASH**	
Band/nm	E_A	E_R (%)	E_A	E_R (%)	E_A	E_R (%)	E_A	E_R (%)
485	0.0386	8.9	0.0981	22.7	0.0098	24.7	0.0496	124.9
555	0.0241	5.0	0.0712	14.7	0.0123	30.9	0.0349	87.8
607.5	0.023	4.5	0.051	10.0	0.019	47.7	0.0729	183.0
660	0.0176	3.4	0.0303	5.9	0.0109	27.3	0.0209	52.4
725	0.0416	8.1	0.0411	8.0	0.0176	43.5	0.0723	178.7
830	0.0194	3.8	0.0759	15.0	0.0219	53.5	0.0476	116.3
950	0.0107	2.2	0.0117	2.5	0.0364	96.5	0.0884	234.4

As for the case of the moderately polluted atmosphere, the second case of Songshan on 4 February 2021 was analyzed. The original image and the corrected images with thin cloud effectively removed are depicted in Figure 12. The contrastive results are displayed in Figure 13 and Table 10, and the values of Syn-AC are almost identical to the field-measured values. The results of FLAASH are significantly less than the field-measured values. There is some difference between the reflectance retrievals of the black target of Syn-AC and the measured values, but the relative error is smaller than the relative error between FLAASH and the measured value. For the white target, the absolute error values of Syn-AC are within 0.012, and the max absolute error of FLAASH is 0.0927. The mean relative error values of Syn-AC and FLAASH are 1.3% and 17.4%, respectively. For the black target, the absolute error values of Syn-AC are within 0.0257, and the max absolute error of FLAASH is 0.0736. The mean relative error values of Syn-AC and FLAASH are 36.1% and 156.1%, respectively.



(**a**) (**b**) (**c**)

Figure 12. Images of Songshan on 4 February 2021. (**a**) Original image; (**b**) corrected image after Syn-AC; (**c**) corrected image after FLAASH. The retrieved AOD at 550 nm and retrieved CWV are 0.421 and 0.42 g/cm^2, respectively.

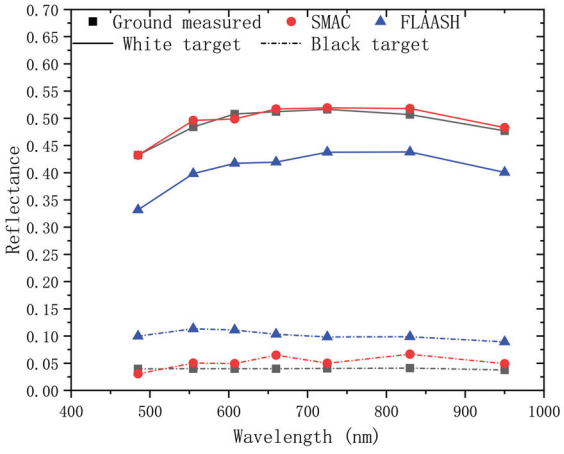


Figure 13. The average surface reflectance of white and black targets in the corrected image of Songshan on 4 February 2021 obtained from Syn-AC and FLAASH and the field-measured reflectance.

Table 10. Performance comparison between Syn-AC and FLAASH, basing on Example 3.

Site	**Songshan—Example 3**							
Target	**White Target**				**Black Target**			
	Syn-AC		**FLAASH**		**Syn-AC**		**FLAASH**	
Band/nm	E_A	E_R (%)	E_A	E_R (%)	E_A	E_R (%)	E_A	E_R (%)
485	0.0002	0.1	0.1007	23.3	0.0092	23.2	0.0599	150.9
555	0.012	2.5	0.0858	17.7	0.0106	26.7	0.0736	185.1
607.5	0.0091	1.8	0.0905	17.8	0.0096	24.1	0.071	178.2
660	0.005	1.0	0.0927	18.1	0.0249	62.5	0.0633	158.7
725	0.0028	0.5	0.0785	15.2	0.0095	23.5	0.0577	142.6
830	0.0111	2.2	0.0688	13.6	0.0257	62.8	0.0577	141.0
950	0.006	1.3	0.0762	16.0	0.0114	30.2	0.0513	136.0

Considering the case of the heavily polluted atmosphere, the surface reflectance images of Syn-AC and FLAASH are shown in Figure 14b,c. The contrastive results are illustrated in Figure 15. The results of the two models are all less than the measured values, and the relative errors of Syn-AC are smaller than those of FLAASH. As shown in Table 11, the correction accuracy of the band centered on 950 nm of Syn-AC is not as good as that of other bands. The surface reflectance of black target of FLAASH is significantly different from the ground measurements. For the white target, the absolute error values of Syn-AC are within 0.0505, and the max absolute error of FLAASH is 0.1621. The mean relative error values of Syn-AC and FLAASH are 6.6% and 27.4%, respectively. For the black target, the absolute error values of Syn-AC are within 0.0625, and the max absolute error of FLAASH is 0.2063. The mean relative error values of Syn-AC and FLAASH are 96.3% and 458.7%, respectively.

- Baotou



(**a**) (**b**) (**c**)

Figure 14. Images of Songshan on 8 February 2021. (**a**) Original image; (**b**) corrected image after Syn-AC; (**c**) corrected image after FLAASH. The retrieved AOD at 550 nm and retrieved CWV are 1.19, and the CWV of 0.72 g/cm^2, respectively.

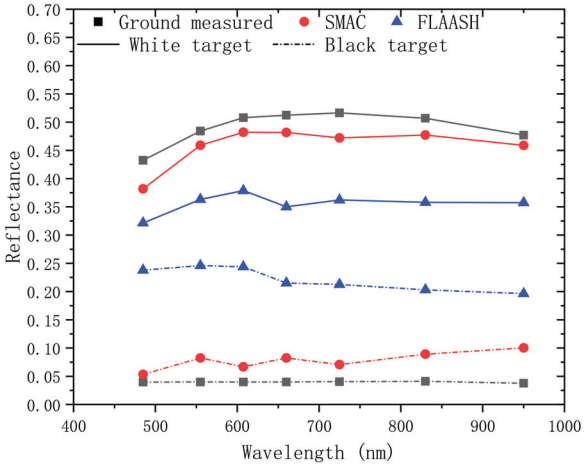


Figure 15. The average surface reflectance of white and black targets in the corrected image of Songshan on 8 February 2021 obtained from Syn-AC and FLAASH and the field-measured reflectance.

Table 11. Performance comparison between Syn-AC and FLAASH, based on Example 4.

Site	Songshan—Example 4							
Target	White Target				Black Target			
	Syn-AC		FLAASH		Syn-AC		FLAASH	
Band/nm	E_A	E_R (%)	E_A	E_R (%)	E_A	E_R (%)	E_A	E_R (%)
485	0.0505	11.7	0.111	25.7	0.0137	34.5	0.1982	499.2
555	0.0253	5.2	0.1211	25.0	0.0427	107.4	0.2063	518.7
607.5	0.0258	5.1	0.1292	25.4	0.0269	67.5	0.204	512.1
660	0.0305	5.9	0.1621	31.7	0.0425	106.6	0.1752	439.3
725	0.0442	8.6	0.1543	29.9	0.0303	74.9	0.1721	425.4
830	0.0297	5.9	0.149	29.4	0.0481	117.6	0.162	395.9
950	0.0181	3.8	0.1195	25.1	0.0625	165.7	0.1586	420.5

For Baotou, two multispectral images under different atmospheric conditions were selected for a comparative analysis of Syn-AC and FLAASH. The atmospheric correction parameter retrievals are obtained from the SMAC with AOD of 0.338 and 0.092, and CWV of 1.42 and 1.14 g/cm^2 for Figures 16a and 17a, respectively.



(**a**) (**b**) (**c**)

Figure 16. Images of Baotou on 26 August 2020. (**a**) Original image; (**b**) corrected image after Syn-AC; (**c**) corrected image after FLAASH. The retrieved AOD at 550 nm and retrieved CWV are 0.338 and 1.42 g/cm^2, respectively.



(**a**) (**b**) (**c**)

Figure 17. Images of Baotou on 31 August 2020. (**a**) Original image; (**b**) corrected image after Syn-AC; (**c**) corrected image after FLAASH. The retrieved AOD at 550 nm and retrieved CWV are 0.092 and 1.14 g/cm^2, respectively.

For the first case on 26 August 2020, the average surface reflectance in the white, gray, and black targets of each image illustrated in Figure 16 was analyzed. The reflectance retrievals and the contrastive results of white, gray, and black target are depicted in Figure 18 and Table 12. The retrieved reflectance of white, gray, and black targets of Syn-AC are in good agreement with the field-measured values. Notably, the FLAASH reflectance is higher than the measured reflectance. The absolute error values of three targets (white, gray, and black) of Syn-AC are within 0.0403, 0.0282, and 0.0315, respectively. The max absolute error values of FLAASH are 0.0919, 0.0237, and 0.0886, respectively. For the white target, the mean relative error values of Syn-AC and FLAASH are 4.7% and 13.2%, respectively. For the gray target, the mean relative error values of Syn-AC and FLAASH are 9.6% and 45.6%, respectively. For the black target, the mean relative error values of Syn-AC and FLAASH are 25.8% and 85.2%, respectively.

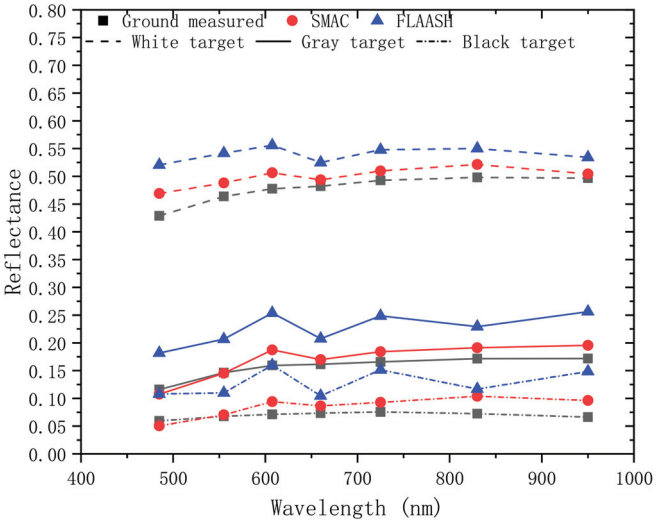


Figure 18. The average surface reflectance of white, gray, and black targets in the corrected image of Baotou on 26 August 2020 obtained from Syn-AC and FLAASH and the field-measured reflectance.

Table 12. Performance comparison between Syn-AC and FLAASH, based on Example 5.

Site	**Baotou—Example 5**											
Target	**White Target**				**Gray Target**				**Black Target**			
	Syn-AC		**FLAASH**		**Syn-AC**		**FLAASH**		**Syn-AC**		**FLAASH**	
Band/nm	E_A	E_R (%)	E_A	E_R (%)	E_A	E_R (%)	E_A	E_R (%)	E_A	E_R (%)	E_A	E_R (%)
485	0.0403	9.4	0.0919	21.4	0.0084	7.2	0.0659	56.8	0.009	15.1	0.0485	81.6
555	0.024	5.2	0.0777	16.8	0.0012	0.8	0.0602	41.1	0.0027	4.0	0.0424	62.6
607.5	0.0286	6.0	0.0783	16.4	0.0282	17.7	0.0944	59.3	0.0229	32.1	0.0886	124.2
660	0.0115	2.4	0.0427	8.9	0.0083	5.1	0.0462	28.6	0.0132	18.0	0.0313	42.7
725	0.0169	3.4	0.055	11.2	0.0184	11.1	0.083	50.1	0.0174	23.1	0.0759	100.5
830	0.0232	4.7	0.0519	10.4	0.0197	11.5	0.0578	33.7	0.0315	43.5	0.0445	61.5
950	0.0078	1.6	0.0378	7.6	0.0237	13.8	0.0846	49.3	0.0299	45.0	0.0821	123.7

For the image on 31 August 2020, the AOD retrieved from SMAC was 0.092. As depicted in Figure 17, the atmospheric condition is clear. As shown in Figure 19 and Table 13, the average reflectance of white, gray, and black targets obtained from the surface

reflectance image of Syn-AC are identical to the field-measured values. The correction precision of FLAASH is inferior to that of Syn-AC. The absolute error values of three targets (white, gray, and black) of Syn-AC are within 0.0285, 0.0258, and 0.0077, respectively. The max absolute error values of three targets of FLAASH are 0.119, 0.0226, and 0.0106, respectively. For the white target, the mean relative error values of Syn-AC and FLAASH are 3.2% and 14.3%, respectively. For the gray target, the mean relative error values of Syn-AC and FLAASH are 4.7% and 7.3%, respectively. For the black target, the mean relative error values of Syn-AC and FLAASH are 7.6% and 10.7%, respectively.

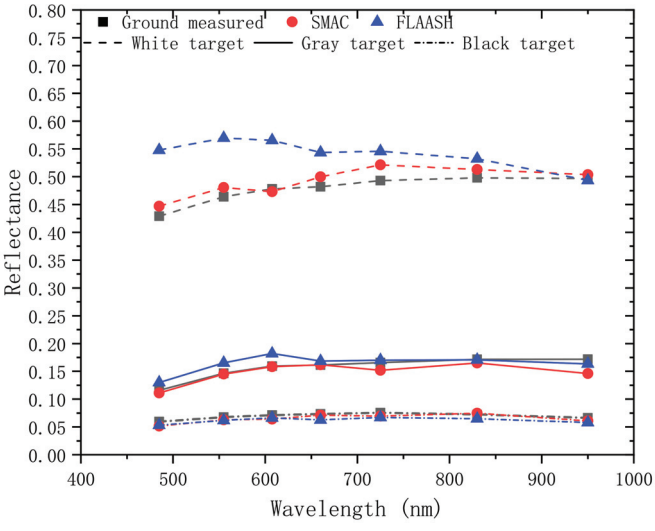


Figure 19. The average surface reflectance of white, gray, and black targets in the corrected image of Baotou on 31 August 2020 obtained from Syn-AC and FLAASH and the field-measured reflectance.

Table 13. Performance comparison between Syn-AC and FLAASH, based on Example 6.

Site	**Baotou—Example 6**											
Target	**White Target**				**Gray Target**				**Black Target**			
	Syn-AC		**FLAASH**		**Syn-AC**		**FLAASH**		**Syn-AC**		**FLAASH**	
Band/nm	E_A	E_R (%)	E_A	E_R (%)	E_A	E_R (%)	E_A	E_R (%)	E_A	E_R (%)	E_A	E_R (%)
485	0.0183	4.3	0.119	27.8	0.0048	4.1	0.0139	12.0	0.0077	13.0	0.0062	10.4
555	0.0166	3.6	0.1056	22.8	0.0014	1.0	0.0187	12.8	0.0052	7.7	0.0061	9.0
607.5	0.0046	1.0	0.0877	18.4	0.0009	0.6	0.0226	14.2	0.0072	10.1	0.005	7.0
660	0.0176	3.7	0.0613	12.7	0.0004	0.3	0.0071	4.4	0.0021	2.9	0.0106	14.5
725	0.0285	5.8	0.0529	10.7	0.0137	8.3	0.0044	2.7	0.006	8.0	0.0082	10.0
830	0.0149	3.0	0.0341	6.9	0.0064	3.7	0.0008	0.5	0.0023	3.2	0.0077	10.6
950	0.0072	1.5	0.003	0.6	0.0258	15.0	0.0083	4.8	0.0056	8.4	0.0084	12.7

6. Discussion

High-precision atmospheric parameters are critical for atmospheric correction based on the radiative transfer model and quantitative application of high spatial resolution remote sensing images. However, due to the spatial-temporal variation of atmospheric parameters, the traditional method of obtaining atmospheric parameters based on ground-based sites or other satellite products is difficult to ensure the spatial and temporal matching between

atmospheric parameters and images, resulting in the error of atmospheric correction. The present paper has demonstrated that the solution to obtain atmospheric parameters synchronously by the equipment on-board the satellite platform is effective.

Based on the synchronous atmospheric parameters, atmospheric correction experiments of GFDM satellite images were conducted. Compared with the original image, the visual effects of corrected image were improved with the blurring effect removed. In addition, the better clarity and contrast were achieved after adjacency effect correction. In the case of lower atmospheric visibility, the correction effect was more obvious, and the image quality was of greater improvement.

The correction precision of Syn-AC was verified by comparing with the field-measured reflectance, and the same analysis was performed for FLAASH. The two methods are both based on radiative transfer models, and other inputs including satellite imaging parameters, atmospheric model, and aerosol model are the same except for the sources of atmospheric parameters. The results indicate that both methods performed well. However, most of the reflectance retrievals error of Syn-AC were less than those of FLAASH, and the correction performance of Syn-AC was more stable. It is considered that FLAASH estimates atmospheric parameters based on the spectral information in the remote sensing image, whereas the band settings of the main sensor may not meet the requirements of FLAASH to retrieve atmospheric parameters. On the other hand, the atmospheric parameters of Syn-AC were retrieved from SMAC, which is specifically designed to detect atmospheric information. Therefore, most of the retrieved values of Syn-AC were closer to the field-measured values.

The acquisition of satellite image of study area requires the imaging schedule submitted by CNSA in advance, so the image data of the region of interest is limited. According to the current experimental results, more image data are required for the analysis of the correction performance under different atmospheric states and underlying surface, as well as the influence of atmospheric model and aerosol model on correction accuracy.

7. Conclusions

In view of the temporal and spatial variation of the atmospheric state, the atmospheric correction on remote sensing images based on synchronous atmospheric parameters could provide a higher precision. An atmospheric correction method was proposed based on the synchronization atmospheric parameters retrieved from SMAC, including the processing steps for the SMAC data, main ideas of atmospheric parameters inversion, and the principles of atmospheric correction of GFDM satellite images. Additionally, based on the atmospheric parameters retrieved from SMAC data, experiments were conducted to investigate the performance and verify the correction precision of the Syn-AC method.

In the present study, six images of three radiometric calibration sites were selected. First, the data obtained from ground-based sites were used to analyze the accuracy of the atmospheric parameters retrieved from SMAC. The max relative errors of AOD and CWV were 22% and 17%, respectively. The results show that the atmospheric parameters retrieved from SMAC in the study are in good agreement with the ground observations, and the atmospheric retrievals could be used in atmospheric correction of GFDM satellite imagery.

For the selected images, Syn-AC and FLAASH were applied to conduct correction experiments. Then, the average reflectance of the targets from the corrected image of Syn-AC and FLAASH were compared with the field-measured reflectance to test correction precision. The max absolute error of Syn-AC was 0.0625, representing a higher precision than the FLAASH (the max absolute error was 0.2063). The mean relative error of Syn-AC and FLAASH were 19.3% and 76.6%, respectively (in the view of the fact that the reflectance of the black target is close to 0, and the measured value is within 0.1. Even if the deviation between the retrieved reflectance and the measured reflectance value is small, a large relative error may be calculated).

Preliminary analyses of the performance of Syn-AC indicate that the atmospheric parameters measured synchronically are useful to improve image quality and obtain high-

precision surface reflectance than those based on image spectral information inversion. The SMAC is of great potential to further meet the demand of high-precision data for remote sensing application, which indicates the necessity of synchronous atmospheric parameters.

At present, an atmospheric synchronization correction instrument capable of imaging is being developed. Therefore, it is urgent to conduct research on atmospheric correction based on image of the atmospheric corrector and spectral polarization information, and the study of this paper is an important part.

Author Contributions: Conceptualization, W.C.; data curation, Z.Q. and W.H.; formal analysis, L.X. and T.W.; methodology, Z.L.; project administration, X.L.; resources, J.L. and Z.H.; software, D.Z. and W.F.; supervision, W.X. and W.Y.; validation, L.X.; writing—original draft, L.X.; writing—review and editing, L.X. All authors have read and agreed to the published version of the manuscript.

Funding: This work was supported in part by the GF-7 Project (Grant No. 30-Y20A010-9007-17/18), the Aerospace Science and Technology Innovation and Application Research Project (Grant No. 2022000351), and the National Natural Science Foundation of China (Grant No. 41871269).

Data Availability Statement: The GFDM satellite images and SMAC data can be obtained from China Centre for Resources Satellite Data and Application (Available online: http://www.cresda.com/CN/ (accessed on 21 July 2022)). AERONET data can be downloaded from the official website of AERONET (https://aeronet.gsfc.nasa.gov (accessed on 21 July 2022)).

Acknowledgments: The authors would like to extend our deep gratitude to Li Kaitao of the Aerospace Information Research Institute, Chinese Academy of Sciences for the supply of SONET data.

Conflicts of Interest: The authors declare no conflict of interest.

References

1. Goody, R.M.; Yung, Y.L. *Atmospheric Radiation: Theoretical Basis*; Oxford University Press: New York, NY, USA, 1989. [CrossRef]
2. Shettle, E.P. Models of aerosols, clouds, and precipitation for atmospheric propagation studies. In *AGARD, Atmospheric Propagation in the UV, Visible, IR, and MM-Wave Region and Related Systems Aspects*; The SAO/NASA Astrophysics Data System: Silicon Valley, SF, USA, 1990; 14p.
3. Guzzi, D.; Nardino, V.; Lastri, C.; Raimondi, V. A Fast Iterative Procedure for Adjacency Effects Correction on Remote Sensed Data. *Remote Sens.* **2021**, *13*, 1799. [CrossRef]
4. Wang, T.; Du, L.; Yi, W.; Hong, J.; Zhang, L.; Zheng, J.; Li, C.; Ma, X.; Zhang, D.; Fang, W.; et al. An adaptive atmospheric correction algorithm for the effective adjacency effect correction of submeter-scale spatial resolution optical satellite images: Application to a WorldView-3 panchromatic image. *Remote Sens. Environ.* **2021**, *259*, 112412. [CrossRef]
5. Li, Z.Q.; Chen, X.F.; Ma, L.Y.; Qie, L.L.; Hou, W.Z.; Qiao, Y.L. Review of atmospheric correction for optical remote sensing satellites. *J. Nanjing Univ. Inf. Sci. Technol. Nat. Sci. Ed.* **2018**, *10*, 10. [CrossRef]
6. Smirnov, A.; Holben, B.N.; Eck, T.F.; Slutsker, I.; Chatenet, B.; Pinker, R.T. Diurnal variability of aerosol optical depth observed at AERONET (Aerosol Robotic Network) sites. *Geophys. Res. Lett.* **2002**, *29*, 30-1–30-4. [CrossRef]
7. Ma, Y. *Study on Synchronous Atmospheric Correction of High Spatial Resolution Optical Remote Sensing Satellite*; University of Chinese Academy of Sciences: Beijing, China, 2016.
8. Kaufman, Y.J.; Sendra, C. Algorithm for automatic atmospheric corrections to visible and near-IR satellite imagery. *Int. J. Remote Sens.* **1988**, *9*, 1357–1381. [CrossRef]
9. Levy, R.C.; Mattoo, S.; Munchak, L.A.; Remer, L.A.; Sayer, A.M.; Patadia, F.; Hsu, N.C. The Collection 6 MODIS aerosol products over land and ocean. *Atmos. Meas. Tech.* **2013**, *6*, 2989–3034. [CrossRef]
10. Dubovik, O.; Schuster, G.L.; Xu, F.; Hu, Y.; Bösch, H.; Landgraf, J.; Li, Z. Grand Challenges in Satellite Remote Sensing. *Front. Remote Sens.* **2021**, *2*, 619818. [CrossRef]
11. Reuter, D.C.; McCabe, G.H.; Dimitrov, R.; Graham, S.M.; Jennings, D.E.; Matsumura, M.M.; Rapchun, D.A.; Travis, J.W. The LEISA/Atmospheric Corrector (LAC) on EO-1. In *Proceedings of the IEEE International Geoscience & Remote Sensing Symposium, Sydney, NSW, Ausralia, 9–13 July 2001*; IEEE: Piscataway, NJ, USA, 2001. [CrossRef]
12. Barazzetti, L.; Roncoroni, F.; Brumana, R.; Previtali, M. Georeferencing accuracy analysis of a single worldview-3 image collected over Milan. In Proceedings of the XXIII ISPRS Congress, Prague, Czech Republic, 12–19 July 2016; pp. 429–434. [CrossRef]
13. Fu, Q.Y.; Min, X.J.; Li, X.C.; Sha, C.; Li, X. Study on on-orbit absolute radiometric calibration of CBERS-02 CCD sensor at Dunhuang Site. *Natl. Remote Sens. Bull.* **2006**, *10*, 433–439. [CrossRef]
14. Li, Z.Z.; Xu, W.; Fu, Q.Y.; Min, X.J.; Zhang, L.M.; Pan, Z.Q.; Qiao, Y.L.; Zheng, X.B.; Fan, Y.T.; Su, B.J.; et al. Construction and application of fixed target site in Songshan Mountains, China. *J. Atmos. Environ. Opt.* **2014**.
15. Li, C.R.; Ma, L.L.; Tang, L.L.; Gao, C.X.; Qian, Y.G.; Wang, N.; Wang, X.H. A comprehensive calibration site for high resolution remote sensors dedicated to quantitative remote sensing and its applications. *Natl. Remote Sens. Bull.* **2021**, *25*, 198–219. [CrossRef]

16. Li, Z.; Hou, W.; Qiu, Z.; Ge, B.; Xie, Y.; Hong, J.; Ma, Y.; Peng, Z.; Fang, W.; Zhang, D.; et al. Preliminary On-Orbit Performance Test of the First Polarimetric Synchronization Monitoring Atmospheric Corrector (SMAC) On-Board High-Spatial Resolution Satellite Gao Fen Duo Mo (GFDM). *IEEE Trans. Geosci. Remote Sens.* **2022**, *60*, 4104014. [CrossRef]
17. Fan, L.J.; Wang, Y.; Yang, W.T.; Yu, L.J.; Zhang, G.B. Scheme design and technical characteristics of high-resolution multimode satellite. *Spacecr. Eng.* **2021**, *30*, 10–19. [CrossRef]
18. Jiang, W.; Huang, Q.L. The high-resolution Multimode Integrated Imaging satellite was successfully launched. *Spacefl. Return Remote Sens.* **2020**, *41*, 2.
19. Hu, Y.D.; Hu, Q.Y.; Sun, B.; Wang, X.J.; Qiu, Z.W.; Hong, J. Polarization Atmospheric corrector with dual angle for remote sensing image. *Opt. Precis. Eng.* **2015**, *023*, 652–659. [CrossRef]
20. Kang, Q.; Yuan, Y.L.; Li, J.J.; Yang, W.F.; Fan, H.M.; Qian, H.H.; Wu, H.Y.; Zheng, X.B. Experimental study on filter screening method and accuracy verification of atmospheric synchronous corrector. *Acta Opt. Sin.* **2017**, *37*, s11. [CrossRef]
21. Deuzé, J.L.; Bréon, F.M.; Devaux, C.; Goloub, P.; Herman, M.; Lafrance, B.; Maignan, F.; Marchand, A.; Nadal, F.; Perry, G.; et al. Remote sensing of aerosols over land surfaces from POLDER-ADEOS-1 polarized measurements. *J. Geophys. Res. Atmos.* **2001**, *106*, 4913–4926. [CrossRef]
22. Dubovik, O.; Herman, M.; Holdak, A.; Lapyonok, T.; Tanré, D.; Deuzé, J.L.; Ducos, F.; Sinyuk, A.; Lopatin, A. Statistically optimized inversion algorithm for enhanced retrieval of aerosol properties from spectral multi-angle olarimetric satellite observations. *Atmos. Meas. Tech.* **2011**, *4*, 975–1018. [CrossRef]
23. Dubovik, O.; Li, Z.; Mishchenko, M.I.; Tanré, D.; Karol, Y.; Bojkov, B.; Cairns, B.; Diner, D.J.; Espinosa, W.R.; Goloub, P.; et al. Polarimetric remote sensing of atmospheric aerosols: Instruments, methodologies, results, and perspectives. *J. Quant. Spectrosc. Radiat. Transf.* **2018**, *224*, 474–511. [CrossRef]
24. Ge, B.; Mei, X.; Li, Z.; Hou, W.; Xie, Y.; Zhang, Y.; Xu, H.; Li, K.; Wei, Y. An improved algorithm for retrieving high resolution fine-mode aerosol based on polarized satellite data: Application and validation for POLDER-3. *Remote Sens. Environ.* **2020**, *247*, 111894. [CrossRef]
25. Levy, R.C.; Remer, L.A.; Kleidman, R.G.; Mattoo, S.; Ichoku, C.; Kahn, R.; Eck, T.F. Global evaluation of the collection 5 MODIS darktarget aerosol products over land. *Atmos. Chem. Phys.* **2010**, *10*, 10399–10420. [CrossRef]
26. Ciren, P.; Kondragunta, S. Dust aerosol index (DAI) algorithm for MODIS. *J. Geophys. Res. Atmos.* **2014**, *119*, 4770–4792. [CrossRef]
27. Hall, D.K.; Riggs, G.A.; Salomonson, V.V. Development of methods for mapping global snow cover using Moderate Resolution Imaging Spectroradiometer data. *Remote Sens. Environ.* **1995**, *54*, 127–140. [CrossRef]
28. Zheng, F.; Li, Z.; Hou, W.; Qie, L.; Zhang, C. Aerosol retrieval study from multiangle polarimetric satellite data based on optimal estimation method. *J. Appl. Remote Sens.* **2020**, *14*, 014516. [CrossRef]
29. Waquet, F.; Léon, J.F.; Cairns, B.; Goloub, P.; Deuzé, J.L.; Auriol, F.J.A.O. Analysis of the spectral and angular response of the vegetated surface polarization for the purpose of aerosol remote sensing over land. *Appl. Opt.* **2009**, *48*, 1228. [CrossRef]
30. Litvinov, P.; Hasekamp, O.; Cairns, B. Models for surface reflection of radiance and polarized radiance: Comparison with airborne multiangle photopolarimetric measurements and implications for modeling top-of-atmosphere measurements. *Remote Sens. Environ.* **2011**, *115*, 781–792. [CrossRef]
31. Zheng, F.X.; Hou, W.Z.; Li, Z.Q. Optimal estimation retrieval for directional polarimetric camera onboard Chinese Gaofen-5 satellite: An analysis on multi-angle dependence and a posteriori error. *Acta Phys. Sin.* **2019**, *68*, 040701. [CrossRef]
32. Wang, J.; Xu, X.; Ding, S.; Zeng, J.; Spurr, R.; Liu, X.; Chance, K.; Mishchenko, M. A numerical testbed for remote sensing of aerosols, and its demonstration for evaluating retrieval synergy from a geostationary satellite constellation of GEO-CAPE and GOES-R. *J. Quant. Spectrosc. Radiat. Transf.* **2014**, *146*, 510–528. [CrossRef]
33. Vermote, E.F.; Tanre, D.; Deuze, J.L.; Herman, M.; Morcette, J.J. Second simulation of the satellite signal in the solar spectrum, 6S: An overview. *IEEE Trans. Geosci. Remote Sens.* **2002**, *35*, 675–686. [CrossRef]
34. Vermote, E.F.; Kotchenova, S. Atmospheric correction for the monitoring of land surfaces. *J. Geophys. Res. Atmos.* **2008**, *113*, D23. [CrossRef]
35. Bennartz, R.; Fischer, J. Retrieval of columnar water vapour over land from backscattered solar radiation using the Medium Resolution Imaging Spectrometer. *Remote Sens. Environ.* **2001**, *78*, 274–283. [CrossRef]
36. Bouffies, S.; Tanre, D.; Bréon, F.-M.; Dubuisson, P. Atmospheric water vapor estimate by a differential absorption technique with the POLDER instrument. *Int. Soc. Opt. Photonics* **1995**, *2582*, 131–143. [CrossRef]
37. Barducci, A.; Guzzi, D.; Marcoionni, P.; Pippi, I. Atmospheric effects on hyperspectral data acquired with aerospace imaging spectrometers. In Proceedings of the Optics in Atmospheric Propagation and Adaptive Systems V (9th International Symposium on Remote Sensing), Crete, Greece, 22–27 September 2003; Volume 4884, pp. 1–9.
38. Verhoef, W.; Bach, H. Simulation of hyperspectral and directional radiance images using coupled biophysical and atmospheric radiative transfer models. *Remote Sens. Environ.* **2003**, *87*, 23–41. [CrossRef]
39. Vermote, E.; Tanre, D.; Deuzé, J.L.; Herman, M.; Morcrette, J.J. *Second Simulation of the Satellite Signal in the Solar Spectrum*; 6S User Guide Version 1; NASA Goddard Space Flight Center: Greenbelt, MD, USA, 1996.
40. Tang, X.; Yi, W.; Du, L.; Cui, W. Adjacency effect correction of GF-1 satellite multispectral remote sensing images. *Acta Opt. Sin.* **2016**, *36*, 0228003-1. [CrossRef]
41. Wang, Q.; Chen, X.; Ma, J.W.; Chen, J. A comparative study of two remote sensing image adjacency effect correction algorithms based on SHDOM empirical equation and synchronized measured spectral data. *Acta Opt. Sin.* **2010**, *30*, 3324–3348. [CrossRef]

42. Zhang, H.B.; Li, F. ASD spectrometer measurement technology and application method. *Shandong Weather* **2014**, *34*, 46–48. [CrossRef]
43. Richter, R. Atmospheric correction of DAIS hyperspectral image data. *Comput. Geosci.* **1996**, *22*, 785–793. [CrossRef]
44. Viallefontrobinet, F.; Léger, D. Improvement of the edge method for on-orbit MTF measurement. *Opt. Express* **2010**, *18*, 3531. [CrossRef]
45. Remer, L.A.; Mattoo, S.; Levy, R.C.; Munchak, L.A. MODIS 3 km aerosol product: Algorithm and global perspective. *Atmos. Meas. Tech.* **2013**, *6*, 1829–1844. [CrossRef]
46. Minomura, M.; Kuze, H.; Takeuchi, N. Adjacency effect in the atmospheric correction of satellite remote sensing data: Evaluation of the influence of aerosol extinction profiles. *Opt. Rev.* **2001**, *8*, 133–141. [CrossRef]
47. Ma, J.W.; Qin, D.; Feng, C. Target adjacency influence estimation using ground spectrum measurement and Landsat-5 data. In Proceedings of the 2005 IEEE International Geoscience and Remote Sensing Symposium, Seoul, Korea, 25–29 July 2005.
48. Adler-Golden, S.; Berk, A.; Bernstein, L.S.; Richtsmeier, S.; Acharya, P.K.; Matthew, M.W.; Anderson, G.P.; Allred, C.L.; Jeong, L.S.; Chetwynd, J.H. FLAASH, a MODTRAN4 atmospheric correction package for hyperspectral data retrievals and simulations. In Proceedings of the 7th Annual JPL Airborne Earth Science Workshop, Pasadena, CA, USA, 12–16 January 1998; JPL Publication: Pasadena, CA, USA, 1998.
49. Research System Inc. *FLAASH User's Guide*; ENVI FLAASH Version 1.0; Research System Inc.: Norwalk, CT, USA, 2001; pp. 8–40.

remote sensing

MDPI

Article

An Improved Aerosol Optical Depth Retrieval Algorithm for Multiangle Directional Polarimetric Camera (DPC)

Bangyu Ge [1], Zhengqiang Li [1,2,*], Cheng Chen [3,4], Weizhen Hou [1,2], Yisong Xie [1], Sifeng Zhu [1,2], Lili Qie [1], Ying Zhang [1,2], Kaitao Li [1], Hua Xu [1,2], Yan Ma [1], Lei Yan [5] and Xiaodong Mei [2]

[1] State Environmental Protection Key Laboratory of Satellite Remote Sensing, Aerospace Information Research Institute, Chinese Academy of Sciences, Beijing 100101, China
[2] University of Chinese Academy of Sciences, Beijing 100049, China
[3] Laboratoire d'Optique Atmosphérique (LOA), UMR8518 CNRS, Université de Lille, 59655 Villeneuve-D'ascq, France
[4] GRASP-SAS, Remote Sensing Developments, Université de Lille, 59655 Villeneuve-D'ascq, France
[5] Institute of Remote Sensing and Geographic Information System, School of Earth and Space Sciences, Peking University, Beijing 100871, China
* Correspondence: lizq@radi.ac.cn

Abstract: The DPC is a multiangle sensor that detects atmospheric parameters. However, the retrieval of high-precision and high-spatial-resolution aerosol products from the DPC remains a great challenge due to the ill-posed nature of the problem. Thus, a novel aerosol optical depth (AOD) retrieval algorithm was proposed using visible surface reflectance relationships (VISRRs). The VISRR algorithm accounts for the surface anisotropy and needs neither a shortwave infrared band nor a surface reflectance database that can retrieve AOD over dark and bright land cover. Firstly, moderate-resolution imaging spectroradiometer (MODIS) surface reflectance (MYD09) products were used to derive the preceding surface reflectance relationships (SRRs), which are related to surface types, scattering angle, and normalized difference vegetation index (NDVI). Furthermore, to solve the problem of the NDVI being susceptible to the atmosphere, an innovative method based on an iterative atmospheric correction was proposed to provide a realistic NDVI. The VISRR algorithm was then applied to the thirteen months of DPC multiangle data over the China region. AOD product comparison between the DPC and MODIS showed that they had similar spatial distribution, but the DPC had both high spatial resolution and coverage. The validation between the ground-based sites and the retrieval results showed that the DPC AOD performed best, with a Pearson correlation coefficient (R) of 0.88, a root mean square error (RMSE) of 0.17, and a good fraction (Gfrac) of 62.7%. Then, the uncertainties regarding the AOD products were discussed for future improvements. Our results revealed that the VISRR algorithm is an effective method for retrieving reliable, simultaneously high-spatial-resolution and full-surface-coverage AOD data with good accuracy.

Keywords: DPC; Gaofen-5; aerosol retrieval; surface reflectance; surface types; bidirectional reflectance distribution function (BRDF); NDVI; new retrieval algorithm

Citation: Ge, B.; Li, Z.; Chen, C.; Hou, W.; Xie, Y.; Zhu, S.; Qie, L.; Zhang, Y.; Li, K.; Xu, H.; et al. An Improved Aerosol Optical Depth Retrieval Algorithm for Multiangle Directional Polarimetric Camera (DPC). *Remote Sens.* **2022**, *14*, 4045. https://doi.org/10.3390/rs14164045

Academic Editor: Carmine Serio

Received: 7 June 2022
Accepted: 16 August 2022
Published: 19 August 2022

Publisher's Note: MDPI stays neutral with regard to jurisdictional claims in published maps and institutional affiliations.

Copyright: © 2022 by the authors. Licensee MDPI, Basel, Switzerland. This article is an open access article distributed under the terms and conditions of the Creative Commons Attribution (CC BY) license (https://creativecommons.org/licenses/by/4.0/).

1. Introduction

Aerosol particles are widely suspended in the Earth's atmosphere, which greatly impacts the Earth's radiation balance and climate change by scattering and absorbing solar light. Meanwhile, aerosol particles can cause adverse effects on the atmospheric environment, human health, satellite image quality, etc. Thus, monitoring and determining aerosols' optical, physical, and chemical properties are necessary for different research fields. There are two main aerosol monitoring methods based on the principle of aerosols' extinction effect on solar radiation. One uses ground-based sun photometers, and the other uses satellite-based sensors. Aerosol products are often measured via ground-based observations with high precision that are also used to validate satellite-based aerosol

product measurements. There are several famous observation networks, for example, the globally distributed Aerosol Robotic Network (AERONET), whose overall aerosol optical depth (AOD) uncertainty is estimated to be between 0.01 and 0.02 [1], and the Chinese Sun–Sky Radiometer Observation Network (SONET), which uses the multiwavelength polarized sun–sky radiometer CE318-DP [2].

Satellite-based aerosol remote sensing can monitor large-scale and inaccessible areas, in contrast to the limited distribution of ground-based sites [3]. Satellite-based aerosol remote sensing has been undergoing development for almost 50 years, ever since Griggs [4] began using a multispectral scanner (MSS) onboard the Earth Resources Technology-1 (ERTS-1) satellite to retrieve the AOD over water. Various satellite sensors have been designed for monitoring aerosols, which can be roughly divided into four categories: (1) single-angle non-polarized sensors, such as the advanced very-high-resolution radiometer (AVHRR), the moderate-resolution imaging spectroradiometer (MODIS), the visible infrared imaging radiometer suite (VIIRS), the medium-resolution imaging spectrometer (MERIS), and the ocean and land colour instrument (OLCI) [5–9]; (2) multiangle non-polarized sensors, such as the multiangle imaging spectroradiometer (MISR), the along-track scanning radiometer (ATSR), the advanced along-track scanning radiometer (AATSR), and the sea and land surface temperature radiometer (SLSTR) [10–12]; (3) single-angle polarized sensors, such as the cloud and aerosol polarization imager (CAPI) [13]; and (4) multiangle polarized sensors, such as the second-generation global imager (SGLI), the polarization and directionality of the Earth's reflectance instrument (POLDER), and the directional polarimetric camera (DPC) [14–16]. Correspondingly, based on the characteristics of these sensors, different specific aerosol retrieval algorithms have been proposed. The basic principle of satellite-based aerosol retrieval is to decouple the surface and atmosphere signals. However, satellite-based aerosol retrieval is an ill-posed problem due to the unknowns being more numerous than the measurements [17]. Therefore, no matter which algorithm is implemented, it must solve two basic problems: the prior estimation of the surface reflectance (SR) and the hypothesis of the aerosol components.

There are two common tools for solving the first of these problems: spectral SR relationships (SRRs) and SR databases (SRDs). For example, the dark target (DT) method, an official MODIS aerosol retrieval algorithm, uses the simple SRRs between shortwave infrared (SWIR) and visible (VIS) bands as the a priori constraints over dark surface types (i.e., vegetated and dark-soiled regions) and assumes that the SWIR band is initially less affected by the atmosphere [18]. Furthermore, Levy et al. [19] improved these SRRs by considering the scattering angle (SCA or Θ) and vegetation index. However, the DT algorithm cannot be applied to bright land surfaces (i.e., desert and semiarid regions), where the SRRs between SWIR and VIS bands is poor. To address this issue, Hsu et al. [17] proposed a novel algorithm called deep blue (DB), which takes advantage of the fact that bright land surfaces are much darker in the blue spectral region and then constructs absolute VIS SRDs by using the minimum reflectivity technique to determine the constraints. However, due to the presence of clouds, gaps still exist over certain regions even when multiyear data are used [20]. In addition, static SRDs may not be suitable for aerosol retrieval where vegetation cover changes seasonally. Subsequently, Hsu et al. [20] combined the SRR and SRD methods to retrieve aerosol properties over dark and bright land covers. Many researchers have applied spectral SRRs, SRDs, or similar modified methods to sensors other than MODIS and have achieved good results [7,21–26]. In addition to these two common methods, Veefkind et al. [27] proposed a dual-view algorithm (DVA) for ATSR-2, which assumes that the spectral SR ratios between forward and nadir view angles are independent. Thus, the VIS SR ratios can be determined by the SWIR band. However, the DVA method is unreliable over bright surfaces [11]. For the multiangle sensor MISR, Diner et al. [28] applied the mathematical empirical orthogonal functions (EOF) method to remove the surface contribution for aerosol retrieval; the advantage of the EOF method is that it does not need to prescribe the spectral absolute SR or SRRs in advance. However, the implementation of EOF is based on the assumption that the atmosphere is homogeneous

and surface contrast is sufficient in a certain size window. Thus, it requires a reduction in spatial resolution, and it is hard to retrieve the aerosol properties at the intrinsic spatial resolution [29]. For polarized sensor aerosol retrieval, the surface polarized reflectance (SPR) estimation is usually derived using the bidirectional polarization distribution function (BPDF) model [14]. However, the BPDF may yield relatively large estimation errors in some surface types. To solve this problem, Ge et al. [30] provided an alternative approach that utilizes the spectral neutrality characteristic of SPR as a constraint to retrieve higher-precision fine-mode aerosol products. In addition, a statistically optimized algorithm called generalized retrieval of aerosol and surface properties (GRASP) was designed for characterizing atmosphere and surface properties simultaneously from a diversity of remote sensing measurements [31]. The aerosol products of GRASP have been validated as high-quality at a global and regional scale [32,33].

Regarding prior knowledge of the aerosol components, the common method is to construct typical aerosol models using ground-based observations. Aerosol model properties usually include the imaginary and real part of the refractive index, parameters of size distribution, and the single-scattering albedo. For example, Dubovik et al. [34] derived the aerosol absorption and other properties in several key locations based on the long time-series data of global AERONET sites. Omar et al. [35] derived six aerosol models, i.e., biomass burning, urban industrial pollution, rural background, polluted marine, dirty pollution, and desert dust; Levy et al. [36] used the cluster analysis method and derived four aerosol models that varied according to the location and season, i.e., moderately absorbing, absorbing, non-absorbing, and spheroid; and Lee et al. [37] derived six aerosol models for East Asia and showed that the models were strongly affected by their sources. Meanwhile, these aerosol models have been widely used in satellite remote sensing aerosol retrieval [7,19,23,38,39]. However, due to the sites being sparse and distributed unevenly, the aerosol models based on AERONET may not be representative of China. Thus, Li et al. [40] used the long time-series of SONET observations to derive fundamental aerosol models for China.

When the two basic problems have been solved, a look-up table (LUT) method is often used in operational retrieval algorithms, such as the MODIS, VIIRS, AATSR, and MISR, to save computation time. Meanwhile, aerosol products retrieved from different sensors have been well-validated globally [10,41,42]. However, these aerosol products may have the shortcomings of low spatial resolution (e.g., the aerosol products (MXD04) of DT and DB have a spatial resolution of 10 km) and low precision for local and regional research [43–48].

In May 2018, the multiangle multispectral polarized sensor directional polarimetric camera (DPC) onboard the Chinese GaoFen-5 (GF-5 01) satellite was successfully launched [13]. The DPC is equipped with three polarized bands (490, 670, and 865 nm) and five non-polarized bands (443, 565, 763, 765, and 910 nm). The spatial resolution and swath width of the DPC are 3.3 and 1850 km, respectively, and the maximum observation angle of the DPC can be up to 12. The DPC is evidently a powerful tool for monitoring atmospheric parameters such as aerosols, clouds, and water vapor. Unfortunately, due to the failure of the solar panel, DPC observation only lasted until April 2020. It provided us with 13 months of continuous observational data, that is, from March 2019 to March 2020. However, as described above, the current operational algorithms have some shortcomings. Furthermore, most of them do not consider surface anisotropy. Thus, to retrieve high-spatial-resolution and high-precision aerosol products over both dark and bright land cover based on multiangle intensity data from the DPC, a novel aerosol retrieval algorithm based on the visible spectral surface reflectance relationships (VISRR) method was proposed (the detailed VISRR algorithm is introduced in Section 3.3). In addition to the DPC/GF-5 (01), the VISRR algorithm can also be applied to similar sensors, such as the advanced DPCs onboard the Chinese GF-5 (02), carbon monitoring (CM-1), and atmospheric environmental monitoring (DQ-1 and DQ-2) satellites and the European multi-view multi-channel multi-polarization imaging (3MI) onboard EPS-SG, etc. [49]. When combined with the fine-model AOD, e.g., our previous fine-model aerosol algorithm 'spectral neutrality of

surface polarized reflectance' (SNOSPR), based on multiangle polarized data [30], the fine-model aerosol fraction (FMF) can be calculated, which can characterize the weight of aerosols from anthropogenic and natural sources.

This paper is structured as follows: In Section 2, the study area and datasets are presented. Section 3 introduces the basic principles of aerosol retrieval based on satellite remote sensing and the VISRR algorithm. Then, in Section 4, the spatial distribution of daily and average DPC AOD products is presented and compared with that of MODIS products. Then, all aerosol products are validated with ground-based (i.e., AERONET and SONET) products, and the uncertainties regarding the AOD are analyzed and discussed. Section 5 presents the conclusions.

2. Study Area and Datasets

2.1. Study Area

The territory of China was the study area, and its land cover types are shown in Figure 1. According to the MODIS Land Cover Type (MCD12Q1) International Geosphere-Biosphere Programme (IGBP) classification, China has 17 land cover types (as shown in Table 1). The spatial resolution was 500 m [50]. It can be seen that China comprises all surface types, with vast deserts and grasslands distributed in the northwest, croplands mainly located in the east and northeast, forests in the south and northeast, and urban cities mainly distributed in the east and along the coastal area. Furthermore, China is currently the biggest developing country globally and has the largest population; with its rapid development in the past few decades, China has become one of the primary sources of aerosols globally. Thus, satellite aerosol remote sensing over China is necessary and has always been a research hotspot. However, due to the complexity of the aerosol sources and land cover, aerosol retrieval over China is still a great challenge.

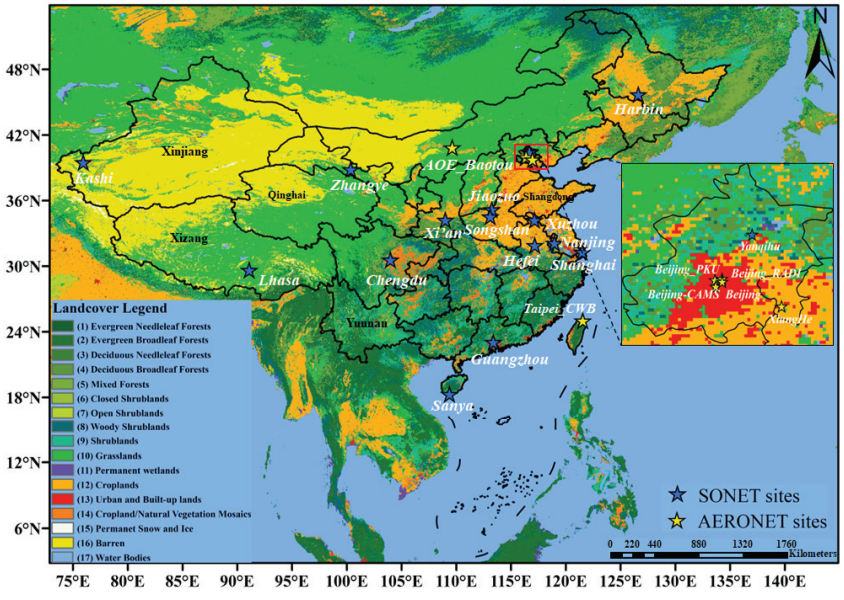


Figure 1. Land cover types of the study area and locations of AERONET (yellow stars) and SONET (blue stars) sites.

Table 1. Seventeen land cover types of MCD12Q1 IGBP classification.

Number	Land Cover Type	Number	Land Cover Type
(1)	Evergreen Needleleaf Forests	(10)	Grasslands
(2)	Evergreen Broadleaf Forests	(11)	Permanent Wetlands
(3)	Deciduous Needleleaf Forests	(12)	Croplands
(4)	Deciduous Broadleaf Forests	(13)	Urban and Built-up Lands
(5)	Mixed Forests	(14)	Cropland/Natural Vegetation Mosaics
(6)	Closed Shrublands	(15)	Permanent Snow and Ice
(7)	Open Shrublands	(16)	Barren
(8)	Woody Savannas	(17)	Water Bodies
(9)	Savannas		

2.2. Datasets

2.2.1. DPC Data

The DPC is the first Chinese multiangle polarized satellite sensor. A two-day revisit period enables the DPC to effectively monitor the temporal variation in aerosols, and it crosses the equator at about 13:30 local solar time. A more detailed introduction to the DPC can be found in Li et al. [15]. According to Zhu et al. [51], the calibration uncertainties of the DPC are about 1–7% depending on the wavelength and view zenith angle. This study used thirteen months (March 2019 to March 2020) of DPC multiangle multispectral (443, 490, 670, and 865 nm) intensity data to retrieve AOD using the VISRR algorithm. The DPC data can be downloaded from the High-Resolution Earth Observation System Grid Platform/Chinese National Space Administration Earth Observation and Data Center website (https://www.cheosgrid.org.cn/) (accessed on 17 May 2022).

2.2.2. MODIS Products

MODIS is a multispectral sensor with 36 channels ranging from 0.412 to 14.2 μm onboard the Terra and Aqua satellites, which cross the equator at about 10:30 and 13:30 local solar time each day, respectively. MODIS has observed the earth for more than 20 years and provided many land and atmospheric products from both the Terra ('MOD') and Aqua ('MYD') satellites. Bands 1–10 (b1–10) are as follows: b1 (620–670 nm), b2 (841–876 nm), b3 (459–479 nm), b4 (545–565 nm), b5 (1230–1250 nm), b6 (1628–1652 nm), b7 (2105–2155 nm), b8 (405–420 nm), b9 (438–448 nm), and b10 (483–493 nm). MODIS products can be downloaded from the website of NASA (https://ladsweb.modaps.eosdis.nasa.gov/) (accessed on 15 August 2022). The MODIS products used here included MYD09; MCD43D; MYD08_D; MCD12Q1; and some aerosol products (MYD04_L2_DT, MYD04_L2_DB, and MYD04_3k_DT). Detailed information on these products is listed in Supplementary Materials Section S1.

2.2.3. Elevation Data

Global Multiresolution Terrain Elevation Data 2010 (GMTED2010) is a global elevation model developed by the U.S. Geological Survey (USGS, https://usgs.gov/) (accessed on 15 August 2022) and National Geospatial Intelligence Agency (NGA), which has three spatial resolutions of about 1 km, 500 m, and 250 m [52]. In this study, GMTED2010 data were used to determine the altitude and correct the influence of Rayleigh scattering for the DPC.

2.2.4. Spectral Library

The USGS spectral library is a reference database containing seven categories of reflectance spectra (artificial materials, coatings, liquids, minerals, organic compounds, soils and mixtures, and vegetation) measured using laboratory, field, and airborne spectrometers [53]. The Spectral Library Version07b (Splib07b) datasets were used to analyze the characteristic variety of the surface spectra between different bands, in order to adjust the spectral response function (SRF) differences between DPC and MODIS for corresponding bands.

2.2.5. Ground-Based Products

Ground-based aerosol products are widely used to validate satellite aerosol remote sensing. AERONET (https://aeronet.gsfc.nasa.gov/) (accessed on 15 August 2022) is a global network established by NASA GSFC (Goddard Space Flight Center) and PHOTONS (PHOtométrie pour le Traitement Opérationnel de Normalisation Satellitaire), according to Giles et al. [1], and the uncertainty of the VIS and NIR AERONET AOD is estimated to be 0.01 for Version 3 (V3) products. However, AERONET sites are rare and distributed unevenly over China. Thus, the Chinese ground-based aerosol observation network SONET (http://www.sonet.ac.cn/en/index.php) (accessed on 15 August 2022) was built by the Chinese Academy of Sciences in collaboration with universities and institutes. The sites of SONET are widely distributed in the typical area of China [2]. In this study, twenty-two AERONET and SONET sites were chosen to validate the DPC and MODIS aerosol products. The spatial distribution and detailed information related to these sites are presented in Figure 1 and Table 2. In addition, these sites were divided into five surface types according to MCD12Q1 [54].

Table 2. Twenty-two ground-based sites of AERONET and SONET and their locations, elevations, surface types, and network.

Number	Site Name	Longitude (°E)	Latitude (°N)	Elevation (m)	Surface Type	Network
1	Hefei	117.162	31.905	36	Cropland	SONET
2	XiangHe	116.962	39.754	36	Cropland	AERONET
3	Zhangye	100.364	38.854	1364	Cropland	SONET
4	AOE_Baotou	109.629	40.852	1314	Grassland	AERONET
5	Lhasa	91.088	29.648	3678	Grassland	SONET
6	Sanya	109.379	18.290	29	Forest	SONET
7	Yanqihu	116.674	40.408	100	Forest	SONET
8	Kashi	75.930	39.504	1320	Mixed	SONET
9	Jiaozuo	113.253	35.187	59	Mixed	SONET
10	Songshan	113.096	34.535	475	Mixed	SONET
11	Beijing	116.381	39.977	92	Urban	AERONET
12	Beijing_PKU	116.310	39.992	53	Urban	AERONET
13	Beijing_RADI	116.379	40.005	59	Urban	AERONET
14	Beijing-CAMS	116.317	39.933	106	Urban	AERONET
15	Chengdu	103.9891	30.5839	510	Urban	SONET
16	Guangzhou	113.381	23.06	28	Urban	SONET
17	Harbin	126.614	45.705	223	Urban	SONET
18	Nanjing	118.957	32.115	52	Urban	SONET
19	Xi'an	109.001	34.223	389	Urban	SONET
20	XuZhou	117.142	34.217	60	Urban	SONET
21	Shanghai	121.481	31.284	84	Urban	SONET
22	Taipei_CWB	121.538	25.015	26	Urban	AERONET

3. Basic Principles and New Methodology

3.1. Surface BRDF Model

This study adopted a linear semi-empirical kernel-driven RossThick LiSparseReciprocal (RTLSR) BRDF model to describe the anisotropic SR [55,56]. The RTLSR model has been widely used in many types of research and has obtained good results [57,58]. Meanwhile, the RTLSR model was adopted to produce MODIS and VIIRS global operational BRDF products [59,60]. The equation of the RTLSR model is as follows:

$$R_{SR}(\lambda, \theta_s, \theta_v, \varnothing) = f_{iso}(\lambda)\, K_{iso}(\theta_s, \theta_v, \varnothing) + f_{vol}(\lambda)\, K_{vol}(\theta_s, \theta_v, \varnothing) + f_{geo}(\lambda)\, K_{geo}(\theta_s, \theta_v, \varnothing) \quad (1)$$

where λ is the wavelength; θ_s, θ_v, and $\varnothing$ are solar zenith angle, sensor zenith angle, and relative azimuth angle, respectively; R_{SR} represents the surface directional reflectance; K_{iso}, K_{vol}, and K_{geo} represent the isotropic, volumetric, and geometric kernels, respectively, where $K_{iso} = 1$, and the expression of K_{vol} and K_{geo}, which are fixed functions and only dependent on the solar and viewing geometry, can be found in Wanner et al. [61]; and $f_{iso}(\lambda)$, $f_{geo}(\lambda)$, and $f_{vol}(\lambda)$ are the coefficients of the three kernels, which were varied according to the wavelength and surface characteristics. Furthermore, Equation (1) could be separated into two terms:

$$R_{SR}(\lambda, \theta_s, \theta_v, \varnothing) = \rho(\lambda)\left[1 + \alpha_1(\lambda)\, K_{vol}(\theta_s, \theta_v, \varnothing) + \alpha_2(\lambda)\, K_{geo}(\theta_s, \theta_v, \varnothing)\right] \quad (2)$$

where $\rho(\lambda) = f_{iso}(\lambda)$ indicates the "reflectance magnitude", which is governed by surface type microphysical properties and changes rapidly with wavelength and time; α_1 and α_2 represent the geometric factor and volumetric factor, respectively; $\alpha_1(\lambda) = \frac{f_{vol}(\lambda)}{f_{iso}(\lambda)}$; and $\alpha_2(\lambda) = \frac{f_{geo}(\lambda)}{f_{iso}(\lambda)}$. The part in the square bracket is the BRDF shape ($BRDF_s$) function (Equation (3)), which is based on the macroscopic structure of the surface types, remains nearly independent of the wavelength, and changes slowly in a short time [62]:

$$BRDF_s = 1 + \alpha_1(\lambda)\, K_{vol}(\theta_s, \theta_v, \varnothing) + \alpha_2(\lambda)\, K_{geo}(\theta_s, \theta_v, \varnothing) \quad (3)$$

3.2. Atmospheric Radiative Transfer Model

Overlying the Lambertian homogeneous surface and under cloud-free, plane-parallel atmosphere conditions, the satellite sensor received reflectance (R_{TOA}) at the top of atmosphere (TOA) can be written as:

$$R_{TOA}(\lambda, \tau, \theta_s, \theta_v, \varnothing) = T_g(R_{atm}(\lambda, \tau, \theta_s, \theta_v, \varnothing) + \frac{T^{\downarrow}(\theta_s) R_{SR} T^{\uparrow}(\theta_v)}{1 - R_{SR} S}) \quad (4)$$

where τ is the optical depth; T_g indicates the gaseous transmission caused by gases such as column water vapor (CWV) and ozone (O_3); R_{atm} refers to the aerosol and molecular intrinsic reflectance; $T^{\downarrow}$ and $T^{\uparrow}$ are transmission; S is the spherical albedo of the atmosphere; and R_{SR} is the angular SR.

SR is an anisotropic Lambertian surface hypothesis can affect the accuracy of the R_{TOA} simulation, especially for multiangle data, ultimately transferring the error to the aerosol retrieval [63]. To avoid this problem in the present study, a fast, accurate, non-Lambertian atmospheric radiative transfer function considering the anisotropy of the surface based on the four-stream theory was adopted. This function has high precision, with mean relative differences in the spectral (range from UV to NIR) TOA simulation of less than 0.7% for different surface types [64]. This forward model has been widely used for aerosol and surface parameter retrieval [65–67], and the equation can be expressed as:

$$R_{TOA}(\lambda, \tau, \theta_s, \theta_v, \varnothing) = T_g(R_{atm}(\lambda, \tau, \theta_s, \theta_v, \varnothing) + \frac{\overrightarrow{T}(\theta_s)^T \boldsymbol{R} \overrightarrow{T}(\theta_v) - e^{-\tau/\theta_s}|\boldsymbol{R}|e^{-\tau/\theta_v} S}{1 - R_{BHR} S}) \quad (5)$$

where $\overrightarrow{T}(\theta_s) = \left[e^{-\tau/\theta_s},\ t_s(\theta_s)\right]^T$; $\overrightarrow{T}(\theta_v) = \left[e^{-\tau/\theta_v},\ t_s(\theta_v)\right]^T$; $t_s(\theta_{s/v})$ refers to the diffuse transmission; $\boldsymbol{R}$ is the reflectance matrix; and $|\boldsymbol{R}|$ is the determinant of $\boldsymbol{R}$.

$$\boldsymbol{R} = \begin{bmatrix} R_{SR} & R_{DHR} \\ R_{HDR} & R_{BHR} \end{bmatrix} \quad (6)$$

$$|\boldsymbol{R}| = (R_{SR} R_{BHR} - R_{DHR} R_{HDR}) \quad (7)$$

where R_{DHR} represents the directional–hemispherical reflectance (DHR), i.e., black-sky albedo (R_{bs}), which describes the diffuse reflection of the incoming direct beam over the hemisphere; R_{HDR} refers to the hemispherical–directional reflectance (HDR), which

describes the direct reflection of the incoming diffuse radiation from the whole hemisphere; and R_{BHR} is the bi-hemispherical reflectance (BHR), i.e., white-sky albedo.

When the coefficients of the three kernels are obtained, the SR for any angle can be calculated with Equation (1). Meanwhile, the R_{DHR} and R_{BHR} can be computed using the following Equations (8)–(11) [67]:

$$R_{DHR}(\lambda, \theta_s) = f_{iso}(\lambda)h_{iso}(\theta_s) + f_{vol}(\lambda)h_{vol}(\theta_s) + f_{geo}(\lambda)h_{geo}(\theta_s) \quad (8)$$

$$R_{HDR}(\lambda, \theta_v) = f_{iso}(\lambda)h_{iso}(\theta_v) + f_{vol}(\lambda)h_{vol}(\theta_v) + f_{geo}(\lambda)h_{geo}(\theta_v) \quad (9)$$

$$R_{BHR}(\lambda) = f_{iso}(\lambda)H_{iso} + f_{vol}(\lambda)H_{vol} + f_{geo}(\lambda)H_{geo} \quad (10)$$

$$h_k(\theta_s) = g_{0k} + g_{1k}\theta_s + g_{2k}{\theta_s}^2 + g_{3k}{\theta_s}^3 \quad (11)$$

where H_k and g_{ik} (i = 0, 1, 2, 3; k = iso, vol, geo) are the regression coefficients listed in Table 3.

Table 3. Regression coefficients used to calculate black-sky and white-sky albedo.

Term g_{ik} for Kernel	k = iso	k = vol	k = geo
g_{0k}	1.0	−0.0374	−1.2665
g_{1k}	0.0	0.5699	−0.1662
g_{2k}	0.0	−1.1252	0.1829
g_{3k}	0.0	0.8432	−0.1489
White-sky integral (H_k)	1.0	0.189184	−1.377622

3.3. VISRR Algorithm

VISRR is a novel AOD retrieval algorithm, which uses the SRRs between VIS bands as constraints and considers the influence of surface anisotropy. VISRR can simultaneously retrieve AOD over dark and bright land covers; the algorithm derivation and retrieval strategies are described in detail below.

3.3.1. SR Characteristics Analysis

Firstly, we used the Splib07b spectral library to analyze which bands were suitable for aerosol retrieval. Figure 2 shows the SRFs of the DPC in the 443, 490, 565, 670, and 865 nm bands (red dotted line) and the corresponding MODIS b9, b10, b5, b1, and b2 bands (gray dotted line). Curves of different colors represent the SR spectral curves of typical surface materials (i.e., blackbrush, sand, brick, and acmite) from Splib07b. From the picture, it can be seen that the surface contribution of VIS is much lower than that of NIR; the SR of non-green vegetation (i.e., sand and brick) is higher than that of green vegetation (i.e., blackbrush); and for green vegetation, there exist two high-reflection peaks near 565 and 865 nm. These features mean that VIS bands are more suitable for aerosol retrieval than NIR bands; aerosol retrieval over green vegetation is easier than over non-green vegetation; and the green band (565 nm) may not be suitable for aerosol retrieval over green vegetation cover. Furthermore, we analyzed the SRRs between the VIS and NIR bands; Figure 3a,b show the SRRs between 490 and 670 nm and between 490 and 865 nm, respectively. It can be seen that the SRRs between VIS bands are more stable than those between VIS and NIR bands, which is consistent with Levy's research [19]. This phenomenon can be explained by the fact that most ground objects have similar spectral reflectance changes in the VIS spectrum range but large changes in the NIR or SWIR bands. Thus, the 443, 490, and 670 nm bands were chosen to build the SRRs in this study.

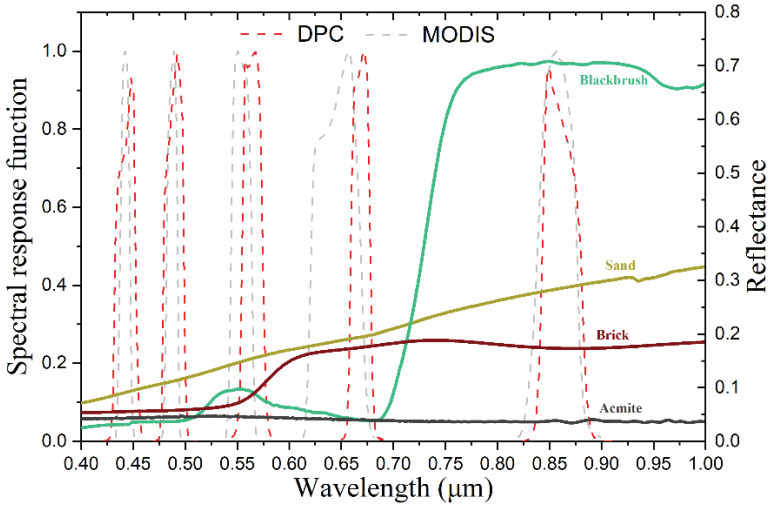


Figure 2. SRFs of DPC (red dotted line) and MODIS (gray dotted line), from left to right, are 443, 490, 565, 670, and 865 nm. The solid lines show the spectral reflectance of typical surface materials in Splib07b, i.e., blackbrush, sand, brick, and acmite, representing vegetation, soil, artificial material, and minerals, respectively. The abscissa represents the wavelength, the left ordinate represents the spectral response function value, and the right represents the surface reflectance value.

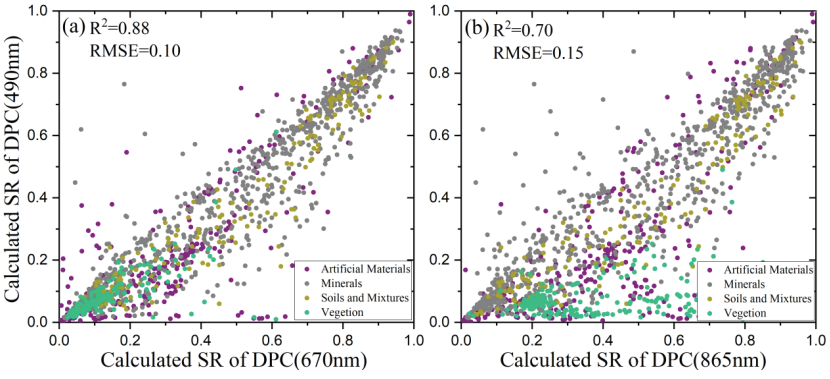


Figure 3. Relationship between SR calculated for DPC 490 and that calculated for 670 nm (**a**) and 865 nm (**b**). The differently colored dots represent different surface materials.

3.3.2. SR Relationship Analysis

Within a satellite sensor's instantaneous field of view, individual pixels detected by the scanning device often include more than one object, especially those with a spatial resolution at the kilometer level. Thus, the determination of SRRs requires real satellite data. Two common methods are used to construct the target sensor's prior knowledge of spectral SR for aerosol retrieval. One is to apply a minimum reflectivity technique [17,68] or atmospheric correction to the target sensor's data [7,19]. This method is suitable for target sensors with long-time-series data that can provide enough samples. The other method is to use the mature SR products from other satellite sensors, such as MODIS [69,70]. This method is generally applicable to new sensors. In this study, owing to the limitation of the relatively small amount of DPC data, the second method was chosen, and three years (2016–2018) of MYD09 SR products pertaining to China and its surrounding areas (Figure 1) were used to derive the DPC equivalent spectrum SR over different surface types. To ensure

the accuracy of the SR, only the pixels with an AOD at 470 nm smaller than 0.2 and the highest quality assurance (QA) of MYD09 were chosen for analysis.

However, two problems needed to be solved beforehand, since DPC and MODIS differ in terms of spatial resolution (3.3 versus 1 km) and SRFs (as shown in Figure 2). To make the spatial resolution consistent, about 3 × 3 pixels of MYD09 and MYD03 were averaged at 3.3 km. As shown in Figure 2, the SRFs of DPC and MODIS do not exactly match; if we did not consider these differences, it would have led to errors in the derived equivalent spectral SR of DPC and affected the accuracy of the aerosol retrieval [70]. We adopted the singular-value decomposition (SVD) method to predict the DPC equivalent spectral SR from the corresponding MODIS channels to solve this problem. The steps were as follows: (1) we used the SRFs and the spectral curves of typical surface materials from Splib07b to calculate the DPC and MODIS spectral SR; (2) we calculated the SVDs, which included the singular vectors V_{modis} and V_{DPC}, based on the calculated spectral SR from step (1); (3) we used the V_{modis} and MYD09 SR products to calculate the conversion coefficient vector C; and (4) the DPC equivalent spectrum SR could be calculated using the C and the V_{DPC}. Detailed information on this method can be found in Sayer et al. [70].

After obtaining the equivalent spectrum SR and geometric information on the DPC over different surface types (except for permanent snow, ice, and water), we analyzed the SRRs between 443, 490, and 670 nm. The normalized difference vegetation index (NDVI) is an important adjustment parameter to estimate the SR for aerosol retrieval [19,20,71], and it can be calculated by the SR of 670 and 865 nm using Equation (12):

$$NDVI = \frac{SR(865) - SR(670)}{SR(865) + SR(670)} \tag{12}$$

The statistical results of the SRRs are shown in Figure 4. It can be seen that the Pearson correlation coefficient (R) of 443 versus 670 nm ranged from 0.82 to 0.98, the root mean square error (RMSE) ranged from 0.003 to 0.012, and the average SR ratios (K_{443_670}) over different surface types varied from 0.43 to 0.63. For 490 and 670 nm, the R ranged from 0.90 to 0.99, the RMSE ranged from 0.002 to 0.011, and the K_{490_670} over different surface types varied from 0.51 to 0.68. These statistical parameters showed that: (1) the SRRs between VIS bands had a high correlation, which was consistent with the conclusion of Section 3.3.1; (2) the SRRs between VIS bands needed to be divided according to the surface types due the substantial differences; (3) the correlation of SRRs between 490 and 670 nm was higher than that between 443 and 670 nm overall; and (4) the NDVI could indicate the surface type and the change in the SR over time to a certain extent—for example, the NDVI of evergreen vegetation (e.g., Figure 4(1,2)) usually has a high value, while over bare soil (e.g., Figure 4(16)) it has a low value. When the surface types vary significantly with the seasons, the NDVI also has a wider range of changes (e.g., Figure 4(10,13)). It is necessary to consider surface types and NDVI when using the SRRs between VIS bands as constraints for aerosol retrieval.

In addition, to make the SRRs between VIS bands more accurate, the SCA was also taken into account when determining the K_{443_670} and K_{490_670} over different surface types. The final values of K_{443_670} and K_{490_670} over each typical surface type are shown in Tables 4–8 (mixed forests, grasslands, croplands, urban and built-up lands, and barren land). The NDVI was set from 0 to 1 with an interval of 0.2; the SCA was set from 60° to 100° and from 100° to 180° with an interval of 20°. The ratios over other surface types (i.e., (1)–(4), (6)–(9), (14), and (18)–(21)) are shown in Supplemental Materials Section S2, Tables S1–S10.

$$\Theta = cos^{-1}(-cos\theta_s cos\theta_v - sin\theta_s sin\theta_v cos\varnothing) \tag{13}$$

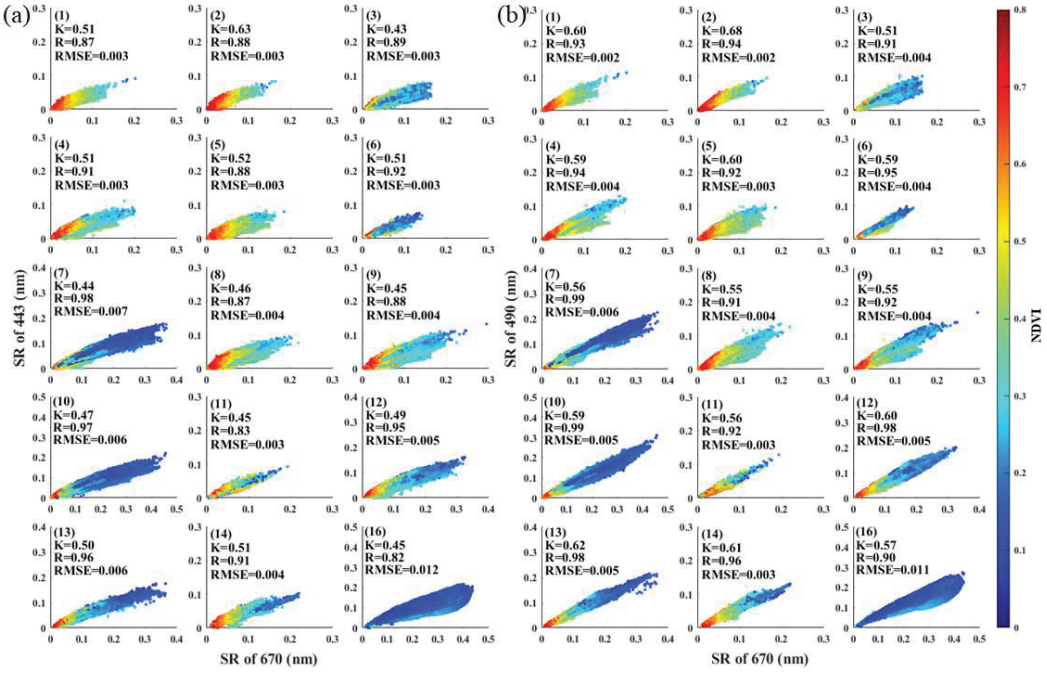


Figure 4. SRRs between DPC (**a**) 443 and (**b**) 490 versus 670 nm, respectively. The serial numbers (1)–(16) of each subgraph (except for (15) permanent snow and ice and (17) water) represent different surface types, as shown in Figure 1. The abscissa represents the SR of 670 nm, and the ordinate represents (**a**) 443 and (**b**) 490 nm, respectively. The color bar represents the NDVI value.

Table 4. Variation in K_{443_670} and K_{490_670} with NDVI and SCA over (5) mixed forests.

NDVI/SCA	(60°, 100°)		(100°, 120°)		(120°, 140°)		(140°, 160°)		(160°, 180°)	
	K_{443_670}	K_{490_670}	K_{443_670}	K_{490_670}	K_{443_670}	K_{490_670}	K_{443_670}	K_{490_670}	K_{443_670}	K_{490_670}
(0.0, 0.2)	0.51	0.68	0.49	0.60	0.47	0.57	0.49	0.58	0.56	0.60
(0.2, 0.4)	0.49	0.61	0.50	0.61	0.48	0.56	0.51	0.59	0.56	0.62
(0.4, 0.6)	0.49	0.64	0.50	0.63	0.47	0.57	0.52	0.61	0.59	0.65
(0.6, 0.8)	0.53	0.64	0.51	0.63	0.51	0.62	0.53	0.61	0.59	0.64
(0.8, 1.0)	0.51	0.62	0.51	0.62	0.58	0.66	0.62	0.65	0.62	0.62

Table 5. Same as Table 4, but for (10) grasslands.

NDVI/SCA	(60°, 100°)		(100°, 120°)		(120°, 140°)		(140°, 160°)		(160°, 180°)	
	K_{443_670}	K_{490_670}	K_{443_670}	K_{490_670}	K_{443_670}	K_{490_670}	K_{443_670}	K_{490_670}	K_{443_670}	K_{490_670}
(0.0, 0.2)	0.49	0.68	0.43	0.53	0.43	0.54	0.48	0.56	0.49	0.52
(0.2, 0.4)	0.53	0.65	0.44	0.56	0.45	0.55	0.46	0.55	0.44	0.50
(0.4, 0.6)	0.51	0.65	0.42	0.55	0.44	0.56	0.47	0.57	0.48	0.54
(0.6, 0.8)	0.53	0.64	0.48	0.62	0.48	0.60	0.48	0.57	0.49	0.55
(0.8, 1.0)	0.53	0.64	0.53	0.64	0.56	0.64	0.59	0.65	0.56	0.61

Table 6. Same as Table 4, but for (12) croplands.

NDVI/SCA	(60°, 100°)		(100°, 120°)		(120°, 140°)		(140°, 160°)		(160°, 180°)	
	K_{443_670}	K_{490_670}	K_{443_670}	K_{490_670}	K_{443_670}	K_{490_670}	K_{443_670}	K_{490_670}	K_{443_670}	K_{490_670}
(0.0, 0.2)	0.47	0.61	0.50	0.64	0.45	0.57	0.44	0.54	0.52	0.61
(0.2, 0.4)	0.49	0.62	0.52	0.64	0.52	0.65	0.45	0.56	0.43	0.52
(0.4, 0.6)	0.46	0.60	0.50	0.66	0.46	0.63	0.46	0.57	0.46	0.55
(0.6, 0.8)	0.53	0.67	0.51	0.65	0.50	0.65	0.47	0.57	0.47	0.56
(0.8, 1.0)	0.57	0.65	0.57	0.65	0.57	0.65	0.63	0.68	0.63	0.68

Table 7. Same as Table 4, but for (13) urban and built-up lands.

NDVI/SCA	(60°, 100°)		(100°, 120°)		(120°, 140°)		(140°, 160°)		(160°, 180°)	
	K_{443_670}	K_{490_670}	K_{443_670}	K_{490_670}	K_{443_670}	K_{490_670}	K_{443_670}	K_{490_670}	K_{443_670}	K_{490_670}
(0.0, 0.2)	0.49	0.62	0.47	0.60	0.49	0.60	0.52	0.60	0.56	0.63
(0.2, 0.4)	0.48	0.60	0.47	0.60	0.49	0.60	0.52	0.60	0.55	0.61
(0.4, 0.6)	0.50	0.64	0.48	0.63	0.49	0.62	0.52	0.62	0.53	0.61
(0.6, 0.8)	0.48	0.61	0.48	0.62	0.50	0.63	0.52	0.63	0.54	0.62
(0.8, 1.0)	0.49	0.62	0.49	0.64	0.52	0.64	0.53	0.62	0.54	0.63

Table 8. Same as Table 4, but for (16) barren land.

NDVI/SCA	(60°, 100°)		(100°, 120°)		(120°, 140°)		(140°, 160°)		(160°, 180°)	
	K_{443_670}	K_{490_670}	K_{443_670}	K_{490_670}	K_{443_670}	K_{490_670}	K_{443_670}	K_{490_670}	K_{443_670}	K_{490_670}
(0.0, 0.2)	0.45	0.70	0.49	0.63	0.49	0.62	0.52	0.60	0.50	0.54
(0.2, 0.4)	0.52	0.64	0.50	0.63	0.51	0.63	0.52	0.61	0.50	0.55
(0.4, 0.6)	0.51	0.60	0.51	0.66	0.51	0.63	0.53	0.62	0.51	0.58
(0.6, 0.8)	0.46	0.56	0.50	0.64	0.54	0.64	0.54	0.63	0.52	0.58
(0.8, 1.0)	0.57	0.64	0.57	0.64	0.60	0.68	0.61	0.67	0.52	0.57

3.3.3. Aerosol Models

The aerosol model is another essential prior knowledge component, and its accuracy plays a vital role in the satellite remote sensing of aerosols [72]. Several global and regional aerosol models derived from AERONET measurements [35–37] have been used for many research satellite aerosol retrieval methods. However, these models may not be very representative in China, where ground-based sites are sparse and distributed unevenly. For example, the aerosol models used in the VIIRS enterprising processing system (EPS) aerosol retrieval algorithm have been validated as unsatisfactory in China [44]. Thus, based on the long-time-series data of the SONET, Li et al. [40] used the K-means cluster analysis approach and obtained ten fundamental aerosol models for China, including five typical fine-particle aerosol models ((1) urban polluted, (2) secondary polluted, (3) combined polluted, (4) polluted fly ash, and (5) continental background) and five coarse models ((6) summer fly ash, (7) winter fly ash, (8) primary dust, (9) transported dust, and (10) background dust). Li et al. [40] also provided the probability of the appearance of fine-mode aerosols and coarse-mode aerosols. In this study, we adopted the six combinations with the highest probability of appearance for aerosol retrieval, i.e., urban polluted and summer fly ash, secondary polluted and summer fly ash, combined polluted and winter fly ash, continental background and background dust, continental background and winter fly ash, and continental background and transported dust. The microphysical parameters of these aerosol models can be found in Li et al. [40].

3.3.4. Retrieval Scheme

In this study, the VISRR algorithm was implemented based on the precalculated LUTs, which were built by the second simulation of a satellite signal in the solar spectrum

vector (6SV) radiative transfer (RT) model [73]. The input parameters of the 6SV RT model included the SRFs of DPC 443, 490, 670, and 865 nm; six combinations of fine-mode aerosols and coarse-mode aerosols, as shown in Section 3.3.3; θ_s and θ_v ranging from 0° to 80° with an interval of 6°; ∅ ranging from 0° to 180° with an interval of 12°; 11 AOD values (550 nm)—0, 0.01, 0.25, 0.5, 1, 1.5, 2, 2.5, 3, 4, 5; and elevation set to sea level. Then, atmospheric parameters (i.e., R_{atm}, $\overrightarrow{T}(\theta_s)$, $\overrightarrow{T}(\theta_v)$, $t_s(\theta_s)$, and $t_s(\theta_v)$ in Equation (4)) for various observational and atmospheric scenarios were built in the LUTs. Similarly, the LUTs of CWV and O_3 gas transmission were also built by the 6SV RT model. The value of CWV was set in the range of 0 to 7 g/cm^2 with an interval of 0.5, and the value of O_3 was set in the range of 0 to 5 cm-atm with an interval of 0.5. In this study, the prior knowledge of BRDF shape (Equation (3)) was assumed to be unchanged for one month and independent of bands [62,65]. When the LUTs and related auxiliary data were ready, the VISRR algorithm could be performed based on the multiangle multispectral DPC intensity data. All procedures were applied to the individual pixels, and the output result at each pixel was recorded. The schematic flowchart is shown in Figure 5, and the specific retrieval steps are described below.

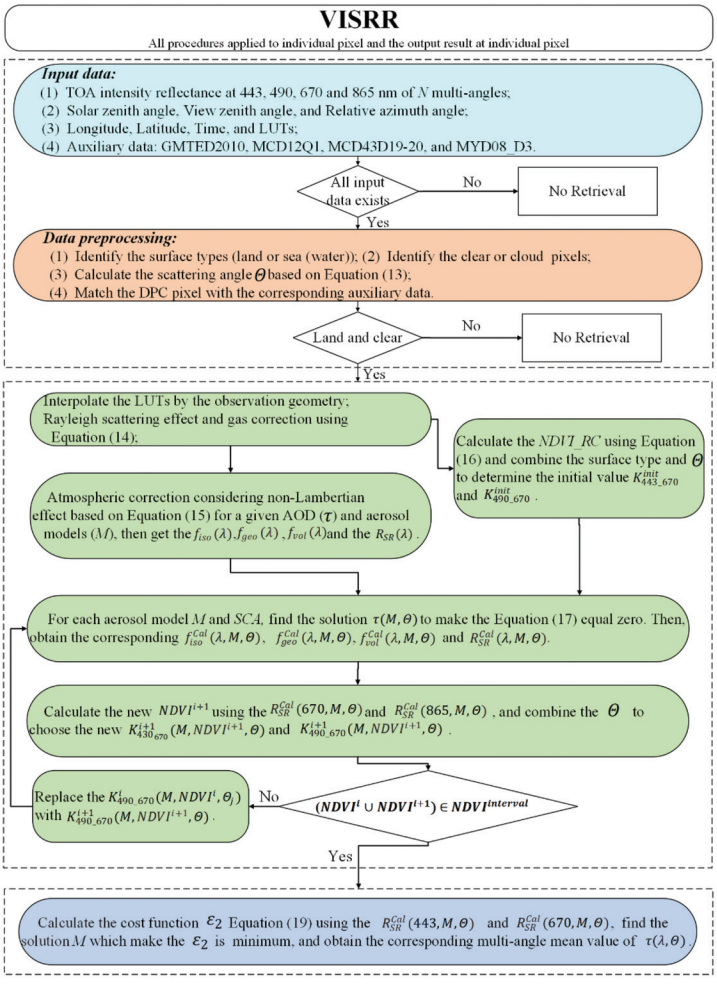


Figure 5. Flowchart of the main steps of the VISRR aerosol and surface retrieval algorithm.

(a) Preprocessing the input data

The input parameters of the DPC included the measured TOA reflectance ($R_{TOA}^{Meas}(\lambda)$) of 443, 490, 670, and 865 nm, with N (maximum of 12) multiangle ($\theta_s, \theta_v, \varnothing$), and the auxiliary datasets included month-averaged MCD43D19-21, MYD08_D3, GMTED2010, MCD12Q1, and the LUTs.

The first step was the identification of the land surface type for each pixel using the MCD12Q1 products; second was the recognition of cloud-contaminated pixels, as only cloud-free and land (except for permanent snow, ice, or inland water) pixels were further processed in the next step; and third was to match and extract the auxiliary data according to the longitude, latitude, the corresponding geometric factor α_1 and volumetric factor α_2 of the BRDF shape, the daily O_3 and CWV, and the elevation from the month-averaged MCD43D19-20, MYD08_D3, and GMTED2010 products. The global mean values were adopted if the O_3 and CWV were missing from MYD08_D3, as shown in Levy et al. [74].

(b) Atmospheric correction method considering the non-Lambertian effect

(1) According to the observation angle ($\theta_s, \theta_v, \varnothing$), the atmospheric parameters $R_{atm}(\lambda, \tau, \theta_s, \theta_v, \varnothing)$, $\overrightarrow{T}(\lambda, \theta_s)$, $\overrightarrow{T}(\lambda, \theta_v)$, and S varied with τ and aerosol model (M), and the gas transmission $T_g(\lambda)$ varied with CWV and O_3, as could be interpolated from the LUTs.

(2) We utilized the Rayleigh scattering correction method proposed by Fraser et al. [75] to remove its contribution to the reflectance at TOA [19] and then obtained the gas corrected reflectance ($R_{TOA}^{Meas_gasc}(\lambda)$).

$$R_{TOA}^{Meas_gasc}(\lambda) = R_{TOA}^{Meas}(\lambda)/T_g(\lambda) \tag{14}$$

(3) Considering the non-Lambertian characteristics of the surface, the atmospheric correction (AC) was implemented to calculate accurate directional surface reflectance $R_{SR}(\lambda)$. The AC equation is Equation (15), and the detailed derivation process is shown in Supplementary Section S3.

$$F_1 = \frac{f_{iso}(\lambda)(F_2' - F_3')}{1 - f_{iso}(\lambda)F_4'} \tag{15}$$

where the definitions of F_1, F_2', F_3', F_4' can be found in Supplementary Section S3. Then, the three kernel coefficients $f_{iso}(\lambda)$, $f_{geo}(\lambda)$, and $f_{vol}(\lambda)$ of the RTLSR BRDF model and the directional surface reflectance $R_{SR}(\lambda)$ could be obtained as follows: $f_{iso}(\lambda) = F_1/(F_2'+F_3' + F_4' * F_1)$, $f_{vol}(\lambda) = f_{iso}(\lambda)\alpha_1$, $f_{geo}(\lambda) = f_{iso}(\lambda)\alpha_2$, $f_{geo}(\lambda) = f_{iso}(\lambda)\alpha_2$, $R_{SR}(\lambda) = f_{iso}(\lambda)BRDF_s$.

(c) Determination of the initial NDVI value and prior knowledge of K_{443_670} and K_{490_670}

The NDVI is an important adjustable parameter for estimating SR and has been widely used for aerosol retrieval. However, the NDVI usually cannot be obtained before aerosol retrieval due to the effects of the atmosphere. Thus, some researchers directly use the reflectance at TOA to calculate the NDVI (NDVI_TOA) [76,77] or use the Rayleigh corrected reflectance at TOA to calculate the NDVI (NDVI_RC) to reduce the impact of the atmosphere [20,78]. However, NDVI_TOA and NDVI_RC are still susceptible to aerosols and rapidly decrease with increasing AOD [79–81]. The use of NDVI_TOA or NDVI_RC can lead to the selection of the wrong K_{443_670} and K_{490_670} values (as shown in Tables 3–7) under some atmospheric conditions and can cause further errors in aerosol retrieval. Thus, to solve this problem, we developed a novel iterative AC method to calculate the real NDVI. Firstly, we used the Rayleigh scattering and gas correction NDVI_RC, which was calculated via Equation (16), as the initial NDVI value (recorded as $NDVI^{init}$); then, after combining the SCA and surface type, the initial $K_{443_670}^{init}$ and $K_{490_670}^{init}$ could be determined as:

$$\text{NDVI_RC} = \frac{R_{TOA}^{Meas_gasc}(865) - R_{TOA}^{Meas_gasc}(670)}{R_{TOA}^{Meas_gasc}(865) + R_{TOA}^{Meas_gasc}(670)} \tag{16}$$

(d) AOD retrieval

There were three problems to be solved in this step. The first was the determination of the solution τ for each aerosol model, the second was the determination of the NDVI, and the third was the determination of the best aerosol model. The steps are described in detail as follows:

(1) For each aerosol model M and Θ, we found the solution $\tau(M, \Theta)$ that made the cost function ε_1 (Equation (17)) equal to 0 (i.e., $\varepsilon_1 = 0$). Then, we obtained the $R_{SR}^{Cal}(\lambda, M, \Theta)$ of 443, 490, 670, and 865 nm:

$$\varepsilon_1(M, \Theta) = \frac{R_{SR}^{Cal}(490, M, \Theta_j, \tau)}{R_{SR}^{Cal}(670, M, \Theta_j, \tau)} - K_{490_670}^{i}(M, NDVI^i, \Theta_j) \quad (17)$$

where $R_{SR}^{Cal}(\lambda, M, \Theta, \tau)$ is the directional surface reflectance calculated using the AC method considering the non-Lambertian effect, as shown in step (c); the superscript i of $NDVI^i$ and $K_{490_670}^{i}$ represents the number of iterations; and the $NDVI^{init}$ and $K_{490_670}^{init}$ determined in step (d) are the initial values of the iteration (i.e., i = 0).

(2) We calculated the new $NDVI^{i+1}$ using the $R_{SR}^{Cal}(670, M, \Theta)$ and $R_{SR}^{Cal}(865, M, \Theta)$ obtained from step (1) and determined the new $K_{430_{670}}^{i+1}(M, NDVI^{i+1}, \Theta)$ and $K_{490_670}^{i+1}(M, NDVI^{i+1}, \Theta)$ values using the $NDVI^{i+1}$ and Θ. Then, we considered Formula (18); if the $NDVI^i$ and $NDVI^{i+1}$ belonged to the same NDVI interval ($NDVI^{interval}$) defined in Section 3.3.2, we proceeded to step (3). Otherwise, we repeated (1) and (2) until Formula (18) was satisfied.

$$(NDVI^i \cup NDVI^{i+1}) \in NDVI^{interval} \quad (18)$$

(3) We calculated the cost function ε_2 (Equation (19)) using $R_{SR}^{Cal}(443, M, \Theta)$, $R_{SR}^{Cal}(670, M, \Theta)$, and $K_{430_{670}}^{i+1}(M, NDVI^{i+1}, \Theta)$, with some fitting error; the solution M was that which minimized ε_2. Then, the corresponding multiangle mean value of $\tau(550\text{ nm}, \Theta)$ was the retrieval solution $\tau(550\text{ nm})$.

$$\varepsilon_2 = \sqrt{\frac{1}{N}\sum_{j=1}^{N}\left(\frac{R_{SR}^{Cal}(443, M, \Theta_j)}{R_{SR}^{Cal}(670, M, \Theta_j)} - K_{443_670}^{i+1}(M, NDVI^{i+1}, \Theta_j)\right)^2} \quad (19)$$

4. Results and Discussion

4.1. Case Results over Typical Surface Covers

Figure 6 shows the spatial distribution of the DPC AOD (550 nm) products retrieved from the VISRR on 3 April 2019 over eastern China; the main surface types of this region are grass, croplands, urban land, and water (lake and sea), as shown in Figure 1. Figure 6a is the DPC TOA true-color image (RGB) consisting of $R_{TOA}^{Meas}(670)$, $R_{TOA}^{Meas}(565)$, and $R_{TOA}^{Meas}(490)$. It can be seen that most regions were cloud-free, except for some areas in the south and west, where an obvious strip of white cloud and some flocculent clouds existed; in addition, grey haze aerosols were distributed in most areas and blurred the surface. Figure 6b shows the DPC AOD (3.3 km) products: the blank areas represent those pixels identified as clouds, ice, and water; the blue regions with a low AOD (<0.2) indicate a clean atmosphere and were mainly distributed in the northern and eastern parts of the Shandong peninsula; the slight-pollution ($0.25 < \text{AOD} < 0.5$) regions were spread over southern Beijing–Tianjin–Hebei (BTH), western Shandong, northern Jiangsu, etc.; and moderate- and heavy-pollution regions with a high AOD (>0.5) could be found over most areas of Henan, central Anhui, and southern Jiangsu. Meanwhile, the DPC surface products' RGB consisting of $R_{SR}(670)$, $R_{SR}(565)$, and $R_{SR}(490)$ is shown in Figure 6c. It can be seen that the surface features became more distinguishable after removing the coupling effect of the atmosphere. In addition, the AOD products of the MYD04_3k_DT AOD (3 km), MYD04_L2_DB AOD (10 km), and MYD04_L2_DT AOD (10 km) results were chosen for comparison and are shown in Figure 6c–e, respectively. Overall, the spatial distribution between the DPC

and MODIS AOD products was similar, but there were some differences. First, the AOD from the DPC and MYD04_L2_DB had high spatial coverage. However, the products from MODIS DT were missing in areas such as BTH and the Liaoning region, even if there was no cloud shown in the TOA reflectance RGB. The reason for this might be that the pixels were over-recognized as clouds, or that the DT algorithm cannot be implemented over bright land cover. Second, the spatial resolutions of the DPC and MYD04_3k_DT AOD were 3.3 km (individual pixel) and 3 km, respectively, while that of the MYD04_L2_DT and MYD04_L2_DB AOD was 10 km. In addition to the increased detail, the variations between different gradients of 3.3 or 3 km AOD products are also smoother than those of 10 km products. Third, the four AOD products were of different magnitudes on the whole; the DT AOD products had the highest value, while the DPC products had the lowest value. In this case, the DPC VISRR algorithm can simultaneously retrieve AOD products with the advantages of fine spatial resolution and high coverage.

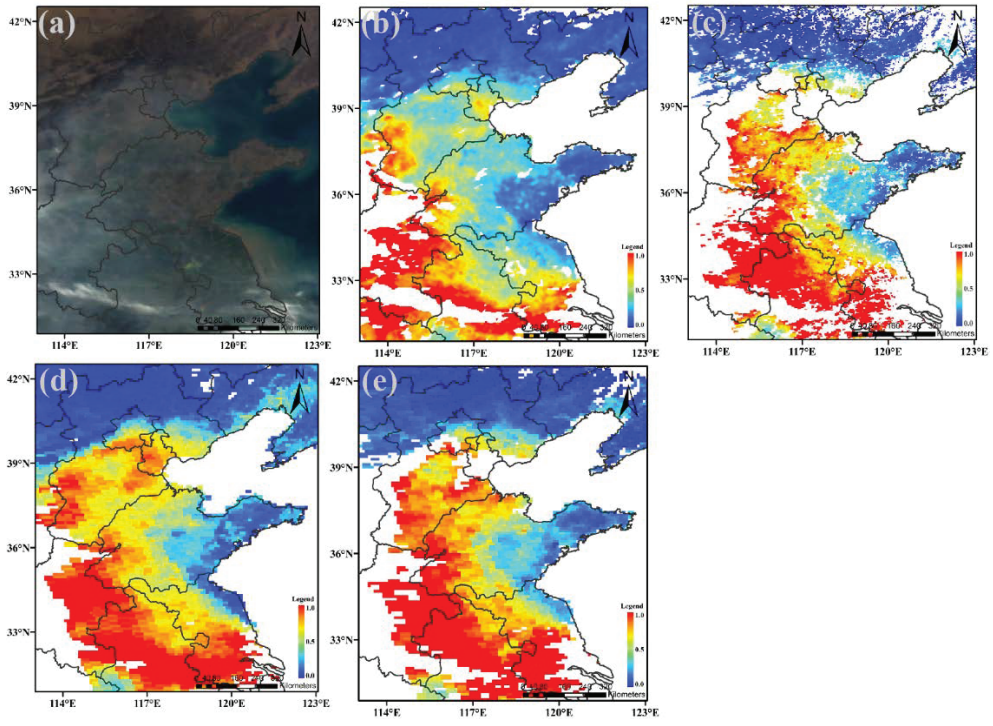


Figure 6. AOD (550 nm) distribution on 3 April 2019: (**a**) DPC true-color image (670,565 and 490 nm) of TOA, (**b**) DPC AOD (3.3 km) results from VISRR, (**c**) AOD (3 km) results from MYD04_3k_DT, (**d**) AOD (10 km) results from MYD04_L2_DB, (**e**) AOD (10 km) results from MYD04_L2_DT.

Figure 7 shows another example of AOD products over western China and its surrounding areas on 30 May 2019, where the main surface types are barren land, grass, permanent snow, ice, and water (lake). From the TOA RGB (a), it can be seen that the permanent snow and ice cover was mainly located in the Himalayas, Kunlun, and the Tianshan Mountains. Thick, thin, and broken clouds were distributed in the Qinghai–Tibet Plateau and east of the Taklimakan Desert. Figure 7b presents the AOD products retrieved from the DPC, which show that the high aerosol loadings were distributed in the oases around the Taklimakan Desert and the Tarim River. Figure 7c–e display the AOD products of MODIS. It is evident that the DT algorithm is ineffective when applied to bright land cover compared to the VISRR and DB products. The DPC AOD products had a higher

value over north Taklimakan and were more detailed than the DB products due to their fine spatial resolution.

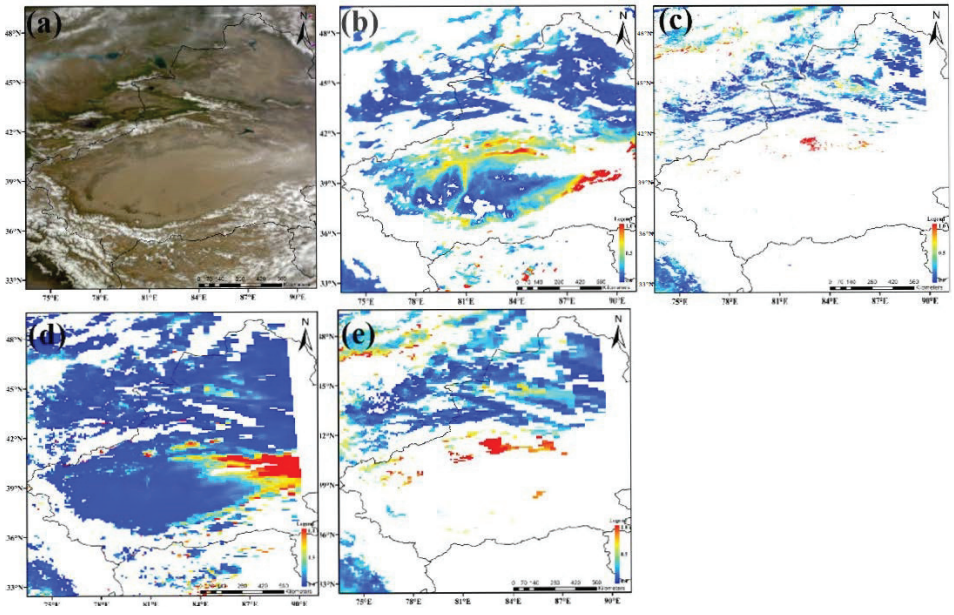


Figure 7. AOD (550 nm) distribution on 30 May 2019: (**a**) DPC true-color image (670,565 and 490 nm) of TOA, (**b**) DPC AOD (3.3 km) results from VISRR, (**c**) AOD (3 km) results from MYD04_3k_DT, (**d**) AOD (10 km) results from MYD04_L2_DB, (**e**) AOD (10 km) results from MYD04_L2_DT.

4.2. Average Results over the Study Area

Figure 8a shows the average DPC VISRR AOD products (March 2019 to March 2020) over China. There were four main high-value regions: (1) the northern and eastern plain of China, mainly including BTH, Shandong, Henan, Anhui, and Shanghai, where the aerosol emissions may be related to the fact that this region contains the largest population and the most industries; (2) the Sichuan Basin, mainly including eastern Sichuan and western Chongqing, where, in addition to industrial emissions, topographic and meteorological factors contribute to aerosol pollution [82,83]; (3) southern China, mainly including the south of Yunnan, Guangxi, and Hainan, where smoke aerosol pollution is transported in significant amounts from biomass burning in Southeast Asia [84,85]; (4) western China, mainly including the Taklimakan Desert and its surrounding areas—Taklimakan is the largest desert in China, and dust events often break out here, which are likely responsible for the aerosol pollution over this region [86]. Figure 8b–d present the AOD products from MYD04_3k_DT, MYD04_DB, and MYD04_DT and compare them with the MODIS products. In general, the spatial distributions of the AOD between the DPC and MODIS were similar. However, the AOD magnitude differed in that the MODIS AOD products were slightly higher than those of the DPC over northeastern China and the Qinghai–Tibet Plateau region. According to the validation of He et al. [47], MODIS 3 km and 10 km aerosol products are generally overestimated over China, and the error derives from two main sources. The first is the surface reflectance, and the second is the aerosol models in the LUT.

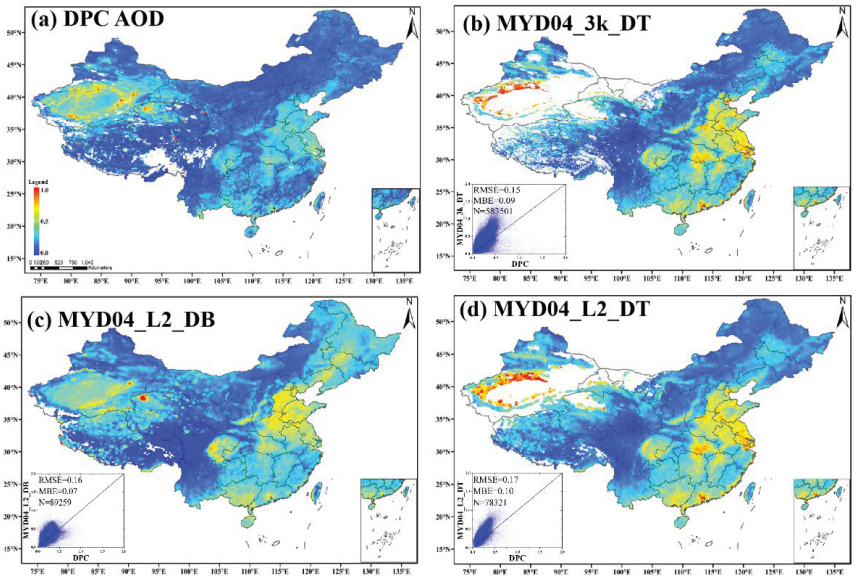


Figure 8. Spatial distribution of average AOD products from March 2019 to March 2020. (**a**) DPC AOD (3.3 km) products from VISRR, (**b**) AOD (3 km) results from MYD04_3k_DT, (**c**) AOD (10 km) results from MYD04_L2_DB, (**d**) AOD (10 km) results from MYD04_L2_DT. The scatter plots on the bottom left of subgraph (**b**,**c**) show the comparison between DPC and MODIS AOD products, based on the spatial interpolation of DPC data. The RMSEs between DPC and MYD04_3k_DT, MYD04_L2_DB, and MYD04_L2_DT were 0.15, 0.16, and 0.17, and the mean bias errors (MBEs) were 0.09, 0.07, and 0.10, respectively.

4.3. Validation Using Ground-Based Aerosol Products

In this study, twenty-two AERONET and SONET sites (Figure 1 and Table 2) were chosen to validate the AOD (550 nm) products from the DPC and MODIS. Due to the lack of ground-based measurements with 550 nm AOD products, a second-order polynomial fitting method was chosen to calculate the 550 nm AOD using the 440, 500, and 675 nm values [87]. Furthermore, for the spatiotemporal matching between the ground and the satellites, the ground-based valid AOD products were averaged within one hour (30 min before or after the overpass of the satellite), and the satellite-based available AOD products were averaged within a sampling window (5×5 pixels) centered on the ground site [88]. Figure 9 shows the validation results for the DPC (a) and MODIS (MYD04_3k_DT (b), MYD04_L2_DB (c), and MYD04_L2_DB (d)) AOD products compared to the ground-based products from March 2019 to March 2020. $y = a \times x + b$ is a linear fitting equation, where a and b are the slope and intercept, respectively; N is the number of AOD pairs; and the good fraction (Gfrac) refers to the fraction of AOD pairs within the expected error $EE = \pm(0.05+20\%)$. The evaluating indicators of the four aerosol products (a–d) were as follows: a and b were (0.96, 0.01), (1.03, 0.12), (0.98, 0.05), and (0.97, 0.1); the R was 0.88, 0.87, 0.82, and 0.87; the RMSE was 0.17, 0.21, 0.27, and 0.20; the N was 971, 1413, 2539, and 1997; and the Gfrac(s) was 62.7%, 51.7%, 60.6%, and 58.5%. The best evaluating indicators are presented in bold. The fact that the revisitation period of the DPC was longer than that of MODIS caused the total number of collected DPC AOD retrievals to be the lowest. At the same time, MYD04_L2_DB had the most retrieval results. The slopes of all products were close to 1; however, the DPC AOD products had the lowest intercept and RMSE and the highest R and Gfrac, demonstrating that the DPC AOD products had the highest accuracy over the study area. Specifically, compared with the AOD products at the 3 km level (i.e., Figure 9a versus Figure 9b), although they had a similar R value (0.88 vs. 0.87), the

MYD04_3k_DT products had a low Gfrac (51.7%), a slope (1.03) greater than 1, and a high bias of intercept (0.12), revealing that these AOD products were generally overestimated. Compared with the AOD products at the 10 km level (i.e., Figure 9a versus Figure 9c,d), although they had similar Gfrac values (62.7%, 60.6%, and 58.5%), the MYD04_L2_DB products had a high RMSE (0.27) and a low R (0.82), and the MYD04_L2_DT products were similar to MYD04_3k_DT with a high bias of intercept (0.1). The slope smaller than 1 and the intercept greater than 0 implied that these AOD products were overestimated for small values but underestimated for large values. The validation results of three MODIS AOD products in this study were consistent with previous research [47,54].

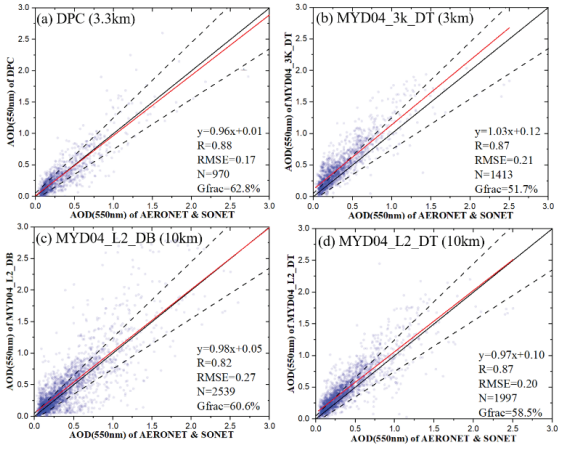


Figure 9. Validation of AOD (550 nm) products between ground-based and satellite-based measurements: (**a**) DPC (3.3 km), (**b**) MYD04_3k (3 km), (**c**) MYD04_L2_DB (10 km), and (**d**) MYD04_L2_DT (10 km). Black solid and dashed lines are the 1:1 lines and EE (±(0.05 + 20%) envelope lines, respectively. Blue dots and red fitting lines represent the satellite-based and ground-based measurements, respectively.

To better understand and analyze the uncertainties of the DPC VISRR AOD products, Figure 10 shows the validation results over different land cover types: (a) urban, (b) cropland, (c) mixed, (d) forest, and (e) grassland. The evaluating indicators over the four surface types (a–d) are shown in Table 9, where the best evaluating indicators are presented in bold. There were 12 ground-based sites covering urban land; therefore, most of the collected DPC AOD retrievals were over this surface type. The slopes and intercepts of all the products were close to 1 and 0; the R was higher than 0.85, and the RMSE was lower than 0.22. Specifically, the accuracy of the DPC AOD over forests and croplands was highest among the surface types, with Gfrac values of 77.3% and 69.3%, respectively. The reasons for this can be summarized as follows: (1) compared to bright land cover, aerosol retrieval over vegetation (dark) surface types has advantages, as the surface signal accounts for a relatively low proportion of the VIS reflectance at TOA; (2) the VIS SRR with the NDVI and SCA constraints proposed in this study can well express the change in vegetation with time. The Gfrac (61.6%) of urban land was lower than that of forests and croplands, possibly because urban land cover is very complex, consisting of buildings, trees, water, roads, etc., and, with the rapid development of urbanization, urban land cover can change substantially over a short time [89]. Although the VISRR algorithm considers the discrepancies in the SRR over different surface types, it does not consider the change in the surface type over a short period of time, which can result in an estimation error for the surface that can be further transmitted to AOD retrieval. The mixed surface type was represented by three sites (Kashi, Jiaozuo, and Songshan): the Jiaozuo site was mainly a mix of urban land (56%) and cropland (46%); the Songshan site was mainly a mix of forests

(36%), grassland (36%), and cropland (28%); and the Kashi site was mainly a mix of barren land (49%), cropland (40%), and grassland (20%). Over mixed-surface-type regions, there will be many mixed pixels. Although these pixels are identified as a certain surface type in advance, the selected prior SRRs may not represent the real relationship of the mixed pixels, which results in retrieval errors. Figure 10e shows the time series of the DPC AOD (blue dot) products against ground-based (red triangle) measurements over grassland (including the AOE_Baotou and Lhasa sites). The first 16 points are matchups from the AOE_Baotou site, and the rest are from the Lhasa site; the evaluating indicators N, RMSE, and Gfrac were 35, 0.1, and 62.9%, respectively. Although most of the valid matched AOD values were lower than 0.2 for AOD_Baotou and 0.1 for Lhasa, it can be seen that DPC AOD products were in better agreement with the ground-based measurements and showed the gradual process of AOD change.

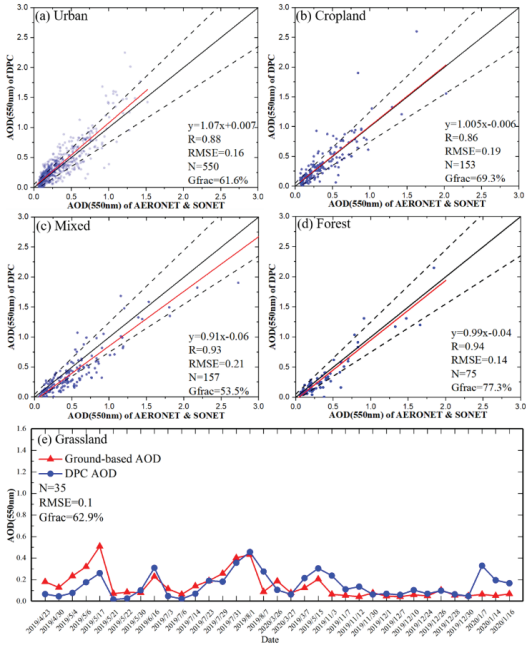


Figure 10. Validation of DPC AOD (550 nm) products against ground-based measurements over different surface types: (**a**) urban, (**b**) cropland, (**c**) mixed, (**d**) forest, and (**e**) grassland. Blue dots and red triangles represent the DPC AOD and ground-based measurements.

Table 9. Statistical parameters of Figure 10a–d. The best evaluating indicators are presented in bold.

Land Cover	a	b	N	R	RMSE	Gfrac
Urban	1.07	**0.007**	**550**	0.88	0.16	61.6
Cropland	**1.005**	−0.006	153	0.86	0.19	69.3
Mixed	0.91	0.11	157	0.93	0.21	53.5
Forest	0.96	−0.06	75	**0.94**	**0.14**	**77.3**

5. Conclusions

In this study, an innovative algorithm called VISRR was proposed and applied to DPC multiangle intensity data to simultaneously retrieve AOD at an intrinsic spatial resolution (3.3 km) over dark and bright land cover. The VISRR algorithm considers surface anisotropy and neither requires a shortwave infrared band nor establishes SRDs. The VISRR's previous SRRs were built based on long-time-series MYD09 products and consideration of surface

types, SCA, and NDVI. Meanwhile, to address the issue of the NDVI being susceptible to the atmosphere, an innovative iterative AC method was proposed to obtain realistic NDVI values. Then, by combining the fundamental aerosol models across China with a LUT method, the proposed algorithm was applied to thirteen months of DPC multiangle intensity data.

A long-time-series comparison and validation of the AOD products were performed, and the results showed that the VISRR algorithm is suitable for dark and bright land cover. The DPC and three MODIS AOD products had similar spatial distribution, but the DPC AOD products had both high spatial resolution and coverage. Validation using twenty-two ground-based sites over different surface types showed that the DPC AOD had the best performance (R of 0.88, RMSE of 0.17, and Gfrac of 62.7%) among the four products over the study area. Then, the uncertainties of the AOD products were comprehensively analyzed and discussed for future improvements. First, the DPC AOD products were validated over five typical surface types: forests had the best Gfrac (77.3%), while mixed land cover had the lowest Gfrac (53.5%). The possible source of error was the chance that the selected prior SRRs did not represent the real relationships of the mixed pixels.

In addition to the DPC/GF-5(01), VISRR can be applied to similar sensors, such as the advanced DPC/GF-5 (02), CM-1, DQ-1, DQ-2, and 3MI [49]. When combined with our previous fine-model aerosol algorithm SNOSPR, based on multiangle polarized data [30], the fine-model aerosol friction can be calculated, a key aerosol optical parameter retrieved from satellite remote sensing for distinguishing aerosol sources.

Supplementary Materials: The following supporting information can be downloaded at: https://www.mdpi.com/article/10.3390/rs14164045/s1, Table S1. K_{443_670} and K_{490_670} varies with *NDVI* and *SCA* over (1) Evergreen Needleleaf Forests; Table S2. Same as Table S1, but for (2) Evergreen Broadleaf Forests, Table S3. Same as Table S1, but for (3) Deciduous Needleleaf Forests, Table S4. Same as Table S1, but for (4) Deciduous Broadleaf Forests, Table S5. Same as Table S1, but for (6) Closed Shrublands, Table S6. Same as Table S1, but for (7) Open Shrublands, Table S7. Same as Table S1, but for (8) Woody Savannas, Table S8. Same as Table S1, but for (9) Savannas, Table S9. Same as Table S1, but for (11) Permanent Wetlands, Table S10. Same as Table S1, but for (14) Cropland/Natural Vegetation Mosaics.

Author Contributions: This work was carried out through the collaboration of all the authors. Conceptualization, B.G., Z.L. and C.C.; methodology, B.G. and Z.L.; validation, B.G. and W.H.; writing—original draft, B.G., Z.L., C.C., W.H., Y.X., S.Z., L.Q., Y.Z., K.L., H.X., Y.M., L.Y. and X.M.; All authors have read and agreed to the published version of the manuscript.

Funding: This work was supported by the National Natural Science Foundation of China (grant No. 42105134, 42175147, and 41871269); the China Postdoctoral Science Foundation (grant No. 2020M680684); the National Outstanding Youth Foundation of China (grant No. 41925019); the Fundamental Research Funds for the Central Universities (E0E48967); and the Special Research Assistant Project of CAS (E0Z103010F).

Data Availability Statement: Data used in the reported studies were obtained from websites as indicated in the text.

Acknowledgments: The authors would like to express our gratitude to AOE Baotou, Beijing, Beijing PKU, XiangHe and Taipei CWB AERONET sites for ground-based data. The authors would also like to thank the Chinese National Space Administration Earth Observation and Data Center for providing the DPC/GF-5 data, NASA for providing the MODIS products data, and USGS for providing the GMTED2010 and Splib07b datasets. The authors deeply appreciate the detailed comments and valuable suggestions from the anonymous reviewers.

Conflicts of Interest: The authors declare no conflict of interest.

References

1. Giles, D.M.; Sinyuk, A.; Sorokin, M.G.; Schafer, J.S.; Smirnov, A.; Slutsker, I.; Eck, T.F.; Holben, B.N.; Lewis, J.R.; Campbell, J.R.; et al. Advancements in the Aerosol Robotic Network (AERONET) Version 3 database–automated near-real-time quality control algorithm with improved cloud screening for Sun photometer aerosol optical depth (AOD) measurements. *Atmos. Meas. Tech.* **2019**, *12*, 169–209. [CrossRef]
2. Li, Z.; Xu, H.; Li, K.; Li, D.; Xie, Y.; Li, L.; Zhang, Y.; Gu, X.; Zhao, W.; Tian, Q. Comprehensive study of optical, physical, chemical and radiative properties of total columnar atmospheric aerosols over China: An overview of Sun-sky radiometer Observation NETwork (SONET) measurements. *Bull. Am. Meteor. Soc.* **2018**, *99*, 739–755. [CrossRef]
3. Dubovik, O.; Schuster, G.L.; Xu, F.; Hu, Y.; Bösch, H.; Landgraf, J.; Li, Z. Grand Challenges in Satellite Remote Sensing. *Front. Remote Sens.* **2021**, *2*, 619818. [CrossRef]
4. Griggs, M. Measurements of atmospheric aerosol optical thickness over water using ERTS-1 data. *J. Air Pollut. Control. Assoc.* **1975**, *25*, 622–626. [CrossRef]
5. Hauser, A.; Oesch, D.; Foppa, N.; Wunderle, S. NOAA AVHRR derived aerosol optical depth over land. *J. Geophys. Res. Atmos.* **2005**, *110*, D08204. [CrossRef]
6. Von Hoyningen-Huene, W.; Joon, Y.; Vountas, M.; Istomina, G.; Rohen, G.; Dinter, T.; Kokhanovsky, A.; Burrows, J. Retrieval of spectral aerosol optical thickness over land using ocean color sensors MERIS and SeaWiFS. *Atmos. Meas. Tech.* **2011**, *4*, 151–171. [CrossRef]
7. Jackson, J.M.; Liu, H.; Laszlo, I.; Kondragunta, S.; Remer, L.A.; Huang, J.; Huang, H.C. Suomi-NPP VIIRS aerosol algorithms and data products. *J. Geophys. Res. Atmos.* **2013**, *118*, 12673–12689. [CrossRef]
8. Kaufman, Y.J.; Sendra, C. Algorithm for automatic atmospheric corrections to visible and near-IR satellite imagery. *Int. J. Remote Sens.* **1988**, *9*, 1357–1381. [CrossRef]
9. Mei, L.; Rozanov, V.; Vountas, M.; Burrows, J.P.; Richter, A. XBAER-derived aerosol optical thickness from OLCI/Sentinel-3 observation. *Atmos. Chem. Phys.* **2018**, *18*, 2511–2523. [CrossRef]
10. Garay, M.J.; Witek, M.L.; Kahn, R.A.; Seidel, F.C.; Limbacher, J.A.; Bull, M.A.; Diner, D.J.; Hansen, E.G.; Kalashnikova, O.V.; Lee, H.; et al. Introducing the 4.4 km spatial resolution Multi-Angle Imaging SpectroRadiometer (MISR) aerosol product. *Atmos. Meas. Tech.* **2020**, *13*, 593–628. [CrossRef]
11. Kolmonen, P.; Sogacheva, L.; Virtanen, T.H.; Leeuw, G.D.; Kulmala, M. The ADV/ASV AATSR aerosol retrieval algorithm: Current status and presentation of a full-mission AOD dataset. *Int. J. Digit. Earth* **2015**, *9*, 545–561. [CrossRef]
12. Luffarelli, M.; Govaerts, Y.; Franceschini, L. Aerosol Optical Thickness Retrieval in Presence of Cloud: Application to S3A/SLSTR Observations. *Atmosphere* **2022**, *13*, 691. [CrossRef]
13. Chen, X.; Wang, J.; Liu, Y.; Xu, X.G.; Cai, Z.N.; Yang, D.X.; Yan, C.X.; Feng, L. Angular dependence of aerosol information content in CAPI/TanSat observation over land: Effect of polarization and synergy with A-train satellites. *Remote Sens. Environ.* **2017**, *196*, 163–177. [CrossRef]
14. Tanré, D.; Bréon, F.; Deuzé, J.; Dubovik, O.; Ducos, F.; François, P.; Goloub, P.; Herman, M.; Lifermann, A.; Waquet, F. Remote sensing of aerosols by using polarized, directional and spectral measurements within the A-Train: The PARASOL mission. *Atmos. Meas. Tech.* **2011**, *4*, 1383–1395. [CrossRef]
15. Li, Z.; Hou, W.; Hong, J.; Zheng, F.; Luo, D.; Wang, J.; Gu, X.; Qiao, Y. Directional Polarimetric Camera (DPC): Monitoring aerosol spectral optical properties over land from satellite observation. *J. Quant. Spectrosc. Radiat. Transf.* **2018**, *218*, 21–37. [CrossRef]
16. Sano, I.; Mukai, S.; Nakata, M. An effective method for retrieval of three kinds of aerosol properties focusing on a coming GCOM-C1/SGLI in December of 2017. In Proceedings of the Remote Sensing of Clouds and the Atmosphere XXII, Warsaw, Poland, 13 October 2017; p. 1042403.
17. Hsu, N.C.; Tsay, S.-C.; King, M.D.; Herman, J.R. Aerosol properties over bright-reflecting source regions. *IEEE Trans. Geosci. Remote Sens.* **2004**, *42*, 557–569. [CrossRef]
18. Kaufman, Y.J.; Wald, A.E.; Remer, L.A.; Gao, B.; Li, R.; Flynn, L. The MODIS 2.1-μm channel-correlation with visible reflectance for use in remote sensing of aerosol. *IEEE Trans. Geosci. Remote Sens.* **1997**, *35*, 1286–1298. [CrossRef]
19. Levy, R.C.; Remer, L.A.; Mattoo, S.; Vermote, E.F.; Kaufman, Y.J. Second-generation operational algorithm: Retrieval of aerosol properties over land from inversion of Moderate Resolution Imaging Spectroradiometer spectral reflectance. *J. Geophys. Res. Atmos.* **2007**, *112*, D13211. [CrossRef]
20. Hsu, N.; Jeong, M.J.; Bettenhausen, C.; Sayer, A.; Hansell, R.; Seftor, C.; Huang, J.; Tsay, S.C. Enhanced Deep Blue aerosol retrieval algorithm: The second generation. *J. Geophys. Res. Atmos.* **2013**, *118*, 9296–9315. [CrossRef]
21. Ge, B.; Li, Z.; Liu, L.; Yang, L.; Chen, X.; Hou, W.; Zhang, Y.; Li, D.; Li, L.; Qie, L. A Dark Target Method for Himawari-8/AHI Aerosol Retrieval: Application and Validation. *IEEE Trans. Geosci. Remote Sens.* **2019**, *57*, 381–394. [CrossRef]
22. Su, X.; Wang, L.; Zhang, M.; Qin, W.; Bilal, M. A High-Precision Aerosol Retrieval Algorithm (HiPARA) for Advanced Himawari Imager (AHI) data: Development and verification. *Remote Sens. Environ.* **2021**, *253*, 112221. [CrossRef]
23. Gao, L.; Chen, L.; Li, J.; Li, C.; Zhu, L. An improved dark target method for aerosol optical depth retrieval over China from Himawari-8. *Atmos. Res.* **2021**, *250*, 105399. [CrossRef]
24. Choi, M.; Kim, J.; Lee, J.; Kim, M.; Park, Y.-J.; Jeong, U.; Kim, W.; Hong, H.; Holben, B.; Eck, T.F.; et al. GOCI Yonsei Aerosol Retrieval (YAER) algorithm and validation during the DRAGON-NE Asia 2012 campaign. *Atmos. Meas. Tech.* **2016**, *9*, 1377–1398. [CrossRef]

25. Zhang, Y.; Li, Z.; Zhang, Y.; Hou, W.; Xu, H.; Chen, C.; Ma, Y. High temporal resolution aerosol retrieval using Geostationary Ocean Color Imager: Application and initial validation. *J. Appl. Remote Sens.* **2014**, *8*, 083612. [CrossRef]
26. Thomas, G.E.; Carboni, E.; Sayer, A.M.; Poulsen, C.A.; Siddans, R.; Grainger, R.G. Oxford-RAL Aerosol and Cloud (ORAC): Aerosol retrievals from satellite radiometers. In *Satellite Aerosol Remote Sensing over Land*; Springer: Berlin/Heidelberg, Germany, 2009; pp. 193–225.
27. Veefkind, J.P.; de Leeuw, G.; Durkee, P.A. Retrieval of aerosol optical depth over land using two-angle view satellite radiometry during TARFOX. *Geophys. Res. Lett.* **1998**, *25*, 3135–3138. [CrossRef]
28. Diner, D.J.; Abdou, W.A.; Bruegge, C.J.; Conel, J.E.; Crean, K.A.; Gaitley, B.J.; Helmlinger, M.C.; Kahn, R.A.; Martonchik, J.V.; Pilorz, S.H.; et al. MISR aerosol optical depth retrievals over southern Africa during the SAFARI-2000 Dry Season Campaign. *Geophys. Res. Lett.* **2001**, *28*, 3127–3130. [CrossRef]
29. Martonchik, J.V.; Kahn, R.A.; Diner, D.J. Retrieval of aerosol properties over land using MISR observations. In *Satellite Aerosol Remote Sensing over Land*; Springer: Berlin/Heidelberg, Germany, 2009; pp. 267–293.
30. Ge, B.; Mei, X.; Li, Z.; Hou, W.; Xie, Y.; Zhang, Y.; Xu, H.; Li, K.; Wei, Y. An improved algorithm for retrieving high resolution fine-mode aerosol based on polarized satellite data: Application and validation for POLDER-3. *Remote Sens. Environ.* **2020**, *247*, 111894. [CrossRef]
31. Dubovik, O.; Herman, M.; Holdak, A.; Lapyonok, T.; Tanré, D.; Deuzé, J.; Ducos, F.; Sinyuk, A.; Lopatin, A. Statistically optimized inversion algorithm for enhanced retrieval of aerosol properties from spectral multi-angle polarimetric satellite observations. *Atmos. Meas. Tech.* **2011**, *4*, 975–1018. [CrossRef]
32. Chen, C.; Dubovik, O.; Fuertes, D.; Litvinov, P.; Lapyonok, T.; Lopatin, A.; Ducos, F.; Derimian, Y.; Herman, M.; Tanré, D.; et al. Validation of GRASP algorithm product from POLDER/PARASOL data and assessment of multi-angular polarimetry potential for aerosol monitoring. *Earth Syst. Sci. Data* **2020**, *12*, 3573–3620. [CrossRef]
33. Wei, Y.; Li, Z.; Zhang, Y.; Chen, C.; Dubovik, O.; Zhang, Y.; Xu, H.; Li, K.; Chen, J.; Wang, H.; et al. Validation of POLDER GRASP Aerosol Optical Retrieval Over China Using SONET Observations. *J. Quant. Spectrosc. Radiat. Transf.* **2020**, *246*, 106931. [CrossRef]
34. Dubovik, O.; Holben, B.; Eck, T.F.; Smirnov, A.; Kaufman, Y.J.; King, M.D.; Tanré, D.; Slutsker, I. Variability of absorption and optical properties of key aerosol types observed in worldwide locations. *J. Atmos. Sci.* **2002**, *59*, 590–608. [CrossRef]
35. Omar, A.H.; Won, J.G.; Winker, D.M.; Yoon, S.C.; Dubovik, O.; McCormick, M.P. Development of global aerosol models using cluster analysis of Aerosol Robotic Network (AERONET) measurements. *J. Geophys. Res. Atmos.* **2005**, *110*, D10S14. [CrossRef]
36. Levy, R.C.; Remer, L.A.; Dubovik, O. Global aerosol optical properties and application to Moderate Resolution Imaging Spectroradiometer aerosol retrieval over land. *J. Geophys. Res. Atmos.* **2007**, *112*, D13210. [CrossRef]
37. Lee, J.; Kim, J.; Song, C.; Kim, S.; Chun, Y.; Sohn, B.; Holben, B. Characteristics of aerosol types from AERONET sunphotometer measurements. *Atmos. Environ.* **2010**, *44*, 3110–3117. [CrossRef]
38. Mei, L.; Rozanov, V.; Vountas, M.; Burrows, J.P.; Levy, R.C.; Lotz, W. Retrieval of aerosol optical properties using MERIS observations: Algorithm and some first results. *Remote Sens. Environ.* **2017**, *197*, 125–140. [CrossRef]
39. Omar, A.H.; Winker, D.M.; Vaughan, M.A.; Hu, Y.; Trepte, C.R.; Ferrare, R.A.; Lee, K.-P.; Hostetler, C.A.; Kittaka, C.; Rogers, R.R.; et al. The CALIPSO automated aerosol classification and lidar ratio selection algorithm. *J. Atmos. Ocean. Technol.* **2009**, *26*, 1994–2014. [CrossRef]
40. Li, Z.; Zhang, Y.; Xu, H.; Li, K.; Dubovik, O.; Goloub, P. The Fundamental Aerosol Models Over China Region: A Cluster Analysis of the Ground-Based Remote Sensing Measurements of Total Columnar Atmosphere. *Geophys. Res. Lett.* **2019**, *46*, 4924–4932. [CrossRef]
41. Levy, R.; Mattoo, S.; Munchak, L.; Remer, L.; Sayer, A.; Patadia, F.; Hsu, N. The Collection 6 MODIS aerosol products over land and ocean. *Atmos. Meas. Tech.* **2013**, *6*, 2989–3034. [CrossRef]
42. Sayer, A.M.; Hsu, N.C.; Lee, J.; Kim, W.V.; Dutcher, S.T. Validation, stability, and consistency of MODIS Collection 6.1 and VIIRS Version 1 Deep Blue aerosol data over land. *J. Geophys. Res. Atmos.* **2019**, *124*, 4658–4688. [CrossRef]
43. Tao, M.; Wang, J.; Li, R.; Chen, L.; Xu, X.; Wang, L.; Tao, J.; Wang, Z.; Xiang, J. Characterization of aerosol type over East Asia by 4.4 km MISR product: First insight and general performance. *J. Geophys. Res. Atmos.* **2020**, *125*, e2019JD031909. [CrossRef]
44. Li, C.; Li, J.; Xu, H.; Li, Z.; Xia, X.; Che, H. Evaluating VIIRS EPS Aerosol Optical Depth in China: An intercomparison against ground-based measurements and MODIS. *J. Quant. Spectrosc. Radiat. Transf.* **2019**, *224*, 368–377. [CrossRef]
45. Wei, J.; Sun, L.; Huang, B.; Bilal, M.; Zhang, Z.; Wang, L. Verification, improvement and application of aerosol optical depths in China Part 1: Inter-comparison of NPP-VIIRS and Aqua-MODIS. *Atmos. Environ.* **2018**, *175*, 221–233. [CrossRef]
46. Sogacheva, L.; de Leeuw, G.; Rodriguez, E.; Kolmonen, P.; Georgoulias, A.K.; Alexandri, G.; Kourtidis, K.; Proestakis, E.; Marinou, E.; Amiridis, V. Spatial and seasonal variations of aerosols over China from two decades of multi-satellite observations–part 1: ATSR (1995–2011) and MODIS C6. 1 (2000–2017). *Atmos. Chem. Phys.* **2018**, *18*, 11389–11407. [CrossRef]
47. He, Q.; Zhang, M.; Huang, B.; Tong, X. MODIS 3 km and 10 km aerosol optical depth for China: Evaluation and comparison. *Atmos. Environ.* **2017**, *153*, 150–162. [CrossRef]
48. Huang, G.; Chen, Y.; Li, Z.; Liu, Q.; Wang, Y.; He, Q.; Liu, T.; Liu, X.; Zhang, Y.; Gao, J. Validation and Accuracy Analysis of the Collection 6.1 MODIS Aerosol Optical Depth Over the Westernmost City in China Based on the Sun-Sky Radiometer Observations From SONET. *Earth Space Sci.* **2020**, *7*, e2019EA001041. [CrossRef]

49. Dubovik, O.; Li, Z.; Mishchenko, M.I.; Tanré, D.; Karol, Y.; Bojkov, B.; Cairns, B.; Diner, D.J.; Espinosa, W.R.; Goloub, P.; et al. Polarimetric remote sensing of atmospheric aerosols: Instruments, methodologies, results, and perspectives. *J. Quant. Spectrosc. Radiat. Transf.* **2018**, *224*, 474–511. [CrossRef]
50. Friedl, M.A.; Sulla-Menashe, D.; Tan, B.; Schneider, A.; Ramankutty, N.; Sibley, A.; Huang, X. MODIS Collection 5 global land cover: Algorithm refinements and characterization of new datasets. *Remote Sens. Environ.* **2010**, *114*, 168–182. [CrossRef]
51. Zhu, S.; Li, Z.; Qie, L.; Xu, H.; Ge, B.; Xie, Y.; Qiao, R.; Xie, Y.; Hong, J.; Meng, B.; et al. In-Flight Relative Radiometric Calibration of a Wide Field of View Directional Polarimetric Camera Based on the Rayleigh Scattering over Ocean. *Remote Sens.* **2022**, *14*, 1211. [CrossRef]
52. Danielson, J.J.; Gesch, D.B. Global Multi-Resolution Terrain Elevation Data 2010 (GMTED2010). US Department of the Interior; US Geological Survey, 2011. Available online: https://pubs.usgs.gov/of/2011/1073/ (accessed on 15 August 2022).
53. Kokaly, R.; Clark, R.; Swayze, G.; Livo, K.; Hoefen, T.; Pearson, N.; Wise, R.; Benzel, W.; Lowers, H.; Driscoll, R.; et al. *Usgs Spectral Library Version 7 Data: Us Geological Survey Data Release*; United States Geological Survey (USGS): Reston, VA, USA, 2017. [CrossRef]
54. Liu, N.; Zou, B.; Feng, H.; Tang, Y.; Liang, Y. Evaluation and comparison of MAIAC, DT and DB aerosol products over China. *Atmos. Chem. Phys. Discuss* **2019**, *19*, 8243–8268. [CrossRef]
55. Li, X.; Strahler, A.H. Geometric-optical bidirectional reflectance modeling of the discrete crown vegetation canopy: Effect of crown shape and mutual shadowing. *IEEE Trans. Geosci. Remote Sens.* **1992**, *30*, 276–292. [CrossRef]
56. Lucht, W.; Schaaf, C.B.; Strahler, A.H. An algorithm for the retrieval of albedo from space using semiempirical BRDF models. *IEEE Trans. Geosci. Remote Sens.* **2000**, *38*, 977–998. [CrossRef]
57. Jiao, Z.; Ding, A.; Kokhanovsky, A.; Schaaf, C.; Bréon, F.-M.; Dong, Y.; Wang, Z.; Liu, Y.; Zhang, X.; Yin, S.; et al. Development of a snow kernel to better model the anisotropic reflectance of pure snow in a kernel-driven BRDF model framework. *Remote Sens. Environ.* **2019**, *221*, 198–209. [CrossRef]
58. Bréon, F.-M.; Vermote, E. Correction of MODIS surface reflectance time series for BRDF effects. *Remote Sens. Environ.* **2012**, *125*, 1–9. [CrossRef]
59. Schaaf, C.B.; Gao, F.; Strahler, A.H.; Lucht, W.; Li, X.; Tsang, T.; Strugnell, N.C.; Zhang, X.; Jin, Y.; Muller, J.-P.; et al. First operational BRDF, albedo nadir reflectance products from MODIS. *Remote Sens. Environ.* **2002**, *83*, 135–148. [CrossRef]
60. Liu, Y.; Wang, Z.; Sun, Q.; Erb, A.M.; Li, Z.; Schaaf, C.B.; Zhang, X.; Román, M.O.; Scott, R.L.; Zhang, Q.; et al. Evaluation of the VIIRS BRDF, Albedo and NBAR products suite and an assessment of continuity with the long term MODIS record. *Remote Sens. Environ.* **2017**, *201*, 256–274. [CrossRef]
61. Wanner, W.; Li, X.; Strahler, A. On the derivation of kernels for kernel-driven models of bidirectional reflectance. *J. Geophys. Res. Atmos.* **1995**, *100*, 21077–21089. [CrossRef]
62. Vermote, E.; Justice, C.O.; Bréon, F.-M. Towards a generalized approach for correction of the BRDF effect in MODIS directional reflectances. *IEEE Trans. Geosci. Remote Sens.* **2009**, *47*, 898–908. [CrossRef]
63. Yang, L.; Xue, Y.; Li, Y.; Li, C.; Guang, J.; He, X.; Dong, J.; Hou, T. Uncertainty from Lambertian surface assumption in satellite aerosol retrieval. In Proceedings of the 2012 IEEE International Geoscience and Remote Sensing Symposium, Munich, Germany, 22–27 July 2012; pp. 3662–3665.
64. Qin, W.; Herman, J.R.; Ahmad, Z. A fast, accurate algorithm to account for non-Lambertian surface effects on TOA radiance. *J. Geophys. Res. Atmos.* **2001**, *106*, 22671–22684. [CrossRef]
65. She, L.; Xue, Y.; Yang, X.; Leys, J.; Guang, J.; Che, Y.; Fan, C.; Xie, Y.; Li, Y. Joint Retrieval of Aerosol Optical Depth and Surface Reflectance Over Land Using Geostationary Satellite Data. *IEEE Trans. Geosci. Remote Sens.* **2018**, *57*, 1489–1501. [CrossRef]
66. Yang, L.; Xue, Y.; Guang, J.; Kazemian, H.; Zhang, J.; Li, C. Improved Aerosol Optical Depth and Ångstrom Exponent Retrieval Over Land From MODIS Based on the Non-Lambertian Forward Model. *IEEE Geosci. Remote Sens. Lett.* **2014**, *11*, 1629–1633. [CrossRef]
67. He, T.; Liang, S.; Wang, D.; Wu, H.; Yu, Y.; Wang, J. Estimation of surface albedo and directional reflectance from Moderate Resolution Imaging Spectroradiometer (MODIS) observations. *Remote Sens. Environ.* **2012**, *119*, 286–300. [CrossRef]
68. Koelemeijer, R.; De Haan, J.; Stammes, P. A database of spectral surface reflectivity in the range 335–772 nm derived from 5.5 years of GOME observations. *J. Geophys. Res. Atmos.* **2003**, *108*, 4070. [CrossRef]
69. Sun, L.; Wei, J.; Bilal, M.; Tian, X.; Jia, C.; Guo, Y.; Mi, X. Aerosol optical depth retrieval over bright areas using Landsat 8 OLI images. *Remote Sens.* **2016**, *8*, 23. [CrossRef]
70. Sayer, A.M.; Thomas, G.E.; Grainger, R.G.; Carboni, E.; Poulsen, C.; Siddans, R. Use of MODIS-derived surface reflectance data in the ORAC-AATSR aerosol retrieval algorithm: Impact of differences between sensor spectral response functions. *Remote Sens. Environ.* **2012**, *116*, 177–188. [CrossRef]
71. Wang, Z.; Deng, R.; Ma, P.; Zhang, Y.; Liang, Y.; Chen, H.; Zhao, S.; Chen, L. 250-m Aerosol Retrieval from FY-3 Satellite in Guangzhou. *Remote Sens.* **2021**, *13*, 920. [CrossRef]
72. Qie, L.; Ma, Y.; Chen, X.; Li, L.; Li, Z.; Zhang, Y. Aerosol model assumption: The retrievals of aerosol optical depth from satellite near-infrared polarimetric measurements. *J. Infrared Millim. Waves* **2016**, *35*, 569–577.
73. Vermote, E.; Tanré, D.; Deuzé, J.; Herman, M.; Morcrette, J.; Kotchenova, S. Second Simulation of a Satellite Signal in the Solar Spectrum-Vector (6SV). Available online: https://salsa.umd.edu/files/6S/6S_Manual_Part_1.pdf (accessed on 30 July 2022).

74. Levy, R.C.; Remer, L.A.; Tanré, D.; Mattoo, S.; Kaufman, Y.J. Algorithm for Remote Sensing of Tropospheric Aerosol over Dark Targets from MODIS: Collections 005 and 051: Revision 2. February 2009. Available online: https://citeseerx.ist.psu.edu/viewdoc/download?doi=10.1.1.386.980&rep=rep1&type=pdf (accessed on 30 July 2022).
75. Fraser, R.S.; Ferrare, R.A.; Kaufman, Y.J.; Markham, B.L.; Mattoo, S. Algorithm for atmospheric corrections of aircraft and satellite imagery. *Int. J. Remote Sens.* **1992**, *13*, 541–557. [CrossRef]
76. Deuzé, J.; Bréon, F.; Devaux, C.; Goloub, P.; Herman, M.; Lafrance, B.; Maignan, F.; Marchand, A.; Nadal, F.; Perry, G.; et al. Remote sensing of aerosols over land surfaces from POLDER-ADEOS-1 polarized measurements. *J. Geophys. Res. Atmos.* **2001**, *106*, 4913–4926. [CrossRef]
77. Von Hoyningen-Huene, W.; Freitag, M.; Burrows, J. Retrieval of aerosol optical thickness over land surfaces from top-of-atmosphere radiance. *J. Geophys. Res. Atmos.* **2003**, *108*, 4260. [CrossRef]
78. She, L.; Mei, L.; Xue, Y.; Che, Y.; Guang, J. SAHARA: A Simplified AtmospHeric Correction AlgoRithm for Chinese gAofen Data: 1. Aerosol Algorithm. *Remote Sens.* **2017**, *9*, 253. [CrossRef]
79. Ge, B.; Li, Z.; Hou, W.; Ma, Y.; Xie, Y.; Wang, H.; Zhu, S.; Chen, J. An impact study of NDVI on the BPDF model under different atmosphere and multi-angles conditions. In Proceedings of the Applied Optics and Photonics China (AOPC2019), Nanjing, China, 22 December 2019; p. 1133834.
80. Liu, G.; Liang, C.; Kuo, T.; Lin, T.; Huang, S. Comparison of the NDVI, ARVI and AFRI Vegetation Index, Along with Their Relations with the AOD Using SPOT 4 Vegetation Data. *Terr. Atmos. Ocean. Sci.* **2004**, *15*, 15–31. [CrossRef]
81. Nagol, J.R.; Vermote, E.F.; Prince, S.D. Effects of atmospheric variation on AVHRR NDVI data. *Remote Sens. Environ.* **2009**, *113*, 392–397. [CrossRef]
82. Zhang, C.; Zhang, Y.; Li, Z.; Wang, Y.; Xu, H.; Li, K.; Li, D.; Xie, Y.; Zhang, Y. Sub-Mode Aerosol Volume Size Distribution and Complex Refractive Index from the Three-Year Ground-Based Measurements in Chengdu China. *Atmosphere* **2019**, *10*, 46. [CrossRef]
83. Liu, X.; Chen, Q.; Che, H.; Zhang, R.; Gui, K.; Zhang, H.; Zhao, T. Spatial distribution and temporal variation of aerosol optical depth in the Sichuan basin, China, the recent ten years. *Atmos. Environ.* **2016**, *147*, 434–445. [CrossRef]
84. Zhu, J.; Xia, X.; Wang, J.; Zhang, J.; Wiedinmyer, C.; Fisher, J.A.; Keller, C.A. Impact of Southeast Asian smoke on aerosol properties in Southwest China: First comparison of model simulations with satellite and ground observations. *J. Geophys. Res. Atmos.* **2017**, *122*, 3904–3919. [CrossRef]
85. Shao, P.; Xin, J.; Zhang, X.; Gong, C.; Ma, Y.; Wang, Y.; Wang, S.; Hu, B.; Ren, X.; Wang, B. Aerosol optical properties and their impacts on the co–occurrence of surface ozone and particulate matter in Kunming City, on the Yunnan–Guizhou Plateau of China. *Atmos. Res.* **2022**, *266*, 105963. [CrossRef]
86. Huang, J.; Minnis, P.; Chen, B.; Huang, Z.; Liu, Z.; Zhao, Q.; Yi, Y.; Ayers, J.K. Long-range transport and vertical structure of Asian dust from CALIPSO and surface measurements during PACDEX. *J. Geophys. Res. Atmos.* **2008**, *113*, D23212. [CrossRef]
87. Eck, T.; Holben, B.; Reid, J.; Dubovik, O.; Smirnov, A.; O'neill, N.; Slutsker, I.; Kinne, S. Wavelength dependence of the optical depth of biomass burning, urban, and desert dust aerosols. *J. Geophys. Res. Atmos.* **1999**, *104*, 31333–31349. [CrossRef]
88. Remer, L.A.; Mattoo, S.; Levy, R.C.; Munchak, L.A. MODIS 3 km aerosol product: Algorithm and global perspective. *Atmos. Meas. Tech.* **2013**, *6*, 1829–1844. [CrossRef]
89. Zhang, H.; Wang, T.; Zhang, Y.; Dai, Y.; Jia, J.; Yu, C.; Li, G.; Lin, Y.; Lin, H.; Cao, Y. Quantifying short-term urban land cover change with time series landsat data: A comparison of four different cities. *Sensors* **2018**, *18*, 4319. [CrossRef]

remote sensing

MDPI

Article

A New Coherence Detection Method for Mapping Inland Water Bodies Using CYGNSS Data

Ji Wang [1,2], Yufeng Hu [1,2,3,*] and Zhenhong Li [1,2,3]

[1] College of Geological Engineering and Geomatics, Chang'an University, Xi'an 710054, China; wj_1998@chd.edu.cn (J.W.); zhenhong.li@chd.edu.cn (Z.L.)
[2] Big Data Center for Geosciences and Satellites (BDCGS), Chang'an University, Xi'an 710054, China
[3] Key Laboratory of Ecological Geology and Disaster Prevention, Ministry of Natural Resources, Xi'an 710054, China
* Correspondence: yfhu@chd.edu.cn

Abstract: Inland water is an important part of the Earth's water cycle. Mapping inland water is vital for understanding surface hydrology and climate change. Spaceborne global navigation satellite systems reflectometry (GNSS-R) has been proven to be an effective technique to detect inland water bodies. This paper proposes a new method to map inland water bodies using the delay-Doppler map (DDM) measurements provided by the GNSS-R platform Cyclone GNSS (CYGNSS). In this new method, we develop a refined power ratio to identify the coherence in DDM caused by the inland water. Processed with an image segmentation method, the refined power ratio is then applied to discriminate the permanent inland water bodies from the land. Using CYGNSS data over the Amazon Basin and the Congo Basin in 2020, we successfully generated water masks with a spatial resolution of 0.01°. Compared with the reference optical water masks, the overall detection accuracy in the Amazon Basin is 94.48% and the water detection accuracy is 92.23%, and the corresponding accuracies in the Congo Basin are 96.12% and 93.16%, respectively. Compared with the previous DDM power-spread detector (DPSD) method, the new method's false alarms and misses in the Amazon Basin are reduced by 17.1% and 9.1%, respectively, while the false alarms and misses in the Congo Basin are reduced by 10.2% and 22%, respectively. Moreover, our method is proven to be useful for detecting short-term flood inundation.

Keywords: GNSS-R; CYGNSS; DDM; coherence; inland water detection; false alarms

Citation: Wang, J.; Hu, Y.; Li, Z. A New Coherence Detection Method for Mapping Inland Water Bodies Using CYGNSS Data. *Remote Sens.* **2022**, *14*, 3195. https://doi.org/10.3390/rs14133195

Academic Editor: Mehrez Zribi

Received: 25 May 2022
Accepted: 1 July 2022
Published: 3 July 2022

Publisher's Note: MDPI stays neutral with regard to jurisdictional claims in published maps and institutional affiliations.

Copyright: © 2022 by the authors. Licensee MDPI, Basel, Switzerland. This article is an open access article distributed under the terms and conditions of the Creative Commons Attribution (CC BY) license (https://creativecommons.org/licenses/by/4.0/).

1. Introduction

Climate change and human activities affect the location and extent of inland water bodies [1]. In turn, inland water also affects human survival, biodiversity [2], and climate [3]. Moreover, inland water bodies play an important role in the terrestrial water cycle, affecting local hydrology and ecosystems. Obtaining the spatial distribution of the inland water is of great significance for understanding the interaction mechanism of regional hydrology and climate change. Due to the complex variety of terrains and water surface characteristics, mapping inland water bodies is challenging [4]. Satellite remote sensing techniques including optical and microwave methods are commonly used for inland water detection over large areas. Optical images derived from satellites such as Landsat are easy to obtain with various sampling intervals, but they suffer from cloud cover and vegetation canopy. This limitation is significant in tropical areas dominated by rainforests since many small streams are fully covered by vegetation and cloud cover prevails in rainy seasons [5]. Microwaves can penetrate clouds, which is the advantage of microwave remote sensing for flood detection. However, the revisit cycle of microwave remote sensing satellites is typically long (>10 days) [6] and is susceptible to buildings, forest cover, etc. [7]. The emergence of spaceborne global navigation satellite systems reflectometry (GNSS-R) provides another method for inland water detection.

GNSS-R is a passive bistatic radar technique. It observes Earth's ground by receiving GNSS L-band signals reflected from the ground surface. All GNSS satellites can be regarded as signal sources, which greatly avoids the cost of instrument implementation. By deploying the receiving system in low Earth orbit, spaceborne GNSS-R measures the signals scattered in the forward direction from an area around the specular reflection point to the receiver in constant changing geometry. UK-DMC-1 is the first experimental GNSS-R satellite launched in 2003, demonstrating the potential of GNSS-R to observe land surfaces with a small amount of raw sampled data [8]. As the following GNSS-R satellite, TechDemoSat-1 (TDS-1) began operation in 2015 in a polar orbit and provides accessible reflection data to the public [9]. In December 2016, the National Aeronautics and Space Administration (NASA) Cyclone Global Navigation Satellite System (CYGNSS) mission consisting of eight small satellites was launched and has recorded abundant reflection observations since then [10]. Although spaceborne GNSS-R has been extensively used to estimate the wind speed on oceans [11,12], its land application is challenging. At present, most of the applications of spaceborne GNSS-R on the land surface used DDM (delay-Doppler map) measurements from the CYGNSS platform and focused on the hydrology variables such as soil moisture [13,14], lake water level [15], wetland extent [16], soil freezing-thawing [17], and flooding area [18–20]. GNSS-R has strong responses to the inland water caused by coherent forward scattering, leading to studies on its ability for permanent inland water detection. Zavorotny et al. [21] found that GNSS signals reflected from water bodies contribute to a higher signal-to-noise ratio (SNR) in DDM than those from the land. Based on the assumption that the peak value is only due to coherent forward scattering from the area of the first Fresnel zone (FFZ), the DDM SNR is used to identify the inland water bodies. Under this simple assumption, one can further derive the ground surface reflectivity from the SNR peak value [20]. Loria et al. [22] corrected the SNR peak value for antenna gain, geometry, and transmit power, and used the scattering model to generate a map of the percentage of the water bodies. Morris et al. [16] introduced thresholds on the SNR-based method to mitigate the overestimates of areas with low water percentages. Ghasemigoudarzi et al. [23] used a machine learning approach to produce a high-precision water map based on the corrected SNR. Gerlein-Safdi and Ruf [24] used the SNR-derived surface reflectivity to produce a water mask of inland water bodies at $0.01^\circ \times 0.01^\circ$ spatial resolution and found it could capture the seasonality of the flooding. However, the SNR-based method ignores the fact that both the scatterings inside and outside the FFZ contribute to the peak SNR. More recently, some scholars inferred the scattering pattern of the ground surface by quantifying the power distribution of the DDM. Al-Khaldi et al. [25] proposed a coherence detection method (DDM power-spread detector, DPSD) for the detection of permanent inland water bodies. This method uses the power ratio to quantify the power spread within the DDM and flag coherency by introducing an empirical power ratio threshold. They believed that the coherent scattering of GNSS-R on land mainly comes from the inland water bodies [26], while the incoherent scattering comes from the land. Based on this idea, they generated dynamic water masks with two spatial resolutions (i.e., 1 km and 3 km) [27].

In this study, we review the DPSD method and propose a new method to map the inland water by detecting the coherence in the CYGNSS DDM. Using the proposed method, we generate the coherence maps in the Amazon Basin and the Congo Basin with a spatial resolution of 0.01°. Then the coherence maps are processed using an image segmentation method to generate the final water masks. The results are qualitatively and quantitatively evaluated with the existing optical water data and compared with the water masks derived from DPSD. Moreover, the effects of the large size of the water body on the coherence method as well as the capacity of our method to detect shorter-lived flooding events are discussed.

2. Data and Methods

2.1. Study Areas

The Amazon Basin and the Congo Basin are selected as the representative areas to perform the proposed method in this study. The Amazon Basin is located in the northern part of South America. It is formed by the Andes, the Guyanese and Brazilian shields, and the Amazon plain [28]. The latitude and longitude coverage ranges are [10°S, 0°N] and [76°W, 56°W], respectively. The Amazon Basin is the world's largest river basin with the most tributaries. It drains about ~5% of global water land, making it the largest hydrological system in the world [29]. This basin is highly interconnected by extensive floodplain-lined river channels and contributes up to 15–20% to the total freshwater discharge to the world oceans [30]. A large amount of open water bodies and flat terrain over the Amazon Basin make it an ideal area to conduct water detection experiments, and it has been extensively investigated by previous GNSS-R studies [20,22,23]. The relief over the Amazon Basin is quite low with most parts below 600 m (Figure 1a). As the largest tropical rainforest in the world, the Amazon Basin contains about 60% of the tropical rainforests in the world [31]. The main rivers along the Amazon Basin are covered by dense tropical rainforest [32]. The size of the entire study area is approximately 2 million square kilometers.

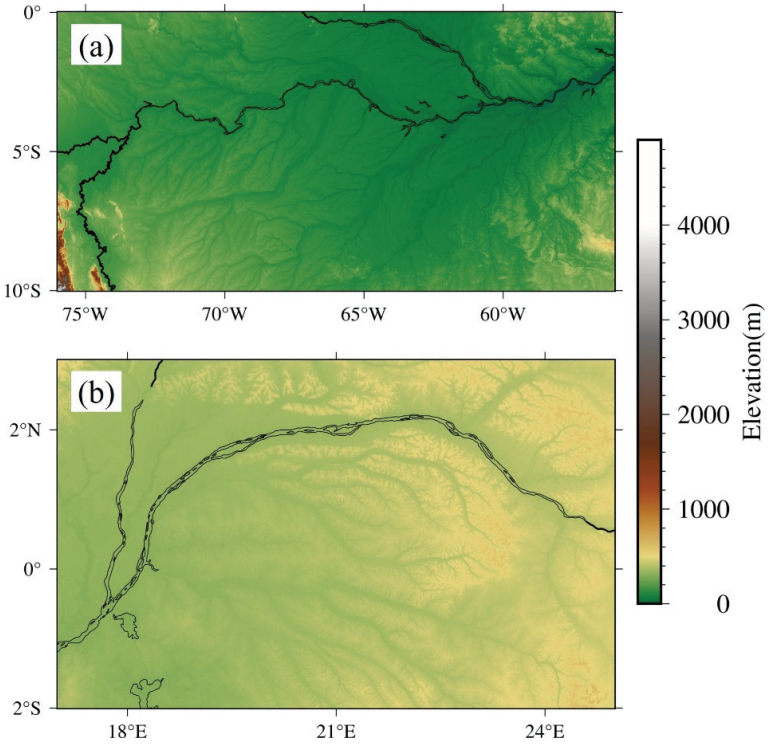


Figure 1. Relief maps of the Amazon Basin (**a**) and the Congo Basin (**b**) with major rivers marked.

The Congo Basin is located in west-central Africa, covering an area of nearly 3.7 million km^2. It stretches from the coast of the Gulf of Guinea to the mountains of the Albertine Rift and is crossed by the equator and the Inter-Tropical Convergence Zone (ITCZ) [33]. The Congo Basin contributes to half of Africa's freshwater discharge into the Atlantic Ocean [34]. It includes the largest and most diverse forest massif on the African continent and the second largest extent of tropical rainforest in the world, next to the Amazon Basin [35]. About 40% of the Congo Basin is covered by the savannas, which are a significant part of the landscape

in Central Africa [36]. The study area is in the Cuvette Centrale spanning from 2°S to 3°N and from 17°E to 25°E (Figure 1b). The terrain over this area is relatively flat with slight slopes (<2 cm km^{-1}) [37].

2.2. Data

2.2.1. CYGNSS DDM

In this paper, we use the data from CYGNSS Level 1 Version 3.0. CYGNSS is a satellite constellation launched by NASA in 2016, consisting of eight tiny satellites equipped with GNSS-R receivers at an altitude of 510 km. The CYGNSS satellites are evenly spaced in an orbit plane inclined at an angle of 35° [10]. Each satellite has four channels receiving GNSS reflected signals from the ground [10,38]. After July 2019, every satellite can generate 32 DDMs at a sampling rate of 2 Hz. The footprint of a single DDM is about 3.5 km × 0.5 km under smooth surface conditions [39]. The short revisit cycle of CYGNSS (median 2.8 h, mean 7.2 h) makes it possible to generate high-resolution water masks. CYGNSS is primarily designed for monitoring sea winds in the Tropics so it only covers the areas from 38°S to 38°N.

DDM is the principal observable of GNSS-R, which is generated by correlating the reflected GNSS signal with the replica in the receiver. It is a two-dimensional correlation function of time delay and Doppler frequency shift in complex form. A single DDM is composed of 17 delay bins and 11 Doppler bins, of which the resolution of the Doppler bin is 500 Hz and the resolution of the delay bin is 249.4 ns. Each CYGNSS DDM is generated by a coherent integration of 1 ms and an incoherent accumulation of 1000 ms [14]. The power scattered by the Earth's surface is mapped in the DDM through lines of constant delay (iso-delay ellipses) and constant Doppler shift (iso-Doppler parabolas) (Figure 2). The power reaches its maximum at the specular point (SP). The application of DDMs for inland water mapping is quite difficult because of the complexity of terrain properties. The power spread of a DDM is affected by the local topography, vegetation coverage, and surface roughness, presenting coherent/incoherent scatterings or mixing features. The power spread of DDM dominated by incoherent scattering from the land is characterized by the shape of a "horseshoe" (Figure 3a), while the power of DDM with coherent reflections from inland water bodies is concentrated in the limited bins about the SP (Figure 3b).

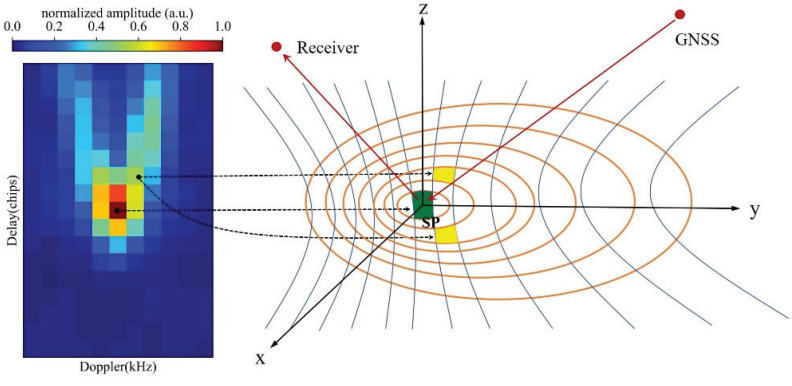


Figure 2. Illustration of the DDM and corresponding surface reflections.

2.2.2. Global Surface Water Data

The Global Surface Water (GSW) data is a water dataset with a spatial resolution of 30 m generated from 3 million Landsat images. GSW comprehensively describes the spatial and temporal dynamics of inland water bodies [40]. The latest GSW-derived seasonality water mask in 2020 is used in this study to evaluate the performance of the proposed method. For comparison, we resampled the original GSW to a 0.01° × 0.01° (about 1 km)

grid. Each grid cell contains the percentage of water bodies averaged from original data falling in it. The grid cells are labeled as water bodies when the water body percentage exceeds 0.2.

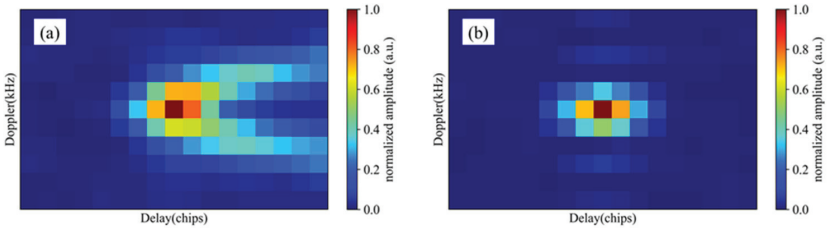


Figure 3. Two distinct DDMs. (**a**) Incoherent DDM. (**b**) Coherent DDM. Note that each DDM is normalized by its maximum power.

2.3. Method

2.3.1. DPSD Method

DPSD is a coherence method using the power ratio (PR) of DDM to detect inland water bodies. According to [26], the DDM from inland water presents strong coherence with power concentrated at the specular bin. While for the DDM from the land surface, the scattering is incoherent with power distribution in a horseshoe shape, as shown in Figure 2. Based on the coherence characteristic, Al-Khaldi developed the DPSD method for the normalized DDM as follows [25]:

$$PR = \frac{C_{in}}{C_{out}} \tag{1}$$

$$C_{in} = \sum_{i=-1}^{1} \sum_{j=-2}^{2} DDM\left(\tau_M + i, f_M + j\right) \tag{2}$$

$$C_{out} = \sum_{i=1}^{N_\tau} \sum_{j=2}^{N_f} DDM\left(i, j\right) - C_{in} \tag{3}$$

where N_τ is the number of delay bins in DDM, N_f is the number of Doppler bins, τ_M and f_M are the delay and Doppler positions of the DDM power maximum (specular bin), respectively, C_{in} is the sum of the power of the 3×5 delay-Doppler region about the specular bin, and C_{out} is the sum of all DDM power bins except C_{in}. Al-Khaldi also proposed a noise exclusion method to reduce the thermal noise before calculating the PR [25]. The threshold of PR (PR = 2) is used to identify the inland water with strong coherence.

2.3.2. New Coherence Detection Method

DPSD is an effective method to detect inland water, but it suffers from the problem of significant false alarms. Figure 4 shows four example DDMs recorded on land. Details of these DDMs are described in Table 1. Figure 4a shows the DDM from the inland water, and Figure 4b–d show the DDMs from the land. The PR values of these four DDMs are 3.61, 2.91, 3.32, and 1.26, respectively. According to the DPSD water detection threshold (i.e., PR = 2), DDMs (a and d) are correctly identified as inland water and land, respectively, while DDMs (b and c) are mistakenly identified. DDM (d) shows significant power spread to the horseshoe region, which is correctly detected as the land by the DPSD method. The slight but obvious power spread is also identified in DDMs (b and c), which are incorrectly detected as the land. Reducing the false alarms in inland water detection motivates us to develop a new coherence detection method.

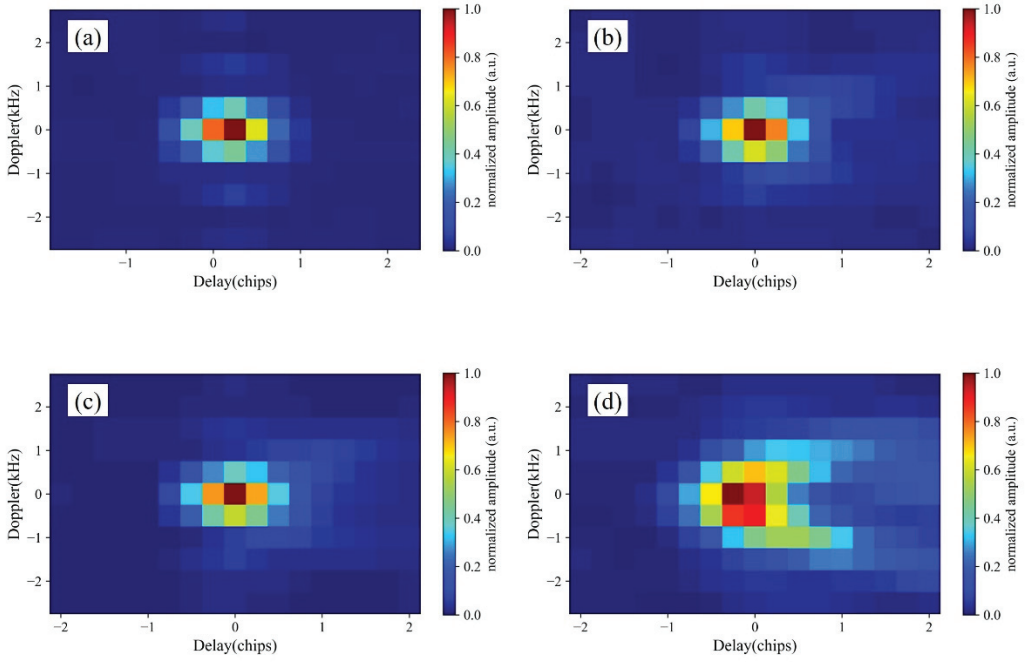


Figure 4. DDMs with specular reflection points falling on land (**a**–**c**) and water (**d**).

Table 1. Information of the example DDMs.

No.	Lon	Lat	SNR (dB)	Type	PR	PHPR
(a)	65.375°W	0.327°S	12.47	Water	3.61	37.78
(b)	66.924°W	2.327°S	11.20	Land	2.91	11.08
(c)	67.098°W	2.456°S	12.96	Land	3.32	10.32
(d)	61.527°W	8.414°S	10.42	Land	1.26	3.22

The power distributes in two regions in DDM. One is the region about the peak and the other one is the horseshoe region outside the peak region. The power ratio of the peak region to the horseshoe region (PHPR) indicates the scattering types, which are defined as:

$$PHPR = \frac{C_{peak}}{C_{horseshoe}} \tag{4}$$

$$C_{peak} = \frac{\sum_{i=-2}^{2}\sum_{j=-1}^{1} DDM(\tau_M + i, f_M + j)}{5 \times 3} \tag{5}$$

$$C_{horseshoe} = \frac{\sum_{i=3}^{N_\tau}\sum_{j=-3}^{3} DDM(\tau_M + i, f_M + j))}{6 \times 7} \tag{6}$$

where τ_M and f_M are the indices of peak power (at specular bin) in DDM. C_{peak} is the 5×3 delay-Doppler where the peak power is located, and $C_{horseshoe}$ is the 6×7 delay-Doppler behind the peak value, as shown in Figure 5.

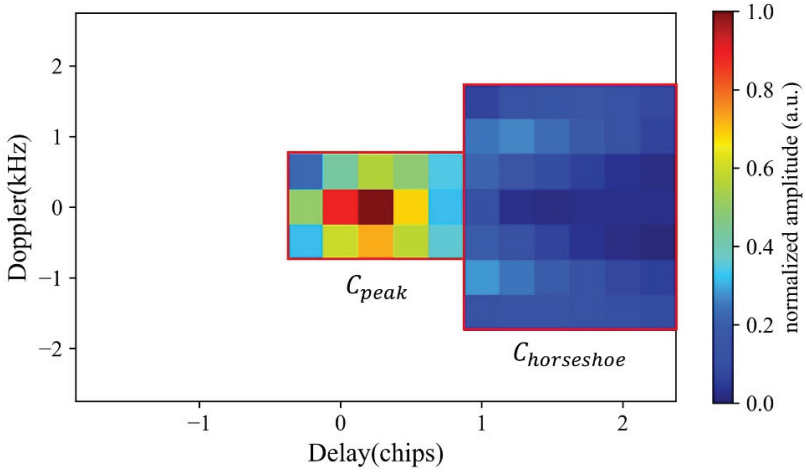


Figure 5. Illustration of the peak region C_{peak} and horseshoe region $C_{horseshoe}$ in DDM defined by the new method.

Compared with coherent DDMs, incoherent DDMs have relatively small PHPR because of the power spread. The new method abandons the power values of the first several delays in DDM, which are often regarded as background noise [41,42]. For the determination of peak region C_{peak}, we referred to the DDMA (DDM average) method in sea-ice detection [43] to set a 5×3 delay-Doppler as the peak region, which is different from the 3×5 delay-Doppler region used by the DPSD method. The determination of 5×3 delay-Doppler region is based on the fact that coherent DDMs resemble the Woodward ambiguity function (WAF) without delay-Doppler spreading [44]. The WAF is defined as the DDM response induced by a point scatter and can be approximated by a delay-spreading function $\bigwedge$ and a Doppler-spreading function S as [27].

$$\chi^2(\tau,\, f_D) \approx \overset{2}{\bigwedge}(\tau - \tau_c) \bullet |\, S(f_D)|^2 \tag{7}$$

$$|\, S(f_D)|^2 = \left| \frac{\sin(\pi f_D T_i)}{\pi f_D T_i} \right|^2 \tag{8}$$

$$\overset{2}{\bigwedge}(\tau) = \begin{cases} \left(1 - \frac{|\tau|}{\tau_c}\right)^2, & |\tau| \le \tau_c \\ 0, & |\tau| \le \tau_c \end{cases} \tag{9}$$

where T_i is the coherent integration time, τ_c is 0.97 μs; τ is the received signal time delays, and f_D is the received signal Doppler frequency shift.

Figure 6 illustrates the WAF calculated in the same delay-Doppler domain as in Figure 5. It can be seen that the main coherent power is concentrated in the central 5×3 delay-Doppler region. The overall similarity of WAF and DDM is often used to determine whether DDM is coherent, with the power concentrative at a specific 5×3 delay-Doppler region.

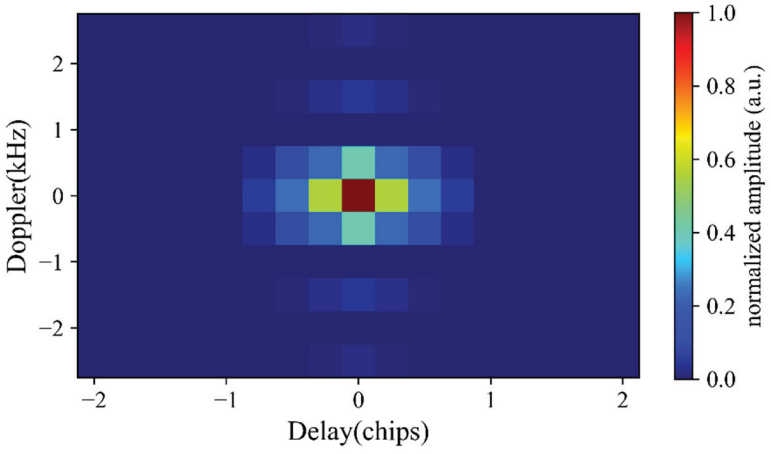


Figure 6. The Woodward ambiguity function in the same delay-Doppler domain as in Figure 5.

For the determination of the $C_{horseshoe}$, we chose the 6 × 7 delay-Doppler region as shown in Figure 5. The power of incoherent DDMs mainly spread in the specific region (e.g., Figures 3a and 4d), which approximately consists of a 5 × 3 peak region C_{peak} and a 6 × 7 delay-Doppler region. The power spread outside this region is very limited, so we keep seven bins along the Doppler domain for $C_{horseshoe}$ and exclude the first and last two bins to increase the sensitivity of PHPR to the coherence reflection. The last column of Table 1 shows the PHPR of the four DDMs. We can see that the PHPR of DDM (a) from inland water is significantly larger than that of the other three DDMs, indicating that the new method has much higher sensitivity to the inland water than the DPSD method.

2.3.3. Random Walker Segmentation

After the generation of the PHPR map using the proposed method, the next step is to discriminate the inland water bodies from the land, which is a classification problem. In this study, we applied an image processing-based technique (i.e., random walker segmentation) to the PHPR map to identify inland water bodies [45]. Gerlein-Safdi and Ruf [24] used this method to the CYGNSS-derived reflectivity to extract water bodies from the land surface and achieved good performance. We followed Gerlein-Safdi and Ruf [24] to use the scikit-image library in Python (https://scikit-image.org, accessed on 27 March 2022) to implement random walker segmentation. In the random walker segmentation, positive and negative samples need to be labeled by corresponding thresholds. The types of rest grid cells are classified by their attributes combined with their similarities to the neighboring samples.

As for the determination of the thresholds for the positive sample (water) and negative sample (land), we experimented a small region ([5°S, 0°N], [65°W, 70°W]) clipped from the study area. Taking the GSW as the reference, we calculated both the water and land detection accuracies for various threshold combinations (Figure 7). From Figure 7a,b, we can see that the water and land detection accuracies have opposite trends with the threshold combinations. We overlaid their contours in Figure 7c and determined a threshold combination (positive threshold = 28; negative threshold = 5) with relatively high accuracies (~0.92) for both.

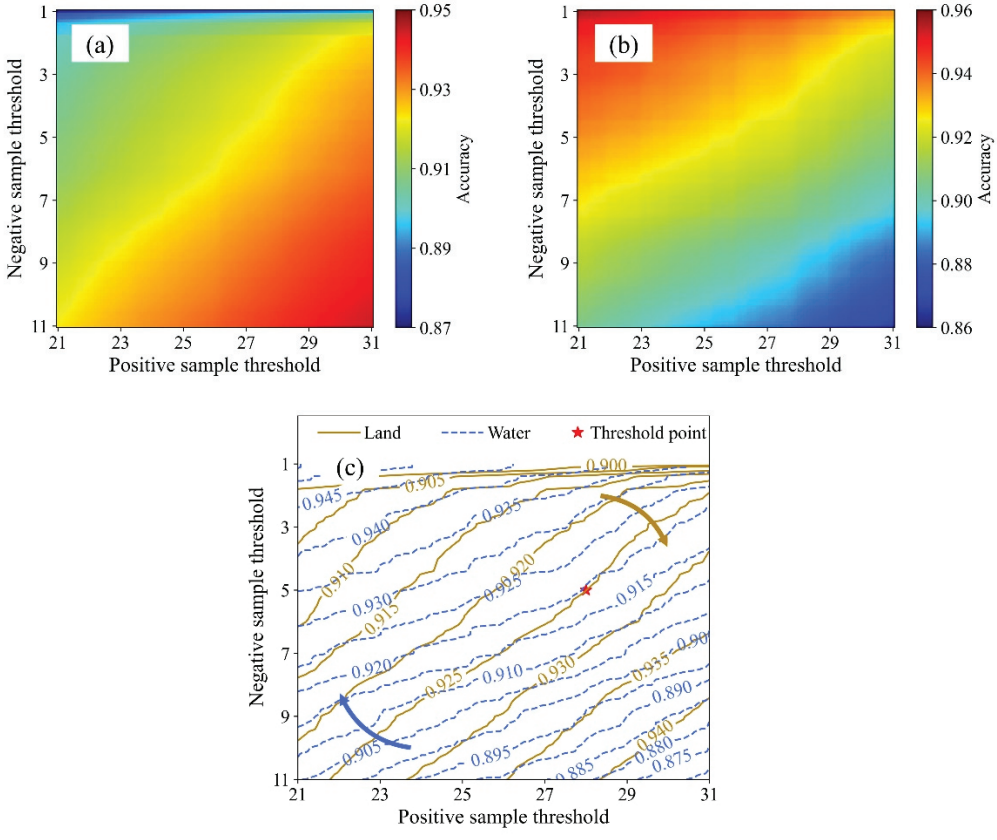


Figure 7. Land (**a**) and water (**b**) detection accuracies with various threshold combinations. (**c**) The contour map with water and land detection accuracies and the determined threshold combination is marked with a red star. The colored arrows indicate the corresponding increased directions of both accuracies.

2.4. Evaluation Indices

We used the confusion matrix to evaluate the performance of inland water detection, which is defined in Table 2.

Table 2. Confusion matrix of the inland water detection.

Reference	Detected Results	
	Land	**Water**
Land	TN	FP
Water	FN	TP

(Note that TP is "true positive", FN is "false negative", FP is "false positive", and TN is "true negative").

In the confusion matrix, TP means the grid cells identified as water in both GSW and CYGNSS; TN means the grid cells identified as land in both data; FP means the grid cells identified as water in CYGNSS but not in GSW; FN means the grid cells identified as land in CYGNSS but not in GSW.

We also used the probability of accurate detection in the study area to evaluate the overall detection accuracy. It is the ratio of the number of correctly identified samples (including both land and water samples) to the total samples, which is determined by:

$$\text{Overall Accuracy} = \frac{\text{TP} + \text{TN}}{\text{TP} + \text{FN} + \text{FP} + \text{TN}} \quad (10)$$

2.5. Steps to Perform New Method

Appling the new method to CYGNSS data, we can detect the inland water bodies and generate the water mask. The steps are summarized as follows (Figure 8):

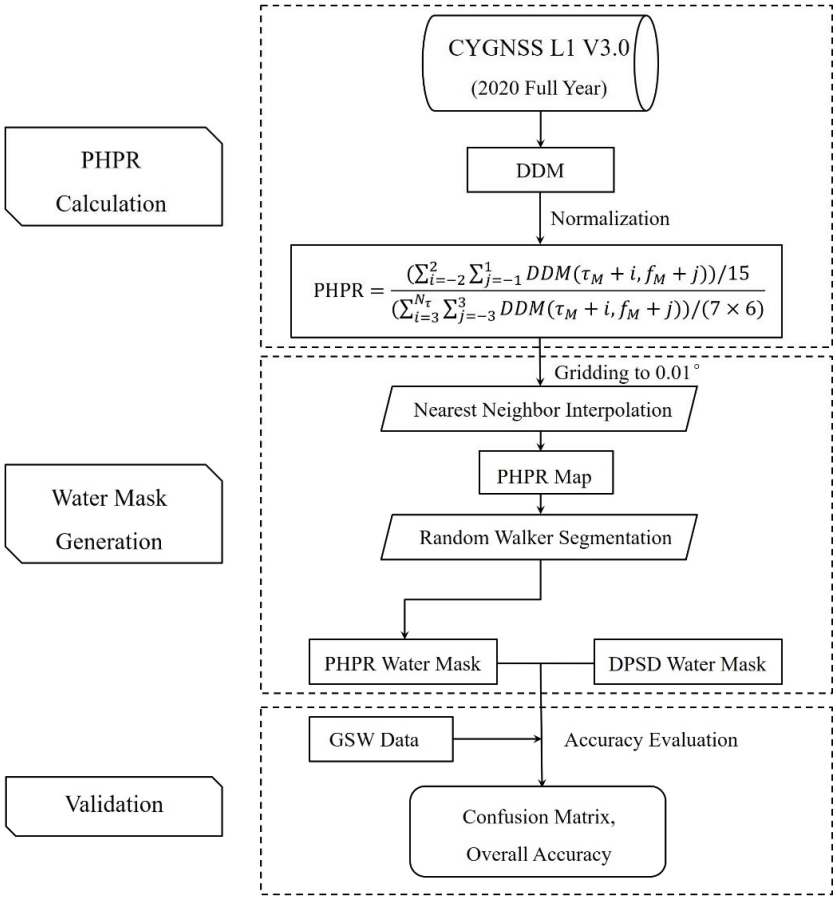


Figure 8. Flowchart of implementation of new coherence method for inland water bodies detection in this study.

Step 1: DDM data from CYGNSS Level 1 Version 3.0 are obtained and each DDM is normalized with its maximum power. Then the PHPR values are calculated with Equations (4)–(6).

Step 2: The PHPR at specular reflection points are spatially scattered, so they are gridded with a specific temporal resolution (0.01° in this study) for further mapping. For specular reflection points falling in the same grid, the average is taken to represent the PHPR value of this grid. The rest empty grid cells were interpolated from the nearest neighbor grid cells.

Step 3: PHPR map generated in step 2 is processed with the random walker segmentation to discriminate the inland water bodies. The identified water bodies and land are flagged with different signs to generate the water mask.

Step 4: Taking the GSW data as references, the confusion matrix and overall accuracy of the PHPR water mask are calculated. For comparison, the evaluation metrics are also calculated for the water mask derived from the DPSD method.

Figure 9 illustrates an example of map generation from step 1 to step 3 in a small region. It can be seen that the water mask is successfully obtained with the water bodies marked out.

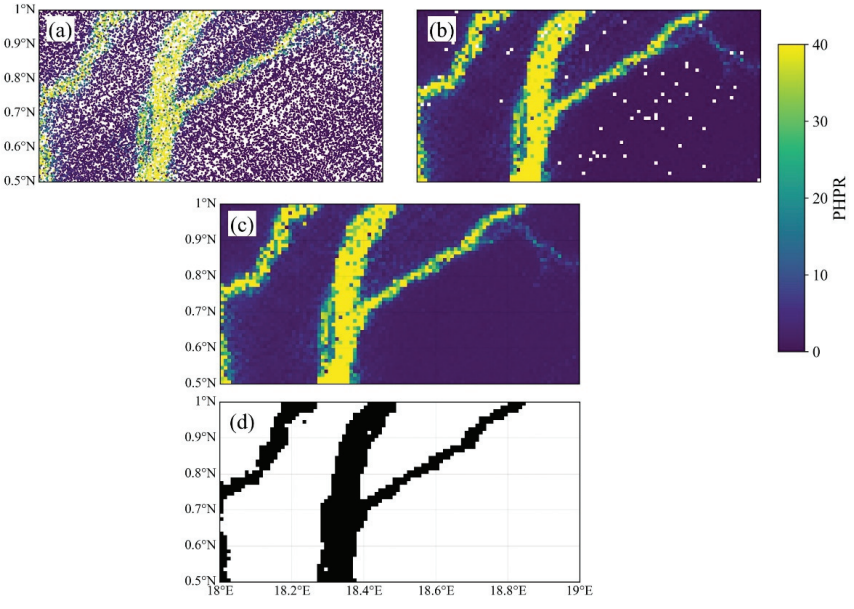


Figure 9. Example generation of PHPR water mask. (**a**) PHPR at specular reflection points. (**b**) Gridded PHPR with a spatial resolution of 0.01°. (**c**) PHPR map with empty grid cells filled through nearest neighbor interpolation. (**d**) PHPR water mask obtained by random walker segmentation with water bodies marked with black color.

3. Results

3.1. Water Detection Results in the Amazon Basin

We used both the proposed new method and the DPSD method to detect inland water bodies in the Amazon Basin. To evaluate the detection performance with the latest 2020 GSW data, we applied our method and the DPSD method to the DDM data through 2020. The power ratio values calculated using both the proposed method and the DPSP method were gridded with a resolution of 0.01° (about 1 km). The remaining empty grid cells were interpolated from the nearest neighboring grid cells.

Figure 10a shows the GSW seasonality water percentages in 2020 over the Amazon Basin and Figure 10b shows the GSW-derived water mask map. The distributions of power ratio derived from our method and DPSD method are illustrated in Figure 10c,d, respectively. It can be seen that the grid cells with a higher percentage of water bodies tend to have higher power ratio values. The water mask maps derived from our method and the DPSD method are shown in Figure 10e,f. Both our method and DPSD can identify the river network in the Amazon Basin, highly consistent with the reference water mask (Figure 10b). We overlaid the water masks obtained by the two methods with the reference water mask and produced the error maps showing grid cells identified as the FN, FP, and Correct (TP + TN), which are shown in Figure 10g,h. As we can see, nearly all water bodies are

identified by both methods but false positives (i.e., false alarms) are found in both. It can be partly attributed to the intrinsic limitation of optical data used by GSW, which are obscured by the dense vegetation in the Amazon Basin. Another possible reason is associated with the coherent reflection footprint of a DDM (i.e., 3.5 km × 0.5 km). Since the power in DDM will be dominated by the coherent reflection from even small water bodies in the footprint and result in a power ratio above the water detection threshold, so the identified rivers in the two methods are wider than that in the reference GSW. Figure 10i,j present the enlarged views of the error maps for both methods. We can see that the false alarms in our method are fewer than those in the DPSD method.

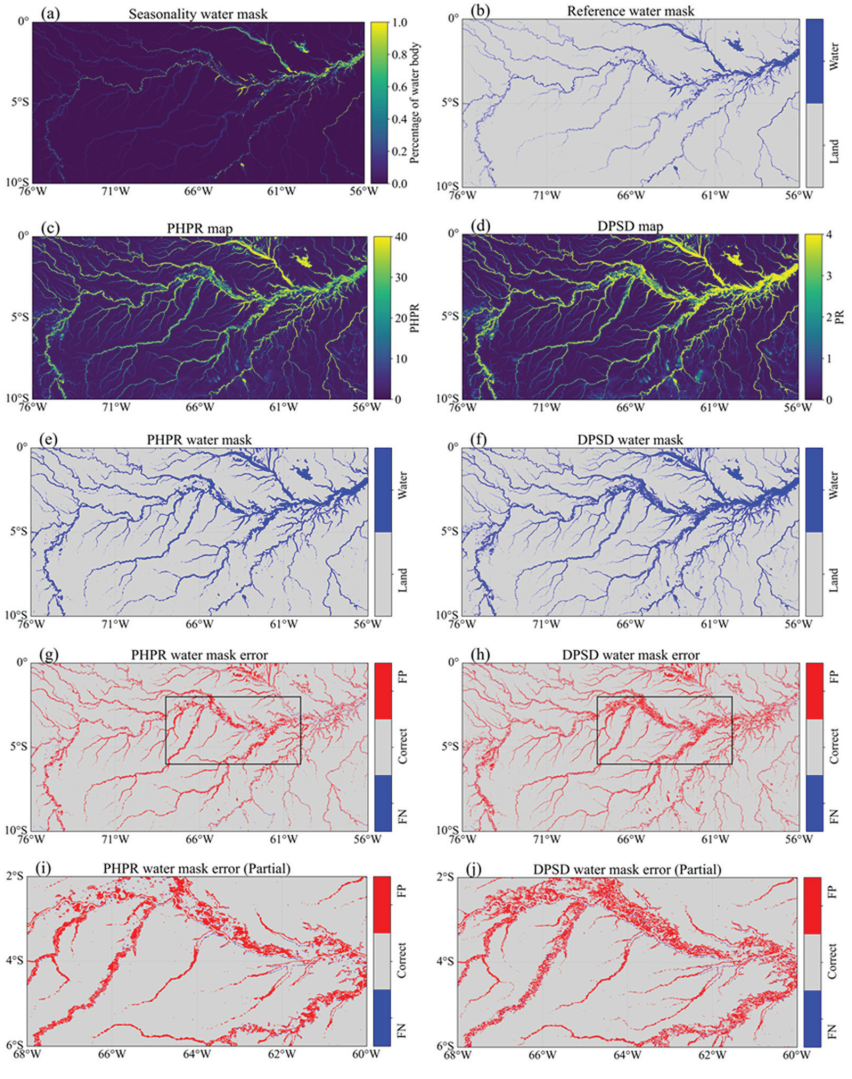


Figure 10. Amazon Basin maps. (**a**) Seasonality water map in 2020 derived from GSW; (**b**) GSW water mask (**c**,**d**) DPSD and PHPR maps; (**e**,**f**) water mask obtained from DPSD and PHRP result maps; (**g**,**h**) error maps obtained by DPSD and PHPR methods; (**i**,**j**) enlarged views of the PHPR and DPSD water mask error maps for the specified area indicated by the black rectangles in (**g**,**h**), respectively.

We took the GSW as references and compared the detection performances of two coherence methods in the Amazon Basin. The result shows that the overall detection accuracies of the DPSD method and our method are 93.36% and 94.48%, respectively. Our method performs slightly better (~1.1%) in terms of overall accuracy. The false alarm rate of our method is 5.44%, which is improved by 17.1% when compared with the DPSD method (6.56%). Moreover, our method significantly reduces the misidentified land grids as water bodies by more than 20,000. The false negative (i.e., misses) rate of our method is 7.77%, which is 9.12% lower than that of the DPSD (8.55%).

3.2. Water Detection Results in the Congo Basin

Figure 11 shows the detection results in the Congo Basin by using both our method and DPSD method, as well as the reference GSW map. Similar to the results in the Amazon Basin, the trunk stream and small tributaries are detected by both methods. Many detected small tributaries are missing in the GSW map, which can be attributed to the vegetation cover along the streams. However, false alarms are also found in the Congo Basin, contributing to the main errors in the water detection.

Compared with the GSW data, the evaluation indices of our method and the DPSD method are summarized in Table 3. It can be seen that our method still performs better than the DPSD method in terms of each evaluation index. Specifically, the false alarms rate is reduced by 10.2% from 4.22% to 3.79% and the false negative rate significantly decreases by 22% from 8.77% to 6.84%. Compared with the results in the Amazon, the results in the Congo Basin are slightly better with the overall accuracies of both methods exceeding 95.6%. The performance improvement of water detection using CYGNSS data in the Congo Basin over the Amazon Basin is also reported by [23]. The possible reason for this discrepancy is that the Congo Basin area is flatter with small slopes and the rivers and streams are fewer, contributing to the higher success rate in water bodies detection.

Table 3. Confusion matrices of the two methods and overall accuracies over the Amazon Basin and the Congo Basin.

Study Area	Method	Reference	Detection *		Overall Accuracy
			Land	Water	
Amazon Basin	PHPR	Land	94.56% (1,821,102)	5.44% (104,689)	94.48%
		Water	7.77% (5767)	92.23% (68,442)	
	DPSD	Land	93.43% (1,799,396)	6.56% (126,395)	93.36%
		Water	8.55% (6348)	91.45% (67,861)	
Congo Basin	PHPR	Land	96.21% (374,256)	3.79% (14,760)	96.12%
		Water	6.84% (751)	93.16% (10,233)	
	DPSD	Land	95.78% (372,616)	4.22% (16,400)	95.66%
		Water	8.77% (963)	91.23% (10,021)	

* The detection rates for classifications are listed with the corresponding number of grid cells in parentheses.

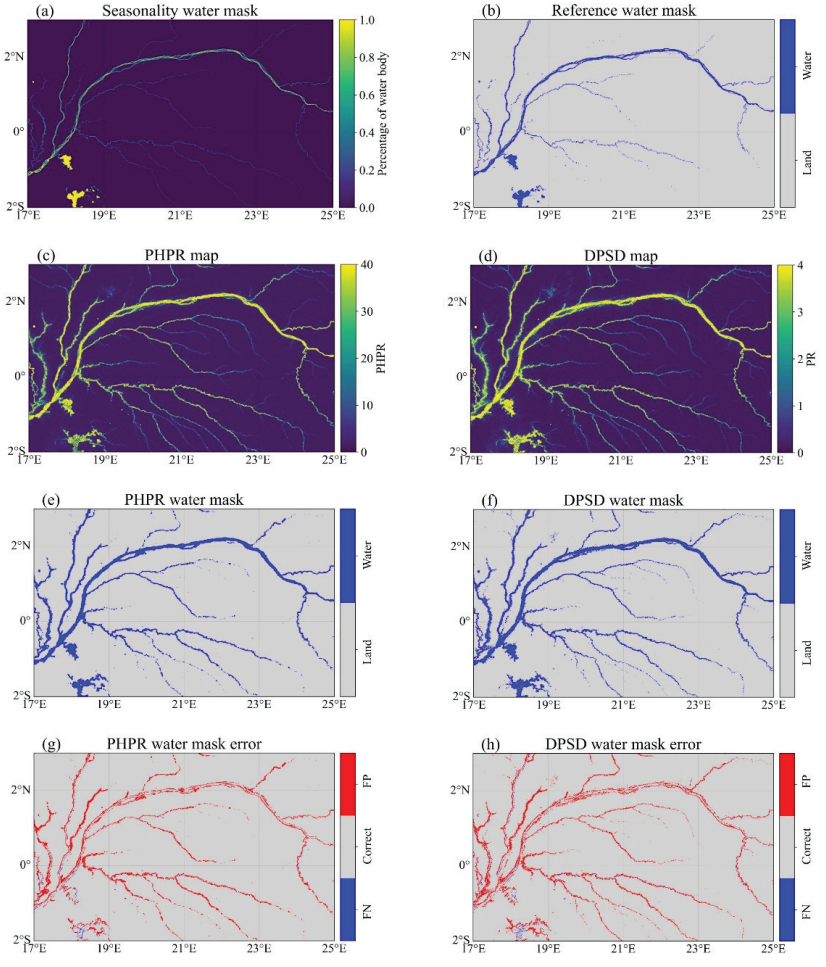


Figure 11. Congo Basin maps. (**a**) Seasonality water map in 2020 derived from GSW; (**b**) GSW water mask; (**c**,**d**) DPSD and PHPR maps; (**e**,**f**) water mask obtained from DPSD and PHRP result maps; (**g**,**h**) error maps obtained by DPSD and PHPR methods.

4. Discussion

4.1. Limitation on Detecting Big Water Bodies

Our method performs well for inland water mapping by detecting the coherence in the DDM. However, it is possible to fail in identifying the inland water bodies of large sizes such as big lakes. Since wind-induced wave heights formed in the lakes will cause incoherent scattering similar to the ocean scene with a rough surface, resulting in significant power spread in the DDM. Figure 12 shows four tracks of derived PHPR over the Tai Lake area in China on 26 February 2020, overlaying with the Lansat-9 image. Three of the four tracks (i.e., numbers 2, 3, and 4) are across Tai Lake and track 1 goes through a small water body. We can see that PHPR significantly increases above the water threshold (PHPR = 28) when it crosses the small water bodies. In contrast to track 1, the PHPR values suddenly decrease below the land threshold (PHPR = 5) in Tai Lake, indicating the wrongly identified land with incoherent scattering. A previous study showed the high sensitivity of the reflected power in DDM to the wind in big inland water bodies [46]. Therefore, it has the potential to detect the big lakes over a long period by investigating the temporal power

response to the wind. Further study on the wind-associated scattering pattern is needed to develop an algorithm to identify the big lakes using CYGNSS DDMs.

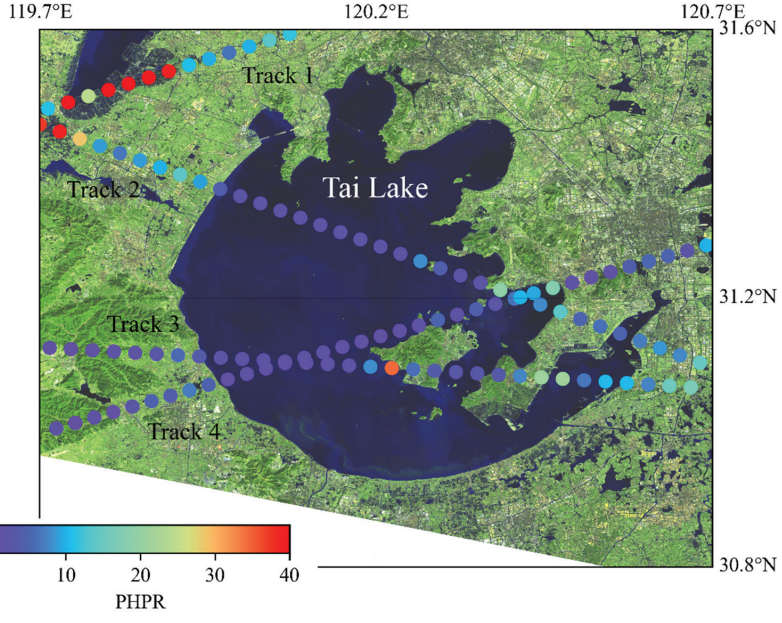


Figure 12. Tracks of the CYGNSS specular reflection points in the Tai Lake area in China on 26 February 2020 with the numbers marked. The corresponding PHPR values are indicated by the color bar. The background image is a fusion of bands 7, 6, and 4 from the image acquired by Landsat 9 on the same day.

4.2. Ability for Flood Inundation Detection

Besides the investigations on the CYGNSS's ability to identify permanent inland water bodies, many studies explored the possibility of monitoring shorter-lived inland water bodies such as floods [18,19,47]. Obscured by cloud cover, optical images are often unusable for water detection during floods. Taking the flood events in Henan Province, China in July 2021 as an example, we discuss the possibility of our method to detect flood inundation in this section.

Since 17 July 2021, extremely heavy rainfall hit the northern parts of Henan Province and caused severe floods in Xinxiang. The floods lasted for over 10 days from the middle to late July 2021. Figure 13 shows two optical images derived from MODIS (moderate-resolution imaging spectroradiometer) before and after the rainfall in the northern parts of Henan Province. We can see significant flood inundation in Xinxiang (red rectangles in Figure 13) after the rainfall with coverage from 35°N to 36°N and from 113°E to 115°E. We used the new coherence method to generate the water masks before and after the rainfall in Henan. The spatial resolution of the water mask is 0.02°. From Figure 14a,c, the PHPR values in several areas of Henan Province increase significantly after rainfall. Especially for the most severe flooding in Xinxiang (shown in the red box in Figures 13 and 14), the PHPR values are very large and significantly exceed the water detection threshold (i.e., 28). Figure 14b,d show the water masks of Henan before and after the rainfall. The area marked by red boxes in Figure 14 is identical to that in Figure 13. We can see that the identified water bodies are consistent overall with those in MODIS image (Figure 13b).

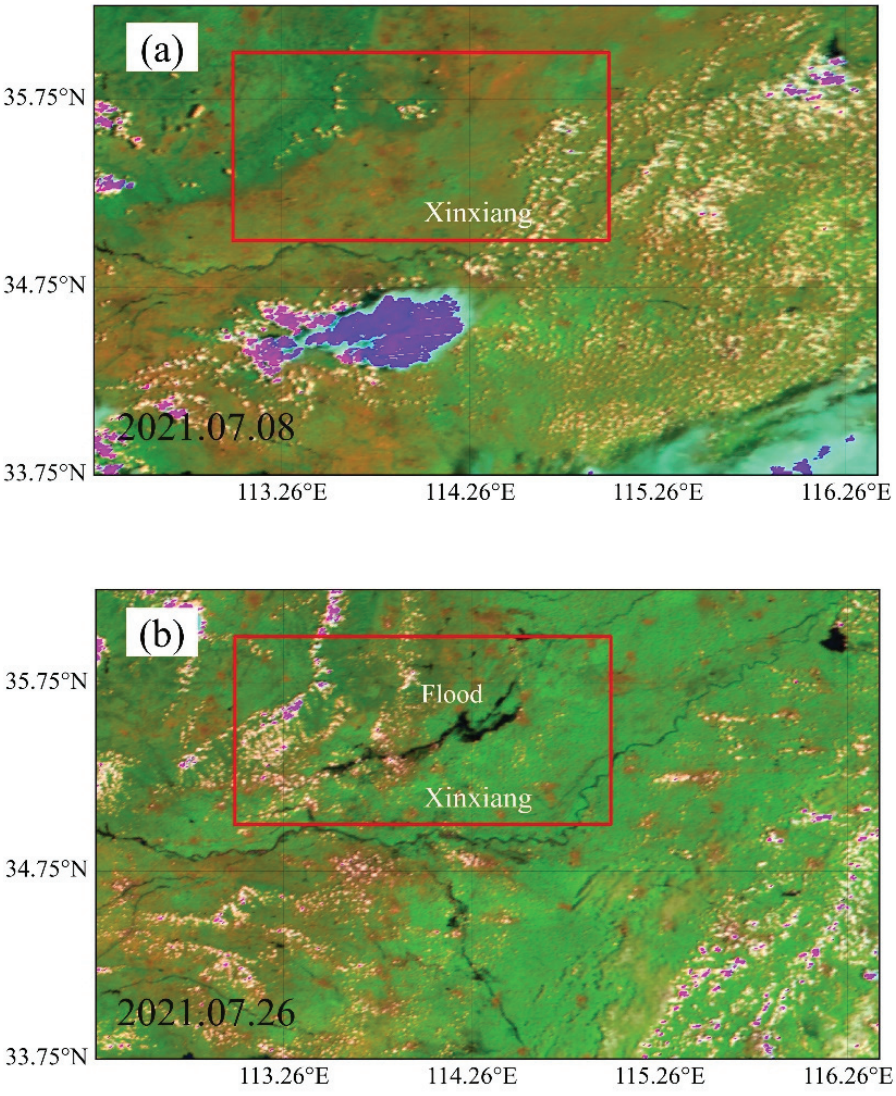


Figure 13. Images of the northern part of Henan Province, China derived from MODIS on 8 July 2021 (**a**) and 26 July 2021 (**b**). Water bodies and clouds are in black color and purple color, respectively. The flooding area in Xinxiang is marked out with red rectangle.

In this case, the PHPR were gridded into 0.02° instead of 0.01° used in the Amazon Basin and the Congo Basin. This is because that data collected over half a month is insufficient to generate the reliable gridded PHPR map with a resolution of 0.01°, in which substantial empty grid cells exhibit. Nevertheless, the method proposed in this paper is feasible for flood inundation detection. A significant increase in the PHPR value was found after the flooding. With a sufficient number of GNSS-R satellites in the future, daily dynamic monitoring of flood changes could become possible.

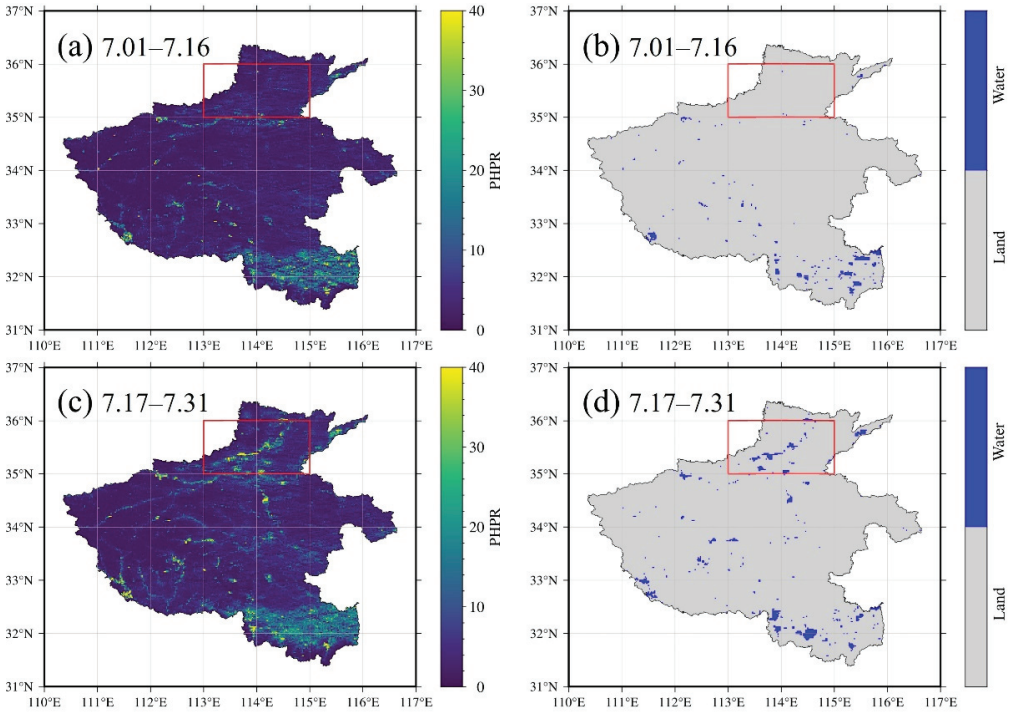


Figure 14. PHPR map (**a**) and PHPR water mask (**b**) of Henan before the rainfall (1 July 2021 to 16 July 2021). PHPR map (**c**) and PHPR water mask (**d**) of Henan after the rainfall (17 July 2021 to 31 July 2021). Red rectangle in each plot represents the flooding area in Xinxiang.

5. Conclusions

In this study, we proposed a new coherence detection method for CYGNSS data (i.e., DDM) based on the power ratio of the peak region to the horseshoe region in DDM. This method is combined with an image segmentation technique to identify the inland water bodies in the Amazon Basin and the Congo Basin in 2020. In the Amazon Basin, compared to the reference GSW data, the overall detection accuracy of our method is 94.48%, which is slightly better than that of the previous DPSD method (93.36%). Specifically, our method's false positive rate (5.44%) and true negative rate (7.77%) are reduced by 17.1% and 9.1%, respectively, compared with the DPSD method, indicating fewer false alarms and misses for inland water detection. In the Congo Basin, compared with the DPSD method, the results show that the false alarm rate of our method is reduced by 10.2% from 4.22% to 3.79% and the false negative rate significantly decreases by 22% from 8.77% to 6.84%. Moreover, the overall accuracies of our method (96.12%) and the DPSD method (95.66%) in the Congo Basin are slightly improved compared with those in the Amazon Basin. Our method works well in most inland areas except over large water bodies such as big lakes, in which the significant wave heights cause incoherence in the DDM. Future study needs to develop an algorithm to discriminate the incoherent scattering of large water bodies from the incoherent scattering of the land in DDM. Besides the permanent water bodies identification, our method was successfully applied to detect the flood inundation in Henan, China in July 2021, proving the ability to monitor short-term inland water bodies. Due to the L-band GNSS signals used in the CYGNSS, our method could be beneficial when the common optical method is hindered by the cloud and vegetation cover, which

can be applied to identify streams under thick vegetation or flood inundation under cloudy weather.

Author Contributions: Conceptualization, J.W., Y.H. and Z.L.; methodology, J.W. and Y.H.; software, J.W.; validation, J.W. and Y.H.; formal analysis, Y.H. and Z.L.; investigation, J.W.; resources, J.W.; data curation, J.W.; writing—original draft preparation, J.W.; writing—review and editing, Y.H. and Z.L.; visualization, Y.H.; supervision, Z.L.; project administration, Y.H. and Z.L.; funding acquisition, Y.H. All authors have read and agreed to the published version of the manuscript.

Funding: This research was funded by the National Natural Science Foundation of China, grant numbers 42041006, 41904020 and 41941019; the National Key Research and Development Program of China, grant number 2020YFC1512000; Shaanxi Province Science and Technology Innovation team, grant number 2021TD-51; Shaanxi Province Geoscience Big Data and Geohazard Prevention Innovation Team (2022); Natural Science Basic Research Program of Shaanxi (2020JQ-350); the Fundamental Research Funds for the Central Universities, CHD, grant numbers 300102260301, 300102262902 and 300102261108; and the European Space Agency through the ESA-MOST DRAGON-5 project, grant number 59339.

Institutional Review Board Statement: Not applicable.

Informed Consent Statement: Not applicable.

Data Availability Statement: The dataset generated in this study are available upon request from the corresponding author.

Acknowledgments: The author would like to thank NASA for providing the CYGNSS data and MODIS data and the Joint Research Centre for providing the GSW data.

Conflicts of Interest: The authors declare no conflict of interest.

References

1. Vorosmarty, C.J.; Green, P.; Salisbury, J.; Lammers, R.B. Global water resources: Vulnerability from climate change and population growth. *Science* **2000**, *289*, 284–288. [CrossRef]
2. Bastin, L.; Gorelick, N.; Saura, S.; Bertzky, B.; Dubois, G.; Fortin, M.J.; Pekel, J.F. Inland surface waters in protected areas globally: Current coverage and 30-year trends. *PLoS ONE* **2019**, *14*, e0210496. [CrossRef]
3. Holgerson, M.A.; Raymond, P.A. Large contribution to inland water CO_2 and CH_4 emissions from very small ponds. *Nat. Geosci.* **2016**, *9*, 222–226. [CrossRef]
4. Alsdorf, D.E.; Rodríguez, E.; Lettenmaier, D.P. Measuring surface water from space. *Rev. Geophys.* **2007**, *45*. [CrossRef]
5. Martins, V.S.; Novo, E.M.L.M.; Lyapustin, A.; Aragão, L.E.O.C.; Freitas, S.R.; Barbosa, C.C.F. Seasonal and interannual assessment of cloud cover and atmospheric constituents across the Amazon (2000–2015): Insights for remote sensing and climate analysis. *ISPRS J. Photogramm. Remote Sens.* **2018**, *145*, 309–327. [CrossRef]
6. Geudtner, D.; Torres, R. Sentinel-1 system overview and performance. In Proceedings of the 2012 IEEE International Geoscience and Remote Sensing Symposium, Munich, Germany, 22–27 July 2012; pp. 1719–1721.
7. Mason, D.C.; Speck, R.; Devereux, B.; Schumann, G.J.P.; Neal, J.C.; Bates, P.D. Flood Detection in Urban Areas Using TerraSAR-X. *IEEE Trans. Geosci. Remote Sens.* **2010**, *48*, 882–894. [CrossRef]
8. Gleason, S.; Hodgart, S.; Yiping, S.; Gommenginger, C.; Mackin, S.; Adjrad, M.; Unwin, M. Detection and Processing of bistatically reflected GPS signals from low Earth orbit for the purpose of ocean remote sensing. *IEEE Trans. Geosci. Remote Sens.* **2005**, *43*, 1229–1241. [CrossRef]
9. Unwin, M.; Jales, P.; Tye, J.; Gommenginger, C.; Foti, G.; Rosello, J. Spaceborne GNSS-Reflectometry on TechDemoSat-1: Early Mission Operations and Exploitation. *IEEE J. Sel. Top. Appl. Earth Obs. Remote Sens.* **2016**, *9*, 4525–4539. [CrossRef]
10. Ruf, C.S.; Atlas, R.; Chang, P.S.; Clarizia, M.P.; Garrison, J.L.; Gleason, S.; Katzberg, S.J.; Jelenak, Z.; Johnson, J.T.; Majumdar, S.J.; et al. New Ocean Winds Satellite Mission to Probe Hurricanes and Tropical Convection. *Bull. Am. Meteorol. Soc.* **2016**, *97*, 385–395. [CrossRef]
11. Li, C.; Huang, W. An Algorithm for Sea-Surface Wind Field Retrieval From GNSS-R Delay-Doppler Map. *IEEE Geosci. Remote Sens. Lett.* **2014**, *11*, 2110–2114. [CrossRef]
12. Jing, C.; Niu, X.; Duan, C.; Lu, F.; Di, G.; Yang, X. Sea Surface Wind Speed Retrieval from the First Chinese GNSS-R Mission: Technique and Preliminary Results. *Remote Sens.* **2019**, *11*, 3013. [CrossRef]
13. Chew, C.C.; Small, E.E. Soil Moisture Sensing Using Spaceborne GNSS Reflections: Comparison of CYGNSS Reflectivity to SMAP Soil Moisture. *Geophys. Res. Lett.* **2018**, *45*, 4049–4057. [CrossRef]
14. Camps, A.; Park, H.; Pablos, M.; Foti, G.; Gommenginger, C.P.; Liu, P.-W.; Judge, J. Sensitivity of GNSS-R Spaceborne Observations to Soil Moisture and Vegetation. *IEEE J. Sel. Top. Appl. Earth Obs. Remote Sens.* **2016**, *9*, 4730–4742. [CrossRef]

15. Li, W.; Cardellach, E.; Fabra, F.; Ribó, S.; Rius, A. Lake Level and Surface Topography Measured With Spaceborne GNSS-Reflectometry From CYGNSS Mission: Example for the Lake Qinghai. *Geophys. Res. Lett.* **2018**, *45*, 13332–13341. [CrossRef]
16. Morris, M.; Chew, C.; Reager, J.T.; Shah, R.; Zuffada, C. A novel approach to monitoring wetland dynamics using CYGNSS: Everglades case study. *Remote Sens. Environ.* **2019**, *233*, 111417. [CrossRef]
17. Wu, X.; Dong, Z.; Jin, S.; He, Y.; Song, Y.; Ma, W.; Yang, L. First Measurement of Soil Freeze/Thaw Cycles in the Tibetan Plateau Using CYGNSS GNSS-R Data. *Remote Sens.* **2020**, *12*, 2361. [CrossRef]
18. Chew, C.; Reager, J.T.; Small, E. CYGNSS data map flood inundation during the 2017 Atlantic hurricane season. *Sci. Rep.* **2018**, *8*, 9336. [CrossRef]
19. Wan, W.; Liu, B.; Zeng, Z.; Chen, X.; Wu, G.; Xu, L.; Chen, X.; Hong, Y. Using CYGNSS Data to Monitor China's Flood Inundation during Typhoon and Extreme Precipitation Events in 2017. *Remote Sens.* **2019**, *11*, 854. [CrossRef]
20. Chew, C.; Small, E. Estimating inundation extent using CYGNSS data: A conceptual modeling study. *Remote Sens. Environ.* **2020**, *246*, 111869. [CrossRef]
21. Zavorotny, V.; Loria, E.; O'Brien, A.; Downs, B.; Zuffada, C. Investigation of Coherent and Incoherent Scattering from Lakes Using Cygnss Observations. In Proceedings of the IGARSS 2020—2020 IEEE International Geoscience and Remote Sensing Symposium, Waikoloa, HI, USA, 26 September–2 October 2020; pp. 5917–5920.
22. Loria, E.; O'Brien, A.; Zavorotny, V.; Downs, B.; Zuffada, C. Analysis of scattering characteristics from inland bodies of water observed by CYGNSS. *Remote Sens. Environ.* **2020**, *245*, 111825. [CrossRef]
23. Ghasemigoudarzi, P.; Huang, W.; De Silva, O.; Yan, Q.; Power, D. A Machine Learning Method for Inland Water Detection Using CYGNSS Data. *IEEE Geosci. Remote Sens. Lett.* **2022**, *19*, 3020223. [CrossRef]
24. Gerlein-Safdi, C.; Ruf, C.S. A CYGNSS-Based Algorithm for the Detection of Inland Waterbodies. *Geophys. Res. Lett.* **2019**, *46*, 12065–12072. [CrossRef]
25. Al-Khaldi, M.M.; Johnson, J.T.; Gleason, S.; Loria, E.; O'Brien, A.J.; Yi, Y. An Algorithm for Detecting Coherence in Cyclone Global Navigation Satellite System Mission Level-1 Delay-Doppler Maps. *IEEE Trans. Geosci. Remote Sens.* **2021**, *59*, 4454–4463. [CrossRef]
26. Al-Khaldi, M.M.; Johnson, J.T.; O'Brien, A.J.; Balenzano, A.; Mattia, F. Time-Series Retrieval of Soil Moisture Using CYGNSS. *IEEE Trans. Geosci. Remote Sens.* **2019**, *57*, 4322–4331. [CrossRef]
27. Al-Khaldi, M.M.; Johnson, J.T.; Gleason, S.; Chew, C.C.; Gerlein-Safdi, C.; Shah, R.; Zuffada, C. Inland Water Body Mapping Using CYGNSS Coherence Detection. *IEEE Trans. Geosci. Remote Sens.* **2021**, *59*, 7385–7394. [CrossRef]
28. Sorribas, M.V.; Paiva, R.C.D.; Melack, J.M.; Bravo, J.M.; Jones, C.; Carvalho, L.; Beighley, E.; Forsberg, B.; Costa, M.H. Projections of climate change effects on discharge and inundation in the Amazon basin. *Clim. Chang.* **2016**, *136*, 555–570. [CrossRef]
29. Villar, J.C.E.; Guyot, J.L.; Ronchail, J.; Cochonneau, G.; Filizola, N.; Fraizy, P.; Labat, D.; de Oliveira, E.; Ordoñez, J.J.; Vauchel, P. Contrasting regional discharge evolutions in the Amazon basin (1974–2004). *J. Hydrol.* **2009**, *375*, 297–311. [CrossRef]
30. Richey, J.E.; Meade, R.H.; Salati, E.; Devol, A.H.; Nordin, C.F., Jr.; Santos, U.D. Water discharge and suspended sediment concentrations in the Amazon River: 1982–1984. *Water Resour. Res.* **1986**, *22*, 756–764. [CrossRef]
31. Laurance, W.F.; Lovejoy, T.E.; Vasconcelos, H.L.; Bruna, E.M.; Didham, R.K.; Stouffer, P.C.; Gascon, C.; Bierregaard, R.O.; Laurance, S.G.; Sampaio, E. Ecosystem decay of Amazonian forest fragments: A 22-year investigation. *Conserv. Biol.* **2002**, *16*, 605–618. [CrossRef]
32. Davidson, E.A.; de Araujo, A.C.; Artaxo, P.; Balch, J.K.; Brown, I.F.; MM, C.B.; Coe, M.T.; DeFries, R.S.; Keller, M.; Longo, M.; et al. The Amazon basin in transition. *Nature* **2012**, *481*, 321–328. [CrossRef]
33. Nicholson, S.E. A revised picture of the structure of the "monsoon" and land ITCZ over West Africa. *Clim. Dyn.* **2009**, *32*, 1155–1171. [CrossRef]
34. Laraque, A.; Castellanos, B.; Steiger, J.; Lòpez, J.L.; Pandi, A.; Rodriguez, M.; Rosales, J.; Adèle, G.; Perez, J.; Lagane, C. A comparison of the suspended and dissolved matter dynamics of two large inter-tropical rivers draining into the Atlantic Ocean: The Congo and the Orinoco. *Hydrol. Process.* **2013**, *27*, 2153–2170. [CrossRef]
35. Hansen, M.C.; Roy, D.P.; Lindquist, E.; Adusei, B.; Justice, C.O.; Altstatt, A. A method for integrating MODIS and Landsat data for systematic monitoring of forest cover and change in the Congo Basin. *Remote Sens. Environ.* **2008**, *112*, 2495–2513. [CrossRef]
36. Laporte, N.T.; Goetz, S.J.; Justice, C.O.; Heinicke, M. A new land cover map of central Africa derived from multi-resolution, multi-temporal AVHRR data. *Int. J. Remote Sens.* **2010**, *19*, 3537–3550. [CrossRef]
37. Laraque, A.; Bricquet, J.P.; Pandi, A.; Olivry, J.C. A review of material transport by the Congo river and its tributaries. *Hydrol. Process.* **2009**, *23*, 3216–3224. [CrossRef]
38. Ruf, C.S.; Gleason, S.; Jelenak, Z.; Katzberg, S.; Ridley, A.; Rose, R.; Scherrer, J.; Zavorotny, V. The CYGNSS nanosatellite constellation hurricane mission. In Proceedings of the 2012 IEEE International Geoscience and Remote Sensing Symposium, Munich, Germany, 22–27 July 2012; pp. 214–216.
39. Chew, C.; Shah, R.; Zuffada, C.; Hajj, G.; Masters, D.; Mannucci, A.J. Demonstrating soil moisture remote sensing with observations from the UK TechDemoSat-1 satellite mission. *Geophys. Res. Lett.* **2016**, *43*, 3317–3324. [CrossRef]
40. Pekel, J.F.; Cottam, A.; Gorelick, N.; Belward, A.S. High-resolution mapping of global surface water and its long-term changes. *Nature* **2016**, *540*, 418–422. [CrossRef]
41. Yan, Q.; Huang, W. Spaceborne GNSS-R Sea Ice Detection Using Delay-Doppler Maps: First Results From the U.K. TechDemoSat-1 Mission. *IEEE J. Sel. Top. Appl. Earth Obs. Remote Sens.* **2016**, *9*, 4795–4801. [CrossRef]

42. Zhu, Y.; Yu, K.; Zou, J.; Wickert, J. Sea Ice Detection Based on Differential Delay-Doppler Maps from UK TechDemoSat-1. *Sensors* **2017**, *17*, 1614. [CrossRef]
43. Alonso-Arroyo, A.; Zavorotny, V.U.; Camps, A. Sea Ice Detection Using U.K. TDS-1 GNSS-R Data. *IEEE Trans. Geosci. Remote Sens.* **2017**, *55*, 4989–5001. [CrossRef]
44. Dong, Z.; Jin, S. Evaluation of the Land GNSS-Reflected DDM Coherence on Soil Moisture Estimation from CYGNSS Data. *Remote Sens.* **2021**, *13*, 570. [CrossRef]
45. Grady, L. Random walks for image segmentation. *IEEE Trans. Pattern Anal. Mach. Intell.* **2006**, *28*, 1768–1783. [CrossRef]
46. Loria, E.; O'Brien, A.; Zavorotny, V.; Zuffada, C. Wind Vector and Wave Height Retrieval in Inland Waters Using CYGNSS. In Proceedings of the IGARSS 2020—2020 IEEE International Geoscience and Remote Sensing Symposium, Waikoloa, HI, USA, 26 September–2 October 2020; pp. 7029–7032.
47. Zhang, S.; Ma, Z.; Li, Z.; Zhang, P.; Liu, Q.; Nan, Y.; Zhang, J.; Hu, S.; Feng, Y.; Zhao, H. Using CYGNSS Data to Map Flood Inundation during the 2021 Extreme Precipitation in Henan Province, China. *Remote Sens.* **2021**, *13*, 5181. [CrossRef]

remote sensing

MDPI

Article

Inter-Annual Climate Variability Impact on Oil Palm Mapping

Fernando Troya [1,*], Paulo N. Bernardino [1] and Ben Somers [1,2]

[1] Division Forest, Nature and Landscape, KU Leuven, Celestijnenlaan 200E, 3001 Heverlee, Belgium; negribernardino.paulo@kuleuven.be (P.N.B.); ben.somers@kuleuven.be (B.S.)
[2] KU Leuven Plant Institute (LPI), Kasteelpark Arenberg 31, 3001 Heverlee, Belgium
* Correspondence: fernando.troyaandrade@kuleuven.be

Abstract: The contribution of oil palm plantations to the economic growth of tropical developing countries makes it essential to monitor their expansion into the tropical forest; consequently, most studies focus on improving mapping accuracy while using satellite imagery. However, accuracy can be hampered by atmospheric phenomena that can drastically change climatic conditions in tropical regions, affecting the spectral properties of the vegetation. In this sense, we studied the accuracy of palm plantation mapping by using features from different regions of the electromagnetic spectrum and a data fusion approach, and then compared the changes in accuracy over the years 2016, 2017, and 2018 (two of them with reported climatic anomalies). Optical-based maps obtained higher accuracy than thermal- and microwave-based maps, but they were the most affected by inter-annual climate variability (error margin between 5 and 10%), while thermal-based maps were the least affected (error margin between 8 and 9%). Data fusion combinations improved accuracy and reduced dissimilarities between years (e.g., phenology-based map accuracy changed by up to 20.8%, while phenology fused with microwave features changed by up to 6.8%). We conclude that inter-annual climate variability on land-cover mapping should be considered, especially if the outputs will be used as input in future·studies.

Keywords: mapping accuracy; oil palm; inter-annual climate variability; remote sensing; tropical forest; spectral region; data fusion; ENSO

Citation: Troya, F.; Bernardino, P.N.; Somers, B. Inter-Annual Climate Variability Impact on Oil Palm Mapping. *Remote Sens.* **2022**, *14*, 3104. https://doi.org/10.3390/rs14133104

Academic Editor: Arturo Sanchez-Azofeifa

Received: 21 April 2022
Accepted: 24 June 2022
Published: 28 June 2022

Publisher's Note: MDPI stays neutral with regard to jurisdictional claims in published maps and institutional affiliations.

Copyright: © 2022 by the authors. Licensee MDPI, Basel, Switzerland. This article is an open access article distributed under the terms and conditions of the Creative Commons Attribution (CC BY) license (https://creativecommons.org/licenses/by/4.0/).

1. Introduction

One of the most important and studied crops in tropical territories, mostly present on the industrial scale, is oil palm, especially due to its high impact in the economic development of tropical countries, but at the same time, also due to its relevant role in the degradation of natural ecosystems [1–3]. Oil palm plantation is a growing business around the world, driven by an increasing demand for palm oil over the last decades, mainly due to its versatility, e.g., used as raw material in the food and cosmetic industries and in the production of biodiesel [4,5]. Thus, palm oil represents one of the biggest pillars of economic growth in tropical developing countries. However, since it shares the same environmental and climatic requirements as lowland tropical rainforest [1], palm plantation is one of the main drivers of deforestation in the tropics, leading to biodiversity loss and the reduction of carbon storage, even inside the limits of protected forest areas [6].

Frequent mapping of palm plantation area is critical for the monitoring of the expansion of its frontier and for a correct management of forest resources. However, up-to-date information on land-cover changes is not common in these remote areas. Because field monitoring is complex and expensive, it does not allow for frequent updates across large regions. Conversely, satellite images can cover remote and extensive areas (at regional or national scale), offering a great advantage in comparison to field monitoring for assessing the impact of palm area expansion [6].

Remotely sensed optical spectra have proven to be useful for mapping land cover, through specific spectral signatures or spectral indices, both created with reflectance

data [7–10]. Thermal imagery has also shown to provide useful information to differentiate between forest and non-forest areas [11,12]. In tropical regions, however, the use of optical and thermal imagery is often complicated by excessive cloud coverage, hampering a continuous monitoring over large areas [13,14]. To address this limitation, SAR (Synthetic Aperture Radar) imagery [5,15–17] can be used to measure the surface backscatter in the microwave spectrum, as it is less affected by clouds.

Moreover, the fusion of spectral features from different spectral regions (i.e., optical, thermal, and microwave) has been reported to improve the accuracy and the spatial resolution of classification efforts [18–21]. Different data fusion techniques (e.g., pixel-based, object-based, or decision-level fusion [22,23]) and different classification algorithms (e.g., Random Forest, Support Vector Machine, and K-Nearest Neighbor [10,16,24]) have been tested to map palm plantations.

Nevertheless, previous studies tested their mapping approach in a single year, but as such, they failed to test the robustness of the methods to inter-annual climate variability. Such a test is important especially in the tropics, where atmospheric phenomena (e.g., the El Niño Southern Oscillation (ENSO) and the Pacific Decadal Oscillation) can drastically change climatic conditions [25].

In such situations, one can expect drastic changes in the rainfall and temperature regimes from one year to another [26], affecting the vegetation condition and, in turn, impacting the spectral properties (i.e., reflectance, emittance, and even backscattering) of the land surface components and, consequently, the mapping accuracy [11,17,27].

Therefore, to fill this gap, our study aims, first of all, to improve our understanding of satellite-based mapping of palm plantations by using features derived from distinct spectral regions (i.e., optical, thermal, and microwave) and a data-fusion approach. We analyzed how variations in climatic conditions might affect palm plantation mapping by evaluating the robustness of our mapping approach with respect to inter-annual climate variability observed across three different years. In this sense, we first focused on comparing the Overall Accuracy obtained by the annual classification maps created from these different features. Then, following the same methodology, we created three annual maps, corresponding to the three years analyzed, to study the changes in the output maps and their accuracies. Observed differences here are assumed to be mainly due to the effect of changing climate conditions.

2. Materials and Methods

2.1. Area of Study and Period

Ecuador is one of the major oil palm producers in Latin America [28], and its largest plantation area is located in the province of Esmeraldas, in the north of the coastal region (1°26′N–0°2′S and 78°22′W–80°10′W; Figure 1). Esmeraldas was once known as the Green Province due to the vast extension of its tropical forest, the Chocó forest, one of the world's biodiversity hotspots [29]. For this reason, the Ecuadorian government has created nine protected areas in its territory [30]. Nevertheless, it has suffered deforestation and a latter growing establishment of palm plantations in the last three decades [31,32]. Currently, it also has a high production of cocoa and banana, and large areas for livestock pasture [33]. Its topography is mostly flat, with elevation not surpassing 800 m above sea level in most of the territory [34], besides the southeast limit, which has borders with the Andes Mountains.

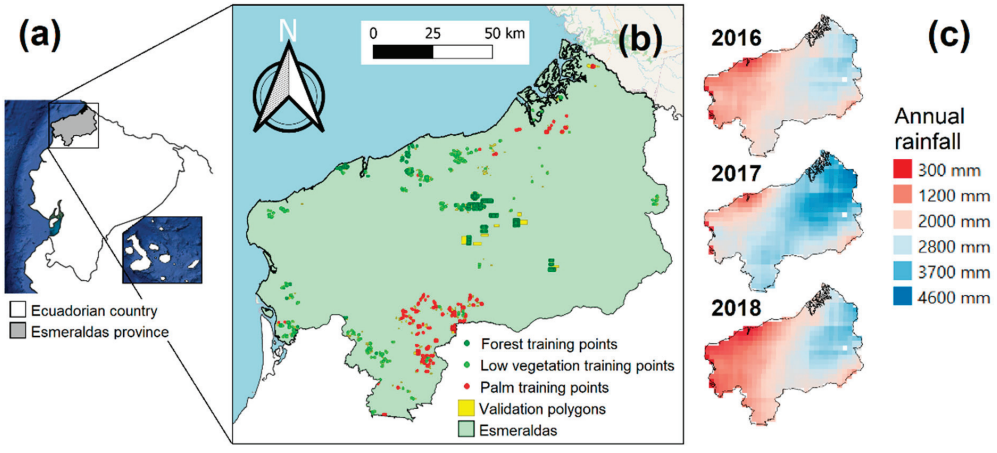


Figure 1. Delimitation of the area of study, comprising the Esmeraldas province (**b**), which is situated in the north of the coastal region of the Ecuadorian Republic (**a**). The central image shows the distribution of the sample points from which the spectral information is extracted to use it in the classifier. (**c**) Annual rainfall of the area of study during the years 2016, 2017, and 2018. Fluctuations among years are observed. Rainfall data retrieved from the Climate Hazards Group InfraRed Precipitation with Station (CHIRPS) dataset [35].

Esmeraldas presents three different types of climate: tropical sub-humid, humid, and very humid, with an average temperature around 23 °C [36]. However, the entire Ecuadorian coastal region is affected by several atmospheric phenomena, such as the ENSO and the Pacific Decadal Oscillation, that result in changes in precipitation, cloud cover, and air temperature [25].

In the present study, we used a three-year period (2016, 2017, and 2018) to assess the impact of distinct inter-annual precipitation regimes on our classification approach. The year of 2016 presented a drought, due to the occurrence of an ENSO event [37], with an average over the area of study of 2200 mm of annual rainfall, ranging from 540 to 3440 mm. In turn, 2017 was a regular year, with average rainfall levels over the area of study: mean annual rainfall of 2975 mm, ranging from 800 mm to more than 4600 mm. In 2018, an ENSO event affected the region again [38], reducing the mean annual rainfall to 2100 mm, which ranged from 340 to 3840 mm over the area of study (Figure 1c).

2.2. Satellite Imagery

We used imagery from the Moderate Resolution Imaging Spectroradiometer (MODIS) sensor (Table 1), a multispectral sensor that acquires images from 36 spectral bands, ranging from the optical to the thermal spectral region. The images have a coarse spatial resolution (250 m, 500 m, and 1 km pixel size) but high temporal resolution, with a revisit time of 1 to 2 days [39]. MODIS is onboard two different satellites, both producing images with the same characteristics: the Terra satellite, which passes the equator at 10:00 a.m.; and the Aqua satellite, which passes the equator at 1:30 p.m. [39,40].

In the present study, we followed a multi-temporal approach by using the MODIS database; in other words, we used all available images over a one-year period, i.e., 23 images in the case of the Vegetation Index product, and 46 in the case of Land Surface Reflectance and Land Surface Temperature and Emissivity products (Table 1). The multi-temporal approach has been reported to increase mapping accuracy in comparison with a single-date approach [21].

Table 1. List of the satellite imagery and products used in this study.

Sensor	Product	EM Region	Image Characteristics	Spatial and Temporal Resolution	# Scenes per Year	Acquisition Time (Julian Days)
MODIS Terra	MOD13Q1	Optical	Vegetation Index (VI)	250 m—16 days	23	001,017,033,049,065,081,097, 113,129,145,161,177,193,209, 225,241,257,273,289,305,321, 337,353
	MOD09A1	Optical	Land Surface Reflectance (LSR)	500 m—8 days	46	001,009,017,025,033,041,049, 057,065,073,081,089,097,105, 113,121,129,137,145,153,161, 169,177,185,193,201,209,217, 225,233,241,249,257,265,273, 281,289,297,305,313,321,329, 337,345,353,361
	MOD11A2	Thermal	Land Surface Temperature and Emissivity (LST)	1 km—8 days	46	
MODIS Aqua	MYD13Q1	Optical	VI	250 m—16 days	23	009,025,041,057,073,089,105, 121,137,153,169,185,201,217, 233,249,265,281,297,313,329, 345,361
	MYD09A1	Optical	LSR	500 m—8 days	46	001,009,017,025,033,041,049, 057,065,073,081,089,097,105, 113,121,129,137,145,153,161, 169,177,185,193,201,209,217, 225,233,241,249,257,265,273, 281,289,297,305,313,321,329, 337,345,353,361
	MYD11A2	Thermal	LST	1 km—8 days	46	
PALSAR 2	FNF	Microwave	Dual polarization (HH and HV)	25 m—1 per year	1	Ranging from 180 to 295

However, to deal with cloud contamination, we created composite images and combined features coming from both satellites (Terra and Aqua). Finally, we smoothed the data by using the Savitzky–Golay (S–G) filter, adjusting its parameters (e.g., window size and number of envelop iterations) to remove outliers but preserving the main characteristics of the data (e.g., relative minimum and maximum), as better explained in the following paragraphs. The S–G filter was applied by using the TIMESAT software [41,42].

We also used the microwave images from the Phased Array type L-band Synthetic Aperture Radar 2 (PALSAR 2), which provides fine-beam dual-polarization images. The specific band (L-band) and polarizations (HH and HV) of PALSAR 2 allows it to penetrate the canopy and differentiate between forest and other land-cover types [43]. However, PALSAR 2 is a sensor with commercial purposes, meaning that the images are not free. To deal with this limitation, we used the features provided with the Forest/Non-Forest (FNF) annual map product [44], which is a classification map of forest and non-forest land cover of 25 m spatial resolution; this product includes a global mosaic of SAR features, which are freely available to download at the JAXA website (https://www.eorc.jaxa.jp/ALOS/en/palsar_fnf/data/index.htm, accessed on 4 January 2021). This also implies that the map created with SAR data, contrary to MODIS data, follows a single-date approach.

2.3. Preprocessing

In total, we tested eleven approaches, six of them using features from a single spectral region and five using a data-fusion approach that combines features from different spectral regions. Three of the evaluated approaches used optical features: (i) a vegetation-index approach (VI), (ii) a phenology-metrics approach (PHENO), and (iii) a spectral-reflectance approach (SRB).

VI uses mathematical equations created to summarize the information contained in different spectral bands to facilitate the analysis of intra-annual changes in

vegetation [9,45]. We followed a multi-index method [8] that incorporates different information from the land cover provided by different Vegetation Indices. We combined the widely used NDVI (Normalized Difference Vegetation Index) with EVI (Enhanced Vegetation Index), both related to photosynthetic activity, and both retrieved directly from MOD13Q1 and MYD13Q1 products, calculated according to the following formulas:

$$\text{NDVI} = (\text{NIR} - \text{red})/(\text{NIR} + \text{red}) \quad (1)$$

$$\text{EVI} = 2.5 \times (\text{NIR} - \text{red})/(\text{NIR} + \text{C1} \times \text{red} - \text{C2} \times \text{blue} + \text{L}) \quad (2)$$

Both NDVI and EVI consist in the ratio of the red band (wavelength: 620 to 670 μm), which is related to photosynthetic activity, and NIR band (wavelength: 841 to 876 μm), which is related to leaf/canopy structure. In the case of EVI, adjustment factors are included (L = 1, C1 = 6, and C2 = 7.5) to make EVI less prone to saturation in densely vegetated areas, as is the case with NDVI; however, EVI is more sensitive to variations in viewing geometry [46].

We also include the NDII (Normalized Difference Infrared Index), which was computed with the following equation:

$$\text{NDII} = (\text{NIR} - \text{SWIR7})/(\text{NIR} + \text{SWIR7}) \quad (3)$$

The NDII index used the SWIR7 band (wavelength: 2105 to 2155 μm), which is sensitive to the water content in vegetation [47]. Knowing that cloud presence results in sudden drops in Vegetation Index values [48], after combining the images from both satellites (i.e., a total of 46 images per year), we applied the S–G filter, setting the window size to 10 and the number of envelope iterations to 3 in order to filter out extremely low values and keep the high ones.

PHENO uses the time series of the three Vegetation Indices used in the VI approach to extract phenology metrics [42]. We extracted these metrics from the fitted time series by using the S–G filter and 20% of the seasonal amplitude to establish the start of the season. We fed the classification algorithm with the thirteen metrics that TIMESAT allowed us to extract: time and value of the start and end of the season; base value, length, and amplitude of the season; large and small growing season integrals; value and time of the peak of the season; and left and right derivatives.

SRB uses the reflectance values from all available optical spectral bands. This approach is most common when using the Landsat dataset [2,7,10], and it consists of using raw spectral information from all the bands to differentiate among land-cover types through their multispectral signatures. We used two different MODIS products (Table 1), totaling seven optical spectral bands (i.e., blue, green, red, NIR, SWIR5, SWIR6, and SWIR7). Contrary to the case of Vegetation Indices, cloud contamination produces higher reflectance values than expected from vegetation in all spectral bands [49]. Therefore, during the preprocessing of the spectral bands coming from the Vegetation Index product (i.e., blue, red, NIR, and SWIR7), we combined the images from both satellites and created a composite, keeping pixels with the lowest values, (corresponding to the highest absorption), resulting in 23 images per band and per year. Then all images were smoothed with the S–G filter, adjusting the window size to 4 and the number of envelope iterations to 1, this time to filter out extremely high values and keep the low ones. In the case of the bands from the Land Surface Reflectance product (i.e., green, SWIR5, and SWIR6), we combined the images from the Terra and the Aqua satellites and then created composites, keeping the pixels with the lowest values, resulting again in 23 images per band and per year. Finally, we smoothed the data with the S–G filter, adjusting the parameters in the same way as with the Vegetation Index product.

The fourth and fifth approaches evaluated used the thermal spectral bands from the MODIS instrument. More specifically, we used (iv) the Daytime Surface Temperature (DST) and (v) the Nighttime Surface Temperature (NST) features. The thermal bands are also highly affected by cloud contamination, which impacts the retrieval of surface emittance

data by the MODIS sensors, preventing the derivation of the Land Surface Temperature and Emissivity (LST) product (Table 1) in contaminated pixels [39]. To address the lack of data, we combined both sources (Terra and Aqua satellites) to create composite images (i.e., 46 images per year), keeping pixels with the highest values, although we expected to find small differences in the temperature due to the different acquisition times. MODIS LST products have a pixel size of 1 km. Thus, to combine this product with features from different spectral regions (described before), we resampled the images to 250 m, using the bilinear method [4]. Finally, we applied the S–G filter—in this case, to preserve original values and, at the same time, fill in missing values in the time series through interpolation. We set the window size to 2 and the number of envelope iterations to 1.

The sixth approach assessed was (vi) the microwave feature approach (hereafter, SAR map); in order to create the SAR map, we masked low-quality pixels (with shadows or layover issues) and generated two new features: the ratio (HH/HV) and the difference (HH − HV) between both polarization images [16]. Then we removed the speckle effect by applying the Refined Lee speckle filter [50] on the Sentinel Application Platform (SNAP) [51]. Next, we resampled the features to a 250 m resolution, using the bilinear method, since it has been reported that an increased accuracy can be obtained with resampled SAR images at a coarser spatial resolution, mainly because of a greater speckle reduction [15]. Finally, all features were converted to a logarithmic scale (decibels, dB) in order to enhance their visualization.

The last five evaluated approaches from the eleven initially proposed were the data-fusion combinations. We followed a simple but effective data-fusion approach that is mostly used with the Sentinel 1 and 2 dataset, combining optical, thermal, and/or SAR images by resampling the images from the different sources to get the same spatial resolution (250 m), and stacking all the images from a year together [21,52,53]. This way, each pixel contains properties and qualities extracted from the different spectral regions and the temporal information of each feature [54]. Following this method, we formulated the five combinations of features: (vii) SAR + VI map [4,55], (viii) SAR + PHENO map [56], (ix) SAR + SRB map [57,58], (x) SAR + DST map [59], and (xi) VI + DST map [60,61].

2.4. Reference Data and Classification Algorithm

In the present study, we used the pixel-based Random Forest (RF) classifier, a non-parametric statistical model that creates a combination of uncorrelated decision trees based on random samples of predictors or variables [7,28]. RF is capable of managing a large number of variables in a fast and robust way, selecting the most important ones for the differentiation among categories [57,62,63]. We chose the RF algorithm since it has been reported to perform better than, for example, the Support Vector Machine, when coarse-spatial-resolution images are used [64].

Using high-spatial-resolution images from Google Earth and Bing Maps, and following a stratified random sampling, we gathered regions of interest (ROIs) of ground truth data for training the classification algorithm and to validate the results (Figure 1b). We looked for the three main land-cover types in the region: forest (natural and forest plantation), palm plantation (industrial and small scale), and low vegetation (pasture, grassland, annual crop). We used the manual digitizing method, specifically the on-screen digitizing process, which consists of manually choosing and drawing the ROIs on the high-resolution images. These areas were selected under two criteria: (1) the source image must have been taken between the year 2016 and 2018, and (2) the land cover must have remained unchanged during the study period.

Around 5000 sample points were obtained from the ROIs; half of them were used as a training dataset (1050 points of forest cover, 800 points of palm plantation, and 655 points of low vegetation), and the other half for validation. All non-vegetative cover (i.e., cities, main rivers, and aquaculture farms) were masked due to their marginal presence in the area of study and to avoid classification errors. These areas were identified with the Map of Homogeneous Accessibility Areas of the Ministry of Agriculture of Ecuador [65].

An accuracy assessment was performed by using the Overall Accuracy (OA), the Kappa coefficient, the Producer's Accuracy (PA), and the User's Accuracy (UA) [66,67]. However, our main concern was to obtain a high PA and UA for the palm plantation class, since, ideally, we should have fewer palm plantation pixels omitted from the correct class and also fewer mislabeled in other classes [68].

An overview of the workflow, with the preprocessing of the images and the classification steps to produce the thematic maps, is presented in Figure 2.

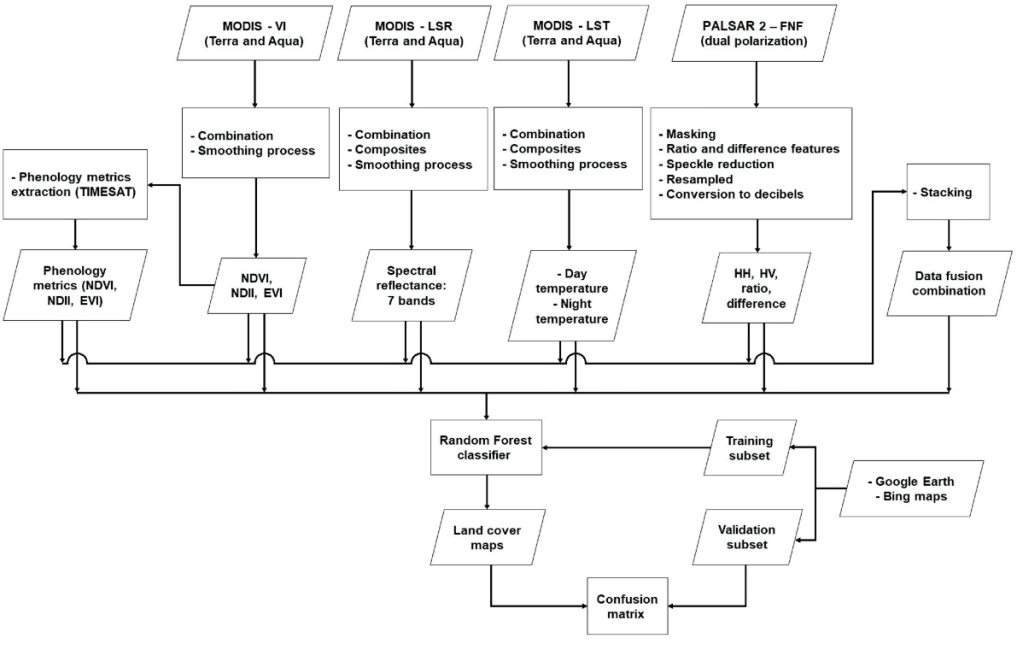


Figure 2. Image preprocessing workflow and classification scheme with the entire dataset. Please note that "combination" refers to the use of both image sources (Terra and Aqua satellites), while "composite" refers to the combination of images from different dates.

3. Results

For the first analysis, we compared the accuracy obtained by the maps created with 2017 data, recognized as the period with regular precipitation regimes (Figure 3; Table 2). It is noticeable that all the annual classification maps displayed a similar distribution of the land-cover types over the area of study.

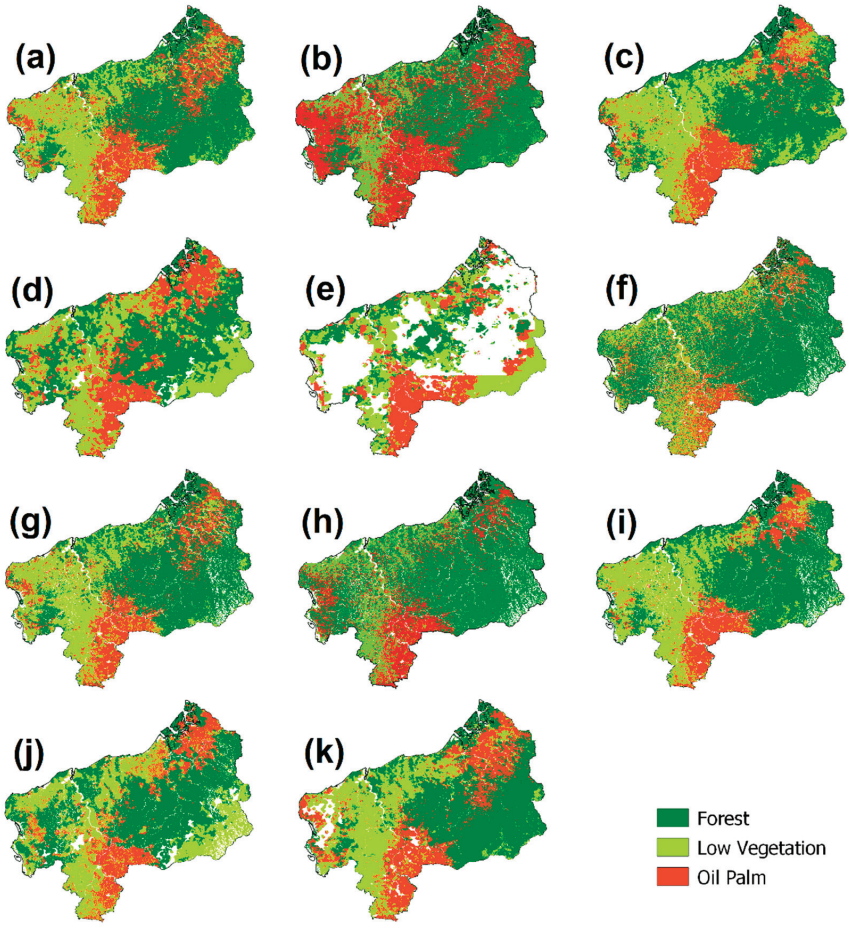


Figure 3. Land-cover maps of the year 2017 based on optical, thermal, and microwave features and data-fusion combinations. (**a**) Vegetation Indices (VIs) map; (**b**) Phenology metrics (PHENO) map; (**c**) Spectral Reflectance Bands (SRBs) map; (**d**) Daytime Surface Temperature (DST) map; (**e**) Nighttime Surface Temperature (NST) map; (**f**) Synthetic Aperture Radar (SAR) map; (**g**) SAR + VI map; (**h**) SAR + PHENO map; (**i**) SAR + SRB map; (**j**) SAR + DST map; and (**k**) VI + DST map.

Table 2. Accuracy metrics obtained from each approach across the three years analyzed. The metrics are Overall Accuracy (OA), Kappa coefficient (Kappa), Producer's Accuracy (PA), and User's Accuracy (UA). The listed approaches are Vegetation Indices (VIs), Phenology metrics (PHENO), Spectral Reflectance Bands (SRBs), Daytime Surface Temperature (DST), Synthetic Aperture Radar (SAR), and five data-fusion combinations.

			OA (%)	Kappa	PA Forest (%)	UA Forest (%)	PA Low Vegetation (%)	UA Low Vegetation (%)	PA Palm (%)	UA Palm (%)
Optical, Thermal, and Microwave Feature Maps	VI maps	2016	84.1	0.75	92.6	86.6	74.2	87.7	80.6	77.9
		2017	91.7	0.87	96.2	91	88.4	94.7	88.1	90.3
		2018	87.6	0.81	95.8	87.8	74.5	92.1	87	84.2
	PHENO maps	2016	67.2	0.49	83.1	75.1	35.7	75.6	71.4	54.8
		2017	88	0.81	95.3	85	86.4	95	79.2	87.3
		2018	70.8	0.54	87.3	87.8	74.5	92.1	87.1	84.2
	SRB maps	2016	90.1	0.85	97.3	92.7	70.7	93.9	96.4	84.4
		2017	94.6	0.92	98.4	95.4	86	94.9	96.5	93.1
		2018	89.8	0.84	97.9	87.4	75.2	96	90.5	89.3
	DST maps	2016	93.7	0.9	98	97.8	84.9	93.7	94.9	88.1
		2017	92.9	0.89	96.3	97.6	88.2	85.5	92.1	92.8
		2018	91.4	0.87	96.6	93.3	77.3	94	96.2	87.2
	NST maps	2016	87.9	0.78	85.9	98.6	75.4	86.4	94.8	86.3
		2017	82.8	0.74	77.7	92.4	74.6	64.7	96	87.6
		2018	76.5	0.65	81.7	66.9	56.6	77.8	90.4	83.6
	SAR maps	2016	87.1	0.8	96.8	90.9	71.3	86.6	86.9	82
		2017	87.1	0.8	97.2	92.1	74.1	83.2	83.8	82.7
		2018	84.8	0.77	93.7	90.8	70.7	79.8	84.2	80
Data-Fusion Combination Maps	SAR + VI maps	2016	90.8	0.86	98.3	92.9	78.5	92.8	90.4	86.2
		2017	95.3	0.93	98.6	95	90.9	96.9	93.9	93.9
		2018	93.1	0.89	97.9	94.6	85.7	93.3	92.6	90.9
	SAR + PHENO maps	2016	81.1	0.7	98.5	83.4	45.8	98.1	86.4	72.2
		2017	87.9	0.81	99.4	93.3	89.9	98	92.5	94.5
		2018	86.8	0.79	98.1	85.7	65.5	95.4	89	83.8
	SAR + SRB maps	2016	92.7	0.89	98.9	94.3	77	96.2	97.2	88.2
		2017	96.5	0.95	99.2	89.9	98.2	97.3	97.1	94.8
		2018	92.1	0.88	98.7	89.9	80	97.3	93	91.9
	SAR + DST maps	2016	95.8	0.94	99.3	99	90	94.7	95.9	92.3
		2017	95.5	0.93	98	98.9	92	90.9	94.8	94.6
		2018	93.9	0.91	97.9	95.2	83.5	95.3	97.3	91.1
	VI + DST maps	2016	92.3	0.88	94.5	98.6	86	90.3	94.4	85.8
		2017	95.3	0.93	96.9	97	90.8	96.8	96.8	91.7
		2018	92.3	0.88	97.8	95	79.4	93	95.6	88.2

3.1. Classification Performance of Maps from Single Data Source and Data Fusion

Comparing the maps created by using the different features from the optical spectral region, we observed that the SRB map obtained the highest OA (94.6%; Table 2) and Kappa (0.92), and also the highest PA (96.5%) and UA (93.1%) for the palm plantation class. It is, however, noteworthy how the irregularity of the topography affects the classification of the low vegetation class, due to the incorrect assignment of this class in an area of protected natural forest located in the southeast region of Esmeraldas (Figure 3c). On the other hand, the PHENO map displayed a much larger number of pixels assigned to the palm plantation class (Figure 3b), especially at the west side of the area of study, and, consequently, the lowest accuracy (OA of 88% and Kappa of 0.81) from the optical-based maps.

The DST map obtained high OA (92.9%; Table 2) and Kappa (0.89), and high PA (92.1%) and UA (92.8%) for the palm plantation class, similar to the SRB map results. Likewise, it is observable how the DST map (as well as the NST map) is affected by irregularities in the topography, similar to the case of the SRB map, but to a greater extent. Moreover, both DST and NST maps are greatly affected by cloud cover (Figure 3d,e), even after preprocessing the LST images to decrease the amount of missing values. In the NST maps, almost half

of the area of study was impacted by cloud cover, leaving no data to be analyzed. This resulted in a bias in the metrics obtained from the accuracy assessment, which obtained a high OA (82.8%) and Kappa (0.74), but, as a consequence of the massive presence of blank spaces, leaving just few pixels to validate the map. For this reason, the NST map was discarded for further analysis.

The SAR map presented a high OA (87.1%; Table 2) and Kappa (0.80), but contrary to our expectations, its accuracy was not the best one when compared to the optical and thermal feature maps. This might be due to the speckle effect that persisted in the input images even after the preprocessing steps and was consequently reproduced in the final map (Figure 3f).

Finally, all data-fusion combinations obtained higher accuracy metrics than the ones obtained from the maps created by using each data source individually (Figure 3g–k; Table 2). However, our data-fusion approach, while straightforward, also allowed the issues inherent to each data source to remain in the resulting maps. For instance, combinations using thermal data are still highly impacted by irregular topography and also presented missing data due to cloud-cover contamination (Figure 3j,k). In yet another example, maps that were created from the optical or thermal data together with SAR features kept the missing data in the southeast region of the area of study due to shadow and overlay problems (Figure 3g–j).

3.2. Inter-Annual Comparison of Classification Performance

To test how differences in precipitation regimes could affect palm plantation mapping, we generated a map for each year between 2016 and 2018, knowing that these three years were subjected to distinct precipitation regimes (mainly due to ENSO events in 2016 and 2018). For this analysis, we did not use the maps PHENO, PHENO + SAR, and NST, due to their low performance when compared with the rest of the optical-based maps and with the DST map, respectively (Table 2). We also did not use the SAR maps because, as mentioned before, they are the only map that follow a single-date approach, and the source images were specifically chosen to be the least affected by rainfall and surface moisture. For these reasons, SAR maps presented a high stability across the years. We focused on the best maps of the previous analysis, comparing the accuracy metrics that take into account all classes together: OA and Kappa coefficient. We chose three maps from the single-data-source approach (i.e., VI, SRB, and DST maps) and three from the data-fusion approach (i.e., SAR + SRB, SAR + DST, and VI + DST maps).

The images for each one of the tested approaches and over the three years analyzed are presented in Supplementary Figures S1 and S2, and the actual values for the OA, Kappa, and per-class accuracy metrics (i.e., PA and UA) are presented in Table 2.

Both the OA and Kappa varied across the three years analyzed (Figure 4) when comparing the performance for distinct years within approaches. Overall, the year 2017 presented the best results (except for the SAR + DST, and DST maps, for which the 2016 classification presented higher accuracies). Even for the classifications that retrieved the highest accuracies (e.g., VI, SRB, DST, VI + DST, SAR + SRB, and SAR + DST), the metrics changed from one year to another (with differences in the OA as low as 0.4%, and as high as 7.6% across the three years analyzed). It is also noteworthy that, following Landis and Koch (1977) nomenclature to label Kappa values, all output maps achieved excellent results, reaching "substantial" and "almost perfect" categories [69,70].

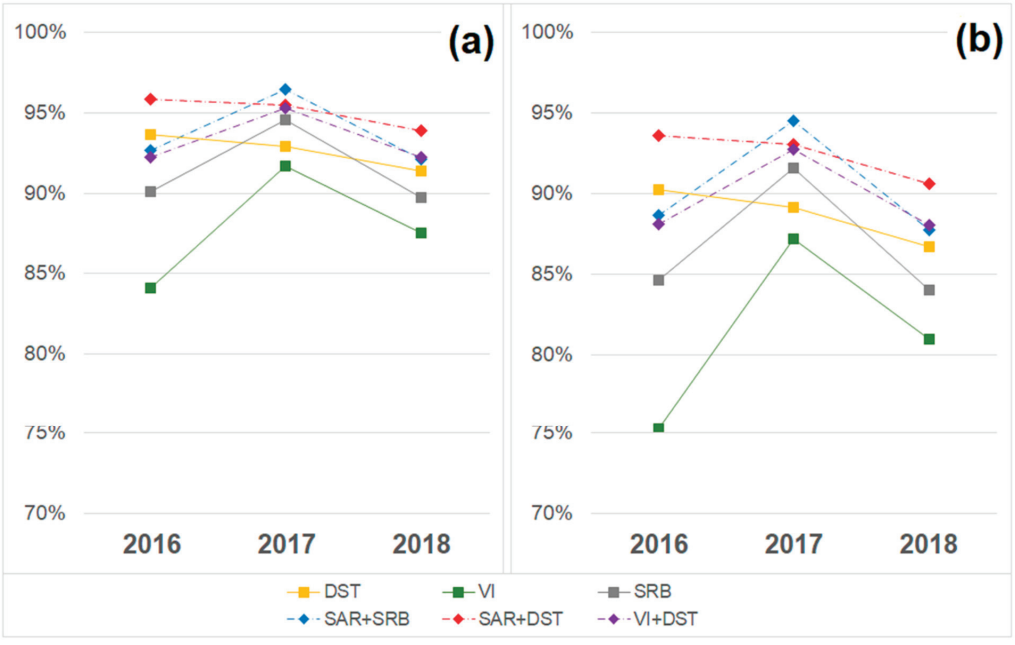


Figure 4. (**a**) Overall Accuracy and (**b**) Kappa coefficient for the best classification maps from the different approaches proposed across the three years analyzed. Full lines represent approaches using features from a single spectral region, while dashed lines represent data-fusion approaches.

Next, for a more comprehensive analysis of the changes produced by inter-annual climate variability in land-cover mapping, we evaluated the PA and the UA of each class in the produced maps across the three years analyzed (Figure 5) as a way of better comparing per-class accuracy [68,70].

Overall, the maps which used optical data in the single-region-feature approach and in the data-fusion approach (VI, SRB, and SAR + SRB) displayed a similar behavior: the accuracy was higher in 2017, the year with a regular precipitation regime, and lower during drought years (2016 and 2018; Supplementary Figure S1). The maps involving thermal features (DST and SAR + DST) presented a non-uniform behavior, presumably not driven by changes in precipitation regimes.

SAR data in the data-fusion approaches (SAR + SRB and SAR + DST) contributed to reduce the differences of PA and UA values of the palm plantation class among the years analyzed. For instance, in the SRB map of the year 2017, the PA value of the palm plantation class decreased by 0.1% in 2016 and 6% in 2018, and the UA decreased by 8.7% in 2016 and 3.8% in 2018. Meanwhile, in the SAR + SRB maps, the PA value obtained in the year 2017 increased by 0.1% in 2016 and decreased by 4.1% in 2018, and the UA value decreased by 6.6% in 2016 and 2.9% in 2018.

In yet another example, the PA value of the palm plantation class of the DST map of 2017 increased by 2.8% in 2016 and 4.1% in 2018, and the UA value decreased by 4.7% in 2016 and 5.6% in 2018. Meanwhile, in the SAR + DST map, the PA of the year 2017 increased by 1.1% in 2016 and 2.5% in 2018, and the UA value decreased by 2.3% in 2016 and 3.5% in 2018.

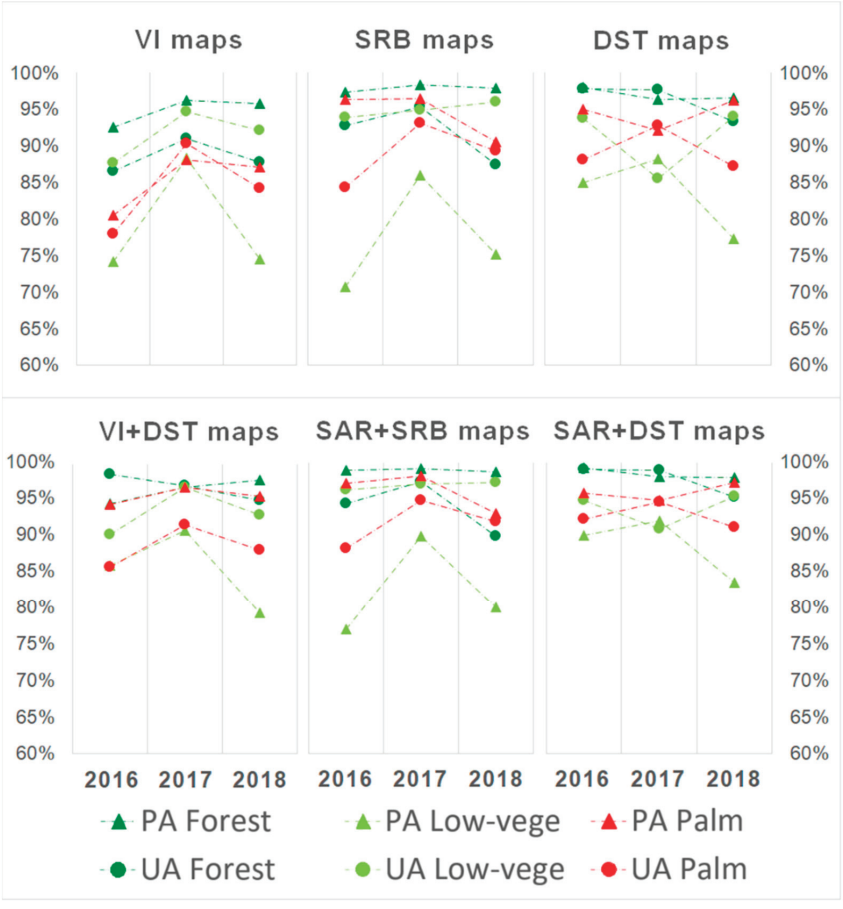


Figure 5. Comparison of Producer's Accuracy (PA) and User's Accuracy (UA) of the three land-cover types over the three-year analysis of the selected thematic maps (i.e., the maps with the highest OA and Kappa, three maps created by using single-data-sources approach and three with data-fusion approach).

However, data-fusion-approach maps still displayed differences among years. For example, Figure 6a shows the capture of a Google Earth image of an area corresponding to low vegetation cover unchanged from 2015 to 2018; Figure 6b shows that, in the SAR + SRB maps, the classifier assigned the palm plantation class in almost half of the pixels in the years 2016 and 2018, while, in the year 2017, the land cover is correctly assigned. Figure 6c displayed also in the year 2016 a great number of pixels assigned to the palm plantation class in the middle-west of the area of study, while those same pixels were assigned mainly as low vegetation in the other two maps (2017 and 2018).

Finally, since we focused on the accuracy obtained specifically for mapping palm plantation, we averaged the values of the two class-specific accuracy measurements, PA and UA, to obtain the mean accuracy value for the palm plantation class (hereafter, mean accuracy). This combined measure will give us an idea of the number of pixels correctly assigned to this class and the number of pixels mislabeled at the same time [15].

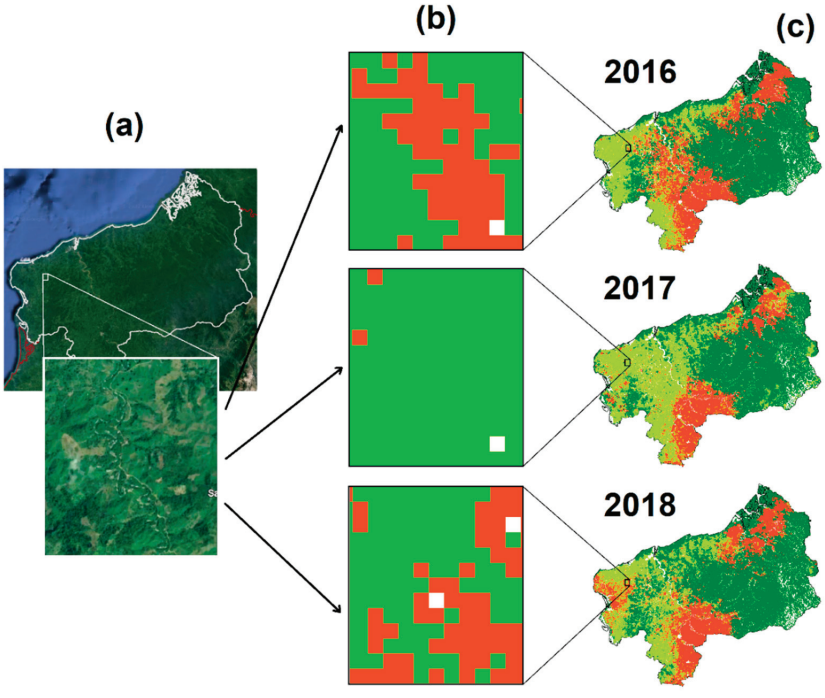
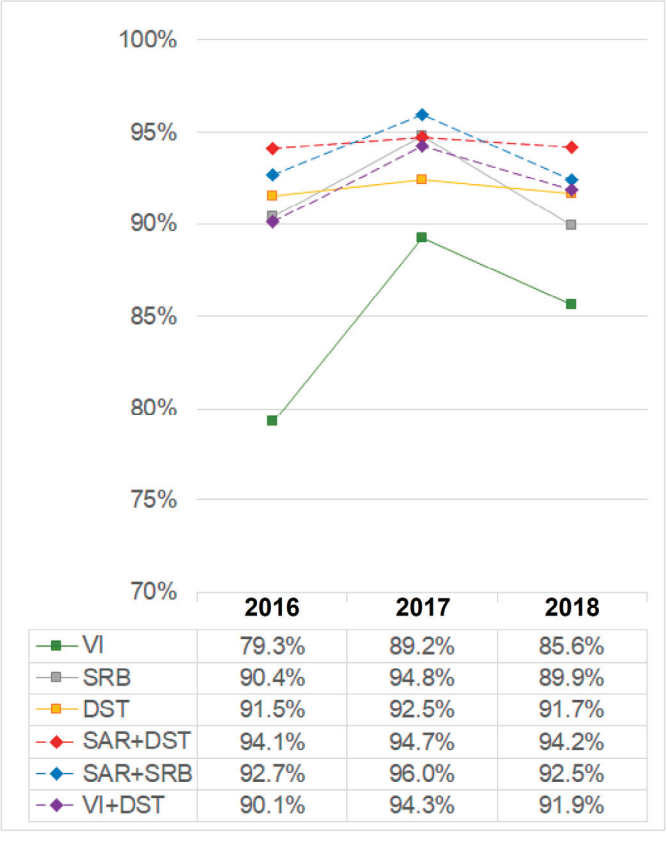


Figure 6. (**a**) True color satellite image of the area of study, with an enlarged square area dominated by low vegetation. (**b**) Enlargement of the classification map corresponding to the area of the square panel of the image (**a**). (**c**) SAR + SRB classification maps of the three years analyzed. The enlargement square of the 2017 map corresponds with the real land-cover type, while, in 2016 and 2018, the pixels were incorrectly assigned mostly as palm plantation.

This analysis suggested that all selected maps performed better during the year 2017 (Figure 7). For instance, the SAR + SRB maps obtained the highest mean accuracy, with an average error of only 4.5% in 2017, which rose to 7.4% in 2016 and 2018 due to the impact of inter-annual climate variability. On the other hand, the SAR + DST map obtained high and consistent mean accuracies across the three years (94.1%, 94.7%, and 94.2% in the year 2016, 2017, and 2018, respectively). That represents an error margin between 6.9% and 6.3%.



	2016	2017	2018
VI	79.3%	89.2%	85.6%
SRB	90.4%	94.8%	89.9%
DST	91.5%	92.5%	91.7%
SAR+DST	94.1%	94.7%	94.2%
SAR+SRB	92.7%	96.0%	92.5%
VI+DST	90.1%	94.3%	91.9%

Figure 7. Annual differences in the mean accuracy value ((PA + UA)/2) for the palm plantation class across the three years analyzed. Values are presented for each one of the previously selected approaches. Full lines represent approaches using features from a single spectral region, while dashed lines represent data-fusion approaches.

4. Discussion

In this study, we provided insights on land-cover mapping accuracy obtained by using different features of the electromagnetic spectrum and some data-fusion combinations. By correctly preprocessing the available images and decreasing the amount of missing data due to cloud cover, we generated thematic maps with three land-cover types with good Overall Accuracies. However, it is noteworthy that the inter-annual climate variability affected the vegetation in such a way that it produced changes in its spectral properties during the years analyzed, resulting in inaccuracies in land-cover mapping.

The low vegetation class showed the lowest accuracy and the lowest consistency over the years when compared to the other classes. This is a consequence of the mixture of vegetation cover that this class contains (e.g., annual crops, shrubs, grassland, pasture, and bare lands), which translates into a high spectral and structural diversity. The forest class achieved the highest PA and UA in all maps, and this is in line with several other mapping studies [4,7,15,16,71], suggesting that this class is relatively easy to be separated from the other classes. In this sense, contrary to what was reported in other studies, we obtained a high spectral differentiation between the forest and the palm plantation classes [7,72]. Additionally, drastic differences in surface backscatter and temperature between palm plantation areas and forest were found [11,12,16,43]. This was potentially a consequence of the type of forest (i.e., native) that has more homogeneous characteristics than secondary

forest, and the type of palm plantation (i.e., industrial) that is more uniform (in terms of canopy closure and vertical structure) than small plots from individual farmers [7,72].

The maps generated from optical features are evidently the most affected by inter-annual climate variability, presenting the greatest differences in PA and UA for all classes among the years analyzed (Table 2 and Figure 5). For instance, in the VI map of the year 2017, the PA value of the palm plantation class decreased 7.5% in 2016 and 1.1% in 2018, and the UA decreased 12.4% in 2016 and 6.1% in 2018.

For palm plantation mapping, the SRB map showed to be the most accurate one (averaging over the three years, the map presented a PA of 94.5% and UA of 88.9%). However, it also presented a notable reduction in the accuracy for all classes during drought years. For example, when comparing the PA and UA of the forest class, the PA and the UA of the year 2016 increased 1.1% and 2.7%, respectively, in the year 2017; the same happened with the low vegetation class, as the PA and UA values increased 15.3% and 1%, respectively; and in the case of the palm plantation class, the PA and UA increased 0.1% and 8.7%, respectively (Table 2 and Figure 5). This is presumably because drought can cause physiological reactions in the vegetation, affecting photosynthetic activity and, thus, the spectral characteristics of the vegetation [27].

The VI-based thematic maps also obtained high accuracy and a distribution of the land-cover types comparable to the SRB maps (Figure 4 and Supplementary Figure S1a). However, contrary to what the literature reports regarding normalized indices compensating for changes in illumination, topographic conditions, and viewing angle, and thus producing better maps than the ones made by spectral data [8], our VI maps did not present better results than the SRB maps (although they were indeed less affected by the irregular topography).

The thematic maps generated with the phenology metrics were the least accurate and, by far, the most affected by inter-annual climate variability (Table 2 and Supplementary Figure S1b). This is understandable due to the close link between the intra-annual climatic conditions (e.g., precipitation regime, solar radiation, and temperature) and the phenology of the vegetation [8,9].

Persistent cloud cover affected most thematic maps that were based on thermal features (Supplementary Figure S1d,e). As already mentioned, the algorithm used to generate MODIS imagery is unable to retrieved LST information if the pixel does not meet certain criteria, such as clear-sky conditions [73]. Thus, since the RF classifier cannot handle missing values [74], this results in blank spots where data are missing. However, the DST maps did present a high PA and UA for the palm plantation class (averaging over the analyzed period a PA of 94.4% and a UA of 89.4%) and also obtained consistent results for all other classes (Table 2 and Figure 4). This could be a consequence of using 8-day average composites basemaps that were created from the daily measurements, but mostly because, when creating the monthly composites, we removed all the variability added by daily energy balances, rainfall events, or soil moisture, while keeping only the seasonal variability that is linked mostly to land-cover types [19,73]. The DST maps were also highly affected by the topography (e.g., irregular slope conditions and shades) present in the southeast limit of Esmeraldas province [75], creating some confusion in the classifier (Supplementary Figure S1d).

The microwave-based thematic maps showed high PA and UA for the palm plantation class (averaging over the three-year period, a PA of 85% and a UA of 81.6) but lower than the optical and thermal-based maps. Nonetheless, it obtained highly consistent results across the study period (Table 2). This is because PALSAR data are considered to be very stable in forested areas, and also as a consequence of the preselection of the SAR images that integrate the global mosaic of the FNF product used in our analysis. The selection of those images took into account seasonality and were taken annually from June to September or from November to January, preferably selecting the ones with lower surface moisture influence [44].

Our data-fusion approach integrates the features from different spectral regions to enhance information contained in each pixel and improve land-cover differentiation and classification. This way, we have additional information coming from each land cover, adding biophysical attributes to the spectral characteristics of the vegetation [18,20,76]. All data-fusion combinations presented improved OA, Kappa, and within-class accuracy (PA and UA) when compared to the ones generated without data fusion. However, they followed a similar pattern as their original data sources when comparing classification stability among the three years (Figure 5). For instance, the maps generated by using the SAR + SRB data fusion were the most accurate in terms of palm plantation classification, but still with a clear variability over different precipitation regimes, which was also the case for the SRB maps (Table 2; Figures 4 and 5). Similarly, the SAR + DST maps obtained the second highest accuracy for the palm plantation class, with more consistent results over the three-year period; this was also the case for the DST maps (Table 2; Figures 4 and 5). On top of that, all data-fusion-based maps displayed a combination of the issues present in the maps created by using each one of their data sources. For instance, all maps with SAR features contained missing values in the southeast areas due to shadow and lay-over problems on irregular topography (Supplementary Figure S2a–d). Likewise, all maps generated with LST data have topography issues and missing values due to cloud contamination (Supplementary Figure S2d,e).

Finally, with the analysis of the mean accuracy value (Figure 7), we obtained a clear idea of the impact caused by inter-annual climate variability in palm plantation mapping. As an illustration, the SAR + DST maps have virtually the same accuracy over the three years, i.e., ~6% of error. In other words, there is a 6% chance of failing to find palm plantations where they actually exist. This error margin was reduced to only 3.5% with the SAR + SRB map, under regular climate conditions (in 2017), but the accuracy decreased over altered conditions (i.e., ~7.5% of error in both 2016 and 2018).

Consequently, we here argue that inter-annual climate variability should be considered during land-cover classification, especially if the output will be used as input in further studies, for example, for the determination of plantation area or yield [77].

The present study was limited to palm plantation mapping due to its high relevance for the global economic growth and its impact in tropical forests. However, future research could perform similar analyses by using different perennial (or even with annual) crops of high importance in tropical areas. This study was also limited to a specific location, but broader scale analysis and studies in other regions that present different atmospheric mechanisms that influence vegetation response are also relevant, both to expand our knowledge and improve land-cover-mapping techniques.

5. Conclusions

Palm plantations, established in tropical rainforest areas, can be mapped with high accuracy, using features from all regions of the electromagnetic spectrum. Our results showed that data fusion combinations can provide a substantial improvement in the Overall Accuracy of the maps. However, the Overall Accuracy and Kappa coefficient alone are not the proper metrics to study, in detail, palm-plantation-mapping accuracy. Instead, the Producer's and User's Accuracy (and also the average of both) allowed us to determine the impact of annual climatic disturbances in palm-plantation mapping.

Our results also suggest that the effect of inter-annual climate variability over vegetation, producing changes in its spectral properties, can lead to mapping inaccuracies.

Thematic maps generated from optical features outperformed thermal and microwave-based maps in terms of Overall Accuracy, but they were the most affected by changing climatic conditions. Thermal features proved to be the most consistent against changes in rainfall regimes, but they were highly affected by persistent cloud cover, as is typical of some tropical regions. Data-fusion combination increased Overall Accuracy and inter-annual consistency in all maps, producing the highest accuracy with the SAR + SRB maps

and the highest stability with the SAR + DST maps (i.e., error margin between 3.5 and 7.5% for the former and an average error of ~6% over the three years analyzed for the latter).

We propose that further studies should take into consideration the effect of climate variability over land-cover classification, especially knowing that phenomena such as the ENSO event will occur more frequently and intensively in the future [25]. Potentially, future studies could also use change detection techniques and trend analysis to help in the differentiation of land-cover types.

Supplementary Materials: The following supporting information can be downloaded at https://www.mdpi.com/article/10.3390/rs14133104/s1. Figure S1: Land-cover maps based on optical, thermal, and microwave features across the three years analyzed. Figure S2: Land-cover maps based on data fusion combinations across the three years analyzed.

Author Contributions: Conceptualization, F.T. and B.S.; methodology, F.T.; software, F.T.; validation, F.T. and B.S.; formal analysis, F.T.; investigation, F.T.; resources, F.T.; data curation, F.T.; writing—original draft preparation, F.T.; writing—review and editing, B.S. and P.N.B.; visualization, F.T. and P.N.B.; supervision, B.S.; project administration, F.T.; funding acquisition, F.T. All authors have read and agreed to the published version of the manuscript.

Funding: This research was funded by National Secretariat of Higher Education, Science, Technology, and Innovation of Ecuador (SENESCYT; contract number CZ05-001245-2018). P.N. Bernardino is funded by the Research Foundation Flanders (grants G0F6922N and G063420N).

Data Availability Statement: Not applicable.

Acknowledgments: The authors would like to thank Jos Van Orshoven, and Guido Wyseure for the support provided in the realization of this research project.

Conflicts of Interest: The authors declare no conflict of interest.

References

1. De Petris, S.; Boccardo, P.; Borgogno-Mondino, E. Detection and characterization of oil palm plantations through MODIS EVI time series. *Int. J. Remote Sens.* **2019**, *40*, 7297–7311. [CrossRef]
2. Vijay, V.; Pimm, S.L.; Jenkins, C.N.; Smith, S.J. The Impacts of Oil Palm on Recent Deforestation and Biodiversity Loss. *PLoS ONE* **2016**, *11*, e0159668. [CrossRef]
3. Gutiérrez-Vélez, V.H.; DeFries, R.; Pinedo-Vásquez, M.; Uriarte, M.; Padoch, C.; Baethgen, W.; Fernandes, K.; Lim, Y. High-yield oil palm expansion spares land at the expense of forests in the Peruvian Amazon. *Environ. Res. Lett.* **2011**, *6*, 044029. [CrossRef]
4. Cheng, Y.; Yu, L.; Xu, Y.; Liu, X.; Lu, H.; Cracknell, A.P.; Kanniah, K.; Gong, P. Towards global oil palm plantation mapping using remote-sensing data. *Int. J. Remote Sens.* **2018**, *39*, 5891–5906. [CrossRef]
5. Pohl, C. Mapping palm oil expansion using SAR to study the impact on the CO_2 cycle. *IOP Conf. Ser. Earth Environ. Sci.* **2014**, *20*, 12012. [CrossRef]
6. Razali, S.M.; Marín, A.; Nuruddin, A.A.; Shafri, H.Z.M.; Hamid, H.A. Capability of Integrated MODIS Imagery and ALOS for Oil Palm, Rubber and Forest Areas Mapping in Tropical Forest Regions. *Sensors* **2014**, *14*, 8259–8282. [CrossRef]
7. Lee, J.S.H.; Wich, S.; Widayati, A.; Koh, L.P. Detecting industrial oil palm plantations on Landsat images with Google Earth Engine. *Remote Sens. Appl. Soc. Environ.* **2016**, *4*, 219–224. [CrossRef]
8. Jin, Y.; Sung, S.; Lee, D.K.; Biging, G.S.; Jeong, S. Mapping Deforestation in North Korea Using Phenology-Based Multi-Index and Random Forest. *Remote Sens.* **2016**, *8*, 997. [CrossRef]
9. Wardlow, B.D.; Egbert, S.L. A comparison of MODIS 250-m EVI and NDVI data for crop mapping: A case study for southwest Kansas. *Int. J. Remote Sens.* **2010**, *31*, 805–830. [CrossRef]
10. Nooni, I.K.; Duker, A.; Van Duren, I.; Addae-Wireko, L.; Jnr, E.O. Support vector machine to map oil palm in a heterogeneous environment. *Int. J. Remote Sens.* **2014**, *35*, 4778–4794. [CrossRef]
11. Sabajo, C.R.; le Maire, G.; June, T.; Meijide, A.; Roupsard, O.; Knohl, A. Expansion of oil palm and other cash crops causes an increase of the land surface temperature in the Jambi province in Indonesia. *Biogeosciences* **2017**, *14*, 4619–4635. [CrossRef]
12. Ramdani, F.; Moffiet, T.; Hino, M. Local surface temperature change due to expansion of oil palm plantation in Indonesia. *Clim. Chang.* **2014**, *123*, 189–200. [CrossRef]
13. Li, M.; Liew, S.C.; Kwoh, L.K. Producing cloud free and cloud-shadow free mosaic from cloudy IKONOS images. In Proceedings of the IGARSS 2003—2003 IEEE International Geoscience and Remote Sensing Symposium, Toulouse, France, 21–25 July 2003; pp. 3946–3948. [CrossRef]
14. Tseng, D.-C.; Tseng, H.-T.; Chien, C.-L. Automatic cloud removal from multi-temporal SPOT images. *Appl. Math. Comput.* **2008**, *205*, 584–600. [CrossRef]

15. Cheng, Y.; Yu, L.; Xu, Y.; Lu, H.; Cracknell, A.P.; Kanniah, K.; Gong, P. Mapping oil palm extent in Malaysia using ALOS-2 PALSAR-2 data. *Int. J. Remote Sens.* **2017**, *39*, 432–452. [CrossRef]
16. Li, L.; Dong, J.; Tenku, S.N.; Xiao, X. Mapping Oil Palm Plantations in Cameroon Using PALSAR 50-m Orthorectified Mosaic Images. *Remote Sens.* **2015**, *7*, 1206–1224. [CrossRef]
17. Oon, A.; Ngo, K.D.; Azhar, R.; Ashton-Butt, A.; Lechner, A.; Azhar, B. Assessment of ALOS-2 PALSAR-2L-band and Sentinel-1 C-band SAR backscatter for discriminating between large-scale oil palm plantations and smallholdings on tropical peatlands. *Remote Sens. Appl. Soc. Environ.* **2018**, *13*, 183–190. [CrossRef]
18. Hong, G.; Zhang, A.; Zhou, F.; Brisco, B. Integration of optical and synthetic aperture radar (SAR) images to differentiate grassland and alfalfa in Prairie area. *Int. J. Appl. Earth Obs. Geoinf. ITC J.* **2014**, *28*, 12–19. [CrossRef]
19. Lambin, E.F.; Ehrlich, D. Combining vegetation indices and surface temperature for land-cover mapping at broad spatial scales. *Int. J. Remote Sens.* **1995**, *16*, 573–579. [CrossRef]
20. Lambin, E.F.; Ehrlich, D. International Journal of Remote Sensing The surface temperature-vegetation index space for land cover and land-cover change analysis. *Int. J. Remote Sens.* **1996**, *17*, 463–487. [CrossRef]
21. Lopes, M.; Frison, P.; Durant, S.M.; Bühne, H.S.T.; Ipavec, A.; Lapeyre, V.; Pettorelli, N. Combining optical and radar satellite image time series to map natural vegetation: Savannas as an example. *Remote Sens. Ecol. Conserv.* **2020**, *6*, 316–326. [CrossRef]
22. Sarzynski, T.; Giam, X.; Carrasco, L.; Lee, J.S.H. Combining Radar and Optical Imagery to Map Oil Palm Plantations in Sumatra, Indonesia, Using the Google Earth Engine. *Remote Sens.* **2020**, *12*, 1220. [CrossRef]
23. Yusoff, N.M.; Muharam, F.M.; Khairunniza-Bejo, S. Towards the use of remote-sensing data for monitoring of abandoned oil palm lands in Malaysia: A semi-automatic approach. *Int. J. Remote Sens.* **2016**, *38*, 432–449. [CrossRef]
24. Ramdani, F. Recent expansion of oil palm plantation in the most eastern part of Indonesia: Feature extraction with polarimetric SAR. *Int. J. Remote Sens.* **2018**, *40*, 7371–7388. [CrossRef]
25. Vicente-Serrano, S.M.; Aguilar, E.; Martínez, R.; Martín-Hernández, N.; Azorin-Molina, C.; Sanchez-Lorenzo, A.; El Kenawy, A.; Tomás-Burguera, M.; Moran-Tejeda, E.; López-Moreno, J.I.; et al. The complex influence of ENSO on droughts in Ecuador. *Clim. Dyn.* **2016**, *48*, 405–427. [CrossRef]
26. Poveda, G.; Álvarez, D.M.; Rueda, Ó.A. Hydro-climatic variability over the Andes of Colombia associated with ENSO: A review of climatic processes and their impact on one of the Earth's most important biodiversity hotspots. *Clim. Dyn.* **2010**, *36*, 2233–2249. [CrossRef]
27. Fatin, M.N.; Razali, S.M.; Ahmad, A.A.; Shafri, Z.M.S.M. Oil palm dry season analysis based on moderate-resolution imaging spectroradiometer (MODIS) satellite indices. *Int. J. Remote Sens.* **2019**, *40*, 7663–7678. [CrossRef]
28. Furumo, P.R.; Aide, T.M. Characterizing commercial oil palm expansion in Latin America: Land use change and trade. *Environ. Res. Lett.* **2017**, *12*, 024008. [CrossRef]
29. Rival, L. The meanings of forest governance in Esmeraldas, Ecuador. *Oxf. Dev. Stud.* **2003**, *31*, 479–501. [CrossRef]
30. Ortiz, S.Y.C.; Valencia, K.L.P.; Estacio, J.R. Presión-Estado-Respuesta en la gestión de las áreas protegidas de la provincia de Esmeraldas. *Gestión Ambient.* **2019**, *17*, 21–22.
31. Movimiento Mundial por los Bosques Tropicales, El Amargo Fruto de la Palma Aceitera: Despojo y Deforestación. Movimiento Mundial por los Bosques Tropicales. 2001. Available online: http://wrm.org.uy/es/files/2013/04/El_amargo_fruto_de_la_palma_aceitera.pdf (accessed on 10 January 2021).
32. USAID. Innovación Productiva en el Ecuador Aceite de Palma. *Innov. Product. Ecuad.* **2013**, *4*, 1689–1699. Available online: https://core.ac.uk/download/pdf/235988344.pdf (accessed on 10 January 2021).
33. Ministerio de Agricultura y Ganadería. Cifras Agroproductivas. Available online: http://sipa.agricultura.gob.ec/index.php/cifras-agroproductivas (accessed on 5 January 2021).
34. Provincia de Esmeraldas-Geografía del Ecuador Enciclopedia del Ecuador. Available online: http://www.enciclopediadelecuador.com/geografia-del-ecuador/provincia-de-esmeraldas/ (accessed on 5 January 2021).
35. Funk, C.; Peterson, P.; Landsfeld, M.; Pedreros, D.; Verdin, J.; Shukla, S.; Husak, G.; Rowland, J.; Harrison, L.; Hoell, A.; et al. The climate hazards infrared precipitation with stations—A new environmental record for monitoring extremes. *Sci. Data* **2015**, *2*, 150066. [CrossRef] [PubMed]
36. Provincia de Esmeraldas (Ecuador)-EcuRed. Available online: https://www.ecured.cu/Provincia_de_Esmeraldas_(Ecuador) (accessed on 6 January 2021).
37. Erfanian, A.; Wang, G.; Fomenko, L. Unprecedented drought over tropical South America in 2016: Significantly under-predicted by tropical SST. *Sci. Rep.* **2017**, *7*, 5811. [CrossRef] [PubMed]
38. Petrova, D.; Rodó, X.; Sippy, R.; Ballester, J.; Mejía, R.; Beltrán-Ayala, E.; Borbor-Cordova, M.J.; Vallejo, G.M.; Olmedo, A.J.; Stewart-Ibarra, A.M.; et al. The 2018–2019 weak El Niño: Predicting the risk of a dengue outbreak in Machala, Ecuador. *Int. J. Clim.* **2020**, *41*, 3813–3823. [CrossRef]
39. MODIS Web. Available online: https://modis.gsfc.nasa.gov/data/dataprod/ (accessed on 5 January 2021).
40. Mas, J.-F. Aplicaciones del sensor MODIS para el monitoreo del territorio. *Educ. Divulg.* **2011**, *7*, 2.
41. Jönsson, P.; Eklundh, L. TIMESAT—A program for analyzing time-series of satellite sensor data. *Comput. Geosci.* **2004**, *30*, 833–845. [CrossRef]

42. Htitiou, A.; Boudhar, A.; Lebrini, Y.; Hadria, R.; Lionboui, H.; Benabdelouahab, T. A comparative analysis of different phenological information retrieved from Sentinel-2 time series images to improve crop classification: A machine learning approach. *Geocarto Int.* **2020**, *37*, 1426–1449. [CrossRef]
43. Miettinen, J.; Liew, S.C. Separability of insular Southeast Asian woody plantation species in the 50 m resolution ALOS PALSAR mosaic product. *Remote Sens. Lett.* **2010**, *2*, 299–307. [CrossRef]
44. Shimada, M.; Itoh, T.; Motooka, T.; Watanabe, M.; Shiraishi, T.; Thapa, R.; Lucas, R. New global forest/non-forest maps from ALOS PALSAR data (2007–2010). *Remote Sens. Environ.* **2014**, *155*, 13–31. [CrossRef]
45. Karlsen, S.R.; Tolvanen, A.; Kubin, E.; Poikolainen, J.; HøGda, K.A.; Johansen, B.; Danks, F.S.; Aspholm, P.; Wielgolaski, F.E.; Makarova, O. MODIS-NDVI-based mapping of the length of the growing season in northern Fennoscandia. *Int. J. Appl. Earth Obs. Geoinf.* **2008**, *10*, 253–266. [CrossRef]
46. Garroutte, E.L.; Hansen, A.J.; Lawrence, R.L. Using NDVI and EVI to Map Spatiotemporal Variation in the Biomass and Quality of Forage for Migratory Elk in the Greater Yellowstone Ecosystem. *Remote Sens.* **2016**, *8*, 404. [CrossRef]
47. Lewińska, K.E.; Ivits, E.; Schardt, M.; Zebisch, M. Alpine Forest Drought Monitoring in South Tyrol: PCA Based Synergy between scPDSI Data and MODIS Derived NDVI and NDII7 Time Series. *Remote Sens.* **2016**, *8*, 639. [CrossRef]
48. Bojanowski, J.; Kowalik, W.; Bochenek, Z. Noise reduction of NDVI time-series: A robust method based on Savitzky-Golay filter. *Rocz. Geomatyki* **2009**, *7*, 13–21.
49. Wen, G.; Marshak, A.; Song, W.; Knyazikhin, Y.; Mõttus, M.; Wu, D. A Relationship Between Blue and Near-IR Global Spectral Reflectance and the Response of Global Average Reflectance to Change in Cloud Cover Observed From EPIC. *Earth Space Sci.* **2019**, *6*, 1416–1429. [CrossRef]
50. Argenti, F.; Lapini, A.; Bianchi, T.; Alparone, L. A Tutorial on Speckle Reduction in Synthetic Aperture Radar Images. *IEEE Geosci. Remote Sens. Mag.* **2013**, *1*, 6–35. [CrossRef]
51. SNAP–STEP. Available online: http://step.esa.int/main/toolboxes/snap/ (accessed on 8 January 2021).
52. Lopes, M.; Frison, P.-L.; Crowson, M.; Warren-Thomas, E.; Hariyadi, B.; Kartika, W.D.; Agus, F.; Hamer, K.C.; Stringer, L.; Hill, J.K.; et al. Improving the accuracy of land cover classification in cloud persistent areas using optical and radar satellite image time series. *Methods Ecol. Evol.* **2020**, *11*, 532–541. [CrossRef]
53. Kempeneers, P.; Sedano, F.; Seebach, L.; Strobl, P.; San-Miguel-Ayanz, J. Data Fusion of Different Spatial Resolution Remote Sensing Images Applied to Forest-Type Mapping. *IEEE Trans. Geosci. Remote Sens.* **2011**, *49*, 4977–4986. [CrossRef]
54. Orynbaikyzy, A.; Gessner, U.; Conrad, C. Crop type classification using a combination of optical and radar remote sensing data: A review. *Int. J. Remote Sens.* **2019**, *40*, 6553–6595. [CrossRef]
55. Torbick, N.; Salas, W.; Xiao, X.; Ingraham, P.; Fearon, M.; Biradar, C.; Zhao, D.; Liu, Y.; Li, P.; Zhao, Y. Integrating SAR and optical imagery for regional mapping of paddy rice attributes in the Poyang Lake Watershed, China. *Can. J. Remote Sens.* **2011**, *37*, 17–26. [CrossRef]
56. Ghazaryan, G.; Dubovyk, O.; Löw, F.; Lavreniuk, M.; Kolotii, A.; Schellberg, J.; Kussul, N. A rule-based approach for crop identification using multi-temporal and multi-sensor phenological metrics. *Eur. J. Remote Sens.* **2018**, *51*, 511–524, Correction in *Eur. J. Remote Sens.* **2018**, *51*. [CrossRef]
57. Zhang, X.; Wu, B.; Ponce-Campos, G.E.; Zhang, M.; Chang, S.; Tian, F. Mapping up-to-Date Paddy Rice Extent at 10 M Resolution in China through the Integration of Optical and Synthetic Aperture Radar Images. *Remote Sens.* **2018**, *10*, 1200. [CrossRef]
58. Laurin, G.V.; Liesenberg, V.; Chen, Q.; Guerriero, L.; Del Frate, F.; Bartolini, A.; Coomes, D.; Wilebore, B.; Lindsell, J.; Valentini, R. Optical and SAR sensor synergies for forest and land cover mapping in a tropical site in West Africa. *Int. J. Appl. Earth Obs. Geoinf. ITC J.* **2013**, *21*, 7–16. [CrossRef]
59. Kaplan, G.; Avdan, Z.Y.; Avdan, U. Mapping and Monitoring Wetland Dynamics Using Thermal, Optical, and SAR Remote Sensing Data. *Wetl. Manag. Assess. Risk Sustain. Solut.* **2019**, *87*, 88–89. [CrossRef]
60. Zhang, G.; Xiao, X.; Dong, J.; Kou, W.; Jin, C.; Qin, Y.; Zhou, Y.; Wang, J.; Menarguez, M.A.; Biradar, C. Mapping paddy rice planting areas through time series analysis of MODIS land surface temperature and vegetation index data. *ISPRS J. Photogramm. Remote Sens.* **2015**, *106*, 157–171. [CrossRef] [PubMed]
61. Xiao, H.; Weng, Q. The impact of land use and land cover changes on land surface temperature in a karst area of China. *J. Environ. Manag.* **2007**, *85*, 245–257. [CrossRef] [PubMed]
62. Gislason, P.O.; Benediktsson, J.A.; Sveinsson, J.R. Random Forests for land cover classification. *Pattern Recognit. Lett.* **2006**, *27*, 294–300. [CrossRef]
63. Pal, M. Random forest classifier for remote sensing classification. *Int. J. Remote Sens.* **2005**, *26*, 217–222. [CrossRef]
64. Sheykhmousa, M.; Mahdianpari, M.; Ghanbari, H.; Mohammadimanesh, F.; Ghamisi, P.; Homayouni, S. Support Vector Machine Versus Random Forest for Remote Sensing Image Classification: A Meta-Analysis and Systematic Review. *IEEE J. Sel. Top. Appl. Earth Obs. Remote Sens.* **2020**, *13*, 6308–6325. [CrossRef]
65. Ministerio de Agricultura y Ganadería. *Mapa de Zonas Homogéneas de Accesibilidad*; Ministerio de Agricultura y Ganadería: Carchi, Ecuador, 2015; p. 81.
66. Chabalala, Y.; Adam, E.; Ali, K.A. Machine Learning Classification of Fused Sentinel-1 and Sentinel-2 Image Data towards Mapping Fruit Plantations in Highly Heterogenous Landscapes. *Remote Sens.* **2022**, *14*, 2621. [CrossRef]
67. Randazzo, G.; Cascio, M.; Fontana, M.; Gregorio, F.; Lanza, S.; Muzirafuti, A. Mapping of Sicilian Pocket Beaches Land Use/Land Cover with Sentinel-2 Imagery: A Case Study of Messina Province. *Land* **2021**, *10*, 678. [CrossRef]

68. Foody, G.M. Status of land cover classification accuracy assessment. *Remote Sens. Environ.* **2002**, *80*, 185–201. [CrossRef]
69. Landis, J.R.; Koch, G.G. The Measurement of Observer Agreement for Categorical Data. *Biometrics* **1977**, *33*, 159–174. [CrossRef] [PubMed]
70. Foody, G.M. Explaining the unsuitability of the kappa coefficient in the assessment and comparison of the accuracy of thematic maps obtained by image classification. *Remote Sens. Environ.* **2020**, *239*, 111630. [CrossRef]
71. Kamiran, N.; Sarker, M.L.R. Exploring the Potential of High Resolution Remote Sensing Data for Mapping Vegetation and the Age Groups of Oil Palm Plantation. *IOP Conf. Ser. Earth Environ. Sci.* **2014**, *18*, 12181. [CrossRef]
72. Santos, C.; Messina, J.P. Multi-Sensor Data Fusion for Modeling African Palm in the Ecuadorian Amazon. *Photogramm. Eng. Remote Sens.* **2008**, *74*, 711–723. [CrossRef]
73. Sharma, L.D.; Kumar, M.; Gupta, J.K.; Rana, M.S.; Dangwal, V.S.; Dhar, G.M. MODIS Land Surface Temperature Products Users' Guide. *Indian J. Chem. Technol.* **2001**, *8*, 169–175.
74. Carranza, E.J.M.; Laborte, A.G. Random forest predictive modeling of mineral prospectivity with small number of prospects and data with missing values in Abra (Philippines). *Comput. Geosci.* **2015**, *74*, 60–70. [CrossRef]
75. Hais, M.; Kučera, T. The influence of topography on the forest surface temperature retrieved from Landsat TM, ETM + and ASTER thermal channels. *ISPRS J. Photogramm. Remote Sens.* **2009**, *64*, 585–591. [CrossRef]
76. Sano, E.E.; Ferreira, L.G.; Huete, A.R. Synthetic Aperture Radar (L band) and Optical Vegetation Indices for Discriminating the Brazilian Savanna Physiognomies: A Comparative Analysis. *Earth Interact.* **2005**, *9*, 1–15. [CrossRef]
77. Olofsson, P.; Foody, G.M.; Stehman, S.V.; Woodcock, C.E. Making better use of accuracy data in land change studies: Estimating accuracy and area and quantifying uncertainty using stratified estimation. *Remote Sens. Environ.* **2013**, *129*, 122–131. [CrossRef]

remote sensing

MDPI

Technical Note

Arctic Sea-Ice Surface Elevation Distribution from NASA's Operation IceBridge ATM Data

Donghui Yi [1,2,*], Alejandro Egido [1,2], Walter H. F. Smith [2], Laurence Connor [2], Christopher Buchhaupt [2,3] and Dexin Zhang [1,2]

[1] GST Inc., 5830 University Research Court, E/RA3, College Park, MD 20740, USA; alejandro.egido@noaa.gov (A.E.); dexin.zhang@noaa.gov (D.Z.)
[2] Laboratory for Satellite Altimetry, Center for Satellite Applications and Research, NOAA, 5830 University Research Court, E/RA3, College Park, MD 20740, USA; walter.hf.smith@noaa.gov (W.H.F.S.); laurence.connor@noaa.gov (L.C.); christopher.buchhaupt@noaa.gov (C.B.)
[3] Earth System Science Interdisciplinary Center, University of Maryland, 5830 University Research Court, E/RA3, College Park, MD 20740, USA
* Correspondence: donghui.yi@noaa.gov

Abstract: In this paper, we characterize the sea-ice elevation distribution by using NASA's Operation IceBridge (OIB) Airborne Topographic Mapper (ATM) L1B data over the Arctic Ocean during 94 Spring campaigns between 2009 and 2019. The ultimate objective of this analysis is to better understand sea-ice topography to improve the estimation of the sea-ice freeboard for nadir-looking altimeters. We first introduce the use of an exponentially modified Gaussian (EMG) distribution to fit the surface elevation probability density function (PDF). The characteristic function of the EMG distribution can be integrated in the modeling of radar altimeter waveforms. Our results indicate that the Arctic sea-ice elevation PDF is dominantly positively skewed and the EMG distribution is better suited to fit the PDFs than the classical Gaussian or lognormal PDFs. We characterize the elevation correlation characteristics by computing the autocorrelation function (ACF) and correlation length (CL) of the ATM measurements. To support the radar altimeter waveform retracking over sea ice, we perform this study typically on 1.5 km ATM along-track segments that reflect the footprint diameter size of radar altimeters. During the studied period, the mean CL values range from 20 to 30 m, which is about 2% of the radar altimeter footprint diameter (1.5 km).

Keywords: sea ice; altimetry; algorithms; remote sensing

Citation: Yi, D.; Egido, A.; Smith, W.H.F.; Connor, L.; Buchhaupt, C.; Zhang, D. Arctic Sea-Ice Surface Elevation Distribution from NASA's Operation IceBridge ATM Data. *Remote Sens.* **2022**, *14*, 3011. https://doi.org/10.3390/rs14133011

Academic Editor: Nereida Rodriguez-Alvarez

Received: 20 April 2022
Accepted: 21 June 2022
Published: 23 June 2022

Publisher's Note: MDPI stays neutral with regard to jurisdictional claims in published maps and institutional affiliations.

Copyright: © 2022 by the authors. Licensee MDPI, Basel, Switzerland. This article is an open access article distributed under the terms and conditions of the Creative Commons Attribution (CC BY) license (https://creativecommons.org/licenses/by/4.0/).

1. Introduction

The satellite altimeter footprint size ranges from 17 m (ICESat-2) [1] to 70 m (ICESat) [2] to more than 1 km for radar altimeters [3,4]. Assuming the height variations in these footprints arise from a stationary random process, aspects of the altimeter's measurement can be related to low-order moments of the surface height probability density function (PDF) [5,6], provided that the horizontal correlation scale of the random process is small compared to the horizontal dimensions of the footprint [5], so that both high and low random height fluctuations are contained within the footprint. Satellite altimeters measure the mean (or median) height, root-mean-square roughness, etc., within the footprint area, and retrieval of this information is simplified if the PDF or its Fourier transform has a simple functional form.

Conventional satellite radar altimetry was developed to measure ocean surfaces, on which the surface height variations produced by wind waves and swell have a very near-Gaussian distribution [7] and a correlation length less than the footprint size [5]. Our motivation is to support the satellite radar altimetry of sea ice by the CryoSat-2 and Sentinel-3 missions, the pulse echoes of which arise from rough surface backscatter distributed over an area approximately 1.5 km in diameter. We, therefore, are interested in

characterizing the sea-ice elevation fluctuations that occur over distances of 1.5 km and less. Applying Doppler beam sharpening to the pulse echoes of these missions can narrow the measurement footprint in the direction of flight [3,8–10]; thus, we also aim to characterize the horizontal correlation scale of the elevation variations.

The sea-ice height variations that occur over 1.5 km are not well-approximated by a Gaussian distribution [11–16]. Many studies of sea ice have used a lognormal distribution [13–16]. Landy et al. [11] demonstrated that at the radar altimeter footprint scale, a lognormal distribution can better describe sea-ice topography than a Gaussian; assuming a Gaussian distribution for the surface elevation of sea ice may be introducing significant error into the Cryosat-2 waveform retracking process. We characterize the PDF of sea-ice elevation using an exponentially modified Gaussian (EMG) distribution, as this form can be incorporated into a radar altimeter waveform retracker. We also compare the EMG to the Gaussian and lognormal distributions in this study.

2. Data

This study used NASA Operation IceBridge (OIB) Airborne Topographic Mapper (ATM) L1B [17,18] and Digital Mapping System (DMS) imagery [19] L1B data [20] from the National Snow and Ice Data Center (NSIDC) collected over the Arctic Ocean in March, April, and May from 2009 to 2019. The geographical coverage of these data is shown in Figure 1. OIB is a NASA airborne mission that monitored Arctic and Antarctic ice sheets, ice shelves, and sea ice. It collected data between the ICESat (2003–2009) and ICESat-2 (2018-present) missions in an effort to fill the data gap of the two satellites. Its airborne conical-scanning laser ranging system has an off-nadir angle (15 degrees for wide swath) and a scan rate of 20 Hz. Its output laser wavelength is 532 nm and the pulse repetition rate is 5 kHz [17,18]. At its wide swath scan angle and at an altitude of 500 m above the surface, the laser footprint diameter is about 1 m and the laser swath width is about 250 m. The absolute elevation accuracy is about 0.1 m or better [21,22]. For IceBridge campaigns, the estimated elevation accuracy and precision are 0.066 and 0.030 m, respectively [18].

The ATM elevation data are heights with respect to the WGS-84 ellipsoid. We adjusted these to measure height with respect to the Danish Technical University mean sea surface (MSS) model DTU18 [23,24]. Because DTU18 gives the MSS height with respect to the TOPEX ellipsoid, we accounted for the difference in ellipsoidal heights [25] and then used bilinear interpolation of the DTU18 grid to evaluate the height correction to apply to each ATM footprint. We did not apply the ATM-azimuth-scan-angle-related elevation bias correction [26] in this study. We tested the application of the bias correction and found the impact on the 1.5 km section mean/STD insignificant.

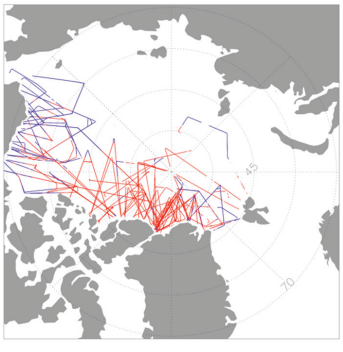


Figure 1. OIB ground tracks from 2009 to 2019. There are 94 spring flights over the Arctic Ocean. Land cover is in gray. Blue tracks are for first-year ice (FYI) and red tracks are for multi-year ice (MYI). FYI and MYI are based on OSISAF sea surface types [27]. The majority of the campaigns are between March and April. There are three campaigns from early May in 2015 and 2016. For overlapping tracks, later tracks will cover early tracks.

The DMS is an airborne digital camera system that records natural color and panchromatic imagery [19]. The DMS level-1b image spatial resolution ranges from 0.015 to 2.5 m. The pixel size is dependent on flight altitude. For a flight at 460 m above ground level, the pixel size is about 0.1 m.

The OSISAF sea ice surface type data of 2009–2019 [27] were used to estimate FYI and MYI. Each ATM footprint can be assigned to an OSISAF sea ice surface type, FYI or MYI, based on the OSISAF sea ice surface type grids.

3. Methods and Analysis

We grouped the ATM data into segments, each segment spanning 1.5 km in the along-track direction of the OIB aircraft. We calculated the sea-ice surface elevation PDF for each 1.5 km segment. In this section, we discuss candidate models that describe the PDFs, cluster analysis to distinguish floe heights from lead heights, ATM elevation measurement noise, and elevation correlation length (CL).

3.1. Candidate Models for the PDFs

Three different surface elevation distribution models: (1) Gaussian, (2) lognormal, and (3) EMG, are evaluated here to describe the sea-ice surface elevation distribution PDFs.

3.1.1. Gaussian Distribution

A Gaussian distribution with mean μ and standard deviation σ is defined as:

$$g(x) = \frac{1}{\sigma\sqrt{2\pi}} \exp(-\frac{(x-\mu)^2}{2\sigma^2}) \quad (1)$$

While this model has been widely used to describe the sea-ice surface elevation distribution, over the satellite radar altimeter scale of 1.5 km horizontally, the Gaussian distribution may not fit the elevation PDF very well and other distribution models need to be considered [11,12].

3.1.2. Lognormal Distribution

A lognormal distribution with mean = $\exp(\mu_l + \sigma_l^2/2)$ and variance = $[\exp(\sigma_l^2) - 1] \times \exp(2\mu_l + \sigma_l^2)$ is defined as:

$$\mathrm{LN}(x) = \frac{1}{x\sigma_l\sqrt{2\pi}} \exp(-\frac{(lnx - \mu_l)^2}{2\sigma_l^2}). \quad (2)$$

This model is also used in the sea-ice study [11,13–16]. Landy and others [11] demonstrated that at the satellite radar altimeter scale, a lognormal distribution can better describe sea-ice topography than a Gaussian.

3.1.3. EMG Distribution

The EMG distribution [28] with mean = $\mu_e + 1/\lambda^2$ and variance = $\sigma_e^2 + 1/\lambda$ is defined as:

$$EG(x) = \frac{\lambda}{2} e^{\frac{\lambda}{2}(2\mu_e + \lambda\sigma_e^2 - 2x)} \,\mathrm{erfc}(\frac{\mu_e + \lambda\sigma_e^2 - x}{\sqrt{2}\sigma_e}). \quad (3)$$

where erfc is the complementary error function defined as $\mathrm{erfc}(x) = 1 - \mathrm{erf}(x) = \frac{2}{\sqrt{\pi}} \int_x^\infty e^{-t^2} dt$.

In this study, we introduce the EMG distribution, as it fits the sea-ice surface elevation PDF nicely and its characteristic function can be applied in an algorithm for floe height retrieval from satellite radar altimeter waveforms.

3.2. Cluster Analysis to Distinguish Floe Heights from Lead Heights

Over sea ice, a satellite radar altimeter will receive specular reflections from leads and rough surface backscatter from the floes [4]; the latter process will sense the entire footprint

as one realization of a single random process. Onana et al. [29] applied a sophisticated method to distinguish leads for the ATM data. Here, we apply a more efficient cluster analysis to separate the floe and lead. This enables us to analyze data with and without leads. Especially when there are a large number of lead footprints, the elevation PDFs will have more than one peak and all three models used here, Gaussian, Lognormal, and EMG, will not fit. Generally, the lead surface has a lower RTratio and lower elevation, and the scatterplot of elevation vs. RTratio will show 2 distinguished clusters of the two types of surfaces. The cluster function used here is from Interactive Data Language (IDL) [30,31]. Figure 2 shows an example of the cluster analysis method. Figure 2b,c show the ATM elevation and the ratio of the received power to transmitted power (RTratio) on top of the DMS images. Figure 2f shows an elevation-RTratio scatterplot and the result from cluster analysis. Figure 2g shows the PDFs of the floe and lead.

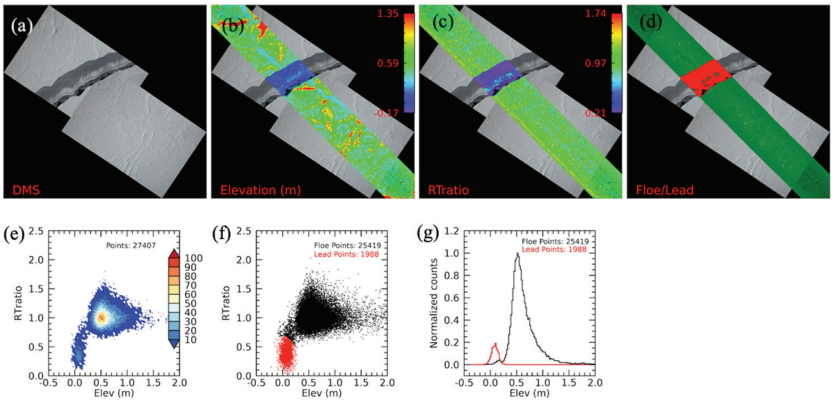


Figure 2. An example from 21 April 2016 shows the cluster analysis method results. (**a**) DMS images. (**b**–**d**) ATM elevation, RTratio, and floe (green) and lead (red) footprints on top of the DMS images. (**e**) Color-coded Elevation-RTratio scatter plot. (**f**) Elevation-RTratio scatterplot, and floe (black) and lead (red) from the cluster analysis. (**g**) The pdf of floe (black) and lead (red) normalized by floe pdf amplitude.

The following data analysis is restricted to the floe elevations identified by this cluster analysis method and separated from the lead elevations.

3.3. Weakly Stationary Surface Processes

We suppose that the floe heights within any data segment are a realization of a random process that is at least weakly stationary over the segment. At any horizontal point position P in the segment, the height $h(P) = \overline{h} + z(P)$, where $\overline{h}$ is the mean height and $z(P)$ is a zero-mean random process having variance v^2. If P and Q are two points within the ice floe segment, the semi-variogram can be defined as:

$$V(r,\theta) = \frac{1}{2}E\langle[h(P) - h(Q)]^2\rangle = v^2\,[1 - C(r,\theta)], \tag{4}$$

in which $E\langle\ \ \rangle$ indicates the statistical expectation and $C(r,\theta)$ is the normalized auto-covariance function for z, so $v^2\,C(r,\theta) = E\langle[z(P)z(Q)]\rangle$. In these expressions, r and θ are the distance and azimuth from P to Q, respectively; stationarity requires that $C(r,\theta)$ and $V(r,\theta)$ are even functions of r and have period π, not 2π, in θ.

3.4. ATM Measurement Noise

We suppose that at each ATM measurement point P_k, the measured floe elevation above the MSS contains a random measurement error, ε_k, so the elevation is measured as $h_k = h(P_k) + \varepsilon_k$. Assuming that the random processes for ε and for h are independent and

weakly stationary over a segment, the PDF for $(h + \varepsilon)$ is the convolution of the individual PDFs of ε and h taken separately, and means and variances will combine additively. Then, by estimating the variance of the measured elevations and subtracting the variance of the measurement noise process, we can obtain the noise-free variance of the ice surface heights. In addition, the semi-variogram estimated from noisy ATM measurements, $\hat{V}$, is related to the noise-free h process semi-variogram, V, simply as $\hat{V} = V + Var\langle\varepsilon\rangle$, where $Var\langle\varepsilon\rangle$ is the variance of the measurement noise.

For each ATM L1b data file, we found all point pairs P_j, P_k such that $P_k \neq P_j$ and the distance between P_j and P_k was less than 0.25 m. For each such pair, we formed the measured height difference $\tau = (h_j - h_k)/2$, and then we tested the set of all τ values obtained from the file to see whether it fit a Gaussian distribution. The Kolmogorov–Smirnov and Anderson–Darling tests for normality found that the τ data appear Gaussian at the 99.99% confidence level, and quantile-quantile (QQ) plots show a straight line out to $\pm$3.7 standard deviations. The fact that ε appears Gaussian is particularly convenient, as it allows us to simply remove the measured measurement noise from the elevation statistics, and describe the noise-free h process by the aforementioned Gaussian, log-normal, or EMG distribution.

As the ATM measurement footprint diameter is ~1 m, for a 0.25 m footprint separation, the ATM measurement footprint overlap in area is about 68%. If the slope of the noise-free surface is small enough that the mean square change in the noise-free height over 0.25 m is less than $Var\langle\varepsilon\rangle$, then $E\langle\tau^2\rangle$ is a good estimate of $Var\langle\varepsilon\rangle$. The standard deviation of τ ranges between 2 and 7 cm, as shown in Figure 3, as the laser instrument, aircraft and aircraft altitude, weather condition, and other phenomena change during OIB flights and can influence this parameter. It is very likely that the measurement noise decreases after 2016 are due to the instrument improvement (for example, the decreased laser pulse width) [32]. We computed $E\langle\tau^2\rangle$ for each file and used this to estimate $Var\langle\varepsilon\rangle$ for each segment. This assumes that $Var\langle\varepsilon\rangle$ changes only slowly during each flight. We made this assumption in order to obtain a large number of samples of τ to make a reliable estimate of the measurement noise.

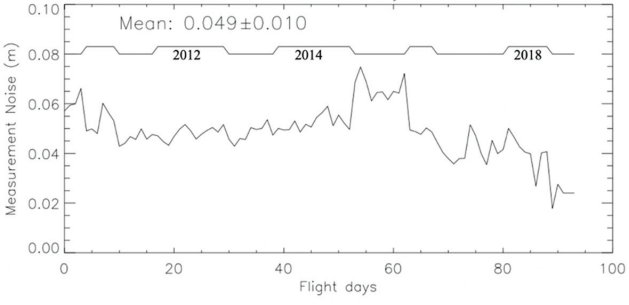


Figure 3. ATM measurement noise for the 94 campaigns from 2009 to 2019. The upper curve marks the measurement years.

Analysis of τ cannot determine $E\langle\varepsilon\rangle$. The spatial resolution of the MSS is such that the mean MSS error will be effectively constant over any one segment of data, consistent with the weak stationarity assumption for ε. If $E\langle\varepsilon\rangle \neq 0$, the effect of this is a shift in location between the PDFs of the noisy and the noise-free h processes. This is not a problem for our application, as the location of h is a parameter to be estimated during satellite radar altimeter waveform modeling; our study aims to determine the shape of the PDF for h, but its accurate location is not needed for our purpose.

3.5. Local Anisotropy and Segment-Scale Isotropy

Figure 4 shows two 1.5 km segments of ATM data, one typical of FYI and one typical of MYI. In each elevation map, there are features that are clearly elongated in one direction or

another, and over a horizontal scale of approximately 100 m, the surfaces appear anisotropic. Because the elevations of the elongated features are more pronounced in the MYI segment in Figure 4, we estimated $\hat{V}(r,\theta)$ for this segment, at sample steps of 0.1 m in r and 10° in θ, by forming all possible P,Q point pairs and assigning each pair's measured height difference to the (r,θ) bin it was closest to, and then taking the sample average over all values assigned in each bin. We found that the resulting $\hat{V}(r,\theta)$ estimates appeared to show the same variation with r at all estimated θ values; that is, the height variation appears statistically isotropic when the expectation is taken over the entire 1.5 km long segment. The limitation of the swath width is not a problem, because the correlation length estimated is quite short compared to the swath width.

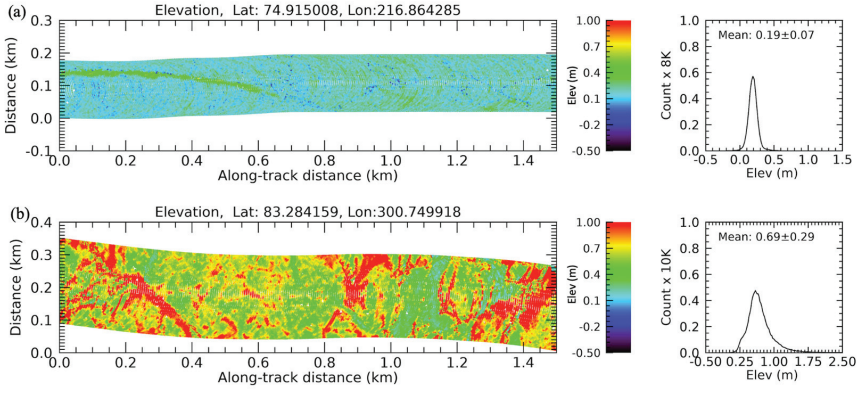


Figure 4. (**a**) Typical first-year flat thin ice and the histogram of a 1.5 km section, 21 April 2016. (**b**) Typical multi-year rough thick ice and the histogram of a 1.5 km section in central Arctic, 9 March 2017. The cross-track swath width is related to the ATM laser scan angle and airplane flight height. Latitude and longitude are the center locations of the two 1.5 km sections.

We believe this apparent isotropy is due to the fact that there are many elongated structures in a segment, and over the length of the segment, the elongation directions vary randomly enough that the overall behavior appears isotropic over a 1.5 km scale. This is convenient, because it simplifies the surface statistical description needed for satellite radar altimetry, and it also allowed us to simplify our subsequent analyses by assuming that $V(r)$ and $C(r)$ are independent of θ, which saved considerable computation. We did not test a large set of surfaces, because this is computationally prohibitive.

3.6. Correlation Length Estimation

For our application, the exact specification of the surface process-normalized autocorrelation function $C(r)$ is not needed if we can determine that the process decorrelates over a distance that is short compared to the satellite radar altimeter footprint. If this is true, then we may use any reasonable estimate of correlation length (CL), so long as we use it consistently. Here, we define CL as that horizontal distance at which $C(r)$ drops to $1/e$ [33].

One may obtain CL from $\hat{V}$, but this is computationally expensive, so we also tried a less computationally expensive approach as follows. We projected the data in each 1.5 km segment into distance coordinates x along-track and y across-track and gridded the data to a grid with samples every 5 by 5 m. We also tried using a 2 by 2 m grid to calculate CL. The CL results from 2 by 2 and 5 by 5 m grids are very similar. We chose to use the 5 by 5 m grid in this study. Along each row of constant y values in the grid, we removed the sample mean elevation and then computed the sample autocovariance function:

$$\mathrm{ACF}(y,\, l_j) = \frac{1}{N}\sum_{i=0}^{N-1} \tilde{z}(x_i)\tilde{z}(x_i + l_j) \tag{5}$$

where l_j is a lag step along the x direction and $\widetilde{z}$ is the height that remains after removing the mean along each row. We then averaged, across the y direction, the ACF estimates obtained from each row. We then normalized the averaged ACF by its value at lag $l = 0$. Finally, we estimated CL from the averaged and normalized ACF.

We applied both the ACF method (method 2) and the $\hat{V}$ method (method 1) to all segments from two days of OIB flight data and compared the results. Figure 5 shows the CL estimates obtained by applying the two methods to 1191 1.5 km long segments from the flight data of 9 March 2017. The mean CL difference between the two methods is 0.2 ± 9.5 m. As the mean difference is small, we decided to use the faster ACF method for the data analyses for all 94 ATM campaigns.

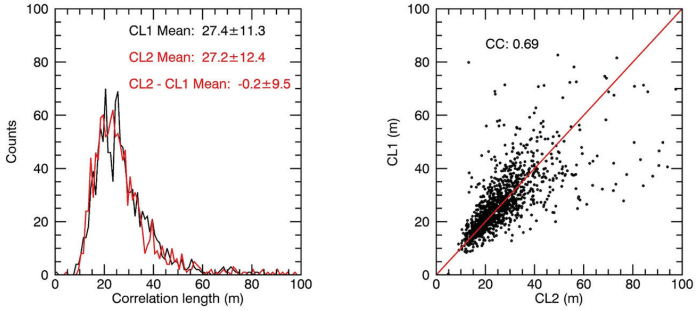


Figure 5. CL values calculated from method 1 (CL1) and method 2 (CL2) for 9 March 2017. The mean of CL1 is 27.4 ± 11.3 m. The mean of CL2 is 27.2 ± 12.4 m. The mean of CL2 $-$ CL1 is -0.2 ± 9.5 m. The correlation coefficient (CC) of CL1 and CL2 is 0.69.

4. Results and Discussion

As described in the previous section, for the calculation of the PDF parameters and CL, we grouped the ATM data into segments, each segment spanning 1.5 km in the along-track direction of the OIB aircraft; we applied the cluster analysis presented in Section 3.2 to discriminate between floe and lead returns. We then computed the histogram of sea-ice floe elevations and fitted the data with the PDF candidate models presented in Section 3.1, and we obtained the segment CL as explained in Section 3.6.

4.1. Elevation PDF Model Fitting

Model fitting to the 1.5 km ATM elevation PDFs: Examples of ATM 1.5 km floe elevation PDFs and their lognormal and EMG model Levenberg–Marquart fitting are shown in Figure 6. A typical PDF is asymmetric and positively skewed, with a shorter, steeper leading edge and a longer, more gradual trailing edge. As a Gaussian model is not fitting the unsymmetric PDF very well, only lognormal and EMG fitting results are presented here. Both the lognormal and the EMG models fit the PDFs. While the lognormal model requires elevation $x > 0$, the EMG does not have this requirement. The PDF mean and STD are compared with the mean and STD calculated from lognormal and EMG fitting parameters for all 11 years of ATM data in Figure 7. There are a total of 108,309 1.5 km segments that have both EMG and lognormal fitting results. The overall mean elevation is 0.670 ± 0.238 m and the overall STD of the elevation is 0.254 ± 0.108 m. The correlation coefficient between the PDF elevation and elevation calculated from lognormal parameters is 0.980, slightly smaller than the value calculated from EMG parameters, 0.993. The correlation coefficient between the PDF elevation STD and the elevation STD calculated from lognormal parameters is 0.807, smaller than the value calculated from EMG parameters, 0.914. Figure 7g shows that the EMG modeled elevation will have an overall elevation bias of 0.006 ± 0.030 m and the lognormal modeled elevation will have an overall elevation bias of -0.010 ± 0.049 m. Both biases are small. The elevation STD biases are -0.017 ± 0.052 and -0.032 ± 0.084 for EMG and lognormal models, respectively (Figure 7h). These results allow us to conclude

that EMG is an excellent candidate PDF and, in some cases, superior to log-normal, for the description of sea-ice roughness.

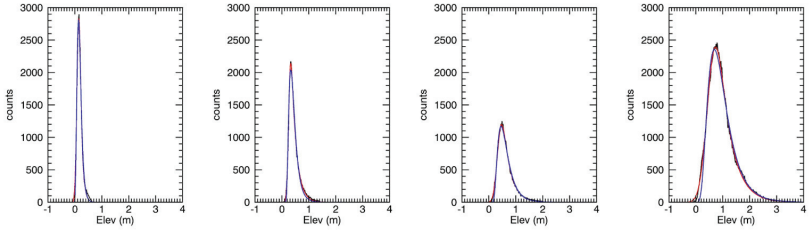


Figure 6. Examples of lognormal (blue) and EMG (red) pdf fitting.

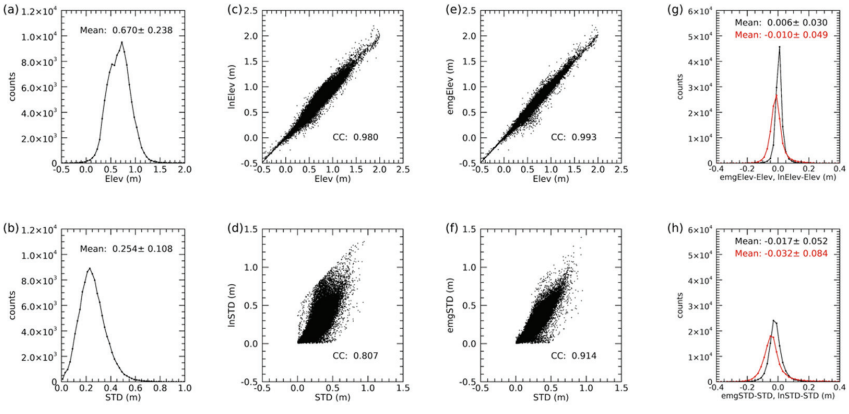


Figure 7. Mean elevation and standard deviation of elevation for each 1.5 km section along-track compared with values calculated from EMG and lognormal fitting parameters. (**a**) 1.5 km mean elevation histogram. (**b**) 1.5 km STD of the elevation histogram. (**c**) Mean elevation (Elev) vs. mean elevation from lognormal model (lnElev). (**d**) STD vs. STD from lognormal model (lnSTD). (**e**) Mean elevation vs. mean elevation from EMG model (emgElev). (**f**) STD vs. STD from EMG model (emgSTD). (**g**) Histograms of emgElev–Elev (black) and lnElev–Elev (red). (**h**) Histograms of emgSTD–STD (black) and lnSTD–STD (red). Measurement noise is removed from STD, lnSTD, and emgSTD.

The spatial variation in the eight parameters derived from the surface elevation (mean, STD, skewness, and kurtosis) and EMG model fitting to the elevation PDF (μ_e, $1/\lambda$, and σ_e) and from ACF functions (CL) for 2014 are shown in Figure 8. There are five parameters (mean, STD, μ_e, $1/\lambda$, and σ_e) that show smaller values over the thinner-ice-dominated Chukchi and Beaufort seas and larger values over the Arctic Ocean north of Ellesmere Islands and Greenland dominated by thicker ice. The skewness and kurtosis show the opposite pattern, smaller values over the thicker ice and larger values over the thinner ice. The mean elevation for 2014 is 0.704 ± 0.251 m and the mean STD is 0.265 ± 0.110 m. The dominant positive skewness values 1.332 ± 0.362 indicate that the elevation PDFs are skewed positively most of the time. The pattern for CL spatial distribution is less obvious. Both smaller and larger values are shown in the FYI regions in the Chukchi and Beaufort seas.

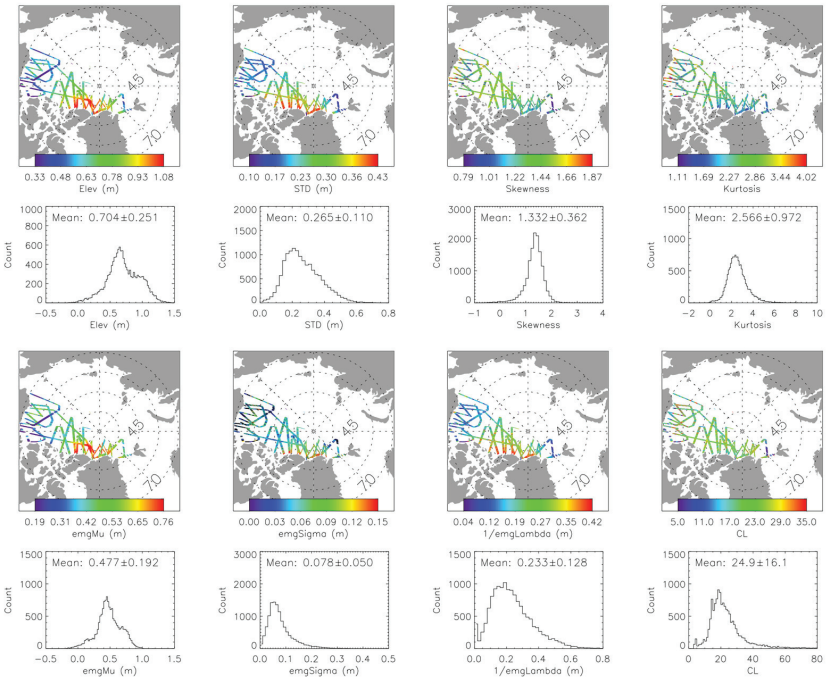


Figure 8. The mean elevation, standard deviation of elevation, skewness, kurtosis, μ_e (emgMu), σ_e (emgSigma), $1/\lambda$ (emgLambda), and CL of the 1.5 km sections of 2014. Measurement noise is removed from the standard deviation of elevation.

4.2. CL Distribution over the Arctic

Examples of ACFs and CL for 8 April 2018 are shown in Figure 9. Although outliers for CL can be as large as over 200 m (typically for "irregular" surfaces that have more than one distinguished peak in floe elevation PDFs), the mean is about 30 m with a standard deviation of about 20 m. The box-whisker plot of CL from 2009 to 2019 for FYI, MYI, and all ice are shown in Figure 10. The mean CL values of the FYI are slightly smaller than those of the MYI. The FYI and MYI CL differences are not significant. The mean and standard deviation of CL for each year, for FYI and MYI, are summarized in Table 1. The 20~30 m of CL values are less than 2% of the radar altimeter footprint diameter (1.5 km).

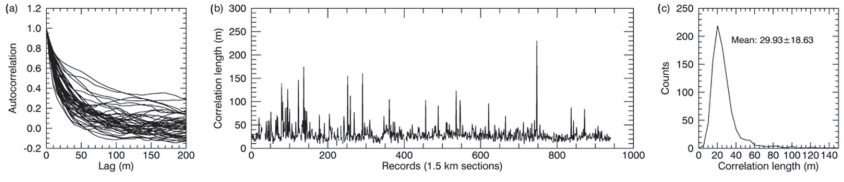


Figure 9. An example of autocorrelation and correlation length of 8 April 2018. All data here are over FYI. (**a**) Examples of autocorrelation vs. lag along the profiles (one for every 20 1.5 km sections is plotted). (**b**) Correlation length for each 1.5 km section. (**c**) Histogram of correlation length. The mean correlation length for the day is 29.93 ± 18.63 m.

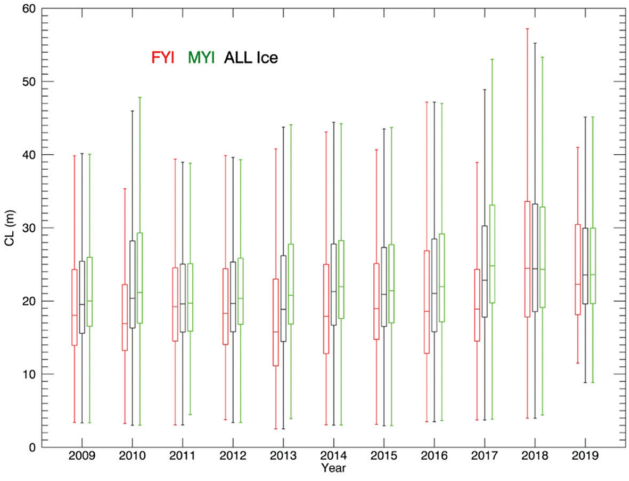


Figure 10. The box-whisker plot of correlation length (CL) of FYI (red), MYI (green), and all ice (black) from 2009 to 2019. The medians of CL show a trend of increase for all FYI, MYI, and all ice.

Table 1. The mean and standard deviation of correlation length (CL) of FYI, MYI, and all ice.

Year	FYI CL (m)	MYI CL (m)	All Ice CL (m)
2009	21.51 ± 14.33	23.28 ± 12.28	22.66 ± 13.06
2010	19.78 ± 13.88	26.47 ± 18.71	25.45 ± 18.22
2011	22.12 ± 15.44	22.42 ± 12.25	22.39 ± 12.58
2012	20.90 ± 12.06	22.99 ± 12.01	22.23 ± 12.07
2013	21.10 ± 19.80	25.12 ± 15.68	23.37 ± 17.70
2014	20.86 ± 15.85	25.60 ± 15.95	24.87 ± 16.09
2015	21.80 ± 13.40	24.66 ± 14.80	24.13 ± 14.59
2016	23.18 ± 19.36	25.40 ± 15.99	24.72 ± 17.12
2017	21.74 ± 14.44	29.64 ± 18.16	26.85 ± 17.36
2018	28.92 ± 20.13	29.54 ± 19.29	29.21 ± 19.75
2019	29.30 ± 19.78	27.62 ± 15.51	27.67 ± 15.65

Upper CL limit set at 150 m.

A previous study by Rivas et al. [12] using ATM data in March 2003 over the Alaskan Arctic [34] derived CL values of 3 to 8 m over deformed FYI and 6 to 9 m over the MYI. Their data were from regions close to the coast and the data sample sizes were relatively small. Similar CL values for similar regions can be found in this study. However, their CL values were at the lower end of the CL values we observe here. It is not clear why the CL results from the two studies differ. A possible reason could be the different sampling sizes used by the two studies.

4.3. Snow Depth Impact and Future Work

A radar altimeter signal typically penetrates a dry snow surface and the main return power is from the snow/ice interface [4]. The return power can also be impacted by the snow depth and snow density [35]. The surface elevation distribution from the ATM laser altimeter is for the snow/air interface. The elevation PDF for the snow/air interface and snow/ice interface can be different due to the irregular snow depth and snow density distributions. Applying the EMG surface elevation distribution derived from ATM data to the modeling of radar altimeter return waveforms inherently assumes that the snow/ice interface has a similar elevation distribution within its footprint. Landy et al. [13] found that the snow and sea ice surfaces exhibit similar roughness properties, and their results support the argument that snow surface roughness is primarily controlled by the roughness

of the underlying sea ice [36–38]. Landy et al. [13] also found that the variable ice surface roughness contributes a systematic uncertainty in sea ice thickness of up to 20% over FYI and 30% over MYI. The error due to the irregular snow distribution impact needs to be studied further.

In this study, we focused on the 1.5 km segments of the ATM along-track data for the typical radar altimeter footprint. For studies related to different altimeter footprint sizes, such as ICESat (~70 m) and ICESat-2 (~17 m), further studies are needed and the PDFs should be evaluated from data grids similar to their corresponding footprint sizes.

5. Conclusions

In this study, we re-analyzed the entirety of NASA's OIB ATM lidar data over the Arctic sea ice for the spring season to better characterize the sea-ice surface elevation PDF. The ultimate objective of this analysis was to better understand the sea-ice surface topography to improve the estimation of the sea-ice freeboard, particularly from nadir-looking radar altimeters. We found that the EMG function fit the surface elevation PDF extremely well for a wide range of sea-ice conditions, from thin FYI to rough MYI, and, therefore, it is possible to characterize the sea-ice surface roughness by just the three parameters describing the EMG function. In addition, the EMG function has a closed mathematical form for its characteristic function, allowing us to integrate this surface elevation PDF in the modeling of radar altimeter waveforms. Our results indicate that the Arctic sea-ice surface elevation PDF is dominantly positively skewed and this function is better suited to fit the PDFs than the classical Gaussian or lognormal functions.

The results presented in this paper are relevant to researchers studying sea-ice dynamics in the Arctic as sea-ice surface roughness modulates the energy and momentum exchange between the atmosphere and ocean and controls the distribution of melt ponds through spring and summer. All of the surface roughness PDF data from the re-analyzed ATM data will be shared through the NOAA's Laboratory for Satellite Altimetry public ftp.

We also characterized the surface elevation correlation characteristics by computing ACF and CL of the ATM measurements along the ground tracks. During the studied period, the mean CL values ranged from 20 to 30 m, which is about 29–43% of the size of the ICESat laser footprint (~70 m), larger than the ICESat-2 footprints (~17 m), and about 2% of the radar altimeter footprint diameter (1.5 km).

Author Contributions: Each of the authors were actively involved in the preparation of the paper. Conceptualization and methodology, A.E., D.Y., C.B. and W.H.F.S.; software, D.Y., A.E., L.C., W.H.F.S. and D.Z.; investigation, validation, and formal analysis, D.Y., A.E., W.H.F.S., L.C., C.B. and D.Z.; writing—original draft preparation, D.Y., A.E. and W.H.F.S.; supervision, A.E. All authors have read and agreed to the published version of the manuscript.

Funding: This research was partially funded by the NASA ROSES, Studies with ICESat-2, grant number NNH19ZDA001N and by the NOAA Product Development, Readiness, and Application (PDRA)/Jason Program.

Data Availability Statement: Sea ice surface elevation distribution data derived from the methodology described in this publication are freely available and accessible at https://www.star.nesdis.noaa.gov/socd/lsa/SeaIce/SurfaceTopography.php.

Acknowledgments: The scientific results and conclusions, as well as any views or opinions expressed herein, are those of the authors and do not necessarily reflect the views of NOAA or the Department of Commerce. We thank the five reviewers for their useful and detailed comments that improved this paper.

Conflicts of Interest: The authors declare no conflict of interest.

References

1. Kwok, R.; Petty, A.; Cunningham, G.F.; Hancock, D.W.; Ivanoff, A.; Wimert, J.T.; Bagnardi, M.; Kurtz, N. Algorithm Theoretical Basis Document (ATBD) For Sea Ice Products. In *ICESat-2 Algorithm Theoretical Basis Document, Version 4*; NASA Goddard Space Flight Center: Greenbelt, MD, USA, 2021.
2. Brenner, A.C.; Zwally, H.J.; Bentley, C.R.; Csatho, B.M.; Harding, D.J.; Hufton, M.A.; Minster, J.B.; Roberts, L.; Saba, J.L.; Thomas, R.H.; et al. Derivation of Range and Range Distributions from Laser Pulse Waveform Analysis for Surface Elevations, Roughness, Slope, and Vegetation Heights. In *ICESat Algorithm Theoretical Basis Document, Version 5*; NASA Goddard Space Flight Center: Greenbelt, MD, USA, 2011.
3. Wingham, D.J.; Francis, C.R.; Baker, S.; Bouzinac, C.; Brockley, D.; Cullen, R.; Chateau-Thierry, P.; Laxon, S.W.; Mallow, U.; Mavrocordatos, C.; et al. Cryosat: A mission to determine the fluctuations in Earth's land and marine ice fields. *Adv. Space Res.* **2006**, *37*, 841–871. [CrossRef]
4. Laxon, S.W.; Giles, K.A.; Ridout, A.L.; Wingham, D.J.; Willatt, R.; Cullen, R.; Kwok, R.; Schweiger, A.; Zhang, J.; Haas, C.; et al. CryoSat-2 estimates of Arctic sea ice thickness and volume. *Geophys. Res. Lett.* **2013**, *40*, 732–737. [CrossRef]
5. Berger, T. Satellite altimetry using ocean backscatter. *IEEE Trans. Antennas Propag.* **1972**, *20*, 295–309. [CrossRef]
6. Brown, G.S. The average impulse response of a rough surface and its applications. *IEEE Trans. Antennas Propag.* **1977**, *25*, 67–74. [CrossRef]
7. Tayfun, M.A. Narrow-Band Nonlinear Sea Waves. *J. Geophys. Res.* **1980**, *85*, 1548–1582. [CrossRef]
8. Raney, R.K. The Delay/Dopper Radar Altimeter. *IEEE Trans. Geosci. Remote Sens.* **1998**, *36*, 1578–1588. [CrossRef]
9. Egido, A.W.; Smith, H.F. Fully Focused SAR Altimetry: Theory and Applications. *IEEE Trans. Geosci. Remote Sens.* **2017**, *55*, 392–406. [CrossRef]
10. Egido, A.; Smith, W.H.F. Pulse-to-Pulse Correlation Effects in High PRF Low-Resolution Mode Altimeters. *IEEE Trans. Geosci. Remote Sens.* **2019**, *57*, 2610–2617. [CrossRef]
11. Landy, J.C.; Tsamados, M.; Scharien, R.K. A Facet-Based Numerical Model for Simulating SAR Altimeter Echoes from Heterogeneous Sea Ice Surfaces. *IEEE Trans. Geosci. Remote Sens.* **2019**, *57*, 4164–4180. [CrossRef]
12. Rivas, M.B.; Maslanik, J.A.; Sonntag, J.G.; Axelrad, P. Sea Ice Roughness from Airborne LIDAR Profiles. *IEEE Trans. Geosci. Remote Sens.* **2006**, *44*, 3032–3037. [CrossRef]
13. Landy, J.C.; Petty, A.A.; Tsamados, M.; Stroeve, J.C. Sea ice roughness overlooked as a key source of uncertainty in CryoSat-2 ice freeboard retrievals. *J. Geophys. Res. Ocean* **2020**, *125*, e2019JC015820. [CrossRef]
14. Hughes, B.A. On the use of lognormal statistics to simulate one- and two-dimensional under-ice draft profiles. *J. Geophys. Res.* **1991**, *96*, 22101–22111. [CrossRef]
15. Davis, N.; Wadhams, P. A statistical analysis of Arctic pressure ridge morphology. *J. Geophys. Res.* **1995**, *100*, 10915–10925. [CrossRef]
16. Castellani, G.; Lüpkes, C.; Hendricks, S.; Gerdes, R. Variability of Arctic sea-ice topography and its impact on the atmospheric surface drag. *J. Geophys. Res. Ocean* **2014**, *119*, 6743–6762. [CrossRef]
17. Krabill, W.B.; Abdalati, W.; Frederick, E.B.; Manizade, S.S.; Martin, C.F.; Sonntag, J.; Swift, R.N.; Thomas, R.H.; Yungel, J.G. Aircraft laser altimetry measurement of elevation changes of the Greenland ice sheet: Technique and accuracy assessment. *J. Geodyn.* **2002**, *34*, 357–376. [CrossRef]
18. Martin, C.F.; Krabill, W.B.; Manizade, S.S.; Russell, R.L.; Sonntag, J.G.; Swift, R.N.; Yungel, J.K. *Airborne Topographic Mapper Calibration Procedures and Accuracy Assessment*; Technical Report NASA/TM-2012-215891; NASA Goddard Space Flight Center: Greenbelt, MD, USA, 2012. Available online: https://ntrs.nasa.gov/archive/nasa/casi.ntrs.nasa.gov/20120008479.pdf (accessed on 1 March 2022).
19. Dominguez, R. *IceBridge DMS L1B Geolocated and Orthorectified Images, Version 1*; Technical Report updated 2018; NASA National Snow Ice Data Center Distributed Active Archive Center: Boulder, CO, USA, 2018. [CrossRef]
20. Studinger, M. *IceBridge ATM L1B Elevation and Return Strength, Version 2*; updated 2020; NASA National Snow and Ice Data Center Distributed Active Archive Center: Boulder, CO, USA, 2020. [CrossRef]
21. Krabill, W.B.; Thomas, R.H.; Martin, C.F.; Swift, R.N.; Frederick, E.B. Accuracy of airborne laser altimetry over the Greenland ice sheet. *Int. J. Remote Sens.* **1995**, *16*, 1211–1222. [CrossRef]
22. Brunt, K.M.; Hawley, R.L.; Lutz, E.R.; Studinger, M.; Sonntag, J.G.; Hofton, M.A.; Andrews, L.C.; Neumann, T.A. Assessment of NASA airborne laser altimetry data using ground-based GPS data near Summit Station, Greenland. *Cryosphere* **2017**, *11*, 681–692. [CrossRef]
23. Andersen, O.B.; Stenseng, L.; Piccioni, G.; Knudsen, P. The DTU15 MSS (Mean Sea Surface) and DTU15LAT (Lowest Astronomical Tide) Reference Surface. In Proceedings of the ESA Living Planet Symposium, Prague, Czech Republic, 9–13 May 2016. Available online: https://ftp.space.dtu.dk/pub/DTU15/DOCUMENTS/MSS/DTU15MSS+LAT.pdf (accessed on 1 March 2022).
24. Andersen, O.B.; Knudsen, P. DNSC08 mean sea surface and mean dynamic topography models. *J. Geophys. Res.* **2009**, *114*, C11001. [CrossRef]
25. Smith, W.H.F. Direct conversion of latitude and height from one ellipsoid to another. *J. Geod.* 2022, *in press*. [CrossRef]
26. Yi, D.; Harbeck, J.P.; Manizade, S.S.; Kurtz, N.T.; Studinger, M.; Hofton, M. Arctic Sea Ice Freeboard Retrieval with Waveform Characteristics for NASA's Airborne Topographic Mapper (ATM) and Land, Vegetation, and Ice Sensor (LVIS). *IEEE Trans. Geosci. Remote Sens.* **2015**, *53*, 1403–1410. [CrossRef]

27. Aaboe, S.; Breivik, L.-A.; Sorense, A.; Eastwood, S.; Lavergne, T. *Ocean & Sea Ice SAF, Global Sea Ice Edge and Type, Product User's Manual, OSI-402-c & OSI-403-c, Version 2.3*; Norwegian Meteorological Institute: Oslo, Norway, 2018.
28. Exponentially Modified Gaussian Distribution. Available online: https://en.wikipedia.org/wiki/Exponentially_modified_Gaussian_distribution (accessed on 1 March 2021).
29. Onana, V.D.P.; Kurtz, N.T.; Farrell, S.L.; Koenig, L.S.; Studinger, M.; Harbeck, J.P. A sea-ice lead detection algorithm for use with high resolution airborne visible imagery. *IEEE Trans. Geosci. Remote Sens.* **2013**, *51*, 38–56. [CrossRef]
30. CLUSTER. Available online: https://www.l3harrisgeospatial.com/docs/cluster.html (accessed on 15 March 2021).
31. Everitt, B.S. *Cluster Analysis*; Halsted Press: New York, NY, USA, 1993; ISBN 0-470-22043-0.
32. MacGregor, J.A.; Boisvert, L.N.; Medley, B.; Petty, A.A.; Harbeck, J.P.; Bell, R.E.; Blair, J.B.; Blanchard-Wrigglesworth, E.; Buckley, E.M.; Christoffersen, M.S.; et al. The scientific legacy of NASA's Operation IceBridge. *Rev. Geophys.* **2021**, *59*, e2020RG000712. [CrossRef]
33. Church, E.L. Comments on the Correlation Length. In Proceedings of the SPIE 0680, Surface Characterization and Testing, Bay Point, FL, USA, 23 March 1987. [CrossRef]
34. Cavalieri, D.J.; Markus, T.; Maslanik, J.; Sturm, M.; Lobl, E. March 2003 EOS Aqua AMSR-E Arctic Sea Ice Field Campaign. *IEEE Trans. Geosci. Remote Sens.* **2006**, *44*, 3003–3008. [CrossRef]
35. Willatt, R.; Laxon, S.; Giles, K.; Cullen, R.; Haas, C.; Helm, V. Ku-band radar penetration into snow cover Arctic sea ice using airborne data. *Ann. Glaciol.* **2011**, *52*, 197–205. [CrossRef]
36. Doble, M.; Skourup, H.; Wadhams, P.; Geiger, C. The relation between Arctic sea ice surface elevation and draft: A case study using coincident AUV sonar and air-borne scanning laser. *J. Geophys. Res.* **2011**, *116*, C00E03. [CrossRef]
37. Iacozza, J.; Barber, D. An examination of the distribution of snow on sea-ice. *Atmos. Ocean* **1999**, *37*, 21–51. [CrossRef]
38. Kurtz, N.T.; Farrell, S.L.; Studinger, M.; Galin, N.; Harbeck, J.P.; Lindsay, R.; Onana, V.D.; Panzer, B.; Sonntag, J.G. Sea ice thickness, freeboard, and snow depth products from Operation IceBridge air-borne data. *Cryosphere* **2013**, *7*, 1035–1056. [CrossRef]

remote sensing

MDPI

Article

Observation on the Droplet Ranging from 2 to 16 μm in Cloud Droplet Size Distribution Based on Digital Holography

Pan Gao, Jun Wang *, Yangzi Gao, Jingjing Liu and Dengxin Hua

School of Mechanical and Precision Instrument Engineering, Xi'an University of Technology, Xi'an 710048, China; 2190220081@stu.xaut.edu.cn (P.G.); 2200221159@stu.xaut.edu.cn (Y.G.); jingjingliu@xaut.edu.cn (J.L.); dengxinhua@xaut.edu.cn (D.H.)

* Correspondence: wangjun790102@xaut.edu.cn

Abstract: Cloud droplets size distribution (DSD) is one of the significant characteristics for liquid clouds. It plays an important role for the aerosol–droplet–cloud mechanism and variation in cloud microphysics. However, the minuscule sampling space is insufficient for the observation of whole DSD when using high-magnification optical systems. In this paper, we propose an observation method for cloud droplets ranging from 2 to 16 μm, by which the balance relationship between sampling space and optical magnification is realized. The method combines an in-line digital holographic interferometer (DHI) with the optical magnification of 5.89× and spatial stitching technique. The minimum size in DSD is extended to 2 μm, which improves the integrity of size distribution. Simultaneously, the stability of DSD is enhanced by increasing the tenfold sampling volume of cloud droplets. The comparative experiment between the in-line DHI and fog monitor demonstrates that the DSD obtained by this method is reliable, which can be used for the analysis of microphysical parameters. In the Beijing Aerosol and Cloud Interaction Chamber (BACIC), the observation results show that the size of cloud droplets follows the Gamma distribution, which is consistent with the theoretical DSD. The results of cloud microphysical parameters indicate that each pair of parameters has a positive correlation, and then the validity of observation method is confirmed. Additionally, the high-concentration aerosol condition significantly mitigates the effect of random turbulence and enhances the robustness of the microphysical parameter data.

Keywords: liquid cloud; size distribution; microphysical characteristics; cloud droplet observation; digital holography

Citation: Gao, P.; Wang, J.; Gao, Y.; Liu, J.; Hua, D. Observation on the Droplet Ranging from 2 to 16 μm in Cloud Droplet Size Distribution Based on Digital Holography. *Remote Sens.* **2022**, *14*, 2414. https://doi.org/10.3390/rs14102414

Academic Editor: Maria João Costa

Received: 1 April 2022
Accepted: 16 May 2022
Published: 18 May 2022

Publisher's Note: MDPI stays neutral with regard to jurisdictional claims in published maps and institutional affiliations.

Copyright: © 2022 by the authors. Licensee MDPI, Basel, Switzerland. This article is an open access article distributed under the terms and conditions of the Creative Commons Attribution (CC BY) license (https://creativecommons.org/licenses/by/4.0/).

1. Introduction

Cloud microphysics, which is used for the investigation of precipitation mechanisms and construction of climate models [1–5], is one of the important parameters for investigating clouds and climates. In order to simulate the cloud processes under different conditions, many research institutions have established different types of cloud chambers, such as the Beijing Aerosol and Cloud Interaction Chamber (BACIC), Michigan Technological University Π chamber, and European Council for Nuclear Research cloud chamber [6,7]. The reproducible experimental processes are carried out in cloud chamber with variable experimental conditions of temperature, humidity, and number concentration of aerosols [8]. Desai et al. [9] observed the cloud droplets size distribution (DSD) and number concentration in a Π cloud chamber with an in-line digital holographic interferometer (DHI), in order to observe the DSD variation caused by condensation growth processes. However, due to the limit of optical magnification (2.85×), the observed smallest droplet size was 7 μm. Chandrakar et al. [10] used a Phase-Doppler Interferometer to measure the diameter of cloud droplets and estimated the DSD in a Π cloud chamber. The author suggested that the number concentration of smaller droplets was underestimated. During the measurement, the smallest credible droplet size was 7.5 μm. In the natural environment, Beals et al. [11]

measured centimeter-scale heterogeneous cloud mixing based on digital holography. The DSD was divided into three channels, and the smallest credible droplet size was 10 μm. However, the size of liquid cloud droplets is usually 2–100 μm [12–15]. Here, the size is the diameter of a droplet. Especially with the increase in the number of cloud condensation nuclei (CCN) [16–25], the number of droplets close to 2 μm is increased. Hence, in order to investigate physical processes such as condensation and collision in the cloud, 2 μm droplets should be measured in a cloud chamber or high-altitude cloud layer to acquire the complete DSD.

A Charge Coupled Device (CCD) or Complementary Metal-Oxide-Semiconductor Transistor Device (CMOS) is used to record digital holograms [26–30]. The recording processes and processing procedures of holograms are greatly simplified by using a DHI [31–36]. Due to the advantages of fast, real-time, non-contact, and full-field measurement, DHI is regarded as a technology for simultaneous observation of dynamic multi-parameter physical fields. It has been successfully applied in the fields of particle three-dimensional motion [37–42], biological cell imaging [43–47], holographic subsurface radar [48,49], and other fields. In this paper, the in-line DHI with high optical resolution is proposed to observe the droplets ranging from 2 to 16 μm in the BACIC. In order to increase the proportion of small droplets, the high concentration CCN is added to BACIC. In the absence of the droplets ranging from 2 to 6 μm, the experimental results show that the pattern of microphysical parameters is changed, and the reliability of observation data is reduced. Some important patterns are ignored, and even the opposite patterns are caused in cloud microphysical processes. The research contributes to data support for the theoretical analysis of cloud physical processes and development of parameterization schemes. Cloud microphysical data is provided for research in the fields of weather, climate, artificial weather modification, and atmospheric chemistry.

2. Theory

In in-line DHI, the mutual interference between a droplet and its twin image is small. When a plane wave is used to irradiate droplets, the diffracted light of the droplets (as the object light) interferes with the undisturbed plane wave (as the reference light) and is recorded as a digital hologram by a CMOS. By using numerical reconstruction, a two-dimensional amplitude distribution with the reconstruction distance z_r can be obtained on the reconstruction plane, given by [50]

$$U_R(u,v) = \frac{1}{\mathrm{j}\lambda}\iint_{\infty} R(x,y) I_H(x,y) \frac{\exp\left(\mathrm{j}k\sqrt{(u-x)^2+(v-y)^2+{z_r}^2}\right)}{\sqrt{(u-x)^2+(v-y)^2+{z_r}^2}}\mathrm{d}x\mathrm{d}y, \quad (1)$$

where, λ is the wavelength, $R(x, y)$ is the reference light, $I_H(x, y)$ is the intensity of interference fringes on the recording medium, k is the wave number. When $z_r = z_i$ (i = 1, 2, 3, ...), the droplets with the reconstruction distance z_i in the reconstructed hologram are focused, and other droplets are out of focus.

However, it is more suitable for batch processing to sample the 12 mm length on the z-axis at equal interval of 0.35 mm. So, z_r can be regarded as a constant set in advance. The reference light of the in-line DHI is a parallel beam, so $R(x, y) = 1$. With the convolution operation, the integral of Equation (1) can be expressed as [50,51]

$$\begin{cases} U_R(u,v) = I_H(x,y) \otimes g(x,y) \\ g(x,y) = \frac{1}{\mathrm{j}\lambda}\frac{\exp\left(\mathrm{j}k\sqrt{x^2+y^2+{z_r}^2}\right)}{\sqrt{x^2+y^2+{z_r}^2}} \end{cases}. \quad (2)$$

Since the convolution operation in Equation (2) is still complicated, the frequency domain multiplication operation can be used instead to reduce the complexity. Therefore, Equation (2) is expressed by Fourier transform as

$$U_R(u,v) = \mathcal{F}^{-1}\{\mathcal{F}[I_H(x,y)]\mathcal{F}[g(x,y)]\}. \tag{3}$$

The 35 reconstruction images $U_R(u,v)$ obtained by sampling are used to identify the focused droplets to obtain the three-dimensional positions and diameters of droplets. The number of droplets in the sampling space is counted as N_c, and the number concentration N can be expressed as N_c divided by volume V. Diameters of all droplets are averaged, the mean volume diameter (MVD) can be obtained as

$$\mathrm{MVD} = \sum_{i=1}^{N_c} l_i, \tag{4}$$

where, l_i is the diameter of the i-th droplet and N_c is the number of droplets in sampling space. Through the statistics of droplet size information in 35 reconstructed images, the actual DSD can be acquired. The above distribution is considered to obey the Gamma distribution. It can be expressed by a corrected Gamma distribution function $n(l)$, given by

$$n(l) = al^5 \exp(-bl^c), \tag{5}$$

where, a, b, and c are three fitting parameters of $n(l)$. They are assigned by the principle of least square method, and the residual sum of squares of Equation (5) is the smallest. The effective diameter (ED) can be calculated based on $n(l)$, given by

$$\mathrm{ED} = \frac{\int_0^\infty l^3 n(l)dl}{\int_0^\infty l^2 n(l)dl}, \tag{6}$$

Here, MVD and number concentration N are directly obtained from the holographic measurement result, which does not depend on the fitting result of $n(l)$. Hence, MVD is used for the analysis of microphysical variations instead of ED, and $n(l)$ is only used to verify the integrity of size distribution. The diameter of each droplet in sampling space can be used to calculate the liquid water content (LWC) of the current environment [52], given by

$$\mathrm{LWC} = \sum_{i=1}^{N_c} \frac{4\pi\rho_c}{3V}\left(\frac{l_i}{2}\right)^3, \tag{7}$$

where, ρ_c is the density of water and V represents the volume of sampling space.

3. Experimental Setup

The evolution processes of cloud can be simulated by expanded form in the BACIC. By continuously reducing pressure and temperature, the aerosols acting as CCN become cloud droplets under high relative humidity conditions. In the experiment, a high-resolution DHI is used to measure the microphysical parameters in the BACIC, as shown in Figure 1. The Condensation Particles Counter (CPC) is used to measure the aerosol number concentration and the DHI is placed on the experimental platform at the bottom. The cloud chamber is a cylindrical structure (the diameter of 2.6 m and volume of 70.5 m^3) with approximately uniform distribution of cloud droplets at the bottom. In DHI, a frequency-doubled solid-state laser produced by the German LASOS company is used as the light source. The wavelength is 532 nm and the output power is 120 mW. In order to ensure the stability of the laser in complex environments, a beam splitting prism with a transmission–reflection ratio of 99:1 is used to divide the beam into two parts. In total, 1% of the beam is reflected to the photodiode (PD) to measure the energy fluctuation of the laser caused by environment temperature and feed it back to the laser control system. The promotion integration differentiation (PID)

algorithm dynamically adjusts the drive current of the laser. A total of 99% of the light beam is collimated and expanded acting as a broad beam using three aspherical lenses (L1–L3), and irradiates the measured cloud droplets. The diameters of L1, L2, and L3 are 10, 30, and 40 mm, respectively. The interference image formed by the droplet diffracted light and the unmodulated transmitted light is zoomed 5.89 times by the microscope lens (ML). The working distance is 20 mm from the ML. The enlarged image is recorded by a CMOS. The minimum exposure time and resolution are 10 μs and 5120 H × 5120 W, respectively. The minimum sampling frequency of CMOS at full resolution is 15 Hz. The chip of CMOS is produced by China Daheng (Group) Company. In order to reduce the influence of field curvature and distortion, the pixels of 3200 W × 3200 H in the central area of CMOS are used. Therefore, the sampling area in the *x*-*y* section is 1.35 × 1.35 mm, the sampling distance along the beam direction (*z*-axis) is 12 mm, and the zero point of the *z*-axis is set on the focal plane of ML. A polarizer (P) is placed behind the ML to improve the contrast of interference fringes.

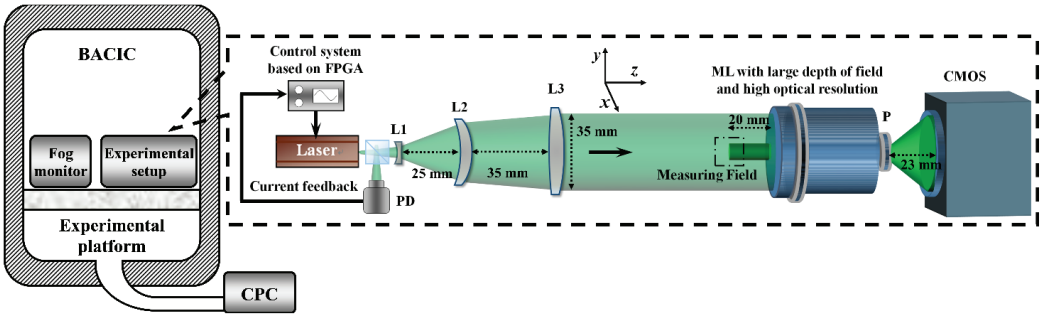


Figure 1. The measurement method of the DHI.

Due to the limitation of target surface size of commercial cameras, high resolution and sample volume are a contradictory relationship. By limiting the sampling volume, the holographic device achieves a high resolution. To ensure complete the observation of 2 μm particles, the sampling volume is reduced to 0.2187 cm^3. The USAF1951 resolution board is observed to verify the optical resolution of the DHI. Figure 2 shows the reconstructed images at −6, 0, and 6 mm on the *z*-axis. The smallest distinguishable line pairs in Figure 2a–c are labeled 7–6, and the corresponding line width is 2.19 μm. By observing standard particle glass plates with diameters of 2, 10, and 20 μm, the accuracy of diameter identification is verified. The particles of 2 and 10 μm are arranged in a square array at an interval of 8 times the diameter, and the interval of 20 μm particles is set to 12 times the diameter. The image algorithms of corrosion and expansion are used for particle identification, which results in a deviation of 1 equivalent pixel. So, the theoretical error of diameter measurement is ± 0.42 μm. The reconstructed image of the particle glass plate at 6 mm from the focal plane is shown in Figure 3. In Figure 3a–c, 795, 236, and 36 particles are identified, and the measurement uncertainties are (2.05 ± 0.53) μm, (10.12 ± 0.86) μm, and (19.89 ± 1.24) μm, respectively. In the cloud chamber, the number of particles in the sampling space of DHI is usually less than 50, so the accuracy of cloud droplet identification is higher than the particle glass plate.

In order to promote the application of in-line DHI in meteorological detection and atmospheric cloud microphysics research, it is necessary to carry out various comparison experiments with recognized cloud droplet detection instruments. The fog monitor [53–60] is widely used in mountain stations and cloud chambers to observe the cloud and fog processes. The measurement results of fog monitors are considered reliable by the majority of researchers. Therefore, we chose the fog monitor as the reference device to verify the accuracy of the holographic device in the measurement of cloud droplet size, number concentration *N*, and other parameters. In this cloud chamber measurement experiment,

the holographic device and the fog monitor are placed 15 cm apart on the experimental platform at the bottom of the cloud chamber. Due to the fact that the distance between two devices is narrow, it can be considered that the cloud droplet groups measured by two devices are highly similar. Then, the most important item in the comparison of measurement results is the size distribution of cloud droplets. The DSDs of fog monitors and in-line DHI are divided by the sampling volume for normalization. Additionally, the DSDs of two devices are nearly identical, as illustrated in Figure 4. The measurement result of the fog monitor is represented by the bold black line and the measurement result of the in-line DHI used in the experiment is represented by the green bar graph.

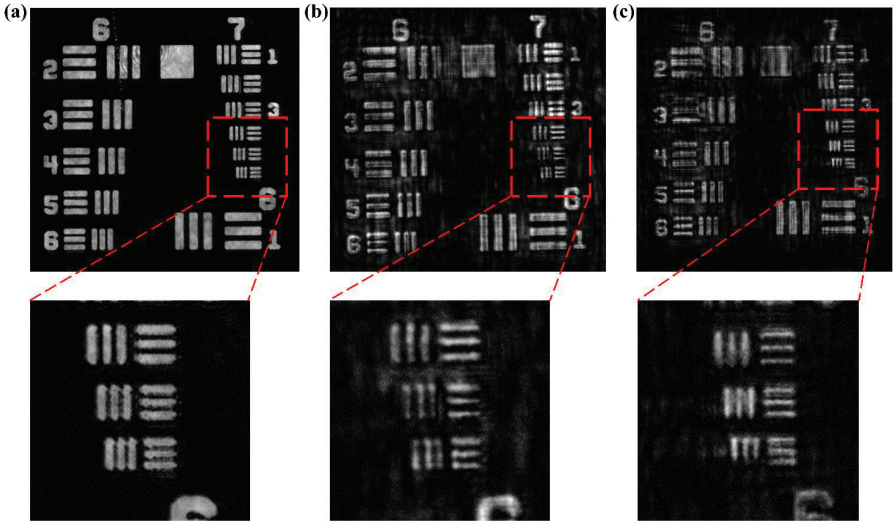


Figure 2. The reconstructed image of the USAF 1951 resolution plate. (**a**) At 0 mm. (**b**) At 6 mm. (**c**) At −6 mm.

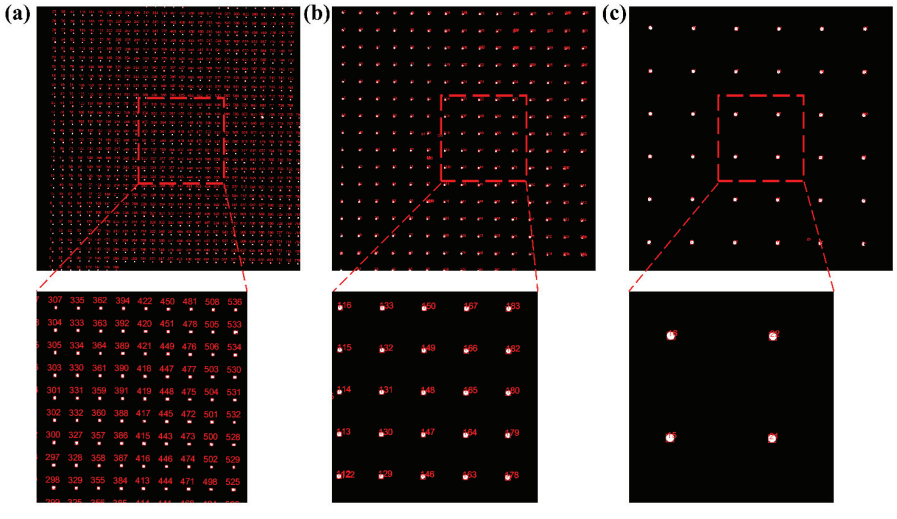


Figure 3. Experimental results of the standard particle glass plate at the distance of 6 mm from the focal plane. (**a**) 2 μm particles. (**b**) 10 μm particles. (**c**) 20 μm particles.

Typically, researchers are interested in the size range corresponding to the maximum value of the DSD, which is used to denote the center of the size distribution. The centers of the size distributions in Figure 4a–d are all 6–7 μm, indicating that the four size distributions collected exhibit similar characteristics. On the one hand, the DSD of two instruments is concentrated at 4–8 μm, as a result of cloud droplet competition for growth. Therefore, the observed cloud droplet exhibits a normal distribution or Gamma distribution. Here, the competitive growth refers to the fact that, as the cloud chamber expands, the majority of CCNs absorb water vapor at the same rate in order to grow in volume. Cloud chamber expansion is achieved by extracting the internal gas. Due to the gas exchange in the extraction processes, a large amount of turbulent flow field is introduced into the cloud chamber. Simultaneously, the entrainment of dry and wet air is also formed. A part of CCN is accelerated by the turbulent flow field, while another part was entrained by moist and dry air, thereby slowing the growth rate. On the other hand, two devices have similar characteristics in the gradient change in the size distribution. The ascending gradient of the cloud droplet size distribution remains slow and uniform below 6 μm, while the descending gradient increases above 6 μm. However, there are slight differences in the results of the two devices due to the difference in measurement principle and observation volume. Compared with the DSD shape of the fog monitor, the DSD shape measured by the holographic device has a larger gradient of rising and falling. Simultaneously, the measurement value of the holographic device in the range of 3–4 μm is less than that of the fog monitor. Except for Figure 4c, the measured values of the holographic device in the range of 8–12 μm are less than that of the fog monitor. These differences can be explained by the measurement principle of the fog monitor. This modifies the spatial distribution of cloud droplets to a certain extent, bringing the resultant DSD closer to statistical distribution, and improving the uniformity of the change in the entire DSD shape. The measurement method of DHI does not alter the spatial distribution of cloud droplets. The gradient of size distribution varies significantly due to the volume (0.219 cm^3) constraint of the sampling space. As a result, each device has distinct advantages and disadvantages. In summary, the DSDs of the DHI and fog monitor are nearly identical, which satisfies the requirements for cloud droplet observation and subsequent cloud microphysical parameter analysis.

The size distribution of cloud droplets can be used to determine the state of cloud droplets at various times. However, the analysis of these distribution characteristics in time series should be performed using the parameter of MVD. In meteorological research, more attention is paid to the formation and dissipation processes of cloud droplets. The dissipation stage lasted approximately 60 s, and 600 holograms are processed to obtain the time-series contrast curve of MVD, as shown in Figure 5. Here, the sampling frequency of the holographic device is 10 Hz, while the sampling frequency of the fog monitor is 1 Hz. To facilitate data comparison, the frequency of the holographic device is reduced to 1 Hz by averaging 10 data points, as shown in Figure 5a. The MVD curves of both devices reflect the dissipating pattern of cloud droplets. Within 60 s, the MVD of both devices followed a similar downward pattern, demonstrating the reliability of holographic device. The MVD of the droplet spectrometer is generally 2 μm higher than that of the holographic device during the last 20 s. This is because the holographic device has a "0 value" during the 20 s, as indicated by the three points with ordinates of 0 in Figure 5a. The binary transitions between 0 and a fixed value are referred to as "zero-sampling". To more clearly represent this "zero-sampling", the sampling frequency of DHI is reduced from 10 to only 5 Hz, as shown in Figure 5b. From the 30th to the 60th second, there are 48 "zero-sampling" points out of 150 data points, which is quite a novel phenomenon. Combined with the related research of Desai et al. [9] in turbulent cloud entrainment, they proposed that the change in the average droplet diameter at the entrainment boundary is binary, abruptly jumping between 0 and a fixed value, which corresponds to the "zero-sampling" effect in Figure 5b. As a result, the dissipation of cloud droplets leads to the appearance of a large number of entrained and mixed regions in the BACIC. Here, the phenomenon of "zero-sampling" indicates that the distribution of cloud droplets is extremely uneven during

the cloud dissipation. It can be considered that the spatial distribution characteristics of cloud droplets are still retained in the cloud microphysical parameters obtained by three-dimensional measurement. Therefore, the DHI device also contributes to the study of small-scale phenomena such as clusters, voids, and random condensation in clouds, which is an exciting area of research to pursue.

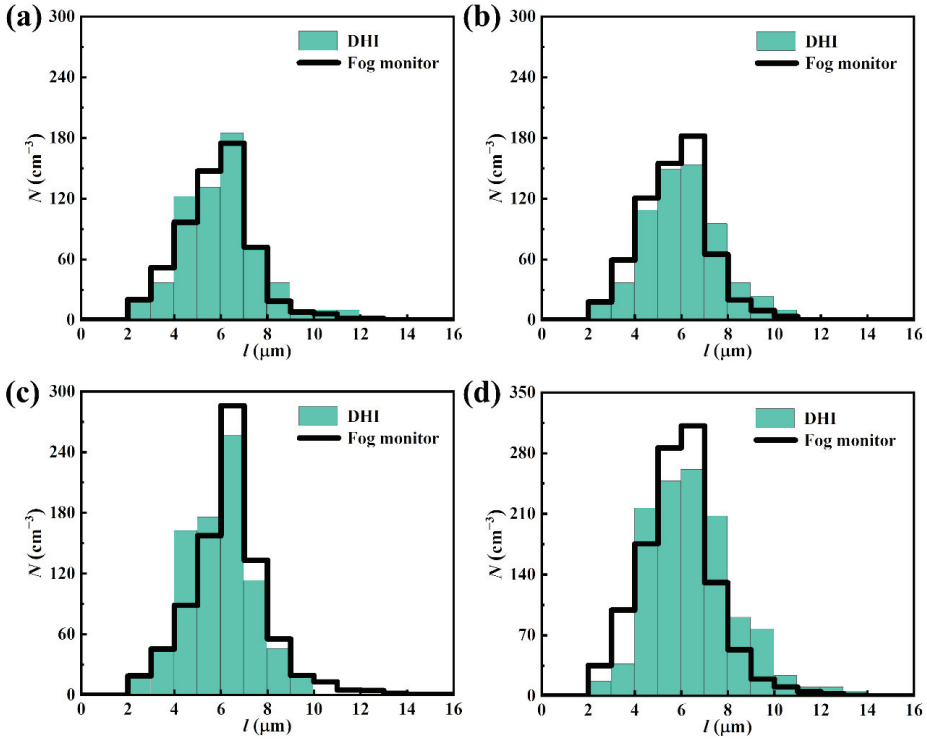


Figure 4. Comparison of DHI and fog monitor on the DSD. (**a**) Size distribution at 1.0 min. (**b**) Size distribution at 4.0 min. (**c**) Size distribution at 2.0 min. (**d**) Size distribution at 3.0 min.

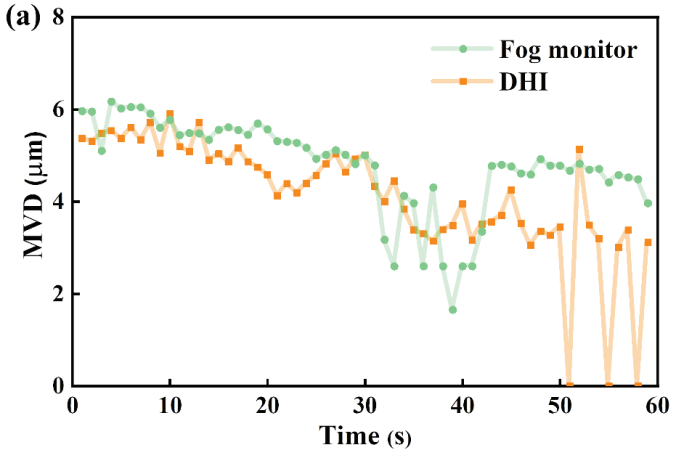


Figure 5. *Cont.*

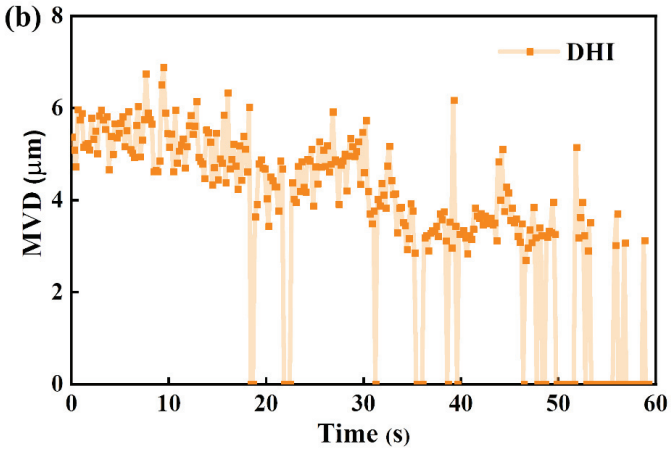


Figure 5. Comparison of DHI and fog monitor in relation to MVD during the last 60 s of the cloud processes. (**a**) The sampling frequency of both DHI and fog monitor is 1 Hz. (**b**) The MVD results of DHI with sampling frequency of 5 Hz.

4. Results Analysis and Discussion

4.1. Size Distribution

The cloud chamber is used as a device for simulating the cloud processes, and the external gas is inhaled by a filter device to fill the interior with aerosol particles. Experiments in the cloud chamber are carried out to verify the accuracy of cloud droplet measurements and the reliability of the software for real-time reproduction of digital holograms. By spraying small liquid droplets (mean diameter 50 μm) above the cloud chamber, the water vapor content in the BACIC is increased. After the spraying operation is completed, the pressure is reduced at a rate of 61 hPa per minute, and cloud droplets are generated 20 s later. The cloud processes last about 5 min, the pressure is reduced by 307 hPa, and the temperature is reduced by 9.5 K. The experimental conditions of the cloud chamber in three experiments are set to the same value, and the environmental parameters of the initial state are relative humidity (95%), temperature (296.2 K), and pressure (998 hPa). The sampling frequency of the in-line DHIis set to 10 Hz for stable image acquisition. In the experiment, the first 10 holograms are averaged to obtain the background hologram of the 11th hologram. By subtracting the obtained background image from the 11th hologram, the noise such as background light is removed. Except for the first 10 holograms, every hologram is processed by the above method. The processes from the hologram to reconstructed image and droplet recognition are shown in Figure 6. During the sampling processes of 12 mm in the z-axis direction at a 0.35 mm interval, the droplet recognition algorithm is used for cloud droplet detection in 35 reconstructed images. Here, the recognition processing of five cloud droplets in the hologram is shown in detail. By droplet recognition, the x, y, and z axis coordinates and diameters of droplets are obtained. Software processes of real-time reconstruction are shown in Figure 7. The steps of droplet recognition are marked by dashed lines, which correspond to the schematic diagram of Figure 6.

DHI is used as a three-dimensional display technology for cloud droplet measurements. The three-dimensional position and size of droplets are obtained at the same time, as shown in Figure 8a–k. DSD can be obtained by counting the diameters of all droplets, and the DSD shape reflects the characteristics of droplet size. The 5 min cloud processes in the first experiment are recorded, and the DSD at the 90th second is provided in Figure 8m. The fitting curve follows the Gamma distribution, and the area between 2 and 6 μm exceeds half of the total area. Hence, for environments with high aerosol number concentrations, the full distribution of DSD can be improved by using an in-line DHI to observe droplets greater than or equal to 2 μm.

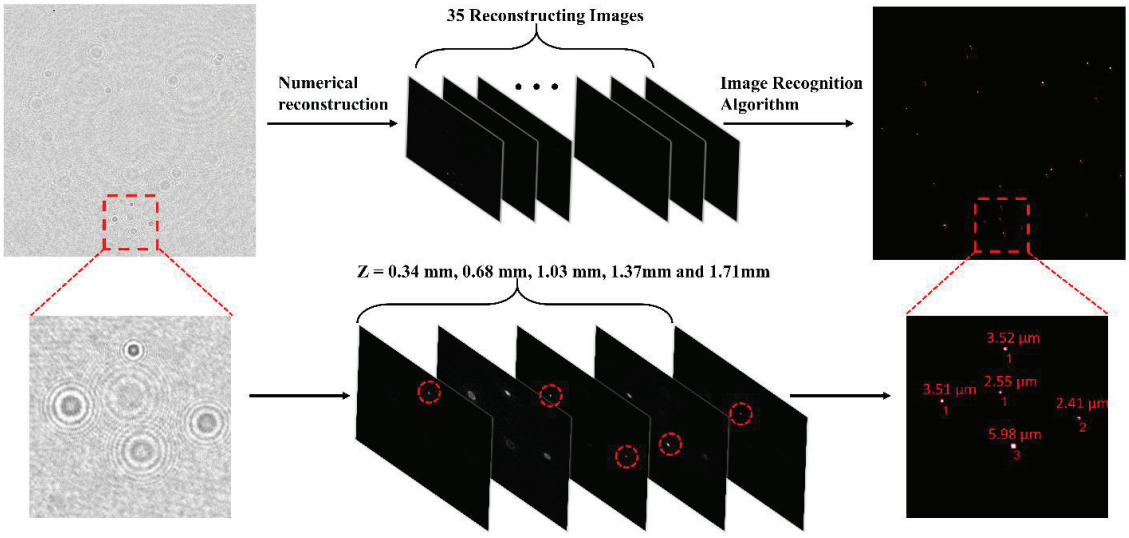


Figure 6. The schematic diagram of droplet recognition.

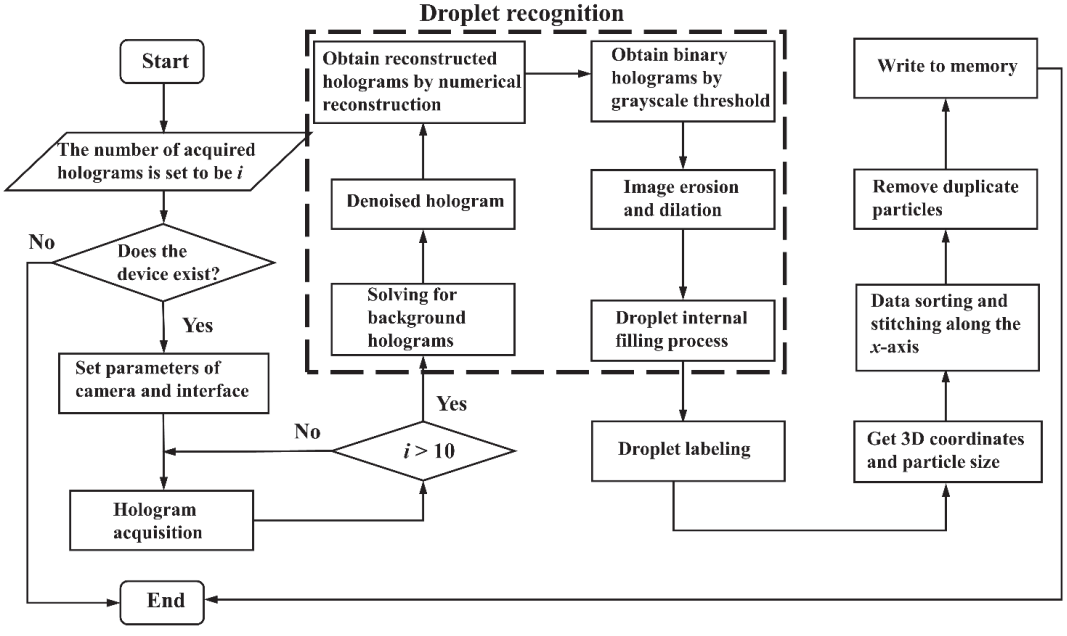


Figure 7. Software processes of real-time reconstruction.

According to the statistical results of 3000 holograms at the first experiment, the number of droplets in each hologram is found to be between 30 and 50. There are not enough overall size characteristics to be represented. The 10 sampling areas are spliced along the positive *x*-axis in time series to expand the sampling space and reduce the randomness of data, as shown in the sampling area of Figure 8k. The spliced area is a rectangular parallelepiped of 13.5 × 1.35 × 12 mm, and the sampling frequency is reduced to 1 Hz. The DSD is usually divided into 1 μm channels according to cloud microphysics

theory, as shown in Figures 8m and 9. The experimental processes were observed in three experiments for analyzing the influence of aerosol number concentration at the DSD.

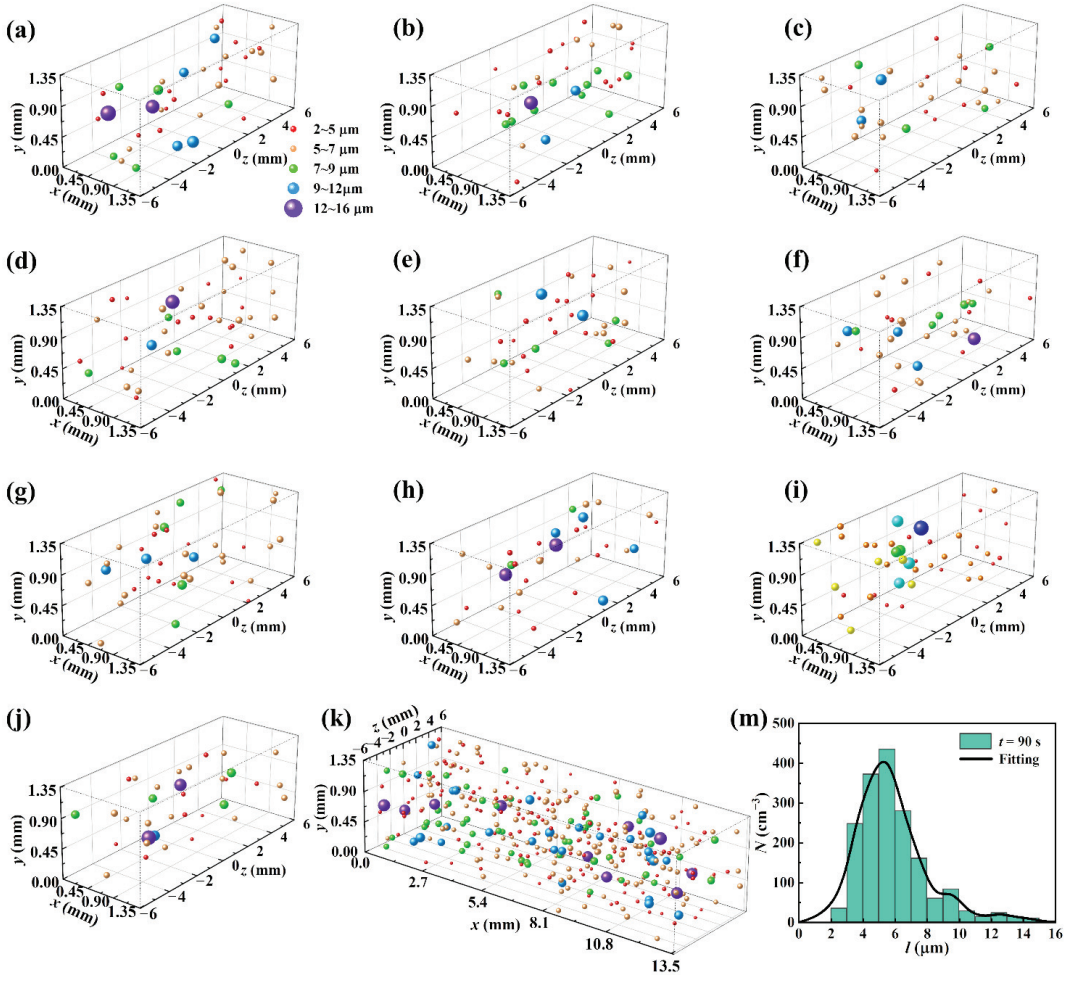


Figure 8. The three-dimensional distribution and DSD in the 90th second. (**a**–**j**) show the 10 three-dimensional distributions of cloud droplets in the detection area within 1 s. (**k**) The three-dimensional distribution fused by 10 distributions. (**m**) The DSD corresponding to the 90th second.

In three experiments, aerosol number concentrations N_a measured by CPC are 10,390, 9150, and 7370 cm^{-3}, respectively. The CCN in the cloud chamber is reduced from the first experiment to the third experiment. By distinction of size, the DSD is divided into smaller droplets (2 μm–l_{mid}), medium droplets (l_{mid}–l_{mid+1}), and oversized droplets (l_{mid+1}–16 μm), as shown in Figure 9a. Figure 9a–c show the three size distributions at equal intervals in the first experiment. The value of l_{mid} is 5 μm, and the proportion of smaller droplets is significantly higher than oversized droplets. This is due to the reduced average water vapor absorption of the droplets at high aerosol number concentration. The l_{mid} increased to 6 μm in the second experiment as shown in Figure 9d–f. Under the condition that N_a is reduced by 11.9%, the proportion of smaller droplets is close to oversized droplets. In the third experiment, the aerosol number concentration of the experiment is reduced by 19.4%, and l_{mid} remains at 6 μm. However, the proportion of smaller droplets is already

less than that of oversized droplets, as shown in Figure 9g–i. The above results describe that the right shift of DSD is caused by the decrease in N_a, and the proportion of smaller droplets is gradually reduced. This indicates that the competitive growth of droplets is weakened as the total number of droplets decreases, resulting in the increase in droplet size. Therefore, compared with l_{mid}, the change in N_a can be more reflected by the proportion of smaller droplets.

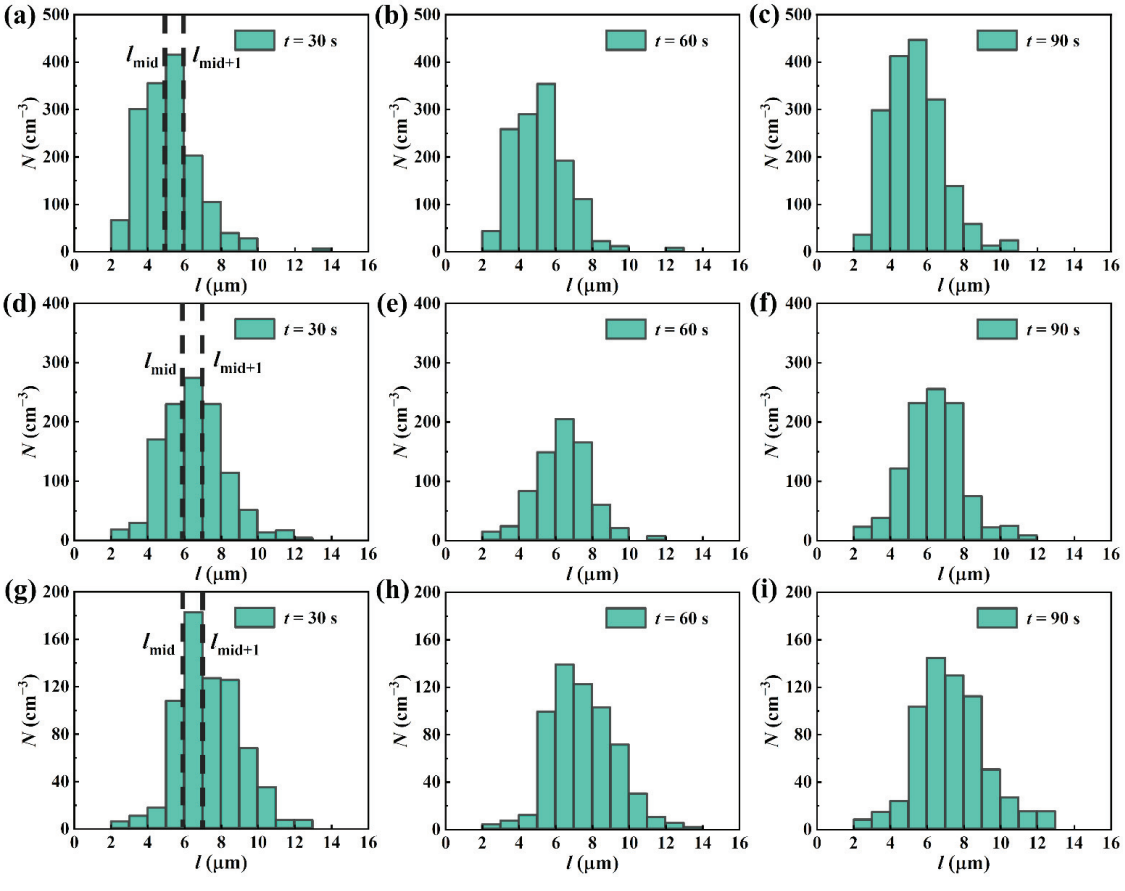


Figure 9. The DSD in cloud chamber. (**a**–**c**) show the size distribution with N_a = 10,390 cm^{-3}. (**d**–**f**) show the size distribution with N_a = 9150 cm^{-3}. (**g**–**i**) show the size distribution with N_a = 7370 cm^{-3}.

The contribution of each size channel is counted. From Figure 10a, the number concentration is represented by the height of histogram, and the range of mean diameter is reflected in the line graph. The overall number concentration is reduced, and the mean diameter is slowly increasing. As for 2 μm–l_{mid}, Figure 10b shows the proportion of the divided three types of droplet sizes. The proportion of smaller droplets in the entire DSD is reduced from 45.47% to 38.70% in the second experiment, and then reduced to 21.26% in the third experiment. Therefore, the statistical result shows that the proportion of smaller droplets is positively correlated with N_a.

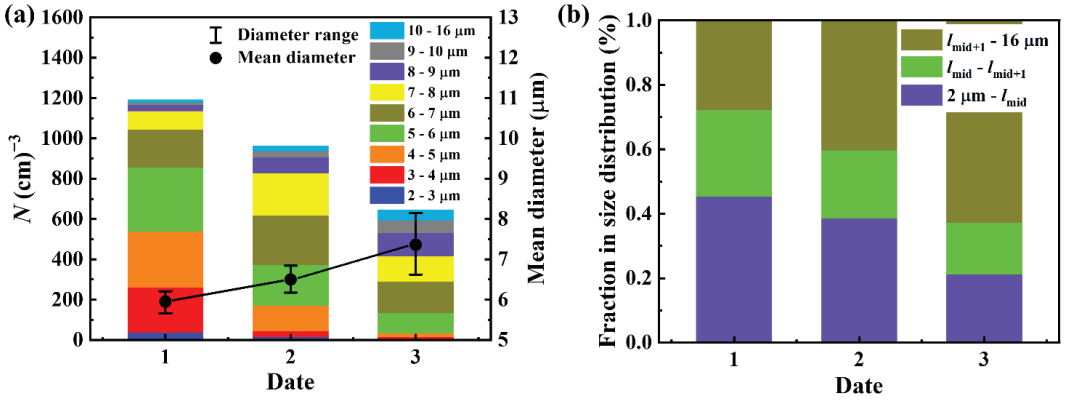


Figure 10. The average statistical results of DSD in three experiments. (**a**) The number concentration distribution of nine size channels. (**b**) The proportion of three types of droplets: smaller, medium, and oversized droplets.

4.2. Microphysical Parameters

The droplet size characteristics at the current moment can be reflected by the DHI in the real-time detection processes. However, the expanding cloud processes last 5 min. The entire experimental processes obviously cannot be represented by the DSD within 1 s. Therefore, the time-series variations in the DSD are transformed into microphysical variations, such as the number concentration N and the LWC. In Figure 11a,c, the data is low-pass filtered to show the pattern of the whole processes. As the N of cloud droplets is increased and decreased by fluctuations, the processes of cloud droplet growth and dissipation are reflected. Due to the weak upward and downward patterns, the original data of MVD is used, as shown in Figure 11b. The comparison results of parameters at the three concentrations show that the decrease in N, the increase in MVD, and the decrease in LWC are caused by the decrease in N_a. At the same time, the pattern of LWC is basically the same as N, and the rate of increase or decrease is related to MVD. However, due to the long-term growth processes (2.1–2.8 min) at N_a = 7370 cm^{-3}, the values of other LWC curves are exceeded, as shown in Figure 11c. It is worth noting that the MVD curve rises rapidly at 2.2–2.8 min, as shown in Figure 11b. This indicates that the monotonic growth of LWC is caused by the volatility growth of MVD. Here, the ratio of standard deviation to average value is usually used to characterize the deviation degree of data, denoted as S. As the proportion of 2–6 μm droplets is reduced, the S of N is 0.198, 0.248, and 0.335, the S of MVD is 0.058, 0.066, and 0.132, and the S of LWC is 0.162, 0.259, and 0.416, respectively. Hence, the decrease in the measurement stability of cloud microphysical parameters is caused by the decrease in the proportion of 2–6 μm droplets.

For the whole cloud processes, the growth and dissipation processes of cloud droplets are usually divided by the rising and falling patterns of N. Due to the influence of the turbulent field and the limitation of the sampling volume, multiple wave crests appear on the time series curve of N. Here, the maximum value in the wave crest is considered as the sign of the end of the growth phase, and its corresponding time is the duration of cloud droplet growth. With the increase in N_a, the growth time of cloud droplets under the three aerosol concentrations is 2.9, 2.4, and 1.5 min, respectively. This shows that, with the same initial water vapor content, the greater the number of CCNs per unit volume, the easier it is to reach the saturation state of water vapor absorption. Here, the MVD curve maintained a downward pattern between 4.0 and 6.0 min, especially the green curve corresponding to the lowest concentration. Therefore, the last 60 s are used to compare holographic devices with fog monitors.

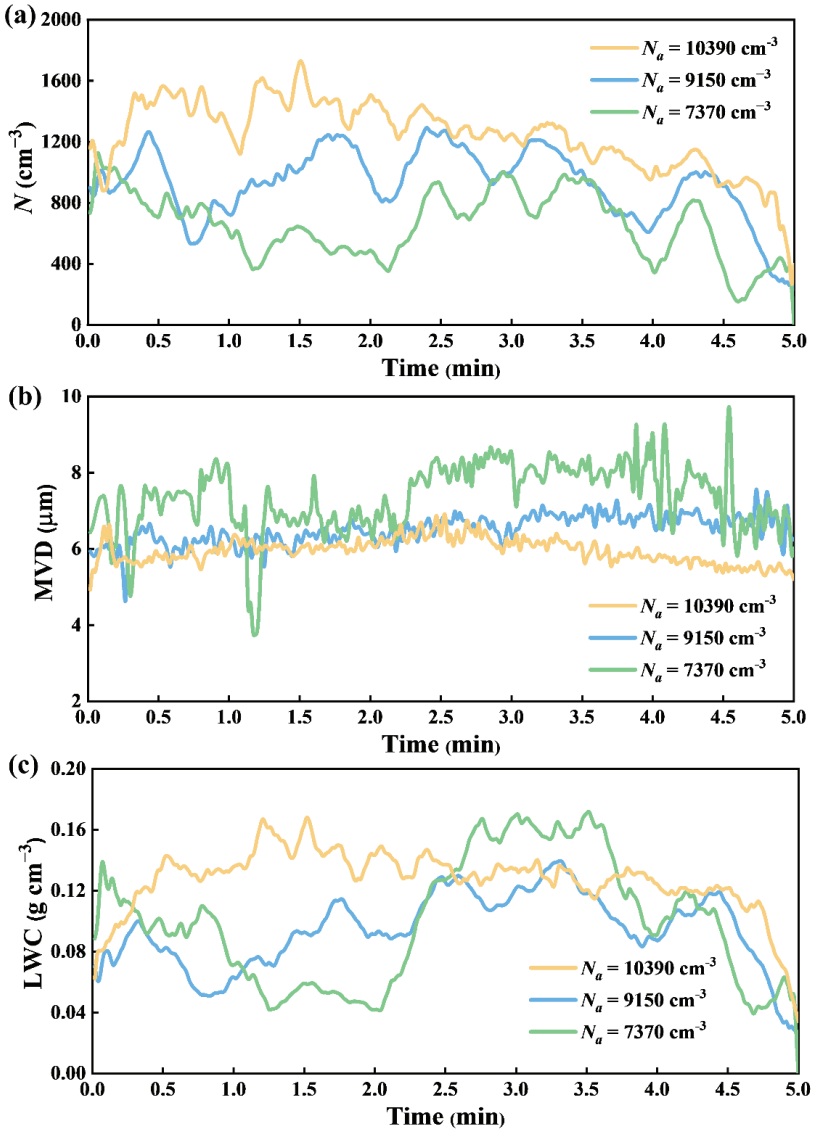


Figure 11. The microphysical parameters of cloud droplets under the different aerosol number concentrations. (**a**) Time-series variation in *N*. (**b**) Time-series variation in MVD. (**c**) Time-series variation in LWC.

In order to investigate the influence of the integrity of DSD on the microphysical processes, the 2–6 μm droplets in the third experiment are deleted, as shown in Figure 12. From the dotted area in Figure 12a, due to the random turbulence in cloud chamber, there are ascending, descending, and ascending processes at 1.0–1.2, 1.2–1.3, and 2.1–2.7 min, respectively. However, for the MVD with 2–6 μm droplets deleted, the steady variation at 2.1–2.7 min does not conform to the upward pattern of original curve. The absence of upward pattern is caused by the incomplete DSD, and the actual change in cloud is ignored. For the observing system, the absence of such a process is essentially considered the defect of data reliability. From the dotted area in Figure 12b, for the LWC with missing

droplets of 2–6 μm, the monotonic growth processes are reduced from 2.0–2.7 to 2.1–2.4 min. Compared with Figure 12a, the upward pattern is completely reversed to the downward pattern at 2.5 min. The faint fluctuations of 2.7–3.6 min are turned into two prominent wave crests. This shows that the interference of turbulence is enlarged by the absence of droplets. The above results indicate that the absence of 2–6 μm in DSD changes the actual pattern of cloud processes in some periods and reduces the reliability of observation data to cloud variations.

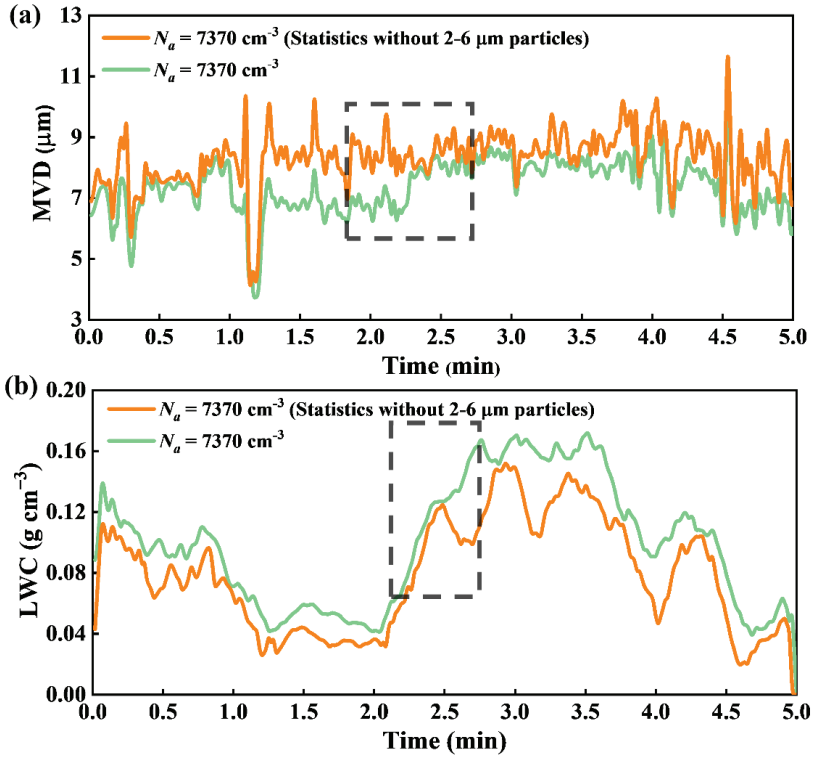


Figure 12. The changes in microphysical parameters at N_a = 7370 cm^{-3}. (**a**) The original MVD and the MVD without 2–6 μm droplets. (**b**) The original LWC and the LWC without 2–6 μm droplets.

The microphysical parameters can reflect the quantity and size characteristics of particles. Among them, the *N* and LWC are primarily used to describe quantitative characteristics, while the MVD, ED, and LWC are primarily used to describe size characteristics. The correlation between *N* and LWC is shown in Figure 13a,b for N_a of 9150 and 7370 cm^{-3}. According to the results of the linear fitting of LWC, there is a positive correlation between *N* and LWC at both concentrations. In the analysis of Figure 11, the change pattern of *N* and LWC curves is similar, which is a manifestation of positive correlation. It is worth noting that as *N* increases, the fluctuation range of LWC is gradually increased. Especially under the condition that N_a is 7370 cm^{-3}, the maximum fluctuation difference reaches 0.14 g cm^{-3}. Correlations of *N* and LWC with N_a of 9150 and 7370 cm^{-3} are shown in Figure 13a,b. The results of the linear fitting reveal a positive correlation between ED and MVD. Unlike the fluctuation change in LWC, the fluctuation change in ED around the fitted curve is kept to a maximum of 1.3 μm in Figure 13c. In Figure 13d, this fluctuation is limited to a range of no more than 2.1 μm. In this case, the fluctuation of the curve represents a data bias, and the fitted curve represents an estimate of the data that approaches the true value. Thus, the

increase in aerosol concentration reduces the deviation degree of the data and improves the anti-interference ability of the data, which is also called the robustness.

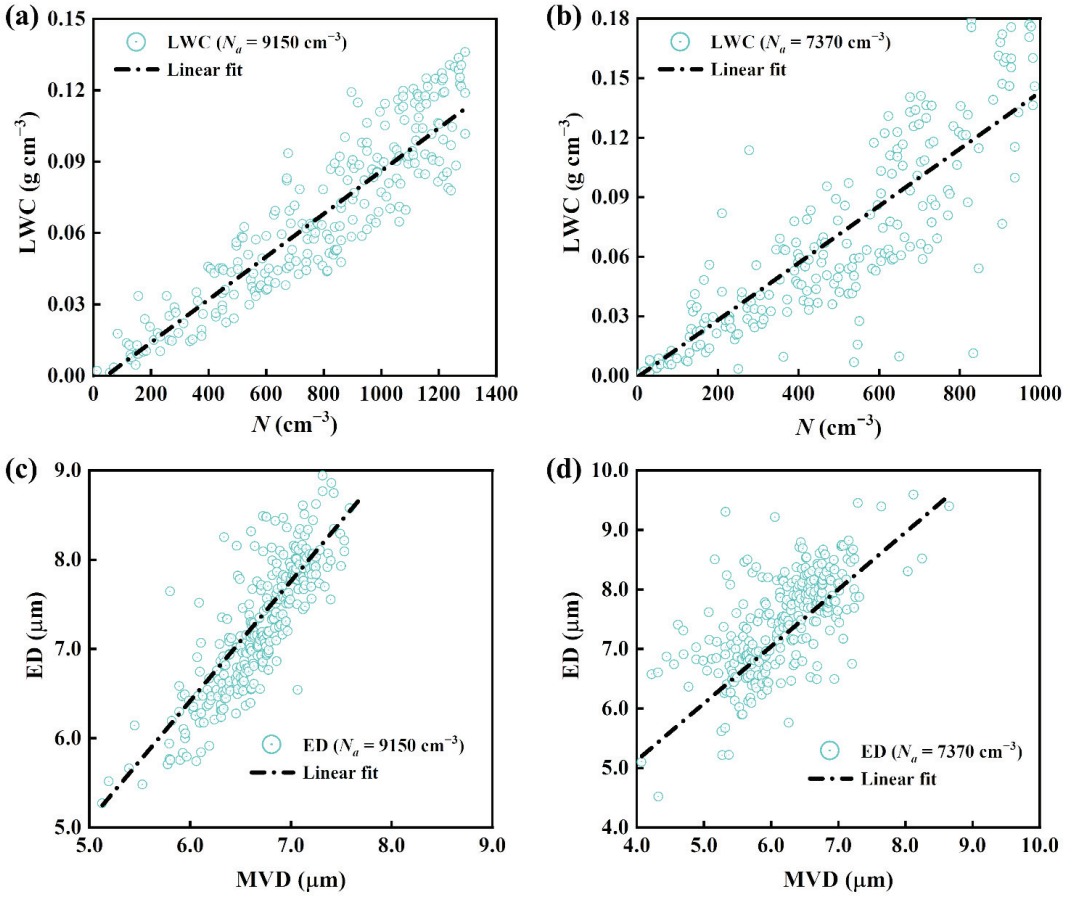


Figure 13. Microphysical parameter correlation curves are shown for N_a of 9150 and 7370 cm^{-3}, respectively. (**a**,**b**) show the relationship between N and LWC. (**c**,**d**) show the relationship between ED and MVD.

To conduct a qualitative analysis of the potential association between MVD and N, we classify the aerosol concentrations across three experiments into three categories based on their numerical magnitude: high, moderate, and low. In Figure 14, the fitting curve for MVD maintained an upward pattern as the number concentration increased, demonstrating a slight positive correlation between MVD and N. Notably, the data distributions at the three concentrations showed obvious stratification. There are two main reasons for the stratification. On the one hand, the values of N_a differ by more than 1000 cm^{-3} in three experiments. A large concentration gradient results in the stratification of MVD. On the other hand, the maximum deviation distance between discrete point and fit curve is less than 2 μm in Figure 14. The limited deviation distance also causes the stratification. In addition, there are some differences in the dispersion degree of data between three concentrations. When N is in the range from 800 to 1100 cm^{-3}, the dispersion degree of data is increased as the aerosol concentration is decreased. With the high-concentration condition of aerosol, the fitted curve grows approximately linearly at N in the range of 800–1400 cm^{-3}, which is consistent with the theoretically proportional relationship. Since

the fluctuation in the fitted curve is mainly affected by the uneven distribution under the action of turbulence, the high-concentration aerosol condition effectively weakens this effect and enhances the robustness of the data.

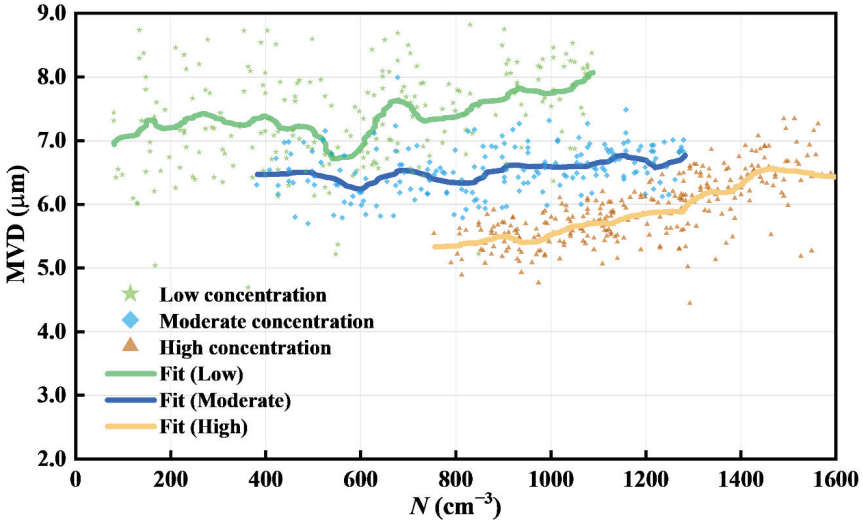


Figure 14. Correlation analysis between N and MVD at three different aerosol concentration levels: high, moderate, and low.

Here, the correlation analysis is performed on several cloud microphysical parameters in Figures 13 and 14. The concentration of aerosols directly influences the correlation between any two microphysical parameters. Regardless of whether Figures 13 or 14 is shown, the data distribution associated with the high concentration is denser, and the data deviation is smaller in the vicinity of the fitted curve. This indicates that DHI device may be better suited for particle detection at higher concentrations of particles. Naturally, there is a limit to the aerosol concentration inside the cloud chamber for cloud droplet observation experiments. Simultaneously, as DHI is a three-dimensional imaging device, the extremely high density of cloud droplets will result in increased particle overlap, lowering the accuracy of particle identification. Therefore, the initial aerosol concentration around 9150 cm^{-3} is an optimal choice.

5. Conclusions

In the paper, the observation method based on DHI of the liquid cloud droplets with the size of 2–16 μm is proposed for extending the observed DSD in the BACIC. With the USAF 1951 resolution plate and the glass plate of 2 μm particles, the minimum reliable size observed by DHI is 2 μm. The sampling volume is increased tenfold by stitching three-dimensional space along the x-axis. After the particle identification, the 3D position and DSD of cloud droplets are obtained. The comparative experimental results demonstrate that the DSDs observed by the DHI and fog monitor follow the Gamma distribution, and that the measured results of MVD are highly comparable. The analysis results of DSD reveal that the absence of the droplets with the size of 2–6 μm alters several patterns of microphysical parameters, and then the reliability of some observational data on cloud variations is diminished. As a result, the minimum size in DSD should be extended to 2 μm. The measured results of cloud microphysical parameters indicate a stronger positive correlation and increased robustness between microphysical parameters under the condition of high concentration aerosols. To further research the interaction mechanism of cloud microphysics and turbulence, an engineering prototype with higher sampling

frequency is required. Future research will examine the mechanism by which aerosol concentration influences the fluctuation of microphysical parameters.

Author Contributions: Conceptualization, P.G. and J.L.; methodology, P.G.; software, P.G. and J.W.; validation, P.G., J.W. and D.H.; formal analysis, P.G.; investigation, Y.G.; resources, Y.G.; data curation, P.G.; writing—original draft preparation, P.G.; writing—review and editing, P.G. and J.W.; visualization, P.G.; supervision, J.W.; project administration, Y.G.; funding acquisition, J.W. All authors have read and agreed to the published version of the manuscript.

Funding: This work was supported by the National Natural Science Foundation of China (41875034, 52127802 and 41975045) and scientific research project of Shanghai Meteorological Service (MS202004).

Data Availability Statement: Not applicable.

Conflicts of Interest: The authors declare no conflict of interest.

References

1. Bhatia, K.; Vecchi, G.; Murakami, H.; Underwood, S.; Kossin, J. Projected response of tropical cyclone intensity and intensification in a global climate model. *J. Clim.* **2018**, *31*, 8281–8303. [CrossRef]
2. Gettelman, A.; Morrison, H.; Santos, S.; Bogenschutz, P. Advanced two-moment bulk microphysics for global models. Part II: Global model solutions and aerosol–cloud interactions. *J. Clim.* **2015**, *28*, 1288–1307. [CrossRef]
3. Lohmann, U.; Stier, P.; Hoose, C.; Ferrachat, S.; Kloster, S.; Roeckner, E.; Zhang, J. Cloud microphysics and aerosol indirect effects in the global climate model ECHAM5-HAM. *Atmos. Chem. Phys.* **2007**, *7*, 3425–3446. [CrossRef]
4. Revell, L.E.; Kremser, S.; Hartery, S.; Harvey, M.; Mulcahy, J.P.; Williams, J.; Morgenstern, O.; McDonald, A.J.; Varma, V.; Bird, L.; et al. The sensitivity of Southern Ocean aerosols and cloud microphysics to sea spray and sulfate aerosol production in the HadGEM3-GA7.1 chemistry-climate model. *Atmos. Chem. Phys.* **2019**, *19*, 15447–15466. [CrossRef]
5. Zhang, Y.; Fan, J.; Li, Z.; Rosenfeld, D. Impacts of cloud microphysics parameterizations on simulated aerosol-cloud interactions for deep convective clouds over Houston. *Atmos. Chem. Phys.* **2021**, *21*, 2363–2381. [CrossRef]
6. Shaw, R.A.; Cantrell, W.; Chen, S.; Chuang, P.; Donahue, N.; Feingold, G.; Kollias, P.; Korolev, A.; Kreidenweis, S.; Krueger, S.; et al. Cloud–aerosol–turbulence interactions: Science priorities and concepts for a large-scale laboratory facility. *Bull. Amer. Meteorol. Soc.* **2020**, *101*, E1026–E1035. [CrossRef]
7. Dias, A.; Ehrhart, S.; Vogel, A.; Williamsonet, C.; Almeida, J.; Kirkby, J.; Mathot, S.; Mumford, S.; Onnela, A. Temperature uniformity in the CERN CLOUD chamber. *Atmos. Meas. Tech.* **2017**, *10*, 5075–5088. [CrossRef]
8. Zhao, X.; Heidinger, A.K.; Walther, A. Climatology analysis of aerosol effect on marine water cloud from long-term satellite climate data records. *Remote Sens.* **2016**, *8*, 300. [CrossRef]
9. Desai, N.; Chandrakar, K.K.; Chang, K.; Cantrell, W.; Shaw, R.A. Influence of Microphysical Variability on Stochastic Condensation in a Turbulent Laboratory Cloud. *J. Atmos. Sci.* **2018**, *75*, 189–201. [CrossRef]
10. Chandrakar, K.K.; Saito, I.; Yang, F.; Cantrell, W.; Gotoh, T.; Shaw, R.A. Droplet size distributions in turbulent clouds: Experimental evaluation of theoretical distributions. *Q. J. R. Meteorol. Soc.* **2020**, *146*, 483–504. [CrossRef]
11. Beals, M.J.; Fugal, J.P.; Shaw, R.A.; Lu, J.; Spuler, S.M.; Stith, J.L. Holographic measurements of inhomogeneous cloud mixing at the centimeter scale. *Science* **2015**, *350*, 87–90. [CrossRef] [PubMed]
12. Pinsky, M.B.; Khain, A.P.; Shapiro, M. Collisions of cloud droplets in a turbulent flow. Part IV: Droplet hydrodynamic interaction. *J. Atmos. Sci.* **2007**, *64*, 2462–2482. [CrossRef]
13. Chen, R.; Chang, F.L.; Li, Z.; Ferraro, R.; Weng, F. Impact of the vertical variation of cloud droplet size on the estimation of cloud liquid water path and rain detection. *J. Atmos. Sci.* **2007**, *64*, 3843–3853. [CrossRef]
14. Li, J.; Wang, X.; Chen, J.; Zhu, C.; Li, W.; Li, C.; Liu, L.; Xu, C.; Wen, L.; Xue, L.; et al. Chemical composition and droplet size distribution of cloud at the summit of Mount Tai, China. *Atmos. Chem. Phys.* **2017**, *17*, 9885–9896. [CrossRef]
15. Lu, C.; Liu, Y.; Yum, S.S.; Chen, J.; Zhu, L.; Gao, S.; Yin, Y.; Jia, X.; Wang, Y. Reconciling contrasting relationships between relative dispersion and volume-mean radius of cloud droplet size distributions. *J. Geophys. Res. Atmos.* **2020**, *125*, e2019JD031868. [CrossRef]
16. Broekhuizen, K.; Chang, R.Y.W.; Leaitch, W.R.; Li, S.M.; Abbatt, J.P.D. Closure between measured and modeled cloud condensation nuclei (CCN) using size-resolved aerosol compositions in downtown Toronto. *Atmos. Chem. Phys.* **2006**, *6*, 2513–2524. [CrossRef]
17. Petters, M.D.; Kreidenweis, S.M. A single parameter representation of hygroscopic growth and cloud condensation nuclus activity. *Atmos. Chem. Phys.* **2007**, *7*, 1961–1971. [CrossRef]
18. Huang, Z.; Nee, J.B.; Chiang, C.W.; Zhang, S.; Jin, H.; Wang, W.; Zhou, T. Real-Time Observations of Dust-Cloud Interactions Based on Polarization and Raman Lidar Measurements. *Remote Sens.* **2018**, *10*, 1017. [CrossRef]
19. Wang, J.; Lee, Y.N.; Daum, P.H.; Jayne, J.; Alexander, M.L. Effects of aerosol organics on cloud condensation nucleus (CCN) concentration and first indirect aerosol effect. *Atmos. Chem. Phys.* **2008**, *8*, 6325–6339. [CrossRef]

20. Riipinen, I.; Pierce, J.R.; Yli-Juuti, T.; Nieminen, T.; Hakkinen, S.; Ehn, M.; Junninen, H.; Lehtipalo, K.; Petaja, T.; Slowik, J.; et al. Organic condensation: A vital link connecting aerosol formation to cloud condensation nuclei (CCN) concentrations. *Atmos. Chem. Phys.* **2011**, *11*, 3865–3878. [CrossRef]
21. Lambe, A.T.; Onasch, T.B.; Massoli, P.; Croasdale, D.R.; Wright, J.P.; Ahern, A.T.; Williams, L.R.; Worsnop, D.R.; Brune, W.H.; Davidovits, P. Laboratory studies of the chemical composition and cloud condensation nuclei (CCN) activity of secondary organic aerosol (SOA) and oxidized primary organic aerosol (OPOA). *Atmos. Chem. Phys.* **2011**, *11*, 8913–8928. [CrossRef]
22. Gunthe, S.S.; Rose, D.; Su, H.; Garland, R.M.; Achtert, P.; Nowak, A.; Wiedensohler, A.; Kuwata, M.; Takegawa, N.; Kondo, Y.; et al. Cloud condensation nuclei (CCN) from fresh and aged air pollution in the megacity region of Beijing. *Atmos. Chem. Phys.* **2011**, *11*, 11023–11039. [CrossRef]
23. Zheng, G.; Kuang, C.; Uin, J.; Watson, T.; Wang, J. Large contribution of organics to condensational growth and formation of cloud condensation nuclei (CCN) in the remote marine boundary layer. *Atmos. Chem. Phys.* **2020**, *20*, 12515–12525. [CrossRef]
24. Bauer, H.; Ciebl, H.; Hitzenberger, R.; Kasper-Giebl, A.; Reischl, G.; Zibuschka, F.; Puxbaum, H. Airborne bacteria as cloud condensation nuclei. *J. Geophys. Res.-Atmos.* **2003**, *108*, 4658. [CrossRef]
25. Gustafson, W.I., Jr.; Chapman, E.G.; Ghan, S.J.; Easter, R.C.; Fast, J.D. Impact on modeled cloud characteristics due to simplified treatment of uniform cloud condensation nuclei during NEAQS 2004. *Geophys. Res. Lett.* **2007**, *34*, L19809. [CrossRef]
26. Kumar, M.; Birhman, A.S.; Kannan, S.; Shakher, C. Measurement of initial displacement of canine and molar in human maxilla under different canine retraction methods using digital holographic interferometry. *Opt. Eng.* **2018**, *57*, 094106. [CrossRef]
27. Das, B.; Yelleswarapu, C.S. Dual plane in-line digital holographic microscopy. *Opt. Lett.* **2010**, *35*, 3426–3428. [CrossRef]
28. Sang, X.; Yu, C.; Yu, M.; Hsu, D. Applications of digital holography to measurements and optical characterization. *Opt. Eng.* **2011**, *50*, 091311. [CrossRef]
29. Pan, G.; Jun, W.; Cheng-Cheng, Z.; Jia-Bin, T.; Jing-Jing, L.; Qing, Y.; Deng-Xin, H. Simultaneous measurement of cloud microphysical parameters based on digital holographic interferometry. *Acta Phys. Sin.* **2021**, *70*, 099201. [CrossRef]
30. Bellanger, C.; Brignon, A.; Colineau, J.; Huignard, J.P. Coherent fiber combining by digital holography. *Opt. Lett.* **2008**, *33*, 2937–2939. [CrossRef]
31. Alvarez, A.S.; Manuel, H.; Santoyo, F.M.; Anaya, T.S. Strain determination in bone sections with simultaneous 3D digital holographic interferometry. *Opt. Lasers Eng.* **2014**, *57*, 101–108. [CrossRef]
32. Kumar, M.; Shakher, C. Experimental characterization of the hygroscopic properties of wood during convective drying using digital holographic interferometry. *Appl. Opt.* **2016**, *55*, 960–968. [CrossRef] [PubMed]
33. Sánchez, A.; Manuel, H.; Santoyo, F.M.; Saucedo-A, T.; Reyes, R. Simultaneous 3D digital holographic interferometry for strain measurements validated with FEM. *Opt. Lasers Eng.* **2014**, *52*, 178–183. [CrossRef]
34. Kumar, V.; Kumar, M.; Shakher, C. Measurement of natural convective heat transfer coefficient along the surface of a heated wire using digital holographic interferometry. *Appl. Opt.* **2014**, *53*, G74–G83. [CrossRef] [PubMed]
35. Gorthi, S.S.; Rajshekhar, G.; Rastogi, P. Strain estimation in digital holographic interferometry using piecewise polynomial phase approximation based method. *Opt. Express* **2010**, *18*, 560–565. [CrossRef]
36. Vincitorio, F.; Bahuer, L.; Fiorucci, M.P.; López, A.J.; Ramil, A. Improvement of crack detection on rough materials by digital holographic interferometry in combination with non-uniform thermal loads. *Optik* **2018**, *163*, 43–48. [CrossRef]
37. Sheng, J.; Malkiel, E.; Katz, J. Digital holographic microscope for measuring three-dimensional particle distributions and motions. *Appl. Optics.* **2006**, *45*, 3893–3901. [CrossRef]
38. Yu, X.; Hong, J.; Liu, C.; Kim, M.K. Review of digital holographic microscopy for three-dimensional profiling and tracking. *Opt. Eng.* **2014**, *53*, 112306. [CrossRef]
39. Dubois, F.; Callens, N.; Yourassowsky, C.; Hoyos, M.; Kurowski, P.; Monnom, O. Digital holographic microscopy with reduces spatial coherence for three-dimensional particle flow analysis. *Appl. Opt.* **2006**, *45*, 864–871. [CrossRef]
40. Latychevskaia, T.; Fink, H.W. Holographic time-resolved particle tracking by means of three-dimensional volumetric deconvolution. *Opt. Express* **2014**, *22*, 20994–21003. [CrossRef]
41. Lee, S.J.; Seo, K.W.; Choi, Y.S.; Sohn, M.H. Three-dimensional motion measurements of free-swimming microorganisms using digital holographic microscopy. *Meas. Sci. Technol.* **2011**, *22*, 064004. [CrossRef]
42. Dimiduk, T.G.; Perry, R.W.; Fung, J.; Manoharan, V.N. Random-subset fitting of digital holograms for fast three-dimensional particle tracking. *Appl. Opt.* **2014**, *53*, G177–G183. [CrossRef] [PubMed]
43. Marquet, P.; Depeursinge, C.; Magistretti, P.J. Exploring Neural Cell Dynamics with Digital Holographic Microscopy. *Annu. Rev. Biomed. Eng.* **2013**, *15*, 407–431. [CrossRef] [PubMed]
44. Krenkel, M.; Toepperwien, M.; Alves, F.; Salditt, T. Three-dimensional single-cell imaging with X-ray waveguides in the holographic regime. *Acta Crystallogr. Sect. A* **2017**, *73*, 282–292. [CrossRef]
45. Langehanenberg, P.; Kemper, B.; Dirksen, D.; Bally, G. Autofocusing in digital holographic phase contrast microscopy on pure phase objects for live cell imaging. *Appl. Opt.* **2008**, *47*, D176–D182. [CrossRef]
46. Bartels, M.; Krenkel, M.; Haber, J.; Wilke, R.N.; Salditt, T. X-Ray Holographic Imaging of Hydrated Biological Cells in Solution. *Phys. Rev. Lett.* **2015**, *114*, 048103. [CrossRef]
47. Singh, A.S.G.; Anand, A.; Leitgeb, R.A.; Javidi, B. Lateral shearing digital holographic imaging of small biological specimens. *Opt. Express* **2012**, *20*, 23617–23622. [CrossRef]

48. Chen, C.; Liu, T.; Liu, Y.; Yang, B.; Su, Y. Learning-Based Clutter Mitigation with Subspace Projection and Sparse Representation in Holographic Subsurface Radar Imaging. *Remote Sens.* **2022**, *14*, 682. [CrossRef]
49. Ivashov, S.I.; Capineri, L.; Bechtel, T.D.; Razevig, V.V.; Inagaki, M.; Gueorguiev, N.L.; Kizilay, A. Design and Applications of Multi-Frequency Holographic Subsurface Radar: Review and Case Histories. *Remote Sens.* **2021**, *13*, 3487. [CrossRef]
50. Kreis, T.M. Frequency analysis of digital holography with reconstruction by convolution. *Opt. Eng.* **2002**, *41*, 1829–1839. [CrossRef]
51. Picart, P.; Tankam, P. Analysis and adaptation of convolution algorithms to reconstruct extended objects in digital holography. *Appl. Opt.* **2013**, *52*, A240–A253. [CrossRef]
52. Zhang, Y.; Chen, S.; Tan, W.; Chen, S.; Chen, H.; Guo, P.; Sun, Z.; Hu, R.; Xu, Q.; Zhang, M.; et al. Retrieval of Water Cloud Optical and Microphysical Properties from Combined Multiwavelength Lidar and Radar Data. *Remote Sens.* **2021**, *13*, 4396. [CrossRef]
53. Tav, J.; Masson, O.; Burnet, F.; Paulat, P.; Bourrianne, T.; Conil, S.; Pourcelot, L. Determination of fog-droplt deposition velocity fron a simple weighing method. *Aerosol Air Qual. Res.* **2018**, *18*, 103–113. [CrossRef]
54. Wei, M.; Xu, C.; Chen, J.; Zhu, C.; Li, J.; Lv, G. Characteristics of bacterial community in cloud water at Mt Tai: Similarity and disparity under polluted and non-polluted cloud episodes. *Atmos. Chem. Phys.* **2017**, *17*, 5253–5270. [CrossRef]
55. Alfonso, L.; Raga, G.B.; Baumgardner, D. The impact of fluctuations and correlations in droplet growth by collision–coalescence revisited–Part 2: Observational evidence of gel formation in warm clouds. *Atmos. Chem. Phys.* **2019**, *19*, 14917–14932. [CrossRef]
56. La, I.; Yum, S.S.; Gultepe, I.; Yeom, J.M.; Song, J.I.; Cha, J.W. Influence of Quasi-Periodic Oscillation of Atmospheric Variables on Radiation Fog over A Mountainous Region of Korea. *Atmosphere* **2020**, *11*, 230. [CrossRef]
57. Liu, Q.; Wu, B.; Wang, Z.; Hao, T. Fog droplet size distribution and the interaction between fog droplets and fine particles during dense fog in Tianjin, China. *Atmosphere* **2020**, *11*, 258. [CrossRef]
58. Weston, M.; Francis, D.; Nelli, N.; Fonseca, R.; Temimi, M.; Addad, Y. The first characterization of fog microphysics in the United Arab Emirates, an arid region on the Arabian Peninsula. *Earth Space Sci.* **2022**, *9*, e2021EA002032. [CrossRef]
59. Koike, M.; Ukita, J.; Ström, J.; Tunved, P.; Shiobara, M.; Vitale, V.; Lupi, A.; Baumgardner, D.; Ritter, C.; Hermansen, O.; et al. Year-round in situ measurements of Arctic low-level clouds: Microphysical properties and their relationships with aerosols. *J. Geophys. Res.-Atmos.* **2019**, *124*, 1798–1822. [CrossRef]
60. Chen, C.; Zhang, M.; Perrie, W.; Chang, R.; Chen, X.; Duplessis, P.; Wheeler, M. Boundary layer parameterizations to simulate fog over Atlantic Canada waters. *Earth Space Sci.* **2020**, *7*, e2019EA000703. [CrossRef]

remote sensing

MDPI

Article

A Novel Ultra−High Resolution Imaging Algorithm Based on the Accurate High−Order 2−D Spectrum for Space−Borne SAR

Tao He [1], Lei Cui [2], Pengbo Wang [1,*], Yanan Guo [1] and Lei Zhuang [2]

[1] School of Electronics and Information Engineering, Beihang University, Beijing 100191, China; tao_h@buaa.edu.cn (T.H.); gyanan@buaa.edu.cn (Y.G.)
[2] Shanghai Institute of Satellite Engineering, Shanghai 201109, China; clei117@163.com (L.C.); zhuanglei0411@163.com (L.Z.)
* Correspondence: wangpb7966@buaa.edu.cn; Tel.: +86-10-823-386-70

Abstract: Ultra−high spatial resolution, which can bring more detail to ground observation, is a constant pursuit of the modern space−borne synthetic aperture radar. However, the exact imaging in this case has always been a complex technical problem due to its complicated imaging geometry and signal structure. To achieve those applications' strict requirements, a novel ultra−high resolution imaging algorithm based on an accurate high−order 2−D spectrum is presented in this paper. The only first two Doppler parameters needed as range models in the defective spectrum are replaced by a polynomial range model, which can derive coefficients from the relative motion between the radar and the targets. Then, the new spectrum is calculated through the Lagrange inversion formula. Based on this, the novel imaging algorithm is elaborated in detail as follows: The range high−order term of the spectrum is compensated completely, and the range chirp rate space variance is eliminated by the cubic phase term. Two steps of range cell migration correct are applied in this algorithm before and after the range compression; one is the traditional linear chirp scaling method, and another is the interpolation to correct the quadratic range cell migration introduced by the range chirp rate equalization. The simulation results illustrate that the proposed algorithm can handle the exact imaging processing with a 0.25 m resolution around the azimuth and range in 2 km × 6 km, which validates the feasibility of the proposed algorithm.

Keywords: space−borne SAR; ultra−high resolution; high−order 2−D spectrum; Lagrange inversion formula; chirp rate space variance

Citation: He, T.; Cui, L.; Wang, P.; Guo, Y.; Zhuang, L. A Novel Ultra−High Resolution Imaging Algorithm Based on the Accurate High−Order 2−D Spectrum for Space−Borne SAR. *Remote Sens.* **2022**, *14*, 2284. https://doi.org/10.3390/rs14092284

Academic Editors: Kai Qin, Zhengqiang Li, Zhongwei Huang, Chi Li, Han Wang, Jie Luo and Tianhe Wang

Received: 2 April 2022
Accepted: 6 May 2022
Published: 9 May 2022

Publisher's Note: MDPI stays neutral with regard to jurisdictional claims in published maps and institutional affiliations.

Copyright: © 2022 by the authors. Licensee MDPI, Basel, Switzerland. This article is an open access article distributed under the terms and conditions of the Creative Commons Attribution (CC BY) license (https://creativecommons.org/licenses/by/4.0/).

1. Introduction

Space−borne synthetic aperture radar (SAR) is an ideal approach in earth observation, which has risen in recent years, both in military and civil applications, due to its advantages of capability with all−time and all−weather. To receive more detailed information in SAR images, the requirement of the resolution becomes higher. Currently, many advanced orbiting space−borne SARs such as TerraSAR−X [1–3], Cosmo−SkyMed [4,5], and GaoFen−3 are capable of reaching the 1 m resolution, and the TerraSAR NEXT GENERATION (TerraSAR NG) [6] plans to enhance this ability to 0.25 m.

In the traditional space−borne SAR system, many classic imaging algorithms possess great ability with the simple air−borne imaging geometry assumptions like the range Doppler algorithm (RDA) [7] and the chirp scaling algorithm (CSA) [8]. The hyperbolic range equation model (HREM) [9] or equivalent squint range model (ESRM) [10] applied in RDA and CSA only require the Doppler centroid and Doppler rate, which supposes the satellite trajectory as a straight line during the integration time. Meanwhile, these methods regard the three− and higher−terms of the signal spectrum as the phase error and ignore them. Conversely, the wavenumber domain algorithm (ωkA) [11] is a classic

high−resolution imaging processor. There is no range cell migration (RCM) approximation in ωkA, and the Stolt interpolation is used to finish the range cell migration correction (RCMC). However, along with the increasing resolution, the apparent curve of the satellite trajectory appears in the long duration time, the high−order phase terms are no longer negligible, and the Stolt interpolation will be highly cumbersome in the immense volume of data. Furthermore, back−projection algorithm (BPA) [12] is another accurate image processor applied in the time domain; it utilizes every radar pulse back−projected in every pixel in the imaging scene to acquire the SAR image exactly. However, the classic BPA requires $N \times N \times N$ times back−projection operations, while N is the number of the azimuth pulses (suppose the azimuth samples are equal to the range samples). This is a large burden for the computers. Many researchers have optimized it and proposed relatively efficient methods such as the fast factorized back−projection algorithm (FFBPA) [13] and the modified FFBPA [14,15], but they still have a considerable amount of calculation.

Under the requirements of processing efficiency and accuracy, many scholars have focused their research on the improvement of the frequency domain imaging algorithm. A four−order processing algorithm was proposed by Eldhuset [16–18] in 1998, which established an extended exact transfer function by the four−order range model in the space−borne SAR geometry. It assumes the RCM does not vary in the one data block so that the RCMC and the range compression are completed together in the 2−D frequency domain and achieve the targets well−focusing with the resolution around 1 m after the azimuth compression. To obtain further results, in 2013, Wang [19] applied this Eldhuset's range model in the modified chirp scaling algorithm. The new four−order 2−D spectrum is derived and improves the imaging algorithm to a large extent, which finally achieved results under 0.3 m. This is a tremendous improvement from the conventional CSA, but its performance is still limited because the spectrum term more than five−order is neglected. Luo [20] proposed an extended range Doppler domain algorithm in 2013. A sinc interpolation is applied in this method to remove the differential RCM and uses the range segmenting to strengthen the focus depth by eliminating the residual cross−coupling phase increased with the slant range displacement. This algorithm has a large image width (above 10 km) in range direction and reaches the resolution around 0.3 m. A year later, another advanced imaging algorithm evolved from the hybrid correlation algorithm was proposed by Wang [21]. A modified ESRM is proposed in this paper by adding an equivalent radar acceleration, and the hybrid correlation factor is constructed through it. It starts with the coarse focusing by the azimuth reference function multiplication to remove the bulk RCM, and the differential RCM is then corrected through the hybrid correlation processing in the refined focusing. A higher resolution is obtained in this method, which is near 0.25 m.

It is obvious that a significant improvement is made in the modified CSA [19], but its performance is limited along the azimuth resolution increasing due to the insufficient 2−D spectrum. The last two methods make a breakthrough at the resolution, but they all avoid the 2−D spectrum calculation and apply their kernels in the range time domain most of the time. However, the accurate 2−D spectrum is necessary to research the ultra−high−resolution space−borne SAR. It contains much important information about the echo properties. This paper proposes an accurate high−order 2−D spectrum brought by the Lagrange inversion formula to meet the above requirements. The ordinary HREM or ESRM is replaced by an infinite polynomial range model, while coefficients can be computed by the satellite and target's relative motion vectors, or obtained from other high−precision range models through the Taylor series directly. After this, the principle of stationary phase (POSP) [22] is applied to both the range and azimuth directions, and the Lagrange inversion, which is widely used in the complex spectrum calculation for SAR imaging [23,24], is employed to obtain the analytical expression of the spectrum.

Based on the aforementioned accurate 2−D spectrum, a novel ultra−high−resolution imaging algorithm is presented as follows. The range high−order term is derived by the Taylor series on the proposed spectrum, directly and completely compensated. Moreover, drawing lessons from the principle of chirp scaling [8], the RCM caused by the relative mo-

tion between the satellite and the targets is accomplished by complex multiplication in the RD domain. Furthermore, to get enough focus depth, the range chirp rate's space variance, which will render the range defocused, is non−negligible in this case. A non−linear FM filter method proposed by Davidson [25] is a common approach to compensate the residual phase raised by the squint angle in the quadratic range compression (SRC). It was validated through the simulation based on Seasat and ERS−1 and achieves the well−focusing with squint angle of up to 35 deg for L−band and 50 deg for C−band. Moreover, the article mentions a limitation: the reference Doppler frequency must be selected outside of the Doppler bandwidth, which will introduce the extra phase error. Another efficient method proposed by Wong [26] in 2008 is applied in this paper. The range chirp rate is assumed to vary linearly, so the cubic phase function can equalize the dominant quadratic phase term of each target, which is like the chirp scaling principle. Nevertheless, there is still a problem that needs to be handled. The residual linear phase introduced above would cause the chirp phase center to shift in range direction with the Doppler frequency and be reflected as the quadratic RCM after the range compression due to the corresponding square of range difference. This quadratic RCM is usually neglected because of the slight variation of chirp rate for low resolution. In contrast, it must be corrected for our research case, so the interpolation is applied to fulfill the correction and finish the range processing. Finally, the well−focused targets can be obtained after the azimuth processing.

This paper is organized as follows: The Infinite polynomial range model and the accurate high−order signal spectrum are introduced in Section 2. In Section 3, the proposed imaging algorithm for the ultra−high space−borne SAR is described in detail. In addition, an analysis of the proposed algorithm's performance and an integrated simulation is presented in Section 4. Finally, conclusions are drawn in Section 5.

2. Infinite Polynomial Range Model and Signal Spectrum

Eldhuset gives a four−order range model to describe the SAR range history in [16], but it only corresponds to the first four−order relative motion parameters between the satellite and the targets. To describe the exact range history of the long illumination time, a general infinite polynomial is presented in this paper. The range history vector $\vec{R}(\eta)$ [16] can be expressed through the Taylor expansion in azimuth time η as

$$\vec{R}(\eta) = \sum_{i=0}^{\infty} \frac{1}{i!} \vec{X}_i \eta^i \tag{1}$$

while $\vec{X}_i$ is the ith−order relative motion parameters. Modulo both sides of Equation (1) and processed through the binomial theorem, the scalar value of the range history can be acquired in Equation (2).

$$R(\eta) = \sqrt{\left|\vec{R}(\eta)\right|^2} = \sqrt{\left(\sum_{i=0}^{\infty} \frac{1}{i!} \vec{X}_i \eta^i\right) \cdot \left(\sum_{i=0}^{\infty} \frac{1}{i!} \vec{X}_i \eta^i\right)} = \sqrt{\sum_{i=0}^{\infty} Y_i \eta^i} \tag{2}$$

while

$$\begin{cases} Y_0 = \vec{X}_0 \cdot \vec{X}_0 \\ Y_1 = 2\vec{X}_0 \cdot \vec{X}_1 \\ Y_2 = \vec{X}_1 \cdot \vec{X}_1 + \vec{X}_0 \cdot \vec{X}_2 \\ Y_3 = \frac{1}{3}\vec{X}_0 \cdot \vec{X}_3 + \vec{X}_1 \cdot \vec{X}_2 \\ Y_4 = \frac{1}{4}\vec{X}_2 \cdot \vec{X}_2 + \frac{1}{12}\vec{X}_0 \cdot \vec{X}_4 + \frac{1}{3}\vec{X}_1 \cdot \vec{X}_3 \\ Y_i = \sum\limits_{n=0}^{i} \left(\frac{1}{n!}\vec{X}_n \frac{1}{(i-n)!}\vec{X}_{i-n}\right) \end{cases} \tag{3}$$

Expanding Equation (2) by the Taylor series, the no error polynomial range model is given as

$$R(\eta) = \sum_{i=0}^{\infty} R_i \eta^i, \text{ where } R_i = \frac{R^{(i)}(0)}{i!} \tag{4}$$

while R_i represents the ith−order range model coefficient.

The space−borne SAR received echo from a point target, after demodulated to the baseband, can be derived as

$$s(\tau, \eta) = \sigma_0 \omega_r \left(\tau - \frac{2R(\eta)}{c} \right) \omega_a(\eta - \eta_c) exp\left\{ -j\frac{4\pi f_0 R(\eta)}{c} \right\} exp\left\{ j\pi K_r \left(\tau - \frac{2R(\eta)}{c} \right)^2 \right\} \tag{5}$$

where the σ_0 represents the target's back scattering coefficient; $\omega_r(\cdot)$ and $\omega_a(\cdot)$ denote the antenna pattern functions on the range and azimuth directions, respectively; c is the velocity of light; η_c is the Doppler central time; f_0 is the signal carrier frequency; K_r is the range chirp rate; τ is the range time.

To acquire the 2−D spectrum of the echo, the POSP is applied. It is easy to achieve this operation on the range direction and obtain the signal in the range−frequency (RD) domain as

$$S(f_\tau, \eta) = \sigma_0 \omega_r(f_\tau) \omega_a(\eta - \eta_c) exp\left\{ -j\frac{4\pi(f_0 + f_\tau)R(\eta)}{c} \right\} exp\left\{ -j\frac{\pi f_\tau^2}{K_r} \right\} \tag{6}$$

where the f_τ is the range frequency. However, in the azimuth direction, the stationary phase point cannot work out through differentiating η on the integrand phase Equation (7) directly, so we must find other ways to solve this problem.

$$\theta(\eta) = -\frac{4\pi(f_0 + f_\tau)R(\eta)}{c} - 2\pi f_\eta \eta = -\frac{4\pi(f_0 + f_\tau)}{c} \sum_{i=0}^{\infty} R_i \eta^i - 2\pi f_\eta \eta \tag{7}$$

According to the time−frequency properties of the Fourier transform, the linear term multiplied in the time domain is equivalent to a frequency shift. Therefore, we can extract the linear term in Equation (3) and acquire the new form of the signal as

$$S(f_\tau, \eta) = S'(f_\tau, \eta) exp\left\{ -j\frac{4\pi(f_0 + f_\tau)R_1 \eta}{c} \right\} \tag{8}$$

while

$$S'(f_\tau, \eta) = \sigma_0 \omega_r(f_\tau) \omega_a(\eta - \eta_c) exp\left\{ -j\frac{4\pi(f_0 + f_\tau)}{c} \sum_{\substack{i=0 \\ i \neq 1}}^{\infty} R_i \eta^i \right\} exp\left\{ -j\frac{\pi f_\tau^2}{K_r} \right\} \tag{9}$$

The new integrand phase of Equation (9) can be expressed as Equation (10), and the stationary phase point can be derived from its differential.

$$\theta(\eta) = -\frac{4\pi(f_0 + f_\tau)}{c} \sum_{\substack{i=0 \\ i \neq 1}}^{\infty} R_i \eta^i - 2\pi f_\eta \eta \tag{10}$$

$$\frac{d\theta(\eta)}{d\eta} = -\frac{4\pi(f_0 + f_\tau)}{c} \frac{d}{d\eta} \sum_{\substack{i=0 \\ i \neq 1}}^{\infty} R_i \eta^i - 2\pi f_\eta = -\frac{4\pi(f_0 + f_\tau)}{c} \sum_{i=2}^{\infty} i R_i \eta^{i-1} - 2\pi f_\eta = 0 \tag{11}$$

To make the followed steps more intuitive, variable P is used to simplify the differential equation as

$$P = \sum_{i=2}^{\infty} iR_i \eta^{i-1} \tag{12}$$

while

$$P = -\frac{cf_\eta}{2(f_0 + f_\tau)} \tag{13}$$

Obviously, Equation (12) is an infinite series without any constant term. Therefore, we can use the Lagrange inversion [27] to obtain its inverse function as another infinite series by

$$\eta = \sum_{i=2}^{\infty} C_i P^{i-1} \tag{14}$$

while

$$\begin{cases} C_2 = \frac{1}{2R_2} \\ C_3 = -\frac{3R_3}{8R_2^3} \\ C_4 = \frac{9R_3^2 - 4R_2R_4}{16R_2^5} \\ C_5 = \frac{-20R_5R_2^2 + 120R_4R_2R_3 - 135R_3^3}{128R_2^7} \\ C_6 = \frac{-24R_6R_2^3 + \left(96R_4^2 + 180R_3R_5\right)R_2^2 - 756R_3^2R_4R_2 + 567R_3^4}{256R_2^9} \\ \cdots \end{cases} \tag{15}$$

So that the 2−D spectrum of $S'(f_\tau, \eta)$ can be achieved by introducing Equation (14) to Equation (10), and the result is given as

$$S'(f_\tau, f_\eta) = \sigma_0 \omega_r(f_\tau) \omega_a \left(f_\eta - f_{\eta_c} - \frac{2(f_0 + f_\tau)R_1}{c} \right) exp\{ j\Phi'(f_\tau, f_\eta) \} \tag{16}$$

$$\begin{aligned} \Phi'(f_\tau, f_\eta) = &-\tfrac{4\pi(f_0+f_\tau)}{c} \sum_{i=2}^{+\infty} \tfrac{i-1}{i} C_i \left[P(f_\eta) \right]^i \\ &-2\pi f_\eta \textstyle\sum_{i=2}^{+\infty} C_i \left[P(f_\eta) \right]^{i-1} - \tfrac{\pi f_\tau^2}{K_r} - \tfrac{4\pi(f_0+f_\tau)R_0}{c} \end{aligned} \tag{17}$$

Finally, the linear term $R_1\eta$ is added as a frequency bias into the Equation (16) and the precise high−order 2−D spectrum of $s(\tau, \eta)$ is elaborated as

$$S(f_\tau, f_\eta) = \sigma_0 \omega_r(f_\tau) \omega_a (f_\eta - f_{\eta_c}) exp\{ j\Phi(f_\tau, f_\eta) \} \tag{18}$$

while

$$\begin{aligned} \Phi(f_\tau, f_\eta) &= \Phi'\left(f_\tau, f_\eta + \tfrac{2\pi(f_0+f_\tau)R_1}{c} \right) \\ &= -\tfrac{4\pi(f_0+f_\tau)}{c} \sum_{i=2}^{+\infty} \tfrac{i-1}{i} C_i \left[P\left(f_\eta + \tfrac{2\pi(f_0+f_\tau)R_1}{c} \right) \right]^i \\ &-2\pi \left(f_\eta + \tfrac{2\pi(f_0+f_\tau)R_1}{c} \right) \sum_{i=2}^{+\infty} C_i \left[P\left(f_\eta + \tfrac{2\pi(f_0+f_\tau)R_1}{c} \right) \right]^{i-1} \\ &-\tfrac{\pi f_\tau^2}{K_r} - \tfrac{4\pi(f_0+f_\tau)R_0}{c} \end{aligned} \tag{19}$$

3. Imaging Algorithm

Based on the high−order 2−D spectrum proposed above, a novel ultra−high−resolution imaging algorithm for space−borne SAR is presented in this section. The sever azimuth aliasing caused by the spotlight or sliding spotlight mode is eliminated by the two−step processing method [28,29]. Then, a range high−order phase filter and a linear RCMC filter are applied to fulfill the range preprocessing. Further, a cubic phase function is introduced to eliminate the space−variance of the range chirp rate, and a quadratic RCMC filter (after the range SRC) is employed to correct the new RCM generated by the chirp rate

equalization. Finally, the azimuth compression filter is applied to focus the targets, and the azimuth scaling is adopted to avoid the azimuth time domain aliasing caused by the deramp operation. Figure 1 gives the block diagram of the proposed imaging algorithm, and all these parts mentioned above are illustrated in the following:

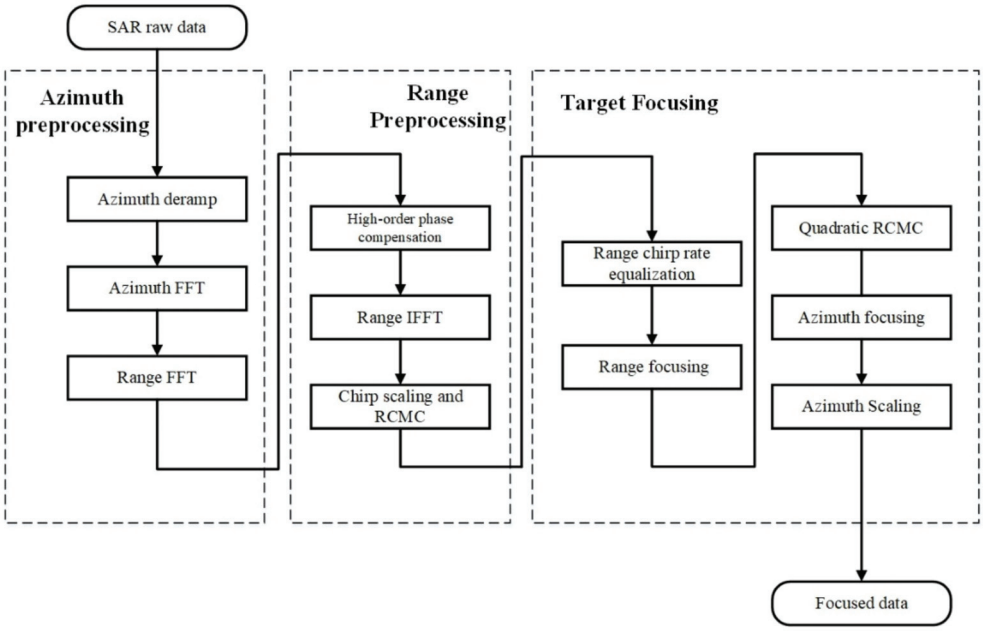


Figure 1. Detailed implementation of the proposed algorithm.

3.1. Azimuth Preprocessing

The total Doppler bandwidth of an ultra−high−resolution space−borne SAR echo is always far larger than the pulse repetition frequency (PRF), which is limited by the range ambiguity and data volume. Therefore, the signal spectrum suffered from the severe aliasing at the azimuth direction. The time−frequency diagram of the sliding spotlight, which is widely developed in many advanced SAR systems and applied in our simulations, is elaborated in Figure 2. The azimuth bandwidth of the whole scene B_{total} is composed of B_{steer} and B_{3dB}, while B_{steer} is rendered by the azimuth antenna steering and B_{3dB} is the antenna beam 3 dB bandwidth. B_T is the single point target's azimuth bandwidth and T_B is the azimuth integration time. As shown in Figure 2, the aliasing is inevitable and must be removed for post−processing.

The two−step processing method is an efficient method and is employed in our algorithm. It utilizes a reference LFM signal with an opposite Doppler chirp rate convoluted with the received signal in the azimuth direction. B_{steer} is removed through this operation and the processed signal can be expressed as Equation (20)

$$s'(\tau,\eta) = s(\tau,\eta) * exp\left\{-j\pi K_{r_rot}\eta^2\right\} \tag{20}$$

while K_{r_rot} is the azimuth chirp rate introduced by the antenna steering and $*$ is the convolution operator. The sketches of the spectrum, whether processed by this method or not, are elaborated in Figure 3, which demonstrate the azimuth wrapping is eliminated clearly in Figure 3b.

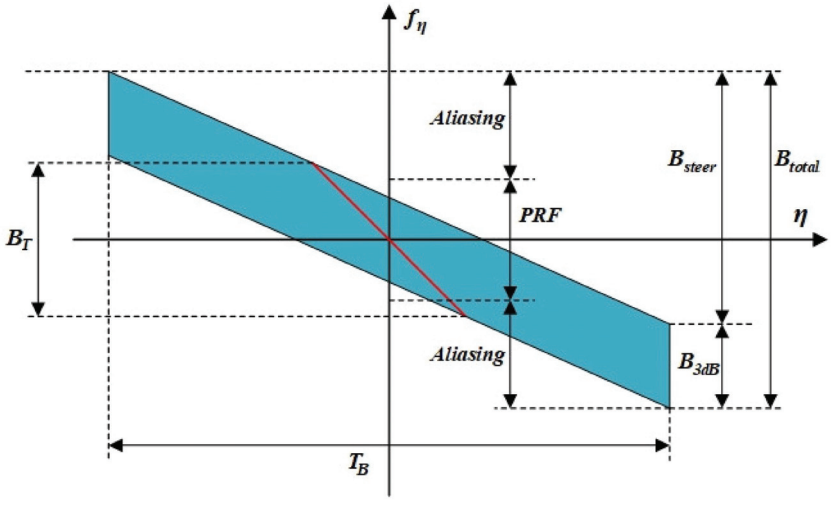


Figure 2. Time−frequency diagram of the sliding spotlight SAR.

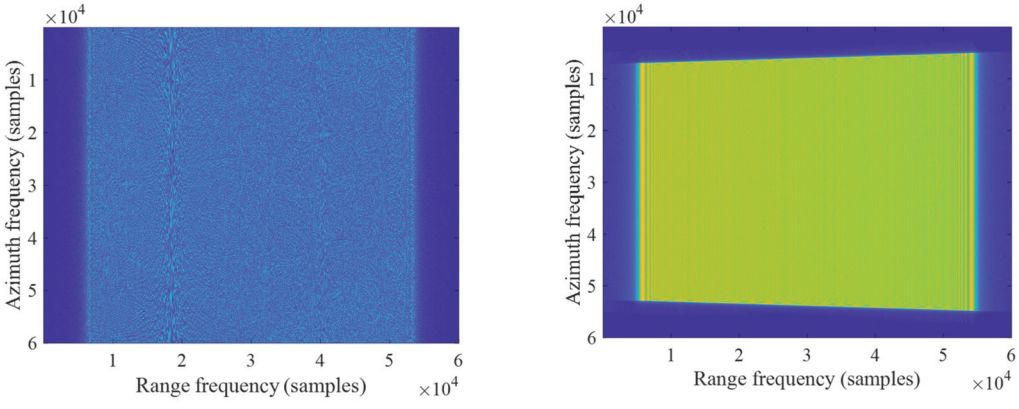


Figure 3. The 2−D spectrum of the echo whether the two−step processing is applied. (**a**) The original spectrum. (**b**) the unwrapped spectrum.

In addition, the convolution operation requires many computing resources. To simplify the calculation, it can be divided into three parts [30]: the two complex multiplications and one Fast Fourier Transform (FFT) as Equation (21)

$$s_{deramp}(\tau,\eta_1) = exp\left\{-j\pi\frac{\eta_1}{K_{r_rot}}\right\} \times IFFT\left[s(\tau,\eta)exp\left(-j\pi K_{r_ref}\eta^2\right)\right] \tag{21}$$

while $\eta_1 = K_{r_rot}\eta$, and the PRF is increased equivalently as

$$PRF_{new} = \frac{N_a K_{r_rot}}{PRF} \tag{22}$$

while N_a is the azimuth sampling number. The unwrapped 2−D dimension signal spectrum can be obtained based on the time−frequency properties of the Fourier transform as Equations (23) and (24).

$$S_{deramp}(f_\tau, f_\eta) = \sigma_0 \omega_r(f_\tau)\omega_a(f_\eta - f_{\eta_c}) exp\left\{ j\Phi_{deramp}(f_\tau, f_\eta) \right\} \tag{23}$$

$$\begin{aligned} \Phi_{deramp}(f_\tau, f_\eta) = & -\frac{4\pi(f_0+f_\tau)}{c} \sum_{i=2}^{+\infty} \frac{i-1}{i} C_i \left[P\left(f_\eta + \frac{2\pi(f_0+f_\tau)R_1}{c} \right) \right]^i \\ & -2\pi\left(f_\eta + \frac{2\pi(f_0+f_\tau)R_1}{c} \right) \sum_{i=2}^{+\infty} C_i \left[P\left(f_\eta + \frac{2\pi(f_0+f_\tau)R_1}{c} \right) \right]^{i-1} \\ & -\frac{\pi f_\tau^2}{K_r} - \frac{4\pi(f_0+f_\tau)R_0}{c} - \frac{\pi f_\eta^2}{K_{r_rot}} \end{aligned} \tag{24}$$

3.2. High−Order Phase Compensation

The phase mathematical expression of the 2−D spectrum is portrayed in Equation (24), which embodies significant range−azimuth coupling. To illustrate validly, the phase of spectrum can be decomposed by the Taylor series with f_τ and expressed as Equation (25).

$$\Phi_{deramp}(f_\tau, f_\eta) = \sum_{i=0}^{+\infty} D_i(f_\eta) f_\tau^i \tag{25}$$

while $D_0(f_\eta)$ is the term of azimuth Doppler frequency modulation, which is recognized as the LFM term in most instances. $D_1(f_\eta)$ includes the information of the RCM for each target, and $D_2(f_\eta)$ corresponds to the range modulation. Their approximate expression is given in Appendix A, and the remaining higher order terms donate the high−order range–azimuth coupling.

Many frequency algorithms are based on the first−three order of the spectrum and focus less on the others, such as the RDA and CSA. However, the negligence of the high−order term does not work for the high−resolution case. The range distortion caused by it is elaborated in Figure 4. [24] gives an analysis of phase error introduced by each order term of the resolution of 1 m, and concludes that the sixth order coupling phase term still requires considering. Through this, it is evident that the higher resolution required, the higher phase terms need to be considered.

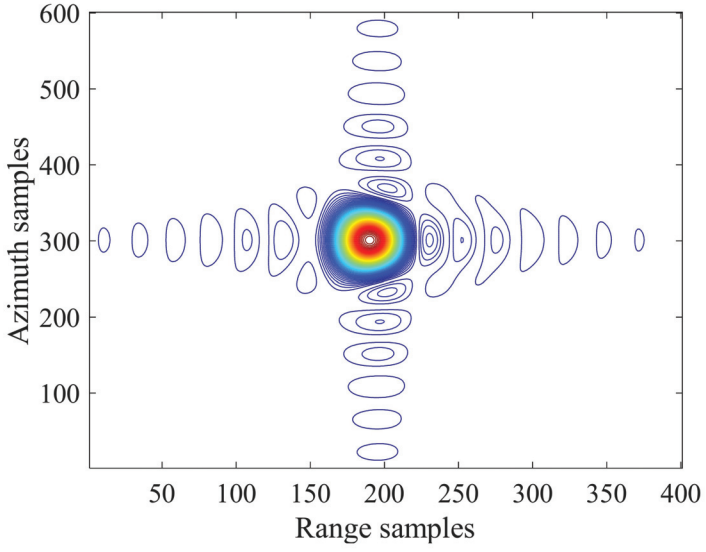


Figure 4. The range distortion caused by the high−order phase term.

To obtain the well−focused targets, the high−order phase term is compensated in this paper, which can be calculated by

$$\Phi_{high_order}(f_\tau, f_\eta) = \Phi_{deramp}(f_\tau, f_\eta) - \left(D_0(f_\eta) + D_1(f_\eta)f_\tau + D_2(f_\eta)f_\tau^2\right) \tag{26}$$

and the compensated 2−D spectrum can be achieved by

$$\begin{aligned} S_c(f_\tau, f_\eta) &= S_{deramp}(f_\tau, f_\eta) \times exp\left\{-j\Phi_{high_{order}}(f_\tau, f_\eta)\right\} \\ &= \sigma_0\omega_r(f_\tau)\omega_a(f_\eta - f_{\eta_c})exp\{j(D_0(f_\eta) + D_1(f_\eta)f_\tau + D_2(f_\eta)f_\tau^2)\} \end{aligned} \tag{27}$$

Transforming the signal to the range time domain by a range inverse fast Fourier transform (IFFT), at last, the compensated signal in the RD domain is achieved by

$$S_c(\tau, f_\eta) = \sigma_0\omega_r(\tau - E_2(f_\eta))\omega_a(f_\eta - f_{\eta_c})exp\{jE_0(f_\eta)\}exp\left\{-jE_1(f_\eta)(\tau - E_2(f_\eta))^2\right\} \tag{28}$$

while

$$\begin{cases} E_0(f_\eta) = D_0(f_\eta) \\ E_1(f_\eta) = \frac{\pi^2}{D_2(f_\eta)} \\ E_2(f_\eta) = -\frac{D_1(f_\eta)}{2\pi} \end{cases} \tag{29}$$

3.3. Linear RCMC

As the principle of chirp scaling, the chirp signal can adjust the phase center by multiplying itself with another chirp signal. By these means, the different RCM produced by each target, which is located in different range gates, can be adjusted to the same, and this is named differential RCMC in many papers.

For the expression, according to the Equations (28) and (29), the range chirp rate $br(f_\eta)$ and range cell migration(RCM) $R_{rd}(f_\eta)$ in the RD domain can be derived as

$$br(f_\eta) = \frac{E_1(f_\eta)}{\pi} \tag{30}$$

$$R_{rd}(f_\eta) = \frac{cE_2(f_\eta)}{2} \tag{31}$$

Therefore, the chirp scaling factor is

$$\Phi_{cs}(\tau, f_\eta) = exp\left\{-j\pi br\left(f_\eta, R_{ref}\right)Cs(f_\eta)\left(\tau - \tau_{ref}(f_\eta)\right)^2\right\} \tag{32}$$

where

$$Cs(f_\eta) = \frac{R\left(f_\eta, R_{ref}\right)}{R_0} - 1 = \frac{cE_2\left(f_\eta, R_{ref}\right)}{2R_{ref}} - 1 \tag{33}$$

$$\tau_{ref}(f_\eta) = \frac{2R_{rd}\left(f_\eta, R_{ref}\right)}{c} \tag{34}$$

R_{ref} represented the referenced slant range of the referenced range gate. The differential RCMC is achieved by multiplying $\Phi_{cs}(\tau, f_\eta)$ with $S_c(\tau, f_\eta)$ in the RD domain.

$$\begin{aligned} S_{cs}(\tau, f_\eta) &= S_c(\tau, f_\eta) \times exp\{j\Phi_{cs}(\tau, f_\eta)\} \\ &= \sigma_0\omega_r(\tau - E_2(f_\eta))\omega_a(f_\eta - f_{\eta_c})exp\{jE_0(f_\eta)\} \\ &\times exp\left\{-j\pi br(f_\eta)\left[1 + Cs(f_\eta)\right]\left[\tau - \frac{E_2(f_\eta) + Cs(f_\eta)\tau_{ref}(f_\eta)}{1 + Cs(f_\eta)}\right]^2\right\} \\ &\times exp\left\{j\pi br(f_\eta)\left[\frac{\left(E_2(f_\eta) + Cs(f_\eta)\tau_{ref}(f_\eta)\right)^2}{1 + Cs(f_\eta)} - E_2^2(f_\eta) - Cs(f_\eta)\tau_{ref}^2(f_\eta)\right]\right\} \end{aligned} \tag{35}$$

After the chirp scaling operation is finished, the remaining RCMC can be achieved together by the RCM of the referenced range gate and is always realized by a complex multiplication in the 2−D frequency domain. According to the time−frequency properties of the Fourier transform, the remaining RCMC filter in the 2−D frequency domain can be expressed as Equation(36)

$$H_{rcmc}(f_\tau, f_\eta) = exp\left\{ j\frac{4\pi f_\tau R_{ref} Cs(f_\eta)}{c} \right\} \tag{36}$$

and the signal in RD domain after finished the linear RCMC is

$$\begin{aligned} S_{rcmc}(\tau, f_\eta) &= IFFT\left[FFT\left[S_{cs}(\tau, f_\eta), \tau\right] \times H_{rcmc}(f_\tau, f_\eta), f_\tau\right] \\ &= \sigma_0 \omega_r \left(\tau - \tfrac{2R}{c}\right) \omega_a (f_\eta - f_{\eta_c}) \\ &\times exp\left\{ -j\pi br(f_\eta)\left[1 + Cs(f_\eta)\right]\left[\tau - \tfrac{2R}{c}\right]^2 \right\} \\ &\times exp\{jE_0(f_\eta)\} exp\left\{ j\pi br(f_\eta)\left[\frac{\left(E_2(f_\eta) + Cs(f_\eta)\tau_{ref}(f_\eta)\right)^2}{1 + Cs(f_\eta)} - E_2^2(f_\eta) - Cs(f_\eta)\tau_{ref}^2(f_\eta) \right] \right\} \end{aligned} \tag{37}$$

while the R is the referenced slant range for each range gate.

3.4. Chirp Rate Equalization and Quadratic RCMC

The chirp rate is space−variant in the RD domain. This variance is always regarded as a system error for the traditional imaging algorithm and neglected because of the low resolution. However, for the ultra−high−resolution case, this is sufficient to lead the targets at the edge to defocus seriously. Based on the first exponential term in Equation (37), the range chirp rate in the RD domain can be expressed as $K_r(f_\eta, R)$

$$K_r(f_\eta, R) = br(f_\eta, R)\left[1 + Cs(f_\eta)\right] \tag{38}$$

while it is assumed to vary linearly with R in this paper like Equation (39)

$$K_r(f_\eta, R) = K_r\left(f_\eta, R_{ref}\right) + A(f_\eta)\left(R - R_{ref}\right) \tag{39}$$

and $A(f_\eta)$ is the rate of the $K_r(f_\eta, R)$. So, this quadratic exponential term can be re−expressed as

$$\begin{aligned} &exp\left\{ -j\pi K_r(f_\eta, R)\left[\tau - \tfrac{2R}{c}\right]^2 \right\} \\ &= exp\left\{ -j\pi\left[K_r\left(f_\eta, R_{ref}\right) + A(f_\eta)\left(R - R_{ref}\right)\right]\left[\tau - \tfrac{2R}{c}\right]^2 \right\} \end{aligned} \tag{40}$$

Based on [26], it is feasible to apply a cubic phase perturbation factor, given in Equation (41), to equalize the chirp rate, like the chirp scaling principle

$$H_{ec}(f_\eta) = exp\left\{ -j\pi\frac{A(f_\eta)}{3}\left[\tau - \frac{2R_{ref}}{c}\right]^3 \right\} \tag{41}$$

the quadratic term after multiplied with Equation (41) becomes Equation (42).

$$\begin{aligned} & exp\left\{-j\pi K_r\left(f_\eta, R\right)\left[\tau-\tfrac{2R}{c}\right]^2\right\} \times H_{ec}\left(f_\eta\right) \\ = & exp\left\{-j\pi \tfrac{A\left(f_\eta\right)}{3}\left(\tau-\tfrac{2R}{c}\right)^3\right\} \\ \times & exp\left\{-j\pi K_r\left(f_\eta, R_{ref}\right)\left[\tau-\tfrac{2R}{c}\right]^2\right\} \\ \times & exp\left\{-j\pi A\left(f_\eta\right)\left(\tfrac{2R}{c}-\tfrac{2R_{ref}}{c}\right)^2\left(\tau-\tfrac{2R}{c}\right)\right\} \\ \times & exp\left\{-j\pi \tfrac{A\left(f_\eta\right)}{3}\left(\tfrac{2R}{c}-\tfrac{2R_{ref}}{c}\right)^3\right\} \end{aligned} \tag{42}$$

The chirp rate for each target located at each range gate is equalized to the reference chirp rate in Equation (42), and it can be well−compressed with a match filter Equation (43) in the RD domain accurately. The first exponential term is the cubic phase term, which can be compensated in the RD domain by the POSP, and the last exponential term is constant.

$$H_{rc}\left(f_\tau, f_\eta\right) = exp\left\{-j\pi \frac{f_\tau^2}{K_r\left(f_\eta, R_{ref}\right)}\right\} \tag{43}$$

The most difficult is the remaining linear term. It will cause the phase center shift in the range time domain and bandwidth shift in the frequency domain. Moreover, a false target will be produced if the bandwidth shifts too much. To explain this phenomenon straightforwardly, Figure 5 shows the false target caused by the spectrum wrapping. The bandwidth of the original spectrum is included in $[-F_s/2 : F_s/2]$, so its compressed result is well−focused and located at the phase center of the chirp signal. However, if the bandwidth shifts out of the sampling frequency, as illustrated in Figure 5a, the energy leakage will occur, and the false target will emerge, as shown in Figure 5b. Therefore, the sampling frequency must be large enough to ensure the bandwidth does not alias after the shift.

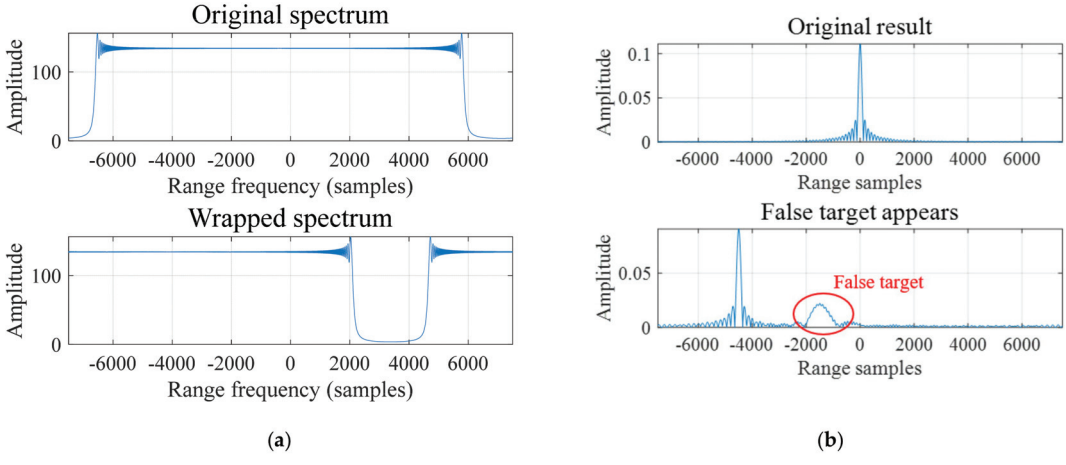


Figure 5. (**a**) The original spectrum and the wrapped spectrum due to the linear term. (**b**) The original focused result and the false target formed by wrapping.

Nevertheless, phase center shifting is inevitable in the range time domain. Figure 6a gives a plot of a real part from a chirp signal, adjusted to the chirp rate by the aforementioned cubic phase perturbation factor. The phase center of the original signal is located at the center of the plot. However, it shifted to the left after applying the chirp rate equal-

ization, displayed in Figure 6a below. Their compressed results, focused on the reference chirp rate, are displayed in Figure 6b. The defocusing emerges on the original signal due to the mismatch of the match filter, and the equalized signal reflects the well−focusing. The peaks of each pulse appear in the phase center so that there is a deviation of location between them. When this bias varies along with the azimuth frequency, it manifests as the RCM introduced artificially. Furthermore, due to the shifts corresponding to the square of the range difference, which embodies the third exponential of Equation (40), the newly generated RCM is represented as quadratic and toward the same direction as illustrated in Figure 7.

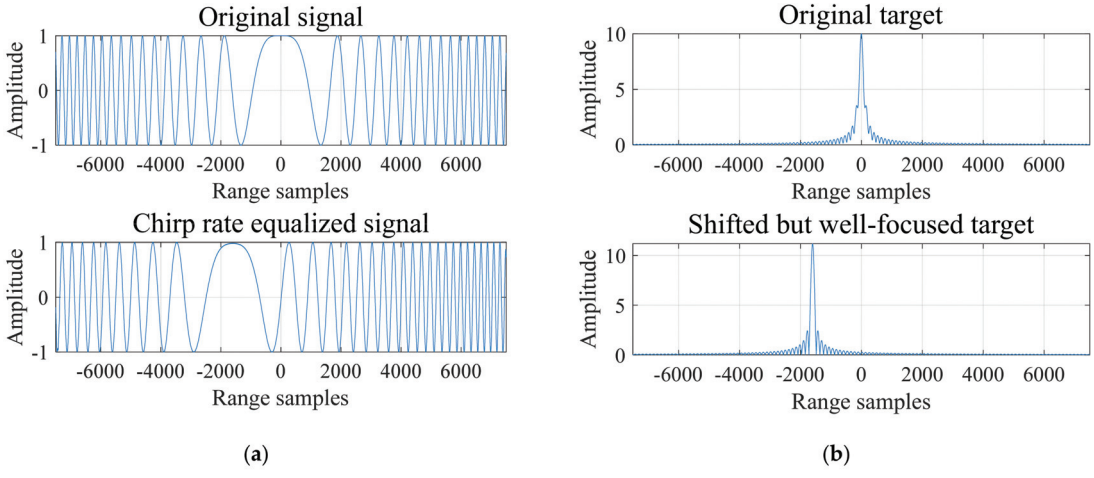


Figure 6. (**a**) The real part of the chirp signal before and after the chirp rate equalization. (**b**) the range compression result focused by the reference chirp rate before and after the chirp rate equalization.

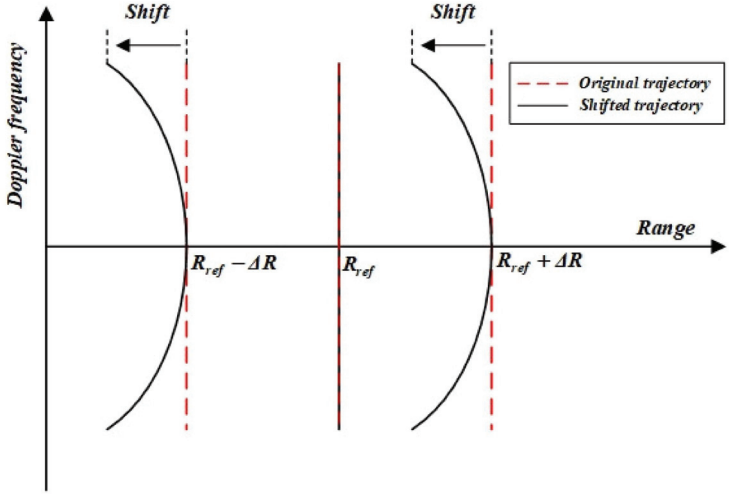


Figure 7. The diagram of quadratic RCM.

The principle of chirp scaling is no longer applicable for the correction because the quadratic RCM is introduced by itself. To accomplish the RCMC, interpolation is employed in this paper. The shift of each range bin can be calculated in Equation (44) precisely without any high−order term. Therefore, the interpolation kernel is longer, and the RCMC by this

method is more accurate. At last, the expression of the signal after RCMC and residual phase compensation is given in Equation (45).

$$RCM_{quadratic}(f_\eta) = \frac{A(f_\eta)\left(\frac{2R}{c} - \frac{2R_{ref}}{c}\right)^2}{2K_r\left(f_\eta, R_{ref}\right)} \tag{44}$$

$$\begin{aligned} S_{rc}(\tau, f_\eta) = {} & \sigma_0 A_r\left(\tau - \tfrac{2R_{ref}}{c}\right)\omega_a(f_\eta - f_{\eta_c}) \\ & \times exp\{jE_0(f_\eta)\}exp\left\{j\pi br(f_\eta)\left[\tfrac{\left(E_2(f_\eta)+Cs(f_\eta)\tau_{ref}(f_\eta)\right)^2}{1+Cs(f_\eta)} - E_2^2(f_\eta) - Cs(f_\eta)\tau_{ref}^2(f_\eta)\right]\right\} \end{aligned} \tag{45}$$

while the $A_r(\cdot)$ is the range envelope after range compression and usually as a sinc function.

3.5. Azimuth Compression and Resampling

According to the Equation (45), the remaining phase includes two parts. The penultimate term is the azimuth modulation phase mentioned above. The last exponential term is introduced by the chirp scaling operation, both of which need to be compensated accurately. Therefore, the azimuth compression filter can be obtained through the conjugate of these parts.

$$H_{ac}(\tau, f_\eta) = exp\left\{-j\left[E_1(f_\eta)\left(\frac{\left(E_2(f_\eta) + Cs(f_\eta)\tau_{ref}(f_\eta)\right)^2}{1 + Cs(f_\eta)} - E_2^2(f_\eta) - Cs(f_\eta)\tau_{ref}^2(f_\eta)\right) + E_0(f_\eta)\right]\right\} \tag{46}$$

To eliminate the azimuth time domain aliasing caused by the deramp, the azimuth scaling option is necessary to achieve the azimuth resampling. The scaling function is given in Equation (47) as

$$H_{scaling}(f_\eta) = exp\left\{-j\pi\frac{H_f}{K_{r_rot}}f_\eta^2\right\} \tag{47}$$

while the H_f is the hybrid factor. After performing the azimuth IFFT, the residual phase is given in Equation (48), and the focused target can be expressed as Equation (49).

$$H_{residual}(\eta) = exp\left\{-j\pi\frac{K_{r_rot}}{H_f}\eta^2\right\} \tag{48}$$

$$\begin{aligned} S_{focused}(\tau, \eta) &= IFFT\left[IFFT\left[S_{rc}(\tau, f_\eta) \times H_{ac}(\tau, f_\eta) \times H_{scaling}(f_\eta), f_\eta\right] \times H_{residual}(\eta'), \eta'\right] \\ &= \sigma_0 A_r\left(\tau - \tfrac{2R_{ref}}{c}\right)A_a(\eta - \eta_c) \end{aligned} \tag{49}$$

while the $A_a(\cdot)$ is the azimuth envelope function.

4. Discussion and Simulation Results

The discussion and experiment results of simulation are presented in this section. To verify the proposed algorithm, the main simulation parameters are given in Table 1.

Table 1. Simulation Parameters.

Description	Value	Units
Orbit Parameters		
Semi−major	514	km
Eccentricity	0.0011	–
Inclination	98	deg
Longitude of ascend note	0	deg
Argument of perigee	90	deg
Radar Parameters		
Carrier frequency	9.6	GHz
Bandwidth	1.25	GHz
Sampling frequency	1.5	GHz
Look angle	30	deg
Antenna width	0.7	m
Antenna Length	6	m
Target Parameters of Scene Center		
Azimuth resolution	0.25	m
Hybrid factor	0.075	–
R_0 of scene center	593.42	km
f_d of scene center	4.969	Hz
f_r of scene center	5909.132	Hz/s
f_{r3} of scene center	0.019894	Hz/s^2
f_{r4} of scene center	2.765661	Hz/s^3

4.1. The Discussion of The Polynomial Range Model and High−Order 2−D Spectrum Analyses

The infinite range model is unachievable in engineering. Therefore, the truncation of it is necessary. There are two infinite series while the range model deduction. First is the range vector illustrated in Equation (1). Each order relative motion parameter vector is required in this expression. However, the higher−order term is non−essential because the illumination time is limited. Figure 8 shows the phase error calculated by the modulus of the low−order truncated range vector and the real range history, and the red line annotates the safe line under the azimuth phase error criterion of 0.25 π. As portrayed in Figure 8, the first four−order relative motion parameters can fit the real range history in 20 s. This is enough to meet the requirement of the ultra−high−resolution imaging for now, and for some time to come.

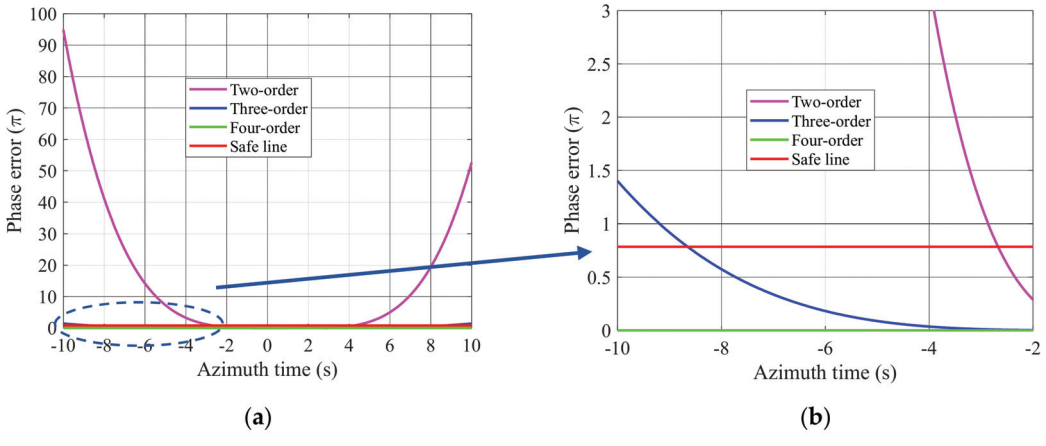


Figure 8. (**a**) The phase error introduced by the truncated range vector. (**b**) the detail view of the circled place.

The second infinite series is the scalar expression of the range model acquired by the Taylor expansion. Similarly, it is not necessary and impossible to apply all coefficients to obtain the no error range history. The first several order approximations will offer acceptable performance and reduce the calculation in engineering. Figure 9 portrays the approximation results based on the first−four order relative motion parameters in the same manner as above. Moreover, the only even−order truncated results are elaborated in the plot because the odd−order coefficients are calculated close to zero through the simulation parameters presented in Table 1. The six−order approximated range model is enough for the 20 s integration time, while the requirement of the ultra−high−resolution imaging is already achieved. However, the curve has an apparent upward trend after −6 s, so to satisfy the development of the SAR system in the future, the eight−order range model will be a better choice, and the remaining experiments are based upon it.

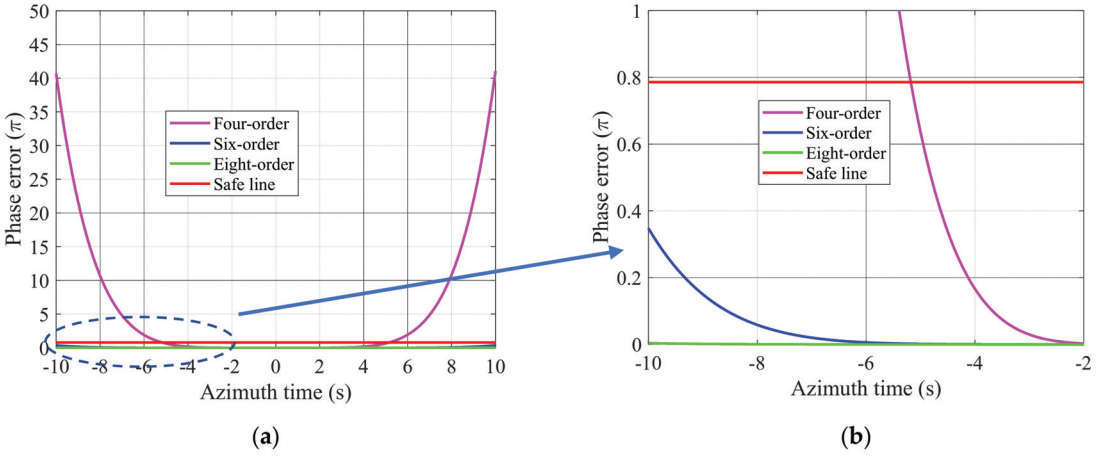
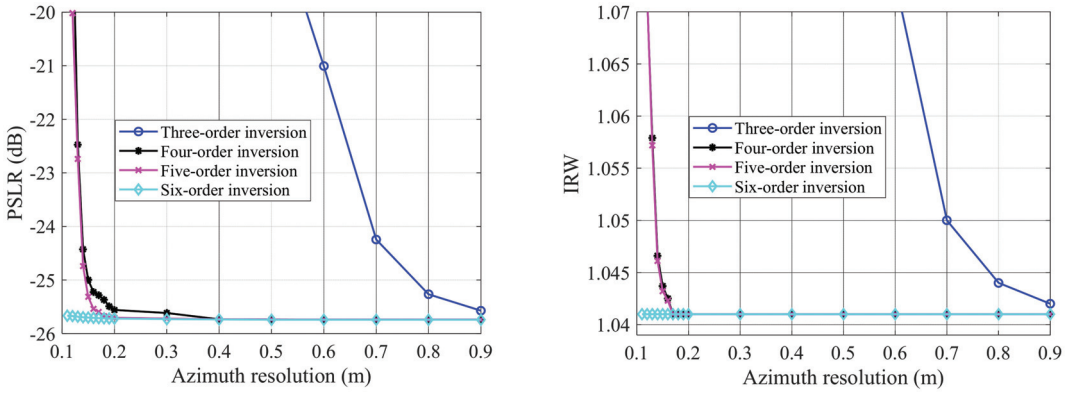


Figure 9. (**a**) The phase error introduced by the truncated range model. (**b**) the detail view of the circled place.

Furthermore, we aimed to verify the accuracy of the high−order 2−D spectrum generated by the Lagrange inversion. The peak sidelobe ratio (PSLR) and the normalized impulse response width (IRW) measured from the point targets, compressed by the calculated spectrum directly based on the different order truncated Lagrange inversion, are presented in Figure 10. Obviously, the three−order Lagrange inversion is far from reaching the requirement of ultra−high−resolution imaging. Serious defocusing has emerged since the 0.8 m of the azimuth resolution. In addition, the four− and five−order inversions exhibit the near−precision of the derived spectrum because the fifth−order coefficient is too small to affect the precision, which is almost the same as the sixth−order parameter in this experiment. Moreover, they are all invalid since the azimuth resolution is higher than 0.17 m, where the spectrum obtained by the six−order inversion still performs well. Similarly, the accuracy of the 2−D spectrum can be improved by increasing the order of the Lagrange inversion to approach the actual accuracy like the Taylor series, and the six−order inversion is employed in the next simulation experiment to calculate the 2−D spectrum.



(**a**) (**b**)

Figure 10. (**a**). PSLR of the compressed point targets. (**b**). IRW of the compressed point targets.

4.2. Image Quality Evaluation and Analysis

The simulated scene is shown in Figure 11, the nine point targets arranged evenly along with the range, and azimuth in 6 km and 2 km as illuminated in the sliding spotlight mode. The main simulation parameters are given in Table 1. To fit the engineering applications, all simulation results are weighted by the 1/3 simplified Taylor window both in range and azimuth, which can reduce the sidelobe level and avoid flooding the weak targets [31].

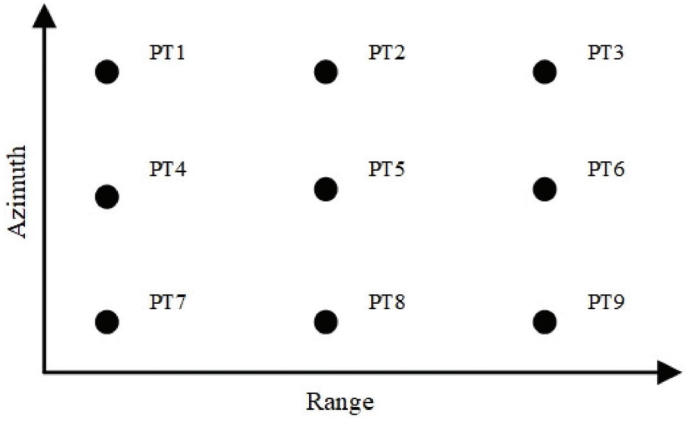


Figure 11. The ground scene of simulation.

Figure 12 illustrates the necessity of the range chirp rate equalization. The diagrams of the PT1, whether it eliminated the chirp rate space variance or not after the range compression in the RD domain, is given in Figures 12a and 12b respectively. As seen in Figure 12a, the mismatch of the match filter is reflected obviously, especially at the edge of the Doppler bandwidth. This leads the results to range defocusing finally. In contrast, Figure 12b shows the influence of the chirp rate equalization achieved by the cubic phase function. The mismatch is eliminated effectively through this method. Conversely, a tiny shift in the range direction corresponding to the Doppler frequency is caused and brings the azimuth distortion for each target in the end. To fulfill the quadratic RCMC, the interpolation is employed, and its result is presented in Figure 12c, in which it can be observed that every shift at each Doppler frequency is removed clearly, and the whole energy of a target is well−compressed.

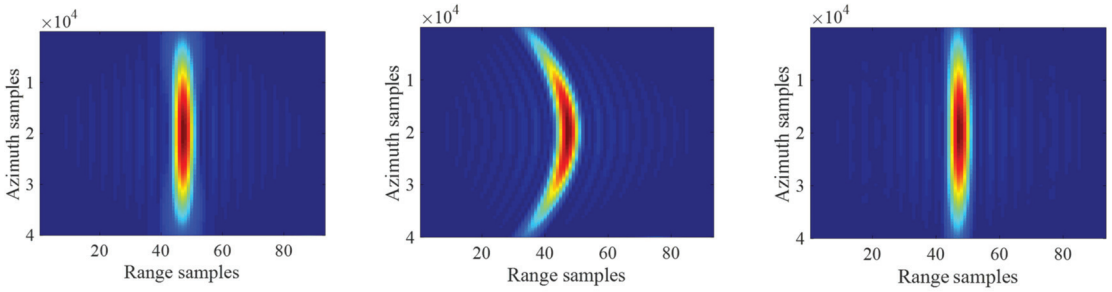


Figure 12. The sketch map of the range compression results. (**a**) Compressed signal with a mismatch chirp rate. (**b**) Only the chirp rate equalization is employed and the quadratic RCM appeared. (**c**) Corrected quadratic RCM by means of interpolation.

The interpolated slices of PT1, PT5, and PT9 focused by the proposed algorithm are displayed in Figure 13. In contrast, Figure 14 gives the same targets focused by the conventional CSA, and Figure 15 gives the results from the BPA. The range and azimuth profiles of the PT5 are presented in Figure 15.

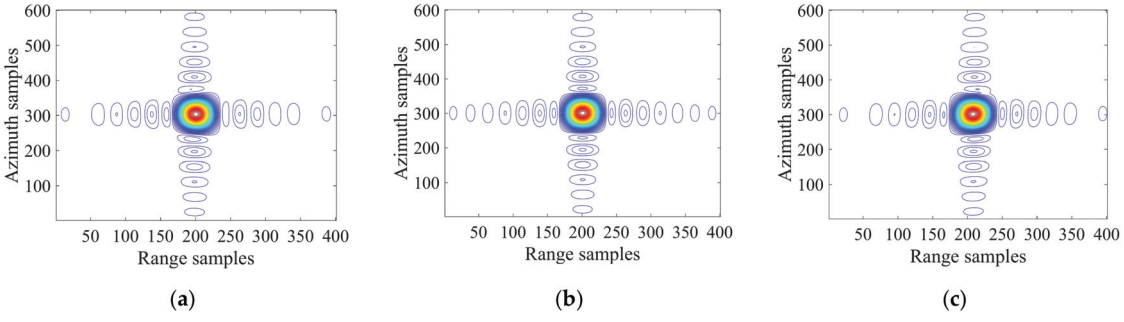


Figure 13. Interpolated results of (**a**) PT3, (**b**) PT5, (**c**) PT7 focused by the proposed algorithm.

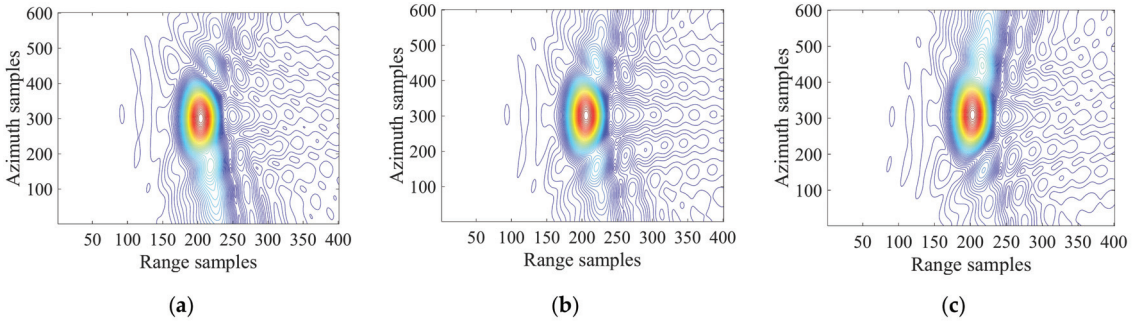


Figure 14. Interpolated results of (**a**) PT3, (**b**) PT5, (**c**) PT7 focused by the conventional CSA.

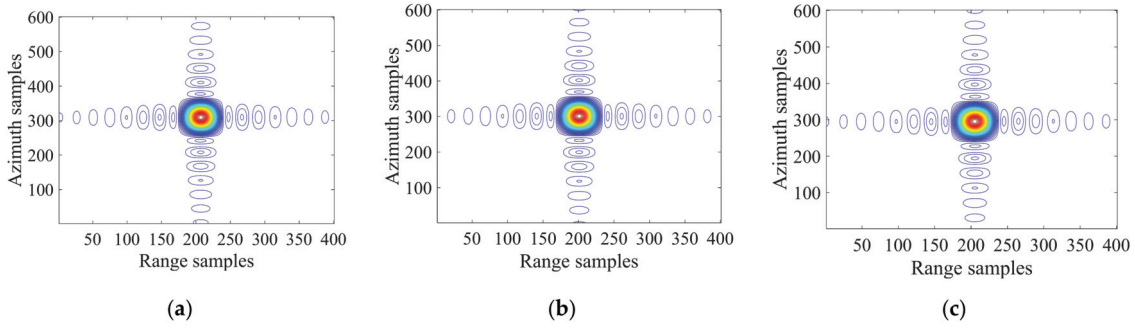


Figure 15. Interpolated results of (**a**) PT3, (**b**) PT5, (**c**) PT7 focused by the back−projection algorithm.

As seen from the results processed by CSA, due to the tremendous phase error introduced by the ESRM in the ultra−high−resolution case, each point target suffers from severe degradation, especially at the edge of the azimuth extent. The insufficient precision of the 2−D spectrum computed in CSA causes the rise of PSRL and the widening of IRW. In Figure 16, the profile cannot be recognized as the sinc function.

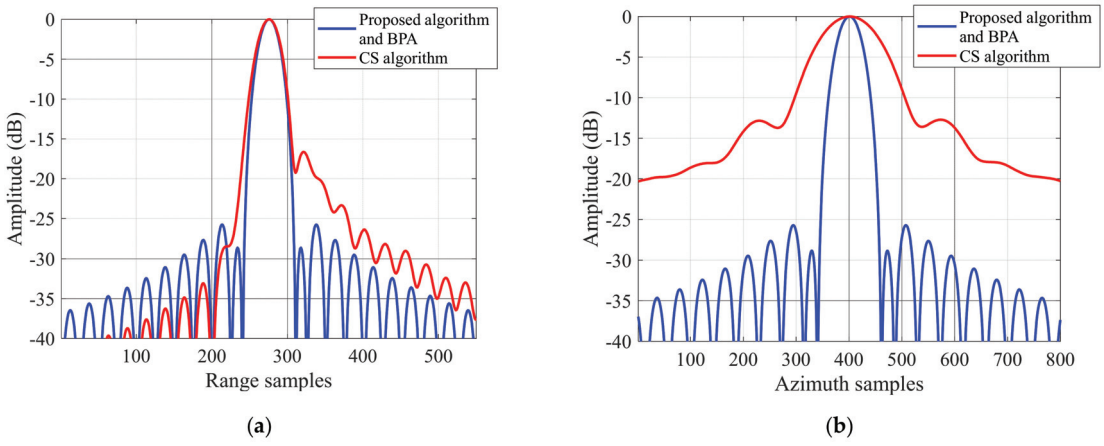


Figure 16. The (**a**) range and (**b**) azimuth profile of PT5 focused by the proposed algorithm, BPA, and the conventional CSA.

Conversely, the results from the proposed algorithm, as presented in Figure 13, indicate that with the more accurate range model and the 2−D spectrum based on it, the focusing performance is dramatically improved. Every point target on the scene is well−focused. The results from the BPA are displayed in Figure 15 as a reference. The well−focused targets validate the high imaging accuracy of the time domain algorithm. Compared with Figure 13, two imaging algorithms have similar performances in image quality, but the proposed algorithm only requires eight times FFT, seven times complex multiplication, and one interpolation, which is far more efficient than the BPA.

To better quantify the image quality, the point target analysis results are listed in Table 2. The theoretical resolution, weighted by the 1/3 simplified Taylor window, is calculated in

$$\begin{cases} \rho_r = 1.09\frac{c}{2B_r} \\ \rho_a = 1.09\frac{L_a H_f}{2} \end{cases} \tag{50}$$

where L_a is the antenna length and H_f is the hybrid factor.

Table 2. Image quality analysis of point targets in small scene obtained by the proposed algorithm.

Target No.	Range			Azimuth		
	ρ_r(m)	PSLR(dB)	ISLR(dB)	ρ_a(m)	PSLR(dB)	ISLR(dB)
1	0.1357	−25.856	−20.807	0.2433	−25.901	−21.327
2	0.1348	−25.753	−20.529	0.2427	−25.729	−21.123
3	0.1357	−25.968	−20.845	0.2437	−25.789	−21.035
4	0.1352	−25.725	−20.655	0.2428	−25.721	−21.225
5	0.1349	−25.755	−20.571	0.2427	−25.737	−21.195
6	0.1352	−25.793	−20.595	0.2428	−25.725	−21.228
7	0.1356	−25.894	−20.736	0.2435	−25.897	−21.050
8	0.1348	−25.764	−20.518	0.2427	−25.729	−21.138
9	0.1356	−25.930	−20.815	0.3435	−25.794	−21.322

It can be observed from Table 2 that the deterioration of the IRW is less than 1%, both in range and azimuth direction. Meanwhile, the PSRL degradation in the table is less than 2%. These promising results prove the proposed algorithm has remarkable performance and can meet the requirement of the ultra−high−resolution imaging for the space−borne SAR for the present and future.

4.3. Geolocation Analysis

The information of geolocation, which is widely used in the post−processing of SAR images, is another criterion for evaluating the performance of the imaging algorithm. Table 3 gives the deviation of the positioning results for every focused target in the image scene, while the targets are located in the WGS84 coordinate system. These results indicate that the deviation at each coordinate axis is less than 10^{-2} m, proving the proposed algorithm's high position accuracy.

Table 3. The deviation of the focused targets in WGS84.

Target No.	X (m)	Y(m)	Z(m)
1	0.000013	−0.000237	0.000134
2	0.000013	0.000300	−0.001480
3	−0.000013	0.000232	−0.000029
4	0.000013	−0.000248	−0.000050
5	0.000000	0.000000	0.000000
6	−0.000013	0.000211	0.000043
7	0.000013	−0.000249	0.000029
8	0.000013	−0.000456	0.002241
9	−0.000013	0.000244	0.000139

4.4. The Discussion of the LEO SAR Motion Error and Autofocus Algorithms

As can be observed from the infinite polynomial range model, the exact relative motion parameters are required for every order. Nevertheless, the parameters error, especially for the higher order, is inevitable in engineering and degrades the image quality. Motion compensation is a common method of handling this problem. It relies on the inertial navigation system installed on the SAR load to record the movement of the radar and compensate for the residual phase through the stored data. This method requires very high accuracy of the inertial navigation system, which increases the system's final cost.

Autofocus is another way to solve the problem. This algorithm is driven by the echo or image data without any auxiliary equipment. The phase gradient autofocus (PGA) [32] algorithm is the most widely used autofocus method, and the maximum likelihood estimation is employed in the kernel to calculate the phase gradient based on the strongest scattering point in the defocused SAR image, and the estimated phase error gradient compensates the phase error. It is worth noting that PGA can eliminate any order of phase error so that it has a good performance in the high−resolution space−borne SAR. With the

development of deep learning, many autofocus algorithms based on the neural network are proposed now [33,34]. They treat the entire imaging process as a linear transformation of the SAR signal and use the neural network to accomplish the linear mapping. Under certain conditions, they have a similar or even better performance than the classic autofocus algorithm, but they still have some limitations, such as only being applied on the polynomial form phase error [34] and the vast number of samples required while the neural network is training.

5. Conclusions

In this paper, a novel 2−D spectrum required imaging algorithm for the ultra−high−resolution space−borne SAR is proposed. To achieve the accuracy of ultra−high−resolution, a high−precision high−order 2−D spectrum is illustrated in detail at the beginning. The infinite polynomial range model is introduced to the 2−D spectrum analysis, and the expression of the new spectrum is derived from it through the Taylor expansion and Lagrange inversion. In addition, the novel imaging algorithm kernel is presented. The azimuth spectrum aliasing caused by the antenna rotation of the sliding spotlight mode is eliminated by the two−step processing. Moreover, to keep the symmetry on the range direction of the point target's impulse response, the high−order phase term of the echo's spectrum is compensated through the derived new spectrum expression. The linear RCM is corrected through the principle of chirp scaling. The space variance of the chirp rate in the range direction is non−negligible in the ultra−high−resolution case. To solve this problem, a cubic phase function is introduced to equalize the chirp rate and guarantee the quality of range focusing. Meanwhile, the quadratic RCM introduced by the cubic phase function is corrected by interpolating after the range compression. In the end, the azimuth compression is implemented, and the well−focused targets of the large scene can be obtained.

The accuracy of the new spectrum is discussed with the order of the Taylor and Lagrange series in the experiment in this paper, and it verifies that the new spectrum can achieve the requirement of ultra−high−resolution. Then, the image quality of the algorithm is evaluated by the simulation. As a comparison, the imaging results from the traditional CSA are also presented. From the detailed view, it is obvious that every well−focused target derived from the proposed algorithm is defocused and distorted by the CSA. The table of the PSLR and ISLR, calculated from the well−focused targets, further proved the performance of the proposed algorithm. Additionally, the geolocation analysis is also given in this paper. The high positioning accuracy shown in the table ensures the post−processing of a SAR image. All these results verify the effectiveness of the proposed imaging algorithm.

Author Contributions: Conceptualization, L.C.; methodology, T.H. and L.C.; software, T.H.; validation, T.H.; formal analysis, T.H.; investigation, T.H.; resources, T.H.; data curation, T.H.; writing original draft preparation, T.H. and Y.G.; writing—review and editing, T.H., L.C., and P.W.; visualization, Y.G. and L.Z.; supervision, L.C. and P.W.; project administration, L.C.; funding acquisition, L.C. All authors have read and agreed to the published version of the manuscript.

Funding: This research was funded by National Natural Science Foundation of China (NNSFC) under Grant No. 61861136008 and Shanghai Aerospace Science and Technology Innovation Fund SAST2020−038.

Data Availability Statement: All data generated or analyzed during this study are included in this article.

Acknowledgments: We thank anonymous reviewers for their comments towards improving this manuscript.

Conflicts of Interest: The authors declare no conflict of interest.

Appendix A

The approximated expression of the first three order term in Equation (25) is given below, and they are all calculated by the first seven order truncated phase Equation (A1).

$$\begin{aligned}\Phi_{deramp_7th}(f_\tau, f_\eta) = &-\tfrac{4\pi(f_0+f_\tau)}{c}\sum_{i=2}^{7}\tfrac{i-1}{i}C_i\left[P\left(f_\eta+\tfrac{2\pi(f_0+f_\tau)R_1}{c}\right)\right]^i\\ &-2\pi\left(f_\eta+\tfrac{2\pi(f_0+f_\tau)R_1}{c}\right)\sum_{i=2}^{7}C_i\left[P\left(f_\eta+\tfrac{2\pi(f_0+f_\tau)R_1}{c}\right)\right]^{i-1}\\ &-\tfrac{\pi f_\tau^2}{K_r}-\tfrac{4\pi(f_0+f_\tau)R_0}{c}-\tfrac{\pi f_\eta^2}{K_{r_rot}}\end{aligned} \tag{A1}$$

$$D_0(f_\eta) = -\pi\left(2f_\eta+\frac{4R_1f_0}{c}\right)*\sum_{i=2}^{7}(-1)^{i-1}C_i\left[\frac{cd(f_\eta)}{2f_0}\right]^{i-1} - \frac{4\pi f_0\left(R_{ref}+\sum_{i=2}^{7}(-1)^i\frac{i-1}{i}C_i\left[\frac{cd(f_\eta)}{2f_0}\right]^i\right)}{c} - \frac{\pi f_\eta^2}{K_{r_rot}} \tag{A2}$$

where

$$d(f_\eta) = \left(f_\eta+\frac{2R_1f_0}{c}\right) \tag{A3}$$

$$\begin{aligned}D_1(f_\eta) = \;&\pi\Bigg[\begin{pmatrix}-1920C_7R_1^7+2240C_6R_1^6-2688C_5R_1^5+3360C_4R_1^4\\-4480C_3R_1^3+6720C_2R_1^2-13340R_{ref}\end{pmatrix}*f_0^7\\ &+\begin{pmatrix}10080C_7R_1^5c^2f_\eta^2-8400C_6R_1^4c^2f_\eta^2+6720C_5R_1^3c^2f_\eta^2\\-5040C_4R_1^2c^2f_\eta^2+3360C_3R_1c^2f_\eta^2-1680C_2c^2f_\eta^2\end{pmatrix}*f_0^5\\ &+\begin{pmatrix}16800C_7R_1^4c^3f_\eta^3-11200C_6R_1^3c^3f_\eta^3+6720C_5R_1^2c^3f_\eta^3\\-3360C_4R_1c^3f_\eta^3+1120C_3c^3f_\eta^3\end{pmatrix}*f_0^4\\ &+\left(12600C_7R_1^3c^4f_\eta^4-6300C_6R_1^2c^4f_\eta^4+2520C_5R_1c^4f_\eta^4-630C_4c^4f_\eta^4\right)*f_0^3\\ &+\left(5040C_7R_1^2c^5f_\eta^5-1680C_6R_1c^5f_\eta^5+336C_5c^5f_\eta^5\right)*f_0^2\\ &+\left(1050C_7R_1c^6f_\eta^6-175C_6c^6f_\eta^6\right)*f_0+90C_7c^7f_\eta^7\Big]/\left(3360cf_0^7\right)\end{aligned} \tag{A4}$$

$$\begin{aligned}D_2(f_\eta) = \;&\pi\Bigg[\begin{pmatrix}-96C_7K_rR_1^5cf_\eta^2+80C_6K_rR_1^4cf_\eta^2-64C_5K_rR_1^3cf_\eta^2\\+48C_4K_rR_1^2cf_\eta^2-32C_3K_rR_1cf_\eta^2+16C_2K_rcf_\eta^2\end{pmatrix}*f_0^5-32f_0^8\\ &+\begin{pmatrix}-240C_7K_rR_1^4c^2f_\eta^3+160C_6K_rR_1^3c^2f_\eta^3-96C_5K_rR_1^2c^2f_\eta^3\\+48C_4K_rR_1c^2f_\eta^3-16C_3K_rc^2f_\eta^3\end{pmatrix}*f_0^4\\ &+\left(-240C_7K_rR_1^3c^3f_\eta^4+120C_6K_rR_1^2c^3f_\eta^4-48C_5K_rR_1c^3f_\eta^4+12C_4K_rc^3f_\eta^4\right)*f_0^3\\ &+\left(-120C_7K_rR_1^2c^4f_\eta^5+40C_6K_rR_1c^4f_\eta^5-8C_5K_rc^4f_\eta^5\right)*f_0^2\\ &+\left(-30C_7K_rR_1c^5f_\eta^6+5C_6K_rc^5f_\eta^6\right)*f_0-3C_7K_rR_1c^6f_\eta^7\Big]/\left(32K_rf_0^8\right)\end{aligned} \tag{A5}$$

References

1. Werninghaus, R.; Buckreuss, S. The TerraSAR−X Mission and System Design. *IEEE Trans. Geosci. Remote Sens.* **2010**, *48*, 606–614. [CrossRef]
2. Breit, H.; Fritz, T.; Balss, U.; Lachaise, M.; Niedermeier, A.; Vonavka, M. TerraSAR−X SAR Processing and Products. *IEEE Trans. Geosci. Remote Sens.* **2010**, *48*, 727–740. [CrossRef]
3. Pitz, W.; Miller, D. The TerraSAR−X Satellite. *IEEE Trans. Geosci. Remote Sens.* **2010**, *48*, 615–622. [CrossRef]
4. Covello, F.; Battazza, F.; Coletta, A.; Lopinto, E.; Fiorentino, C.; Pietranera, L.; Valentini, G.; Zoffoli, S. COSMO−SkyMed an existing opportunity for observing the Earth. *J. Geodyn.* **2010**, *49*, 171–180. [CrossRef]
5. Mezzasoma, S.; Gallon, A.; Impagnatiello, F.; Angino, G.; Fagioli, S.; Capuzi, A.; Caltagirone, F.; Leonardi, R.; Ziliotto, U. COSMO−SkyMed system commissioning: End−to−end system performance verification. In Proceedings of the 2008 IEEE Radar Conference, Rome, Italy, 26–30 May 2008; pp. 1–5. [CrossRef]

6. Janoth, J.; Gantert, S.; Schrage, T.; Kaptein, A. Terrasar next generation—Mission capabilities. In Proceedings of the 2013 IEEE International Geoscience and Remote Sensing Symposium—IGARSS, Melbourne, VIC, Australia, 21–26 July 2013; pp. 2297–2300. [CrossRef]
7. Smith, A.M. A new approach to range−Doppler SAR processing. *Int. J. Remote Sens.* **1991**, *12*, 235–251. [CrossRef]
8. Raney, R.K.; Runge, H.; Bamler, R.; Cumming, I.G.; Wong, F.H. Precision SAR processing using chirp scaling. *IEEE Trans. Geosci. Remote Sens.* **1994**, *32*, 786–799. [CrossRef]
9. Cafforio, C.; Prati, C.; Rocca, F. SAR data focusing using seismic migration techniques. *IEEE Trans. Aerosp. Electron. Syst.* **1991**, *27*, 194–207. [CrossRef]
10. Sun, X.; Yeo, T.S.; Zhang, C.; Lu, Y.; Kooi, P.S. Time−varying step−transform algorithm for high squint SAR imaging. *IEEE Trans. Geosci. Remote Sens.* **1999**, *37*, 2668–2677. [CrossRef]
11. Bamler, R. A comparison of range−Doppler and wavenumber domain SAR focusing algorithms. *IEEE Trans. Geosci. Remote Sens.* **1992**, *30*, 706–713. [CrossRef]
12. Yegulalp, F.A. Fast backprojection algorithm for synthetic aperture radar. In Proceedings of the 1999 IEEE Radar Conference. Radar into the Next Millennium (Cat. No.99CH36249), Waltham, MA, USA, 22 April 1999; pp. 60–65. [CrossRef]
13. Ulander, L.M.H.; Hellsten, H.; Stenstrom, G. Synthetic−aperture radar processing using fast factorized back−projection. *IEEE Trans. Aerosp. Electron. Syst.* **2003**, *39*, 760–776. [CrossRef]
14. Xu, G.; Zhou, S.; Yang, L.; Deng, S.; Wang, Y.; Xing, M. Efficient Fast Time−Domain Processing Framework for Airborne Bistatic SAR Continuous Imaging Integrated With Data−Driven Motion Compensation. *IEEE Trans. Geosci. Remote Sens.* **2022**, *60*, 1–15. [CrossRef]
15. Xie, H.; Shi, S.; An, D.; Wang, G.; Wang, G.; Xiao, H.; Huang, X.; Zhou, Z.; Xie, C.; Wang, F.; et al. Fast Factorized Backprojection Algorithm for One−Stationary Bistatic Spotlight Circular SAR Image Formation. *IEEE J. Sel. Top. Appl. Earth Obs. Remote Sens.* **2017**, *10*, 1494–1510. [CrossRef]
16. Eldhuset, K. A new fourth−order processing algorithm for spaceborne SAR. *IEEE Trans. Aerosp. Electron. Syst.* **1998**, *34*, 824–835. [CrossRef]
17. Eldhuset, K. Spaceborne Bistatic SAR Processing Using the EETF4 Algorithm. *IEEE Geosci. Remote Sens. Lett.* **2009**, *6*, 194–198. [CrossRef]
18. Eldhuset, K. Ultra high resolution spaceborne SAR processing. *IEEE Trans. Aerosp. Electron. Syst.* **2004**, *40*, 370–378. [CrossRef]
19. Wang, P.; Han, Y.; Chen, J.; Cui, Z.; Yang, W.; Li, S. A refined chirp scaling algorithm for high−resolution spaceborne SAR based on the fourth−order model. In Proceedings of the 2013 IEEE International Geoscience and Remote Sensing Symposium—IGARSS, Melbourne, VIC, Australia, 21–26 July 2013; pp. 2051–2054. [CrossRef]
20. Luo, Y.; Zhao, B.; Han, X.; Wang, R.; Song, H.; Deng, Y. A Novel High−Order Range Model and Imaging Approach for High−Resolution LEO SAR. *IEEE Trans. Geosci. Remote Sens.* **2014**, *52*, 3473–3485. [CrossRef]
21. Wang, P.; Liu, W.; Chen, J.; Niu, M.; Yang, W. A High−Order Imaging Algorithm for High−Resolution Spaceborne SAR Based on a Modified Equivalent Squint Range Model. *IEEE Trans. Geosci. Remote Sens.* **2015**, *53*, 1225–1235. [CrossRef]
22. Vizitiu, I.; Anton, L.; Popescu, F.; Iubu, G. The synthesis of some NLFM laws using the stationary phase principle. In Proceedings of the 2012 10th International Symposium on Electronics and Telecommunications, Timisoara, Romania, 15–16 November 2012; pp. 377–380. [CrossRef]
23. Li, C.; Zhang, H.; Deng, Y. Focus Improvement of Airborne High−Squint Bistatic SAR Data Using Modified Azimuth NLCS Algorithm Based on Lagrange Inversion Theorem. *Remote Sens.* **2021**, *13*, 1916. [CrossRef]
24. Chen, X.; Yi, T.; He, F.; He, Z.; Dong, Z. An Improved Generalized Chirp Scaling Algorithm Based on Lagrange Inversion Theorem for High−Resolution Low Frequency Synthetic Aperture Radar Imaging. *Remote Sens.* **2019**, *11*, 1874. [CrossRef]
25. Davidson, G.W.; Cumming, I.G.; Ito, M.R. A chirp scaling approach for processing squint mode SAR data. *IEEE Trans. Aerosp. Electron. Syst.* **1996**, *32*, 121–133. [CrossRef]
26. Wong, F.H.; Cumming, I.G.; Neo, Y.L. Focusing Bistatic SAR Data Using the Nonlinear Chirp Scaling Algorithm. *IEEE Trans. Geosci. Remote Sens.* **2008**, *46*, 2493–2505. [CrossRef]
27. Jeffrey, D.J.; Kalugin, G.A.; Murdoch, N. Lagrange Inversion and Lambert W. In Proceedings of the 2015 17th International Symposium on Symbolic and Numeric Algorithms for Scientific Computing (SYNASC), Timisoara, Romania, 21–24 September 2015; pp. 42–46. [CrossRef]
28. An, D.; Huang, X.; Jin, T.; Zhou, Z. Extended Two−Step Focusing Approach for Squinted Spotlight SAR Imaging. *IEEE Trans. Geosci. Remote Sens.* **2012**, *50*, 2889–2900. [CrossRef]
29. Lanari, R.; Tesauro, M.; Sansosti, E.; Fornaro, G. Spotlight SAR data focusing based on a two−step processing approach. *IEEE Trans. Geosci. Remote Sens.* **2001**, *39*, 1993–2004. [CrossRef]
30. Pengbo, W.; Zhou, Y.; Chen, J.; Li, C.; Yu, Z.; Min, H. A Deramp Frequency Scaling Algorithm for Processing Space−Borne Spotlight SAR Data. In Proceedings of the 2006 IEEE International Symposium on Geoscience and Remote Sensing, Denver, CO, USA, 31 July–4 August 2006; pp. 3148–3151. [CrossRef]
31. Deng, R.; Tian, X.; Kang, Z.−M.; Hong, B.; Wang, W.−Q. Linear Programming Based Sidelobe Suppression for SAR Image Optimization. In Proceedings of the 2021 IEEE International Geoscience and Remote Sensing Symposium IGARSS, Brussels, Belgium, 11–16 July 2021; pp. 3157–3160. [CrossRef]

32. Li, J.; Wu, R.; Chen, V.C. Robust autofocus algorithm for ISAR imaging of moving targets. *IEEE Trans. Aerosp. Electron. Syst.* **2001**, *37*, 1056–1069. [CrossRef]
33. Pu, W. SAE−Net: A Deep Neural Network for SAR Autofocus. *IEEE Trans. Geosci. Remote Sens.* **2022**, *60*, 5220714. [CrossRef]
34. Liu, Z.; Yang, S.; Feng, Z.; Gao, Q.; Wang, M. Fast SAR Autofocus Based on Ensemble Convolutional Extreme Learning Machine. *Remote Sens.* **2021**, *13*, 2683. [CrossRef]

remote sensing

MDPI

Article

Estimates of Hyperspectral Surface and Underwater UV Planar and Scalar Irradiances from OMI Measurements and Radiative Transfer Computations

Alexander Vasilkov [1,*], Nickolay Krotkov [2], David Haffner [1], Zachary Fasnacht [1] and Joanna Joiner [2]

[1] Science Systems and Applications, Inc., 10210 Greenbelt Road, Lanham, MD 20706, USA; david.haffner@ssaihq.com (D.H.); zachary.fasnacht@ssaihq.com (Z.F.)
[2] NASA Goddard Space Flight Center, Greenbelt, MD 20771, USA; nickolay.a.krotkov@nasa.gov (N.K.); joanna.joiner@nasa.gov (J.J.)
* Correspondence: alexander.vasilkov@ssaihq.com

Abstract: Quantitative assessment of the UV effects on aquatic ecosystems requires an estimate of the in-water hyperspectral radiation field. Solar UV radiation in ocean waters is estimated on a global scale by combining extraterrestrial solar irradiance from the Total and Spectral Solar Irradiance Sensor (TSIS-1), satellite estimates of cloud/surface reflectivity, ozone from the Ozone Monitoring Instrument (OMI) and in-water chlorophyll concentration from the Moderate Resolution Imaging Spectroradiometer (MODIS) with radiative transfer computations in the ocean-atmosphere system. A comparison of the estimates of collocated OMI-derived surface irradiance with Marine Optical Buoy (MOBY) measurements shows a good agreement within 5% for different seasons. To estimate scalar irradiance at the ocean surface and in water, we propose scaling the planar irradiance, calculated from satellite observation, on the basis of Hydrolight computations. Hydrolight calculations show that the diffuse attenuation coefficients of scalar and planar irradiance with depth are quite close to each other. That is why the differences between the planar penetration and scalar penetration depths are small and do not exceed a couple of meters. A dominant factor defining the UV penetration depths is chlorophyll concentration. There are other constituents in water that absorb in addition to chlorophyll; the absorption from these constituents can be related to that of chlorophyll in Case I waters using an inherent optical properties (IOP) model. Other input parameters are less significant. The DNA damage penetration depths vary from a few meters in areas of productive waters to about 30–35 m in the clearest waters. A machine learning approach (an artificial neural network, NN) was developed based on the full physical algorithm for computational efficiency. The NN shows a very good performance in predicting the penetration depths (within 2%).

Keywords: UV satellite measurements; radiative transfer computations; underwater irradiance

Citation: Vasilkov, A.; Krotkov, N.; Haffner, D.; Fasnacht, Z.; Joiner, J. Estimates of Hyperspectral Surface and Underwater UV Planar and Scalar Irradiances from OMI Measurements and Radiative Transfer Computations. *Remote Sens.* **2022**, *14*, 2278. https://doi.org/10.3390/rs14092278

Academic Editors: Kai Qin, Zhengqiang Li, Zhongwei Huang, Chi Li, Han Wang, Jie Luo and Tianhe Wang

Received: 1 April 2022
Accepted: 3 May 2022
Published: 9 May 2022

Publisher's Note: MDPI stays neutral with regard to jurisdictional claims in published maps and institutional affiliations.

Copyright: © 2022 by the authors. Licensee MDPI, Basel, Switzerland. This article is an open access article distributed under the terms and conditions of the Creative Commons Attribution (CC BY) license (https://creativecommons.org/licenses/by/4.0/).

1. Introduction

An interest in ultraviolet (UV) radiation effects on aquatic ecosystems is particularly driven by increased levels of biologically harmful UV radiation (290–400 nm) resulting from the depletion of Earth's ozone layer. A recent review of studies of the UV radiation effects on aquatic ecosystems and interactions with other environmental factors is provided in Hader et al. [1]. One of the important effects of enhanced levels of UV radiation is a reduction in the productivity of phytoplankton, caused by inhibition of photosynthesis due to damage to the photosynthetic apparatus, see, e.g., [2]. This effect is described by the spectral biological weighting functions (BWF), which depend on wavelength, phytoplankton species and environmental factors [3–5]. Knowledge of UV radiation penetration is important for the evaluation of ecosystem properties, including ecosystem health and primary productivity [1]. Enhanced UV radiation can also affect the photochemical decomposition of dissolved organic matter [6] and the photochemical production of carbonyl sulfide in seawater [7], thereby affecting long-term global biogeochemical cycles.

A few models of the UV radiation field in ocean waters have been developed over the past two decades. An essential component of the in-water radiation field model is a model of ocean water-inherent optical properties (IOPs) in the UV region (290 to 400 nm). A simplified version of the IOP model in UV was already used for calculations of underwater UV radiation fields on local and global scales [8,9]. The IOP model in the UV region was updated [10] and used for radiative transfer (RT) calculations in the ocean with the Hydrolight RT model [11]. With the use of these IOP and RT models, the seasonal variability of the UV radiation field in the ocean was studied [12]. An algorithm for deriving the UV diffuse attenuation coefficient from remote sensing reflectance was proposed [13]. Penetration of UV irradiance into the ocean was studied [14] using empirical diffuse attenuation coefficient relationships derived from in situ measured profiles of IOPs at visible and UV wavelengths. A semianalytical model of the UV diffuse attenuation coefficient based on ocean color remote sensing has been proposed [15]. Wang et al. [16] evaluate several algorithms developed for the diffuse attenuation coefficient in the UV region (specifically 360, 380, and 400 nm), as well as their performance with satellite observations using comparisons with measurements from the open ocean to coastal waters. Algorithms have also been developed to estimate UV and visible underwater light attenuation from satellite hyperspectral observations from the in-water vibrational Raman scattering signal [17–19]. The authors of [20] explained a need for satellite-retrieving underwater ocean radiation in the UV region globally. They suggest utilizing current satellite hyperspectral missions Aura/OMI and Sentinel-5P/TROPOMI for UV products such as "spectral fluxes below the surface and diffuse attenuation in the UV (or integrated over UV-A and UV-B ranges), in both photon and energy units".

In recent years, the interest in UV radiation studies has grown in relation to the future Plankton, Aerosol, Cloud, ocean Ecosystem (PACE) mission scheduled to launch in 2024. The PACE mission includes the hyperspectral Ocean Color Instrument (OCI) that has UV channels down to 340 nm. As compared with other ocean color instruments, the OCI measurements in the UV will help identify phytoplankton composition and quantify the colored dissolved organic matter (CDOM) absorption by discriminating CDOM from other absorbers [21]. A main goal of the current paper is to test our prototype satellite-based algorithms for computing the hyperspectral surface and in-water UV solar radiation being developed for the OCI. For this purpose, we use data from the current Ozone Monitoring Instrument (OMI) flying on the NASA Aura satellite as a proxy for OCI. To calculate the underwater radiation field, we use the Hydrolight radiative transfer (RT) model [11] with our extensions for ocean IOPs into the UV wavelength range [10]. The boundary conditions at the ocean surface for the underwater computations are provided by the atmospheric RT model, which was first developed for the OMI UV surface irradiance algorithm [22] and extended for the computation of hyperspectral surface irradiance in the present work. The OCI prototype algorithms include both physics-based and neural network (NN) approaches. Training of the NN algorithm is performed on results of the physics-based algorithm.

2. Data and Methods

We have developed a hyperspectral surface and underwater hyperspectral UV irradiance algorithm for the future hyperspectral OCI on board of NASA's upcoming PACE mission [21]. The width of the OCI swath will be 2663 km, and the spatial resolution will be 1 km for nadir viewing pixels. OCI will make hyperspectral solar irradiance measurements once per day and Earthshine radiance measurements for each pixel at a spectral resolution of 5 nm, covering the spectral range from 340 nm to 885 nm.

2.1. TSIS-1 Data

In the atmospheric RT model, we use the Total and Spectral Solar Irradiance Sensor (TSIS-1) Hybrid Solar Reference Spectrum (HSRS) [23]. We smoothed the 0.1 nm spectral resolution TSIS-1 HSRS spectrum with a 5 nm boxcar rolling filter to create a proxy of the OCI extraterrestrial solar irradiance (ETS) (Figure 1). At wavelengths below 2400 nm, the original TSIS-1 HSRS hybrid spectrum was constructed by adjusting the absolute irradiance

scale of high spectral resolution solar irradiance datasets with measurements from the Spectral Irradiance Monitor (SIM) on the TSIS-1 mission aboard the International Space Station (ISS). The TSIS-1 SIM instrument is a prism-CCD spectrometer with SI-traceable calibration monitored carefully on-orbit [24]. The uncertainties reported for the TSIS-1 HSRS are 1.3% in the UV region used in this study. Daily TSIS-1 SIM measurements from one week in early December 2019 when solar activity was near minimum were used to construct the reference spectrum. The TSIS-1 HSRS spectrum is recommended by the PACE science team for the use in OCI L2 algorithms. We corrected TSIS-1 HSRS, reported at a standard distance of 1 AU, for the variation of ETS with the Sun-Earth distance (±3.5%).

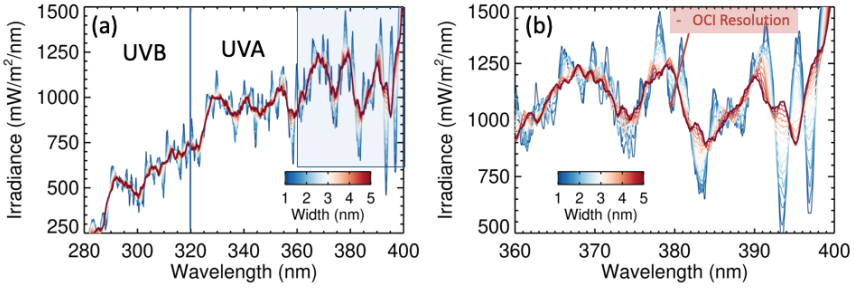


Figure 1. Extraterrestrial spectral irradiance at different spectral resolutions shown for (**a**) the entire UV spectral range and (**b**) the OCI spectral range shown in the light blue cutout in (**a**). The color bar represents the boxcar smoothing width in nanometers.

Figure 1a shows TSIS-1 high spectral resolution extraterrestrial solar irradiance measurements at varying boxcar smoothing widths from 1 to 5 nm (OCI 5 nm resolution in dark red). The spectral shape was chosen because OCI data will be collected at a higher resolution in orbit and averaged onboard to 5 nm resolution. Figure 1b shows spectral details in the UV-A region. The high-frequency structure in the irradiance spectra results from solar Fraunhofer features, resulting from absorption in the Sun's photosphere. The depth of the prominent Ca H and K Fraunhofer lines at 396.847 and 393.366 nm diminishes rapidly as smoothing is applied, and a notable distortion and spectral shift in the Fraunhofer features occurs as the smoothing width is increased from 3 to 5 nm.

2.2. OMI Data

The Ozone Monitoring Instrument (OMI) is a nadir-viewing spectrometer aboard the United States National Aeronautics and Space Administration's (NASA's) Earth Observing System (EOS) atmospheric composition (chemistry) observatory (Aura) that flies in a sun-synchronous orbit with a mean local equator crossing time of about 13:45 (ascending node). Aura is part of the afternoon "A-train" satellite constellation. OMI measures the solar irradiance daily and Earth backscattered radiance from 270–500 nm with a spectral resolution of approximately 0.5 nm [25,26]. It provides near global coverage with a nadir pixel size of 13 × 24 km^2 (along and across the swath, respectively) and a swath width of about 2600 km. OMI made daily global measurements at the start of the mission, but later the global coverage period increased to two days, presumably due to a partial obstruction of the Earth-view port by insulation material on the outside of the instrument. Radiance and irradiance measurements from OMI Collection 3 Level 1B (product names OML1BRUG and OML1BIRR, respectively) [27–29] are used in this work. These are obtained from the Collection 3 products at the Goddard Earth Sciences Data and Information Services Center (GES DISC). OMI TOA radiance measurements used in this study are from sensor band 2 (UV-2) and band 3 (Vis). A small angular offset in pointing of the two bands results in differences in FOV location of 2–3 km in rows 10–40 and 15–25 km at the very edges of the OMI swath. These larger differences at swath edges are predominantly in the cross-track direction.

To carry out atmospheric RT computations in UV, we need to know the total column ozone amounts and surface reflectance. The total ozone fields used as input to the atmospheric RT computations are obtained from the NASA OMI Total Ozone Mapping Spectrometer (TOMS)-like product (OMTO3) that has been validated extensively up to a solar zenith angle (SZA) of 80° [30]. We use operational L2 total column ozone measurements from OMI in Dobson Units (1 DU = 2.69×10^{16} molecules/cm^2). The OMI-TOMS V8.5 total ozone data [31] are also obtained from the GES DISC.

As a proxy of the surface reflectance we use a monthly climatology of the so-called minimum Lambertian Equivalent Reflectivity (LER). Given the measured top-of-atmosphere (TOA) radiance, I_m, the LER is defined by inverting the following exact equation:

$$I_m = I_0 + RT/(1 - RS_b), \quad (1)$$

where R is the surface LER, I_0 is the TOA path radiance calculated for a black surface, T is the total (direct + diffuse) solar irradiance reaching the surface converted to the ideal Lambertian reflected radiance (dividing by π) and then multiplied by the transmittance of the reflected radiation between the surface and TOA in the direction of a satellite instrument and S_b is the diffuse flux reflectivity of the atmosphere for the case of its isotropic illumination from below. OMI-derived multi-year gridded LER data are used to create the climatology of the minimum LER (OMLER) [32,33].

2.3. Atmospheric RT Model

RT solutions in the atmosphere and ocean are coupled through the contribution of photons backscattered by the ocean and then scattered back to the ocean by the atmosphere, see, e.g., Ref. [34] and the references therein. However, if the ocean reflectance is small enough, the atmospheric and oceanic RT problems can be treated separately. Vasilkov and Krotkov [8] estimated that the separation of the atmospheric and oceanic RT models produces less than 10% resulting error in UV underwater irradiance. This RT scheme allows us to significantly reduce the computational burden and calculate spectral UV penetration into the ocean using global satellite measurements with reasonable computational resources.

RT calculations of hyperspectral surface planar irradiance, $E(\lambda)$, are needed to create a boundary condition for Hydrolight calculations of underwater downwelling irradiance. $E(\lambda)$ is determined in the presence of Rayleigh scattering from the molecular atmosphere, the absorption of ozone, scattering by clouds, both scattering and absorption by aerosols and reflection from the surface. To accommodate variable BWF spectra, we extended the OMI surface UV algorithm [22] from 4 to 110 wavelengths producing $E(\lambda)$ at every 1 nm from 290 to 399 nm at the OCI spectral resolution of 5 nm. The algorithm is based on interpolation of lookup tables of clear sky irradiance, $E_{clr}(\lambda)$, and cloud/aerosol transmittance factor, C_T, given by:

$$E(\lambda) = E_{clr}(\lambda)\, C_T(\lambda). \quad (2)$$

Calculation of E_{clr} from satellite measurements of total column ozone, Ω and Lambertian equivalent surface reflectivity, R_s, is described in Krotkov et al. [35,36]. We use climatological ozone absorption profiles. Each standard profile represents a multi-year average for a given total ozone bin for all profiles within a latitude band. These profiles cover a range of 225–475 DU for low latitudes and 125–575 DU for middle and high latitudes, in steps of 50 DU. R_s is estimated from a monthly climatology of the minimum LER at 380 nm, which is small over the ocean ($R_s < 0.1$). We screen OMI pixels affected by sun glint, which is highly non-Lambertian.

In practice, we calculate $C_T(\lambda)$ using full radiative transfer calculations for a model of a homogeneous, plane-parallel C1 cloud model [37] embedded in a Rayleigh scattering molecular atmosphere with climatological ozone absorption profiles. The C1 cloud model represents a water cloud model having the modified gamma size distribution of water droplets with the mode radius of 4 microns. The cloud effective optical thickness, τ_c,

assumed spectrally independent, is derived by matching pre-calculated and measured OMI TOA reflectances at 360 nm corrected for non-elastic (Raman) scattering and collision-induced O_2-O_2 absorption [38]. The $C_T(\lambda, \Omega, \tau_c, R_s, \mathrm{SZA})$ lookup table is calculated at multiple wavelengths for a fixed climatological ozone profile (Ω = 300 DU), τ_c (0–100), surface albedo, R_s (0–1) and solar zenith angles (SZA = 0–88°). The cloud height and geometrical thickness are fixed (3–5.5 km).

We use the DIScrete ORdinate Radiation Transfer (DISORT) code [39] for large τ_c, where polarization can be neglected, and the Gauss–Seidel RT code [40] for $\tau_c < 10$, where polarization may have an effect on backscattered radiances. The effective τ_c corresponds to the actual cloud optical thickness only in an idealized case of a homogeneous plane-parallel cloud layer with complete coverage of the satellite field of view (pixel). For inhomogeneous cloud fields, the τ_c and C_T are spatially averaged quantities that depend on the sub-pixel 3D cloud structure and satellite observational geometry in more complex ways [41]. The spectral independence of τ_c is a good approximation in the UV region and was confirmed by Mie calculations. We also neglect the spectral dependence of LER in UV, which is less than 0.05 over both land and ocean in the UV, causing <2% error in E_{clr} (see Figure 6 in Krotkov et al. [35]). Even with spectrally independent τ_c and LER, our algorithm accounts for the spectral dependence of diffuse cloud transmittance, which results from interactions between the cloud and the Rayleigh atmosphere and ozone absorption.

A C_T error analysis [41] shows that the C1 cloud model with OMI-derived effective τ_c at 360 nm can also be used to describe attenuation of surface UV irradiance by non-absorbing aerosols (e.g., sulfates and oceanic) or their mixture with clouds. The surface UV radiation is more strongly attenuated by UV absorbing aerosols (e.g., smoke and dust) of the same optical depth. These transitory plumes of absorbing aerosols are detected using the OMI UV aerosol index (AI). Either C_T or the absorbing aerosol correction is applied for each OMI pixel. The choice between these two alternative techniques is based on the threshold values of LER and AI. Currently, the AI correction technique is applied if AI > 0.5 and LER < 0.15. The error budget is estimated for each OMI pixel assuming a horizontally homogeneous scene. The noise (random error) in OMI radiance measurement is considered to be much smaller than retrieval errors due to uncertainties in the clear sky atmospheric radiative transfer model, E_{clr}, C_T and ETS irradiance (about 3% [23]). The E_{clr} errors are determined by errors in input geophysical parameters: total column ozone amount, surface pressure and reflectivity [35]. The strategy of the C_T error estimate is as follows: we model the TOA reflectance and true cloud transmittance $C_T^{true} = E/E_{clr}$ for different cloud/aerosol scenarios. Next, we use this TOA reflectance to infer the effective cloud optical thickness, τ_c, and C_T specifically for the C1 model (C_T^{C1}) to estimate C_T error, i.e., $C_T^{true} - C_T^{C1}$, for different OMI viewing geometries and cloud/aerosol models (i.e., cloud drop size distribution, cloud height and cloud fraction, aerosol optical properties, etc.). Finally, we combine all errors to estimate the total uncertaintiy in the surface irradiance as $\Delta E \sim 10\%$ in the UVB and $\Delta E \sim 7\%$ in the UVA (see Table 5.5 in [41]).

2.4. Oceanic RT Model

To calculate underwater irradiances, we use a lookup table of scalar and planar irradiances computed with the Hydrolight RT model [11] with our extensions for ocean IOPs into the UV wavelength range [10]. We use the default boundary conditions for Hydrolight. The incident sky radiance is calculated by the incorporation of a clear-sky spectral irradiance model, a cloud cover correction, and a sky radiance distribution model [11]. According to Mobley [11], "These models have proven sufficiently accurate for most HydroLight applications. In particular, apparent optical properties (AOPs) are only weakly dependent on the details of the sky radiance distribution—that is, after all, one of the main reasons for using AOPs".

The sea surface is assumed to be covered with waves that are parameterized as a function of the surface wind speed. We assume the wind speed to be equal to 5 m/s. In our atmospheric RT model, we do not consider a separation of the incident light into a clear-sky fraction and a cloudy fraction. This approach is similar to that described in Frouin et al. [42].

We scale the input surface irradiance for Hydrolight computations by our OMI-retrieved spectral irradiance. We do not apply the default cloud cover correction in the calculations because this correction has effectively been incorporated into the C_T factor.

The IOP model used here is an extension of the Case I water model [43] to the spectral region 290–400 nm. The model has been described in detail in Vasilkov et al. [10,44]; here, we briefly describe the main features of the IOP model and its verification in Appendix A. The only input parameter of the model is chlorophyll concentration.

The RT computations with Hydrolight were conducted for vertically homogeneous waters. We do not account for non-elastic Raman scattering because its contribution to the in-water radiation field in the UV region is small. This is due to a relatively large wavelength shift between the vibrational Raman excitation and emission bands, which is about 40–50 nm. Due to the sharp decrease of solar radiation at shorter wavelengths in the UV region, the vibrational Raman excitation is significantly reduced at shorter wavelengths, and thus the vibrational Raman emission at longer wavelengths is small. This fact substantially limits the spectral performance of algorithms developed to estimate UV underwater light attenuation from satellite hyperspectral observations from the in-water vibrational Raman scattering signal [19]. Reliable results of the light attenuation retrieval can be expected for longer wavelengths of the UV-A spectral range only. The attenuation of the harmful UV-B radiation seems to be hardly estimated using the in-water Raman signal from the theoretical point of view. It should also be noted that the Raman-based approach for retrieving the light attenuation has another limitation; it is applicable for cloud fractions less than 0.05 only [19]. Additionally, the Raman effect is significantly smoothed due to the relatively low spectral resolution of OCI. The Raman effect strongly depends on the spectral resolution of an instrument. Even at the OMI spectral resolution of about 0.5 nm, the Raman effect does not exceed a few percent in the deepest Ca II Fraunhofer lines [45].

Lookup tables for in-water downward and upward irradiances were generated for the UV wavelength range of 290–400 nm, for chlorophyll concentrations that varied from 0.01 to 10 mg/m^3, for SZAs ranging from 0° to 80°, and ozone column amounts from 150 to 550 DU.

2.5. Scalar Irradiance

For studying physical processes in the ocean, e.g., the heating rate, downward or upward planar irradiance (i.e., energy flux through a horizontal plane) is essential. However, in biogeochemical studies, e.g., photosynthesis, photochemistry, UV effects on marine ecosystem, etc., the scalar irradiance (density of radiant energy) is more appropriate [46]. The OMI UV irradiance product provides the planar irradiance, E_d, at the ocean surface. The spectral planar downward irradiance (energy flux through a horizontal plane) is defined as:

$$E_d(\lambda) = \int_{2\pi} I(\lambda, \theta, \phi) cos\theta \, d\omega, \tag{3}$$

where I is the radiance as a function of wavelength λ, zenith angle θ and azimuth angle ϕ; ω is the solid angle, integration is performed over the upper hemisphere. The upward irradiance is defined similarly with integration over the lower hemisphere. The scalar irradiance (i.e., actinic flux in the atmospheric optics) is defined as:

$$E_o(\lambda) = \int_{4\pi} I(\lambda, \theta, \phi) \, d\omega, \tag{4}$$

where the integration is performed over the entire 4π solid angle. The quantity $E_o(\lambda)\lambda/(hc)$ gives a number of photons in a unit of volume. We propose to estimate scalar irradiance, E_o, at the ocean surface by scaling the planar irradiance, E_d, on a basis of Hydrolight computations: $E_o = f(\lambda, \theta, \mathrm{Chl}, \Omega) E_d$, where the scaling factor, f, depends on wavelength, θ, chlorophyll concentration (Chl) and total column ozone amount Ω, is considered in detail in Appendix B.

3. Results

3.1. Surface Irradiance

The Marine Optical Buoy (MOBY) is a facility designed for the vicarious calibration of satellite ocean color instruments [47]. Located in clear ocean waters near the island of Lanai, Hawaii, MOBY measures the upwelling radiance and downwelling irradiance below the ocean surface plus the incident solar irradiance just above the surface. The measurements include a near-UV range down to about 350 nm.

Figure 2 shows the results of comparing the OMI-derived surface irradiance with the MOBY-measured irradiance in the UV. Comparisons were carried out for OMI pixels collocated over the MOBY site. Because the OMI equator crossing time is about 13:45 local time, the MOBY measurements at 14:00 local time are selected to ensure a minimum time difference between the MOBY measurements and OMI overpass time. Only good MOBY measurements under clear skies were used for the comparisons. OMI pixels were collocated for different seasons to encompass the SZA variability over the year 2005. Using the PACE recommended TSIS solar irradiance improved comparisons with MOBY by 2–3%. As can be seen from Figure 2, the computed and measured irradiances agreed rather well; the mean difference was less than 5%.

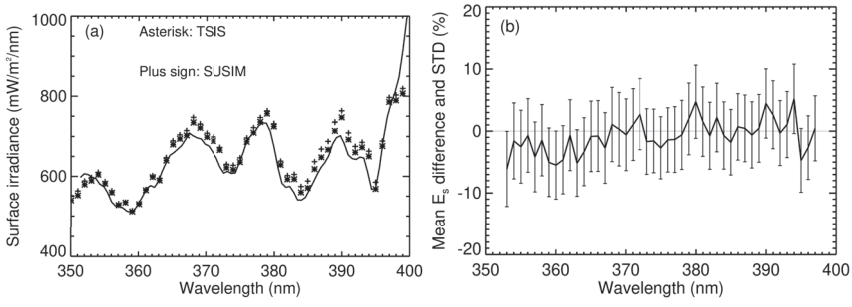


Figure 2. (**a**) A comparison of the smoothed E_s measurements from MOBY (solid line) and OMI (symbols) using the Solar Ultraviolet Spectral Irradiance Monitor (plus signs) and TSIS (asterisks) extraterrestrial solar irradiance spectra for a selected OMI pixel. (**b**) The mean difference and standard deviation between the OMI-derived surface irradiance and the MOBY-measured irradiance.

3.2. In-Water Irradiance

We first present the results, which show the main factors affecting the underwater UV radiation field and then the results of the OMI-retrieved characteristics of the radiation field.

3.2.1. Spectral Irradiance

Here, we consider the spectral dependence of planar and scalar irradiances and DNA action-weighted irradiance. The latter is defined as a product of the spectral irradiance and the DNA damage action spectrum [48] (see also https://www.temis.nl/uvradiation/product/action.html, accessed 30 March 2022). Figure 3 shows an example of absolute values of the hyper-spectral planar and scalar irradiances at different depths and the corresponding normalized irradiances along with the DNA action spectrum.

A comparison of the normalized irradiance spectra (Figure 3 right) near the ocean surface and at the depth of 20 m shows how the spectra changed with depth. The most significant reduction of the irradiance occured at shorter wavelengths. As the depth increased, the ocean water mostly cut down the short-wave part of the solar spectrum due to higher absorption at shorter wavelengths.

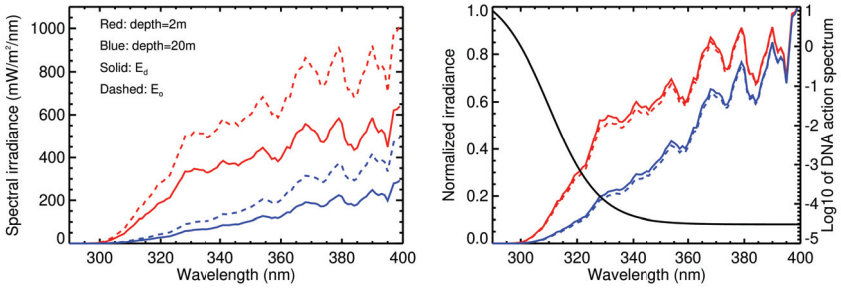


Figure 3. Spectral planar (solid lines) and scalar (dashed lines) irradiances. **Left**: Absolute values of the irradiances at two depths: 2 m (red lines) and 20 m (blue lines). **Right**: Planar and scalar irradiances normalized over their values at 400 nm. The black line shows the DNA damage action spectrum.

The DNA-weighted irradiances are shown in Figure 4. It is interesting to note that the spectral maximum of the DNA-weighted irradiances slightly shifted from 303 nm to about 305 nm with depth increasing from 2 m to 20 m. This is explained by the larger absorption of ocean water at shorter wavelengths resulting in the reduction of contribution of shorter wavelengths to the DNA-weighted irradiance. An estimate of the diffuse attenuation coefficient at 305 nm from in situ measurements [49] or satellite observations [16] can provide information on the DNA damage penetration depth.

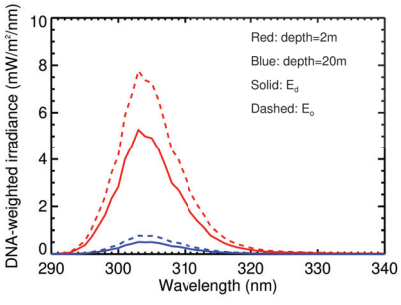


Figure 4. DNA-weighted planar (solid lines) and scalar (dashed lines) irradiances at two depths: 2 m (red lines) and 20 m (blue lines).

3.2.2. K-Functions in the UV

In-water attenuation of E_d and E_o with depth is characterized by the diffuse attenuation coefficient (K-function):

$$K(z) = -d\ln(E)/dz, \tag{5}$$

where E is either E_d or E_o, z is the depth and the wavelength dependence is omitted for briefness. Then, the propagation of E to depth is described by the exponential function:

$$E(z) = E(0)\ \exp(-\int_0^z K(z)dz), \tag{6}$$

where $E(0)$ is the irradiance value at the surface. A penetration depth, z_p, can be defined as a depth at which the quantity E decreases to a pre-defined fraction of its surface value $\varepsilon = E(z_p)/E(0)$. For instance, in the case that K equals a constant and the commonly used value $\varepsilon = 0.1$ for defining the euphotic zone depth, $z_{10\%}$ [50], the penetration depth is $z_p = -\ln(0.1)/K$.

The diffuse attenuation coefficient at a given depth depends on the angular distribution of radiance and IOPs, e.g., [51]. Here, we compare the diffuse attenuation coefficients for downwelling planar irradiance, K_d, and scalar irradiance, K_o, as a function of different input variables. Figure 5 shows the dependence of K_d and K_o on depth, wavelength, chlorophyll concentration and SZA.

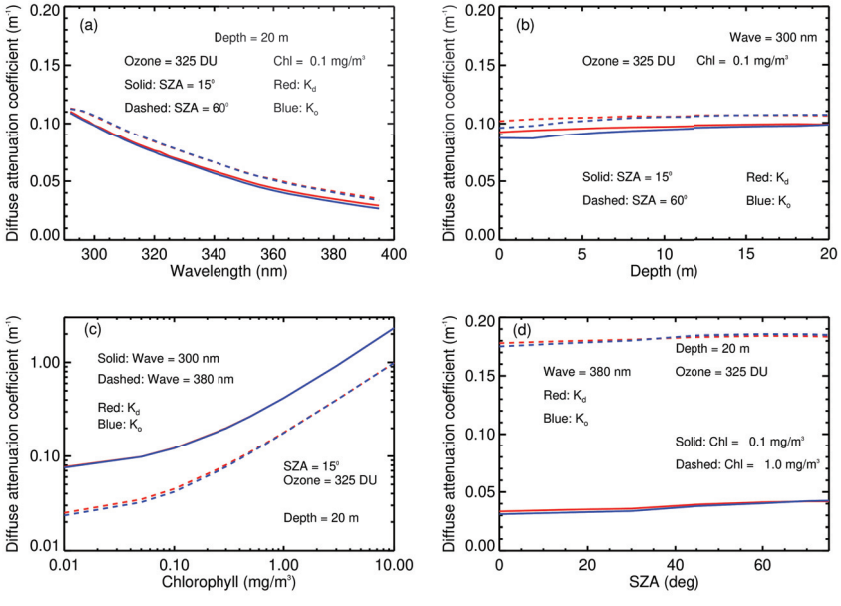


Figure 5. Diffuse attenuation coefficient K_d (red lines) and K_o (blue lines) as a function of: (**a**) wavelength, (**b**) depth for two SZAs of 15° (solid lines) and 60° (dashed lines), (**c**) chlorophyll concentration for two wavelengths 300 nm (solid lines) and 380 nm (dashed lines) and (**d**) SZA for two values of chlorophyll concentration 0.1 mg/m^3 (solid lines) and 1.0 mg/m^3 (dashed lines).

The data in Figure 5 show that the dependences of the diffuse attenuation coefficient of scalar and planar irradiance on depth were quite close to each other. Given that the average cosine of the downwelling radiance is defined as $\mu(z) = E_d(z)/E_0(z)$, this means a weak dependence of μ in UV on depth in the upper layer of the ocean due to the following relationship $d\mu/dz = \mu(K_d - K_o)$. The weak dependence of μ on depth results in a weak dependence of the K functions on depth (see Figure 5b) because we assume a vertically uniform distribution of IOPs. This assumption is well justified for the well-mixed upper layer of the ocean. The weak dependence of the K functions on depth in the upper layer allows for the use of a single value of the K functions averaged over the upper layer for predicting the penetration depths in the UV. This is particularly important for satellite estimates of the diffuse attenuation coefficients [16] because the satellite estimates are based on the measurement of water-leaving radiance, which is primarily formed in the upper layer of the ocean.

The wavelength dependence of the K function shown in Figure 5a was determined by the IOP wavelength dependence. The dominant role in this dependence is played by the spectral dependence of the total absorption coefficient, which significantly increases with decreasing wavelength. Similarly, the dependence of the K functions on chlorophyll (Figure 5c) is explained by the increase in the total absorption coefficient with the increasing chlorophyll concentration (see Appendix A). Figure 5d shows that the K functions increase slightly with increasing SZA. This is explained by the fact that the average cosine of the downwelling radiance decreases due to an increased fraction of the diffuse light in the

incident radiation. The dependence of K_d and K_o on ozone amount is quite small and is not shown in Figure 5.

3.2.3. OMI Retrievals

In this section, OMI retrievals are shown for OMI orbit 2573 on 7 January 2005. All the retrievals are limited to SZA $< 80°$. The retrievals include the surface erythemal dose rates and penetration depths for the DNA damage dose rates. The DNA damage dose rate at a given depth is defined as the integral of the DNA-weighted irradiance over the UV spectral range:

$$D(z) = \int_{290}^{400} E(\lambda, z, \mathrm{SZA}) A(\lambda)\, d\lambda, \tag{7}$$

where $E(\lambda, z)$ is either the planar or scalar irradiance, $A(\lambda)$ is the DNA damage action spectrum [48] and SZA is defined for each OMI pixel at the time of the satellite overpass. The penetration depth is calculated from the following equation: $D(z_p) = \epsilon D(0)$, where $\varepsilon = 0.1$.

Figure 6 shows maps of the main input parameters of orbit 2573 used for the OMI retrievals. The chlorophyll concentrations shown in Figure 6 were obtained from the MODIS/Aqua chlorophyll-a product [52]. We use the monthly averaged Level 3 MODIS chlorophyll product, which is reported at a spatial resolution of 4 km [53]. All available monthly MODIS chlorophyll data within the OMI field-of-view (FOV) were averaged. In the case where MODIS data were not available from the monthly product for an OMI FOV, gap filling was performed using monthly climatology. If monthly data were unavailable, an annual mean was used.

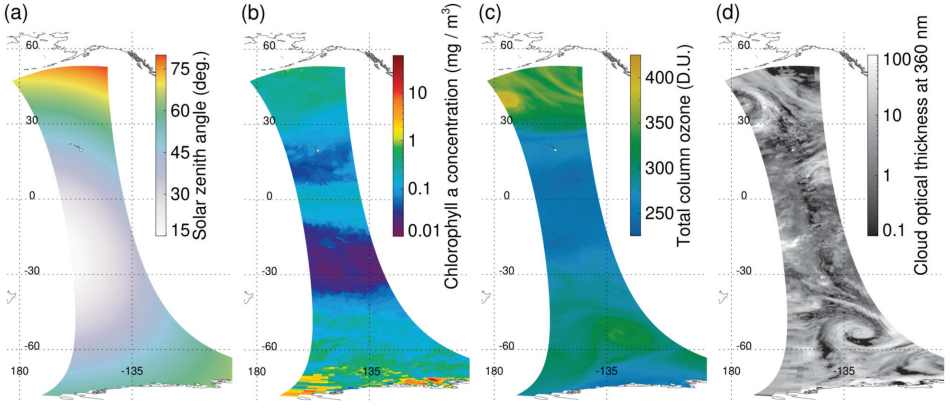


Figure 6. Maps of the main input parameters: (**a**) solar zenith angle; (**b**) chlorophyll concentration in mg/m^3; (**c**) ozone amounts in DU; and (**d**) effective cloud optical depth at 360 nm.

Figure 7 shows maps of the OMI-derived surface erythemal dose rates. The dose rates were calculated using the planar and scalar irradiances convolved with the erythemal action spectrum [54] (see also, https://www.temis.nl/uvradiation/product/action.html, accessed on 30 March 2022).

As expected, the scalar erythemal dose rates were noticeably higher than the planar erythemal dose rates. Both planar-based and scalar-based erythemal dose rates depend on SZA and cloud cover. The erythemal dose rates exhibit a strong spatial correlation with the effective cloud optical depth shown in Figure 6d. The ratio of the scalar dose rates to the planar dose rates (Figure 7c) was highly correlated with SZA (Figure 6a) and increased with SZA except for very high SZA $> 70°$ in the northern part of the orbital swath. For those high SZAs, the ratio decreased with increasing SZA (see Figure A2b of Appendix B). This dependence of the ratio on SZA for high values of SZA was similar to the so-called Umkehr effect that is related to ozone absorption in the atmosphere. In general, the ratio

of the scalar erythemal dose rates to the planar erythemal dose rates varied from 1.5 to about 3.0.

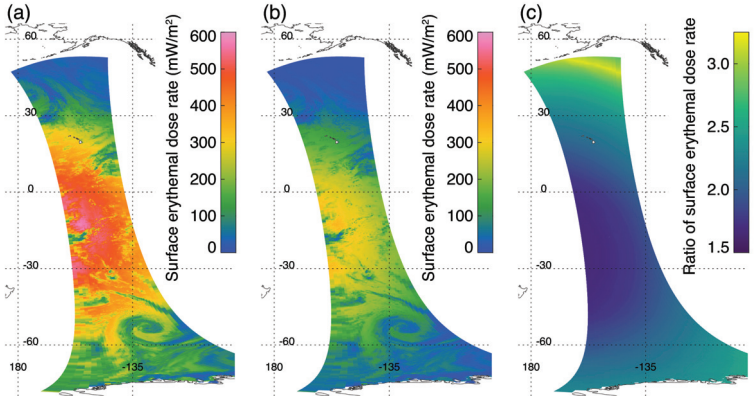


Figure 7. Maps of the surface erythemal dose rates: (**a**) calculated using the scalar irradiance; (**b**) calculated using the planar irradiance; (**c**) ratio of the scalar erythemal dose rate to the planar dose rate.

Figure 8 shows maps of the penetration depths of the DNA damage dose rates calculated using the planar and scalar irradiance and their difference. The maps of the penetration depths show that a governing parameter that mostly defines the penetration depth is chlorophyll concentration. There is a strong spatial correlation between the chlorophyll concentration (Figure 6b) and the penetration depths (Figure 8a,b). Other input parameters play an insignificant role in the spatial distribution of the penetration depths. The penetration depths vary from a few meters in areas of productive waters of the Southern Ocean to about 30–35 m in the clearest waters of the South Pacific Gyre. Differences between the planar penetration and scalar penetration depths are small. They do not exceed a couple of meters (Figure 8c). This fact follows from Hydrolight computations that show a small difference between K functions for the planar and scalar irradiances for a wide range of input parameters (Figure 5).

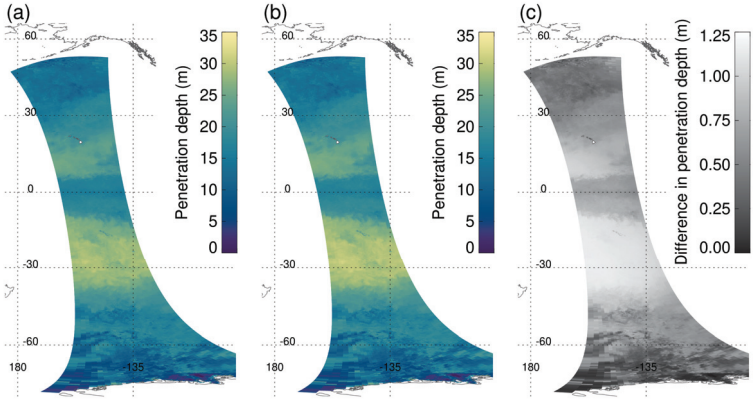


Figure 8. Maps of the penetration depths for the DNA damage dose rates: (**a**) calculated using the planar irradiance; (**b**) calculated using the scalar irradiance. (**c**) The difference between the planar penetration and scalar penetration depths. The color bars represent the penetration depths in meters.

3.3. Machine Learning Results

Forward radiative transfer modeling from tools such as Hydrolight can be computationally inefficient due to the large number of complex non-linear physical equations. The current and future Earth observing satellites continue to provide measurements at higher spectral, spatial and temporal resolutions. As a result of the increased number of measurements, traditional physically based radiative transfer models will not be feasible in operational processing. Machine learning approaches have been proposed to overcome these computational challenges. Machine learning models such as neural networks (NNs) can learn how to represent the complex physical relationships in the radiative transfer simulations through statistical equations [55,56].

Here, we explore the feasibility of using an NN to reproduce the physics-based penetration depth simulations from Hydrolight so that the retrieval algorithm can be applied to an operational sensor such as OMI. The inputs used to estimate penetration depth are SZA, chlorophyll concentration, total column ozone and surface irradiance. For this work, we used a simple four-layer feed-forward neural network with an input layer, two hidden layers and an output layer that predicts planar and scalar penetration depth. The neural network uses a sigmoid activation function for each hidden layer and an adaptive moment estimation optimizer was used to minimize the error with a learning rate of 0.01. We trained the NN with 80% of the samples from two orbits from 7 January 2005 (orbits 2570 and 2572), which include a well-distributed sampling of Case I open waters (low chlorophyll concentration) as well as Case II coastal waters (higher chlorophyll concentration). The neural network was able to predict the penetration depth in approximately two seconds of the computer time for a single orbit as compared with a few minutes of the computer time needed for processing a single orbit by the physics-based algorithm.

Figure 9 shows comparisons of the NN estimates of penetration depth compared to those from the Hydrolight simulations. This figure shows comparisons for orbits included in the training (left panel) as well as additional independent testing orbits not included in the NN training (right panel). There was excellent agreement between the NN results and the Hydrolight simulations with an R^2 of nearly 1 and RMS error of 0.08–0.1 m. The comparisons were quite similar for the training orbits and independent orbits, suggesting that the NN works well for all conditions and is not overfitting to the training samples.

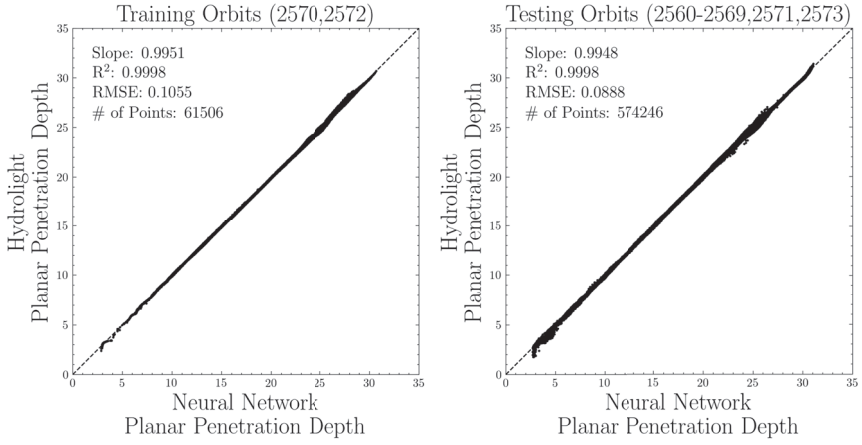


Figure 9. Comparisons of Hydrolight penetration depth simulations and neural network estimate for 7 January 2005. Left panel shows comparisons for orbits included in neural network training while right panel shows orbits on this date not included in the training.

Figure 10 shows maps of the planar penetration depth from Hydrolight (top) and the estimated planar penetration depth from the NN (middle). The NN does well in reproducing the planar penetration depth; differences with Hydrolight were generally

$<\pm 2\%$. There were some larger differences off the immediate coast of Antarctica, which are likely due to misclassification of snow or sea ice.

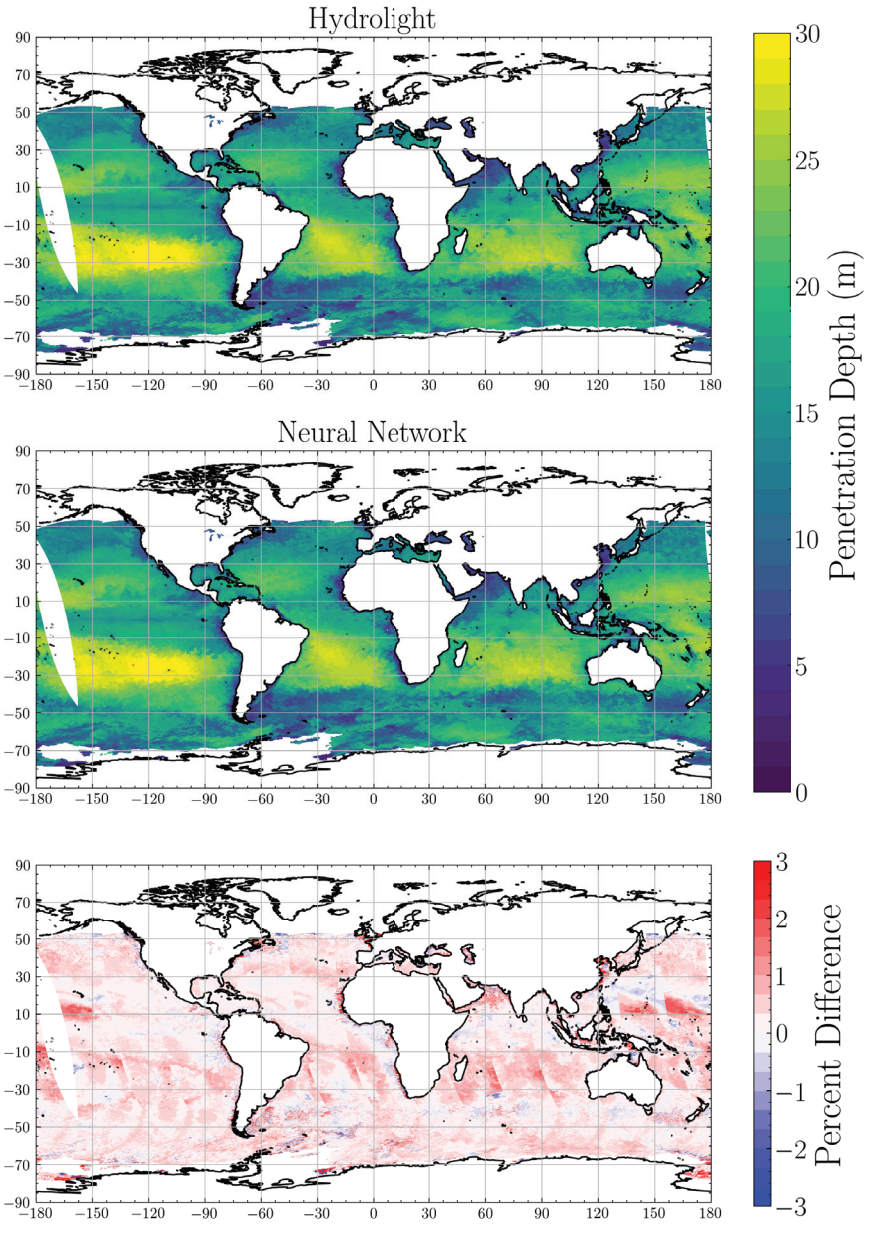


Figure 10. Map of planar penetration depth on 7 January 7 2005. Top panel shows planar penetration depth from Hydrolight, middle panel shows planar penetration depth from the neural network and the bottom shows the percent difference of Hydrolight versus the neural network estimate. The color bars represent the penetration depths in meters and the percent difference.

4. Discussion

4.1. IOP Model Limitations

The largest source of uncertainty in the estimation of UV penetration into the ocean is related to the IOP model used in RT computations with Hydrolight. HydroLight is a radiative transfer numerical model that computes radiance distributions and derived quantities for natural water bodies. This model solves the unpolarized RT equation to obtain the radiance distribution within a plane-parallel water body. We neglect the errors of solving the RT equation with Hydrolight because a main source of the errors in the Hydrolight output is related to uncertainties in the Hydrolight input. In general, the Hydrolight inputs consist of the absorbing and scattering properties of water, the properties of the wind-blown ocean surface, the reflectance of the bottom in the case of shallow waters and the angular distribution of radiance incident on the ocean surface.

Here, we assume the Case I model of IOPs that allows us to minimize the number of input parameters and, therefore, to use the standard satellite ocean color product as input for Hydrolight. Within the Case I model, the IOPs of ocean water are assumed to be fully correlated and can be parameterized through chlorophyll concentration. The Case I ocean water model is supposed to work well for open ocean waters where the influence of terrigenic matter is negligible. The Case I model is not applicable for coastal zones of the world ocean where suspended particulate matter and CDOM may not be fully correlated with chlorophyll concentration.

Our parameterization of the particulate-matter absorption coefficient, a_{ph}, Ref. [10] is based on in situ data collected on the California Cooperative Oceanic Fisheries Investigations (CalCOFI) cruises in different areas and seasons. The CalCOFI region encompasses a large dynamic range of coastal and open ocean trophic structures. The optics data have been collected for Chl-a concentrations at the surface, ranging four orders of magnitude, from 0.05 mg m^{-3} for offshore stations to about 20 mg m^{-3} and higher. The taxonomic composition across the onshore-offshore gradient ranges from a dinoflagellate/diatom-dominated coastal community to a pico-plankton-dominated community offshore. The offshore region of CalCOFI is typical of the open ocean oligotrophic subtropical gyres with low surface Chl-a and a deep Chl-a maximum between 100–130 m.

Unfortunately, there are few measurements of particulate-matter absorption below 350 nm. That is why a direct comparison of our parameterization with other data is limited. The lack of the $a_{ph}(\lambda)$ data compels us to assume an arbitrary spectral dependence of a_{ph} in the UV. For instance, Westberry et al. [57] assume that a_{ph} is spectrally flat for $\lambda < 412$ nm, which is rather unrealistic. However, this model is currently embedded in NASA's SeaDAS software. A classification of $a_{ph}(\lambda)$ measured down to the 350 nm at 5 nm step was proposed in [58]. The a_{ph} spectra were divided into twelve groups based on a value of $a_{ph}(440)$, covering oligotrophic oceanic waters to waters with phytoplankton blooms. However, a parameterization of a_{ph} in UV that would be suitable for a global application was not proposed. Morrison et al. [59] show two normalized phytoplankton absorption spectra from 300 to 750 nm taken at the Bermuda Atlantic Time Series (BATS) site. Their spectra are highly variable with seasons and depths between 300 and 365 nm. This variability is likely due to mycosporine-like amino acids (MAAs), which strongly absorb near 320 nm. The shape of the summer spectrum [59] is quite different from our paramterization. This is explained by averaging many spectra collected in different seasons in our parameterization, while Morrison et al. [59] show examples of the phytoplankton absorption spectra. This discussion suggests the development of a new parameterization based on simultaneous measurements of chlorophyll and MAA concentrations. Hedley and Mobley [60] attempted to combine the data from Vasilkov et al. [10] with the spectra from Morrison et al. [59] in the latest version of Hydrolight. Their attempt gives an absorption model that roughly corresponds to the mid-range of UV absorptions seen in Morrison et al. [59]. We think that this model may be too speculative and do not use it in our computations.

Quantifying the pure water absorption coefficient, a_w, is important because there is no consensus on the a_w values. There are significant differences between different

datasets of a_w in the UV. We have discussed the pure water absorption and compared the different datasets in Vasilkov et al. [44,61] (see, e.g., Figure 12 in Vasilkov et al. [61]). The estimates from Vasilkov et al. [61] show that the IOP model could be improved for very low chlorophyll concentrations if we use the data from Lee et al. [62]. However, those data were not derived from direct measurements; they were retrieved from comparisons of the modelled and measured remote sensing reflectances. Moreover, the spectral range of a_w data in Lee et al. [62] is not suitable for our purposes because it is limited by the shortest available wavelength (350 nm). That is why we do not use those data.

4.2. Verification of the IOP Model

We have verified the ocean RT and IOP model by comparing the calculated and measured diffuse attenuation coefficients in Vasilkov et al. [10]. Here, we briefly describe the results of the verification. In situ data used in the comparisons are from measurements taken during the Aerosol Characterization Experiment. The (ACE)-Asia experiment was carried out in 2001 in the Pacific Ocean. The dataset includes profile measurements of downward irradiance E_d and upward irradiance E_u at 17 wavelengths ranging from 313 to 710 nm. In the field measurements of K_d, the surface-wave introduced fluctuations in the subsurface light field make it hard to accurately determine $K_d(z)$. To compare with the calculated K_d, we averaged the measurements over a 10 m layer using linear regression analysis between $\ln(E_d(z))$ and z. Comparisons of the calculated and measured K_d, which were completed for chlorophyll concentrations less than 0.7 mg/m^3 to ensure the validity of the Case I water model, showed that the correlation coefficient varied from 0.89 at 313, 320 and 340 nm to 0.87 at 380 nm. The relative RMS error for all the cruise stations was less than 20%. There was no obvious bias between the measured and calculated K_d, suggesting that the IOP model reasonably reflects the observed absorption and scattering in the ocean. Comparisons between the calculated and measured quantities were also carried out for the diffuse reflectance, $R = E_u/E_d$ in Vasilkov et al. [44]. The comparisons showed a good agreement between the data: the correlation coefficient varied from 0.85 to 0.90 depending on wavelength.

4.3. Ozone Availability for OCI

Daily column ozone fields are necessary to apply our underwater UV retrieval algorithm to OCI. OMI no longer achieves daily global coverage due to a partial instrument blockage at the Earth-view entrance port. Total column ozone is also available from the series of Ozone Mapping and Profiler Suite (OMPS) nadir mapper (NM) instrument, which will be operating on the Joint Polar Satellite System (JPSS) missions into the next decade. However, it would be preferable for our retrievals to use total ozone produced from the OCI itself. Mannino et al. [63] demonstrated the feasibility of retrieving ozone from PACE, if the UV spectral range of OCI could be extended to bands centered at 322 and 325 nm. They find the quality of retrieved ozone from their approach suitable for the atmospheric correction of ocean color products, and the same is true for underwater UV irradiances.

Another possibility to obtain total column ozone is the use of monthly climatological values. However, some differences between the daily ozone and climatological amounts will inevitably exist. They will lead to errors in the surface and underwater irradiances. For the typical 5 DU (2%) ozone uncertainty, the surface UV uncertainty is 1–3% at 310 nm, increasing to 5–8% at 300 nm and 10–15% at 295 nm. The UV sensitivity to total ozone and its vertical distribution increases for high SZAs and short UVB wavelengths due to the Umkehr effect (see the discussion of Figures 3 and 4 in Krotkov et al. [35]).

5. Conclusions

Scalar irradiance at the ocean surface can be derived from satellite estimates of planar irradiance using the scaling factor from Hydrolight computations. For a clear sky, the scaling factor is a function of wavelength, SZA and ozone amount. The scalar erythemal dose rates calculated at the ocean surface are noticeably higher than the planar erythemal dose rates; their ratio varies from 1.5 to about 3.0. In-water attenuation of E_d and E_o with

depth is quite similar. Differences in the corresponding K-functions are very small for the wide range of input parameters, which include depth, wavelength, SZA, chlorophyll concentration and ozone amount.

A dominant factor defining the UV penetration depths is chlorophyll concentration. Other input parameters play a less significant role in the spatial distribution of the penetration depths. The penetration depths vary from a few meters in areas of productive waters to about 30–35 m in the clearest waters. The machine learning algorithm shows a very good performance with the selected NN architecture in predicting the penetration depths. The NN reproduces the planar penetration depth with errors $<\pm 2\%$.

Author Contributions: Conceptualization, A.V. and N.K.; methodology, A.V. and N.K.; software, D.H.; validation, A.V., D.H. and Z.F.; formal analysis, A.V.; investigation, A.V.; resources, Z.F.; data curation, Z.F.; writing—original draft preparation, A.V. and N.K.; writing—review and editing, J.J., D.H. and Z.F.; visualization, A.V. and D.H.; supervision, N.K. and J.J.; project administration, N.K.; funding acquisition, N.K. All authors have read and agreed to the published version of the manuscript.

Funding: This research was funded by NASA through the PACE science team program.

Data Availability Statement: OMI Level 1b UV radiance data are available through NASA's Goddard Earth Sciences Data and Information Services Center (GES DISC) at https://disc.gsfc.nasa.gov/datasets/OML1BRUG_004/summary. The TSIS-1 HSRS 0.1 nm spectral resolution ("p1nm") dataset was obtained from the Laboratory for Atmospheric and Space Physics (LASP) at the University of Colorado, Boulder, https://lasp.colorado.edu/lisird/data/tsis1_hsrs. OMI Level 2 total ozone data are available at https://disc.gsfc.nasa.gov/datasetsOMTO3_003/summary. MODIS Level 3 4 km chlorophyll data are available at https://oceancolor.gsfc.nasa.gov/. All accessed on 30 March 2022.

Acknowledgments: We are grateful to the OMI processing team for providing OMI data.

Conflicts of Interest: The authors declare no conflict of interest.

Abbreviations

The following abbreviations are used in this manuscript:

AU	Astronomical Unit
BWF	Biological Weighting Function
CDOM	Colored Dissolved Organic Matter
DNA	Deoxyribonucleic Acid
DU	Dobson Unit
FOV	Field of View
IOP	Inherent Optical Property
MOBY	Marine Optical Buoy
MODIS	Moderate Resolution Imaging Spectroradiometer
OCI	Ocean Color Instrument
OMI	Ozone Monitoring Instrument
RMS	Root Mean Square
RT	Radiative Transfer
SZA	Solar Zenith Angle
TOA	Top of the Atmosphere
TSIS-1 HSRS	Total and Spectral Solar Irradiance Sensor Hybrid Solar Reference Spectrum
UV	Ultraviolet

Appendix A. IOP Model

To carry out RT computations with Hydrolight we need to specify the absorption and scattering coefficients of ocean water along with a phase-scattering function. The total IOPs are built up as a sum of IOPs attributable to the various components of the water body. Thus, the total absorption coefficient is:

$$a(\lambda) = a_w(\lambda) + a_{ph}(\lambda) + a_{CDOM}(\lambda), \quad \text{(A1)}$$

where a_w is the pure ocean water absorption coefficient, a_{ph} is the particulate-matter absorption coefficient and a_{CDOM} is the CDOM absorption coefficient. Similarly, the total scattering coefficient is calculated as follows:

$$b(\lambda) = b_w(\lambda) + b_{ph}(\lambda), \tag{A2}$$

where b_w is the pure ocean water scattering coefficient, and b_{ph} is the particulate-matter scattering coefficient.

Additionally, we need to specify a phase-scattering function. An intercomparison of different phase scattering functions was carried out in Vasilkov et al. [10] by comparing the calculated K_d with the measured K_d for different chlorophyll concentrations. Data in this paper show that the physically-based Fournier–Forand (FF) phase function [64] is better in predicting downwelling irradiances than the average Petzold phase function. The FF phase function with a backscatter fraction of 0.003 was used in the computations. This conclusion was confirmed by Vasilkov et al. [44], where comparisons of the calculated diffuse reflectance and measured reflectance were performed.

An important feature of the IOP model in the UV region is quantifying the pure water absorption coefficient, a_w. At present, there are significant differences between different datasets of a_w in the UV region. A detailed discussion on pure water absorption and comparisons of the different datasets can be found in Vasilkov et al. [44,61]. In this study, we use interpolation between data given in Pope and Fry [65] and Quickenden and Irvin [66], as suggested by Fry [67].

To reduce a number of input parameters to the IOP model, we assume the so-called Case I water model [43,68]. According to this model, all ocean water constituents are of biogenic origin and can be related to a single parameter—chlorophyll concentration. A parameterization of the particulate matter absorption coefficient in the UV as a function of chlorophyll concentration is based on in situ data collected in the framework of the California Cooperative Oceanic Fisheries Investigations (CalCOFI) [10].

The particulate matter absorption coefficient is expressed through a chlorophyll-a concentration and a chlorophyll-specific absorption coefficient similar to that used in the visible part of the spectrum:

$$a_{ph}(\lambda) = A(\lambda)\,\mathrm{Chl}^{1-B(\lambda)}, \tag{A3}$$

where the coefficients $A(\lambda)$ and $B(\lambda)$ are tabulated in [10]. The spectral dependence of a_{ph} and its dependence on chlorophyll concentration are shown in Figure A1 for low chlorophyll concentrations, which are typical for open ocean waters (Case I waters).

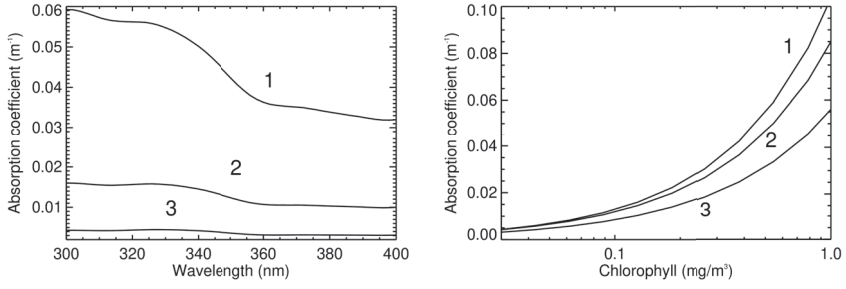


Figure A1. The particulate-matter absorption coefficient. Left panel: a_{ph} as a function of wavelength for different chlorophyll concentrations: 1—Chl = 0.55 mg/m^3; 2—Chl = 0.13 mg/m^3; 3—Chl = 0.03 mg/m^3. Right panel: a_{ph} as a function of chlorophyll concentration for different wavelengths: 1–300 nm; 2–340 nm; 3–380 nm.

An important absorber in UV is the colored (or chromophoric) dissolved organic matter (CDOM). The spectral CDOM absorption is parameterized in the conventional form:

$$a_{CDOM}(\lambda) = a_{CDOM}(\lambda_0)\exp[-S(\lambda - \lambda_0)], \tag{A4}$$

where $\lambda_0 = 440\,\text{nm}$ is the reference wavelength, and S is the spectral slope. The CDOM spectral slope typically has somewhat higher values in the UV region as compared with the Vis region. We assume $S = 0.017\,\text{nm}^{-1}$, as recommended for the UV [69]. Following Morel and Maritorena [68], the CDOM absorption coefficient at 440 nm is parameterized as:

$$a_{CDOM}(440) = 0.2[a_w(440) + 0.06\,\text{Chl}^{0.65}], \tag{A5}$$

where $a_w = 0.0063\,\text{m}^{-1}$ is the pure seawater absorption coefficient [70]. This parameterization assumes that there is some CDOM absorption even in the absence of chlorophyll and models the presence of background CDOM in ocean waters.

The spectral dependence of the particulate matter scattering coefficient is approximated by a power law:

$$b_p(\lambda) = b_0(\lambda/\lambda_0)^n, \tag{A6}$$

where $\lambda_0 = 550\,\text{nm}$ is the reference wavelength and the power-law exponent is set to $n = 1$ [43]. A value of the particulate matter scattering coefficient at the reference wavelength is parameterized through the chlorophyll concentration [68]:

$$b_0 = 0.416\,\text{Chl}^{0.766}$$

Thus, all the input parameters are functions of only one input quantity—the chlorophyll concentration.

Appendix B. Scaling Factor

The scaling factor $f(\lambda, \text{SZA}, \text{Chl}, \text{Ozone}) = E_o/E_d$ derived from Hydrolight computations allows us to estimate the scalar irradiance at the ocean surface provided the planar irradiance is known from an external source. In our case, the external source is satellite-derived planar irradiance at the surface. Then we can propagate the scalar irradiance into the ocean body using Hydrolight. The Hydrolight computations are carried out for a specified angular distribution of incoming radiance at the surface, which may differ from the actual angular distribution of incoming radiance. The below results refer to the default boundary conditions of Hydrolight.

Figure A2 shows the scaling factor just above the ocean surface as a function of different input variables.

The most notable dependence of the scaling factor on input parameters is its dependence on SZA (Figure A2b). The scaling factor increases with SZA increasing up to SZA $\approx 70^\circ$. Then, the scaling factor decreases with increasing SZA. This dependence of the scaling factor on SZA for high values of SZA is similar to the so-called Umkehr effect. Such a dependence of the scaling factor on SZA is explained by a different ozone absorption of the direct and diffuse solar light as a function of SZA in the atmosphere.

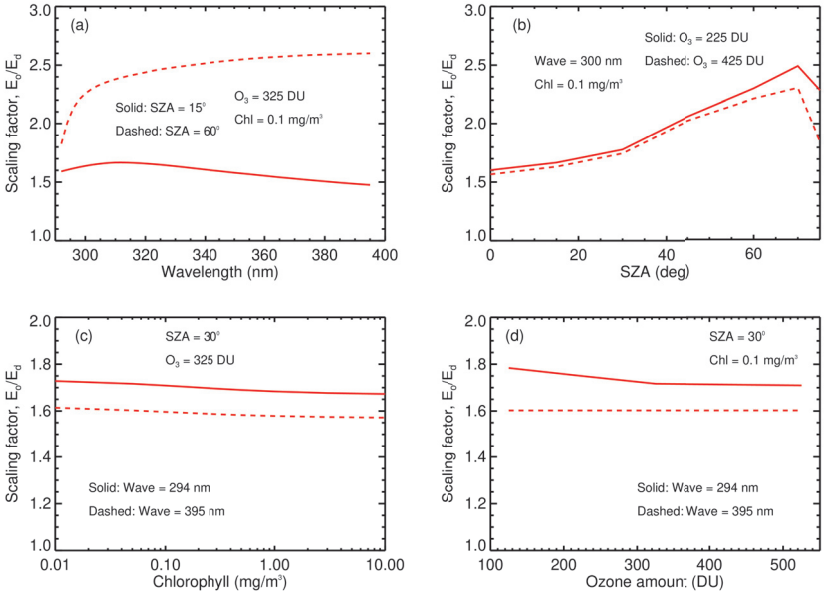


Figure A2. The scaling factor dependence on different variables; (**a**) the f dependence on wavelength for different SZAs; (**b**) the f dependence on SZA at 300 nm for different ozone amounts; (**c**) the f dependence on chlorophyll concentration for different wavelengths. (**d**) The f dependence on ozone amount for different wavelengths.

References

1. Häder, D.-P.; Williamson, C.E.; Wängberg, S.-A.; Rautio, M.; Rose, K.C.; Gao, K.; Helbling, E.W.; Sinhahand, R.P.; Worrest, R. Effects of UV radiation on aquatic ecosystems and interactions with other environmental factors. *Photochem. Photobiol. Sci.* **2015**, *14*, 108–126. [CrossRef] [PubMed]
2. Litchman, E.; Neale, P.J. UV effects on photosynthesis, growth and acclimation of an estuarine diatom and cryptomonad. *Mar. Ecol. Prog. Ser.* **2005**, *100*, 53–62. [CrossRef]
3. Cullen, J.J.; Neale, P.J.; Lesser, M.P. Biological weighting function for the inhibition of phytoplankton photosynthesis by ultraviolet radiation. *Science* **1992**, *258*, 646–650. [CrossRef] [PubMed]
4. Boucher, N.P.; Prezelin, B.B. An in situ biological weighting function for UV inhibition of phytoplankton carbon fixation in the Southern Ocean. *Mar. Ecol. Prog. Ser.* **1996**, *144*, 223–236. [CrossRef]
5. Neale, P.J.; Pritchard, A.L.; Ihnacik, R. UV effects on the primary productivity of picophytoplankton: Biological weighting functions and exposure response curves of Synechococcus. *Biogeosciences* **2014**, *11*, 2883–2895. [CrossRef]
6. Bélanger, S.; Xie, H.; Krotkov, N.; Larouche, P.; Vincent, W.F.; Babin, M. Photomineralization of terrigenous dissolved organic matter in Arctic coastal waters from 1979 to 2003: Interannual variability and implications of climate change. *Global Biogeochem. Cycles* **2006**, *20*, GB4005. [CrossRef]
7. Moran, M.A.; Zepp, E.G. Role of photoreactions in the formation of biologically labile compounds from dissolved organic matter. *Limnol. Oceanogr.* **1997**, *42*, 1307–1316. [CrossRef]
8. Vasilkov, A.P.; Krotkov, N.A. Modeling the effect of seawater optical properties on the ultraviolet radiant fluxes in the ocean. *Izv. Atmos. Ocean. Phys.* **1997**, *33*, 349–357.
9. Vasilkov, A.P.; Krotkov, N.; Herman, J.R.; McClain, C.; Arrigo, K.; Robinson, W. Global mapping of underwater UV irradiance and DNA-weighted exposures using TOMS and SeaWiFS data products. *J. Geophys. Res.* **2001**, *106*, 27205–27219. [CrossRef]
10. Vasilkov, A.; Herman, J.; Ahmad, Z.; Kahru, M.; Mitchell, B.G. Assessment of the ultraviolet radiation field in ocean waters from space-based measurements and full radiative-transfer calculations. *Appl. Opt.* **2005**, *44*, 2863–2869. [CrossRef]
11. Mobley, C.D. *Light and Water: Radiative Transfer in Natural Waters*; Academic Press: Cambridge, MA, USA, 1994; 592p.
12. Ahmad, Z.; Herman, J.R.; Vasilkov, A.; Tzortziou, M.; Mitchell, G.; Kahru, M. Seasonal variation of UV radiation in the ocean under clear and cloudy conditions. In *Ultraviolet Ground-and Space-Based Measurements, Models, and Effects III*; Slusser, J.R., Herman, J.R., Gao, W., Eds.; SPIE: Bellingham, WA, USA, 2003; pp. 63–73.
13. Fichot, C.G.; Sathyendranath, S.; Miller, W.L. SeaUV and SeaUVC: Algorithms for the retrieval of UV/visible diffuse attenuation coefficients from ocean color. *Remote Sens. Environ.* **2008**, *112*, 1584–1602. [CrossRef]

14. Smyth, T.J. Penetration of UV irradiance into the global ocean. *J. Geophys. Res.* **2011**, *116*. [CrossRef]
15. Lee, Z.; Hu, C.; Shang, A.; Du, K.; Lewis, M.; Arnone, R.; Brewin, R. Penetration of UV-visible solar radiation in the global oceans: Insights from ocean color remote sensing. *J. Geophys. Res. Oceans* **2013**, *118*, 4241–4255. 10.1002/jgrc.20308. [CrossRef]
16. Wang, Y.; Lee, Z.; Ondrusek, M.; Li, X.; Zhang, S.; Wu, J. An evaluation of remote sensing algorithms for the estimation of diffuse attenuation coefficients in the ultraviolet bands. *Opt. Express* **2022**, *30*, 6640–6655. [CrossRef] [PubMed]
17. Dinter, T.; Rozanov, V.V.; Burrows, J.P.; Bracher, A. Retrieving the availability of light in the ocean utilising spectral signatures of vibrational Raman scattering in hyper-spectral satellite measurements. *Ocean Sci.* **2015**, 11, 373–389. [CrossRef]
18. Oelker, J.; Richter, A.; Dinter, T.; Rozanov, V.V.; Burrows, J.P.; Bracher, A. Global diffuse attenuation derived from vibrational raman scattering detected in hyperspectral backscattered satellite spectra. *Opt. Express* **2019**, *27*, A829–A855. [CrossRef]
19. Oelker, J.; Losa, S.N.; Richter, A.; Bracher, A. TROPOMI-Retrieved underwater light attenuation in three spectral regions in the ultraviolet and blue. *Front. Mar. Sci.* **2022**, *9*, 296. [CrossRef]
20. Frouin, R.; Ramon, D.; Boss, E.; Jolivet, D.; Compiègne, M.; Tan, J.; Bouman, H.; Jackson, T.; Franz, B.; Platt, T.; Sathyendranath, S. Satellite radiation products for ocean biology and biogeochemistry: Needs, State-of-the-Art, Gaps, Development Priorities, and Opportunities. *Front. Mar. Sci.* **2018**, *5*, 3. [CrossRef]
21. Cetinić, I.; McClain, C.R.; Werdell, P.J. (Eds.) *PreAerosol, Clouds, and ocean Ecosystem (PACE) Mission Science Definition Team Report*; PACE Tech. Rep. NASA/TM2018-219027; NASA: Greenbelt, MD, USA, 2018; Volume 2, p 316.
22. Tanskanen, A.; Krotkov, N.; Herman, J.R.; Bhartia, P.K.; Arola, A. Surface UV irradiance from OMI. *IEEE Trans. Geosci. Remote Sens.* **2006**, *44*, 1267–1271. [CrossRef]
23. Coddington, O.M.; Richard, E.C.; Harber, D.; Pilewskie, P.; Woods, T.N.; Chance, K.; Liu, X.; Sun, K. The TSIS-1 Hybrid Solar Reference Spectrum. *Geophys. Res. Lett.* **2021**, *48*, e2020GL091709. [CrossRef]
24. Richard, E.; Harber, D.; Coddington, O.; Drake, G.; Rutkowski, J.; Triplett, M.; Pilewskie, P.; Woods, T. SI-traceable spectral irradiance radiometric characterization and absolute calibration of the TSIS-1 Spectral Irradiance Monitor (SIM). *Remote Sens.* **2020**, *12*, 1818. [CrossRef]
25. Levelt, P.F.; Joiner, J.; Tamminen, J.; Veefkind, J.P.; Bhartia, P.K.; Stein Zweers, D.C.; Duncan, B.N.; Streets, D.G.; Eskes, H.; van der A.R.; et al. The Ozone Monitoring Instrument: Overview of 14 years in space. *Atmos. Chem. Phys.* **2018**, *18*, 5699–5745. [CrossRef]
26. Levelt, P.F.; van den Oord, G.H.J.; Dobber, M.R.; Mälkki, A.; Visser, H.; de Vries, J.; Stammes, P.; Lundell, J.; Saari, H. The Ozone Monitoring Instrument. *IEEE Trans. Geosci. Remote* **2006**, *44*, 1093–1101. [CrossRef]
27. Dobber, M.R. OMI/Aura Level 1B UV Global Geolocated Earthshine Radiances (V003) [Dataset], Goddard Earth Sciences Data and Information Services Center (GES DISC). 2007. Available online: https://disc.gsfc.nasa.gov/datasets/OML1BRUG_003/summary (accessed on 30 March 2022).
28. Dobber, M.R. OMI/Aura Level 1B IRR Solar Irradiances (V003) [Dataset], Goddard Earth Sciences Data and Information Services Center (GES DISC). 2007. Available online: https://disc.gsfc.nasa.gov/datasets/OML1BIRR_003/summary (accessed on 30 March 2022).
29. Schenkeveld, V.M.E.; Jaross, G.; Marchenko, S.; Haffner, D.; Kleipool, Q.L.; Rozemeijer, N.C.; Veefkind, J.P.; Levelt, P.F. In-flight performance of the Ozone Monitoring Instrument. *Atmos. Meas. Tech.* **2017**, *10*, 1957–1986. [CrossRef] [PubMed]
30. Balis, D.; Kroon, M.; Koukouli, M.E.; Brinksma, E.J.; Labow, G.; Veefkind, J.P.; McPeters, R.D. Validation of Ozone Monitoring Instrument total ozone column measurements using Brewer and Dobson spectrophotometer ground-based observations. *J. Geophys. Res.* **2007**, *112*. [CrossRef]
31. Bhartia, P.K. OMI/Aura Ozone (O3) Total Column 1-Orbit L2 Swath 13 × 24 km V003, Greenbelt, MD, USA, Goddard Earth Sciences Data and Information Services Center (GES DISC). 2005. Available online: https://disc.gsfc.nasa.gov/datasets/OMTO3_003/summary (accessed on 30 March 2022).
32. Kleipool, Q.L.; Dobber, M.R.; de Haan, J.F.; Levelt, P.F. Earth surface reflectance climatology from 3 years of OMI data. *J. Geophys. Res.* **2008**, *113*, D18308. [CrossRef]
33. Kleipool, Q.L. OMI/Aura Surface Reflectance Climatology L3 Global Gridded 0.5 degree x 0.5 degree V3, Greenbelt, MD, USA, Goddard Earth Sciences Data and Information Services Center (GES DISC). 2010. Available online: https://disc.gsfc.nasa.gov/datasets/OMLER_003/summary (accessed on 30 March 2022).
34. Zhai, P.; Hu, Y.; Chowdhary, J.; Trepte, C.R.; Lucker, P.L.; Josset, D.B. A vector radiative transfer model for coupled atmosphere and ocean systems with a rough interface. *J. Quant. Spectr. Radiat. Trans.* **2010**, *111*, 1025–1040. [CrossRef]
35. Krotkov, N.A.; Bhartia, P.K.; Herman, J.R.; Fioletov, V.; Kerr, J. Satellite estimation of spectral surface UV irradiance in the presence of tropospheric aerosols 1. Cloud-free case. *J. Geophys. Res.* **1998**, *103*, 8779–8794. [CrossRef]
36. Krotkov, N.A.; Herman, J.R.; Bhartia, P.K.; Fioletov, V.; Ahmad, Z. Satellite estimation of spectral surface UV irradiance 2. Effects of homogeneous clouds and snow. *J. Geophys. Res.* **2001**, *106*, 11743–11760. [CrossRef]
37. Deirmendjian, D. *Electromagnetic Scattering on Spherical Polydispersions*; Elsevier: New York, NY, USA, 1969; 290p.
38. Joiner, J.; Vasilkov, A.P.; Flittner, D.E.; Gleason, J.F.; Bhartia, P.K. Retrieval of cloud pressure and oceanic chlorophyll content using Raman scattering in GOME ultraviolet spectra. *J. Geophys. Res.* **2004**, *109*, D01109. [CrossRef]
39. Stamnes, K.; Tsay, S.C.; Wiscombe, W.; Jayaweera, K. Numerically stable algorithm for discrete-ordinate-method radiative transfer in multiple scattering and emitting layered media. *Appl. Opt.* **1988**, *27*, 2502–2509. [CrossRef] [PubMed]
40. Ahmad, Z.; Fraser, R. An iterative radiative transfer code for ocean-atmosphere systems. *J. Atrnos. Sci.* **1982**, *39*, 656–665.%3C0656:AIRTCF%3E2.0.CO;2. [CrossRef]

41. Krotkov, N.A.; Herman, J.R.; Bhartia, P.K.; Seftor, C.; Arola, A.; Kaurola, J.; Taalas, P.; Vasilkov, A.P. OMI Surface UV Irradiance Algorithm. OMI Algorithm Theoretical Basis Document. Clouds, Aerosols, and Surface UV Irradiance. Available online: http://eospso.gsfc.nasa.gov/sites/default/files/atbd/ATBD-OMI-03.pdf (accessed on 30 March 2022).
42. Frouin, R.; Tan, J.; Ramon, D.; Franz, B.; Murakami, H. Estimating photosynthetically available radiation at the ocean surface from EPIC/DSCOVR data. In *Remote Sensing of the Open and Coastal Ocean and Inland Waters*; International Society for Optics and Photonics:Bellingham, WA, USA, 2018; Volume 10778, p. 1077806.
43. Morel, A. Optical modeling of the upper ocean in relation to its biogeneous matter content (Case I waters). *J. Geophys. Res.* **1988**, *93*, 10749–10768. [CrossRef]
44. Vasilkov, A.; Lyapustin, A.; Mitchell, B.G.; Huang, D. UV Reflectance of the Ocean from DSCOVR/EPIC: Comparisons with a Theoretical Model and Aura/OMI Observations. *J. Atmos. Oceanic Tech.* **2019**, *36*, 2087–2099. [CrossRef]
45. Vasilkov, A.P.; Joiner, J.; Gleason, J.; Bhartia, P.K. Ocean Raman scattering in satellite backscatter UV measurements. *Geophys. Res. Lett.* **2002** *29*, 14–18. [CrossRef]
46. Liu, C.-C.; Carder, K.L.; Miller, R.L.; Ivey, J.E. Fast and accurate model of underwater scalar irradiance. *Appl. Opt.* **2002**, *41*, 4962–4974. [CrossRef]
47. Clark, D.K.; Feinholz, M.E.; Yarbrough, M.A.; Johnson, B.C.; Brown, S.W.; Kim, Y.S.; Barnes, R.A. Overview of the radiometric calibration of MOBY. In *Earth Observing Systems VI*; International Society for Optics and Photonics: Bellingham, WA, USA, 2002; Volume 4483, pp. 64–76.
48. Setlow, R.B. The wavelengths in sunlight effective in producing skin cancer: A theoretical analysis. *Proc. Natl. Acad. Sci. USA* **1974**, *71*, 3363–3366. [CrossRef]
49. Tedetti, M.; Sempere, R.; Vasilkov, A.; Charriere, B.; Nerini, D.; Miller, W.L.; Kawamura, K.; Raimbault, P. High penetration of ultraviolet radiation in the south east Pacific waters. *Geophys. Reas. Lett.* **2007**, *34*, L12610. [CrossRef]
50. Lee, Z.; Weidemann, A.; Kindle, J.; Arnone, R.; Carder, K.L.; Davis, C. Euphotic zone depth: Its derivation and implication to ocean-color remote sensing. *J. Geophys. Res.* **2007**, *112*, C03009. [CrossRef]
51. Lee, Z.-P.; Du, K.-P.; Arnone, R. A model for the diffuse attenuation coefficient of downwelling irradiance. *J. Geophys. Res.* **2005**, *110*, C02016. [CrossRef]
52. Hu, C.; Lee Z.; Franz, B.A. Chlorophyll-a algorithms for oligotrophic oceans: A novel approach based on three-band reflectance difference. *J. Geophys. Res.* **2012**, *117*, C01011. [CrossRef]
53. NASA Goddard Space Flight Center, Ocean Ecology Laboratory, Ocean Biology Processing Group. *Moderate-Resolution Imaging Spectroradiometer (MODIS) Aqua Chlorophyll Data; 2018 Reprocessing*; NASA OB.DAAC: Greenbelt, MD, USA, 2018. [CrossRef]
54. McKinlay, A.; Diffey, B. A reference action spectrum for ultraviolet induced erythema in human skin. *CIE J.* **1987**, *6*, 17–22.
55. Fan, Y.; Li, W.; Chen, N.; Ahn, J.-H.; Park, Y.-J.; Kratzer, S.; Schroeder, T.; Ishizaka, J.; Chang, R.; Stamnes, K. A machine learning based data analysis platform for satellite ocean color sensors. *Remote Sens. Environ.* **2021**, *253*, 112236. [CrossRef]
56. Fasnacht, Z.; Joiner, J.; Haffner, D.; Qin, W.; Vasilkov A.; Castellanos, P.; Krotkov, N. Using machine learning for timely estimates of ocean color information from hyperspectral satellite measurements in the presence of clouds, aerosols, and sunglint. *Front. Remote Sens.* **2022**, *2*, 34. [CrossRef]
57. Westberry, T.K.; Boss, E.; Lee, Z. Influence of Raman scattering on ocean color inversion models. *Appl. Opt.* **2013**, *52*, 5552–5561. [CrossRef]
58. Chowdhary, J.; Zhai, P.-W.; Boss, E.; Dierssen, H.; Frouin, R.; Ibrahim, A.; Lee, Z.; Remer, L.A.; Twardowski, M.; Xu, F.; et al. Modeling atmosphere-ocean radiative transfer: A PACE mission perspective. *Front. Earth Sci.* **2019**, *7*, 100. [CrossRef]
59. Morrison, J.R.; Nelson, N.B. Seasonal cycle of phytoplankton UV absorption at the Bermuda Atlantic Time-series Study (BATS) site. *Limnol. Oceanogr.* **2004**, *49*, 215–224. [CrossRef]
60. Hedley, J.D.; Mobley, C.D. *HYDROLIGHT 6.0 ECOLIGHT 6.0 Technical Documentation*; Numerical Optics Ltd.: Tiverton, UK, 2019.
61. Vasilkov, A.; Herman, J.; Krotkov, N.A.; Kahru, M.; Mitchell, B.G.; Hsu, C. Problems in assessment of the ultraviolet penetration into natural waters from space-based measurements. *Opt. Eng.* **2002**, *41*, 3019–3027. [CrossRef]
62. Lee, Z.; Wei, J.; Voss, K.; Lewis, M.; Bricaud, A.; Huot, Y. Hyperspectral absorption coefficient of "pure" seawater in the range of 350–550 nm inverted from remote sensing reflectance. *Appl. Opt.* **2015**, 54, 546–558. [CrossRef]
63. Mannino, A.; Haffner, D.; Robinson, W.; Ahmad, Z. *Extended UV Capability on OCI for Ozone Retrieval, in PACE Technical Report Series: Ocean Color Instrument (OCI) Concept Design Studies (NASA/TM-2018-2018–219027-)*; Cetinić, I., McClain, C.R., Werdell, P.J., Eds.; NASA Goddard Space Flight Space Center Greenbelt: Prince George's County, MD, USA, 2018; Volume 7.
64. Fournier, G.; Forand, J.L. Analytic phase functions for ocean water. *Proc. SPIE* **1994**, *2258*, 194–201.
65. Pope, R.M.; Fry, E.S. Absorption spectrum (380–700 nm) of pure water. II. Integrating cavity measurements. *Appl. Opt.* **1997**, *36*, 8710–8723. [CrossRef] [PubMed]
66. Quickenden, T.I.; Irvin, J.A. The ultraviolet absorption spectrum of liquid water. *J. Chem. Phys.* **1980**, *72*, 4416–4428. [CrossRef]
67. Fry, E.S. Visible and near ultraviolet absorption spectrum of liquid water. *Appl. Opt.* **2000**, *39*, 2743–2744. [CrossRef] [PubMed]
68. Morel, A.; Maritorena, S. Bio-optical properties of oceanic waters: A reappraisal. *J. Geophys. Res.* **2001**, *106*, 7163–7180. [CrossRef]
69. Kopelevich, O.V.; Lutsarev, S.V.; Rodionov, V.V. Light spectral absorption by yellow substance of ocean water. *Oceanology* **1989**, *29*, 409–414.
70. Morel, A.; Gentili, B.; Claustre, H.; Babin, M.; Bricaud, A.; Ras, J.; Tieche, F. Optical properties of the "clearest" natural waters. *Limnol. Oceanogr.* **2007**, *52*, 217–229. [CrossRef]

MDPI AG
Grosspeteranlage 5
4052 Basel
Switzerland
Tel.: +41 61 683 77 34

MDPI Books Editorial Office
E-mail: books@mdpi.com
www.mdpi.com/books



Disclaimer/Publisher's Note: The title and front matter of this reprint are at the discretion of the Topic Editors. The publisher is not responsible for their content or any associated concerns. The statements, opinions and data contained in all individual articles are solely those of the individual Editors and contributors and not of MDPI. MDPI disclaims responsibility for any injury to people or property resulting from any ideas, methods, instructions or products referred to in the content.





Academic Open
Access Publishing

mdpi.com

ISBN 978-3-7258-1480-0